

Fifth International Symposium on Liquid Space Propulsion

R. Garcia, Compiler

Marshall Space Flight Center, Marshall Space Flight Center, Alabama

Proceedings of a conference
held in Chattanooga, Tennessee,
October 27–30, 2003

The NASA STI Program Office...in Profile

Since its founding, NASA has been dedicated to the advancement of aeronautics and space science. The NASA Scientific and Technical Information (STI) Program Office plays a key part in helping NASA maintain this important role.

The NASA STI Program Office is operated by Langley Research Center, the lead center for NASA's scientific and technical information. The NASA STI Program Office provides access to the NASA STI Database, the largest collection of aeronautical and space science STI in the world. The Program Office is also NASA's institutional mechanism for disseminating the results of its research and development activities. These results are published by NASA in the NASA STI Report Series, which includes the following report types:

- **TECHNICAL PUBLICATION.** Reports of completed research or a major significant phase of research that present the results of NASA programs and include extensive data or theoretical analysis. Includes compilations of significant scientific and technical data and information deemed to be of continuing reference value. NASA's counterpart of peer-reviewed formal professional papers but has less stringent limitations on manuscript length and extent of graphic presentations.
- **TECHNICAL MEMORANDUM.** Scientific and technical findings that are preliminary or of specialized interest, e.g., quick release reports, working papers, and bibliographies that contain minimal annotation. Does not contain extensive analysis.
- **CONTRACTOR REPORT.** Scientific and technical findings by NASA-sponsored contractors and grantees.

- **CONFERENCE PUBLICATION.** Collected papers from scientific and technical conferences, symposia, seminars, or other meetings sponsored or cosponsored by NASA.
- **SPECIAL PUBLICATION.** Scientific, technical, or historical information from NASA programs, projects, and mission, often concerned with subjects having substantial public interest.
- **TECHNICAL TRANSLATION.** English-language translations of foreign scientific and technical material pertinent to NASA's mission.

Specialized services that complement the STI Program Office's diverse offerings include creating custom thesauri, building customized databases, organizing and publishing research results...even providing videos.

For more information about the NASA STI Program Office, see the following:

- Access the NASA STI Program Home Page at <http://www.sti.nasa.gov>
- E-mail your question via the Internet to help@sti.nasa.gov
- Fax your question to the NASA Access Help Desk at 301-621-0134
- Telephone the NASA Access Help Desk at 301-621-0390
- Write to:
NASA Access Help Desk
NASA Center for AeroSpace Information
7121 Standard Drive
Hanover, MD 21076-1320
301-621-0390



Fifth International Symposium on Liquid Space Propulsion

R. Garcia, Compiler

Marshall Space Flight Center, Marshall Space Flight Center, Alabama

Proceedings of a conference
held in Chattanooga, Tennessee,
October 27–30, 2003

National Aeronautics and
Space Administration

Marshall Space Flight Center • MSFC, Alabama 35812

Acknowledgments

The symposium could not have occurred without the strong support, leadership, and personal involvement of the executive committee: Bob Sackheim, Dr. Koschel, Paul Kuentzman, Jue Wang, Keiichi Hasegawa, and In-Seuck Jeung.

The strong technical content of the symposium is a result of the hard work and commitment of the following technical committee members: Vigor Yang, Mohammed Habiballah, Oskar Haidn, Chuck Merkle, Bill Anderson, Doug Talley, Robert Garcia, Joe Ruf, Mike Popp, and Stephen Richardson.

There were many who supported the organization and logistics of the meeting. In particular, Vanessa Suggs, Bennie Jacks, and Wayne Bordelon merit special acknowledgment in this regard. And finally, the executive committee wishes to thank the sponsors that were so helpful in making the symposium a great success.

Available from:

NASA Center for AeroSpace Information
7121 Standard Drive
Hanover, MD 21076-1320
301-621-0390

National Technical Information Service
5285 Port Royal Road
Springfield, VA 22161
703-487-4650

INTRODUCTION

The International Liquid Space Propulsion Symposia provides the principal forum for all aspects of liquid rocket propulsion. The aim of the symposium series is to gather international experts in the field of liquid rocket engines on a regular basis for presentations and discussions of the current status of research and development. Besides an exchange of information about future trends, it also fosters existing cooperations and acts as a nucleus to establish networks to enhance international scientific collaboration in the liquid rocket propulsion area.

The Fifth International Symposium on Liquid Space Propulsion, held October 27–30, 2003, in Chattanooga, TN, was focused on long-life combustion devices technologies for liquid space propulsion, including all aspects of analysis, modeling, and design. In addition to an introductory topical session on current national programs given by representatives from agencies and industries from across the world, invited speakers presented recent technical work of particular relevance in the following main categories:

- **Component-Level Processes**

Ignition, chamber life, injector life, nozzle loads

- **Engine Cycle and Material Considerations**

Transient load issues, oxygen-rich environments, hydrocarbon environments, material limitations, hydrogen environment issues, injector considerations

- **Design Environments—Predictions**

Damage assessment, CFD, validation of codes

- **Design Environments—Measurements**

Data requirements, advance diagnostics, scaling considerations

- **System-Level Effects**

Component interactions, in-space propulsion, tri-propellant engines.

Use of this CD requires Adobe® Acrobat® Reader 4.0. To access the Fifth International Symposium on Liquid Space Propulsion documents, double-click the Start.pdf file. If you do not have access to or are unfamiliar with Acrobat® Reader, please open the Readme file on the CD for more information and help installing the program on Macintosh, Windows, or Unix computers.

TABLE OF CONTENTS

Welcome and Symposium Overview

Symposium Overview

Bob Sackheim, NASA MSFC, U.S.A.

Delivering the Future: NASA's Integrated Space Transportation Plan

John Rogacki, NASA Headquarters, U.S.A.

Session I: Welcome and International Perspectives

Future Directions for Space Transportation and Propulsion at NASA

Bob Sackheim, NASA MSFC, U.S.A.

European Space Propulsion Perspective

Alain Souchier, Snecma, France

Overview of Japanese Research and Development Program on Liquid Rocket Engine Combustor

Keiichi Hasegawa, National Aerospace Laboratory, Japan

Development of KSR-III Liquid Propulsion System

Yeon-Seok Chae, Director, Korea Aerospace Research Institute, Korea

(Paper also available)

Session II: System-Level Effects

Combustion Device Failures During Space Shuttle Main Engine Development

Jan Monk (retired) and Otto Goetz (retired), NASA MSFC, U.S.A.

Operational Issues in the Development of a Cost-Effective Reusable Lox/LH₂ Engine

Rick Ballard, NASA MSFC, U.S.A.

(Paper also available)

Lifetime Issues for In-Space Propulsion Systems

Gordon Dressler, Northrop Grumman, U.S.A.

Research Achievements on Long-Life Thrust Chambers at NAL/KPL

Akinaga Kumakawa, National Aerospace Laboratory, Japan

(Paper also available)

Lox/Kerosene Oxygen-Rich Staged Combustion Rocket Engine Design and Life Issues

Feliks Y. Chelkis, NPO Energomash, Russia

(Paper also available)

History of Rocket Propulsion at Rocketdyne

Steve Fisher, Boeing-Rocketdyne Propulsion and Power, U.S.A.

Session III: Component-Level Processes

Transient Mathematical Modeling for Liquid Rocket Engine Systems: Methods, Capabilities, and Experience

Bill Greene, David C. Seymour (retired), Michael A. Martin, and Huy H. Nguyen, NASA MSFC, U.S.A.

(Paper also available)

Experimental Investigation and Modeling of the Ignition Transient of a Coaxial H₂/O₂ Injector

Michael Oswald, DLR, Germany, and Mohammed Habiballah, ONERA, France

(Paper also available)

Cooling and Life Issues for Long Life Combustion Chambers

Mike Popp, Pratt and Whitney, U.S.A.

Experimental Results for an Annular Aerospike With Differential Throttling

Joe Ruf and David McDaniels, NASA MSFC, U.S.A.

Session IV: Material Considerations

Material Requirements and Limitations for Liquid Rocket Engines

Genevieve Inglebert, ISMCM-CESTI (LISMMA Groupe Tribologie), France

(Paper also available)

Materials Issues Arising From Transient and Unsteady Loads in Combustion Devices

Thomas Farris, Purdue University, U.S.A.

Damage Assessment of Combustion Devices

Peter J. Bonacuse, NASA Glenn Research Center, U.S.A.

(Paper also available)

Advances in High-Temperature (Viscoelastoplastic) Material Modeling for Thermal Structural Analysis

Steve Arnold, NASA Glenn Research Center, U.S.A.

Session V: Design Environments—Predictions

Using CFD as a Rocket Injector Design Tool: Recent Progress at Marshall Space Flight Center

Kevin Tucker, NASA MSFC, U.S.A.

(Paper also available)

CFD Code Validation for Space Propulsion Applications

Francois Vuillot, Mohammed Habiballah, and Dominique Scherrer, ONERA, France

(Paper also available)

Liquid Propellant Injection Mixing and Combustion at Supercritical Conditions

Vigor Yang, Pennsylvania State University, U.S.A.

Session VI: Injector Design Technology

Injector Issues With Different Propellant Combinations

Dietrich Haesler, EADS, Germany

(Paper also available)

Injectors for Long-Life Combustion Devices

Vladimir Bazarov, Moscow International University of Engineering, Russia

(Paper also available)

Gas-Centered Swirl Coaxial Liquid Injector Evaluations

A.K. Cohn, AFRL, U.S.A.

(Paper also available)

Session VII: Design Environments—Measurements

Required Data for Code Validation

Richard Farmer, University of Nevada, U.S.A., and Robert Santoro, Pennsylvania State University, U.S.A.

(Paper also available)

Subscale Test Methods for Combustion Devices

Bill Anderson, Purdue University, U.S.A.

Investigations of Subcritical and Transcritical Cryogenic Combustion Using Imaging and Laser Techniques

Sebastien Candel, Ecole Centrale de Paris, France

(Paper only)

Understanding Injection Into High-Pressure Supercritical Environments

Doug Tally, AFRL, U.S.A. and Wolfgang Mayer, DLR, Germany

Subscale Testing and Design Issues of Injectors

Youngbin Yoon and In-Seuck Jeung, Seoul National University, Seoul Korea
(Paper only)



Fifth International Symposium on Liquid Space Propulsion



Symposium Overview

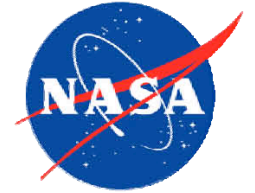
Robert L. Sackheim

Executive Chair

October 27, 2003



Fifth International Symposium on Liquid Space Propulsion

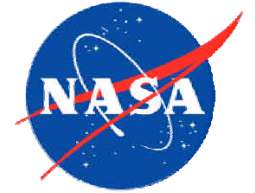


Purpose:

- Provide principal international forum for all aspects of liquid space propulsion
- Gather international experts to discuss current research and development activities in the field of liquid space propulsion
- Foster international technical collaboration and networking in the area of liquid space propulsion



Fifth International Symposium on Liquid Space Propulsion

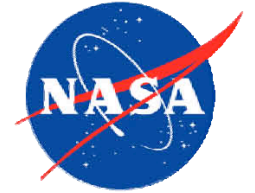


Approach:

- Meet every two to three years with rotation to different host country
- Organized by executive and technical committees
- Expert presentations and discussions, exhibits, and panel discussions



Fifth International Symposium on Liquid Space Propulsion

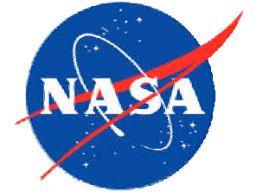


Executive Committee:

- Bob Sackheim
- Keiichi Hasegawa
- In-Seuck Jeung
- Wolfgang Koschel
- Alexander Kuznetsov
- Paul Kuentzmann
- Jue Wang



Fifth International Symposium on Liquid Space Propulsion

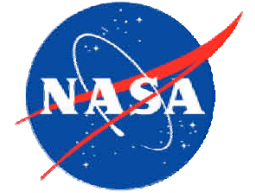


Technical Committee:

- Robert Garcia
- Bill Anderson
- Mohammed Habiballah
- Oskar Haidn
- Chuck Merkle
- Mike Popp
- Joe Ruf
- Doug Talley
- Vigor Yang



Fifth International Symposium on Liquid Space Propulsion

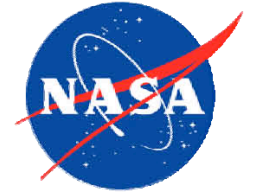


Organizing Committee:

- Vanessa Suggs
- Wayne Bordelon
- Robert Garcia
- Bennie Jacks

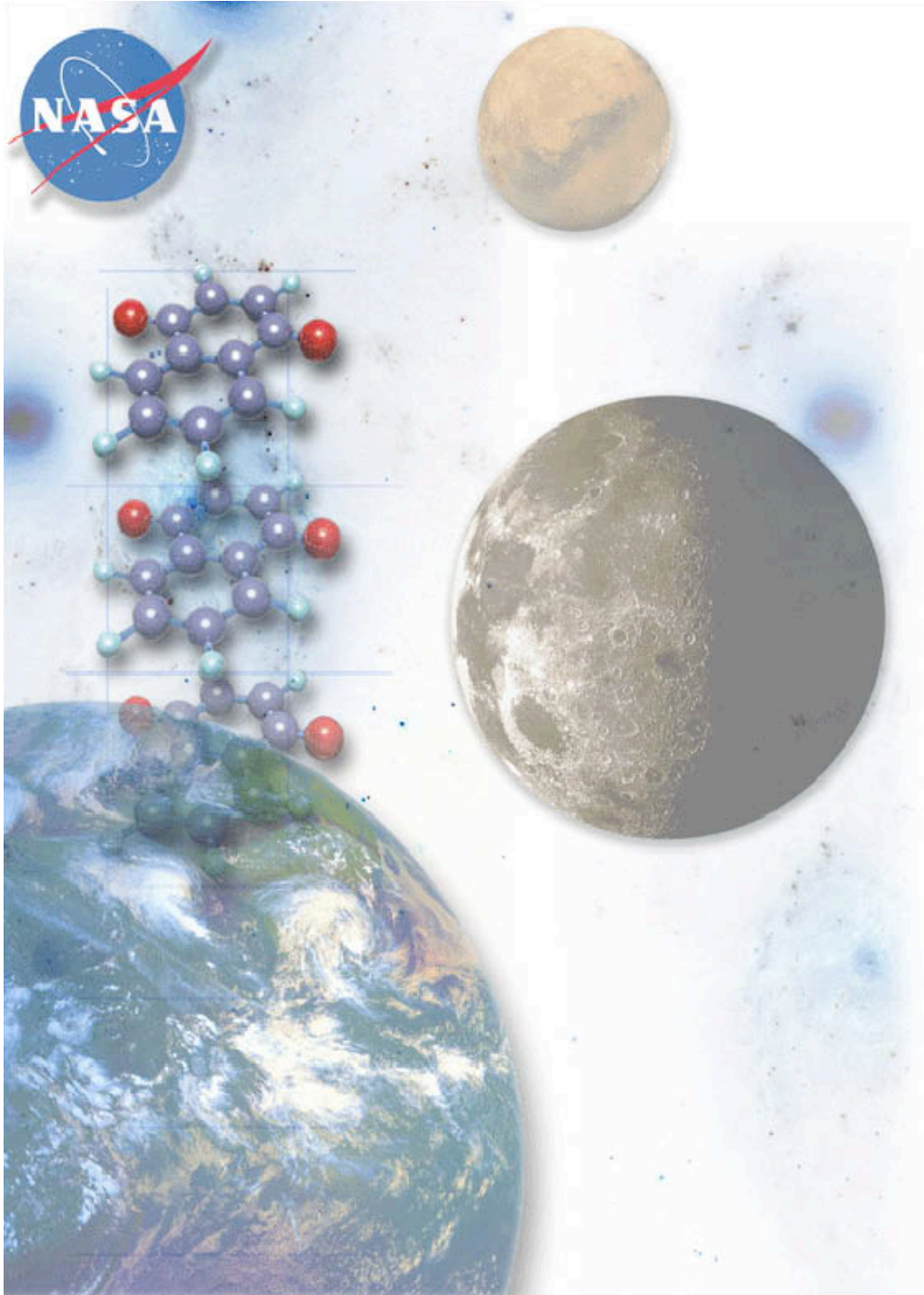


Fifth International Symposium on Liquid Space Propulsion



Overview:

- Theme: Life-life Combustion Devices Technology
- Technical Sessions:
 - **International Perspectives**
 - **System Level Effects**
 - **Component Level Processes**
 - **Material Considerations**
 - **Design Environments -- Predictions**
 - **Injector Design Technology**
 - **Design Environments -- Measurements**
- Panel Discussion: Views on future research and development needs and Symposium observations
- Aquarium Welcome and Southern Belle Riverboat Recognition Banquet evening events



Delivering the
Future:

NASA'S Integrated Space Transportation Plan

Dr. Row Rogacki
Office of Aerospace
Technology

Space Exploration



“This cause of exploration and discovery is not an option we choose; it is a desire written in the human heart”

George W. Bush, Feb. 4, 2003



www.nasa.gov

The NASA Vision

To improve life here,
To extend life to there,
To find life beyond.

The NASA Mission

To understand and protect our home planet,
To explore the universe and search for life,
To inspire the next generation of explorers
... as only NASA can.



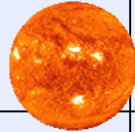

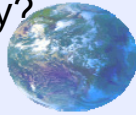

Forging New Frontiers: Space Exploration Requires ...

- **Technology** -- the enabling capabilities
- **Scientific Research Agenda** -- a purposeful objective
- **Engineering** -- the application of required technologies
- **Human Judgment** -- the ability to assess and adapt to a complex situation, balance risk and reward, decide to abort or continue -- in time critical situations

We have equipment today that incorporates “artificial intelligence” -- but there is no such thing as “artificial wisdom.”



Science Drivers Determine Destinations (Selected Examples)

	Science Questions	Pursuits	Activities	Destinations
How did we get here?	<ul style="list-style-type: none"> How did the Solar System evolve? 	<ul style="list-style-type: none"> History of major Solar System events 	<ul style="list-style-type: none"> Planetary sample analysis: absolute age determination “calibrating the clocks” 	<ul style="list-style-type: none"> Asteroids Moon Mars Venus
	<ul style="list-style-type: none"> How do humans adapt to space? 	<ul style="list-style-type: none"> Effects of deep space on cells 	<ul style="list-style-type: none"> Measurement of genomic responses to radiation 	<ul style="list-style-type: none"> Beyond Van Allen belts
Where are we going?	<ul style="list-style-type: none"> What is Earth’s sustainability and habitability? 	<ul style="list-style-type: none"> Impact of human and natural events upon Earth 	<ul style="list-style-type: none"> Measurement of Earth’s vital signs “taking the pulse” 	<ul style="list-style-type: none"> Earth orbits Libration points
Are we alone?	<ul style="list-style-type: none"> Is there Life beyond the planet of origin? 	<ul style="list-style-type: none"> Origin of life in the Solar System Origin of life in the Universe 	<ul style="list-style-type: none"> Detection of bio-markers and hospitable environments 	<ul style="list-style-type: none"> Cometary nuclei Europa Libration points Mars Titan



Robust Exploration Strategy

Traditional Approach: A Giant Leap (Apollo)



New Strategy: Stepping Stones and Flexible Building Blocks

- Cold War competition set goals, National Security justified the investment
- Singular focus on the Moon
- Humans in space an end unto itself
- Robotic exploration secondary to crewed missions
- Rigid timeframe for completion with unlimited resources
- Technologies are destination- and system-specific
- Inspirational outreach and education secondary to programs

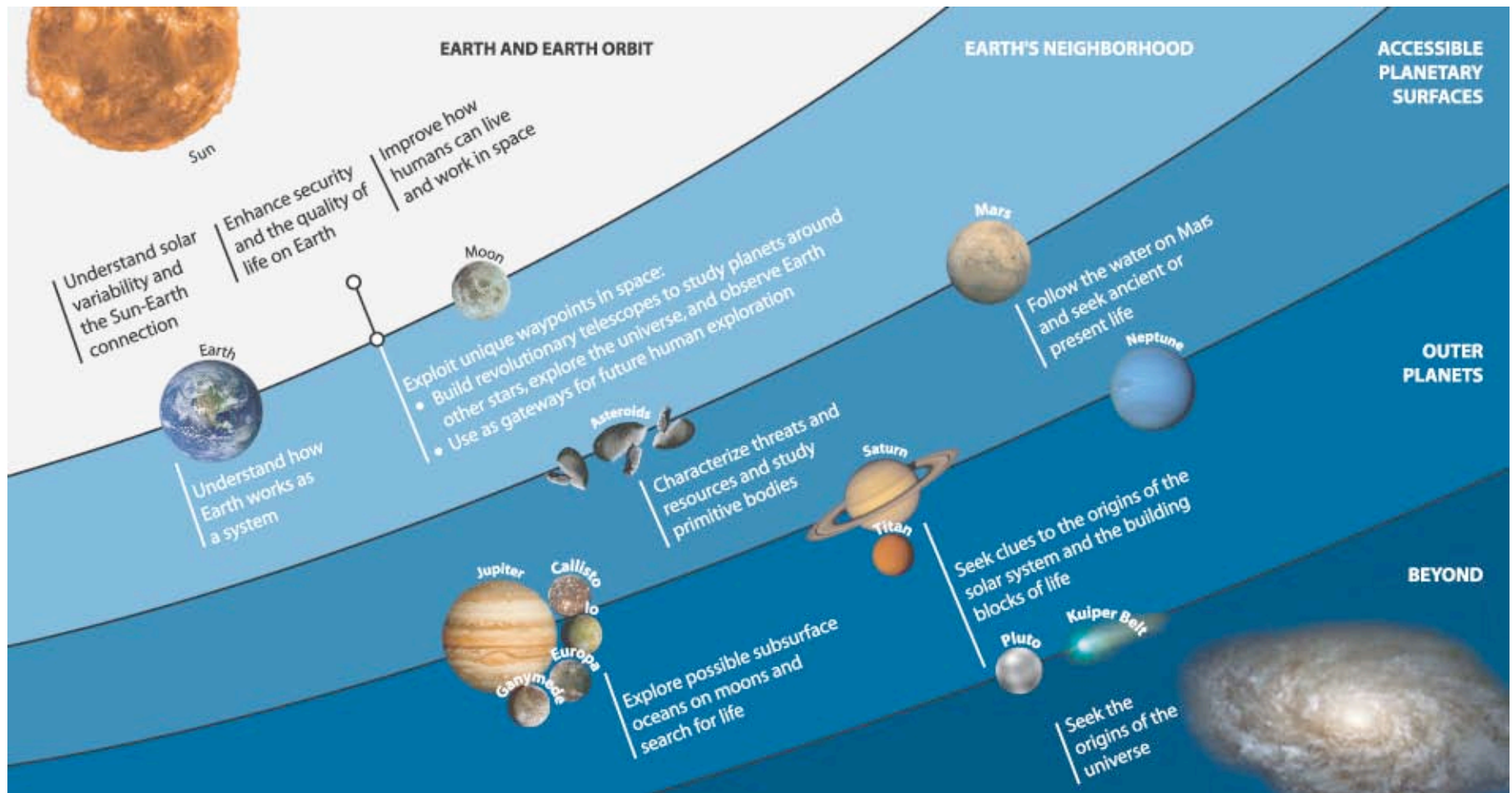
- NASA Vision and Mission drive goals and must justify investment
- Robust and flexible capability to visit several potential destinations
- Human presence is a means to enable scientific discovery
- Integrate/optimize human-robotic mix to maximize discovery
- Timeframe paced by capabilities and affordability
- Key technologies enable multiple, flexible capabilities
- Inspiration and educational outreach integral to programs

In today's environment, this approach to exploration is high-risk with limited vision beyond demonstrating a technology capability

This approach is robust and flexible, driven by discovery, and firmly set in the context of national priorities



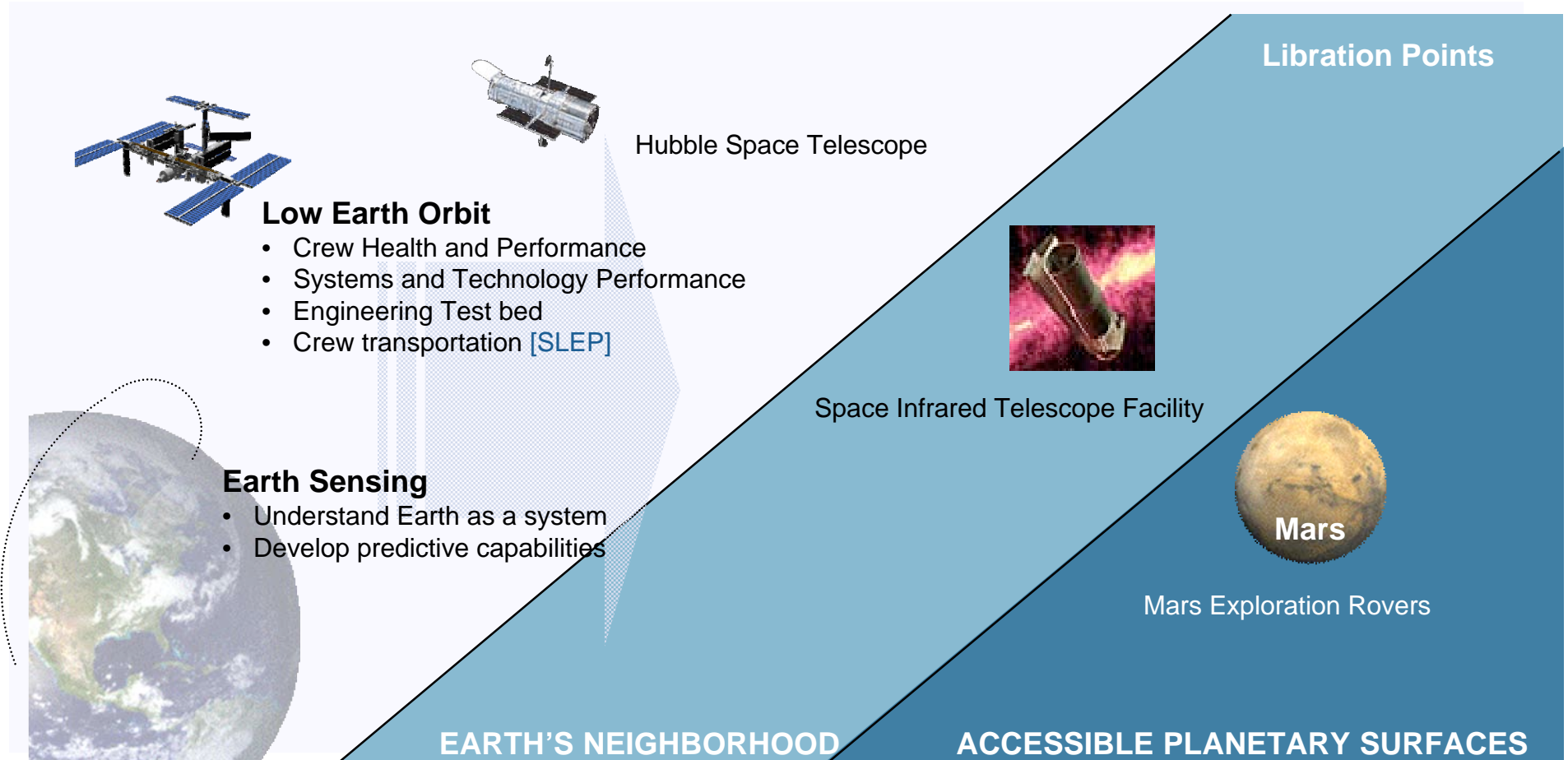
Stepping Stone Strategy





Stepping Stone Approach

Current Capabilities





Stepping Stone Approach

Near-term Next Steps for Human and Robotic Exploration

Key Investments

- Transformational Space Infrastructures
- Sustainable Human Presence
- Revolutionary Robotics

Low Earth Orbit

- Crew Health and Performance
- Systems and Technology Performance
- Engineering Test bed
- Crew transportation [OSP]
- Heavy Lift [NGLT]
- Cargo



Earth Sensing

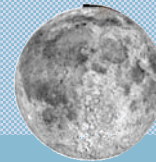
- Understand Earth as a system
- Develop predictive capabilities



High Earth Orbit/High Inclination (above the Van Allen Belts)



- Assembly, Maintenance, and Servicing
- Initial Deep Space Crew Transfer



Moon (14 day + missions)

- Surface Systems
- Operations
- Resource Utilization
- High Power Systems

Libration Points (60-100 day missions)



- Breakthrough Science Capabilities
- Deep Space Systems Development

EARTH'S NEIGHBORHOOD

ACCESSIBLE PLANETARY SURFACES

Potential Sites for Operations Above Low Earth Orbit



Stepping Stone Approach

Far-Term Next Steps for Human and Robotic Exploration

Key Investments

- Transformational Space Infrastructures
- Sustainable Human Presence
- Revolutionary Robotics

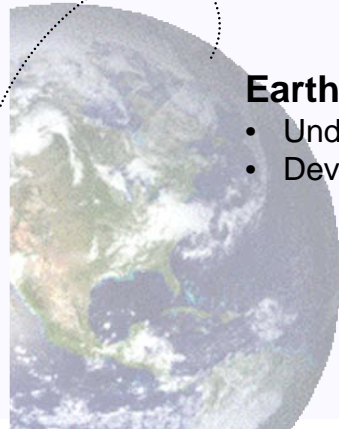
Low Earth Orbit

- Crew Health and Performance
- Systems and Technology Performance
- Engineering Test bed
- Crew transportation [OSP]
- Heavy Lift [NGLT]
- Cargo



Earth Sensing

- Understand Earth as a system
- Develop predictive capabilities



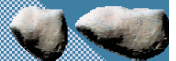
High Earth Orbit/High Inclination (above the Van Allen Belts)

- Assembly, Maintenance, and Servicing
- Initial Deep Space Crew Transfer

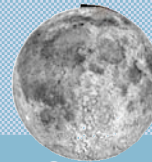
Libration Points (60-90 day missions)

- Breakthrough Science Capabilities
- Deep Space Systems Development

Asteroids



Moon (14 day + missions)



- Surface Systems
- Operations
- Resource Utilization
- High Power Systems



Mars (365 day + missions)

- Explore a New World
- Search for Life
- Resource Utilization
- High Power Systems

EARTH'S NEIGHBORHOOD

ACCESSIBLE PLANETARY SURFACES

Potential Sites for Operations Above Low Earth Orbit



Key Technology Challenges

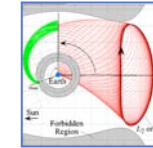
- Space Transportation
 - **Safe, fast, and efficient**
- Affordable, Abundant Power
 - **Solar and nuclear**
- Crew Health and Safety
 - **Counter measures and medical autonomy**
- Optimized Robotic and Human Operations
 - **Dramatically higher productivity; on-site intelligence**
- Space Systems Performance
 - **Advanced materials, low-mass, self-healing, self-assembly, self-sufficiency...**



RLV



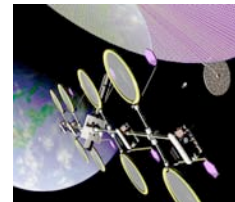
NEP



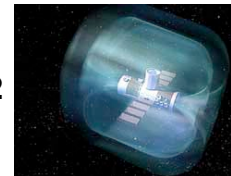
Invariant Manifolds



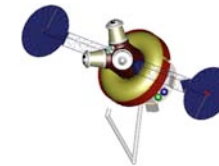
Aerobraking



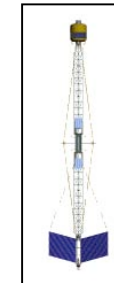
Space Solar Power



M2P2



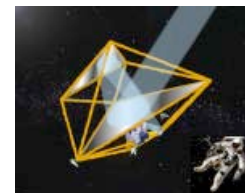
L₁ Outpost



Artificial Gravity



Robonaut



Gossamer Telescopes



Nanotube Space Elevator



Strategic Building Block Investments: High-Leverage, Broadly Enabling Capabilities

Technological Barriers

Power:

Providing ample power for propulsion and science

Transportation:

Providing safe, reliable and economical transportation to and from space and throughout the solar system

Human Capabilities:

Understanding and overcoming human limitations in space

Communications:

Providing efficient data transfer across the solar system

FY 2003 Request

Nuclear Systems Initiative

- Greatly increased power for space science and exploration

Integrated Space Transportation Plan

- Orbital Space Plane
- Extended Shuttle Operations
- Next Generation Launch Systems

In-Space Propulsion Program

- Efficient Solar System Transportation

Space Station Restructuring

- Research Priority Focused
- Management Reforms
- Sound Financial Base

Bioastronautics Program

- Roadmap to address human limitations

FY 2004 Request

Project Prometheus

- Nuclear power and propulsion for revolutionary science and orbital capabilities
- First mission to Jupiter's Moons

Human Research Initiative

- Accelerate research to expand capabilities
- Enable 100-plus day missions beyond low-Earth orbit

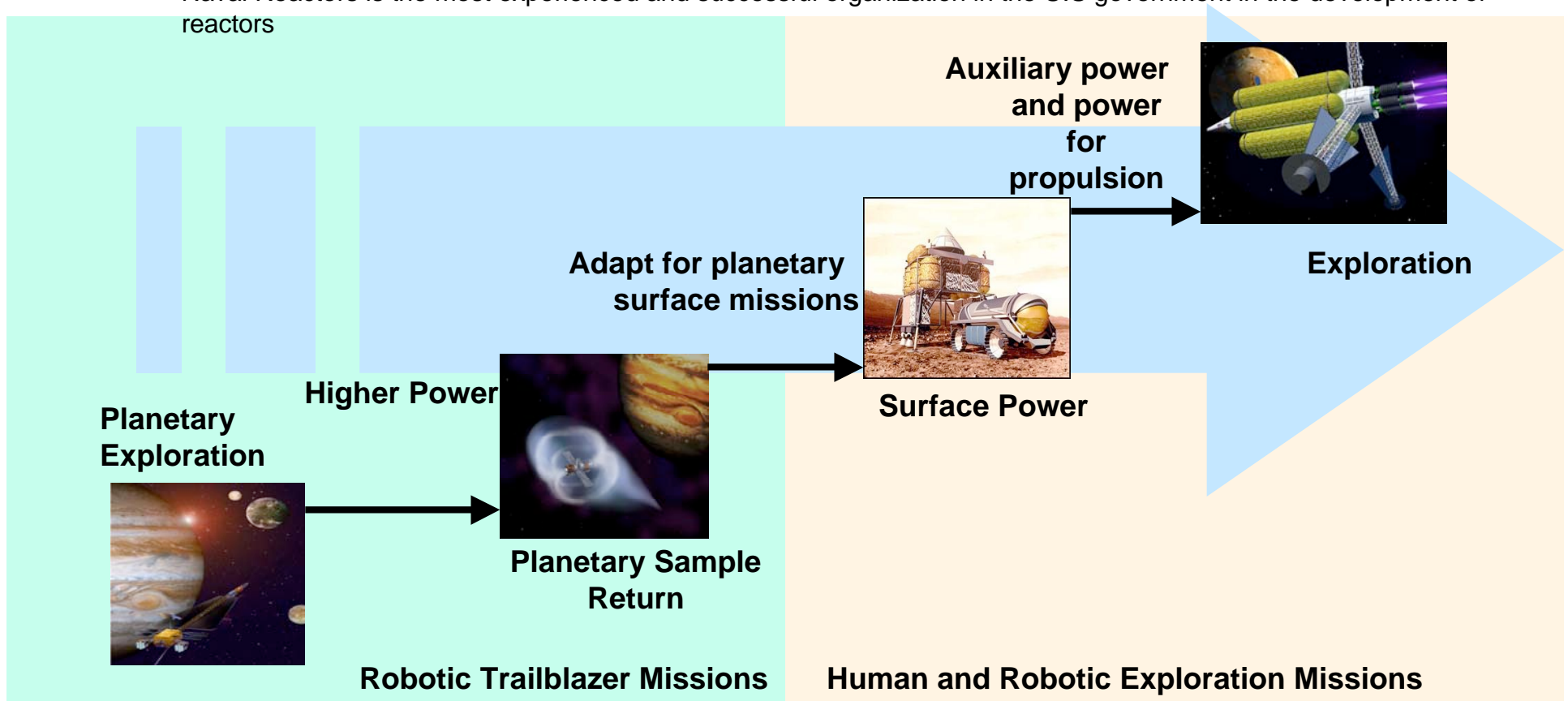
Optical Communications

- Vastly improve communication to transform science capability
- First demonstration from Mars



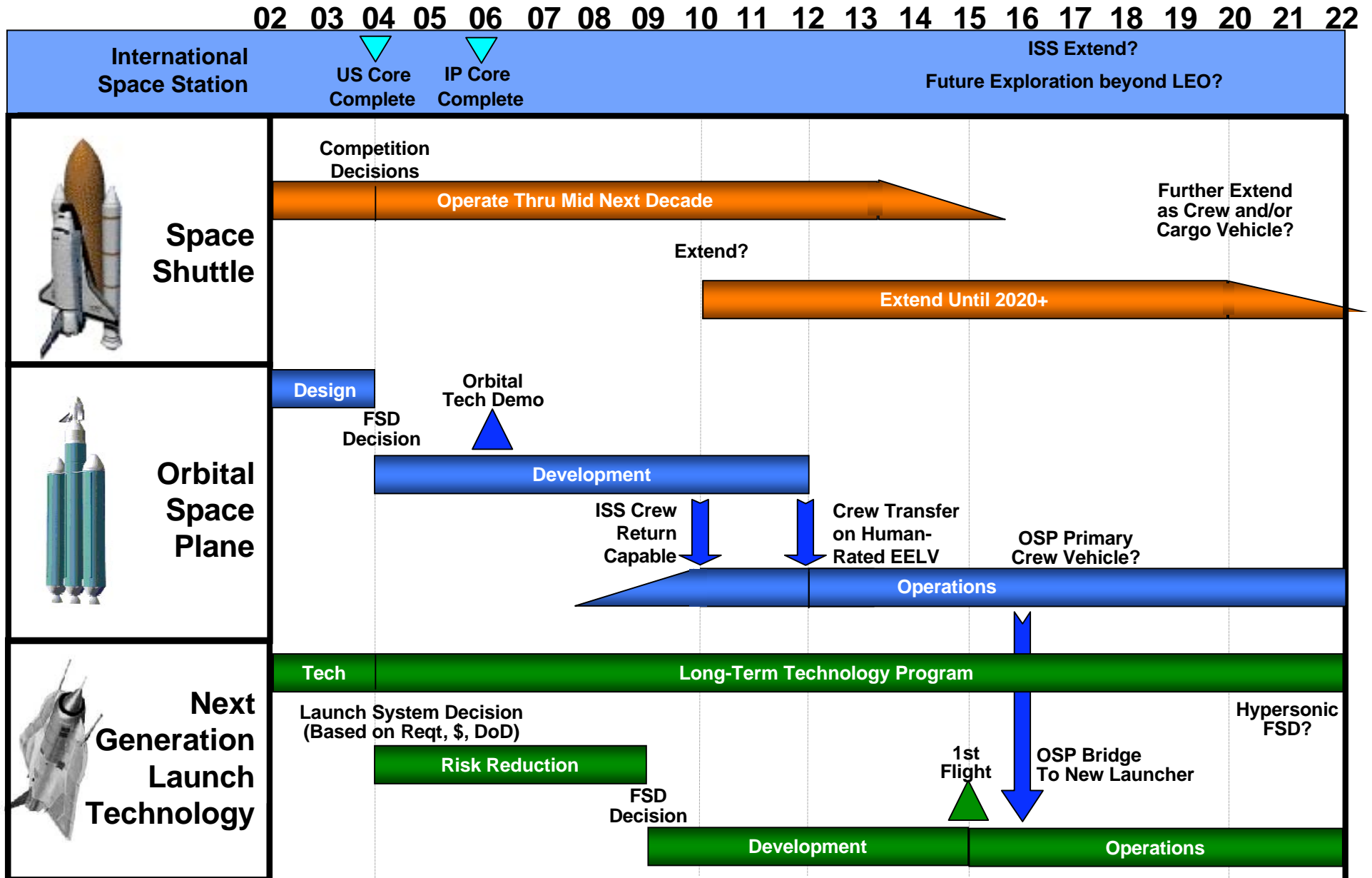
Enabling Knowledge and Technology: Power and Propulsion

- More capable science missions to the outer planets (kW)
- Surface systems for future human/robotic missions (kW)
- Electric or thermal propulsion for human/robotic missions (MW)
- The Vice President endorsed the cooperative venture of DOE/Naval Reactors to NASA's Project Prometheus to develop space reactors
 - Decision supports the high priority placed on Project Prometheus in the President's FY04 budget
 - Naval Reactors is the most experienced and successful organization in the U.S government in the development of reactors





Integrated Space Transportation Plan



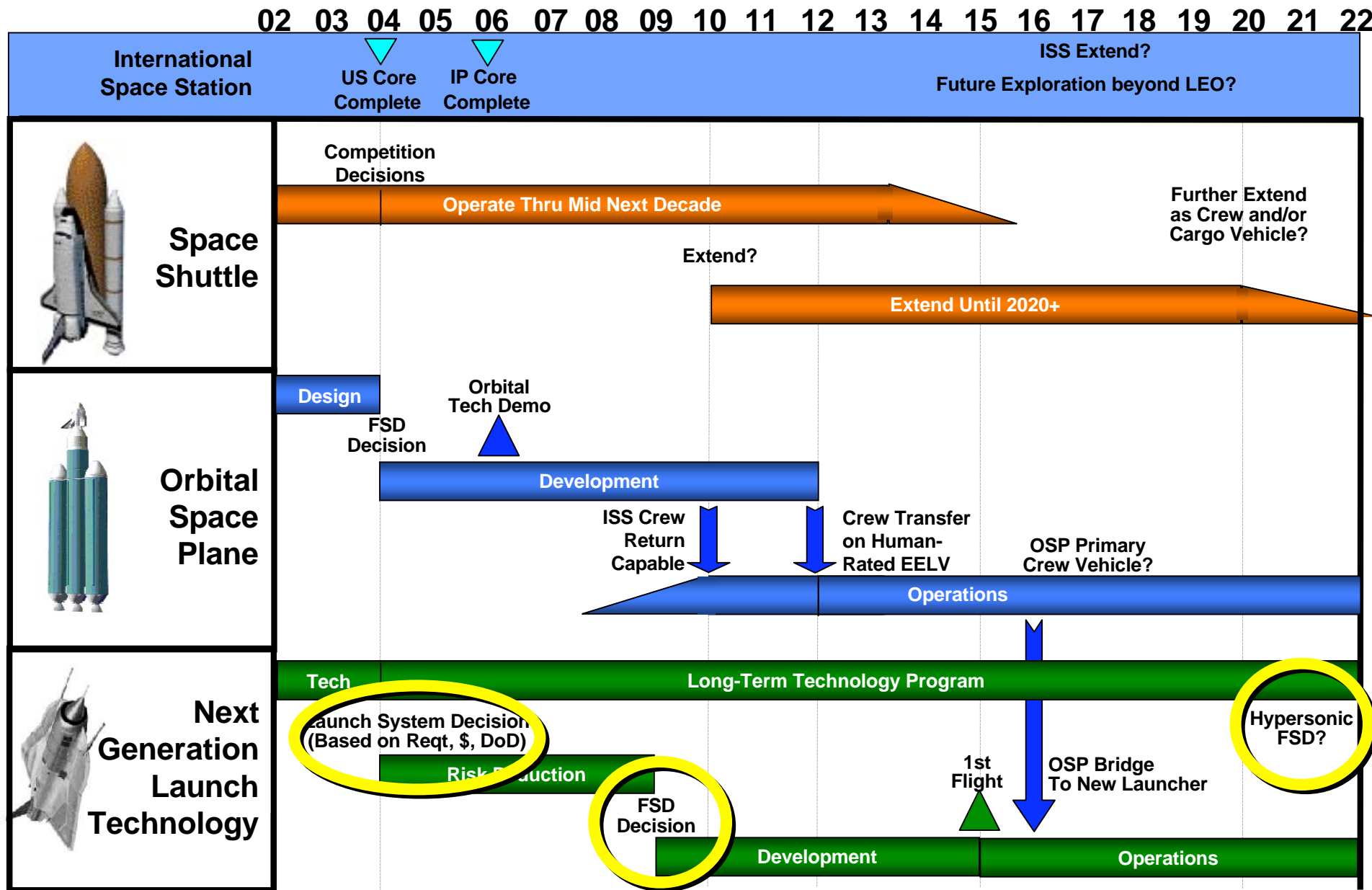


Next Generation Launch Technology Program Overview

- Technology program addresses critical space access needs of cost, operability, safety, and reliability, technology areas include:
 - Propulsion
 - Durable Structures
 - Operations
- Conduct in-depth trade studies to steer overall program direction to meet evolving customer requirements
- Enable human exploration beyond LEO for Earth Neighborhood missions with focused effort toward – 40 mT class launch vehicle
- Full Scale Development for heavy lift launch vehicle decision planned for in 2008



Integrated Space Transportation Plan

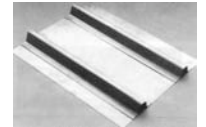




Significant NGLT Products

Near- and Mid-term

- **Hydrocarbon Engine Prototype and Supporting Technologies**
 - Higher reliability and operability than current state of the art
 - NASA launch vehicles (Shuttle Derived or Exploration) will require Hydrocarbon first stage propulsion
 - Current Hydrocarbon engines represent 15 - 40 year-old foreign technology
 - Funding phased for technology transition in 2008 - Potential IOC in 2015
- **Non-Toxic Auxiliary Propulsion**
 - Lower operations cost, speed up turnaround time
 - Major operations driver, phased for transition in 2008 - Potential IOC in 2015
- **Vehicle Systems Ground Technologies**
 - Lower cost through more robust vehicle systems
 - Integrated tanks and newer airframe materials lead to higher performance, lower cost systems
 - Airframe and Subsystem Component, and Space-Based Range Technologies
 - Partial funding to support to near and mid objectives



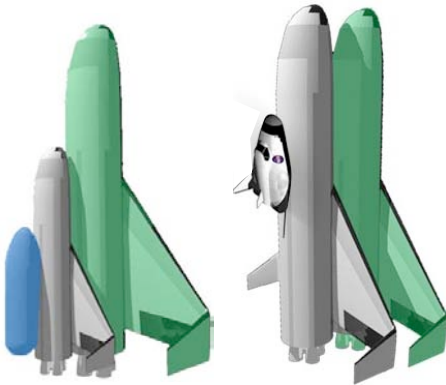
Long-term

- **Airbreathing Propulsion Ground Demonstrators & Supporting Technologies**
 - Mach 4 Turbine Engine
 - High temperature materials, sensors and components
 - *Rocket-Based Combined Cycle content deferred to future flight demonstrator options*
- **Scramjet Flight Demonstrators**
 - X-43C Hydrocarbon Scramjet (Joint with DoD)
 - Supports time critical long term objectives





LOX/RP Engine Prototype RFP



Common Booster
NASA / USAF RLVs



Heavy Lift Booster
40mT - 80mT
Expendable/Partially
Reusable/Common Booster Options



1Mlb Class
LOX/RP Engine



Potential EELV
U.S. Booster Engine
6000lb payload gain



Shuttle
Liquid Booster Upgrade



Next Generation Launch Technologies

Long Term Activities – Hypersonics

- **Joint program with DOD as part of the National Aerospace Initiative (NAI)**
- **Air-breathing propulsion ground demonstrators and supporting technologies**
 - Mach 4 Turbine Engine
 - High temperature materials, sensors and components
- **Scramjet flight demonstrators**
 - X-43C Hydrocarbon Scramjet (Mach 5-7)
 - Supports time critical long term objectives



Heavy Lift Launch Vehicle

- Minimize the number of launches required for Earth Neighborhood Missions and the number of elements while keeping the launch package mass as low as reasonable
- Current studies show the mass in LEO (IMLEO) required to land people on the Moon and return them to Earth ranges between 120 - 220 mT
- Most architecture elements developed in Earth's neighborhood studies have an initial launch mass between 30 – 50 mT
 - Earth and Lunar orbital fuel storage depots
 - Exploration transfer vehicle with high-energy transfer stage
 - Fueled Lunar lander vehicle
- Launch vehicle payload capability between approx. 40 mT represents a balance between the desire to minimize # of launches and # of elements while minimizing launch vehicle size
- Approx. 40 mT launch vehicle may also offer a growth path to the larger launchers required for Mars exploration



Heavy Lift Launch Capability Needs

- Provide the capability to Launch a 40 Metric Ton payload to Low Earth Orbit by 2015
 - 407km 28.5 deg. Circular
 - Volume - 6.5 meters in diameter x 15 meters in length
 - LOV Target- 0.998 Probability of Survival per Launch
 - If Human-rated, LOC Target– 0.9995 Probability of Survival per Launch
- Trade Study Criteria for Level I Requirements and System Solution
 - Reliability, Safety, and Cost
 - For the Exploration mission alone
 - Across all NASA missions
 - Includes leverage opportunity with the DoD
 - Schedule and technical risk



Space Transportation Summary

- **Space Station Assembly**
 - Complete assemble of the International Space Station by 2010
- **Space Station Utilization**
 - Determine if recertification of the Space Shuttle for extended life should be performed in CY 2010
 - Complete development of the Orbital Space Plane to provide safe and efficient transportation of Crew to and from the International Space Station
- **Exploration**
 - Develop transportation systems required to meet exploration objectives
 - Complete the NGLT derived 40 mT Launcher to provide high reliable low cost access to space for exploration class payloads



Summary: Committing to a New Course in Space

- **Fundamental U.S. national interest at stake in forging the space frontier**
 - Enriching our understanding of our place in the Universe
 - Setting an example for Americans and for all humanity
 - Pursuing answers to some of the most fundamental questions
 - Improving life here at home
- **Long-term Vision: To Enable Human Exploration Beyond Low Earth Orbit**
 - Near, mid and far-term opportunities identified
 - Transformational approach
- **Enabling Knowledge and Technology**
 - Crew health and systems performance requires ISS research
 - Transportation performance requires Orbital Space Plane and Next Generation Launch Technology
 - Power and propulsion investments create an important foundation for future exploration missions

A bold agenda for civil space leadership

Great Nations do Great Things

“I believe that you must spend political capital, or it withers and dies. Now is the time to spend that capital on a bold agenda...the need for a rousing call to make the most of every moment, discard reservations, throw caution to the wind, rise to the challenge”

George W. Bush



BACKUP SLIDES



Orbital Space Plane

The Orbital Space Plane (OSP) will:

- Support NASA's strategic goals and science objectives by achieving assured access to the International Space Station (ISS) and Low Earth Orbit (LEO)
 - Crew return capability from the International Space Station as soon as practical but no later than 2010 (Goal is now 2008)
 - Crew transfer to and from the ISS as soon as practical but no later than 2012 (Goal is now 2010)
- Provide the basis for future exploration beyond Low Earth Orbit



Orbital Space Plane

Level One Requirements Summary

- OSP Improves Astronaut Safety
 - Requires crew escape system during launch
 - Provides crew survivability system during launch
 - Provides emergency crew rescue capability from the ISS
 - Required to be safer than Soyuz or Shuttle
- Enables expanded science on ISS by supporting increased crew size
- Provides Assured U.S. crew access to ISS
 - Reduces dependence on Shuttle for crew access to/from space
 - Enables eventual transition of crew access to/from space from Shuttle
 - Enhances robustness of ISS support to help ensure science productivity



Shuttle

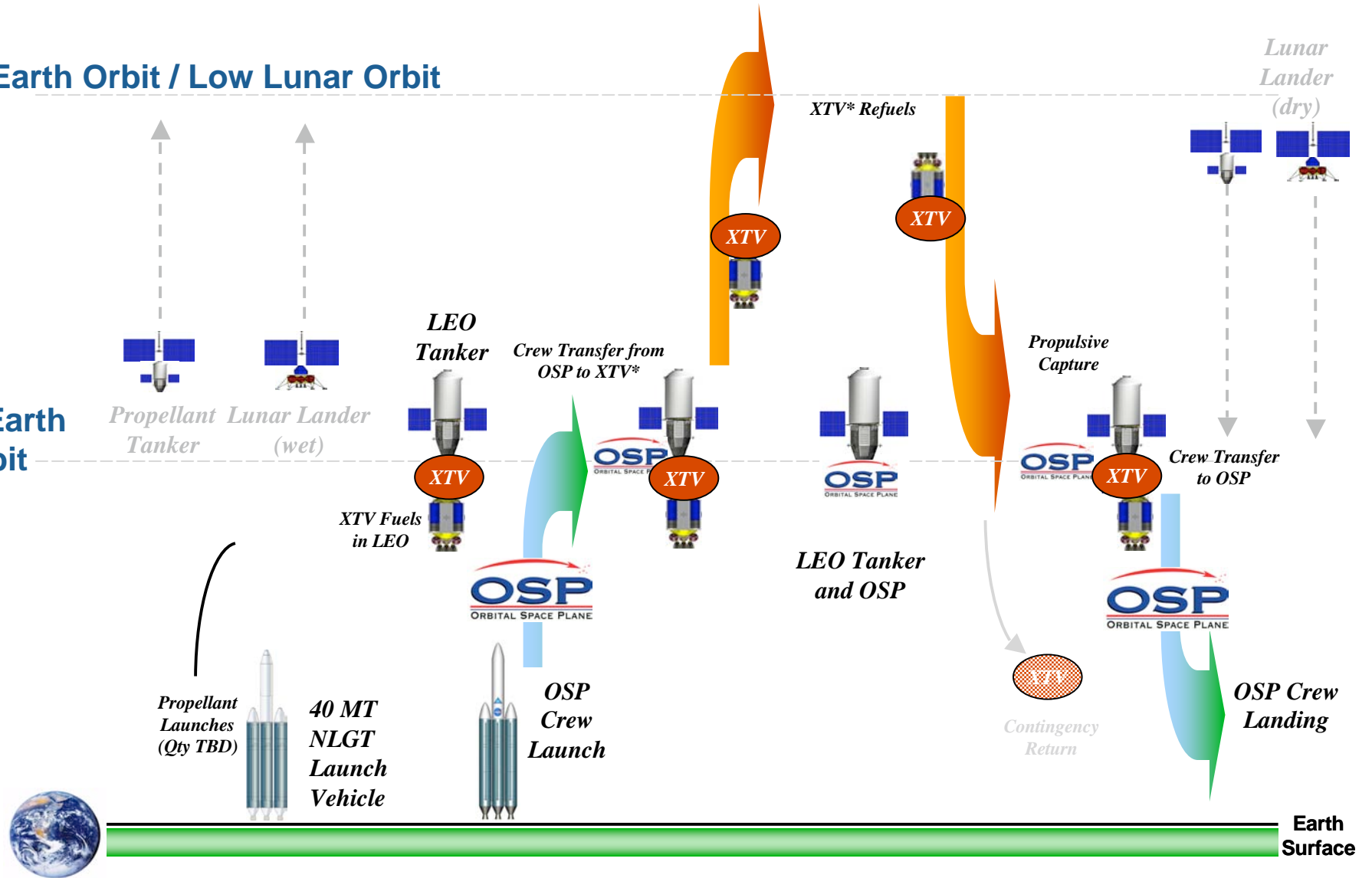
- The current Agency-wide commitment to support Return-To-Flight of the Space Shuttle fleet preserves existing space transportation capabilities and commitments.
 - *Complete Space Station Assembly*
 - *Post Station assembly cargo up-lift/down-lift*
 - *Station crew transfer operations*
- Continue to fly safely
 - Complete all CAIB recommendations in a timely manner
 - Recertification decision to extend life CY2010
- Maintenance of the Service Life Extension Program (SLEP) insures that Agency missions, National capabilities and International agreements can be sustained until capability replacement options are in place.
 - *Enhanced flight and ground safety enhancements*
 - *Infrastructure revitalization*
 - *Vehicle health monitoring enhancements*
 - *Identify and mitigate near term sustainability risk*
 - *Improve Probabilistic Risk Assessment tools and metrics*



OSP Primary Earth-to-LEO Transportation

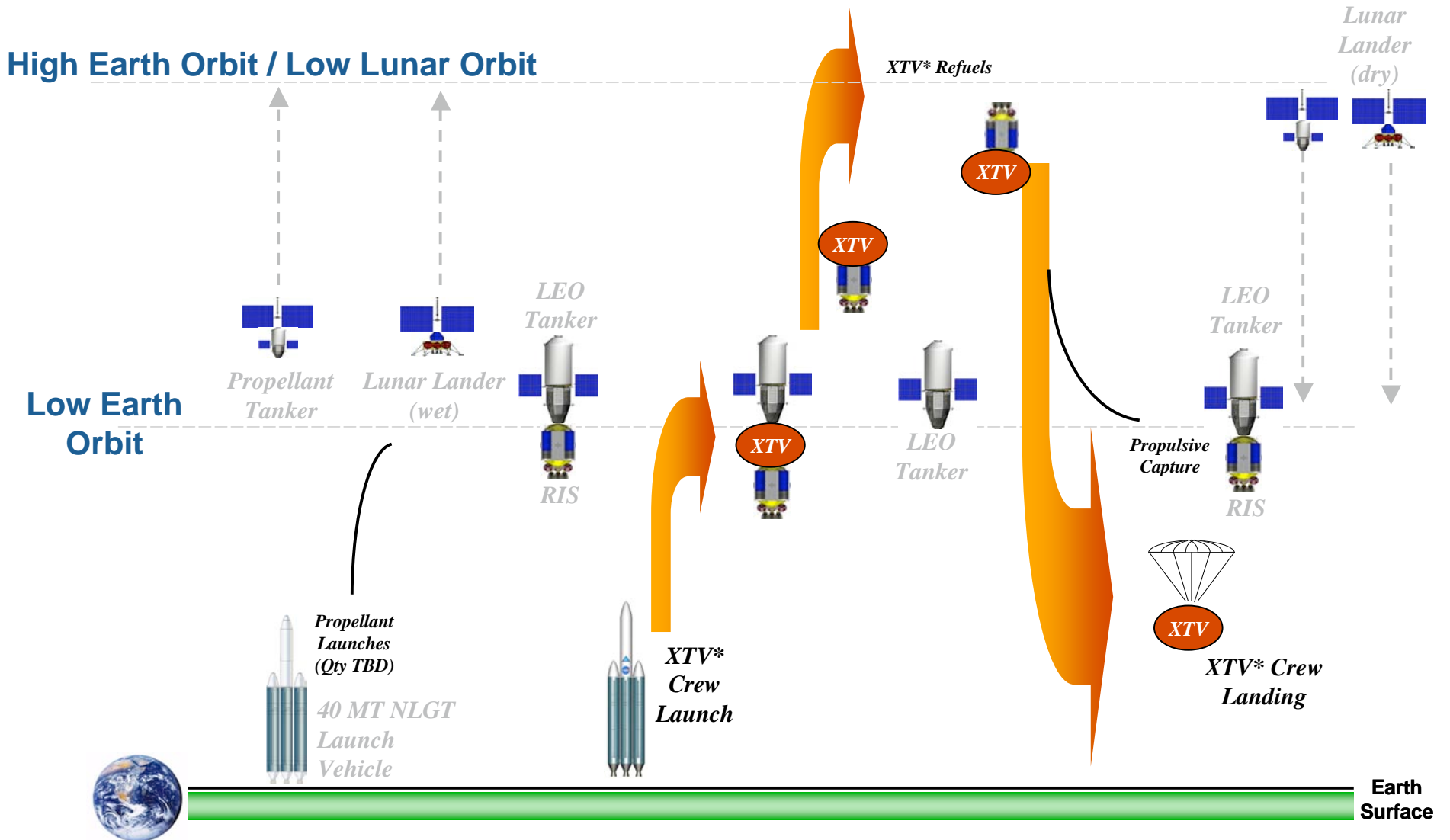
High Earth Orbit / Low Lunar Orbit

Low Earth Orbit





High Commonality between OSP and Transfer Vehicle



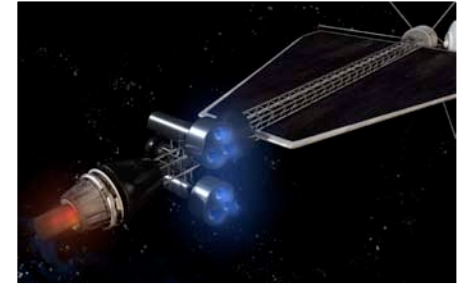
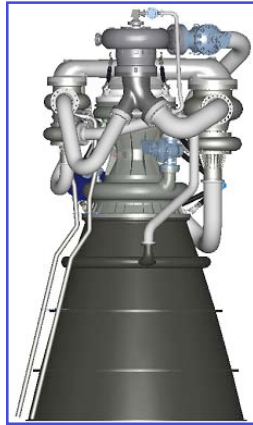


OSP Evolvability

Subsystem	Crew Rescue Vehicle	Crew Transfer Vehicle	Exploration Transfer Vehicle
Avionics	GREEN	GREEN	GREEN
Crew Accommodations	GREEN	GREEN	GREEN
Thermal Control System	GREEN	GREEN	GREEN
Propulsion	GREEN	GREEN	GREEN
Structures and Mechanisms	GREEN	GREEN	YELLOW
ECLSS	GREEN	GREEN	GREEN
Electric Power	GREEN	GREEN	GREEN
Landing and Recovery	GREEN	GREEN	GREEN*
TPS	GREEN	GREEN	YELLOW*

* Impractical if OSP is winged vehicle

RED	Incompatible or Impractical	YELLOW	Significant changes required	GREEN	Potentially Common or minor differences
------------	-----------------------------	---------------	------------------------------	--------------	---



Future Directions for Space Transportation and Propulsion at NASA

5th International Symposium on Liquid Space Propulsion
Long-Life Combustion Devices Technology
Chattanooga, TN
October 27-30, 2003

Robert L. Sackheim
Assistant Director and
Chief Engineer for Propulsion
NASA Marshall Space Flight Center

The NASA Mission:

To understand and protect our home planet,

To explore the universe and search for life,

To inspire the next generation of explorers . . .

. . . as only NASA can.

Space Is Critical to the World

The New International "Ocean"

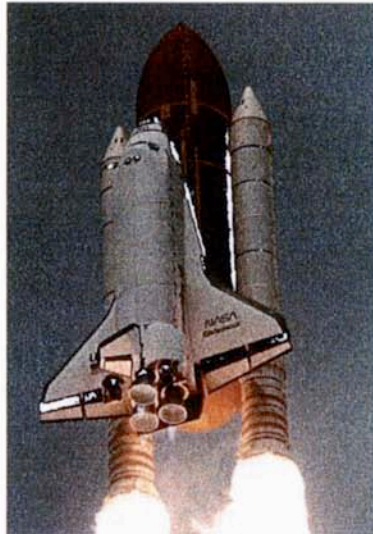
- ◆ Scientific Discovery
 - The Search for Life Beyond Earth
 - Understanding our Planet
 - Understanding our Universe
 - Exploration of the Planets and Beyond
- ◆ The Ultimate High Ground for National Security
 - Intelligence, Communications, Rapid Response, GPS . . . World Wide
- ◆ "Space-Based" Commerce
 - Communications and Earth Observing

Yet it Remains the Last, Largely Untapped Frontier

MSFC's Heritage – Complex Programs Requiring a Strong Systems Engineering Focus



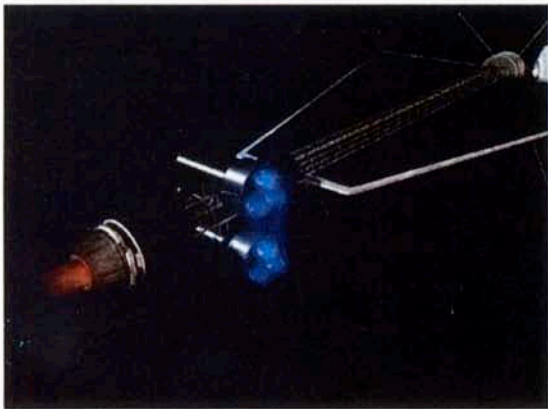
SATURN V



SHUTTLE



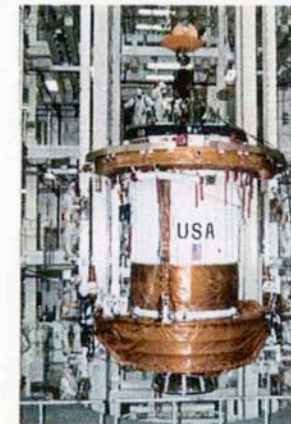
SPACE STATION



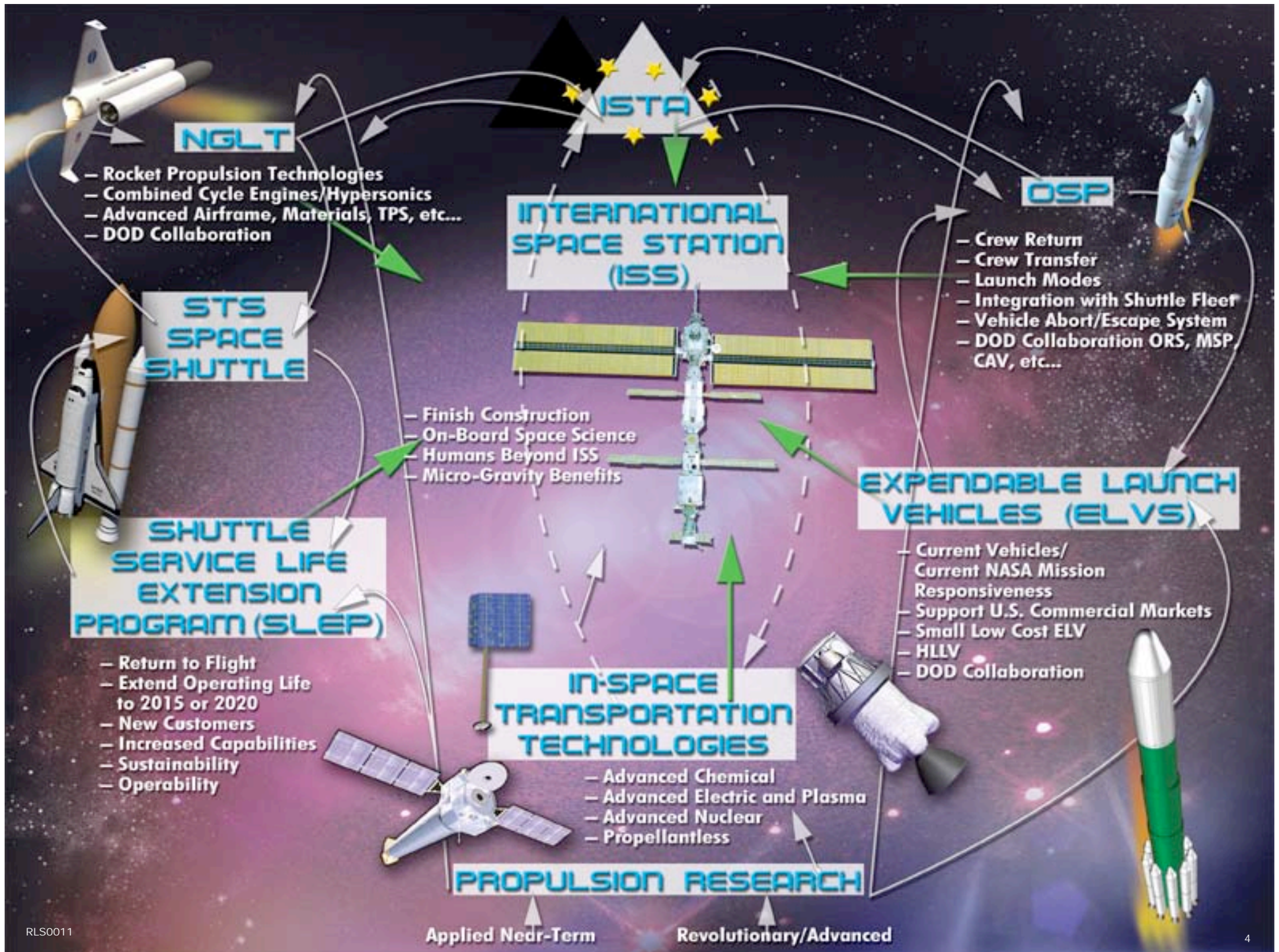
NEP VEHICLE DESIGN

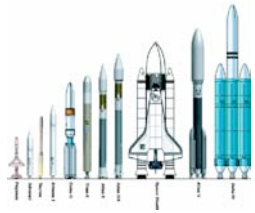


CHANDRA

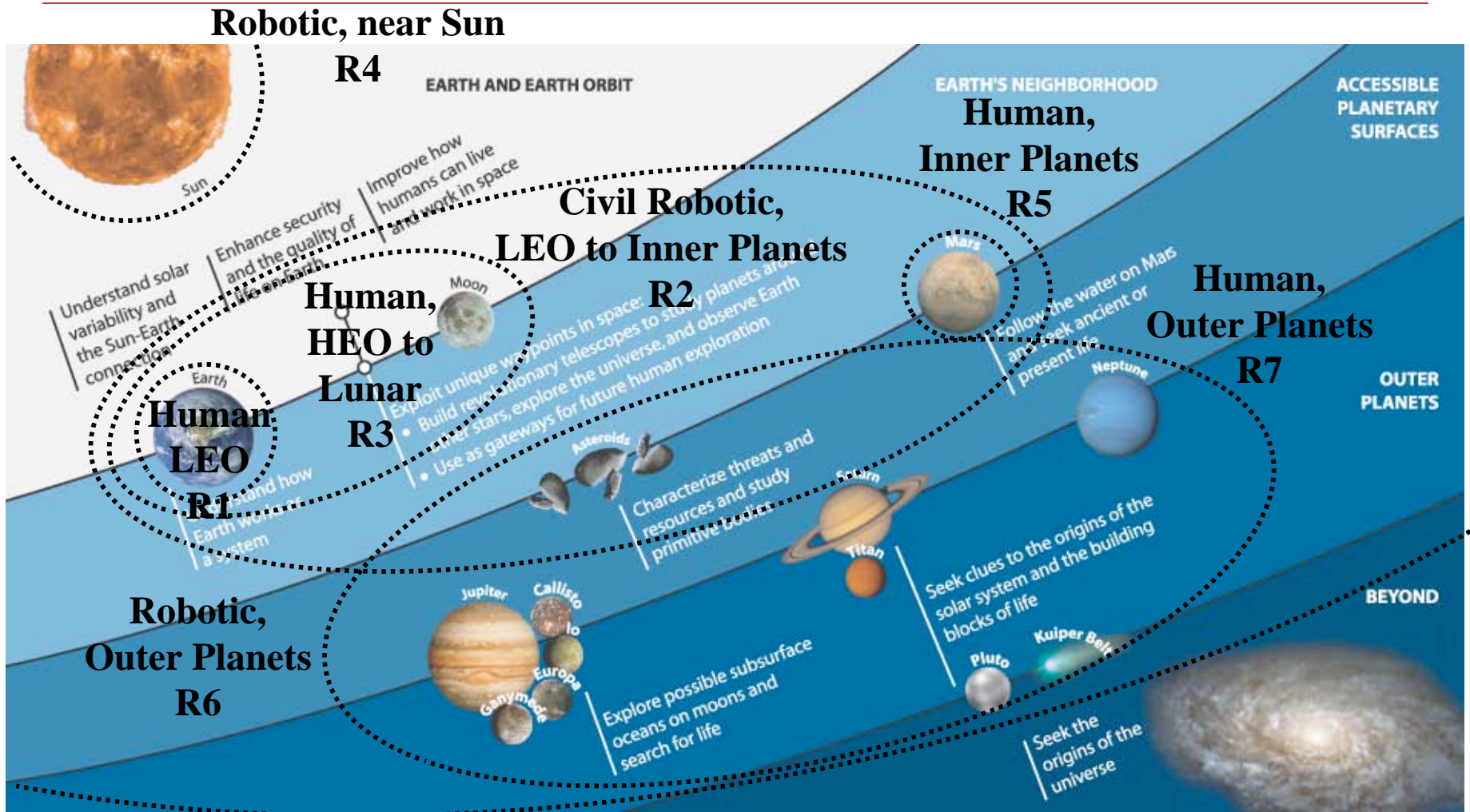


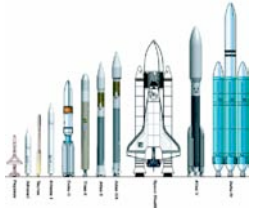
INERTIAL UPPER STAGE





Stepping Stones Overlay on Space Transportation Regimes

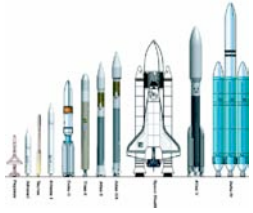




Regime Descriptors and Needs



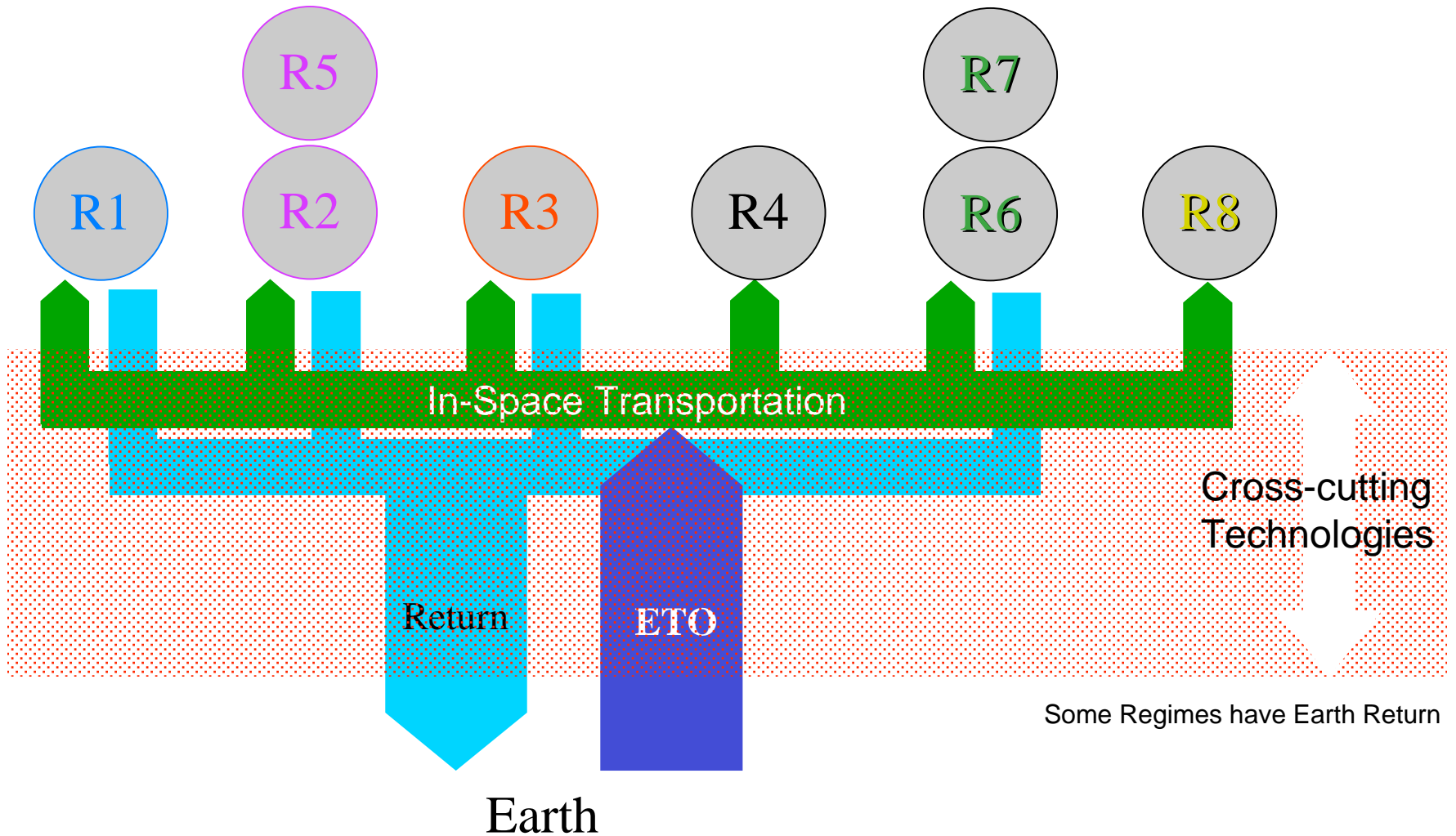
R1	Human Earth Orbit	ISS and other near-Earth missions	Frequent access; safety; medium cargo; reduced cost
R2	Robotic LEO to near planets	Earth & space observation; planetary science; sample return	State of art mainly OK; reduced cost; higher reliability; landing & ascent systems
R3	Human HEO and lunar	Missions in cislunar space & lunar surface and basing	Medium space transfer/cargo, landing, safety, reduced cost
R4	Robotic near-Sun	Mercury, solar probes, solar polar	High delta V, reduced cost, ETO state of art OK
R5	Human near planets	Mars and Mars surface, asteroids, exploration and basing	Increased lift to LEO, heavy space transfer, short trip time, reduced cost, safety, artificial g
R6	Robotic outer planets	Orbiters, probes, landers, sample return	Reduced trip time, high/very high delta V, nuclear electric power, reduced cost, ETO state of art OK
R7	Human outer planets	To Jupiter and Saturn moons, landing, return	Fast trips, very high delta V, heavy space transfer, nuclear power
R8	Robotic beyond planetary system	Kuiper belt, Oort cloud, interstellar medium	Very/extremely high delta V, nuclear electric power

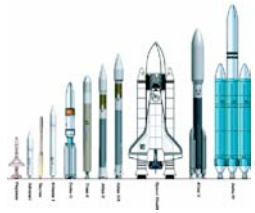


End-to-End Regimes Capture Mission Requirements

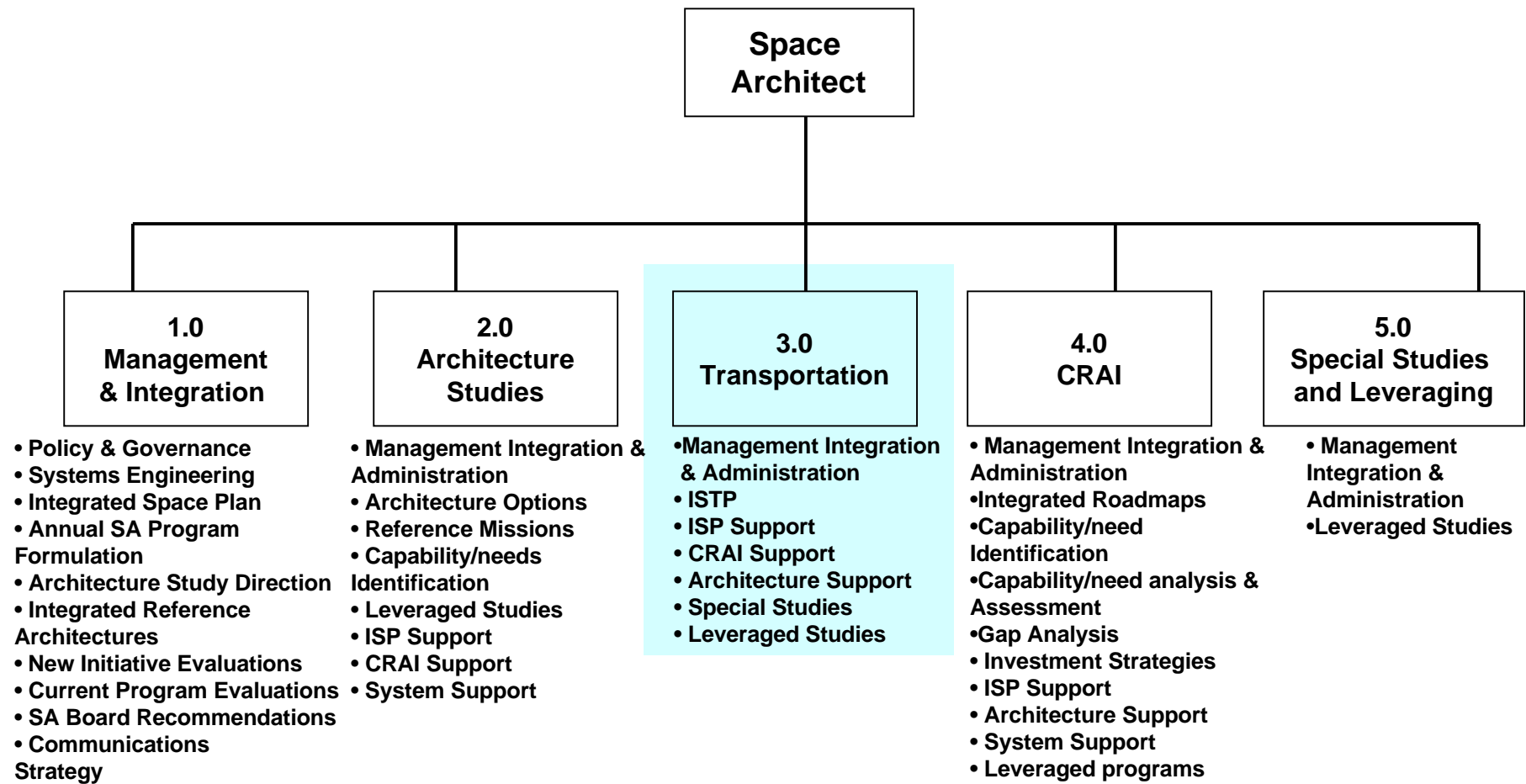


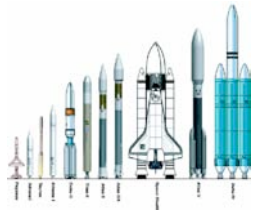
Equal emphasis over all Regimes favors NASA-Wide Propulsion Requirements



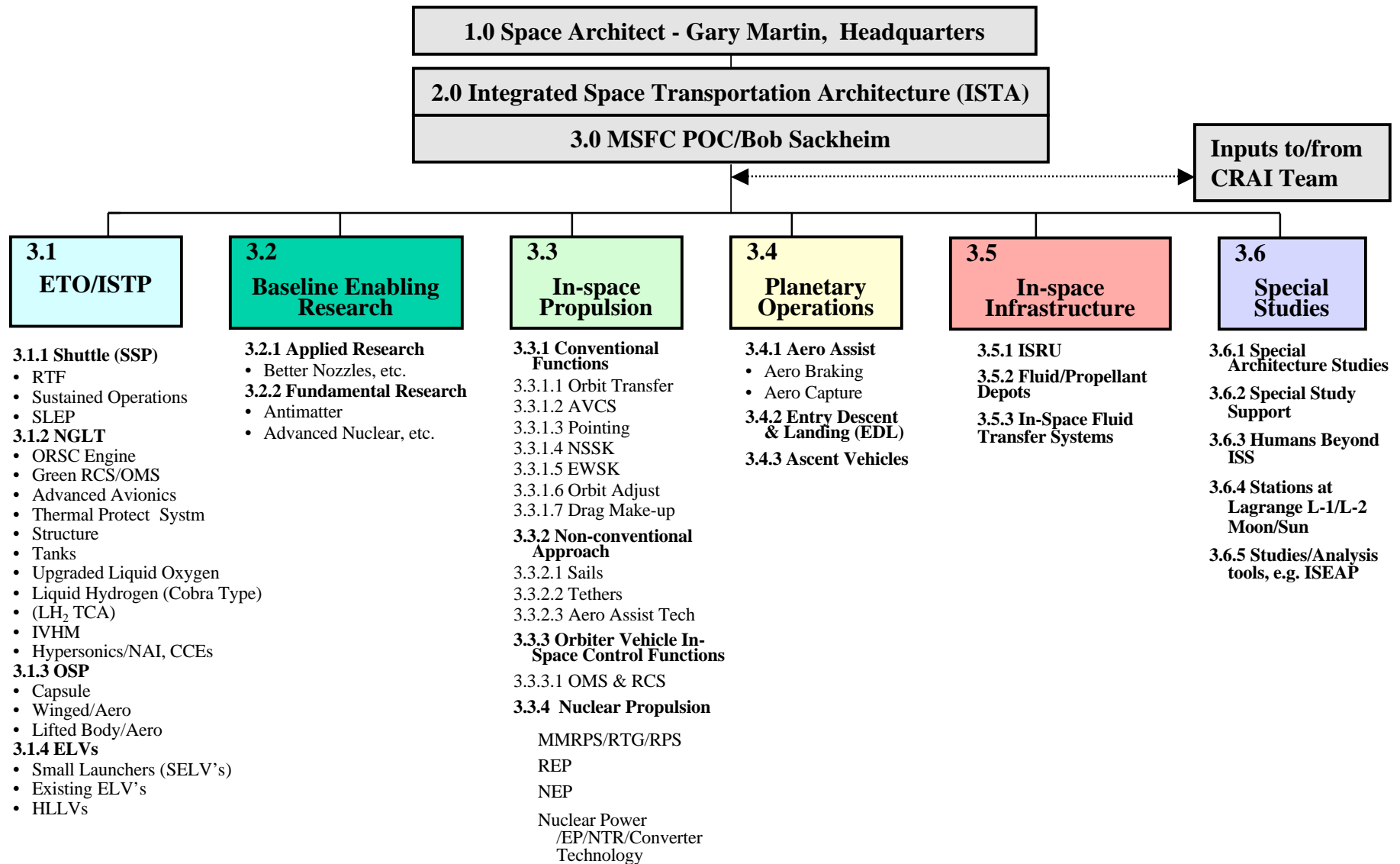


Work Breakdown Structure





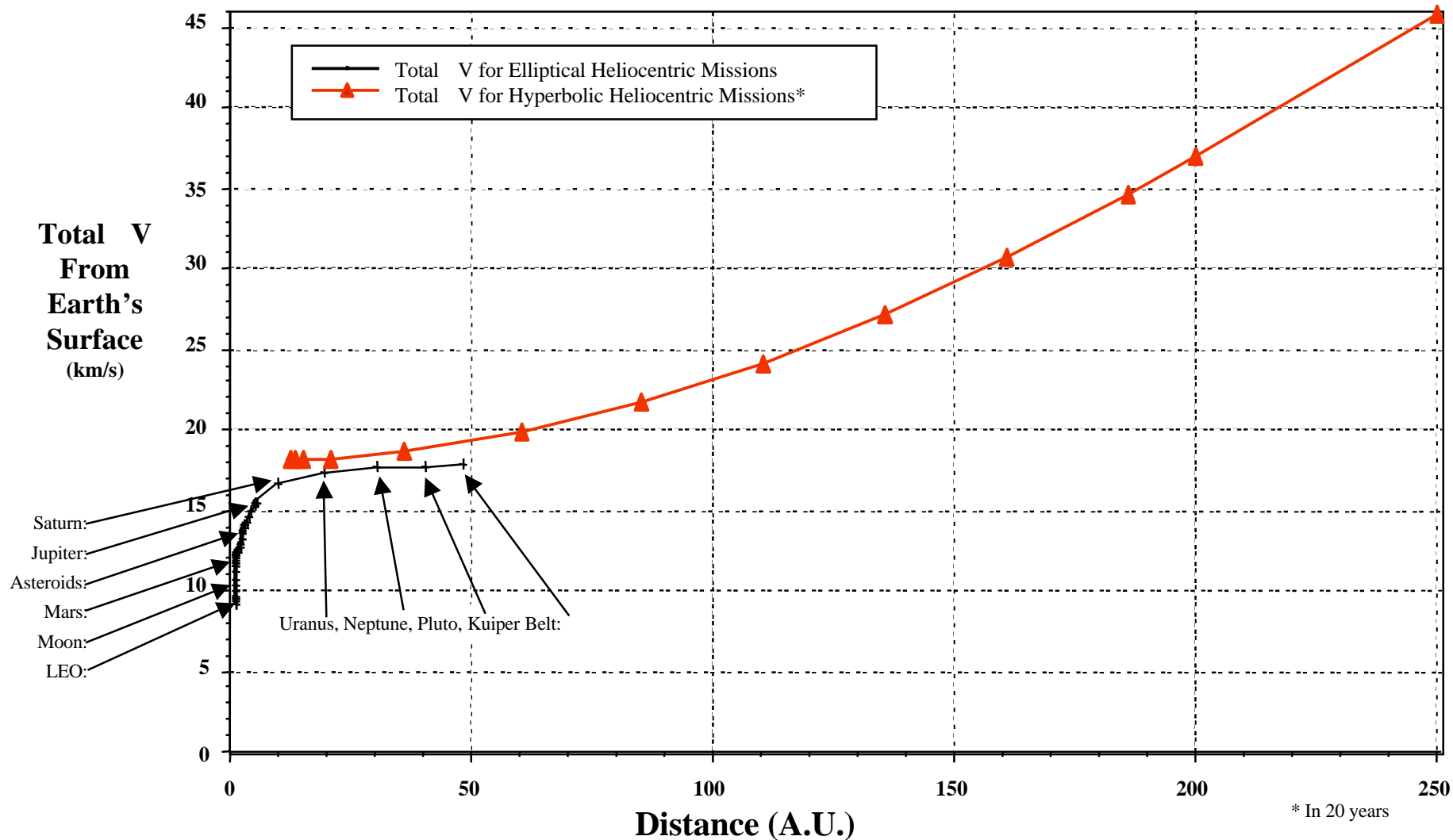
Integrated Space Transportation Architecture Inputs to the Space Architecture Work Breakdown Structure Format



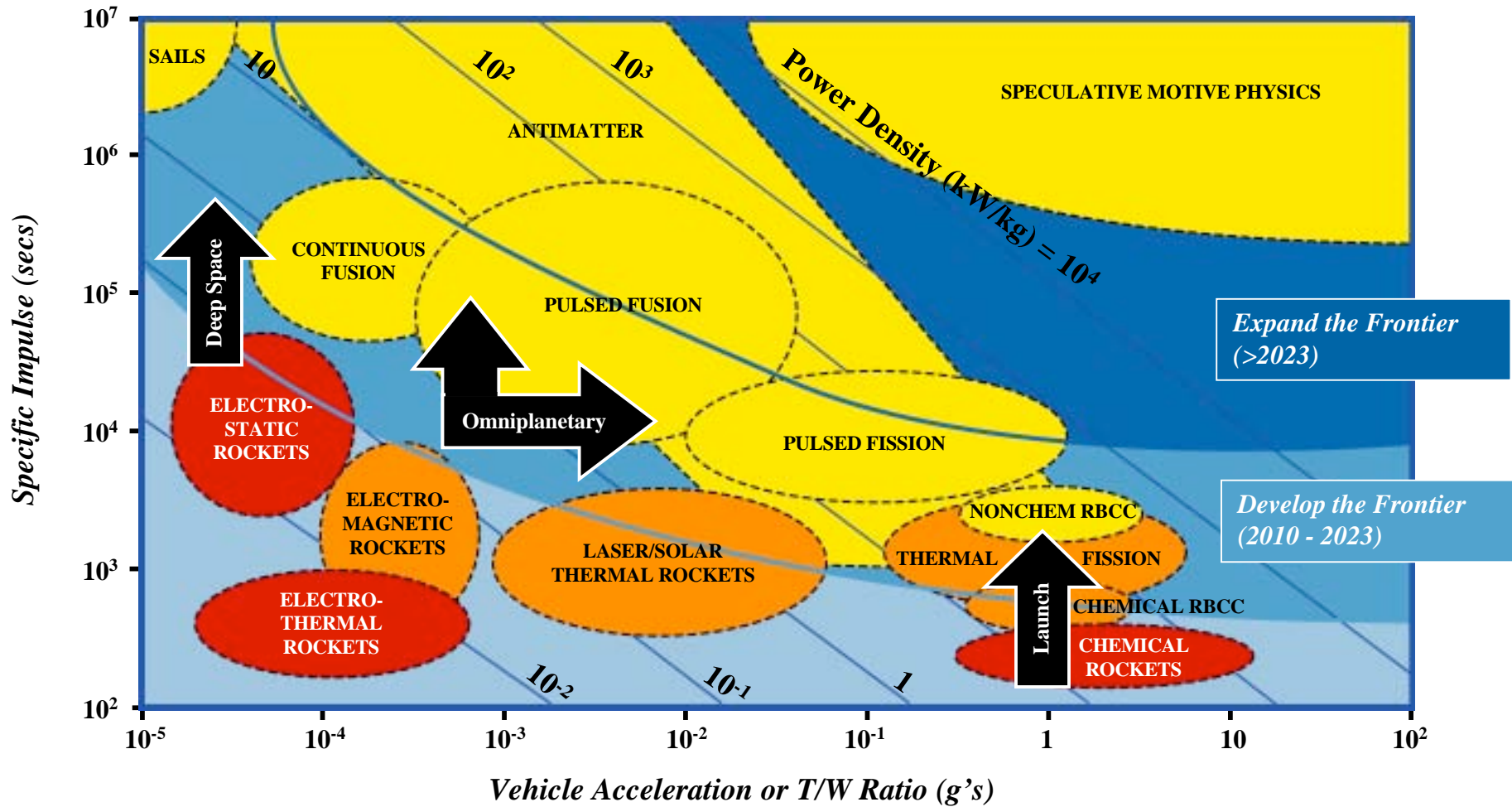


The Physics Problem

Energy Comparison for Various Distances Single Burn Delta V From LEO, ETO $V = 9.3$ km/s



New Propulsion Technologies are Needed to Meet NASA's Most Ambitious Goals



Unproven Technology (TRL 1-3)

Demonstrated Technology (TRL 4-6)

Operational Systems (TRL 7-9)

NASA's New Integrated Space Transportation Plan (ISTP)

Space Shuttle Life Extension Upgrades

Orbital Space Plane (OSP)

- ISS Crew Rescue by 2010
- ISS Crew Transfer by 2012

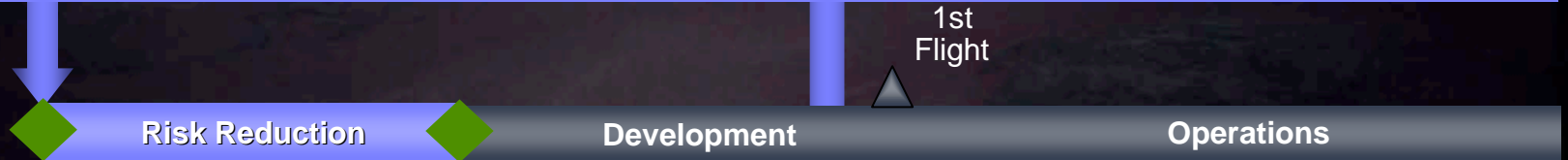
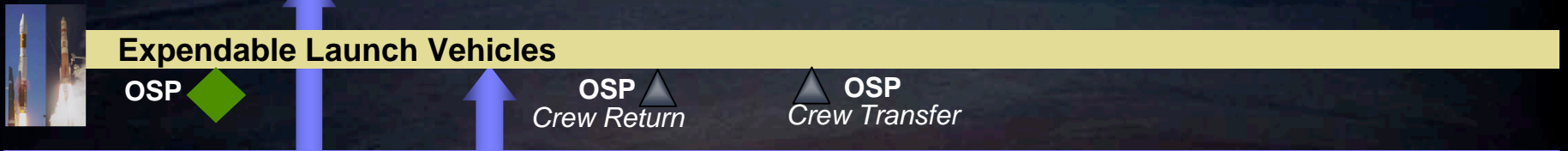
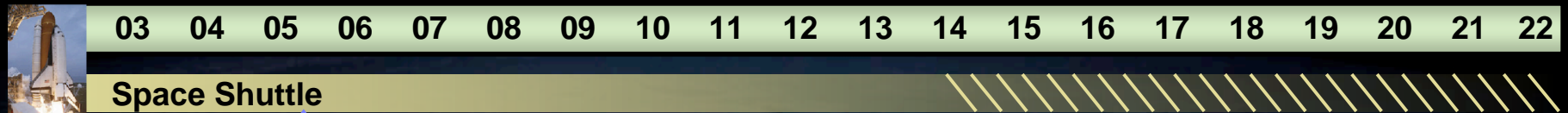


Next Generation Launch Technology (NGLT)

- Enabling Future National Launch Capabilities



Enabling Near and Long Term Improvements in U.S. Launch



■ NGLT Program

◆ Decision Point



Near Term Options

- Shuttle Upgrades / Derived System
- New Rocket RLV
- Heavy Lift Expendable Launch

Longer Term Options

- New Rocket RLV
- Hypersonic RLV
- Very Heavy Lift Launch



Imagine the Possibilities....

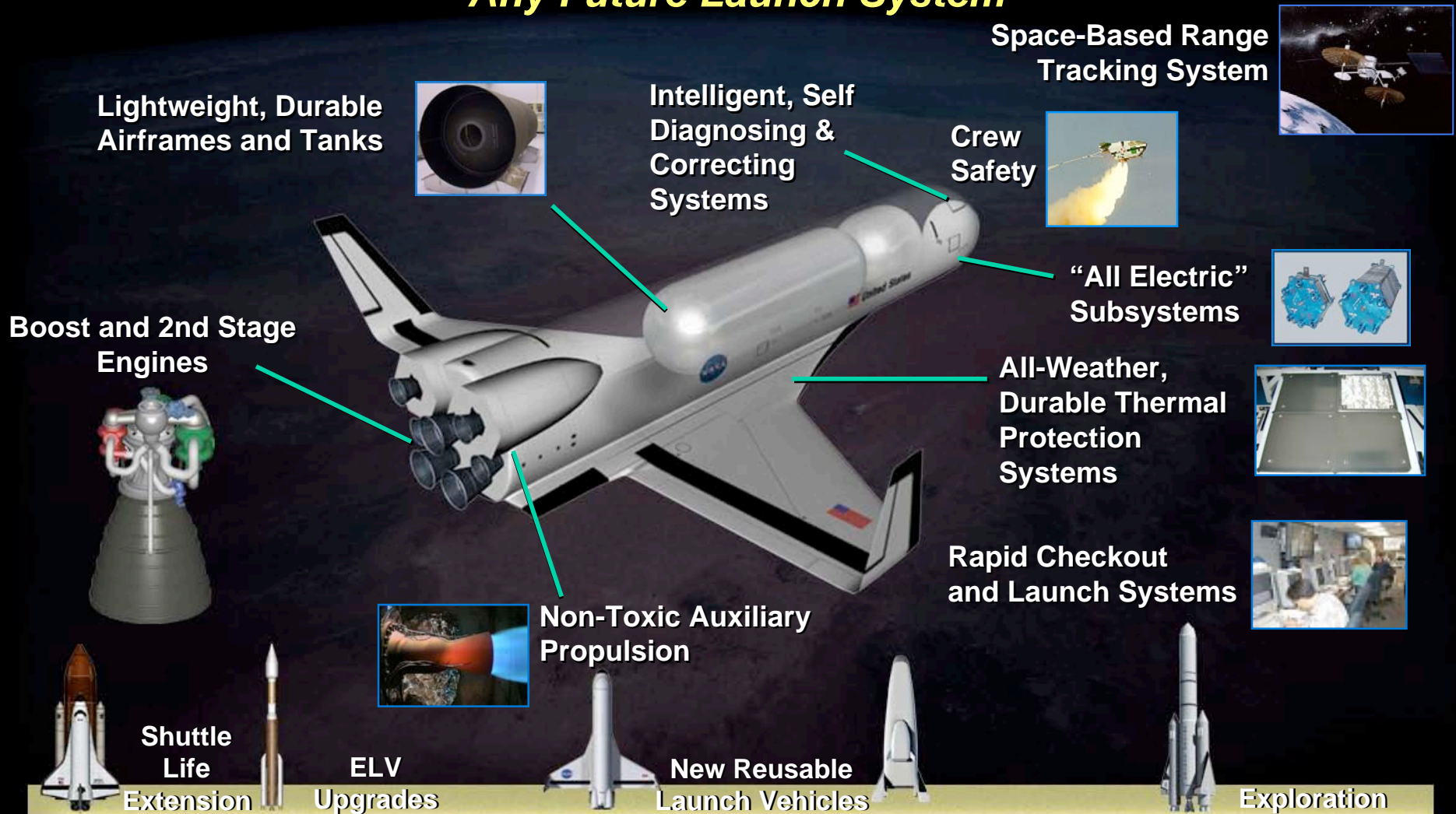


- Significant Expansion in Robotic Probes Going Throughout the Solar System and Beyond
- Humans Exploring Space Beyond Low Earth Orbit
- Space Solar Power Systems Supplying Cheap Electricity Around the Globe
- Daily Tours To and From Space
- Industrial Space Platforms Developing New Materials and Medicines

*A Primary Limitation is
Safe, Reliable and Affordable Space Launch*

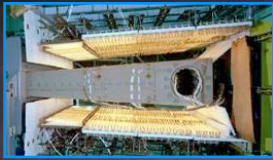


High Leverage, Cross-Cutting Technologies for Any Future Launch System





Cutting Edge Hypersonics Technologies for Future, Aircraft-like Operations



Long Life, High Temperature Structures and Materials



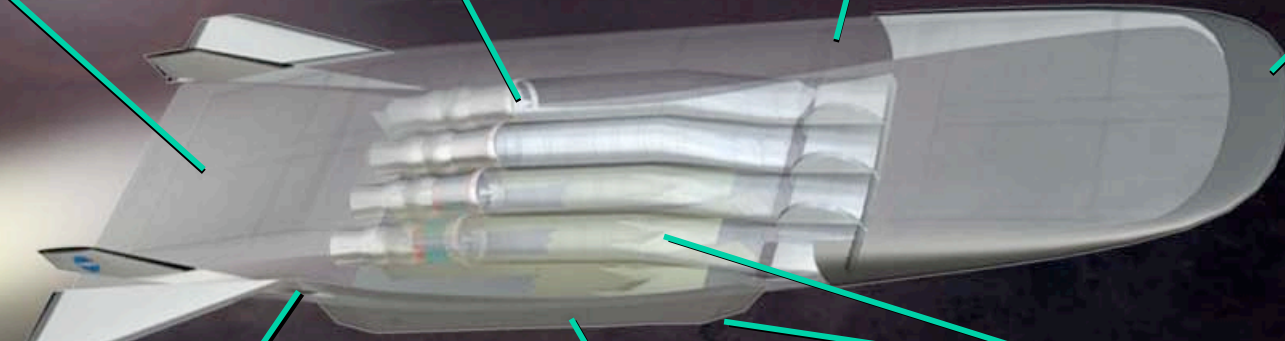
Mach 4 Turbine Engines



Highly Integrated Airframe Systems



Ultra High-Temp Leading Edges



Integrated Rockets



Ram / Scramjets



Combined Cycle Propulsion Systems



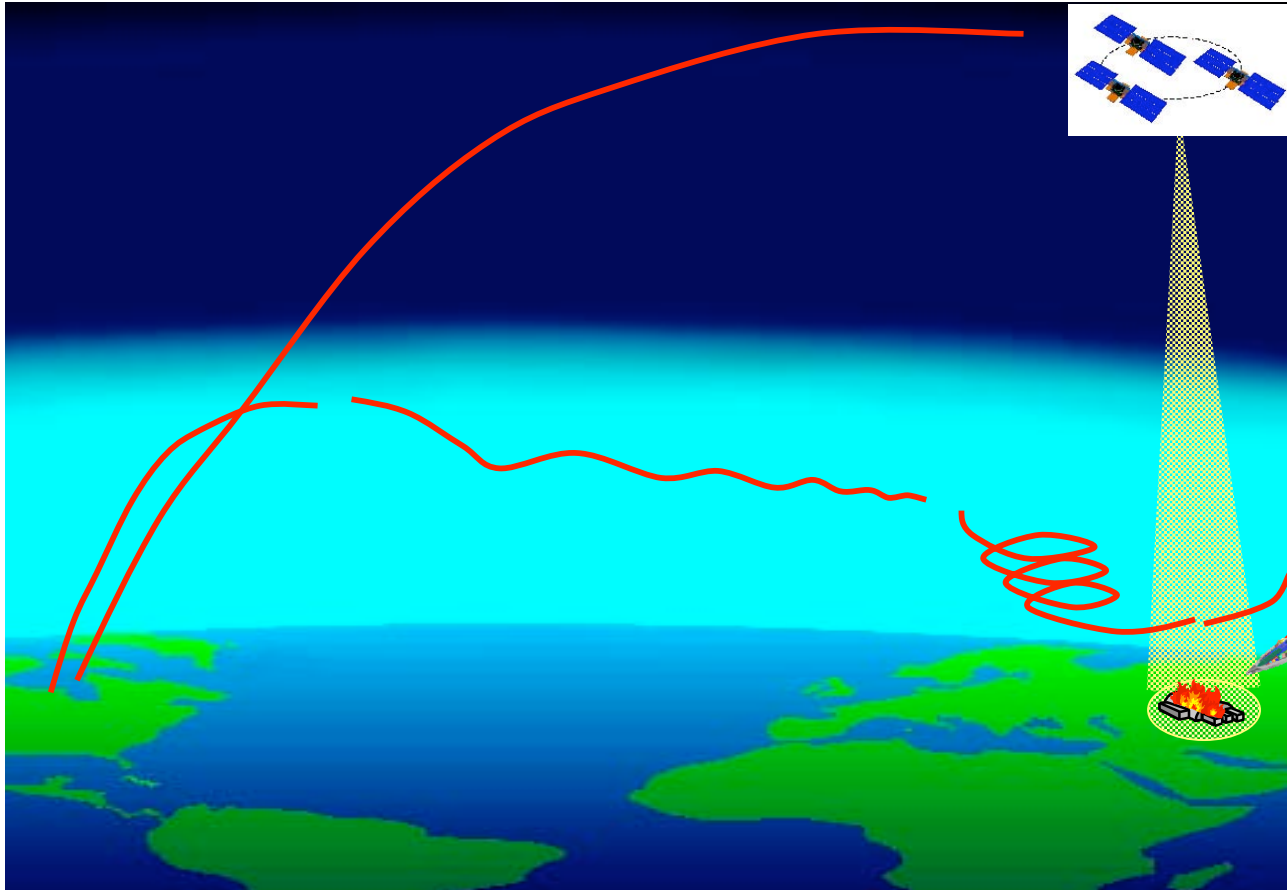
DARPA/USAF Small Launcher Initiative



- DARPA and the Air Force have established a joint program
- DARPA has overall program management primacy
- The program is called FALCON (Force Application Launch from CONUS)
- FALCON RFP released on July 29, 2003
- The FALCON SLV initiative has some similarities to MSFC's original Bantam Project



FALCON





FALCON

Many respondents to
FALCON RFI (1/30/2003)





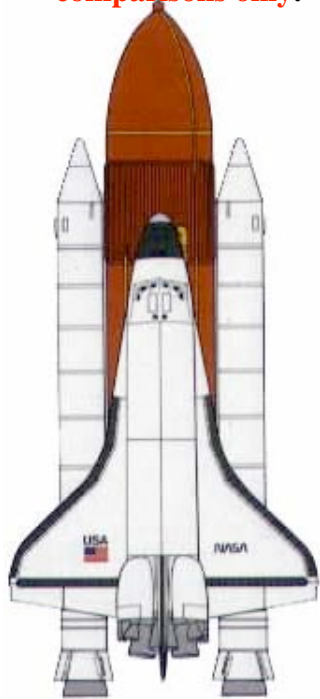
Why Will It Work This Time?

- **Simplicity of Design**
 - Some simple designs are inherently more reliable and lower cost than others
 - See RLS papers for last 20 years
 - NASA and DOD have really shown zero interest in inherently low costs
- **Trade Design Margin Against Performance and Weight**
 - Nontraditional aerospace design philosophy
 - Greater design margins enhance reliability
 - Very high Thrust-to-Weight is not that critical for low cost, vertical launch
 - Lower Thrust-to-Weight is more reliable (but vehicle T/W >1.1 @ liftoff)
- **Trade Design Margin Against Redundant Systems**
 - Redundancy adds complexity and cost
- **Use Rack and Stack Design Approach to Achieve Component Commonality**
 - Commonality enables simplicity and lowers cost
 - Commonality enhances reliability
 - Provides evolutionary design approach for heavy lift using flight-proven building blocks
- **Use Commercial (non-aerospace) Processes and Components As Much as Possible**
 - Leverage commercial industry's production rate
 - Commercial components are inherently higher margin; not optimized for performance
 - Commercial hardware is dramatically lower cost than comparable aerospace hardware

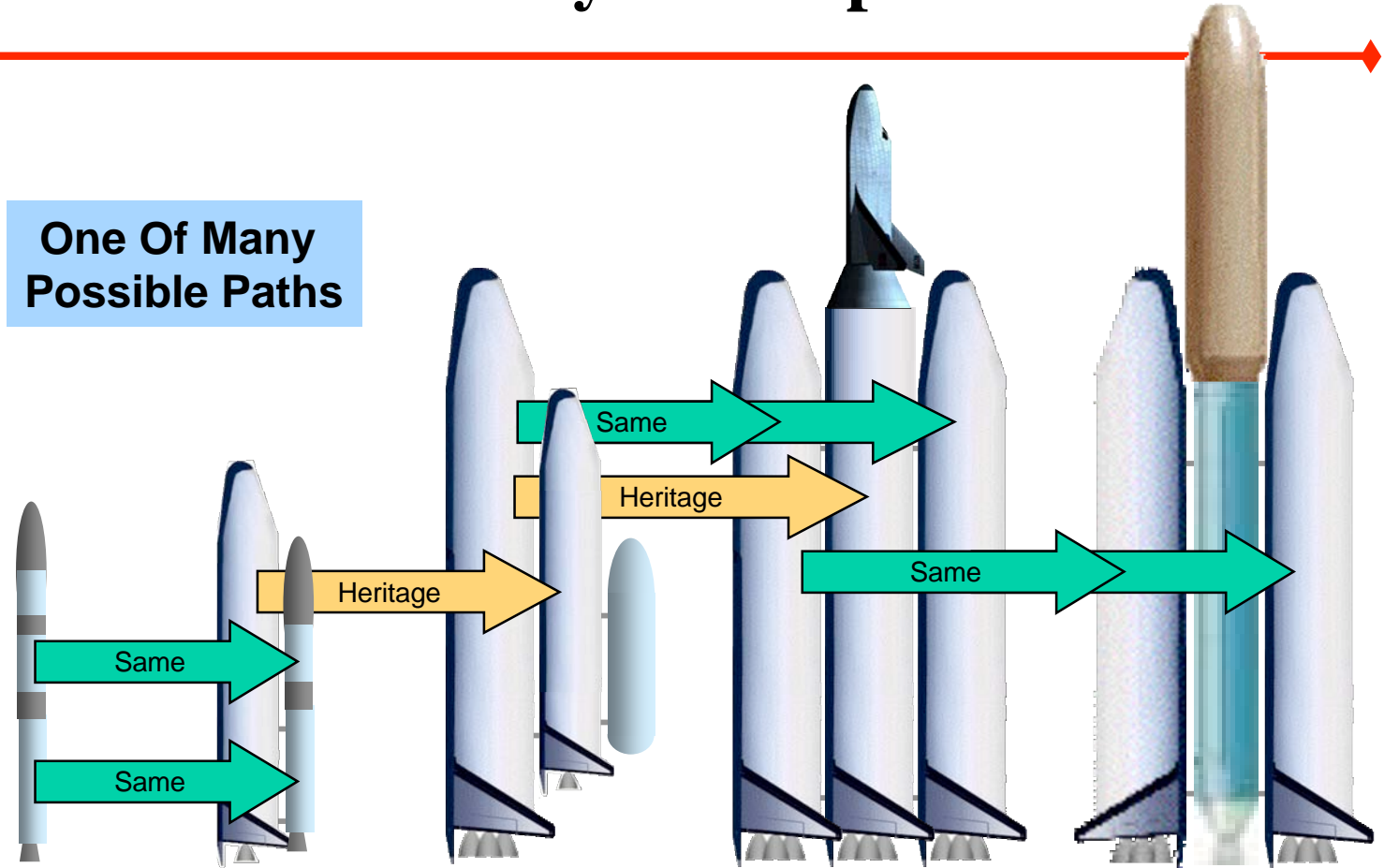


Notional Evolutionary Development Path

Shuttle depicted for size comparisons only.



One Of Many Possible Paths



Stage 1 Engine
Stage 2 Engine
Stage 3 Engine

FALCON

New RP
New RP
New RP

Spiral 1

2 SSME
FALCON Stage 2
FALCON Stage 3

Spiral 2

New LH Engine (4)
Spiral 1 Stage 1
--

Spiral 3

Same as Spiral 2
Same as Stage 1
--

Spiral 4

Same as Spiral 2
EELV Core
EELV US



Technology Application to Shuttle Upgrades (Initial NGLT Assessment)

External Tank

- Self Reacting Friction Stir Welding
- Advanced Cryoinsulation

Booster

- LOx/RP liquid booster replacement (1+Mlb Prototype Engine)

Airframe Structure

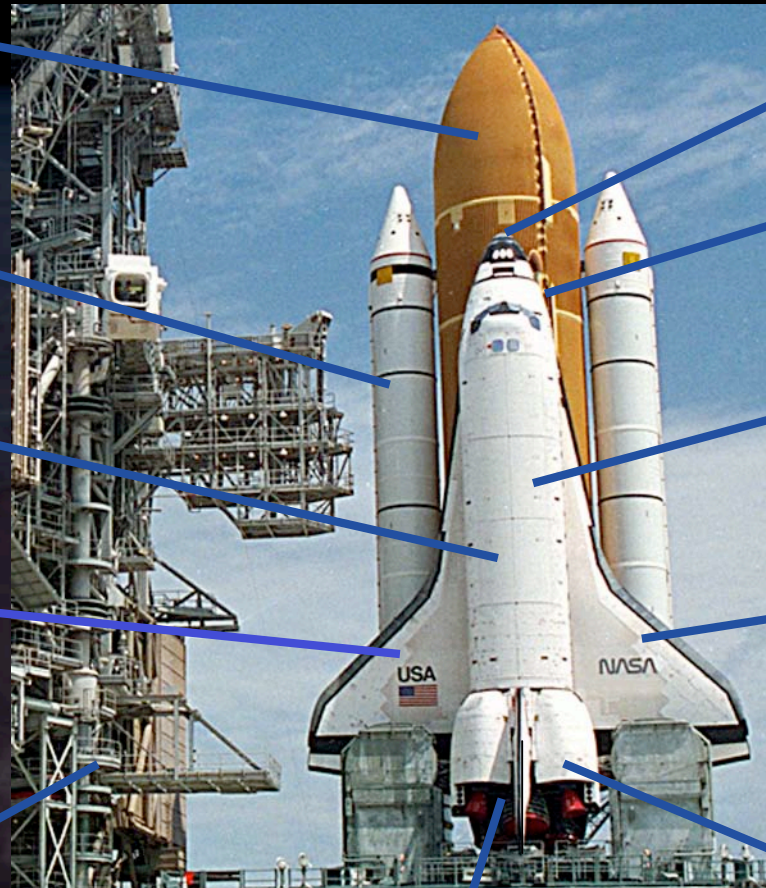
- Ceramic Matrix Composite Control Surfaces
- Structural Health Monitoring Sensors

Thermal Protection Systems

- Light Weight, Intelligent Micrometeoroid Resistant Ceramic TPS
- Durable, Conformal Reusable Insulation
- Long Life, Durable Thermal Seals
- Rapid Waterproofing

Ground Operations

- Space Based Telemetry and Range Safety
- Silent Sentry/Passive Coherent Location (Advanced Range Technology)
- Range Architecture Development
- Advanced Umbilical Development
- Improved Propellant Management
- Densified Propellants
- Advanced Checkout Control and Maintenance System
- Launch Acoustic Environment Prediction



RCS/OMS

- LOx/Ethanol Dual-Thrust Level RCS Thrusters

IVHM System Integration

- Advanced Systems/Subsystems Diagnostic Algorithms
- IVHM/Flight Operations Integration

Subsystems

- High Horsepower, Electrically Driven Actuators
- PEM Fuel Cells
- Nontoxic Turbine Power Unit

Aero & GN&C Tools

- Separation and Abort Scenarios
- Reentry Heating Environments
- Localized Heating
- Integrated Development and Operations System
- Integrated Aerothermal/TPS Sizing

Aft Compartment

- Oxygen and Hydrogen Leak Detectors

SSME

- IPD Channel Wall Nozzle
- Advanced Turbomachinery
- GRCop-84 Main Combustion Chamber Liner
- Advanced Engine Health Management



Technology Application to Expendable Launch Upgrades (*Initial NGLT Assessment*)

Tanks

- Self Reacting Friction Stir Welding
- Advanced Cryoinsulation

Structures

- Structural Health Monitoring Sensors
- Lightweight metal matrix and polymer matrix composite structures

Ground Operations

- Space Based Telemetry and Range Safety
- Silent Sentry/Passive Coherent Location (Advanced Range Technology)
- Range Architecture Development
- Advanced Umbilical Development
- Improved Propellant Management
- Densified Propellants
- Advanced Checkout Control and Maintenance System
- Launch Acoustic Environment Prediction



IVHM System Integration

- Advanced Systems/Subsystems Diagnostic Algorithms
- IVHM/Flight Operations Integration

Subsystems

- High Horsepower, Electrically Driven Actuators
- PEM Fuel Cells
- Nontoxic Turbine Power Unit

Aero & GN&C Tools

- Separation and Abort Scenarios
- Reentry Heating Environments
- Localized Heating
- Integrated Development and Operations System

Aft Compartment

- Oxygen and Hydrogen Leak Detectors

Replacement RP Engine

- LOx/RP liquid booster replacement (1+MIb Prototype Engine)

LH₂ Engine Upgrades

- IPD Channel Wall Nozzle
- Advanced Turbomachinery
- GRCop-84 Main Combustion Chamber Liner
- Advanced Engine Health Management



Enabling "Firsts" in Space Launch Technology

Booster Engine Prototype



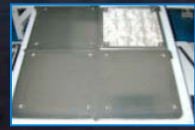
- Highly reliable hydrocarbon fueled rocket booster engine
- High reliability, long life hydrogen rocket engines

Auxiliary Propulsion



- Non-toxic propellants for orbital propulsion

Vehicle Research and Technology



- Airframes capable of containing cryogenic propellants and reentering the Earth's atmosphere
- Durable high temperature thermal protection systems
- An intelligent, autonomous "all electric" launch system

Propulsion Research & Technology



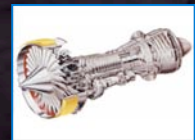
- Long life, lightweight high temperature materials, seals and components

X-43A and C



- 1st controlled flight of a vehicle powered by a scramjet from Mach 5 - 7 and 10

Revolutionary Turbine Accelerator



- Lightweight, long life jet engines capable of flight at Mach 4



**Think of What We Have Accomplished
in the 100 years Since the Wright
Brothers 1st Flight**



**..... Imagine What We Will Do On the
New "Ocean of Space"**



In-Space Focused Scope

Orbital Transfer Vehicles



Reusable Upperstage



Tethers

Interplanetary Transfer Stages



Solar Electric

Planetary Capture



Aerocapture

Ascent/Descent Stages

Sample return



In-Situ Prop/
Ascent Chem
Prop Stage

Enabling New Scientific Discoveries

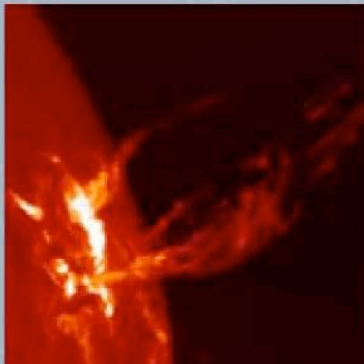
Solar System Exploration



◆ Planetary Exploration Examples:

- Orbiters
- Landers
- Sample Return

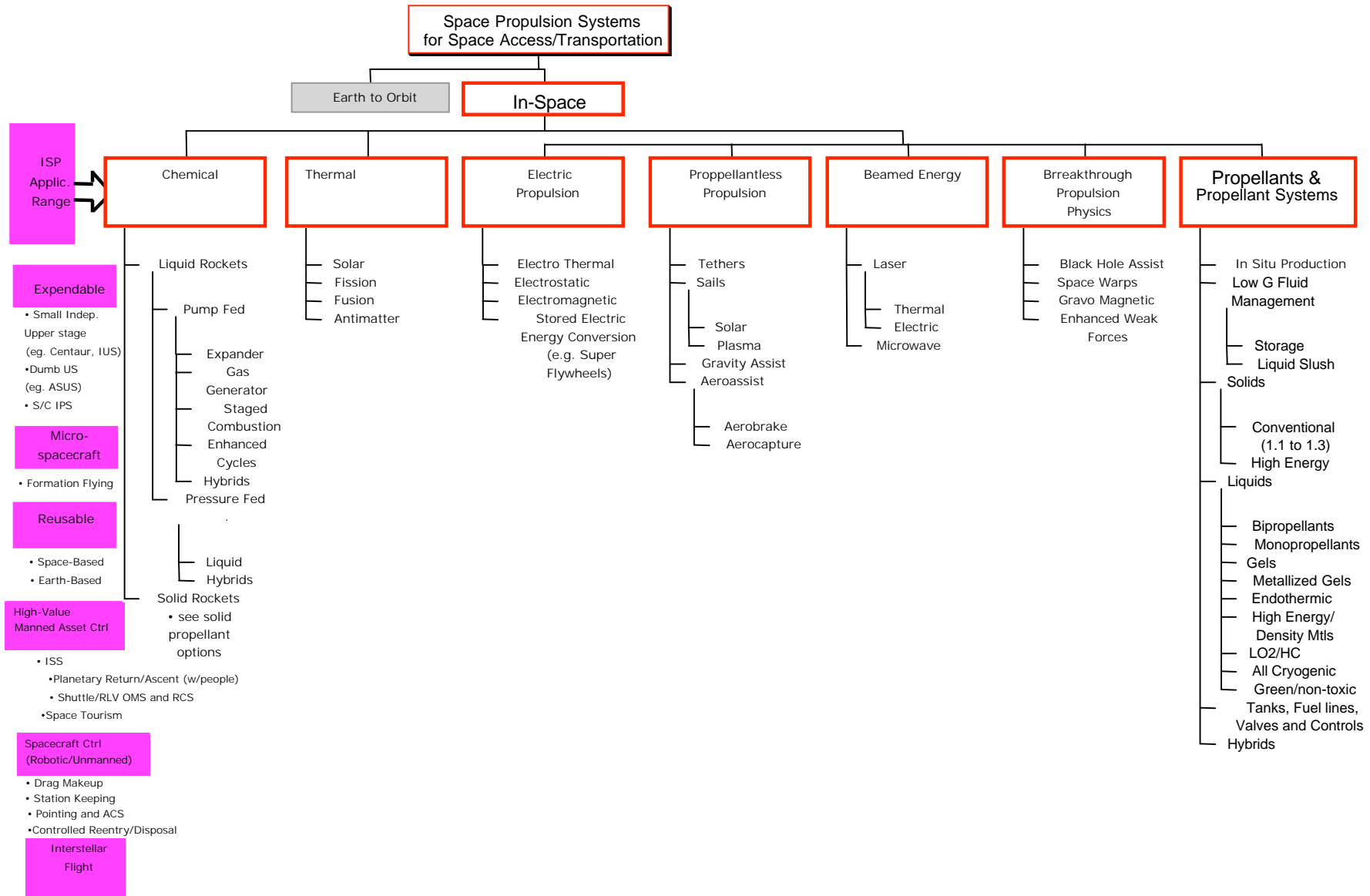
Sun Earth Connection



◆ Solar Science Examples (inc. Solar Sails):

- LaGrange Missions
- Orbiters
- Pole Sitters

In-Space Propulsion Systems



Missions Often Characterized by "Delta V"



Typical Mission Examples

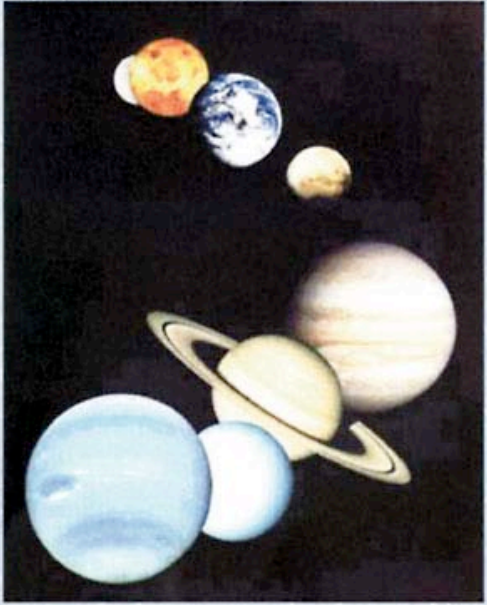
	<u>ΔV Required KM/SEC</u>
• 10 Year GEO Stationkeeping	~0.5
• LEO to GEO (0.3 days)	~4
• LEO to GEO (250 days)	~6
• Titan Orbiter (1way)	~11
• Neptune SR (NEP)	~85
• LEO to Alpha Centauri	30000.0

Far Away Places Truly Stress the Bounds of Propulsion

In-Space Transportation

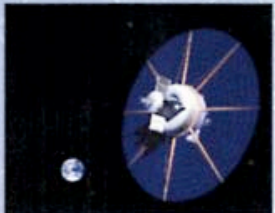


Enabling New Scientific




A central image showing a collection of planets and moons, including Mercury, Venus, Earth, Mars, Jupiter, Saturn, Uranus, and Neptune, arranged in a semi-circle against a black background.

Solar Electric Propulsion




A satellite with large solar panels deployed, orbiting Earth.

Nuclear Electric Propulsion




A satellite with a nuclear reactor and ion thrusters, emitting a blue glow.

Solar and Plasma Sails



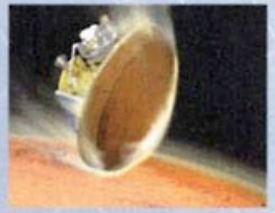
A satellite with a large, pink, triangular sail, orbiting Earth.

Chemical Propulsion



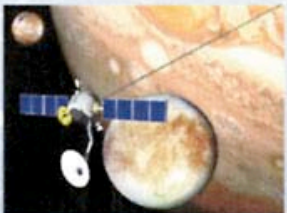
A satellite with a large, spherical, metallic propellant tank, orbiting Earth.

Planetary Aeroassist

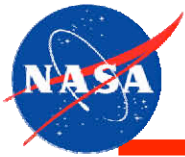


A satellite with a large, conical, metallic heat shield, orbiting Earth.

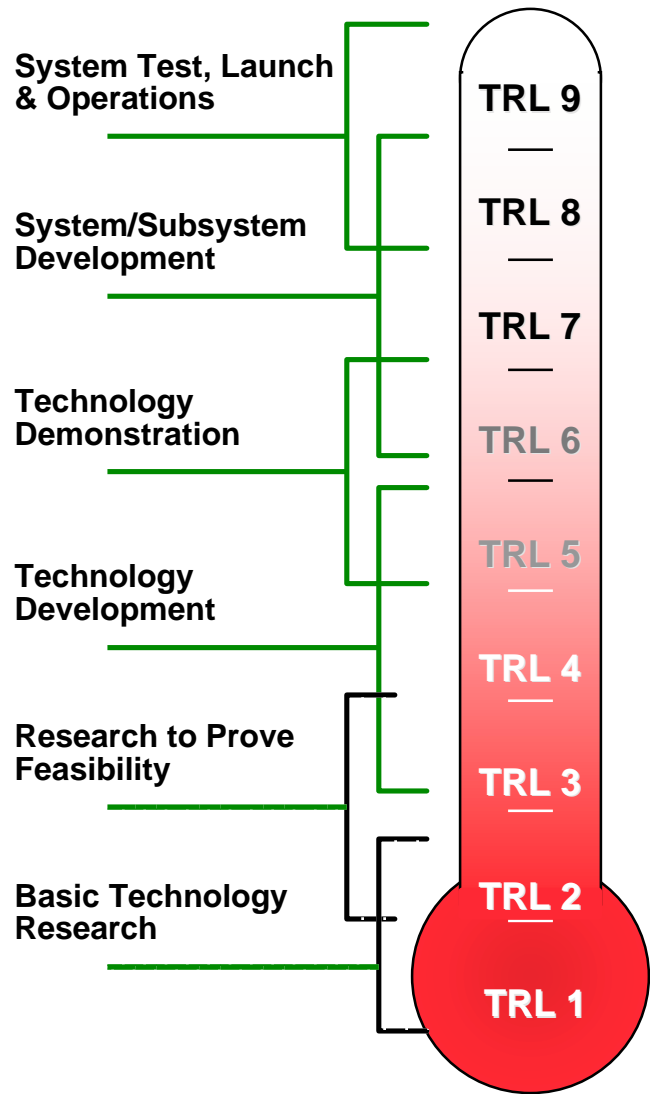
Tethers



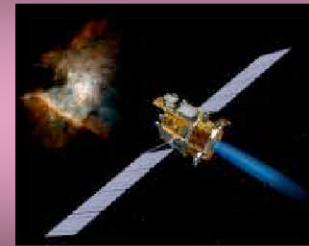
A satellite with a long, thin tether, orbiting Earth.



In-Space Propulsion Program Will Advance Mid-TRL Technologies to Support NASA Mission Applications



NASA Implementation: (Deep Space One Ion Engine Example)

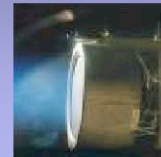


In-Space Propulsion Technologies

Aeroassist



Adv. Electric Propulsion



Solar Thermal



Adv. Chemical



Tethers



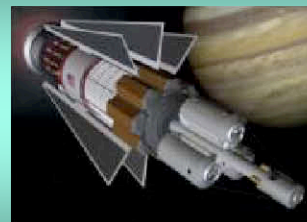
Solar Sails



Plasma Sails



Low-TRL Technologies For the Future



External Pulsed Plasma



Fusion & Antimatter



Beamed Energy

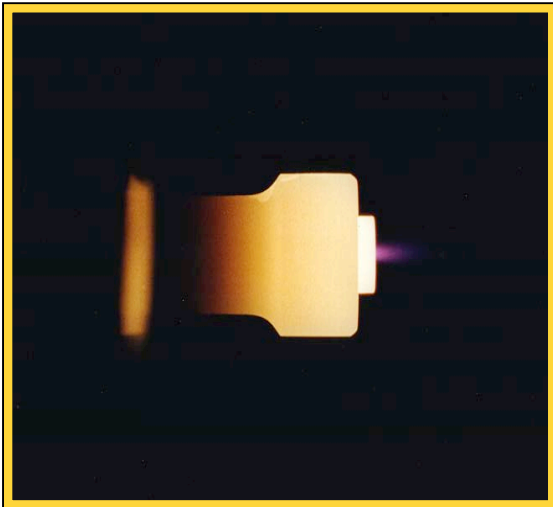
Electric Propulsion Overview

Three Classes of Concepts



Electrothermal:

Gas heated via resistance element or discharge and expanded through nozzle



Examples -

Arcjets
Resistojets
Microwave

Electrostatic:

Ions created and accelerated in an electrostatic field

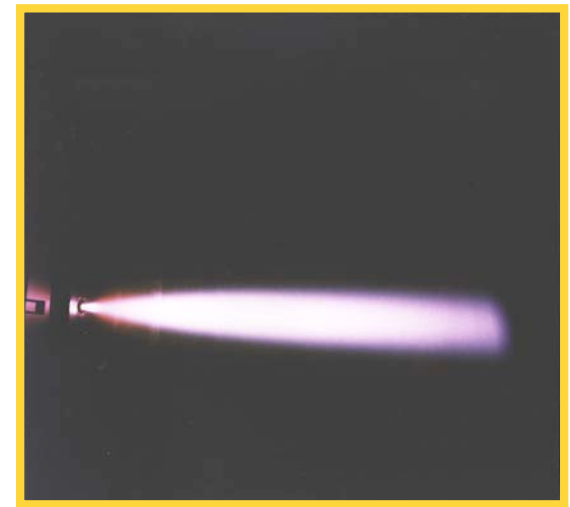


Examples -

Ion Engines
Hall Accelerators

Electromagnetic:

Plasma accelerated via interaction of current and magnetic field



Examples -

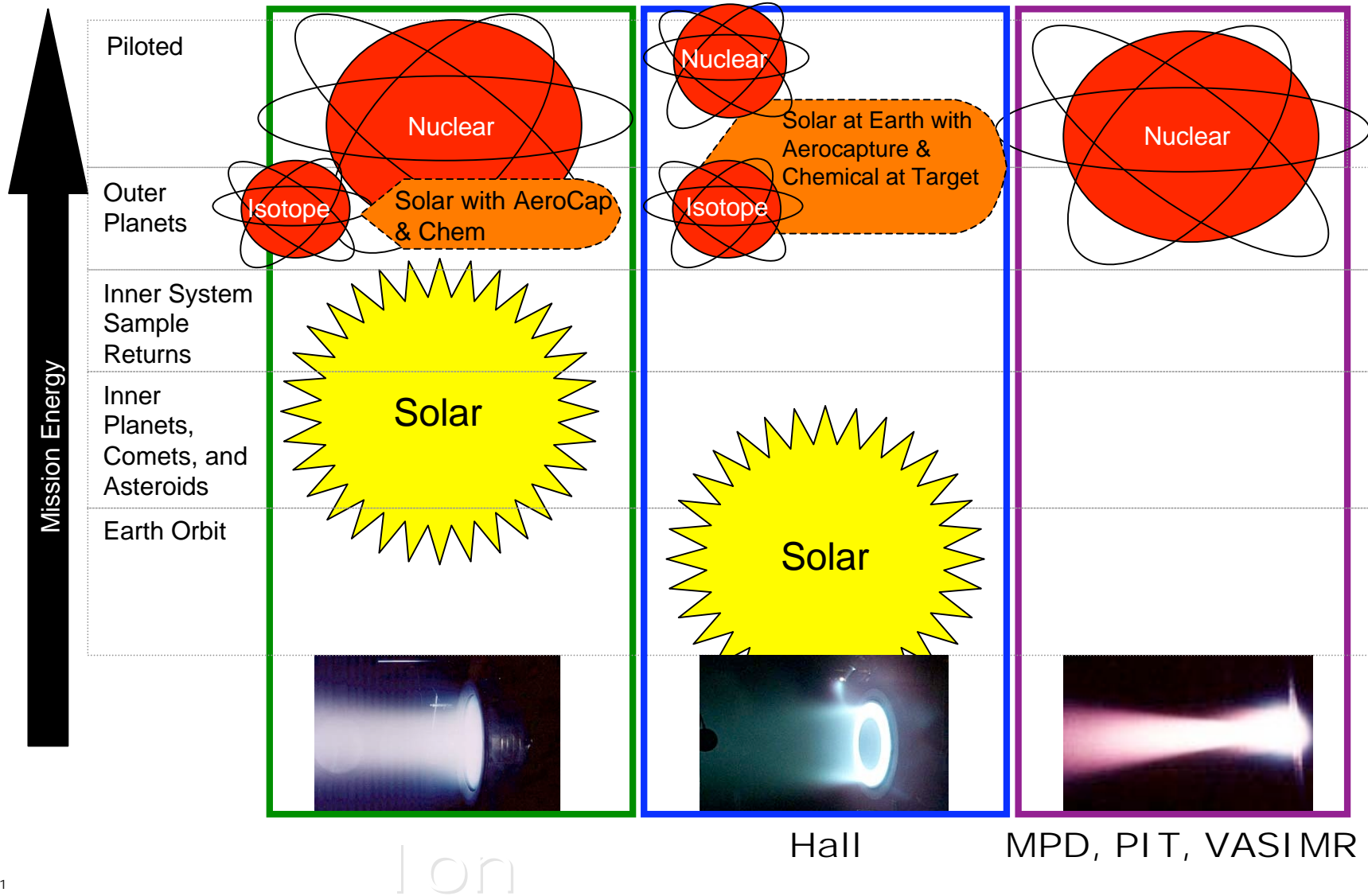
Pulsed Plasma
MPD/LFA
Pulsed Inductive



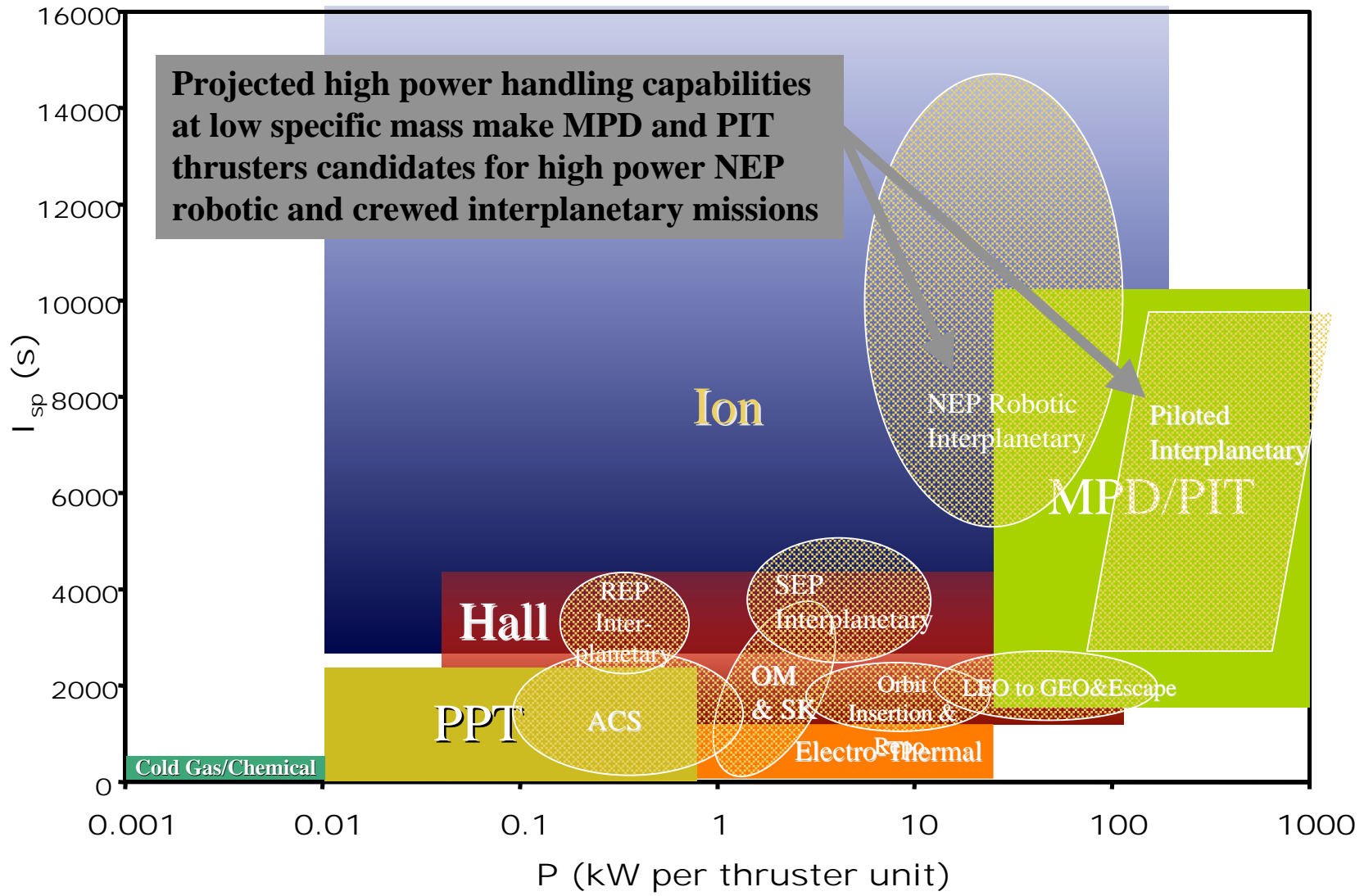
Match the Power System to the Destination

	Main Asteroid Belt	Trojan Asteroids	Centaur Minor Planets	Trans-Neptunian Objects	Kuiper Belt Objects / Comets
	Jupiter and Moons	Saturn and Moons	Uranus and Moons	Neptune and Moons	Pluto/Charon
	<p>Inner Planets</p> <p>Solar Electric Confined to Inner Solar System</p> <ul style="list-style-type: none"> - Also limited reach to large outer planetary bodies with aerocapture (Jupiter, Saturn, Uranus, Neptune only) 			<p>Radioisotope Electric for New Frontiers Class Outer Solar System Missions</p> <ul style="list-style-type: none"> -Targets with low Mass - 500 W Class RTG - <50 kg payload -Delta II Launchers <p>Nuclear Electric for Large Flagship Missions to Outer Planets</p> <ul style="list-style-type: none"> -Large Targets -100 kW Class Reactor ->500 kg Payloads -Delta IV Launch Vehicles 	
	<p>RTG for Surface Lander</p>				

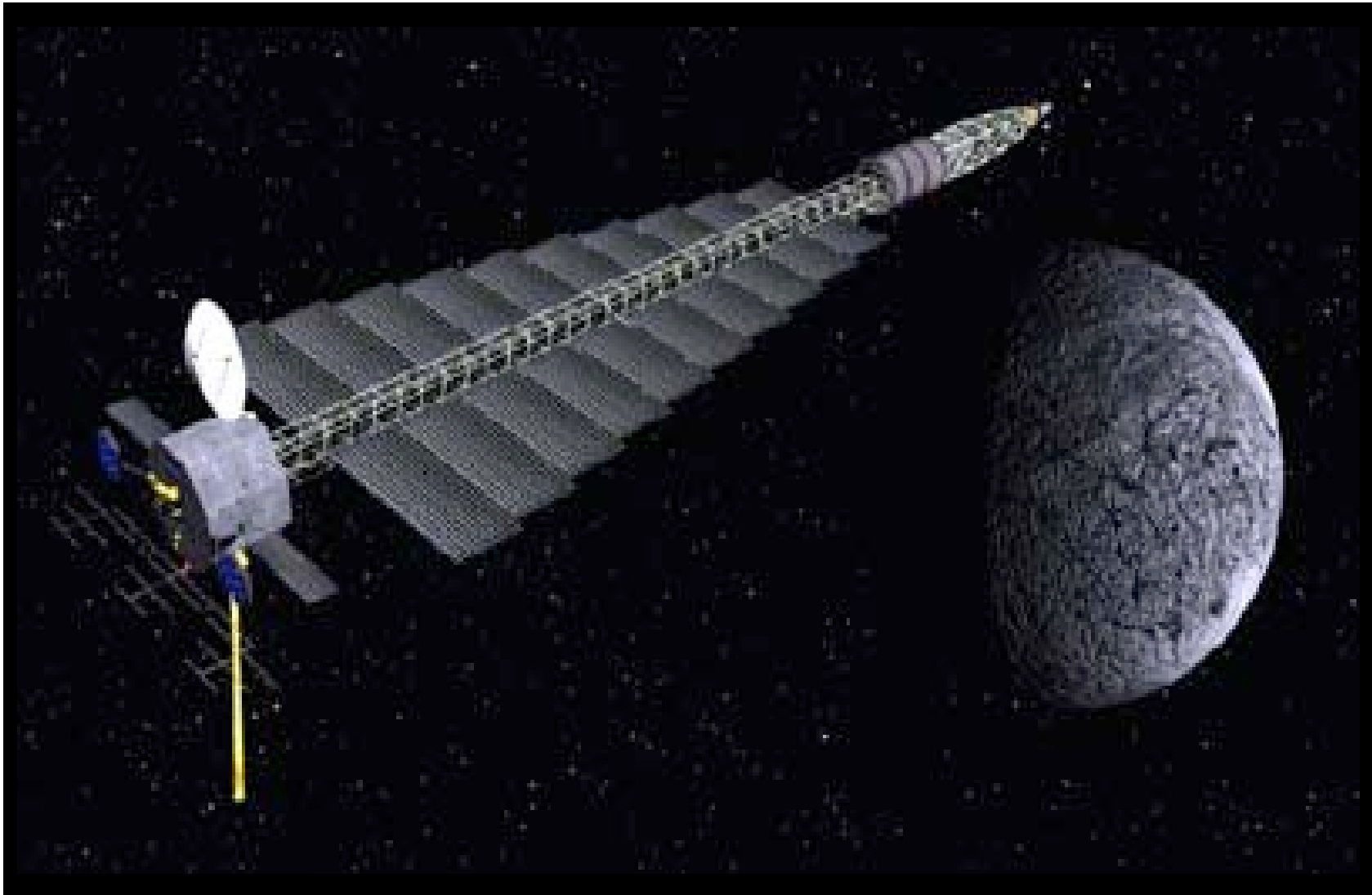
Electric Propulsion and Power Source for Space Missions



Electric Propulsion Performance



Project Prometheus



"Jupiter Icy Moons Orbiter"

Established Nuclear Energy Sources: Fission



= 50 x



Fissioning 12 fl oz (341 ml) of Uranium yields 50 times the energy contained in a Shuttle External Tank
Energy Density: 82 billion joules per gram

- **Overcomes limitations of other candidate power sources**
 - **Chemical:** already near theoretical performance limits
 - **Radioisotopes:** versatile and long-lived, but low power density and limited Pu-238 supply
 - **Natural sources (e.g., solar, EM tethers):** highly dependent on location w/respect to sun or planet
 - **Advanced concepts (e.g., beamed energy, fusion):** too immature, may not work, and/or require substantial in-space infrastructure and investment
- **Greatly extends capability, sophistication and reach of future science missions**
 - **Enables use of high-performance electric propulsion beyond inner solar system**
 - **Provides long-duration, power-rich environments for sophisticated scientific investigations, high-data rate communications and complex spacecraft operations**
- **Improves safety, capability and performance of future human planetary missions**
 - **Power-rich spacecraft and surface operations**
 - **Rapid transportation to reduce extended exposure to solar/cosmic radiation and zero-g**

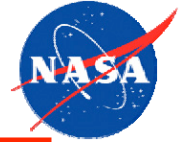
Mission Objectives



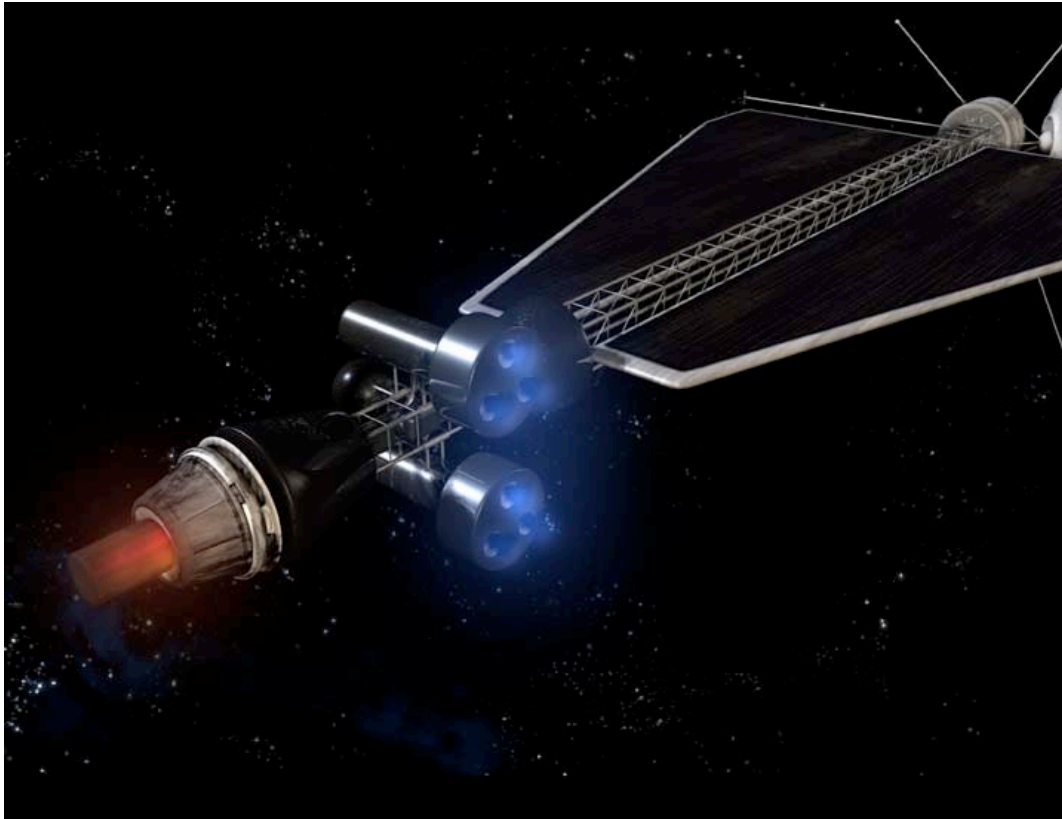
- This mission responds to the National Academy of Sciences' recommendation that a Europa orbiter mission be the number one priority for a flagship mission in Solar System exploration
- JIMO will search for evidence of global subsurface oceans on Jupiter's three icy moons: Europa, Ganymede, and Callisto.
- JIMO will be the first flight mission to use nuclear power and propulsion technologies.
- This mission will set the stage for the next phase of exploring Jupiter and will open the rest of the outer Solar System to detailed exploration.



Nuclear Electric Propulsion



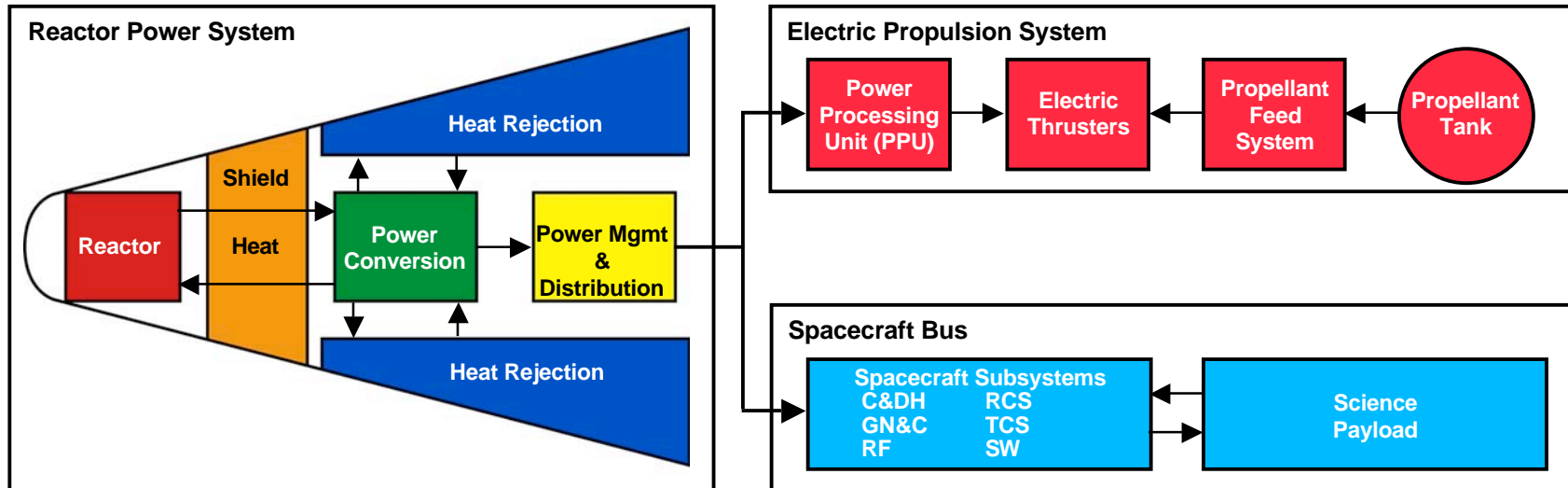
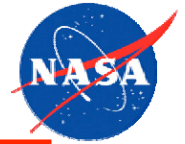
Nuclear Systems Initiative; Revolutionizing Space Exploration



***Broad Set of Concept
Options with Common
Technologies***

- **Faster Missions into Deep Space**
- **Power-rich Spacecraft for Sophisticated Investigations**
- **Ambitious Missions involving Multiple Planetary Destinations**
- **High-data Rate Communication**
- **Civil and Military Power Spinoffs**

Fission Electric Power & Propulsion System Diagram & Representative Technology Options



Reactor

Heat pipe cooled
Liquid metal cooled
Gas cooled

Power Conversion

Thermoelectric
Segmented thermoelectric
Stirling
Brayton
Thermo photovoltaic

Electric Propulsion

Ion thruster
Hall thruster
MPD, PIT

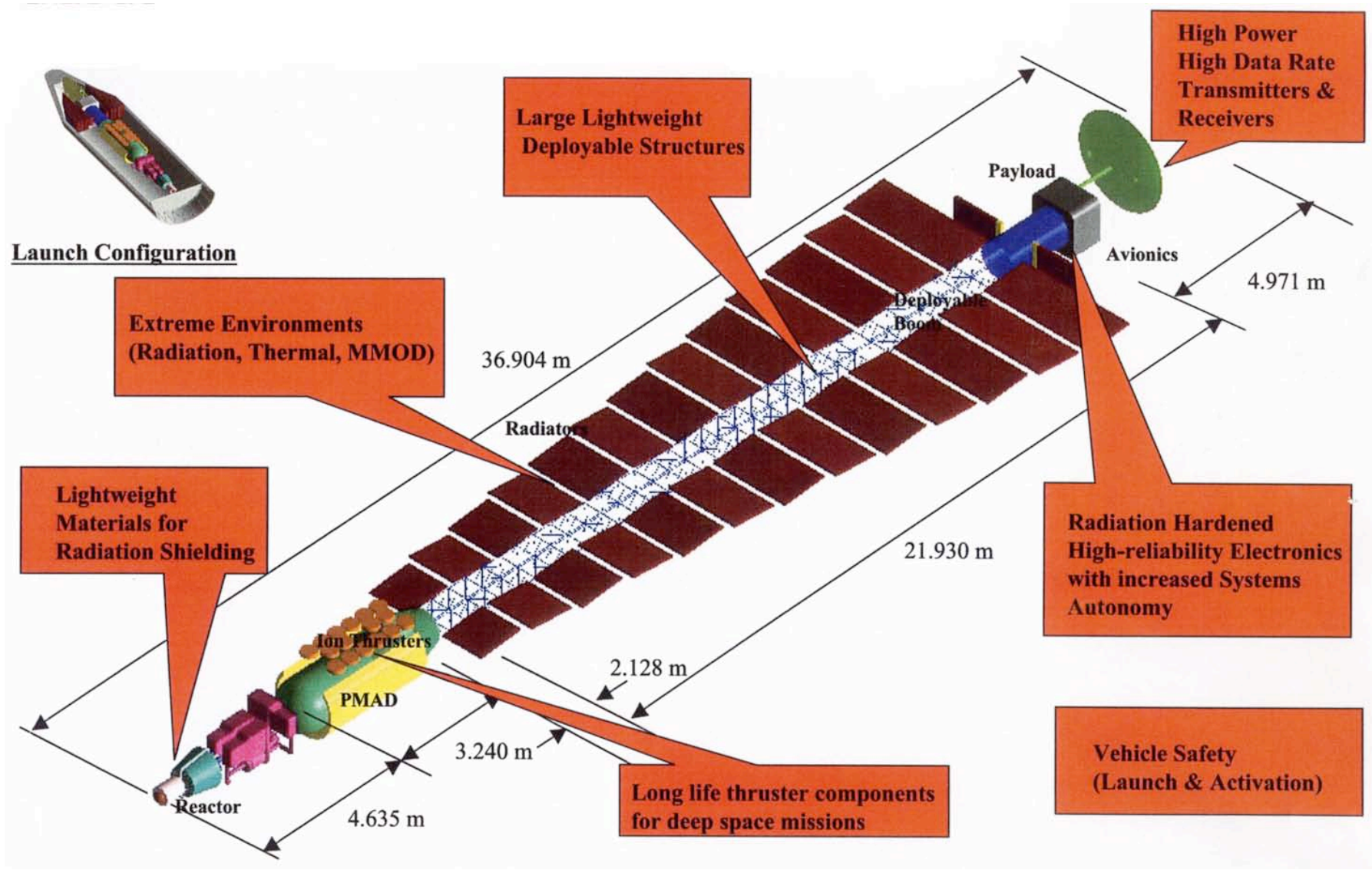
Heat Rejection

2-phase loops (capillary pumped loop, loop heat pipes)
Heat pipes
Pumped loops

Power Management and Distribution

Depends upon power conversion:
AC
DC
Low/high input voltage

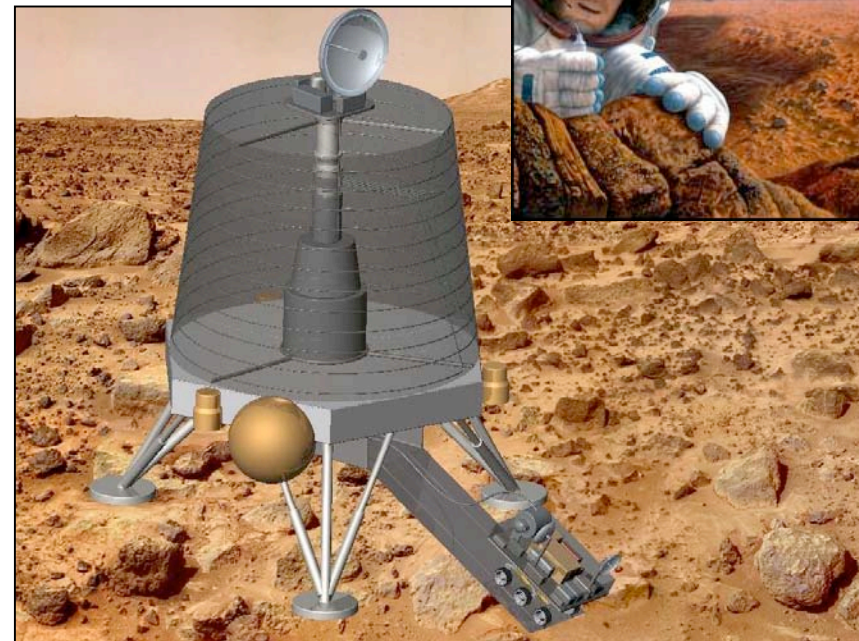
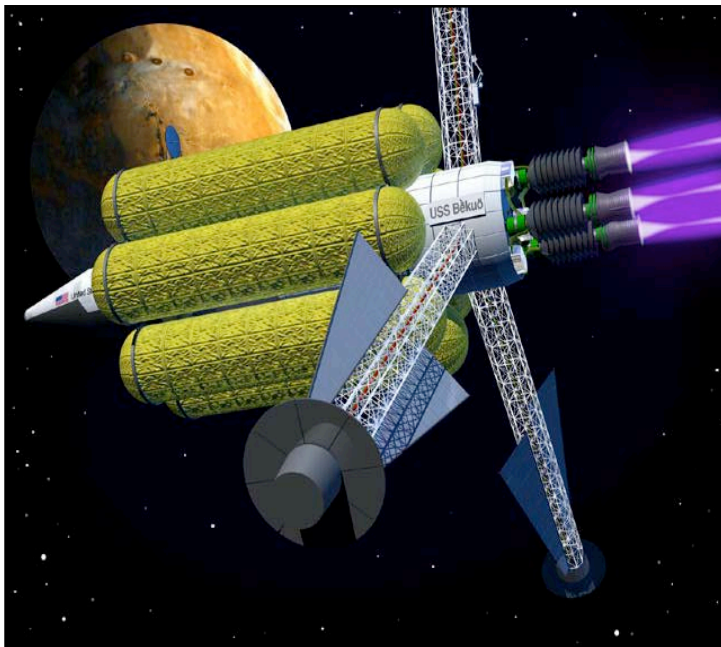
Technical Challenges Required For NEP Systems Development



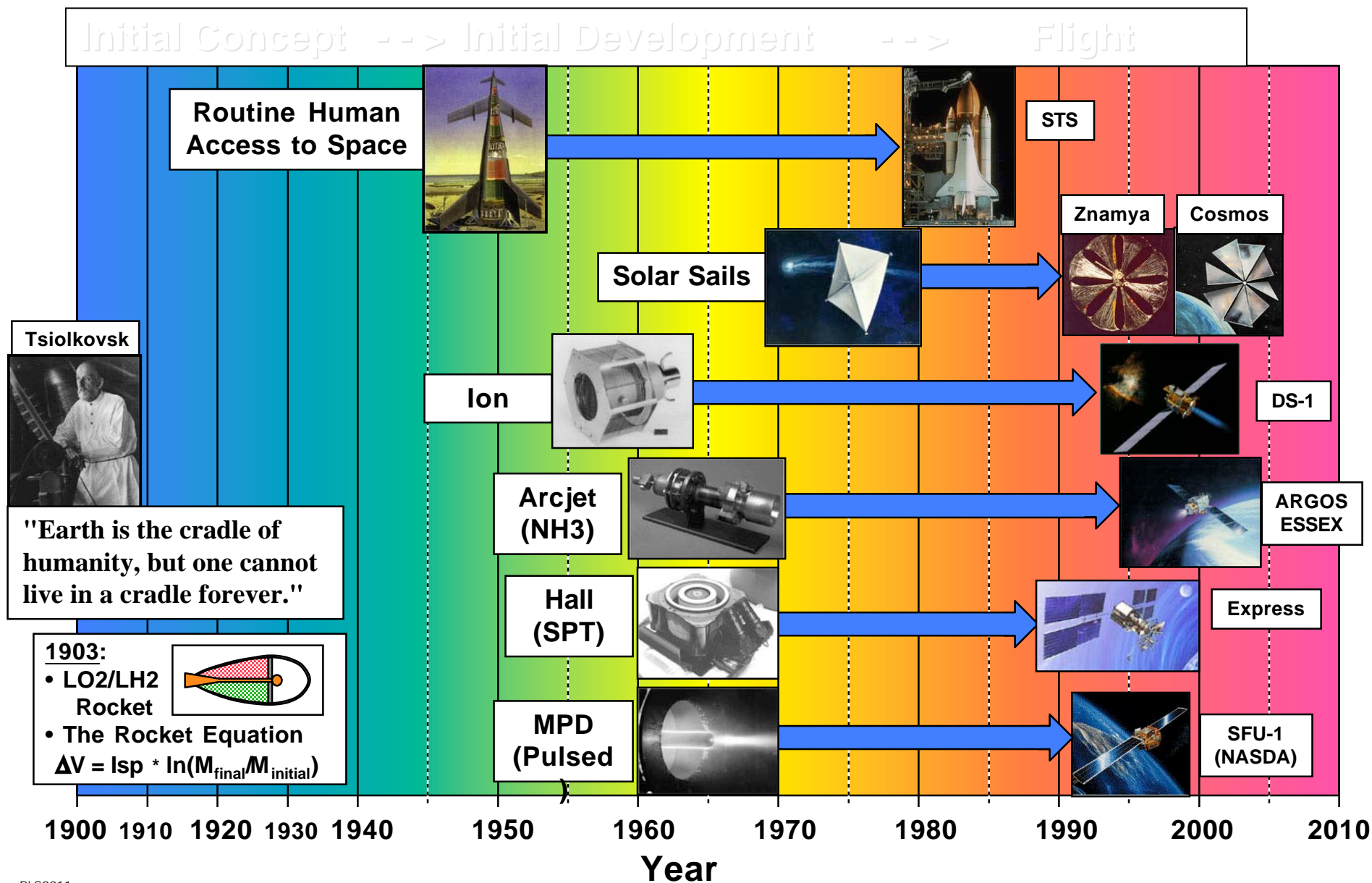
Potential Support to Human Space Exploration



- Nuclear power and propulsion are key enablers of expanded human exploration
 - Enables human exploration beyond earth orbit
 - Provides high power for human protection against charged solar particles
 - Provides abundant power at destination
 - Enables complex, long duration missions
- Nuclear surface power is essential for extended reconnaissance of the Mars surface
 - Long-range surface and sub-surface exploration
 - Human habitat and life support
 - *In-situ* manufacturing of consumables
 - *In-situ* propellant production



Development of Low-TRL Propulsion Technologies Can Take Decades



Propulsion Research

Unlocking the Potential of A Broad Spectrum of Revolutionary Concepts



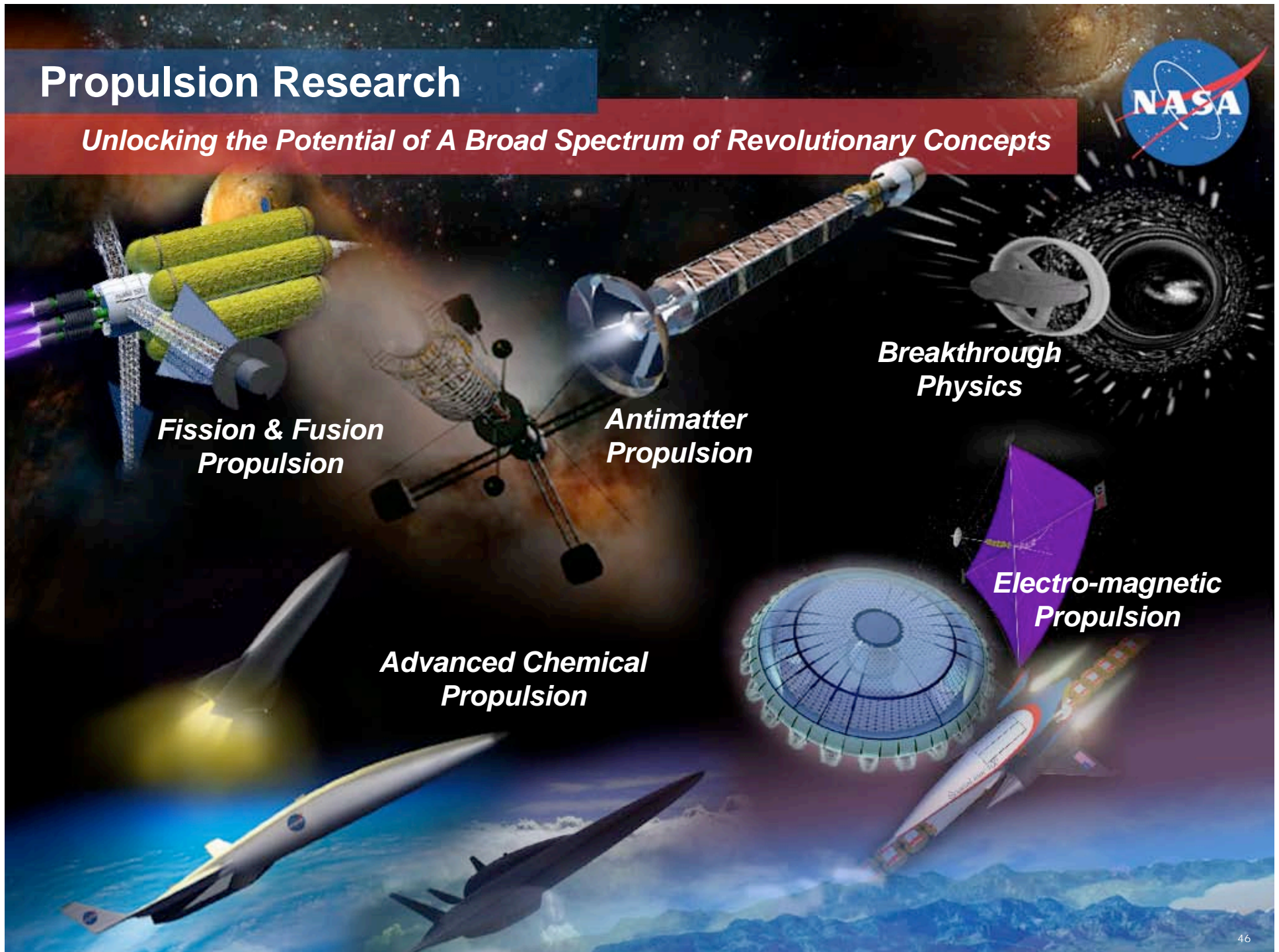
***Fission & Fusion
Propulsion***

***Antimatter
Propulsion***

***Breakthrough
Physics***

***Electro-magnetic
Propulsion***

***Advanced Chemical
Propulsion***



Rocket Engine Prototype (REP) Project Overview

◆ Objectives

- Provide risk mitigation for large class, Oxygen Rich Stage Combustion Engine (ORSC)
- Design and Test a high-fidelity prototype engine
- Validate existing analytical tools
- Develop and validate new analytical tools as required to develop the flight ORSC engine system

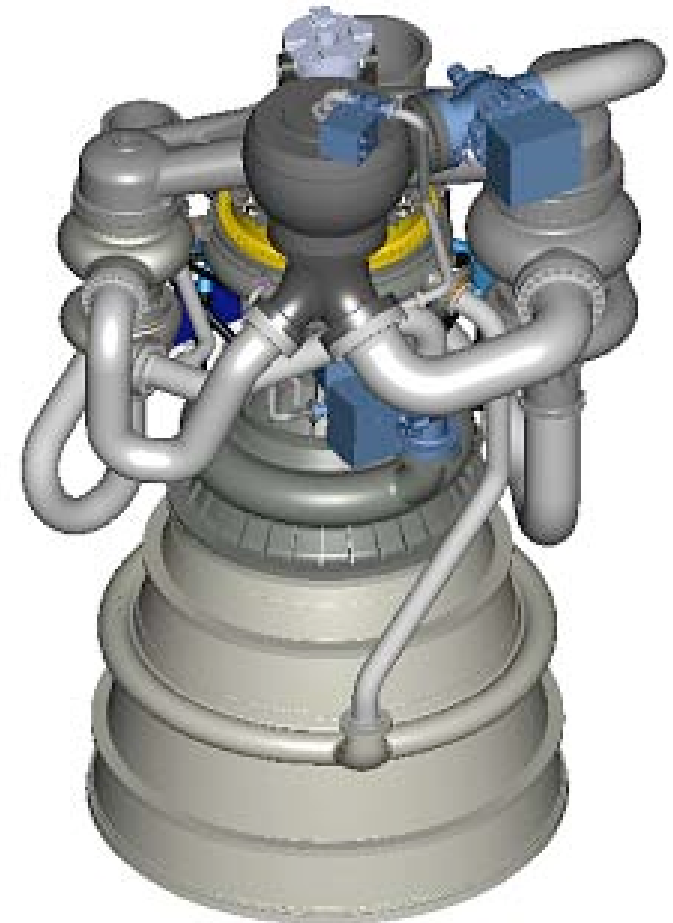
◆ Success Criteria

- ORSC Engine System @ TRL 6 (demonstration in relevant environment)

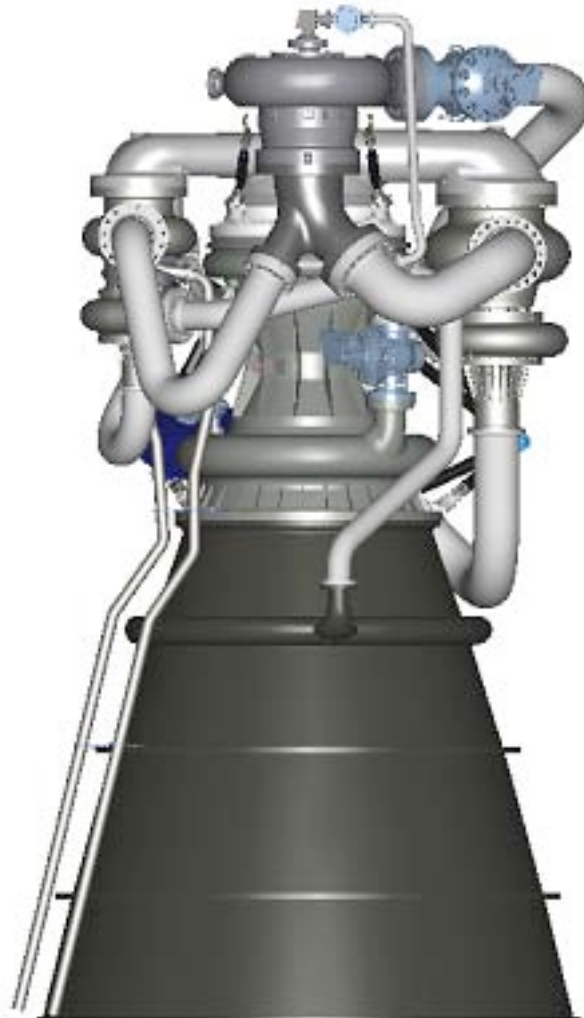
◆ Goals

- Improved Safety
- Reduced Cost
- Improved Operability and Responsiveness

◆ Current Activity limited to Prototype Engine Design and Technology Development



ORSC Prototype Engine Characteristics

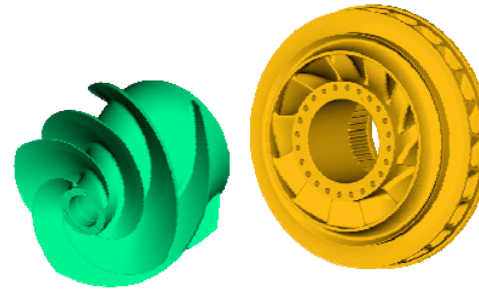


	<u>Prototype</u>	<u>Reference</u>
Thrust		
• Sea Level klb.	1064	1049
• Vacuum klb.	1130	1160
Reliability		
• Failures Per Million Missions traceable		18
Operability		
• Shift turn time	8	8
Specific Impulse		
• Sea level sec.	305	301
• Vacuum sec.	324	335
Weight		
• Dry lbm.	17,922	14,956
Life		
• Missions	100	100
Dimensions		
• Length in.	147	184
• Diameter in.	108	108
• Area Ratio	20:1	36:1

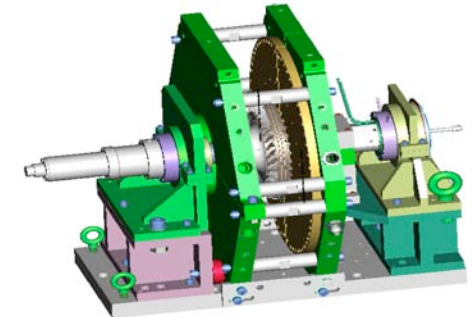
Rocket Engine Prototype Project Overview

◆ Deliverables

- Oxygen Compatible Materials
- Manufacturing Technology Demonstrations
- Turbopump Inducer Waterflow Test
- Turbine Damping “Whirligig” Test
- Single Element Preburner and Main Injector Test
- 40K Multi-Element Preburner and MI
- Full-Scale “Battleship” Preburner
- Prototype Preburner Test Article
- Full-Scale Prototype TCA
- Turbopump Hot-Fire Test Article
- Prototype Engine
- Validated Analytical Models



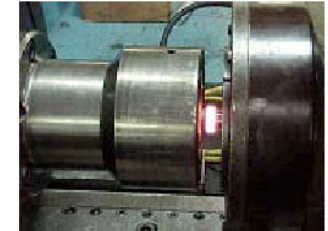
Inducer & Impeller Test Articles



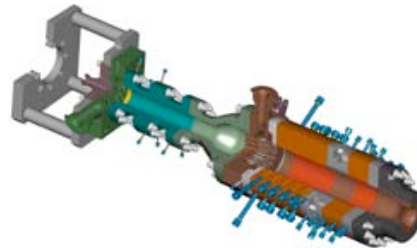
Whirligig Test Article



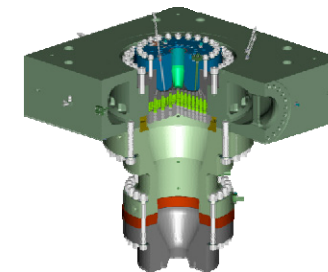
Single Element Test Rig



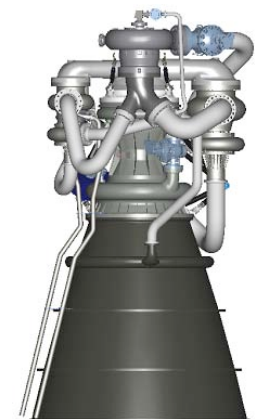
Inertial Weld Sample



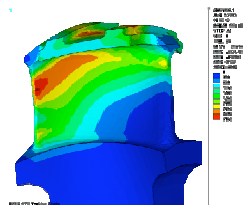
40K Test Rig



Battleship Preburner



Prototype Engine



Turbine Blade Analytical Model

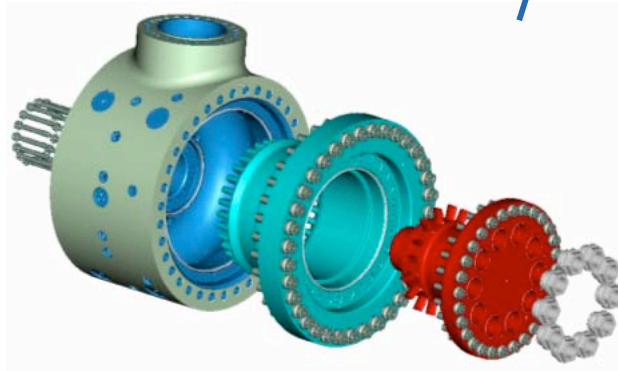
On Current Contract

◆ Full-Scale Preburner

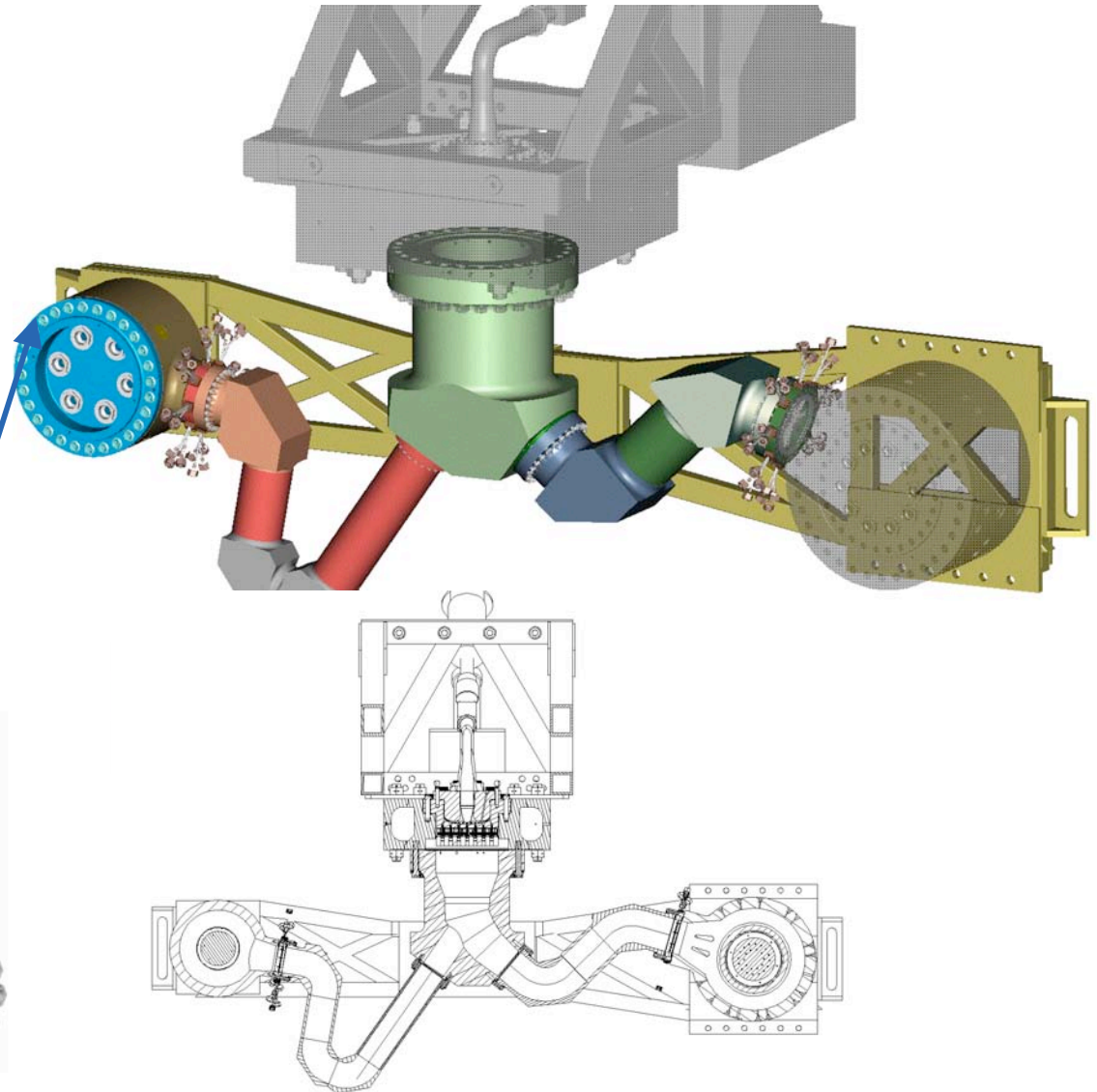
- High fidelity simulation of internal flow geometry
- Injectors, Chamber, Splitter Ducts, and Turbine Simulators

◆ Objectives

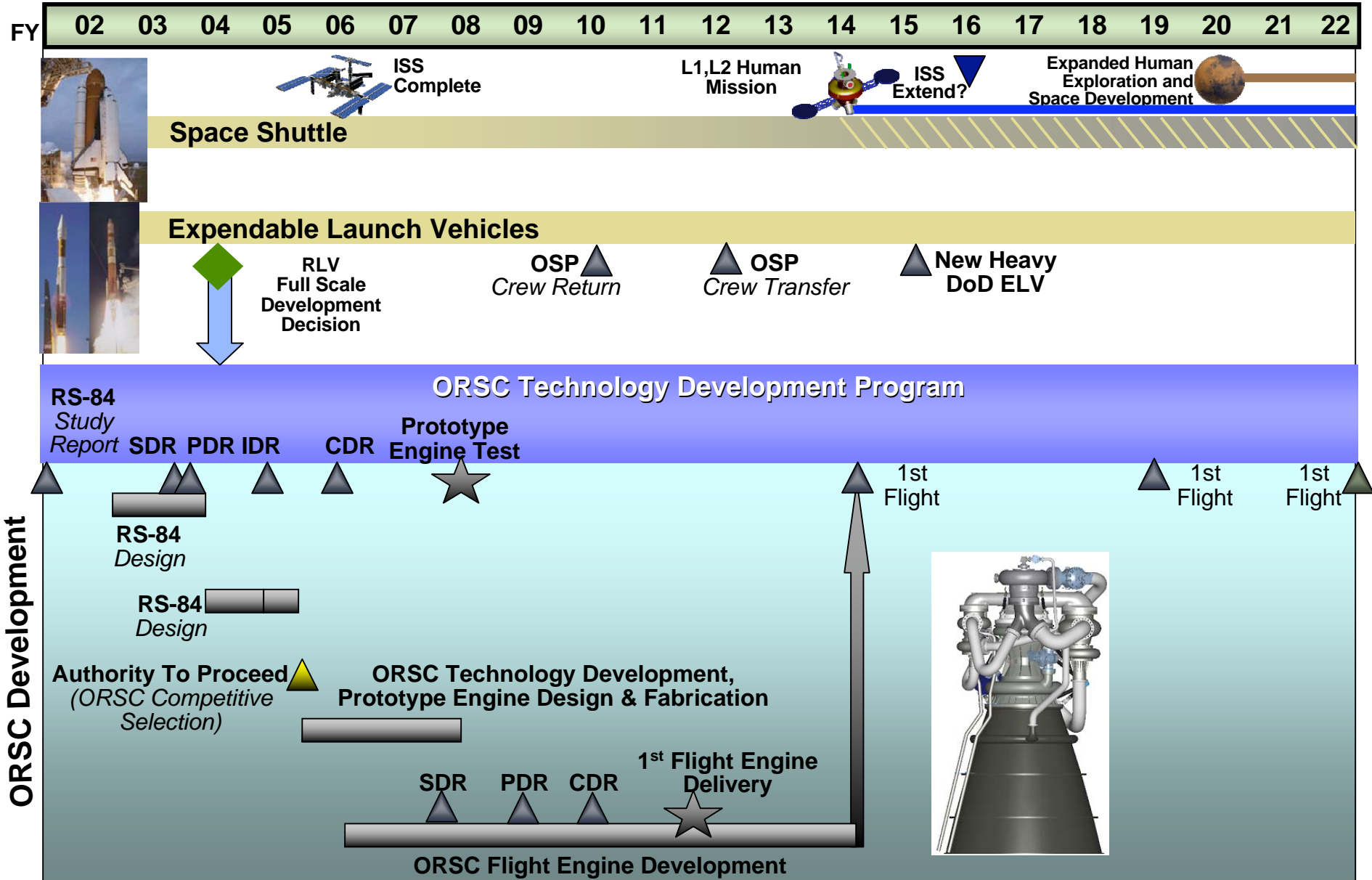
- Stability demonstration
- Flow uniformity at turbine inlets
- Materials usage



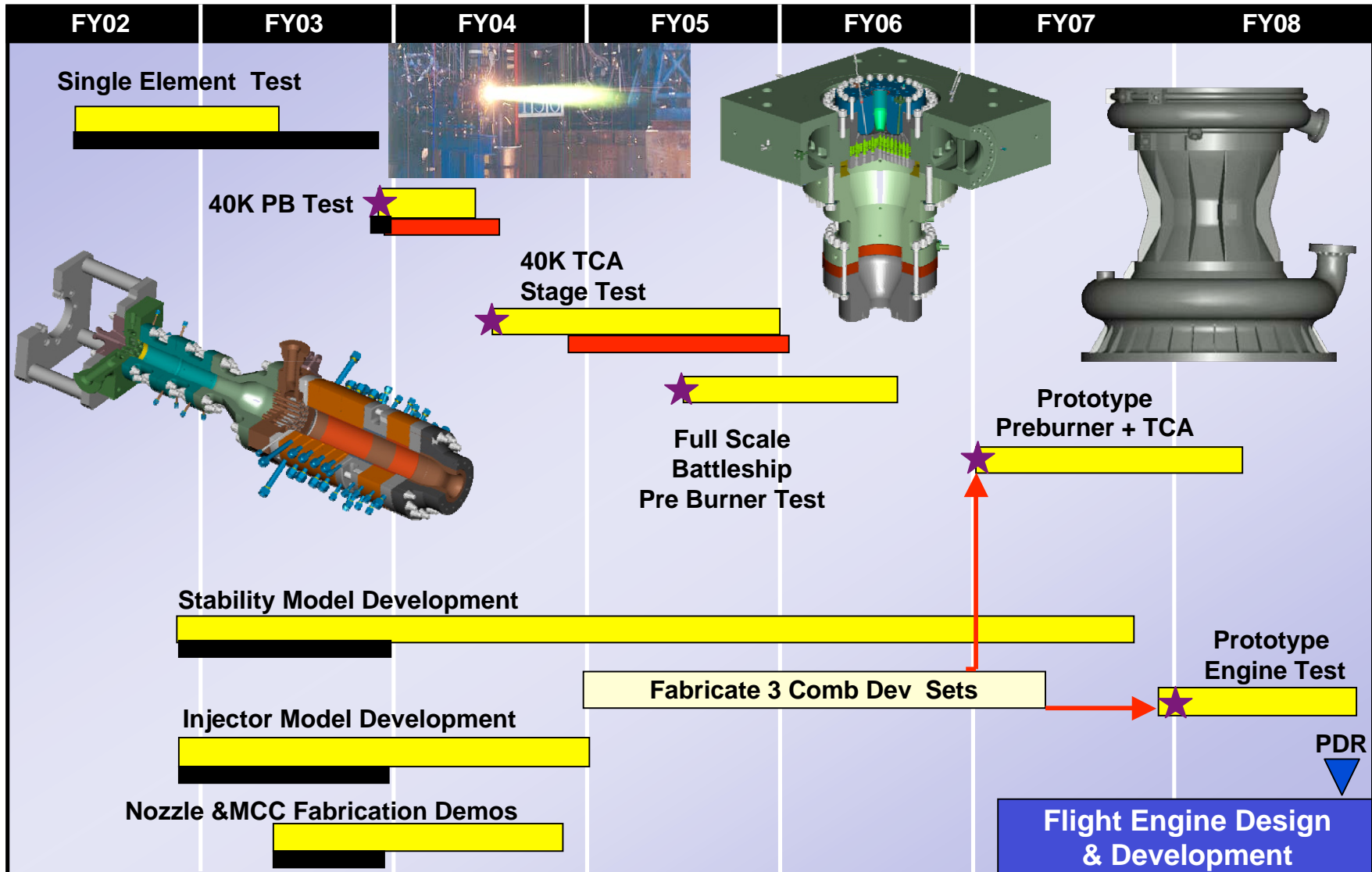
Turbine Simulator



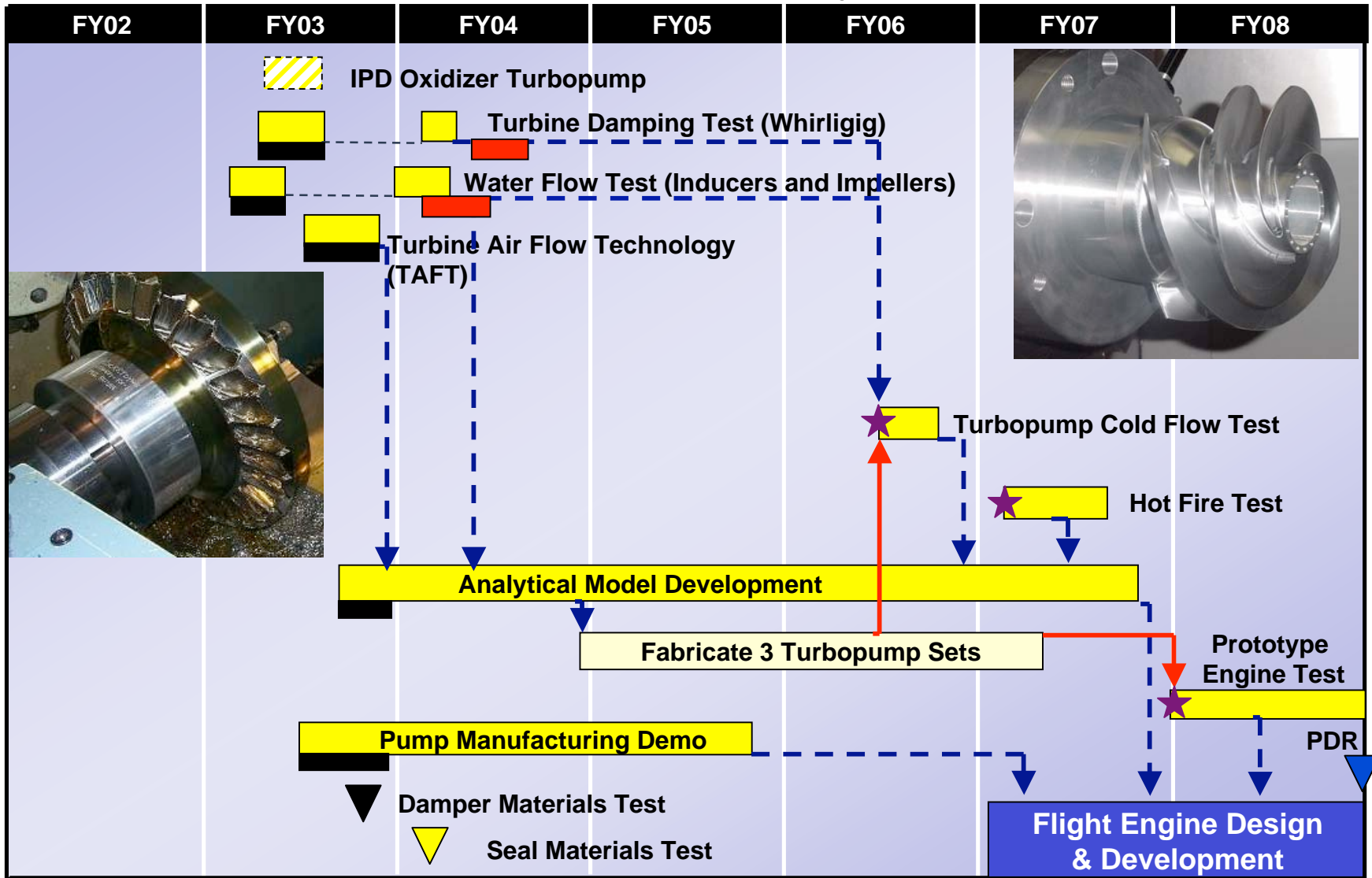
NGLT & REP ORSC Future Space Launch Roadmap



Combustion Devices



Turbomachinery



★ Program Milestone

EUROPEAN SPACE PROPULSION PERSPECTIVE

5TH International Symposium on Liquid Space Propulsion

CHATTANOOGA - OCTOBER 28 2003



European launchers

1979 → 2003

ARIANE 1 → ARIANE 2/3 → ARIANE 4



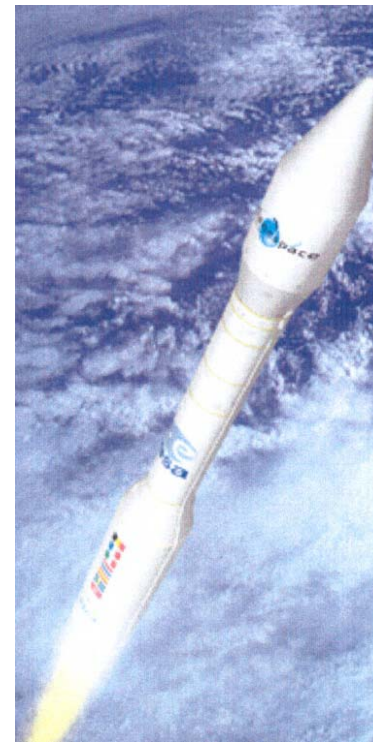
1996 → 2009 →

ARIANE 5 → ARIANE 5 ECA → ARIANE 5 ECB



2006 → ...

VEGA → ...

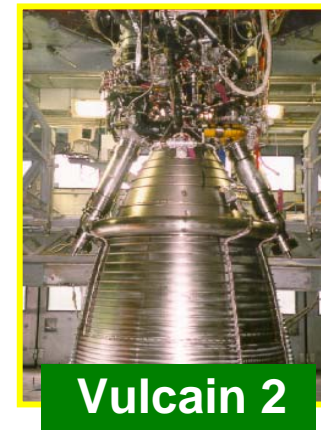
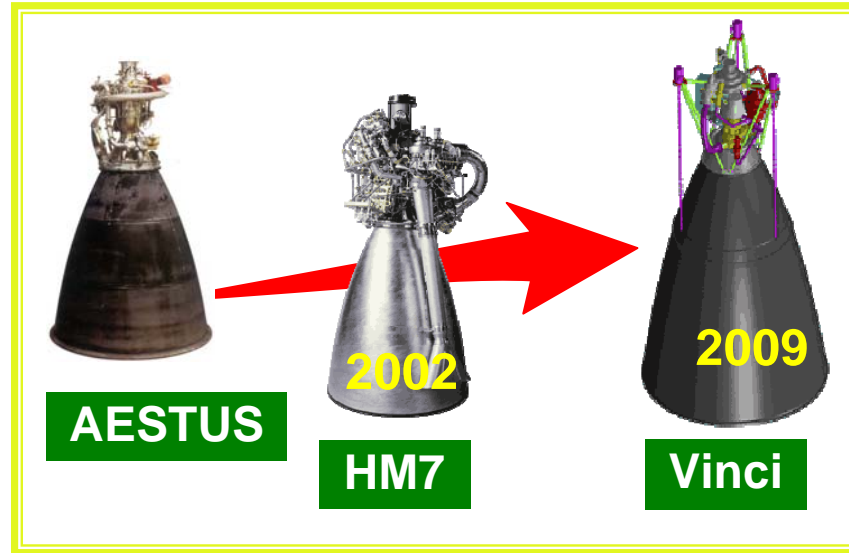
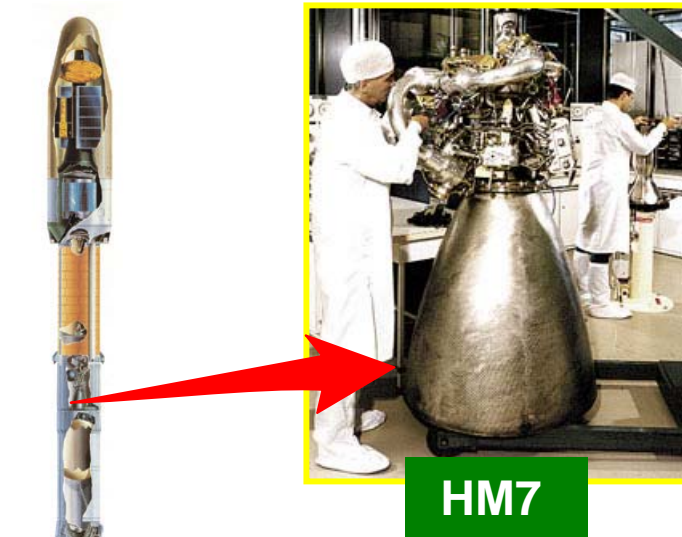


SOYOUZ → ..

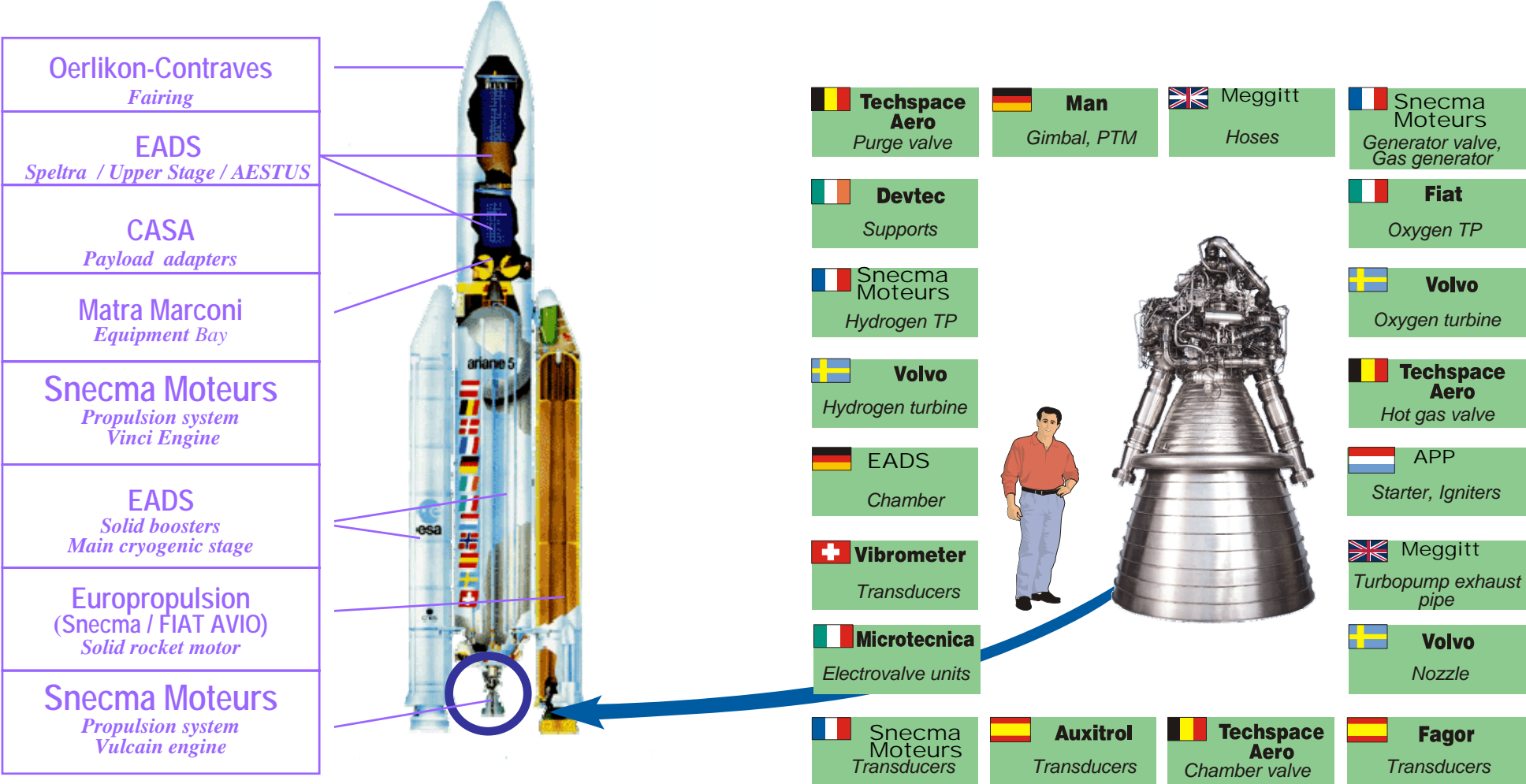


ARIANE LAUNCHERS AND PROPULSION

Ariane's Liquid Rocket Engines




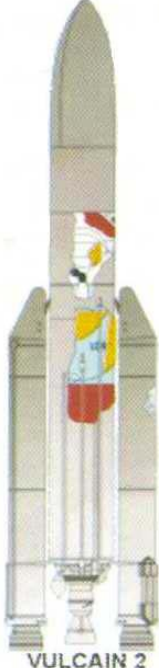

ARIANE 5 main contractors



Ariane 5 Prime Contractors

Snecma leads a European cooperation on the Vulcain engine

Ariane 5 - 1996 → 2009

ANCHER	A5G		A5ECA		A5NG	
PER POSITE	GTO PAYLOAD	6,2	9,5		12	
	STAGE	EPS	ESC-A		ESC-B	
	ENGINE	AESTUS	HM7B		VINCI	
OWER POSITE	SOLID PROPELLANT MASS	238	241	ESCA	241	ESCB
	LIQUID PROPELLANT MASS	158	174		176	
	ENGINE	VULCAIN 1	VULCAIN 2		VULCAIN 2	
AUNCH	1996		2002		2009	
						
	VULCAIN 1		VULCAIN 2		VULCAIN 2	

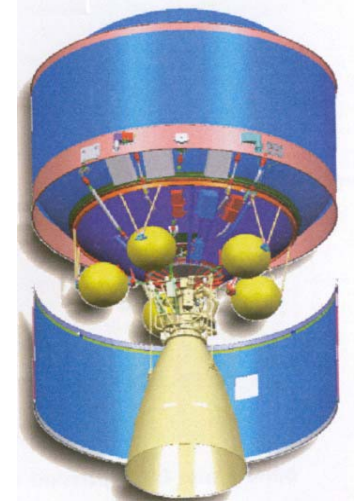
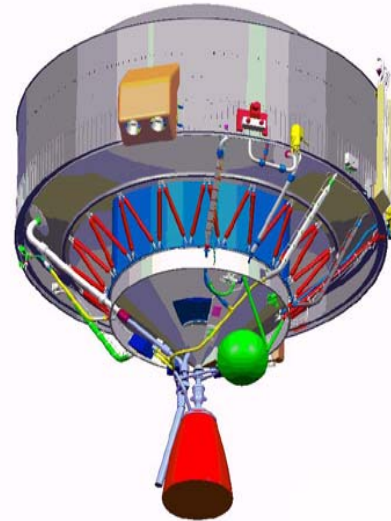
From Vulcain to Vulcain 2



	VULCAIN	VULCAIN 2
Thrust	1150 kN	1250 kN
Isp	431 s	434 s
Mass	1700 kg	2040 kg
Type	Gas generator open cycle	Gas generator open cycle
Fuel and oxidizer	LOX - LH2	LOX - LH2
Chamber pressure	110 bar	115 bar
Production	over 38 engines produced	



ARIANE 5 upper stages



STAGE
STAGE PRIME
ENGINE
ENGINE PRIME
TURBOPUMPS
CHAMBER/NOZZLE

EPS
EADS ST
AESTUS
EADS ST
/
EADS ST

ESCA
EADS ST
HM7
SNECMA
SNECMA
EADS ST

ESCB
EADS ST
VINCI
SNECMA
SNECMA/AVIO
EADS ST/SNECMA

European Space Ministers Conference the 27th of May 2003

- ⇒
- **Restructuring of the Ariane launcher sector**
 - Qualification of the Ariane 5 ECA launcher*
 - Reorganisation of the Ariane launcher sector*
 - Sustaining guaranteed access to space with Ariane 5*
 - **Unblocking of the ISS exploitation programme (2002 - 04)**
 - **Relations between the European Space Agency and the European Union**
 - **2010 perspectives for the European launcher sector**
 - Future launchers preparatory programme (FLPP)*
 - Soyuz at the CSG.*

Ariane 5NG : A new step to answer market needs in 2020

GTO dual launch for 2 medium heavy satellites (6 + 6t) }
 for one heavy + one medium (7 + 5 t) } **12 t GTO**

Flexibility for **new missions** and orbits

Galileo GPS orbit (24 000 / 24 000 km)
High perigee GTO orbits for satellites
with electrical propulsion
Different missions on the same flight
(GTO + scientific probe)

Upper stage
multiple
reignition

Modified cryogenic upper stage ESCA → **ESCB**

New restartable **VINCI** engine (18t thrust)

Same **cost** as ESCA 6 t thrust engine
Increased **reliability**
Better **produceability**.

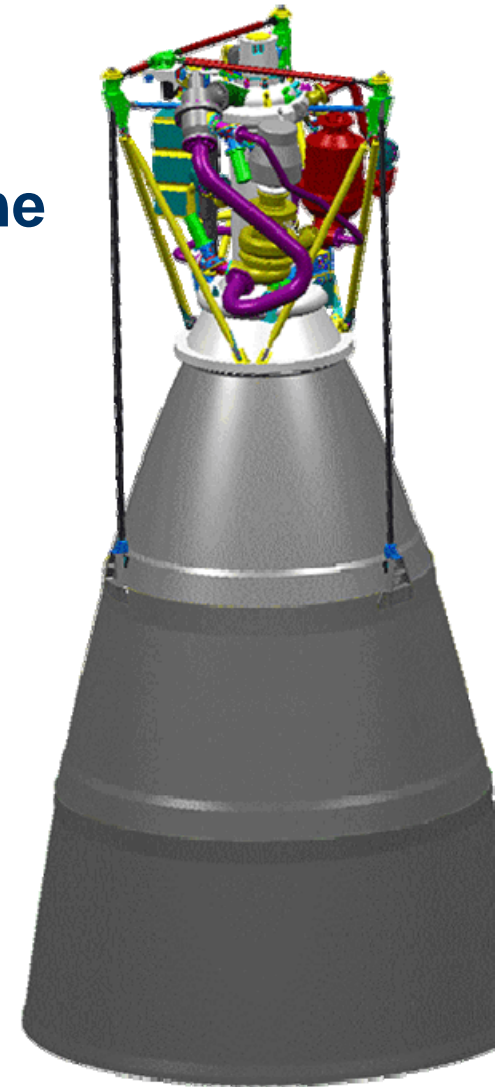


Vinci Engine

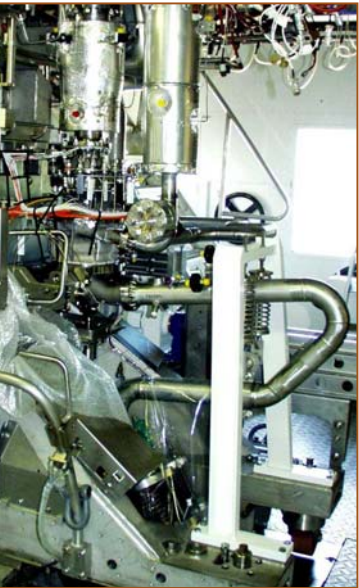


The Ariane 5 upper stage cryogenic engine

Thrust	: 180 kN
Isp	: 464 s
Cycle	: Expander
Re-ignitions	: 5 times
Fuel and oxidizer	: LOX - LH2
Chamber pressure	: 60 bar
Nozzle Extension	: Extendible (240:1)



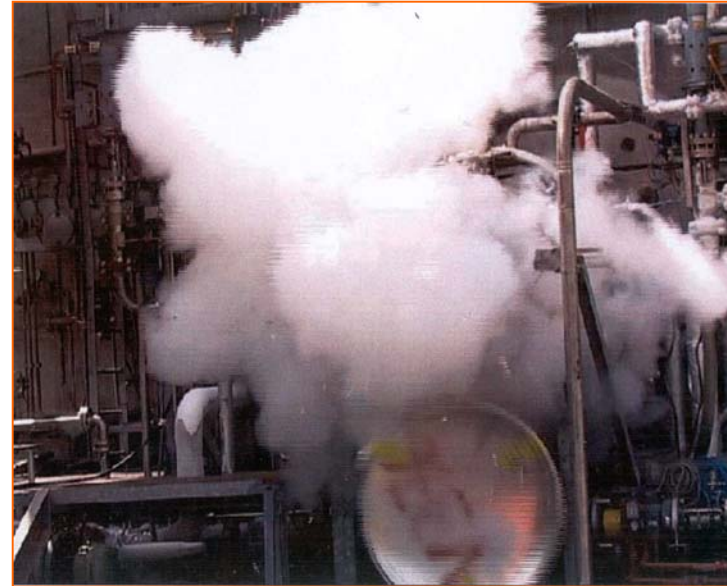
Vinci hardware already in testing



TPH tested



TPO tested



Chamber tested

1st engine assembled



P4-1 test facility (DLR)

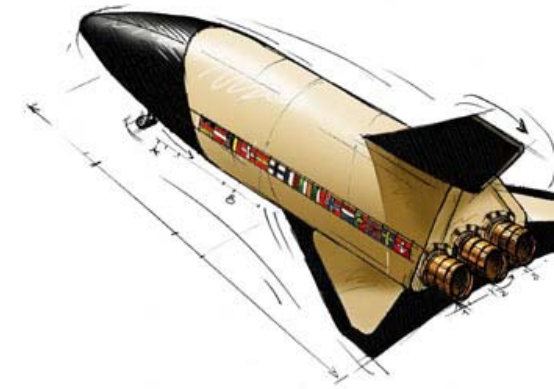


Testing in 2004



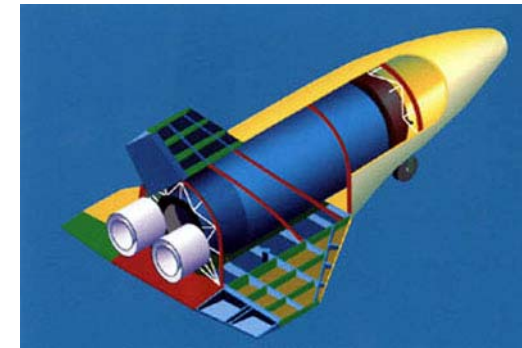
And after 2010

- ⇒ Ariane 5 new evolution
or
 - ⇒ New Expendable Launcher
or
 - ⇒ Totally or partially reusable launcher
- ➤ Preparation in the frame of the Future Launcher Preparatory Programme (FLPP). Three years programme decided at the May 2003 Ministerial Conference



FLPP Content

- Propulsion technologies
- Reusable stages
- Flight demonstrators



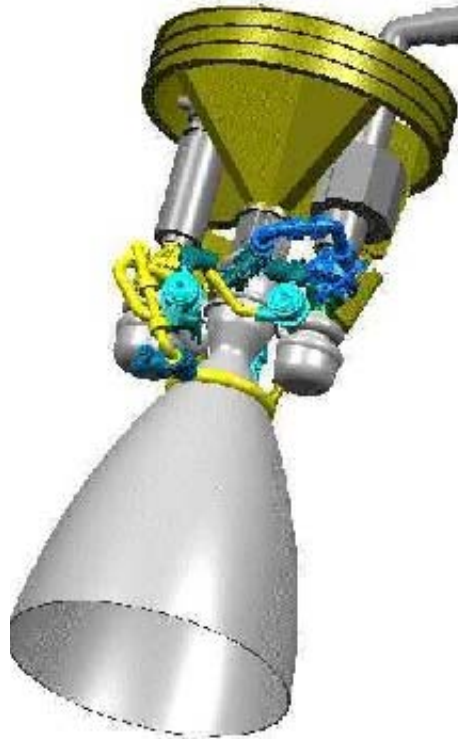
A cooperative effort with Russia

High thrust cryogenic engines for the next 20 years answering to the most probable needs

VULCAIN



**VEDA
MC 2000 E**



**VOLGA
MX 4000**

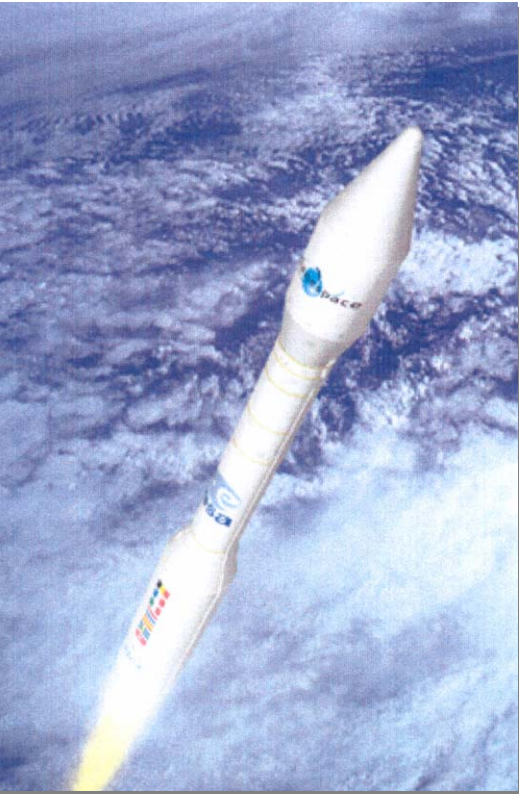


**VIKING K
MBC 2000**



Propellant	LOX / LH2	LOX / LH2	LOX / CH4	LOX / LH2
Thrust (kN)	≤ 1500	2000	2000 - 4000	2000 - 4000
Specific impulse (s)	≤ 440	> 450	> 360	> 400
Mass (kg)	< 2500	< 3000	< 5000	< 6000
Design objective	Ariane 5 main engine	Higher performance reusable engine for 1 st and 2 nd stages possible expendable version	Higher density propellants reusable engine for 1 st stage	Low cost cryogenic engine for expendable launch

VEGA small launcher



- Payload : 1500kg in LEO 700 km
- First flight : 2006
- Italian share : 65%
- Configuration :

	1 ST STAGE P80FW	2 nd STAGE Z23	3 rd STAGE Z9	4 th STAGE AVUM
Propellant	SOLID	SOLID	SOLID	LIQUID
Prop Mass ('T)	88	24	9	0,39
Thrust (kN)	2100	935	221	2,35



- Launcher development contract : ESA → ELV (70% AVIO, 30% ASI)
- 1st stage development contract : CNES → AVIO
 - ↳ P80 is also a technology demonstrator for Ariane 5
- AVUM upper stage developed by AVIO with Ukrainian NPO Yuzhnoye

MAIN NATIONAL ACTIVITIES IN EUROPE

SWEDEN

- **VOLVO** involved in the PW RL 60 programme (Nozzle) in bilateral (with germany) and multinational technological activities on flow separation control devices nozzles



BELGIUM

- **TECHSPACE AERO** involved in the PW RL 60 programme (Valves)

NEDERLANDS

STORK involved in technological activities on LOX/LH2 and LOX/HC igniters

GERMANY

EADS Space transportation and DLR involved in the TEHORA program with Russia (ROSAVIKOSMOS and CADB) in preparation for FLPP :

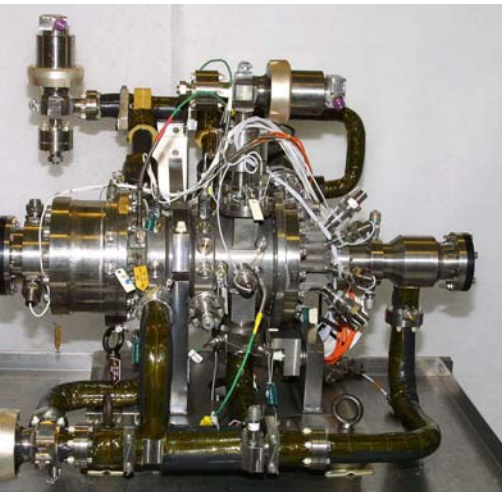
- experimentation on LOX/HC (Kerosene and methane) injectors and combustion chambers
- TEHORA 3 (3rd step in the program) signed in August 2003.
- DLR is conducting in house technological activities on combustion and combustion chambers



FRANCE

- CNES is managing technological activities with SNECMA Moteurs and EADS Space Transportation and scientific organizations (ONERA, CNRS).

Preliminary work with Russia (VOLGA Programme) has started in 2002 for FLPP program preparation.



TP Tech integrated component tester

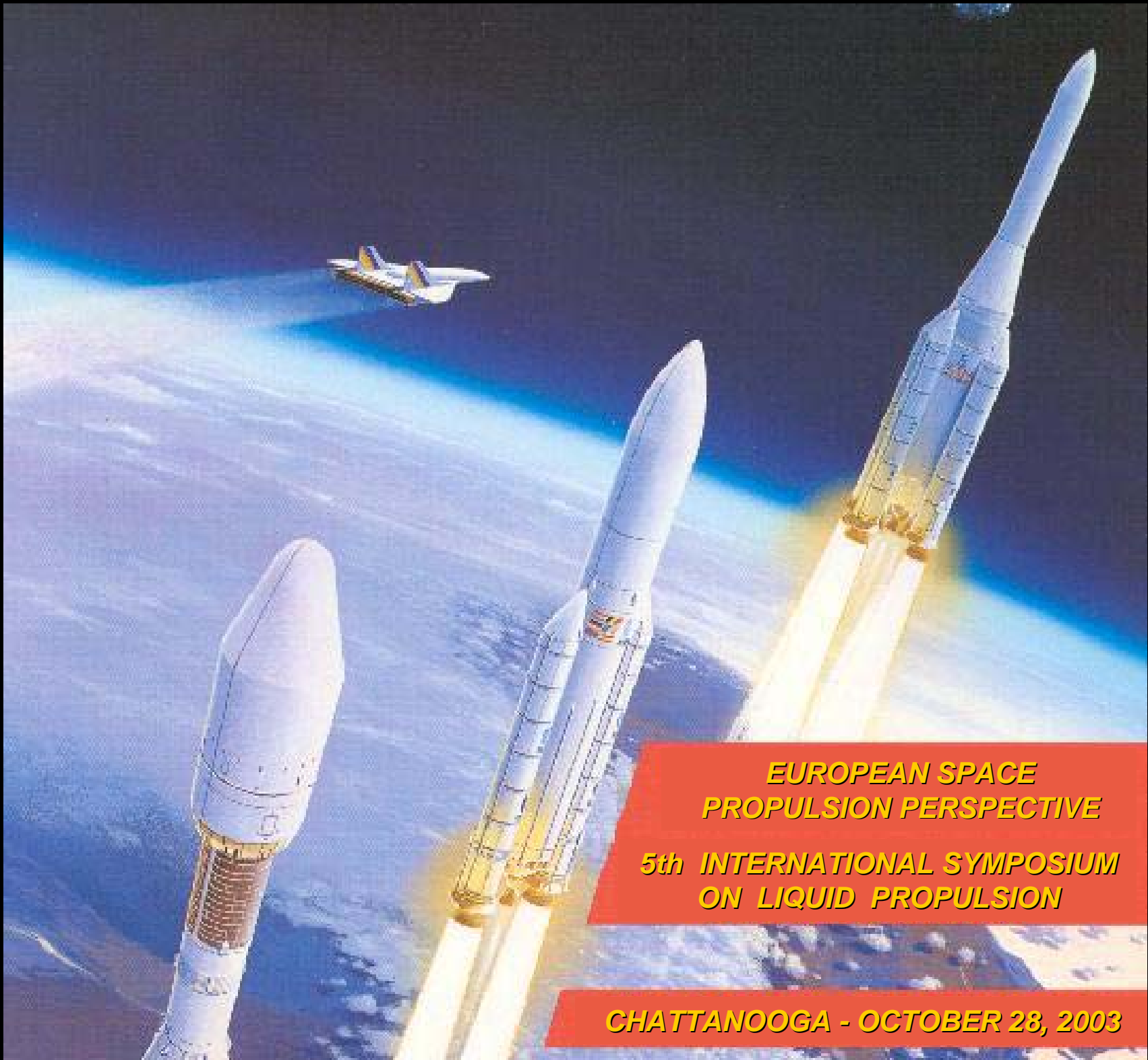


Low cost gas generator

Test at DLR



Snecma Moteurs
snecma group



**EUROPEAN SPACE
PROPULSION PERSPECTIVE**

**5th INTERNATIONAL SYMPOSIUM
ON LIQUID PROPULSION**

CHATTANOOGA - OCTOBER 28, 2003

Overview of Japanese Research and Development Program on Liquid Rocket Engine Combustor

K. Hasegawa, A. Kumakawa, T. Onodera, T. Shimizu,
Y. Watanabe, T. Tomita, H. Taniguchi, Y. Naruo



Japan Aerospace Exploration Agency

5th International Symposium
on Liquid Space Propulsion
Oct 27 – 30, 2003 / Chattanooga, TN

New Organization “JAXA” was Born on Oct 1, 2003

National
Aerospace
Laboratory
of Japan



Institute of
Space and
Astronautical
Science

National
Space
Development
Agency of
Japan

Japan Aerospace Exploration Agency

Web Site <http://www.jaxa.jp/>

Focus on Following Six Topics



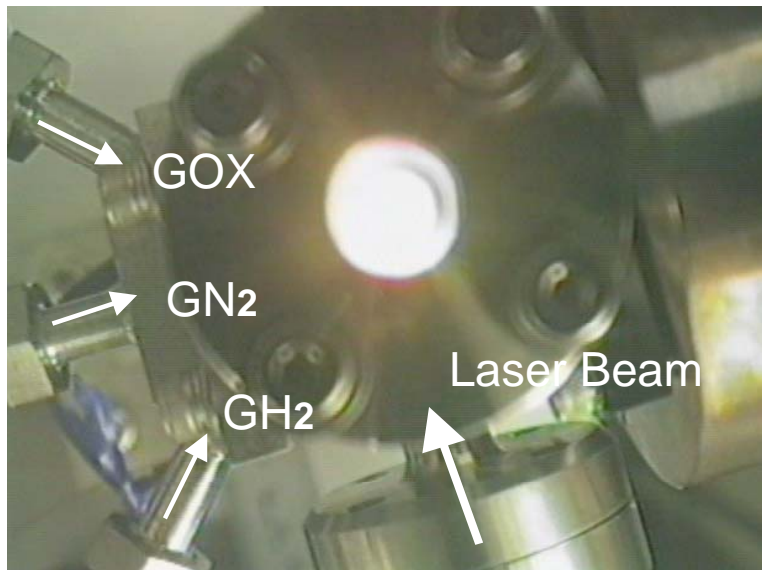
- (1) Laser Ablation Ignition
- (2) Extendible Nozzle and Dual-Bell Nozzle
- (3) LE-7A Nozzle Flow Separation Phenomenon
- (4) Low Cycle Chamber Pressure Fluctuation
- (5) LOX/LH₂ Engine for Reusable Vehicle Test
- (6) Study of Advanced Expander Bleed Cycle

(1) Laser Ablation Ignition

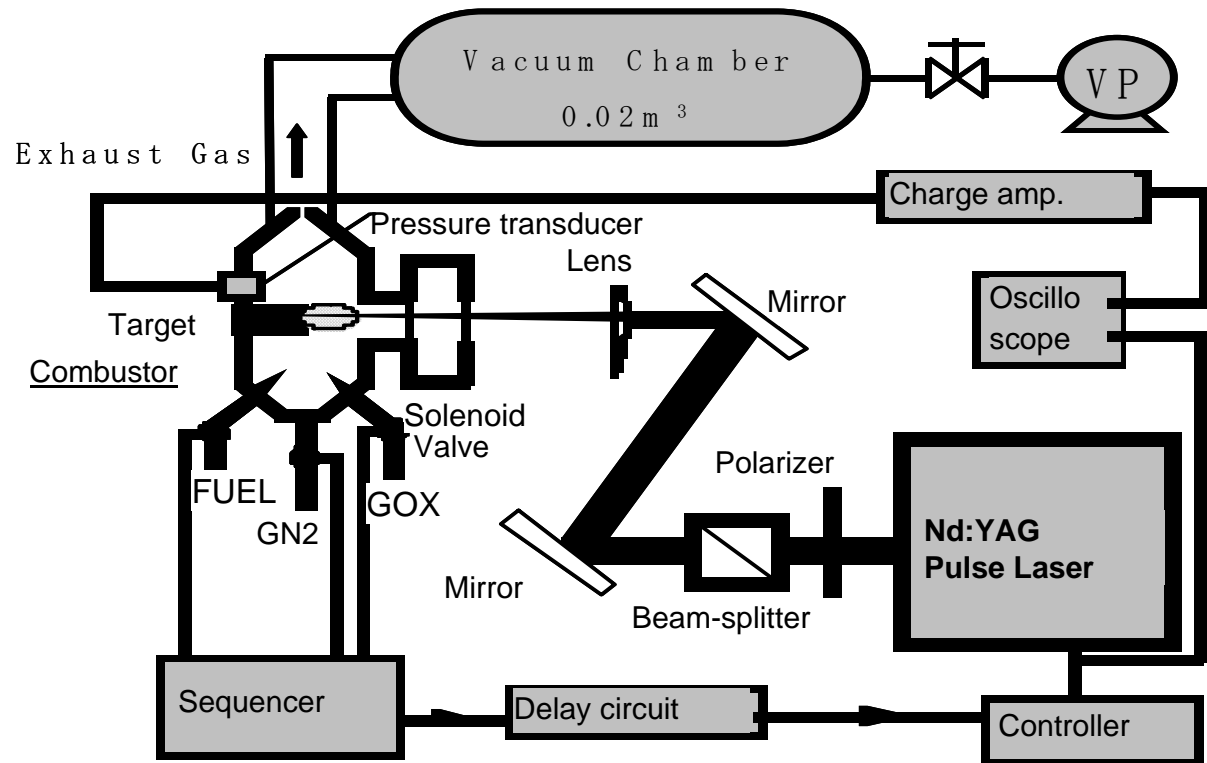


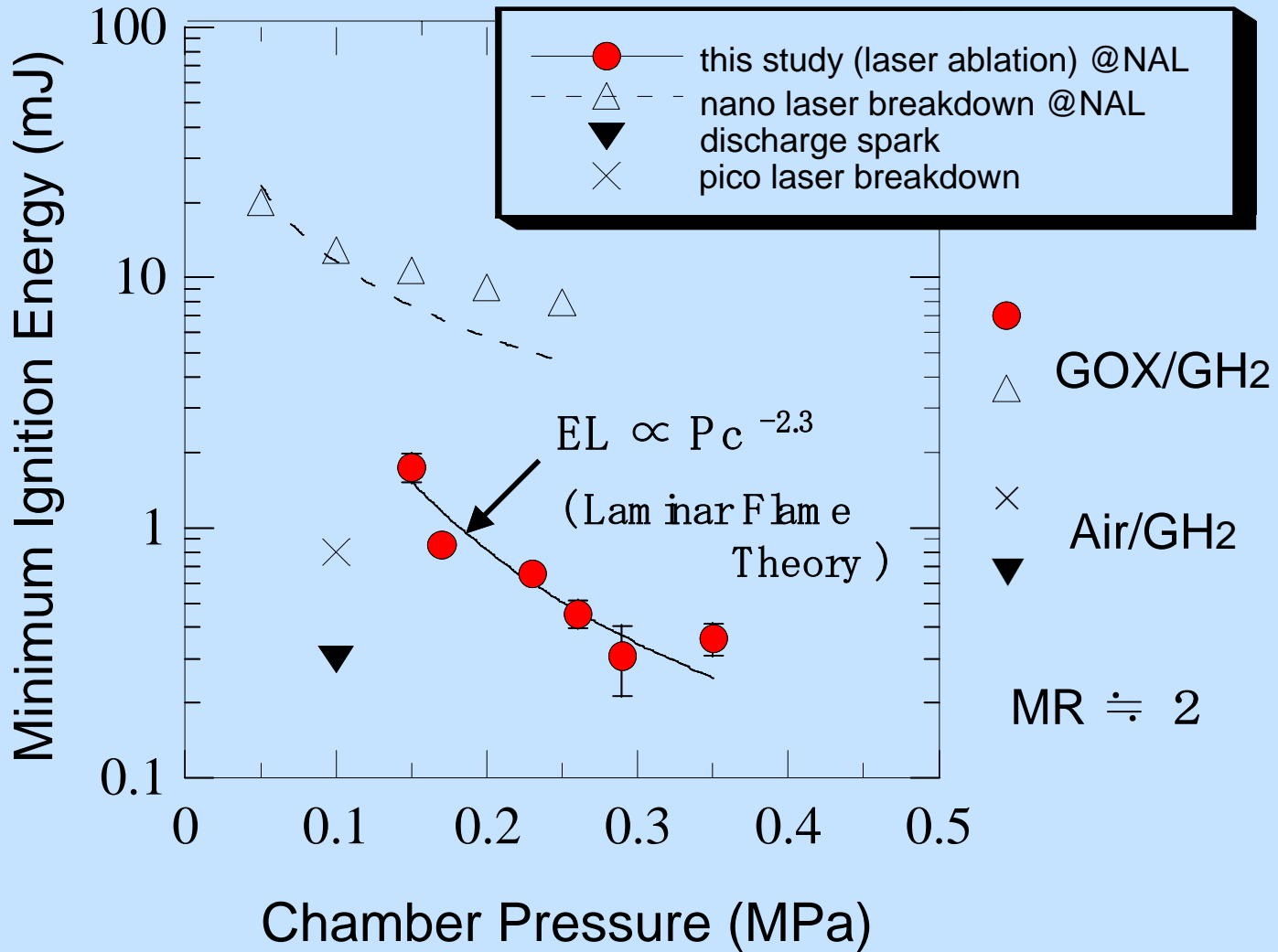
- Laser Type : Flash lamp excited Nd : YAG laser
(Wavelength : 1064nm、 Laser pulse width : 12nsec)
- Ignition Method : Laser Ablation Ignition
(Irradiation by a laser beam on a solid target generates high-temp plume and initiates ignition)
- Cyclic pulse mode operation was demonstrated and optical fiber transmitted laser ignition could be applied to RCS

Photograph taken from Observation Window



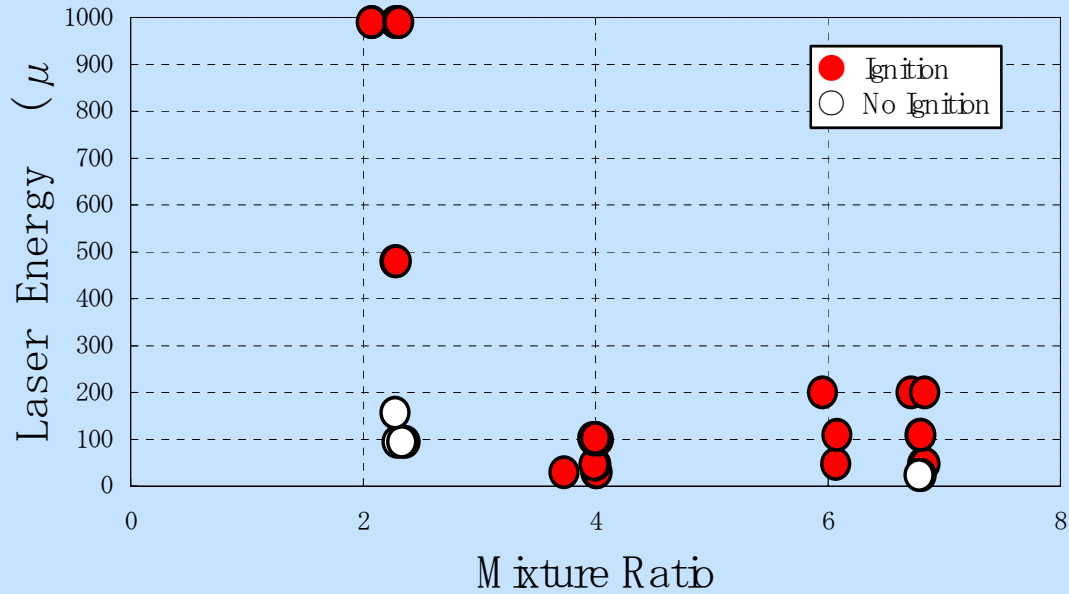
Schematic of Laser Ablation Ignition System



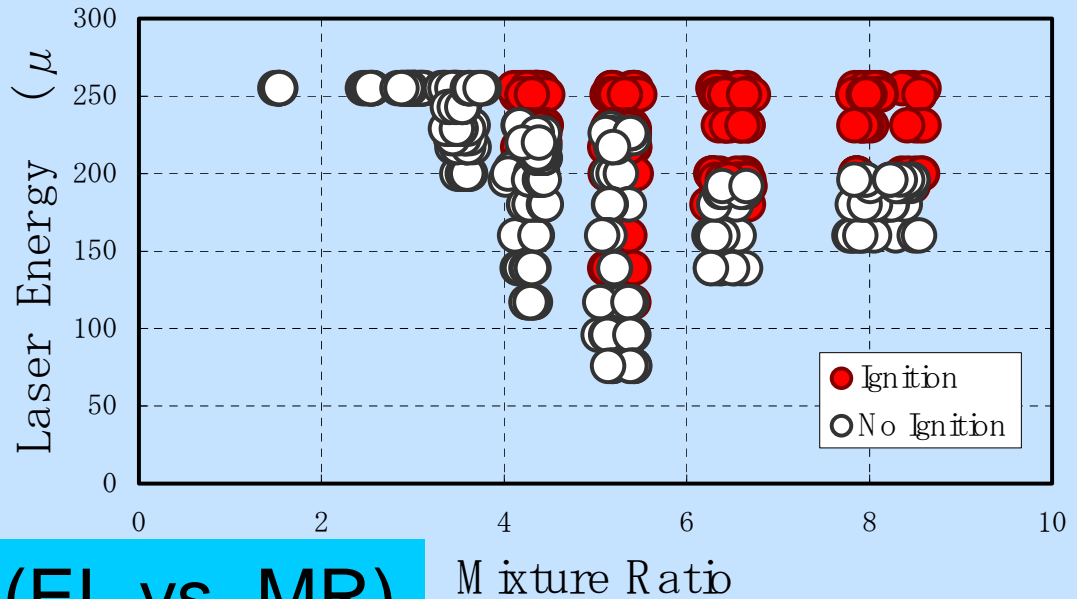


Correlation between Minimum Ignition Energy and Chamber Pressure

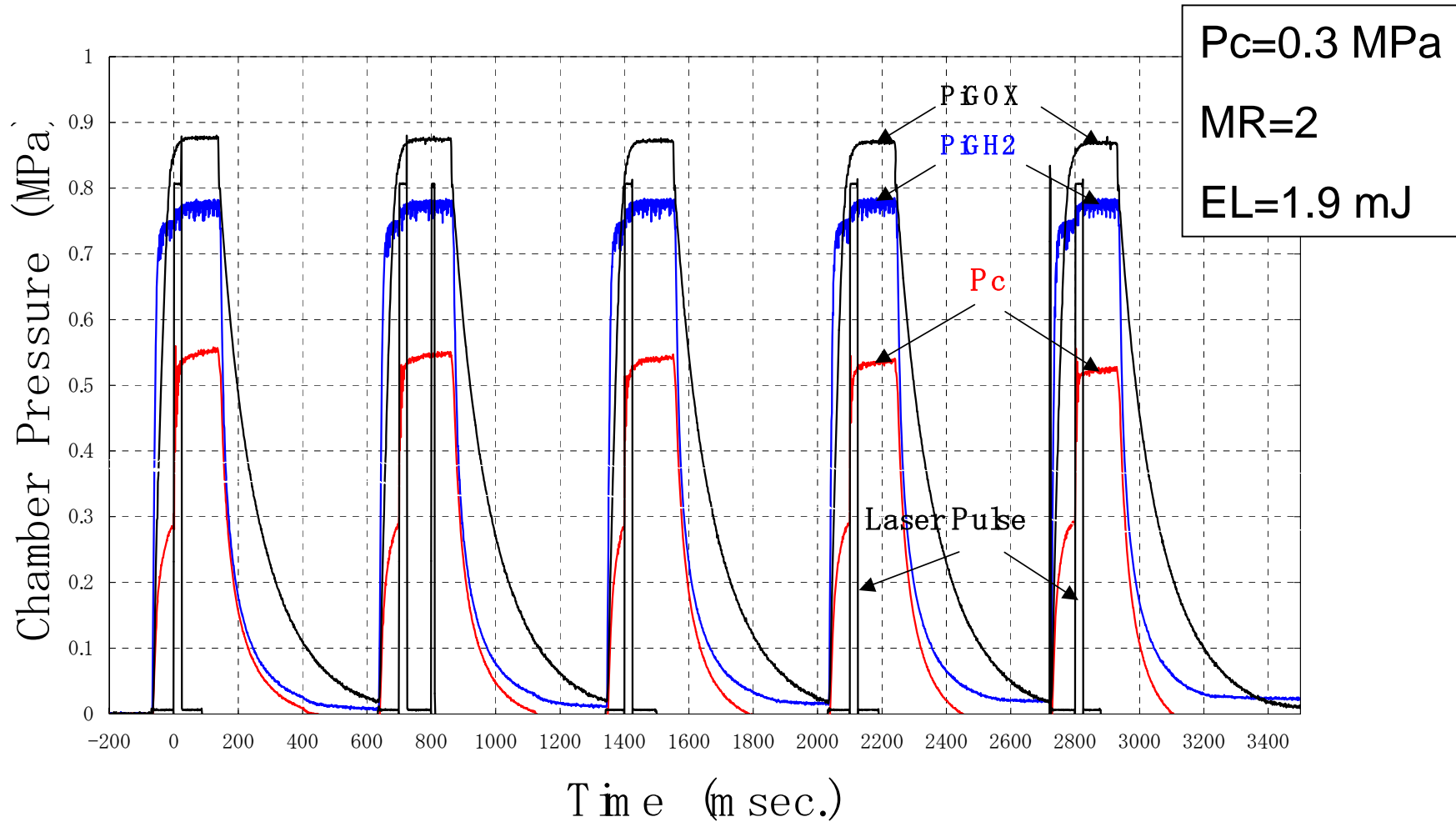
GOX/GH₂
 (P_c=0.3 MPa)



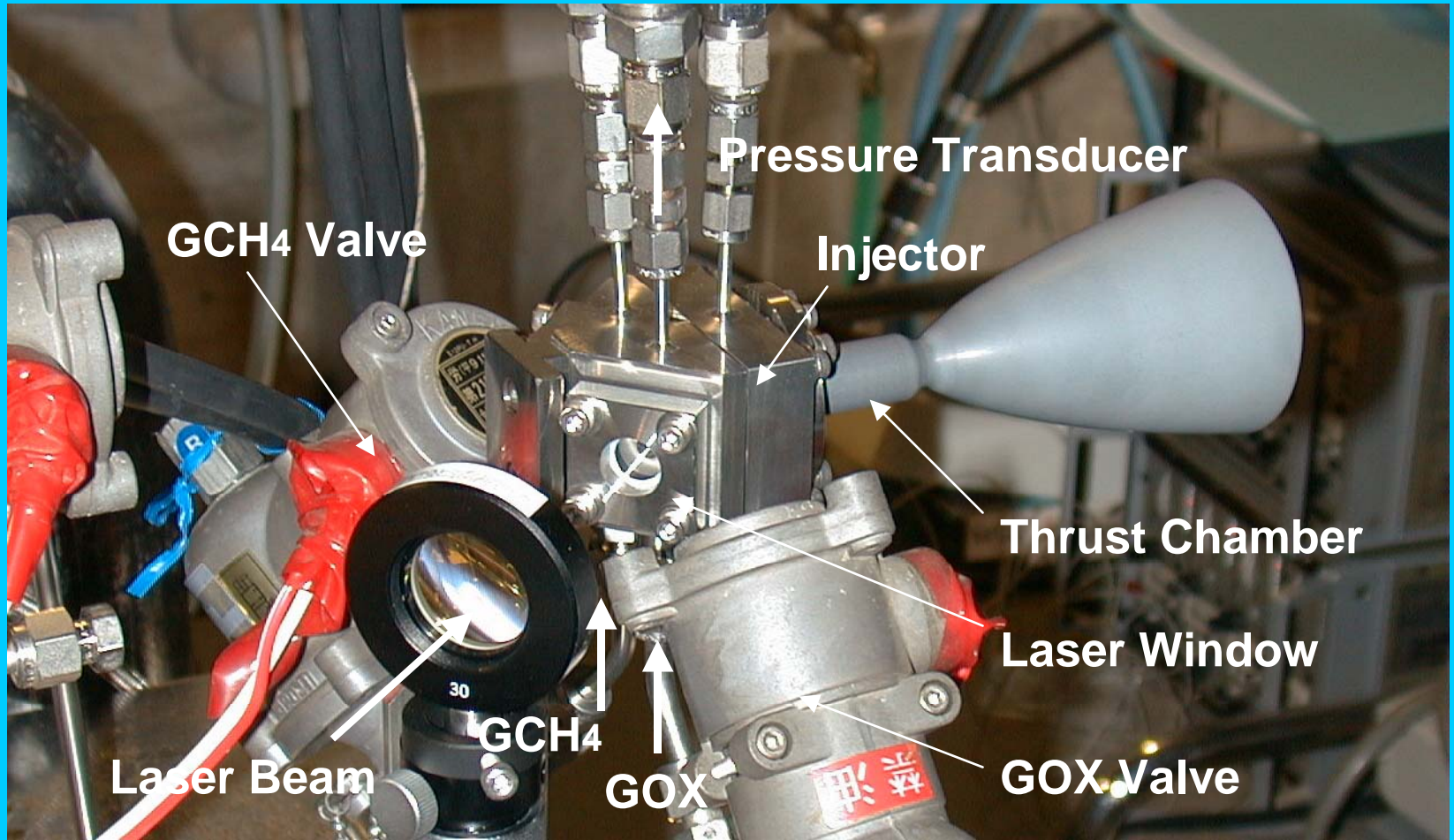
GOX/GCH₄
 (P_c=0.1 MPa)



Ignition Area Map (EL vs. MR)



Pressure History during Cyclic Pulse Mode Operation
(GOX/GH₂, under Vacuum Condition)



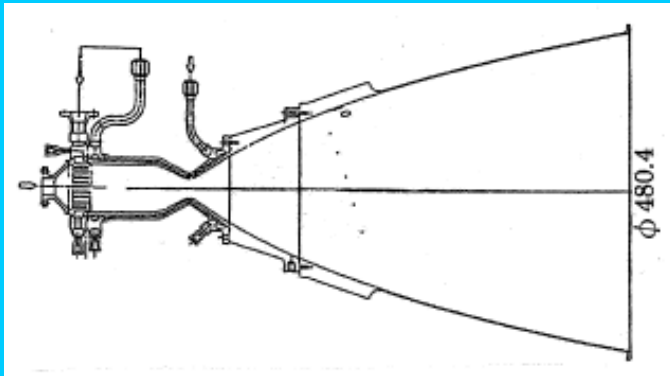
Appearance of Newly Designed Device

VTR

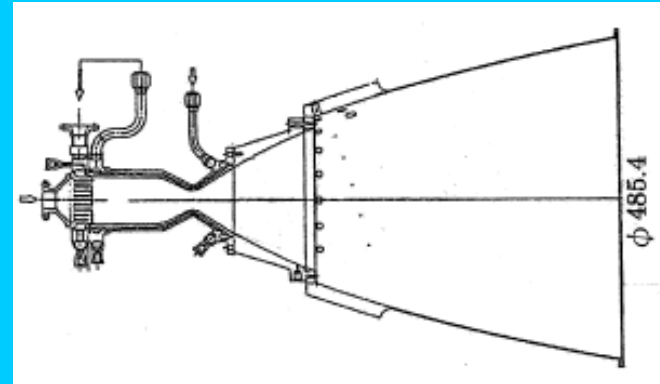
(2) Extendible Nozzle and Dual-Bell Nozzle



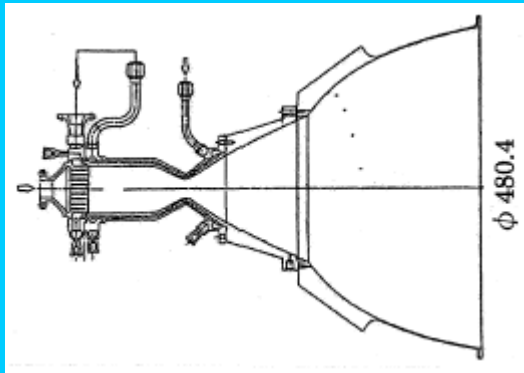
- Both nozzles are considered feasible devices to improve performance of booster engine
- Hot firing tests were conducted on high altitude test stand, using four types of nozzle
- Rapid transition between low exp. mode and high exp. mode in dual-bell nozzle
- No reverse flow of hot gas during deployment of extendible nozzle



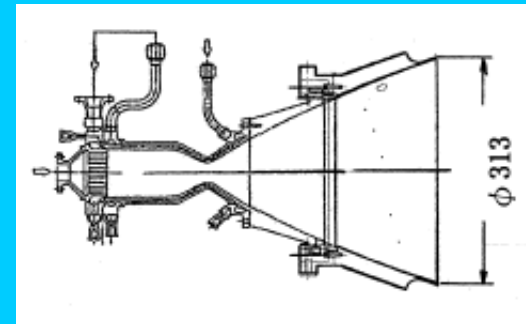
(a) Standard Nozzle



(b) Step Nozzle



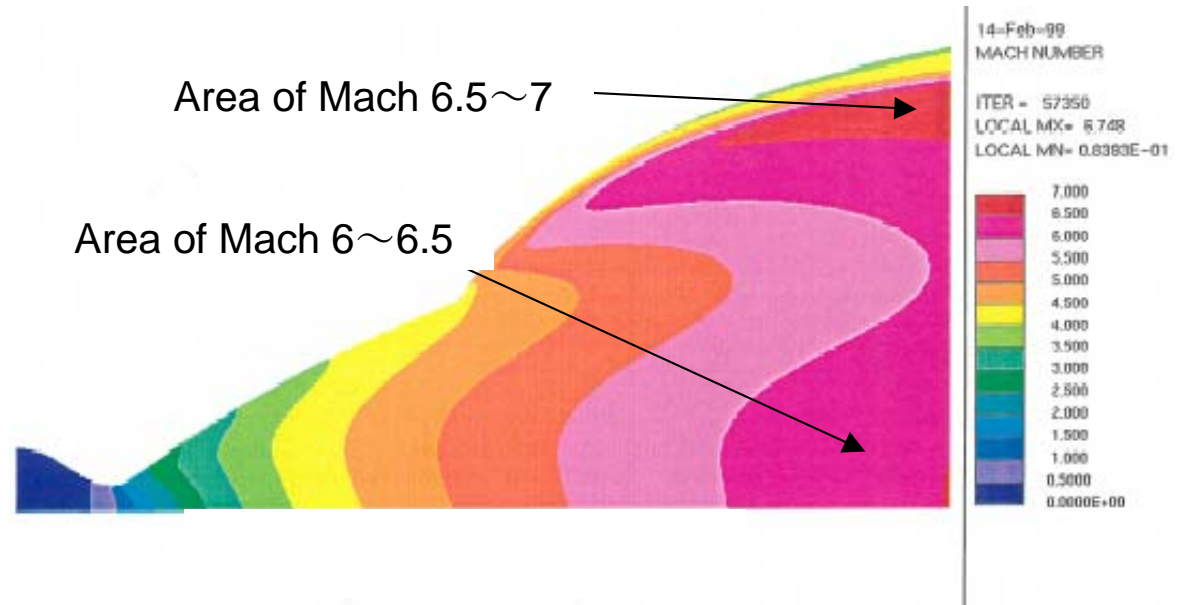
(c) Dual-Bell Nozzle



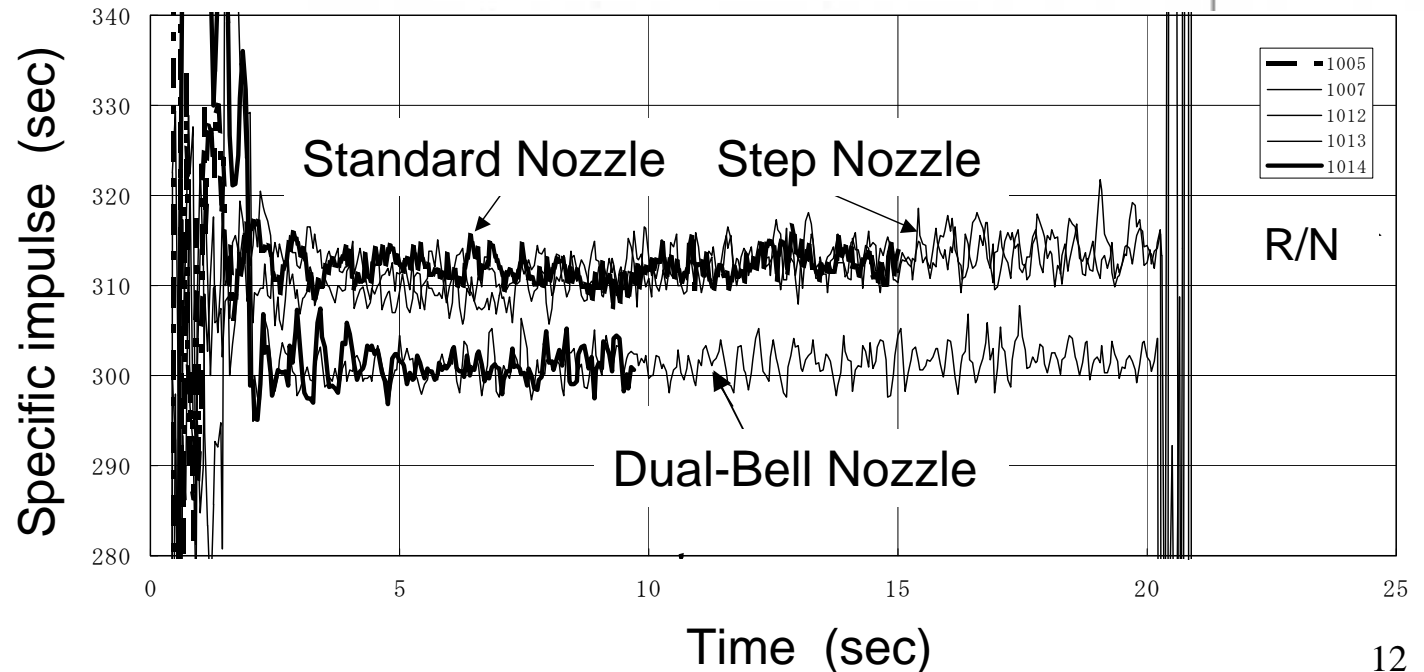
(c) Extendible Nozzle

Four types of Nozzle Configuration

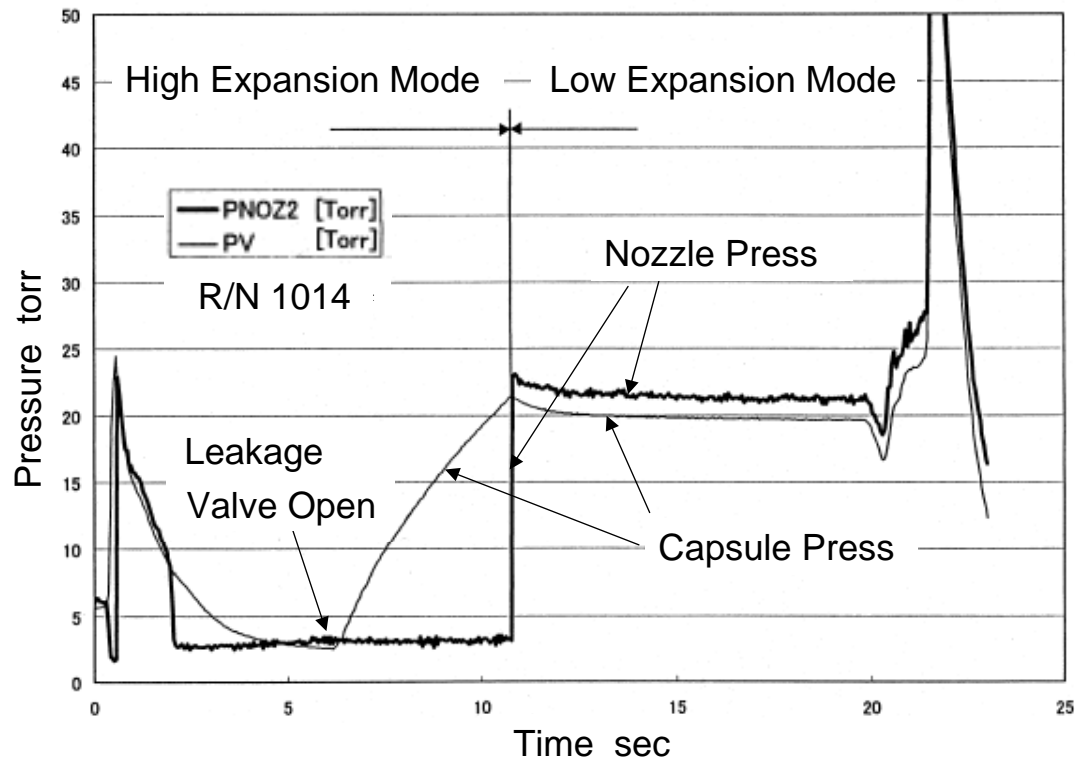
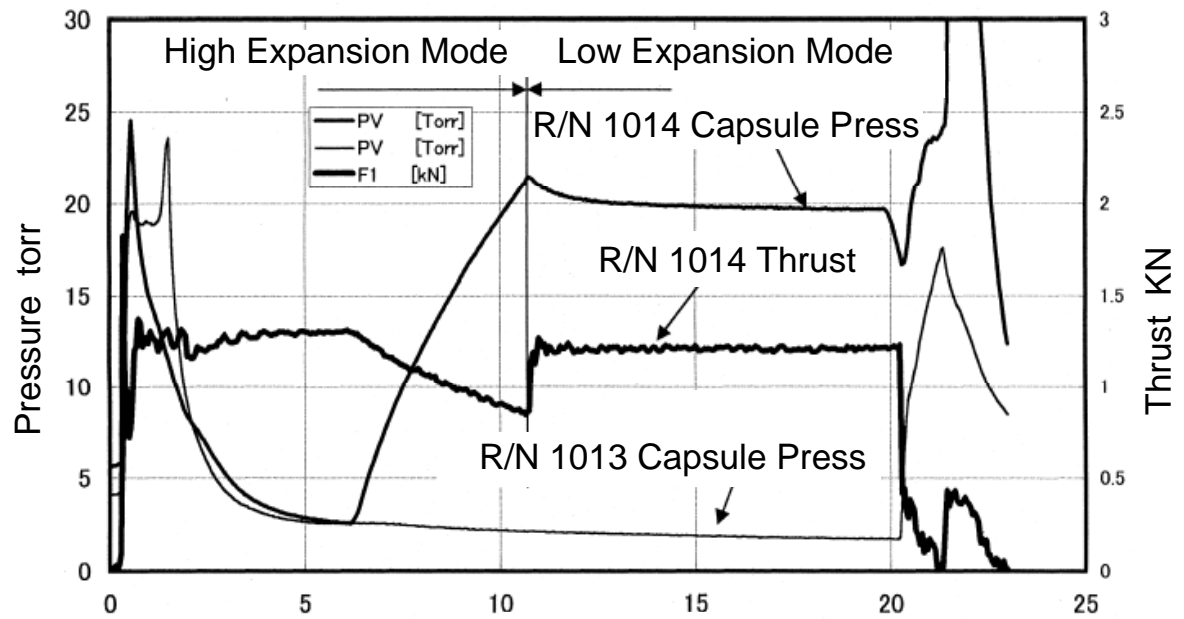
CFD Analysis for Dual-Bell Nozzle



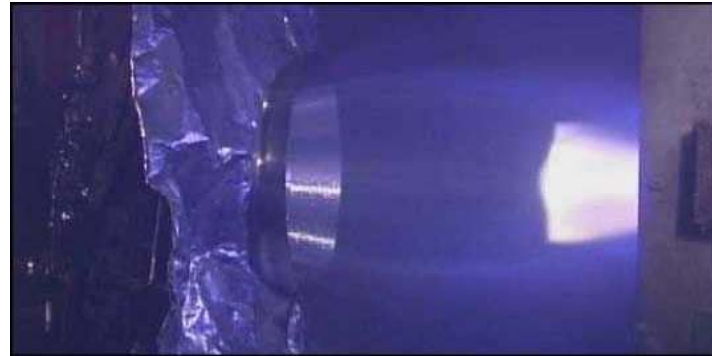
Specific Impulse of Three Nozzles



Pressure and Thrust History of Dual-Bell Nozzle



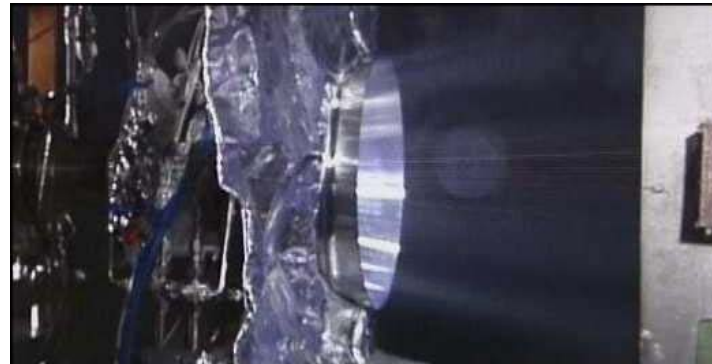
(a)
Stowed
Position



(b)
Deploying
Position

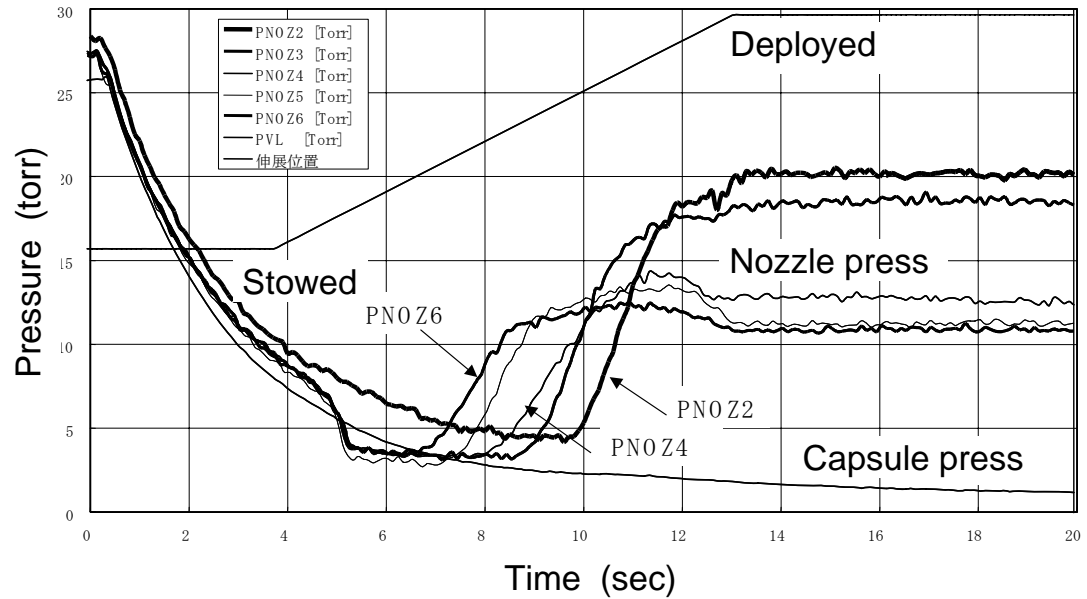


(c)
Fully Deployed
Position

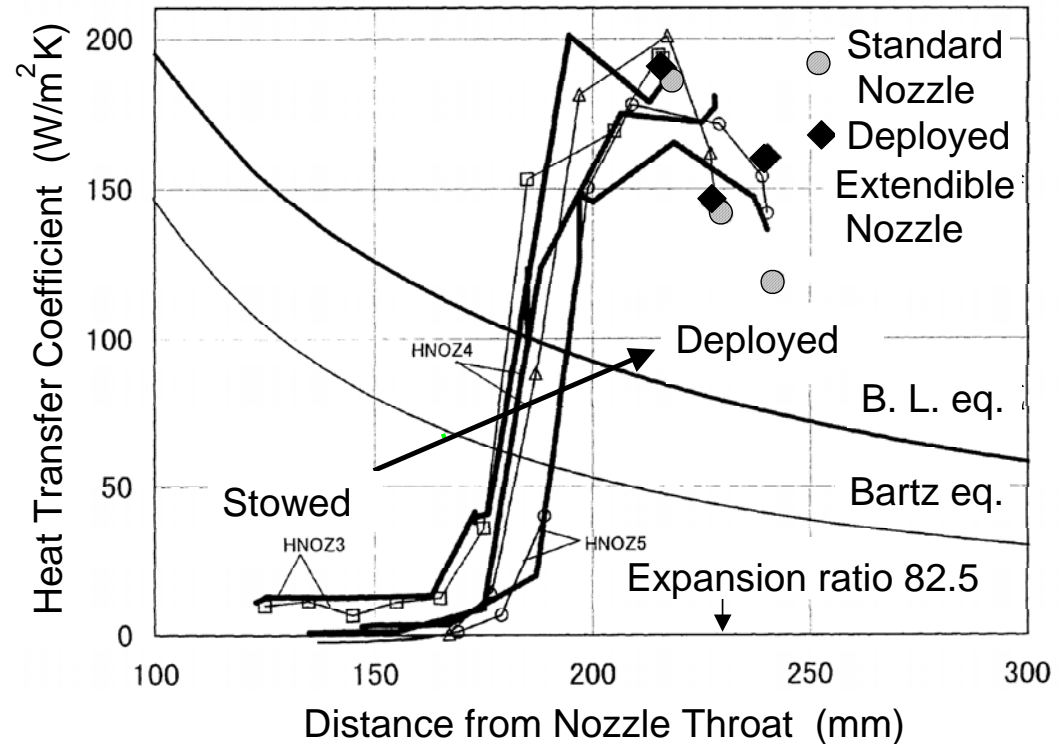


Photographs of Extendible Nozzle Firing Test

Pressure History during Deployment



Heat Transfer Coefficient during Deployment

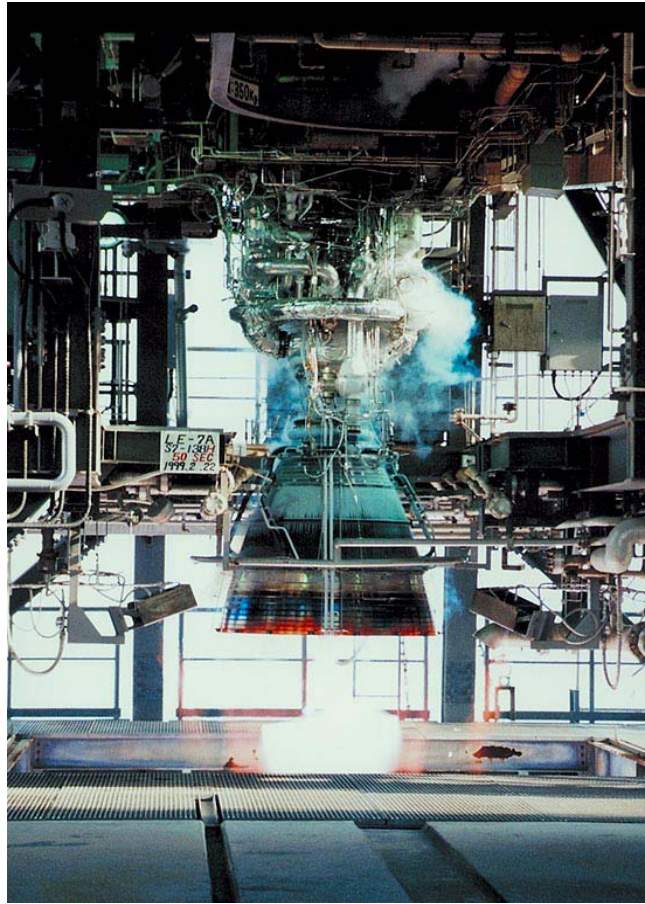


VTR

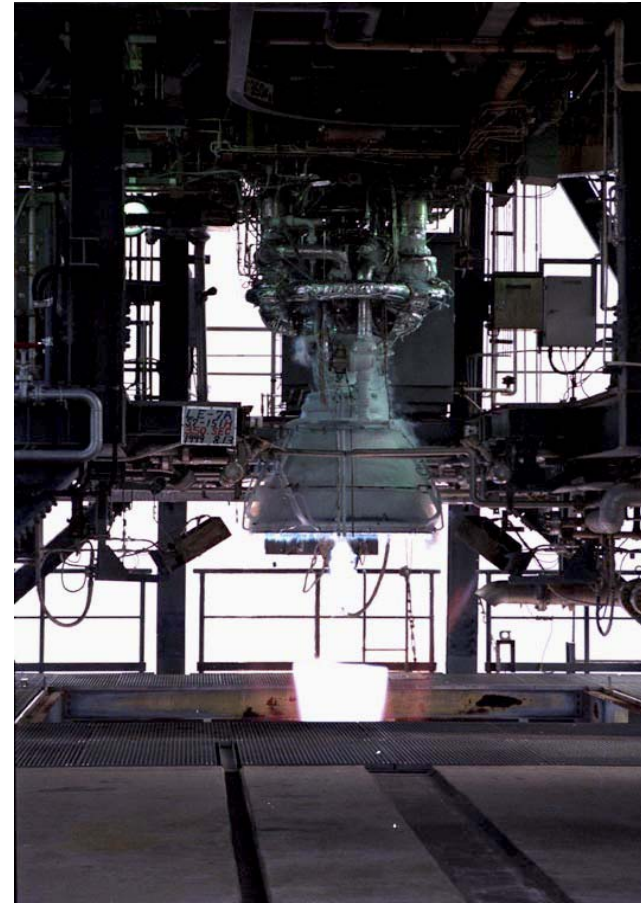


(3) LE-7A Nozzle Flow Separation Phenomenon

- To clarify nozzle flow separation phenomenon, motion picture analysis, cold flow test of step nozzle and CFD analysis were conducted
- First large side load caused by jump phenomenon of nozzle flow separation point
- Second side load due to flow pattern transition from FSS to RSS

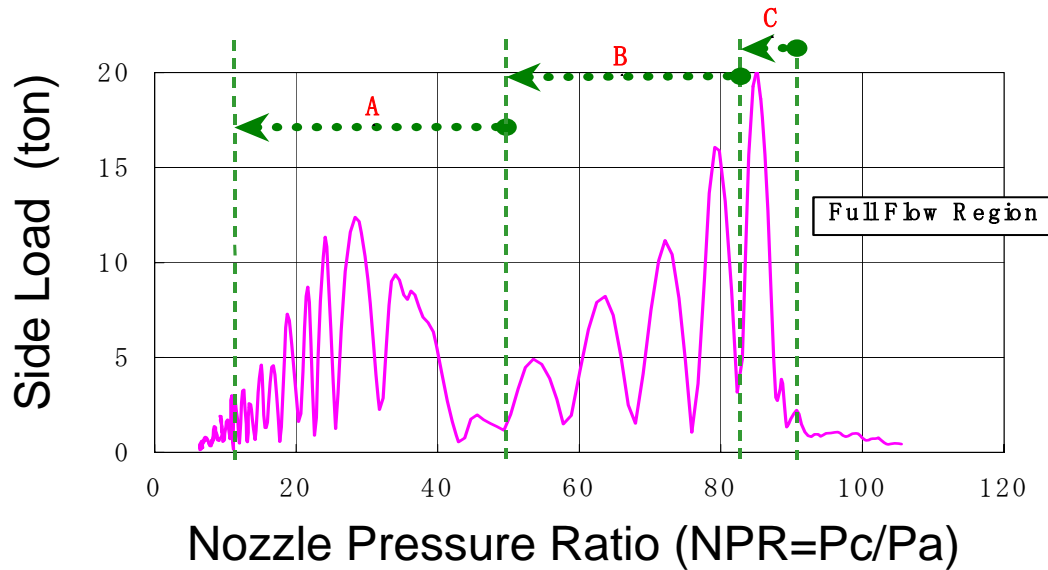
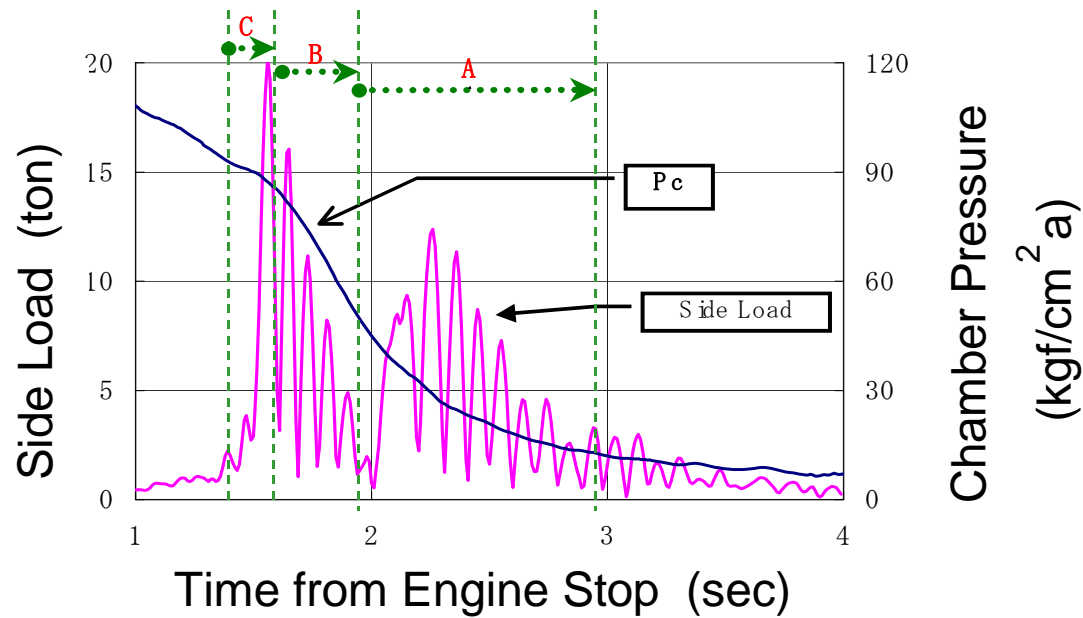


Long Nozzle



Short Nozzle

Photographs of Hot Firing Tests of Two Nozzles



Side Load Test Data of Long Nozzle

Photographs of Nozzle Exit Flame

(a)~(e) : FSS
($60 < \text{NPR}$)

(f)~(i) : RSS
($\text{NPR} < 50$)



(a) $T = \text{Stop} + 1.44 \text{ s}$
 $\text{NPR} = 89.4$

(b) $T = \text{Stop} + 1.54 \text{ s}$
 $\text{NPR} = 86.5$

(c) $T = \text{Stop} + 1.64 \text{ s}$
 $\text{NPR} = 80.0$



(d) $T = \text{Stop} + 1.74 \text{ s}$
 $\text{NPR} = 71.4$

(e) $T = \text{Stop} + 1.84 \text{ s}$
 $\text{NPR} = 60.3$

(f) $T = \text{Stop} + 1.94 \text{ s}$
 $\text{NPR} = 49.5$

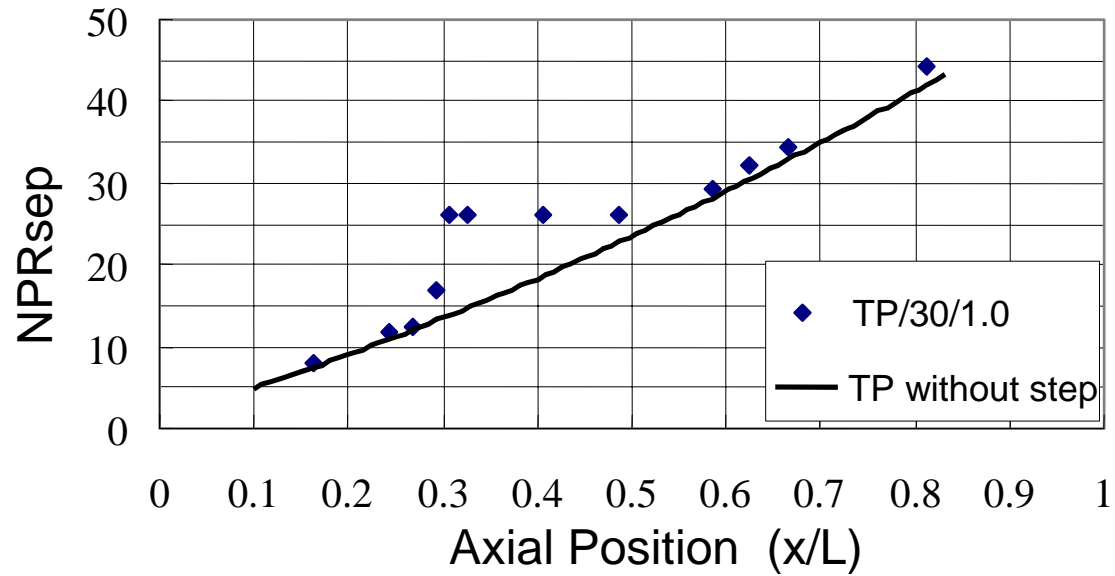


(g) $T = \text{Stop} + 2.04 \text{ s}$
 $\text{NPR} = 40.6$

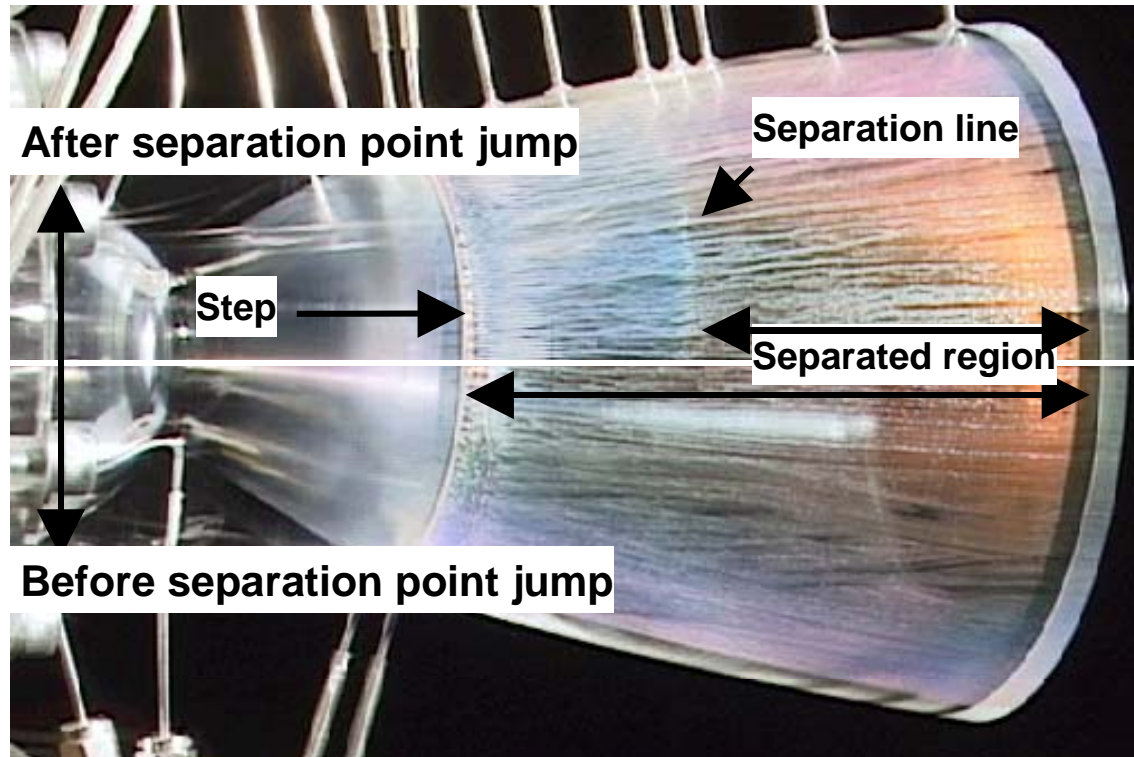
(h) $T = \text{Stop} + 2.14 \text{ s}$
 $\text{NPR} = 34.7$

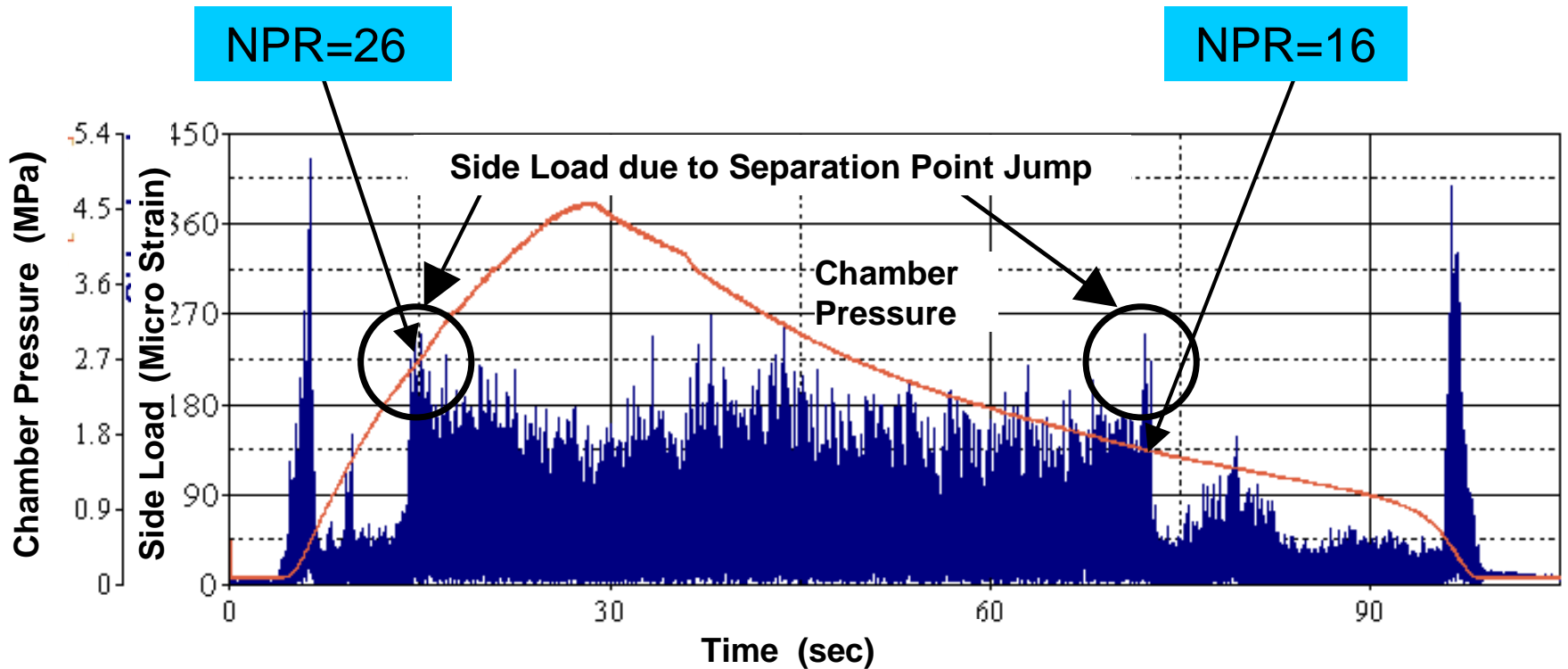
(i) $T = \text{Stop} + 2.24 \text{ s}$
 $\text{NPR} = 29.5$

NPRsep of TP/30/1.0 and TP without Step



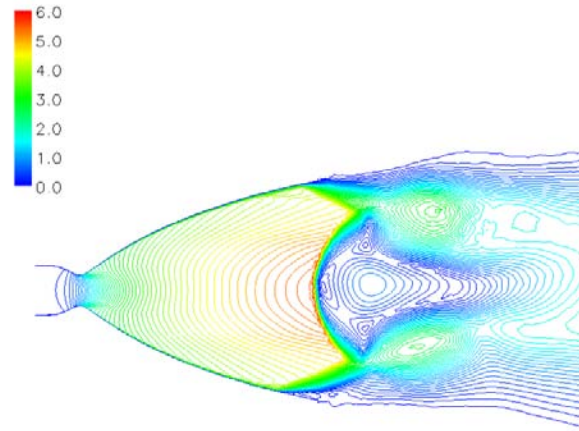
Photographs of Surface Flow by SSLC



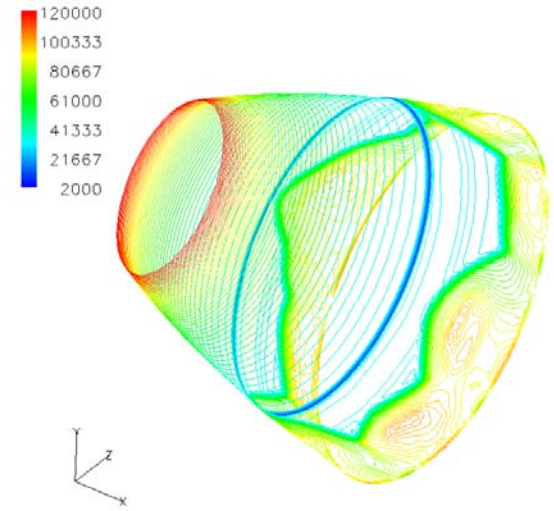


Chamber Pressure and Side Load History of Step Nozzle TP/30/1.0

(a)
NPR : 82
MR : 6
(Phase C)

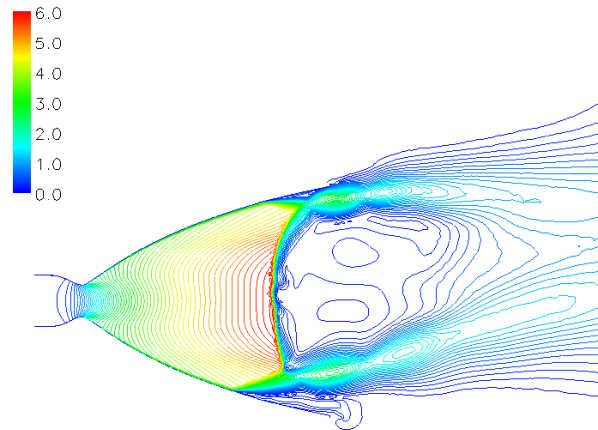


Mach number

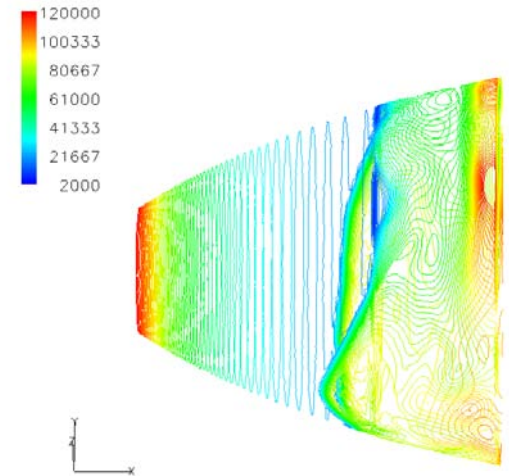


Wall pressure (Pa)

(b)
NPR : 50
MR : 3
(Phase A)



Mach number

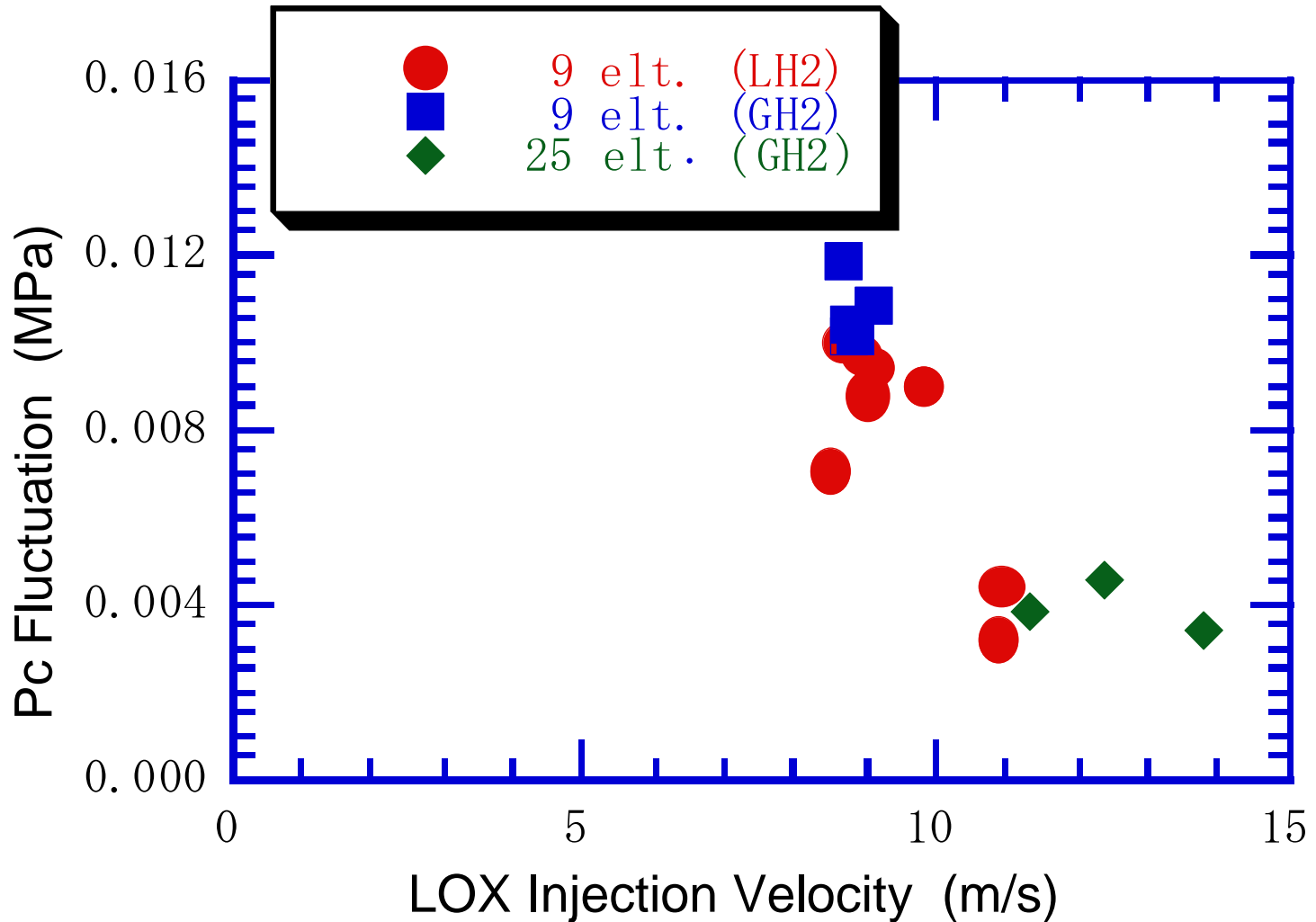


Wall pressure (Pa)

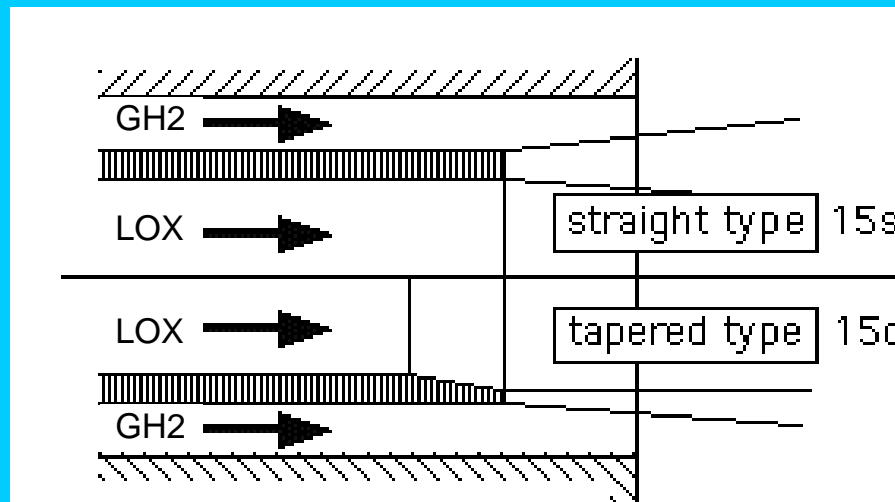
(4) Low Cycle Chamber Pressure Fluctuation



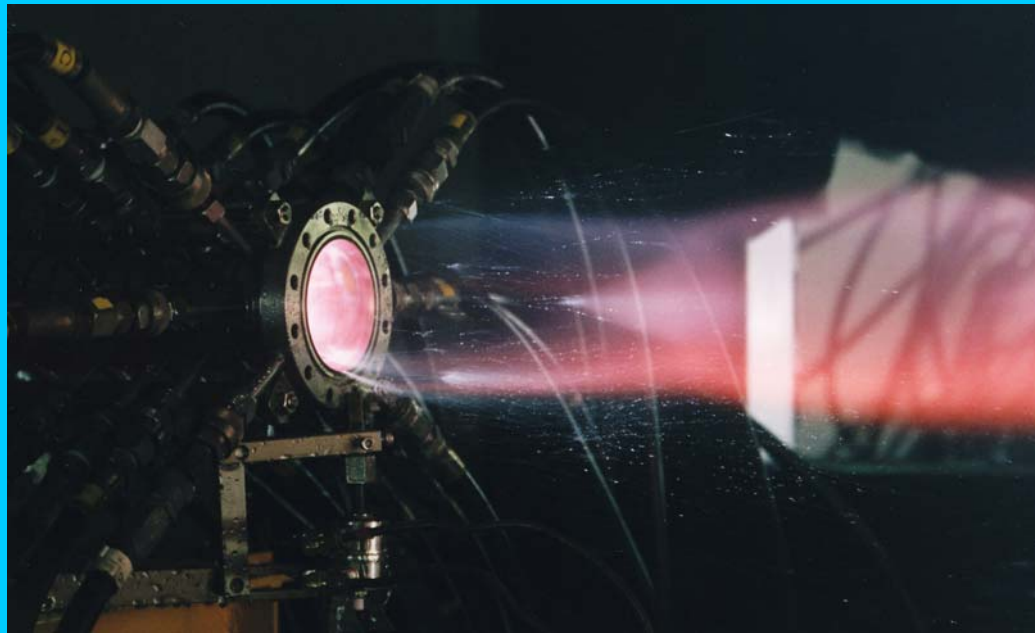
- Low cycle pressure fluctuations in combustion chamber may trigger coupled vibration of vehicle structure and rocket engine
- Hot firing tests were conducted to investigate correlations between chamber pressure fluctuations and several parameters
- Increasing LOX jet breakup frequency could reduce chamber pressure fluctuations



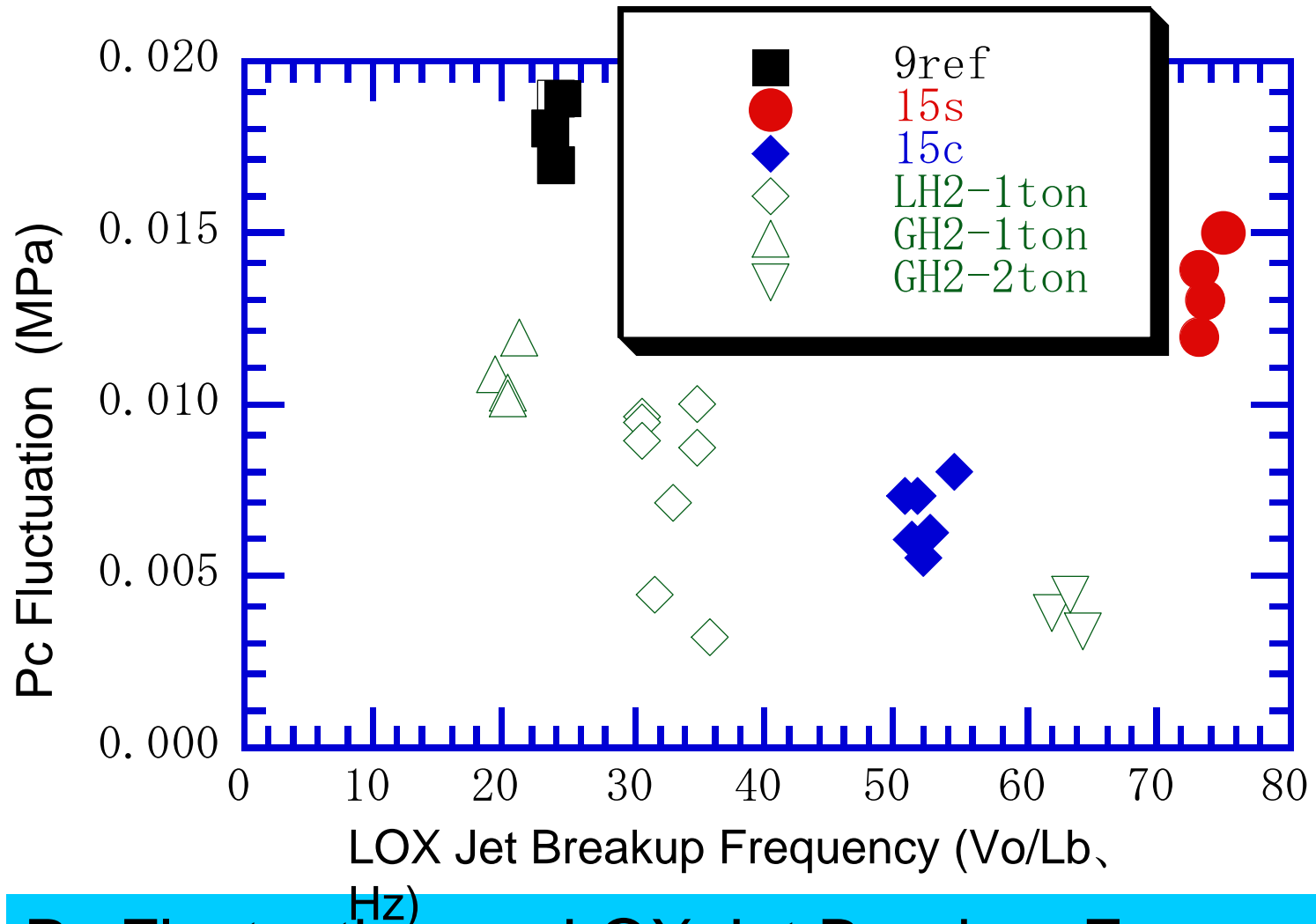
**Pc Fluctuation vs. LOX Injection Velocity
(Previous Test Data)**



Two Types of LOX Post Configuration



Photograph of Hot Firing Test



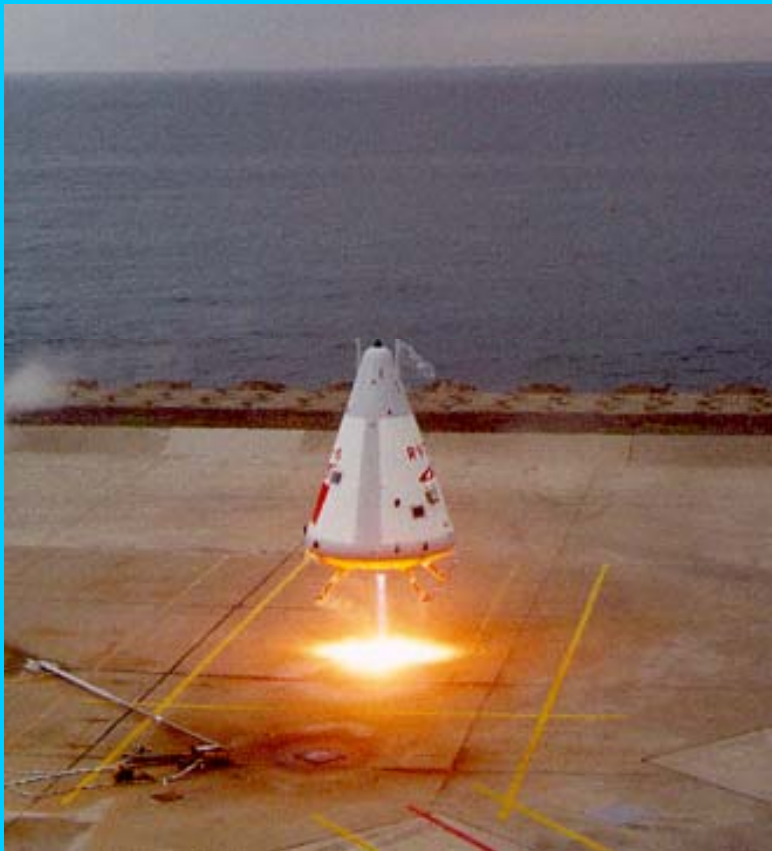
Pc Fluctuation vs. LOX Jet Breakup Frequency

● ◆ : Newly Obtained Data

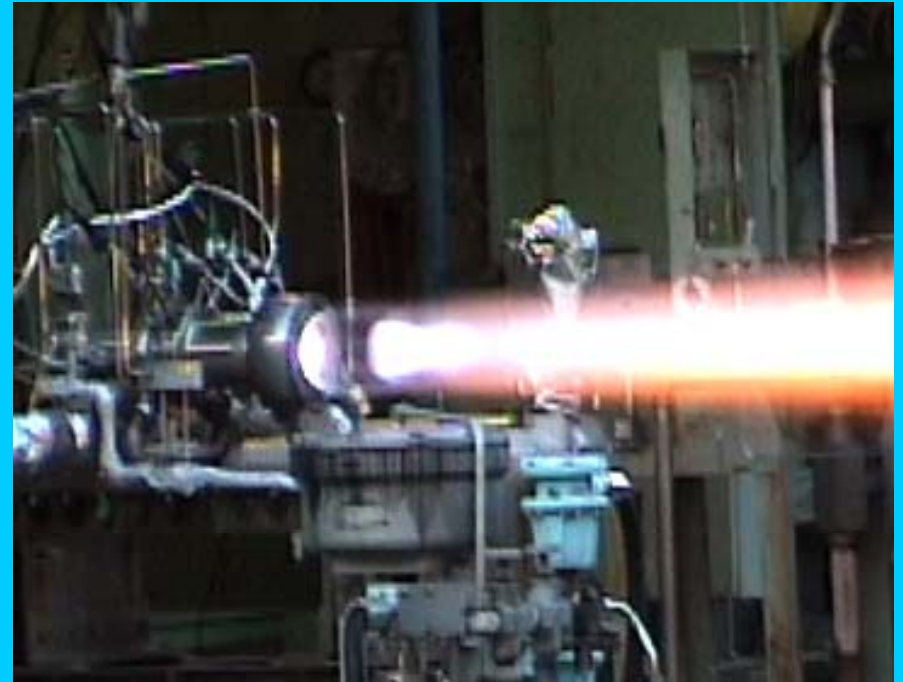
(5) LOX/LH₂ Engine for Reusable Vehicle Test



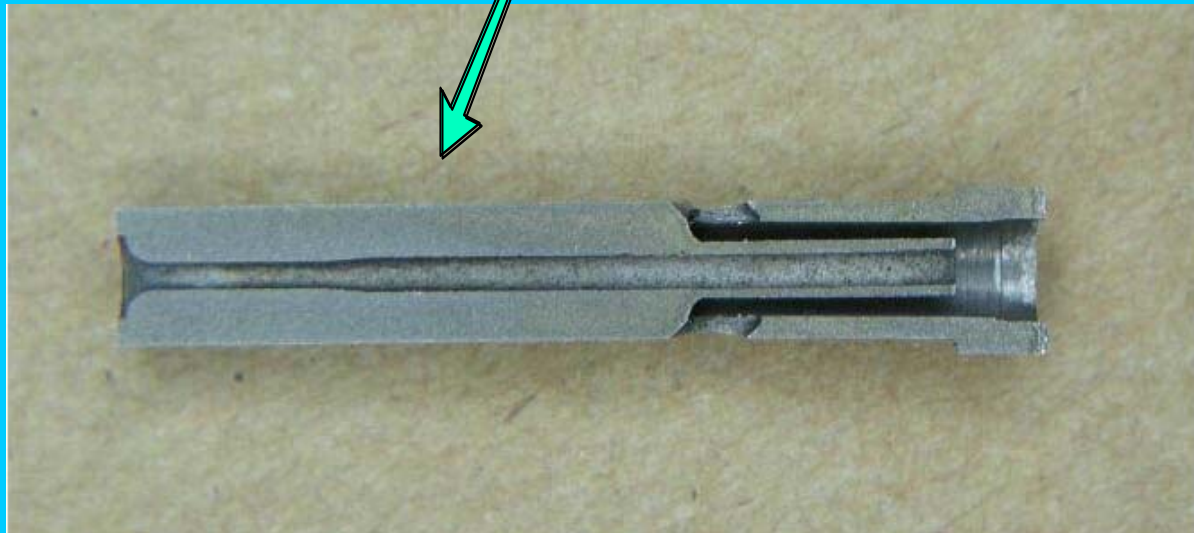
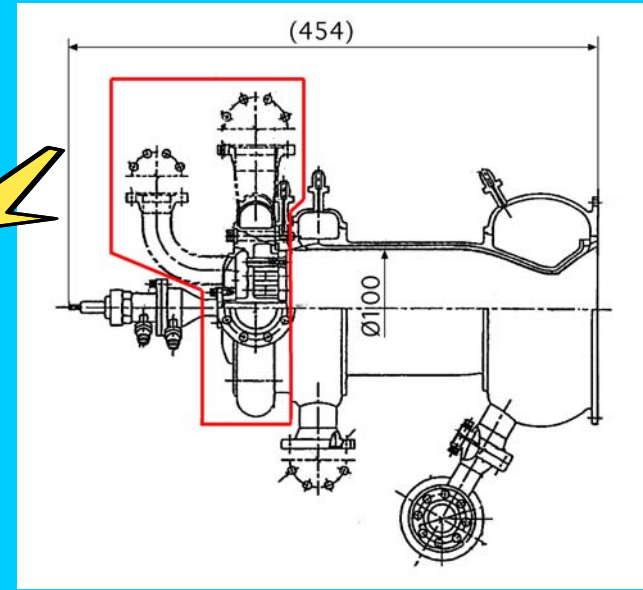
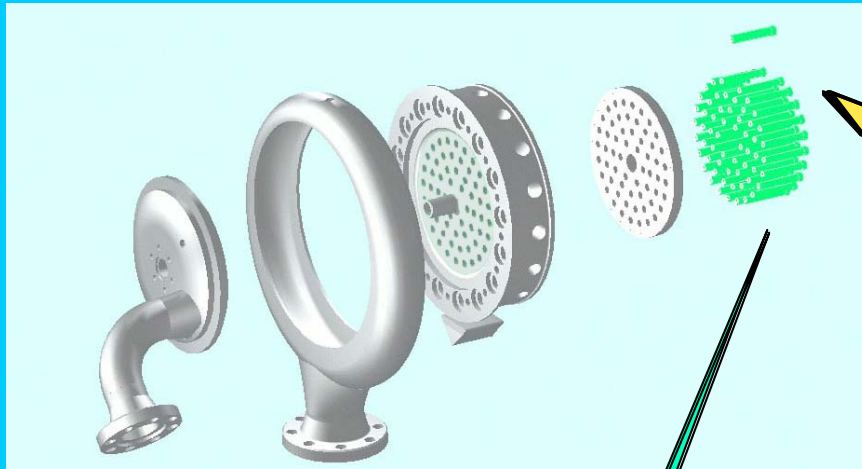
- Demonstration of vertical landing and turnaround operation is underway, using small pressure fed LOX/LH₂ engines
- Electro-formed element injector was fabricated and hot firing tested to meet requirement of long life and deep throttling capabilities
- Good throttling and frequency response capabilities were verified



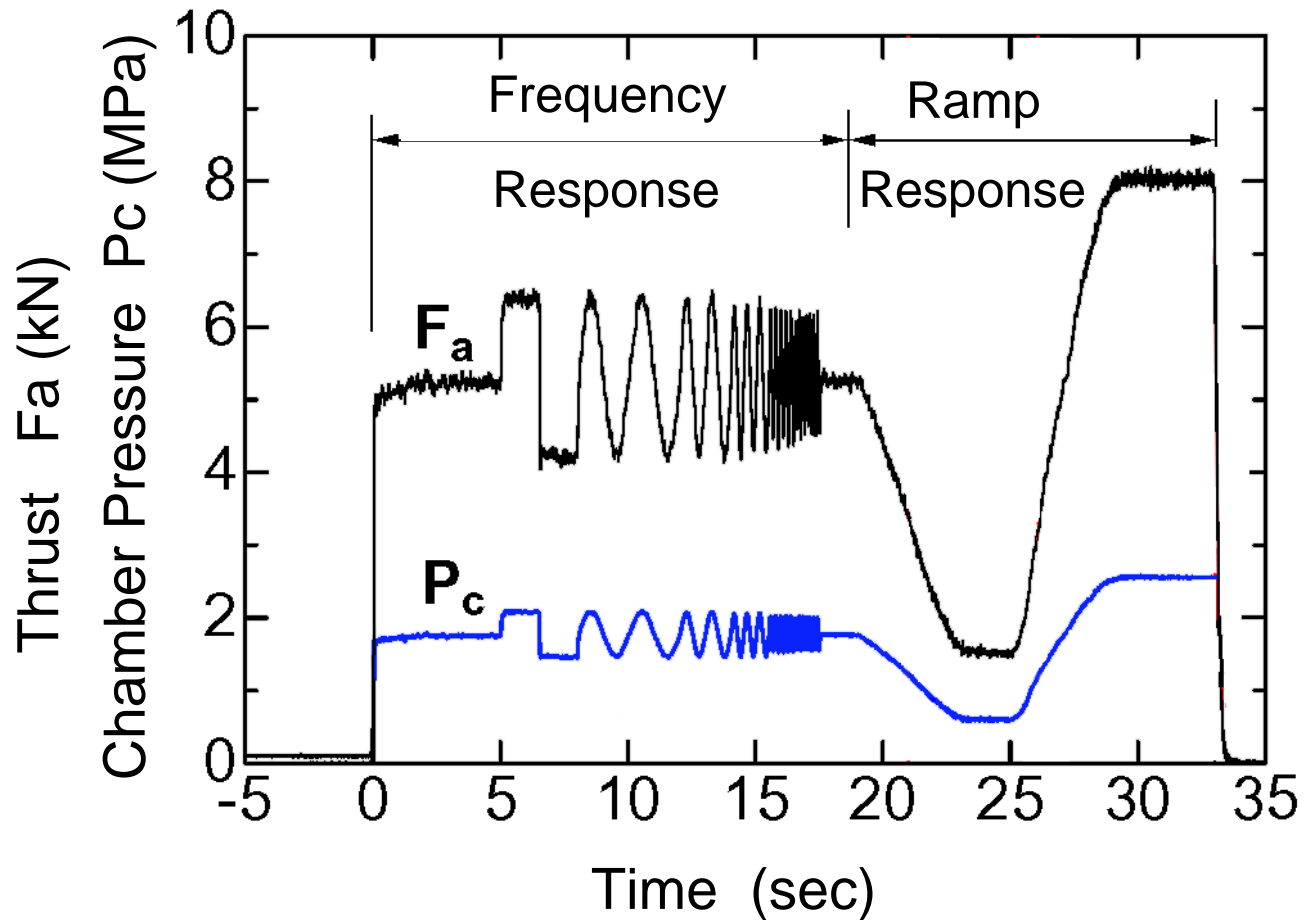
Photograph of
Test Vehicle in Flight



Photograph of
Engine Hot Firing Test



Photograph of Electro-Formed Injector Element



Thrust and Chamber Pressure History of Frequency / Ramp Response Test

(6) Study of Advanced Expander Bleed Cycle



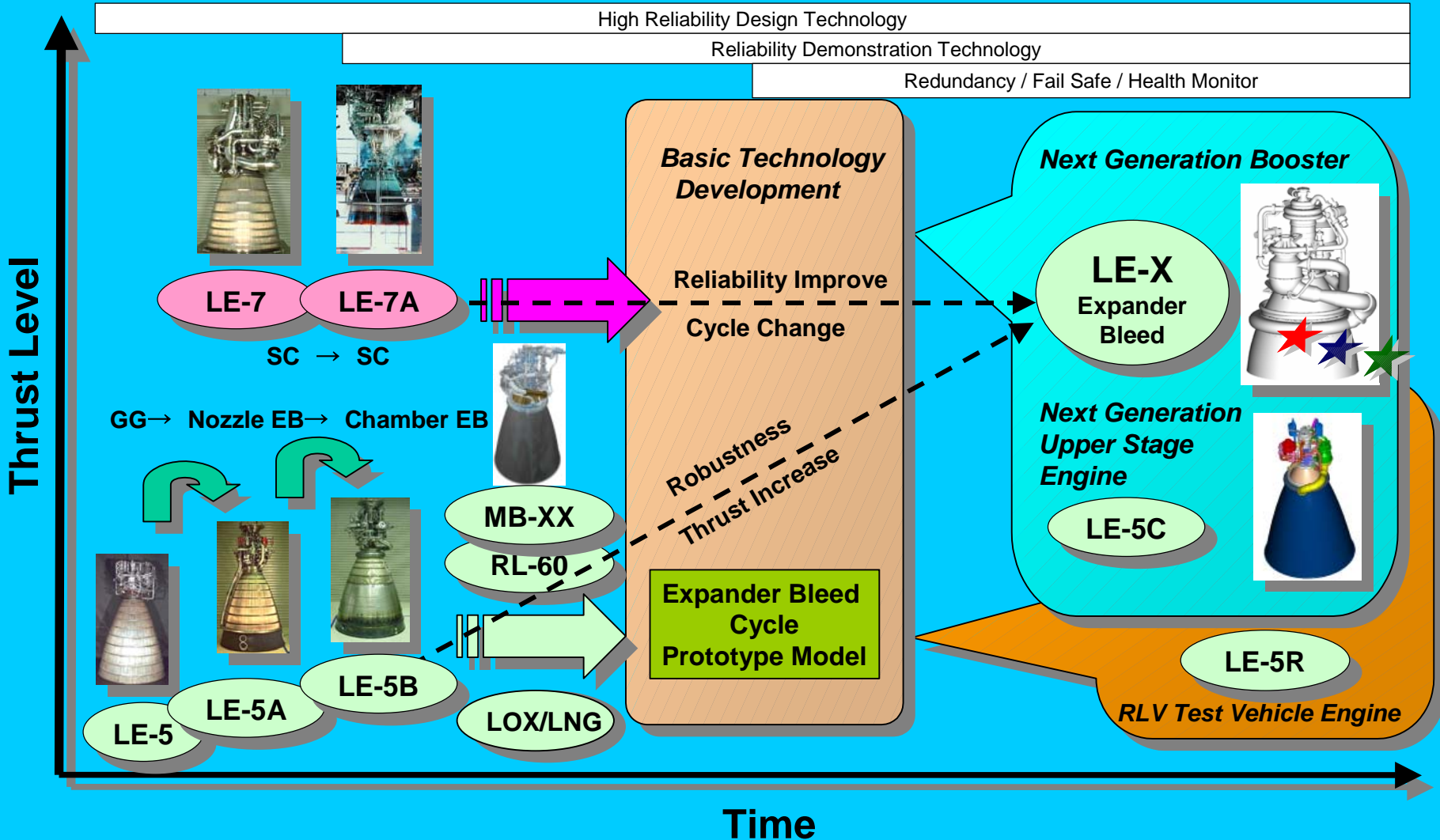
- Advanced expander bleed cycle is now under study for next generation LOX/LH₂ engines
- Advantage of expander bleed cycle is its simplicity and capability of minimizing LH₂ pump pressure, although delivered Isp is a little bit lower than that of full expander cycle
- Expander bleed cycle could be applied also to 200-ton-class booster engine

2000

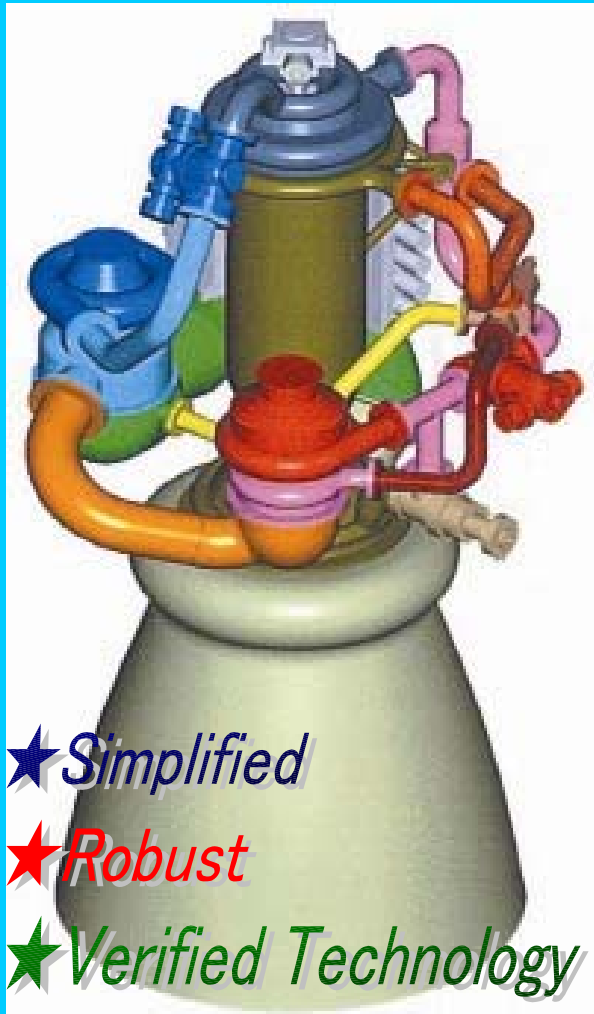
ELV

EELV / RLV 2010~

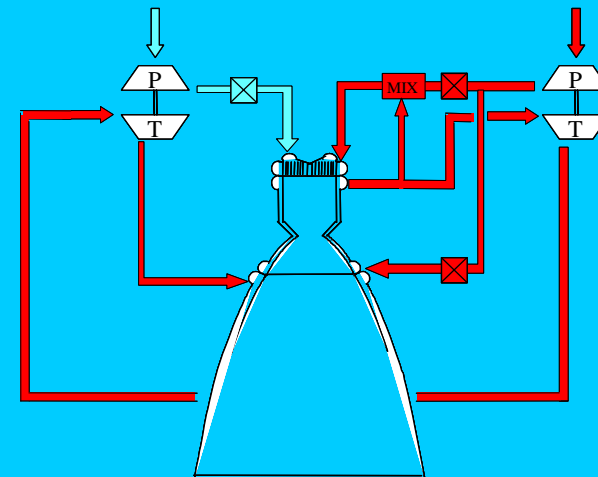
2010~



Development Concept of Advanced Engines

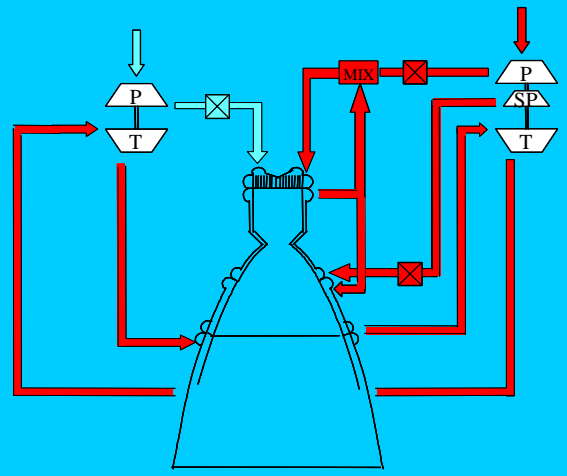
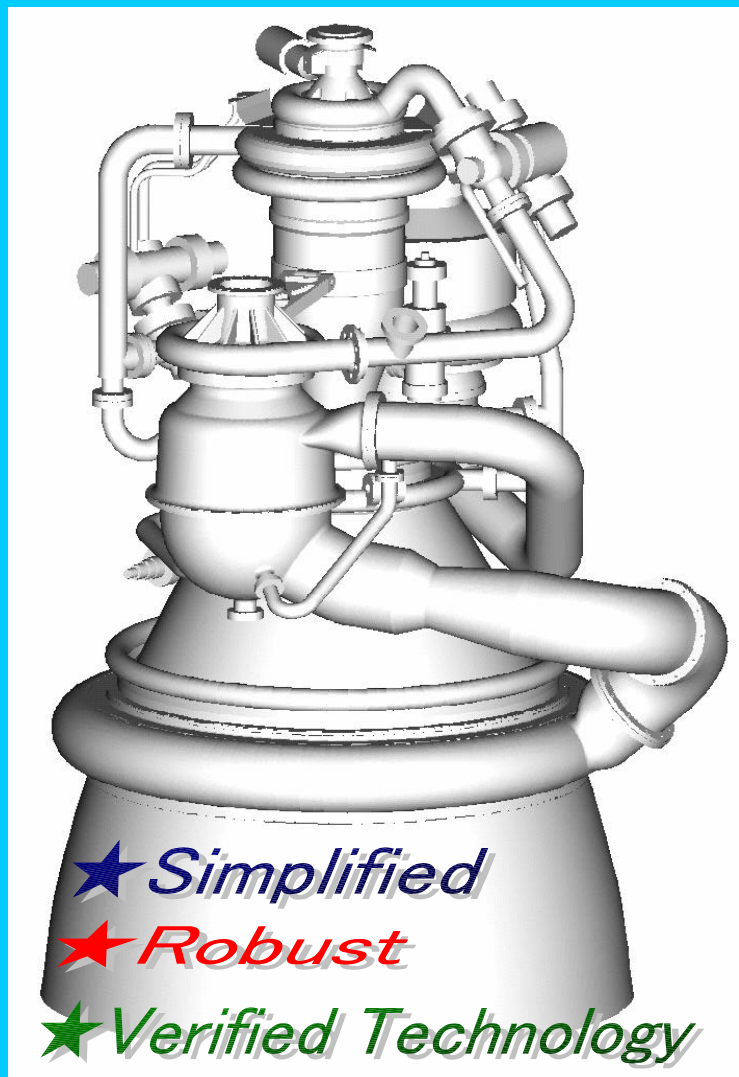


Cycle	Expander Bleed
Thrust (sea level)	20 ton
Specific Impulse (sea level)	429 sec
Mixture Ratio	5.5
Expansion Ratio	45
Chamber Pressure	8.3 MPa
LH2 Pump Pressure	13.5 MPa
Dry Weight	500 kg



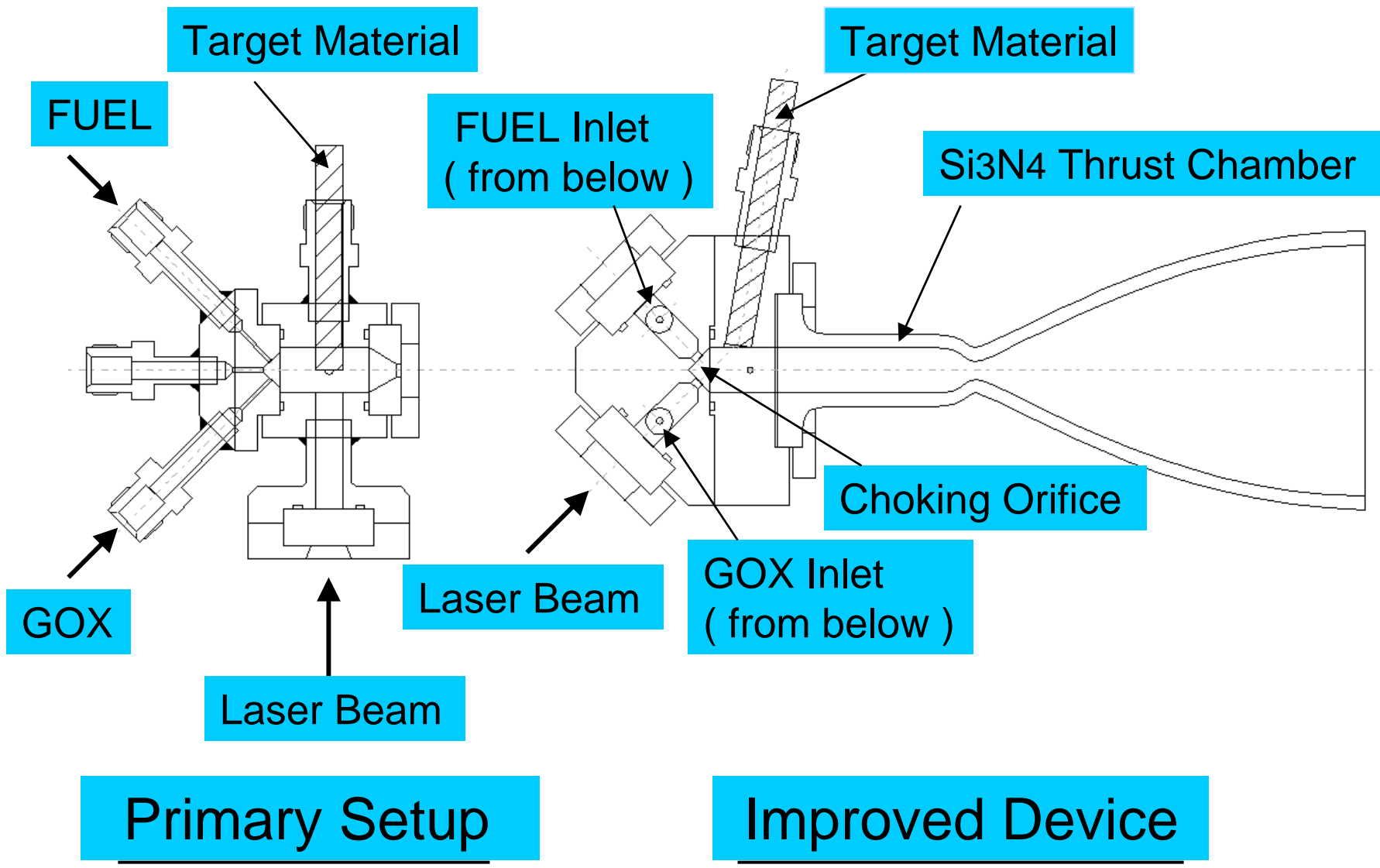
Concept of Prototype Engine

Cycle	Expander Bleed
Thrust (sea level)	110 ton
Specific Impulse (sea level)	440 sec
Mixture Ratio	6.0
Expansion Ratio	60
Chamber Pressure	12.1 MPa
LH2 Pump Pressure	18.7 MPa
Dry Weight	1700 kg



Concept of Advanced Booster Engine

END



Primary Setup

Improved Device

Correlation between EL and Pc

- Minimum ignition energy is expressed by

$$EL \propto \delta^3 \rho_0 C_p (T_\infty - T_0)$$

where δ : flame thickness, ρ_0 : density, T_0 : temp,

C_p : specific heat, T_∞ : flame temp

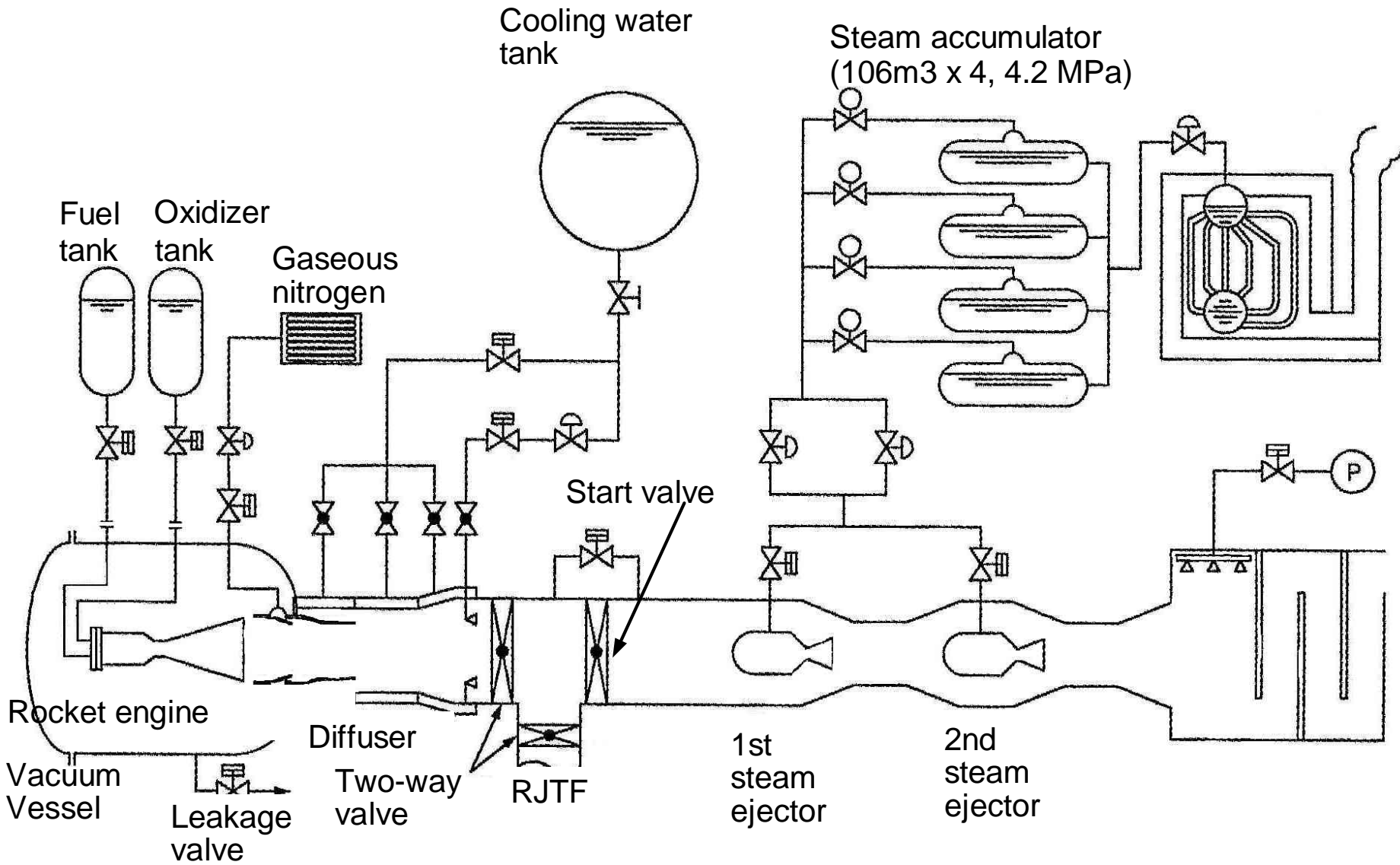
- Based on laminar flame theory, $\delta \propto P_c^{-n/2}$
where, n : the order of reaction, P_c : chamber pressure of the mixture gas before ignition

- Since $\rho_0 \propto P_c$, $EL \propto P_c^{1-3n/2}$

$n=2.17$ for GOX/GH₂, therefore, $EL \propto P_c^{-2.3}$ 36

Allowable Maximum Energy

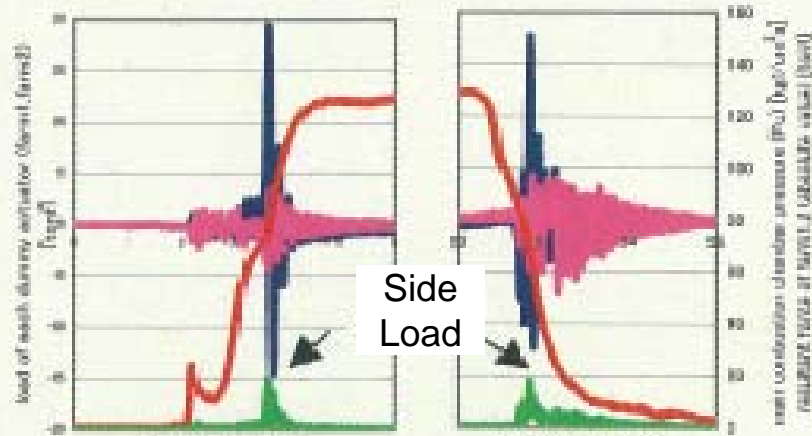
- Allowable max energy density for silicon-based optical fiber $\doteq 1 \text{ MW/mm}^2$
- When the typical fiber of 0.3 mm diameter and 12 nsec pulse width laser are used, max energy $\Rightarrow 1 \text{ mJ}$
- Considering safety factor of 1.5, allowable max energy $\Rightarrow 700 \mu\text{J}$



Schematic of High Altitude Test Stand



Long Nozzle



Side Load during Startup and Shutdown Transient



Damage to Regeneratively Cooled Tubes

DEVELOPMENT OF A LIQUID PROPELLANT ROCKET, KOREA SOUNDING ROCKET (KSR)-III

Yeon Seok Chae, Soo Yong Lee, Seonghyeon Seo

Korea Aerospace Research Institute
Daejeon, 305-333, Korea

ABSTRACT

Korea Sounding Rocket-III has established itself as the first-ever bi-propellant liquid rocket designed and manufactured in Korea, which is fueled by pressure-fed, liquid oxygen and environment-friendly kerosene. The project on KSR-III took its development period of five years to achieve its successful launch campaign on November 28, 2002. The main objectives of the development of KSR-III were to acquire prerequisite experiences in the development of satellite launchers and to further strengthen capability of domestic industries related to space technology. The program has been accomplished by going through many development stages such as subscale model and full-scale engine combustion tests, propellant feeding system tests, integrated power plant tests, and eventually a flight test. Each development stage underwent various technical difficulties and challenges that had to be resolved and verified with reliable processes to minimize trials and errors. The subscale model combustion test provided useful data about the combustion efficiency of a split-triplet (F-OO-F) injector and suggested the best injector arrangement. Two types of subscale thrust chambers allowed us to determine the design of an injector and a faceplate for the full scale thrust chamber. The on-ground combustion tests of a full-scale thrust chamber had verified its performance and the endurance of hardware including ablative material. The thrust and chamber pressure of the engine are 13tonf @ sea level and 13.6atm, respectively, which lasts for 59 seconds. A composite baffle successfully suppressed troublesome high frequency combustion instability at the beginning of the development. Throughout the program, three different versions of full-scale chambers had

been designed and manufactured for the optimization of performance and weight. The propellant feeding system was tested and verified through water flow tests and each component showed acceptable performance for flight use. Eventually, the thrust chamber assembly and the propellant feeding system were vertically integrated to check the functionality of subsystems and verify the performance of the whole propulsion system and thus, a stage qualification test had been conducted before a final flight test. At long last, the series of all these tests resulted in the successful flight test of KSR-III.

INTRODUCTION

After two previous pioneer steps, Korea Sounding Rocket-I and II programs, Korea Sounding Rocket (KSR)-III program had been conducted by Korea Aerospace Research Institute (KARI) to increase the capabilities of domestic space technology towards the development of space launch vehicles. While the prior sounding rocket programs depended solely on solid rocket propulsion technology, KSR-III program was intended to lay a foundation of a liquid propellant propulsion technology for the future development of space launcher vehicles. The execution of these programs, mainly in the fields of a sounding rocket, made sense for Korea to equip itself with independent means to undertake scientific and peaceful use of space technologies.

The first-ever liquid propellant rocket, KSR-III, employs its engine, KL-3, burning liquid oxygen and hydrocarbon fuel. The development of KL-3 had taken almost five years since December of 1997. The main considerations for the development of KL-3 were given to the clear identification of technologies required for a sounding rocket, the minimization of development cost, and the improvement of domestic technologies available for the development. Based on these development concepts and objectives, environment-friendly and cost effective propellants, liquid oxygen and hydrocarbon fuel had been selected and in order to compromise the available domestic technologies, a relatively simple, pressure-fed propellant feeding system has been adopted for KL-3 instead of a power pack propellant feeding system. Consequently, the thrust chamber had to take advantage of ablative material with fuel film cooling for protection of its inner insulation layer.

Table 1. Overview of Korea Sounding Rocket (KSR) programs

	KSR-I	KSR-II	KSR-III
Development Purpose	Measurement of ozone layer	Measurement of ozonosphere, ionosphere and X-ray experiment	Development of basic model for space launcher
Development Period	'90.7 ~ '93.10	'93.11 ~ '98.6	'97.12 ~ '02.12
Altitude	39.0 km, 49.4 km	137.2 km	217 km
Length	6.7 m	11 m	13.4 m
Weight	1.2 ton	2.02 ton	5.2 ton
Payload	150 kg	150 kg	150 kg
Propulsion System	Single Stage : SRM	1st Stage : SRM 2nd Stage : SRM	1st Stage : LRE 2nd Stage : SRM

Here in this paper, the brief description of the development of KSR-III will be presented, and technical concepts and approaches will be provided to give an overall view on the program.

Development Procedure of Propulsion System

Since there had been no previous domestic experiences in developing a rocket engine with a cryogenic liquid propellant, it became one of ultimate objectives from the beginning of the development to secure technologies related to handling cryogenic fluid and establish solid development logic for the future development of more sophisticated liquid rocket engines used for space launchers. From these reasons, it was required to set logical steps for the development based on the indirect acquisition of knowledge available on the public domain. Nonetheless, it seemed natural that trials and errors occurring through the development procedure taught invaluable lessons. The sequences for the development of the propulsion system with brief description are like following.

- Screen out several designs out of preliminary candidate injectors by conducting cold flow tests. An unlike split triplet injector (F-OO-F) as shown in Fig. 1

had been chosen for the best mixing efficiency among several candidates.

Each injector was machined and brazed onto an injector plate.

- Design and fabricate subscale thrust chambers for selected injector types, and perform hot firing tests with variety of injector layout patterns and minor changes on injector dimensions such as an impinging angle. See Fig. 2 for schematics of sub and full-scale thrust chambers.
- Based on hot firing test results from various subscale thrust chambers, manufacture a heavy type Engineering Model (EM), a full-scale thrust chamber.
- Conduct a series of on-ground combustion tests using a horizontal test stand. Characterize the performance and the dynamic stability of the full-scale thrust chambers by the measurement of operating parameters.
- Design and fabricate Power plant Model (PM) thrust chambers, and conduct structure endurance tests since PM thrust chamber housing was manufactured by the application of a filament winding technique for weight reduction.
- Perform on-ground combustion tests of PM thrust chambers for the assessment of performance and function.
- Examine dynamic stability of an acceptance-ready full-scale thrust chamber based on results of stability rating tests.
- In parallel with the development of thrust chambers, a propellant feeding system had been developed through structural and functional tests of each component, and cold flow tests.

Table 2. Specification of KL-3 Engine

Item	Value
Thrust (tonf)	13 @ sea level
Isp (sec)	260 @ vacuum
Chamber Pressure (psia)	200
Design Run Duration (sec)	59
Max. Diameter (m)	0.725 (fuel manifold)
Max. Weight (kg)	200
Mixture Ratio	2.34
Oxidizer/Fuel Mass Flow Rate (kg/sec)	42/18

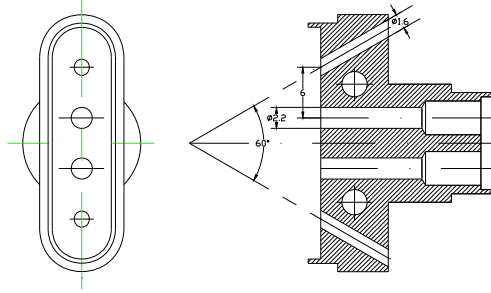


Figure 1. Drawing of an unlike split triplet injector (F-OO-F)

- Integration of a PM thrust chamber with a propellant feeding system for Integrated Power Plant Tests (IPPT) and conduct on-ground combustion tests with a vertically mounted engine.
- Declaration of the development of the propulsion system. See Table 2 for the general specification of KL-3.

Development Features of KL-3

Injector and Injector Faceplate

The early design of the injector faceplate for KL-3 employed the total number of unlike split triplet injectors (F-OO-F), 216, with an impinging angle of 30 degrees and the radial distribution of injectors. This design showed severe thermal damage on the injector faceplate even covered with thermal barrier coating through the hot firing tests of subscale and full-scale thrust chambers and thus, a number of tests with various combinations of impinging angles and layouts of injectors led to an optimized design that the total number of injectors is 228. The injectors were decided to be rearranged on the faceplate in a vertical way for the better uniform distribution of mass flux, which eventually settled thermal damage problem, although design change resulted in minor decrease of a combustion efficiency by two percent. The thrust chamber is ignited by hypergolic fluid, TriEthylALuminum (TEAL), injected into the combustion chamber through the igniter injector centered on the injector faceplate.

As one might easily expect, one of toughest technical problems confronted during the

development of KL-3 burning heavy hydrocarbon fuel with an impinging injector was combustion stability. The thrust chamber designed and tested at the early stage of the development revealed the unsatisfactory margin of dynamic stability even with an acoustic absorber around the perimeter of the injector faceplate. The measurement of dynamic chamber pressures from the number of on-ground combustion tests showed the self-excited oscillations corresponding to the first tangential mode of the combustion chamber occurred at around 20~30 seconds after ignition.

To suppress strong transverse oscillations of pressure, the acoustic baffle had to be adopted on the injector faceplate, which resulted in a reduced total number of injectors having bigger orifice diameters to keep the total mass flow rate fixed. The employment of the acoustic baffle turned out to be very successful in terms of the suppression of combustion instability even though the combustion efficiency of the thrust chamber decreased by about two percent. A number of stability rating tests using an external pressure perturbation device, a pulse gun, confirmed that the thrust chamber operating at the design and off-design working window became decoupled from combustion instability.

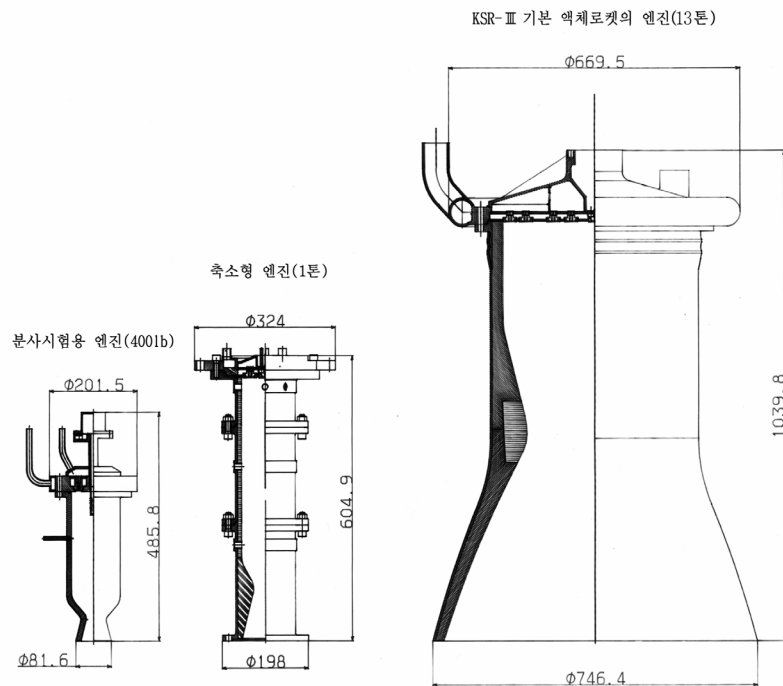


Figure 2. Cutaway views of subscale and full-scale thrust chambers.

Combustion Chamber Housing

Throughout the program, three different types of a chamber housing were developed and tested. At first, a steel case chamber housing as presented in Fig. 3 was fabricated and used for the assessment of performance of injectors in a full-scale chamber by measuring static and dynamic pressures. The choice of material for the inner layer of the housing was considered one of critical technical issues for KL-3 with ablative cooling. The inner layer of the housing contacting hot combustion gas is made of silica/phenolic composite material sustaining in highly thermal environment and a pile-up angle of the material was chosen to be 60 degrees for the minimum abrasive degradation of the layer. This ablative material for the inner layer of the thrust chamber assisted with fuel film cooling could withstand harsh thermal environment and used for all of the full-scale models manufactured throughout the program.

Another composite material was considered for the reduction of weight and manufacturing cost of the thrust chamber. The outer layer of PM and FM chamber housings is made of carbon fiber using a filament winding technique, which is widely utilized in aerospace industry. Pictures in Fig. 3 show PM and FM thrust chambers manufactured by using the technique.

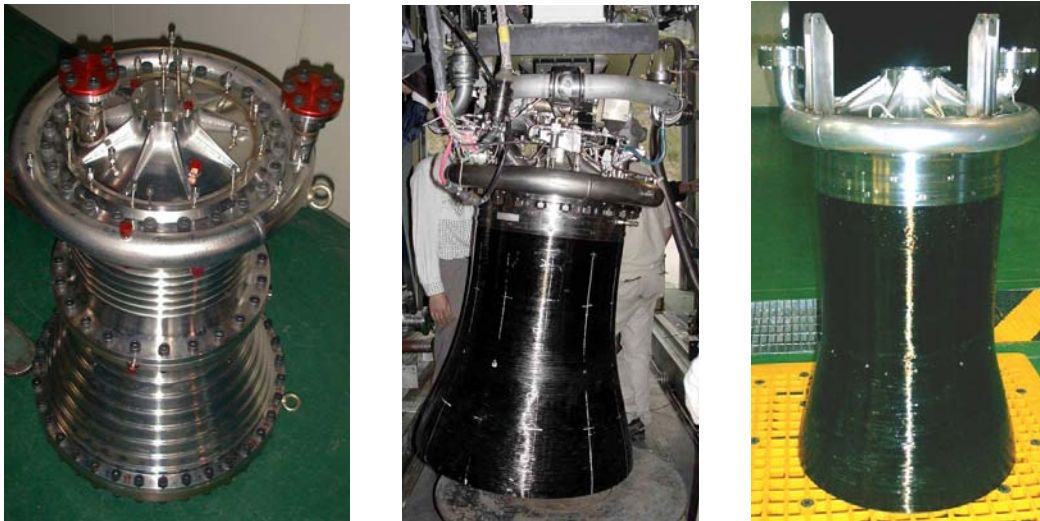


Figure 3. Photographic views of various full-scale thrust chambers. Engineering Model (EM) on the left, Power plant Model (PM) in the middle, and Flight Model (FM) on the right.



Figure 4. Photographic views of (a) a KL-3 EM thrust chamber during a combustion test and (b) a FM thrust chamber installed on the IPPT facility.

Full-Scale Engine Combustion Test

The pressure-fed, thrust chamber becomes an engine itself for the case of KSR-III and thus, an engine test focused on the confirmation of performance of the thrust chamber only. For the on-ground combustion and flight tests of full-scale engine, the total number of nine Engineering Models (EM), five Power plant Models (PM), and eight Flight Models (FM) had been manufactured. The on-ground combustion test time of the thrust chamber accumulated to 772 seconds in total including on-ground horizontal stand tests, integrated power plant tests, and stage qualification test.

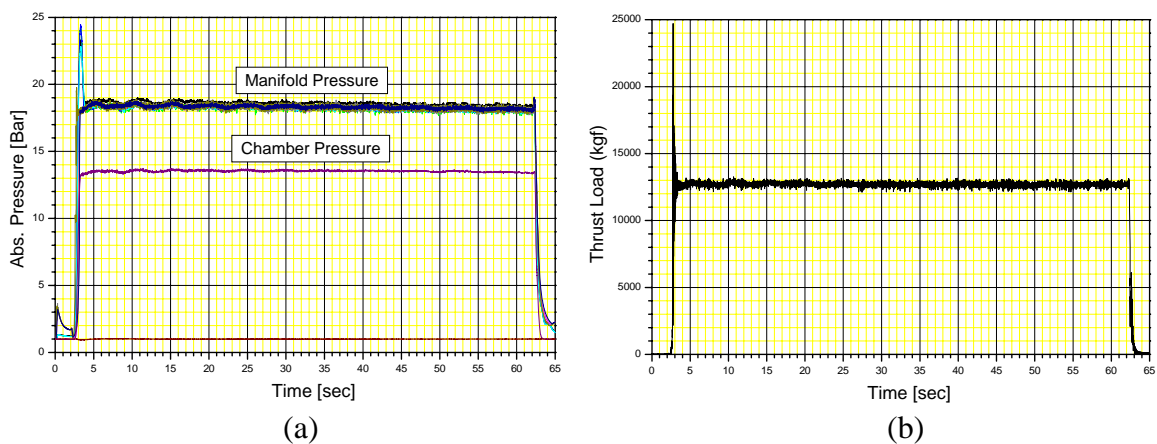


Figure 5. Typical results of an on-ground combustion test; (a) manifold and chamber pressures and (b) thrust measurement.

First, the on-ground combustion test by using only a thrust chamber had been conducted at Rocket Engine Test Facility (RETF) with a horizontal test stand. This facility provides constant mass flow at preset values pressurized by high pressure gaseous nitrogen. The typical combustion test results are shown in Fig. 5.

Development of Propellant Feeding System

KSR-III propellant feeding system consists of pressurization system using helium gas, propellant supply lines, ignition, purge and drain lines. Pressure-fed thrust chamber usually rates at a thrust level of 10 tonf. For the development of KSR-III, it was not possible to utilize a turbo pump due to barely available technologies and experiences in designing turbo machinery operating at such a low temperature. It had been decided to make the best use out of a pressure-fed system relatively simple in terms of realization of the propellant feeding system. Most of all, pressure regulators, which can provide propellants at a constant pressure, had to be developed first. These pressure regulators at low and high working pressures play a critical role in the propellant feeding system since these kept the inlet pressure into the thrust chamber constant from the highly pressurized helium tank at 4000psi. The pressure regulator on the liquid oxygen line working at a very low temperature had to provide more confidence and stability than the one on the kerosene side. The regulators adopt a two-step pressure drop scheme to achieve pressure controlled at a requirement. For the development of these regulators, various tests for the identification of characteristics had been conducted and consequently, many design parameters such as optimum material, operating conditions, and flow coefficients could be determined as a result. See Fig. 6 for the schematic of the system and general specification of the system is listed in Table 3.

The propellant supply line consists of sumps, venturies, shut-off valves, and pipe lines. For the gimbaling of the engine, the three-axis flexible lines were applied and venturies used for mass flow rate control at the beginning of the combustion. The combination of venturi and pressure regulator can provide a stable and fixed mass flow into the chamber for achieving constant thrust. During combustion, the variation of chamber pressure can be minimized by the application of cavitation ventureries. To confirm the operation of the developed venturies, the cold flow test using water and real propellants were carried out.

Ignition fluid stored in an ampule can flow into the thrust chamber with opening of the pyrotechnic valves.

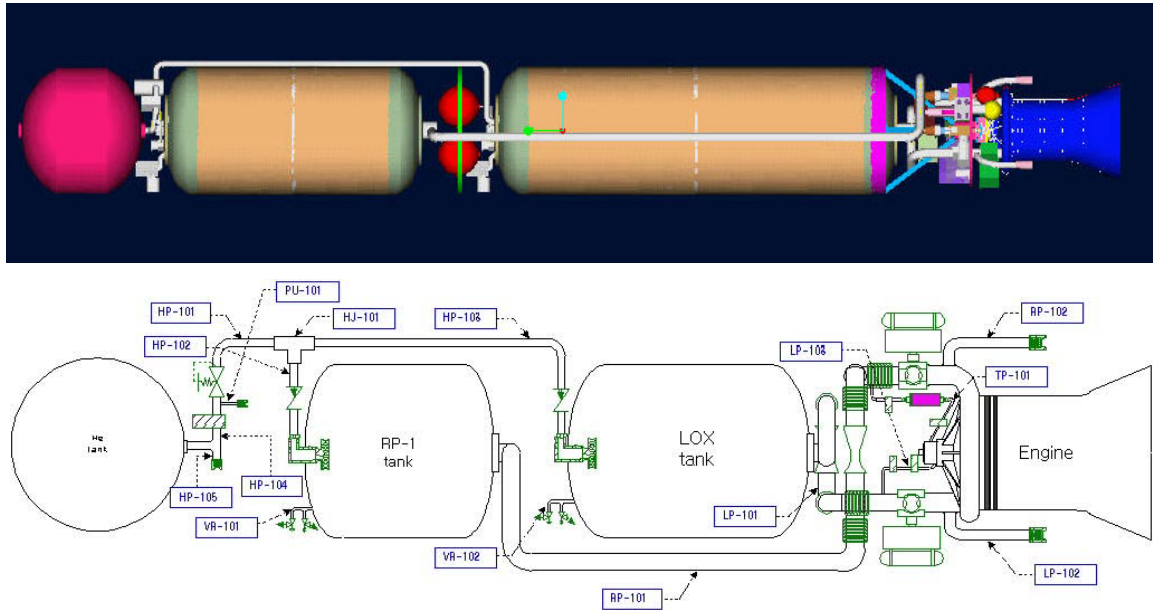


Figure 6. 3-D model and schematic of the propellant feeding system.

Table 3. Specification of KSR-III Propellant Feeding System

	Pressurant	Fuel	Oxidizer
Flow	Gaseous Helium	Liquid Jet A-1	Liquid Oxygen
Tank Pressure (psia)	4,500 (initial) 400 (final)	350	350
Tank Shape	Spherical	Cylindrical	Cylindrical
Length (m)	-	2.145	3.242
Radius (m)	0.7754	0.99	0.99
Volume (m ³)	0.488	1.396	2.246
Propellant Weight (kg)	23.4	1,089	2,513

CONCLUSIONS

Throughout the Korea Sounding Rocket-III program, all the crucial tests required for the development of a liquid propulsion system had been conducted in Korea for the first time. KSR-III rocket powered by the liquid propulsion system successfully finished its Launch campaign on 28th of November, 2002. The program certainly gave valuable experiences to engineers involved in the development of the liquid rocket engine. Also, it is worth to mention that through the program, collaborative work with industries and universities was effective on troubleshooting various problems. Major infrastructures (S/W & H/W) are well set up for developing advanced LREs. KSR-III's lessons will be the sound foreground for the development of space launch vehicles.

ACKNOWLEDGEMENTS

Authors would like to express their sincere gratitude to all the persons who made their efforts to successfully accomplish the program, and without their devotion, this program could have never achieved the goal in time which had been ambitiously set five years ago.

REFERENCE

1. Korea Aerospace Research Institute, "Research and Development of KSR-III," Ministry Of Science and Technology, M1-9702-00-0001, 2002.

CONTACT

Yeon Seok Chae, Ph. D.	President, yschae@kari.re.kr
Soo Yong Lee, Ph. D.	Director, Space Propulsion Division, sylee@kari.re.kr
Seonghyeon Seo, Ph. D.	Senior Researcher, Rocket Engine Dept, Space Propulsion Division, sxs223@kari.re.kr

Development of KSR-III Liquid Propulsion System

October 28, 2003

Yeon Seok Chae

Korea Aerospace Research Institute

Overview of Korea Sounding Rocket (KSR) Projects

	KSR-I	KSR-II	KSR-III
Objectives	Measurement of ozone layer	Measurement of ozonosphere, ionosphere and X-ray experiment	Development of scientific liquid propellant rocket for space launcher
Period	'90.7 ~ '93.10	'93.11 ~ '98.6	'97.12 ~ '02.12
Altitude	39.0 km, 49.4 km	137.2 km	50 km
Length	6.7 m	11 m	13.4 m
Weight	1.2 ton	2.02 ton	6.2 ton
Payload	150 kg	150 kg	150 kg
Propulsion	1 st Stage : SRM	1 st Stage : SRM 2 nd Stage : SRM	1 st Stage : LRE 2 nd Stage : SRM

Development of Liquid Propulsion System for KSR-III Project

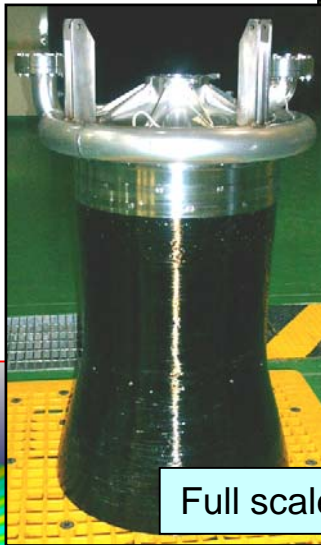
□ Objectives

- First Sounding Rocket with Liquid Propulsion System
 - No Experiences in Handling Liquid Propellants

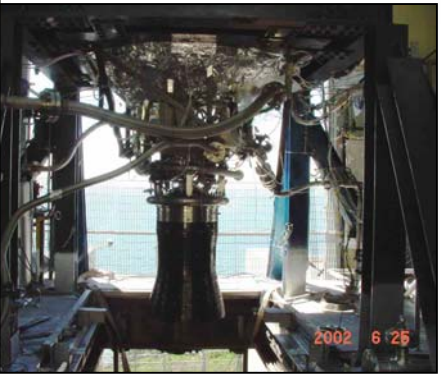
- R&D of Key Technologies for Space Launcher
 - Liquid Propulsion System using Clean Propellants
 - Pressure Fed Propellant Feeding System with Helium
 - Relatively Simple Design of Engine

- Incubation of Domestic Technologies for Space Industry
 - Increasing Capability of Industrial Participants
 - Collaboration with Universities for Key Technologies

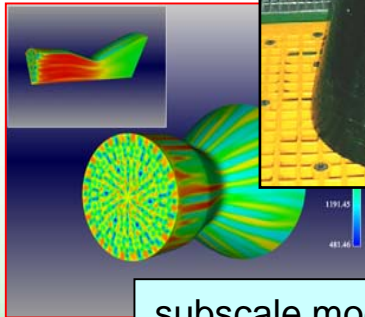
Verification Procedure of KSR-III Propulsion System



Full scale engine test(2001)



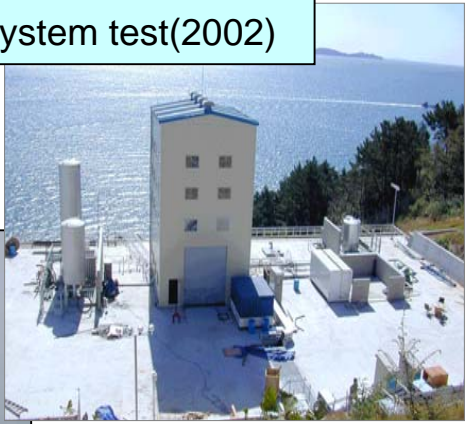
Propulsion system test(2002)



subscale model engine test(1999)



Flight test(2002)



Engine Development Procedure

- ❑ Subscale Model Engine
 - Evaluation of Main Design Parameters

- ❑ Engineering Model (EM) Engine
 - Heavy Case for Structural Safety
 - On & Off-Design Point Performance
 - Heat Resistance Performance
 - Stability Performance

- ❑ Prototype Model (PM) Engine
 - Composite Filament Winding Case

- ❑ Flight Model (FM) Engine



KSR-III Main Engine (EM)

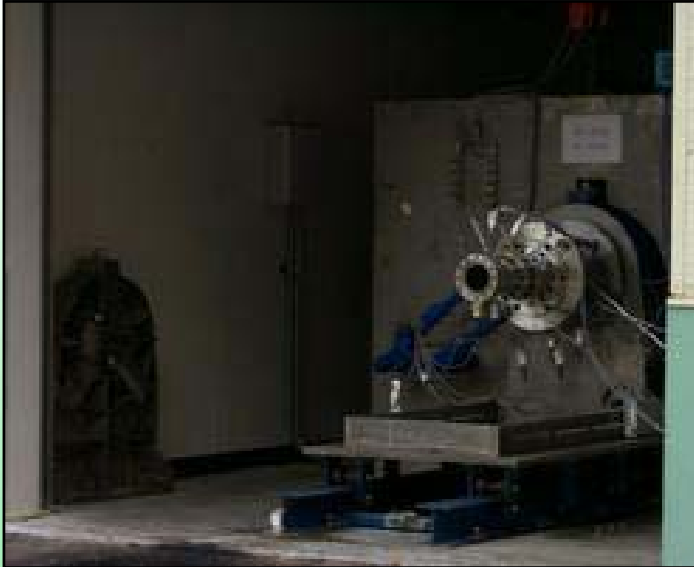
Subscale Model Engine

□ Purpose

- Evaluation of Main Design Parameters
- Injector Characteristics
- Ignition Characteristics
- Verification of Combustion Chamber Design/Manufacturing Methods
- Thermal Performance Evaluation
- Performance Evaluation of Combustion Efficiency



Performance Test of Subscale Model Engine



Firing Test of Modified Subscale Model Engine

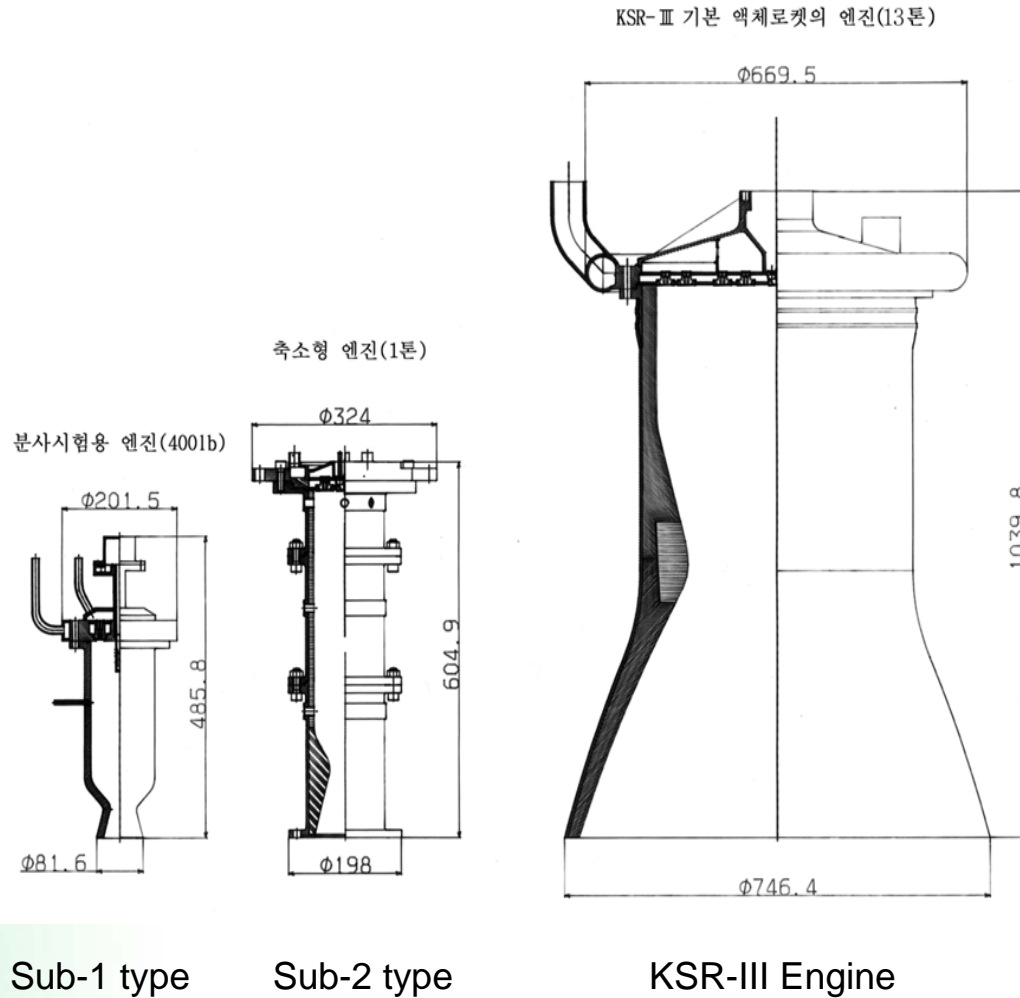


Effects of Injector Arrangement



Effects of Thermal Barrier Coating

Conceptual Comparison between Subscale Model and Full Scale Engine



Full Scale Engine of KSR-III

- KSR-III Engine of the 1st Stage
 - Pressure-fed system with helium
 - Propellants : LOX/Kerosene
 - Ignition : Hypergolic Ignitor
 - Thrust Vector Control : Gimbals



Engineering Model Engine

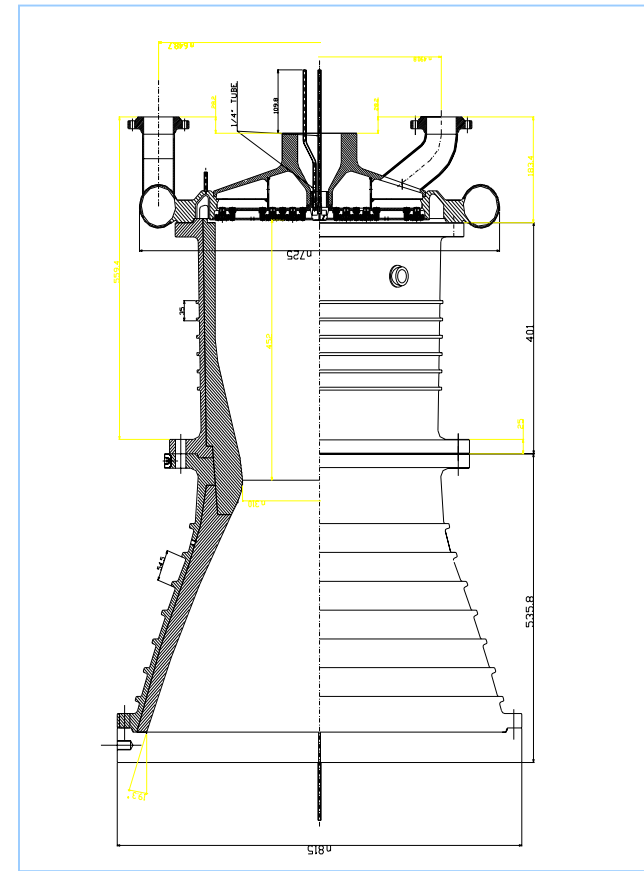
Full Scale Engine Combustion Chamber

□ Main Features

- Injector : Split-triplet impinging type (FOOF)
- Ignition : Hypergolic Ignitor
- Cooling System : Ablation and Film cooling
- No. of Injector Elements : 228

□ Specification

Thrust (ton)	13 @sea level
Isp (sec)	260 @vacuum
Chamber Pressure (psia)	200
Burning Time (sec)	59
Max. Diameter (m)	0.725 (Fuel manifold)
Max. Weight (kg)	200
Mixture Ratio	2.34
Oxidizer/Fuel (kg/sec)	42/18



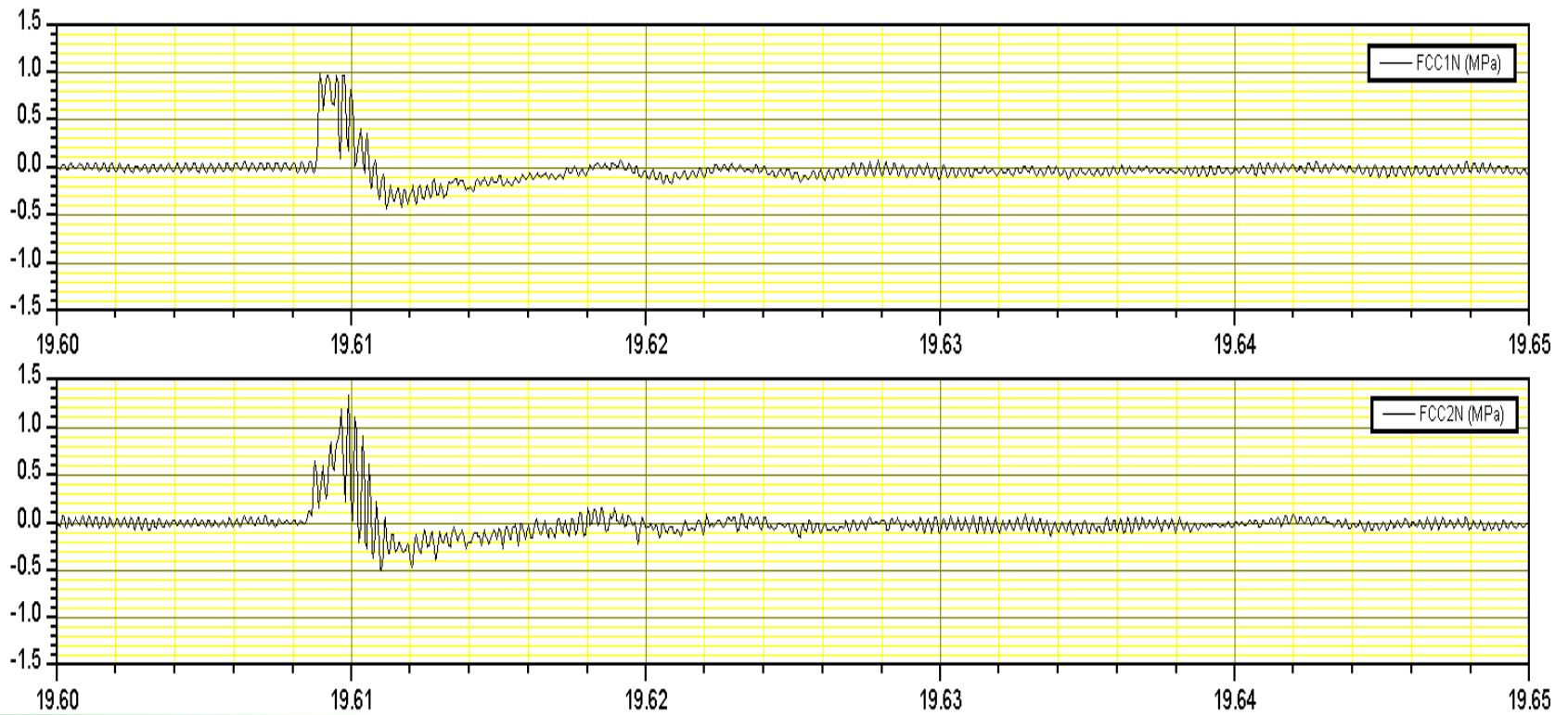
Full Scale Engine Combustion Test

□ Combustion Stability

- Stability rating test showed improper stability margin.
- Nonlinear instability occurred at 20~30 sec.
 - Effect of acoustic cavity was not enough to remove the instability.
- Baffle was adopted.
 - Temporary stainless steel baffle was used for initial test.
 - Bomb test was performed.
 - Composite baffle showed good performance for full duration test.
 - Injector array was rearranged for baffle preservation.

Decay of Artificial Disturbance

Data No. 1739 SRT with Baffle



Comparison between EM, PM and FM Engines



EM Engine

- Heavy Type Case
- Verification of Performance (Combustion Instability)



PM Engine

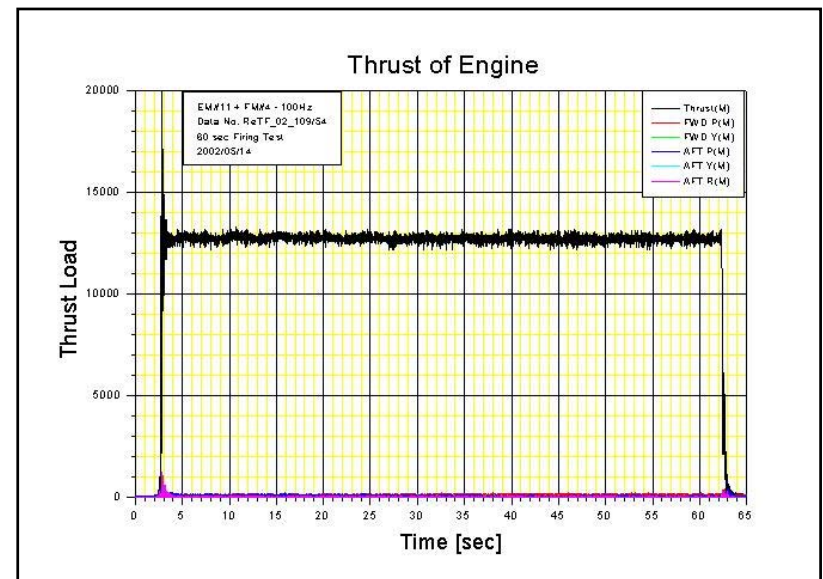
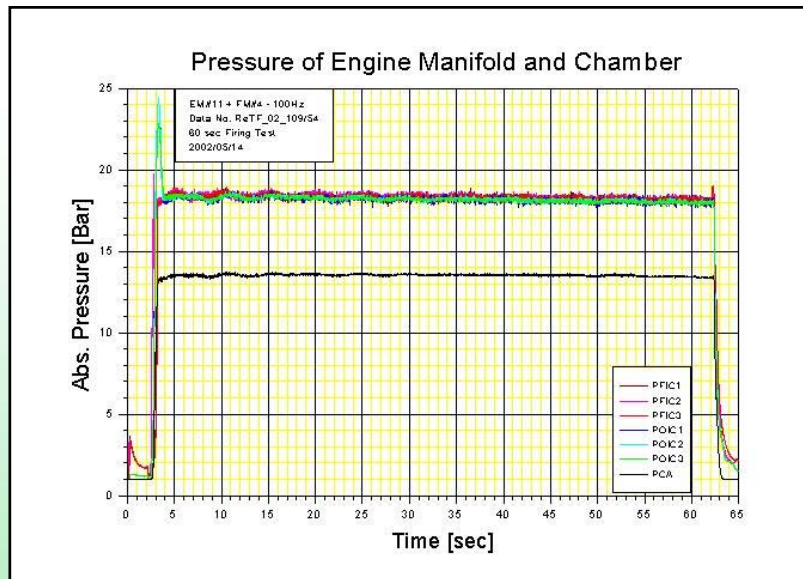
- Large Expansion Ratio
- Filament Winding Combustion Chamber



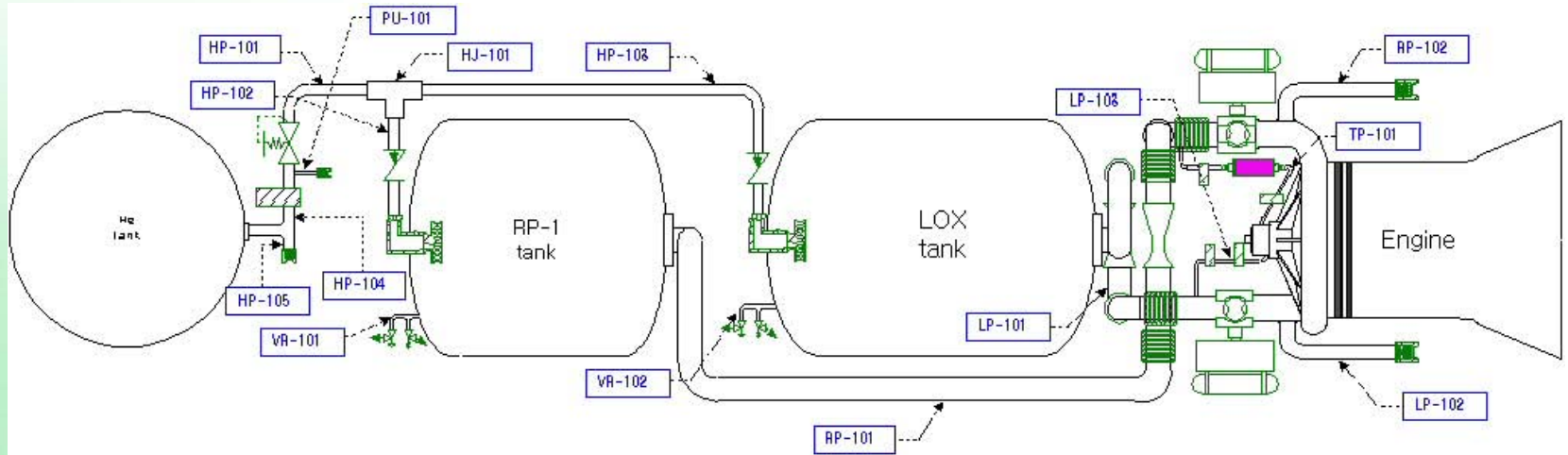
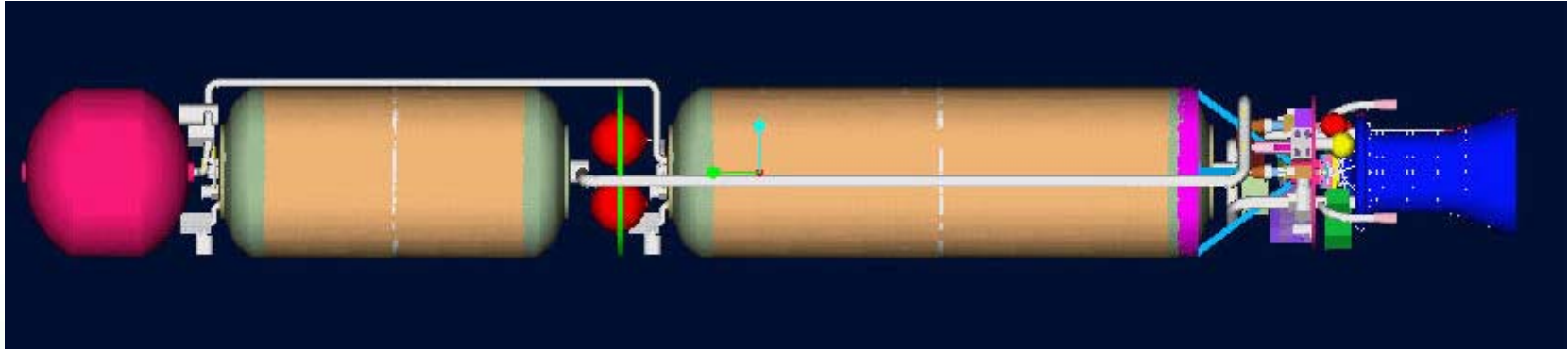
FM Engine

- Optimum Nozzle Expansion

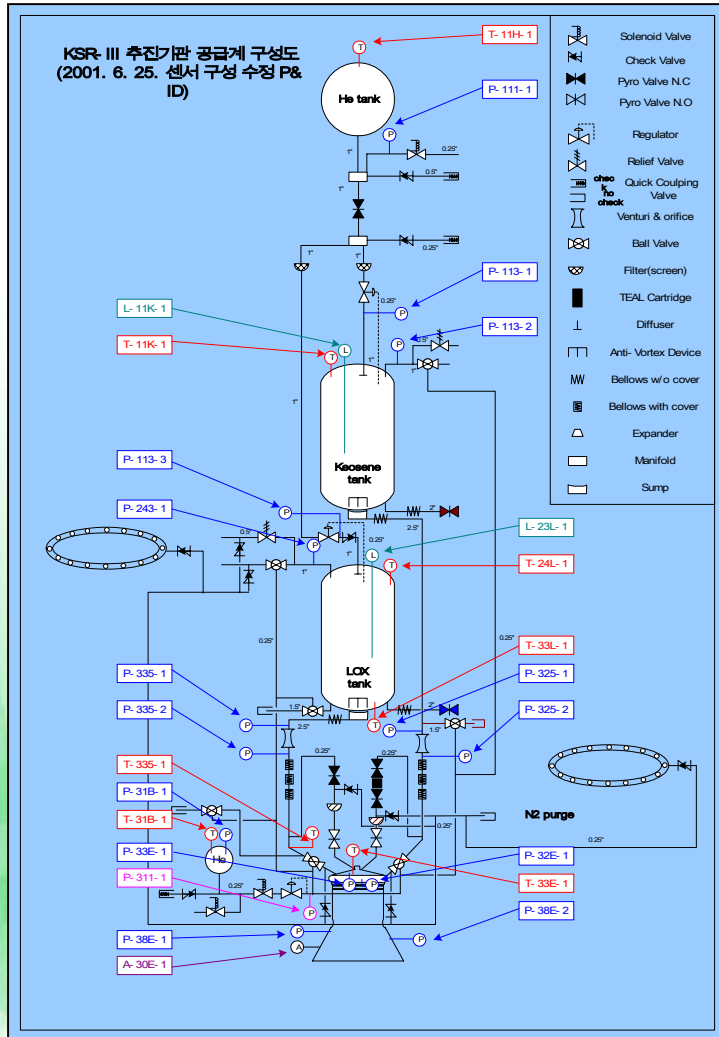
Typical Test Results of KSR-III Engine



Schematic of KSR-III Propulsion System



Propellant Feeding System



□ Main Features

- Pressure-Fed System
- Pressurant : Gaseous Helium
- Fixed Flow Rate using Cavitation Venturi

□ Tank Specification

	Pressurant (He)	Fuel (Kerosene)	Oxidizer (LOX)
Pressure (psia)	4,500 (initial) 400 (final)	-	-
Configuration	Spherical	Cylindrical	Cylindrical
Length (m)	-	2.145	3.242
Radius (m)	0.7754	0.99	0.99
Volume (m ³)	0.488	1.396	2.246
Propellant Weight (kg)	23.4	1,089	2,513

Water Flow Test for Feeding System

□ Objectives

- Functional Test for Every Components of Propellant Feeding System
- Proof Test for Valves and Ducts
- Verification of Sequence Controller
- Water Flow Test for Propellant Feeding System



ETB(Engineering Test Bed) for Water Flow Test

Integrated Power Plant Test

❑ Objectives

- Final Ground Test of LRE and Feeding System
- Ground Stage Test

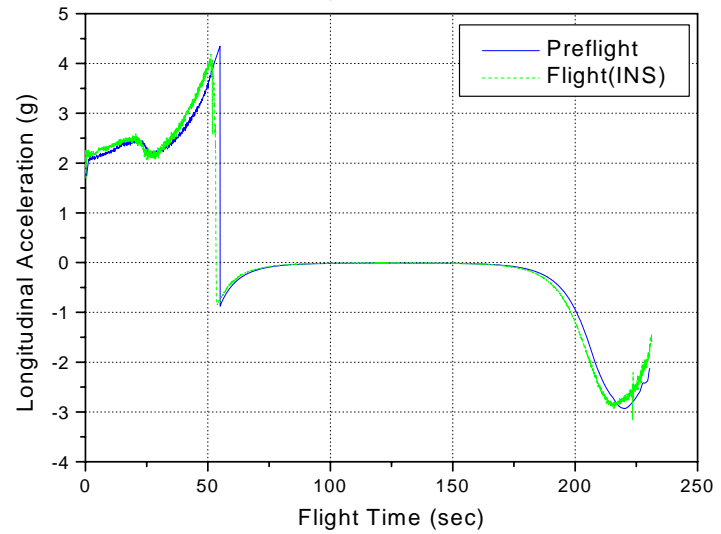
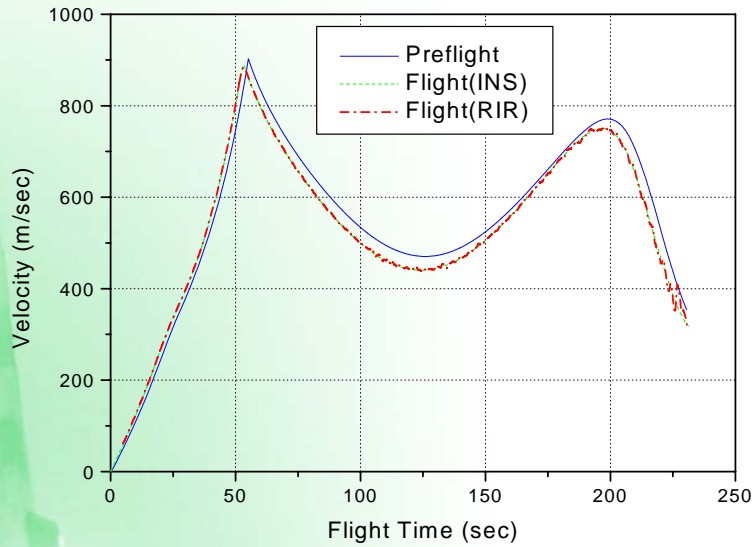
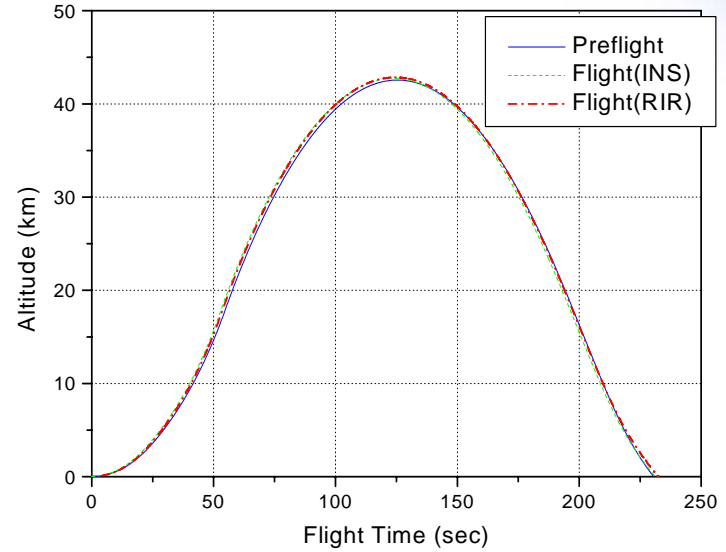
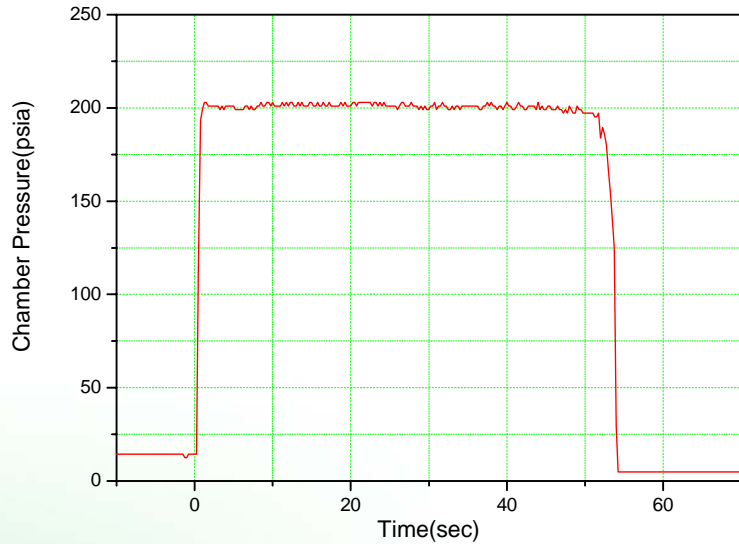
❑ Main Test Items

- Validation of Launch Scenario
- Propellant Flow Test for Feeding System
- Hot Firing Test
- Gimbals Test
- Stage Qualification Test

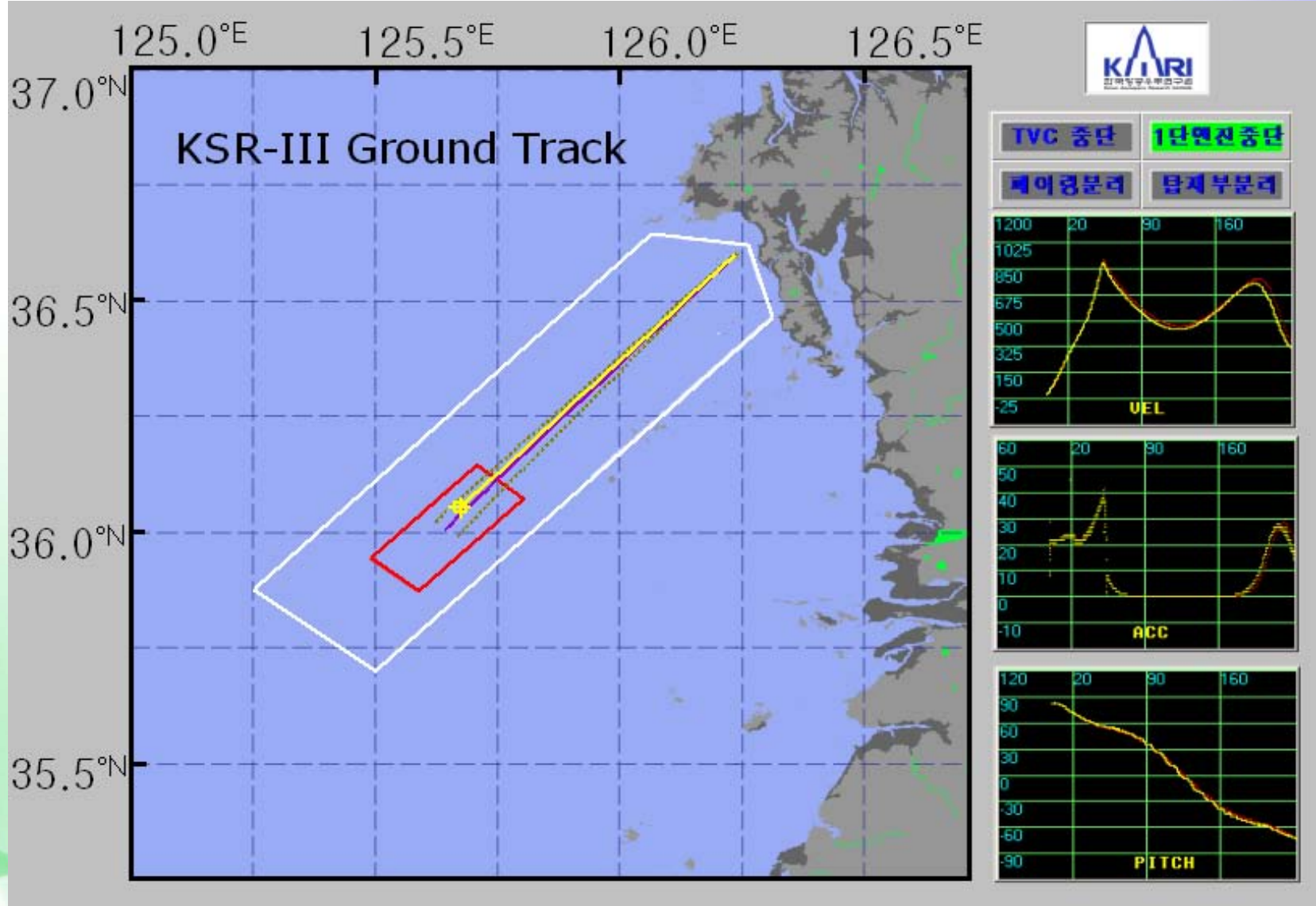
Flight Test



Flight Test Results



Flight Trajectory



Conclusions

- All ground evaluation of LRE was performed.
- Launch campaign was successful on 28th of November, 2002.
- Valuable experiences in development of liquid rocket engine were gained.
- Collaborative work with industries and universities was effective on troubleshooting various problems.
- Major infrastructures (S/W & H/W) are well set up for developing advanced LREs.
- KSR-III's lessons will be the sound foreground for the development of space launch vehicles.

A 3D-rendered rocket is shown in the process of launching from the Earth's surface. The rocket is oriented diagonally from the bottom-left towards the top-right. It has a white nose cone with a red tip, a grey body with a white band, and a tail section with a red and white striped pattern. A large, bright yellow and orange fireball is visible at the base of the rocket, indicating the point of launch. The background shows the Earth's surface with a mix of blue oceans and brownish-green landmasses.

Thank you !

Combustion Device Failures During Space Shuttle Main Engine Development

Otto K. Goetz
NASA

Marshall Space Flight Center (Retired)

Jan C. Monk
NASA

Marshall Space Flight Center (Retired)

5th International Symposium on Liquid Space Propulsion
Long Life Combustion Devices Technology

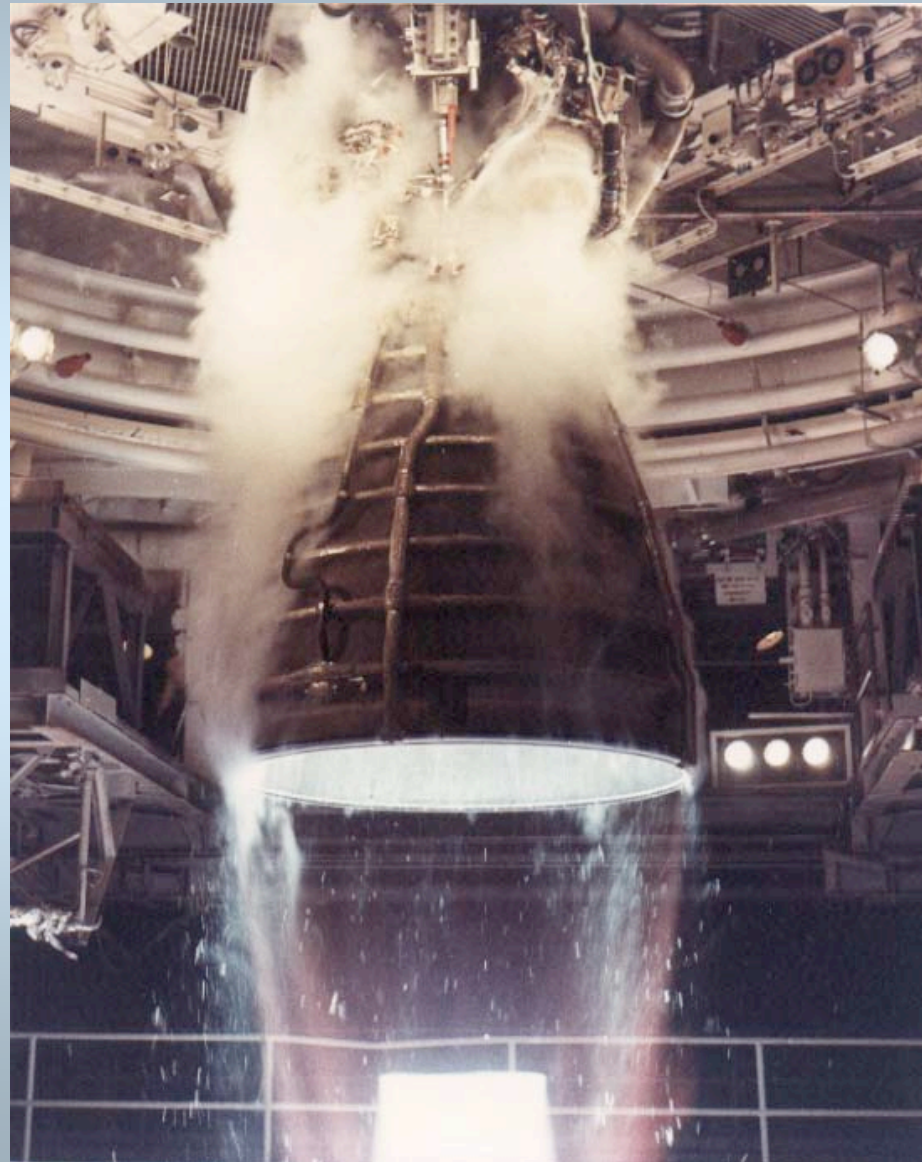
Chattanooga, Tennessee
October 27-30, 2003

The Beginning

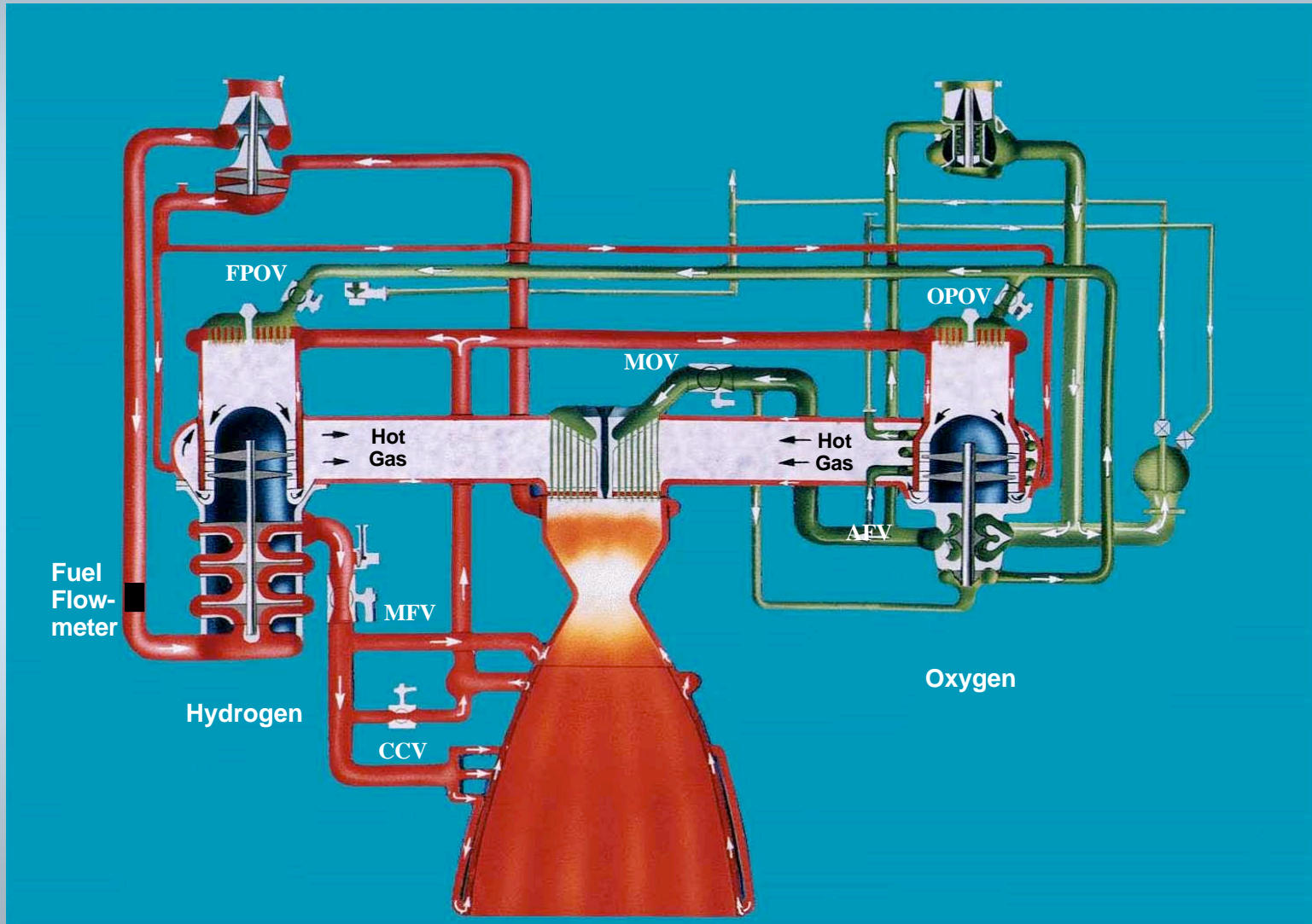
The SSME Full Scale Development Program was initiated in April 1972

- First Fully Reusable Cryogenic Rocket Engine
- First US Staged Combustion Cycle Engine
- Performance Characteristics
 - Rated Power Level (RPL) (100%) - 470,000 lbf vacuum
 - Full Power Level (FPL) (109%) - 512,300 lbf vacuum
 - Throttle Range - 109% to 50% Thrust
 - Mixture Ratio - 6.0
 - Initial Mixture Ratio Range - 5.5 to 6.5
- Life - 55 Missions
- First Flight - April 1981

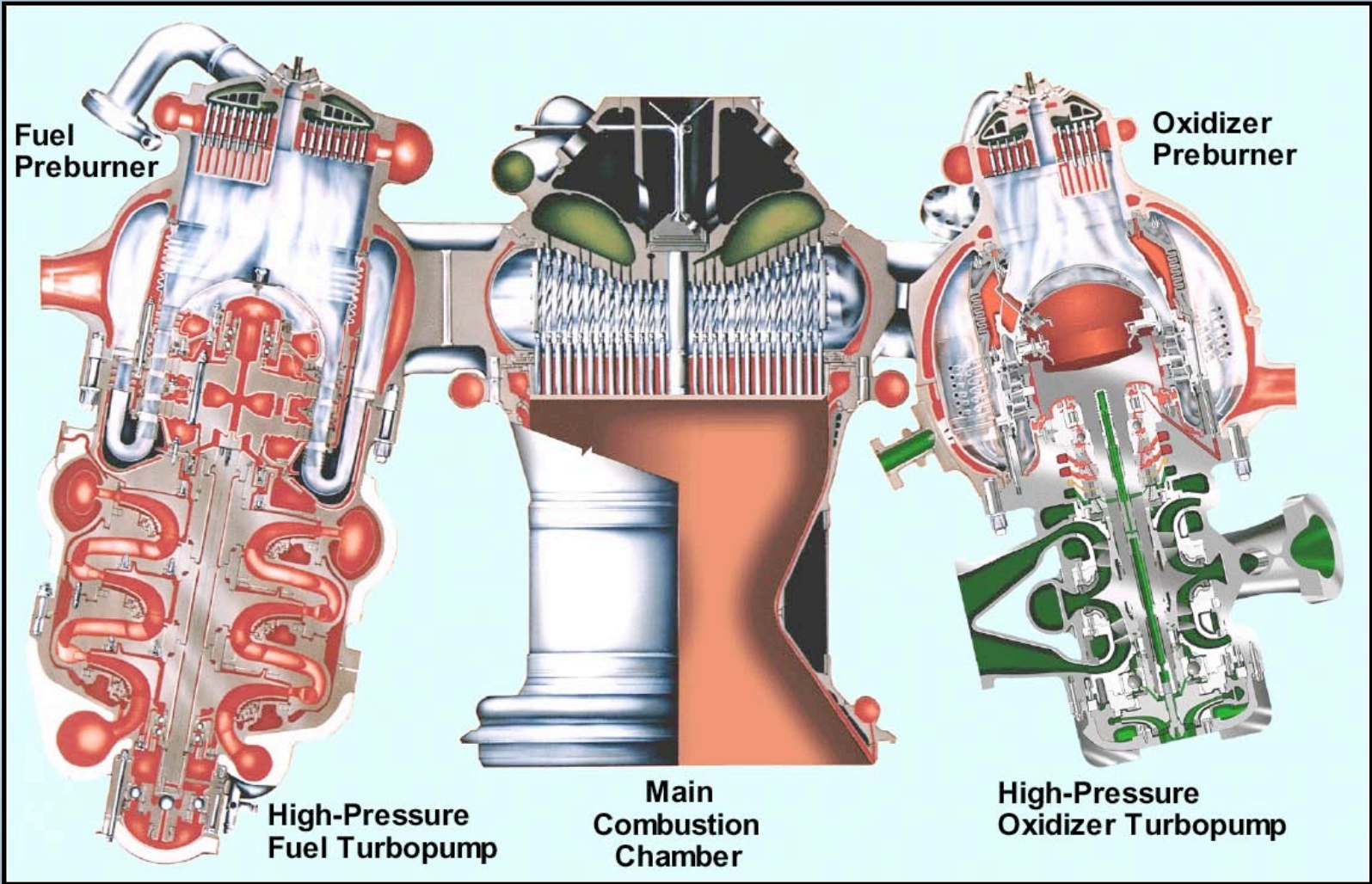
Space Shuttle Main Engine



Flow Schematic



Powerhead Component Arrangement

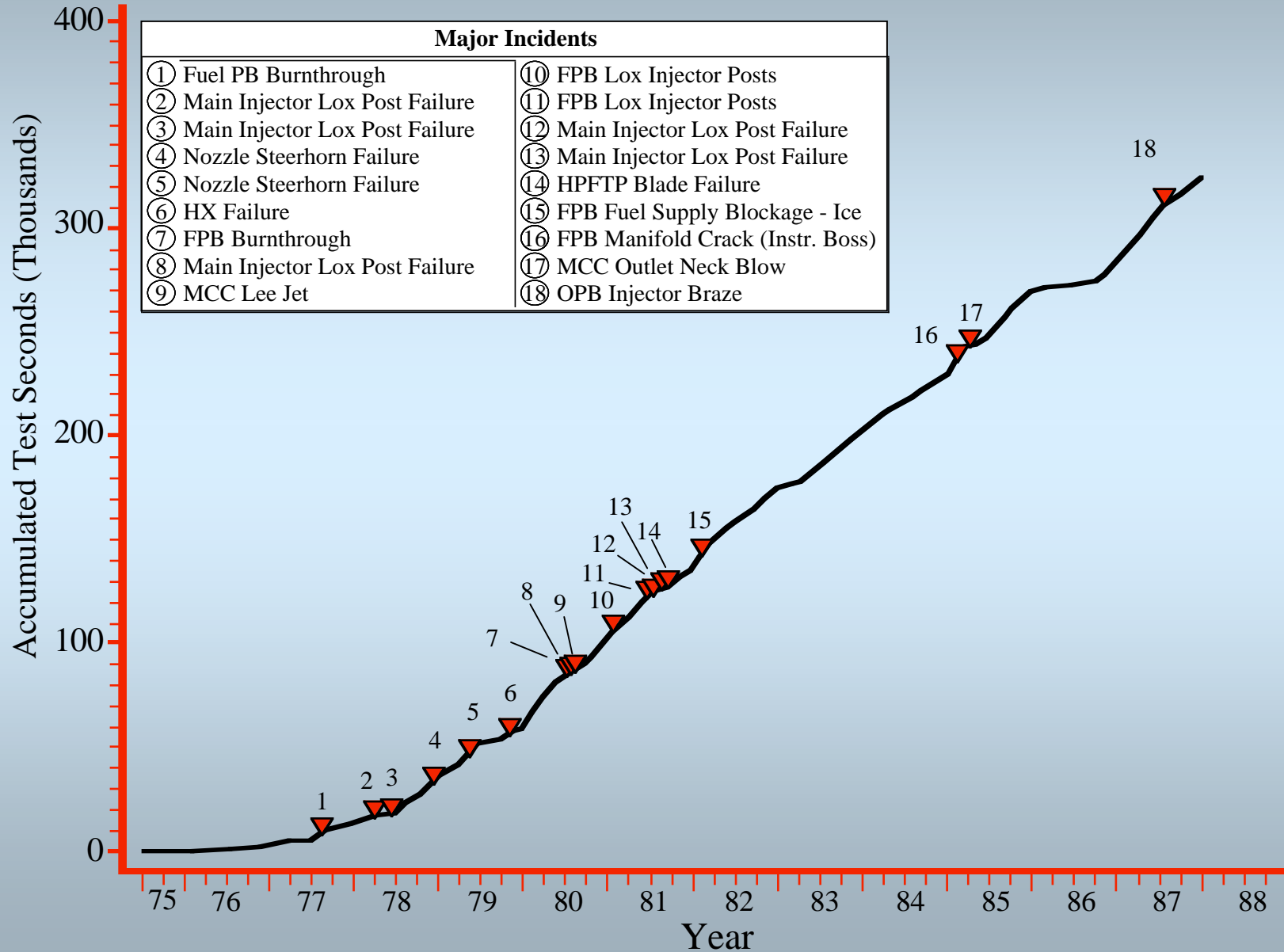


Combustion Device Major Failures

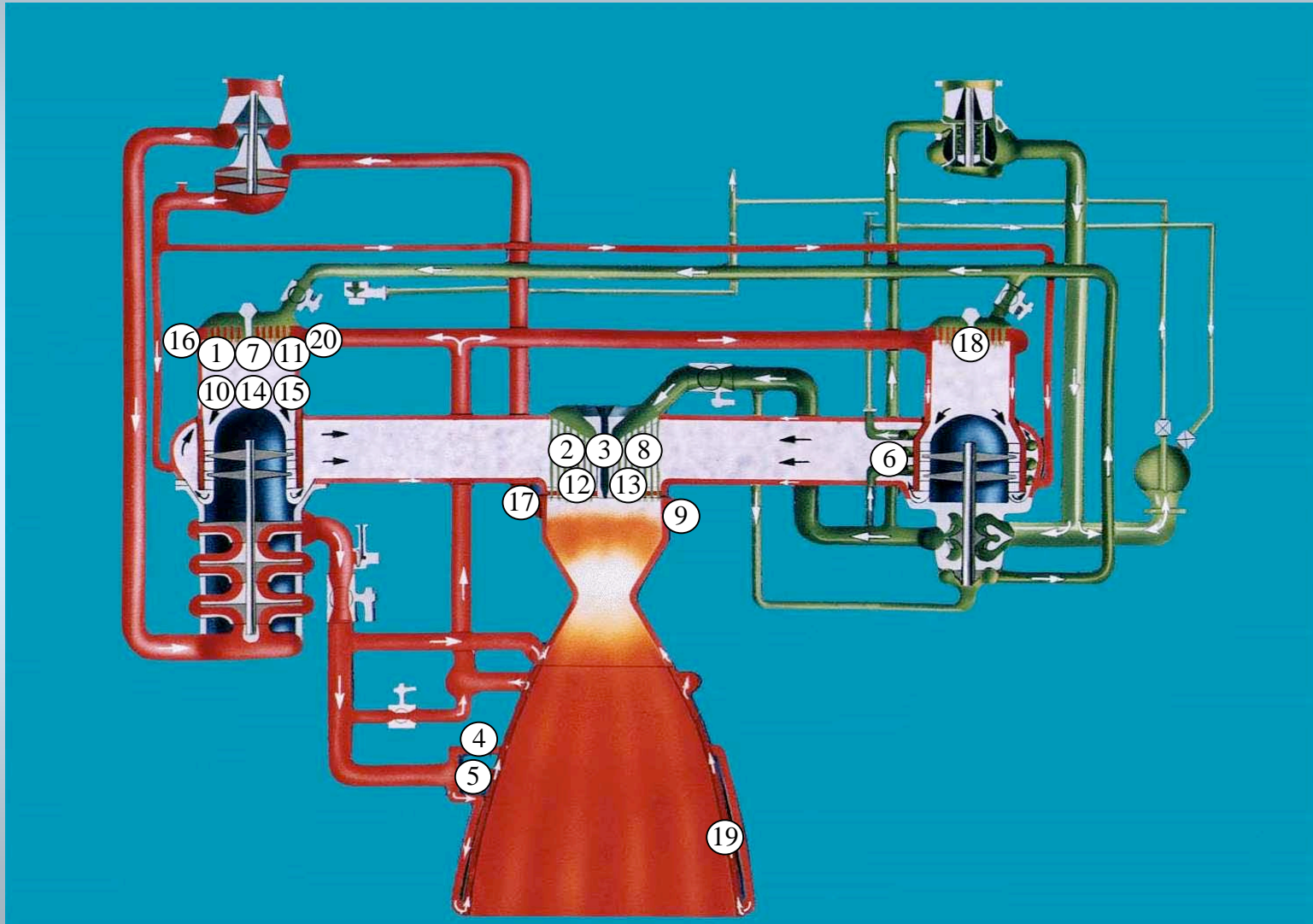
Date	Test Number	Failure	Engine S/N
August 27, 1977	901133	① Fuel PB Burnthrough	0004
March 31, 1978	901173	② Main Injector Lox Post Failure	0002
June 5, 1978	901183	③ Main Injector Lox Post Failure	0005
May 14, 1979	750041	④ Nozzle Steerhorn Failure	0201
November 4, 1979	MPTA SF06-3	⑤ Nozzle Steerhorn Failure	2002
December 6, 1978	901222	⑥ HX Failure	0007
July 12, 1980	MPTA SF10-1	⑦ FPB Burnthrough	0006
July 23, 1980	902198	⑧ Main Injector Lox Post Failure	2004
July 30, 1980	901284	⑨ MCC Lee Jet	0010
January 28, 1981	901307	⑩ FPB Lox Injector Posts	0009
July 14, 1981	902244	⑪ FPB Lox Injector Posts	0204
July 15, 1981	901331	⑫ Main Injector Lox Post Failure	2108
September 2, 1981	750148	⑬ Main Injector Lox Post Failure	0110
September 21, 1981	902249	⑭ HPFTP Blade Failure*	0204
February 12, 1982	750160	⑮ FPB Fuel Supply Blockage - Ice	0110F
February 4, 1985	901468	⑯ FPB Manifold Crack (Instr. Boss)	0207
March 27, 1985	750259	⑰ MCC Outlet Neck Blow	2308
July 1, 1987	902428	⑱ OPB Injector Braze	2106
August 27, 1997	901933	⑲ Nozzle Turbe Rupture	0524
June 6, 2000	902772	⑳ FPB Fuel Manifold Contamination	0523

* Induced by Deactivated FPB Lox Posts

Combustion Devices Major Incident Chronology



Combustion Device Failures



Oxidizer Preburner Failure

Engine 2106, Test 902428, July 1, 1987

Failure: Interpropellant braze joint



Oxidizer Preburner Failures

Engine 2106, Test 902428, July 1, 1987

Failure: Interpropellant braze joint

Incident Description: Test 902428 proceeded normally until 163 seconds when the High Pressure Oxidizer Turbopump (HPOTP) turbine discharge temperature channel A began to increase without any increase in channel B. These changes indicated a hot streak in the Oxidizer Preburner (OPB). The data showed an increasing loss of turbine power beginning at 167 seconds and continuing to 188 seconds. Subsequent to 188 seconds, the overall engine power level decreased until the fuel turbine temperature lower limit was violated at 204.12 seconds and the test was terminated.

Post test inspections revealed moderate erosion in one quadrant on the OPB faceplate and a hole through the HPOTP turbine inlet sheet metal. Leakage tests of the OPB interpropellant plate conducted on the engine revealed leak at baffle number 2, row A pin (2A).

Cause: Poor quality braze joints (greater than 90 percent porosity) at row A baffle pin to interpropellant plate joint. The large porosity was related to poor process control techniques used in the laboratory furnace. The poor quality braze joint failure was most probably due to low cycle fatigue.

Oxidizer Preburner Failures



Test 902428, Engine S/N 2106

Fuel Preburner Failures

Engine 0004, Test 901133, August 27, 1977

Failure: Fuel Preburner Body Burnthrough

Engine 0006, Test MPTA SF10-01, March 31, 1978

Failure: Fuel Preburner Body Burnthrough

Engine 0009, Test 901307, January 28, 1981

Failure: Fuel Preburner Injector Erosion

Engine 0204, Test 902244, July 14, 1981

Failure: Fuel Preburner Injector Erosion

Engine 0204, Test 902249, September 21, 1981

Failure: High Pressure Fuel Turbopump turbine blade failure

Engine 0110F, Test 750160, February 12, 1982

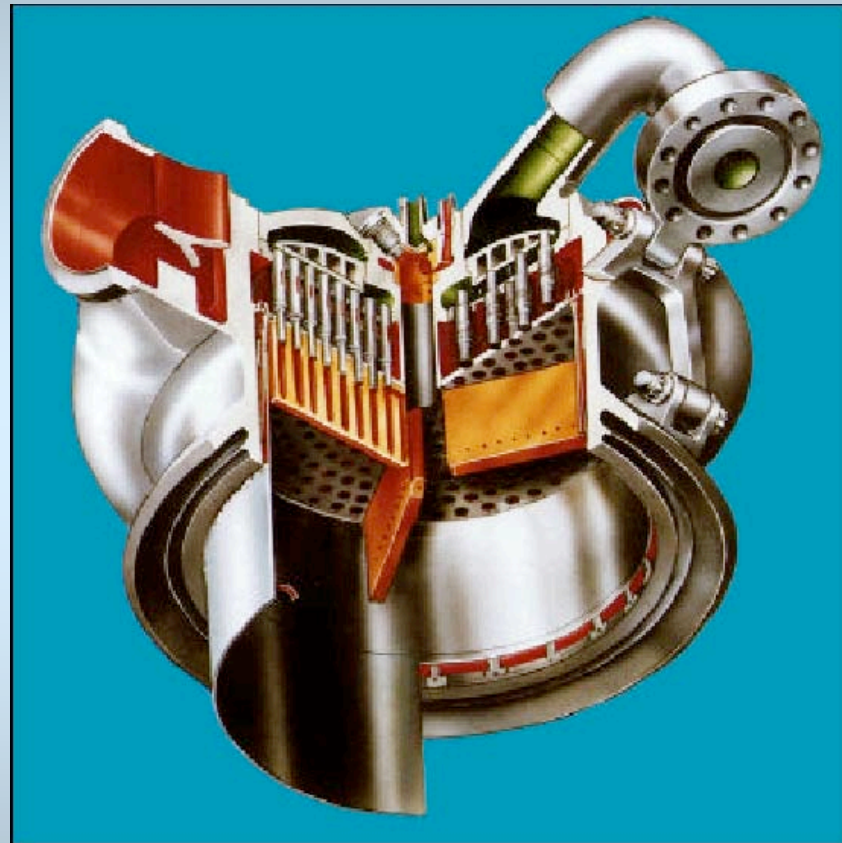
Failure: Fuel Preburner Fuel Supply Blockage - Ice

Engine 0207, Test 901468, February 4, 1985

Failure: Fuel Preburner Instrumentation Boss Crack

Engine 0523, Test 902772, June 6, 1997

Failure: Fuel Preburner Fuel Manifold Contamination



Fuel Preburner Failures

Engine 0004, Test 901133, August 27, 1977

Failure: Fuel Preburner Body Burnthrough

Incident Description: Test 901133 proceeded normally until 35 seconds when burnthrough occurred in the Fuel Preburner (FPB) body. Test was terminated by observer at 48 seconds due to external fire in the fuel preburner area.

Cause: Localized recirculation of Lox from the corner element, causing, burning of the nearby acoustic cavity, which acted as fuel to propagate the burning.

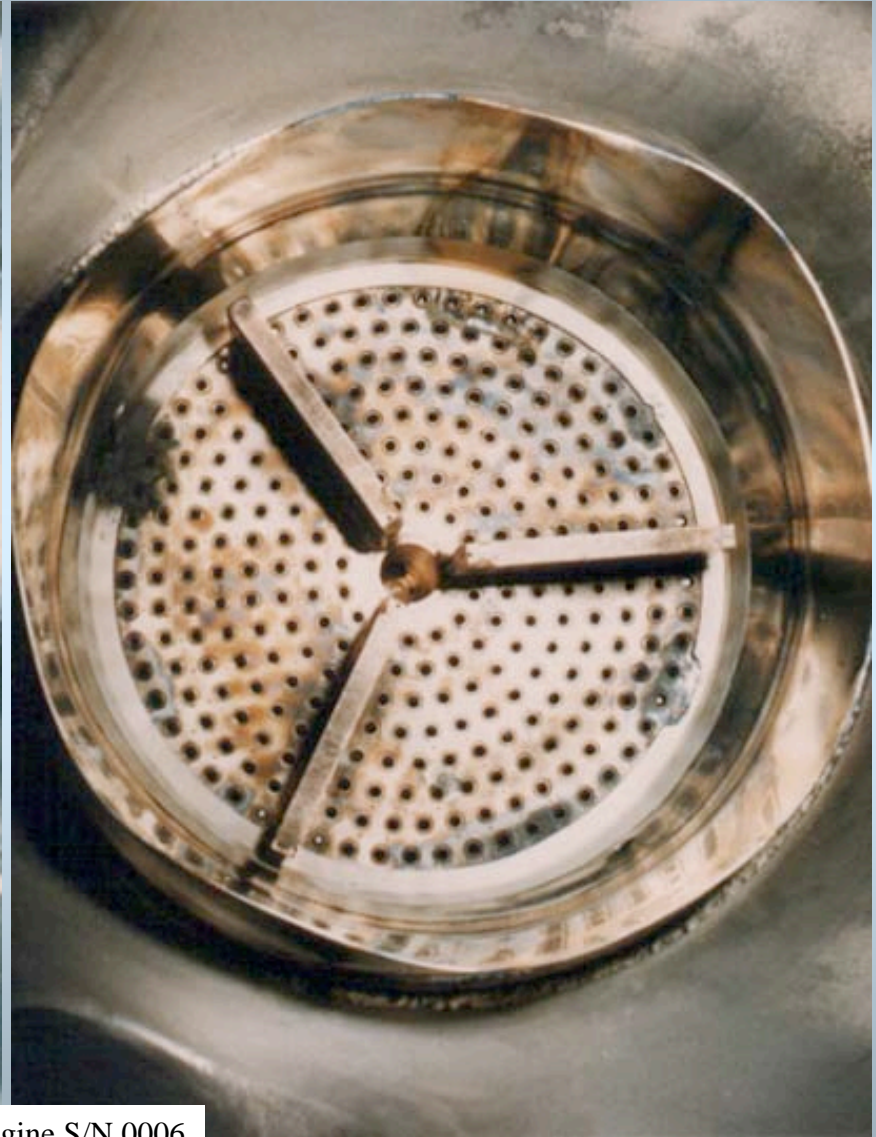
Engine 0006, Test MPTA SF10-1, July 12, 1990

Failure: Fuel Preburner Body Burnthrough

Incident Description: Test SF10-1 was prematurely terminated at 106.6 seconds when fire detectors and hazardous gas detectors triggered in the aft fuselage, and the fire detect redline observer terminated the test.

Cause: Individual element Lox posts were not concentric with the fuel annuli, causing a fuel restriction on the outboard side of the outer row elements.

Fuel Preburner Failures



Test SF10-1, Engine S/N 0006

Fuel Preburner Failures

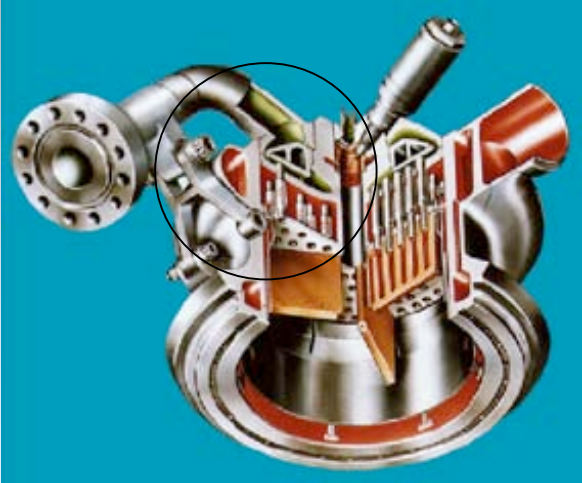
Engine 0009, Test 901307, January 28, 1981

Failure: Fuel Preburner Injector element erosion

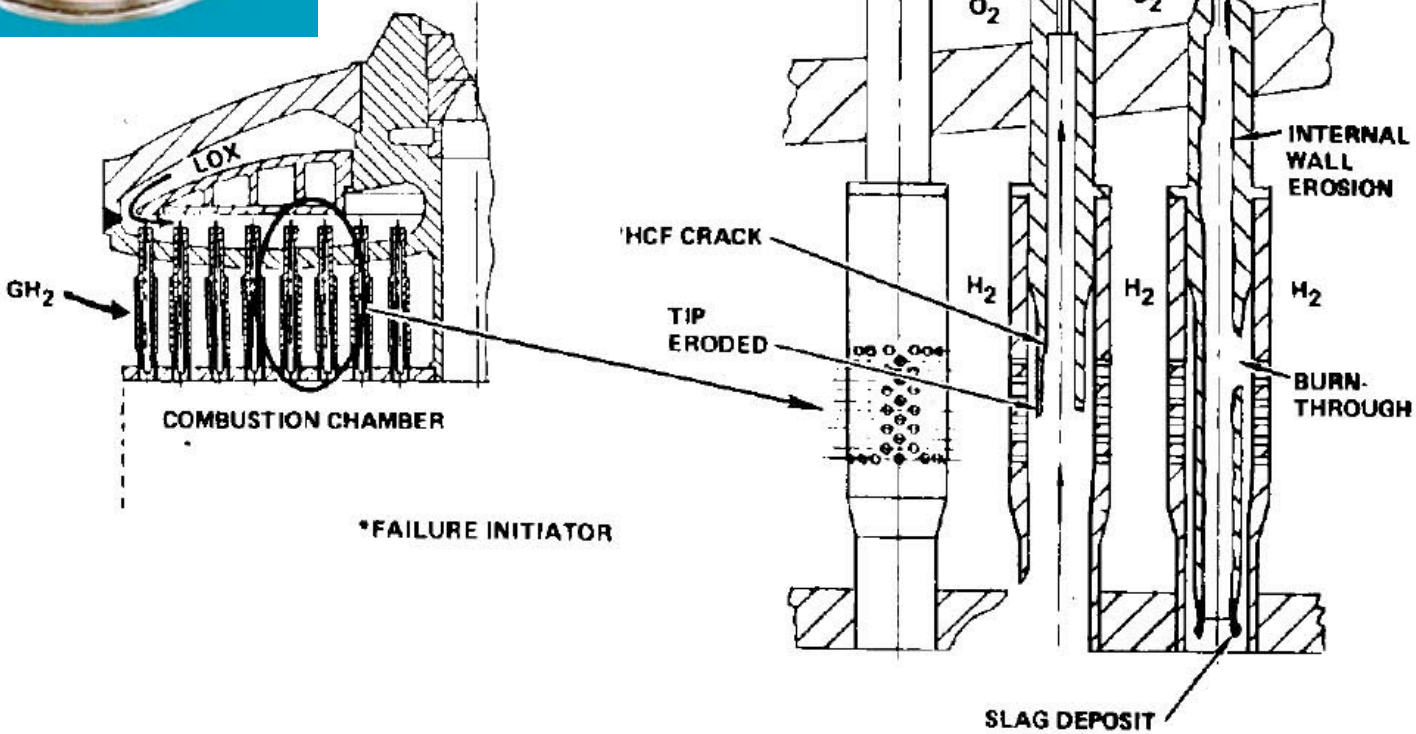
Incident Description: Test 901307 proceeded through programmed shutdown. A metallurgical examination revealed a crack in one Lox post in the fuel preburner. Fuel mixes with Lox through the crack, ignites, and burns the Lox post tip. GH2 backflows into the Lox dome through the damaged element after shutdown has been initiated. The recirculating GH2 ignites with residual Lox and causes additional injector damage.

Cause: High Alternating stresses resulting from combined mainstage mechanical vibration and flow induced vibration associated with element hydrogen flow.

Fuel Preburner Failures



Test 901307, Engine S/N 0009



Fuel Preburner Failures

Engine 0204, Test 902244, July 14, 1981

Failure: Fuel Preburner Injector Element Erosion

Incident Description: Test 902244 proceeded through program duration. Post test inspection revealed erosion and slag deposits on inside of posts.

Cause: High cycle Fatigue (HCF) induced failure in FPB Lox post fillet radius. GH2 flows into Lox post through crack, ignites and erodes Lox post tip. Damage self limiting during mainstage operation. GH2 back flows into Lox dome through damaged element during shutdown. Recirculating GH2 ignites with residual Lox in dome causing remaining damage.

Engine 0204, Test 902249, September 21, 1981

Failure: High Pressure Fuel Turbopump (HPFTP) turbine blade failure

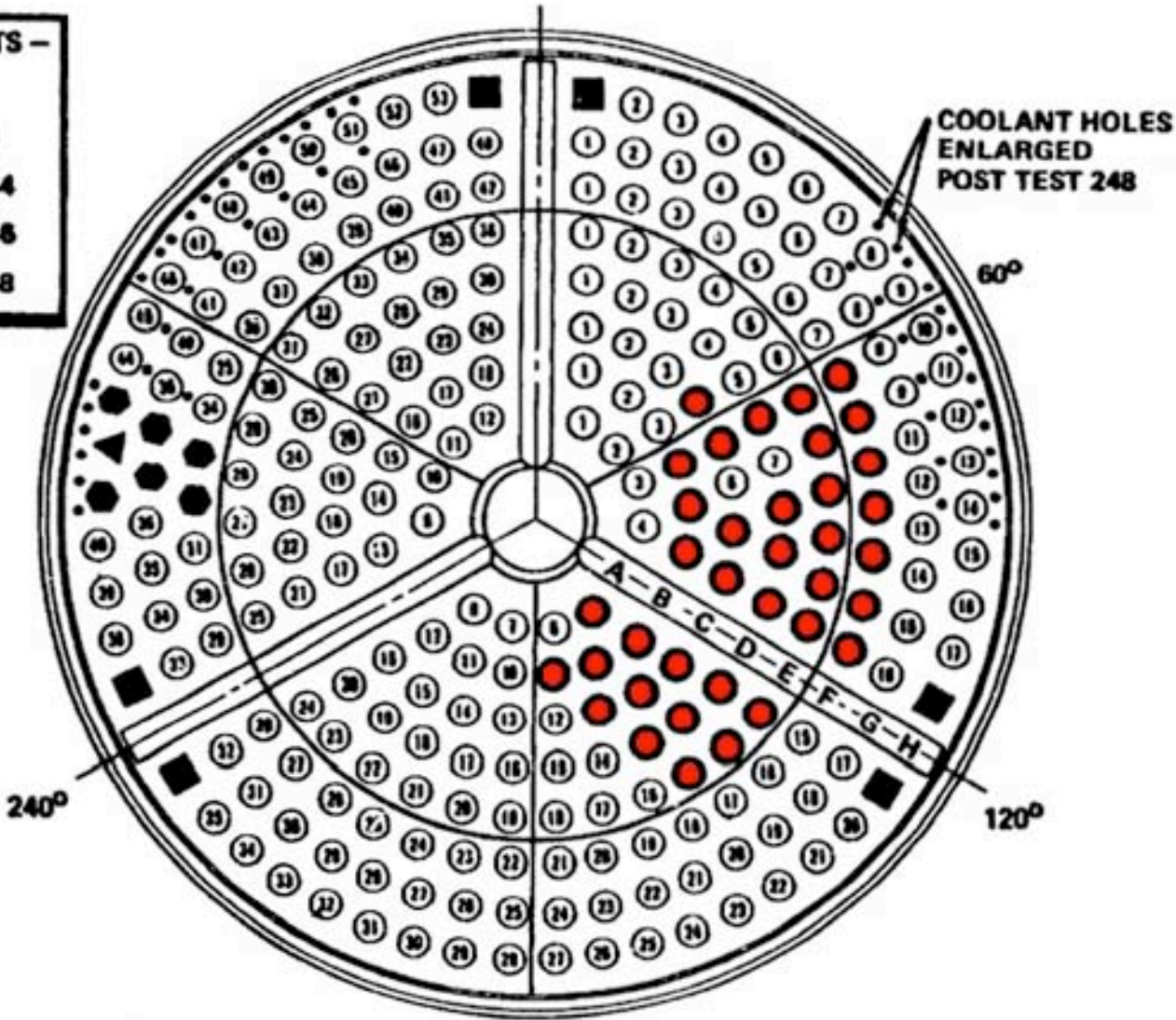
Incident Description: Test 902249 was terminated at 450.58 seconds when the HPFTP accelerometer measurements exceeded the redline value. Posttest inspection of the engine revealed a section of the HPFTP inlet volute missing, severe damage to the Main Combustion Chamber (MCC) and Main Injector, the nozzle, HPFTP and HPOTP turbine sections, the heat exchanger and the Hot Gas Manifold. The missing section of the HPFTP inlet volute caused the loss of all of the fuel from the engine leading to a highly oxygen rich shutdown.

Cause: FPB injector face had experienced damage during a prior test and had been repaired by plugging several oxidizer posts in one quadrant resulting in a circumferential temperature gradient in the preburner. Localized high temperature streaking caused disbonding of the first stage turbine tip seals; excessive rubbing of the blades caused blade failure, sudden rotor speed decay and resulting HPFTP inlet volute rupture and Lox rich shutdown.

Fuel Preburner Failures

**PINNED LOX POSTS –
LEGEND**

- STANDARD
- POST 902-244
- ▲ POST 902-246
- POST 902-248



Fuel Preburner Failures



Test 902249, Engine S/N 0204

Fuel Preburner Failures



Test 902249, Engine S/N 0204

Fuel Preburner Failures

Engine 0110F, Test 750160, February 12, 1982

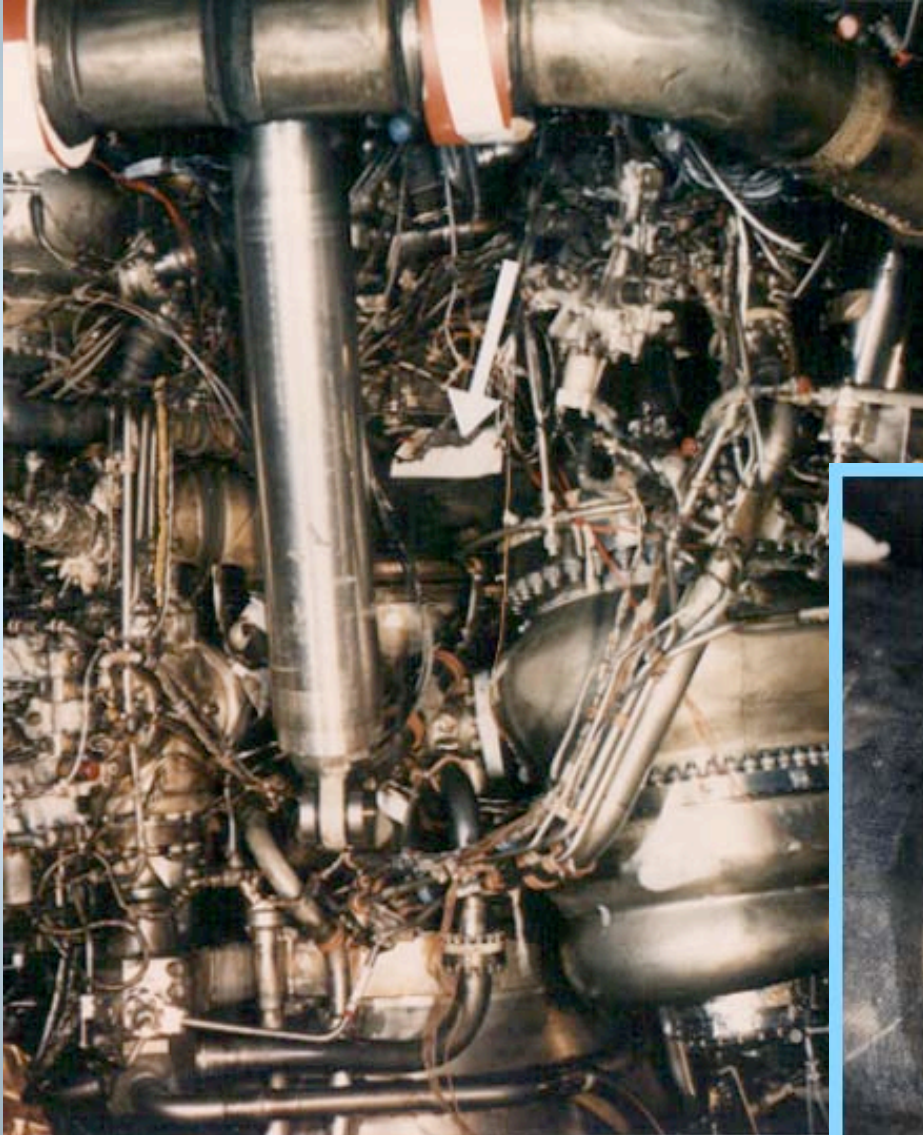
Failure: Fuel Preburner Fuel Supply Blockage - Ice

Incident Description: Test 750160 was prematurely terminated at 3.16 seconds by the HPFTP Turbine discharge temperature redline. Posttest hardware inspection revealed severe erosion damage to the high pressure fuel and oxidizer turbines, main injector, MCC, nozzle, and hot gas manifold. A hole burned through the left side transfer tube resulting in a rupture of the Fuel Preburner Oxidizer Valve actuator hydraulic line and an external fire.

Cause: Data analysis, hardware condition and supporting laboratory tests identified the cause of the incident as EDM water contamination of the fuel system upstream of the fuel preburner. The formation of ice during engine start resulted in fuel flow restriction in some fuel preburner elements. This restriction produced one or more abnormally high temperature combustion gas zones which cause turbine blade erosion and/or failure. The resulting decay in fuel flow to the engine produce excessive combustion gas mixture ratio and subsequent erosion damage.

The primary objective was to evaluate the turning of a combustion gas stream tube during its passage from the preburner, through the turbine and into the hot gas manifold. Ten FPB face coolant holes were enlarged to lower the local combustion gas temperature. An array of 16 thermocouples in the HGM would then be used to locate the cool zone after passage through the turbine. The EDM process used to enlarge the holes produces water into the engine. Normal drying procedures were used and required in excess of 2.5 times the typical time necessary to reach the dryness requirement.

Fuel Preburner Failures



Test 750160, Engine S/N 0110F



Fuel Preburner Failures



Test 750160, Engine S/N 0110F

Fuel Preburner Failures

Engine 0207, Test 901468, February 4, 1985

Failure: FPB Instrumentation Boss Crack

Incident Description: Test 901468 was prematurely terminated at 203.86 seconds when the external powerhead temperature redline was exceeded. Visual inspection revealed a crack in the weld forward of the stub to the joint flange.

Cause: High cycle fatigue of welded in port. Not flight configuration and only power head in service with welded in instrumentation ports.

Engine 0523, Test 902772, June 6, 2000

Failure: High Pressure Fuel Turbopump (HPFTP) Turbine erosion

Incident Description: Test 902772 was prematurely terminated at 5.18 seconds when the HPFTP Turbine Discharge Temperature redline was exceeded. Posttest inspection of the engine revealed FPB liner erosion; MCC hot gas wall forward end had flame spray, slag, and numerous dings and dents; and the HPFTP turbine sustained erosion damage to the turbine housing, struts and blades.

Cause: Tape contamination was introduced into the fuel system during engine assembly. The tape entered the fuel manifold of the FPB causing localized high mixture ratio. The resulting hot streak impinged on the turbine inlet housing struts and first stage vanes. A vane segment burned through and the inner section fell into the first stage blades causing rotor imbalance and significant turbine and pump damage.

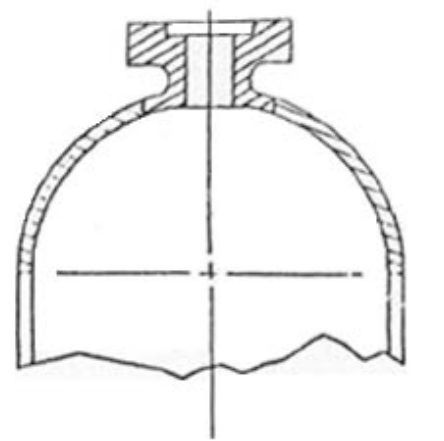
Fuel Preburner Failures

Engine Survey

Fuel Preburner Manifold

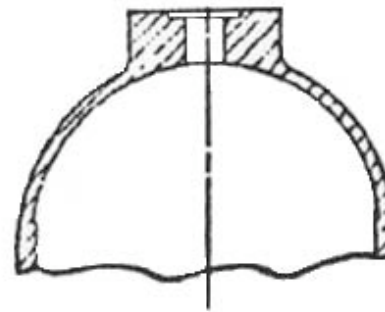
Welded Bosses

Engine S/N 0207 (One of Nine
Powerheads)



Integrally Machined Bosses

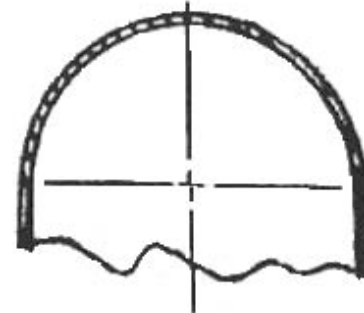
Powerhead 0007 and subs



Bosses Eliminated

Powerhead 2004 and subs

All Flight Engines



Main Injector Failures

Engine 0002, Test 901173, March 31, 1978

Failure: Lox injector post crack

Engine 0005, Test 901183, June 5, 1978

Failure: Lox injector post crack

Engine 2004 Test 902198, January 28, 1981

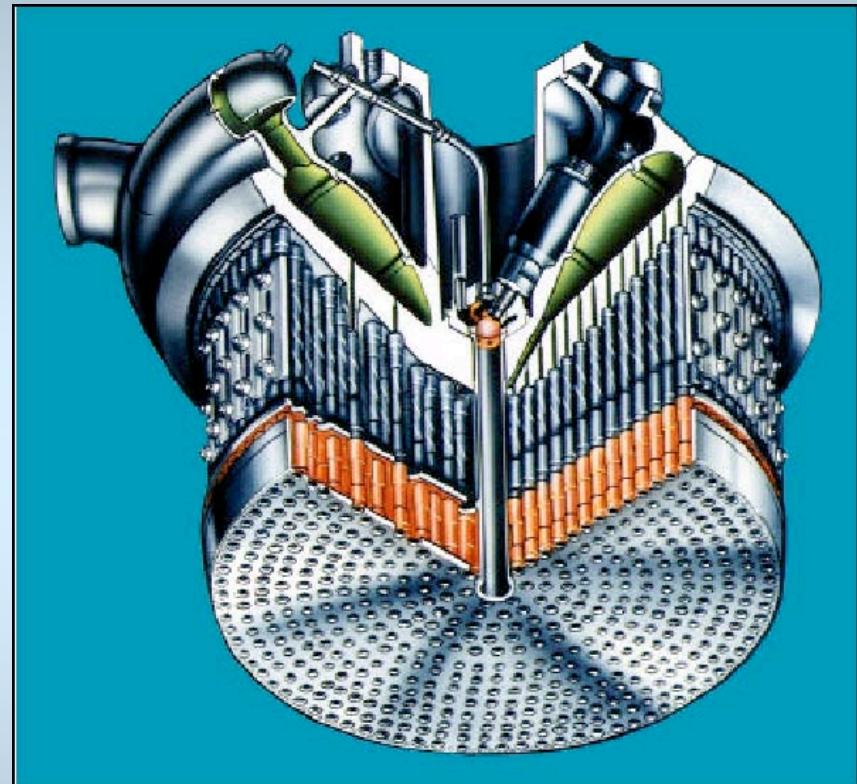
Failure: Lox injector post crack

Engine 0110 Test 750148, July 2, 1981

Failure: Lox injector post crack

Engine 2108 Test 901331, July 15, 1981

Failure: Lox injector post crack



Main Injector Failures

Engine 0002, Test 901173, March 31, 1978

Failure: Lox injector post crack

Incident Description: Test 901173 was terminated at 201.17 seconds when the HPFTP turbine discharge temperature redline was exceeded. At approximately 200.7 seconds, Lox post 10, Row 13 cracked through at the tip radius between the primary and secondary faceplates. Hot gas flow into the lox post ignited and burned out the post. Lox pouring into the face coolant manifold cause burn through of primary and secondary faceplates. Ejection of burned debris caused severe nozzle tube ruptures (46 tubes). Fuel loss couple with engine control reactions to maintain MCC pressure increased the HPFTP turbine temperature to increase until the redline was exceeded.

Cause: High cycle fatigue of the Lox post due to flow and mechanical vibration.

Engine 0005, Test 901183, June 5, 1978

Failure: Lox injector post crack

Incident Description: Test 901183 was terminated at 51.1 seconds by the HPFTP accelerometers because of an unrelated problem. At approximately, 24 seconds, failure of a group of Lox posts began. The condition appears to have limited itself and engine operation stabilized. 15 Lox posts were eroded back to the secondary faceplate and a section of the primary faceplate was burn away. The MCC hot gas wall received minor scalding and the nozzle had a failed saddle patch at one location.

Cause: High cycle fatigue of the Lox post due to flow and mechanical vibration.

Main Injector Failures

Engine 2004 Test 902198, January 28, 1981

Failure: Lox injector post crack

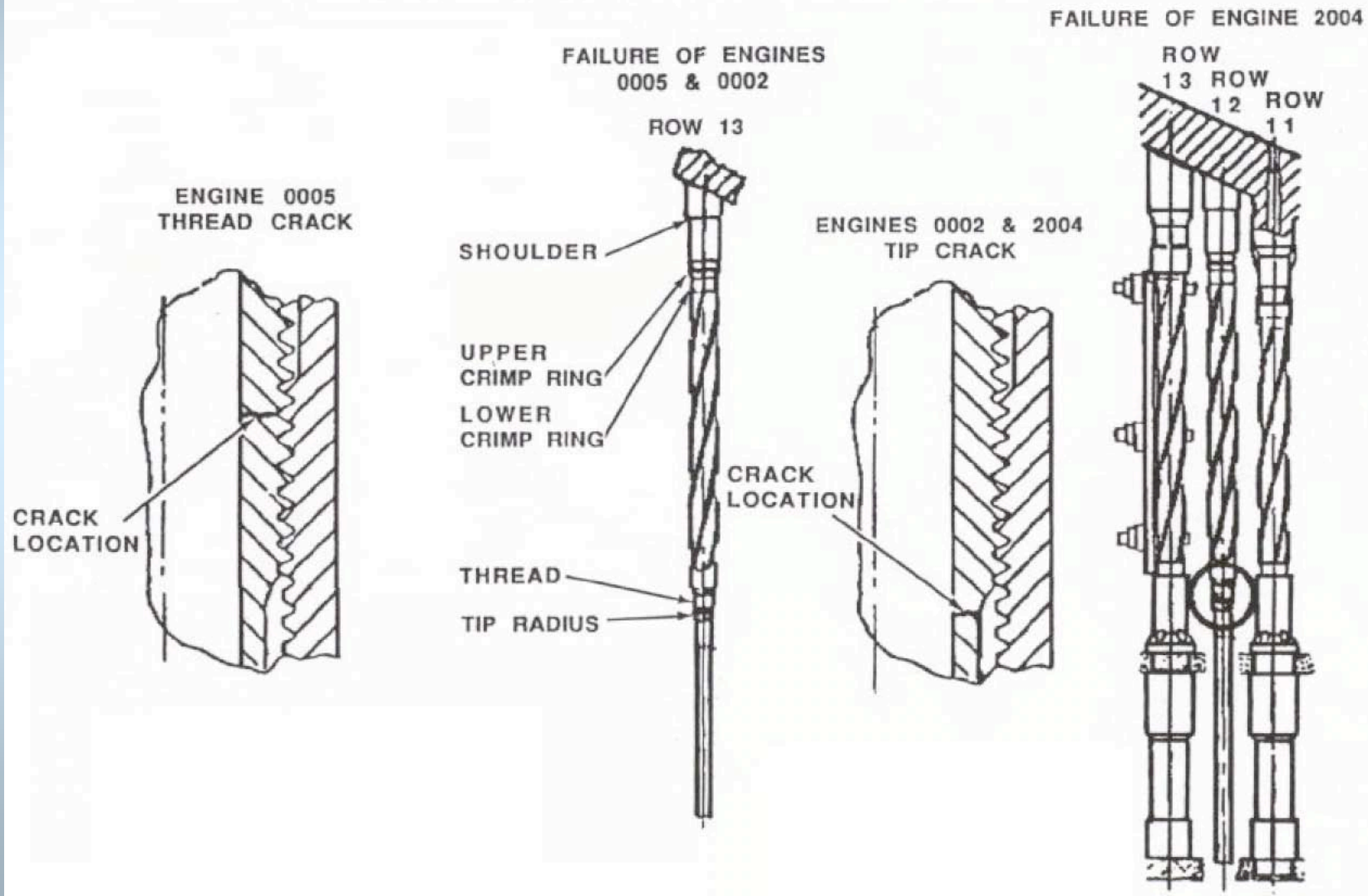
Incident Description: Test 902198 proceeded normally until 5.5 seconds when data indicated an unscheduled decrease in MCC pressure. At this same time, other engine parameters also indicated anomalous engine behavior and that the problem was localized to the MCC injector. The engine system continued to degrade until cutoff was initiated at 8.52 seconds after the HPOTP turbine discharge temperature exceed the redline value.

Posttest hardware inspection and disassembly revealed that the MCC injector was partially damaged, the MCC had slight erosion between two acoustic cavities, and the nozzle had several tubes dented and/or ruptured from the injector debris exiting the engine. No other hardware was damaged.

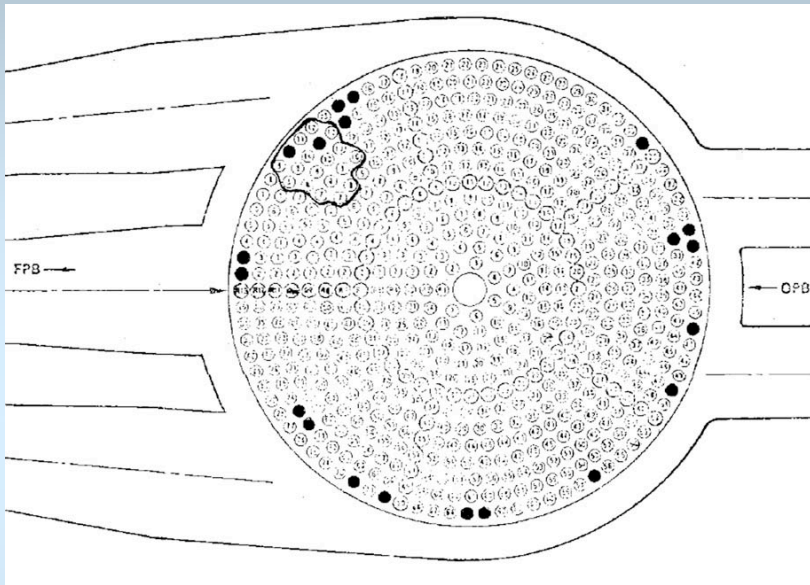
Cause: The cause of the failure was high cycle fatigue of the Lox post due to flow and mechanical vibration. Metallographical examination of the disassembled injector in rows 13, 12, and 11 revealed that 62 posts were cracked. A cross section of the fillet area of post 61 in row 12 revealed longitudinal wavy lines indicative of the type of cold working accompanying HCF. Visual observation earlier in the disassembly of the injector indicated that post 61, row 12, was the failed post. Post 61 had the most uniform burning with molten metal and slag 360°. The high cycle fatigue of the Lox posts was caused by mechanical vibration of the powerhead and flow induced vibration from the hot gas combined with high steady-state stresses.

Main Injector Failures

ENGINE FAILURES IN THE THREAD AREA

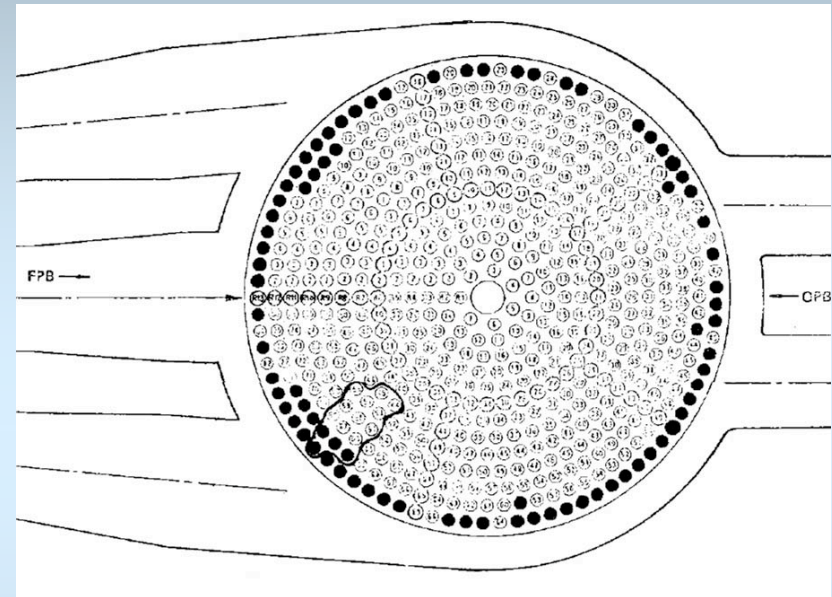


Main Injector Failures



Location of Cracked Posts
and Burnout Area

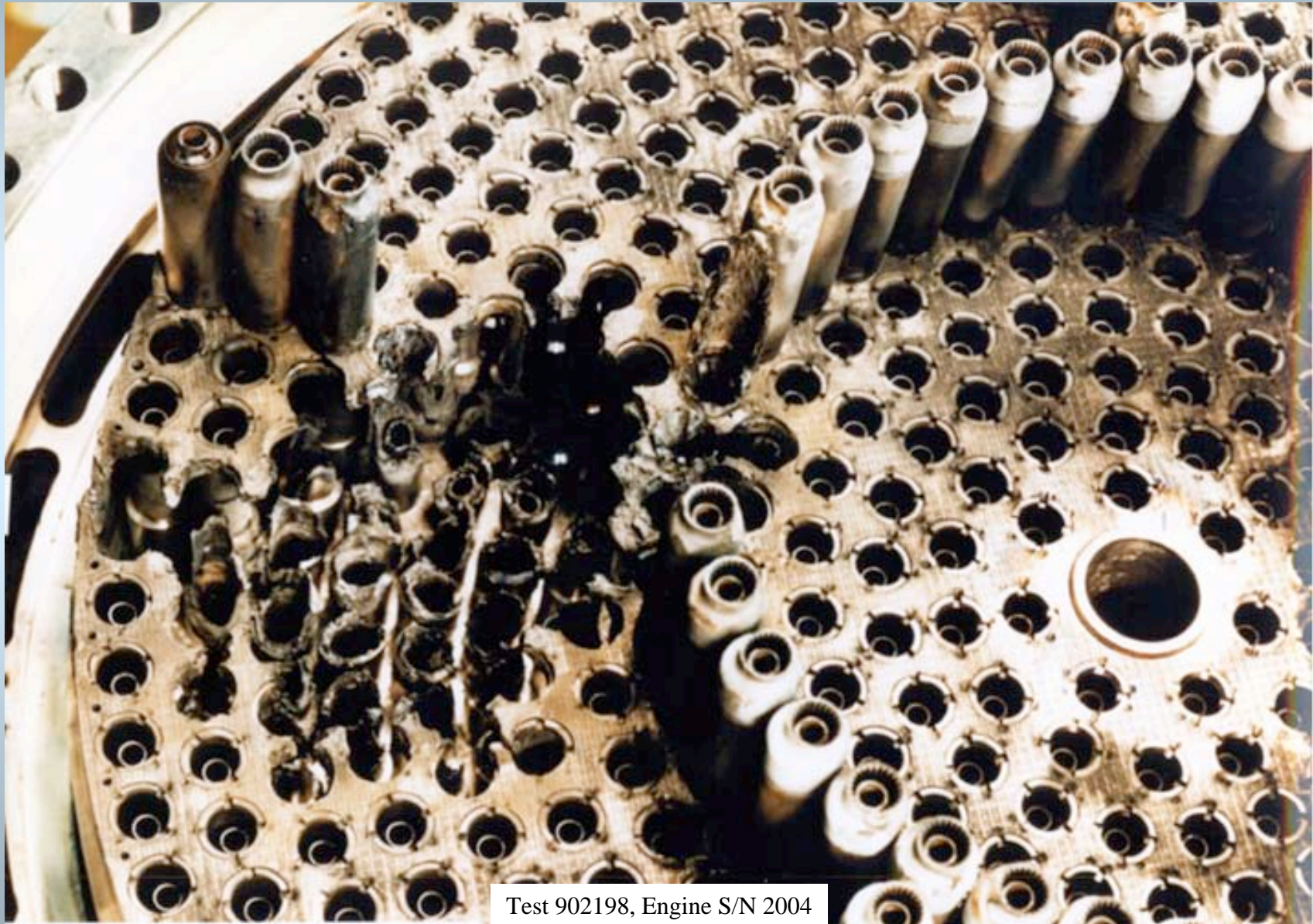
Test 901173, Engine S/N 0002



Location of Cracked Posts
and Burnout Area

Test 901183, Engine S/N 0005

Main Injector Failures



Test 902198, Engine S/N 2004

Main Injector Failures

Engine 0110 Test 750148, July 2, 1981

Failure: Lox injector post crack

Incident Description: Test 750148 proceeded normally until 16.0 seconds when the HPOTP turbine discharge temperature exceeded the redline value.

Inspection of the engine revealed extensive damage of the fuel preburner side of the main injector with burn-through of 149 Lox posts, erosion of the primary and secondary face plates, and erosion of the interpropellant plate. The nozzle sustained shrapnel damage to approximately 150 tubes and the MCC suffered erosion damage.

Cause: High cycle fatigue of Lox post caused by random mechanical vibration of the powerhead and flow induced vibration from the hot gas combined with high steady-state stresses. The damage pattern of the injector indicates the failure occurred at the inertia weld of post 12, row 13. However, the posts in this vicinity were largely consumed by the fire, including the fatigue crack where the failure initiated. Post 12, row 12, which is very near the indicated failure location, had been reworked and the acceptance requirements relaxed, making this post a credible candidate as the failure initiation point. 5. All evidence points to high cycle fatigue near a Lox post inertial weld as being the single cause.

Main Injector Failures

Engine 2108 Test 901331, July 15, 1981

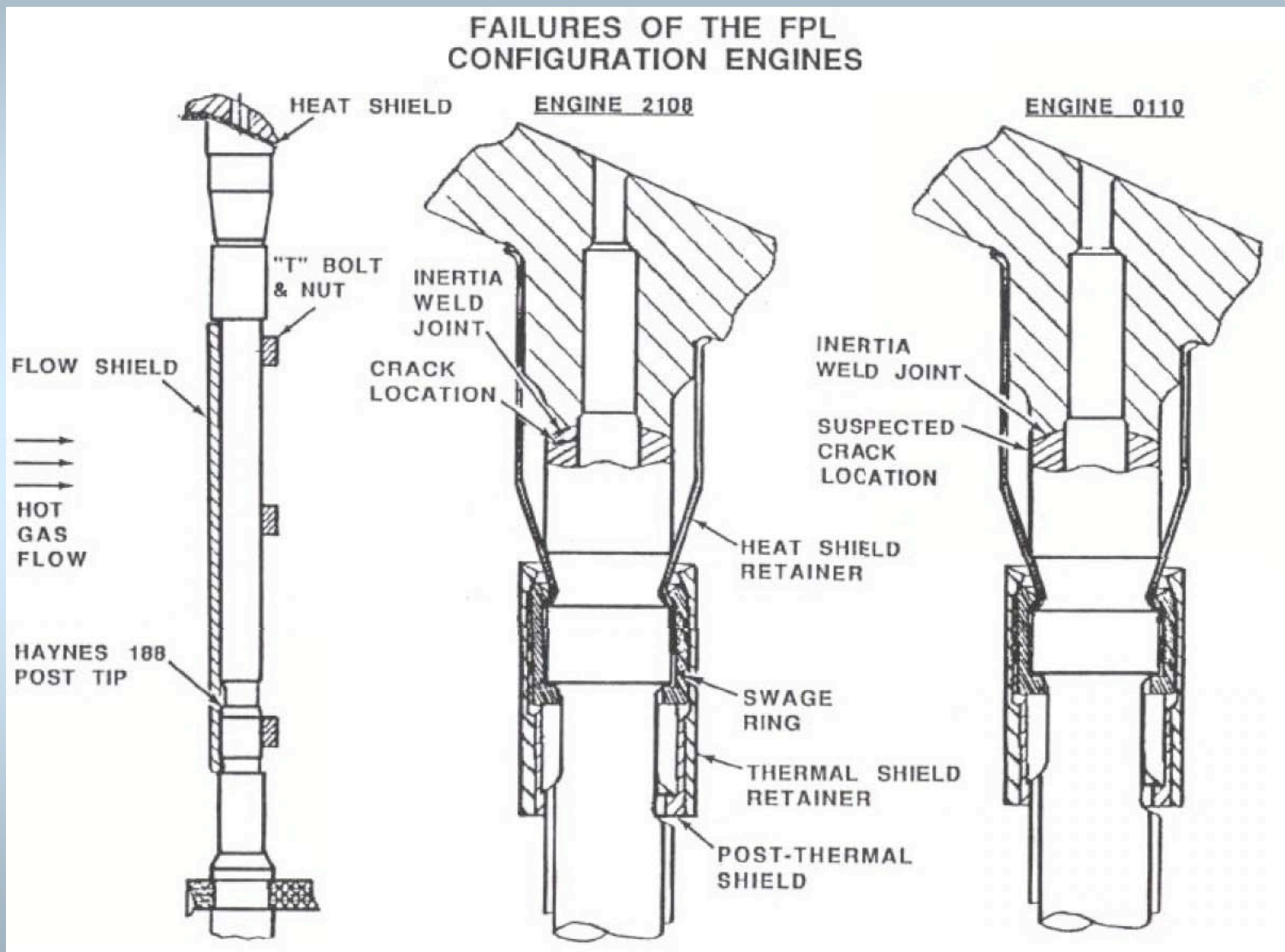
Failure: Lox injector post crack

Incident Description: Test 901331 proceeded normally until 233.14 seconds when the High Pressure Oxidizer Turbopump turbine discharge temperature exceeded the redline value.

Inspection of the engine revealed extensive damage on the fuel preburner side of the main injector with burnthrough of 169 Lox posts, major erosion of the primary and secondary faceplates, major erosion of the interpropellant plate, and six Lox post shields damaged. The nozzle sustained shrapnel damage to approximately 60 tubes, and the MCC acoustic cavity suffered erosion damage.

Cause: Lox post number 79 in row 13 failed in the 316L material at the inertial weld (which joins a 316L post to an INC0718 interpropellant plate stub) . The post failure was caused by high cycle fatigue. There was a much larger increase in flow induced vibration in going from RPL to FPL; than had been estimated in life calculations. Furthermore, the modifications which had been made in the high pressure fuel pump to adapt it to FPL operation increased the severity of the flow induced vibrations at all power levels.

Main Injector Failures

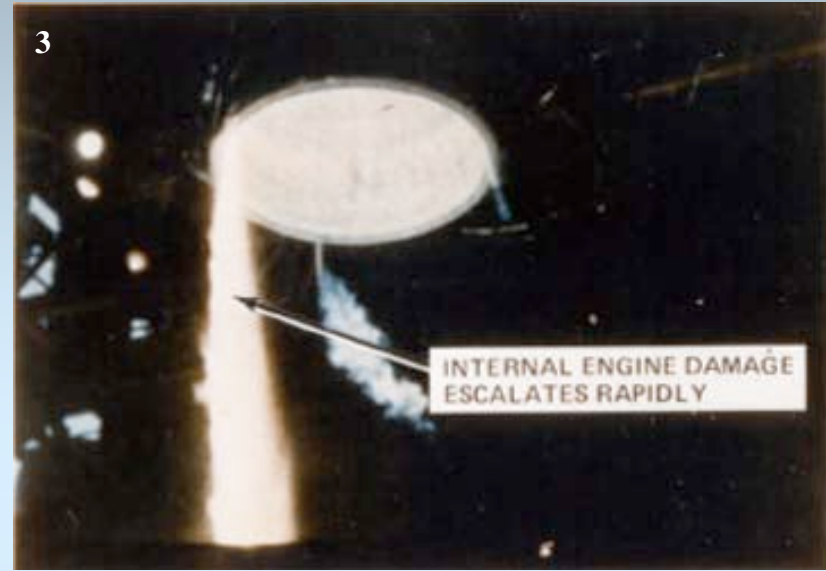
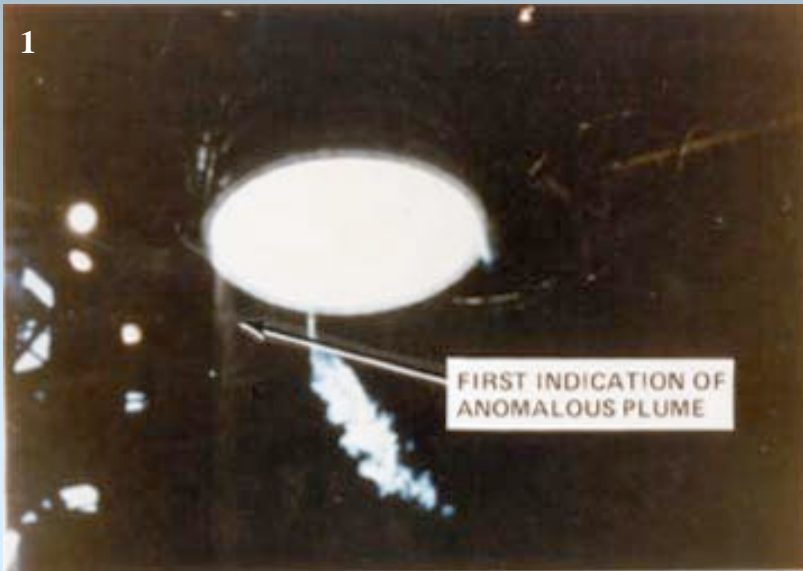


Main Injector Failures

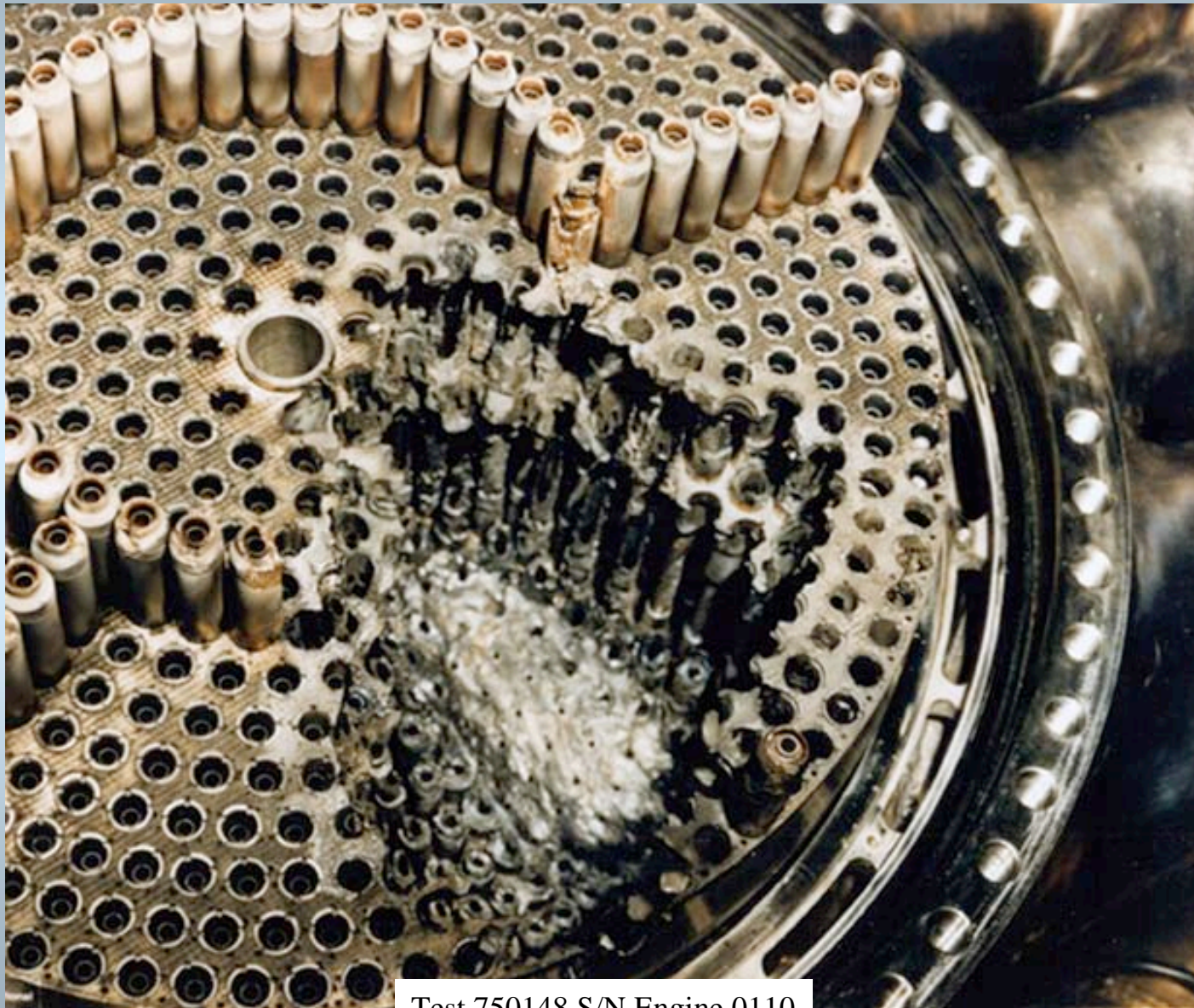


Test 901331 Engine S/N 2108

Main Injector Failures



Main Injector Failures



Test 750148 S/N Engine 0110

Nozzle Failures

Engine 0201, Test 750041, May 14, 1979

Failure: Fuel feed duct (Steerhorn) rupture

Engine 2002, Test MPTA SF06-03, November 4, 1979

Failure: Fuel feed duct (Steerhorn) rupture

Engine 0524, Test 902933, August 27, 1997

Failure: Nozzle coolant tube rupture



Nozzle Failures

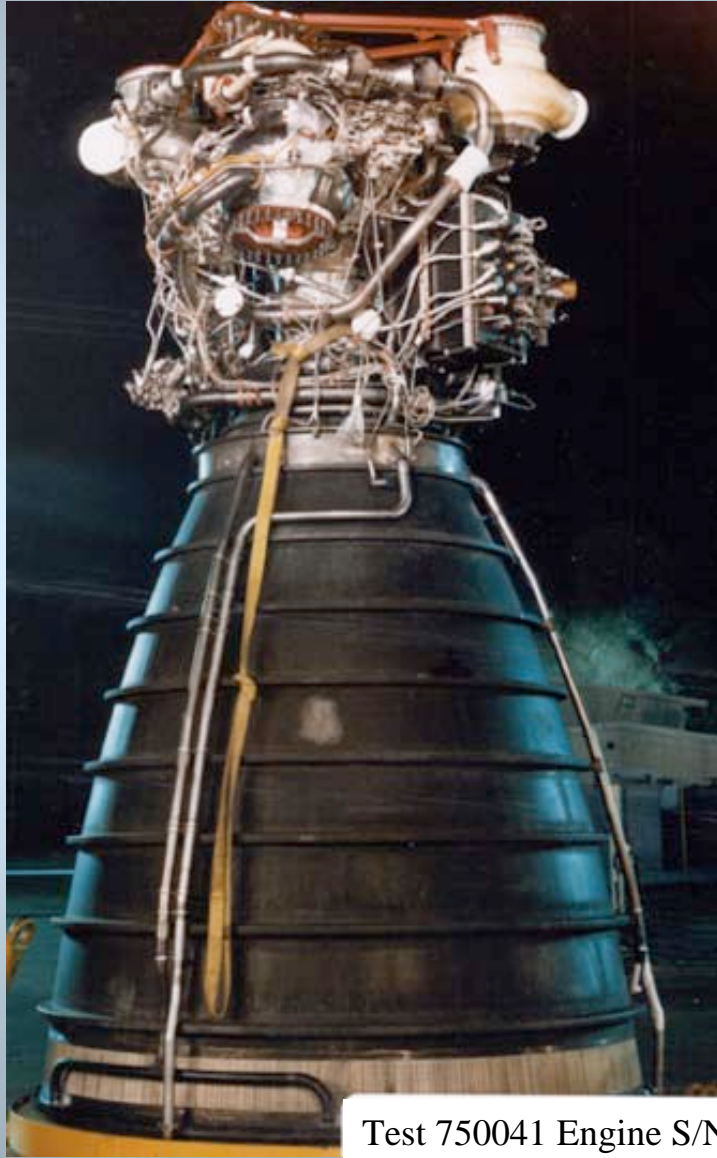
Engine 0201, Test 750041, May 14, 1979

Failure: Fuel feed duct (Steerhorn) rupture

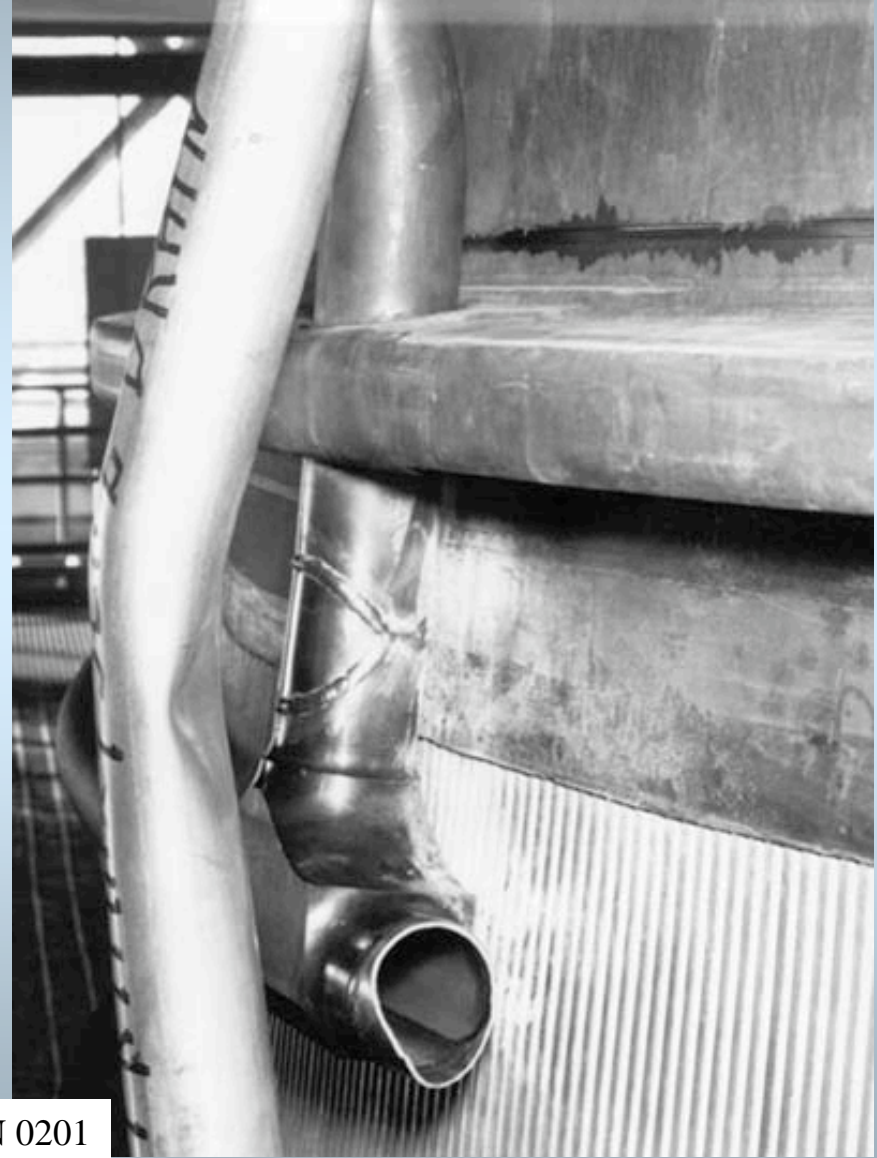
Incident Description: Test 750041 was automatically terminated at 4.296 seconds when the HPFTP turbine discharge temperature exceeded the redline value. The engine sustained considerable damage internally due to the loss of hydrogen flow during shutdown. Review of the motion picture film and data evaluation indicates that there were actually two incidents in this test. The first incident was the hot start which resulted in an high initial temperature spike in the high pressure fuel turbopump turbine discharge temperature. When the engine reached steady state the temperature again exceeded the redline value and shutdown was initiated. The second incident was the failure of the hydrogen feed line (steerhorn) to the nozzle. This occurred as the engine preceded through shutdown. This caused loss of hydrogen to the engine and the resulting damage. Damaged hardware included extensive overheating and erosion of both HPFTP and HPOTP turbines, extensive overheating and massive tube ruptures in the nozzle, extensive erosion of the main injector (not repairable), extensive slag deposited on the MCC, erosion of the fuel preburner liner and body, and extensive erosion of the hot gas manifold liner (fuel side).

Cause: A small crack was found in the failed steerhorn which was the initiation point of the failure. Metallurgical analysis of the failed area indicated that all of the damage may have been accumulated in this one test. Engineering analysis of this test however, could not identify any loads high enough to fail the steerhorn in this one test. It was postulated that the steerhorn could have accumulated damage from previous testing without cracking. Strain gages were place on engines being hot fired and previously unidentified 200-400 Hz oscillations were found during the start and shutdown transients. The loads from these oscillations had not been included in the design of the steerhorn. Utilizing data obtained with strain gages from eleven tests gives a projected life of 44 tests for minimum fatigue properties. The nozzle from engine 0201 had accumulated 12,109 seconds of test time during 48 tests.

Nozzle Failures



Test 750041 Engine S/N 0201



Nozzle Failures



Test 750041 Engine S/N 0201

Nozzle Failures

Engine 2002, Test MPTA SF6-03, November 4, 1979

Failure: Fuel feed duct (Steerhorn) rupture

Incident Description: Test SF6-03 was automatically terminated at simulated liftoff (To plus 4.848 seconds when the HPOTP secondary seal cavity pressure on Engine Position 3 (Engine S/N 0006 exceeded the maximum redline value. During the shutdown sequence, the nozzle steerhorn on Engine Position 1 (Engine S/N 2002) failed. The resulting loss of fuel following the failure caused extensive internal damage due to overheating. Damaged hardware included extensive overheating and erosion of both HPFTP and HPOTP turbines, extensive overheating and massive tube ruptures in the nozzle, extensive erosion of the main injector (not repairable), extensive erosion of the MCC (not repairable), and extensive erosion of the Hot Gas Manifold liner (fuel side).

Cause: The steerhorn failure occurred during the period of maximum nozzle deflections due to exhaust plume separation; however, the data obtained from strain gage measurements located on the steerhorn were below the levels necessary to fail the steerhorn. Subsequent investigations revealed that improper weld rod material was utilized in the fabrication of the steerhorn which significantly reduced the load carrying capability of the assembly.

Nozzle Failures



Test SF6-3, Engine S/N 2002

Nozzle Failures



Test SF6-3, Engine S/N 2002

Nozzle Failures

Engine 0524, Test 901933, August 27, 1997

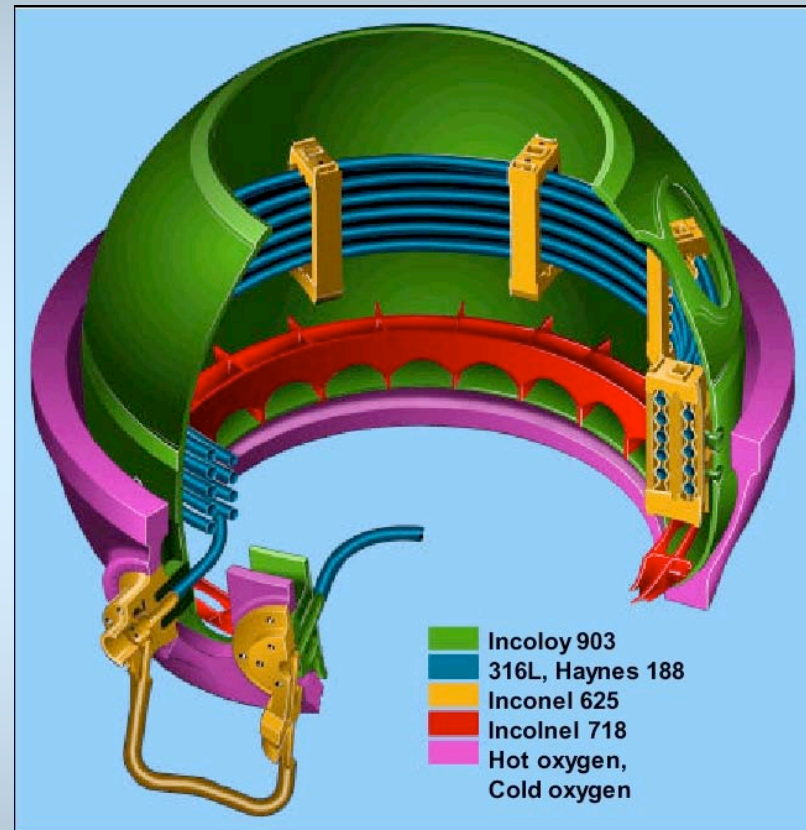
Failure: Nozzle Coolant Tube Rupture

Incident Description: Test 901933 was terminated at 567.96 seconds when the HPFTP turbine discharge temperature and the MCC Chamber pressure versus Pc Reference delta exceeded redline values. Posttest inspection revealed extensive damage to the HPFTP turbine, severe erosion to the Main Injector, the MCC and the nozzle hot wall. The damage resulted from the Lox-rich conditions in the engine following the nozzle rupture.

Cause: The cause of the nozzle tube rupture was an external overpressurization of these tubes due to cold wall tube leakage of hydrogen into the tube/jacket interface. This overpressurization resulted from the inability to vent an increasing amount of cold wall leakage due to fatigue crack initiation and propagation in these tubes. The cold wall leakage was the result of tube-to-jacket braze discontinuities in an area of the nozzle that experiences steady-state and transient loading. Because of the transient loading, circumferential low cycle fatigue cracks were initiated above the aft edge of the nozzle jacket.

Oxygen Heat Exchange Failure

Engine 0007, Test 901222, December 6, 1979
Failure: HEX coil leakage



Oxygen Heat Exchanger Failure

Engine 0007, Test 901222, December 6, 1979

Failure: HEX coil leakage

Incident Description: Test 901222 was terminated at 4.34 seconds by the heat exchanger outlet pressure minimum redline. Simultaneously, external fire was observed in the area of the oxidizer preburner. Extensive occurred to the heat exchanger coil, oxidizer turbine discharge area gas manifold, main injector and heat exchanger discharge line.

Cause: It was concluded that the incident could have been caused by one of two possible failure modes. One possible cause is undetected damage to the inlet tube during failure modes. One possible cause is undetected damage to the inlet tube during manufacturing. Following welding of the inlet, the small diameter inlet passage is reamed to remove weld drop-through. If the reaming operation penetrates past the planned depth or is performed off center, extensive damage may occur to the internal surface of the coil. The key supporting rationale for this failure mode is evidence of reaming penetration. Another possible cause is associated with a heat exchanger bracket welding operation. The No. 1 bracket was weld-repaired near the outlet, in the general area where the failure apparently originated. The exchanger bracket welding operation was conducted after the final proof pressure test. The grounding method -- to the bowl rather than directly to the bracket -- may have caused high frequency current arcing between bracket and tubing, damaging the tubing.

Heat Exchanger Failure



Test 901222, Engine S/N 0007

Main Combustion Chamber Failures

Engine 0010, Test 901284, July 30, 1980

Failure: Lee Jet failure

Engine 2308, Test 750259, March 27, 1985

Failure: Failure: Outlet neck rupture



Main Combustion Chamber Failures

Engine 0010, Test 901284, July 30, 1980

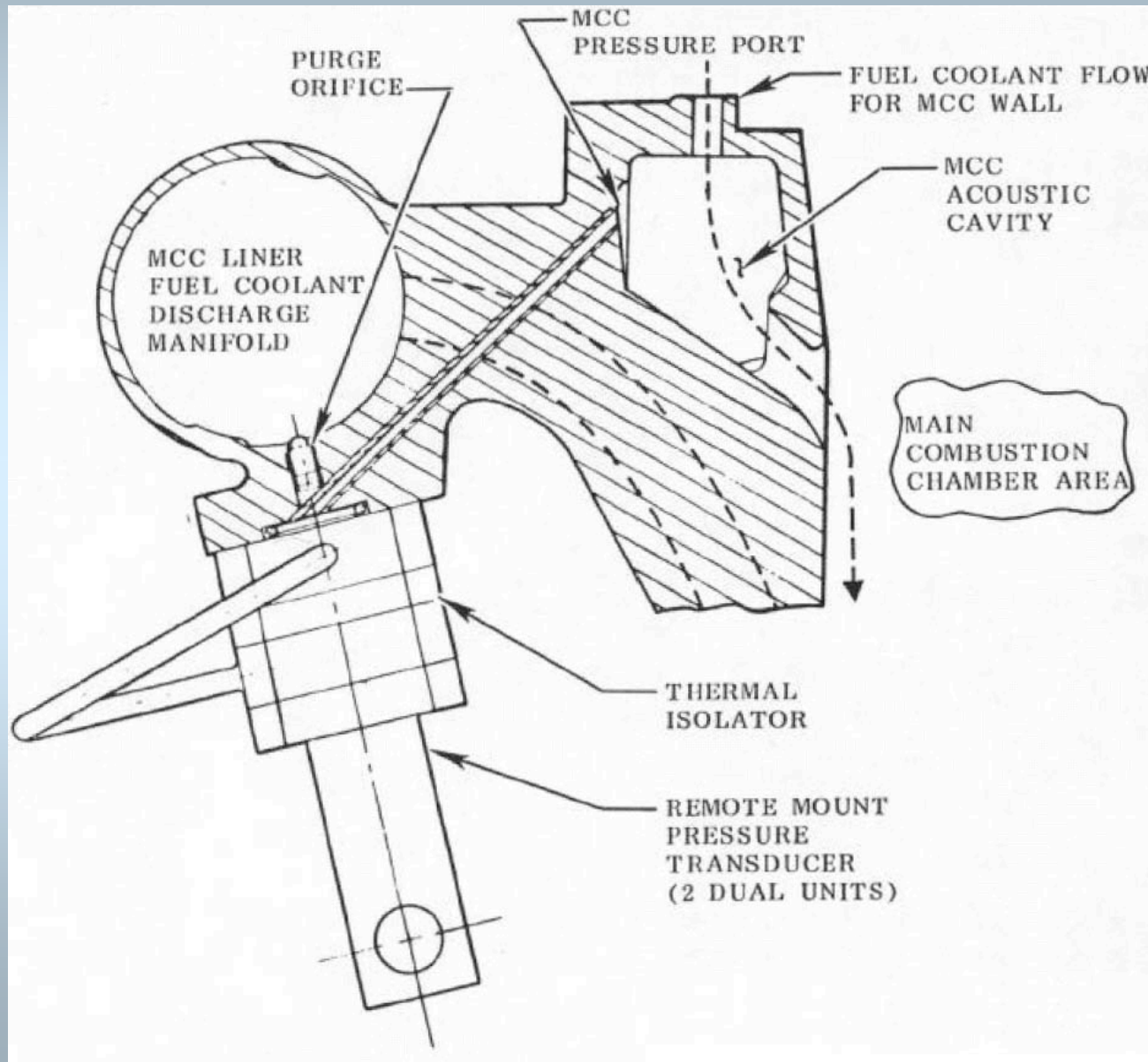
Failure: Lee Jet failure

Incident Description: Test 901284 was prematurely terminated at 9.82 seconds when pneumatic shutdown was initiated due to loss of the engine controller.

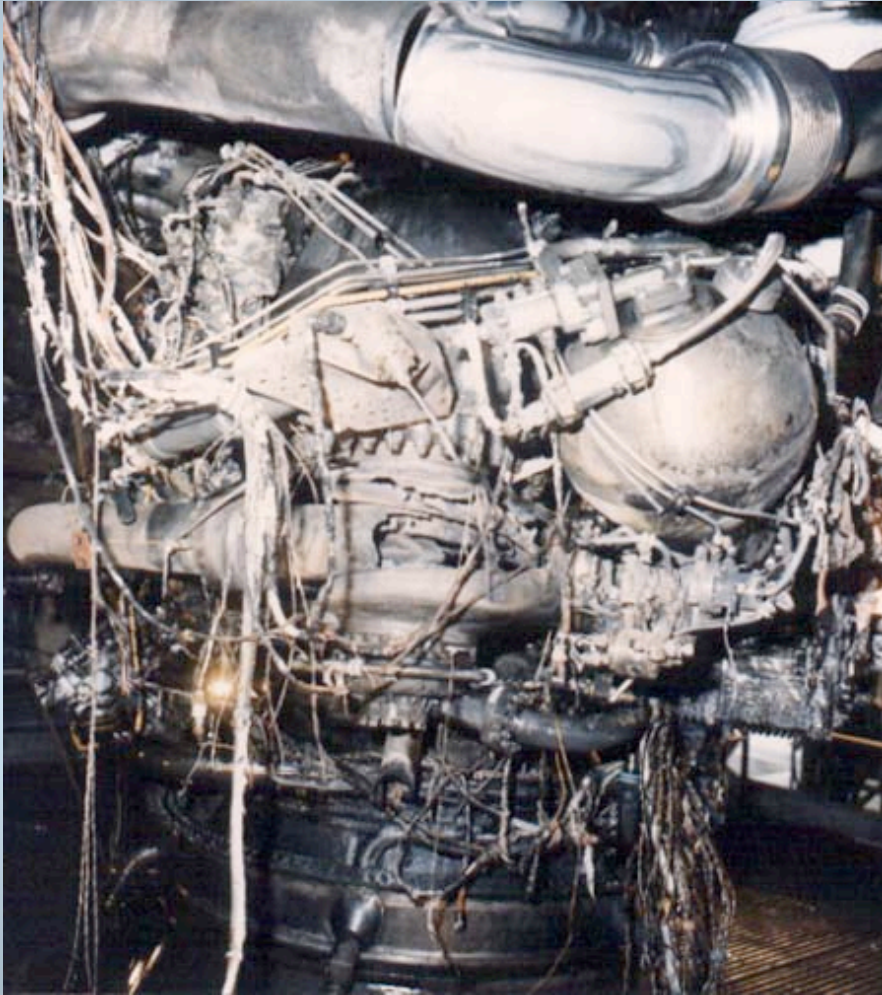
An erroneously high reading combustion chamber pressure caused the Controller to close the Oxidizer Preburner Oxidizer Valve to reduce Pc to the desired value. A few milliseconds later, the Controller calculated a mixture ratio of 9.0 and commanded the Fuel Preburner Oxidizer Valve full open in an attempt to reduce the MR to 6.0. The immediate result of the Controller actions, based on an erroneous Pc, was operation in an abnormal mode, characterized by high fuel flow and low turbine temperature. The HPOTP turbine inlet temperature fell below a value which led to freezing of water in the turbine gases. The ultimate result of the Controller actions was a fire in the HPOTP at about 9.7 seconds due to rubbing in the area of the Lox primary seal. The rubbing was caused by a high axial load which displaced the rotor assembly toward the pump end of the HPOTP housing.

Cause: Two unrelated events caused this failure to prorogate to a catastrophic failure. First, Channel B of the Engine Controller cut itself off at 3.25 seconds because of failure of electronic components in the facility power supply. Secondly, at 3.9 seconds, the Lee Jet orifice, used to purge the Channel A Pc transducer passage, became dislodged and caused the Pc transducer to sense MCC coolant flow pressure instead of Pc. The reason for the Lee Jet orifice dislodging was a poorly machined Lee Jet housing that went undetected. It was out of specification and should have been noted.

Main Combustion Chamber Failures

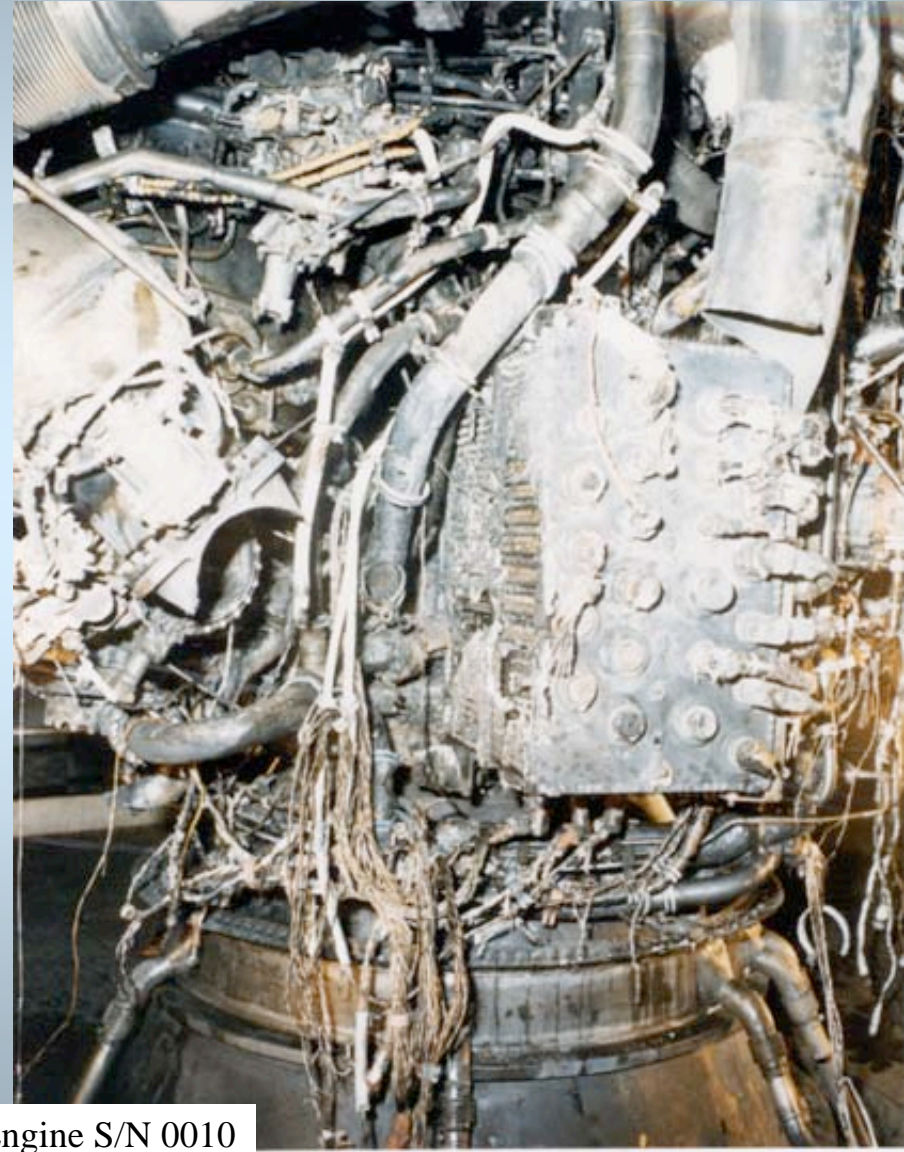


Main Combustion Chamber Failures



Test 901284, Engine S/N 0010

Main Combustion Chamber Failures



Test 901284, Engine S/N 0010

Main Combustion Chamber Failures

Engine 2308, Test 750259, March 27, 1985

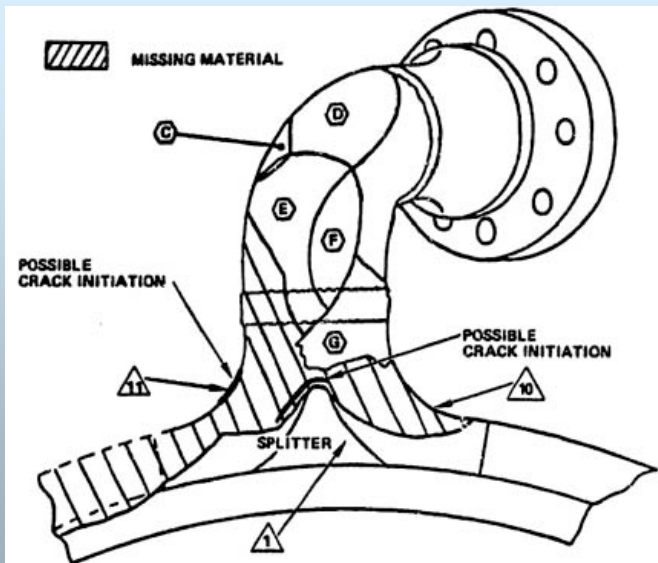
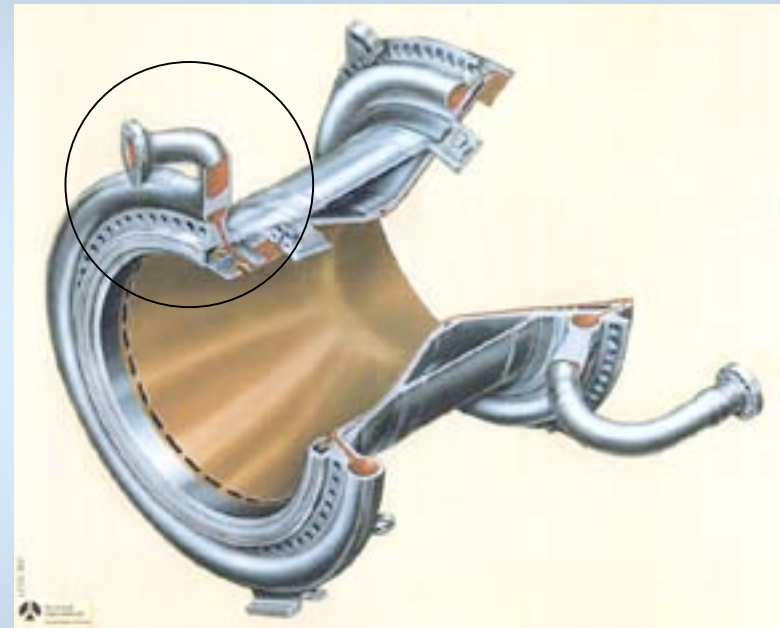
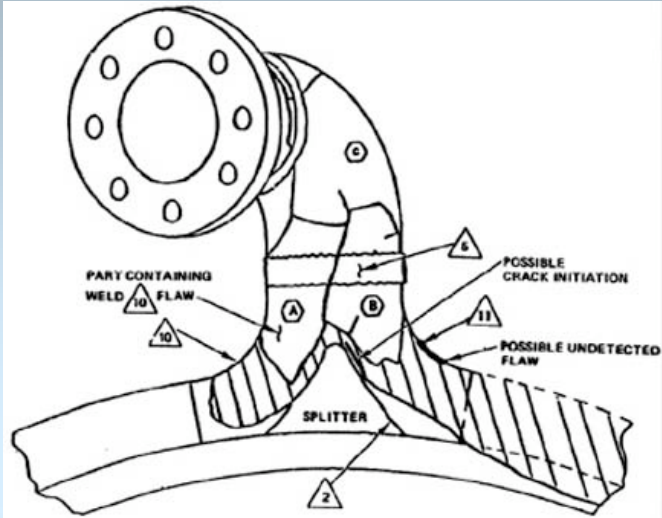
Failure: MCC Coolant Outlet Manifold neck rupture

Incident Description: Test 750259 was prematurely terminated at 101.5 seconds by the HPFTP accelerometer redline. In the incident, the engine was severed from the test stand as a result of an oxygen rich fire and came to rest in the stand spillway.

Catastrophic failure of Engine 2308 was caused by rupture of the MCC outlet manifold neck which resulted from an initial fatigue crack that grew to instability. In response to the rupture, the low-pressure fuel turbopump rapidly decayed in speed, further indicating the source of the leak to be in the MCC outlet system. The speed drop rapidly reduced discharge pressure (inlet pressure to the high-pressure pump) and the high-pressure fuel pump went into deep cavitation. As a result of deep cavitation, the high-pressure fuel pump speed increased to a value 30% over FPL nominal, rapidly increased pump vibration which exceeded the vibration redline, and led to a cutoff command. Following cutoff, the fuel cavitation condition resulted in reduce engine fuel flow and a severe oxygen-rich condition. Burnout of the turbines, burn-through of the hot-gas manifold and severe erosion of the gimbal bearing produced conditions leading to separation of the engine below the low-pressure pumps.

Cause: The precise origin and initiation mechanism for the failure was not established. Fatigue or an undetected defect were both postulated as potential failure modes for welds No. 1, 2, or 11 of the MCC outlet neck. The most probable cause of failure was determined to be fatigue (endurance) crack initiation at splitter welds No. 1 or 2.

Main Combustion Chamber Failures



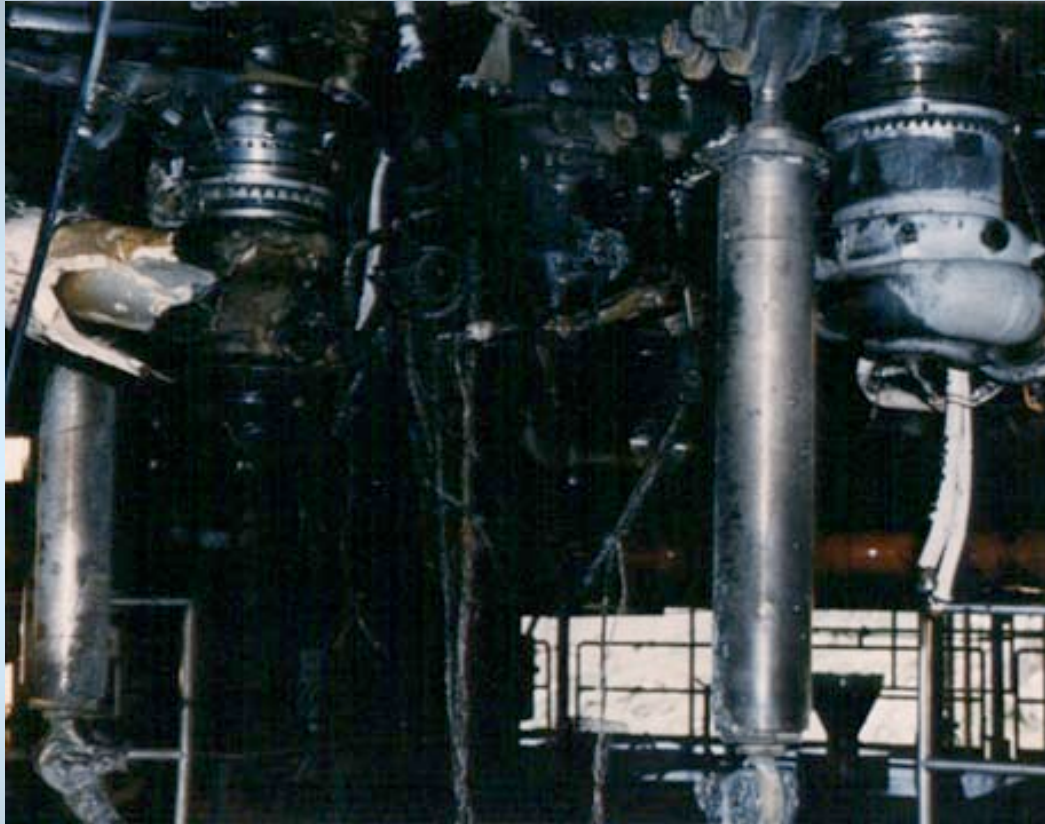
Test 7502594, Engine S/N 2308

Main Combustion Chamber Failures



Test 750259, Engine S/N 2308

Main Combustion Chamber Failures



Test 750259, Engine S/N 2308

Combustion Device Failures Summary

Major Causes

- Limited Initial Materials Properties
- Limited Structural Models - especially fatigue
- Limited Thermal Models
- Limited Aerodynamic Models
- Human Errors

Limited Component Test

- High Pressure
- Complicated Control

The SSME was designed and developed 30 years ago when computational tools were still rather primitive

Space Shuttle





Operational Issues in the Development of a Cost-Effective Reusable LOX/LH2 Engine

29 October 2003

5th International Symposium on
Liquid Space Propulsion

Richard O. Ballard

NASA Marshall Space Flight Center
Space Transportation Directorate



NASA Space Launch Initiative (SLI)

- SLI initiated under NASA Research Announcement (NRA) 8-30
- Strategic Objectives
 - Make spaceflight safer (1 in 10000 mission LOV)
 - Make spaceflight cheaper (\$1000/lb payload)
- Two prototype LOX/LH2 engine systems funded under Cycle-1 of NRA8-30
 - COBRA (Pratt & Whitney / Aerojet)
 - RS-83 (Rocketdyne)



LOX/LH2 Engines Developed for SLI

COBRA



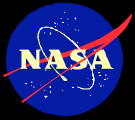
RS-83



SSME

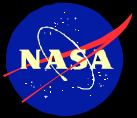


**Both SLI LOX/LH2 Engines
benefited from experience
gained from SSME +25-year
operational history**



Operational Issues

- In order to achieve the SLI goal of economic access to space, a number of propulsion system operational concerns were identified from SSME experience to be addressed through pre-emptive design
- Lengthy post-flight turnaround interval
- Labor/time-intensive maintenance operations



RLV Turnaround Time is Critical

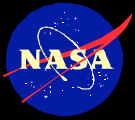
National Aeronautics
and Space Administration

Marshall Sp
Flight Cent



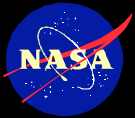
Time on the ground represents lost revenue – which impacts the economic viability of the RLV system.





Post-Flight Turnaround Concerns

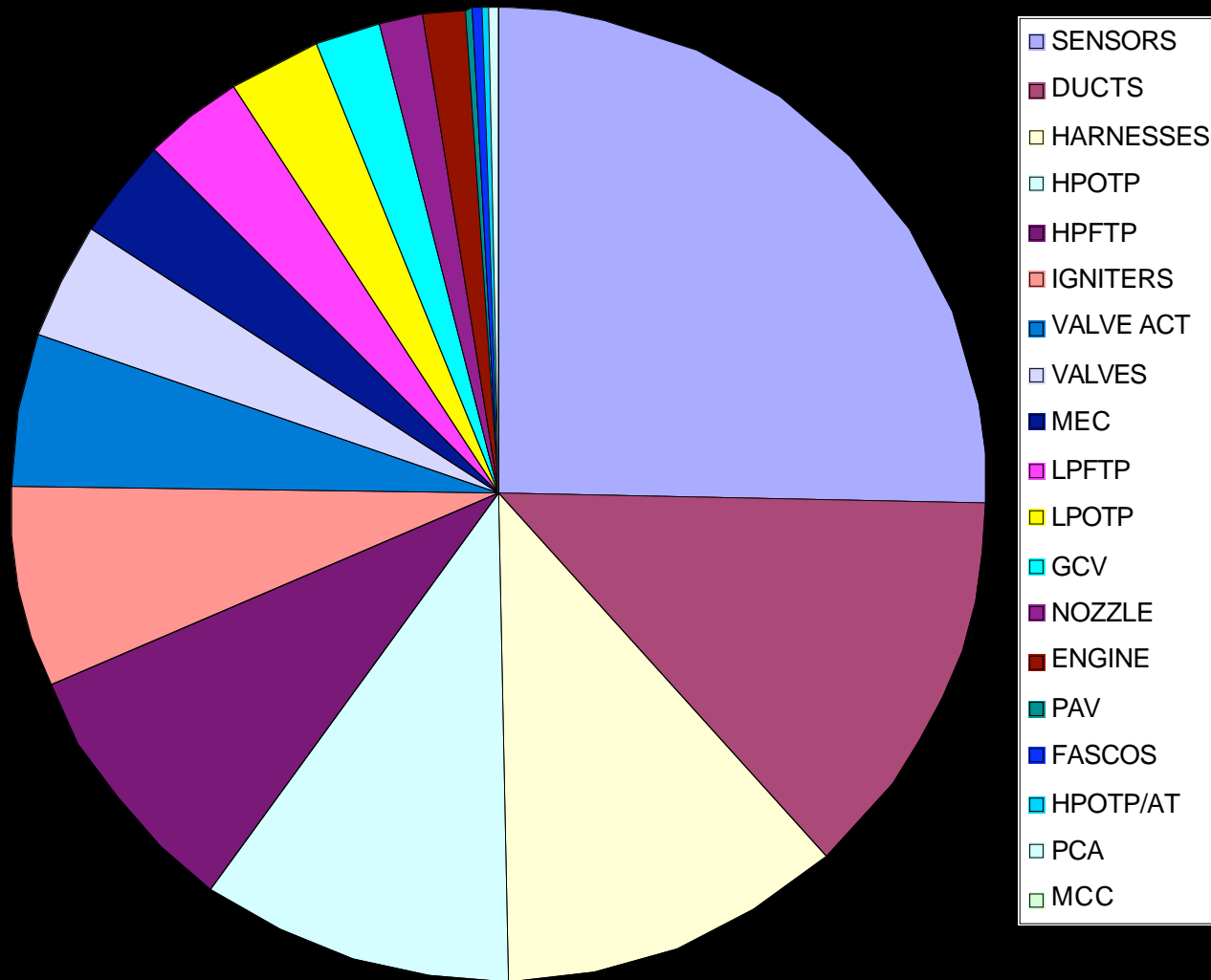
- Engine Drying
 - A necessary but lengthy part of turnaround operations. Offers significant time savings if mitigated early in the design phase.
- Inspections
 - Typically conducted to mitigate technical risk areas in the engine. Can be reduced by designing out risk areas or utilizing alternate mitigation approaches.
- Engine vs. Line Replaceable Unit (LRU) Replacement
 - An LRU philosophy should be established early in the design phase to permit components with a high incidence of replacement to be designed as LRUs. Other non-LRU components would require engine removal for depot-level procedures if they required replacement.



Engine vs. LRU Replacement

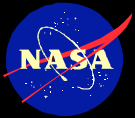
National Aeronautics
and Space Administration

Marshall Sp
Flight Cent



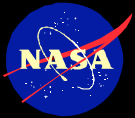
**Development of an
Line Replaceable
Unit (LRU)
philosophy should
be done early in the
engine design and
should take into
account components
that have a high rate
of replacement**

SSME Hardware Replacements for Life & Cause



LRU Design Considerations

- Fasteners
 - Avoid use of time-intensive anti-rotation devices (i.e., lockwire) by using alternatives such as self-locking nuts or torque-stripe.
 - Consider alternate fasteners or latching mechanisms when possible.
- Common Tools
 - Encourage limiting the number of tools required to conduct engine maintenance operations.
- Shallow Engine Layout
 - Organize “one-deep” LRU placement to permit rapid R&R without disturbing other components
- Advanced Interface Design
 - Minimize flange leakage potential and permit larger margin for misalignment.
 - Enable rapid interface mount/dismount.



Useful Tools and Improvement Areas

- REIMR Study
 - Reviewed other engine histories to determine “Fundamental Root Causes” of problems and how they can be avoided in the future.
- Process FMEA (P-FMEA)
 - Identify critical and/or vulnerable processes in the manufacturing and maintenance elements and how to reinforce to prevent flaw infiltration.
 - The P-FMEA is particularly applicable to components with no/few moving parts (i.e., combustion devices), where failure modes can be introduced through process escapes during manufacture.
- Periodic Maintenance Schedule Evaluation
 - Review rationale for specific maintenance operations to enable elimination of those that are invalid or outdated.



- **Minimization of Flight Sensor Suite**
 - Reduce required number of sensors by thorough characterization of engine internal environment during development by test.
 - Utilize multiplexed sensors to sense multiple measurands through one sensor port.
- **Improved Sensor Reliability / Survivability**
 - The high number of sensor replacements on SSME indicate a need for sensor design improvements to better tolerate the extreme engine environment and all operational phases.
 - This is also applicable to connectors and wiring harnesses.
- **EHMS-supported Maintenance Scheduling**
 - Integrate algorithms into EHMS logic to support scheduling of turnaround maintenance operations while the vehicle is still in orbit.



Conclusion

- In Fall 2002, SLI LOX/LH2 engine development was suspended due to reorientation of immediate risk reduction priorities to LOX/kerosene.
 - Both COBRA and RS-83 were proceeding on schedule and on budget.
- Significant improvements in engine operational efficiency were being incorporated into both engine designs when work was suspended.
- Both showed progress toward achieving SLI strategic goals of increased safety and reliability, and reduced operational cost.



Questions?

Operational Issues in the Development of a Cost-Effective Reusable LOX/LH2 Engine

*Richard O. Ballard
Space Transportation Directorate
NASA Marshall Space Flight Center, AL*

Abstract

The NASA Space Launch Initiative (SLI) was initiated in early 2001 to conduct technology development and to reduce the business and technical risk associated with developing the next-generation reusable launch system. In the field of main propulsion, two LOX/LH2 rocket engine systems, the Pratt & Whitney / Aerojet Joint Venture (JV) COBRA and the Rocketdyne RS-83, were funded to develop a safe, economical, and reusable propulsion system. Given that a large-thrust reusable rocket engine program had not been started in the U.S. since 1971, with the Space Shuttle Main Engine (SSME), this provided an opportunity to build on the experience developed on the SSME system, while exploiting advances in technology that had occurred in the intervening 30 years. One facet of engine development that was identified as being especially vital in order to produce an optimal system was in the areas of operability and maintainability. In order to achieve the high levels of performance required by the Space Shuttle, the SSME system is highly complex with very tight tolerances and detailed requirements. Over the lifetime of the SSME program, the engine has required a high level of manpower to support the performance of inspections, maintenance (scheduled and unscheduled) and operations (prelaunch and post-flight). As a consequence, the labor-intensive needs of the SSME provide a significant impact to the overall cost efficiency of the Space Transportation System (STS). One of the strategic goals of the SLI is to reduce cost by requiring the engine(s) to be easier (i.e. less expensive) to operate and maintain. The most effective means of accomplishing this goal is to infuse the operability and maintainability features into the engine design from the start. This paper discusses some of the operational issues relevant to a reusable LOX/LH2 main engine, and the means by which their impact is mitigated in the design phase.

1. Introduction

1.1 The Space Launch Initiative

The NASA SLI program was initiated under NASA Research Agreement (NRA) 8-30 to begin development of a space launch system that would be significantly safer and more economical to operate than current launch systems. SLI was identified as part of the Integrated Space Transportation Plan (ISTP) and followed on the NRA8-27 study to define an optimal roadmap that would produce a 2nd Generation Reusable Launch Vehicle (2GRLV). The objective of the NRA8-27 study was to identify risk reduction areas and was applicable to several 2GRLV architectures by performing cycle analyses and trade studies on applicable propulsion systems. Risk reduction activities were then identified to mature the technologies and engine cycles to production status. Other elements of the ISTP identified at that time included upgrades for safety of NASA's first generation RLV, the space shuttle, and technologies for third and fourth generation transportation systems.

The 2GRLV program was to build on NASA's then-current programs (e.g., X-33, X-34 and X-37) — testing new materials, structures, propulsion, software, and other technologies needed to meet the program's goals of significantly increasing safety to a 1 in 10,000 chance of loss of life and reducing payload launch costs from \$10,000 per pound today to \$1,000 per pound.

The scope of NRA8-30 covered more than just the propulsion facet of space transportation. The ten technology areas (TAs) worked on all elements of the next manned space launch infrastructure. In addition, NRA8-30 was separated into multiple cycles and phases to permit management flexibility. Cycle-1 would focus on initial prototype development and risk reduction, with Cycle-2 culminating in the demonstration by test of the prototype engine. Phase-2 of the SLI program would build on the foundation laid by the prototype engine project by proceeding with the design, development, test, and deployment of the human-rated full-scale development (FSD) flight engine.

Under Cycle-1 of the 2GRLV program, two prototype LOX/LH2 main engines were selected for development to reduce technical risks: the COBRA engine by the Joint Venture (JV) of Pratt & Whitney (P&W) and Aerojet, and the RS-83 by Rocketdyne.



Figure 1: SSME

1.2 The SSME

Rocketdyne initiated the development of the SSME in 1971 under contract to NASA to provide the main propulsion for the Space Shuttle. Engine testing started in May 1975 and was first flown on 12 April 1981 (STS-1). Thirty years, a few thousand tests, over a hundred flights, and one million seconds of operation later, the SSME is still being safely operated as the STS main propulsion system.^[1]

The SSME (Figure 1) is a high-performance 490 Klbf LOX/LH2 rocket engine and is the first large-thrust engine ever developed to be reusable

beyond that typically associated with an expendable engine life cycle (e.g. a few acceptance or calibration tests followed by the mission operation). It was designed to be reusable with the intent of making access to space more economical than that experienced in previous manned space programs. While the engine has succeeded in being capable of multiple uses, the cost benefit was less than envisioned. This was in part due to the increasing operational costs required to maintain the engine in order for it to operate safely and reliably.

Before and after each flight, the SSME is subjected to extensive external and internal inspections, as well as an exhaustive battery of maintenance procedures. In addition, any nonconformances, irregularities, or discrepancies in the engine or its constituent components are meticulously documented and tracked. These operational constraints require a significant level of skilled manpower to support continued operation of the engine. By comparison, the non-recurring cost of manufacturing the engine is of less concern than the recurring operational cost.

SLI is oriented to utilize the operational expertise gained from the SSME to identify areas of focus to optimize the engine design to operate safely and reliably, while requiring labor to maintain and operate it.

1.3 The COBRA Engine

The Co-Optimized Booster for Reusable Application (COBRA) engine (Figure 2) is a reusable, LOX/LH2 600 Klbf class engine system utilizing the Single Burner Fuel-Rich Staged Combustion (SBFRSC) power cycle set up around the upgraded SSME ATD high-pressure turbomachinery. The SBFRSC cycle reduces the potential for oxygen-rich failure modes inherent in the dual-burner cycle, thus increasing engine reliability and safety. The hot combustion gases from the preburner drive both the hydrogen and LOX turbines in parallel before entering main chamber. This design reduces the turbine temperature, increasing engine life. In addition, the use of a single “liquid-liquid” preburner means that the high transient turbine temperatures seen during engine start in the dual-burner staged combustion cycle are eliminated. Additionally,

the fuel and LOX turbine temperatures are essentially “averaged” in the single preburner system, allowing the peak temperature in the system to stay at a more benign level. The Russian RD-0120 engine also uses this cycle, though with an integrated single-shaft LOX and fuel turbopump.

The COBRA engine system was selected for development under the Cycle-1 of the NRA8-30



Figure 2: COBRA

SLI program under contract NAS8-01108. The genesis of the COBRA engine system originated during the development of the P&W XLR129 engine for the USAF in the early 1970's. The system utilized a highly integrated “powerduct” arrangement, with the separate turbopumps mounted in a close-coupled configuration with the single fuel-rich preburner to a double-walled hot gas duct.

1.4 The RS-83 Engine

The RS-83 engine (Figure 3) is a reusable, LOX/LH2 750 Kibf class engine system utilizing the SBFRSC power cycle with the main turbopumps arranged in series as compared to the

parallel configuration used by the COBRA system. The RS-83 is a clean sheet design built on experience gained from the lengthy history of producing the SSME. Its development relies on advanced integration design tools and more rigorous design optimization in a quicker design cycle. Risk reduction activities have included the development of advanced fabrication processes that result in more consistent material properties and shorter production times. The RS-83 is



Figure 3: RS-83

similar to the COBRA system in that it decouples the fuel flow to the preburner from the coolant flow to the nozzle and main combustion chamber, promising a smoother start transient over that of the SSME.

The RS-83 engine system was selected for development under the Cycle-1 of the NRA8-30 SLI program.

2. Operational Issues

The following is a discussion of some of the operational issues associated with a LOX/LH2 engine and some of the means to be considered on how they may be mitigated by pre-emptive design.

2.1 Post-flight Turnaround

The economic viability of a reusable launch system is partially dependent on the ability to support a high launch rate. Like commercial aircraft, time on the ground represents lost revenue. From the time when the vehicle rolls to a stop and support personnel are allowed access to it, the vehicle and its subsystems are in a maintenance pipeline to prepare it for the next launch. Minimizing the post-flight turnaround maintenance requirements is a key objective of the SLI program in its pursuit of developing a safe and reliable propulsion system that is less operations intensive than previous systems.

One focus is to identify what maintenance operations are the most time/labor intensive and then either design out the need for doing the operation or develop a means of using existing or modified data (instrumentation) to eliminate the need. One example is the use of a high-fidelity turbopump speed sensor to evaluate the pump speed decay at engine shutdown to eliminate rotor torque checks.

2.1.1 Engine Drying

During engine operation, the combustion of LOX and LH2 produces steam, which is invasive throughout the hot gas system of the engine. The steam also permeates into the turbomachinery, where it condenses and collects as water. It has been described that “about a cup” of water is drained from the SSME HPOTP following a nominal duration (hotfire) operation.

Regardless of the volume, the presence of water or humidity in the engine is unacceptable and must be thoroughly removed prior to its next operation. Engine drying is generally a lengthy process requiring a heated gaseous nitrogen (GN2) purge through the engine. On the SSME, a drying purge is connected to the engines shortly after the orbiter lands.

While the need to dry the engine after operation cannot be eliminated, the amount of time required to complete it may be reduced. This can be accomplished by minimizing the volumes where the water is known to collect, making it more difficult for steam to invade into areas where it could condense, or designing the volumes to permit them to be easily drained. Another means

of saving time would more efficient positioning and routing of purge and drains, and to have quick disconnects (QDs) in key locations to permit purges or drains to be easily connected/reconnected.

2.1.2 Inspections

In a perfect world, the engine should never require inspections. Inspections are generally conducted to verify the physical integrity of risk areas on the engine and can be separated into external and internal types. With few exceptions, inspections are usually visual, using the “Eyeball, Mark-1” as the primary instrument. External inspections are less problematic than internal ones, because they do not require the engine to be breeched.

Performing an internal inspection on the engine requires the opening of flanges or other component interfaces, or the opening of ports. An internal inspection may be regarded in the same sense as “exploratory surgery” would be regarded on a medical patient – there is always a risk of a “post-operative infection” manifesting itself afterwards. This is generally in the form of FOD (Foreign Object Debris) contamination being introduced into the engine (i.e. LOX tape, cotton swabs, rags, safety wire, nuts, bolts, etc.), which has been known to occur. The following are some means by which inspections can be reduced: ^[2]

- Do concurrent engineering, i.e., design and manufacturing engineers work to together to have parts and assemblies that are simple, easy to make, low cost and do not require post flight inspection.

The use of concurrent engineering can be further utilized on a number of other crosscutting development applications. The expertise provided by the engine maintenance technicians should not go unexploited. They should be recruited into the engine and component design teams to provide valuable maintainability insight.

- Eliminate welds by using castings (welds often require inspection to identify crack initiation / propagation). If they cannot be eliminated, locate them where they can be easily inspected, on both sides if possible.
- Eliminate as many inspection points as is possible make those required easy to do by

placing inspection ports in locations that are easy to access.

- Eliminate fracture critical areas by using generous radius in all applications (i.e., HPF ducts, turbine housings, internal ties on LPF ducts, etc.).
- Develop techniques for performing non-intrusive inspections.
- Eliminate the need for protective coating materials.
- Characterize the internal environment of the engine as fully as possible and as early as possible during development. Do this by actual test of a highly instrumented engine to develop and verify internal models. This is useful in identifying problem areas and correcting them by pre-emptive design early in the design cycle, rather than later mitigating the flight risk by the implementation of a more-expensive maintenance “band-aid” that

has to be added on to the post-flight turnaround procedures. The lack of thorough environment characterization is often mitigated later by limiting engine life to compensate for the lack of design margin.

2.1.3 Engine vs. LRU Replacement

A Line Replaceable Unit (LRU) philosophy should be established early in the engine development that identifies components to be replaced on the engine while it is on the vehicle. Any other components not identified as LRUs would necessitate engine removal if replacement became necessary. In order to reduce the impact to post-flight turnaround time, the engine and all identified LRUs would require design and development to be easily and quickly replaced. One way to optimally develop this philosophy would be to identify those components that have a high incidence of replacement for cause, and for life related. An inventory was conducted by Rocketdyne on the SSME to catalog all the

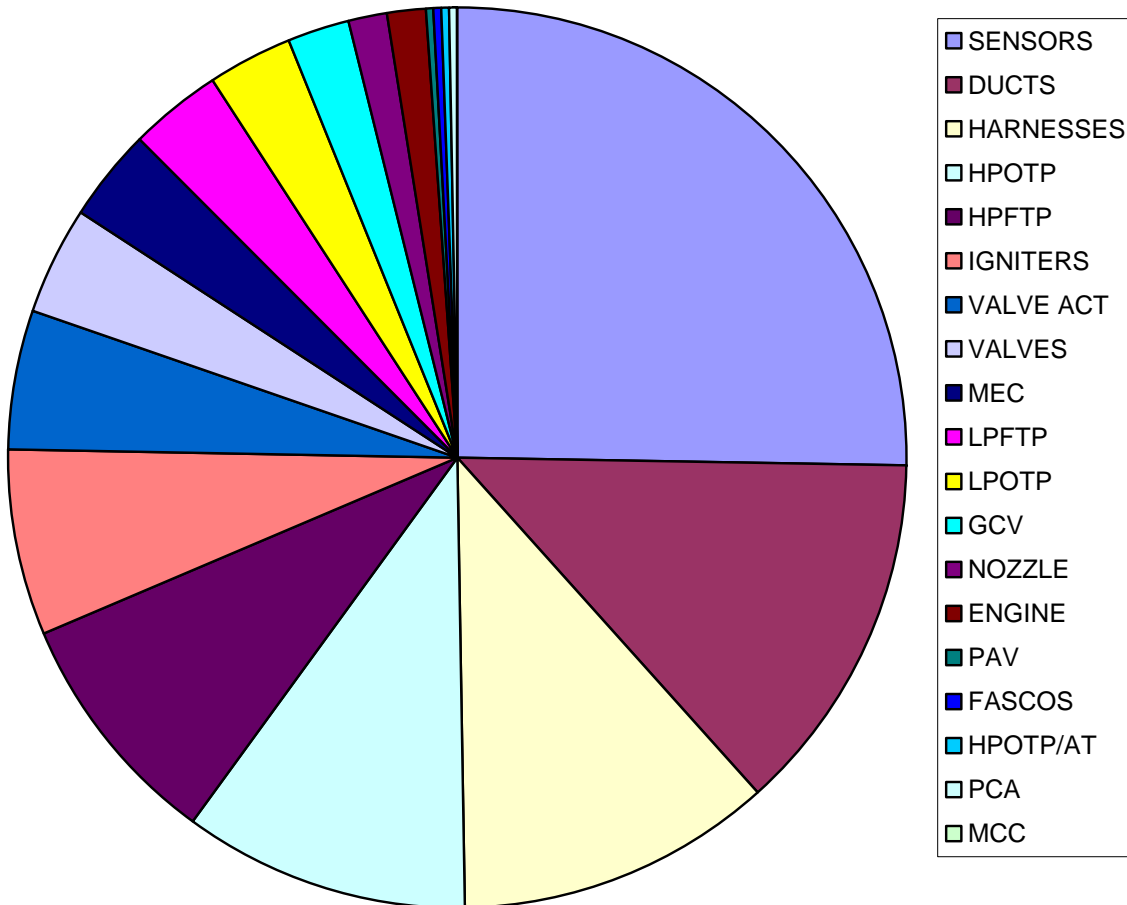


Figure 4: SSME Hardware Replacements for Life & Cause

hardware replacements that had occurred on the SSME during post-flight operations^[3]. This replacement inventory was evaluated to show those components that had the highest rate of replacement (Figure 4). The causes of replacement included:

- Latent defects.
- Flight, checkout, or suspect anomalies (includes NASA- or Rocketdyne-directed removals).
- Damage incurred during turnaround operations.
- Operational/life limits

2.2 Engine or LRU Replacement

If it becomes necessary to remove and replace the engine or a LRU part, the ability to do this quickly is important in order to reduce its impact on the post-flight turnaround schedule. The engine and all identified LRUs should utilize design attributes that permit this to be realized.

2.2.1 Fasteners

Simplification of fasteners and latching devices would be useful in designing expeditious removal features into the engine and LRU component interfaces. Timesaving anti-rotation alternatives to the use of lock-wire should be considered whenever possible and can include self-locking nuts, washers with locking tabs, and torque-stripe compound. One example that would save many hours of turnaround time on the Space Shuttle orbiter is the simplification of the fasteners used on the heat shields enclosing the SSMEs, which consist of several hundred bolts and require approximately eight hours each to remove in order to permit access to the engines.

2.2.2 Common Tools

In the same context as the simplification of fasteners and latching mechanisms, the additional simplification and standardization of tools required to perform maintenance operations can also result in a benefit to the time required to perform post-flight turnaround. The requirements for complex or a large number of tools should be avoided.

2.2.3 Shallow Engine Layout

One guideline in the development of the LRU philosophy is to encourage “one-deep” or a “shallow” engine layout that would permit the removal of the LRU without having to previously remove any other component. By design, parts identified for high instances of maintenance or removal are located at easily accessible locations in the engine layout. If a component is identified as needing to be replaced and can only be done so by the prior removal of one or more other components, then the cost (in turnaournd time) of on-site removal and replacement (R&R) may be excessive and the engine should be removed for depot-level maintenance activities.

2.2.4 Advanced Interface Design

Whenever an interface is disturbed, it must undergo a series of leak-checks and inspections to verify the interface seal integrity is acceptable. Another liability to be considered when a component interface is restored following an LRU replacement is the small misalignment tolerance allowed to prevent seal leakage or the formation of stress concentrations. The development of advanced interfaces (e.g., spherical flanges) that reduce the potential for seal leaks and permits a larger range of misalignment would provide a benefit in LRU replacement times. Development of an operationally efficient vehicle-to-engine interface can decrease maintenance operations and engine R&R time. Design considerations may include: location, number and grouping of interfaces, as well as possible use of automation and innovative use of tooling, ground support equipment (GSE), and infrastructure.

3. Useful Engine Development Tools & Techniques

In response to some of the operational issues identified during the SLI program, tools and techniques have been developed to mitigate the technical risk presented by them. In order to develop the best solutions the design process must consider all phases of handling and operations of the engine, from “cradle-to-grave” (including assembly, test and flight cycles, to final disassembly and deactivation).

3.1 REIMR Study

At the initiation of SLI, MSFC conducted a detailed study of development and operational issues associated with liquid propellant rocket engines. This included many of the “lessons learned” that had been documented for most of the large-thrust rocket engines developed in the United States (i.e. F-1, J-2, and SSME). Emphasis was placed on determining common themes in issues or problem areas in all phases of engine design, development, manufacture and operation. The intent was to provide the results of this study to the different engine development teams (i.e. COBRA and RS-83) to assist them in avoid the development “speed-bumps” that had been encountered previously.

The key difference that separated this study, known as REIMR (Rocket Engine Issue Mitigation Resource), from many previous “lessons learned” studies was that it not only focused on the problem/event and the immediate primary cause of it, but also the “fundamental root cause” that had allowed it to occur and how it could be avoided/mitigated in future engine programs. The Fundamental Root Causes (FRCs) identified were:

- Inadequate understanding of the engine environment.
- Inadequate systems engineering and integration design trades.
- Inadequate resources.
- Overestimation of technology base.
- Immature mission/vehicle design requirements imposed unnecessary engine requirements.
- Inadequate understanding of manufacturing environments and process variability.
- Inadequate understanding of material properties.
- Inadequate design margins.
- Inadequate quality processes.
- Inadequate or loosely worded requirements or specifications.

- High performance requirements (I_{SP} , thrust-to-weight, etc.) drove design to be very sensitive to all design and operations parameters.

3.2 Process FMEA

The function of process FMEA (P-FMEA) is to evaluate critical manufacturing and maintenance processes and procedures to identify the likelihood and consequences of an escape. The P-FMEA is useful for mitigating manufacturing and maintenance risks during the preliminary and design phases. It also is useful in mitigating one of the FRCs identified in the REIMR study (e.g. “Inadequate understanding of manufacturing environments and process variability.”).

3.3 Periodic Maintenance Schedule Evaluation

In the development of the post-flight maintenance schedule, it is obviously important to document the rationale for conducting each maintenance operation. This permits periodic evaluation of the schedule to eliminate those activities that no longer have a valid rationale for performing.

3.4 Minimization of Flight Sensors

Like inspections, a rocket engine in a perfect world is one that doesn’t need sensors. Emphasis should be made to minimize the number of intrusive sensors required by the flight engine. A high number of sensor ports can result in a degradation of reliability by a higher number of potential leak locations, sources of FOD, and sensors that can fail. Sufficient instrumentation should be utilized during engine development to fully characterize the internal environment and model the relationships between the flight sensors and the engine operating condition. This should further reduce the suite of flight instrumentation.

Another means of reducing the number of intrusive instrumentation ports penetrating the engine is through the use of multiplexed sensors that can sense multiple measurands (i.e., temperature, pressure, vibration) through one port.

3.5 Improved Instrumentation

In addition to minimization of sensor quantities, increased performance and robustness of existing

intrusive sensors and associated connectors and wiring/cables can be enhanced. Instruments, connectors, and wiring that can withstand long durations of extreme conditions in all phases of operation are absolutely necessary for increased safety and reliability, quicker turn time, and lower operational costs.

High accuracy, non-intrusive instrumentation is another area that can be developed to enhance full engine environment characterization while minimizing risks and operational concerns.

3.6 EHMS-Supported Maintenance Scheduling

The SLI program is supporting the development of engine health management systems (EHMS) to be part of the integrated vehicle health management (IVHM) system. In addition to providing a reliability benefit provided by failure mode mitigation, the EHMS can be also used to support post-flight maintenance scheduling. The data recorded by the EHMS during the engine flight operation can be downlinked to the ground for analysis. This allows unscheduled maintenance to be identified and prepared for implementation before the vehicle returns to earth.

4. Summary

In the summer of 2002, NASA announced that it would not exercise the contract options to continue development of the COBRA or RS-83 engines. The suspension of development efforts was not due to technical or programmatic deficiencies in either project, but was due to reorientation of SLI priorities to focus on LOX/kerosene booster engine development. With the limited program budget (and manpower), the LOX/LH2 development effort could not be continued in parallel and was suspended.

Although the LOX/LH2 engine programs were discontinued, they were useful in developing and demonstrating the process of infusing the strategic engine attributes (e.g., safety, reliability, operability, maintainability) into the engine design at an early stage. This practice should be further refined and implemented in the design process of future engine development efforts.

¹ Biggs, R.E., "SSME – The First Ten Years," *History of Liquid Rocket Engine Development in the United States*, AAS History Series, Vol. 13, 1992

² Interview with NASA personnel, REIMR Study, 2001

³ RI/RD89-109, "Flight Readiness Firing and Space Transportation System Launch History Data," Rocketdyne Propulsion & Power, 9 June 1998

Lifetime Issues for In-Space Propulsion Systems

28 October 2003

Fifth International Symposium on Liquid Space Propulsion

Gordon Dressler

Northrop Grumman Space Technology



Definition & Scope

Lifetime Issues for In-Space Propulsion

In-Space Propulsion

Any type of propulsion operations—and associated fluids and hardware—used for ΔV or ACS functions on space vehicles outside a celestial body's sensible atmosphere

- *excludes launch vehicle stages unless restartable in space vacuum*

Thus, the Centaur, Proton Block-DM and Rocket Briz-KM (among others) as well as Shuttle OMS/RCS can be considered as In-Space propulsion systems even though typically categorized as launch vehicle stages

Symposium Scope

Liquid Propellant Rocket Engines and Supporting Subsystems

- Focus on long life combustion devices technologies

Major Categories for Discussing Propulsion Lifetime Issues

Major Categories for Discussing Propulsion Lifetime Issues

Category 1. Systems That Reach or Exceed Design Life

Lifetimes generally determined by:

- Commanded deactivation/termination
- Propellant or pressurant depletion
- Other S/C subsystem failures
- Cycle life failures of regulators, valves, control electronics
- Operating life (time and/or cycles) accumulated on catalyst beds (monoprop thrusters), anti-oxidation coatings (biprop thrusters), control valves, etc.

Notable examples:

- *Most “heritage” propulsion systems (the rule, not the exception)*
 - *Geostationary comsats*
 - *Weather and remote sensing satellites*
 - *Military satellites*
- *Most high value scientific spacecraft*
 - *Planetary exploration*
 - *Space-based astronomy*

Major Categories for Discussing Propulsion Lifetime Issues (cont'd)

Category 2. Systems That Reach Design Life (with Good Performance) Despite Significant Degradation

Lifetimes generally determined by:

- Design robustness (operating margins)
- “Fail safe” design implementation
- Degree of redundancy available
- Ability for human intervention and “workaround” skills

Notable examples:

- *Systems incorporating new components or new techniques*
- *Systems accidentally overstressed or outright damaged*
- *Systems forced to operate outside qualification envelopes*

Major Categories for Discussing Propulsion Lifetime Issues (cont'd)

Category 3. Systems That Fail Completely Prior to Reaching Design Life

Lifetimes generally determined by:

- Fundamental design error(s)
- Critical manufacturing defect missed during acceptance screening
- “Random” component failure (statistical outlier present on flight)
- Command error (ground or OBC)
- Misread/misunderstanding of early warning signs (pre-launch or in-flight)
- Lack of effective redundancy
- Ineffective abort or safe-hold mode planning/implementation
- Ground verification testing not representative of flight conditions

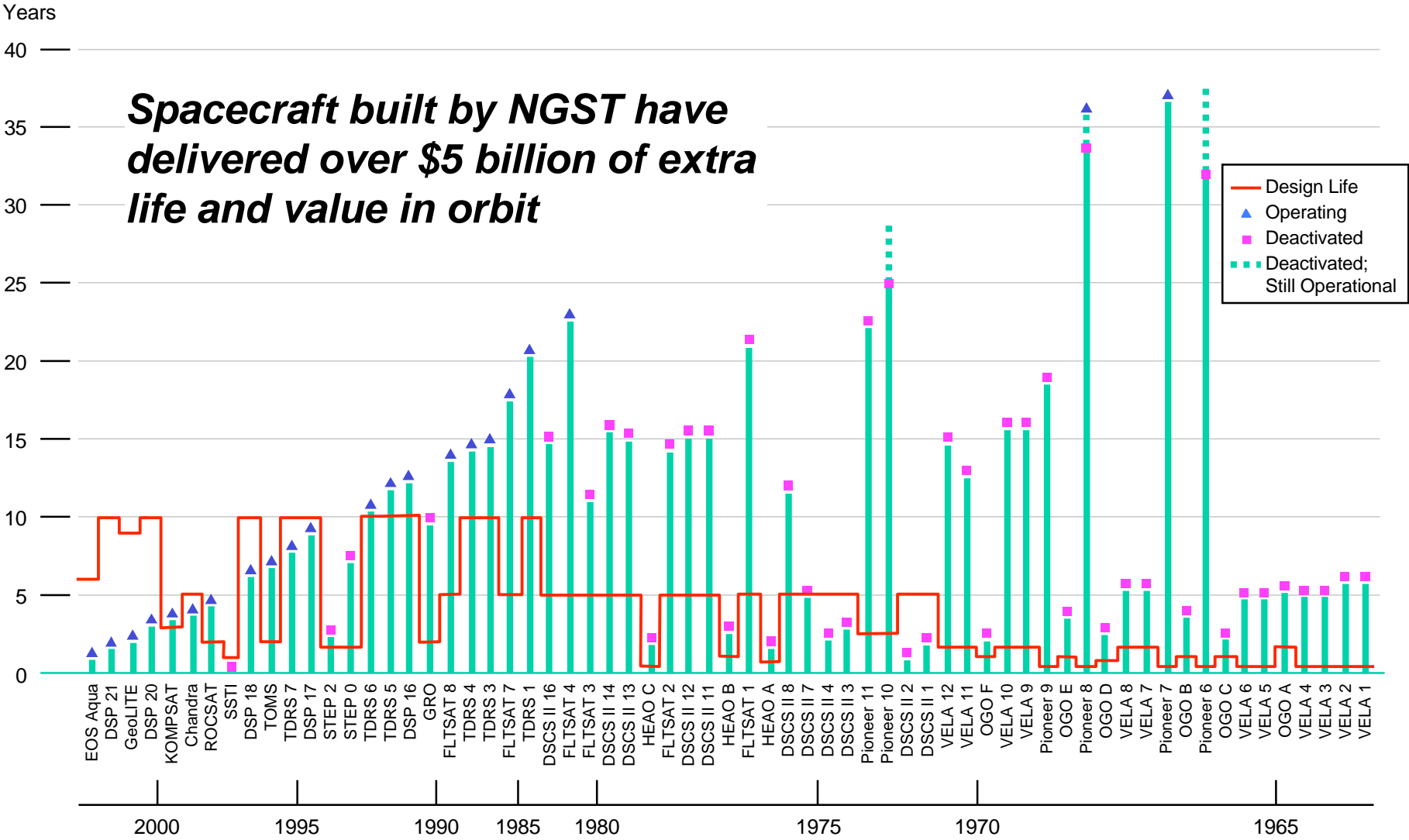
Notable examples:

- ***Most likely for “first of kind” propulsion systems***
- ***Most likely for cost or schedule constrained programs***
- ***Most likely to occur on programs with inexperienced engineering, fabrication, testing or management personnel***

Despite the notoriety of major in-space failures (including a few due to propulsion systems), modern spacecraft systems are quite reliable overall and are increasing in life capability . . .

Longevity of Northrop Grumman Spacecraft

Lifetime Issues for In-Space Propulsion



Broad Factors Affecting Operating Lifetimes of In-Space Propulsion Systems

- **Mission mode**
 - **Expendable vs. reusable**
 - **Degree of normal-operations autonomy**
 - **Capability for ground intervention**
(inc. communication windows and one-way light times)

- **Mission environment:**
 - **Non-operating (inc. pre-launch)**
 - **Operating**

Broad Factors Affecting Operating Lifetimes of In-Space Propulsion Systems (cont'd)

- **Propulsion system design:**

- **Design reliability**
- **Degree of redundancy**
- **Specified and actual design margins**
- **Fault tolerance (inc. contamination sensitivity)**
- **C.g. control, s/c balance and thrust vector alignments**
- **Propellant utilization/residual allocation calculations**
- **Materials/propellants compatibilities**
- **Component and subsystem maturity level (lessons learned)**

Broad Factors Affecting Operating Lifetimes of In-Space Propulsion Systems (cont'd)

- **Propulsion system operation**
 - **Operating modes maturity level (lessons learned)**
 - **Open-loop vs. closed loop (e.g., MR control on biprops)**
 - **State-of-health monitoring and intervention**
 - **“Safe-hold” planning, execution and recovery**
 - **Prevention of critical command mistakes**
 - **Pre-launch operations (e.g., fueling, removal of non-flight items)**

Broad Factors Affecting Operating Lifetimes of In-Space Propulsion Systems (cont'd)

- **Interfaces to other spacecraft systems**
 - **Command**
 - **Electrical power**
 - **Thermal control**
(inc. margins above freezing and below boiling/autodecomposition of propellants)
 - **Structure**

- **Other factors**
 - **Unnoticed pre-launch handling damage/defects**
 - **Unnoticed test-induced damage/defects**
 - **Inadequate parts sampling or testing**

The Complexity Issue

Lifetime Issues for In-Space Propulsion

- A. Increasing complexity in single-strung systems generally leads to decreased reliability and, hence, likelihood of **decreased** operating life
- B. Increasing complexity to effect redundancy generally leads to increased reliability and, hence, likelihood of **increased** operating life
- Mission requirements (allocated cost, volume, weight, power, etc.) generally preclude 100% redundant propulsion systems, so the engineering challenge is to achieve the optimum balance between A and B.

Major In-Space Propulsion Life Extension Activities at Northrop Grumman

Major In-Space Propulsion Life Extension Activities at Northrop Grumman

Lifetime Issues for In-Space Propulsion

Focus on Two Major Areas:

- **Elimination of Life-Limiting, Oxidation-Resistant Coatings on Radiation-Cooled Bipropellant ACS/RCS Engines**
 - **Two Approaches:**
 - **Pt-Ir Thrust chambers (110/3900 N, 25/870 lbf)**
 - **SCAT (18-62 N, 4-14 lbf)**
 - **Addresses Category 1 and 2 Lifetime Issues**

- **On-Orbit Propellant Resupply (Orbital Express Program)**
 - **Addresses Category 1 Lifetime Issue**
 - **Enables partial/full recovery from Category 2 and 3 faults**

Disilicide Coatings are a Life Limiting Item for Space Shuttle Thrusters

Lifetime Issues for In-Space Propulsion

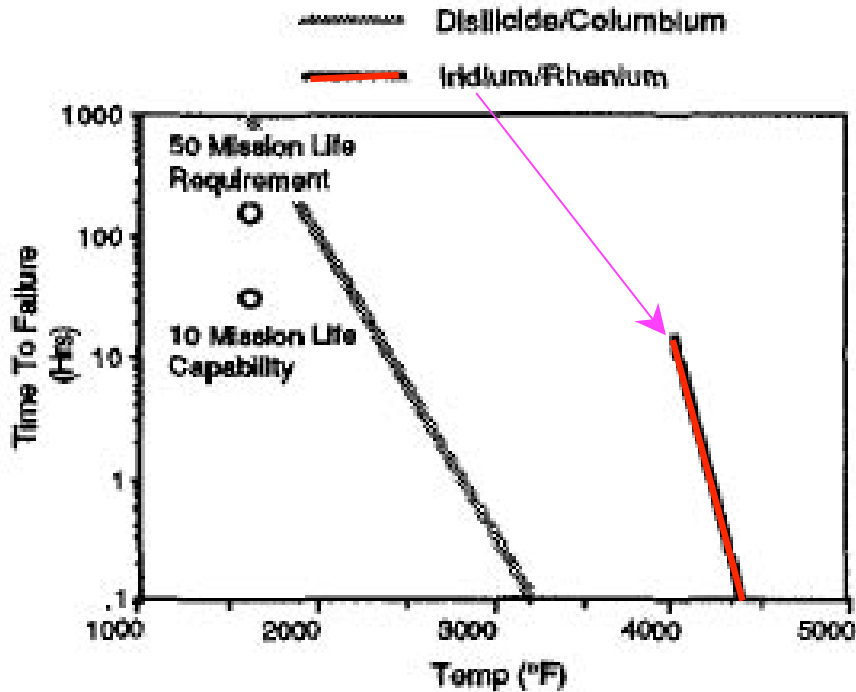


Figure 4. Chamber Operating Life vs Temperature*

*“Through Shuttle flight STS-31, a total of eleven vernier thrusters have required replacement due to chamber (coating) damage.” **

*“The chronic and problematic issues that continue to impact the Orbiter processing are combustion chamber degradation and propellant valve leakage. The combustion chamber degradation is caused by thermal cycles and mechanically induced spalling of the di-silicide R512 coating. At the current failure pattern, an average of one thruster valve replacement is required per flow.” ***

*Ref: “Space Shuttle Vernier Thruster Long-Life Chamber Development,” D. Krohn, NASA JSC, AIAA 90-2744, 26th AIAA/SAE/ASME/ASEE Joint Propulsion Conference, July 16-18, 1990

**Ref: “Space Shuttle Orbital Maneuvering System/Reaction Control System Improvements for the Future Shuttle,” H. Rodriguez and R. Rehagen, The Boeing Company, AIAA 2002-4326, 36th AIAA/SAE/ASME/ASEE Joint Propulsion Conference, July 8-11, 2002

Disilicide Coatings are Damaged by Thermal Cycles and Time-at-Temperature

Lifetime Issues for In-Space Propulsion

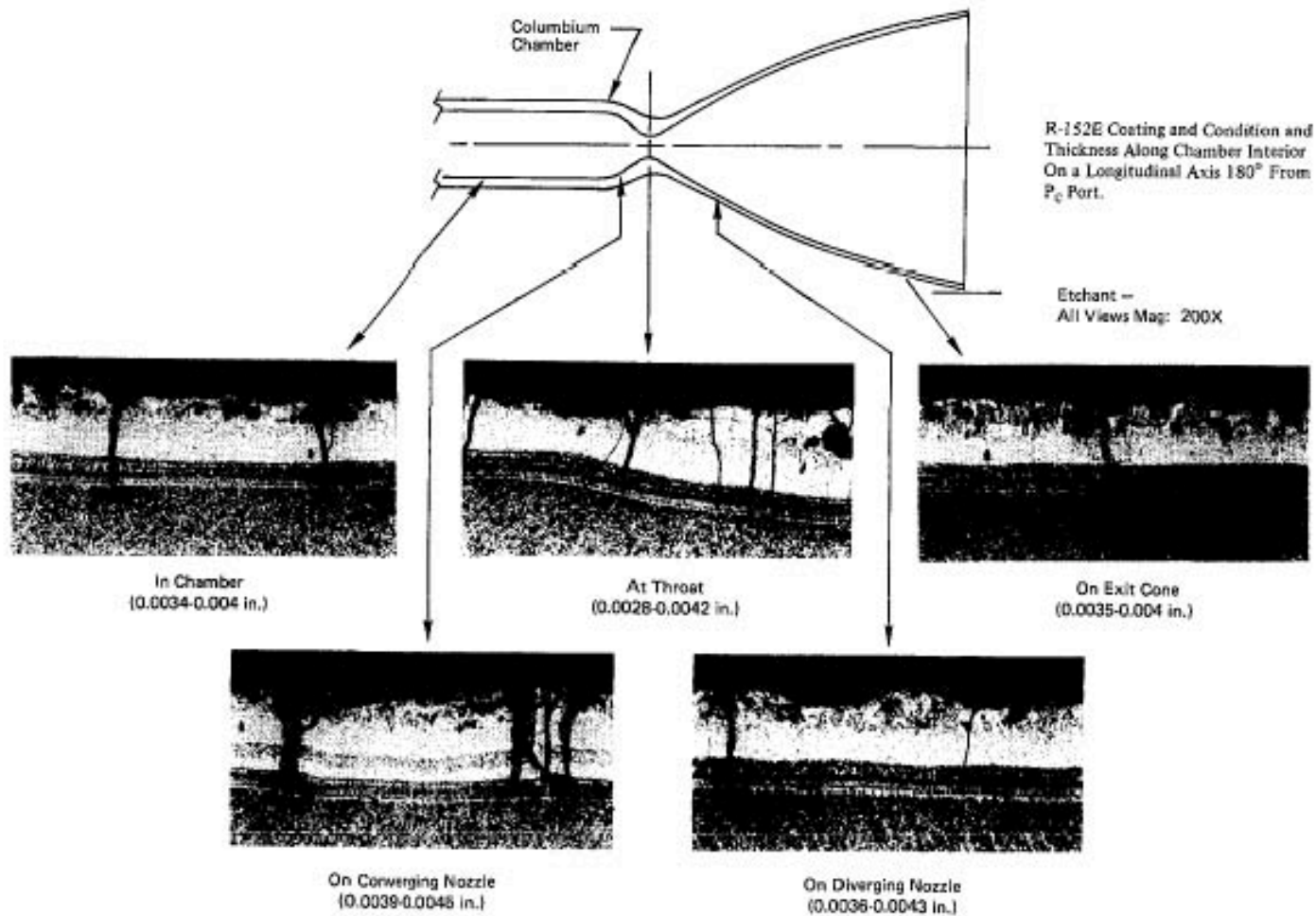


Figure 10. Metallurgical Analysis of R-152E Coating After 29.4 Hours Firing Time

*Ref: "Long Life 5 lbf Bipropellant Engines," M. Chazen, Bell Aerospace Textron, AIAA 85-1378, 21st AIAA/SAE/ASME/ASEE Joint Propulsion Conference, July 8-10, 1985

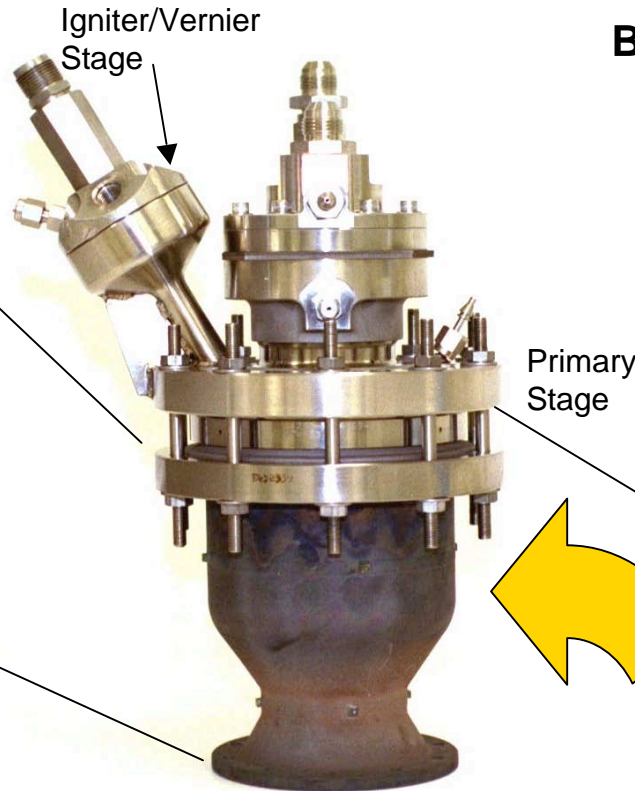
Pt-Ir Chamber Testing with LOX/Ethanol: 3900 N (870 lbf) RCS Thruster

Lifetime Issues for In-Space Propulsion

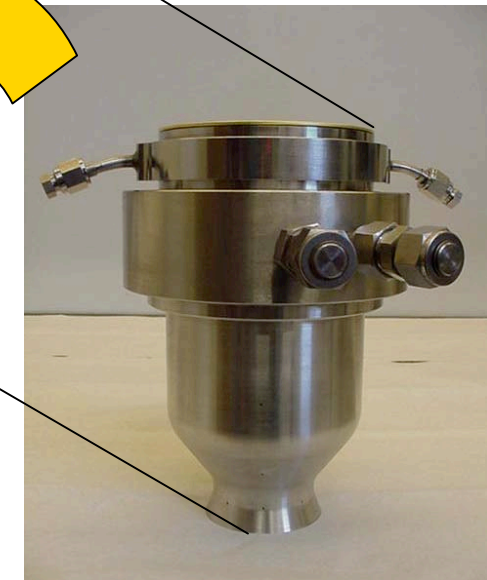
Coated C103 Chamber



**R512 Disilicide-Coated C103 Chamber
Replaced by Pt-Ir Alloy Chamber**



Bare Pt-Ir Metal Chamber



Pt-Ir Chamber Testing with LOX/Ethanol: 3900 N (870 lbf) RCS Thruster (cont'd)

Objectives

- Demonstrate pulse mode capability of a Pt-Ir alloy chamber using LOX/ethanol propellants
- Demonstrate the structural integrity of the chamber and its internal & external surfaces are not adversely affected by exposure to representative RCS temperatures and pressure/thermal cycles

Test Results

- Tested pulse widths of 0.50 and 1.0 seconds and duty cycles of 9, 17 and 20 % over multiple pulse trains
- Smaller pulses and higher duty cycles precluded by use of non-flight, facility valves
- Seven test runs completed, all at full thrust, acceptable c^* and for full duration
- Chamber appeared “as new” at end of testing



Pt-Ir Chamber Testing with LOX/Ethanol: 3900 N (870 lbf) RCS Thruster (cont'd)

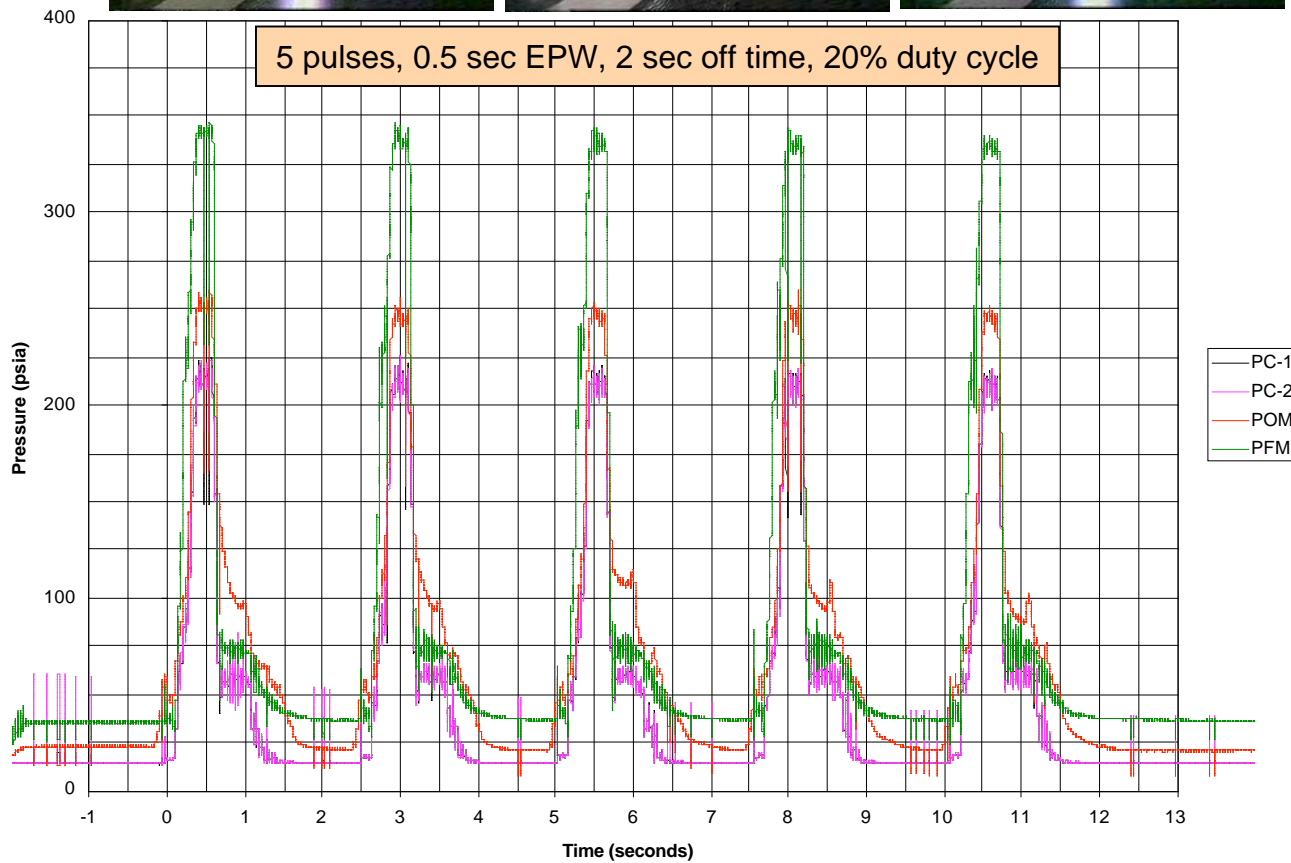
Northrop Grumman
Space Technology

RCS Pt/Ir Chamber Pulse Test
Test No. HB1-2741
10/07/03

20% Duty Cycle
5 pulses x 0.5 sec ON x 2.0 sec OFF

Pt-Ir Chamber Testing with LOX/Ethanol: 3900 N (870 lbf) RCS Thruster (cont'd)

Lifetime Issues for In-Space Propulsion



Post-Test Photo



Secondary Combustion Augmented Thruster (SCAT)

Lifetime Issues for In-Space Propulsion

SCAT Dual Mode Propulsion — An Enabling Development

SCAT is the world's first thruster designed to switch between — as well as operate continuously in — either bipropellant or monopropellant modes

Transformation: use the combination of operating modes to most efficiently use on-board propellant (full tank depletion), and use the unique design features (deep blowdown, thrust modulation) to enhance mission flexibility and effectiveness



Technology Unique to NGST:

Overall SCAT concept (patented)

Oxidizer-cooled flight engine

Long life design & materials of construction

Benefits:

Qualified & flight-proven on GeoLITE spacecraft

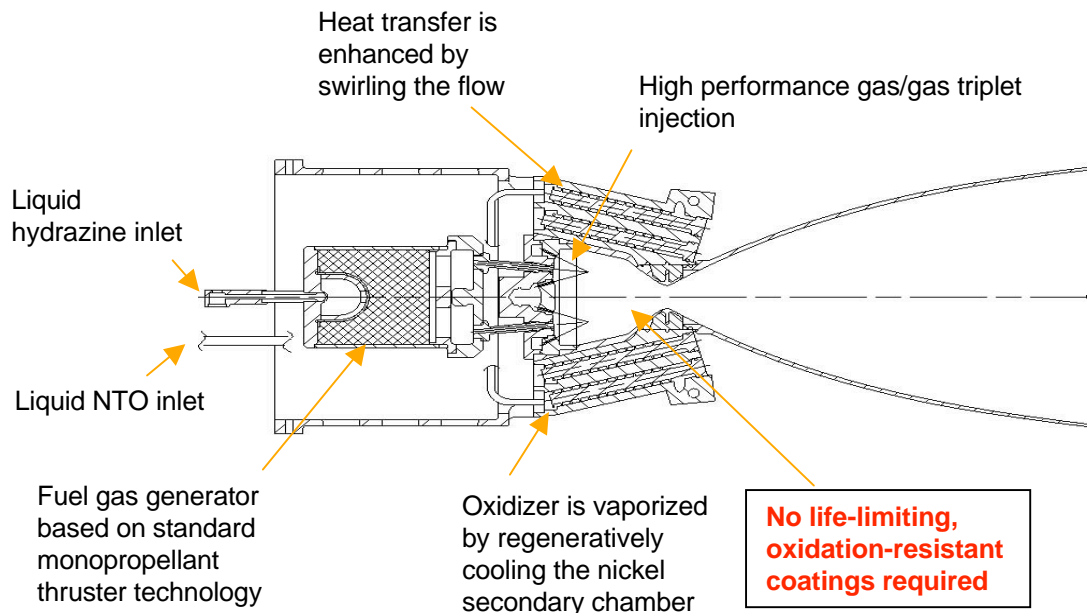
Better cooling margin in biprop mode;
no cooling required in monoprop mode

High reliability: low cost, common alloys used;
life-limiting oxidation-resistant coatings are not used

Secondary Combustion Augmented Thruster (SCAT)

Lifetime Issues for In-Space Propulsion

- SCAT as a bi-propellant thruster uses nitrogen tetroxide (N₂O₄) as the oxidizer and hydrazine (N₂H₄) as the fuel . . . or just hydrazine in monopropellant mode
- The thruster marries a low cost, reliable monopropellant catalyst thruster with a secondary, regenerative-cooled oxidizer chamber . . . This approach makes SCAT uniquely insensitive to mixture ratio swings



Model TR500 Performance Features

Propellants:	N ₂ O ₄ / N ₂ H ₄
Thrust Biprop Mode:	4 lbf to 14 lbf
Mono Mode:	0.75 lbf to 4.5 lbf
Thrust Modulation*:	30% delta max.
Mixture Ratio*:	0.95 to 1.6
Specific Impulse:	325 seconds max.
Mono Mode:	230 seconds
Inlet Pressures:	90 to 600 psia
Qualification Life:	90,000 seconds
Envelope Dimensions:	12.3" x 4.5" x 5.5"
Weight:	4.85 lbm

**Bi-propellant Mode*

Orbital Express Program Overview

Lifetime Issues for In-Space Propulsion

- **Orbital Express demonstration program is a satellite-servicing mission that includes propellant resupply**
- **Planned launch is 2006**
- **The mission has the objective of demonstrating the technologies needed for routine servicing of spacecraft: namely autonomous rendezvous and docking, propellant resupply, and orbital replacement unit transfer.**
- **The demonstration system uses two spacecraft. A servicing vehicle (ASTRO) will perform multiple dockings with a client (NEXTSat) spacecraft, and perform a variety of propellant transfers in addition to exchange of a battery and potentially a computer.**
- **The NGST-designed and fabricated fluid transfer and propulsion system onboard ASTRO, in addition to providing the six degree-of-freedom (6 DOF) thruster system, will demonstrate autonomous transfer of monopropellant hydrazine to and from the NEXTSat spacecraft, including closed-loop pump and pressure transfers**

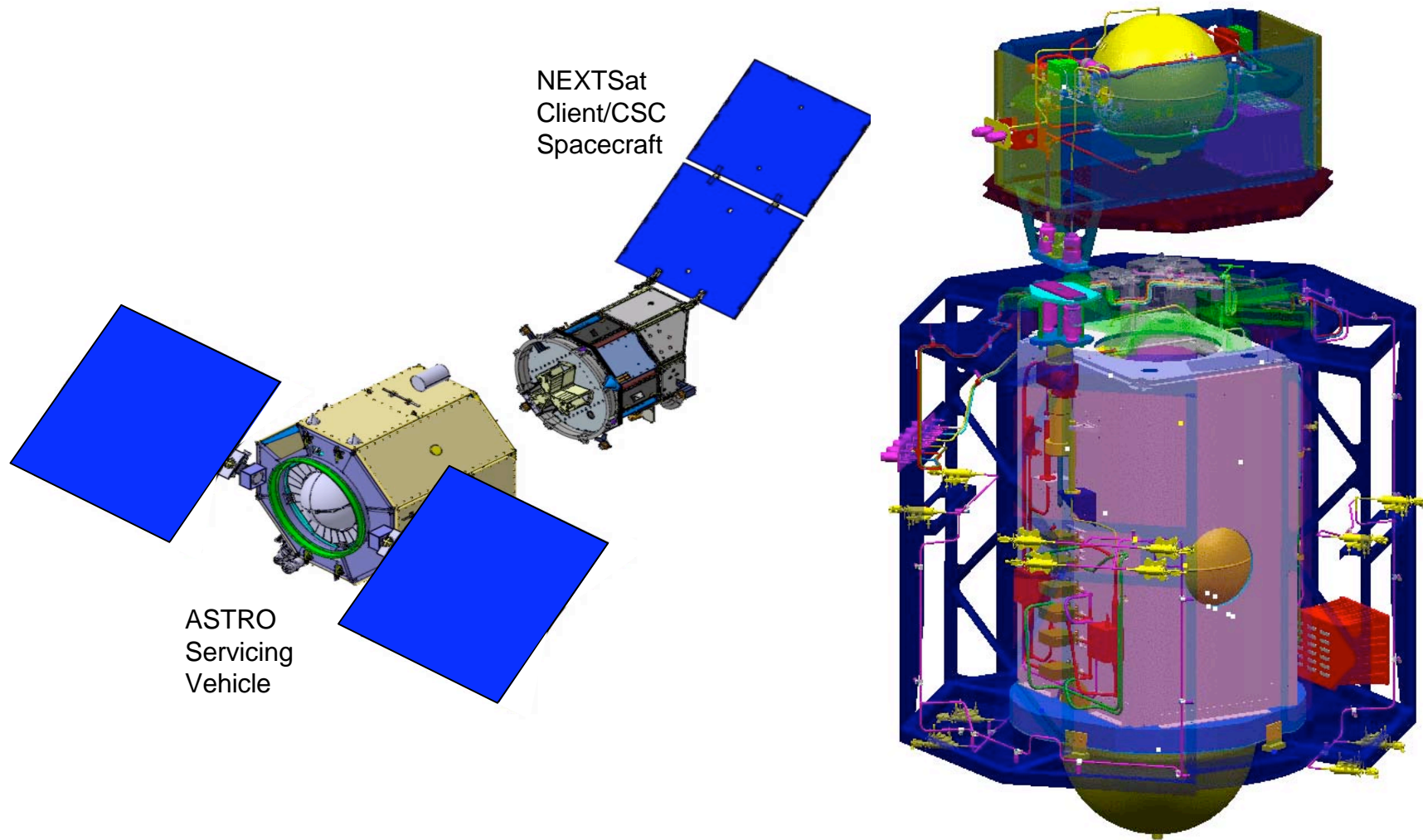
Orbital Express Program Overview (cont'd)

Lifetime Issues for In-Space Propulsion

- **Although on-orbit refueling has been successfully performed numerous times by the Progress resupply vehicle (MIR, ISS), routine servicing of satellites has not followed suit. Impediments for such a transition may be lack of standardized servicing hardware, hardware maturity, and desired spacecraft mission pedigree.**
- **The Orbital Express mission will not demonstrate all potential servicing needs – for example monopropellant hydrazine is the only fluid to be transferred in the Orbital Express demonstration. However, the technology and infrastructure could be readily adapted to bipropellant refueling.**
- **Benefits to having an on-orbit refueling capability generally fall into the categories of reduced launch weight, life extension, system efficiency (enhanced delta V budget, reduced tank volume), maneuverability, and contingency recovery.**

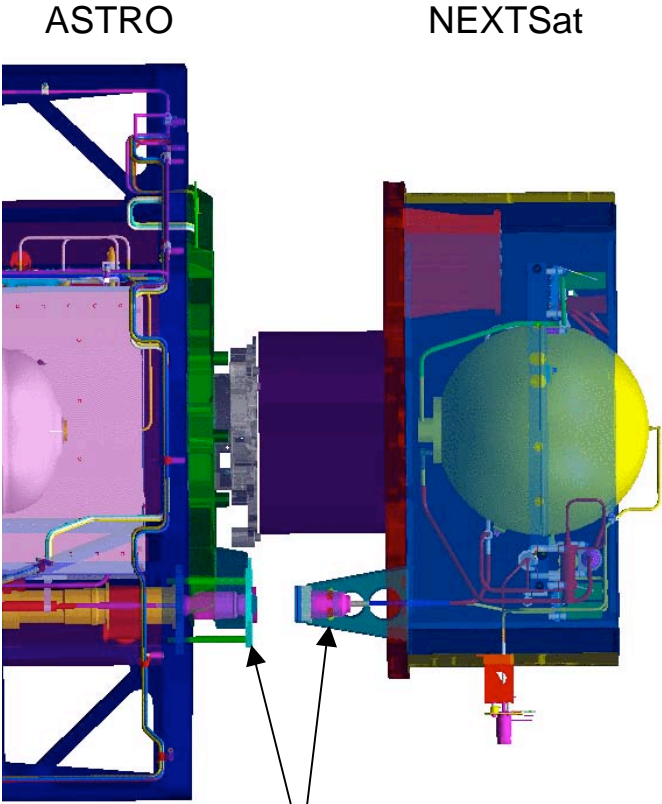
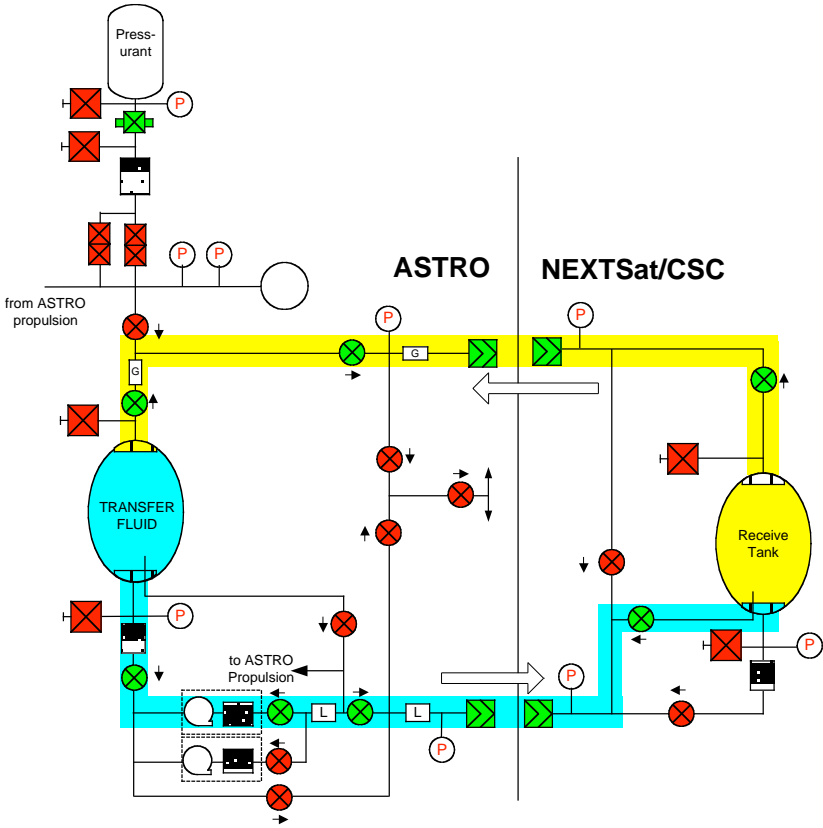
Orbital Express Program Overview (cont'd)

Lifetime Issues for In-Space Propulsion



Orbital Express Program Overview (cont'd)

Lifetime Issues for In-Space Propulsion



Fluid Couplings Not Yet Engaged

Concluding Remarks

Lifetime Issues for In-Space Propulsion

- **Propulsion system complexity for increased performance and capabilities tends to negatively impact meeting mission design life; propulsion system complexity to achieve operational redundancy tends to insure exceeding mission design life**
- **Most of today's spacecraft have in-space propulsion systems that meet or exceed design lifetimes**

Concluding Remarks (cont'd)

Lifetime Issues for In-Space Propulsion

- **Overall, chemical combustion devices and associated systems for in-space propulsion are generally very reliable**
 - **Failing to meet or exceed mission design life is often due to causes other than the specific technology utilized (e.g., command errors, design errors, manufacturing defects, failure to heed “lessons learned”)**
 - **Reflected in general reliance on single main rocket for most large ΔV functions**
 - **Reflected in general lack of full system redundancy for most spacecraft ACS/RCS systems**

Concluding Remarks (cont'd)

Lifetime Issues for In-Space Propulsion

- **The Orbital Express program will be a key flight demonstration that spacecraft can attain many additional years of operational life by in-space refueling of propellants**

- **A major improvement in the mission life capability of current radiation-cooled ACS/RCS thrusters can be obtained by elimination of sensitive anti-oxidation coatings through use of:**
 - **regeneratively-cooled combustion chambers, or**
 - **noble refractory metal combustion chambers**



RESEARCH ACHIEVEMENT ON LONG-LIFE THRUST CHAMBERS AT NAL/KPL

Oct. 28, 2003

5th International Symposium on Liquid Space Propulsion

A. Kumakawa*, S. Moriya and M. Sato
Space Propulsion Research Center, JAXA, JAPAN

Contents

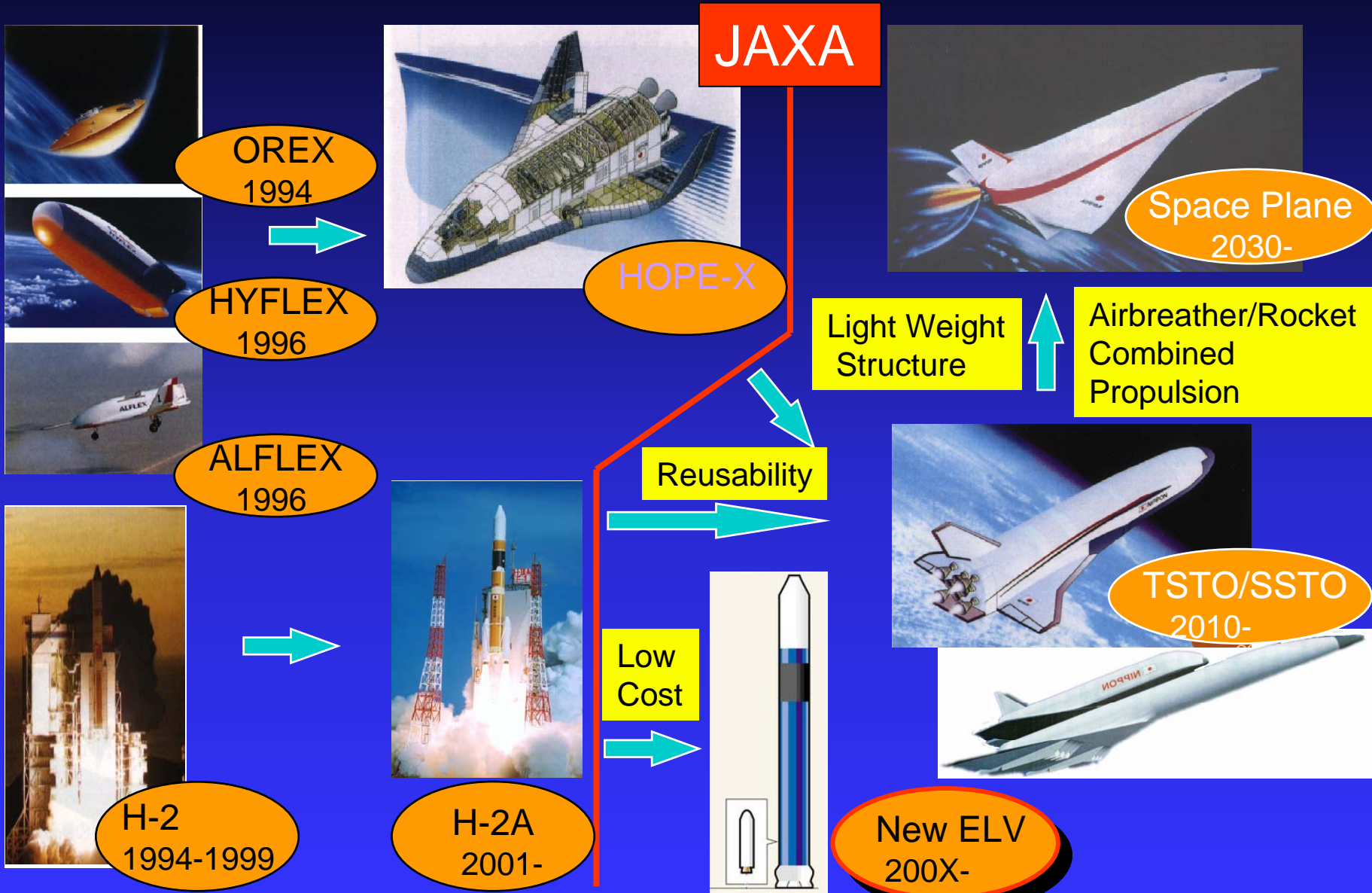
- Introduction
- Compliant structure — Outer shell approach
- Thermal barrier coatings & FGMs
 - Inner shell approach
- Summary

Introduction

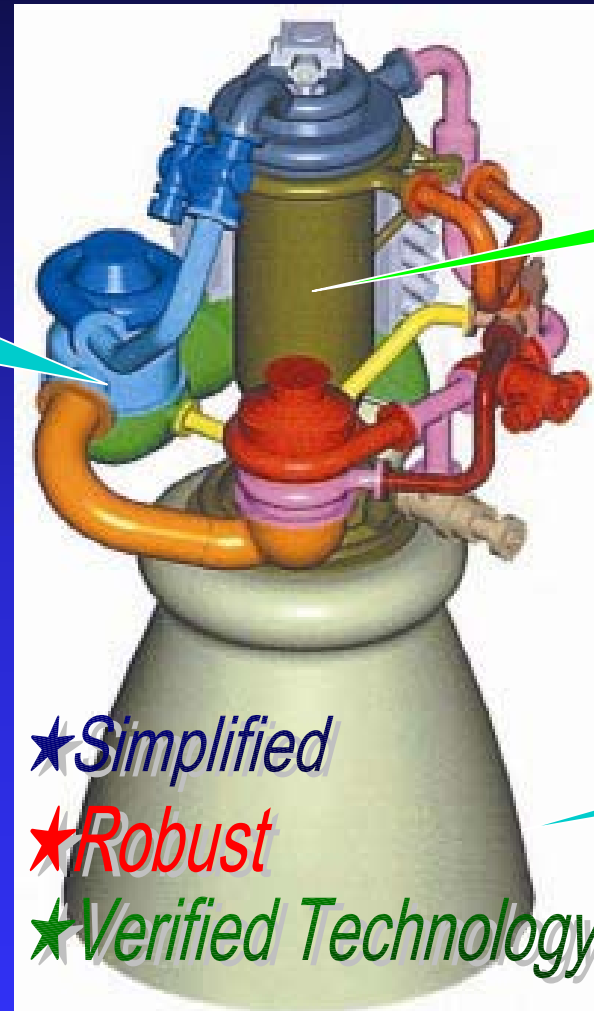


- Since its establishment of in 1965, NAL (National Aerospace Laboratory) /KPL (Kakuda Space Propulsion Laboratory) has contributed to the R&D of Japanese launch vehicles, especially with respect to propulsion.
- It has been involved in the R&D of rocket engines such as the LE-5 engine and the LE-7 engine. These engines have been respectively used for the H-1 and H-2 launch vehicles.
- NAL/KPL has been merged and renamed as Space Propulsion Research Center of JAXA (Japan Aerospace Exploration Agency) this October.

Flowchart of Development of RLV



Subjects for reusable rocket engine



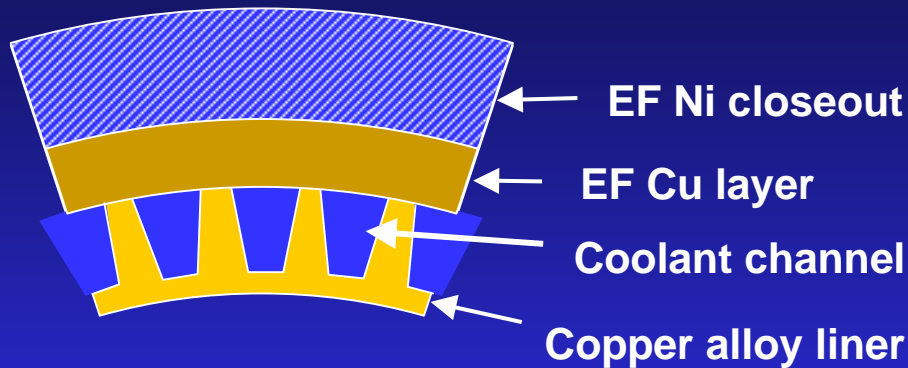
Long-life combustor

High performance & durable T/Ps

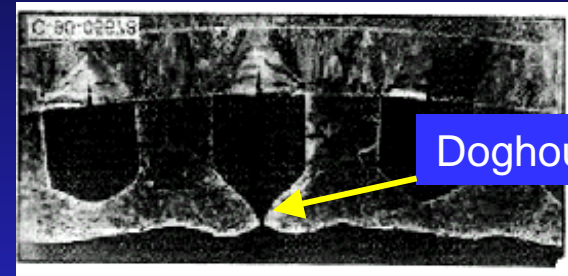
High performance nozzle

★ *Simplified*
★ *Robust*
★ *Verified Technology*

Factors for restricting the life



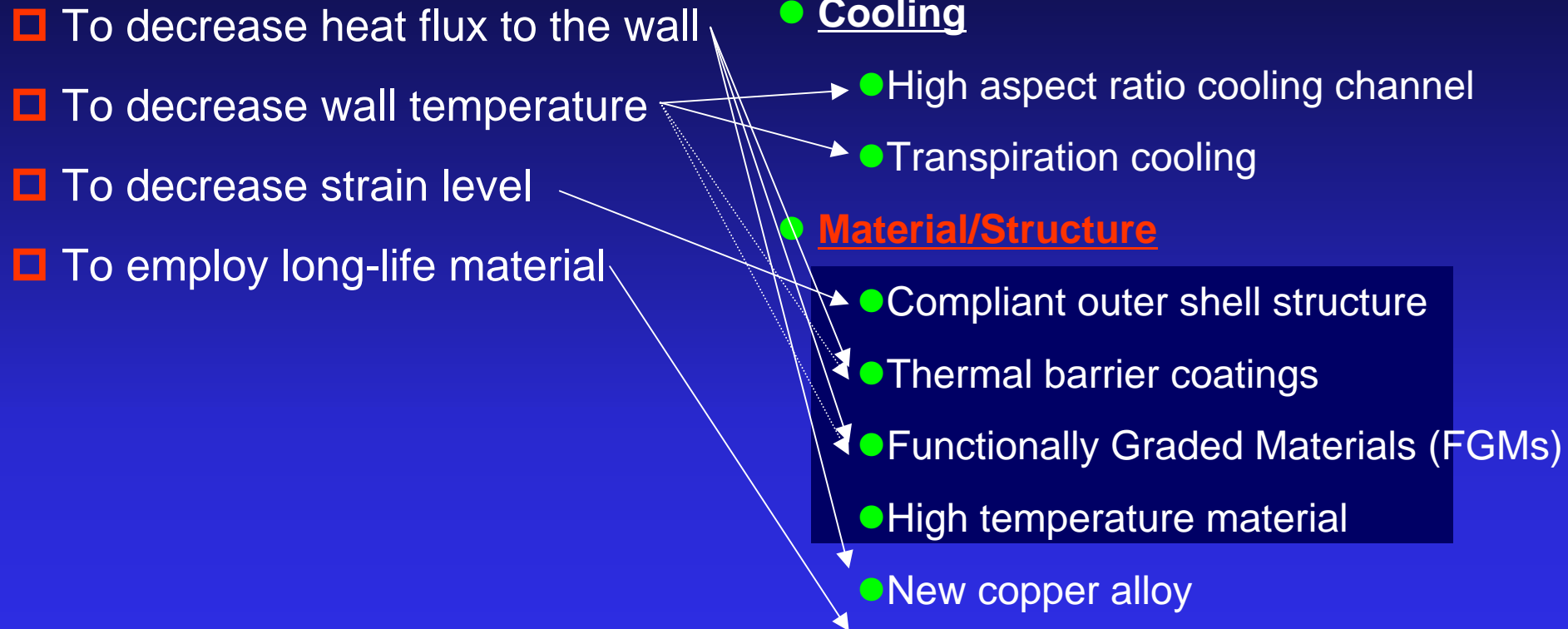
Typical conventional structure of thrust chamber



Typical failure of coolant channel

- Large thermal strain due to large heat flux of 100 MW/m^2
- Strain due to high pressure of hot gas and coolant
- Confinement due to high stiffness of EF Ni or Inconel alloy outer shell

Proposed approach for life extension



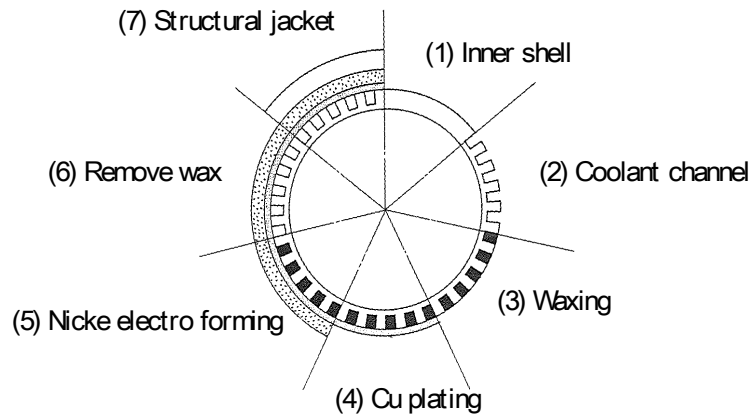
Purposes



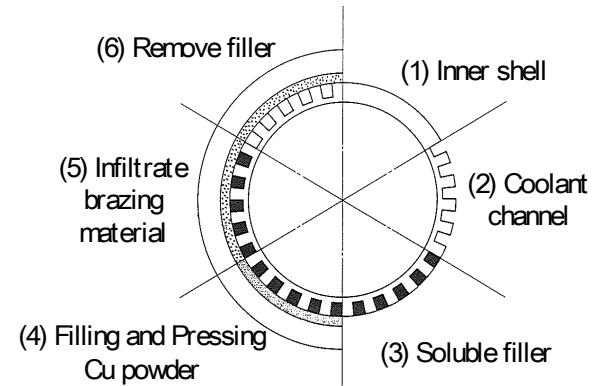
- To introduce research progress on compliant outer shell structures, thermal barrier coatings and FGMs for long-life thrust chambers, which have been studied at NAL/KPL up to now.

I. Outer shell approach

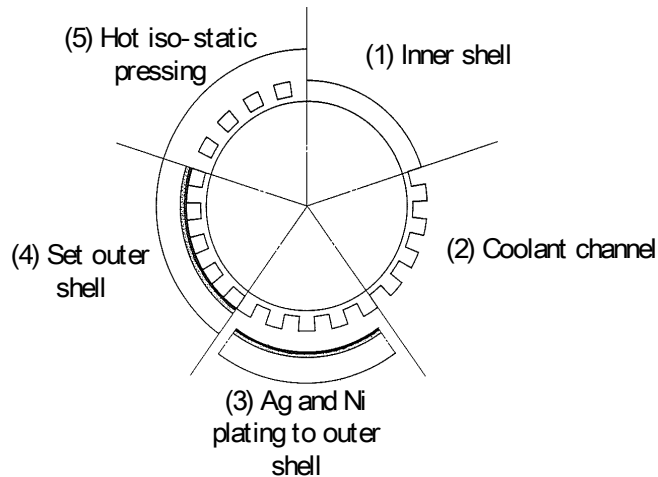
Fabrication methods proposed



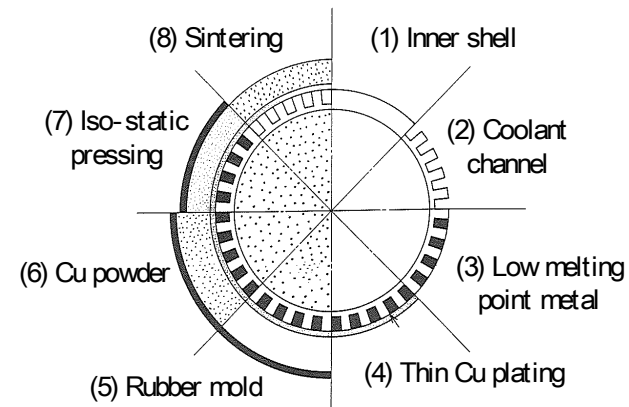
(a) Electro-forming method



(b) Infiltration method

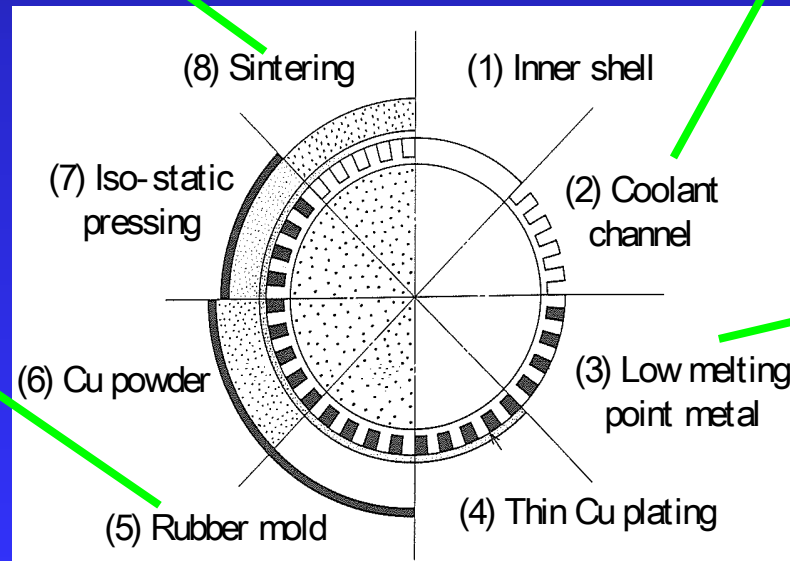
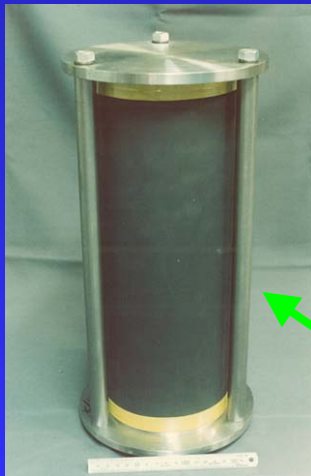
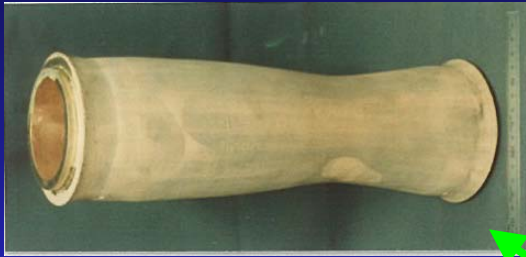


(c) Diffusion bonding method

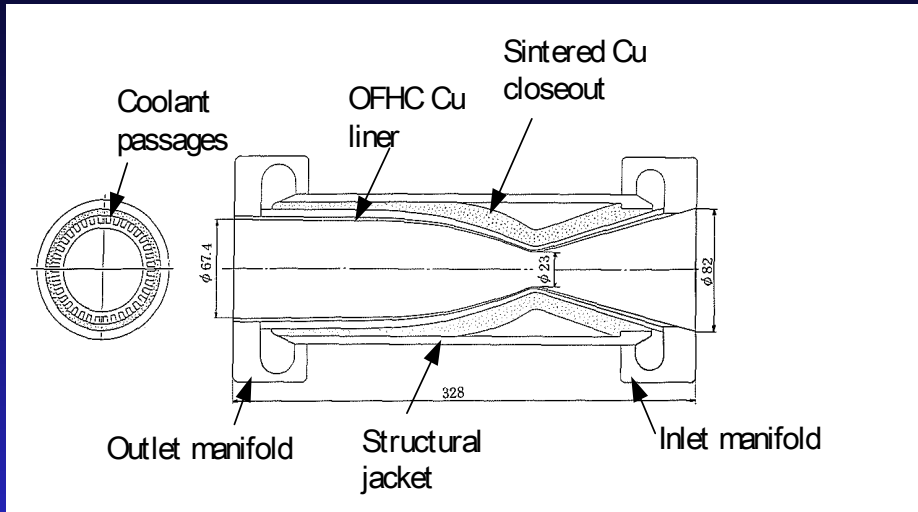


(d) CIP forming method

CIP forming Method



CIP formed chambers



10 kN chamber

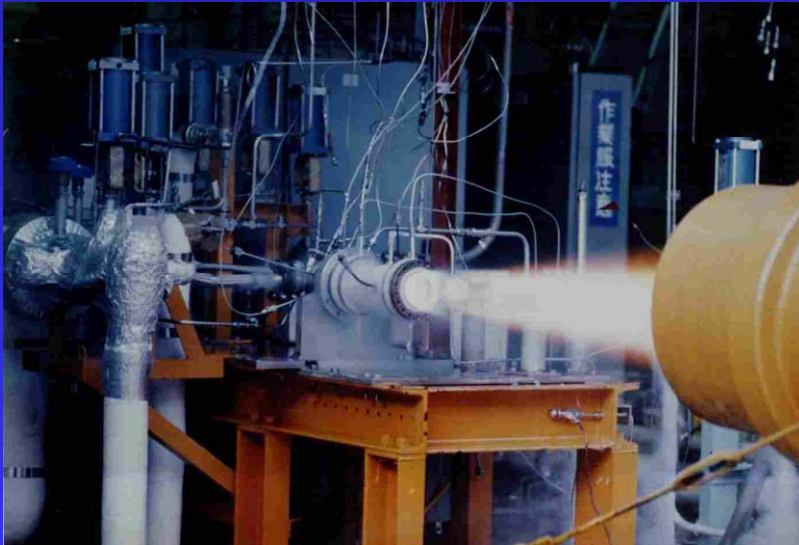


◀ 100 kN chamber

Firing tests of CIP formed combustor

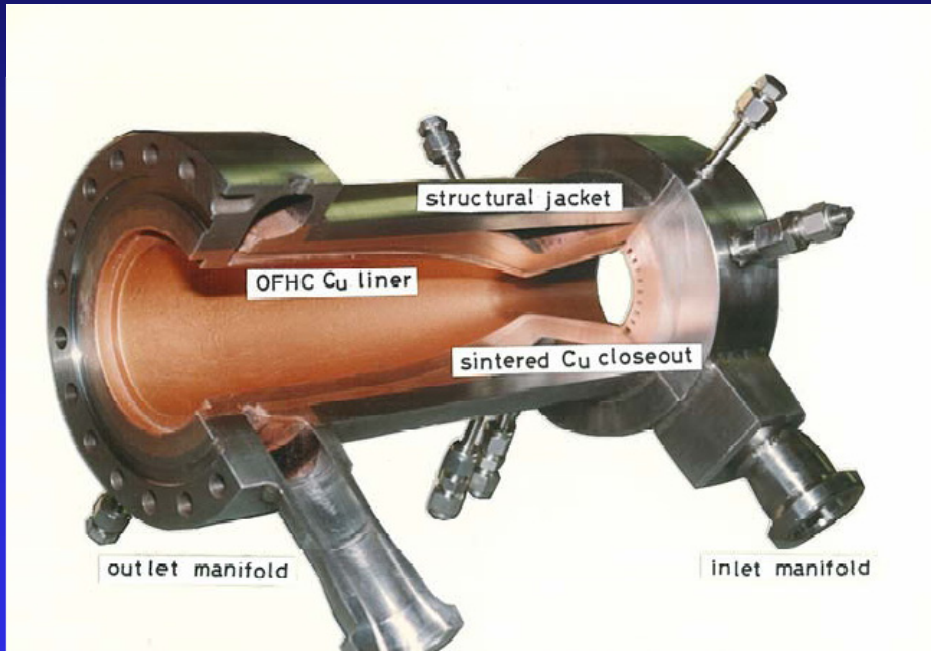


Propellant	Liquid oxygen, /gaseous hydrogen
Chamber pressure	5 - 9 MPa
Thrust	10 kN
Firing Duration	1- 30 sec
Number of test	10 times



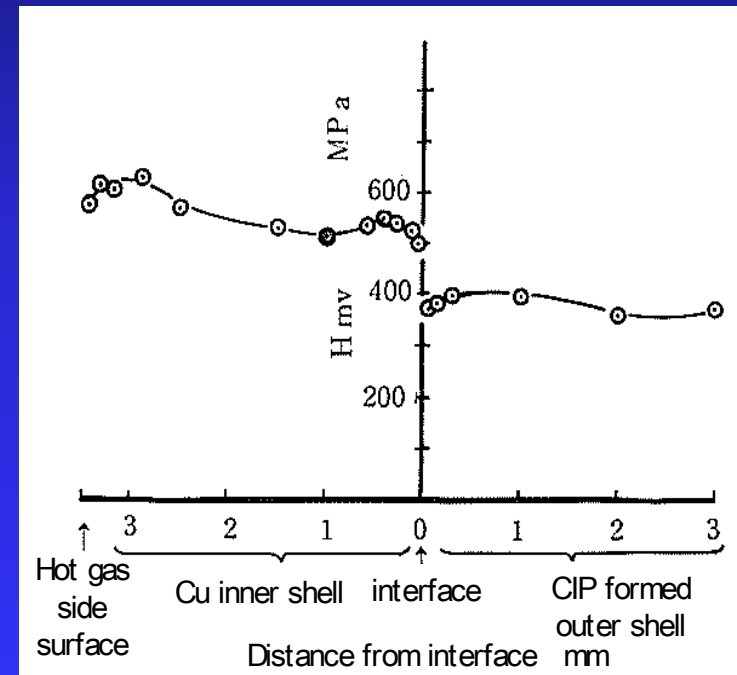
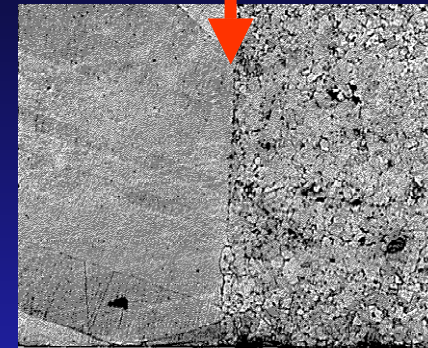
No flaw was observed
after firing tests

Firing tests of CIP formed combustor



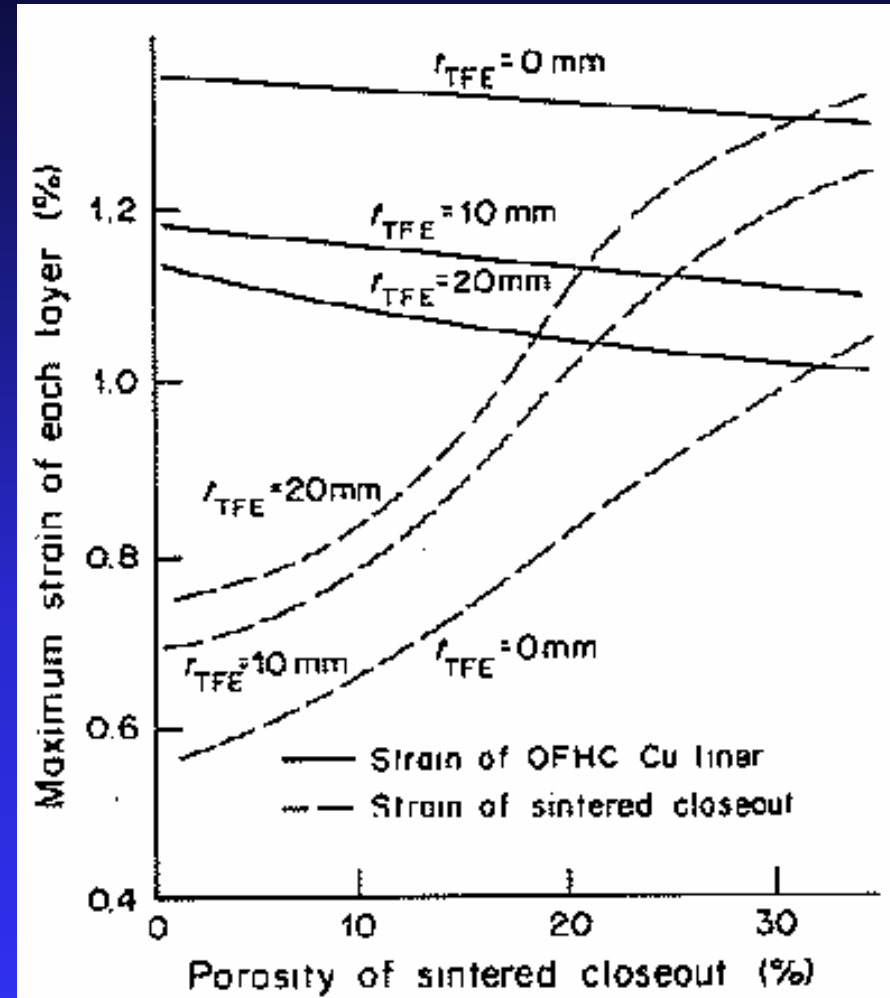
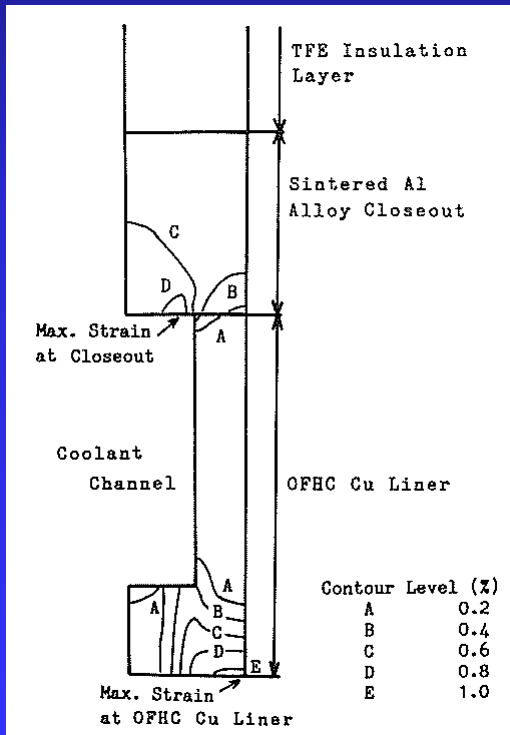
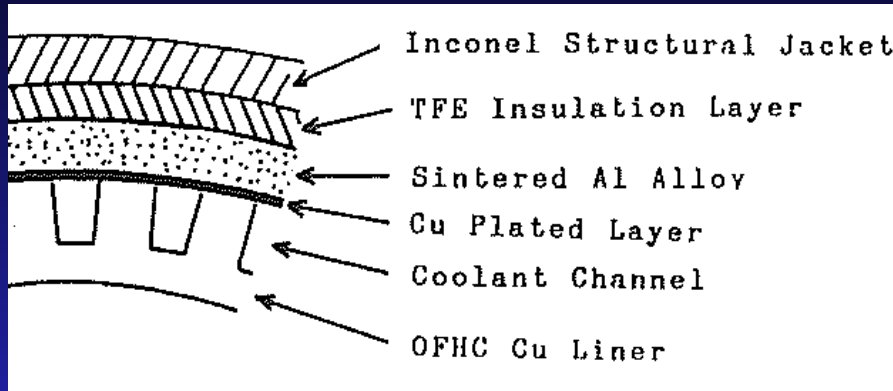
Cut-view after tests

Interface



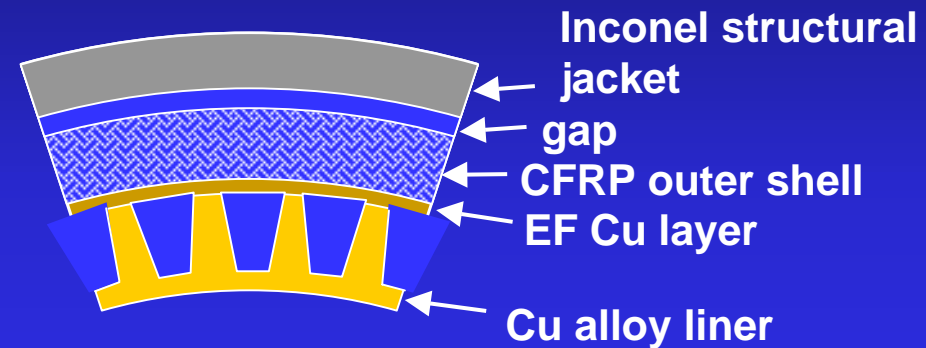
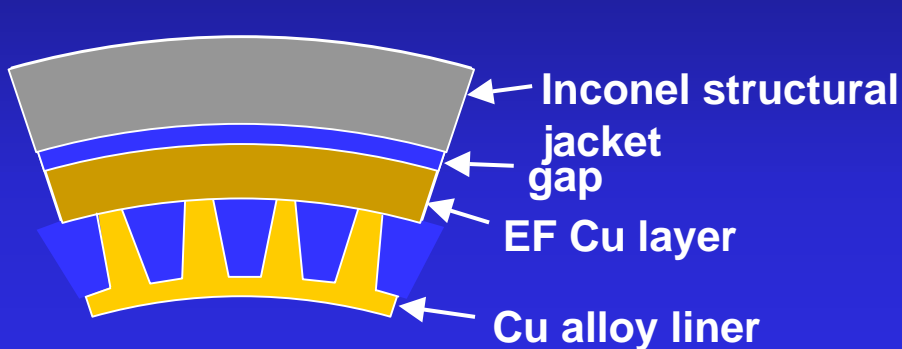
Micro Vickers hardness distribution

Compliant CIP formed structure



Outer shell with compliant structure

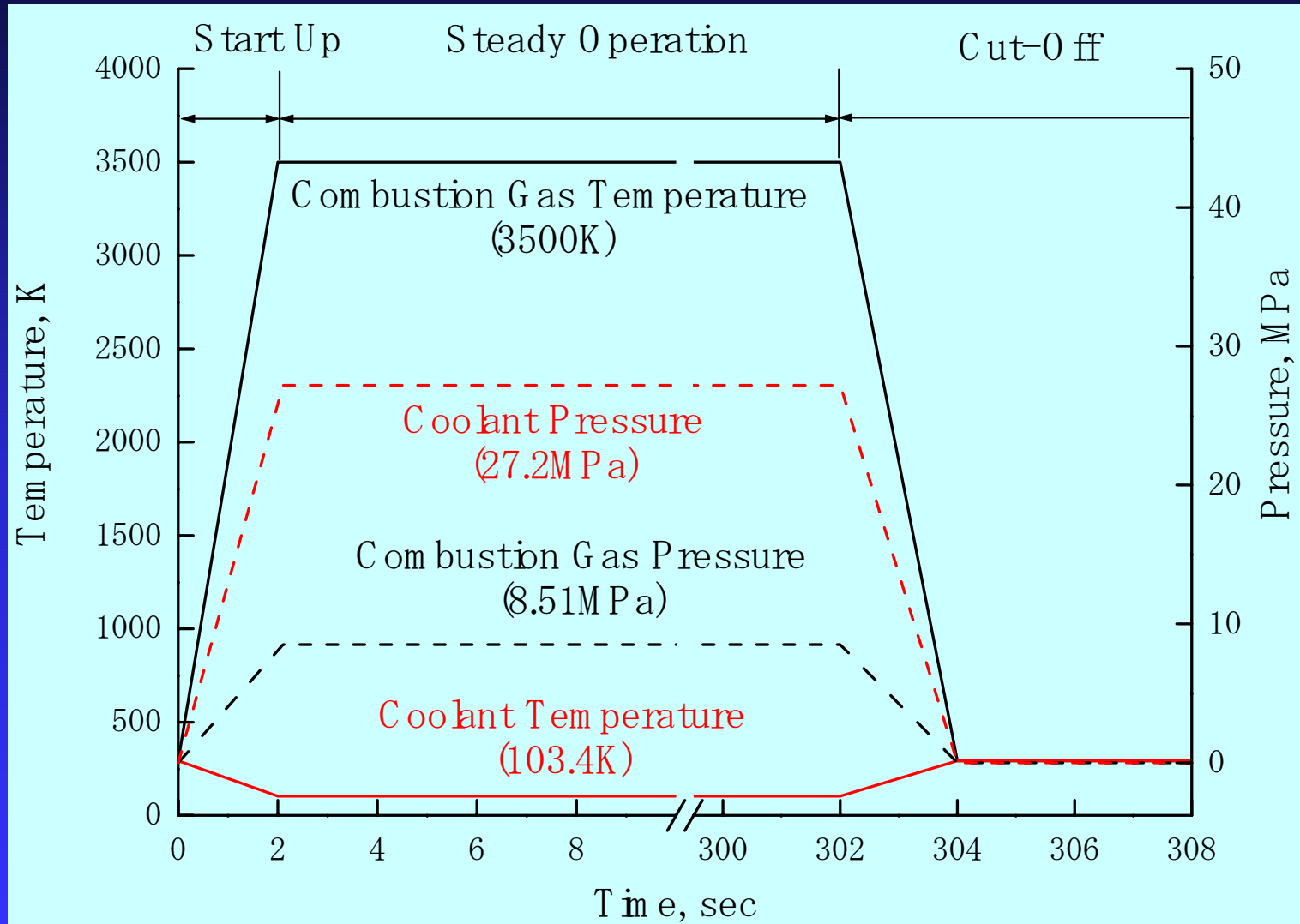
- Separated structure with Inconel outer shell
 - Low-stiffness CFRP outer shell
- ➔ Decrease thermal stress of Copper alloy liner



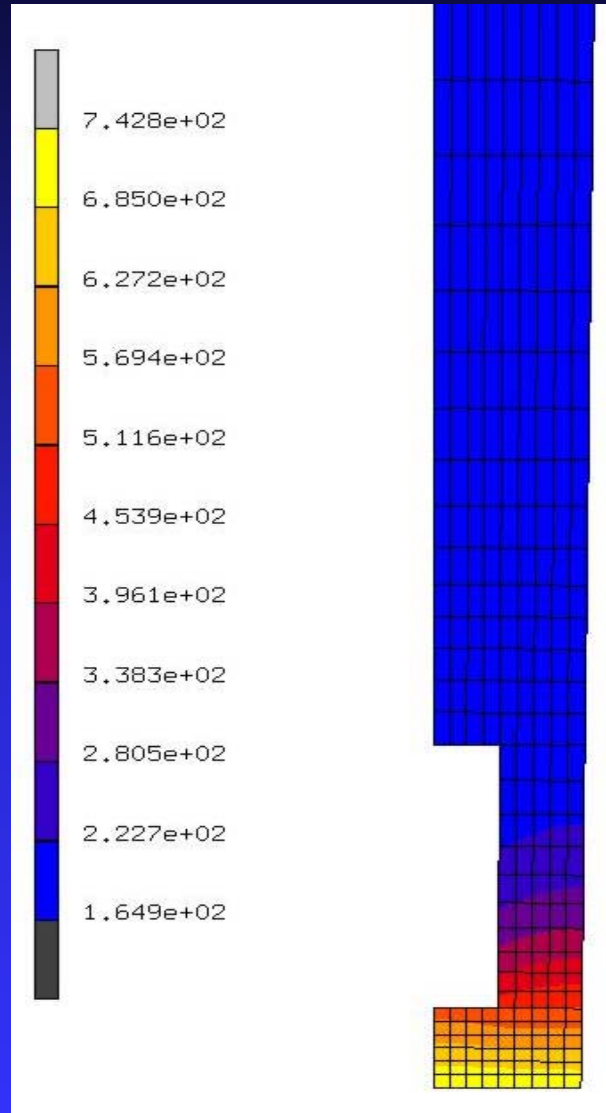
Separated structure

Low-stiffness CFRP
outer shell

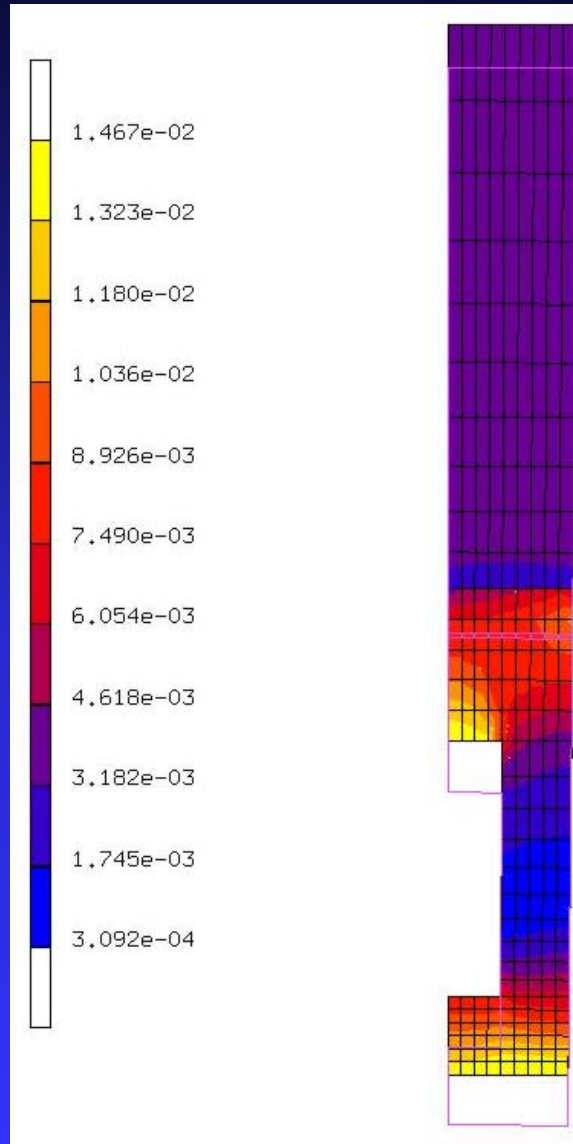
Assumed variation of temperature and pressure



Temperature distribution of Ni closeout model

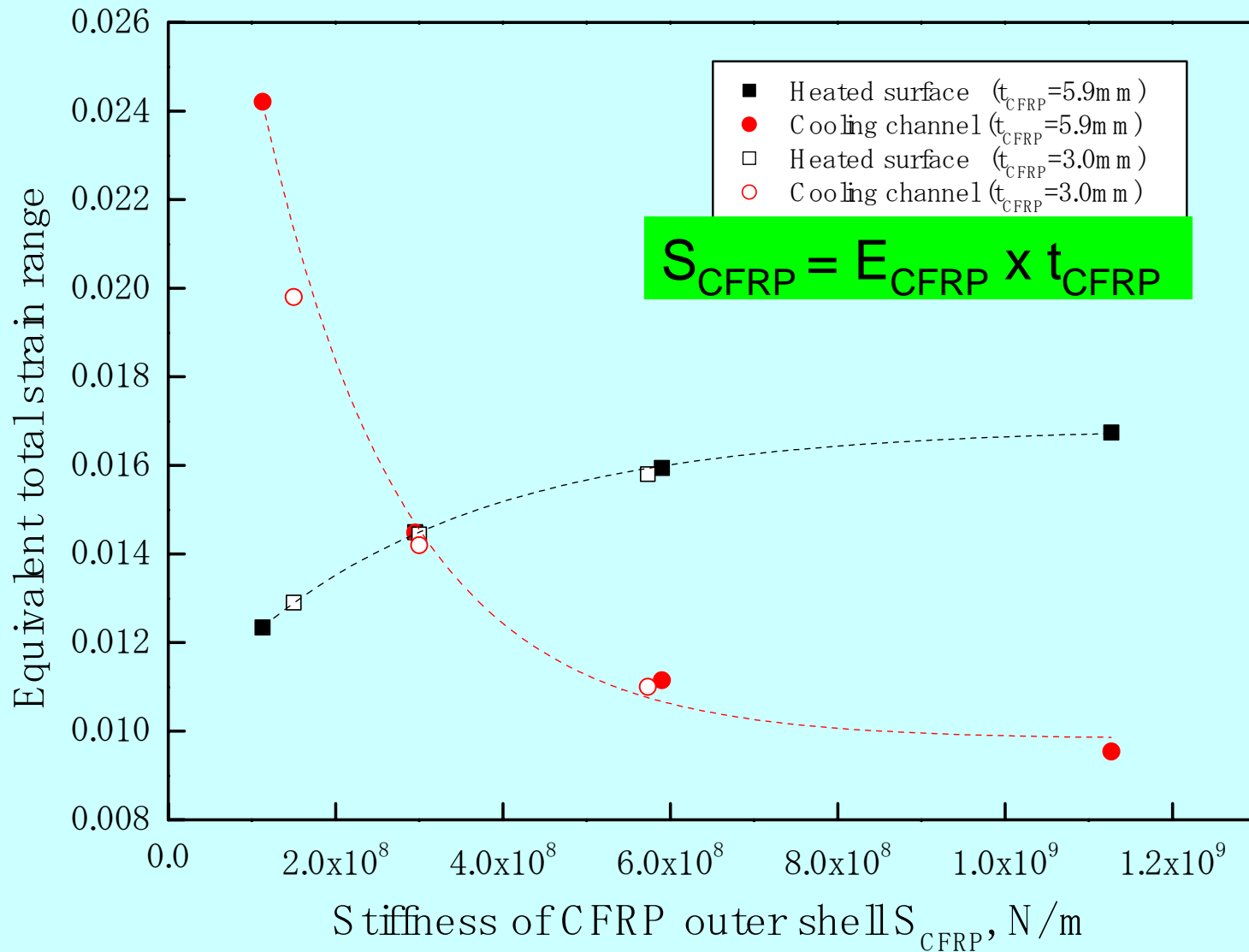


Equivalent total strain of compliant structure model

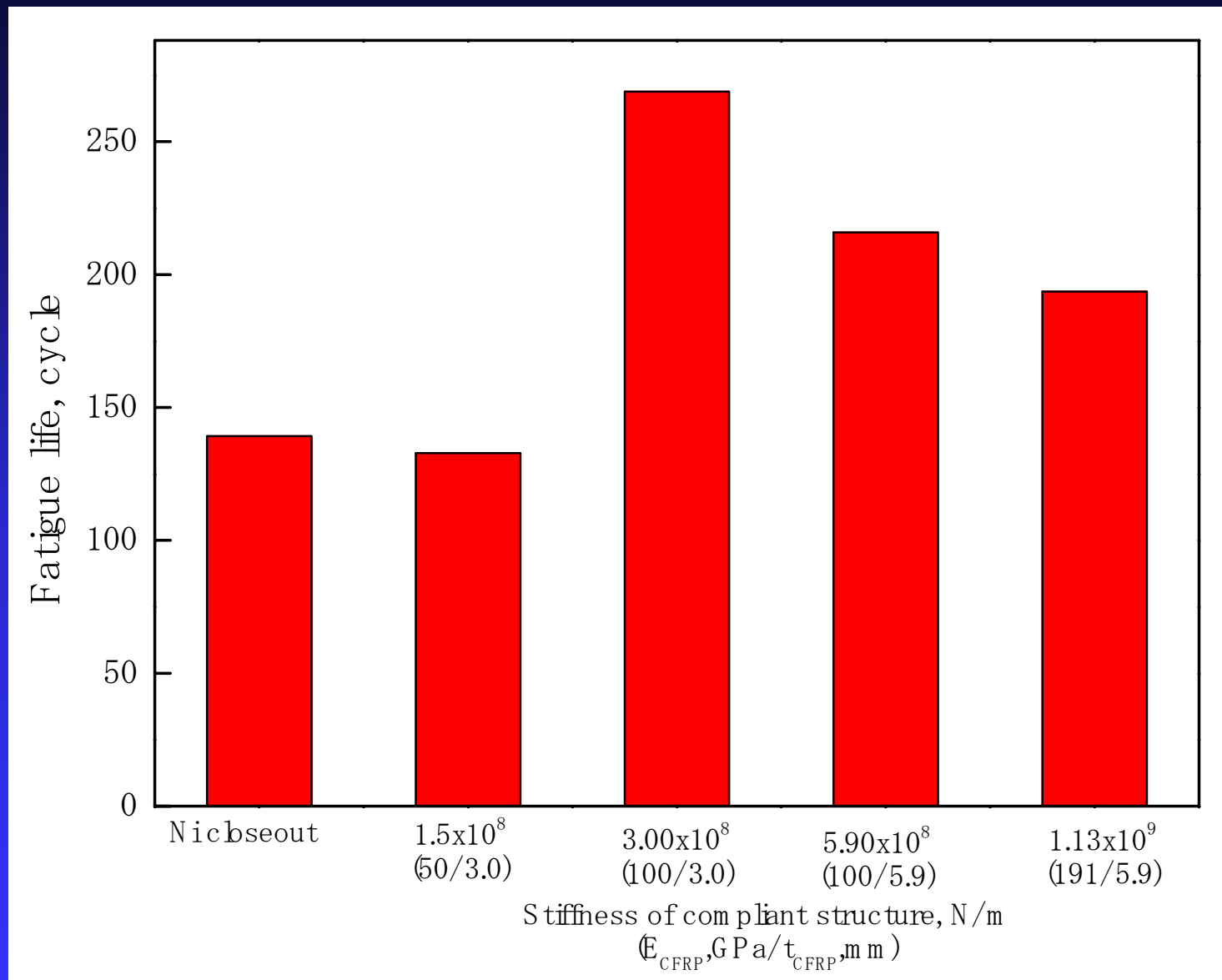


($E_{\text{comp}}=50\text{GPa}$)

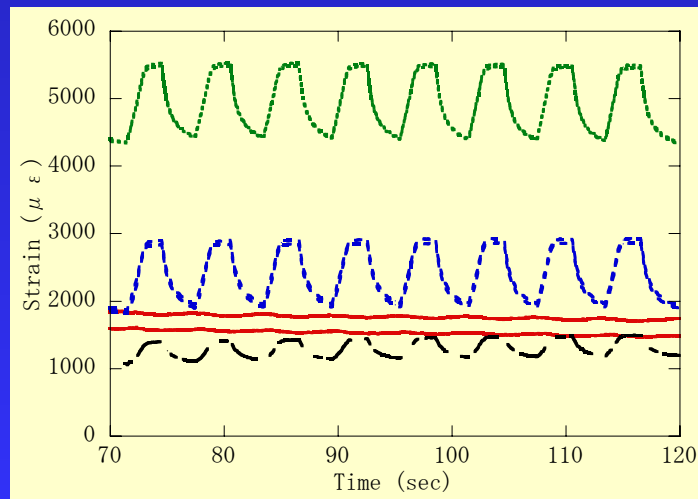
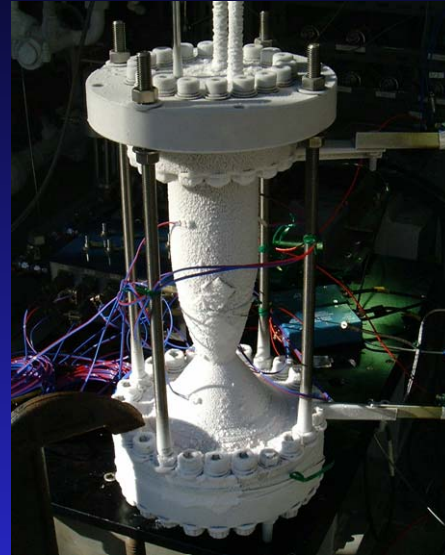
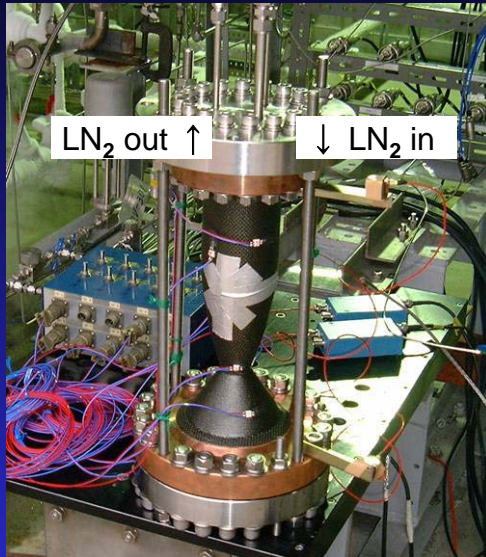
Stiffness of CFRP outer shell, S_{CFRP}



Analyzed fatigue life of each model



Fabrication & Testing of CFRP compliant structure



Pressure : 9MPa

Fluid : Liquid nitrogen

Number of cycle : 100 times

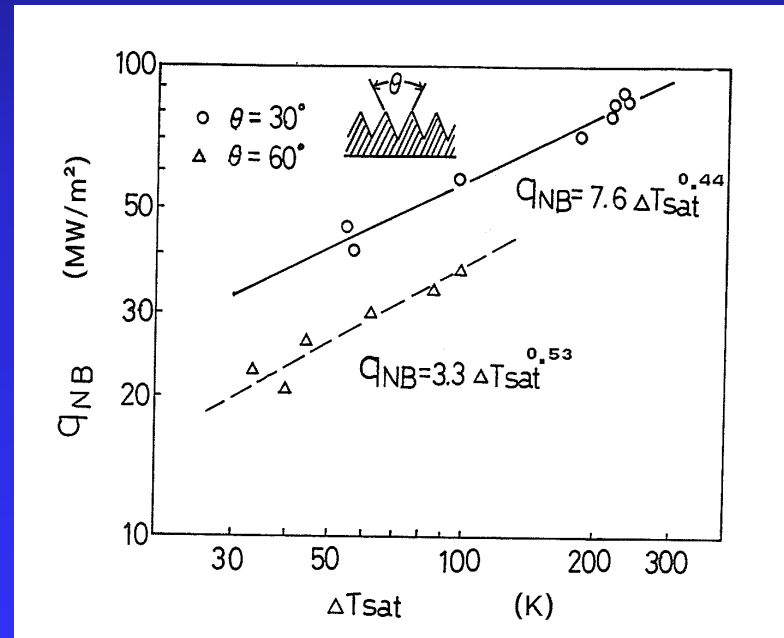
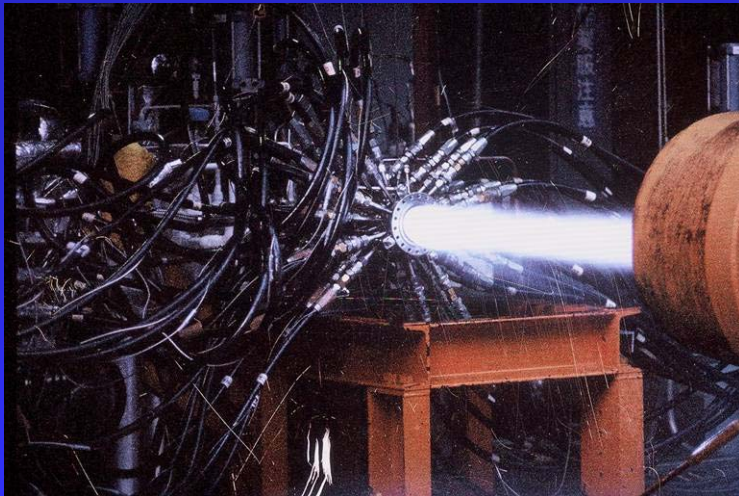
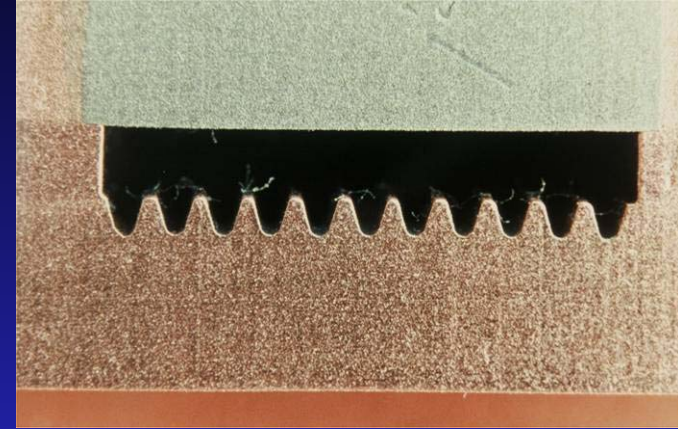
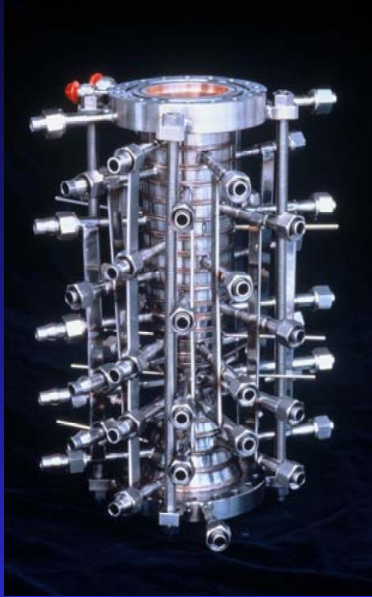
No large flaw



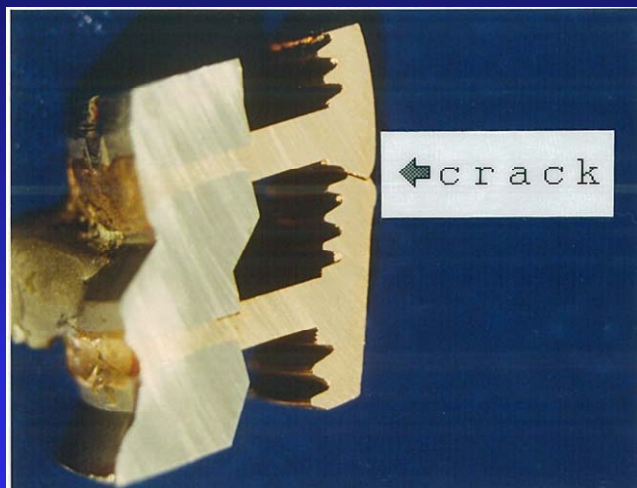
Firing tests are planned

II. Inner shell approach

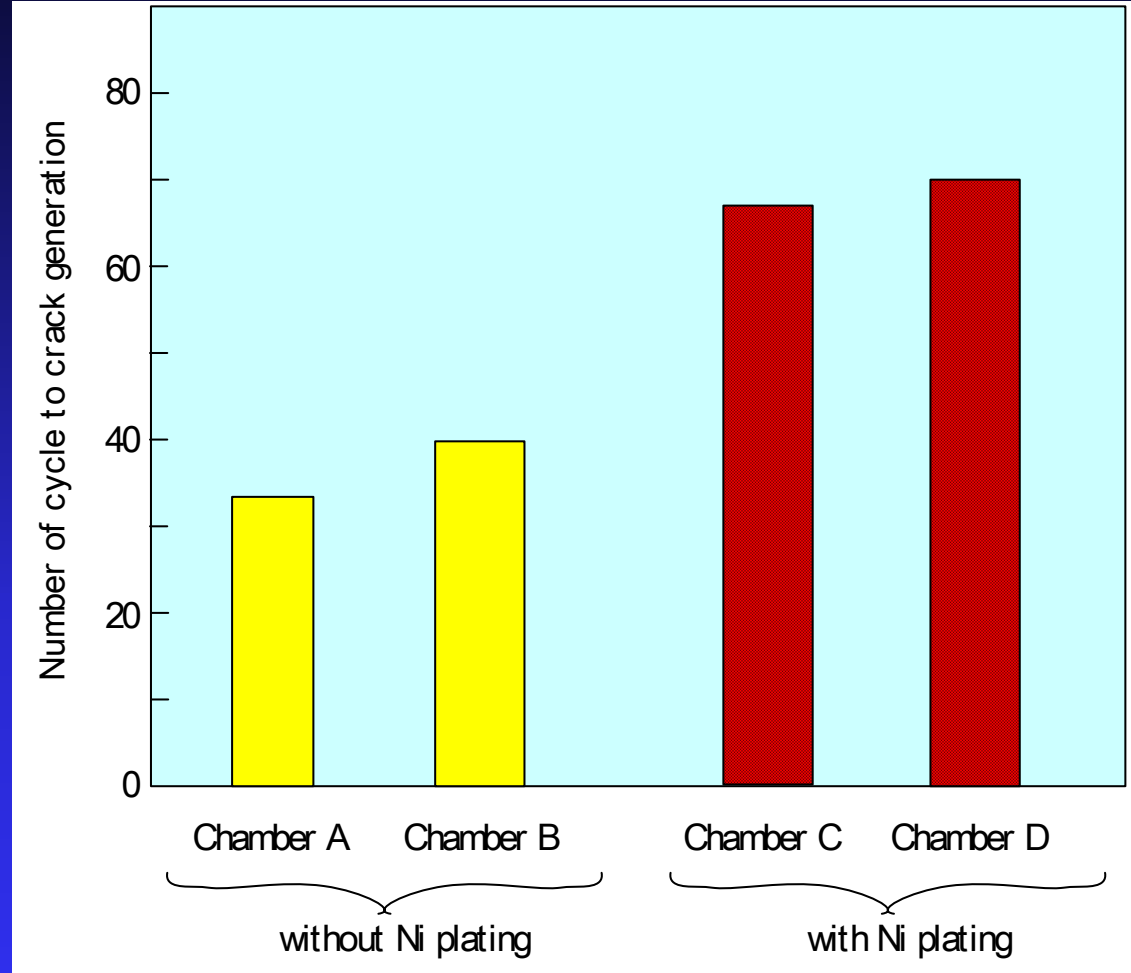
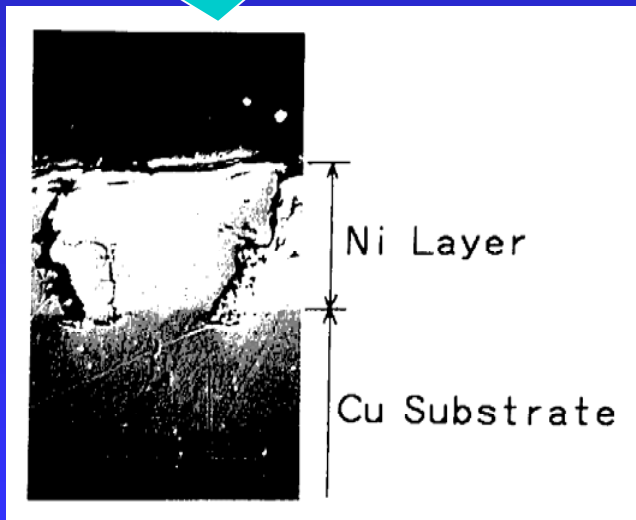
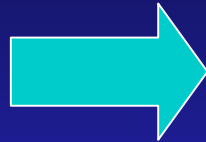
Calorimetric Combustors



Fatigue of calorimetric combustor



Life enhancement by nickel plating

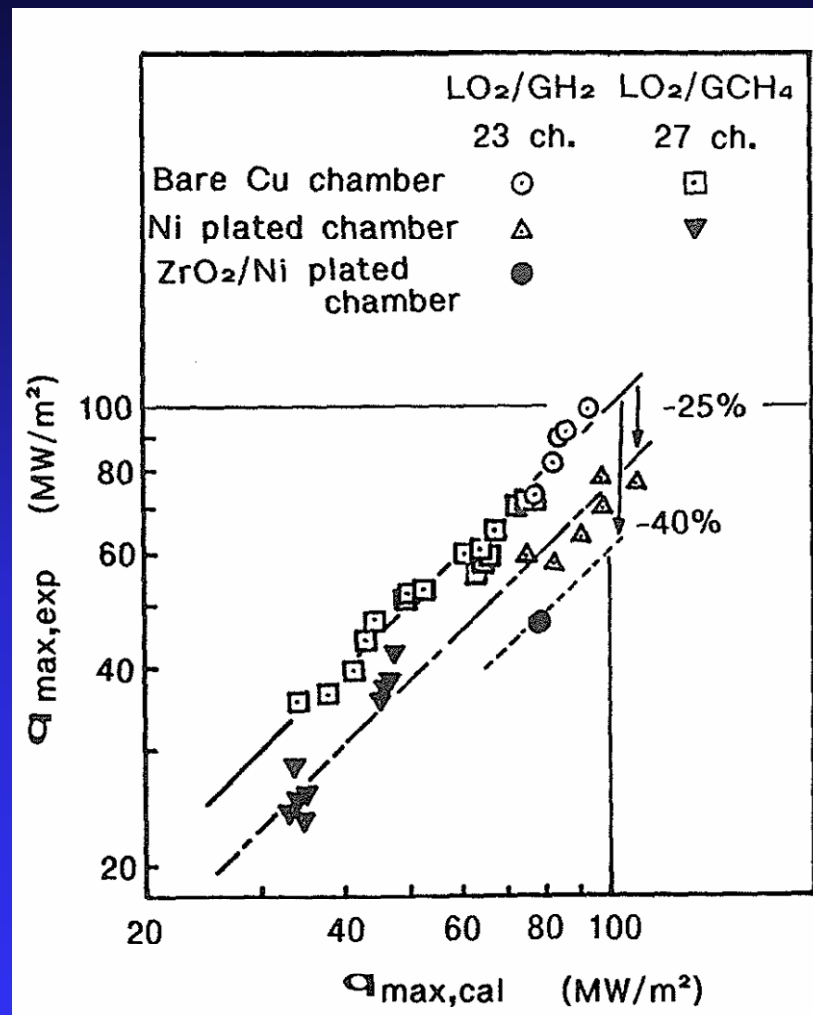
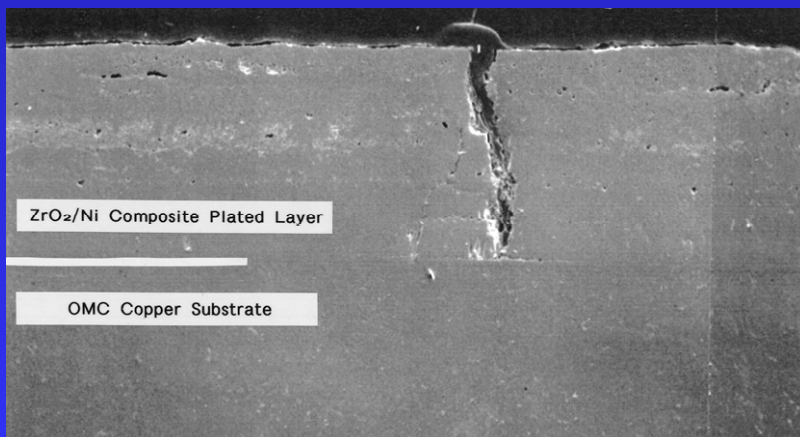


Life enhancement and heat load reduction by composite plating

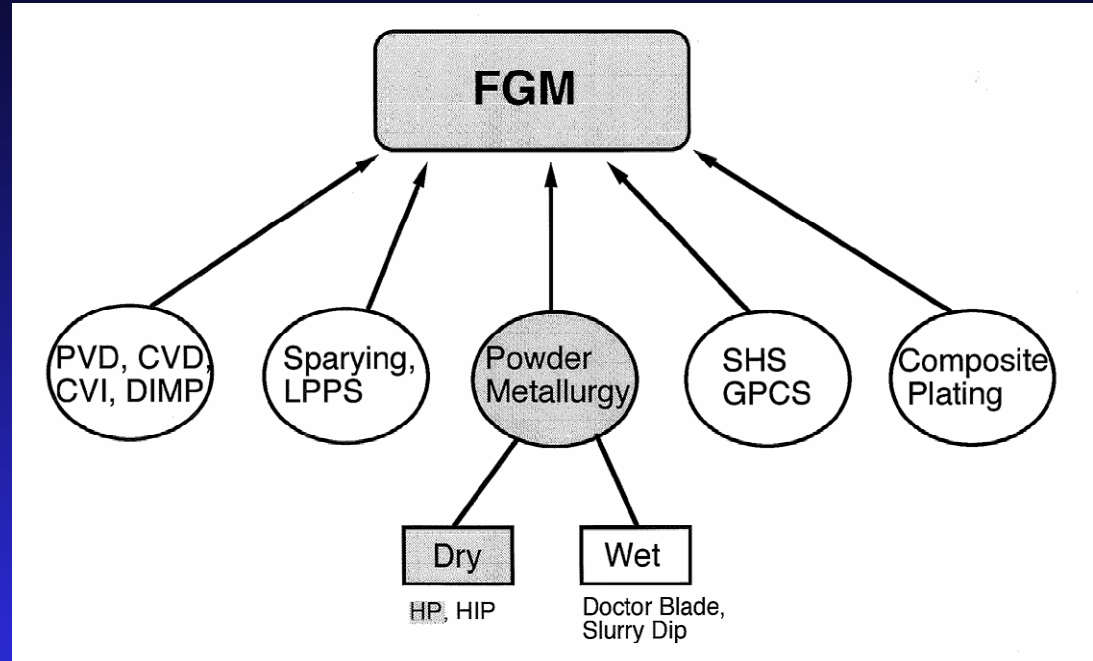
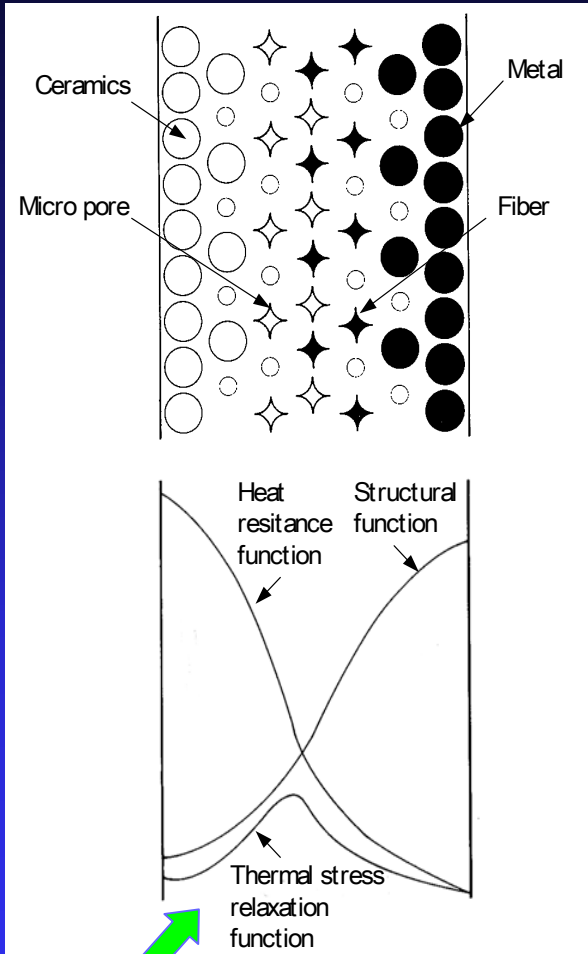


Composite plating:

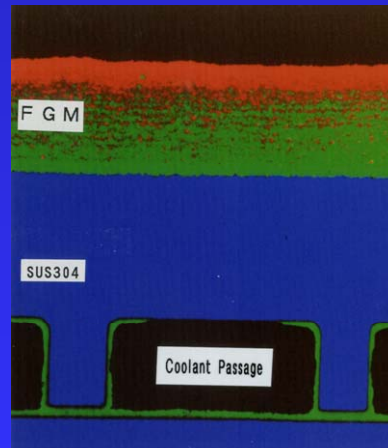
Nickel with 24.4% partially-stabilized zirconia with an average particle diameter of 5 micron meters



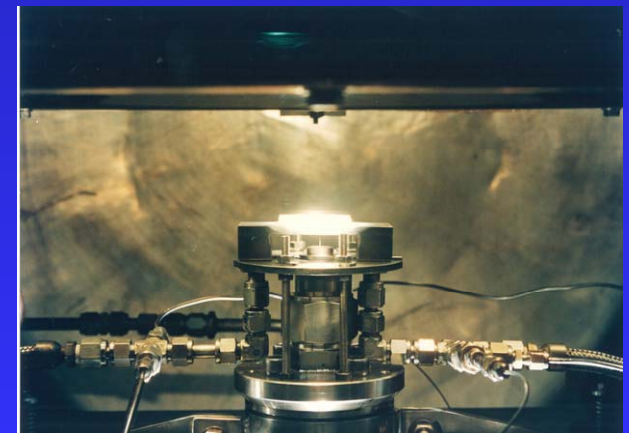
Application of Functionally Graded Materials (FGMs)



Distribution function must be designed to minimize thermal stress.



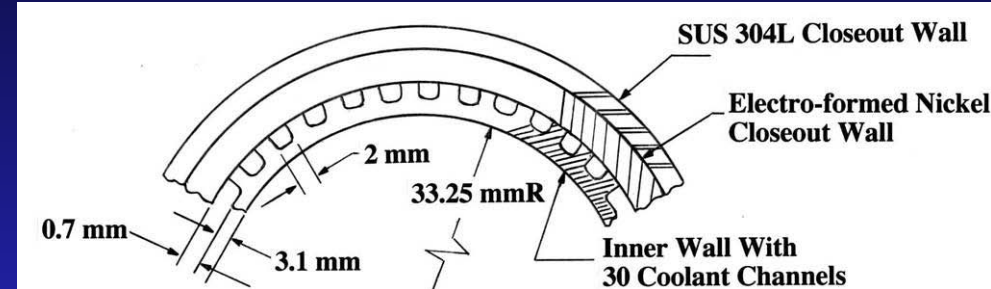
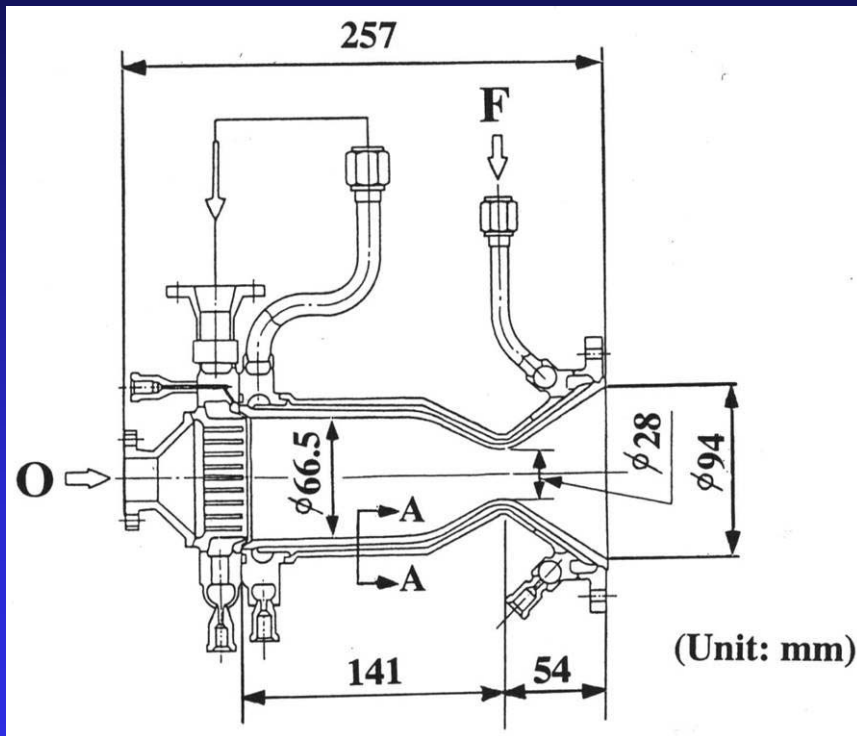
Actively cooled panel



Xe arc-lamp heating/ LH₂ cooling test

Thrust chamber with FGMs liner

SECT. A-A



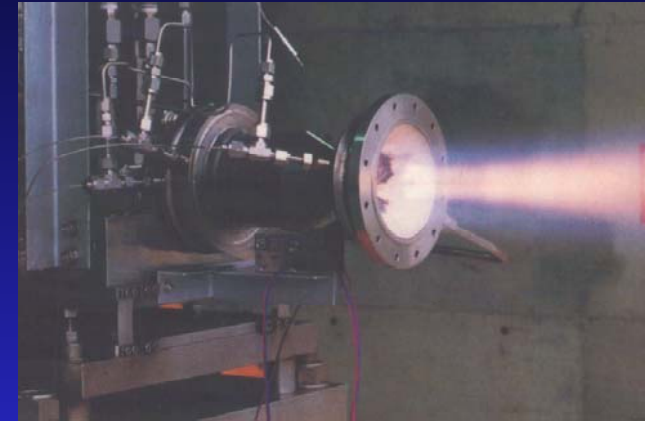
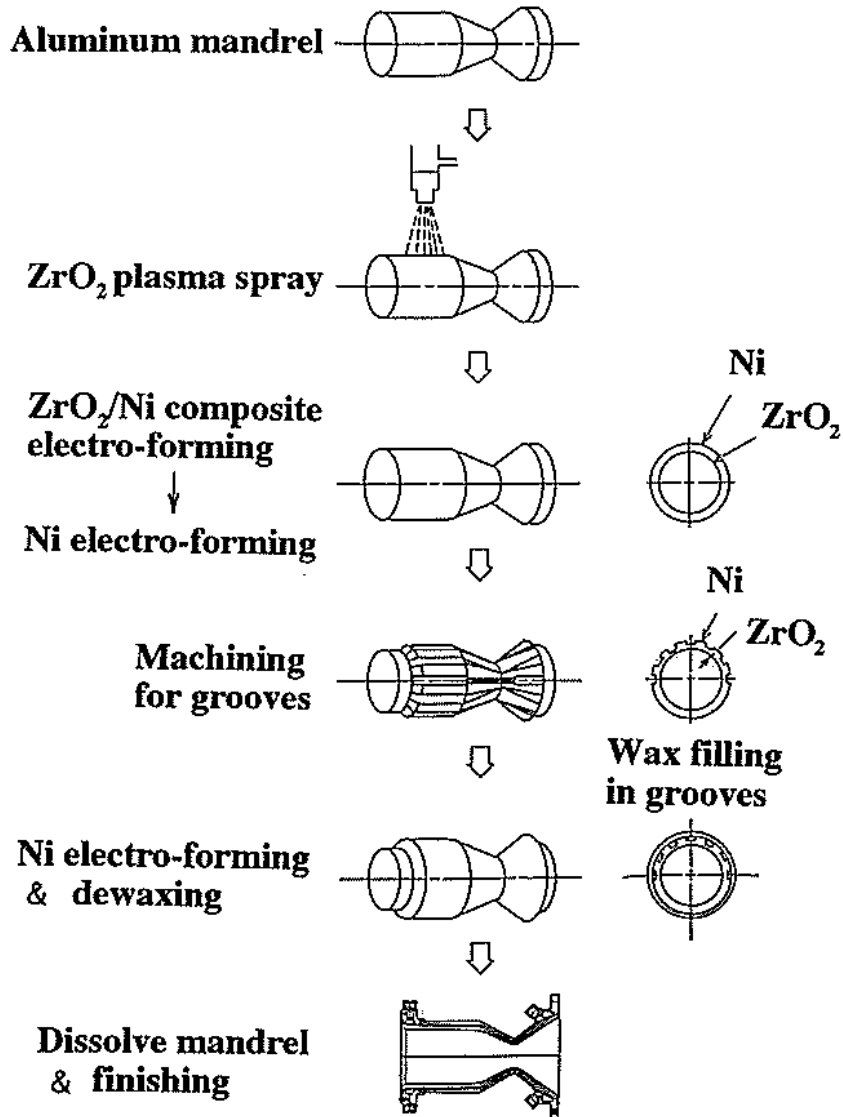
Thickness of TBC

PSZ	0.2mm
LPPS/FGM (PSZ100-25 vol.%)	0.4mm
EF/FGM (PSZ 25-0 vol.%)	2mm

LPPS: Fabricated by Low Pressure Plasma
Splay Method

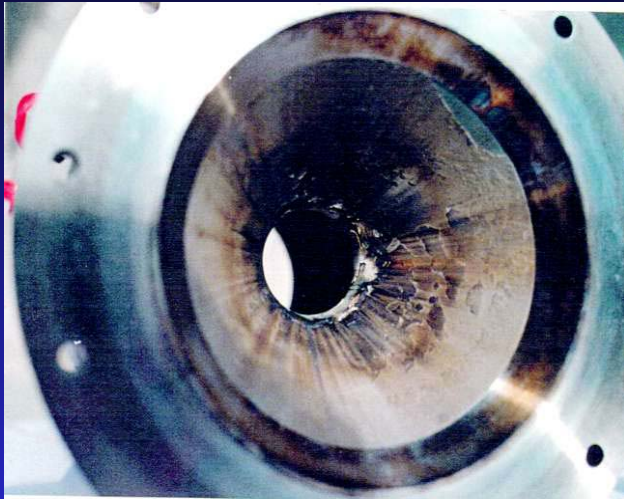
EF: Fabricated Electro Forming Method

Employed process

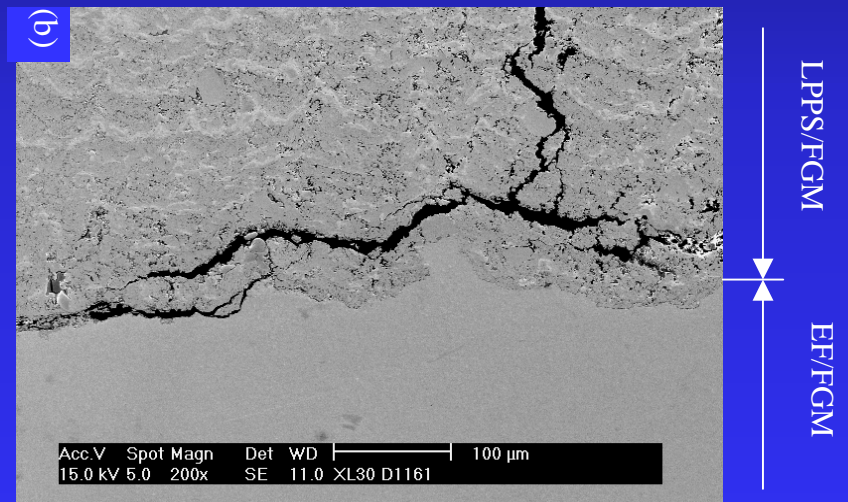
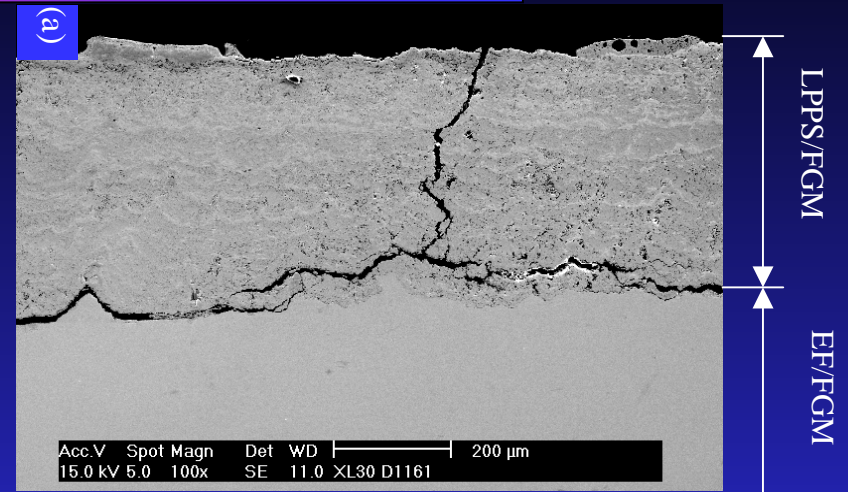


Tested condition:
 Propellants: NTO/MMH
 Chamber pressure: 1 MPa
 Throat heat flux: 9 MW/m²

Damage of FGM after combustion test

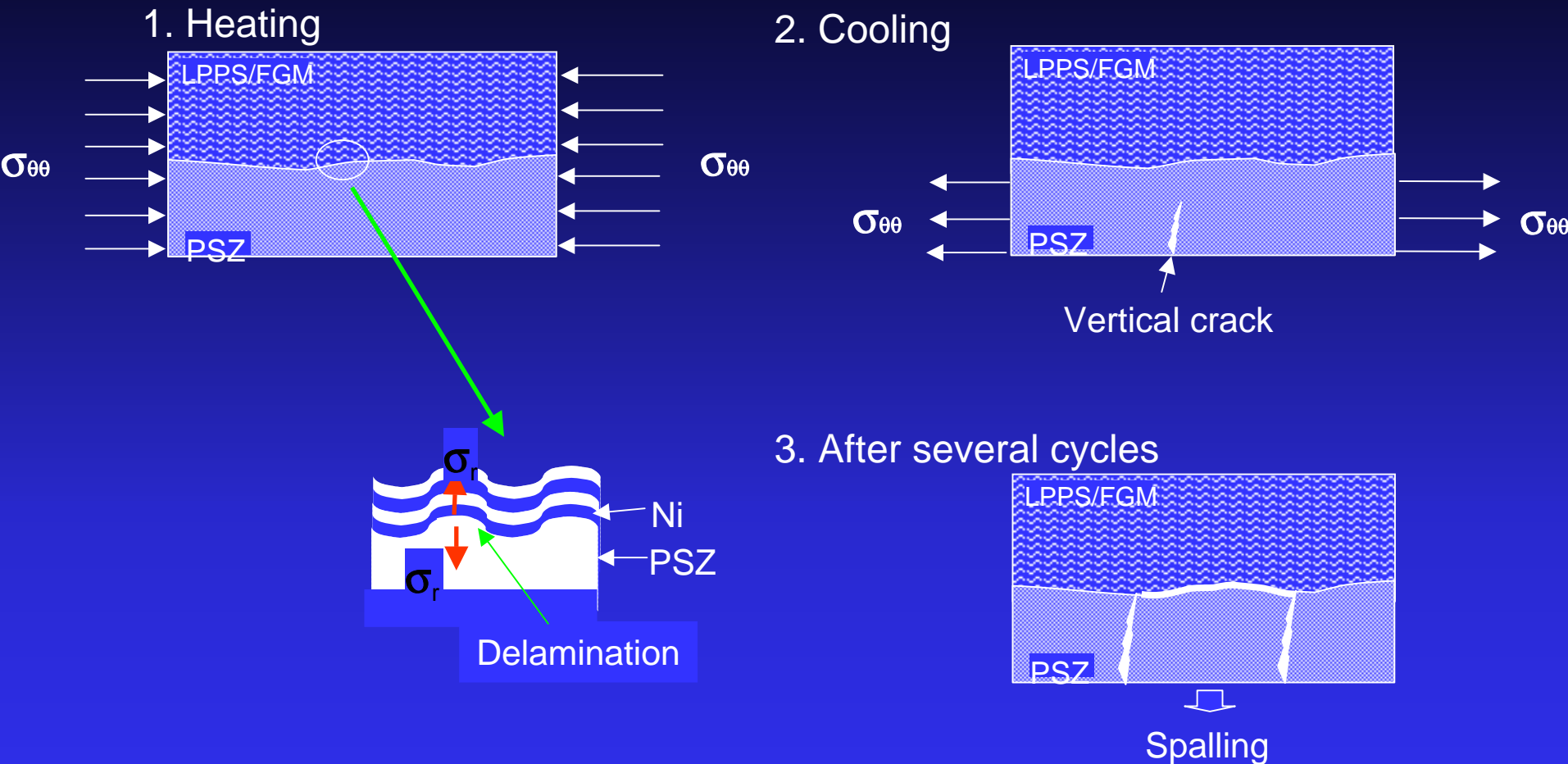


Appearance of the chamber throat after 50 firing cycles



Cross section of the throat section

Schematic illustration of the damage mechanism of the thermal barrier coating



Chamber life reached to 250 cycles after modification

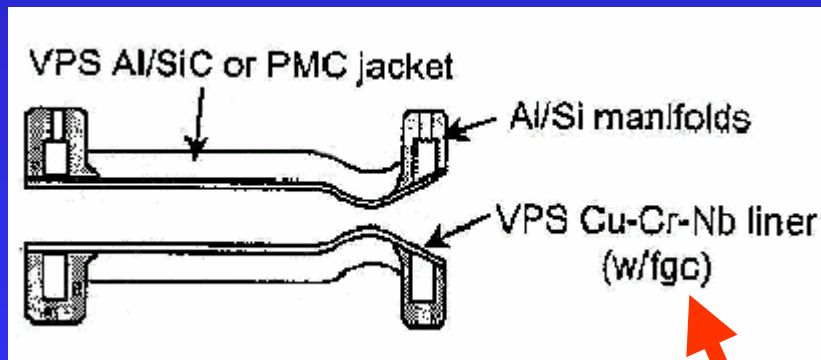
Application of FGMs in other countries



C/C-SiC FGM



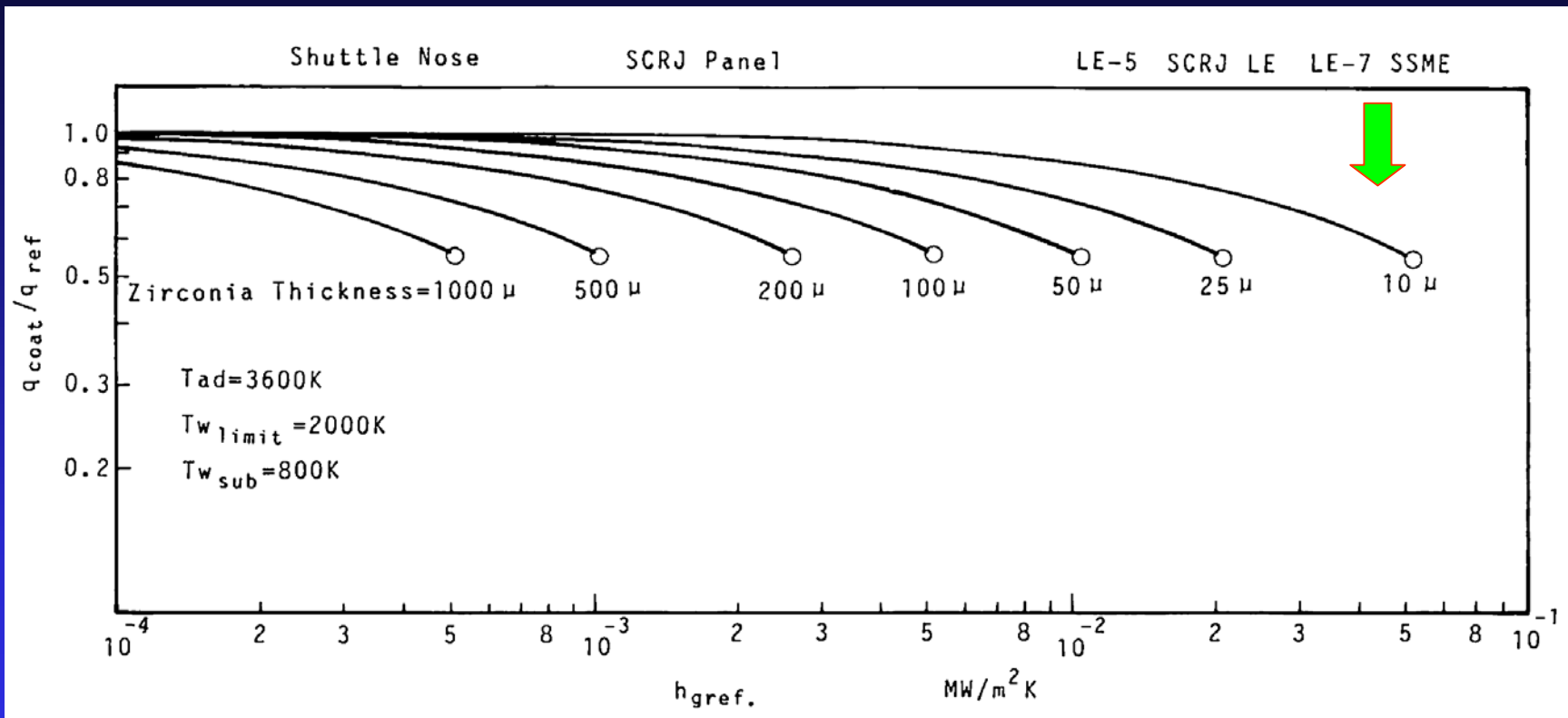
VINCI nozzle



NiCoCrAlY-Cu FGM

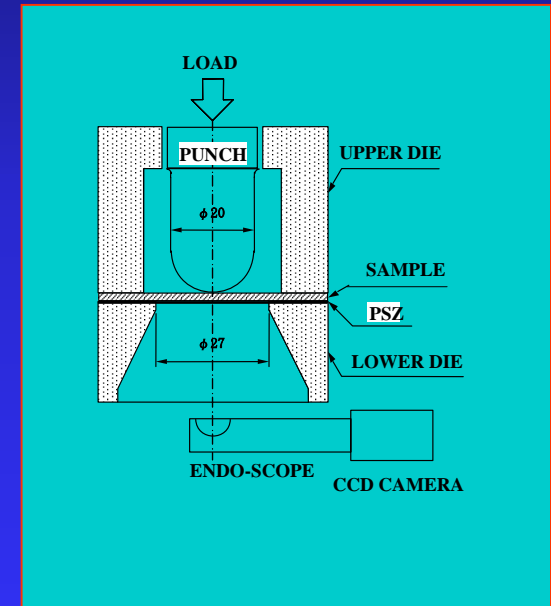
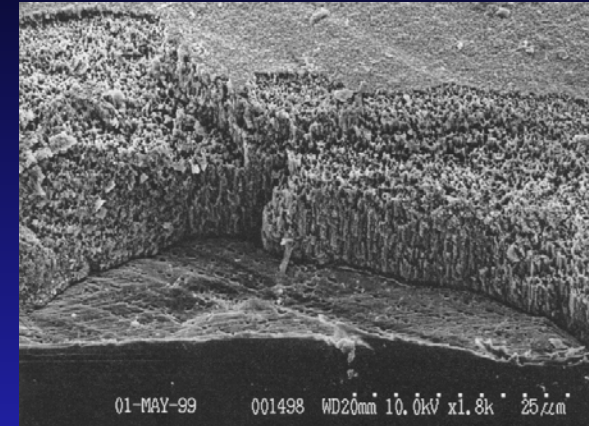
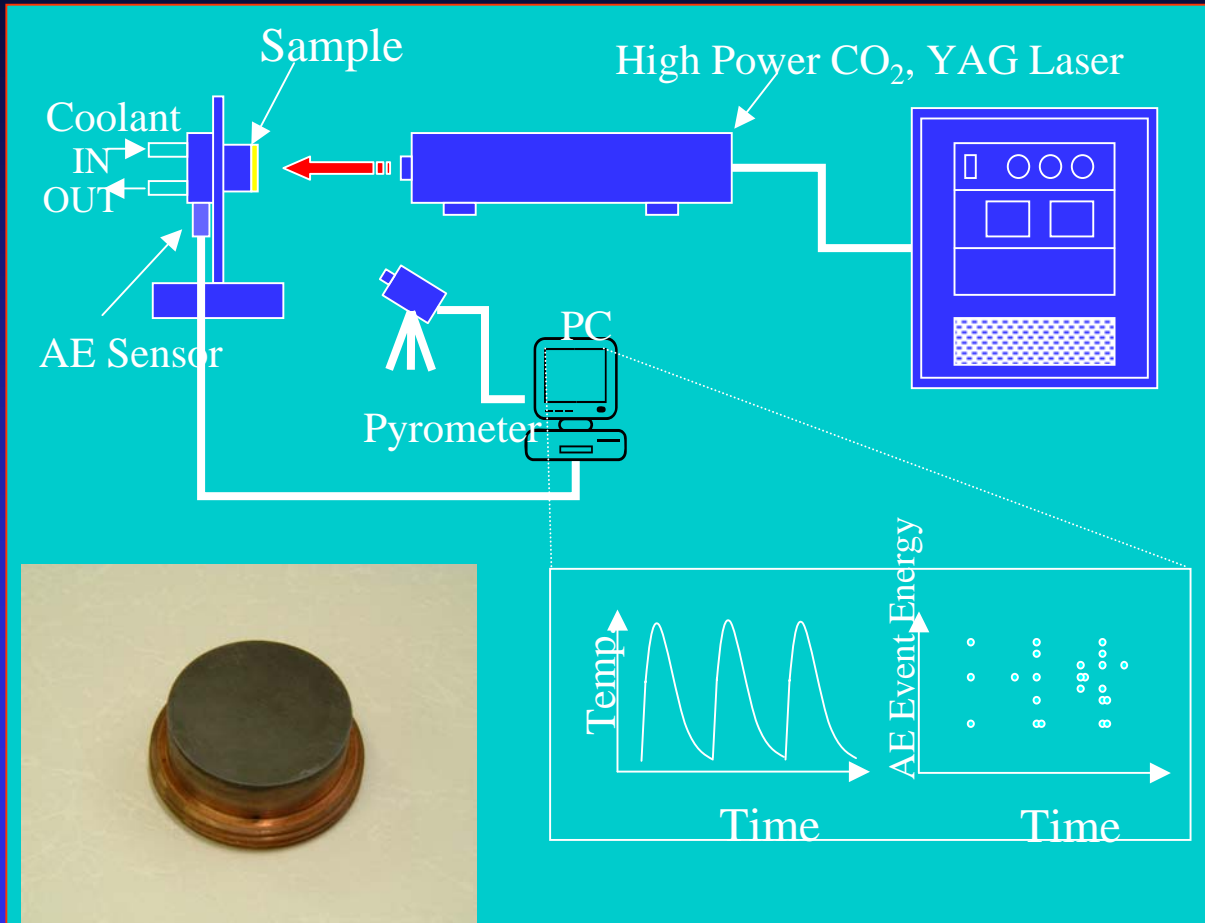


Application of the TBC to high pressure thrust chambers



Require thin coating layer

Testing of specimens prepared by EB-PVD process

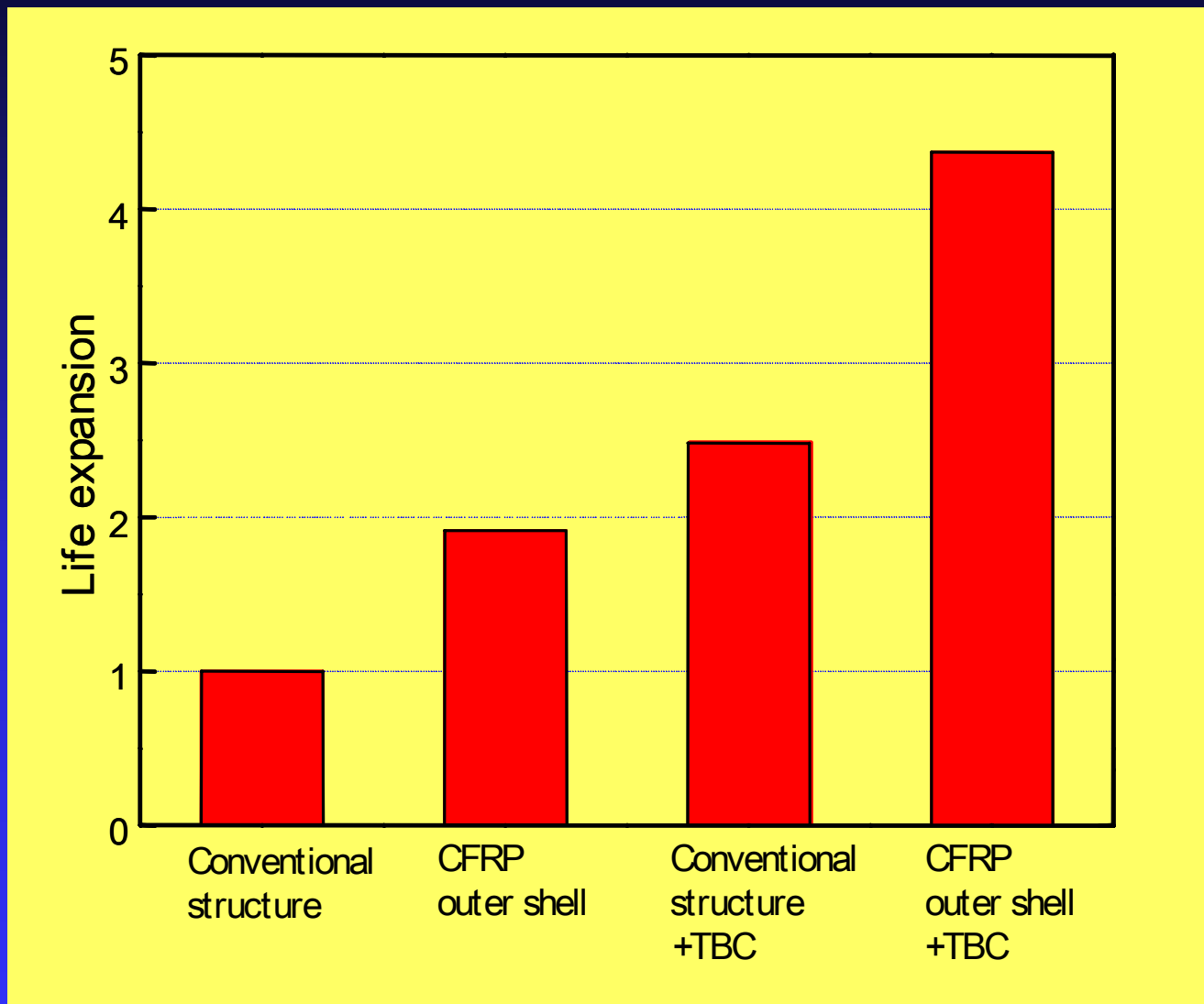


Laser thermal shock test specimen prepared by DLR

How to coat on an inner wall surface with desired thickness distribution?

Cup test for bonding strength

Life enhancement by different approach



Summary

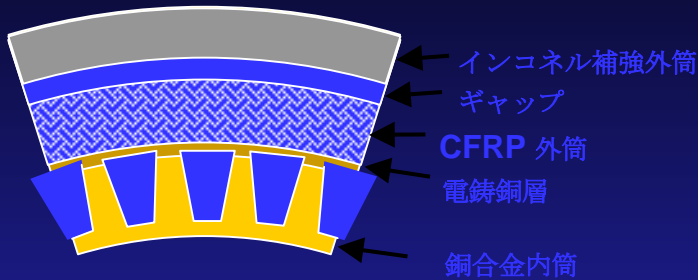


- ◆ Reusable rocket engines will be required to realize TSTO or SSTO in the future.
- ◆ Long-life combustor is one of key technologies for the reusable rocket engines.
- ◆ Outer shell structure using the CIP forming method was demonstrated successfully and CFRP compliant structure is under study for long-life chambers.
- ◆ Metal plating was easy and effective for prolonging the life of calorimetric combustors.
- ◆ FGMs was applied to extend the life of thrusters under relatively lower heating conditions.
- ◆ Reliable thin coating process should be developed for high pressure thrust chambers.

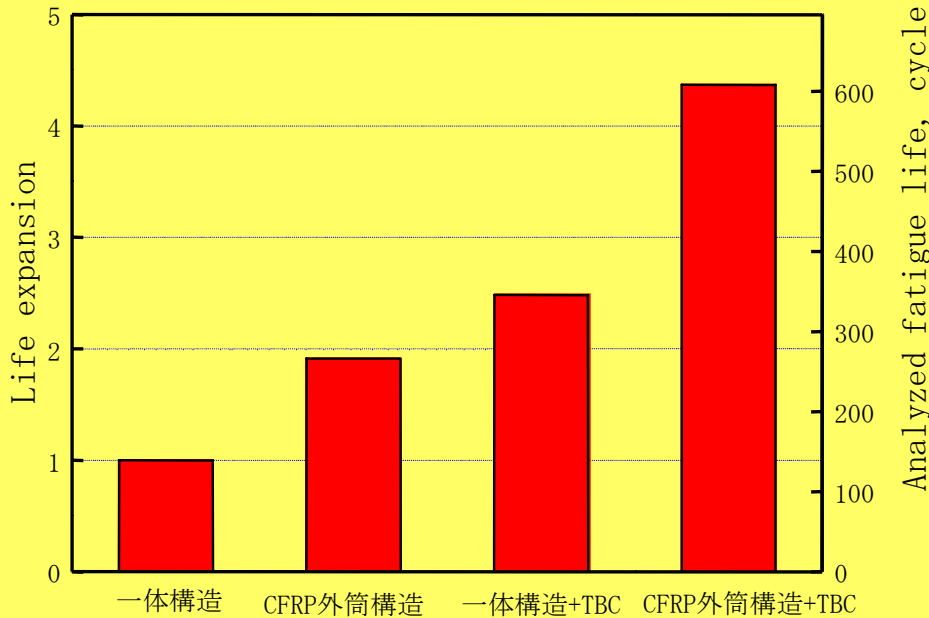


END

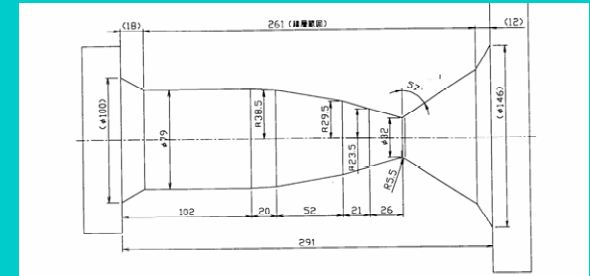
柔構造化による燃焼器の長寿命化



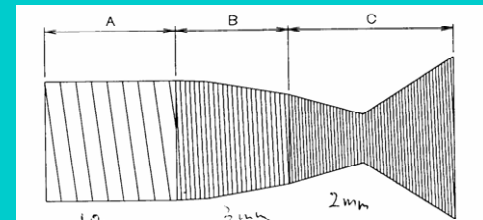
低剛性CFRP外筒



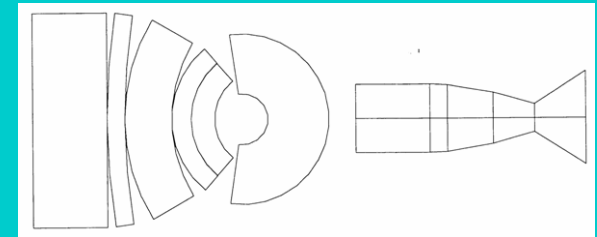
柔構造と遮熱コーティングの組み合わせによる燃焼器の長寿命化



(1) 銅製内筒



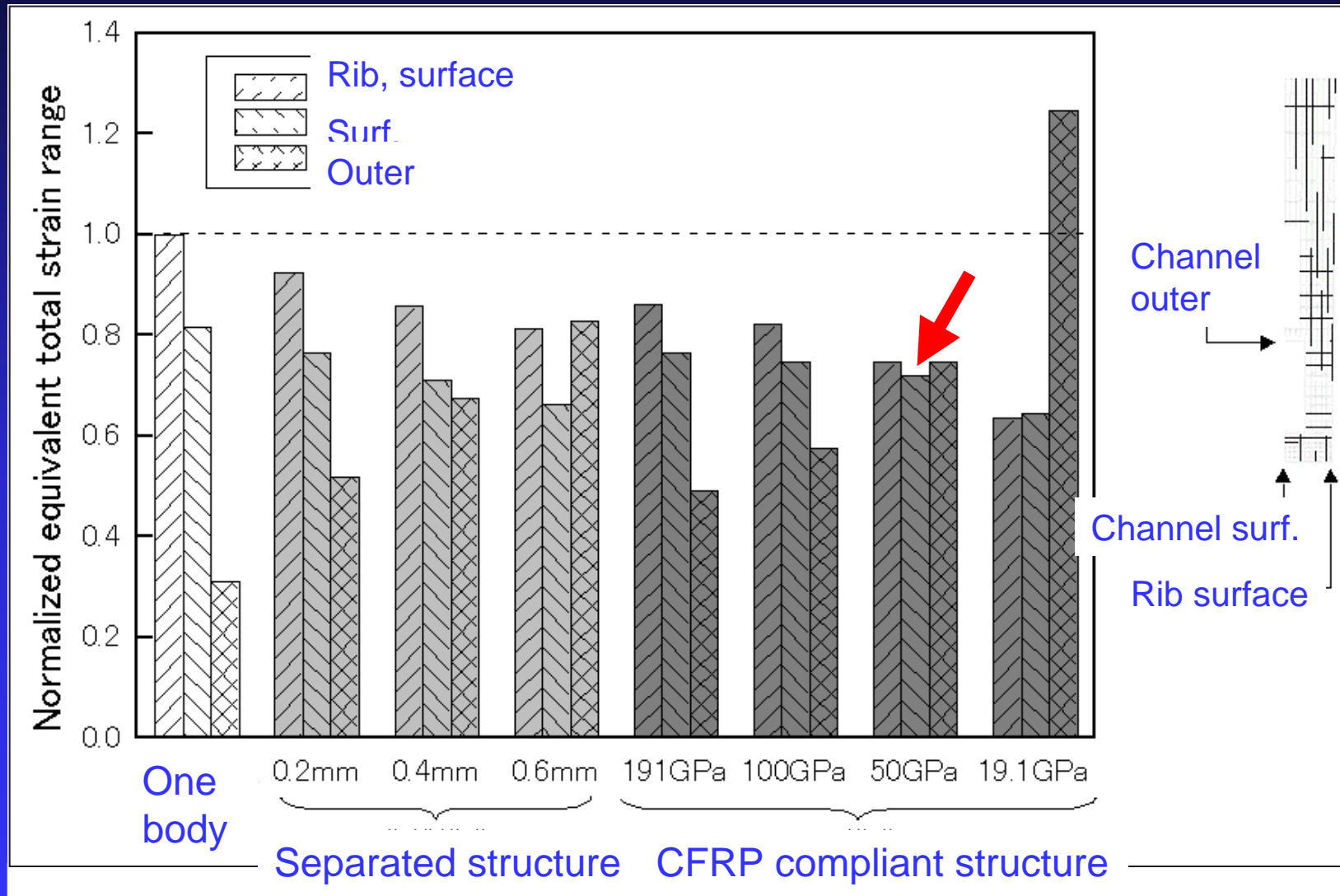
(2) CFRP一方向材層 (耐圧用, 中心層, 2-ply)



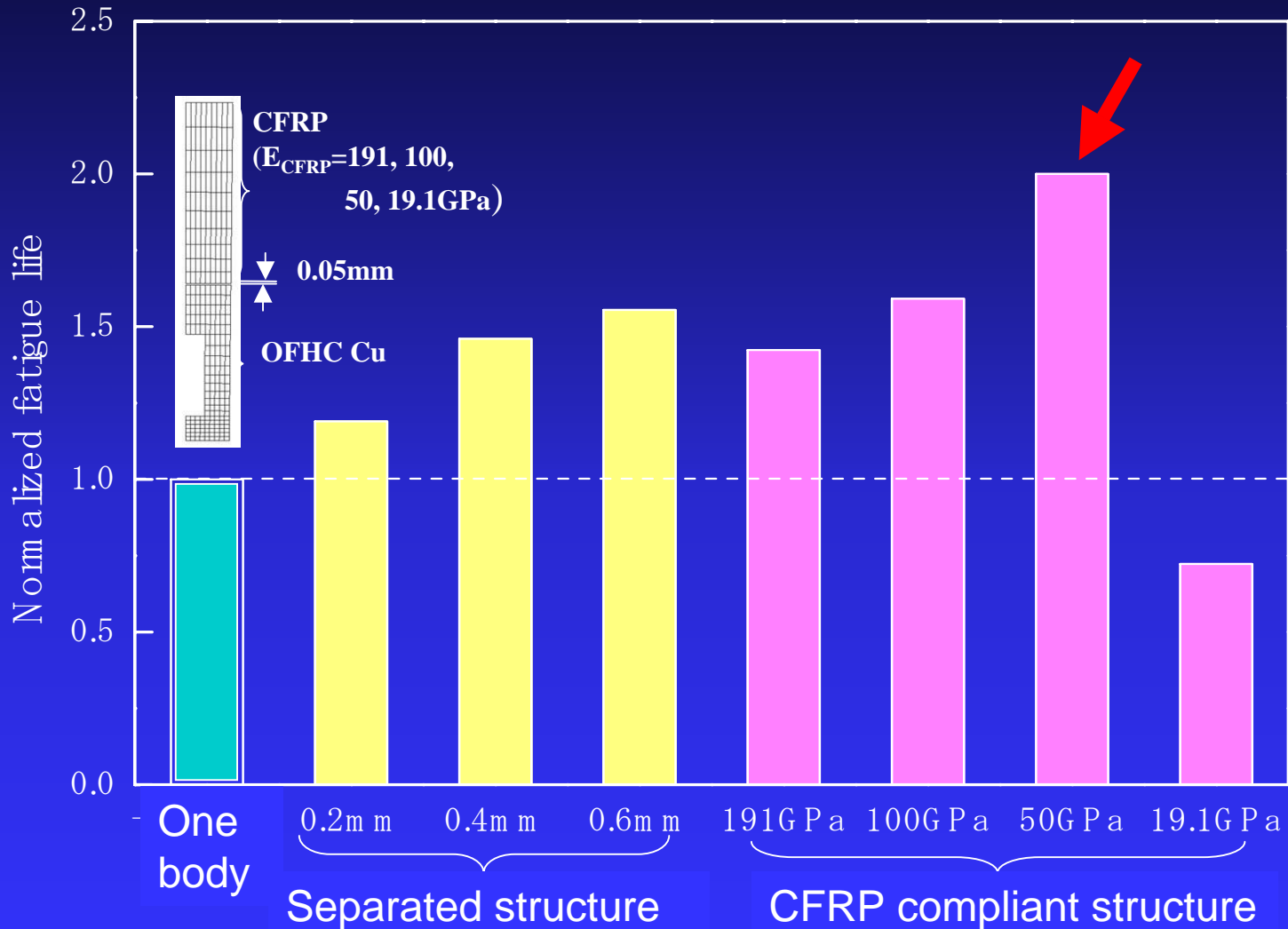
(3) 平織りクロス層 (CFRP外筒の形状保持, 最内外層, 2-ply)

CFRP外筒製作法 (特許申請済)

Total strain range of each model



Life of each model



RESEARCH ACHIEVEMENTS ON LONG-LIFE THRUST CHAMBERS AT NAL/KPL

Akinaga KUMAKAWA, Shin-ichi MORIYA and Masaki SATO
Japan Aerospace Exploration Agency, Space Propulsion Research Center

ABSTRACT

Much effort is being put into prolonging the lives of thrust chambers for future Reusable Launch Vehicles (RLVs). Two approaches were taken to extend the lives of rocket combustors. Compliant structures with a Cold Isostatic Pressing (CIP) formed layer or a (Carbon Fiber Reinforced Plastics) CFRP shell were tested. Combustors with a thermal barrier coating including plating method and functionally graded materials were tested. Test results and their subjects were discussed in this paper.

INTRODUCTION

Since its establishment in 1965, NAL/KPL (currently, Japan Aerospace Exploration Agency (JAXA), Space Propulsion Research Center) has contributed to the R&D of Japanese launch vehicles, especially with respect to propulsion. It has been involved in the R&D of rocket engines such as the LE-5 (upper stage liquid oxygen (LO₂)/liquid hydrogen (LH₂) engine) and the LE-7 (booster stage LO₂/LH₂ engine) series. These engines have been respectively used for the H-1 and H-2 launch vehicles and the technologies involved in these vehicles have reached a high level of development.

A total of five flights of the H-2A launch vehicle, successor of the H-2 launch vehicle, have been successfully conducted since September 2001. The H-2A launch vehicle employs the LE-7A engine, a modified LE-7 engine, for the first stage and the LE-5B engine, a modified LE-5A engine, for the second stage. Both engines are currently under testing to increase their reliability.

In conjunction with these activities, technologies needed for an unmanned reentry vehicle demonstrator, the HOPE-X plane, have also been developed in Japan. The precursors of the HOPE-X plane, i.e., the Orex, Hyflex and Alflex vehicles, were tested to obtain the technology necessary for reentry and automatic landing from 1994 to 1996. The HOPE-X plane project itself has unfortunately been frozen due to the current budgetary constraints.

The direction and plans for R&D of future Japanese space transportation systems have been previously proposed and rocket-powered vehicles for use in the earlier phase as the second stage of the TSTO (Two-Stage-To-Orbit) or in the later phase as the SSTO (Single-Stage-To-Orbit), are expected to be operational in the late 2010s to 2020s, though the plan is under re-discussion after the establishment of the JAXA. Research and development of this vehicle will encompass various aspects such as vehicle system, aerodynamics, structure, a thermal protection system, avionics, navigation, and a propulsion system. Weight reduction and enhancement of engine performance have been mandated as being necessary to realize operation of the vehicle.

Much effort is being put into prolonging the lives of components, reducing their weight and achieving higher performance, namely, studies to realize a higher performance extendible nozzle, a more durable thrust chamber, higher performance T/Ps, long-life bearings, lighter-weight cryogenic tanks, and so on.

The present structure of a high-pressure reusable combustion chamber, such as that

of the SSME (Space Shuttle Main Engine), consists of an inner cylinder made of a high-strength copper alloy with machined coolant channels and a nickel closeout formed by the electroforming method to contain chamber pressure. It has been pointed out that stiffness of the nickel layer constrains the expansion of the inner copper liner and consequently reduces the life of engines.

One way to prolong the lives of thrust chambers is to use a compliant structure for the outer shell to reduce the thermal stresses at the wall of coolant channels. Another way to prolong the lives of thrust chambers is to reduce high heat flux to the wall by using a thermal barrier, such as a ceramic coating, on the hot-gas-side wall. However, such a ceramic coating easily causes spalling or flaws under high temperature gradient conditions due to the mismatch of the thermal expansion between the ceramic layer and the metal substrate. The present authors previously proposed using functionally graded materials (FGMs) and plating the copper chamber wall with high temperature metal.

Research activities on long-life thrust chamber technology for RLVs required for future space transportation systems for these decades are outlined in this paper. Two approaches, namely thermal barrier coating systems including FGMs and compliant structures, which have been taken to prolong the lives of thrust chamber are introduced.

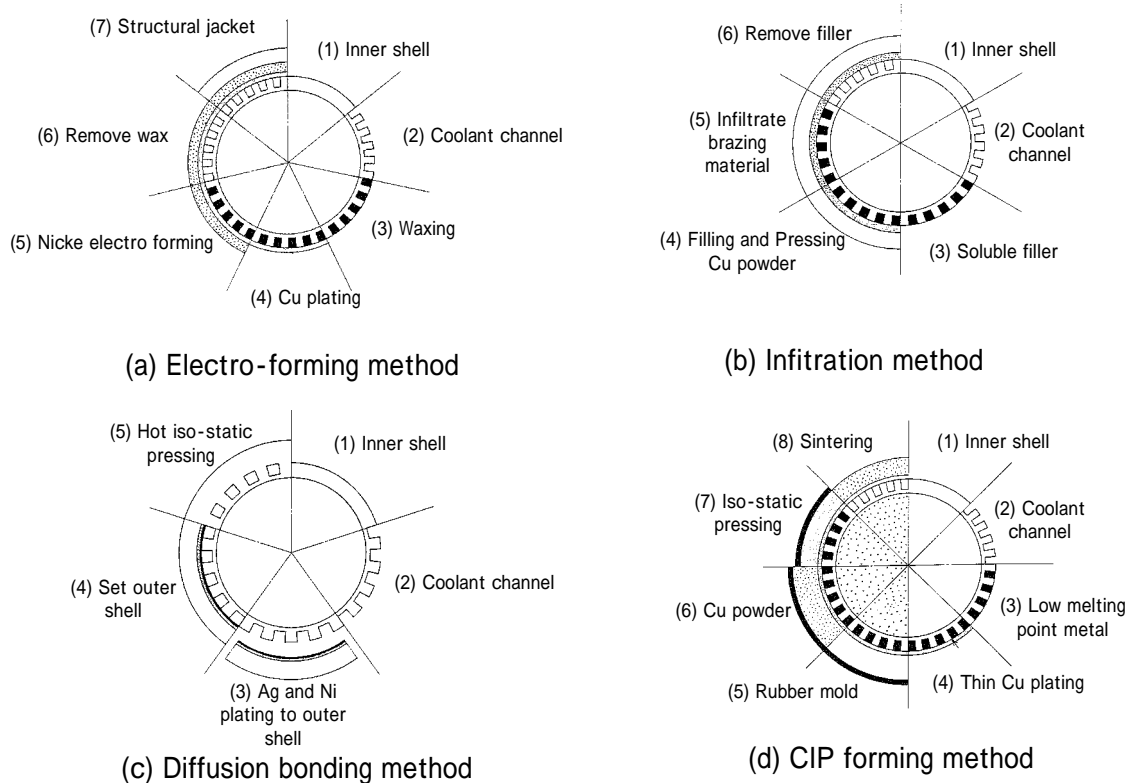


Fig. 1 Typical processes for assembling thrust chambers

COMPLIANT OUTER SHELL STRUCTURE

Background

Before the development of the LE-7 engine, several new methods to bond an outer shell to an inner shell have proposed among institutes and industries in Japan. They

were a conventional brazing method, a diffusion bonding method, an infiltration method and a CIP forming method. Figure 1 shows their typical processes and the detail can be found in Ref. 1.

CIP formed thrust chamber

The CIP forming method was proposed by NAL/KRC based on powder metallurgy. As shown in Fig. 1 (d), the copper or copper alloy liner having cooling channels is temporarily filled with a metal having a low melting point. The space between the liner and a flexible mold is evenly filled with copper powder or a mixture of copper powder and those of other metals. The powder is isostatically compacted. After cold isostatic pressing, the metal filling the cooling channel is removed. Then the compact is sintered in a hydrogen gas flow. By this method, a very compliant closeout is easily obtained, while a sufficient bonding strength is sustained between the copper liner and the closeout, and perfect sealing of the coolant hydrogen channels is achieved. Figure 2 shows a cutaway view of a CIP formed thrust chamber.

Before the firing test, the chamber was hydrostatically tested to assure structural integrity. The pressures during the hydrostatic test were 40 MPa in the coolant channels and 20 MPa in the combustion chamber. A test to confirm the durability at an extremely low temperature, due to liquid hydrogen, was also conducted at a pressure of 15 MPa. Firing tests were conducted at rocket engine test facility of NAL. Firing tests were performed at the combustion pressure of 5- 9 MPa for 28 runs and total firing time amounted to 300 seconds. After the each firing test, the inner dimensions of combustion chamber and the diameter of the throat portion were measured to investigate the deformation at the interface between the sintered layer and combustion chamber. However, the results of these measures indicated that the change incurred by the test was not significant.

Based on the success of the CIP forming methods and the good results of the firing tests, a design consisting of a copper inner cylinder, a CIP (Cold Isostatic Pressing) formed porous aluminum compliant layer, a PTFE (polytetrafluoroethylene) insulation layer, and a nickel alloy outer shell was investigated. Structural analysis of this design concept indicated a life enhancement factor, three-fold that of a conventional structure without porous aluminum and PTFE layers. However, the structure is complicated and an appropriate fabrication process must be established. On the other hand, tremendous progress has been made in carbon composite material technology. Research on the application of a carbon composite material to a low-stiffness outer shell as a compliant structure has commenced, and numerical analysis has been conducted.



Fig. 2 A cutaway view of CIP formed thrust chamber

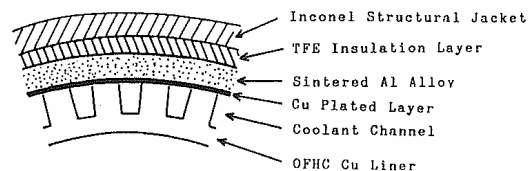


Fig. 3 An advanced concept of a CIP formed thrust chamber

CFRP compliant structure

Before fabrication of the CFRP thrust chamber, transient thermal stress analyses were performed. Nozzle throat section of the LE-7 engine class thrust chamber where the thermal load was the severest was mainly analyzed. Two combustion chamber models were analyzed: a Ni closeout model as a conventional structure and a compliant structure model with a carbon composite outer shell.

(1) Ni closeout model

Figure 4(a) shows the finite element division of the Ni closeout model. Coolant channels engraved on the inner cylinder were closed up with copper alloy, and the inner cylinder was encompassed by a Ni outer shell as the structural jacket; the inner cylinder and the outer shell were joined.

(2) Compliant structure model

The compliant structure model has an outer shell with low stiffness to decrease the restraint force so as to allow expansion of the inner cylinder. The finite element model of compliant structure is shown in Fig. 4 (b). In this study, the stiffness of the outer shell was investigated for eight combinations of elastic moduli, $E_{CFRP} = 191, 100, 50$ and 19.1 GPa, and the thickness of the outer shell, $t_{CFRP} = 3.0, 5.9$ mm, to examine its effect on the life of the combustion chamber. A candidate for the outer shell material is CFRP (Carbon Fiber Reinforced Plastics) because its elastic modulus can be adjusted by changing fibers and because carbon composite materials have lower thermal expansion coefficients compared with metals. The inner cylinder and the outer shell were separated, and the gap between them was assumed to be 0.1 mm.

Temperature and pressure varied linearly with time, and heat transfer coefficients were assumed to be constant for simplicity. Periods of start-up, steady-state operation and shut-down were $2, 300,$ and 2 seconds, respectively. In this study, low cycle fatigue life was evaluated by strain analysis without taking creep deformation into consideration.

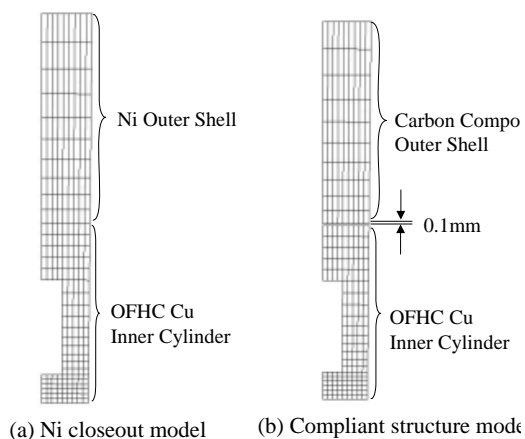


Fig. 4 Schematic diagrams of finite element model

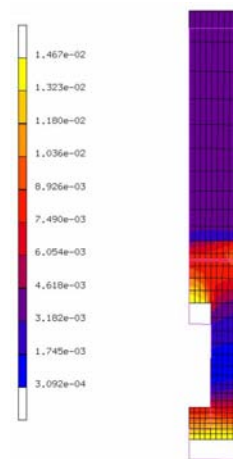


Fig. 5 Contour of equivalent total strain of compliant structure model ($E_{comp} = 50$ GPa)

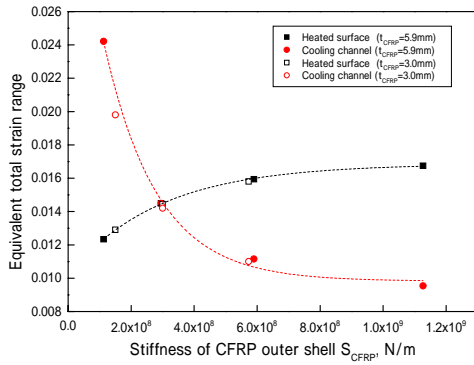


Fig. 6 Dependency of equivalent total strain range at heated surface and cooling channel upon stiffness of CFRP outer shell, S_{CFRP}

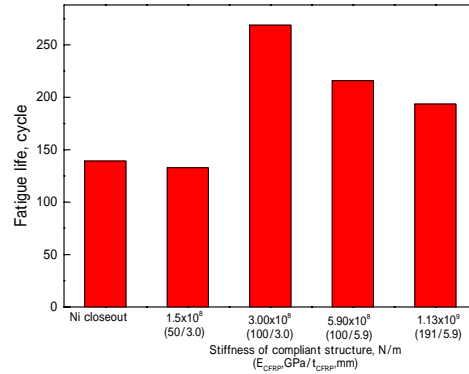


Fig. 7 Analyzed fatigue life of each model

Maximum strain was induced at the hot-gas-side wall surface in the Ni closeout model and the compliant structure model having a CFRP outer shell with a higher stiffness ($E_{CFRP} = 191, 100$ GPa). On the other hand, in the case of the low stiffness compliant structure model ($E_{CFRP} = 50, 19.1$ GPa), the maximum strain was induced at the coolant channels as shown in Fig. 5. Stiffness of the outer shell, S_{CFRP} , can be described as follows:

$$S_{CFRP} = E_{CFRP} \times t_{CFRP} \quad (1)$$

Figure 6 shows the relationship between S_{CFRP} and the equivalent total strain range at the hot-gas-side wall surface and the coolant channel. The relationship can be expressed with curves in spite of the thickness of the CFRP outer shell. As can be seen in Fig. 6, the optimum stiffness is 3.0×10^8 N/m. This stiffness corresponds to the case of $E_{CFRP}/t_{CFRP} = 100$ GPa/3.0 mm. Fatigue life estimated from the analyzed strain level utilizing the S-N curve for the OFHC copper evaluated by Esposito [13] is indicated in Fig. 7. Compliant structure when a low-stiffness outer shell ($S_{CFRP} = 3.0 \times 10^8$ N/m, $E_{CFRP}/t_{CFRP} = 100$ GPa/3.0 mm) was attached indicated a life enhancement factor two-fold that of the Ni closeout model.

Based on these results, trial fabrication and testing of CFRP low-stiffness outer shells with compliant and lightweight structures have commenced. Material tests of CFRP composites at cryogenic temperature and cyclic pressure tests of the outer shell of the CFRP with liquid nitrogen have been conducted as shown in Fig. 8. Firing tests of a thrust chamber with a CFRP compliant structure are planned as well as that of the CIP formed chamber.

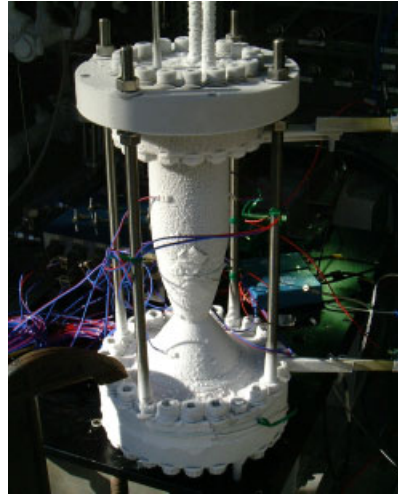
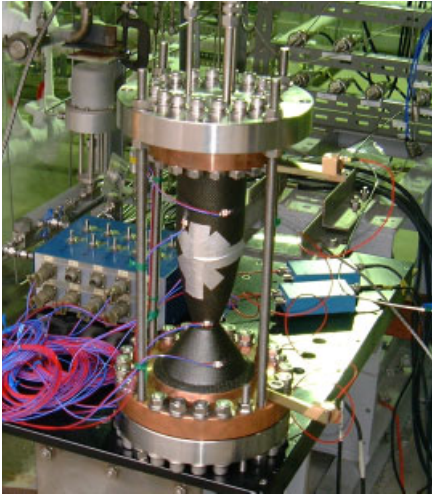


Fig. 8 Cyclic hydrostatic pressure test of CFRP thrust chamber model with liquid nitrogen

THERMAL BARRIER COATINGS

Regards with thermal barrier coatings, we have took several approaches. One is to use metal plating for prolonging the lives of water calorimetric chambers as workhorses. Nickel plating and composite plating have been employed for them until now.

Nickel plating²⁾

Copper, which is a conventional inner shell material, has a relatively lower melting point. However, there are many higher melting point metals like a nickel and they have higher thermal resistances. Therefore, best way to employ their merit is to plate them on the copper inner shell. AS the first trial, nickel was selected due to its easiness for plating.

The cooling channels were machined into an OFHC copper shell and nickel was then plated on the inside wall of the shell as shown in Fig. 9. The thickness of the nickel layer was determined to be between from 0.05 to 0.2 mm in the first trial. The thickness of the nickel layer depended on the plating conditions and it was difficult to get uniform thickness distribution along the axis of the chamber because of the complicated nozzle configuration. Nickel plated chambers were used for many firing tests as workhorse.

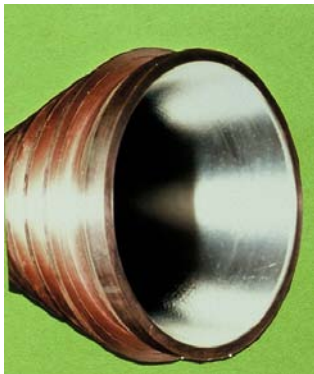


Fig. 9 Nickel plated inner shell

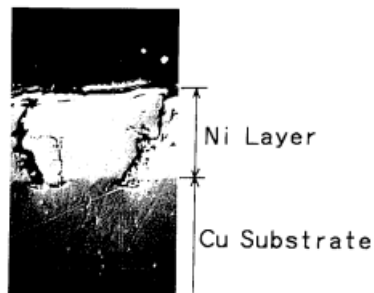


Fig. 10 An SEM photo of nickel plated layer after firing tests

After many firing tests of chamber pressures of 7 to 9 MPa, no visible flaws or spalling were observed on the nickel plated surface walls of either chamber. Figure 10 shows an SEM (Scanning Electron Microscope) photograph of the wall around the nozzle throat section after firing tests. Large vertical or inclined cracks were cyclically observed around the throat section as shown in Fig. 10, while there were not any cracks near the injector end and nozzle end. These cracks seem to have been caused by compression stress due to the high temperature difference in the axial direction. Fine cracks were also detected around these macro-cracks in the throat section. The interfaces between the copper substrate and the nickel layer were tightly bonded, except around the large cracks. It is thought that these sub-critical, macro- and micro-cracks were caused by thermal stress during the start-up of the first combustion test and that they relaxed thermal stress due to the mismatch of thermal expansion of both metals in the following tests, thus preventing crack propagation. The tightly bonded interfaces, except around the large cracks, are thought to have prevented spalling of the nickel layer.

Figure 11 shows photos of cracked nozzle throat section of water cooled thrust chamber without nickel plating after many cycles. Figure 12 shows a comparison the lives of water cooled thrust chambers with and without nickel plating. The lives of chambers with nickel plating were almost 1.6 times longer than those of chambers without such plating.

Composite Plating

Based on previous results, nickel with 24.4% partially-stabilized zirconia with an average particle diameter of 5 micron meters was plated on the inside the chamber wall in order to achieve higher thermal resistance. Though a flaw was observed near the throat section in one firing test, heat flux distribution revealed lower values, especially near nozzle throat section, than those without plating as shown in Fig. 13. As some blisters which were the source of the delamination and spalling were observed on the surface, it was concluded that the plating process had a problem and should be improved.



Fig. 11 Photos of cracked nozzle throat section of a water cooled thrust chamber

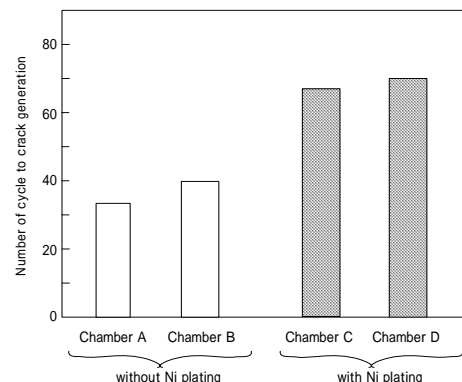


Fig. 12 Comparison of lives of water cooled thrust chambers with and without nickel plating

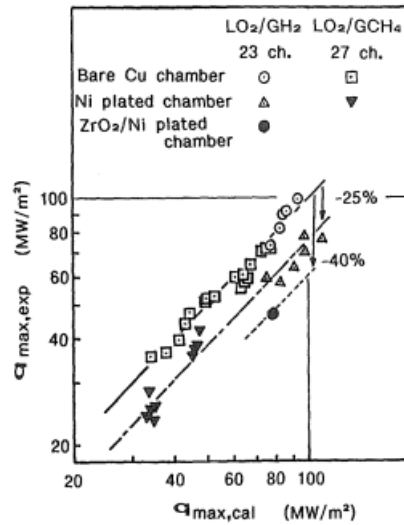
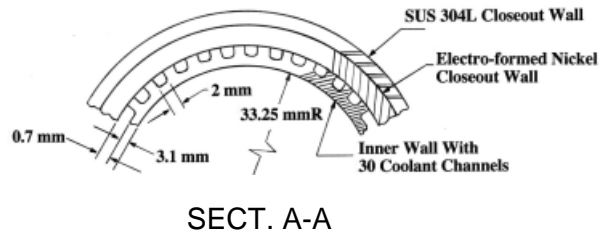
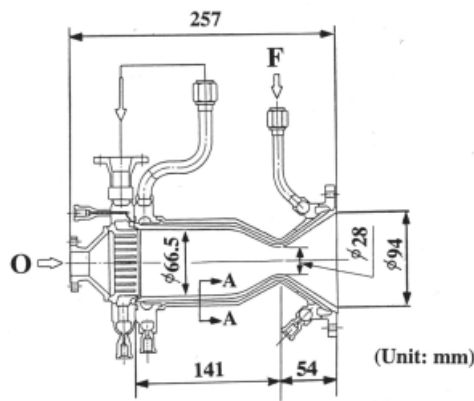


Fig. 13 Heat flux comparison around nozzle throat section

Application of FGMs³⁾

Combustors of the orbital maneuvering system (OMS) employed ZrO₂-Ni FGM, were studied in the HOPE-X program for its durability at a chamber pressure of 1 MPa. In a traditional combustion system, excess heating of the Ni-side surface was prevented by a film coolant, but under this arrangement a certain amount of unburned fuel was lost, inevitably reducing engine performance. Moreover, Ni does not have sufficient heat resistance to realize the required durability. FGMs were employed to solve this problem. Fig. 14 depicts a crosssection of the combustor. The wall of the combustion chamber, with compositional grading from Ni to 25% ZrO₂, was manufactured by composite electroplating, and low-pressure plasma spraying was employed for the part from the 25% ZrO₂ to the 100% ZrO₂. This combustion chamber was finally able to withstand up to 250 cycles of durability testing. Figure 15 shows the cross-sectional appearance of the nozzle throat section of a combustor which was damaged after 50 testing cycles. In addition to a large longitudinal crack, delamination is evident around the joined interface. Figure 16 depicts the mechanism of development of the delamination. Stress analysis indicated that the delamination was influenced by the roughness of the interface, as depicted in Fig. 16. That is, intense compressive stress arose during heating, producing a radial tensile force on the convex face of the ZrO₂ side which caused delamination; during cooling the longitudinal cracking developed as a result of circumferential tensile force on the ZrO₂ side. Thus, cracking was propagated by cyclic heating and cooling, and delamination ultimately occurred. Thanks to a series of combustion tests and improvement measures adopted on the basis of the test results, enhanced engine performance and greater durability were achieved by employment of FGM combustor wall material, significantly reducing the film coolant injection.



Thickness of TBC	
PSZ	0.2mm
LPPS/FGM (PSZ100-25 vol.%)	0.4mm
EF/FGM (PSZ 25-0 vol.%)	2mm

LPPS: Low Pressure Plasma Spray Method
EF: Electro Forming Method

Fig. 14 A combustor with FGM

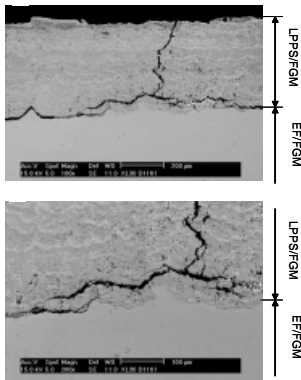


Fig.15 A cross section of nozzle throat section after firing tests

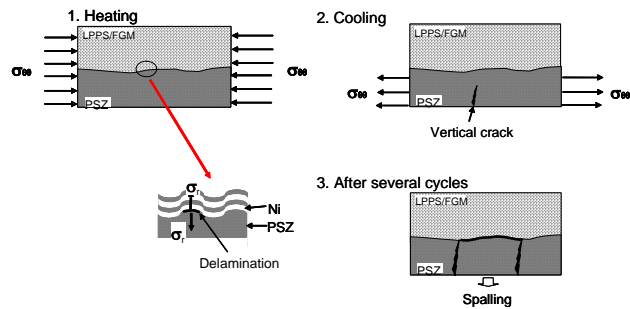


Fig. 16 Damage mechanism of TBC

Application of the TBC to high pressure thrust chambers

From the previous results of plated combustors and ZrO₂-Ni FGM combustors tests, it was pointed out that interface roughness between a coating and a substrate, or a defect in a coating has a significant effect on the durability of a coating. Therefore, the coating process is quite important and should satisfy the following three requirements: (1) a coating layer should be deposited on a smooth surface, (2) adhesion between a coating and a substrate must be strong, and (3) a coating should be highly resistive to thermal shock.

Based on these conclusions, the EB-PVD method is being studied as a coating process at this moment. Because the thickness required for high pressure thrust chambers is quite thin, the EB-PVD method is thought to be approximate for such a thin coating process.

As the first step, PSZ coating layers are deposited on disk-shaped OFHC copper samples. Figure 17 shows an SEM photo of a PSZ coating fabricated experimentally.

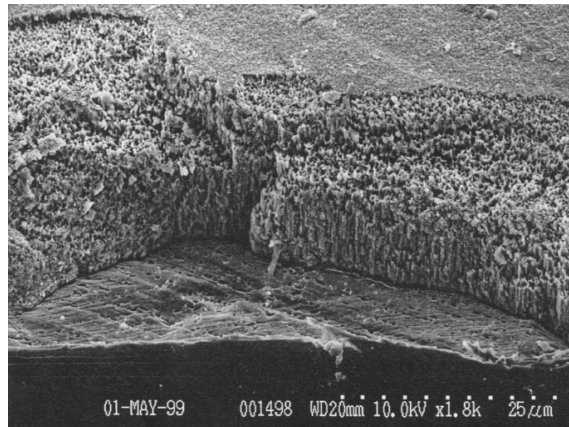


Fig. 17 SEM picture of PSZ coating fabricated on copper substrate

The columnar structure of the PSZ, considered to be effective in reducing thermal stress, can be observed. A thermal shock test utilizing a high power laser to simulate the extremely high heat flux ($> 100 \text{ MW/m}^2$) of the high-pressure combustion chamber is underway, and investigation of a fabrication method to form TBC on the inner wall of a combustor has been commenced.

CONCLUSION

Much effort is being put into prolonging the lives of thrust chambers for future Reusable Launch Vehicles (RLVs).

Compliant structures with a Cold Isostatic Pressing (CIP) formed layer or a (Carbon Fiber Reinforced Plastics) CFRP shell were tested. A combustor with a CIP formed structure was tested under a combustion pressure of 7 to 9 MPa. It revealed a good result and its structure with isolated pores in the CIP formed layer gave a hint for compliant outer shell. Based on this results and analysis of CFRP compliant structure, material tests of CFRP composites at cryogenic temperature and cyclic pressure tests of the outer shell of the CFRP with liquid nitrogen have been conducted. 8. Firing tests of a thrust chamber with a CFRP compliant structure are planned as well as that of the CIP formed chamber.

Combustors with a thermal barrier coating including plating method and functionally graded materials were tested. The effects of nickel plating method to life extension and heat load reduction are about 1.6 times and 80% of those of conventional combustors without the plated layer. The process of the composite plating method should be optimized for obtaining good bonding strength. It was demonstrated that FGMs are effective for prolonging lives of low pressure thrust chambers. New method, which can coat the inside the inner shell with desired thickness distribution, should be developed for high pressure thrust chambers. EB-PVD method might be a candidate of such a method.

References

- 1) M. Nino *et al.*, "Fabrication method of thrust chambers by CIP forming method," NAL TR-858, 1985.
- 2) A. Kumakawa, *et al.*, "Characteristics of heat transfer to nickel plated chamber walls of high pressure rocket combustors," NAL TR-1126T, 1991.
- 3) Y. Kuroda, *et al.*, "Durability test of OMS subscale engine", NAL TR-1294, 1996.



LOX Kerosene Oxygen-Rich Staged Combustion Rocket Engine

5th International Symposium on LSP

LOX Kerosene Oxygen-Rich Staged Combustion Rocket Engine Design and Life Issues

The 28th of October, 2003

The 5th International Symposium
on
Liquid Space Propulsion

Feliks Chelkis
NPO Energomash



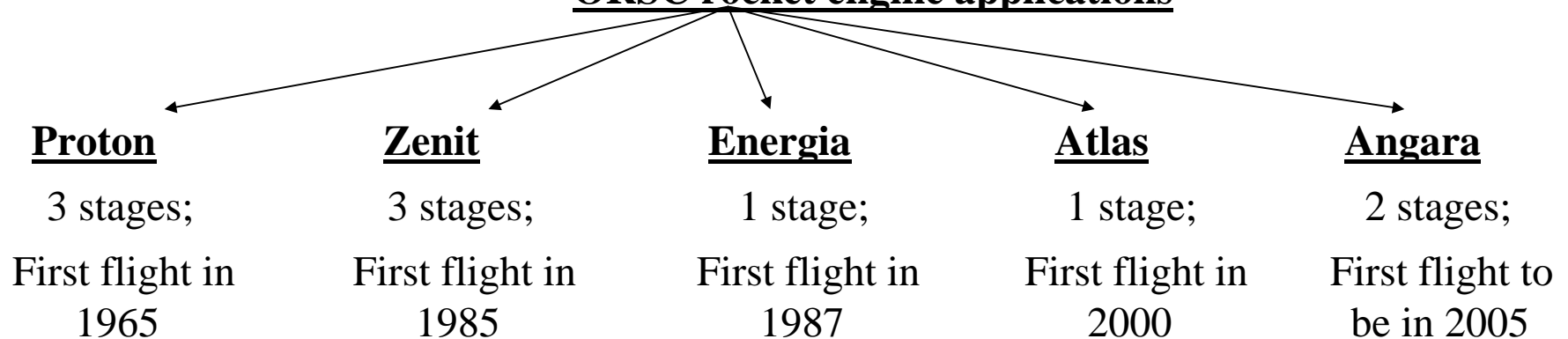
LOX Kerosene Oxygen-Rich Staged Combustion Rocket Engine

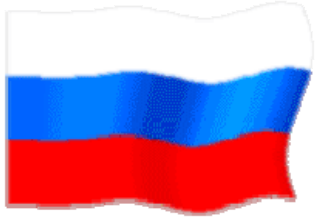
ORSC is a Russian Acronym

40 years of experience

- Designing
- Research & Development
- Manufacturing & Delivery
- Flights

ORSC rocket engine applications





LOX Kerosene Oxygen-Rich Staged Combustion Rocket Engine

Most Prominent ORSC Engines

RD-253	Thrust of 150 tf; 1 st stage of Proton LV	Highest reliability: more than 1,700 engine-flights with no failures
RD-170 (171)	Thrust of 740 tf (1,631 klb) 1 st stage of Zenit LV	The most powerful liquid propellant engine in the world
RD-180	Thrust of 390 tf (860 klb) 1 st stage of Atlas LV	The highest chamber pressure of 261.7 kgf/cm² (3,722 psi)



LOX Kerosene Oxygen-Rich Staged Combustion Rocket Engine

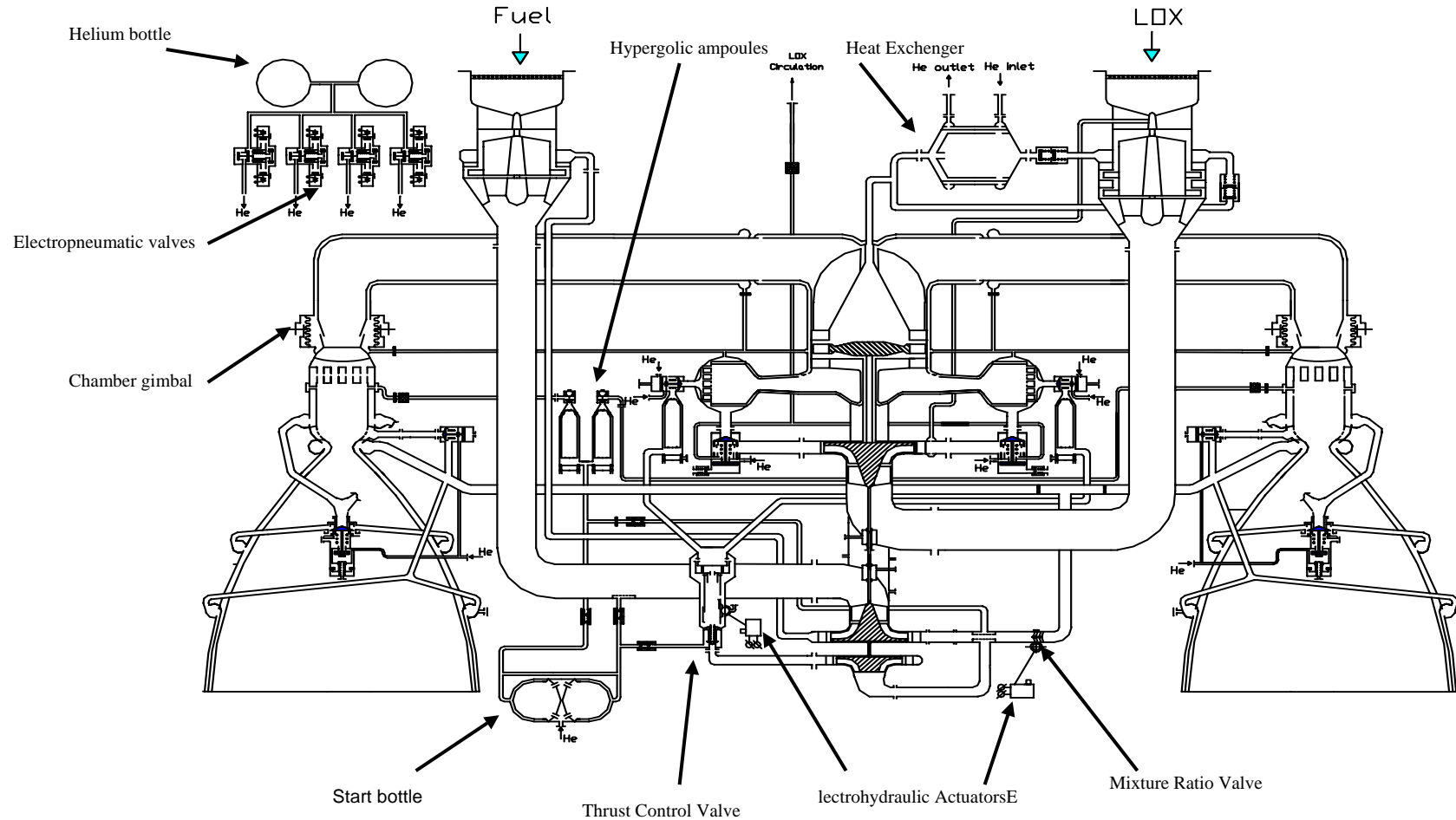
RD170 Engine





LOX Kerosene Oxygen-Rich Staged Combustion Rocket Engine

RD170 Engine Schematic





LOX Kerosene Oxygen-Rich Staged Combustion Rocket Engine

RD170 Design Features

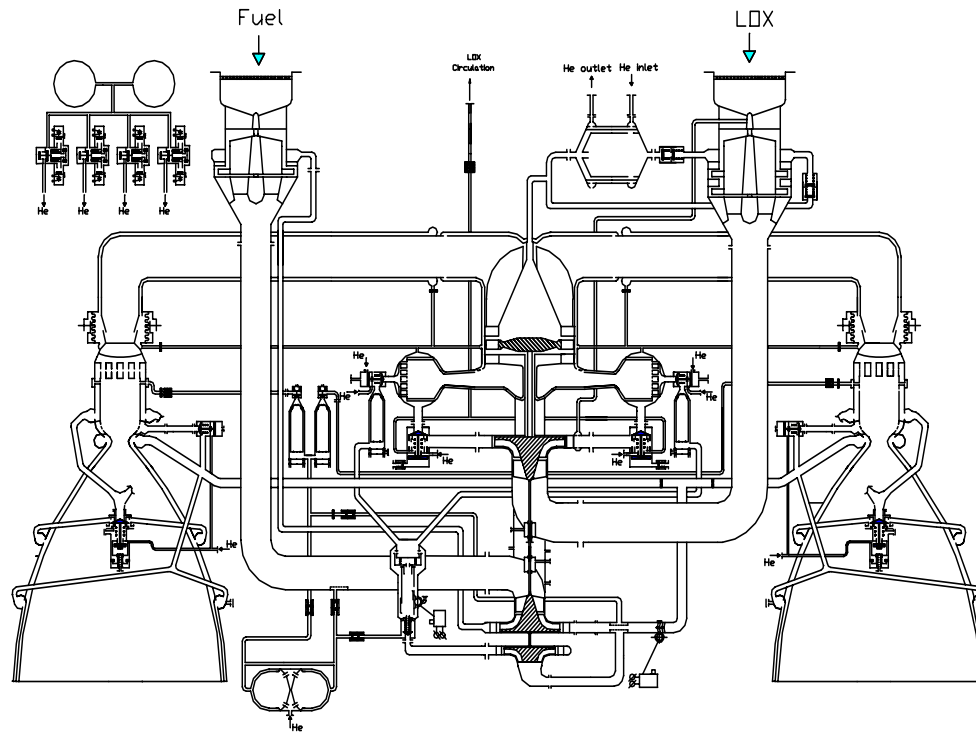


- 4 gimbaling chambers ($\pm 8^\circ$; any direction)
- 2 preburners;
- Single shaft MTU, LOX & fuel boost pumps;
- Hot gas duct is cooled at turbine inlet and outlet by LOX;
- Preburner and chamber propellant ignition with the use of hypergol;
- Gimbal actuators and TCV and MRCV actuators are hydraulic with the use of kerosene;
- Self-contained helium bottles to control valves and purges;
- Self-contained helium heat exchanger for pressurization of LV tanks;
- Engine arrangement provides good access for maintenance;

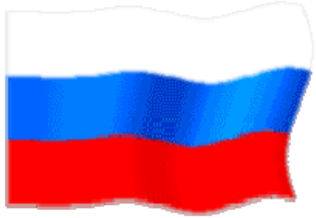


LOX Kerosene Oxygen-Rich Staged Combustion Rocket Engine

RD170 Design Features (cont'd)

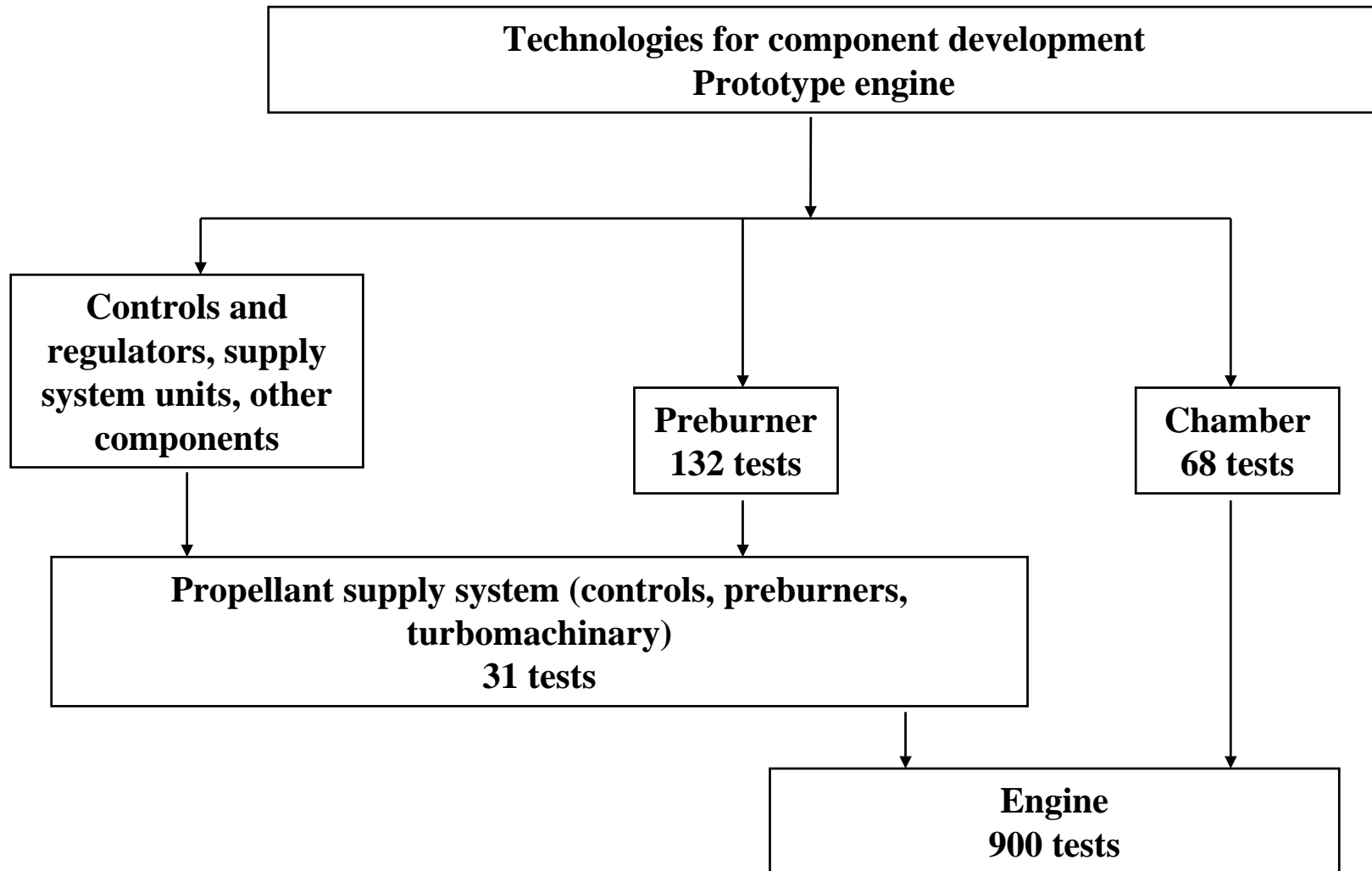


- **Programmable Start-up**
- **LOX Boost Pump turbine operates with oxygen-rich gas**
- **Filters in all external interfaces**
- **Duplication and triplication of electric control circuits**
- **Duplication of solenoids**



LOX Kerosene Oxygen-Rich Staged Combustion Rocket Engine

RD170 Development Plan





LOX Kerosene Oxygen-Rich Staged Combustion Rocket Engine

RD170 Certification Stages

Required

1 A/T + 1 Flight + 5 margin = 7

1 A/T + 4 Flights + 5 margin = 10

1 A/T + 10 Flights + 5 margin = 16

Demonstrated

1987 - expendable engine:

58 tests

8 engines

1990 - reusability of 4 missions:

46 tests

3 engines

1992 - reusability of 10 missions:

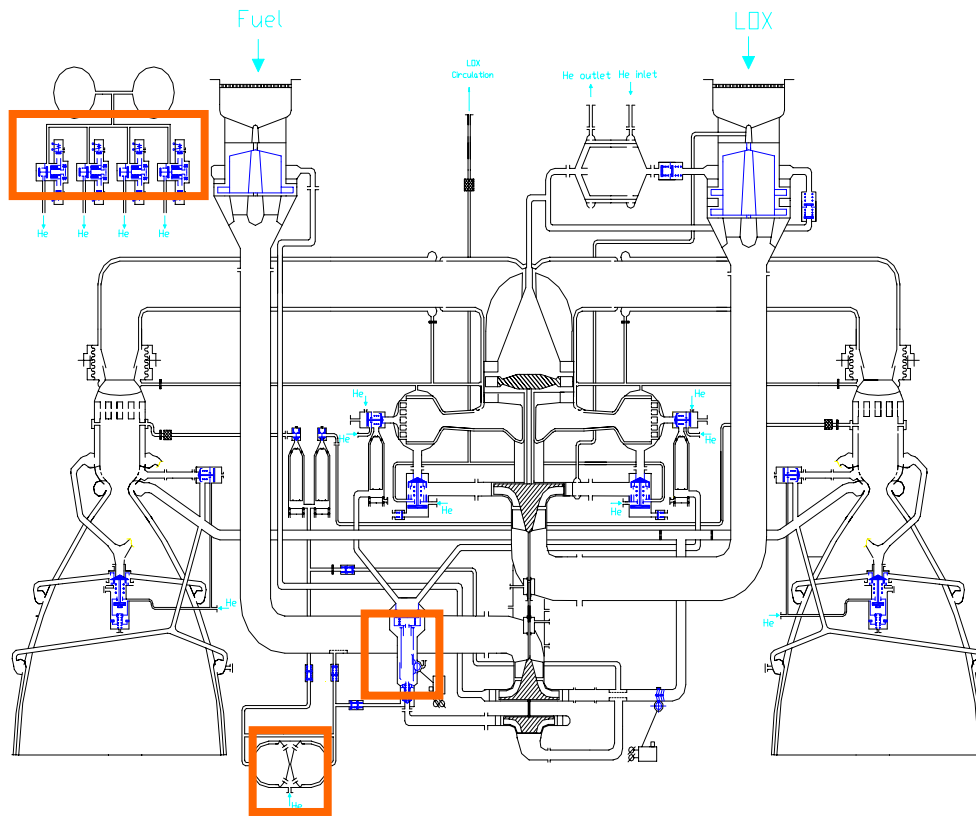
54 tests

3 engines



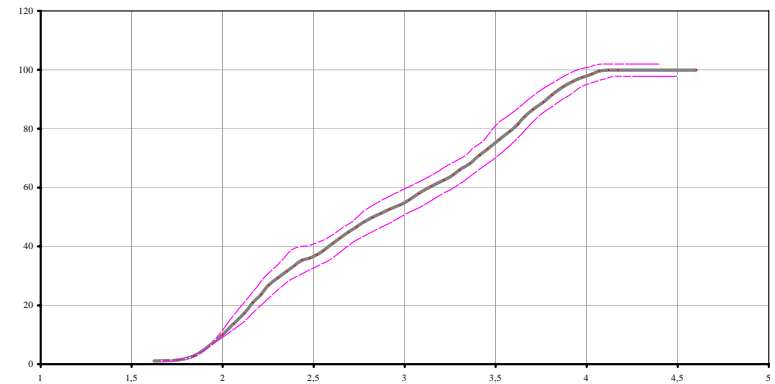
LOX Kerosene Oxygen-Rich Staged Combustion Rocket Engine

Programmed Engine Start



Objective:
minimum dynamic loads
on LV and engine components

Power level (%)

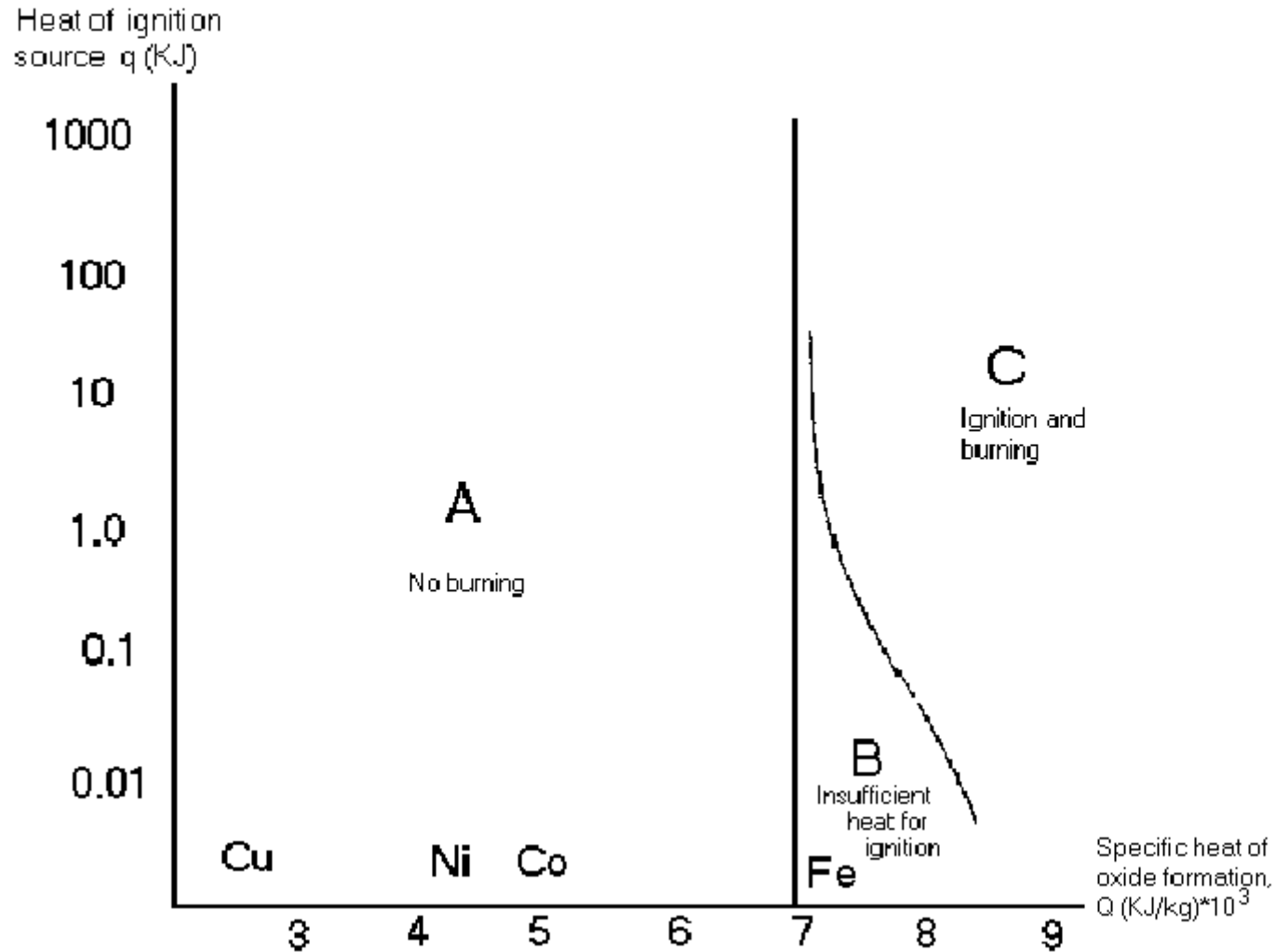


Time, sec



LOX Kerosene Oxygen-Rich Staged Combustion Rocket Engine

Materials of Oxygen Circuits





LOX Kerosene Oxygen-Rich Staged Combustion Rocket Engine

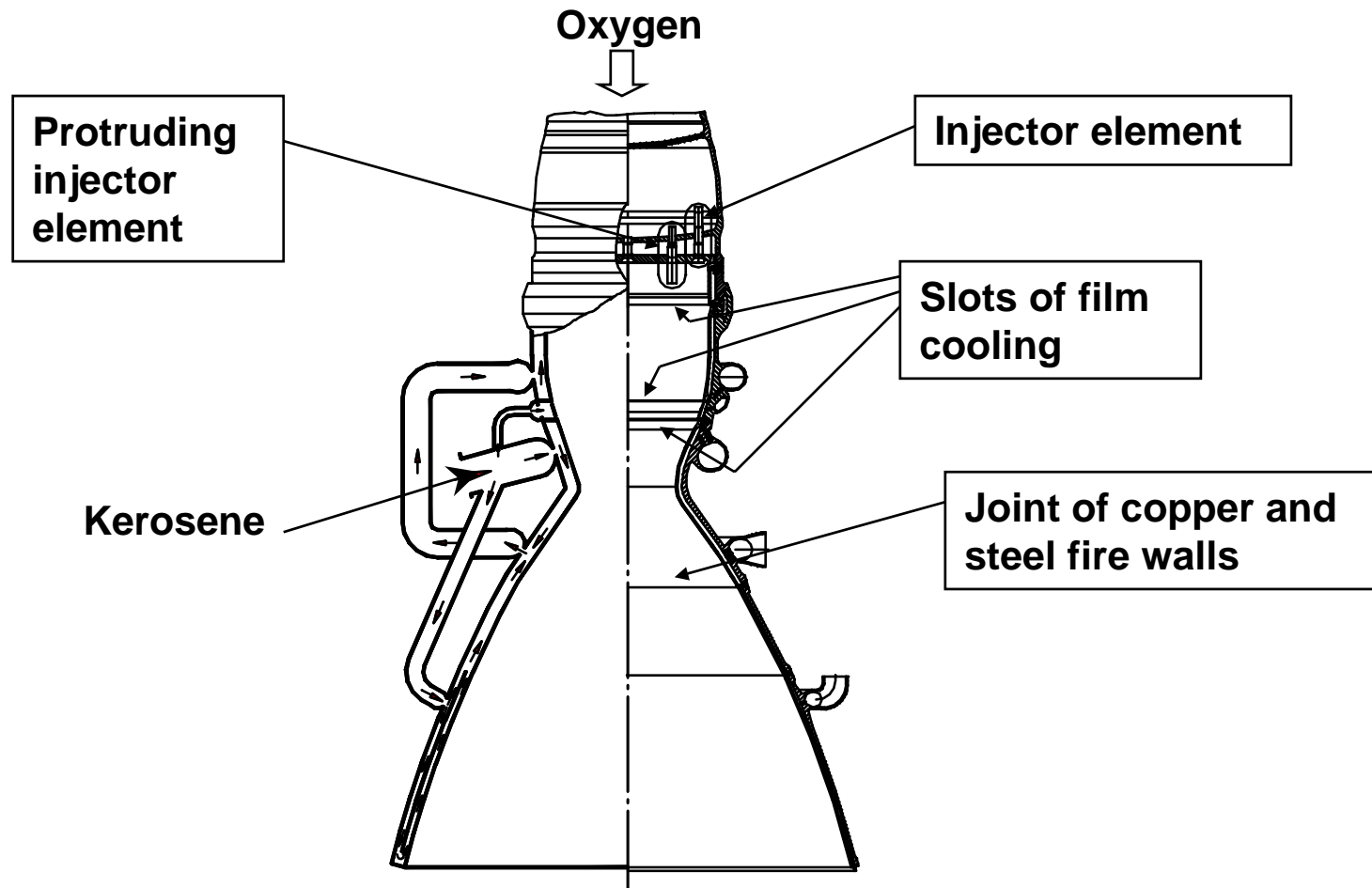
RD170 Chamber Basic Specifications

Thrust, tf (klbf)		Range of thrust throttling, %	
- at sea level	185 (408)	Required	100 - 49
- in vacuum	201.6 (445)	Demonstrated	108 - 30
Specific impulse, s		Range of mixture ratio variation, %	
- at sea level	309.5	Required	±7
- in vacuum	337.2	Demonstrated	+20 -10
Nozzle expansion ratio	36.9	The number of runs	
Chamber pressure, kg/cm ² (psi)	250 (3,556)	Required	11
Nominal mixture ratio	2.63	(1 acceptance test + 10 flights)	
Mass, kg (lb)	500 (1104)	Certified	17
		Demonstrated	25
		Predicted	>100

RD170 Chamber is used on RD171, RD180, RD191 Engines



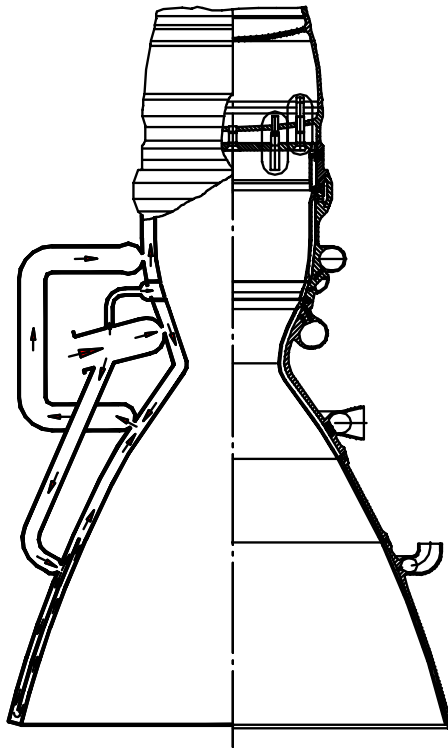
LOX Kerosene Oxygen-Rich Staged Combustion Rocket Engine *RD170 Chamber*



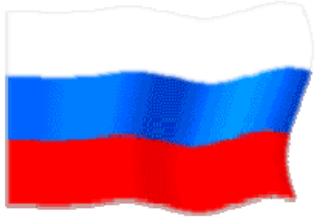


LOX Kerosene Oxygen-Rich Staged Combustion Rocket Engine

RD170 Chamber Design Features



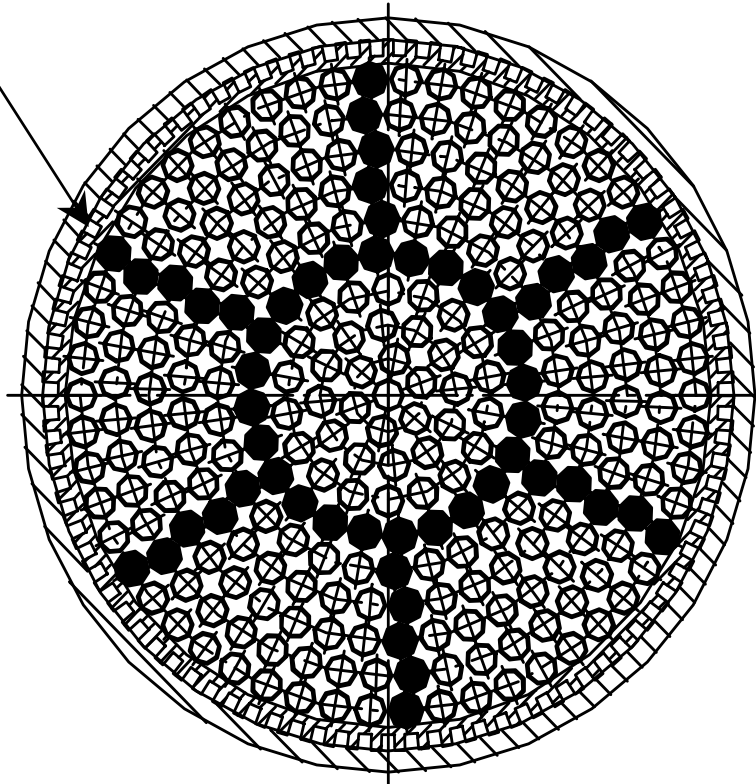
- **Brazing-welding assembly**
- **Fire wall of bronze, steel**
- **Distribution of kerosene flow rate in regenerative cooling passage**
- **Three slots of film cooling**
- **Spiral ribs on copper wall from fluid side**
- **Two-layer coating on bronze wall from gas side: nickel up to 100 μ m, chromium up to 500 μ m**



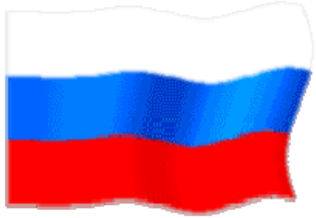
LOX Kerosene Oxygen-Rich Staged Combustion Rocket Engine

RD170 Chamber Injector Head

Protruding injector
elements

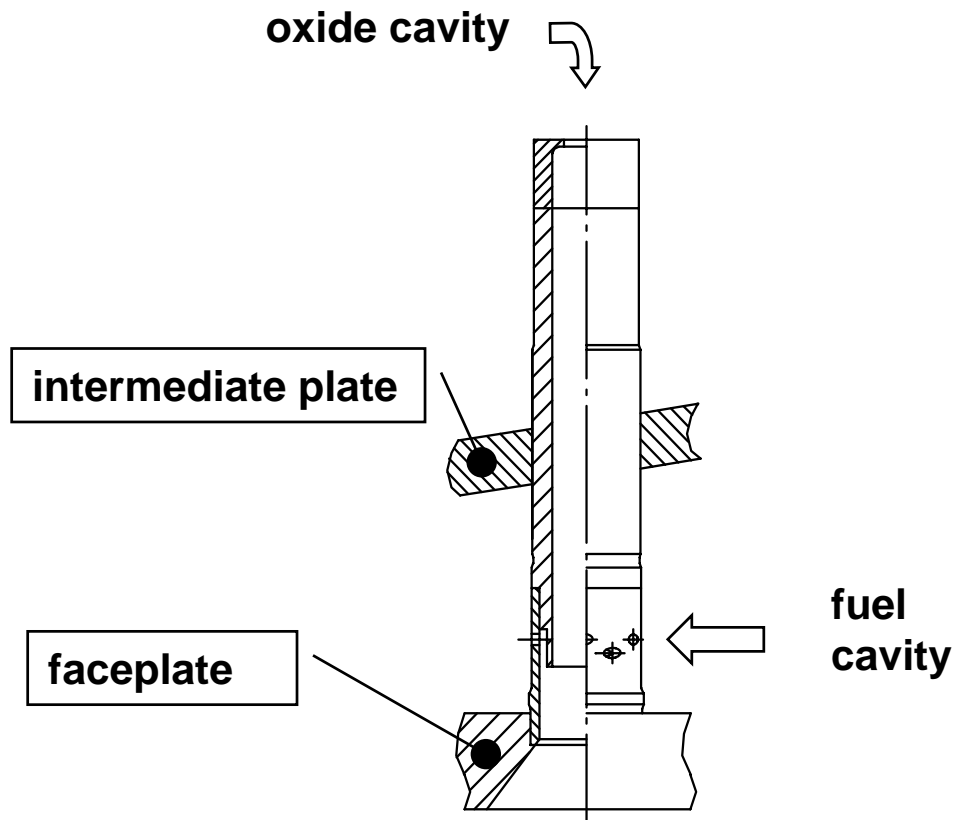


- separation of injector elements into three groups with difference in flowrates up to 10%;
- clustering of injector elements with different flowrate;
- protruding injector elements constitute ring and radial baffles



LOX Kerosene Oxygen-Rich Staged Combustion Rocket Engine

RD170 Chamber Injector Element

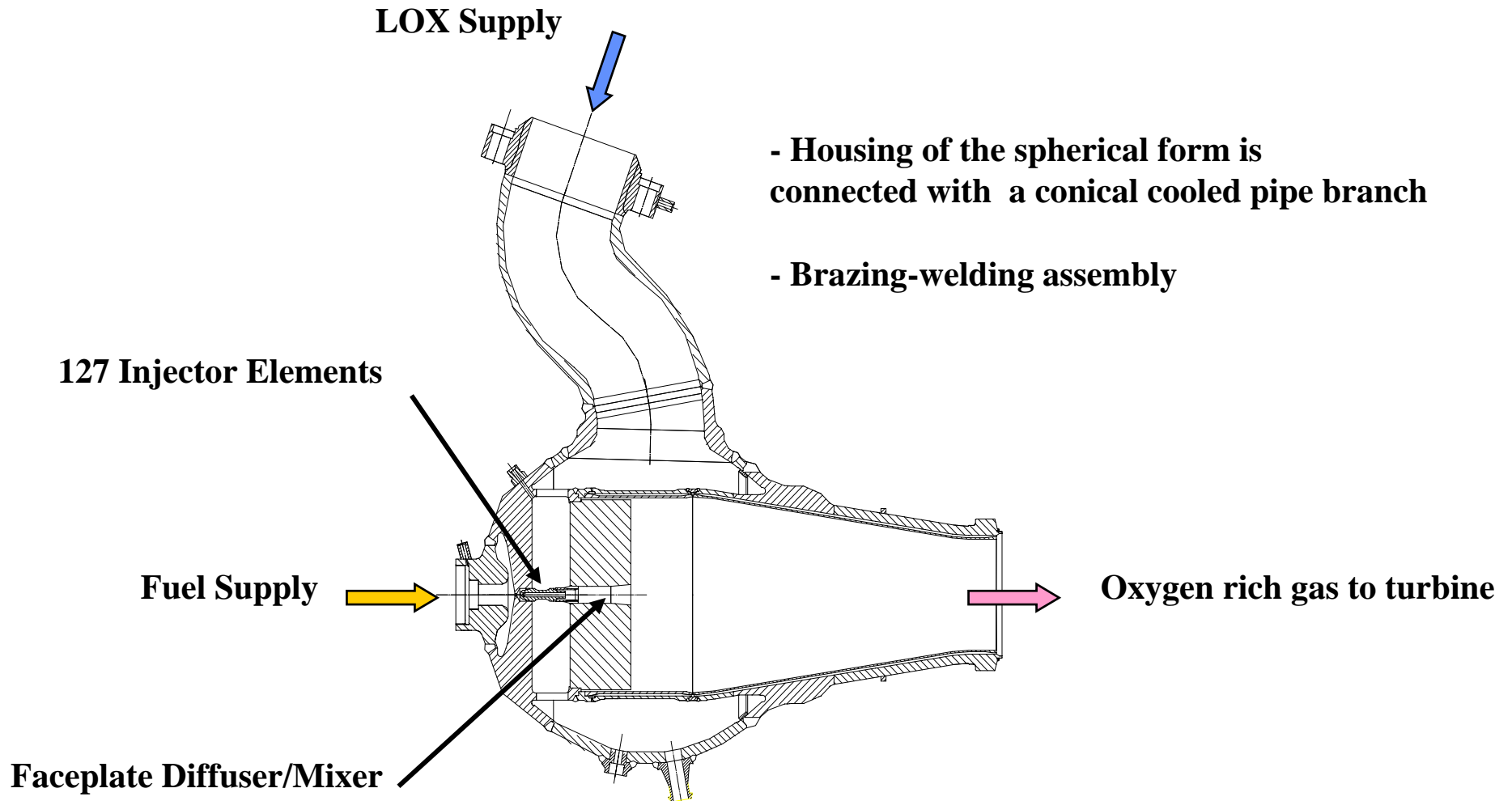


- two component injector elements:
oxygen – axial supply;
kerosene – tangential supply



LOX Kerosene Oxygen-Rich Staged Combustion Rocket Engine

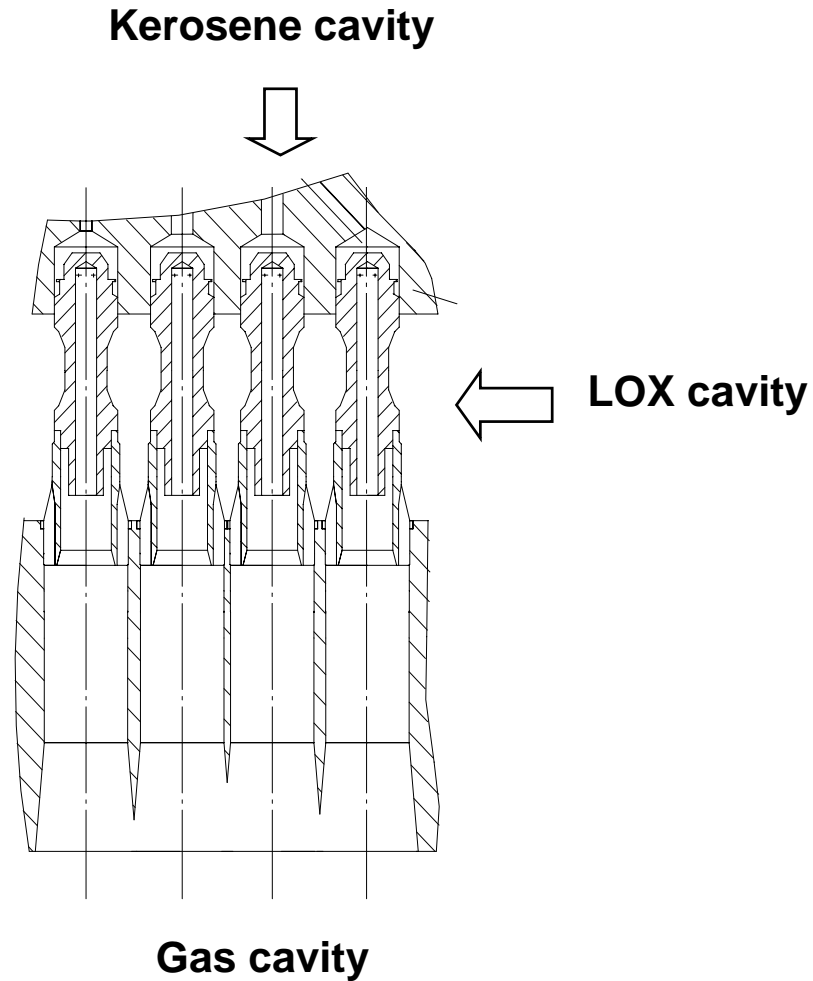
RD170 Preburner Design Features





LOX Kerosene Oxygen-Rich Staged Combustion Rocket Engine

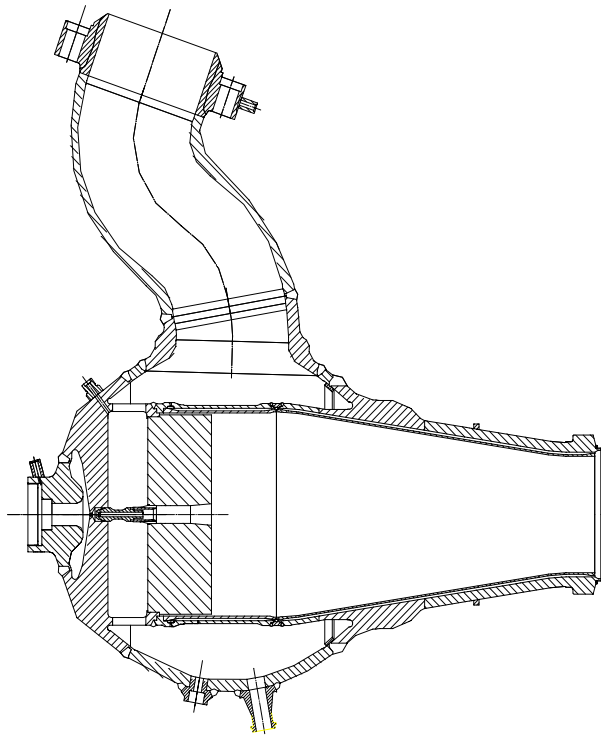
RD170 Preburner Design Features





LOX Kerosene Oxygen-Rich Staged Combustion Rocket Engine

RD170 Preburner Basic Characteristics



Nominal pressure, kgf/cm ² (psi)	600 (8,530)
Nominal LOX flowrate, kg/s	866
Non-uniformity of gas temperature at the outlet	± 30 C
Mass (two preburners), kg (lb)	520 (1,148)

The number of runs:

required -11 (1 acceptance test + 10 launches)

certified – 17

demonstrated – 25

predicted – >100

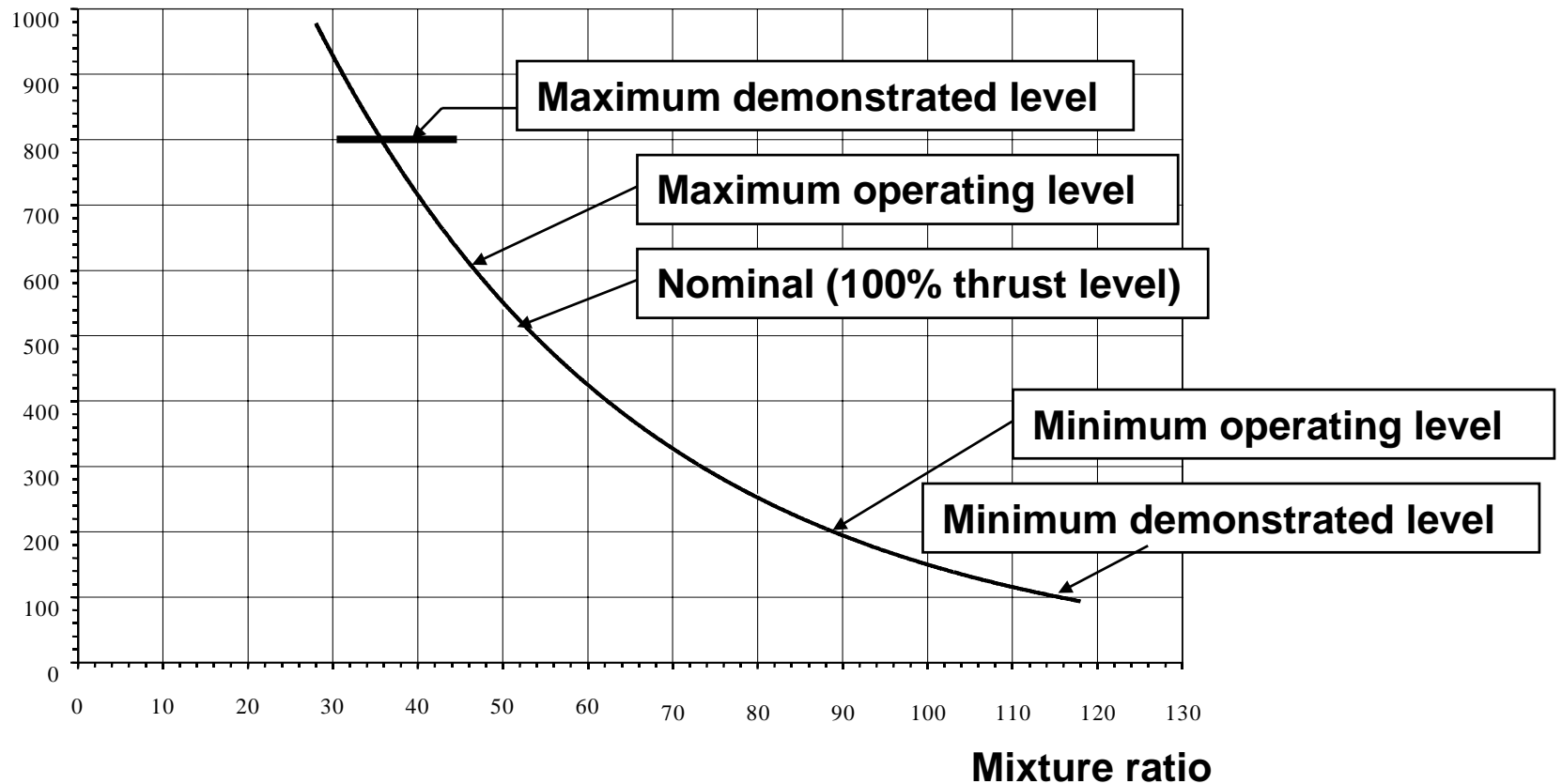
RD170 Preburner is used on RD171 and RD180 Engines



LOX Kerosene Oxygen-Rich Staged Combustion Rocket Engine

RD170 Preburner Temp Operational Range

Outlet temperature (°C)





LOX Kerosene Oxygen-Rich Staged Combustion Rocket Engine *SUMMARY*

- ORSC is the best choice for a LOX/kerosene rocket engine
- The existing ORSC LOX/kerosene rocket engine technology provides compliance with the modern requirements for reliability, safety, reusability, and operations

LOX/KEROSENE OXYGEN RICH STAGED COMBUSTION ROCKET ENGINE DESIGN AND LIFE ISSUES

B.I. Katorgin, V.K. Chvanov, F.Yu.Chelkis

NPO Energomash
28 October 2003

On May 15, 1987 and November 15, 1988 Energia launch vehicles were successfully launched in the Soviet Union. In contrast to the similar U.S. Space Shuttle that has two solid rocket boosters (SRB), Energia had four liquid propellant boosters. Each booster was equipped with one engine designed to be reused for ten missions. In the aforementioned first two launches, the boosters were not equipped with the means that would provide their soft landing.

The Zenit medium class expendable launch vehicle was developed in parallel with the “Energia” launch vehicle. The first stage of the “Zenit” launch vehicle, including the engine (engine designation is RD-171), is similar to the booster of Energia launch vehicle (engine designation is RD-170).

INTRODUCTION

The principal decisions with respect to the design of RD-170 (RD-171) were based on the experience in development of engines with oxygen rich staged combustion (ORSC). Development of engines of such type was initiated in the early sixties of the last century. For the past period of time newly developed engines have been made mainly with ORSC cycle.

This period of time was the most important phase of the history of rocket engineering development in the Soviet Union. A major part of the production and test infrastructure that provided capabilities to develop engines with a high level of combustion chamber pressure was established then. In the same period of time, based on experience in engine development and operations, the modern scientific-engineering methods and standard documentation base now in use were generated.

As of today, some ORSC engines have a very high performance both in Russia and in the whole world.

RD-253. Engine with 150 tf thrust, using N_2O_4 and UDMH fuel, chamber pressure of 150 kgf/cm² (its derivative is RD-257 with 170 tf thrust). The engine is used on the first stage of Proton launch vehicle and has a very high proven reliability level: more than 1,700 engines have been flown without failure.

RD-170 (171). It is the most powerful liquid propellant rocket engine in the world. Its thrust at sea level is 740 tf. Currently, this engine is used on the first stage of the Zenit launch vehicle under the Sea Launch commercial program.

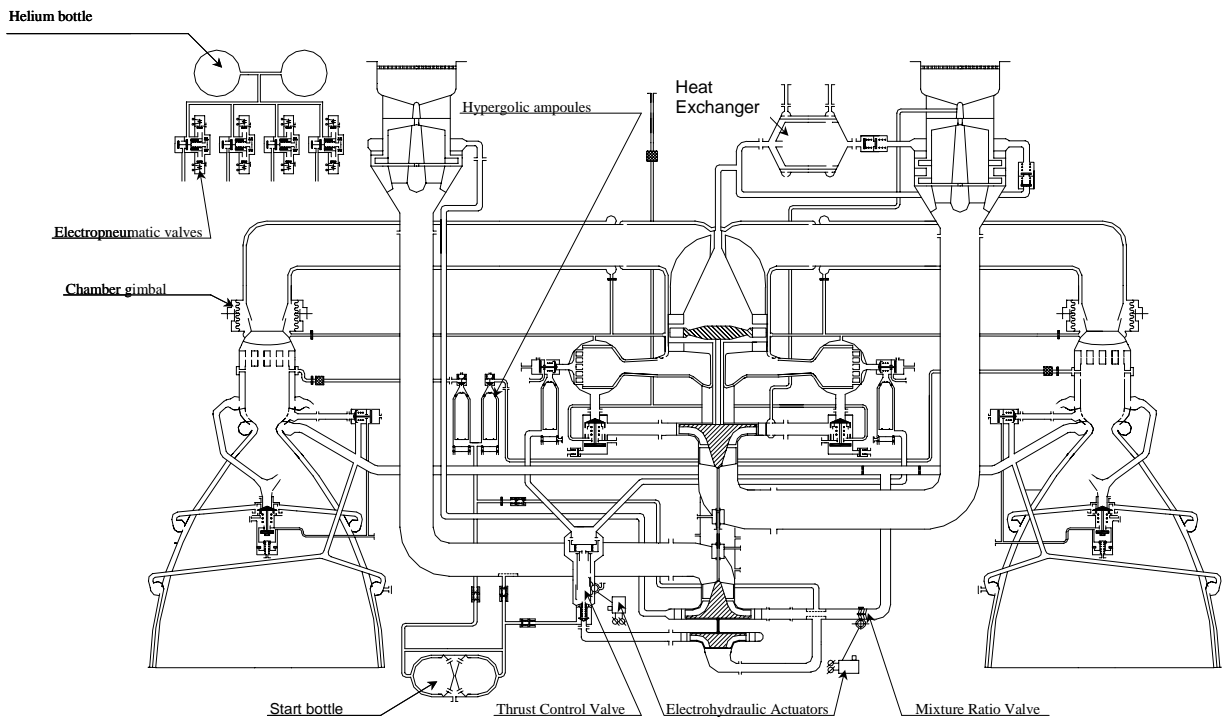
RD-180. It is a two-chamber derivative of the RD-170 engine. This engine is used on the first stage of the Atlas III and Atlas V launch vehicles. The remarkable feature of this engine is the high chamber pressure, the nominal value of which is 261.7 kgf/cm².

This paper is devoted to RD-170, the most remarkable ORSC engine. It is possible to consider this engine remarkable due to the fact that this engine possesses unique combination of extremely high performance and also it gave rise to a large family of engines.

1. RD-170 GENERAL DATA.

Principal Scheme.

RD-170 - four chamber engine with propellant supply system common for all chambers (Figure 1)



The propellant supply system comprises LOX and fuel boost turbopumps, the main turbopump unit (MTU), and two preburners. The boost turbopumps are inducer pumps with turbine rotors. Such being the case, main fuel tapped from the pump first stage outlet is used as the working fluid of the fuel boost turbopump turbine, and oxidizing gas tapped from the MTU turbine outlet - as working fluid of the LOX boost turbopump turbine. The MTU comprises an axial turbine, one-stage radial LOX pump, and a two-stage radial fuel pump.

The propellant ignition system in the preburners and chambers is chemical with the use of start fuel in ampoules. The ampoules, sealed with membrane valves, are installed in engine lines prior to every start-up.

The control system ensures engine thrust and mixture ratio variation. The system includes the thrust control valve (TCV) to provide fuel flow rate to the preburners and a mixture ratio control valve (MRCV) in the line of fuel supply to the chambers. To provide TCV and MRCV operations, two electro-hydraulic actuators are used which are identical in design and are controlled by a digital code.

The engine pneumatic system ensures control of the engine propellant valves and also purging of the preburner and chamber fuel cavities.

A self-contained helium heat exchanger is used for pressurization of launch vehicle tanks. Heating is provided by preburner gas tapped from the LOX boost turbopump turbine supply line.

Engine thrust vector control is provided by synchronized turning of the chambers in any direction by an angle of $\pm 8^\circ$. Electrohydraulic gimbal actuators (two for each chamber), controlled by a digital code, are used to perform such turning.

History of Development

The unique size and high level of parameters (pressures, flow rates, temperatures) presented an unprecedented complexity in the problem of experimental engine development. The feasibility of its successful solution was determined, in many respects, by the chosen strategic plan of development. This plan is represented in Figure 2.

The main idea of the plan is that at every step the key problems of main components/systems development were solved, if possible, independently from each other. The objective at every step was to obtain an operable design of the individual components. Final development should be conducted at the engine system level.

The selected engine design schematic (4 chambers, 2 preburners) made it possible to completely implement this strategic plan.

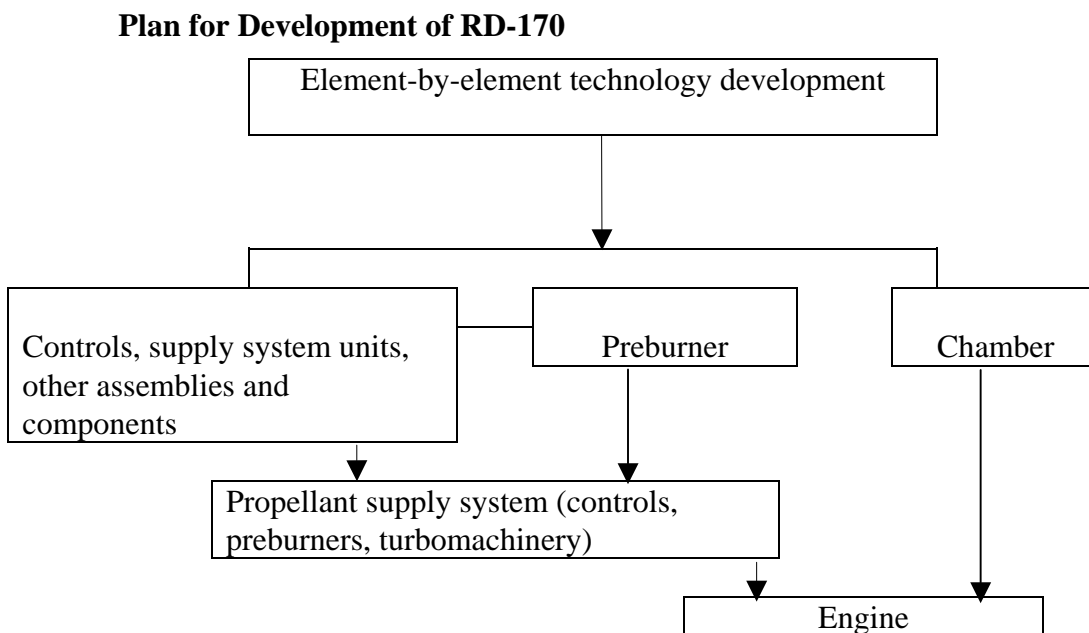


Figure 2.

Development of Certain Technology Elements.

On test rigs designed on the basis of previously developed engines:

- comprehensive studies of propellant ignition start-up and shut-down features were performed;
- technology of processing of engine cavities between tests was developed for multiple testing without engine removal from the test stand;
- Some decisions concerning chamber and preburner injector elements were proven.

Development of Control Valves and Other Components

Control valves, pipeline bellows compensators, the main chamber gimbal unit, heat exchanger, MTU bearings and other components were developed at the component level. In the course of development all possible types of testing for functioning were conducted; hydraulic, proof pressure, vibrational, environmental. The supply system components were proof and rigidity tested (including burst pressure) with measurements of deformation at loaded locations. The pump component rotors passed testing to determine natural frequencies of torsional oscillations and were proof tested on spin test stands. In the course of pump water flow testing, pump suction characteristics and efficiency were investigated.

Development of the Preburner.

The selection of the mixing scheme and injector design, assurance of working process stability, and high uniformity of combustion product temperature were reached in the course of hot fire testing of sub-scale and full-size preburners within test rigs.

In testing of a full-size preburner, the test facility turbopump system of propellant supply ensured flow rate and pressure parameters in the range of 30-80% nominal design values.

132 tests were conducted in total during which about 50 options of mixing schemes and various design solutions were tested (verified).

Results of hot fire tests, proof pressure tests to destruction, cutting and metallographic investigations of assemblies that underwent, among others, multiple hot fire tests showed high reliability of preburner design and the possibility, if required, to further boost its working parameters.

Development of the Chamber.

The development of the chamber was conducted with the use of a rig representing a one-chamber liquid-propellant engine made per the preburner gas afterburning scheme. The RD-170 chamber gimbal assembly and some control components also passed development stage.

The rig provided the possibility to reach 80% of design nominal thrust.

68 tests were conducted in total: six different cooling schemes and more than 20 versions of injectors were tested. Combustion stability of the LOX option design was proved with the use of the bomb method in the combustion chamber.

Development of the Propellant Supply System.

The development of the propellant supply system was conducted on a special assembly that comprised the MTU, boost pumps, preburners, and controls. 31 tests were conducted in total. In fact, during these tests the supply system passed only the initial phase of development. The main phase of development was performed during testing within the full-scale engine.

Engine Development.

The engine development plan included the provision for gradually increasing the engine lifetime, margin testing in more extreme modes (in thrust, mixture ratio, propellant temperature, engine inlet pressure etc.), as well as testing with simulation of defects and failures of certain components.

The final phases of ground development were the formal certification tests and testing within the launch vehicle stage.

Figure 3 represents limits of variations of the thrust in vacuum (P) and mixture ratio (Km) which were verified in the process of testing.

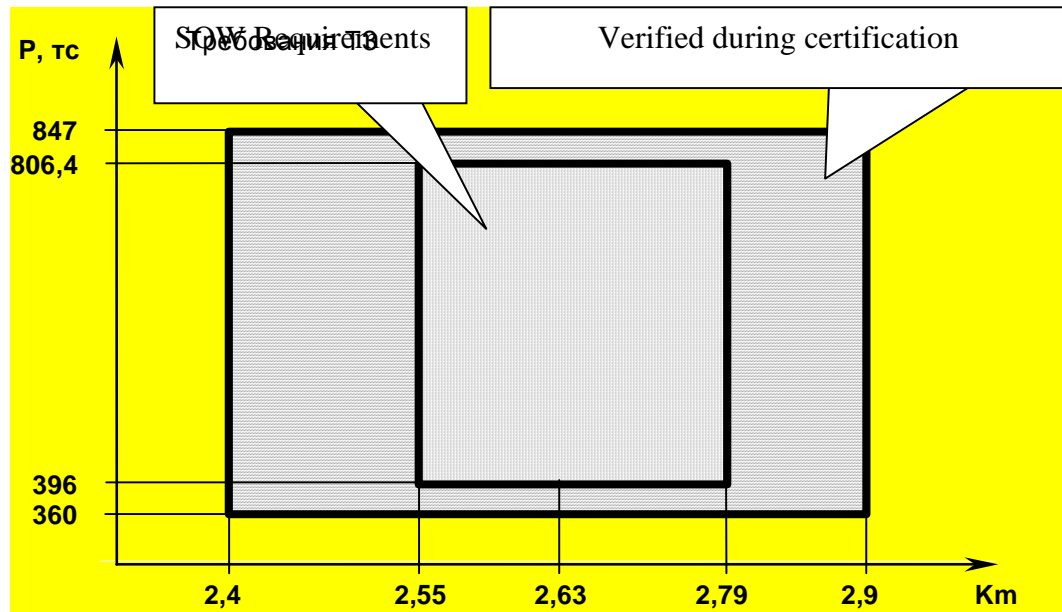


Figure 3

As of the 1st of December, 1992 the total run time of RD-170 (171) including all types of hot fire tests was about 101,300 second, the total number of hot fire tests was 898.

In 1993-1994, 50 tests of 15 modified RD-170 engine assemblies had been conducted for the purpose of determining the potential of increasing its performance.

The RD-170 underwent three phases of certification tests.

In 1987 testing of the phase for an expendable launch vehicle was completed (58 tests on 8 engines).

In 1990 testing of the phase for 4-time reusability was completed (46 tests on 3 engines).

In 1992 testing of the phase for 10-time reusability was completed (54 tests on 3 engines).

The certification test programs made provision for multiple (corresponding to the phase) testing on each engine with variation of operation modes and conditions at worst combinations, as well as disassembly of engines after testing and thorough inspection of hardware condition with the use of destructive and non-destructive inspection methods. Testing was considered successful, if the test plan was fully completed and hardware condition after testing met the technical documentation requirements.

The RD-170 successfully passed through all three phases of certification tests.

2. MAJOR DESIGN FEATURES OF RD-170.

This section describes only some features that directly determine engine reliability and life cycle.

Programmed Engine Start-up.

For the purpose of limiting the level of dynamic loads on the launch vehicle and engine components the RD-170 engine start-up was performed through:

- issuance of commands in a certain sequence to the TCV actuator;
- change of the TCV setting from the initial value at which preburner propellants ignition takes place to the flow rate that corresponds to the nominal thrust;
- supply of fuel to the inlet of the TCV with the use of a start bottle and engine pneumatic system, which provide the required pressure drop across the TCV.

The sequence of all start preparation operations which was determined with the use of mathematical modeling and corrected based on experimental results provides for:

- meeting the launch vehicle requirements to engine thrust increase rate;
- smooth change of engine parameters (no spikes);
- repeatability in start-up time for the complete range of external conditions.

Figure 4 shows MTU rotation speed during the start.

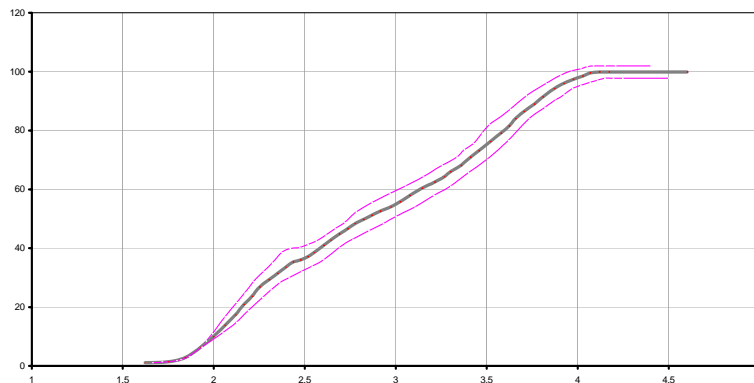


Figure 4 - Percent Speed Vs Time, sec

Selection of Materials used for Engine Oxygen Path Components

Investigations to justify selection of materials and coatings for components of “hot” and cryogenic oxygen path were very important during the development of the RD-170. Because of this the efforts were focused on experimental studies of the sensitivity of various materials under conditions of random ignition sources in oxygen environment. The investigations were conducted by simulation of operating conditions for various engine components within the engine. This research resulted in requirements for the configuration of specific engine components.

The general engineering approach to LOX path material selection is illustrated in Figure 5.

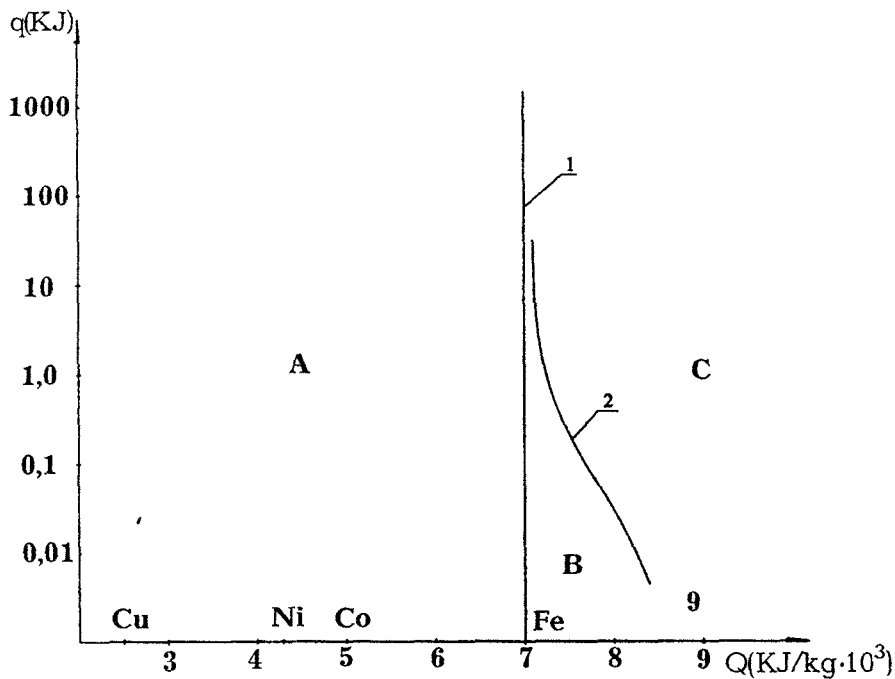


Figure 5

Figure Key:

Abscissa axis Q is specific heat of metal oxide formation;

Ordinate axis (logarithmic scale), q – amount of heat released by an ignition source.

Area A formed between the ordinate axis and vertical line 1 is an area where material is not capable of self-sustained burning (material does not burn at these conditions without a heat supply from an external source). This area comprises silver, copper, nickel, copper-nickel alloys, and other nickel alloys. The position of vertical line 1 on the abscissa axis depends on the oxygen environment parameters, primarily, on temperature and pressure. In particular, a temperature increase results in displacement of vertical line 1 to the area of lower values of Q . The Figure above approximately corresponds to LOX conditions under pressure more than 100 kgf/cm².

Areas B and C located to the right relative to vertical line 1 are areas of metal burning.

Curve 2 separating areas B and C determines the limiting level of the ignition source thermal power.

In area B the source power is insufficient to ignite metal.

In area C metal is ignited and burns.

High-strength design alloys contain various alloying elements that, as a rule, move these alloys relative to its base along the abscissa axis towards the area of higher values of Q .

In its practice NPO Energomash widely uses various types of inactive material coatings. First of all, this relates to turbine components that operate in high-temperature oxygen environment. In cases when the alloy is beyond area A, application of coating makes it possible to shift the ignition boundary (curve 2) towards the area of higher values of q determined by coating properties.

The approach to selection of materials, efficiency and resistance of coatings used by NPO Energomash were successfully proven during material sample and turbine component testing, special hot fire testing of engines with the use of various initiators of burning, as well as during the certification of RD-170 for reusability.

Chamber.

Main characteristics

Thrust, tf	- at sea level	185
	- in vacuum	201.6
Specific impulse, s		
	- at sea level	309.5
	- in vacuum	337.2
Nozzle expansion ratio		36.9
Nominal pressure, kg/cm ²		250
Mass, kg		500
Throttling range, %		
	Required	100 - 49
	Demonstrated	108-30
Nominal mixture ratio		2.63
Mixture ratio excursion range, %		
	Required	± 7
	Certified	> ± 10
The number of runs:		
	Required	11 (1 acceptance test + 10 launches)
	Certified	17
	Demonstrated	25
	Predicted	> 100

Design features:

- integral injector head, combustion chamber and exhaust nozzle design based on brazing and welding;
- dual-propellant injector elements – axial supply of gaseous oxygen, tangential supply of kerosene (Figure 7);
- separation of injector elements into three groups with difference in flow rates up to 10%;
- grouping of injector elements with different flow rates;
- use of injector elements that protrude beyond the face plate and constitute ring and radial buffers (Figure 8);
- fire wall made of bronze;

- regenerative cooling has a certain scheme of kerosene flow rate distribution in combination with three levels of film cooling; in addition, spiral ribs are made on the fire wall from the fluid side (Figure 6);
- the fire wall made of bronze has a two-layer coating: the first layer – nickel of thickness up to 1000 μm , the second – chromium of thickness up to 500 μm .

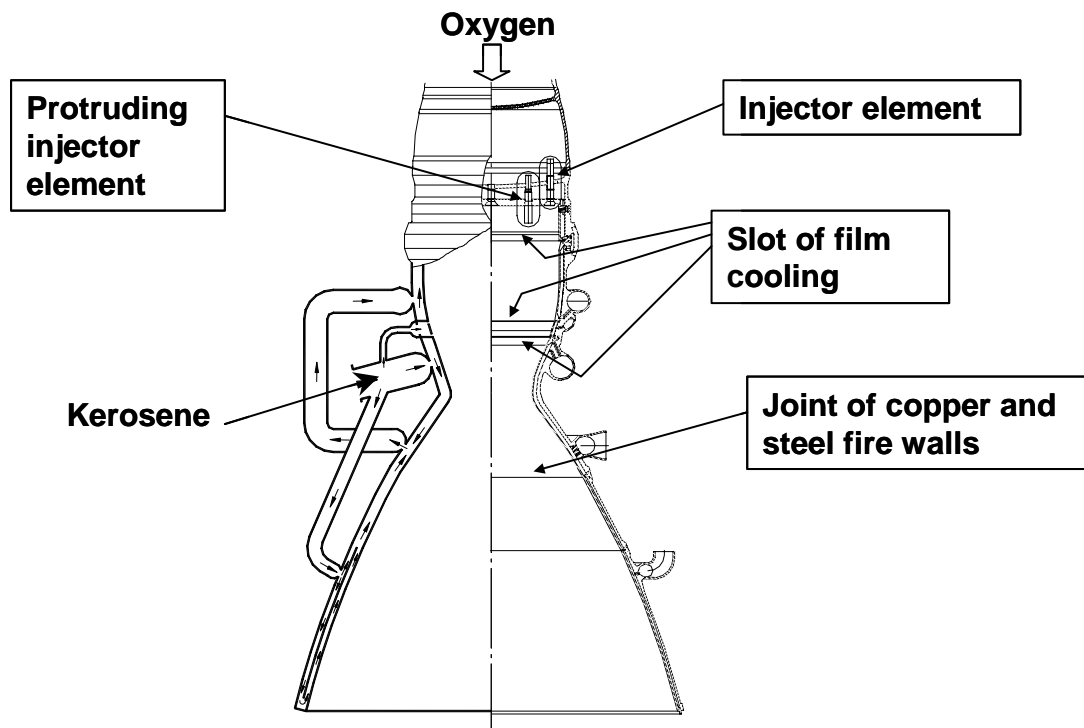


Figure 6 - Chamber

oxide cavity

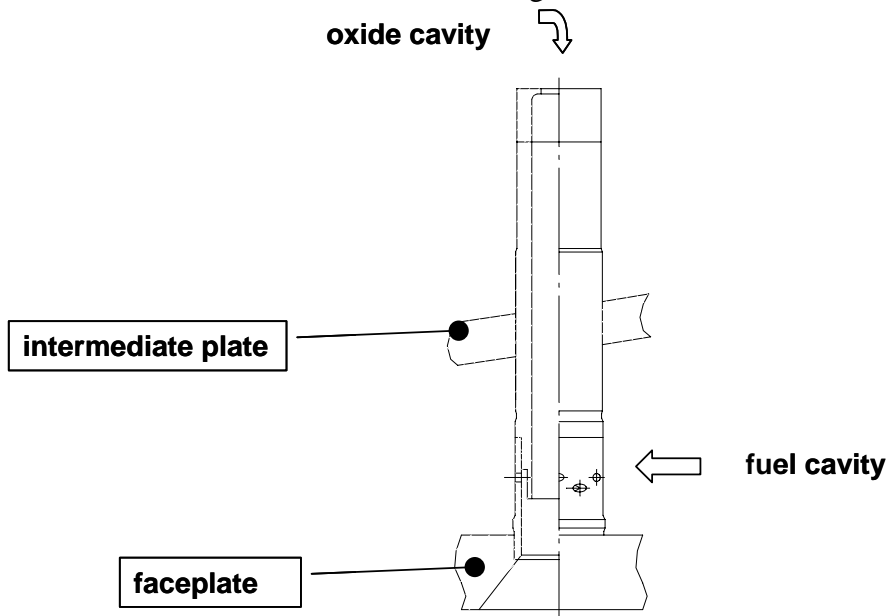


Figure 7, Chamber Injector Element

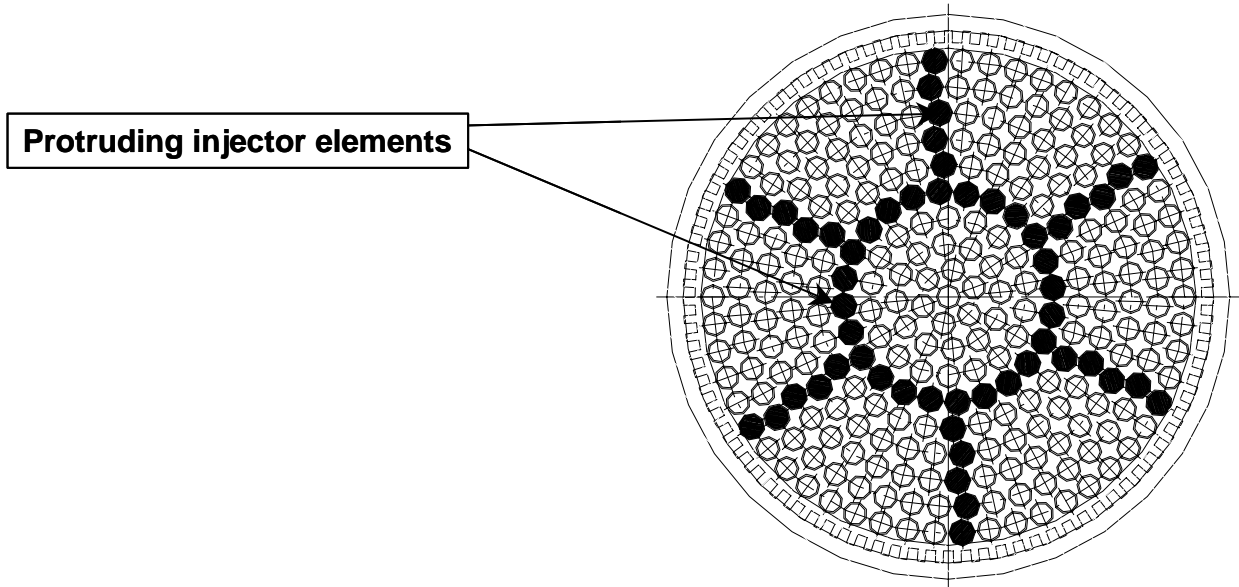


Figure 8, Injection Head

Preburner.

Main characteristics

Nominal pressure, kgf/cm² – 600

Nominal LOX flow rate, kg/s – 866

Operation temperature range is given on Figure 9.

Mass (two preburners), kg - 520

Instability of gas temperature at the outlet - $\pm 30^{\circ}\text{C}$

The number of runs:

required - 11 (1 acceptance test + 10 launches) ;

certified – 17;

demonstrated – 25;

predicted – >100.

Design features:

- Integral design based on brazing and welding;
- The spherical housing is connected with a cooled conical pipe (Figure 10);
- Injector element with tangential kerosene supply and double supply of LOX - tangential and axial;
- Completion of propellant combustion and flow temperature equalization takes place in the individual channel (chamber) of each injector element (Figure 11).

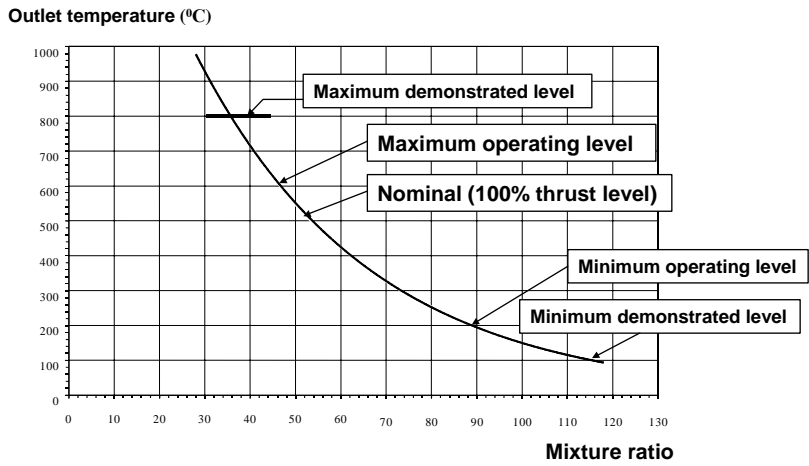


Figure 9 - Operability Temperature Range

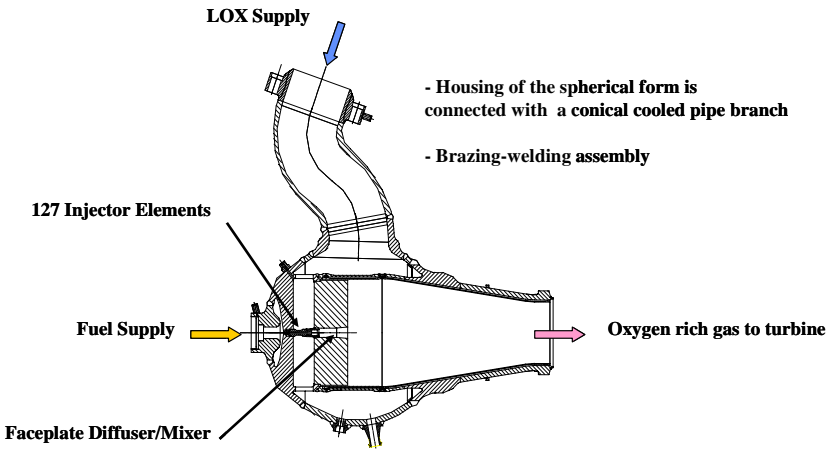


Figure 10 - Preburner Scheme

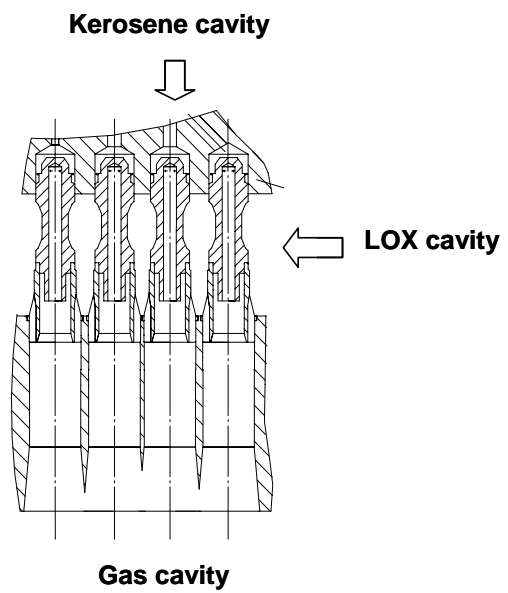


Figure 11 - Injection Head Section

Summary

1. ORSC is the best choice for a LOX/kerosene rocket engine.
2. The existing ORSC LOX/kerosene rocket engine technology provides compliance with the modern requirements for reliability, safety, reusability, and operations.

History of Rocket Propulsion at Rocketdyne

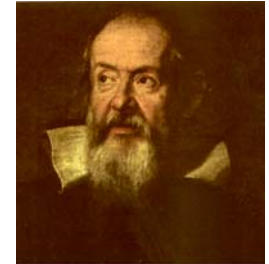
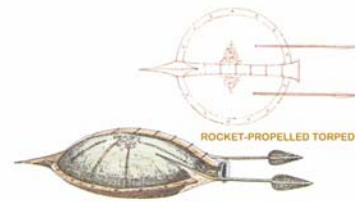
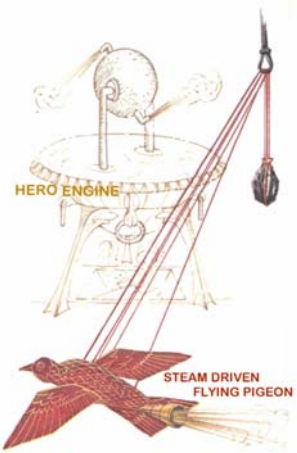
Steve Fisher

October 28, 2003

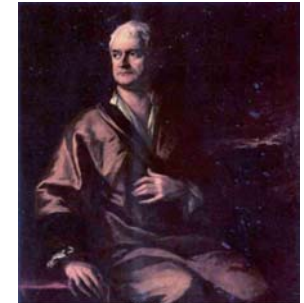
**5th International Symposium on Liquid Propulsion
Chattanooga, Tennessee**

Primal Rocketry Years

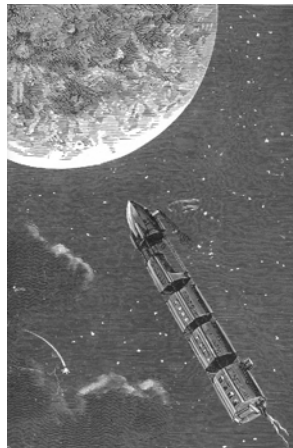
400 B.C. thru 1900



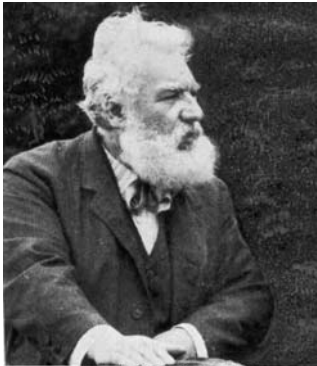
Galileo Galilei



Isaac Newton



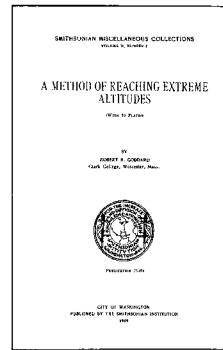
Rocketry Becomes a Science 1900 thru 1930



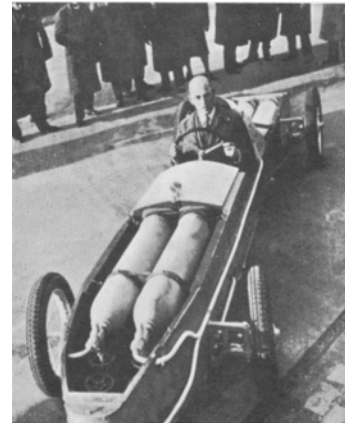
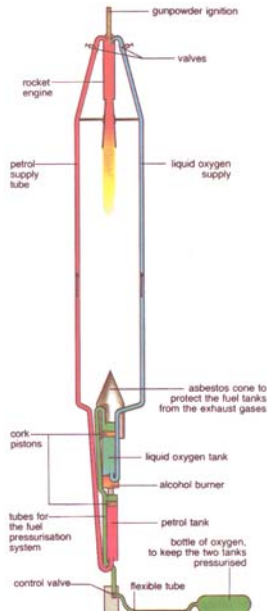
Konstantin Tsiolkovsky



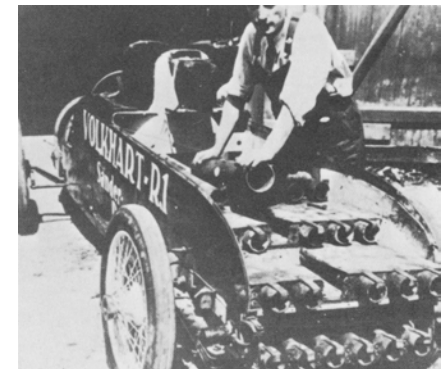
Dr. Robert H. Goddard



Hermann J. Oberth



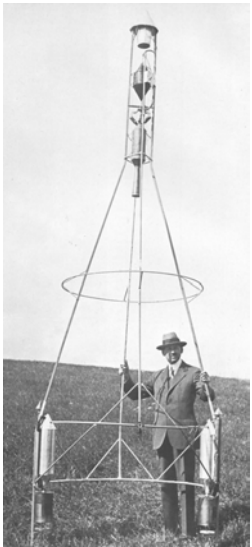
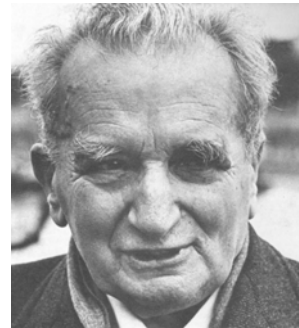
Max Valier in his liquid-propellant rocket car



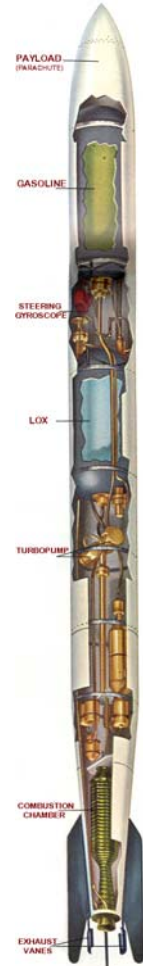
U.S. Rocketry 1930 thru 1945



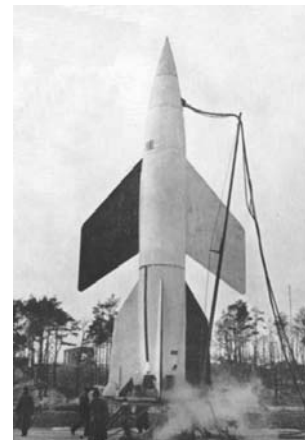
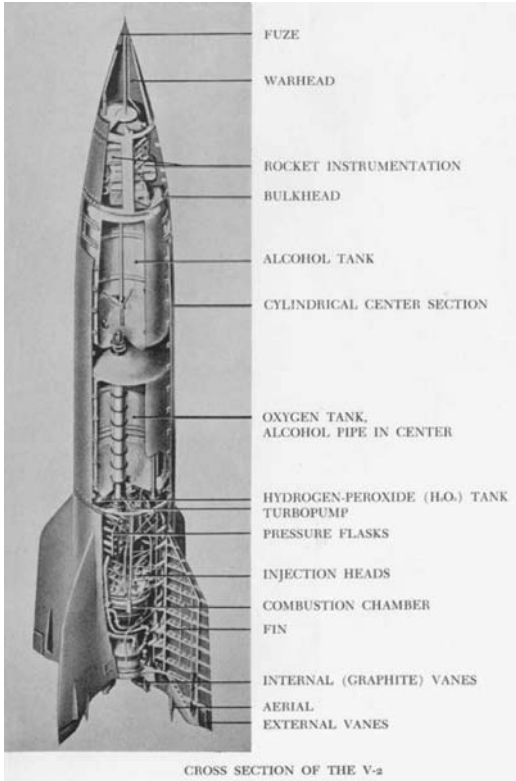
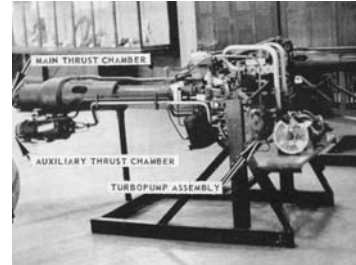
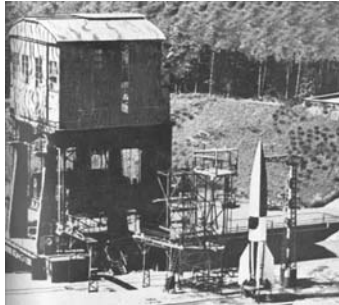
Robert H. Goddard



Rocketayne



German Rocketry 1930 thru 1946



Von Braun (with arm in cast) surrenders to the Americans at Rehrdt, in May 1945. Left to right are Charles L. Stewart, U.S. counter-intelligence agent, Lt. Col. Herbert Isler, attached to Gen. Dornberger's staff, Dieter K. Brand, Werner von Braun, Major von Braun, and Hans Lindbergh.

Rocketdyne Beginnings

1946 thru 1949

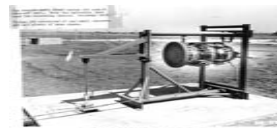
- 1945/1946 - North American Aviation formed Technical Research Laboratory
- 1946 - Letter contract for Phase I for AF MX-770 Navaho Missile
- 1946 - First tests conducted on 3,000 thrust aircraft jet-assisted takeoff (JATO) unit at LA East Parking Lot
- March 1947 - Santa Susana selected for nation's first liquid propellant high-thrust test facility
- 1947 - Technical Research Laboratory, now at 500 personnel, renamed Aerophysics Laboratory
- 1948 - North American test Instrumentation Vehicle (NATIV) launched at Alamogordo Army Base
- 1949 - East Parking Lot testing discontinued as Santa Susana activated



NAA LAX Parking Lot Test Area Aerial View - 1947



NAA LAX Parking Lot Control Center - 1947



NAA LAX Parking Lot JATO Hot Firing - 1947



NATIV Launch - 1948



NATIV Launch - 1948

Rocketdyne Beginnings

1949 thru 1955

- Aerophysics Field Laboratory, now Santa Susana Field Laboratory, activated in 1949 - First tests conducted late 1949/ 1950
- 18 large static test stands with thrust capability up to 1.5 million lbs and five component test laboratories with over 60 positions eventually constructed
- Folding Fin Aircraft Rockets Produced - NALAR, LAR, NAKA, & NASTY
- Engines for Navaho, Redstone, Atlas, Thor, & Jupiter Missiles and Launch Vehicles developed and tested during this period
- Rocketdyne Division of NAA Inc. formed November 7, 1955



Navaho Phase 2 Engine System Installation - 1951



Vertical Test Stand (VTS) - Engine Hot Firing



Folding Fin Aircraft Rockets (FFAR) - NALAR, LAR, NAKA, & NASTY



G-26 Navaho Two Engine Cluster - 1955 (1 of 5)



NAVAHO 120 K ENGINE

REDSTONE A-6 ENGINE

GERMAN A-4 ENGINE

ROCKETDYNE DIVISION CREATED NOVEMBER 7, 1955

- CONSTRUCTION BEGAN IN FEBRUARY OF 1955
- PLANT OPENED ON NOVEMBER 14, 1955
- 850 EMPLOYEES
- ANOTHER 1,700 MOVED FROM SAUCON, BEVERLY HILLS AND DEERING FACILITIES BY THE END OF 1955



Rocketdyne Front Lobby - 1955

Rocketdyne Propulsion & Power Overview



STS SSME



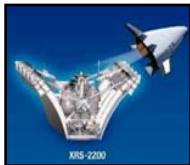
Delta IV RS-68



Delta II/III RS-27



Atlas II MA-5



XRS-2200



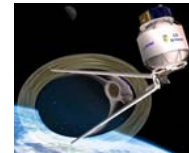
RS-72



MB-60



Technology



Solar/Thermal



Space Power



THAAD



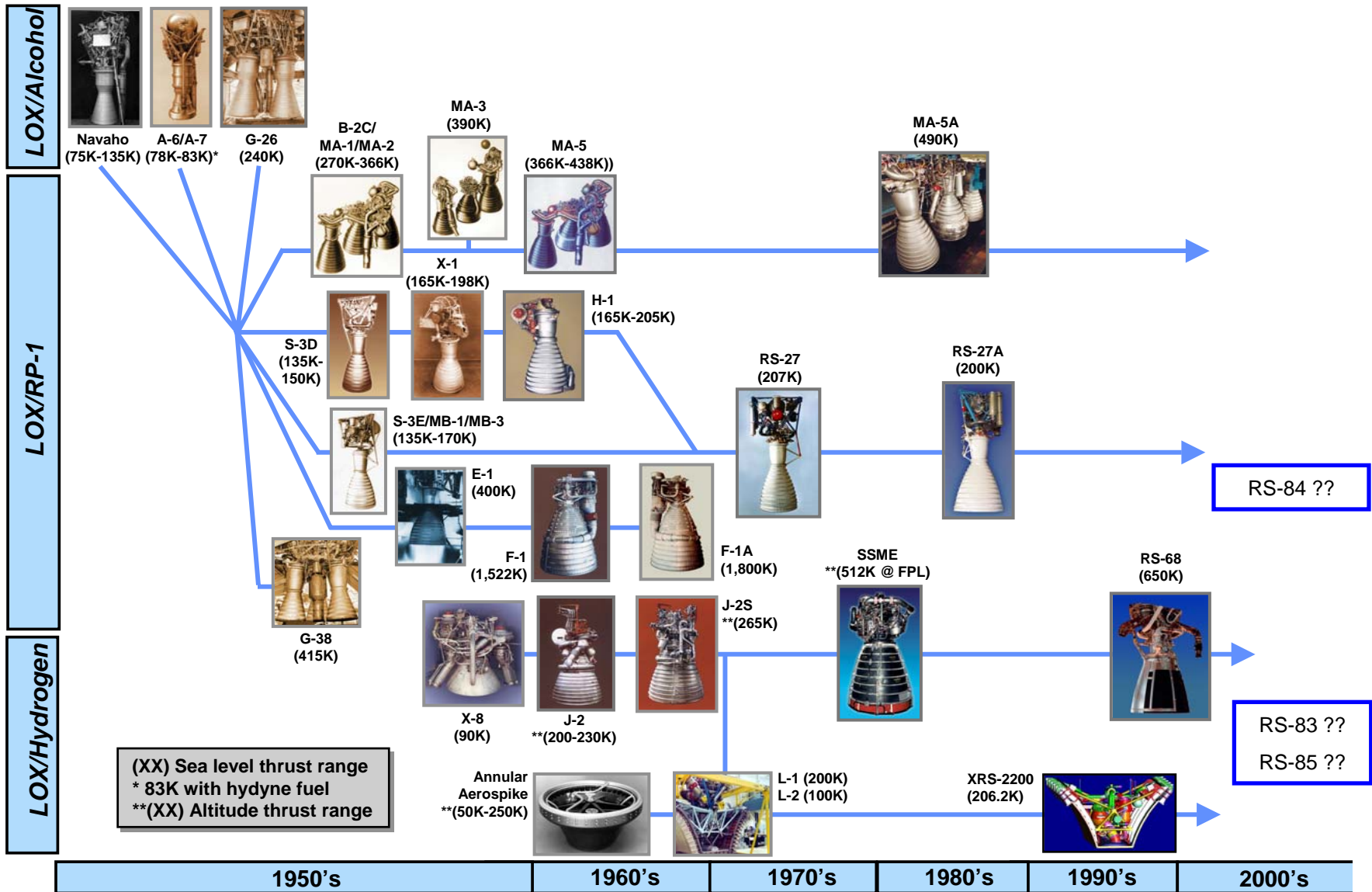
Non-Toxics



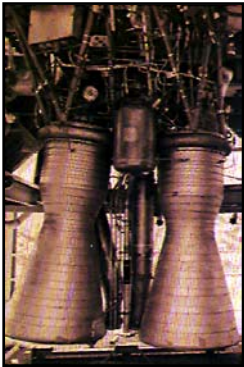
Ion Thrusters



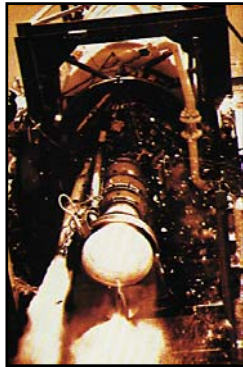
Rocketdyne Propulsion & Power Liquid Propellant Propulsion Booster Evolution



Rocketdyne Family of Engines



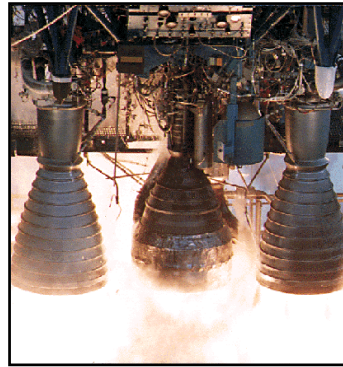
G-26
Navaho II



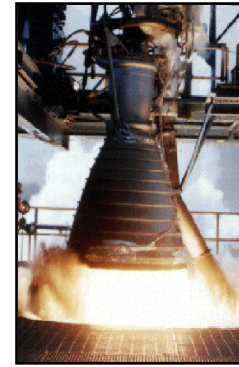
A-7
Redstone



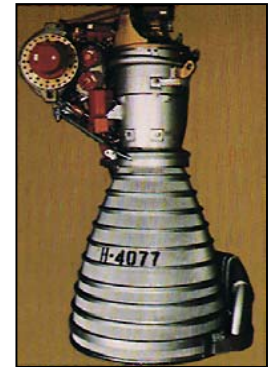
S-3D
Jupiter



MA-5A
Atlas II



RS-27A
Delta II/III



H-1
Saturn I/IB



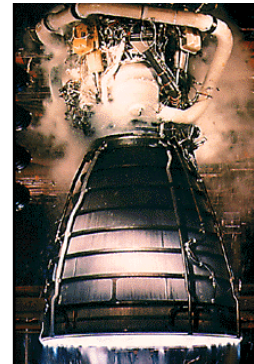
F-1
Saturn V



J-2
Saturn IB/V



RS-68
Delta IV



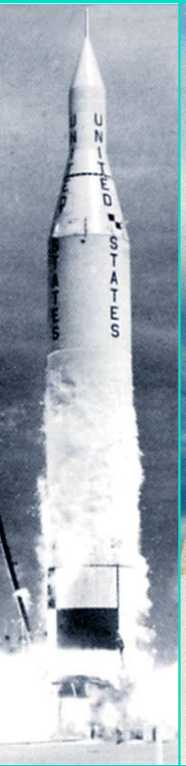







SSME
Space Shuttle



XRS-2200
X-33

Our Engines Have Boosted 1,508 Vehicles

							
Redstone	Navaho	Jupiter	Thor/Delta	Atlas	Saturn I/1B	Saturn V	Space Shuttle
85	11	46	380/284	565	19	13	113

Delta IV – Three launches

First in Space: Boeing/Rocketdyne



Alan Shepard
May 5, 1961



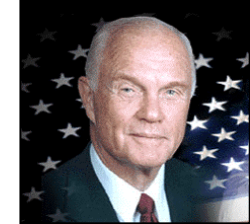
John Glenn
Feb 20, 1962



Neil Armstrong
Mike Collins
Buzz Aldrin
Jul 16, 1969



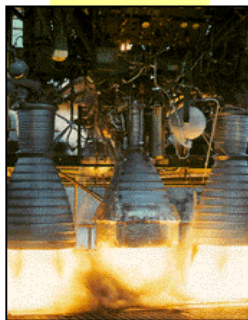
John Young
Bob Crippen
Apr 12, 1981



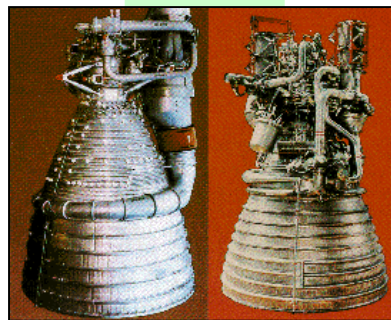
John Glenn
Oct 29, 1998



Redstone



Atlas

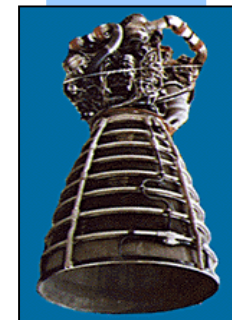


F-1

J-2



SSME Basic



SSME Block IIA

Saturn I/IB H-1 Engine



H-1
Saturn I → IB Booster

Type: Gas Generator, Pump-Fed
Thrust: 165,000 → 205,000 lb SL
Specific Impulse: 260 → 263 sec SL
Propellants: LOX/RP-1
Design Year: 1958



Saturn I



Saturn IB

Initial Saturn Demonstration and Apollo Command Module Launch Vehicles for Earth-Orbit, Skylab, and Soyuz missions.



Saturn I Aft

Saturn I/IB H-1 Engine

1958 thru 1975



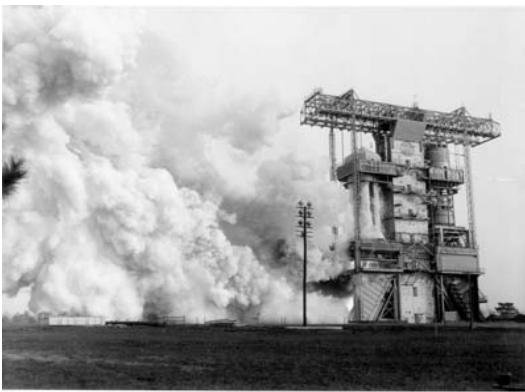
H-1C Inboard S-1B Engine - 1966 (1 of 4)



H-1 Engine Hot Fire Test in Canyon Area - 1967 (1 of 2)



S-1B Vehicle Assembly Sequence at MAF - 1967 (7a of 12)



S-1B Hot Firing at MSFC - 1965

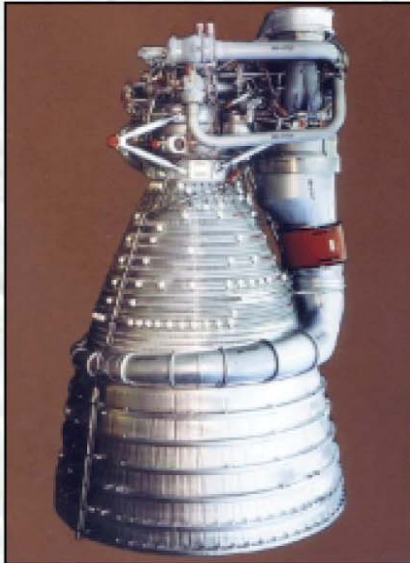


Saturn 1 Eight Engine H-1 Cluster - 1965



Saturn 5-1B Launch

Saturn V S-IC Stage F-1 Engine



F-1
Saturn V S-IC Stage Booster

Type: Gas Generator, Pump-Fed
Thrust: 1,522,000 lb SL
Specific Impulse: 265 sec SL
Propellants: LOX/RP-1
Design Year: 1959



Saturn V Apollo
Missions to the Moon.

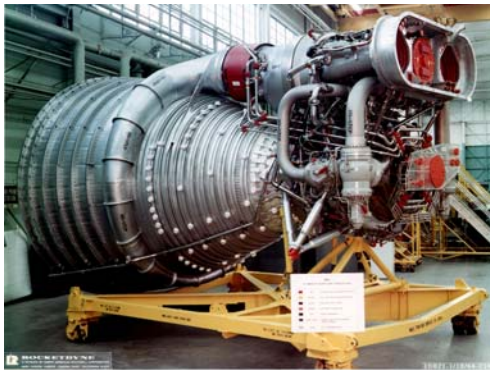


Saturn V Skylab
America's first
Space Station.



Saturn V S-IC Aft

Saturn V S-IC Stage F-1 Engine 1959 - 1973



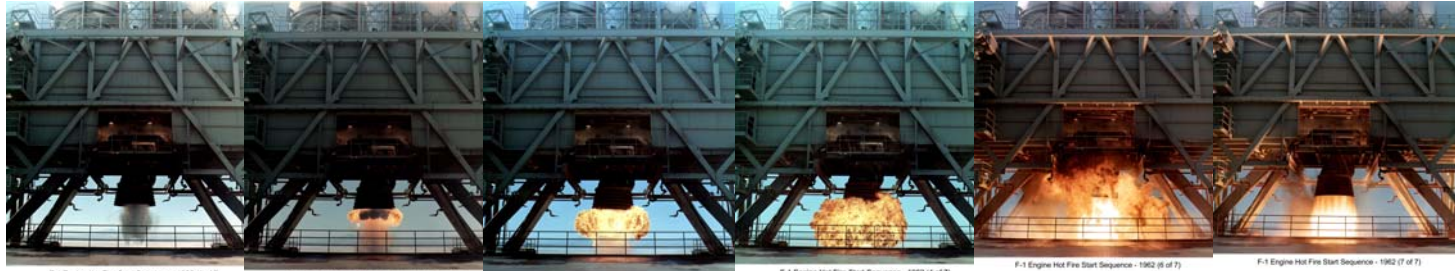
F-1 Engine - 1966



F-1 Engine Production Line - 1965 - 1968



Thermal Protection System (TPS) Installed on Single F-1 engine - 1965



F-1 Engine Hot Fire Start Sequence - 1962 (1 of 7)

F-1 Engine Hot Fire Start Sequence - 1962 (2 of 7)

F-1 Engine Hot Fire Start Sequence - 1962 (3 of 7)

F-1 Engine Hot Fire Start Sequence - 1962 (4 of 7)

F-1 Engine Hot Fire Start Sequence - 1962 (5 of 7)

F-1 Engine Hot Fire Start Sequence - 1962 (7 of 7)



F-1 Engine Hot Fire Test - 1962



F-1 Engine Horizontal Installation into S-1C Stage - 1965 (4 of 4)



S-1C Stage Rollout at Marshall Space Flight Center (MSFC) - 1966 (2 of 2)



S-1C-T Five F-1 Engine Hot Fire Cluster Test at Marshall Space Flight Center (MSFC) - 1965

Saturn S-IVB & S-II Stages J-2 Engine



J-2
Saturn V S-II & S-IVB Stage Engines
Saturn IB S-IVB Stage Engine

Type: Gas Generator, Pump-Fed
Thrust: 200,000 → 230,000 lb vac
Specific Impulse: 425 sec vac
Propellants: LOX/Hydrogen
Design Year: 1960



Saturn V Apollo



Saturn IB



Saturn V S-II Aft



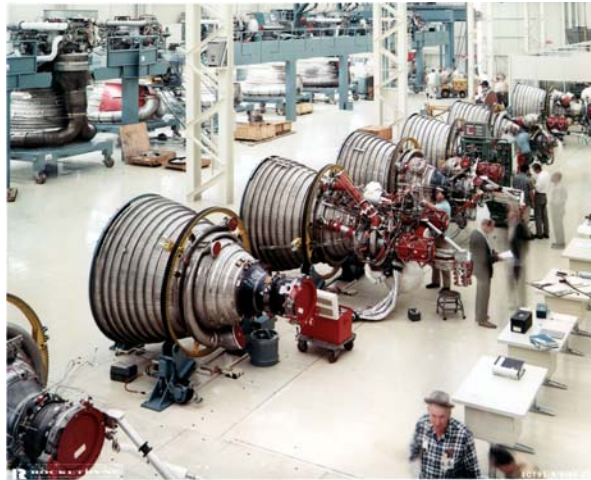
S-IVB Aft

Saturn S-IVB & S-II Stages J-2 Engine

1960 - 1975



J-2 Engine - 1965



J-2 Engine Production Line - 1966 (1 of 3)



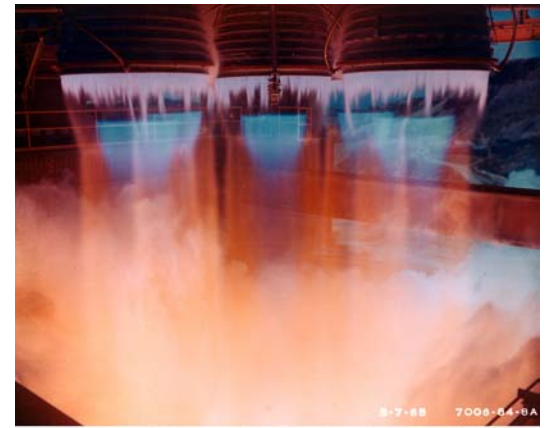
J-2 Engine Hot Fire



J-2 Cluster Engine Exit Cover Removal - 1965



Saturn V Second Stage (S-II) Aft - 1965



Coca Area - S-II Battleship J-2 Five Engine Cluster Hot Fire Test - 1965

Some of Rocketdyne's Small Engine - 1960's

										
THRUST, LB: PROPELLANTS: T/C TYPE: PROGRAM: DESIGN YEAR:	0.01 O ₂ /H ₂ /N ₂ S.S. ADV. TECH. - NASA 1969	1 N ₂ O ₄ / MMH BERYLLIUM ADV. TECH. - NASA 1967	5 N ₂ O ₄ / MMH BERYLLIUM ADV. TECH. - NASA 1966	18/ 23 N ₂ O ₄ / MMH BERYLLIUM PBPS 1966	25 N ₂ O ₄ / MMH ABLATIVE GEMINI AND GEMINI E 1963	25 N ₂ O ₄ / MMH ABLATIVE GEMINI 1963	25 N ₂ O ₄ / 50-50 ABLATIVE TRANSTAGE 1964	45 N ₂ O ₄ / 50-50 ABLATIVE TRANSTAGE 1964	50 N ₂ O ₄ / 75-25 N ₂ H ₄ -MMH ABLATIVE AGENA 1962	72 N ₂ O ₄ / MMH ABLATIVE SIVB 1965
										
THRUST, LB: PROPELLANTS: T/C TYPE: PROGRAM: DESIGN YEAR:	75 N ₂ H ₄ MONOPROP. STAINLESS STEEL ADV. TECH. 1968	85 N ₂ O ₄ / MMH ABLATIVE GEMINI 1963	93 N ₂ O ₄ / MMH ABLATIVE APOLLO 1964	100 N ₂ O ₄ / MMH ABLATIVE GEMINI 1963	100 N ₂ O ₄ / MMH BERYLLIUM ADV. TECH. - AF 1967	100 N ₂ O ₄ / MMH BERYLLIUM ADV. TECH. - NASA 1968	125 TO 80 IRFNA / HYDYNE REGENERATIVE DRONE / NAVY 1963	300 N ₂ O ₄ / MMH BERYLLIUM MARS MARINER 1968	318 N ₂ O ₄ / MMH BERYLLIUM PBPS 1966	700 TO 200 IRFNA/HYDYNE REGENERATIVE DRONE/NAVY 1963
										
THRUST, LB: PROPELLANTS: T/C TYPE: PROGRAM: DESIGN YEAR:	700 ClF ₃ / MHF-3 ABLATIVE CONDOR 1967	1000 N ₂ O ₄ / MMH BERYLLIUM ADV. TECH. - NASA 1966	1000 COMP. A / MMH BERYLLIUM ADV. TECH. - AF 1967	1600 N ₂ O ₄ / 50-50 ABLATIVE RESA-5 1969	3500 N ₂ O ₄ / 50-50 ABLATIVE APOLLO LM 1967	12,000 TO 6,000 H ₂ O ₄ - JP REGENERATIVE AIRCRAFT ROCKET 1955	10,000 - 1,000 N ₂ O ₄ - 50-50 ABLATIVE APOLLO LM 1963	12,000 F ₂ / N ₂ H ₄ REGENERATIVE NOMAD 1958	1,000 TO 287 CPF / MHF ABLATIVE ADV. TECH. - AF 1969	40,000 TO 90 IRFNA / UDMH ABLATIVE LANCE - XRL 1964

Interesting & Unique Engines



P8E-9
Lance Booster and Sustainer System

Type:	Pressure-Fed	
	Booster	Sustainer
Thrust:	46,200 lb SL	14-4,400 lb alt
Specific Impulse:	238 sec SL	227 sec alt
Propellants:	IFRNA/UDMH	IFRNA/UDMH
Design Year:	1964	1964



Lance
Surface-to-Surface Missile



Lance Propulsion System



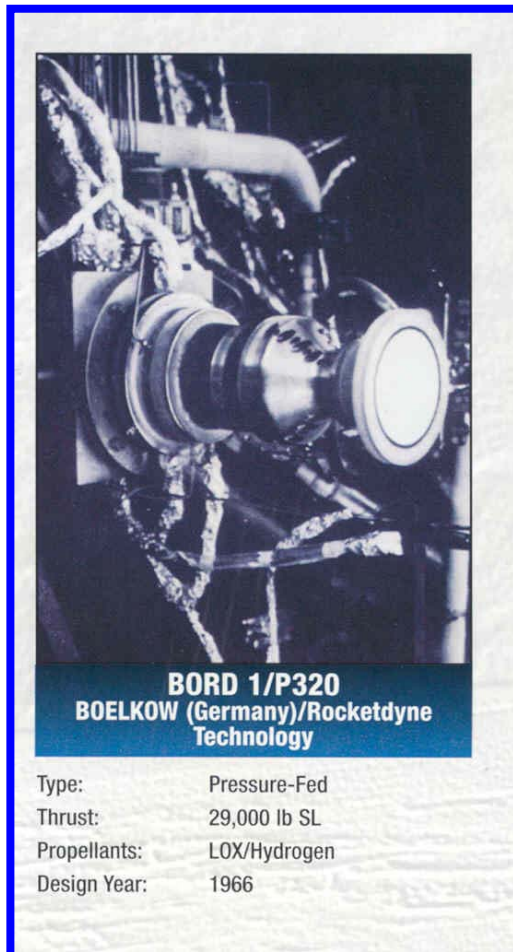
FLEXEM (RS-22)
Flexible Energy Management

Type:	Pressure-Fed	
	Booster	Sustainer
Thrust:	11,000 lb vac	267-4,000 lb vac
Specific Impulse:	275 sec vac	260 sec vac
Propellants:	ClF ₂ /MHF-5	ClF ₂ /MHF-5
Design Year:	1968	1968

Lance Engine Features

- Integrated coaxial booster/sustainer chambers
- Throttling pintle injector
- Ablative chambers
- Highest number of production units

Interesting & Unique Engines, Cont'd



Bord 1 Thrust Chamber

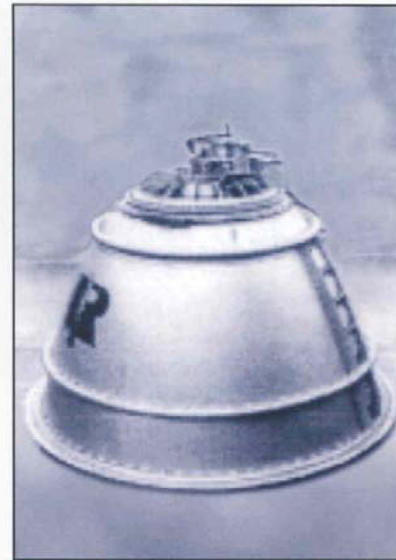
- Paved the way for current high performance milled channel combustion chambers
- High conductivity copper alloy liners
- Very high pressure O₂/H₂ - 4000 psi chamber pressure

Interesting & Unique Engines, Cont'd



**Expansion-Deflection
Booster**

Type: Pressure-Fed
Thrust: 50,000 lb SL
Propellants: NTO/Hydrazine (50%)
UDMH (50%)
Design Year: 1961

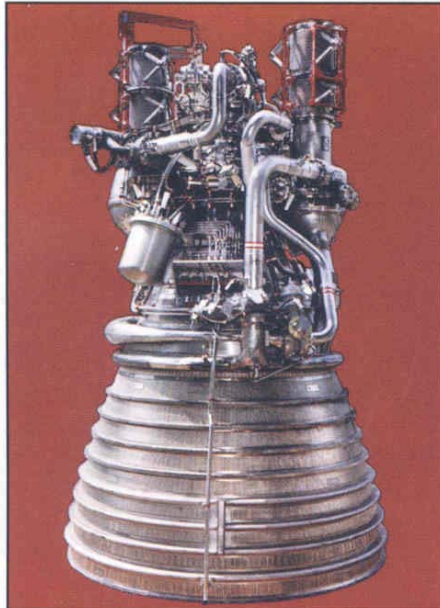


**Expansion-Deflection
Booster**

Type: Pressure-Fed
Thrust: 10,000 lb SL
Propellants: NTO/Hydrazine (50%)
UDMH (50%)
Design Year: 1961

Expansion-Deflection Thrust Chambers

Interesting & Unique Engines, Cont'd



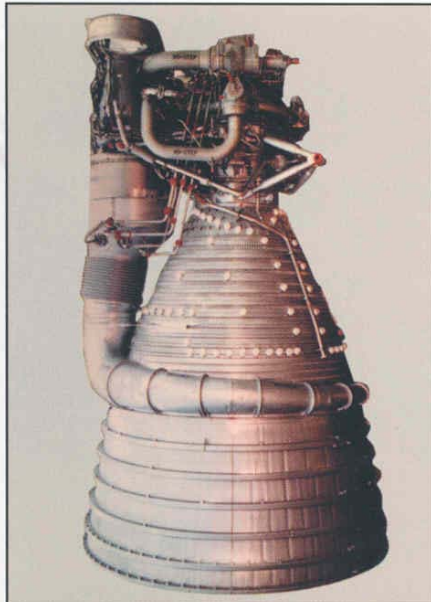
**J-2S
Booster**

Type: Tapoff, Pump-Fed
Thrust: 265,000 lb vac
Specific Impulse: 435 sec vac
Propellants: LOX/Hydrogen
Design Year: 1967
J-2X developed most simplification features for J-2S between 1964 and 1967.

J-2S Booster Engine

- Simplification of very successful J-2
- Gas generator turbine drive system removed
- Replaced with hot-gas tap-off system from main chamber to drive turbine
- Simplified chill and start sequence

Interesting & Unique Engines, Cont'd



**F-1A
Booster**

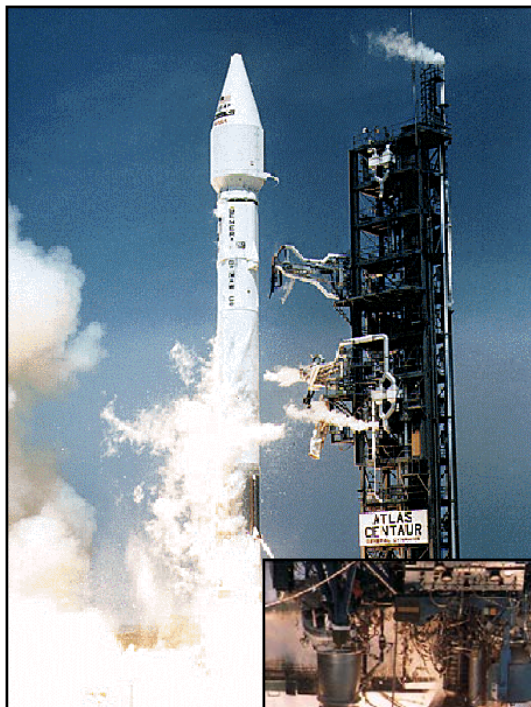
Type: Gas Generator, Pump-Fed
Thrust: 1,800,000 lb SL
Specific Impulse: 272 sec SL
Propellants: LOX/RP-1
Design Year: 1967

F-1A Booster

- Out growth of very successful F-1 program
- Next generation Mark 10A turbopump
- Up-rated from original 1.5 million LB thrust to 1.8 million LB thrust

Rocketdyne ELV Engines

Lockheed Martin



Atlas MA-5A



Boeing Expendable Launch Systems



Delta RS-27A



RS-27A



**Delta II
Space Launch Vehicle**



**Delta III
Space Launch Vehicle**

The Delta II and III first stages are powered by the RS-27A booster engine. Two vernier engines provide roll and attitude control.



RS-27A Delta Vernier Engine



**RS-27A
Delta Booster**

Type:	Gas Generator, Pump-Fed Booster	Vernier
Thrust:	200,000 lb SL	1,015 lb SL
Specific Impulse:	255 sec SL	207 sec SL
Propellants:	LOX/RP-1	LOX/RP-1
Design Year:	1987	1987

MA-5A



Atlas II Space Launch Vehicle

The Atlas II launch vehicle is powered by the MA-5A propulsion system, consisting of two booster engines and one sustainer engine.



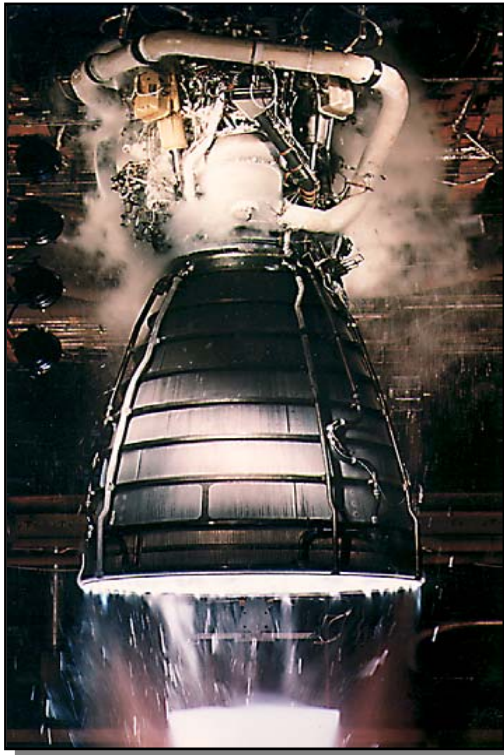
Atlas IIAS Booster Aft



**MA-5A (RS-56)
Atlas Booster**

Type:	Gas Generator, Pump-Fed	
	Booster	Sustainer
Thrust:	429,500 lb SL	60,500 lb SL
Specific Impulse:	265 sec SL	220 sec SL
Propellants:	LOX/RP-1	LOX/RP-1
Design Year:	1988	1988

Space Shuttle Main Engine (SSME)



- **World's only operational, reusable liquid oxygen/hydrogen booster designed for human space flight**
- **World class thrust and specific impulse performance**
- **World's most reliable booster engine**

The SSME Maintains United States Leadership in Global LOX/Hydrogen Booster Technology

SSME



SSME (RS-24)
Space Shuttle Main Engine

Type: Staged Combustion, Pump-Fed
Thrust: 512,264 lb vac (109% Power Level)
Specific Impulse: 453 sec vac
Propellants: LOX/Hydrogen
Design Year: 1972

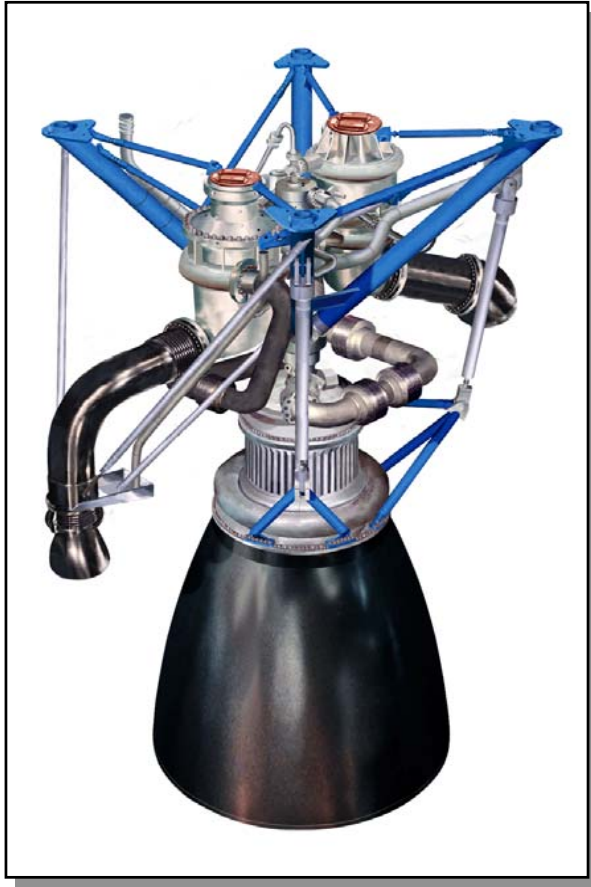


Space Shuttle in Flight



Space Shuttle Orbiter Aft in Flight

RS-68 Engine Design



- **Low-cost simplified liquid oxygen/liquid hydrogen engine**
- **Minimal parts count & low fabrication cost**
- **Low to moderate chamber pressure**
- **Not performance driven**

RS-68



RS-68
Delta IV Development Booster

Type:	Gas Generator, Pump-Fed
Thrust:	650,000 lb SL
Specific Impulse:	365 sec SL
Propellants:	LOX/Hydrogen
Design Year:	1998



Small lift
launch
vehicle

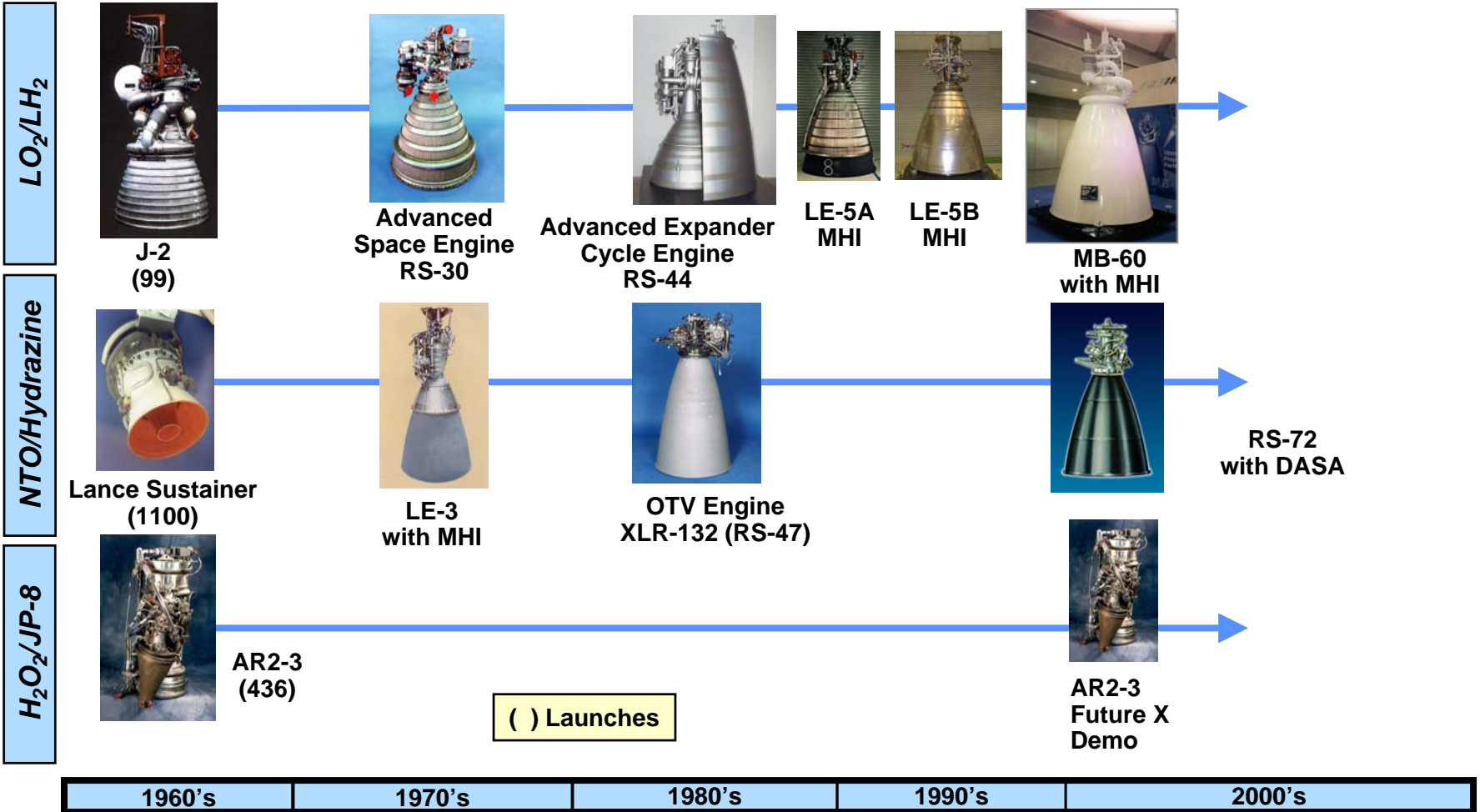
Medium
lift launch
vehicle

Heavy lift
launch
vehicle

Delta IV Launch Vehicles

Boeing small, medium, and heavy lift launch vehicles are configured with common booster cores powered by the RS-68. The design of the engine drastically reduces the number of parts, resulting in lower development and production costs.

Upper Stage Propulsion Evolution

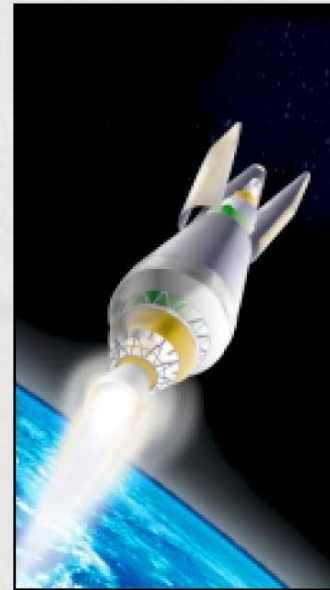


MB-60



MB-60
MHI (Japan)/Boeing
Cryogenic Upper Stage

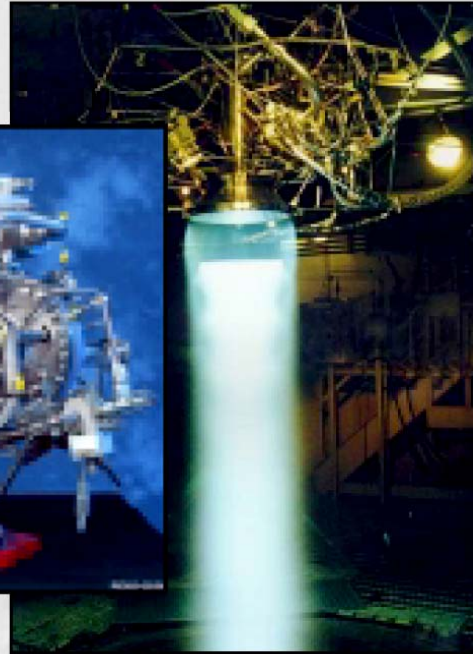
Type: Expander Bleed,
Pump-Fed
Thrust: 60,000 lb vac
Specific Impulse: 467 sec vac
Propellants: LOX/Hydrogen



Boeing Delta IV

Boeing Delta IV medium and heavy lift launch vehicle upper stage configurations will be enhanced by implementing a higher thrust, higher performance cryogenic upper stage engine.

RS-72



RS-72
Astrium GmbH. (Germany)/Rocketdyne
Upper Stage

Type:	Gas Generator, Pump-Fed
Thrust:	12,450 lb vac
Specific Impulse:	338 sec vac
Propellants:	NTO/MMH

AR2-3



AR2-3A
Future-X Demonstrator
Engine

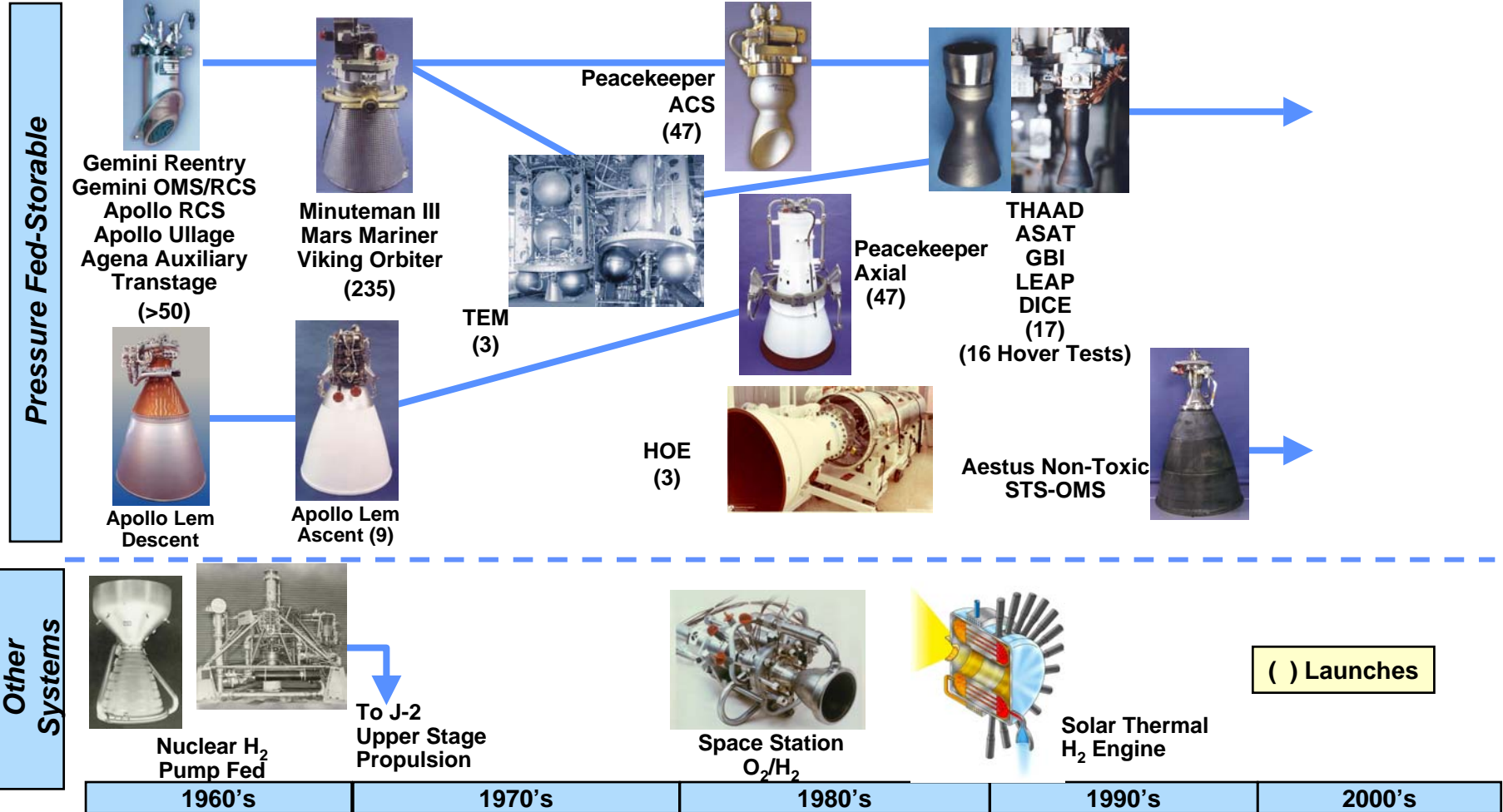
Type: Gas Generator, Pump-Fed
Thrust: 2,150-6,600 lb alt
Specific Impulse: 245 sec alt
Propellants: Hydrogen Peroxide/JP-8
Heritage technology is in evaluation for current applications.



NASA/Boeing X-37

The NASA/Boeing X-37 Reusable Upper Stage Vehicle can deliver small payloads to orbit, sustain on-orbit operations, and return payloads to Earth.

Space Propulsion Evolution



KEW-3 & KEW-4



KEW-3
Kinetic Energy Propulsion

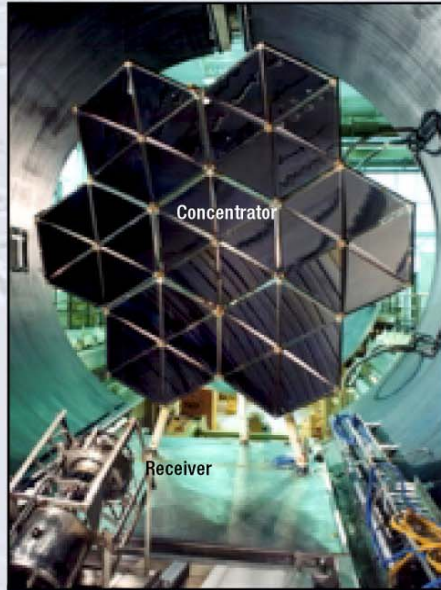
Type: Pressure-Fed
Thrust: 100 lb vac
Specific Impulse: 283 sec vac
Propellants: NTO/MMH
Design Year: 1991



KEW-4
Kinetic Energy Propulsion

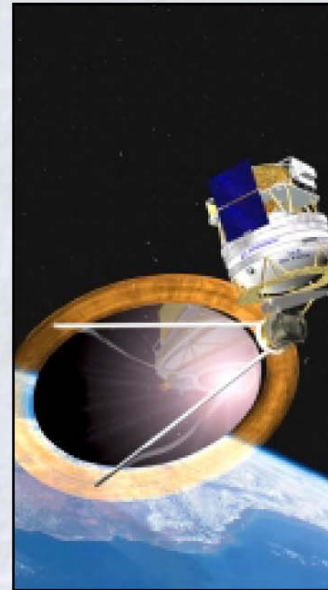
Type: Pressure-Fed
Thrust: 500 lb vac
Specific Impulse: 235 sec vac
Propellants: NTO/MMH
Design Year: 1993

RS-77



RS-77
Solar Thermal Engine

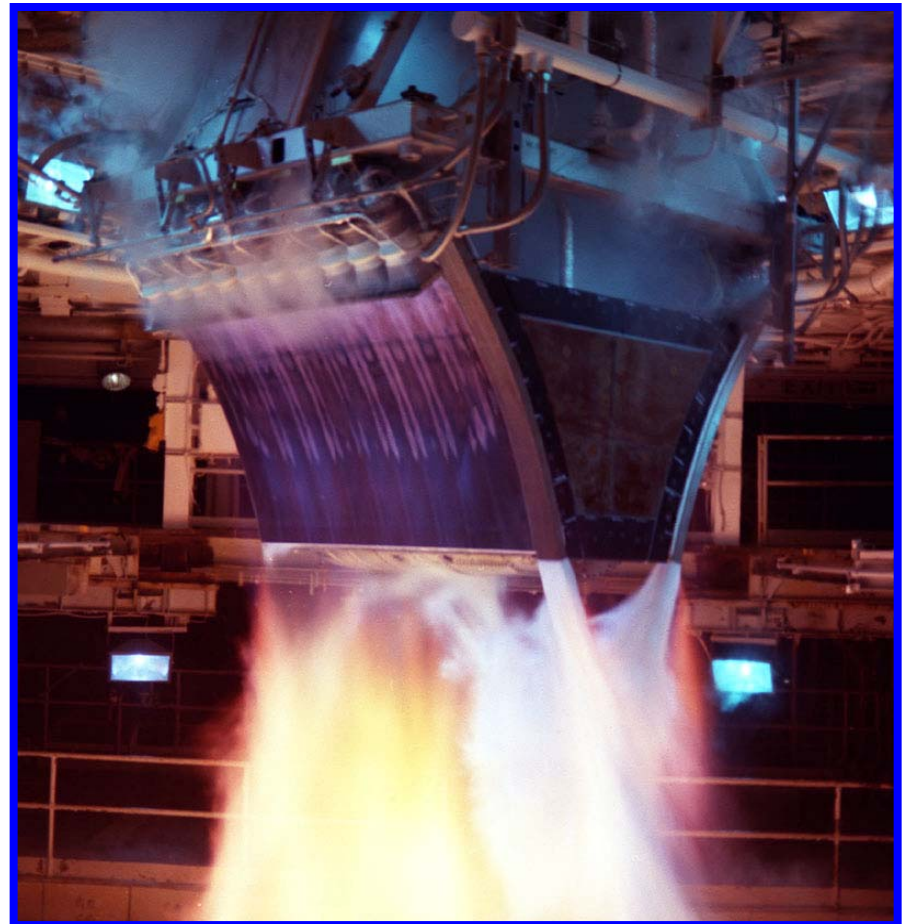
Type: Pressure-Fed
Thrust: 5-40 lb vac
Specific Impulse: 750-870 sec vac
Propellant: Hydrogen



Solar Orbit Transfer Vehicle (SOTV)

The SOTV will transfer satellites from low to high Earth orbits at twice the propulsive efficiency and generate electrical energy once on-orbit with its bimodal solar thermal engine.

X-33 Aerospike



Rocketdyne Liquid Propulsion Systems Represent Over 50 Years of Leading Technology

- **From 0.01 LB thrust space engines to 1.8 million LB thrust F-1A booster**
- **Nearly all propellant combinations: from exotic storables, tri-dyne, LOX/kerosene, LOX/hydrogen, peroxide/hydrocarbons, to LOX/alcohols and everything in between**
- **Nearly all engine cycles: from pressure fed, gas generator, fuel rich staged, “oxidizer rich” staged, various expanders, self pressurizing, hot gas tap-off, to full flow (combined fuel and oxidizer rich) staged**
- **Nearly all thrust chamber configurations: from conventional, dual bell, Aerospike, linear Aerospike, concentric booster/sustainer, to expansion-deflection**



Transient Mathematical Modeling for Liquid Rocket Engine Systems: Methods, Capabilities, and Experience

Authors: David C. Seymour, ERC, Inc. (NASA retired)
 Michael A. Martin, NASA MSFC
 Huy H. Nguyen, NASA MSFC
 William D. Greene, NASA MSFC



***Fifth International Symposium on Space Propulsion
Chattanooga, Tennessee, USA***



Who we are...

National Aeronautics and Space Administration (NASA)



George C. Marshall Space Flight Center (MSFC),
Huntsville, AL



Space Transportation Directorate



Vehicle and Engine Systems Development Department

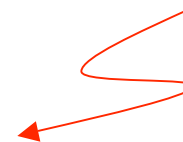


Systems Analysis Group



Engine and Motor System Analysis Team

We Are Here!





Fifth International Symposium on Space Propulsion Chattanooga, Tennessee, USA



Engine and Motor System Analysis Team: Recent Liquid Rocket Engine Experience

Space Shuttle Main Engine (SSME)

- Lox-Hydrogen Staged Combustion
- Contractor: Rocketdyne and Pratt & Whitney
- Operational – large experience base

RS-83

- Lox-Hydrogen Staged Combustion
- Contractor: Rocketdyne
- Completed study

COBRA

- Lox-Hydrogen Staged Combustion
- Contractor: Pratt & Whitney
- Completed study.

Integrated Powerhead Development (IPD)

- Lox-Hydrogen Full-Flow Staged Combustion
- Joint NASA and US Air Force project
- Contractor: Rocketdyne and Aerojet
- Component testing underway

RS-84

- Lox-Kerosene Ox-Rich Staged Combustion
- Contractor: Rocketdyne
- Component testing underway

TR107

- Lox-Kerosene Ox-Rich Staged Combustion
- Contractor: Northrup-Grumman / TRW
- Ongoing study contract

MC-1 (Fastrac)

- Lox-Kerosene Gas Generator
- Contractor: in-house project
- 6 engine tests



Fifth International Symposium on Space Propulsion Chattanooga, Tennessee, USA



Introduction: Liquid Rocket Engine Transient Modeling

- Liquid rocket engine development is expensive under the best of circumstances.
- The “Test-Fail-Fix” method is not the best of circumstances.
- Analytical modeling, specifically transient system modeling, is a means to overcome this.
- Over the past two decades, MSFC has dedicated significant resources to the development of our transient modeling capabilities.

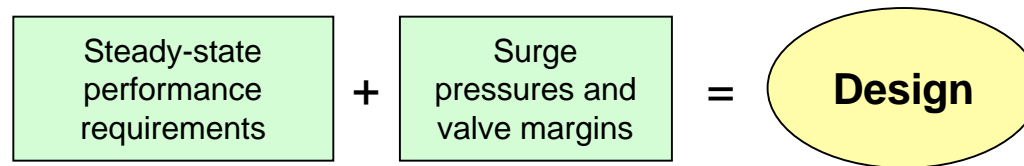


- Space Shuttle Main Engine (SSME) was developed in the mid-1970's.
- It took about 50 tests, lots of hardware, and a year of effort to get the SSME through a repeatable start transient.
- In the 1990's, the MSFC-developed MC-1 engine benefited from the involvement of transient systems modeling in the development process.

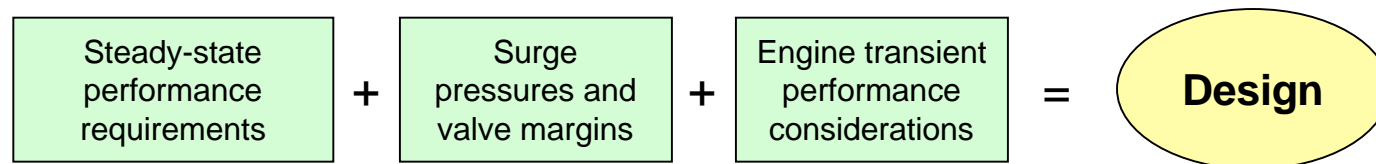


Transient Modeling and Design Considerations

- Typical rocket engine design practice is based primarily on steady-state performance (with some allowance made for surge pressures)



- It is thus often the task of the transient modeling analyst to figure out how to start and shutdown the engine safely with the hardware as given.
- A better approach is to involve transient analysis as a part of the development program early in the process.



- Examples:
 - IPD – spin-assist start
 - MC-1 – addition of rotary damper to valves



Fifth International Symposium on Space Propulsion Chattanooga, Tennessee, USA

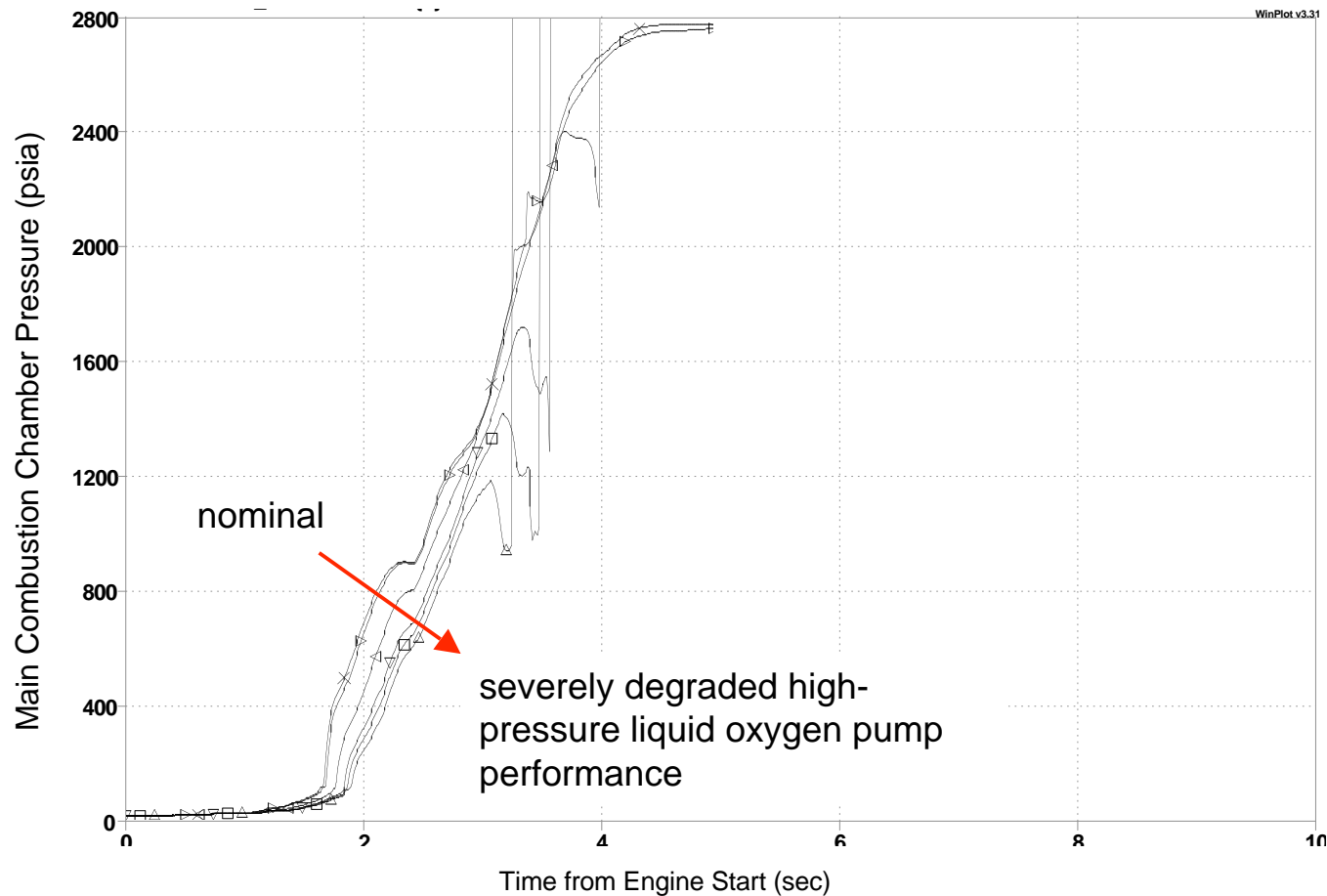


Operations and Failure Considerations

- One thing that definitely cannot be explored, even if a program did have an infinite budget, is the full territory of engine failure modes.
- Instantly catastrophic failures are an inherent element of liquid rocket engine development, but not all failures fall within this category.
- Only through the use of a transient model can “what if” scenarios be explored.
 - What if pump or turbine performance is suddenly degraded?
 - What if ignition of a combustion chamber fails?
 - What if there is a deviation from the scheduled valve sequence?
- The goal is always to avoid a catastrophic situation if at all possible.
 - How can an off-nominal situation be identified?
 - How can a safe shutdown be implemented from these conditions?
 - Are there situations in which shutdown itself causes a catastrophic condition?
(Example: SSME shutdown during start transient)



Failure Scenario Considerations: **SSME Example**

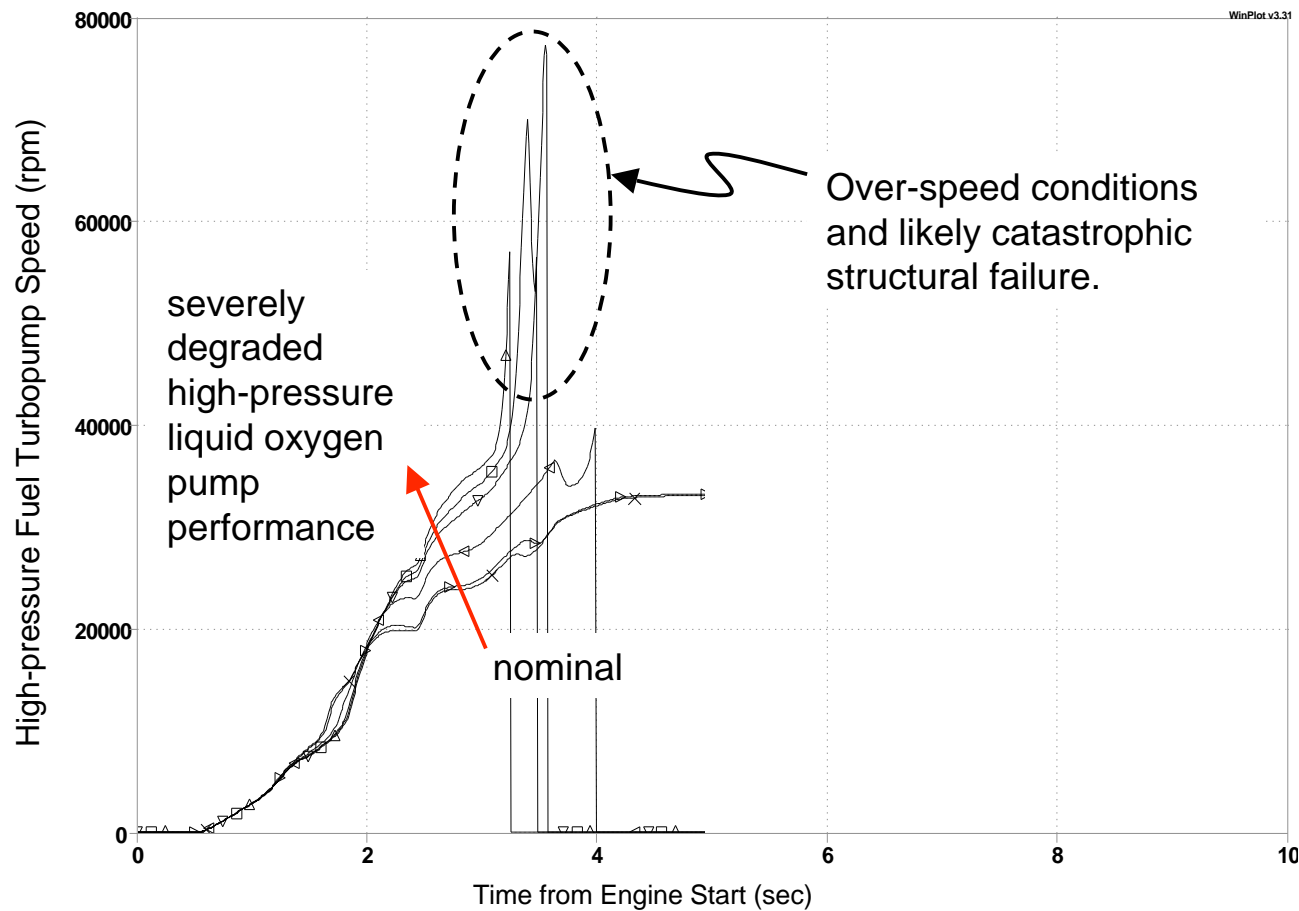




**Fifth International Symposium on Space Propulsion
Chattanooga, Tennessee, USA**



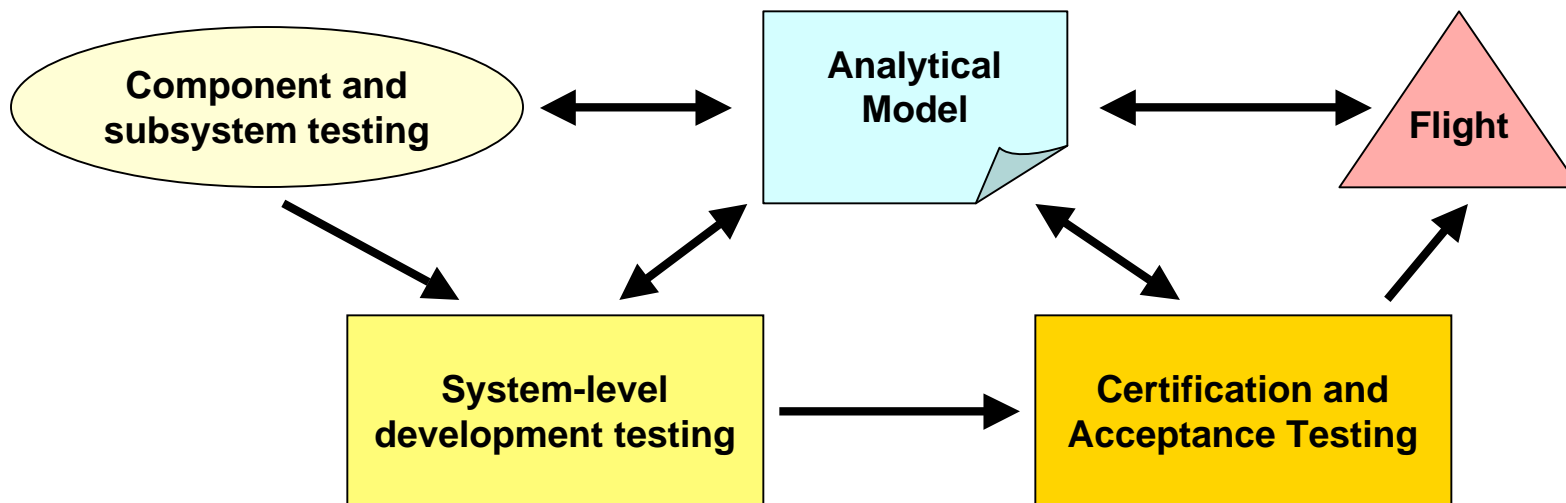
Failure Scenario Considerations: **SSME Example (continued)**





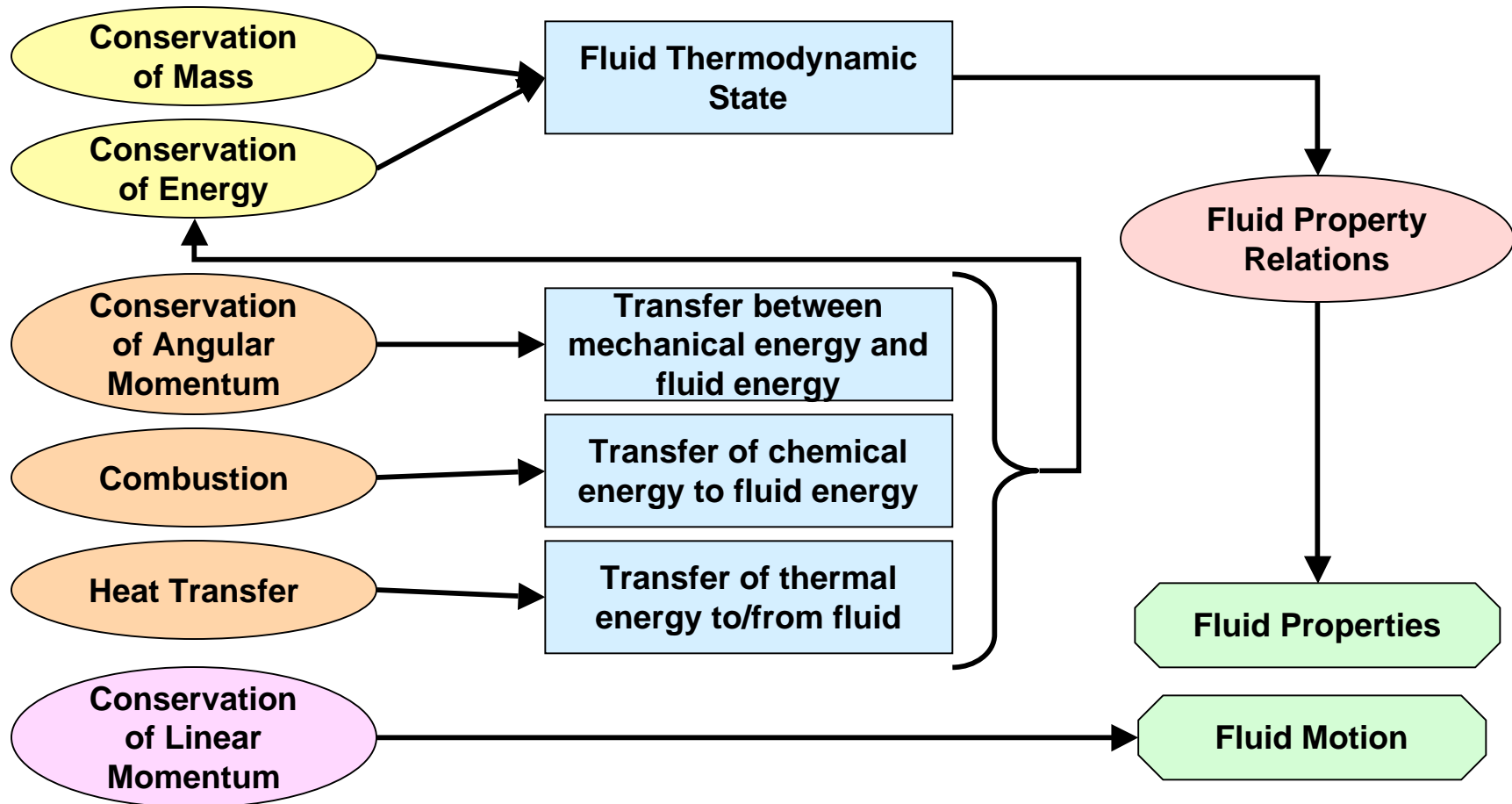
Development Testing and Design Verification

- When engine design requirements cannot be verified by test, then analysis must be used to fill the void.
- However, analysis cannot stand alone. It must be informed by the testing that is performed at the component, subsystem, and system levels.
- Further, the analytical models continue to be informed by engine performance throughout the mission life of the engine. (Example: [SSME DTM – MSFC derived](#))



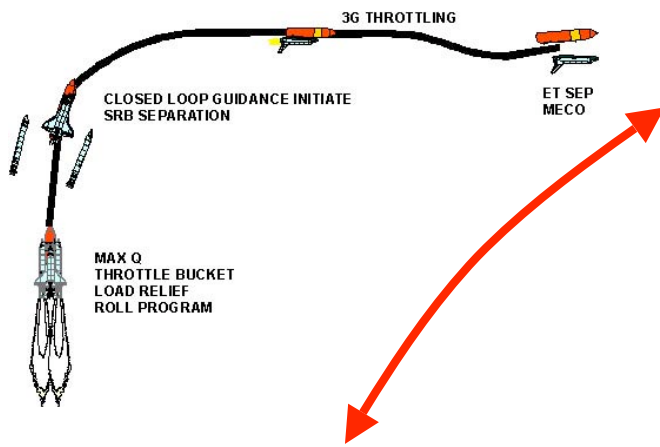


Transient Modeling Overview



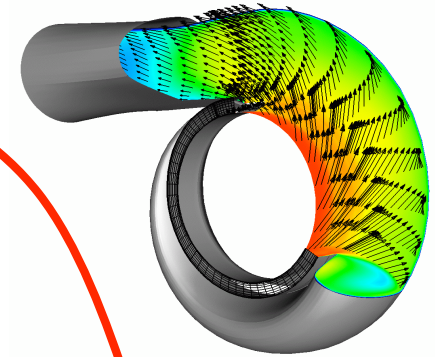


Place of Engine System Modeling within the Community



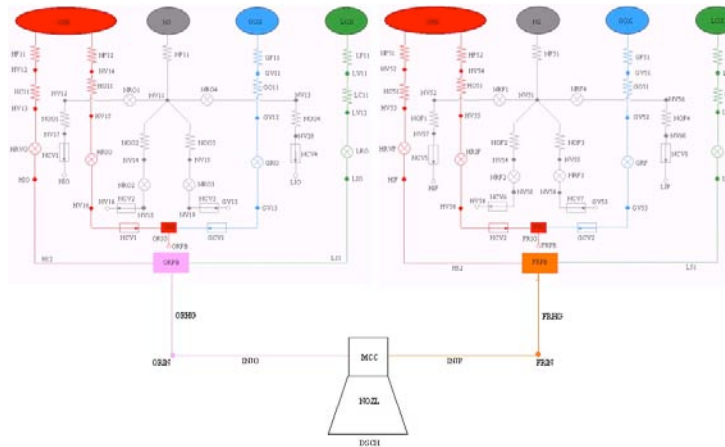
Engine System Modeling (Also called “Lumped-Parameter” Modeling)

- Engine environments at the homogeneous volume level
- Moderate fidelity
- Scope is the engine system
- It is not:
 - Method of characteristics modeling
 - Incompressible fluids modeling
 - Fluid phase-volume modeling



Mission Analysis

- Mission environments
- Low fidelity (w/ regards to engines)
- Global scope



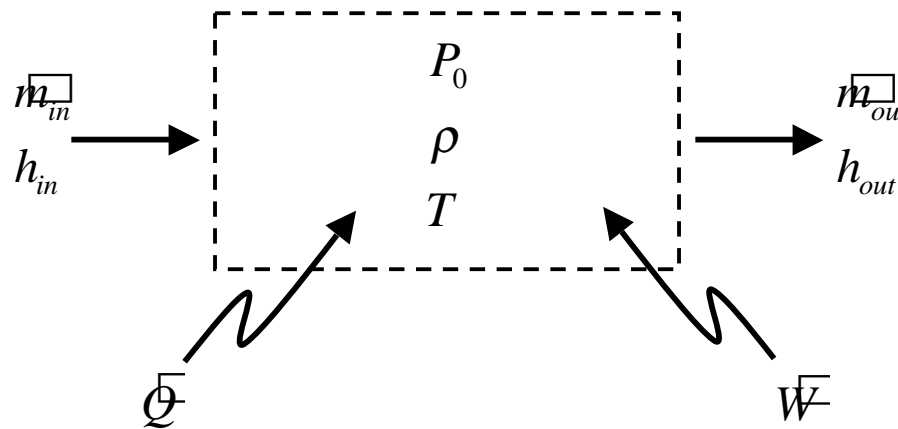
Computational Fluid Dynamics

- Local environments
- Very high fidelity
- Limited scope



Conservation of Mass and Energy

Homogeneous Control Volume: Conditions within the volume determine the fluid state.



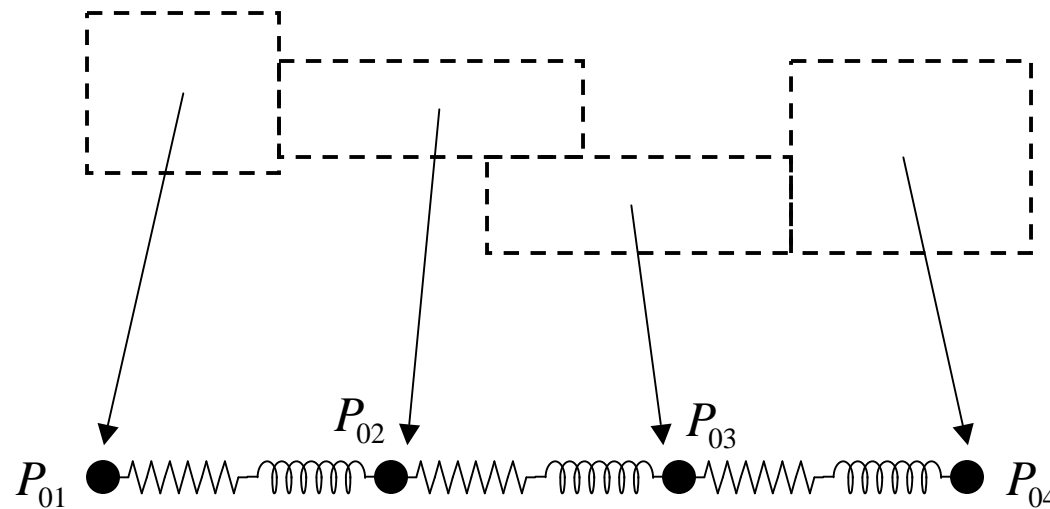
$$\frac{\partial \rho}{\partial t} = \frac{1}{V} (\sum \dot{m}_{in} - \sum \dot{m}_{out})$$

$$\frac{\partial u_{CV}}{\partial t} = \frac{\sum (\dot{m} h_0)_{in} - \sum (\dot{m} h_0)_{out}}{\rho_{CV} V} + \frac{W_{net} + Q_{net} - u_{CV} (\sum \dot{m}_{in} - \sum \dot{m}_{out})}{\rho_{CV} V}$$



Conservation of Linear Momentum

Flow Circuit: Series of homogeneous volumes represented as nodes within a circuit connected by elements of flow resistance and flow inductance.



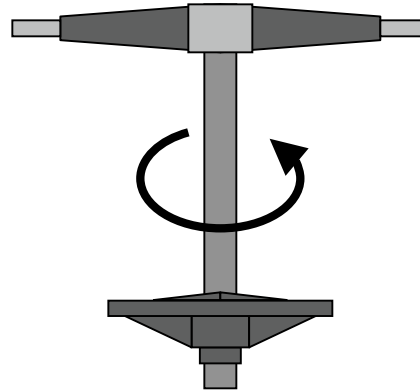
$$\frac{\partial \bar{m}_{ij}}{\partial t} = \frac{A}{L} \left[(P_{0i} - P_{0j}) - \frac{R \bar{m}_{ij}^2}{\rho} \right]$$

One form of many for describing
flow between volumes



Conservation of Angular Momentum

Rotating Machinery: Typically consisting of a turbine element and a pump element.



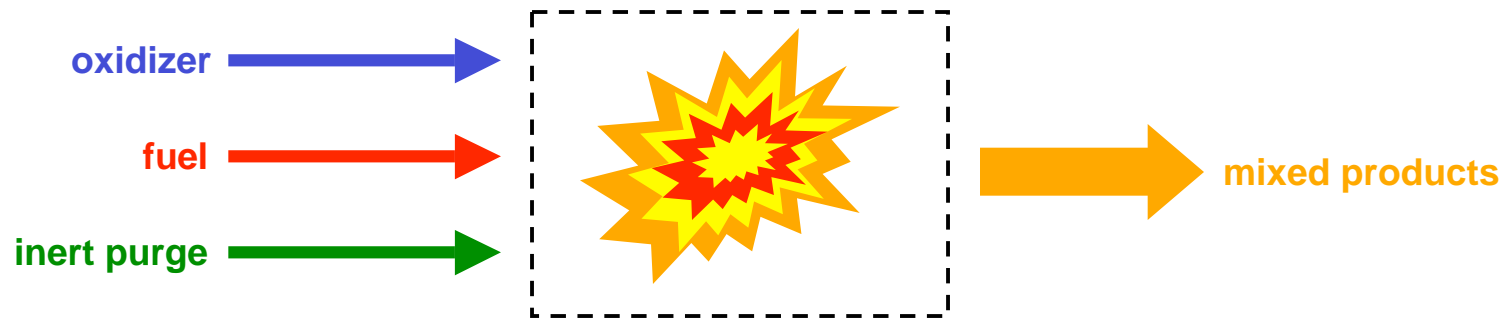
$$\frac{\partial N}{\partial t} = \frac{\sum T_{turbine} - \sum T_{pump}}{I}$$

Also, for turbomachinery performance maps are necessary to form a complete system of equations.



Combustion Devices

*Special Homogeneous Volume -- Combustion Zone:
 Mixing of several constituents and often inert purge
 gases plus the addition of chemical energy to the flow.*



$$OFR = \frac{M_{ox}}{M_{total}} = \frac{M_{ox}}{M_{ox} + M_{fuel}}$$

$$\frac{\partial(OFR_{CV})}{\partial t} = \frac{(\sum \dot{m}_{ox_{in}} - \sum \dot{m}_{ox_{out}})}{M_{total}}$$

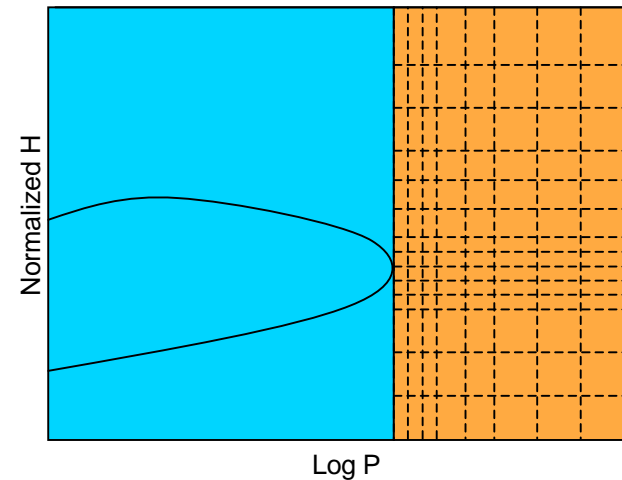
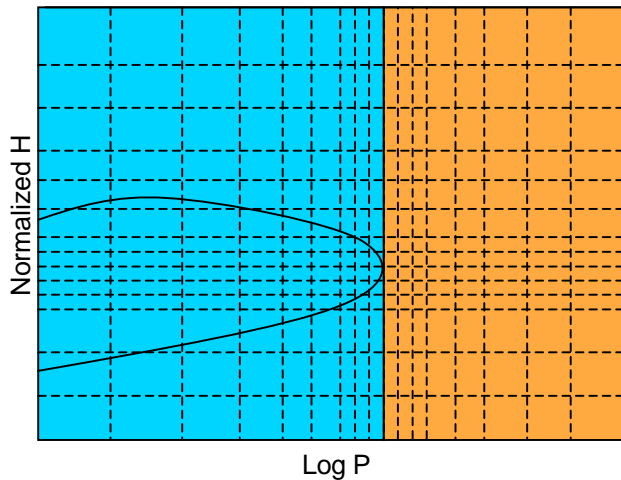
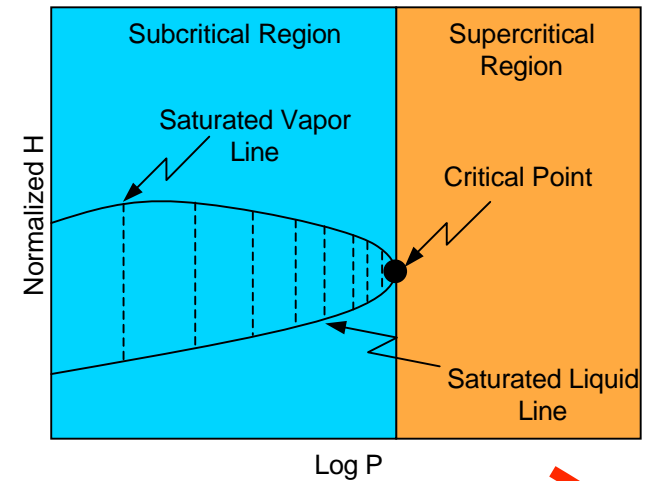
$$OFR_{CV} \frac{(\sum \dot{m}_{total_{in}} - \sum \dot{m}_{total_{out}})}{M_{total}}$$

To the usual Conservation of Mass and Energy considerations must be added a description of mixed fluid composition. Oxidizer fraction (OFR) is the factor.



Fluid Properties

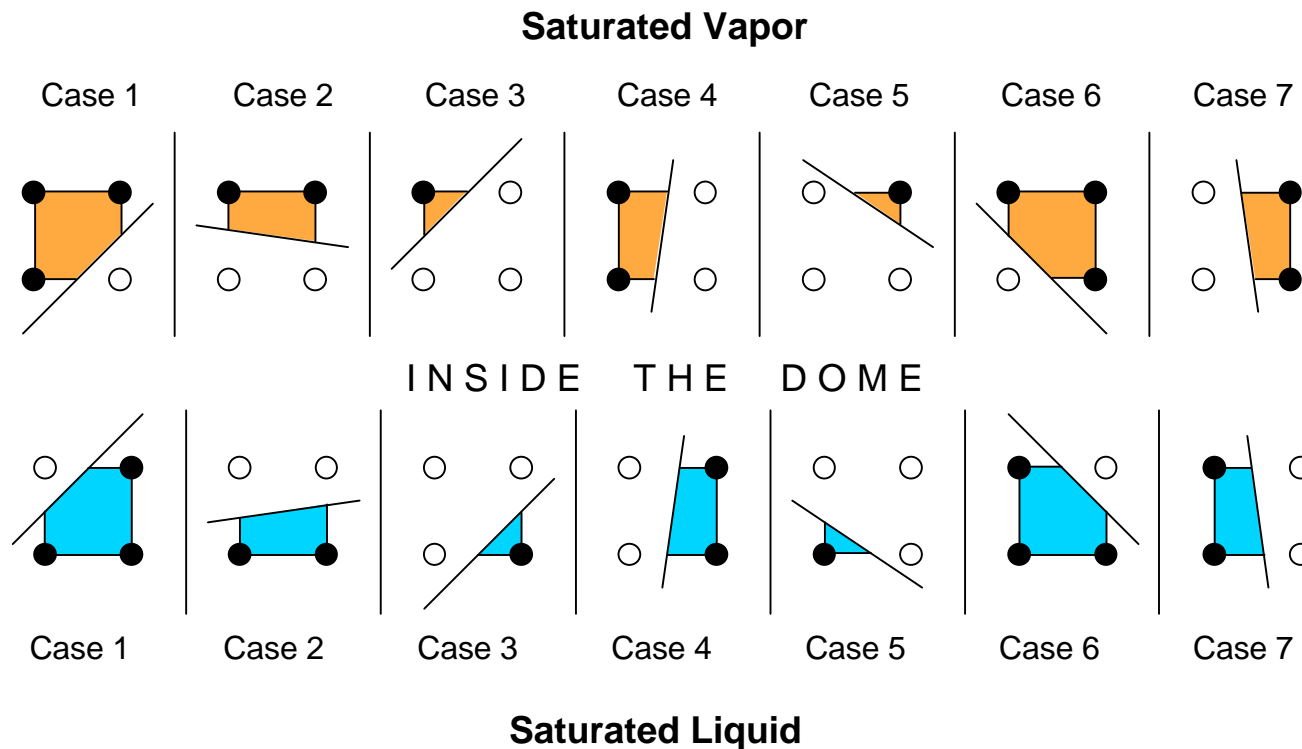
- Fluid property relations are the connection between mathematics and actual fluids.
- In order to run efficient analyses, property tables are used.
- MSFC has developed means of automatically generating these tables to a specified level of interpolation error.





Fluid Properties (continued)

- One tricky aspect of creating propellant tables is dealing with the phase-change dome.
- MSFC has developed interpolation methods for handling these cases where points of interest straddle the phase-change line.





Fifth International Symposium on Space Propulsion Chattanooga, Tennessee, USA



Numerical Issues and Integration

- Engineers at MSFC most commonly use implicit integration for rocket engine transient modeling.
 - Allows larger time step but requires an iteration at each time step
 - Overall more efficient because the number of iterations is automatically variable as the solution proceeds. Equivalent methods of varying the explicit integration time step are not available.
- Current practice is to use a multivariable Newton-Raphson iteration method in conjunction with the Broyden technique of Jacobian evolution during solution progression.
 - Iteration independents are normalized pressure and fluid enthalpy.
 - Iteration dependents are the normalized deviations of the states from the implicit integrated values.
 - To avoid infinite slopes within the Jacobian, flow rate equations are linearized near zero pressure differential conditions.



Fifth International Symposium on Space Propulsion Chattanooga, Tennessee, USA



Future Work

- Upgrades to ROCETS (ROCKET Engine Transient Simulation) code – nonproprietary code open to U.S. Government agencies and U.S. companies.
- Usability improvements
 - Development of a graphical users interface for model creation and results interpretation.
- Modeling improvements
 - Development of a Generalized Combustion (GCOMB) approach to handle complex control volumes in a combustion zone.
 - GCOMB handles arbitrary mixtures of reactants, combustion products, and inert purge fluids.
- Numerical scheme improvements
 - Working with a number of partners on improved computational and mathematical approaches to solving nonlinear sets of equations.
 - Includes line back-search applied to Newton-Raphson-Broyden, simulated annealing, embedding procedure for parametric solutions, and various genetic algorithms.

Transient Mathematical Modeling for Liquid Rocket Engine Systems: Methods, Capabilities, and Experience

Michael A. Martin, Huy H. Nguyen, and William D. Greene
NASA Marshall Space Flight Center, Huntsville, AL

David C. Seymour (NASA-retired)
ERC, Inc., Huntsville, AL

Abstract

The subject of mathematical modeling of the transient operation of liquid rocket engines is presented in overview form from the perspective of engineers working at the NASA Marshall Space Flight Center. The necessity of creating and utilizing accurate mathematical models as part of liquid rocket engine development process has become well established and is likely to increase in importance in the future. The issues of design considerations for transient operation, development testing, and failure scenario simulation are discussed. An overview of the derivation of the basic governing equations is presented along with a discussion of computational and numerical issues associated with the implementation of these equations in computer codes. Also, work in the field of generating usable fluid property tables is presented along with an overview of efforts to be undertaken in the future to improve the tools use for the mathematical modeling process.

Nomenclature

dt	Time increment	L	Length
h_0	Total Enthalpy	M	Mass
\dot{m}	Mass Flow Rate	MR	Mixture Ratio
t	Time	N	Rotational Velocity
u	Internal Energy	OFR	Oxidizer Fraction
\hat{u}	Fluid Velocity	P_0	Total Pressure
A	Area	\dot{Q}	Heat Transfer
CV	Control Volume	R	Fluid Resistance
\dot{E}	Energy Flux	T	Shaft Torque
F	Force	V	Volume
I	Moment of Inertia	\dot{W}	Work
		Y	Generic Fluid Property
		ρ	Density
		τ	Time Constant

This is a work of the U.S. Government and is not subject to copyright protection in the United States. Foreign copyrights may apply.

Introduction

The development of complex and expensive machinery such as liquid propellant rocket engines within the real world of limited budgets requires that analytical tools be used to facilitate the process as much as possible. Rocket engine project managers expect and plan to have detailed engine transient analysis available early in their development program. Because building hardware and conducting testing is exorbitantly expensive, they typically budget only a few tests to develop the engine start and shutdown sequences and they do not plan for the possibility of major hardware damage as part of the process. They can do this because the U.S. rocket engine community has actively developed analytical tools to take advantage of the tremendous increase in computer power over the last twenty years.

At the NASA Marshall Space Flight Center (MSFC), engineers recognized about two decades ago that new ways of rapidly developing moderately detailed models of new engines was needed. Although monetary resources have been very limited, engineers have continued to pursue this goal and today possess very powerful tools to offer the prospective liquid rocket engine program manager.

Despite all of the work to date, however, rocket engine transient analysis remains a very challenging discipline. While steady-state tools have evolved almost to the point that any engineer can use them, transient analysis still requires dedicated specialists experienced in transient analysis to get useful results. The transient analyst must develop and manage a large amount of input data, describe complex physics, and deal with challenging computational and numerical issues. All mathematical modeling requires the utilization of some level of approximation and selecting

the right approximation to the complex physics involved in transient analysis is critical and often unique to the model being developed. The tools developed at MSFC allow the specialist to choose between common generic approximations or generate and implement their own versions.

Having detailed, reliable transient analysis available during the design phase, prior to hardware testing is enormously valuable. For example, the initial design and testing of the Space Shuttle Main Engine (SSME), shown in Figure 1, did not benefit significantly from such analysis. About a year of time, the accumulation of approximately fifty tests, and a significant amount of engine hardware were required to get the engine through a reasonable and repeatable start transient. This was not the fault of the transient analysts, they were exceptionally capable, but rather due to the very limited computer power available at the time.



Figure 1, Space Shuttle Main Engine (SSME)

Subsequent engine development programs, such as the MSFC-developed MC-1 (also called Fastrac), shown in Figure 2, although few in number and of simpler designs, have demonstrated dramatically lower development costs in part due to advances in engine transient modeling analyses and the computers to drive them. Further, this approach of emphasizing transient model development early in the engine design period has become the standard process followed for the next generation of rocket engines being pursued through the NASA Next Generation Launch Technology Program.



Figure 2, MC-1 (Fastrac) thrust chamber assembly being tested at MSFC

Design Considerations

Typical design practice for liquid rocket engines dictates that with the exception for surge pressures and valve margins, most engine components are designed to meet steady-state performance requirements. Thus, most engine elements are not been designed with start and shutdown transient environments in mind. Thus, it becomes the task of the transient analyst to take given component capabilities and find start and shutdown sequences that are safe for the

components and still meets all other performance requirements.

During the preliminary design phase, engine system analysis may be required to set basic engine requirements. For example, in the joint NASA and Air Force Integrated Powerhead Development (IPD) engine program, transient system analysis showed that an engine start sequence based on tank pressure head alone was a risky proposition. This analysis was used to justify the inclusion of provisions for turbopump spin-assist into the engine and facility development.

For most engine development programs, as the engine design matures so does the model detail and fidelity. Model sensitivity analyses can point to component characteristics most critical to successful, repeatable starts and shutdowns.

An example of this can be found during the MC-1 development. Early flow tests of the main propellant valves showed that the valves were “jerking” open instead of opening in a smooth, controlled manner. Simulating this valve behavior in the engine transient model showed that this was an undesirable condition. The quickly opening valves, combined with a helium spin-start on the turbine, resulted pump cavitation. Using the same codes that are used for engine transient models, a detailed transient model of the pneumatic valve itself was able to duplicate the phenomenon. One potential fix was to add a rotary damper to the valve. This fix was added to the valve model to verify the results prior to testing. After adding the rotary damper to the actual valve, the valves opened smoothly. Thus, the model aided in the design of the valve prior to engine hot-fire testing. The model was used not only to show the effects of the valve design on the engine system, but was also used in fixing the design flaw.

The transient system mathematical model predictions are key inputs into the initial engine system test plan and are a vital part of post-test analysis. Final engine start and shutdown sequences are, of course, verified by test. However, some off-nominal start or shutdowns may be impossible, impractical, or unsafe to demonstrate with actual engine hardware and must be verified by the transient model alone.

Design Verification and Operation

When meeting the engine design requirements that cannot be verified by test, it is standard practice to use analysis to fill the void. The transient engine model is anchored to the available test data, specifically for conditions as close as possible to the verification condition, and then used to predict the engine operation at the verification condition.

This approach was taken for SSME to verify safe engine flight shutdown under liquid oxygen depletion conditions. Several attempts to simulate the zero-g flight engine feedline conditions on a ground test stand were made. However, none were judged to satisfactorily simulate the behavior of the saturated liquid oxygen in the feedline and its effect on the low-pressure liquid oxygen pump performance. The transient analysis on this issue performed by Rocketdyne, the SSME prime contractor, was a vital part of the SSME shutdown performance verification for flight.

Verification of safe shutdown at any point in time during engine operation is another area that usually requires analysis. Such an analysis was not formally performed for the SSME during engine development. After about twenty years and several thousand engine tests, a redline engine cut occurred in a ground test during the engine start sequence at a slightly different time than previously tested. This shutdown resulted in a control valve

exceeding its operating limit. The valve was commanded to close but failed to do so under the conditions and the result was extensive engine damage. Because of this engine failure, the software controlling the SSME shutdown sequence was modified to avoid such a situation in the future. Subsequent transient analyses verified the inherent danger in the original sequence and have been used extensively to examine all other points throughout the mission profile.

Failure Scenario Considerations

For liquid rocket engines, many hardware failure modes are classified as inherently catastrophic and are not extensively analyzed. The power unleashed and the speed at which the failures occur are so great that they preclude any possibility of mitigation or minimization. This is simply the nature of the field. However, there are a very large number of failure modes that are not inherently catastrophic but could lead either to an engine shutdown or to engine performance sufficiently off nominal as to prevent the vehicle from fulfilling mission objectives. Many of these failures are too costly or too risky to verify by test and must be assessed by engine system transient analysis.

Some examples from the SSME program include degraded control valve actuator performance, propellant or combustion gas leaks, check valve leaks, flow restrictions due to contamination, and degraded turbopump performance.

The specific example of an engine start being attempted under the conditions of severely degraded turbopump performance is shown in Figures 3 and 4. In this case, the performance of the SSME high-pressure liquid oxygen pump is degraded to differing degrees over a series of transient model runs. After a certain amount of performance degradation, the pump

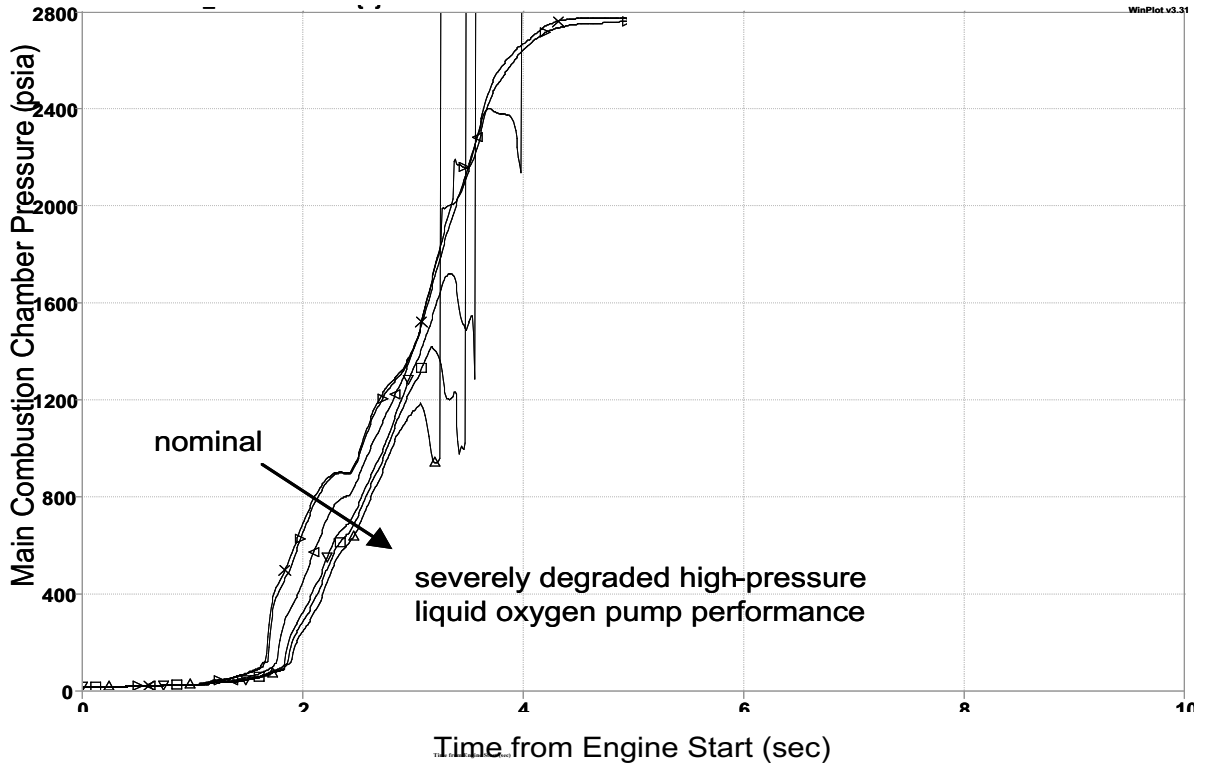


Figure 3, SSME main combustion chamber pressure during the start transient with varying levels of high-pressure oxidizer pump performance degradation.

Obviously, this is not a scenario that would be desirable to actually test with engine hardware. It is, however, a scenario for which controls must be built into the system to prevent. So this is the kind of analysis that is used to derive redline conditions used throughout the start sequence as Go/No-Go gates to proceed with the start sequence. In this case, a redline is set on the main combustion chamber pressure to ensure that sufficient back-pressure is maintained on the high-pressure fuel turbine thereby preventing an over-speed condition.

Engine Development Testing

A transient model of a liquid rocket engine can be a very important tool in determining design considerations for the engine, even very early in the program. Although many design details may not be known, the model can still be used to get a top-level idea of how the engine will behave during start and shutdown. As the design progresses, the transient will evolve into a more accurate representation of the actual final engine design.

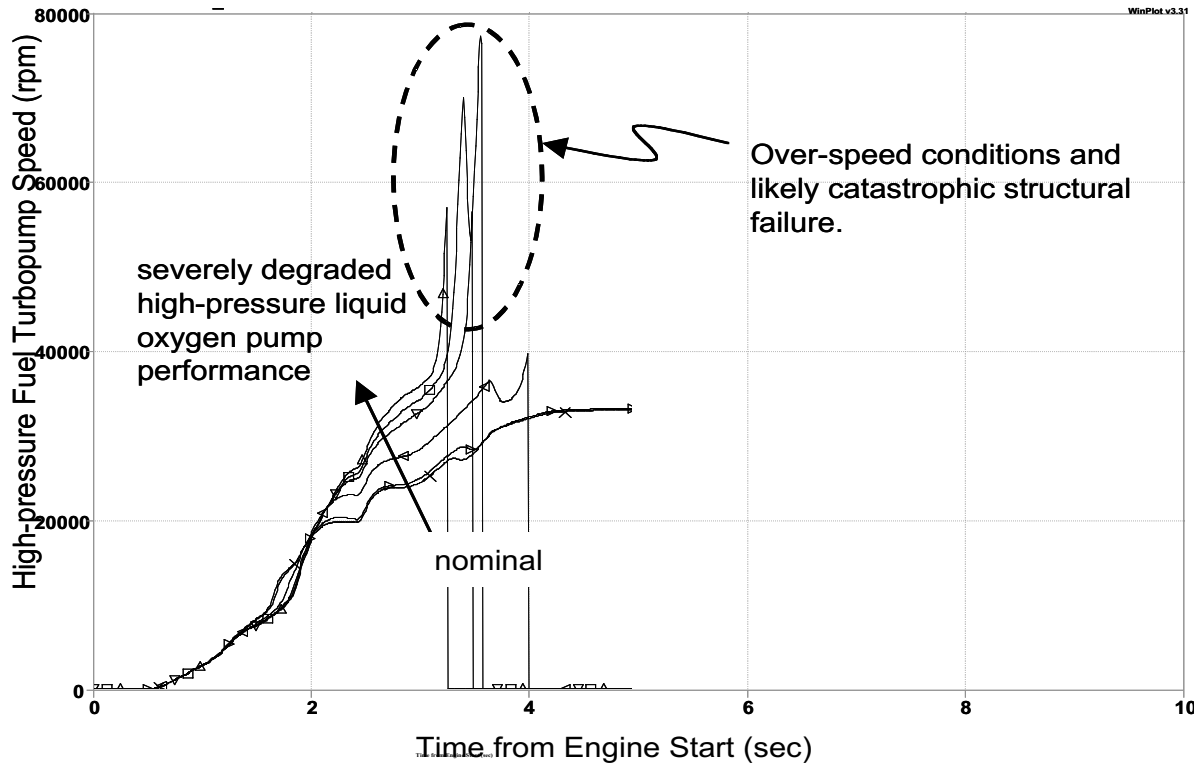


Figure 4, SSME high-pressure fuel turbopump speed during the start transient with varying levels of high-pressure oxidizer pump performance degradation.

Typically, component tests are performed prior to full engine testing to determine operating characteristics and design margins of the individual components in a more benign environment. A transient model can be used at this level as well, though usually component test facilities are not able to perfectly duplicate engine conditions during start and shutdown. Facility-specific sequences are required to keep the components within their acceptable ranges of operations. A transient model of the component test facilities, many times, can yield important clues about how to start the full engine, as well as how to keep the components safe during the tests. Even at this level, model anchoring through detailed post-test data analysis is a vital part of transient system model development.

When the engine finally gets to system-level development testing, the importance of the transient model becomes more critical, especially for the more complex cycles such as staged combustion where multiple control valves must be precisely choreographed to yield a safe start and shutdown. Despite the application of best practices and best efforts, however, unknowns about the complex interactions of the components during the transient operation can still make the transient model less than perfect. This is often illustrated while attempting the initial few tests of an engine. It is incumbent upon the analysts to keep up with the latest test data and attempt to reconcile differences between test data and model predictions. Many times, the model becomes critical in understanding this test data. As development testing continues,

the model should become more refined and consistently accurate.

Once the engine is well into development testing, the model can be used to refine the start and shutdown sequences in an attempt to minimize damaging characteristics of the transients. Examples of this are the minimization of thermal ignition spikes in combustion devices and pressure surges in lines. It is the responsibility of the analyst to recommend ways to improve the operational sequences in order to optimize the start and shutdown. This process continues even as the engine enters the flight program since the transient model becomes a primary tool in the understanding of sequence change impact and the resolution of anomalous situations.

A good example of a transient model utilized and maintained long after an engine has been demonstrated in flight is the SSME Digital Transient Model (DTM). This model is kept under configuration control and is used to resolve transient performance issues after over twenty years of successful flight use. It is used to validate proposed changes to the baseline start and shutdown sequences and to evaluate real and hypothetical anomalous situations.

Thus, a transient model of a liquid rocket engine is important through all phases of an engine program. In fact, as the modeling tools become better and more sophisticated in the future, their importance is likely to increase.

Transient Modeling Physics and Basic Modeling Strategy

Transient modeling of a liquid propellant rocket engine system is typically based upon the assumption of approximating the engine as a series of homogenous control volumes. Within each volume the principles of the conservation of mass and energy are applied.

This includes the incorporation of thermal analysis, where appropriate, when temperature changes in the hardware itself is influencing the fluid conditions. Further, these volumes are connected to create a fluid flow network to which the principle of the conservation of linear momentum is applied as a governing equation to determine the transport of fluid from one volume to another.

Finally, because of the unique aspects of liquid typical, high-power rocket engine systems, special considerations must be made for the inclusion of rotating machinery and the existence of combustion zones. Rotating machinery, otherwise called turbomachinery, is included within the solution process via the use of the conservation of angular momentum. Combustion zones, called combustion devices, require the additional consideration of the addition of chemical energy into the system and the change in the chemical content of the working fluids.

All of this together constitutes the complete system that must be accurately modeled through mathematical and computational analysis.

Conservation of Mass

For a control volume as pictured in Figure 5, the transient form of the conservation of mass equation begins with the definition of density.

$$\rho = \frac{M}{V} \quad (1)$$

By differentiating this equation, the familiar form of the conservation of mass can be derived. This is fundamentally a statement that mass can be transported or accumulated but can neither be created nor destroyed.

$$\frac{\partial \rho}{\partial t} = \frac{1}{V} (\sum \dot{m}_m - \sum \dot{m}_{out}) - \frac{\rho}{V} \frac{\partial V}{\partial t} \quad (2)$$

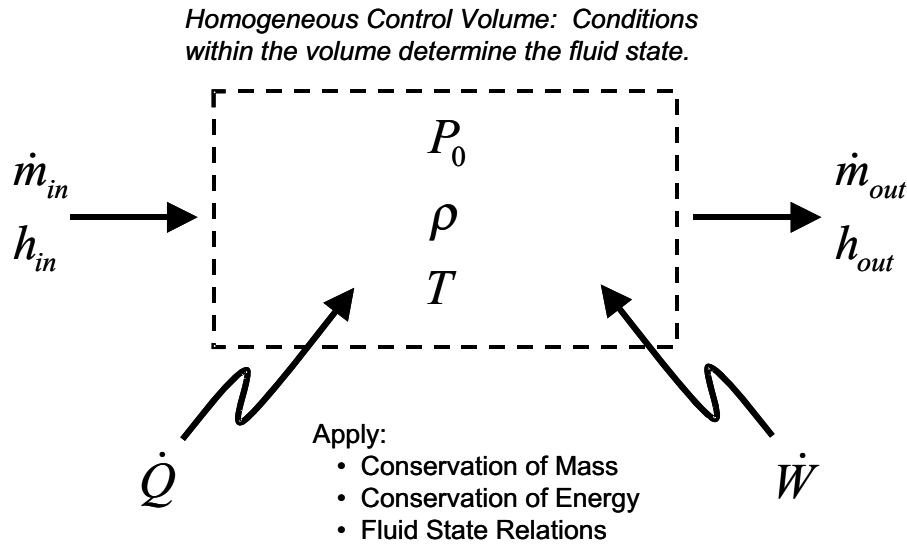


Figure 5, Homogeneous control volume with inputs and outputs.

Equation 2 is the form of the conservation of mass equation most useful for transient modeling. For most applications of this equation, the volume is fixed and, therefore, the equation simplifies to:

$$\frac{\partial \rho}{\partial t} = \frac{1}{V} (\sum \dot{m}_{in} - \sum \dot{m}_{out}) \quad (3)$$

This equation gives one the current rate of change of density based on the current values of flowrates entering and leaving a control volume. This is the first state equation.

Conservation of Energy

The second state equation applicable to the control volume pictured in Figure 5 is derived from the first law of thermodynamics. Just as with mass, the statement of conservation of energy is that the rate of flow of energy into a control volume minus the rate of flow of energy out equals the rate of energy accumulation. Energy is neither created nor destroyed. In mathematical terms this becomes,

$$\frac{\partial E_{CV}}{\partial t} = \dot{E}_{in} - \dot{E}_{out} + \dot{W}_{net} + \dot{Q}_{net} \quad (4)$$

Typically, potential energy in the form of elevation effects is ignored and kinetic energy in the form of fluid velocity is included within the formulation of total enthalpy terms. This leads to the form used for transient analysis,

$$\frac{\partial u_{CV}}{\partial t} = \frac{\sum (\dot{m} h_0)_{in} - \sum (\dot{m} h_0)_{out}}{\rho_{CV} V} + \frac{\dot{W}_{net} + \dot{Q}_{net} - u_{CV} (\sum \dot{m}_{in} - \sum \dot{m}_{out})}{\rho_{CV} V} \quad (5)$$

Within the term \dot{Q}_{net} exists the possibility of heat transfer between the fluid and the engine hardware. This is an important factor for transient analysis, particularly when dealing with cryogenic propellants.

Equation 5 is the state equation for the internal energy of the control volume. Combined with Equation 3, these two derivative equations allow for the determination of two

independent states of the fluid, from which any other required thermodynamic properties can be determined.

Conservation of Linear Momentum

So far, only the state of the fluid can be determined from the equations derived. Motion of the fluid from volume to volume is based upon Newton's Second Law formulated for a control volume.

$$\frac{d(m\hat{u})}{dt} = \sum F \tag{6}$$

This is a statement of the conservation of linear momentum, which is simply that the momentum of fluid will remain unchanged unless acted upon by a force. Within the context of transient analysis, the forces typically acting upon the fluid are pressure and viscous effects.

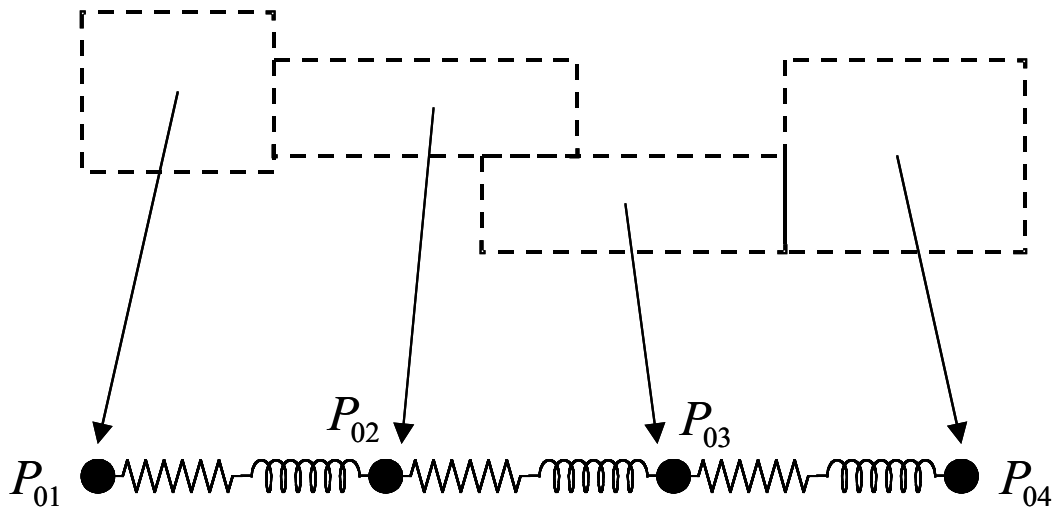
There are a number of different flow processes

that can be modeled. The most common and the most general is the flow through a network represented by a series of homogeneous control volumes. A simple representation of this is shown in Figure 6 where the volumes act as nodes in the network. Solution of this network involves the transformation of Equation 6 into an analogy of electrical circuit solution methods.

$$\frac{\partial \dot{m}_{ij}}{\partial t} = \frac{A}{L} \left[(P_{0i} - P_{0j}) - \frac{R \dot{m}_{ij}^2}{\rho} \right] \tag{7}$$

Where i and j represent two nodes within the network and the variables A and L represent effective cross-sectional area and node-to-node linear distance. For many problems such as flow in a duct these parameters have obvious values but for problems involving complex flow geometry situations, determining the appropriate values for these factors can become problematic. The engineer must often depend upon experience,

Flow Circuit: Series of homogeneous volumes represented as nodes within a circuit connected by elements of flow resistance and flow inductance.



Apply:
 • Conservation of Linear Momentum

Figure 6, Modeling representation of a fluid flow circuit

reasonable approximation, and even empirical data to come to truly representative values for these parameters.

For a steady state problem Equation 7 simplifies to the situation of flow being driven by pressures and being resisted by viscous and friction forces represented by the variable R and called flow resistance, in keeping with the analogy to the electrical circuit. For the case of transient flow, the inertia of the fluid itself must be taken into account unless the fluid is so light that this is a negligible factor as is often the case for gases. For liquid flow, and again in keeping with the electrical circuit analogy, this fluid inertia factor can be thought of as an effective inductance term.

By combining Equation 7 for node-to-node fluid transfer with the fluid state determination represented by Equations 3 and 5 applied to each node in circuit, we now have a solvable transient flow circuit.

It should be noted that formulation of the conservation of linear momentum as shown in Equation 7 does not fully encompass all of the various flow regimes existing within a rocket engine. For example, specialized formulations for compressible gas flow through orifices and converging-diverging nozzle are also used when appropriate. However, regardless of the specific formulation all node-to-node flow calculations are intrinsically rooted in the principle of the conservation of linear momentum.

Combustion Devices

As with the rest of the engine system represented by homogeneous volumes, the concepts of the conservation of mass and energy must be applied to locations within the engine system that have reacted propellant as well. Equations 3 and 5 derived above still apply to these areas, but more information is

needed to determine the properties associated with a chemical reaction.

Equation 3, the conservation of mass equation, applies only to the total flow. The mass of the various combustion reactants and products is, of course, not conserved in the case of chemical reaction. However, combustion properties are a function of the relative amounts of fuel and oxidizer brought together. There are many ways to state the relative of amounts of fuel and oxidizer. Mixture ratio is usually the term of choice. Mixture ratio is defined as the mass of oxidizer divided by the mass of fuel.

$$MR = \frac{M_{ox}}{M_{fuel}} \quad (8)$$

For transient modeling purposes, this term is not convenient numerically because MR can assume a value of infinity. A better way to express this quantity is in terms of fraction of total propellant. Typically used is oxidizer fraction, OFR .

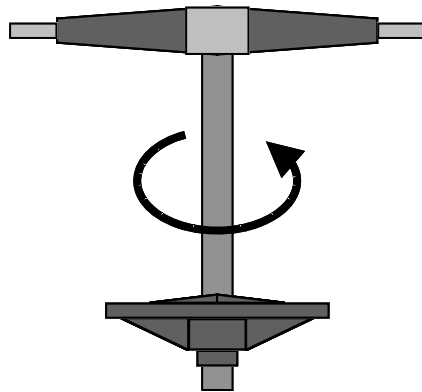
$$OFR = \frac{M_{ox}}{M_{total}} = \frac{M_{ox}}{M_{ox} + M_{fuel}} \quad (9)$$

For modeling purposes, the value of OFR during transient operation can be determined from the differential form of Equation 9:

$$\frac{\partial(OFR_{CV})}{\partial t} = \frac{(\sum \dot{m}_{ox_{in}} - \sum \dot{m}_{ox_{out}})}{M_{total} - OFR_{CV}(\sum \dot{m}_{total_{in}} - \sum \dot{m}_{total_{out}})} \quad (10)$$

Equation 10, representing the time rate of change of the oxidizer fraction, provides the final piece of data needed to calculate combustion properties. By knowing how much oxidizer is leaving and entering the control volume, the rate of oxidizer accumulation can be determined. This information can then be fed into a standard

Rotating Machinery: Typically consisting of a turbine element and a pump element.



Apply:

- Conservation of Angular Momentum
- Pump and turbine relationships between fluid work and shaft torque

Figure 7, Modeling of rotating hardware element of turbomachinery

chemical equilibrium routine [Gordon, 1971 and 1984] to determine the properties of resultant high-energy chemical reaction products.

Turbomachinery

The other piece of hardware that is typical in high-power liquid rocket engine systems that requires special attention is turbomachinery. The energy transfer accomplished by this machine can be modeled through a focus on the rotational acceleration of the shaft connecting the turbine to the pump. This is illustrated in Figure 7. The angular acceleration of a shaft is determined from the application of the conservation of angular momentum.

$$\frac{\partial N}{\partial t} = \frac{\sum T_{turbine} - \sum T_{pump}}{I} \quad (11)$$

In order to determine the summation of torque moments applied to the shaft, the model must

additionally have information relating fluid property and flow parameters in both the turbine and the pump to values of torque. These are collectively referred to as turbomachinery maps. The determination of these maps is largely an empirical matter the details of which are left to the component developers.

Integration and Solution

With all of the necessary governing equations derived for the various elements of the engine system, the next step becomes the generation of a numerical means of solving these equations.

Upon first impression, performing an explicit Eulerian integration of the state equations would appear to be the most straightforward way of completing the transient analysis. This would consist of stepping through time using the conditions of the previous time step to drive the calculations in the current time step.

However, in practice, the time step used for such an integration scheme must be very small. Larger time steps can be taken by using implicit methods. One such approach is the trapezoidal integration as represented in Equation 12.

$$(12)$$

Other similar schemes are also considered. It should be noted that an iteration loop is required as the part of such a scheme because the value of the state at the new point is a function of the derivative evaluated at the current point, which requires knowing the value of the state at the new point. For this reason, the state is iterated until the guessed value is equal to the predicted value.

It has been found that using density and the fluid internal energy, the two most obvious

choices, as the iteration parameter can be numerically unstable. Instead, pressure and enthalpy are used as the iterated state variables. This scheme works so long as density and internal energy can be determined from pressure and enthalpy. However, because pressure and enthalpy are independent properties, this obstacle is easily overcome.

Fluid Properties

A critical element of transient modeling of liquid rocket engines is the utilization of accurate fluid properties. Through the derivation of the governing conservation equations all of the various fluid properties existing as variables within the equations remain generic with no tie to actual propellants. It is through the use of accurate fluid property routines that the transient model is transformed from a mathematical exercise

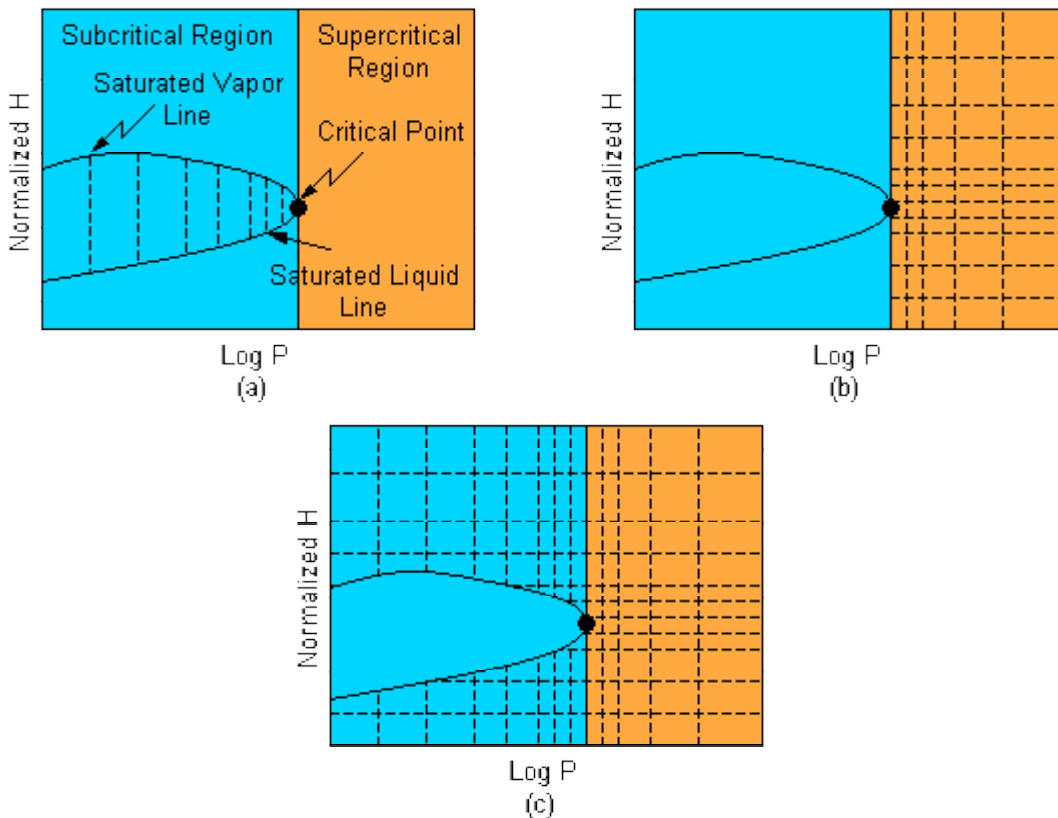


Figure 8, The creation of a grid across the state space for a fluid

to a representation of an actual engine. With this in mind, a great deal of effort has been spent, and continues to be spent, in the creation of efficient and accurate and usable property routines. This section describes a recent effort in which property tables in and around the region of propellant phase change were developed in a unique way.

Real fluid properties were generated using the widely available GAPAK (© copyright Cryodata Inc.) routine by using pressure and enthalpy as input values. Other available routines besides GAPAK could be utilized in the process, such as GASP [Hendricks, 1975] for example, since the process itself is generic even if the generated tables are quite specific. The fundamental goal of this effort was to minimize the number of pressure-enthalpy values necessary to generate property tables that fully described the fluid. To accomplish this, a program was created which indirectly allows the user to determine how many pressure-enthalpy pairs are necessary in order to achieve a prescribed interpolation error. Thus, the desired accuracy of the results across the region of fluid properties considered is used to determine the expanse of the tables generated.

First, the program goes through saturated liquid and vapor lines to determine the necessary number of pressure points and their values so that the interpolation error would be within the specified error. This is illustrated in Figure 8a. The property data is divided into two regions: sub-critical and supercritical. After obtaining the pressure values for saturated lines, the program then determines pressure-enthalpy values for the supercritical region as shown in Figure 8b. For the sub-critical region, the pressure values are the same as the pressure values of the saturated lines, and likewise the enthalpy values were the same as the enthalpy values of the supercritical region as in Figure 8c.

For the supercritical region, a regular linear interpolation routine can be used to retrieve property data from the property tables; however, for the sub-critical region, a special interpolation routine is required for cases where one or more data points were inside the phase-change dome. A new interpolation routine was derived to handle both sub-critical and supercritical regions. Figure 9 shows fourteen possible cases near the saturated lines where the special interpolation routine is

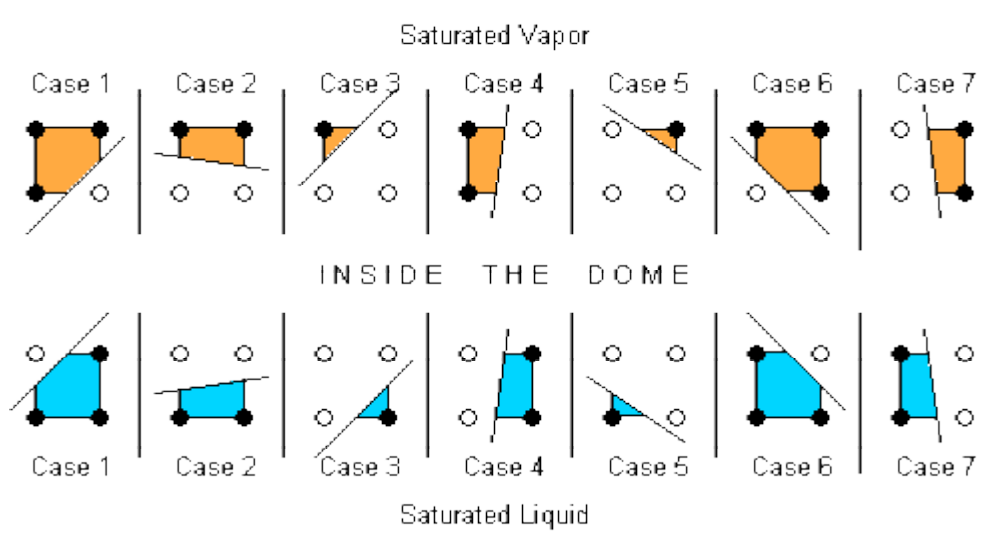


Figure 9, Special interpolation situations around the liquid and vapor saturation lines

required in order to retrieve reasonable property data from the generated tables. For example, Case 2 represents situation straddling the saturated vapor line. The bottom 2 data points within the interpolation rectangle (unshaded) lie inside the phase-change dome; therefore, they will not be used in the interpolation process. Instead, only the top 2 data points (shaded) are used along with data along the saturated vapor line. In this manner the inherent errors associated with using linear interpolation around a zone of discontinuity can be avoided.

Numerical Solution Issues

The application of the conservation equations and the first law of thermodynamics as described above results in a system equations that must be solved in order to define the state of the engine at each point in time. The method currently used at NASA MSFC for doing this is based on the Newton-Raphson scheme as applied to a system of non-linear equations. Newton-Raphson requires the generation of a Jacobian matrix – a collection of the slopes of the equations with respect to each parameter being iterated. These derivatives are determined analytically by individually perturbing each variable and measuring the response of the system of equations to that perturbation. This Jacobian matrix is then used by the solver to iterate the variables until convergence. The theory of Newton-Raphson is well documented; however, in practice, several problems can arise.

One such problem is that the Jacobian is only valid at the initial values of the independents. As the solution progresses, the Jacobian matrix will change. Evaluating the Jacobian is costly in terms of computational resources. For this reason, reevaluation of the Jacobian as the solution progresses is not feasible. This problem is overcome by making use of the

Broyden technique [Broyden, 1965]. This is a technique to evolve the Jacobian matrix during solution progression.

In order to overcome issues of numerical stiffness, convergence of the system is determined based on percent errors, not absolute errors. This in turn creates a problem when the variable being used in the denominator of the percent error equation approaches zero. In practice, this obstacle is overcome by using normalizers. A normalizer is essentially a limit placed on the denominator to prevent it from going to zero. However, when a normalizer value is invoked, the percent error starts to approach an absolute error, as opposed to a percent error so this process must be invoked with considerable care.

When modeling a transient fluid network, progress in the solution through time is made using a time step, or dt . If the dt is too small, the solution takes an excessive amount of time to progress. However, if the dt is too large, the iterations may fail or the results may contain errors. Thus, a balance must be struck between these two extremes. However, even after recognizing this need for balance there exists the problem that the required dt may change depending on what is happening at that time (valves opening/closing, ignition events, etc.). There are no rigorous methods to determine to optimum dt . However, one method used to gauge the time step relative to the system is the concept of the time-constant. The time-constant of a control volume is the mass stored in the volume divided by the flow rate through the volume ($\tau = M/\dot{m}$). This term is a rough approximation of the time a fluid particle resides within the control volume. It is also a measure of how quickly the volume responds to changes. The time constant can be employed to determine if the dt is within the correct order of magnitude. If the time constant of a control volume is much

smaller than the time-step being used, this implies that the changes to the control volume may not be sufficiently captured by the time-step. Another technique is automatic dt reduction. When a solution begins to experience convergence problems, the code automatically reduces the time-step to attempt to obtain a converged solution.

Another common problem occurs when flow rates approach zero. Since flow rate is proportional to the square root of the pressure differential, the slope of changes in flow rate as a function of differential pressure approaches infinity when the differential pressure approaches zero. This large slope creates havoc on the Newton-Raphson solution methodology. Typically, to overcome this issue, the flow rate equation is linearized near zero flow (in other words, near zero differential pressure) to create a finite and constant slope in this region.

Future Work

The process of improving transient mathematical modeling capabilities in the future falls into three basic categories:

- Improvements of the usability of the modeling tools
- Improvements to the approximations used in the modeling to represent complex systems
- Improvements to the numerical schemes used to solve the derived equations and developed computer code.

The task of assembling a complete mathematical model of a complex liquid rocket engine system is a time-consuming process. The use of a modular format for pieces of modeling code that apply to particular hardware elements is well established and is of great utility. However, the text-based format currently used at NASA

MSFC for the assembly of these modules is not easy or quick. To overcome this limitation, work has begun on the development of a graphical users interface (GUI) for this initial assembly procedure. It is hoped that the use of GUI will cut down the basic assembly time and allow analysts to spend a greater amount of time dealing with the more technical aspects of their modeling tasks.

The complex environments contained within liquid rocket engine components require that the analyst make approximations of reality in order to generate a solvable problem. One area where improvements are being made to this approximation is in the combustion devices. Engineers at NASA MSFC are developing a Generalized Combustion (GCOMB) approach that can determine the effective mixed properties of multiple constituents within a volume. This is of particular importance in volumes potentially containing combustion reactants, combustion products, and inert gas purge flows. This overcomes many limitations of previous methods wherein artificial volumes were sometimes added to account for purge flows and real fluid properties could not be used throughout the transient operation regimes being modeled.

And finally, work is being pursued in the area of using more advanced computational and mathematical techniques in the solution of the nonlinear sets of equations used to represent the liquid rocket engine system. In coordination with industry partners and experts from academia, and with support from our Air Force partners, NASA MSFC engineers are examining a number of advanced methods. These include line back-search applied to the currently used Newton/Broyden method [Press, 1986] (pictured in Figure 10), simulated annealing,

NUMERICAL EXPERIMENTS

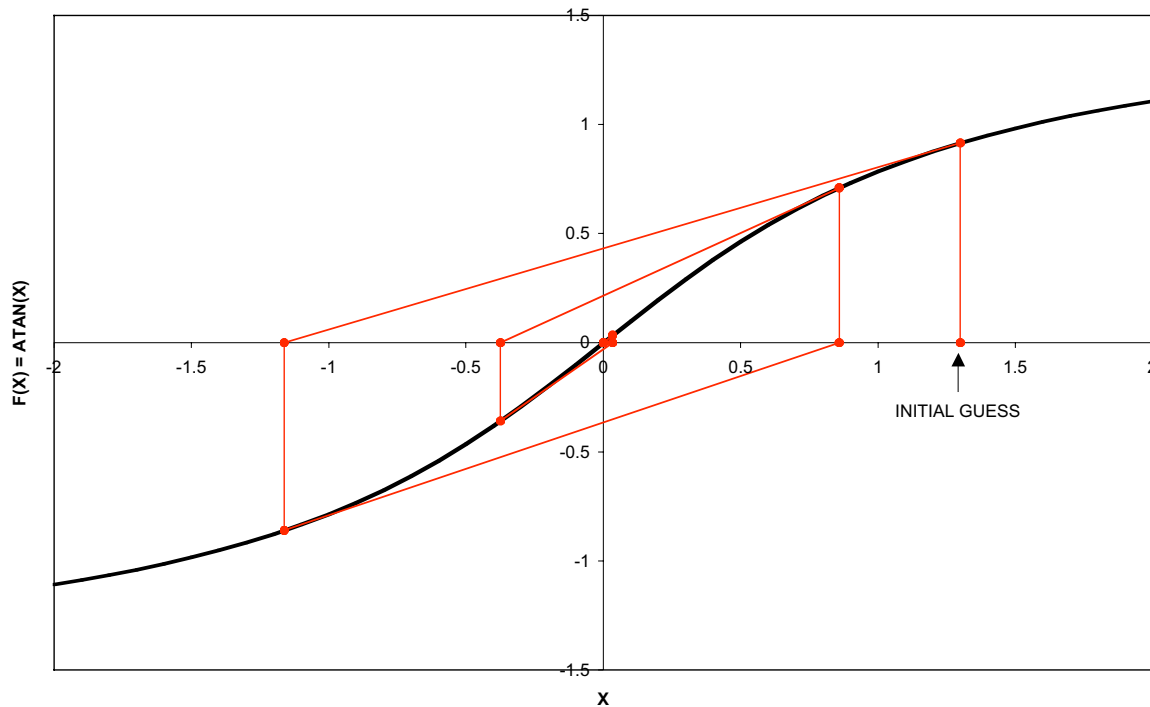


Figure 10, Line back-search method (backtracking) applied to Newton/Broyden method

embedding procedure for parametric solutions, and various genetic algorithms.

Summary / Conclusions

The subject of liquid rocket engine system transient modeling could, if covered in detail, fill several entire textbooks. The reader is directed to the Additional Reading section for just such treatments. It was the purpose of the authors here to present some of the basic principles and some clear rationale why this subject is such a vital aspect of liquid rocket engine development and utilization. Whereas rocket engines are designed to perform at steady state conditions, the only way to get to and from that point is through the potentially treacherous processes of engine start and engine shutdown.

In the past, before the widespread use of high-speed computers, many liquid rocket engine

programs relied on the process of trial and error in developing start and shutdown sequences. Obviously, this approach can work but it is costly, time consuming, and can often result in multiple hardware failures. Further, such an approach cannot fully explore all of the hypothetical failure scenarios that might be lurking just on the edges of nominal performance. Only through the use of transient simulation can these shortfalls be overcome.

However, even with the use of high-speed computers and even with the basic physics of the problem well established, the task of the analyst is hardly straightforward. Every system is unique and presents special challenges. Because any mathematical modeling task is intrinsically a process of making reasonable approximations of reality, the analyst must constantly reevaluate the sufficiency and completeness of his

approximations. This is most effectively accomplished through the analysis of available test data to properly ground the model developed. Further, the analyst must pay attention to the intrinsic limits of the numerical algorithms used and the solution schemes employed.

As the liquid rocket systems of the future are proposed and developed, the task of transient modeling of these systems will likely become more and more important. The process of improving the tools used for this task is an ongoing project being undertaken by the engineers at NASA MSFC.

Acknowledgments

The authors would like to sincerely thank Mr. Bruce Tiller for his invaluable input and oversight regarding this paper.

References

Broyden, C.G., 1965, "A Class of Methods for Solving Nonlinear Simultaneous Equations," Mathematics of Computation, Vol. 19, pp. 577-593 (American Mathematical Institute, 1965).

Gordon, S. and McBride, B.J., "Computer Program for Calculation of Complex Chemical Equilibrium Compositions, Rocket Performance, Incident and Reflection Shocks, and Chapman-Jouquet Detonations," NASA SP- 273, 1971.

Gordon, S., McBride, B.J. and Zeleznik, F.J., "Computer Program for Calculation of Complex Chemical Equilibrium Compositions and Applications Supplement I -Transport Properties," NASA Technical Memo-86885, Oct. 1984.

Hendricks, R.C., Baron, A.K., and Peller, I.C., "GASP - A Computer Code for Calculating

the Thermodynamic and Transport Properties for Ten Fluids: Parahydrogen, Helium, Neon, Methane, Nitrogen, Carbon Monoxide, Oxygen, Fluorine, Argon, and Carbon Dioxide," NASA Technical Note D-7808, Feb. 1975.

Press, W.H., Flannery, B.P., Teukolsky, S.A., and Vetterling, W.T., Numerical Recipes, The Art of Scientific Computing (Cambridge University Press, 1986).

Additional Reading

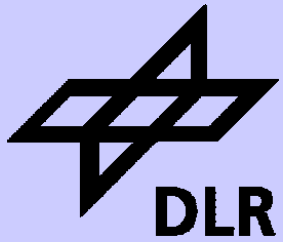
Blevins, R.D., Applied Fluid Dynamics Handbook (Keiger Publishing Company, 1992)

Hodge, B.K., Analysis and Design of Energy Systems (Prentice-Hall, Inc., 1990).

Huzel, D.K., and Huang, D.H., Modern Engineering for Design of Liquid-Propellant Rocket Engines (American Institute of Aeronautics and Astronautics, 1992).

Sutton, G.P., Rocket Propulsion Elements: An Introduction to the Engineering of Rockets (John Wiley & Sons, Inc., 1992).

White, F.M., Fluid Mechanics (McGraw-Hill Book Company, 1979)



ONERA

Experimental Investigation and Modeling of the Ignition Transient of a Coaxial H₂/O₂-Injector

V. Schmidt, D. Klimenko, O. Haidn, M. Oschwald
DLR Lampoldshausen, Institute of Space Propulsion
Germany

A. Nicole, G. Ordonneau, M. Habiballah
ONERA Châtillon, Fundamental and Applied Energetics Department
France

5th International Symposium on Space Propulsion''
27-31 October 2003 – Chattanooga (TE)

Outline

Motivation & objectives

Experiment : DLR micro combustor

Computations

microcombustor

application to VINCI engine

Conclusion



motivation

propellant ignition is still an issue for liquid propellants engines

- reliable ignition
- no overpressure, no blow out
- multiple payload capability requires multiple ignitions in different conditions
- Ariane 4 failure , HM7B ignition problems (V15 and V18)

modeling and simulations is challenging

- two-phase flow
- turbulent diffusion flame
- transient boundary conditions
 - pressure, injection velocity, phase of propellant, atomization regime

today advances in diagnostics and computational capabilities enable to address ignition phenomenon using detail experiments and CFD tools



objectives of the work

take advantage of detailed experiments to get insight into main processes involved in the ignition of cryogenic engines like VINCI and improve modeling

Approach

experimental investigation of the ignition transient in a basic configuration (DLR)

- gaseous propellant (GO₂/GH₂)
- single injector
- laser ignition

use of new generation of CFD tools with existing modeling of ignition transient (ONERA)

- basic configuration test case
- VINCI engine ignition



experimental set-up

micro-combustor test facility M3 injection

- coaxial GH₂/GO₂-injection
- O₂-post Ø: 1.22mm
- width of annular H₂-slit: 1mm

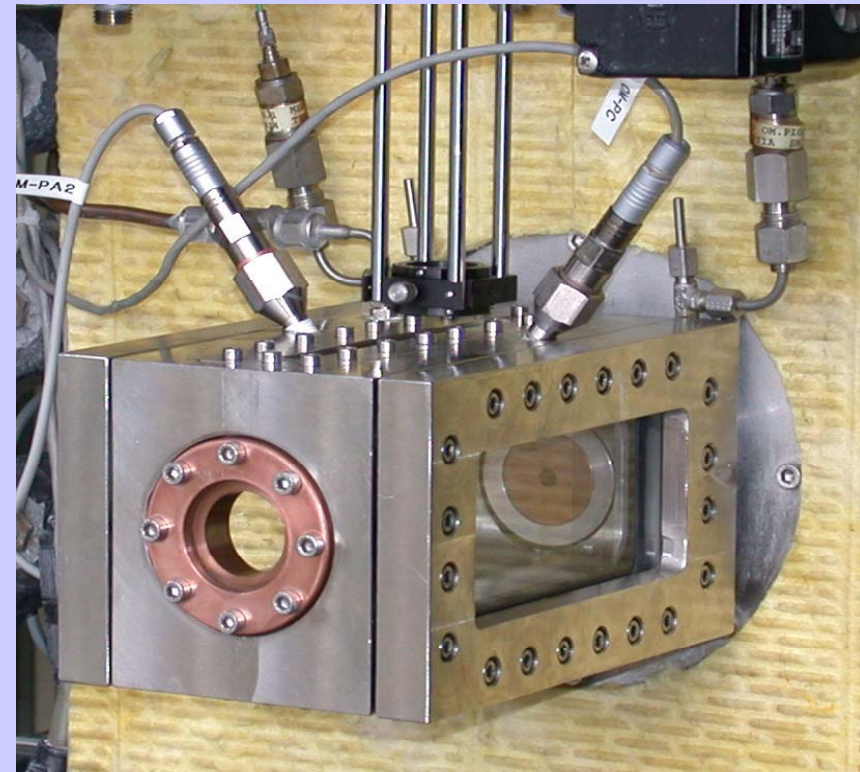
nozzles with Ø6mm and Ø4mm

sequencing

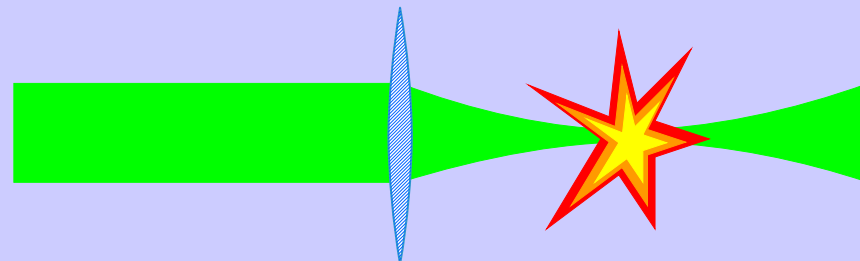
- N₂-purging prior to the test
- O₂-valve opened 20ms after H₂-valve

ignition

- laser ignition
- 40ms after H₂-valve opening
- at stationary cold flow conditions
- ambient chamber pressure



laser ignition



ignition by laser induced gas break down
full control of time and location of ignition
no distortion of the flow due to ignition equipment

Nd:YAG-laser, 532nm , 195 mJ/pulse

focus-position:

- **z = 36 mm downstream injector**
- **r=2.5mm off-axis**

results have been proven to be independent on laser pulse energy (80-195mJ/pulse)

cold flow diagnostics

Rayleigh Scattering

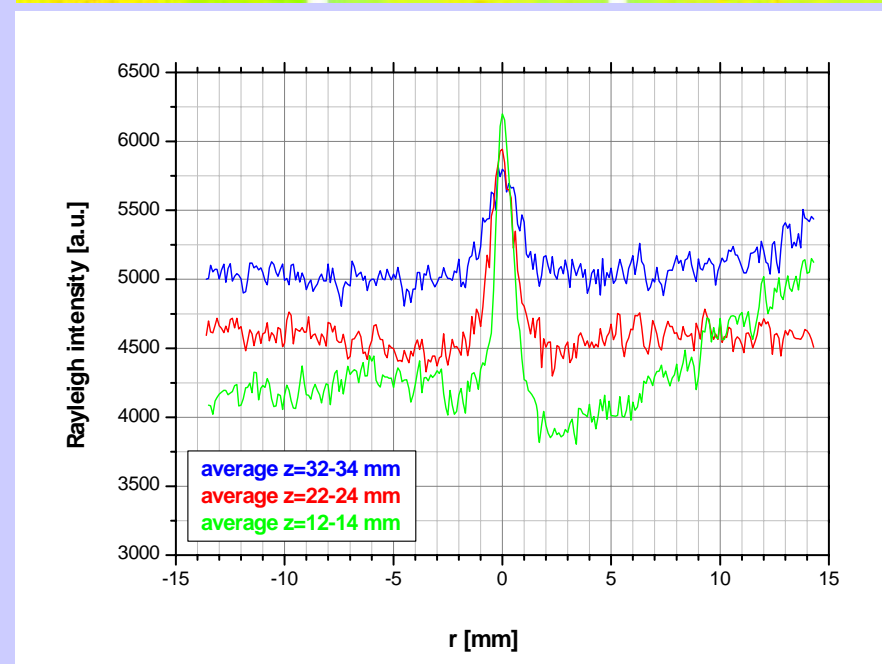
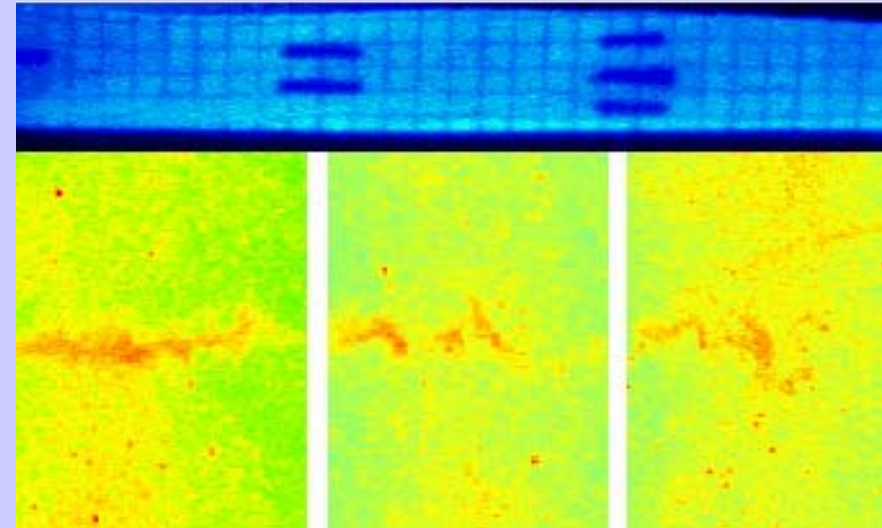
- KrF-laser, planar light sheet, gated ICCD

single shot images

- O₂-jet visible due to high scattering cross section (cross section ratio O₂/H₂ ≈ 3.9)
- zigzag bending of O₂-jet increasing downstream
- separate regions of high O₂-density

averaged images

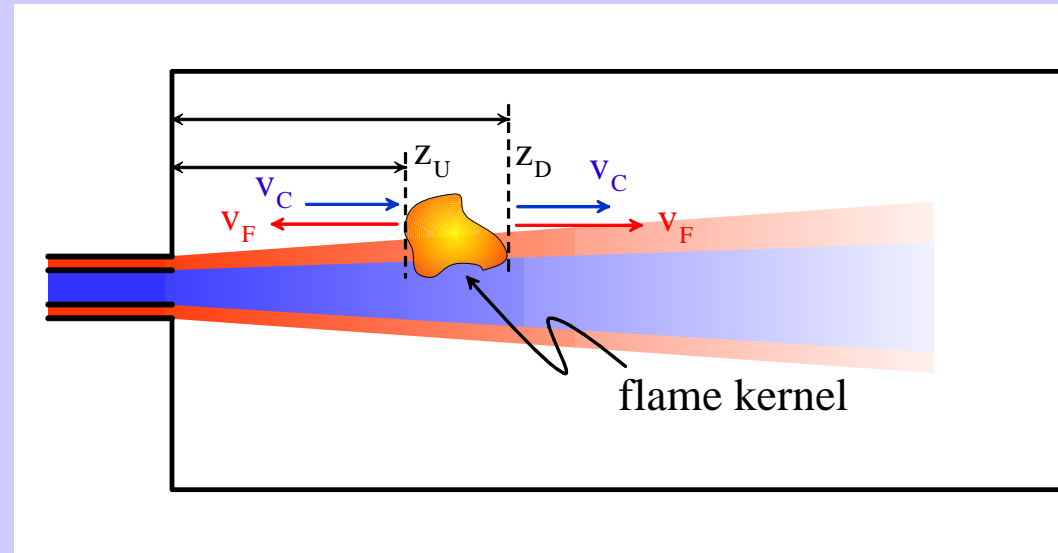
- radial profiles show decreasing peak intensity and jet-broadening with increasing z



transient flame diagnostics

high speed **OH-imaging** for flame detection

- ICCD-camera
- filter 300-310nm
- frame rate 18kHz, 256x128 px², 8bit



flame front velocities

- velocities from displacement of flame front in subsequent images
- downstream front: convection and flame velocity parallel
- upstream front: flame velocity opposite to convection velocity
- derivation of convection and flame velocity

$$v_U = \frac{z_U(t_{i+1}) - z_U(t_i)}{\Delta t}$$

$$v_D(z_D) = v_C(z_D) + v_F(z_D)$$

$$v_U(z_U) = v_C(z_U) - v_F(z_U)$$

$$v_C = \frac{v_D + v_U}{2} \quad v_F = \frac{v_D - v_U}{2}$$

test conditions

m_{H_2} [g/s]	m_{O_2} [g/s]	Re_{H_2}	Re_{O_2}	J	v-ratio	I_{H_2} [kg·m/s ²]
0.58	1.15	18616	43836	~0.2	~1.8	~0.4

momentum flux ratio

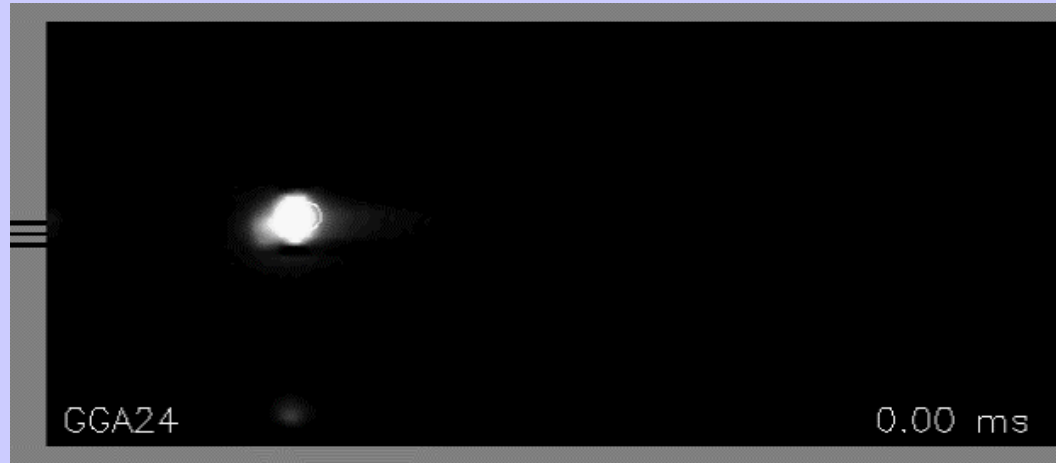
$$J = \frac{(\rho v^2)_{H_2}}{(\rho v^2)_{O_2}}$$

H₂-momentum flow

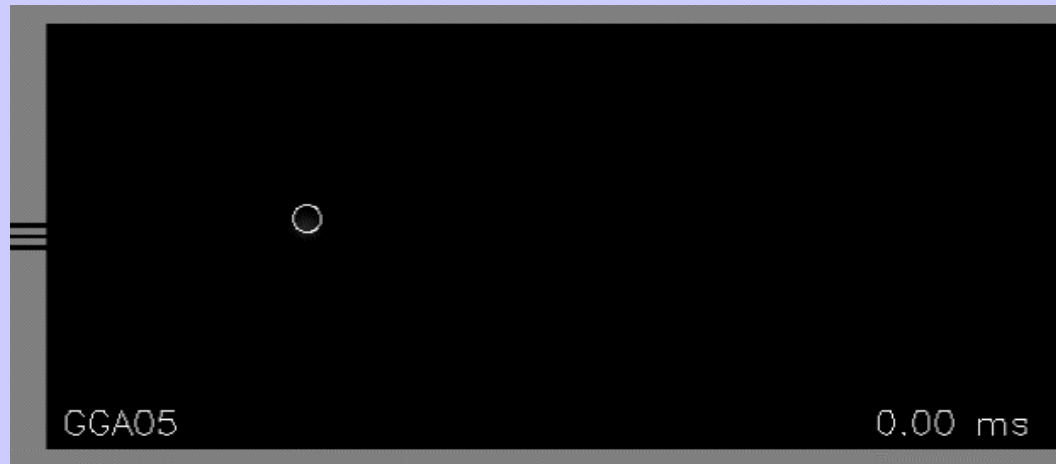
$$I_{H_2} = (\rho v^2 A)_{H_2}$$

video of transient OH-emission

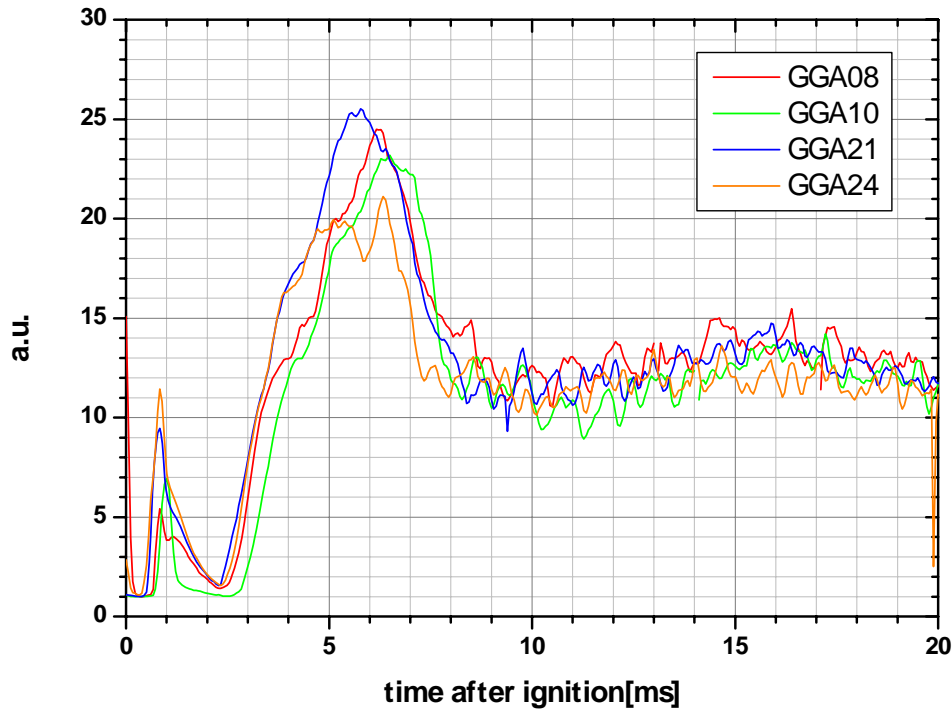
Ø4mm nozzle



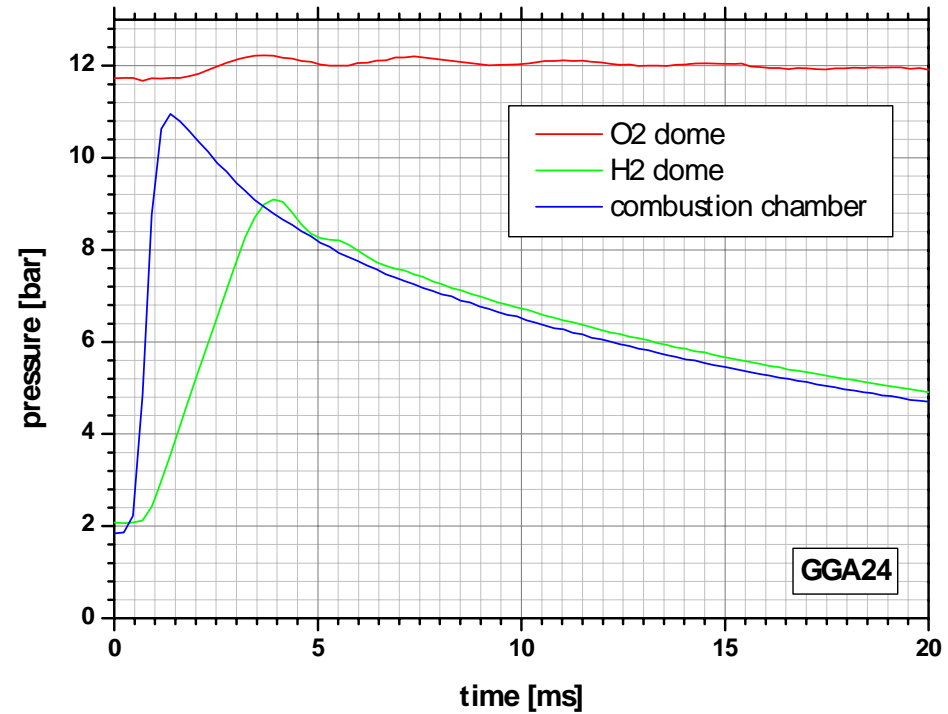
Ø6mm nozzle



transient chamber pressure and OH-emission intensity



OH-emission



dome- and chamber-pressures



Ø4mm nozzle



flame front movement (0.0 - 0.7 ms)

time series of OH-frames

$t < 0.4 \text{ms}$:

- downstream movement of flame
- very low level of OH-emission
- rather constant size of flame kernel

$0.4 < t < 0.7 \text{ms}$:

- upstream movement of flame kernel
- OH-emission increasing
- flame kernel size increasing
- flame attaches to the injector

frame#	time [ms]	GGA05 raw data	GGA05 enhanced gray values
2	0.06		
4	0.17		
6	0.28		
8	0.39		
10	0.50		
12	0.61		
14	0.72		

flame front movement (0.8 - 2.2 ms)

time series of OH-frames

0.8<t<1.1ms:

- unburnt propellants in the combustion chamber react
- OH-emission decreasing
- hot gas is trapped in the recirculation zone at the O2-post

1.1<t<2.2ms:

- flame stabilized at the injector post and starts to expand downstream

frame#	time [ms]	GGA05 raw data	GGA05 enhanced gray values
16	0.83		
20	1.05		
24	1.28		
28	1.50		
32	1.72		
36	1.94		
40	2.16		

flame front movement ($t > 2.4$ ms)

time series of OH-frames

$2.4 < t < \sim 5$ ms:

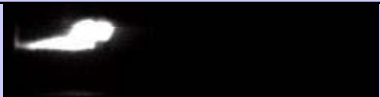
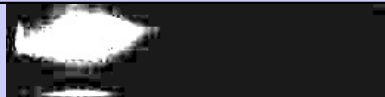

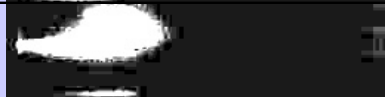







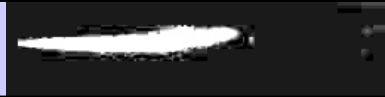

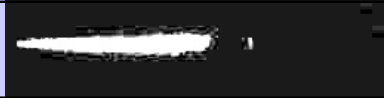
- flame stabilizes in a cylindrical shape around the O_2 -jet

$t > \sim 5$ ms:

- flame contour is stable

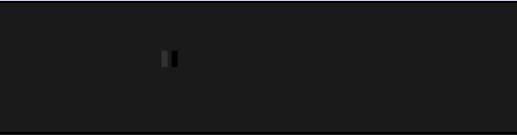
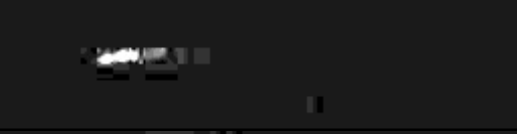


$t \sim 15$ - 17 ms:

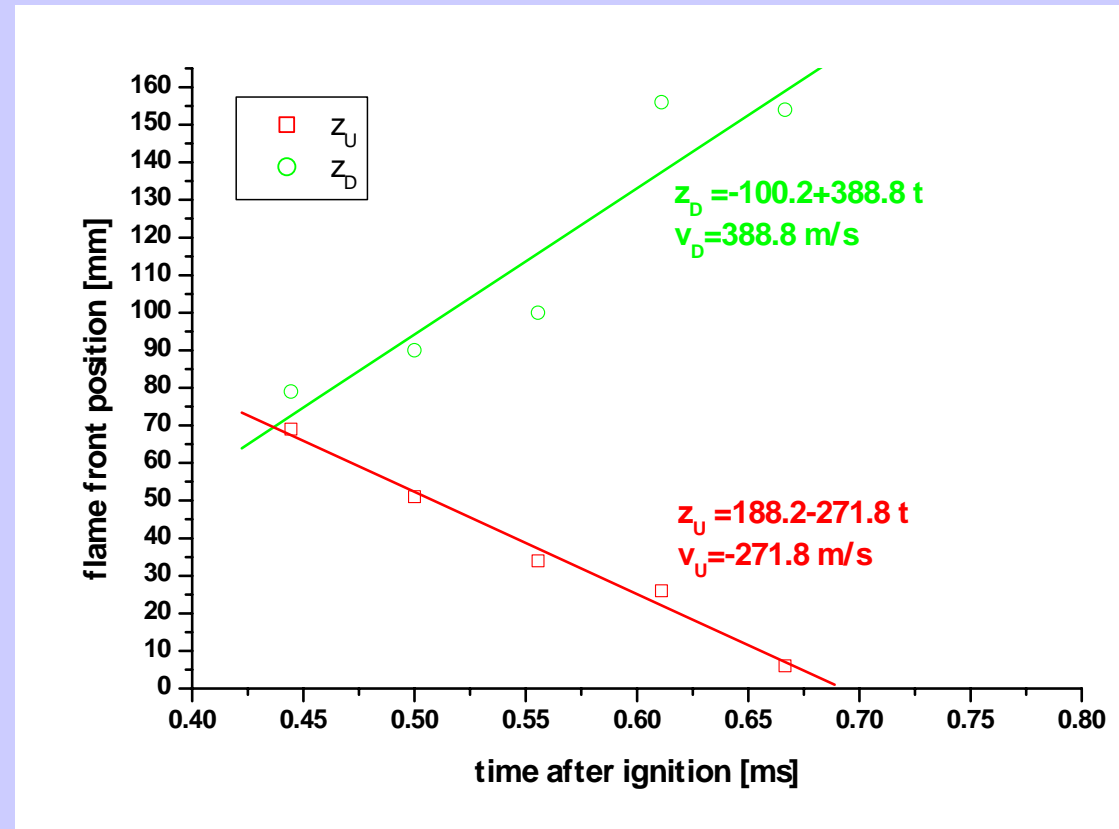
- flame extinction for 46mm-nozzle

frame#	time [ms]	GGA05 raw data	GGA05 enhanced gray values
44	2.39		
50	2.72		
60	3.28		
70	3.83		
80	4.39		
90	4.94		
100	5.50		

flame front and convection velocities

upstream movement of flame kernel ($0.4 < t < 0.7 \text{ms}$)

frame#	time [ms]	GGA05 enhanced gray values
8	0.39	
10	0.50	
12	0.61	
14	0.72	







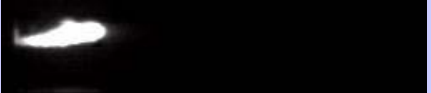
$$V_{\text{conv}} = -52 \pm 67 \text{ m/s}$$

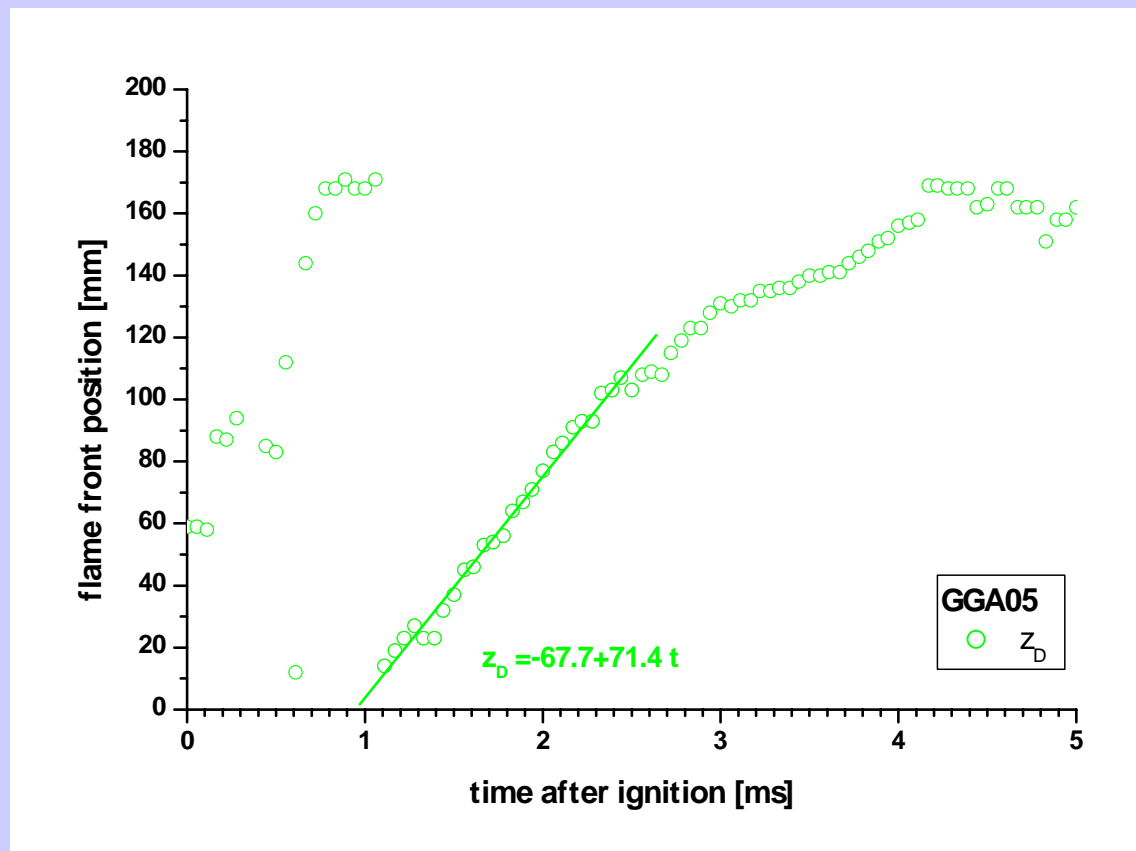
$$V_{\text{flame}} = 300 \pm 22 \text{ m/s} \text{ (mean value of 7 tests)}$$



flame front and convection velocities

downstream movement of flame front of the anchored flame ($1.0 < t < 2.6$ ms)

frame#	time [ms]	GGA05 raw data
24	1.28	
28	1.50	
32	1.72	
36	1.94	
40	2.16	



$$V_{\text{front}} = 62 \pm 8 \text{ m/s (mean value of 7 tests)}$$

comparision of results of tests with Ø4mm and Ø6mm-nozzle

	6mm-nozzle	4mm-nozzle
upstream movement of flame kernel (0.4-0.8ms)		
convection velocity	-52±67m/s	-37±52m/s
flame front velocity	300±22m/s	171±59m/s
anchored flame (~ 1-5ms)		
flame front velocity	62±8m/s	39±5m/s
flame extinction	17ms	no extinction

Outline

Motivation & objectives

Experiment : DLR micro combustor

Computations

microcombustor

application to VINCI engine

Conclusion



Numerical simulation of O₂/H₂ ignition

Objective :

To assess CFD tools to handle correctly ignition transient for space propulsion application

Physical processes

We need to represent :

- temporal pressure evolution
- mixing zone, temperature and species gradients
 - Need to mesh the actual geometry, including nozzle

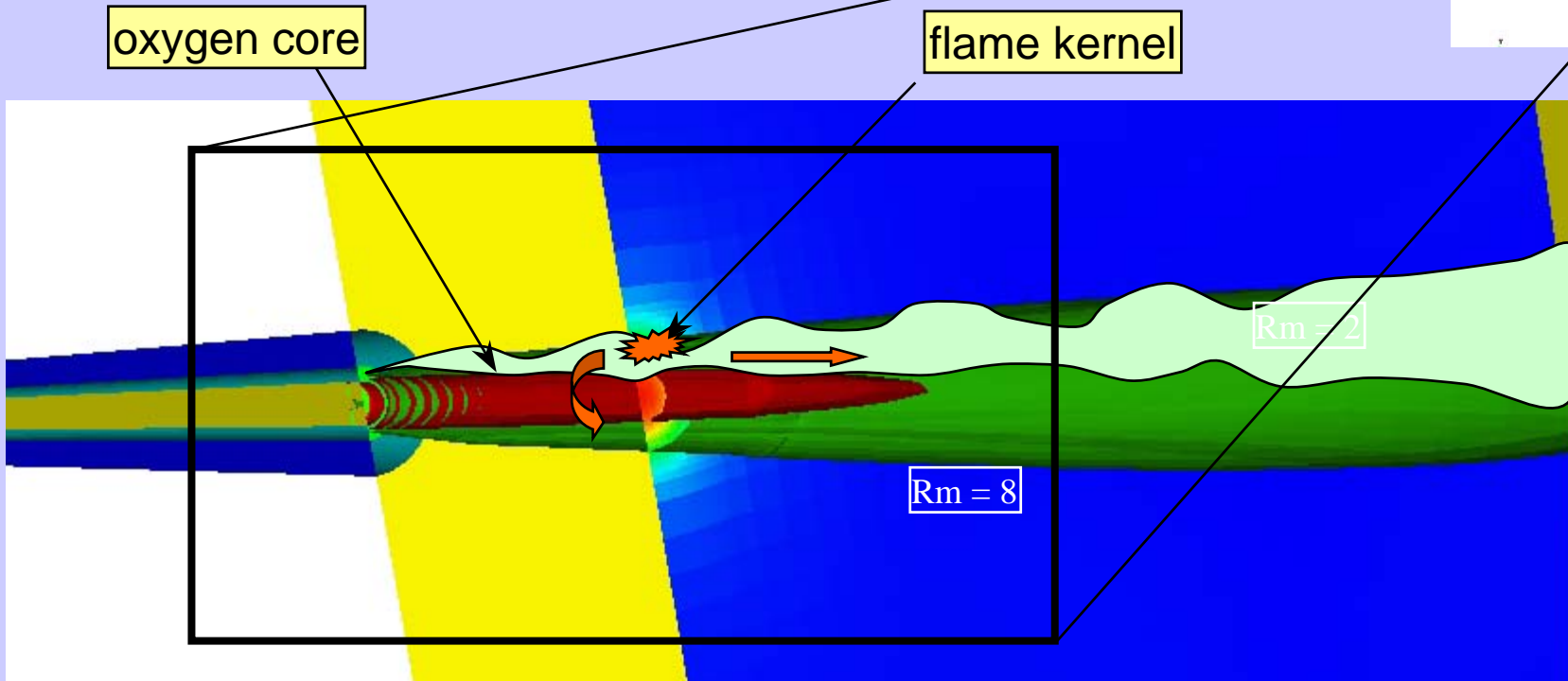
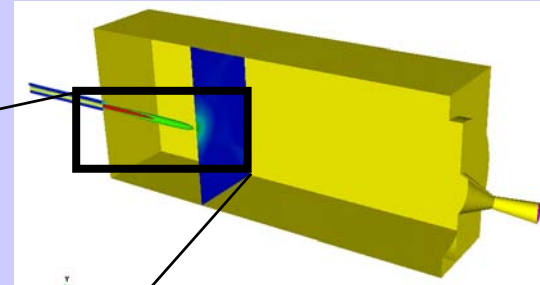
Due to large temperature and species gradients

- A multi step chemical reaction scheme is used to simulate flame propagation under such conditions during ignition transient

Physical processes

Laser pulses in mixing layer induce small flame kernel which propagates in 2 ways

- Radially : as a diffusion flame between oxygen and hydrogen
- Axially : as a premixed flame in the mixing layer



Computation logic

Remark : Geometry and flame kernel position require 3D computations

Acceptable computational time

7 reactions, 6 species chemical kinetics (« Eklund » scheme)

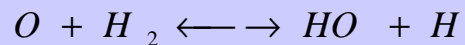
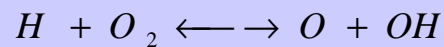
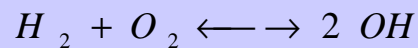
RANS model for fluid flow

Due to the complexity of computation, numerical simulation will be performed step by step, using the microcombustor geometry.

- Firstly, we have performed a 2D axisymmetrical computations to adjust :
 - cold flow simulation,
 - laser phase simulation and spot localization
 - some other parametric studies (turbulent species diffusion, etc.)
- Then 3D computations were conducted
 - computations are performed to be compared with experimental results.

Combustion model

The Eklund mechanism involves 6 species in 7 reactions



Source terms follow Arrhenius law

ONERA codes for energetics and propulsion

- **MSD 3.1 (released, April 2003)**

- more than 15 years in service,
- multi-block, structured meshes, chimera and moving meshes,
- explicit and implicit ADI time integration up to $O(2)$,
- several families of flux-splitting schemes up to $O(3)$,
- elaborated models, multi-species, turbulent reactive flows, two-phase flow (eulerian + lagrangian), LES,
- parallel and vectorized, external coupling capabilities (MpCCI).

- **CEDRE 1.2 (released, November 2003)**

- new generation code (started in 1996, from scratch) builds on MSD,
- multi-domain, generalized unstructured meshes,
- explicit and implicit (GMRES) time integration,
- flux-splitting schemes,
- multi-solver approach: multi-species, turbulent reactive flows (CHARME), two-phase flow (eulerian (SPIREE) + lagrangian (SPARTE)), thermal (ACACIA) and radiative (ASTRE), LES,
- parallel and vectorized, external coupling capabilities (MpCCI),
- integrated graphical user interface,
- geometric preprocessors (fusion, splitting, refinements).

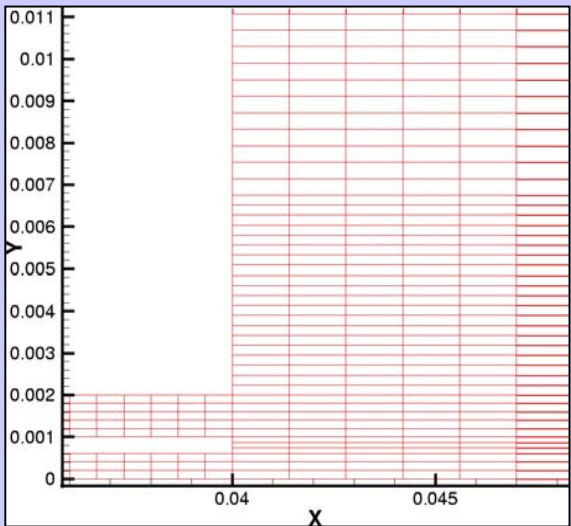
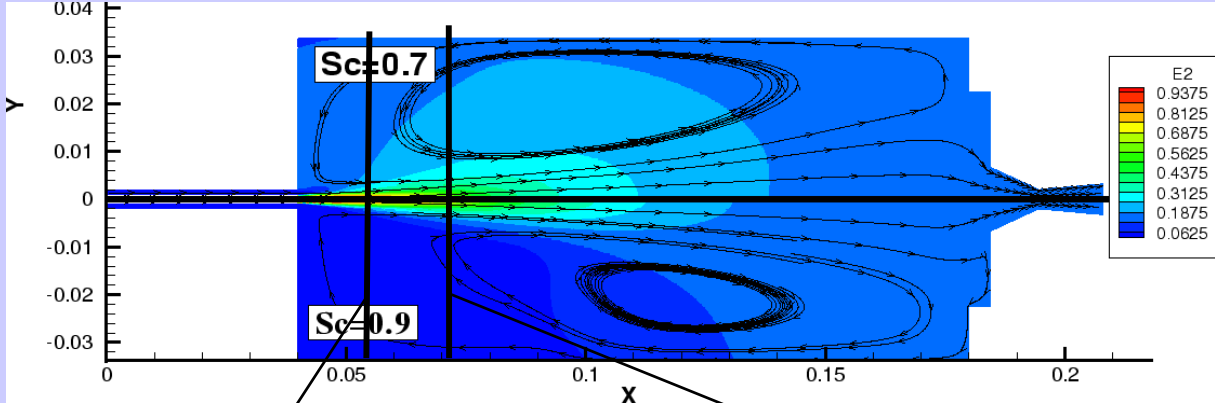


Microcombustor : 2D computations - steady state cold flow – Comparison with experiment

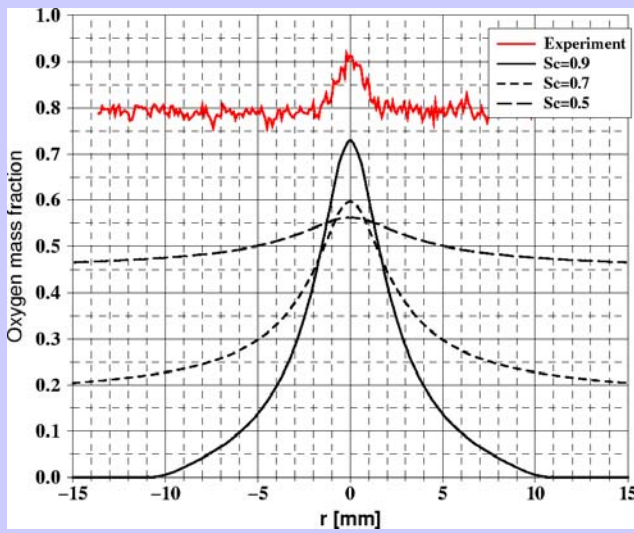
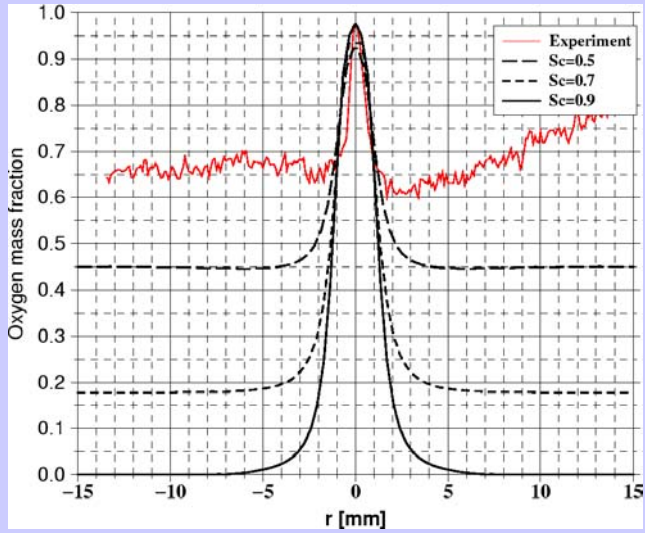
Mesh

17650 elements

- $\delta x = \sim 1 \text{ mm}$
- $\delta y = \sim 0.1 \text{ mm}$



DLR
Grid detail

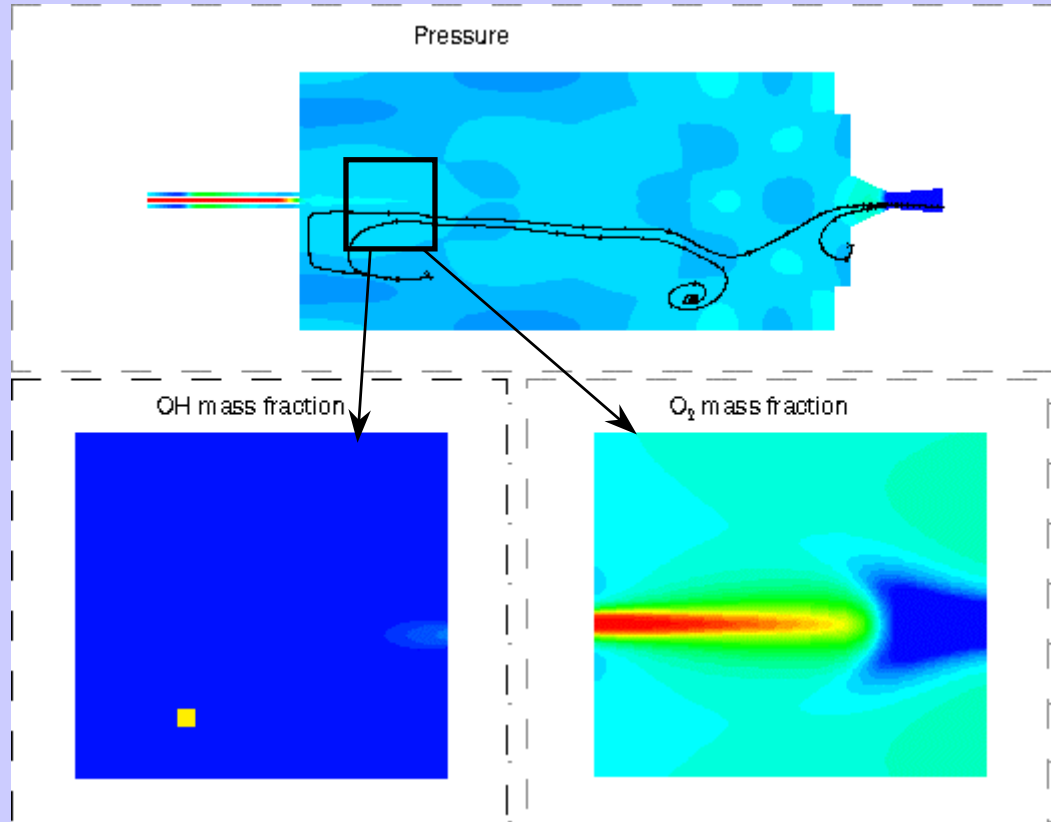


Oxygen mass fraction profiles

ONERA

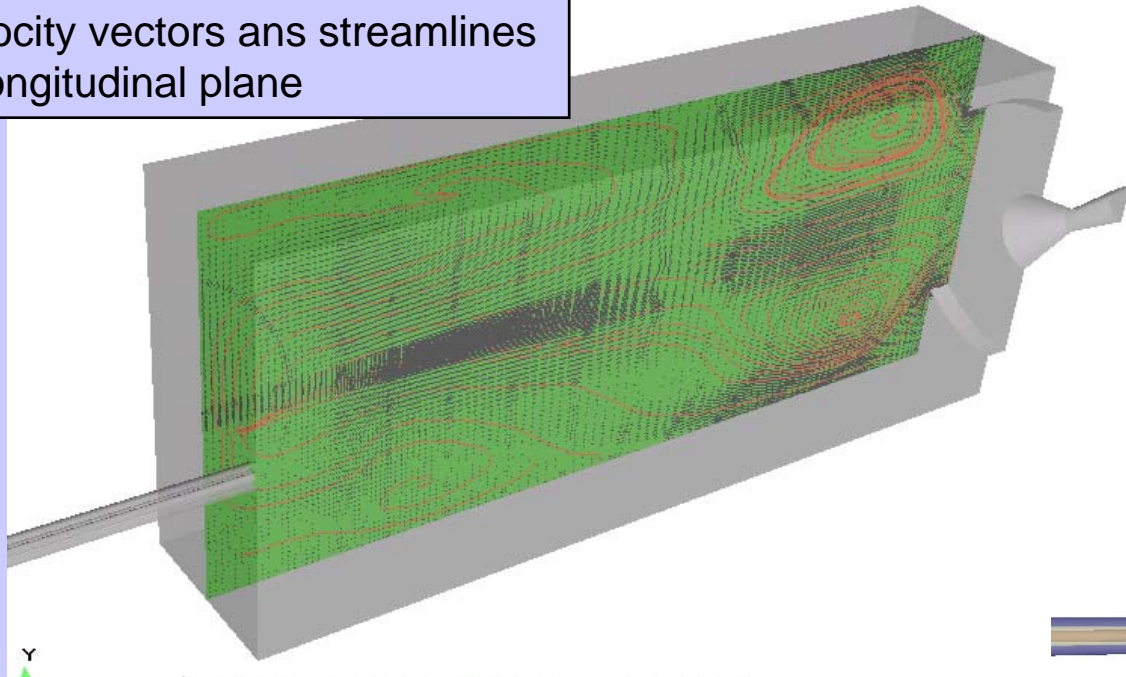
S- ISSN: October 27-31, 2003 - Chattanooga (TN)

Microcombustor : 2D axisymmetrical computations – ignition transient



3D results – Steady state

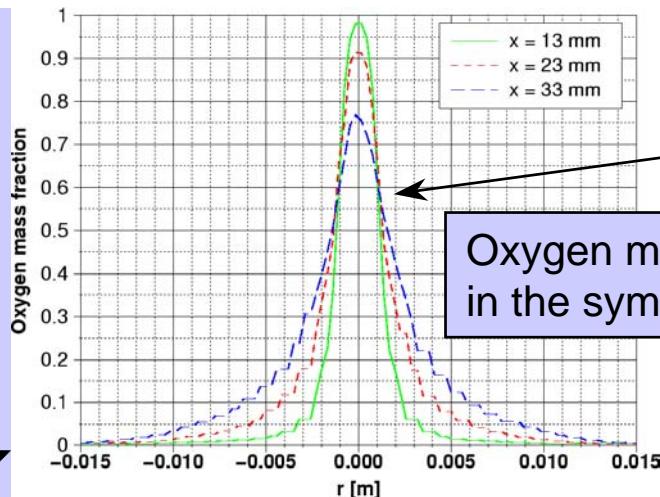
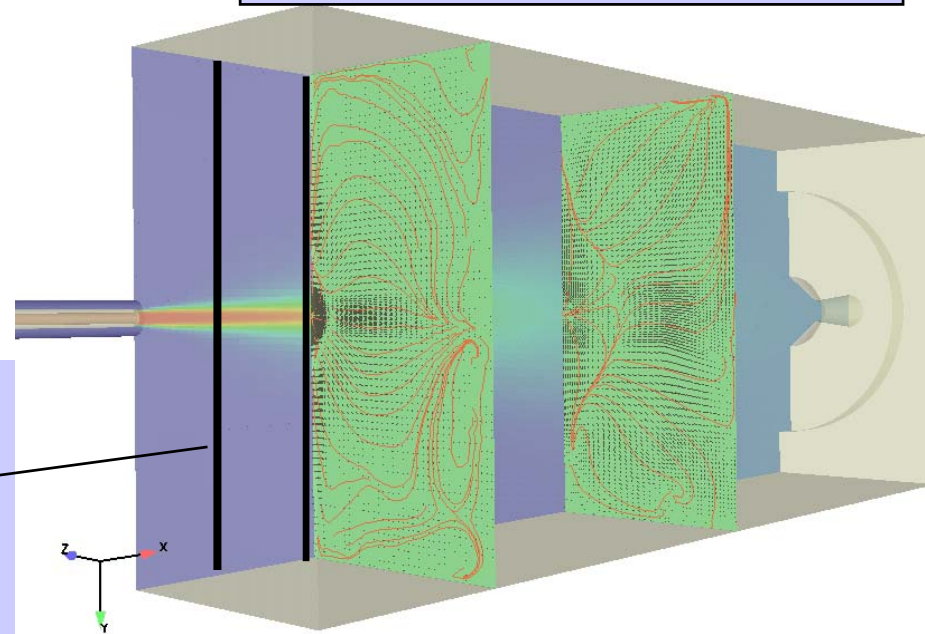
Velocity vectors and streamlines in longitudinal plane



Mesh

500194 elements

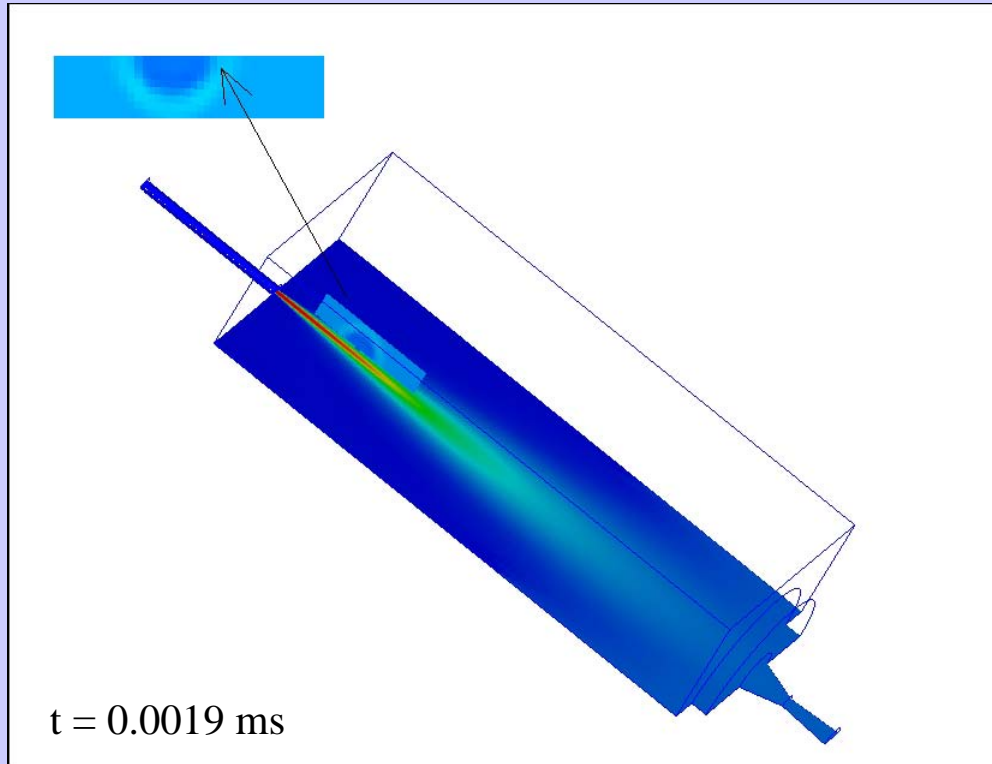
Velocity vectors and streamlines in transverse plane



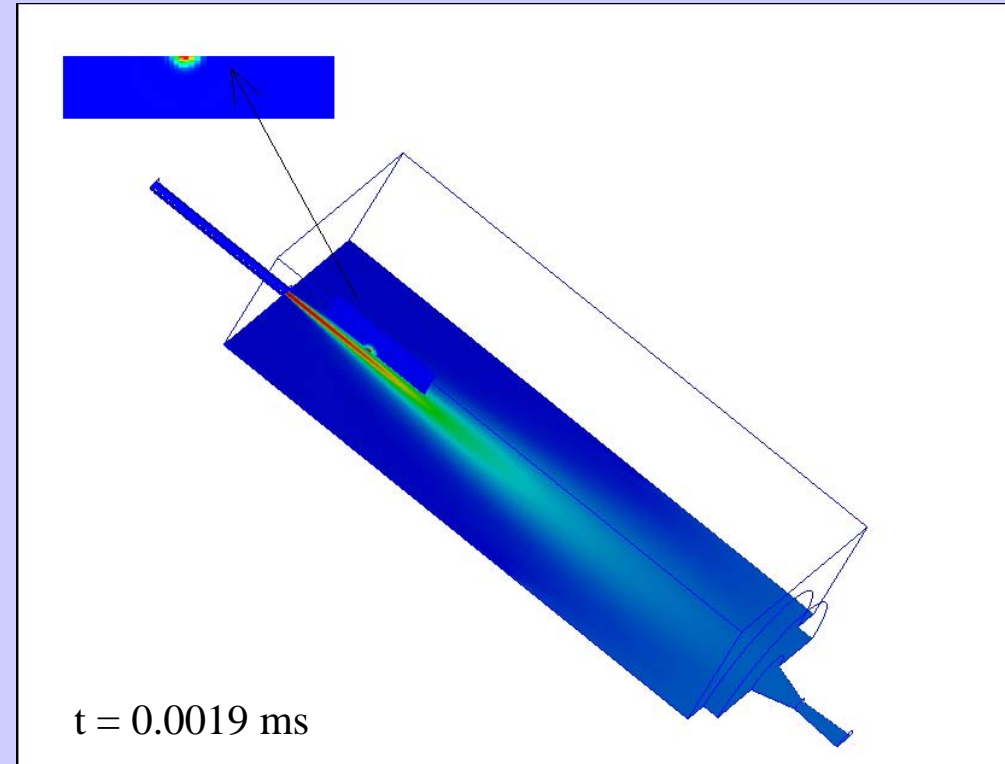
Oxygen mass fraction in the symmetry plane

3D results - Transient

Pressure



Temperature



computational time : 21 000 s ; time step = 10^{-8} s

Summary of preliminary investigation of the microcombustor ignition

- **Real geometry of the combustor is considered for ignition transient**
- **Modeling of laser pulse can be performed by a source term in energy equation.**
- **Preliminary results show :**
 - Chemical reactions are initiated due to high temperature and pressure spots and develop
 - Initial pressure peak modifies strongly the flow field
 - So it was important to describe as well as possible these expansion (adequate integration time step) ;
- **Axisymmetrical configuration induces an axisymmetrical ignition which does not allow a strong interaction of the pressure waves with the jet which may increase mixing and promote propagation of the flame.**
 - Nevertheless, these computations were necessary to adjust ignition model and perform some parametric studies
- **3D steady state cold flow computations could be achieved and show a very complex structure**
- **3D ignition computations under way will be compared to 2D simulations and to experiments**

Application of existing tools to the Vinci ignition transient

Vinci is the future Ariane V cryogenic (Lox/GH2) expander cycle engine which is under development

to match high performance and low cost requirements

- including multiple ignitions

with a H₂/O₂ gas fed torch igniter :

- the igniter design must be optimized in terms of mass versus efficiency and reliability :
 - correct and smooth ignition
 - no damage for igniter and chamber hardware

To support this development, some numerical activities on the engine ignition transient are conducted



Introduction : Physics

Chamber filled with hydrogen

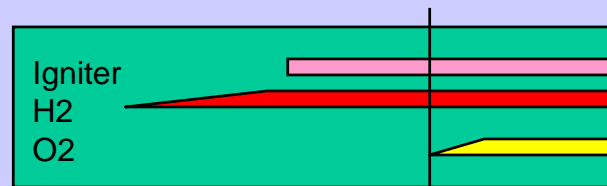
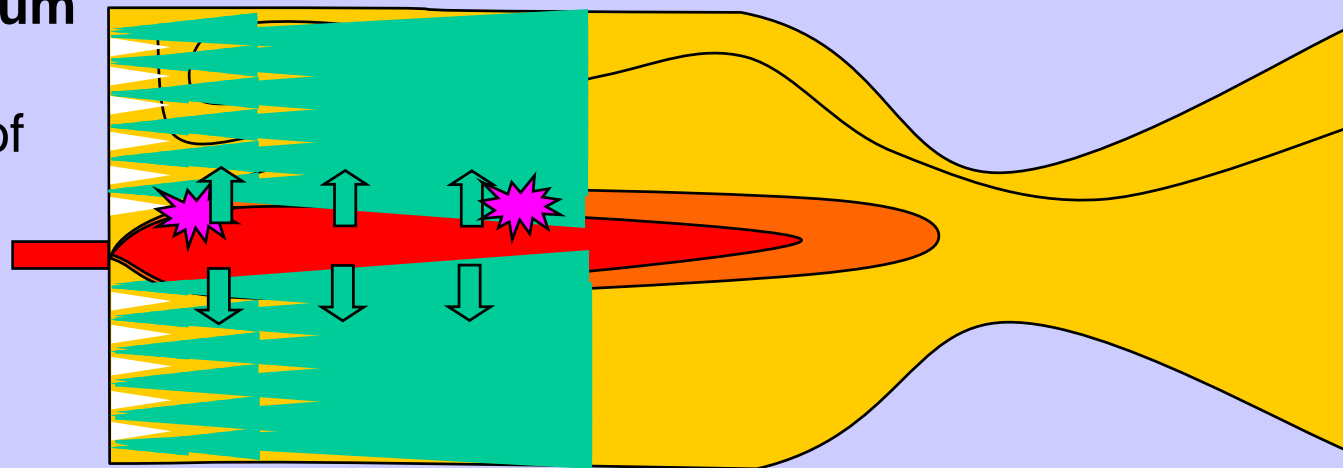
Hot gas jet with high momentum

- Recirculation zone mixing fresh hydrogen with a part of the torch burnt products
- Heat transfer

Injection of Oxygen

- Mixing with hydrogen
- Mixing with burnt products

Ignition in a zone with suitable conditions



Ignition sequence

Computational cases

Simulated ignition

Sea level ignition

In-space ignition

Method

The actual geometry of the Vinci is used

Focus on the mixing of the hot gas jet with fresh propellant flowing through the first injector row, in a *simplified* configuration

- injector geometry
- Injected fluids

The « Eklund » chemical reaction scheme is used

Geometry and grid

Objectives

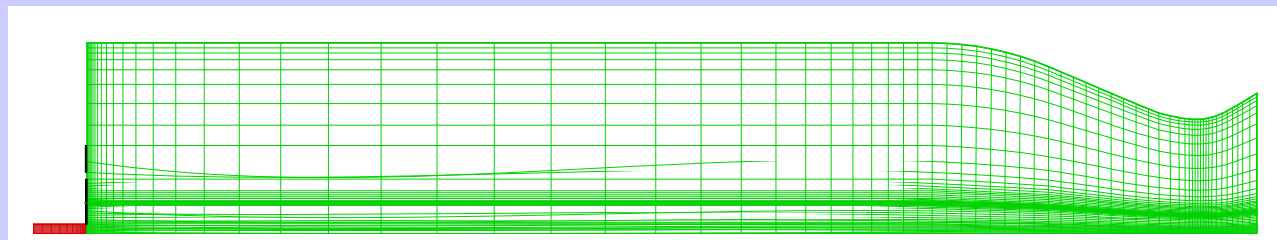
To have a limited number of grid points ,
But enough to capture the vortices near the igniter exit ...

With reasonable computation time

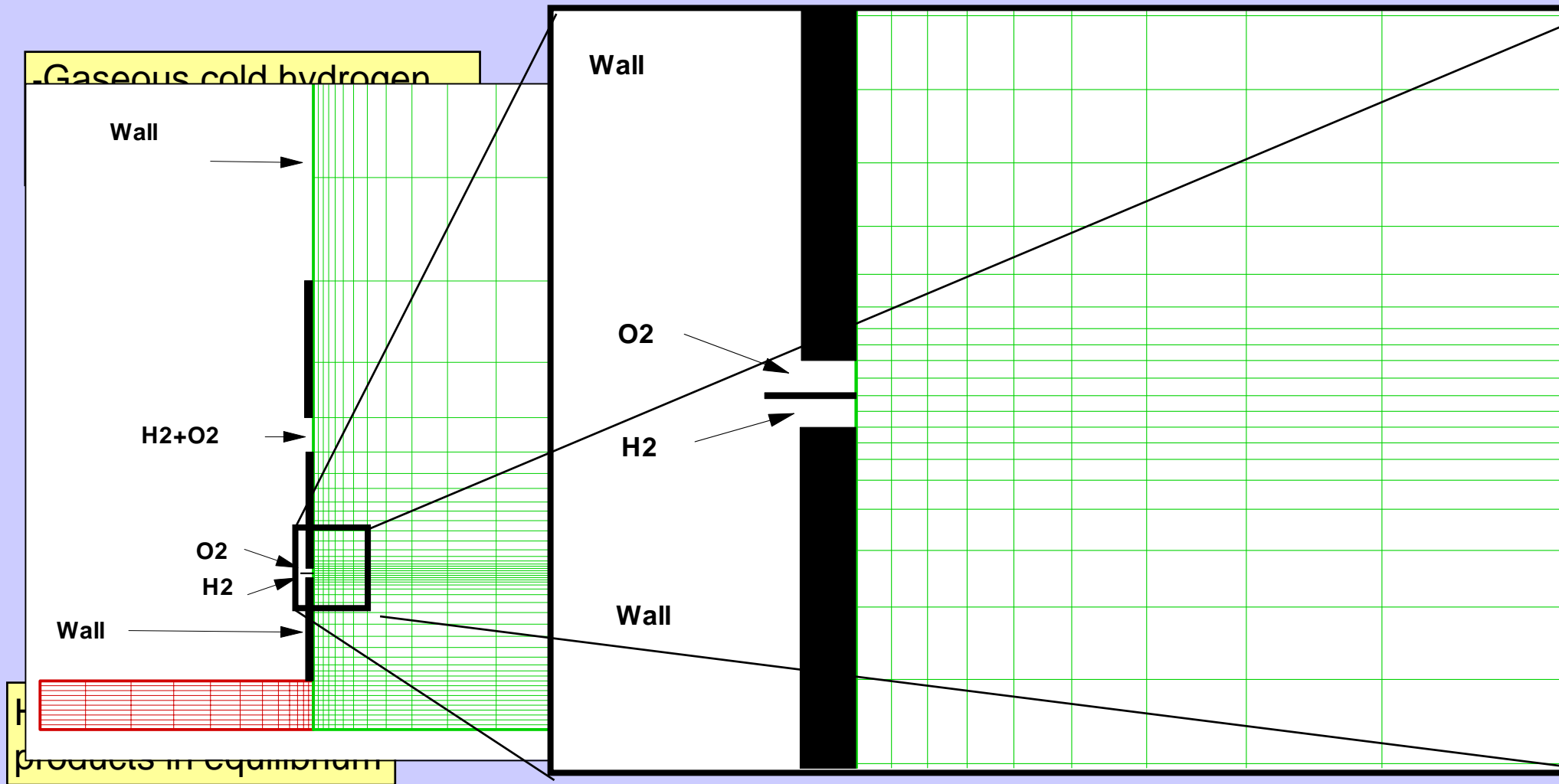
- time step must not be too small

Grid

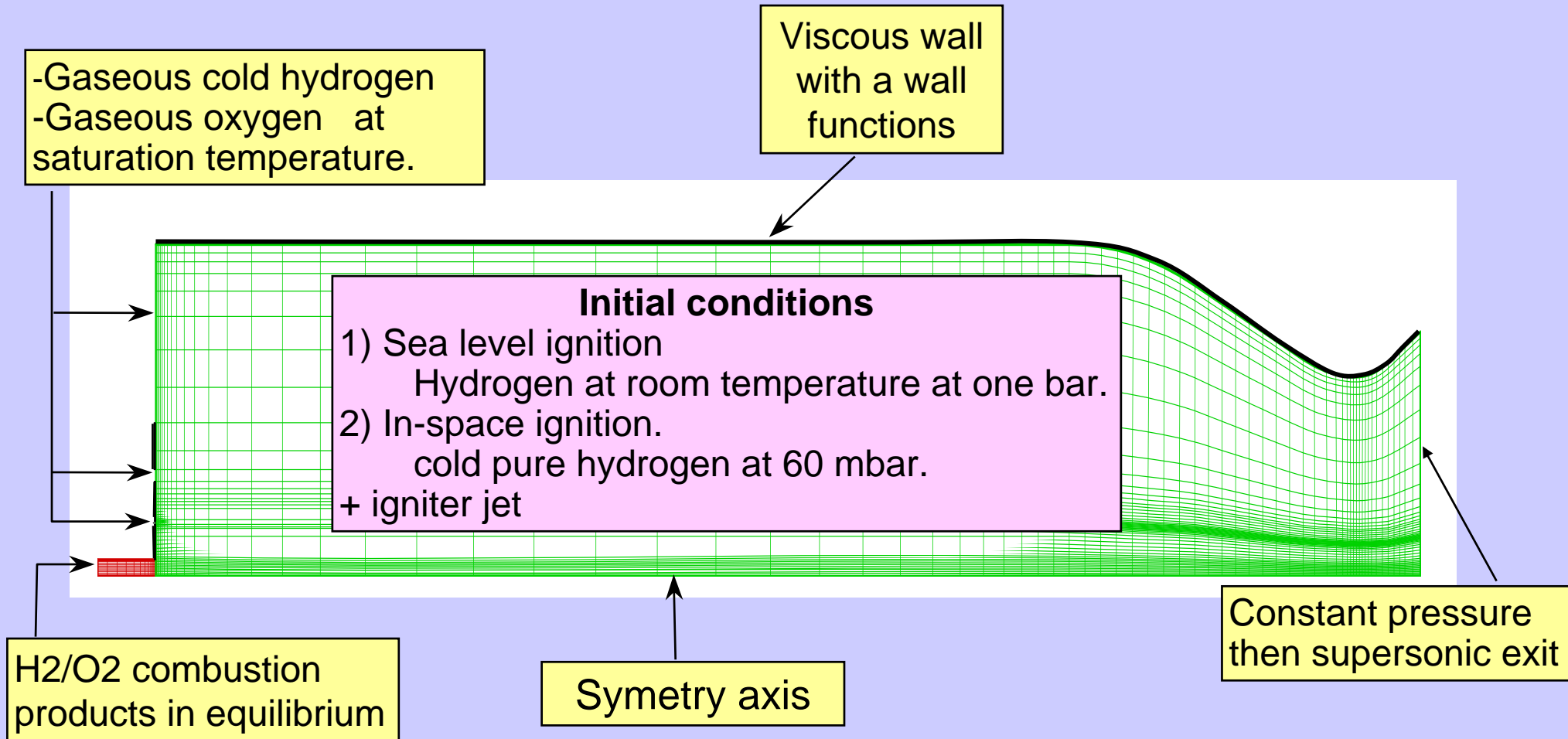
- 2D axisymmetrical
- Refinement near the igniter exit
 - 15 cells between igniter and injector row
 - simplification of injector geometry
 - » Annular slots for injector : conservation of area for the 2 first rows
 - » Uniform injection for outer injector rows
- Coarse grid
- 2 domains
 - Igniter tube
 - » $13 \times 11 = 143$ points
 - Chamber
 - » $73 \times 54 = 3942$ points



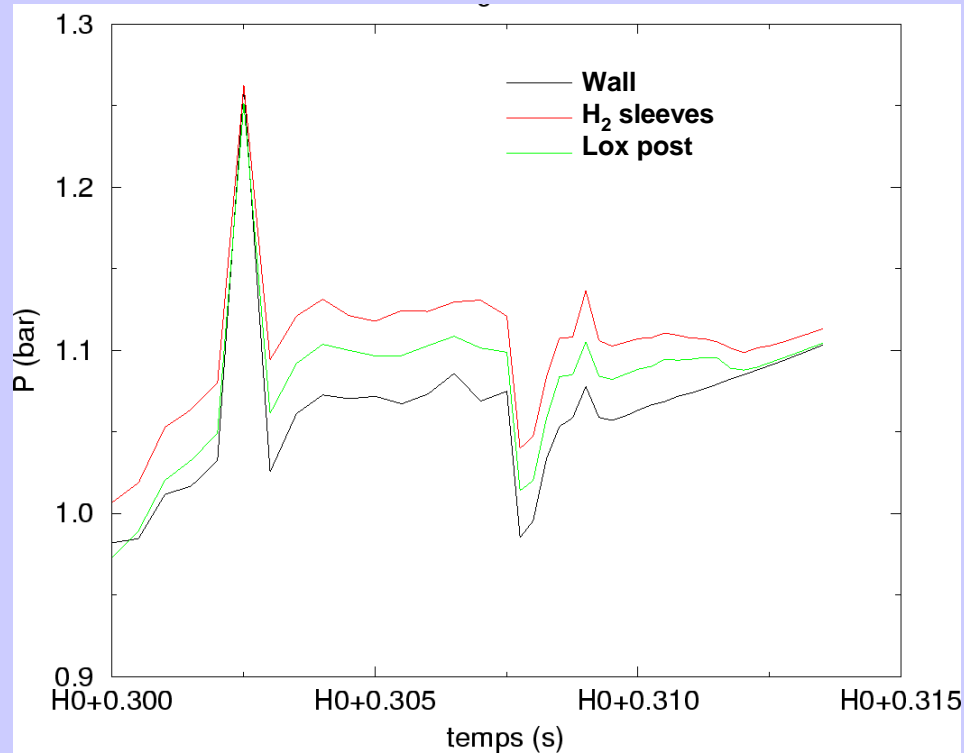
Boundary and initial conditions



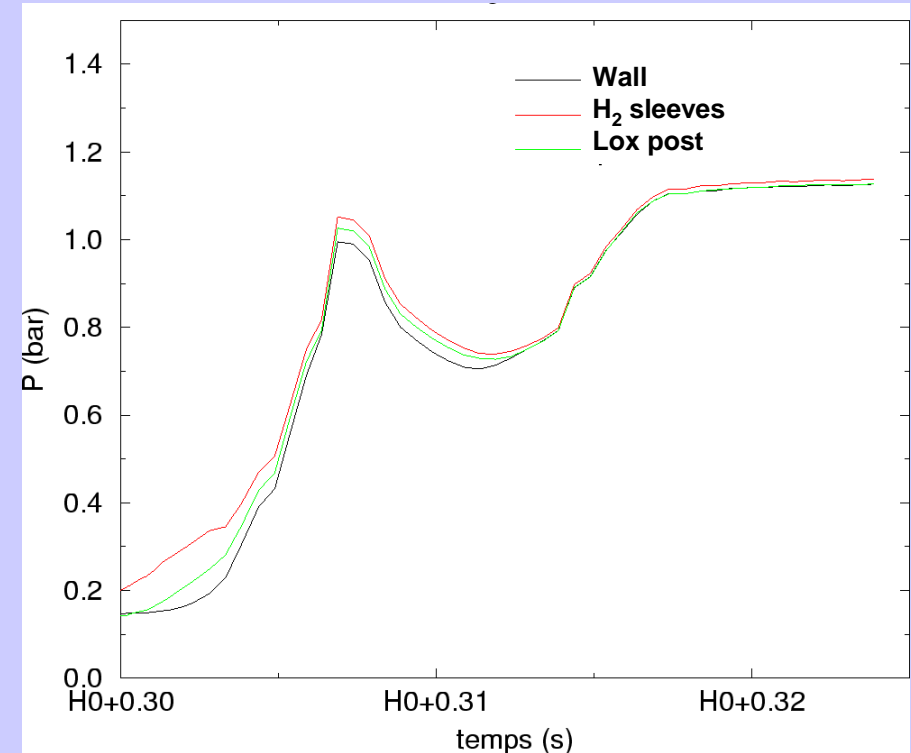
Boundary and initial conditions



Pressure evolution at face plate during ignition transient



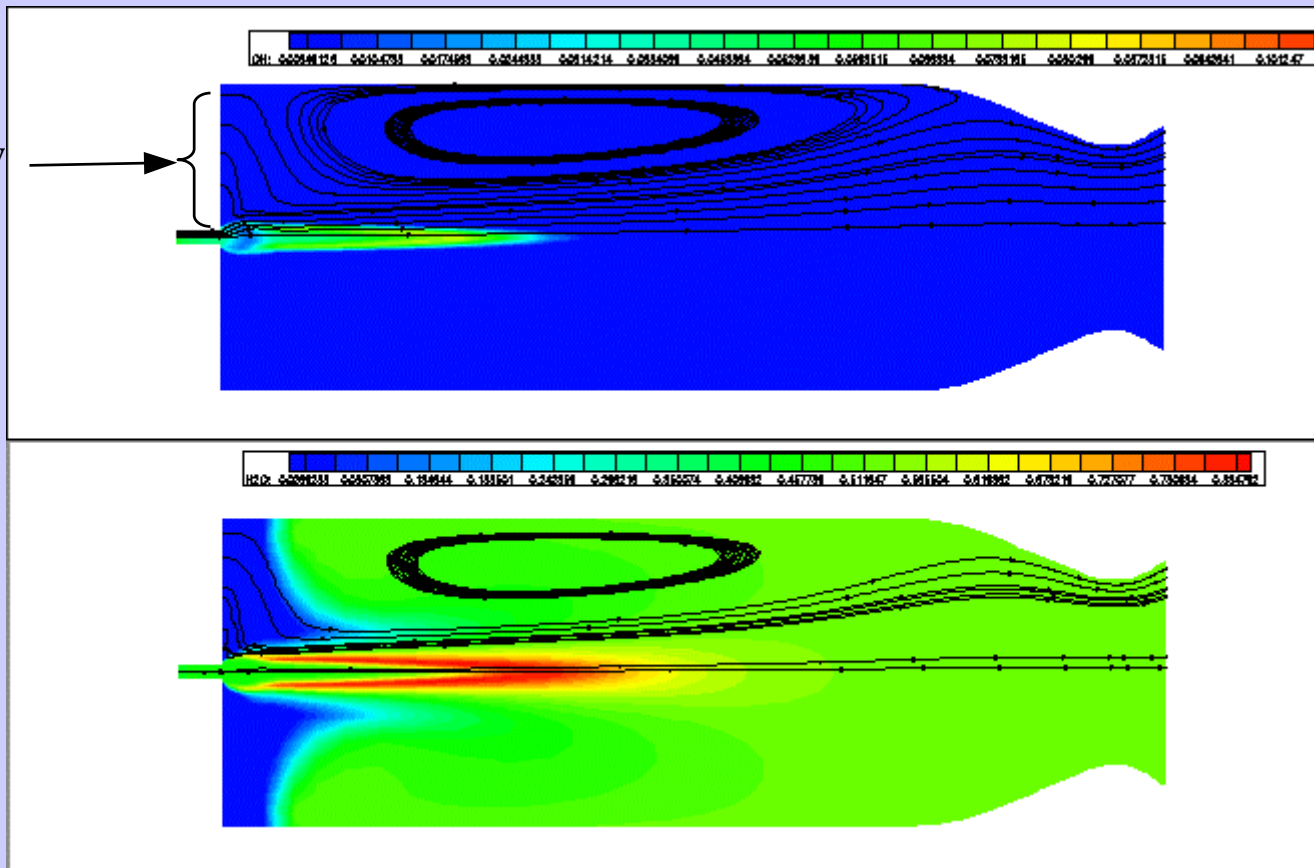
« Sea-level » ignition



« In space » ignition

"Sea level" computation : combustion species

Injection :
H2 : constant mass flow
O2 : variable mass flow



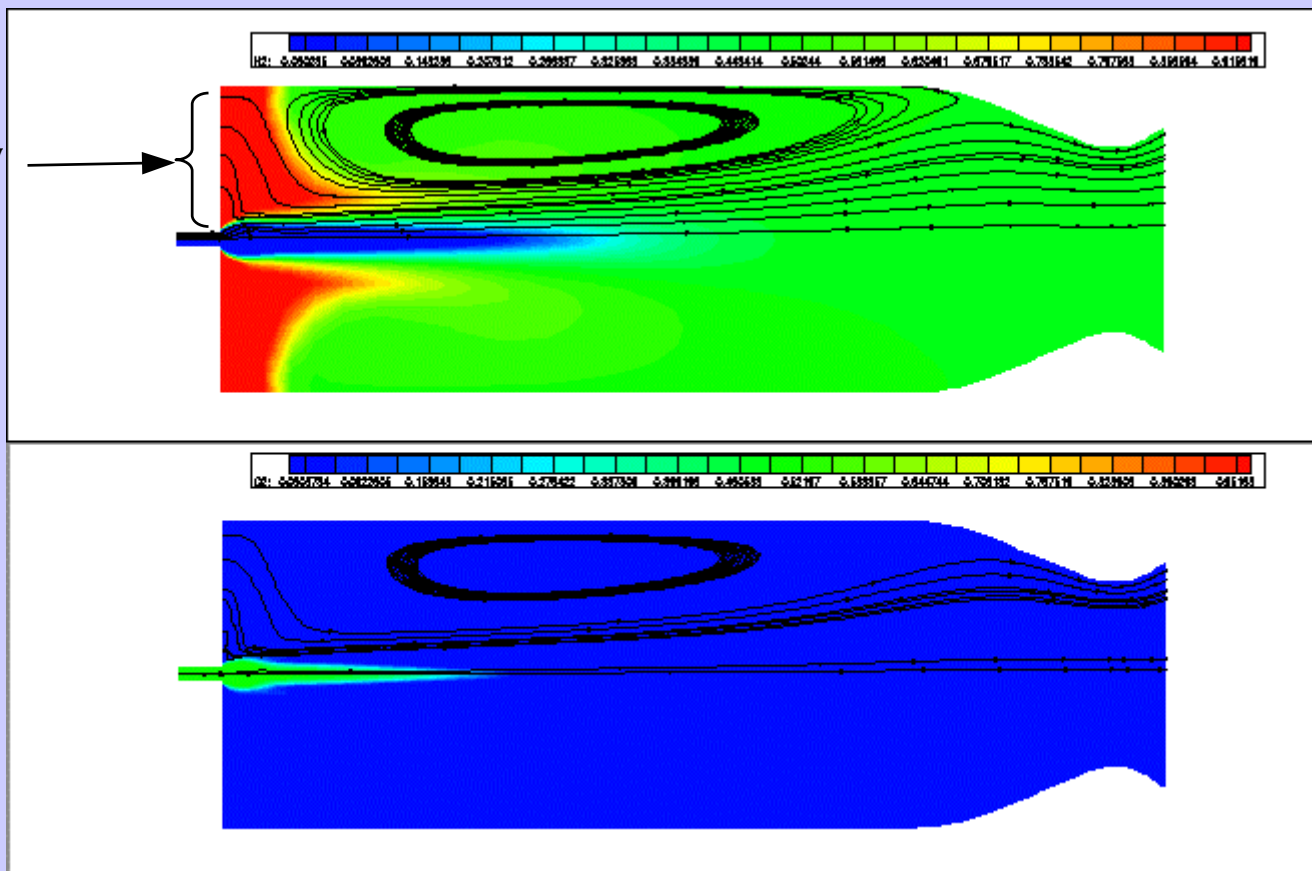
OH

H2O



"Seal level" computation : Propellant mass fraction

Injection :
H2 : constant mass flow
O2 : variable mass flow



H2

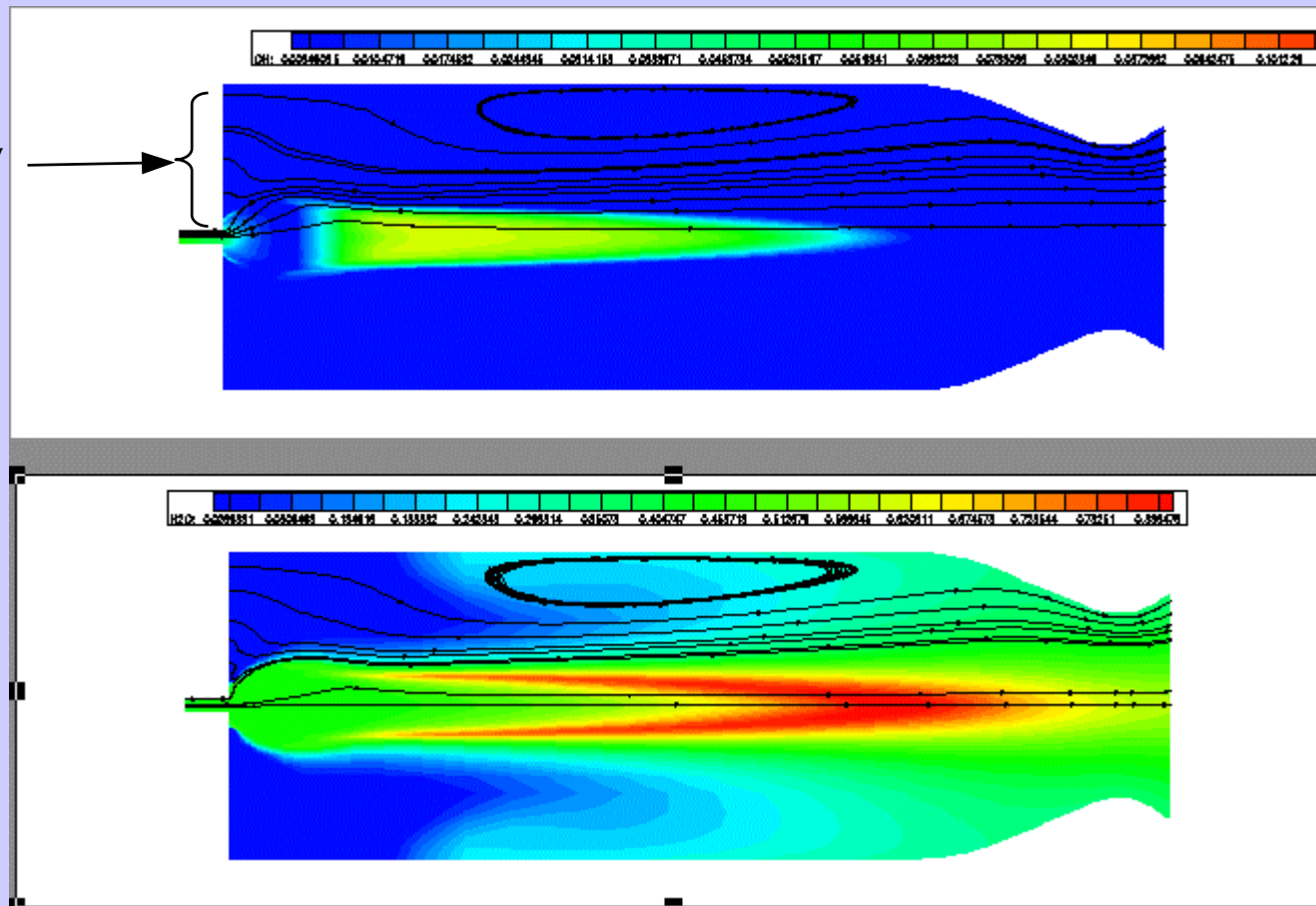
O2

"In-space" computation : combustion species

Injection :

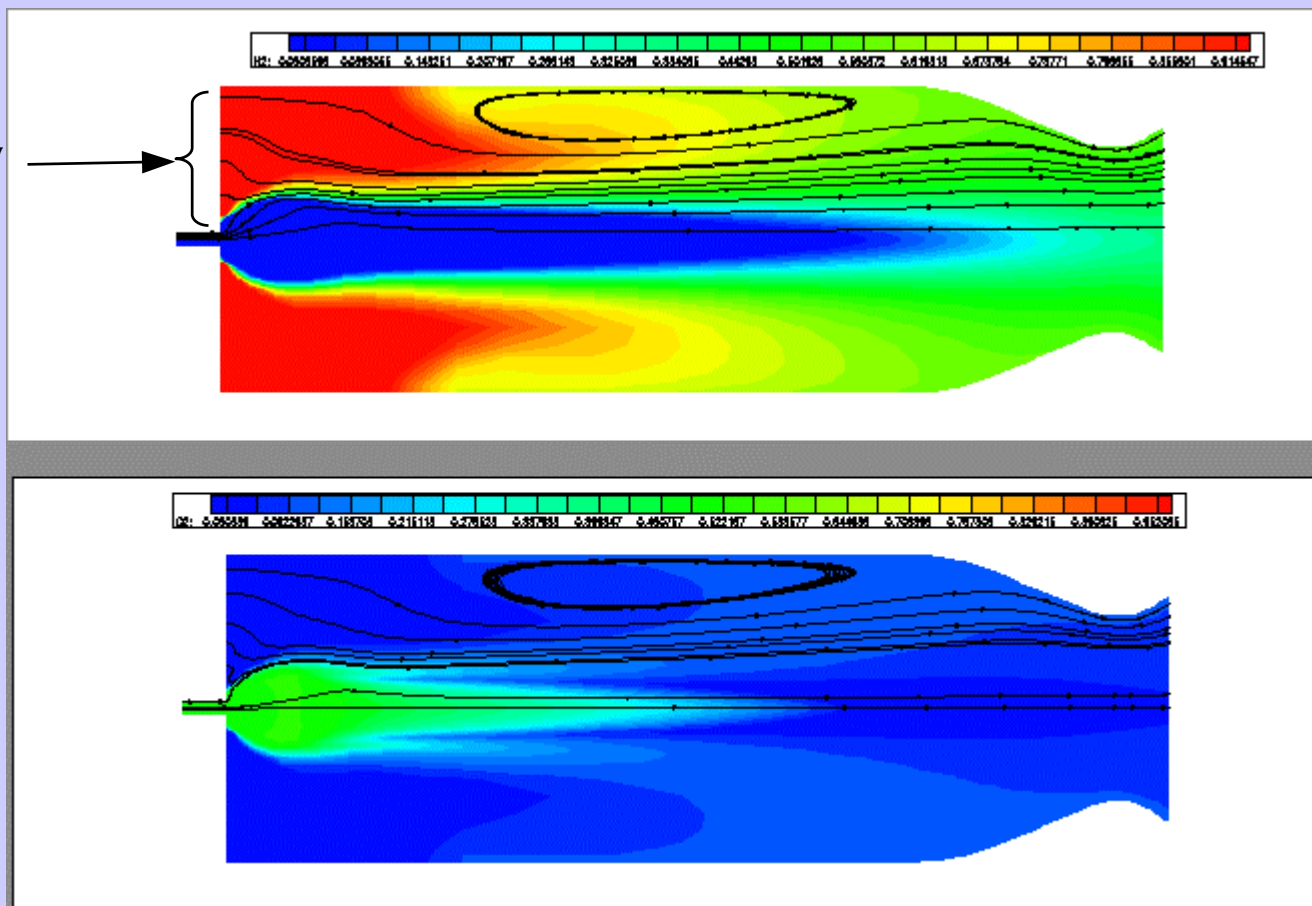
H2 : constant mass flow

O2 : variable mass flow



"In-space" computation : Propellant mass fraction

Injection :
H2 : constant mass flow
O2 : variable mass flow



H2

O2



Vinci application – Summary of results

Ignition driven by the mixing

ignition location in the low mach number zone (end of the jet)

depends on turbulence model

Recirculation zone before oxygen injection depending on

chamber length

turbulence model

flow momentum at injection

Conclusions (1/2)

experimental approach

- laser ignition allows to adjust well defined experimental boundary conditions
- quantitative determination of flame front velocities and characteristic time scales for flame stabilization by high speed visualization

ignition process

- expansion and movement of the flame in the H_2/O_2 -shear layer determined
- pressure peak in the combustion chamber results in back flow
- flame anchoring process due the recirculation zones at the faceplate observed
- early ignition transient: similar flame propagation scenarios for 4mm- and 6mm-nozzle
- flame anchoring at injector sensitive to chamber pressure, no stabilization with 6mm-nozzle

Conclusions (2/2)

Numerical simulations of ignition transient were conducted in extreme cases:

Small scale test : Microcombustor

- Well controlled conditions, laser diagnostics => enables to get insight into basic phenomena and to anchor modeling

full scale engine : Vinci engine

- Use of existing tools and modeling is helpful to support engine igniter system design

First numerical results are encouraging and should be continued to improve our knowledge in this phenomenon

The MSDH-Cedre family code offers high capabilities for ignition simulation such as

- handling actual combustor geometry, with local refinement
- representative ignition sequence
- detection of ignition peak
 - Even if amplitude is lower than expected because of a limiting scheme for kinetics

Outlook

DLR experiment

- variation of injection conditions
- ignition under high altitude conditions
- CH₄/O₂ coaxial injection

computations

- microcombuster experiment
 - Short term : go on 3D computations
 - Mean term
 - Parametric study on turbulence/combustion models
 - Two-phase flow ?
 - » Time-dependant data on droplet distribution are required for injection boundary conditions
- Application to Vinci



Experimental Investigation and Modeling of the Ignition Transient of a Coaxial H₂/O₂-Injector

V. Schmidt, D. Klimenko, O. Haidn, M. Oschwald
DLR Lampoldshausen, Institute of Space Propulsion
D-74239 Hardthausen, Germany

A. Nicole, G. Ordonneau, M. Habiballah
ONERA Chatillon, Fundamental and Applied Energetics Department
BP 72, 92322 Chatillon, France

April 15, 2004

Abstract

A test case have been defined to investigate experimentally and by numerical simulation the transient ignition phenomenology when igniting coaxial injected O₂ and H₂ by a laser. Using high-speed photography the temporal evolution of the flame and its anchoring at the injector could be visualized. From the analysis of the flame front movement flame velocities and convection velocities have been determined at specific phases during the ignition transient.

1 Introduction

The ignition of the propellants injected into a rocket combustion chamber and the subsequent propagation and anchoring of the flame is an important design consideration for all types of rockets [1]. Reliable ignition has to be guaranteed and the initiated turbulent diffusion flame has to stabilize without overpressure or blow out. The analysis of this process has to take into account that the boundary conditions for the flame are changing until stationary combustion chamber conditions are reached: during the ignition transient the pressure is increasing, due to the thermal transient in the injector head the velocities of the injected fluids are changing or the propellants may even change their phase. Atomization is adjusting to the transient injection conditions and the flow field in the combustion chamber has to adapt continuously to the actual status of the flame as well.

The motivation to address the problem of ignition is based on several aspects. The ability to launch multiple payloads into orbit in one flight is an essential feature of the Ariane launcher family with relevant impact on costs/payload. A new cryogenic upper stage Vinci is currently under development aiming to increase the payload capacity of Ariane 5 to 12 tons [2]. The multiple payload capability requires igniter systems guarantying reliable multiple ignitions under vacuum conditions. This has initiated igniter development and ignition research activities [3], [4], [5]. Experiences in former development programs have shown how important a sound understanding of the ignition process is. Anomalies during the ignition process of the HM7 engine resulted in the loss of the Ariane flights V15 and V18 [6]. Another motivation to get more insight into the ignition transient of a coaxial injected cryogenic H₂/O₂ is based on the observation that during this transient low- and high-frequency combustion instabilities may develop [7].

Predicitivity of the models and numerical tools to analyze the ignition transient has still limitations. In H₂/O₂-rocket combustors the injected propellants are ignited by a stream of hot gas originating the igniter device. The hot gases have to mix with the injected propellants and to initiate combustion in a situation which is characterized by strong spatial inhomogeneities e.g. in respect to species, temperature, turbulence and state of mixing. Turbulent transport properties are mainly controlling mixing. The problem of rocket combustor ignition has motivated several experimental investigations [8], [9], [10], [11], [12], [13] and was addressed by modeling and numerical simulation [4], [14], [15]. However, the problem of reliable prediction of the ignition transient in a compressible, reactive, instationary flow is still

pending. Where are regions with ignitable mixtures in the flow? Is the mixing of the igniter jet with the injected propellants efficient? Is there sufficient energy transfer of the hot igniter gases to these regions? When combustion has been initiated, what are then the dominant parameters controlling the flame propagation and stabilization? How can flame blow out and high overpressure during the ignition transient be prevented?

The focus of the work presented here is on the phenomena after combustion has been initiated in the flow. Flame evolution, propagation and its ability to anchor at the injector is investigated experimentally and by numerical simulation. Test conditions are not primarily chosen to represent conditions in real rocket combustors in all aspects. The experiments are dedicated to simplify the situation as much as possible to allow quantitative measurements and a comparison of experimental and numerical results.

The scenario under investigation in this work is the coaxial injection of gaseous oxygen and hydrogen. The propellants are injected at ambient temperature. Ignition is initiated at stationary cold flow conditions at a specified location in the flow. Thus the injector exit conditions, i.e. mass flows, Reynolds numbers, momentum flux ratios, etc. at time of ignition are well known.

2 Experimental Investigation of O₂/H₂-ignition transient

2.1 Experimental set-up

2.1.1 Combustion Chamber

The tests have been done at the M3 test-facility at DLR Lampoldshausen. The micro-combustor has a square cross section (6 x 6cm²) and a length of 14cm (figure 1). It is designed for combustion chamber pressures up to 2MPa. Operation time of the capacitively cooled combustor under hot fire conditions is limited to 1-2s. Quartz windows give complete optical access to the combustor volume. Two slid windows in the upper and lower combustor wall allow access for the igniting laser. The chamber nozzle has a diameter of 6 mm. Optional a nozzle with 4mm diameter could be mounted.

The gaseous propellants at ambient temperature have been injected through a single coaxial injector. The diameter of the O₂-post (1.22mm) is fixed. The outer O₂-post diameter, i.e. the inner diameter of the H₂ annular slit, is 2.0mm. The cross section of the annular H₂-slit can be varied by exchanging the ring defining the outer H₂-slit diameter and was 4.0mm in the tests presented in this paper.

The chamber is continuously purged with nitrogen prior to a test, the N₂-purge is shut off 1s before the H₂-valve is opened. The O₂-valve is opened 20ms after the H₂-valve.

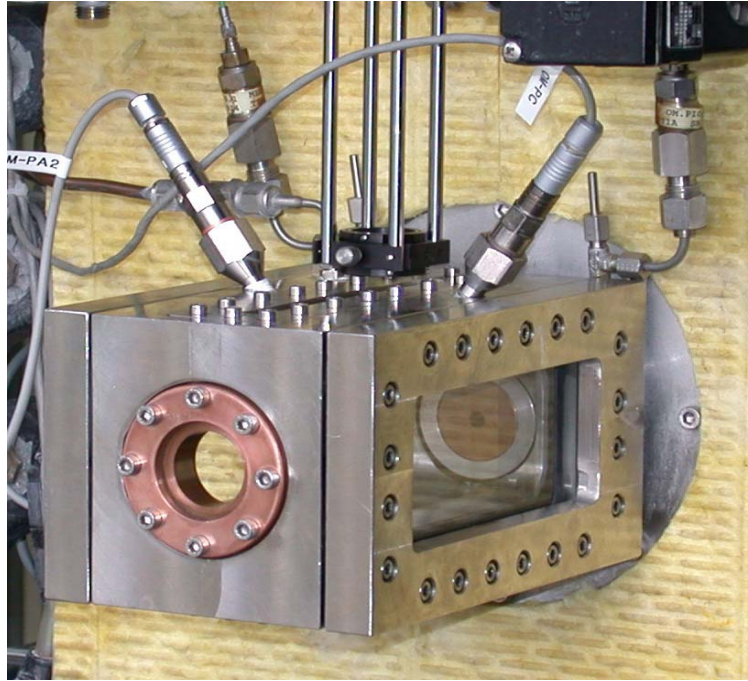


figure 1: Cross section of the micro-combustor

2.1.2 Laser Ignition

Combustion is initiated in these tests by laser induced gas break down. A frequency doubled Nd:YAG laser (523nm, 195mJ/pulse) is focused into the flow. The focus position was $z=36\text{mm}$ downstream the injector exit and $r=2.5\text{mm}$ off-axis from the O_2 -jet.

Laser ignition allows full control of the time of ignition, which is essential for synchronization of the data acquisition systems with the ignition transient. Furthermore as compared to electric spark ignition which has been used by several authors [9], [10], [11], [12], laser ignition gives high flexibility in choosing the location of energy release. The location of ignition can be chosen to be in the central flow region without disturbing this flow by the ignition equipment.

Laser induced gas-break down has been studied intensively since it has been first reported in 1963 by Maker et al. [16]. The leading part of the laser pulse is transmitted in the focal volume until the ionization threshold intensity has been reached. As soon as a plasma is formed laser radiation from later parts in the pulse is absorbed efficiently [17]. Since in our set-up a measurement of the transmitted radiation was not possible, the energy deposited in the flow cannot be deduced. However, our pulse energy is far above the energy required for ignition of H_2/O_2 -mixtures near the flammability limit at ambient conditions [18], thus the major part of the pulse energy is assumed to be absorbed.

The expansion of the plasma immediately after laser absorption results in the formation of an shock front that becomes spherical in time. This blast wave expands and an estimation of McManus et al. for electric spark ignition has shown, that the shock heating of the mixture is not probable [8]. During laser absorption the temperature in the plasma can reach several 10^4K [19]. In the following the plasma cools down by adiabatic expansion. From Schlieren images at about $30\mu\text{s}$ after the laser pulse we determined that the bubble of hot gas had an ellipsoidal shape with an extension of 2mm in axial and of 3.5mm in radial direction. The extension in the radial direction is in the order of the distance of the laser focus from the central axis of the O_2 -jet. The flow induced by the expanding hot gas is therefore probably changing the local parameters in the shear layer between O_2 -jet and hydrogen co-flow.

Tests have been performed with different pulse energies of the ignition laser. No influence of the pulse energy on the temporal evolution of the OH-emission or combustion chamber pressure has been found. It can therefore be assumed the results are not biased by ignition energies in the range from 80mJ to 195mJ.

2.1.3 Diagnostic Techniques

Schlieren Photography: A color-Schlieren set-up has been used to visualize the flow topology. Images have been recorded with a Hasselblad film camera.

Rayleigh Scattering: Using the radiation of an KrF-excimer laser (248nm) a planar light sheet has been illuminated in the flow. An intensified CCD-camera detected the Rayleigh signal. The Rayleigh scattering cross section of O₂ is 4.2 times that of H₂, allowing the observation of the disintegration of the oxygen jet in the annular flow of hydrogen. Under favorable conditions even quantitative mixture ratios can be obtained.

OH-Imaging: The flame evolution is recorded with an intensified high-speed CCD-camera with an interference filter that only transmits light in the range of 300-310nm, i.e. radiation emitted by the OH-radical. The Photron Fastcam Ultima I² allows recording images at a frame rate of 18KHz at a resolution of 256x128 pixel, the dynamic range was 8bit. In regions without chemical activity less than 2 counts have been recorded on the detector. Therefore all pixels with 3 counts or more have been assumed to belong to the flame.

In each frame of the OH-image series the coordinates of flame-pixels at the most upstream position z_U and downstream position z_D have been determined. From these data the velocities at the upstream and downstream flame front as seen by an observer in the laboratory coordinate system can be calculated according to

$$v_U = \frac{z_U(t_{i+1}) - z_U(t_i)}{\Delta t}$$

where Δt is the time between two frames. Similarly the downstream front velocity v_D is determined. The upstream front moves with the difference of flame velocity v_F and convection velocity v_c

$$v_U(z_U) = v_c(z_U) - v_F(z_U)$$

and the downstream front moves with

$$v_D(z_D) = v_c(z_D) + v_F(z_D)$$

With the assumption that the flame- and convection-velocities at $z = z_D$ and $z = z_F$ are identical the flame velocity

$$v_F = \frac{v_D - v_U}{2}$$

as seen by an observer moving with the flow with the convection velocity

$$v_c = \frac{v_D + v_U}{2}$$

can be estimated:

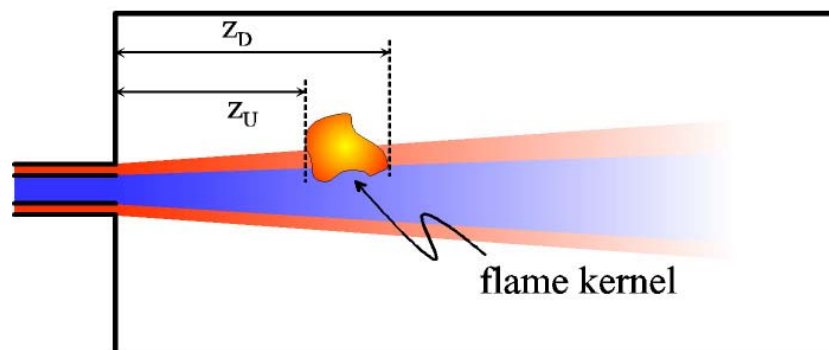


figure 2: Determination of the upstream and downstream flame position

2.2 Test Conditions

The tests presented here have been done at ambient temperature and ambient pressure in the combustion chamber prior to ignition. The propellants have been injected in the gaseous state and ignition has been initiated after stationary cold flow conditions have been approached. Tests have been done at a mixture ratio of $R_{OF}=2$.

The injection conditions as calculated for the injector exit are given in table 1. The injection conditions match realistic conditions in terms of Reynolds-numbers for hydrogen and oxygen. Taking data from Baudart et al. [15] momentum flux ratios $J=(\rho v^2)_{H_2}/(\rho v^2)_{O_2}$ ranging from 0.002 to 0.3 can be estimated at ignition conditions in cryogenic rocket combustors. The integral He-momentum flux $I_{H_2}=(\rho v^2 A)_{H_2}$ which has appeared to be an important parameter to characterize the ignition transient phenomena in the former experiments [13] is given as well in table 1.

v_{H_2} [m/s]	v_{O_2} [m/s]	m_{H_2} [g/s]	m_{O_2} [g/s]	Re_{H_2}	Re_{O_2}	J	v-ratio	I_{H_2} [kg·m/s ²]
653.5	370.6	0.58	1.15	18616	43836	0.195	1.763	1.571

table 1: Injection conditions.

2.3 Results

2.3.1 Conditions before Ignition

A Schlieren image taken 35 μ s after ignition is shown in figure 3. The laser induced flame kernel has just developed and the wake of hot gas can be seen. The O_2 -jet upstream this kernel is still not influenced by the flame and the regular pattern of Mach knots is clearly visible in the sonic O_2 -jet leaving the injector.

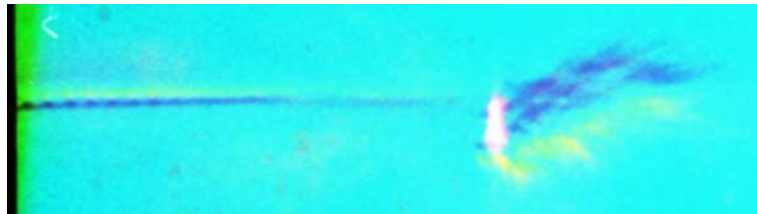


figure 3: Schlieren image 35 μ s after ignition

Single pulse images of the Rayleigh scattering signal are shown in figure 4. The O_2 -jet visible due to its high Rayleigh scattering cross section as compared to H_2 shows an increasing zigzag-like shape on its way downstream until it disintegrates into separate regions of high O_2 -density. The zigzag bending - although not strictly regular - seem to match the periodicity of regular Mach disk pattern of the sonic O_2 -jet seen in the Schlieren images.

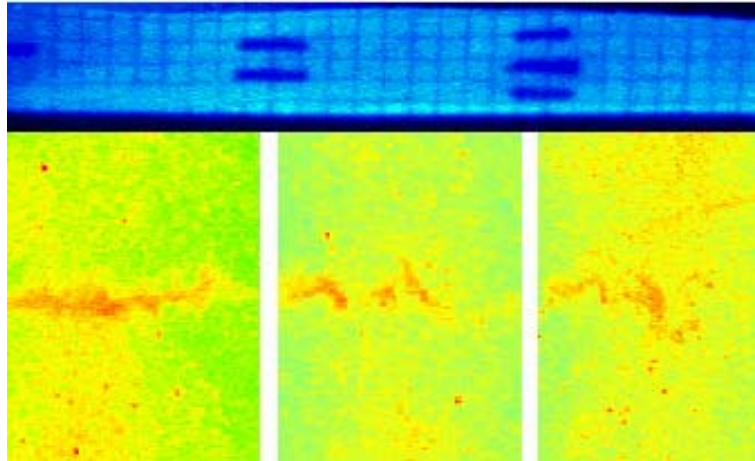


figure 4: Single pulse Rayleigh signal for $z = 10 - 38$ mm

Radial profiles of the Rayleigh signal have been determined from these images averaged over 2mm in axial direction. The results are shown in figure 5 for $z=12-14$ mm and for $z=32-34$ mm. The high Rayleigh intensity on the central line clearly reflects the high O_2 -density, which is decreasing downstream. The width of the O_2 -jet is broadening with increasing distance to the injector.

At large radii there are significant variations in the signal, at positions where we do not expect corresponding changes in the composition of the gas. This indicates problems with background illumination which were mostly related to condensed water vapor from previous hot fire tests on the windows. This unfortunately prohibited to deduce quantitative mixture fractions from these Rayleigh images.

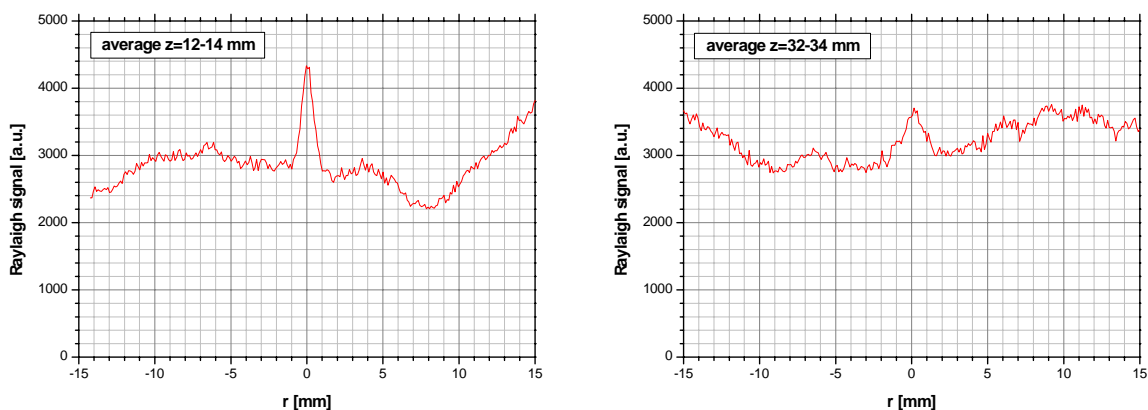


figure 5: Radial profile of the Rayleigh scattering intensity averaged for $z=12-14$ mm (left) and averaged for $z=32-34$ mm (right).

2.3.2 Ignition Transient

According to the phenomenology observed the ignition transient can be divided into 4 phases. The ignition transient follows the general scenario:

- (i) As a result of the deposition of the laser energy a small flame kernel is formed, which is convected downstream. The OH-emission of this flame kernel is decreasing to a level, that is rather not detectable with the intensified high-speed camera. The size of this flame kernel is rather constant.
- (ii) After some time the movement of the flame kernel changes its direction and the flame kernel moves upstream. The size of the kernel is increasing and the OH-emission increases as well. Finally the flame is attached to the injector.
- (iii) The flame separates in a small region attached to the injector and a second region moving downstream. The downstream flame is consuming the unburned propellants

and extinguishes after some time. The flame anchored at the injector is not visible in some tests but from the flame evolution it is obvious that it has to be existent. This flame is becoming longer and extending in the downstream direction.

- (iv) The flame stabilizes around the O₂-jet, but extinguishes, when the combustion chamber pressure falls below a specific level.

Based on the experimental results the phenomenology of the ignition transient is discussed in detail in the following:

phase (i): Frames from the high-speed video of the OH-emission are shown in figure 6. To see the whole story of flame evolution it is necessary to look even at the smallest intensities, in some cases the dynamic range of our camera is not high enough to detect the smallest OH-emission levels. For that reason in figure 6 the raw-data and frames with enhanced gray-values (gray value interval [0-10] extended to [0-255]) are shown.

As a result of the deposition of the laser energy a small flame kernel is formed, which is convected downstream. The size of this flame kernel is rather constant. The OH-emission of this flame kernel is decreasing and rather not detectable with the intensified high-speed camera. Phase (i) ends about 0.3-0.4ms after ignition when the downstream convection of the kernel stops.



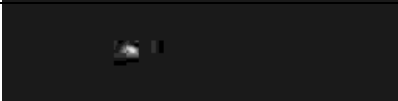

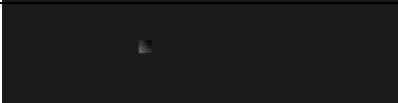
frame#	time [ms]	GGA05 raw data	GGA05 enhanced gray values
2	0.06		
4	0.17		
6	0.28		

figure 6: Flame kernel initiated by the laser induced spark and its downstream convection during phase (i)

phase (ii): After some time the movement of the flame kernel changes its direction and it moves upstream. The size of the kernel is increasing and the OH-emission increases as well. Finally the flame is attached to the injector. Frames of the OH-emission during this phase are shown in figure 7. Simultaneously to the OH-intensity the combustor chamber pressure starts to increase as well (see figure 8). The low pressure loss for H₂ at the injector results in a higher chamber pressure than in the H₂-dome. Just after around 3ms the dome pressure is above the chamber pressure again.

OH-emission of the flame kernel is reaches a maximum near to 0.8ms. The upstream moving flame kernel has now attached to the injector.

The position of the upstream and downstream flame front as determined by image processing routines can be seen for test GGA04 in the left half of figure 9 for 0-3ms after ignition. For $t \in [0.1\text{ms}, 0.4\text{ms}]$ the evaluated z_U and z_D are zero, because no flame has been detected by the image processing software. For $t > 0.7\text{ms}$ the flame is attached to the injector and $z_U = 0\text{mm}$.

In the right half of figure 9 a zoom for $t \in [0.4\text{ms}, 0.7\text{ms}]$ - the time period when the flame kernel grows and moves upstream - is shown. The slopes of the linear fits to the flame front positions correspond to the front velocities v_U and v_D . As explained above with v_U and v_D the convection and flame-velocities can be evaluated. Based on the analysis of 6 tests with the 6mm-nozzle the mean convection velocity $v_C = -52 \pm 67\text{m/s}$ and the mean flame front velocity $v_F = 300 \pm 22\text{m/s}$ have been determined. The uncertainties given are the standard deviation due to the variation of results from tests to test. The negative convection velocity

may be surprising, but can be understood by the pressure increase and related compression of the unburned propellants.

A peak chamber pressure of 6.8bar is reached after about 1.2ms (see figure 8), the average slope of the pressure increase was 8.1bar/ms.

frame#	time [ms]	GGA05 raw data	GGA05 enhanced grey values
8	0.39		
10	0.50		
12	0.61		
14	0.72		

figure 7: Upstream movement and growing of the laser induced flame kernel during phase (ii)

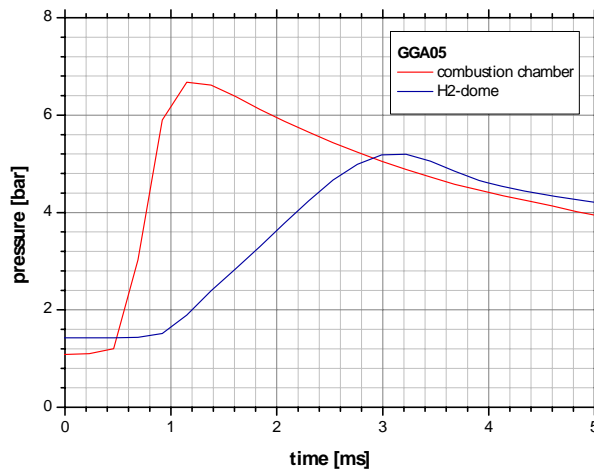


figure 8: Chamber pressure and H₂-dome pressure during the early ignition transient.

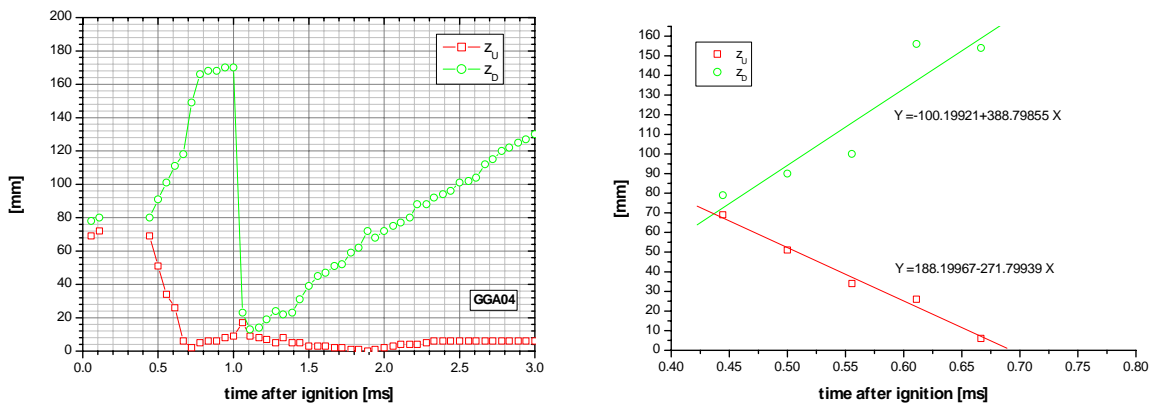


figure 9: Positions of the upstream and downstream flame front (left) and linear fits to determine the flame front velocities during phase (ii) (right) for test GGA04, 6mm-nozzle

phase (iii): Between about 1ms and 3ms after ignition the flame separates in a small region attached to the injector and a second region moving downstream. Frames of the OH-emission during this phase are shown in figure 10.

As soon as the upstream moving flame of phase (ii) has anchored at the injector the OH-emission is decreasing significantly (see frame #20, figure 10). The anchored flame is even not visible in some tests but from the flame evolution it is obvious that it has to be existent during all the time. With increasing time the anchored flame grows along the downstream direction with associated increasing OH-emission intensity. The OH-intensity reaches a peak value around 3.5ms after ignition for the 6mm-nozzle. The length of the flame, i.e. the downstream flame front, as function of time is shown in figure 11. The slope of this curve, i.e. the velocity with which the front moves downstream, has been determined for the time interval $t \in [1\text{ms}, 2.5\text{ms}]$. The mean value for the flame front velocity was $62 \pm 8\text{m/s}$ with the 6mm-nozzle. As can be seen in figure 11 after 2.5ms the flame front velocity slows down.

The second downstream moving flame is shrinking, consuming the unburned propellants and extinguishes after about 2ms (figure 10). From the positions of the upstream and downstream front of this flame the convection and flame velocities have been extracted. An example of the flame front positions during this phase for a test with the 4mm-nozzle is shown in left side of in figure 11. For the tests with the 6mm-nozzles a convection velocity of $v_C = 12 \pm 22\text{m/s}$ and a flame velocity of $v_F = -101 \pm 32\text{m/s}$ are obtained. The negative flame velocity is (as it should be) consistent with the visible shrinking of the flame region.














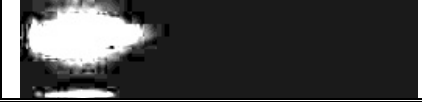
frame#	time [ms]	GGA05 raw data	GGA05 enhanced gray values
16	0.83		
20	1.05		
24	1.28		
28	1.50		
32	1.72		
36	1.94		
40	2.16		

figure 10: Growing of the flame anchored at the injector and separation and burning out of downstream flame during phase (iii)

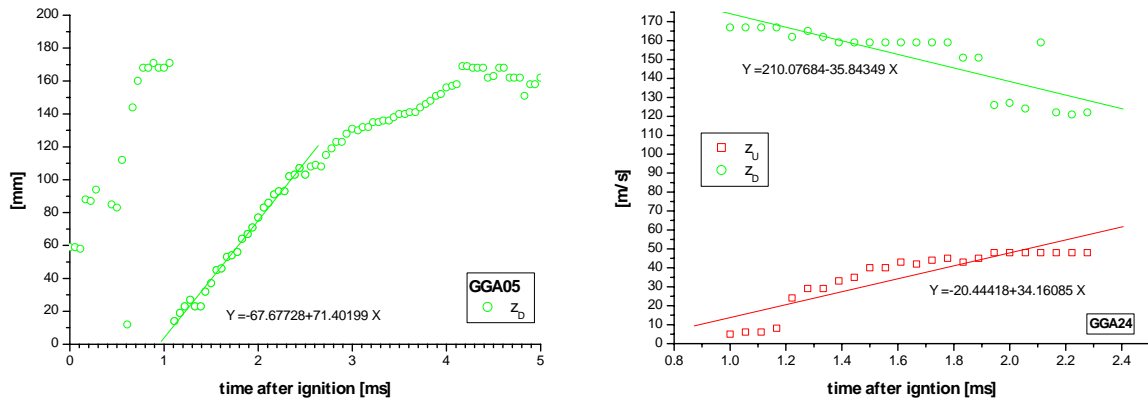


figure 11: Left: downstream position z_D of the flame front attached to the injector (test GGA05, 6mm-nozzle); Right: movement of the fronts of the burning out downstream flame (test GGA24, 4mm-nozzle)

phase (iv): The flame stabilizes into a pencil like shape after about 5ms (figure 12). As seen in figure 13 the OH-emission intensity becomes now rather constant. The chamber pressure built up during phase (ii) has still not relaxed to stationary conditions at this time (figure 8). During the pressure becomes smaller, the flame intensity decreases slowly, until the flame suddenly extinguishes. This happens at 17-19ms, when the chamber pressure falls below around 1.8bar.

With the 4mm-nozzle a stationary combustion chamber pressure of 2.6bar has been reached. No extinction of the flame during the time of observation (100ms) has been detected.

frame#	time [ms]	GGA05 raw data	GGA05 enhanced gray values
44	2.39		
50	2.72		
60	3.28		
70	3.83		
80	4.39		
90	4.94		
100	5.50		

figure 12: Sequence of OH-images during phase (iv)

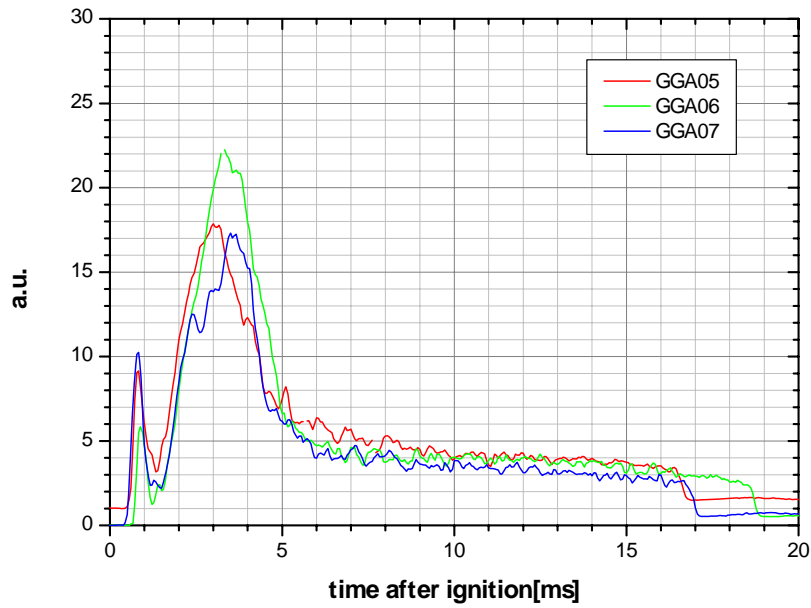


figure 13: Temporal evolution of the mean intensity of the OH-emission for three tests with the 6mm-nozzle.

2.3.3 Comparison of Tests with 6mm- and 4mm-Nozzle

The general ignition scenario is quite similar, independent whether the \varnothing 6mm- or \varnothing 4mm nozzle has been used. However, in some aspects there are differences. The characteristic data are listed in table 2.

Until the laser induced flame kernel has attached to the injector (phases (i) and (ii)) with both nozzles similar characteristic times are observed, the convection velocities of the flame kernel are similar in the frame of the measurement accuracy for both configurations. The growth of the kernel however is significantly faster with the 6mm-nozzle than with the 4mm-nozzle.

The evolution of a conical flame anchored at the injector (phase (iii)) is clearly delayed for the \varnothing 4mm-nozzle-tests. The velocity with which the leading flame front moves downstream is smaller by about 63% as compared to for the \varnothing 6mm-nozzle tests.

A prominent difference is that the flame could be stabilized with the \varnothing 4mm-nozzle at a stationary pressure of 2.6bar.

phase	event	6mm-nozzle	4mm-nozzle
(ii)	flame kernel: start of growing, upstream movement	0.4ms	0.4ms
	chamber pressure: start of pressure increase		
	flame kernel: convection velocity	-52 ± 67 m/s	-37 ± 52 m/s
	flame kernel: flame front velocity	300 ± 22 m/s	171 ± 59 m/s
	flame kernel attaches to the injector, peak OH-emission of flame kernel	0.8ms	0.8ms
(iii)	chamber pressure: slope	8.1bar/ms	11.9bar/ms
	chamber pressure: time of pressure peak	1.2ms	1.6ms
	chamber pressure: peak value	6.8bar	11.1bar
	anchored flame: time of downstream spreading	1-3ms	2-5ms

	anchored flame: downstream flame front velocity	62±8m/s	39±5m/s
	separated flame: convection velocity	12±22m/s	16±25m/s
	separated flame: flame front velocity	-101±32m/s	-29±8m/s
	separated flame: extinction	2ms	3.5ms
	anchored flame: time of OH-peak	3-3.5ms	6.5ms
(iv)	anchored flame: stabilization in pencil shaped form	5ms	8ms
	anchored flame: flame extinction	17ms	no extinction
	chamber pressure: stationary value	-	2.6bar

table 2: Characteristic data for tests with Ø4mm- and Ø6mm-nozzles.

2.4 Summary

There is indication from the Schlieren- and Rayleigh images that the regular Mach-pattern in the sonically injected oxygen leaves its mark on the length scale of ket-disintegration. Coherent structures originating in a H₂/O₂-shear layer entraining H₂ into the O₂-flow could not be seen, neither in the Schlieren, nor in the Rayleigh images.

During the first few milliseconds the combustion chamber pressure is above the H₂-dome pressure. Thus the dynamics during phases (ii) and (iii) is influenced by the dynamic response of the H₂-dome pressure on the transient combustion chamber pressure. During phase (iv) pressures in the H₂-dome and combustion chamber are in dynamic equilibrium.

The reproducibility of the qualitative transient ignition phenomenology was good. Quantitative estimation of flame velocities were possible with variations in the order of 10%-30% from test to test.

A comparison of results with the 4mm and 6mm-nozzle shows, that although mixture ratio and injection conditions are similar at stationary cold flow, during the ignition transient flame-, convection-, and flame front-velocities are significantly different due to the different pressure conditions.

3 Modeling of H₂/O₂ Ignition Transient

4 Conclusions

References

- [1] E. Hurlbert, R.J. Moreland, Propellant Ignition and Flame Propagation, Proceedings of the 2nd International Symposium on Liquid Rocket Propulsion, Chatillon, 1995
- [2] P. Alliot, V. Jover, J.N. Caruana, J.P. Dutheil, A. Juhls, Ariane 5 Cryogenic Upper Stage Propulsion Systems, AIAA 2001-3259
- [3] G. Frenken, E. Vermeulen, F. Bouquet, B. Sanders, Development of the Ignition System for Vinci, 4th International Conference on Launcher Technology "Space Launcher Propulsion", Decemvber 3-6, 2002, Liege, Belgium
- [4] G. Ordonneau, H. Douchet, Numerical Simulation of the Vinci Thrust Chamber Ignition, 4th International Conference on Launcher Technology "Space Launcher Propulsion", Decemvber 3-6, 2002, Liege, Belgium
- [5] C. Hensel, D. Wiemann, W. Oechslein, J. Görden, Ignition Aspects for the Vinci Thrust Chamber, AIAA 2002-4008

- [6] J. Gastal, Ariane 3rd Stage Ignition Improvement, AIAA 88-2931
- [7] D. Preclik, P. Spagna, Low Frequency and High Frequency Combustion Oscillation Phenomena inside a Rocket Combustion Chamber Fed by Liquid or Gaseous Propellants, AGARD CP-450
- [8] K. McManus, F. Aguerre, B. Yip, S. Candel, Analysis of the Ignition Sequence of a Multiple Injector Combustor Using PLIF Imaging, Non Intrusive Combustion Diagnostics, K. Kuo, T. Parr (Eds.), Begell House, 1994
- [9] V. Quintilla, M. Cazalens, R. Lecourt, G. Lavergne, Experimental and Numerical Study to Predict Spray Ignition, Proc. Of ILASS-Europe 2001, (Zurich), (2001).
- [10] R.A. Bjorklund, Very Low Thrust Gaseous Oxygen-Hydrogen Rocket Engine Ignition Technology, 20th JANNAF Combustion meeting, Vol. 1, D.S. Eggleston (Ed.), CPIA PUBL-383, Laurel, MD, 1983, pp. 699-711.
- [11] D.R. Ballal, A.H. Lefebvre, Ignition of Liquid Fuel Sprays at Subatmospheric Pressures, Combustion and Flame, Vol. 31, pp. 115-126, 1978.
- [12] M. Arai, H. Yoshida, H. Hiroyasu, Ignition Process of Compound Spray Combustible Mixtures, Dynamics of heterogeneous Combustion and Reacting Systems, Progress in Astronautics and Aeronautics, Vol. 152, 1993.
- [13] O. Gurliat, V. Schmidt, O.J. Haidn, M. Haidn, Ignition of Cryogenic H₂/LOX-Sprays, submitted for publication to Aerospace Science and Technology, 2003
- [14] P.A. Baudart, V. Duthoit, J.C. Harlay, Numerical Simulation of Cryotechnic Rocket Engine Ignition, AIAA 91-2290, 1991
- [15] P.A. Baudart, V. Duthaut, T. Delaporte, E. Znaty, Numerical modeling of HM7 B main chamber ignition, AIAA 89-2397, 1989
- [16] P.D. Maker, R.W. Terhune, C.M. Savage, Optical Third Harmonic Generation. In III International Conference on Quantum Electronics Proceedings, Paris, 1963
- [17] Y.-L. Chen, J.W.L. Lewis, C. Parriger, Spatial and Temporal Profiles of Pulsed Laser Induced Plasma Emissions, Journal of Quantitative Spectroscopy and Radiative Transfer, 67, 2000, pp. 91-103
- [18] J.A. Syage, E.W. Fournier, R. Rianda, R.B. Cohen, R.B., Dynamics of Flame Propagation using Laser-Induced Spark Ignition: Ignition Energy Measurements, J. Applied Physics 64-3, 1988, pp. 1499-1507.
- [19] I.P. Shkarofski, Review of Gas-Breakdown Phenomena Induced by High-Power Lasers I, RCA Review, Vol. 35, 1974, pp. 48-78

Cooling and Life Issues for Long Life Combustion Chambers

Mike Popp

Pratt & Whitney Space Propulsion
West Palm Beach, Florida

Fifth International Symposium on Liquid Space Propulsion, Chattanooga, Tennessee, October 27-30, 2003

Approved for Public Release - No Export Restrictions

Cooling and Life Issues for Long Life Combustion Chambers

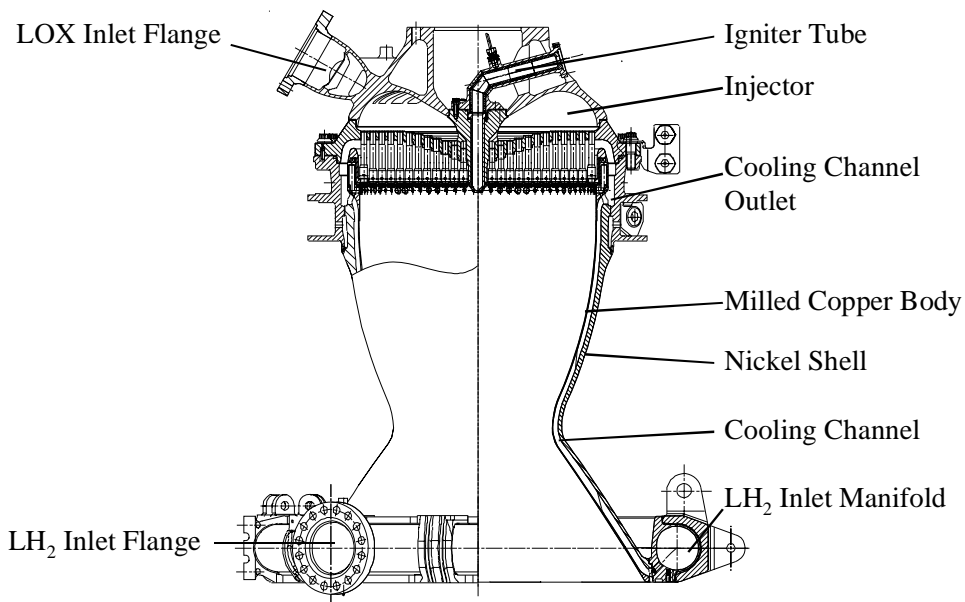
- Introduction
- Chamber Cooling
- Chamber Life
- Long-Life Enablers
- Conclusions
- References



Fifth International Symposium on Liquid Space Propulsion, Chattanooga, Tennessee, October 27-30, 2003

Approved for Public Release - No Export Restrictions

High Pressure Combustion Chambers



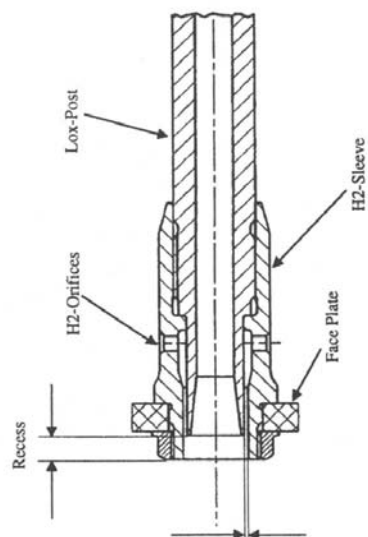
Cryogenic Rocket Engine Injector/Combustion Chamber Assembly (Ariane 5 Vulcain Engine; courtesy of Astrium; from ref. 2)

- Milled Channel Copper-Alloy Chamber Liner
- Regeneratively Cooled (Fuel)
- Chamber Pressure:
~ 100 - 260 bar
- Mixture Ratio:
 - Hydrogen/Oxygen ~ 5.5 - 7.5
 - Kerosene/Oxygen ~ 2.4 - 2.9
- Maximum Heat Flux:
~ 80 - 180 MW/m²

(Cryogenic Rocket Engine Data see ref. 1)

Fifth International Symposium on Liquid Space Propulsion, Chattanooga, Tennessee, October 27-30, 2003

High Pressure Combustion Chamber Injectors



(from ref. 1)



Vulcain Injector (from ref. 3)

Coaxial Injector Elements

Number of Elements:

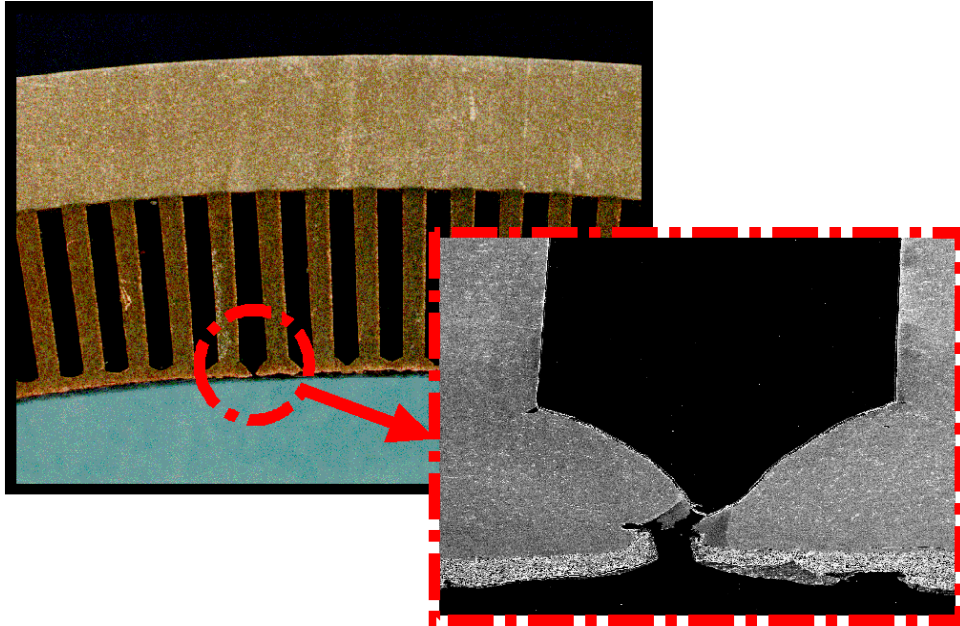
~ 500 - 600

Added Features:

- Outer row element mixture ratio bias
- Film Cooling
- Baffles

Fifth International Symposium on Liquid Space Propulsion, Chattanooga, Tennessee, October 27-30, 2003

Chamber Failure Characteristics



Chamber Liner Life:

- First liner crack develops (life models)
- End of useful life (too much leakage)

Liner Material operates in highly plastic regime, with strain rates up to $\sim 3\%$

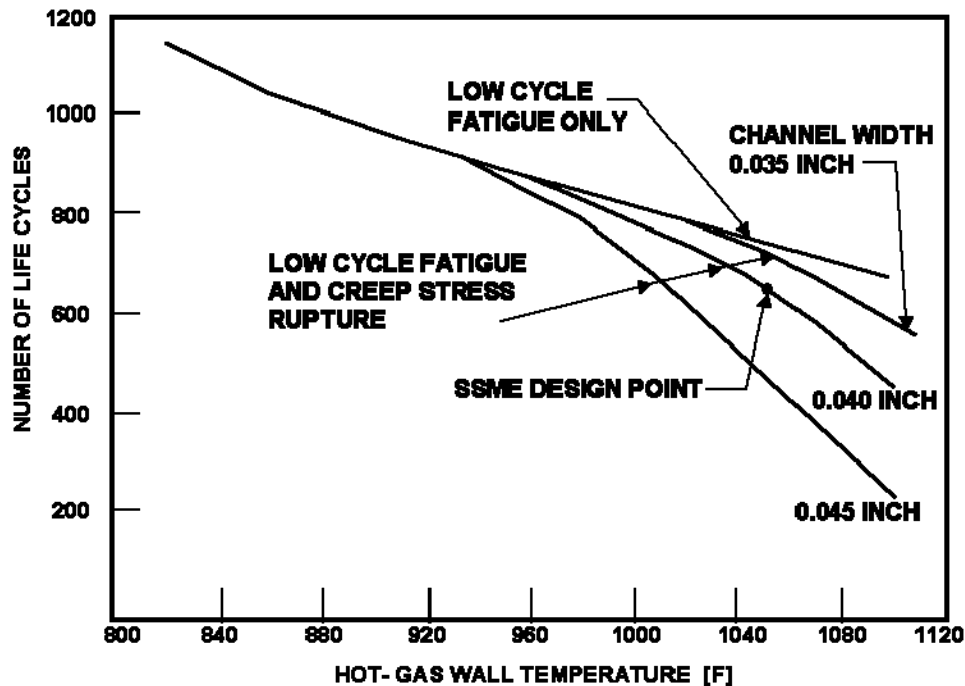
- on/off Cycles (number of starts)
 - material creep (mainstage operation)
- (see refs. 4 - 7)

Liner Material is subject to chemical attack (Blanching)

- surface roughening (increased heat transfer)
 - material porosity (reduced thermal conductivity)
- (see refs. 8, 9)

Fifth International Symposium on Liquid Space Propulsion, Chattanooga, Tennessee, October 27-30, 2003

Chamber Failure Characteristics

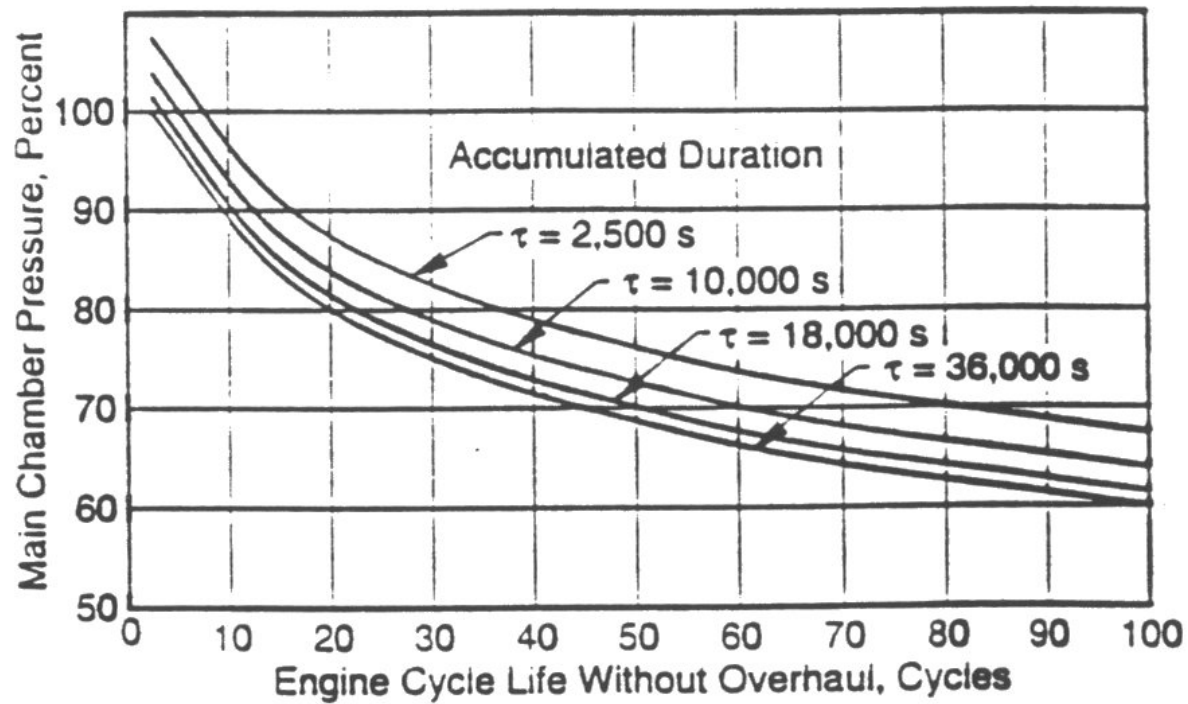


Chamber Liner Life is a Strong Function of Liner Material Temperature and Temperature Differentials

**Early SSME Main Combustion Chamber Life Prediction (from ref. 5):
Life to First Crack**

Fifth International Symposium on Liquid Space Propulsion, Chattanooga, Tennessee, October 27-30, 2003

RD-0120 Engine Life as a Function of Chamber Pressure



(from ref. 10)

Fifth International Symposium on Liquid Space Propulsion, Chattanooga, Tennessee, October 27-30, 2003

Approved for Public Release - No Export Restrictions

Chamber Life and Performance

Lower Material Temperature increases Life !

Reduction of Chemical Attack increases Life !

TRADE

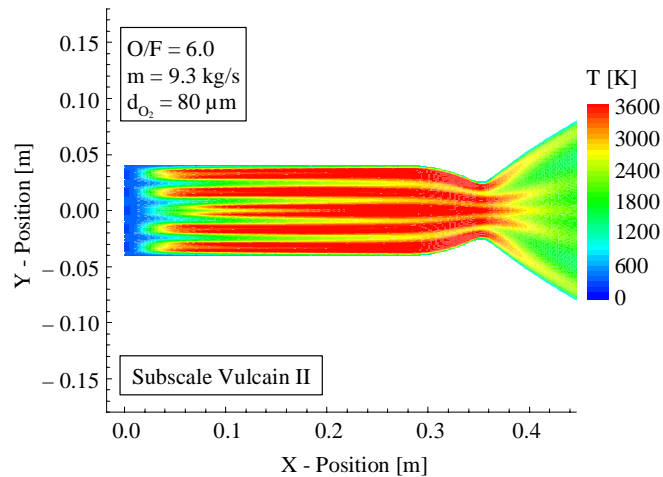
PERFORMANCE

- Specific impulse (Isp)
- Cooling Circuit delta P
- Component Mass

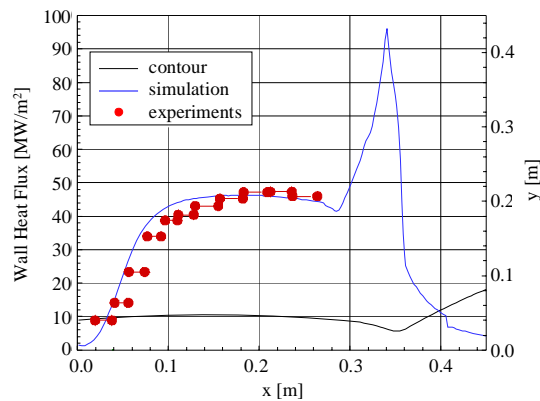
LIFE

- Margin
- Reliability

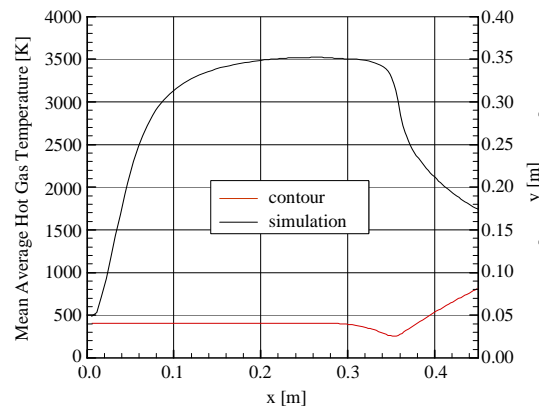
Combustion Chamber Cooling: Hot Gas Side Heat Transfer



- High Pressure reactive gas flow
- Wall Heat Transfer strongly affected by injector characteristics
- Variety of prediction tools exist
 - Non-reactive gas flow (Nu, BL)
 - Reactive gas flow
 - Reactive gas flow with droplet combustion



(from ref. 3)



- All tools need to be anchored and validated experimentally
- Prediction of heat transfer within $\pm 15\%$ for known conditions

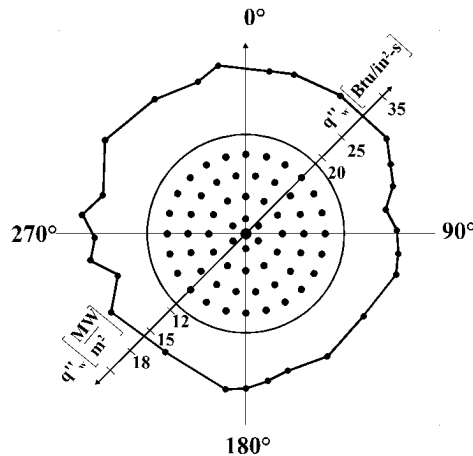
(further information see ref. 2)

Fifth International Symposium on Liquid Space Propulsion, Chattanooga, Tennessee, October 27-30, 2003

Hot Gas Side Heat Transfer: Injector Characteristics

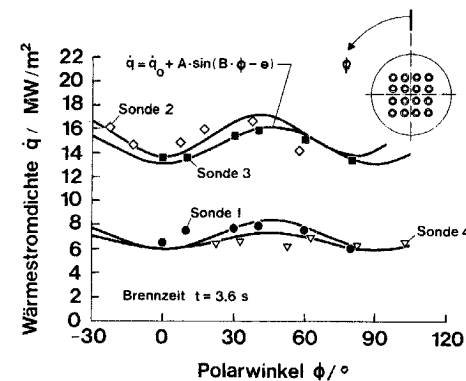


(from ref. 3)



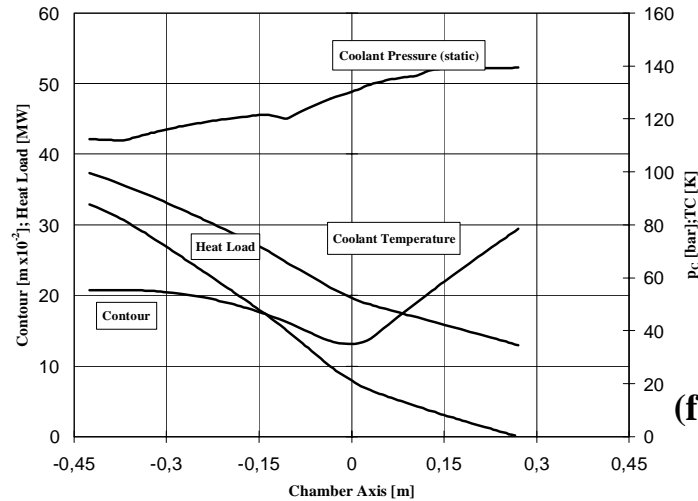
(from ref. 2)

- Non-uniform wall heating circumferentially, due to individual injector streamtube effect
- Hot Spots, non-uniform wall heating, due to
 - Injector streaking
 - Radial winds
 - injector manifolding effects

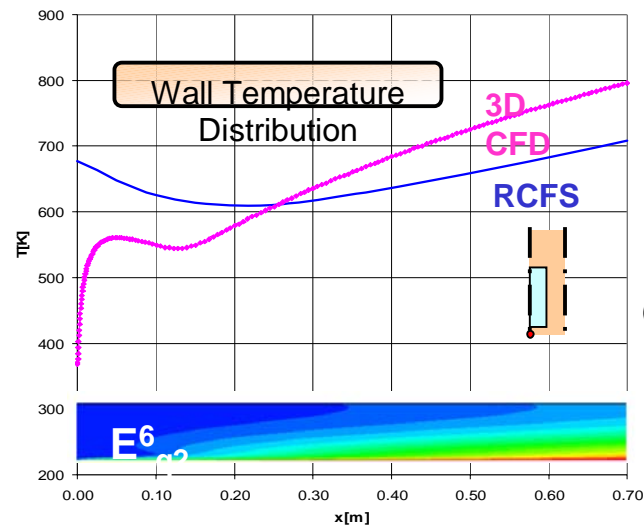


Fifth International Symposium on Liquid Space Propulsion, Chattanooga, Tennessee, October 27-30, 2003

Combustion Chamber Cooling: Coolant Side Heat Transfer



(from ref. 2)



(from ref. 11)

- High velocity channel flow
 - Hydrogen/Oxygen:
 - High aspect ratio cooling channels
 - 3D flow effects/stratification, vortices
 - Kerosene/Oxygen:
 - Low aspect ratio cooling channels
 - Chemical attack
 - Prediction Tools:
 - 1D Nu-type with correction factors (used for thermal design)
 - Stratification models
 - 3D CFD, for specific analyses
 - Further tool development and validation needed for improved hydrogen flow and heat transfer predictions
- (further information see ref. 2)

Fifth International Symposium on Liquid Space Propulsion, Chattanooga, Tennessee, October 27-30, 2003

Flight Engine Chamber Life Data

Engine	Nominal Flight Duration	Required Life	Certified Life	Demonstrated Life	Predicted Life
Vulcain 2*	540 sec	5400 sec 20 starts		6500 sec 24 starts	
SSME LTMCC**	520 sec	26000 sec 50 starts	23060 sec 43 starts	46120 sec 86 starts	
RD-170 / RD-180***	145 sec / 186 - 400	1600 sec 11 starts	2500 sec 17 starts	3200 sec 25 starts	> 100 starts

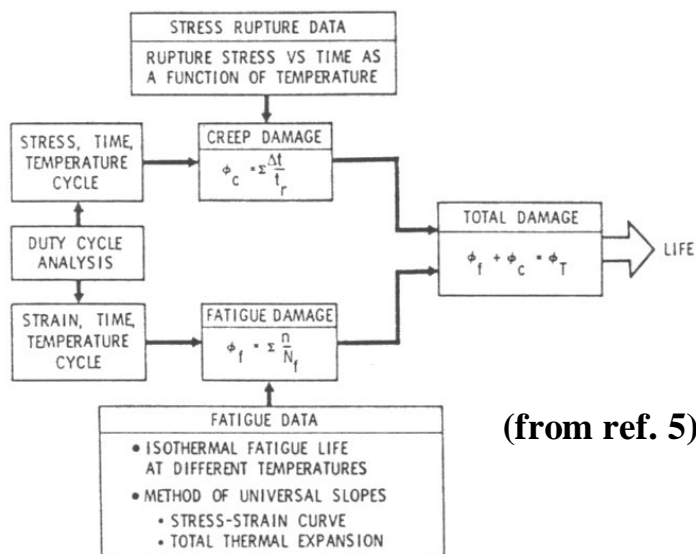
Notes:

* Data from ref. 12

** Data courtesy of NASA MSFC, October 2003; see also ref. 13

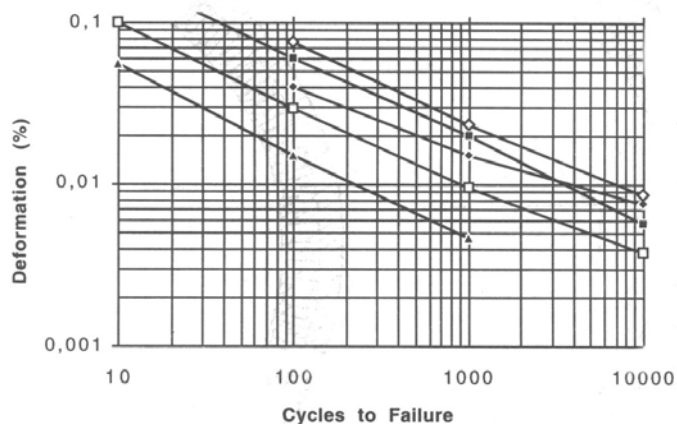
*** Data courtesy of NPO EM / Pratt & Whitney; see also ref. 14

Chamber Life Prediction

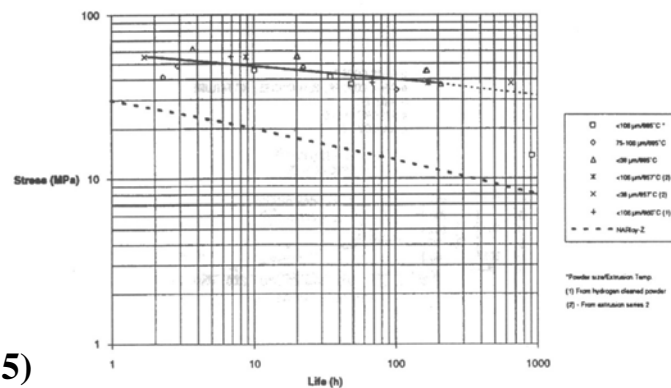


Early 1970s Prediction Method,
(still in use):

Linear Accumulation of Low
Cycle Fatigue (LCF) and Creep
Life (“Minor’s Rule”)



(from ref. 15)



Fifth International Symposium on Liquid Space Propulsion, Chattanooga, Tennessee, October 27-30, 2003

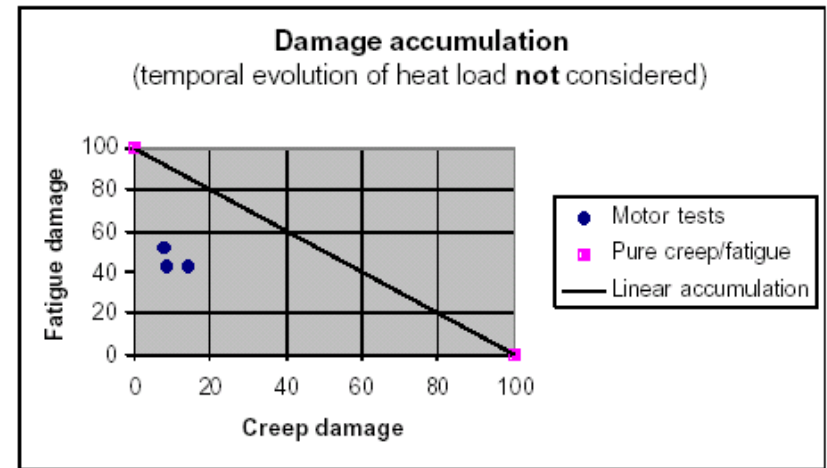
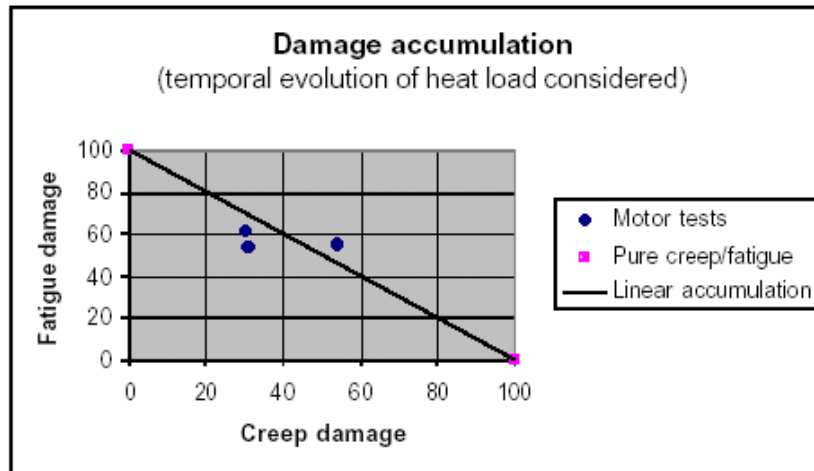
Chamber Life Prediction

- Simple LCF/Creep Model overpredicts Chamber Life by at least a Factor of 2-3
- Cyclic creep (Nasa, 1983; ref. 6)
 - 2D finite element analysis
 - Account for liner geometry change after each cycle
 - Account for hot spots (increase heat transfer for analysis)
- Astrium Model (2002; ref. 7)
 - 2D FEM (MARC)
 - Incorporates increased HGS heat transfer coefficient due to surface roughening (blanching) during mainstage operation
 - Anchored to test data

Fifth International Symposium on Liquid Space Propulsion, Chattanooga, Tennessee, October 27-30, 2003

Chamber Life Prediction

Astrium Results: Prediction of first crack for Vulcain 2 chamber



Creep Damage and Fatigue Damage at First Liner Crack (Vulcain 2 motor test results; from ref. 7)

Fifth International Symposium on Liquid Space Propulsion, Chattanooga, Tennessee, October 27-30, 2003

Approved for Public Release - No Export Restrictions

Chamber Life Prediction

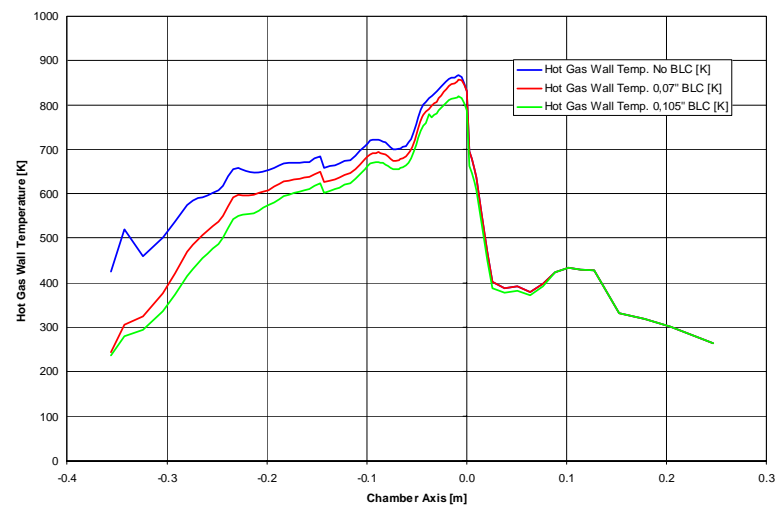
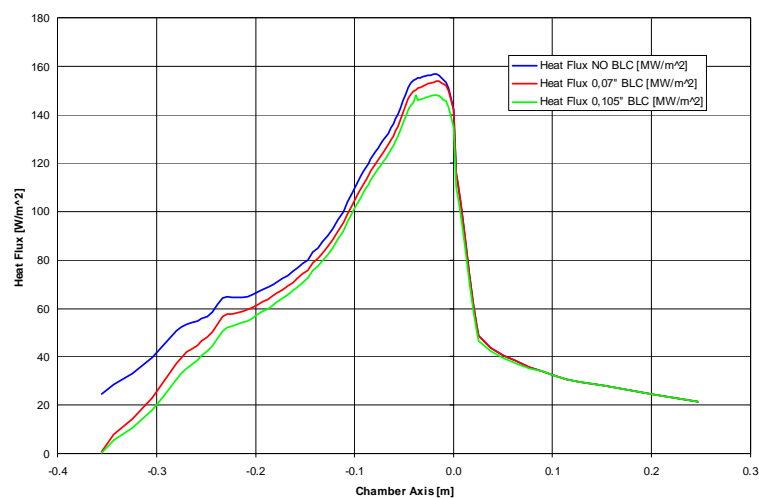
Issues and Improvements

- Use of “standard” linear damage accumulation tool overpredicts chamber liner life in case of long duration firings
- Damage accumulation is not linear
- Creep relaxation must be included
- Research is being conducted in the area of viscoplastic material damage models (improvement potential TBD)
- Always need extensive experimental data base with actual combustors (subscale, full-scale)

SSME MCC Life Improvement: STMCC

Small Life Increase by reducing heat load by small amount:

- outer row MR bias
- LOX post canting
- Film cooling



~5% Heat Flux Reduction by Film Cooling (from ref. 2)

Fifth International Symposium on Liquid Space Propulsion, Chattanooga, Tennessee, October 27-30, 2003

SSME MCC Life Improvement: LTMCC

- Large Life Improvement achieved by reducing thermal loading
 - Increase throat area by 10%
 - Results in 10% decrease of p_c and q_w ”
 - Improved life to 43 starts/23060 sec
- Specific impulse performance penalty largely recovered by other engine system adjustments
- Additional information
 - Liner inspected and polished after every flight
 - Chamber use allowed with liner cracks (safe operating mode)
 - End of life determined when total leakage is $> \sim 4$ lbm/sec

(data courtesy of NASA MSFC, October 2003)

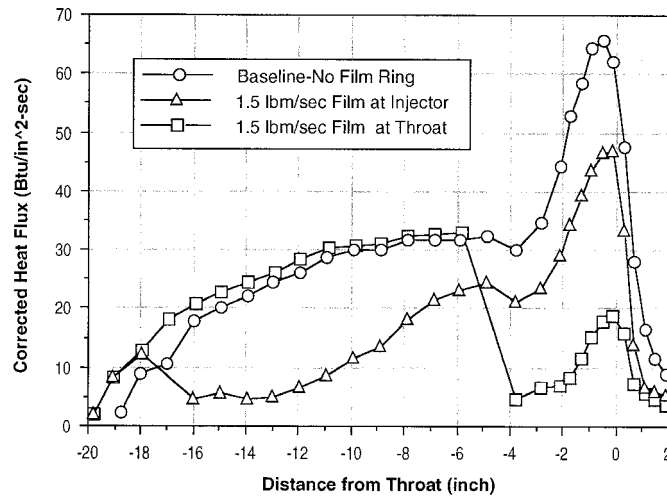
Fifth International Symposium on Liquid Space Propulsion, Chattanooga, Tennessee, October 27-30, 2003

Long Life Enablers

- Key: Keep the Heat Loading low !
 - Film Cooling
 - Transpiration Cooling
 - Thermal Barrier Coating
- Others:
 - Improved Liner Material
 - Microchannel Cooling structure
 - Elastic Cooling Structure
- Further Information: see refs. 15 - 17

Long Life Enablers: Film Cooling

- **Injector-originated Film Cooling**
 - used in SSME, RD-0120, Vulcain 2
 - Very small performance penalty with hydrogen film cooling
- **Chamber wall-originated Film Cooling**
 - used in RD-170/180
- **Example:**



(from ref. 2)

Chamber Pressure: 138 bar / 2000 psia
Mixture Ratio: 2.7
Injector: 120 like-impingement doublets in 3 rings
Film Cooling: RP1; 0.68 kg/s / 1.5 lbm/sec (= ~ 13 % fuel)
Chamber Diameter: 88.9 mm / 3.5"
Chamber Contraction Ratio: 2.53

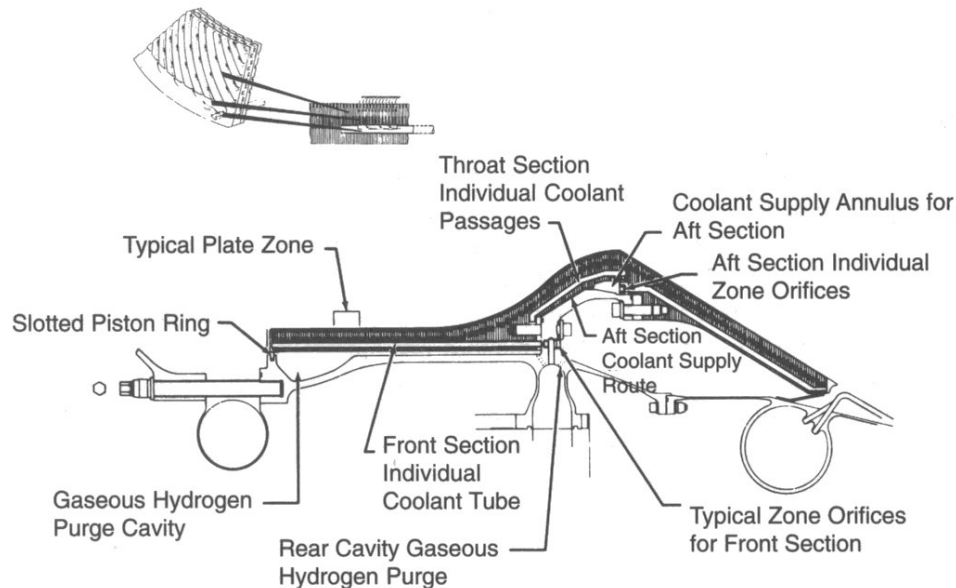
Chamber Wall Heat Flux Reduction by Liquid Film Cooling; RP-1; Rocketdyne subscale tests

- **Injector film cooling: q_w reduced by 28%**
- **Throat film cooling: q_w reduced by 69%**

Fifth International Symposium on Liquid Space Propulsion, Chattanooga, Tennessee, October 27-30, 2003

Long Life Enablers: Transpiration Cooling

- Demonstrated in Subscale and Full Scale Tests in late 1960s/early 1970s (P&W 250k & XLR-129 engines) (see ref. 18)
- Potentially Large Life Increase
- Small Performance Penalty (Isp); added Mass
- Has not been used in any Flight engines



Subscale Tests:

- 10k chamber, copper
- Chamber pressure: ~3300 psia

Full Scale Tests (250k, XLR-129)

- 250k chamber
- 602 seconds / 32 firings
- Chamber pressure: ~ 3000 psia
- Isp Penalty: ~ 0.5 - 1.2 sec
- No chamber damage

Fifth International Symposium on Liquid Space Propulsion, Chattanooga, Tennessee, October 27-30, 2003

Long Life Enablers: Thermal Barrier Coatings

- Thermal Barrier Coating (TBC) on Chamber Hot Gas Side reduces Heat Flux and Liner Temperatures
- Metallic: Ni and Cr used in RD-0120 and RD-170 chambers
- Ceramic Material (ZrO₂): demonstrated in subscale experiments; holds promise for full scale application; needs process development
- Main Design Requirement for any TBC: must be Fail/Safe
- Example: Vulcain 1 (100bar; MR = 6.0), with and without coating (throat conditions)
RD-170-like coating: 0.1 mm Ni bond layer, 0.5mm Cr TBC

	Bulk Coolant Temp.	Coolant Side Wall Temp.	Hot Gas Side Wall Temp.	Heat Flux [MW/m²] (%)
Without Coating	60 K	565 K	810 K	80.0 (100%)
With Coating	60 K	477 K	679 K (Cu) 1217 K (Cr)	65.7 (82%)

Fifth International Symposium on Liquid Space Propulsion, Chattanooga, Tennessee, October 27-30, 2003

Cooling and Life Issues for Long Life Combustion Chambers

Conclusions:

- Long Combustion Chamber Life is enabled by reducing Chamber Liner Temperatures and Chemical Attack
- Injector-originated Film Cooling is widely used
- Chamber Wall-originated Film Cooling and Thermal Barrier Coatings are used successfully in RD-170/180 Flight Engines
- Transpiration Cooling has been successfully demonstrated; further testing and manufacturing process development needed
- Thermal Barrier Coatings must demonstrate Fail/Safe Behavior
- Combination of Thermal Barrier Coating, Film Cooling, Transpiration Cooling (TBD) enables Long Life Chamber Construction

PERFORMANCE must be traded for LIFE: Long Life Design results in reduced Isp and increased mass, however, penalties are relatively small

Fifth International Symposium on Liquid Space Propulsion, Chattanooga, Tennessee, October 27-30, 2003

Cooling and Life Issues for Long Life Combustion Chambers

References:

Note: This is not meant to be an exhaustive list of references, rather it identifies the source of data used in this presentation.

1. Popp, M., and Pekkari, L.-O., "Cryogenic Engine Thrust Chamber Technologies", Paper 4.3, AAAF 5th International Symposium, Propulsion in Space Transportation, Paris, 1996.
2. Fisher, S.C., Popp, M., and Quentmeyer, R.J., "Thrust Chamber Cooling and Heat Transfer", Chapter 17, Liquid Rocket Thrust Chambers: Aspects of Modeling, Analysis, and Design, AIAA Progress in Astronautics and Aeronautics, (to be published 2003/2004).
3. Prelik, D., Knab, O., Görden, J., and Hagemann, G., "Simulation and Analysis of Thrust Chamber Flowfields: Cryogenic Propellant Rockets", Chapter 15, Liquid Rocket Thrust Chambers: Aspects of Modeling, Analysis, and Design, AIAA Progress in Astronautics and Aeronautics, (to be published 2003/2004).
4. Quentmeyer, R.J., "Experimental Fatigue Life Investigation of Cylindrical Thrust Chambers", NASA TM X-73665, and AIAA 77-893, 13th Propulsion Conference, Orlando, FL, July 1977.
5. Cook, R.T., and Coffey, G.A., "Space Shuttle Orbiter Engine Main Combustion Chamber Cooling and Life", AIAA 73-1310, 9th Propulsion Conference, Las Vegas, Nevada, 1973.

Fifth International Symposium on Liquid Space Propulsion, Chattanooga, Tennessee, October 27-30, 2003

Cooling and Life Issues for Long Life Combustion Chambers

References con't:

6. Cook, R.T., Fryk, E.E., and Newell, J.F., "SSME Main Combustion Chamber Life Prediction", NASA CR-168215, May 1983.
7. Fröhlich, A., Weigel, N., and Wiedmann, D., "Critical Topics for Rocket Engine Thrust Chamber Life Prediction", Paper No. 201, 4th International CNES Conference on Launcher Technology: Space Launcher Liquid Propulsion, Liege, Belgium, Dec. 2002.
8. Morgan, D.B., and Franklin, J.E., "Hot-Fire Test Investigation of Copper Combustion Chamber Blanching", The 1989 JANNAP Propulsion Meeting, edited by D.S. Eggleston and K.L. Strange, Publication 515, Vol. 3, Chemical Propulsion Information Agency, pp. 417-426, 1989.
9. Murphy, M., Anderson, R.E., Rousar, D.C., and Van Kleek, J.A., "Effects of Oxygen /Hydrogen Combustion Chamber Environment on Copper Alloys", in NASA, Marshall Space Flight Center, Advanced Earth-To-Orbit Propulsion Technology, Volume 2, pp. 580-617, October 1986.
10. Rachuk, V., Orlov, V., Plis, A., Gontcharov., N., and Fanciullo, T.J., "The Low Risk Development of a Fuel Rich Preburner Tripropellant Engine using the RD-0120", AIAA 94-9465, AIAA Space Technology Conference, Huntsville, AL, Sept. 1994.
11. Knab, O., Fröhlich, A., Wennerberg, D., and Haslinger, W., "Advanced Cooling Circuit Layout for the VINCI Expander Cycle Thrust Chamber", AIAA-2002-4005, 38th Joint Propulsion Conference, Indianapolis, IN, 2002.
12. Caisso, P., Brossel, P., Souchier, A., Illig, M., and Margat, T., "Development Status of the Vulcain 2 Engine", AIAA 2002-3840, 38th Joint Propulsion Conference, Indianapolis, IN, July 2002.

Fifth International Symposium on Liquid Space Propulsion, Chattanooga, Tennessee, October 27-30, 2003

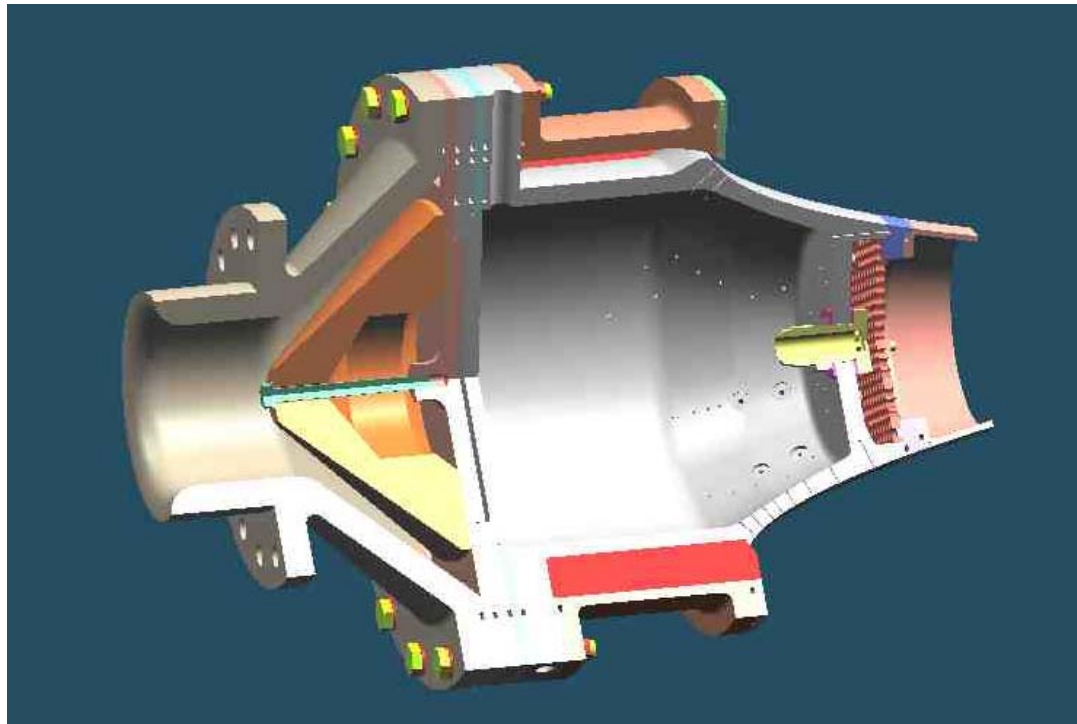
Cooling and Life Issues for Long Life Combustion Chambers

References con't:

13. Worlund, A.L., and Hastings, J.H., "Space Shuttle Main Engine Evolutions", AIAA 2001-3417, 37th Joint Propulsion Conference, Salt Lake City, UT, July 2001.
14. Katargin, B.I., Chvanov, V.K., and Chelkis, F.Yu., "LOX/Kerosene Oxygen-Rich Staged Combustion Rocket Engine Design and Life Issues", 5th International Symposium on Liquid Space Propulsion, Chattanooga, TN, October 2003.
15. Popp, M., and Schmidt, G., "Rocket Engine Combustion Chamber Design Concepts for Enhanced Life", AIAA 96-3303, 32nd Joint Propulsion Conference, Lake Buena Vista, FL, 1996.
16. Cook, R.T., and Quentmeyer, R.J., "Advanced Cooling Techniques for High Pressure Hydrocarbon-Fueled Rocket Engines", AIAA 80-1266, 16th Joint Propulsion Conference, Hartford, CT, 1980.
17. Quentmeyer, R.J., "Rocket Combustion Chamber Life-Enhancing Design Concepts", AIAA 90-2116, 26th Joint Propulsion Conference, Orlando, FL, 1990.
18. D. Mulready, *Advanced Engine Development at Pratt & Whitney*, Chapters 5, 6 and 8, SAE Publications, 2001.

Fifth International Symposium on Liquid Space Propulsion, Chattanooga, Tennessee, October 27-30, 2003

Experimental Results for an Annular Aerospike with Differential Throttling



Joseph H. Ruf and David M. McDaniels
NASA/Marshall Space Flight Center

5th International Symposium on Liquid Space Propulsion
October, 2003. Chattanooga, TN

Overview

- Introduction
- Experimental Hardware
- Results
- Conclusions

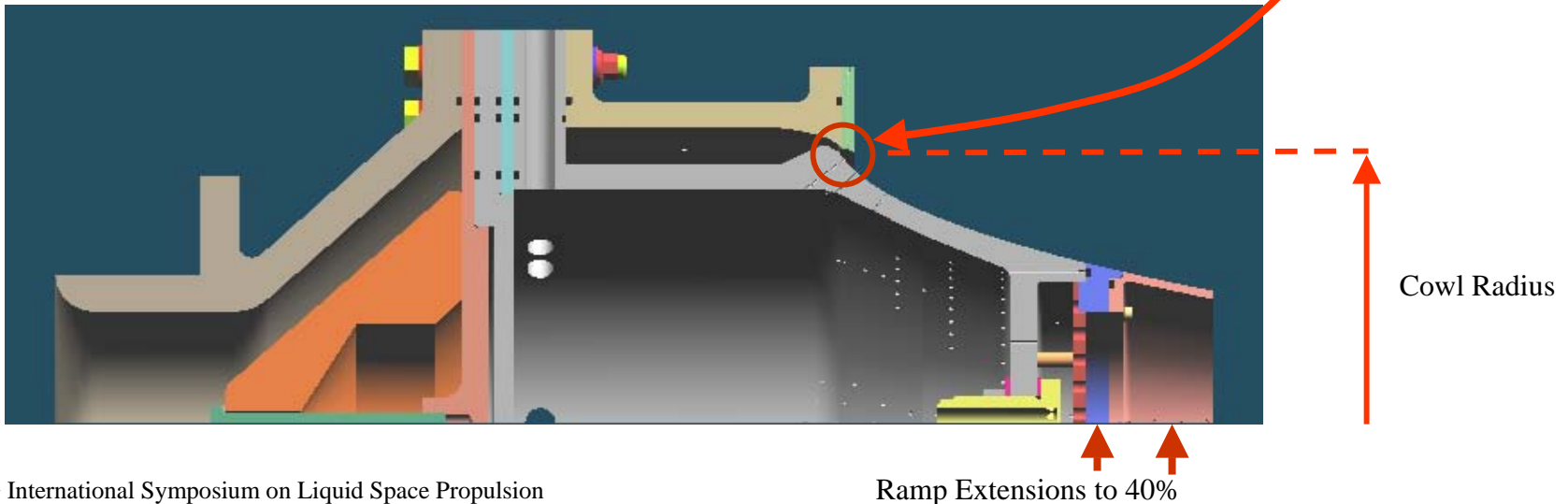
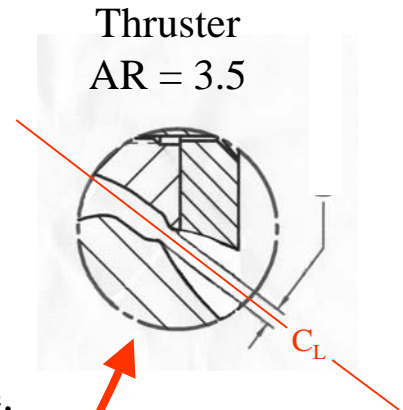


Introduction

- MSFC funded an internal study on Altitude Compensating Nozzles
 - Develop an ACN design and performance prediction tool.
 - Design, build and test cold flow ACN nozzles
 - An annular aerospike nozzle was designed and tested
 - Incorporated differential throttling to assess Thrust Vector Control
- Objective of the test hardware
 - Provide design tool verification
 - Provide benchmark data for CFD calculations
 - Experimentally measure side force, or TVC, for a differentially throttled annular aerospike

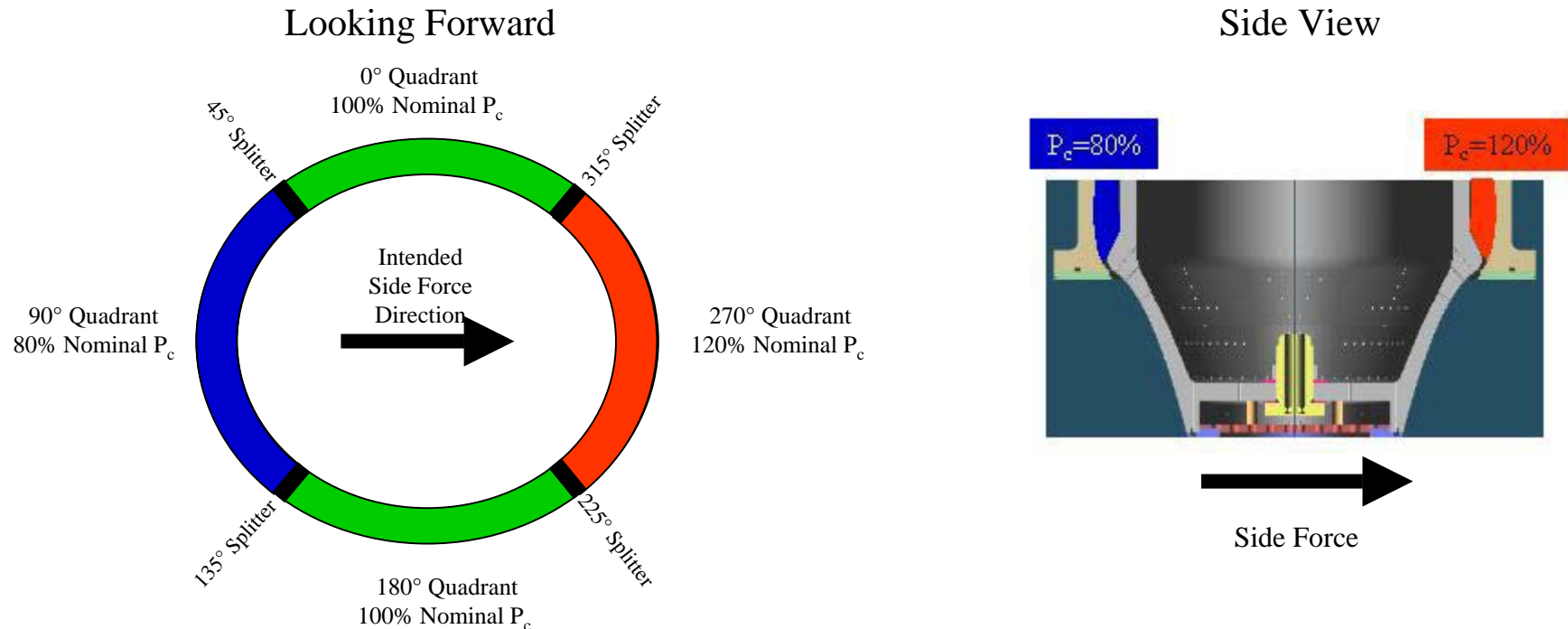
Experimental Hardware

- One Dimensional Design Parameters
 - Overall area ratio, 38:1
 - Internal expansion or ‘thruster’, 3.5:1. Symmetric expansion.
 - Design point Nozzle Pressure Ratio (NPR) = 995
 - Working fluid was warm air.
 - Two spike lengths, 25% and 40% of equivalent conical nozzle.

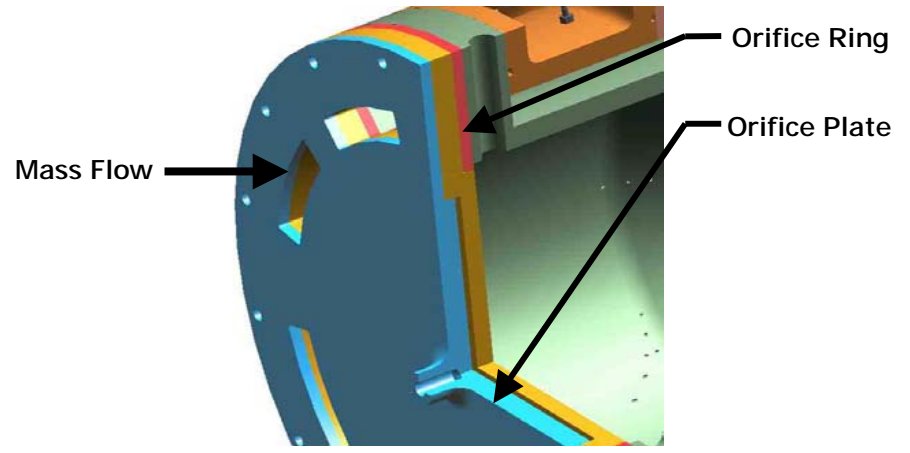
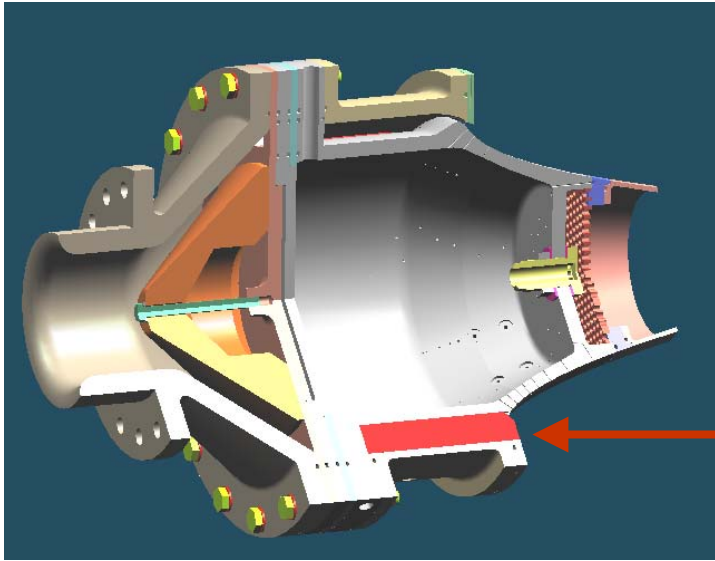


Experimental Hardware, continued

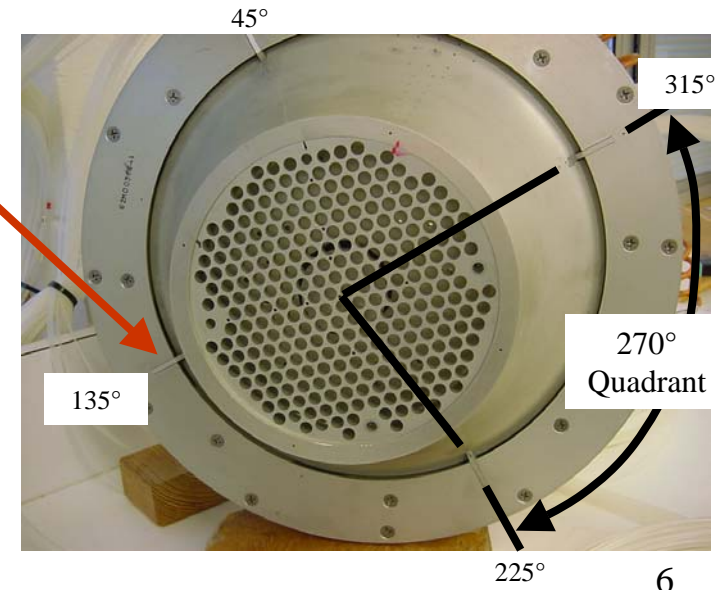
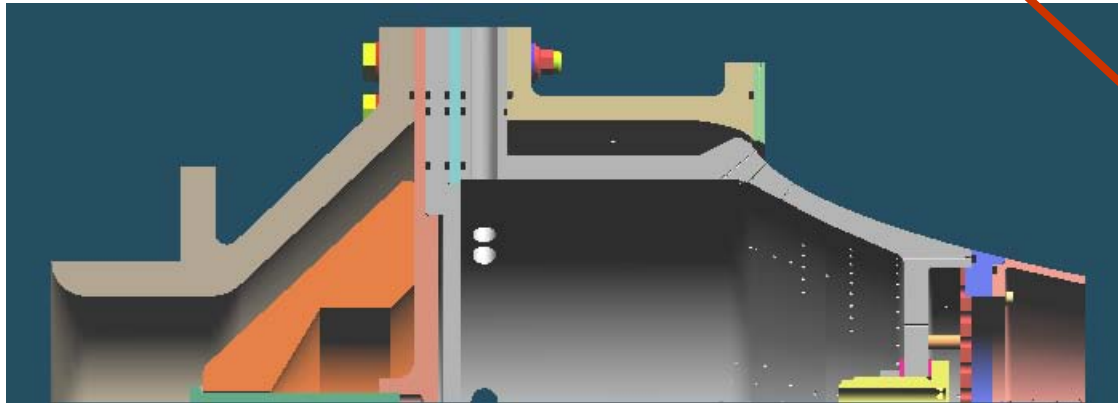
- Differential Throttling
 - Annular manifold and thruster were divided into quadrants with splitter plates
 - Mass flow orificed to produce $\pm 20\%$ differential throttling



Experimental Hardware, continued

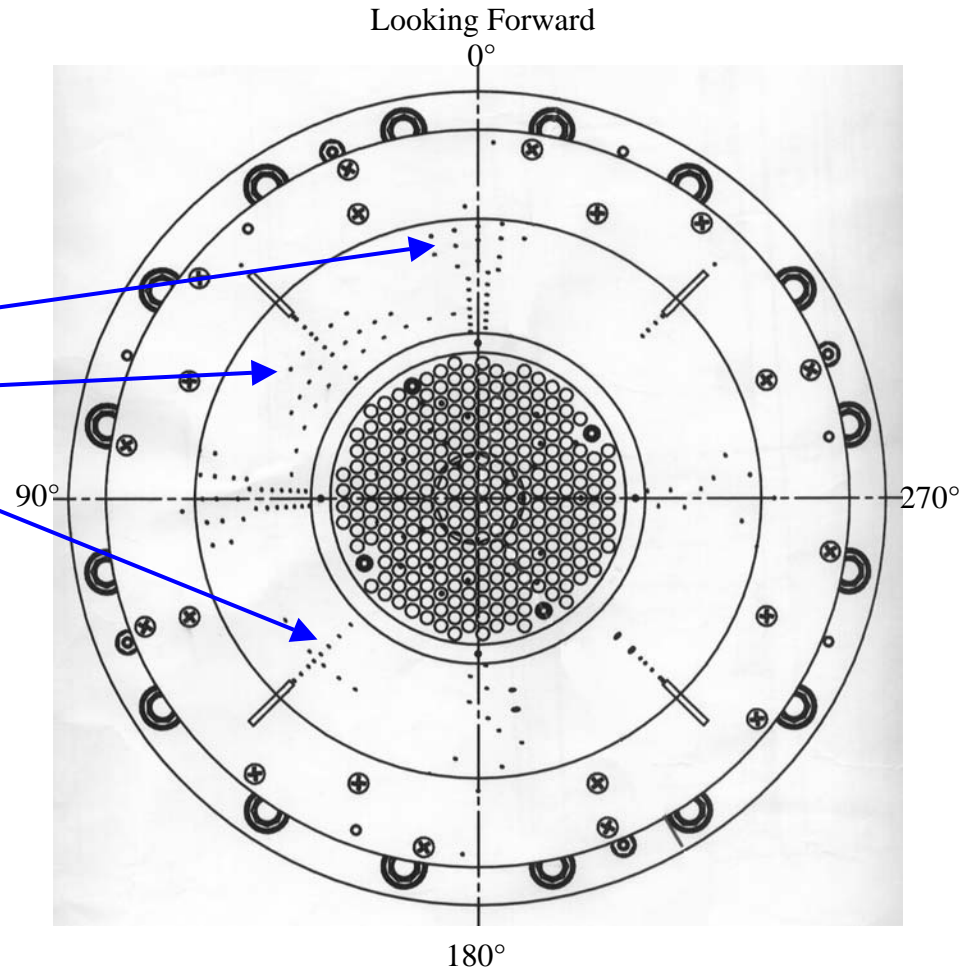


Splitter Plates



Experimental Hardware, continued

- Nozzle Pressure Field Well Mapped
 - P_{total} and P_{static} in each quadrant manifold
 - More than 160 P_{static} on spike
 - Quadrant centerlines
 - Crossflow
 - Splitter plate profiles
 - Nozzle Base
 - High frequency pressures
 - One each in each quadrant manifold
 - Four on spike
 - two on thruster centerlines
 - two on splitter plate centerlines

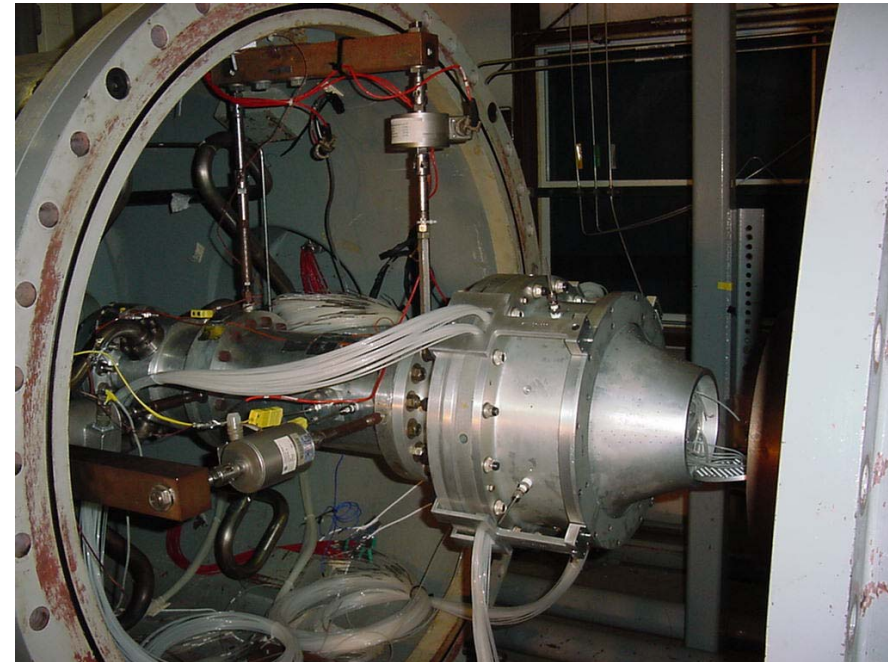


Experimental Hardware, continued

- Test Performed in MSFC's Nozzle Test Facility
 - Test cell evacuated with ejectors
 - Evacuated to near vacuum
 - Measures axial force with load cell
 - Heated Air to 150°C
- Nozzle Efficiency
 - Efficiency = $F_{\text{measured}}/F_{\text{optimum}}$
 - $F_{\text{opt}} = P_c A_{\text{throat}} C_{f_opt}$

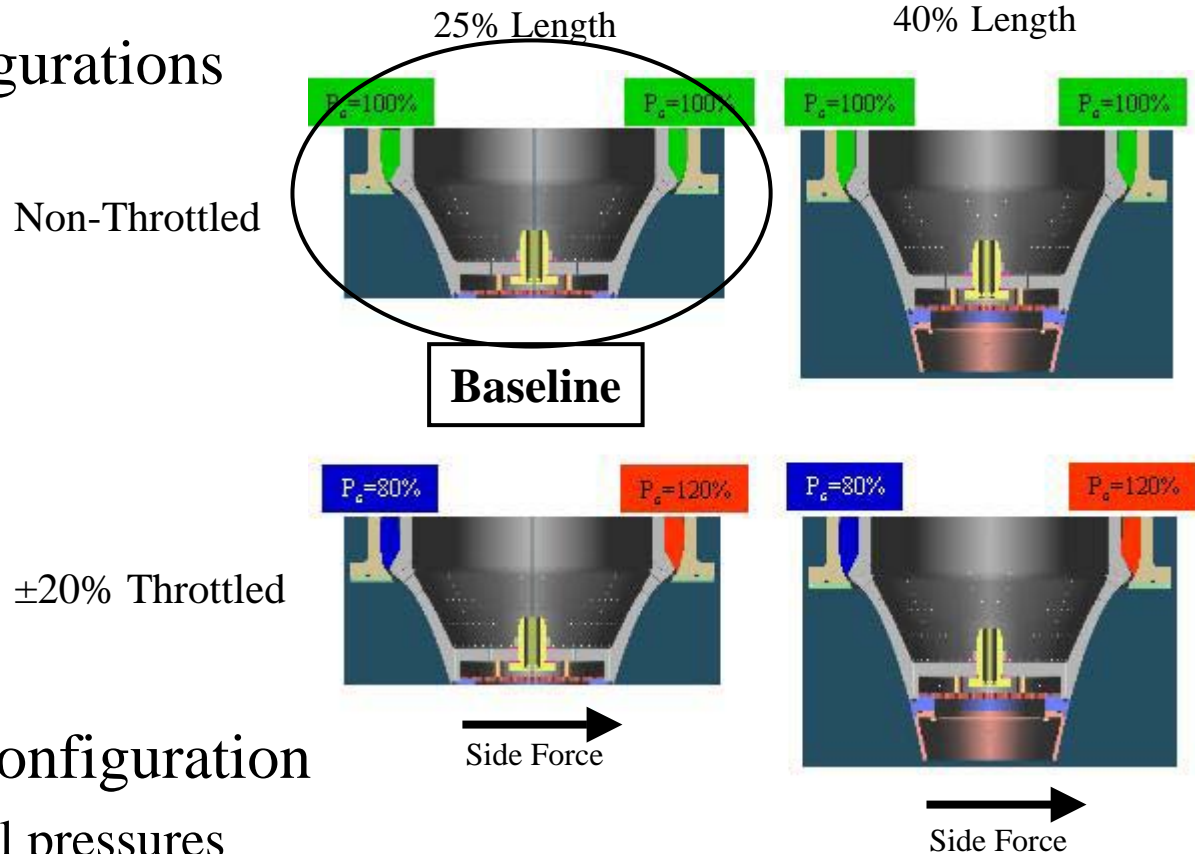
$$C_{f_opt} \equiv \sqrt{\frac{2\gamma^2}{\gamma-1} \left(\frac{2}{\gamma+1}\right)^{\frac{(\gamma+1)}{(\gamma-1)}} \left[1 - \left(\frac{1}{NPR}\right)^{\frac{(\gamma-1)}{\gamma}}\right]}$$

- Side Force
 - Measured with set of small flexures
 - Only measured in horizontal plane



Results

- Four Configurations

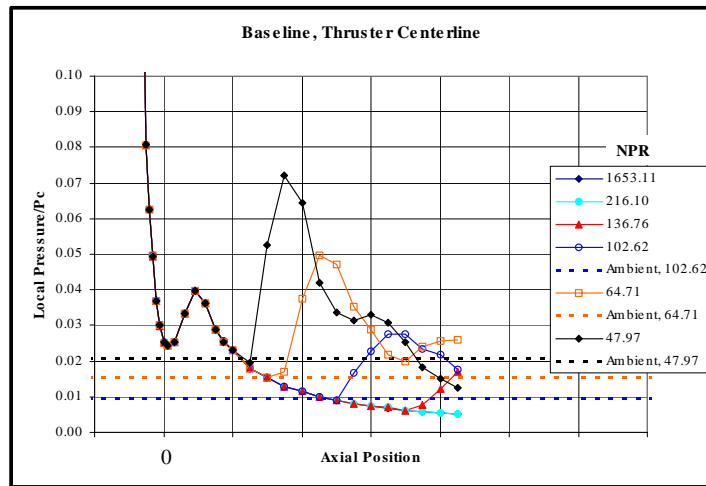


- For Each Configuration

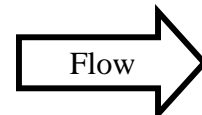
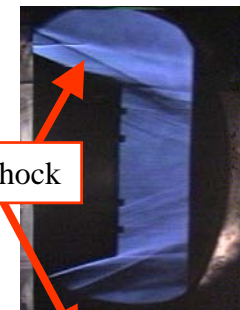
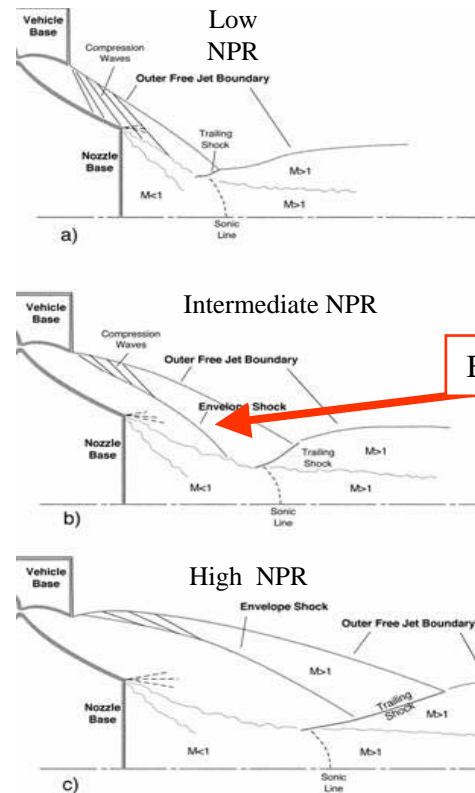
- Spike wall pressures
- Nozzle efficiency
- Side force

Results, continued: Spike Wall Pressures

- Altitude Compensation
 - Altitude compensation at low NPR occurs via recompressions on the spike generated by the Barrel Shock.
 - Barrel, or envelop, shock results from the plume sensing the local ambient pressure.

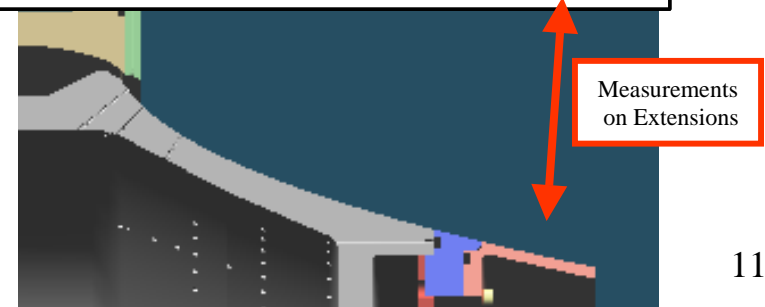
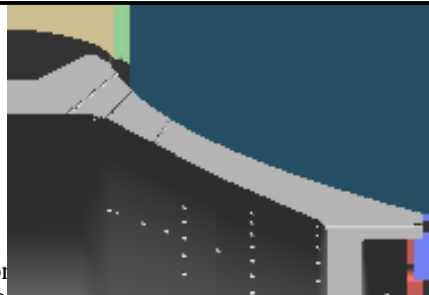
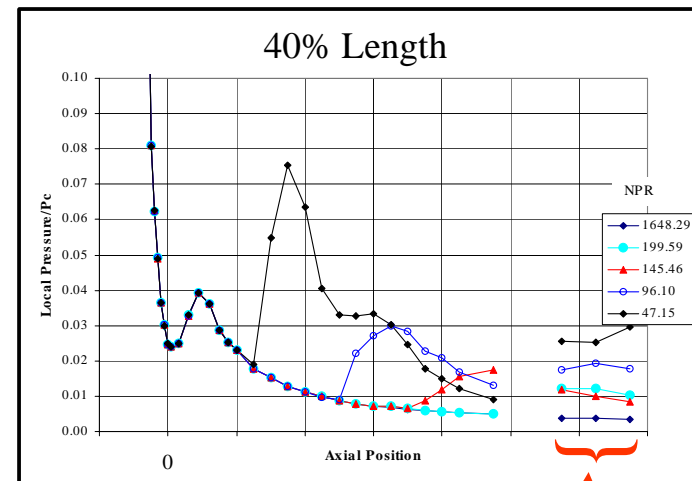
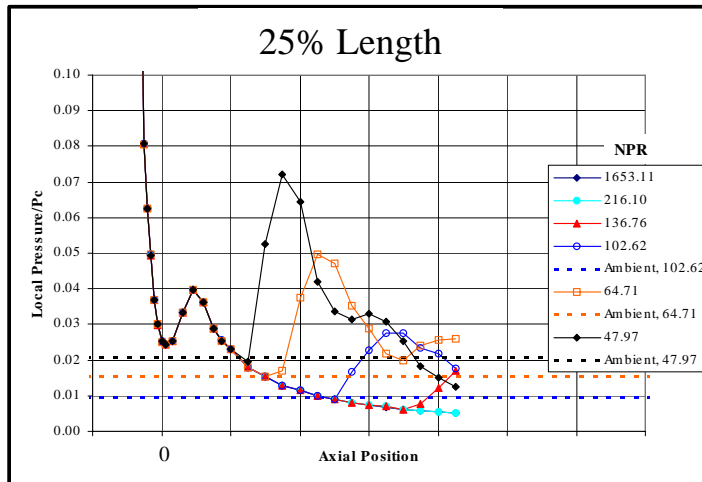


Wall pressure on the annular aerospike centerbody



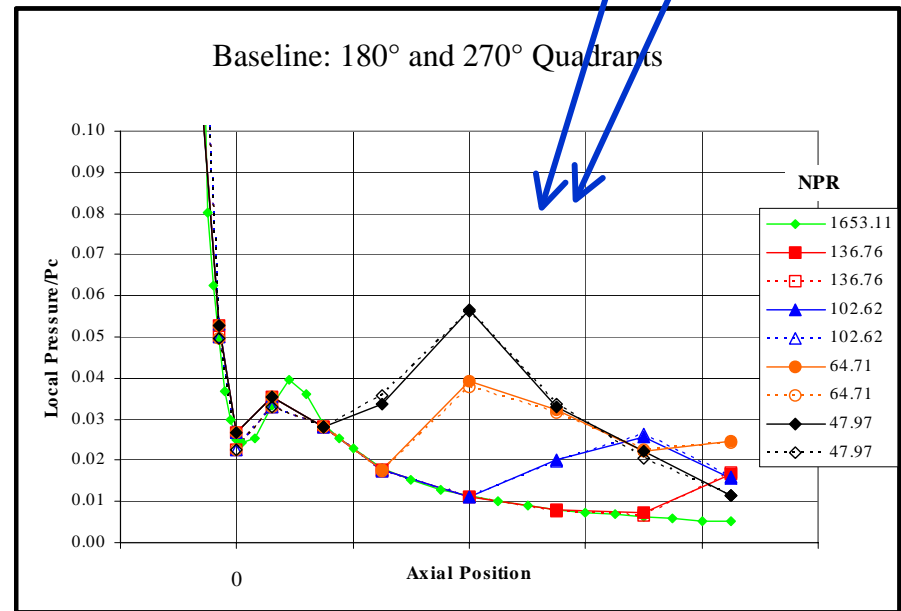
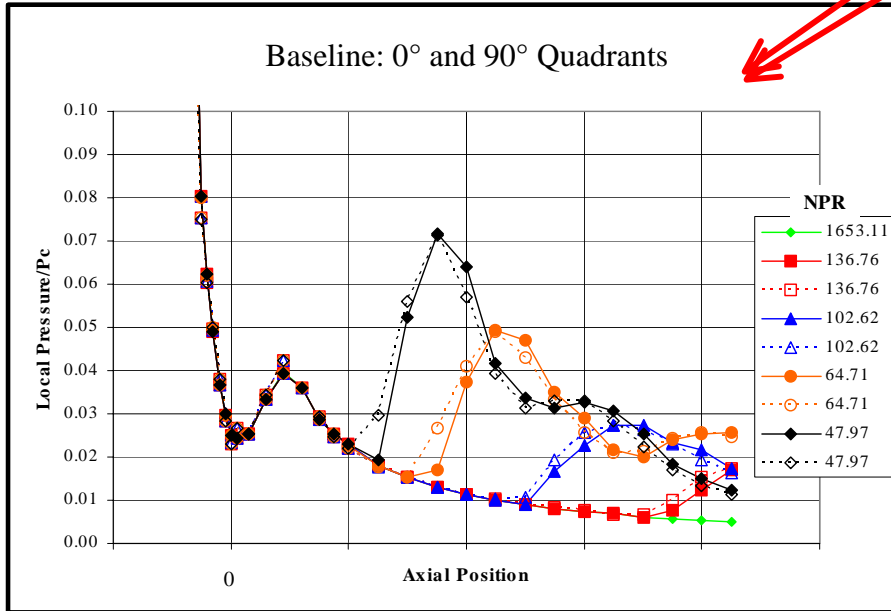
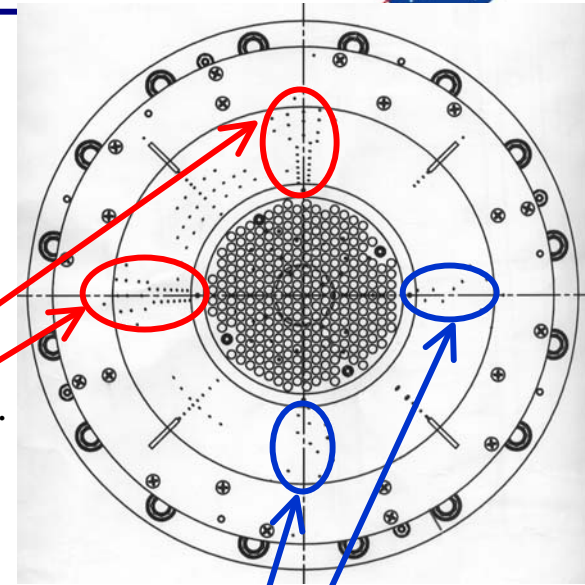
Results, continued: Spike Wall Pressures

- Non-Throttled
 - Recompression on spike
 - 25% Length, barrel shock moved off spike at NPR ~150
 - 40% Length, barrel shock moved off spike at NPR ~200



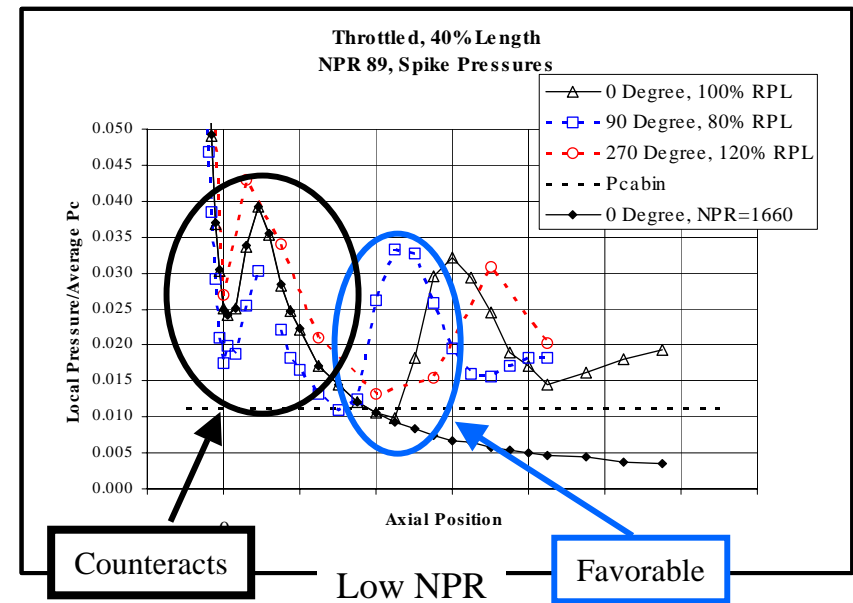
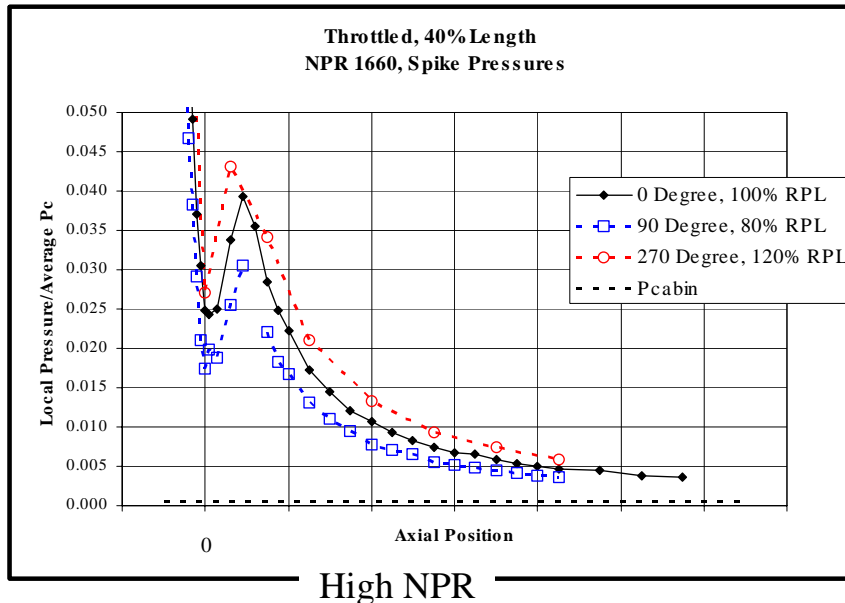
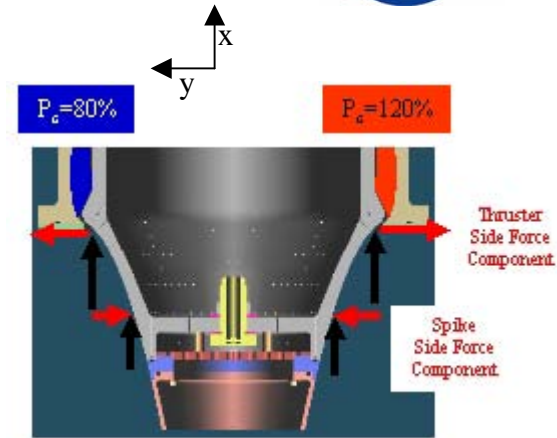
Results, continued: Spike Wall Pressure

- Non-Throttled
 - Quadrant centerline profiles – good agreement
 - 0° & 90° quadrants, high density of measurements.
 - 180° & 270° quadrants, lower density of measurements.
 - 0° & 90 agree with 180 & 270.



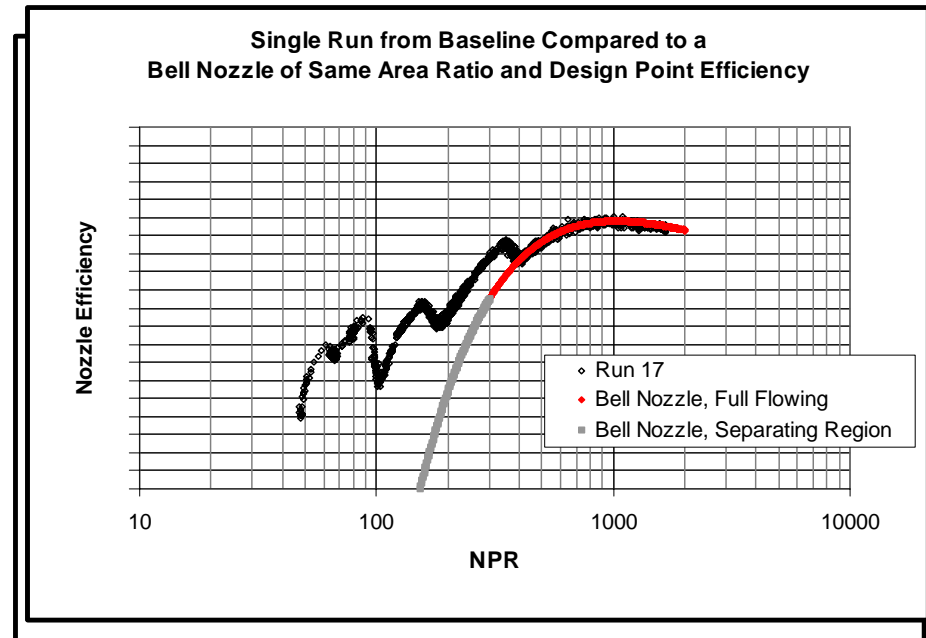
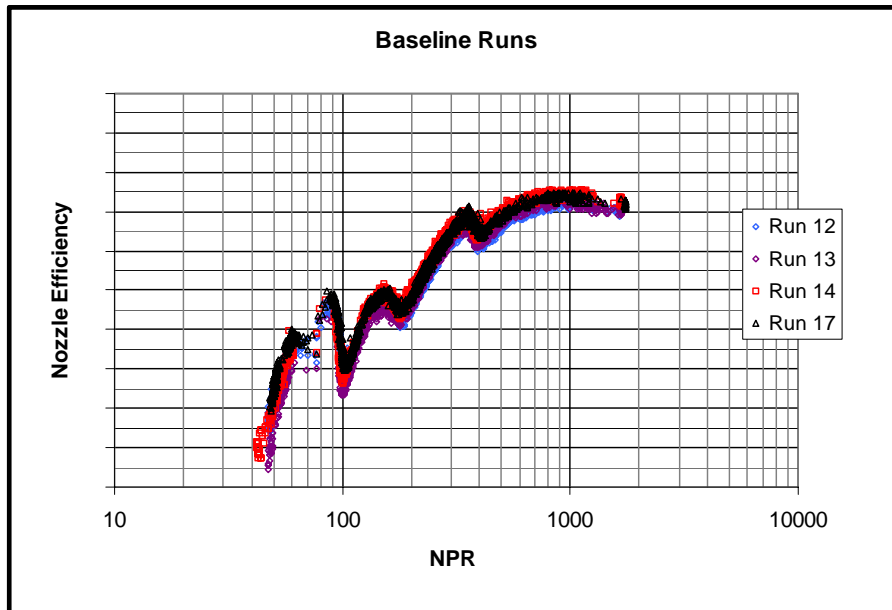
Results, continued: Spike Wall Pressures

- Throttled: 40% Length shown (25% Length Similar)
 - High NPR
 - High pressure quadrant had higher pressures on spike
 - Spike pressures counteract intended side force
 - Low NPR
 - Spike pressures after recompression were favorable to intended side force



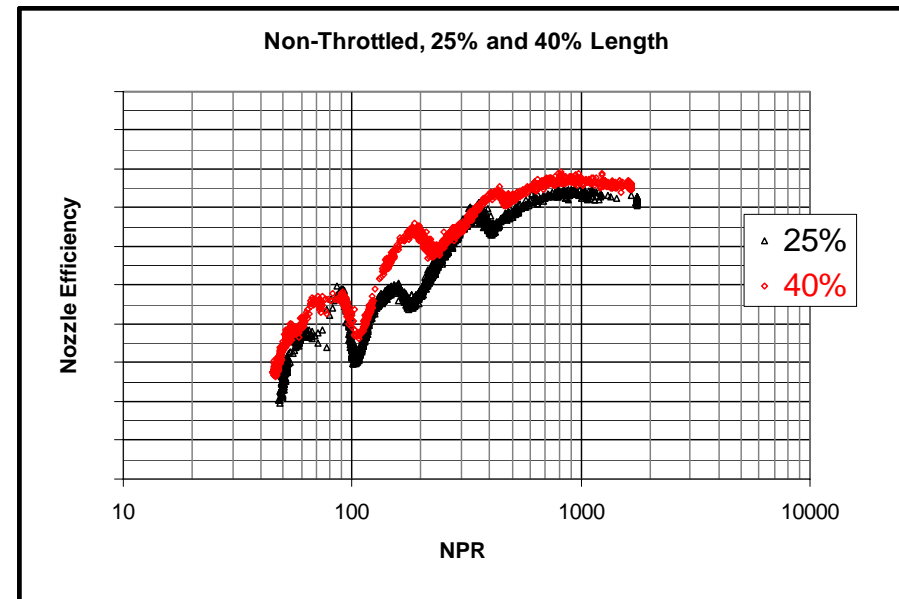
Results, continued: Nozzle Efficiency

- Non-Throttled: 25% Length, 'Baseline'
 - Fairly good repeatability in test data
 - Several discontinuities in the curves
 - At NPR 400, due to rapid decrease in nozzle base pressure at wake closure
 - At NPR 180, due to recompressions moving off the ramp
 - At NPR 100, due to decrease in base pressure related to barrel shock structure



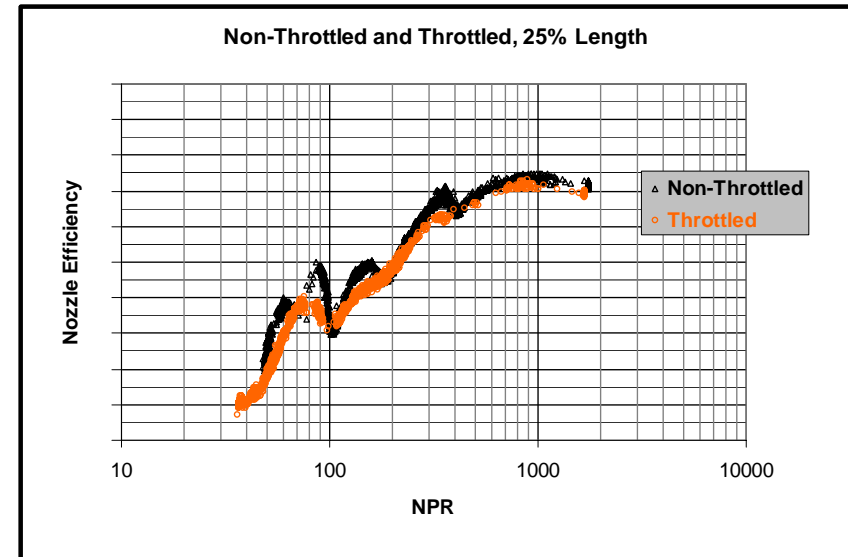
Results, continued: Nozzle Efficiency

- Non-Throttled: 40% vs. 25% Length
 - Length
 - Longer spike increased nozzle efficiency
 - Discontinuities shifted to higher NPR
 - Wake closure at higher NPR
 - Barrel shock moved off spike at higher NPR
 - Decrease in efficiency at wake closure was smaller
 - Nozzle base area smaller, smaller component of axial thrust



Results, continued: Nozzle Efficiency

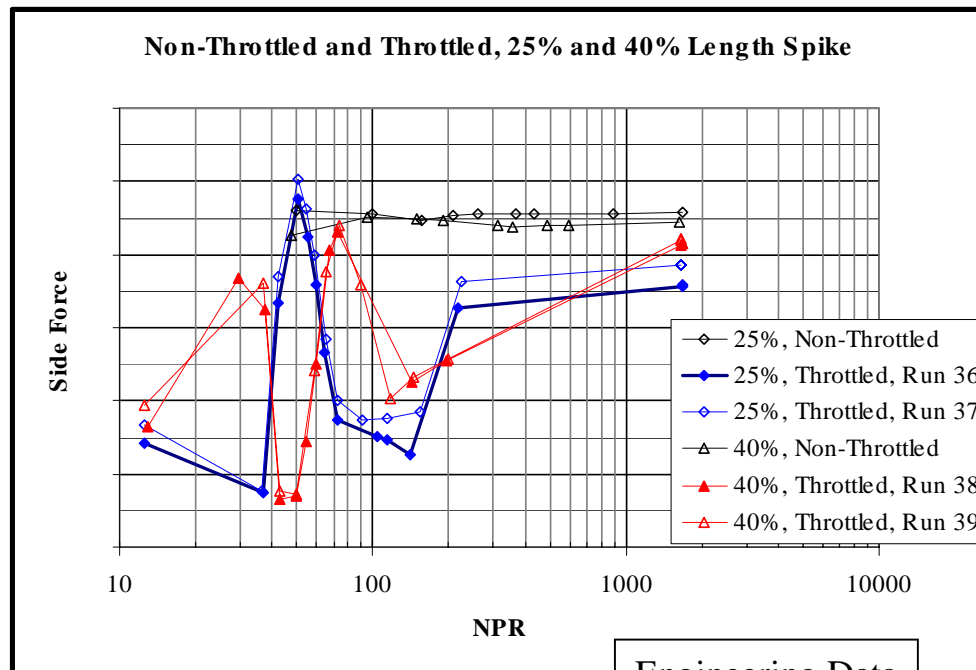
- Throttled: 25% Length
 - Efficiency at the design point was within family of baseline runs
 - Discontinuities smoothed
 - 90° and 270° quadrants had different effective NPR than nominal P_c quadrants
 - Different barrel shock positions on spike smoothed the transitions



- Throttled: 40% Length had Similar Trends

Results, continued: Side Force

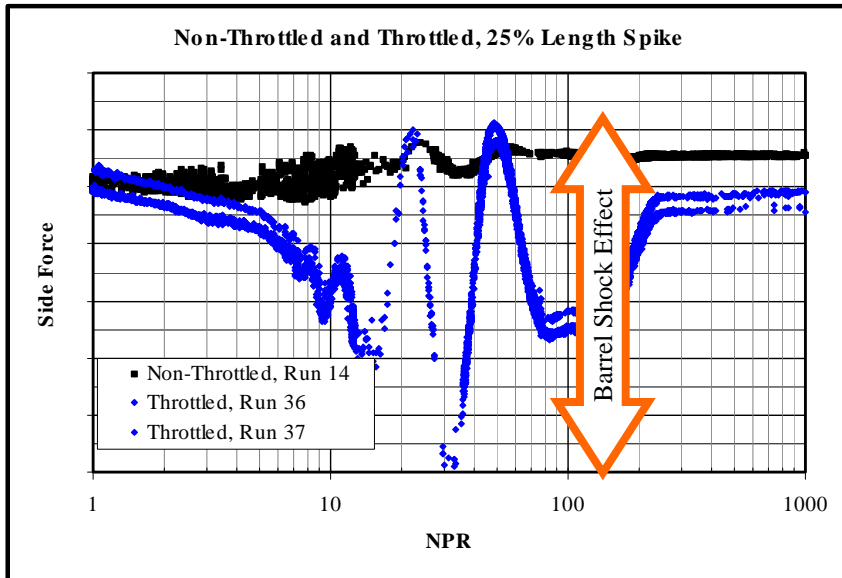
- Overview of 25% and 40% Length Spike
 - Non-Throttled runs plotted as reference
 - Both 25% and 40% length spikes exhibited large variations at low NPR
 - Peaks occurred at different NPR
 - Both had constant value at high NPR
 - 40% length produced less side force at high NPR



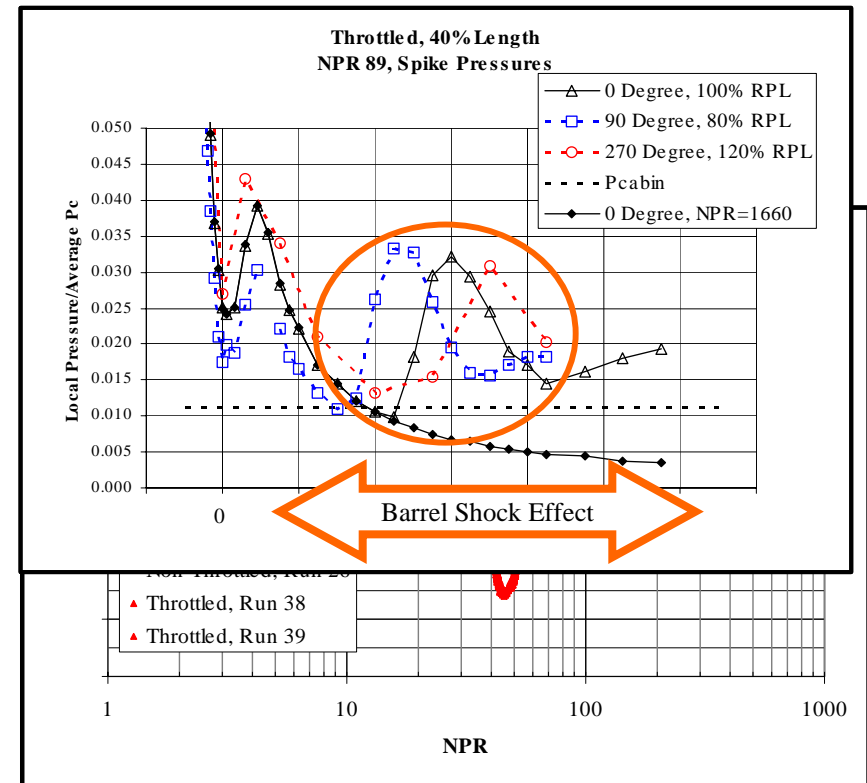
Engineering Data

Results, continued: Side Force

- 25% Length
 - Two peaks of near zero side force. Both indicate TVC reversal.
 - Constant value reached at NPR 230.

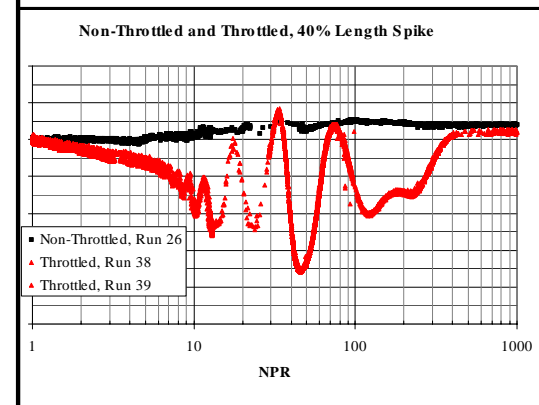
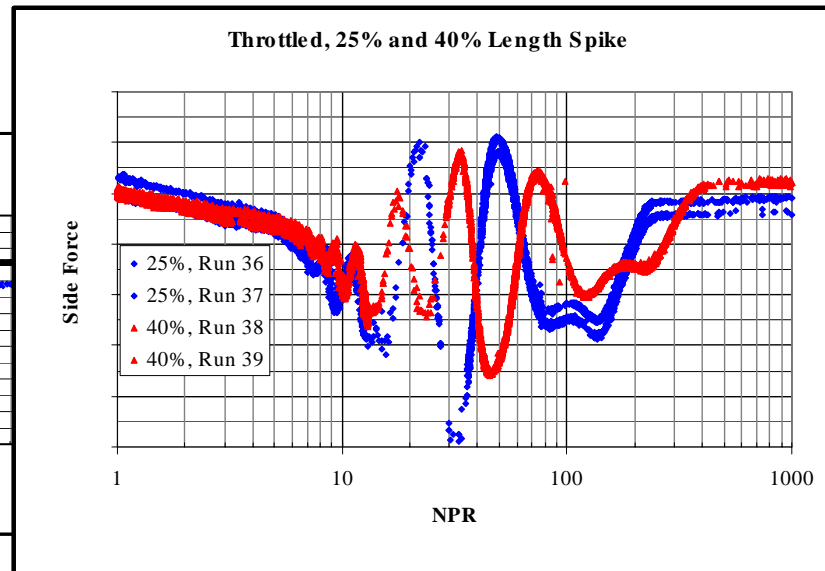
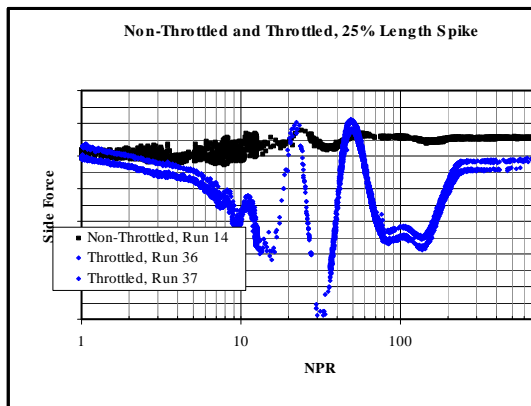


- 40% Length
 - Three peaks of near zero side force. One indicated TVC reversal
 - Constant value reached at NPR 400.



Results, continued: Side Force

- Comparing Side Force Directly
 - 25% length spike's peak to peak variation larger than 40% length
 - Peaks were at different NPR



Conclusions

- Non-Throttled
 - 25% Length
 - Details of aerospike nozzle efficiency curve explained.
 - Discontinuities due to altitude compensation by barrel shock.
 - 40% Length
 - Increased efficiency.
 - Subtle changes in details of efficiency curve.
- Throttled
 - 25% Length
 - No discernable effect on efficiency.
 - Large variation of side force at low NPR resulted from barrel shock impingement at different axial stations.
 - Side force became a constant value when last shock moved off centerbody.
 - 40% Length
 - No discernable effect on efficiency.
 - Large variation, but less than 25% length spike, at low NPR.
 - Side force became a constant value when last shock moved off centerbody.
 - Side force at high NPR was approximately $\frac{1}{4}$ of side force for 25% length spike.

Material requirements and limitations for liquid rocket engines

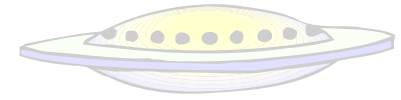
G. Inglebert, R. Gras

Laboratoire d'Ingénierie des Systèmes Mécaniques
et des Matériaux, groupe Tribologie, EA 2336,
ISMCM-CESTI, France

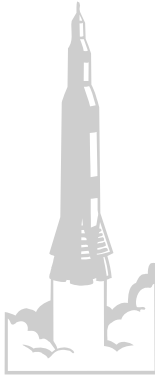
www.ismcm-cesti.fr



Introduction



- ◆ Spatial systems work in severe environment
 - Vacuum, cryogenic fluids, hot gases
- ◆ Key parameters for design :
 - mechanical links, guiding, power transmission systems, sealing
- ◆ Engines for launchers :
 - Turbopumps to compress LH2 and LOx > 100 bars
 - Combustion chamber and nozzle ⇒ specific thrust
- ◆ Deep knowledge of materials
 - Physical properties in the loading range (thermal and mechanical)
 - Accurate enough behavior modeling



Material behavior guidelines

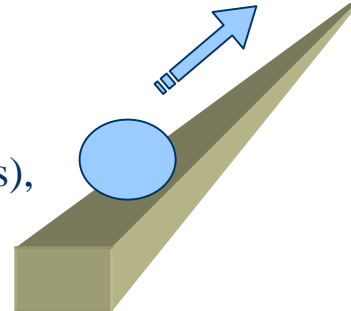
- ◆ Available evidence for material properties
 - no evidence of time dependent effects
 - elastoplastic model (Standard Generalised Materials)
 - ◆ allows simplified search for stabilised cyclic state
 - ◆ Up to 4 plastic constants to be defined for each temperature
 - time dependent effects and wide thermal range
 - Walker and Freed unified model
 - ◆ unique definition for thermal and mechanical loading
 - ◆ complex identification process (12 constants)
 - Damage mechanisms
 - Fatigue HCF or LCF (thermal effect?)
 - Creep damage associated to viscoplastic effects
 - Hydrogen embrittlement

Selected examples

- ◆ The most critical problems (for solid parts) are due to contact (complex stresses) and thermal loadings :
 - Contact range
 - In cryogenic turbopumps
 - ◆ Fretting (splined shafts, blade fir trees, ...)
 - ◆ Contact fatigue (ball bearings)
 - Wide thermal range
 - In combustion chambers or nozzles

Materials for cryogenic turbopumps

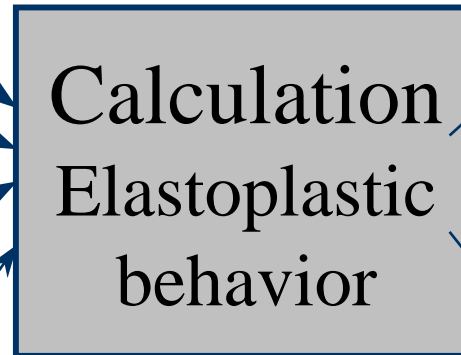
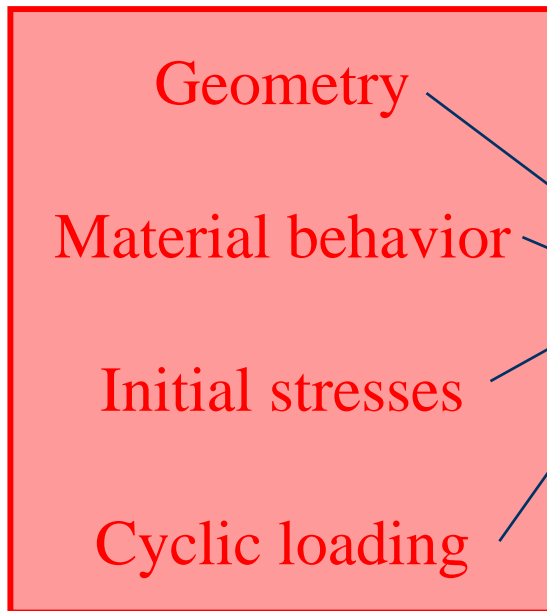
- ◆ Initial purpose
 - Life prediction of Ariane V turbopumps ball bearings from
 - Structural calculations and material properties identified on simple tests
 - Experimental evidence
 - Importance of residual stresses
 - Multiaxial loading
 - ◆ Non proportional principal stresses with rotating principal directions
 - Long life ($\approx 10^7$ cycles)
 - ◆ Elastic shakedown needed
 - ◆ High cycle fatigue techniques and multiaxial fatigue criteria
- ◆ Other applications
 - Elastic shakedown and high cycle fatigue
 - Some examples
 - ◆ Fretting fatigue on titanium grooves (turbopumps shafts),
 - ◆ Fatigue of lubricated carbonitrided gear teeth...
 - 2D + symmetric hertzian contact



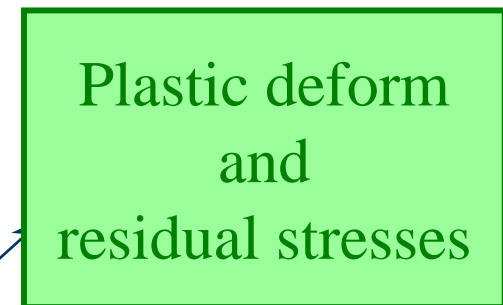
Principle for Life evaluation

Input

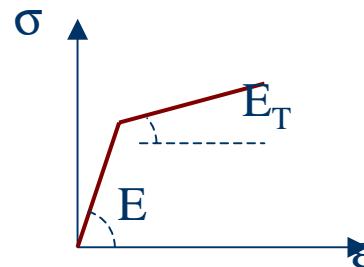
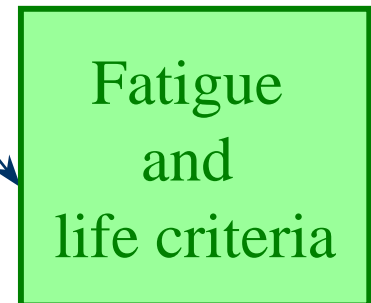
Interactive or data files



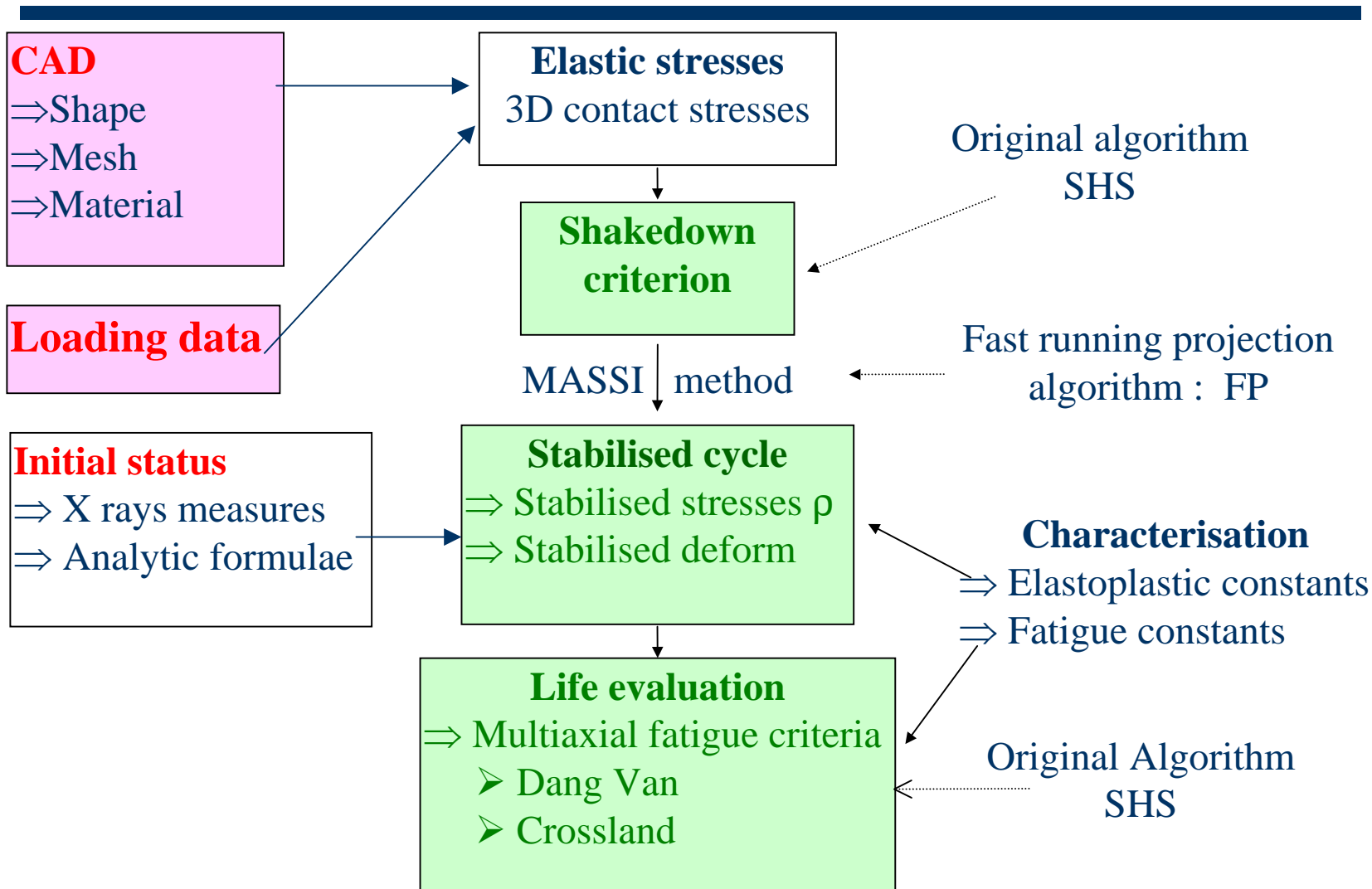
Output



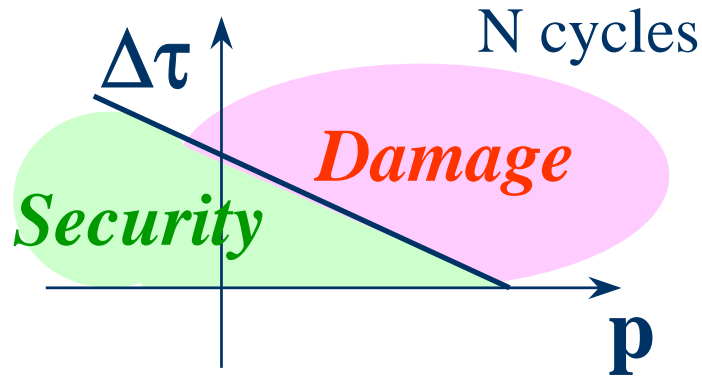
and / or



General flow chart



Multiaxial fatigue criteria



◆ General shape

$$\Delta\tau + a p < b$$

a et *b* material properties

$\Delta\tau$ elastic centered shear stress

p hydrostatic pressure (El+Res)

(El+Res) = elastic+residual

⇒ Crossland:

- * Max ($\Delta\tau_{\text{Von Mises}}$)
- * Max (*p*)

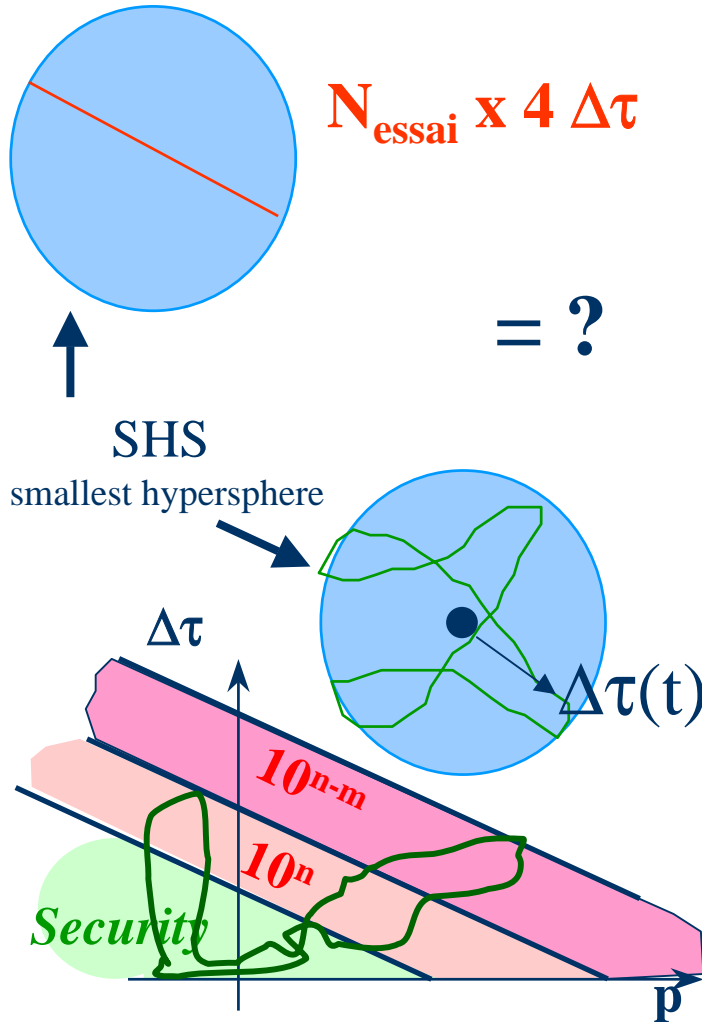
⇒ Sines:

- * Max ($\Delta\tau_{\text{Von Mises}}$)
- * Moy (*p*)

⇒ Dang Van:

- * Max ($\Delta\tau_{\text{Tresca}} + a p$)

Life estimation



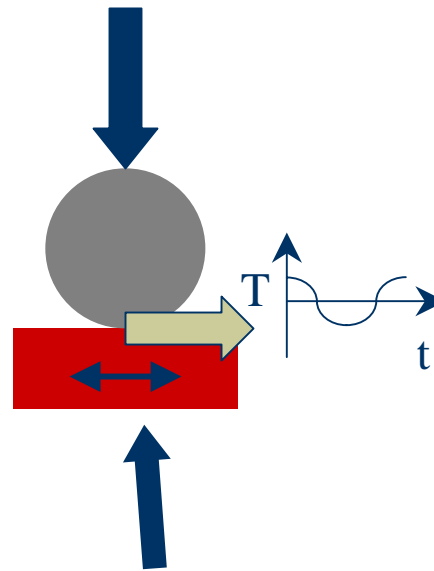
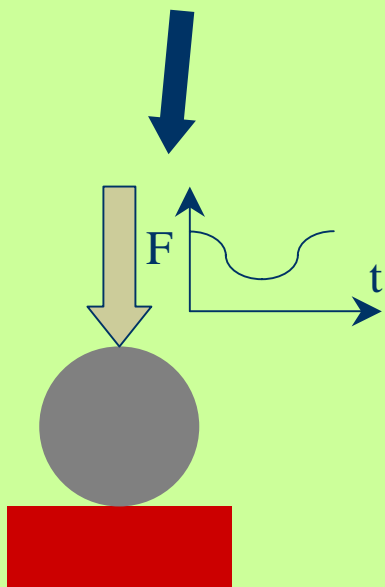
- ◆ Fatigue life known on uniaxial tests : $N(R, \Sigma_{\max})$ tensile or bending test...
- ◆ Complex loading path ???
- ◆ Damaging loading path function of distance to endurance limit ($\Delta\tau$, p plane)

$$D = N \times \left(\frac{1}{10^n} + \frac{1}{10^{n-m}} \right) \leq 1$$

Validation : Contact fatigue tests

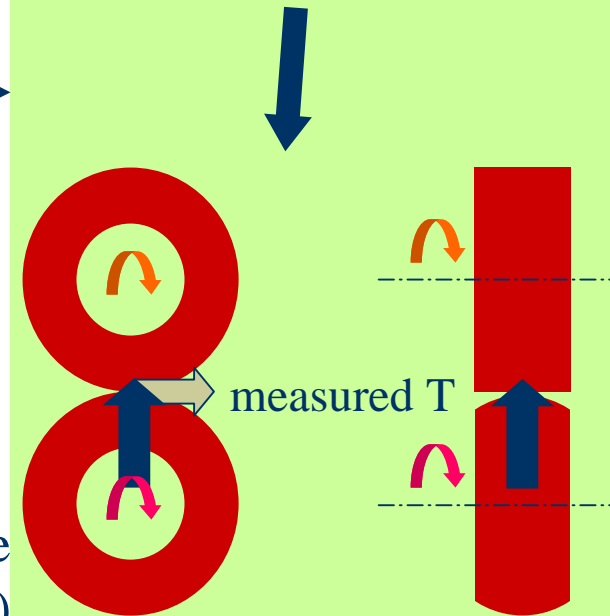
Available volume tests \Rightarrow initial values of fatigue parameters
 If coatings or surface treatments, Hertzian critical depth to be considered

Ball on plane, ondulated normal force (highly symmetric, simple parts)

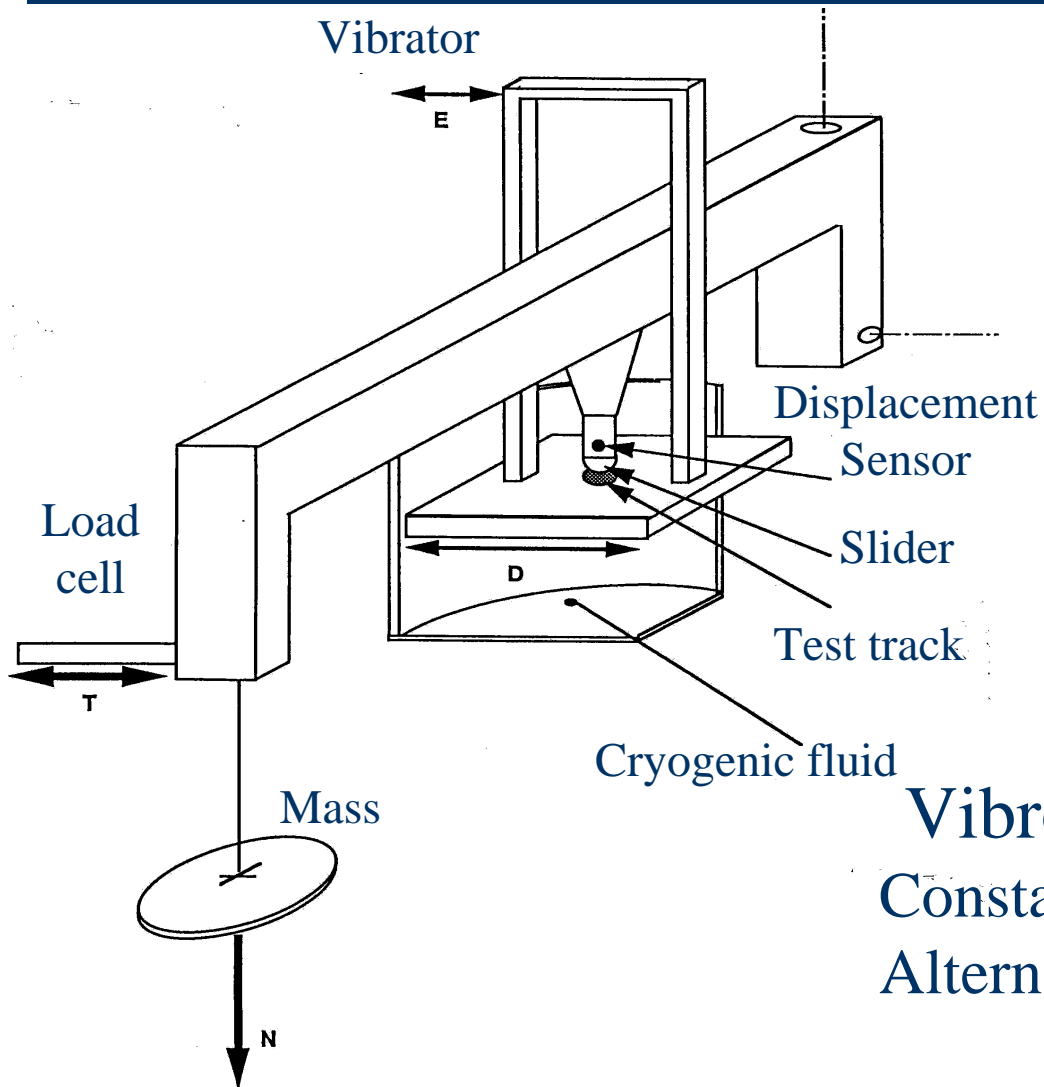


VibroCryoTriboMeter
 Constant normal force
 alternate tangential force
 (constant volume forces)

Disk on disk
 Constant normal force
 2 controlled rotation speeds

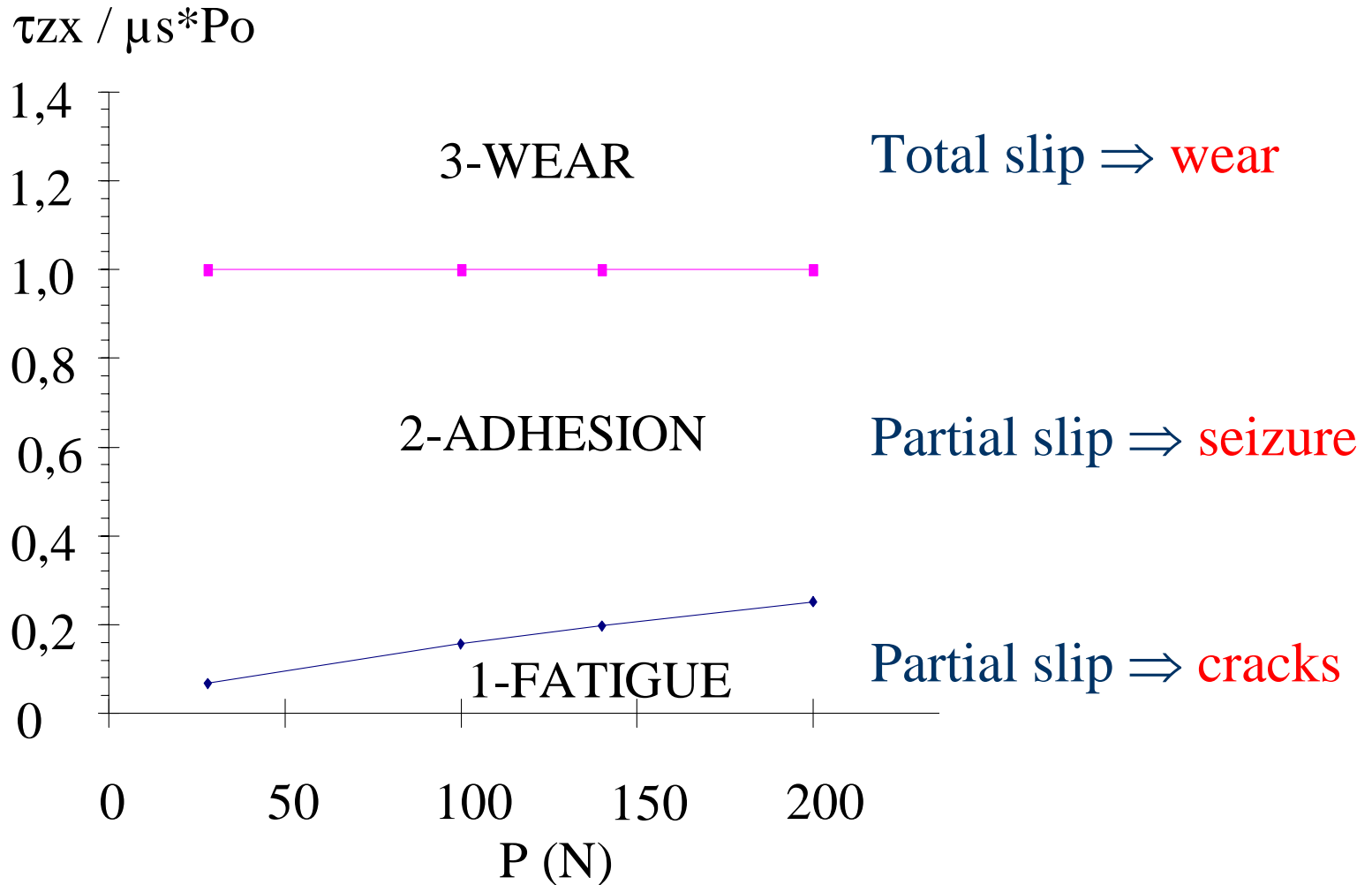


Fretting fatigue and wear



VibroCryoTriboMeter
 Constant normal force
 Alternative tangential force
 or displacement

Fretting fatigue and wear

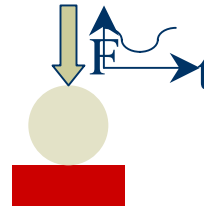


Rolling sliding contact (bearings)

◆ Turbopumps bearings

- plastic and fatigue material properties and 1 validation from :

- ball/plane test



A2DF or A2DF6S

- disk / disk test

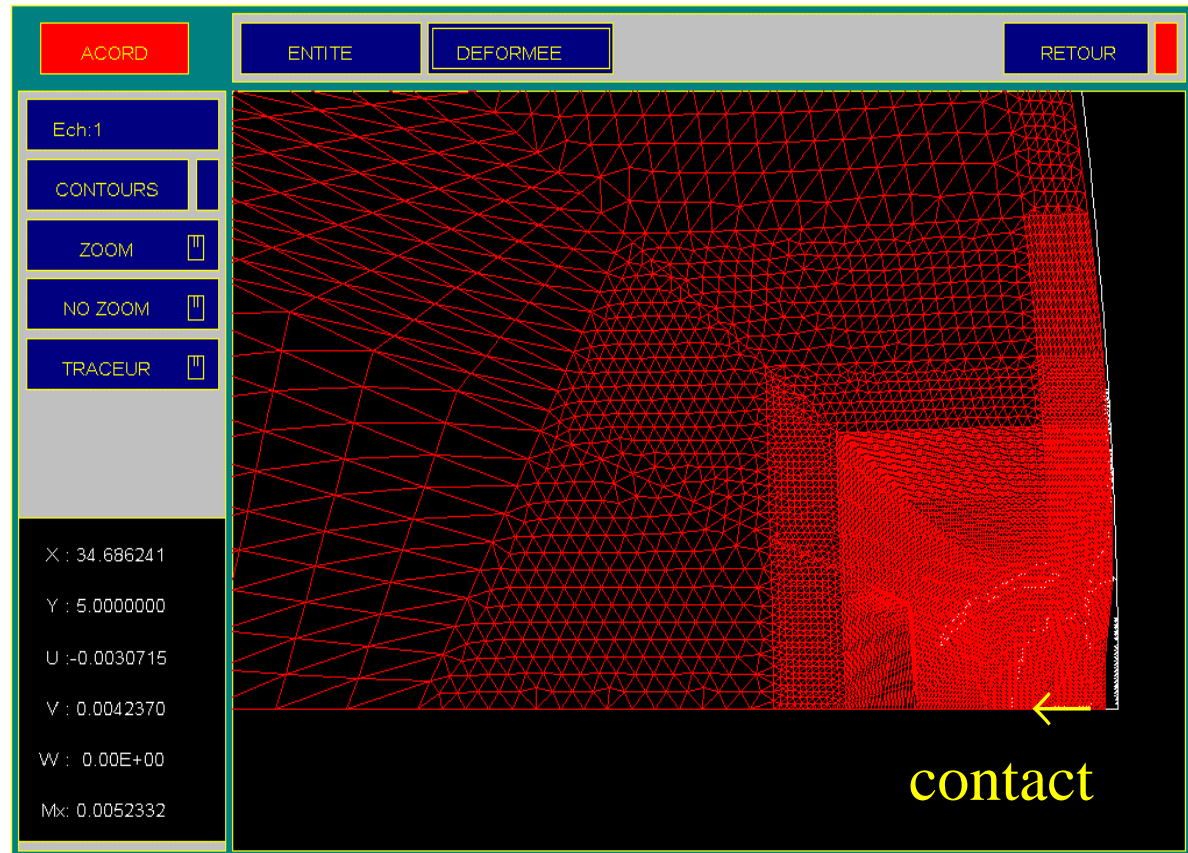
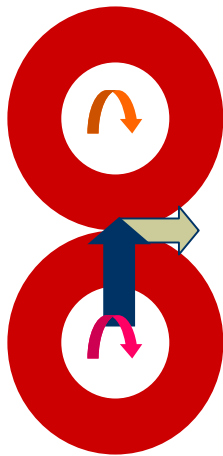


A2DF6S

- Shakedown and life prediction for turbopumps ball bearings

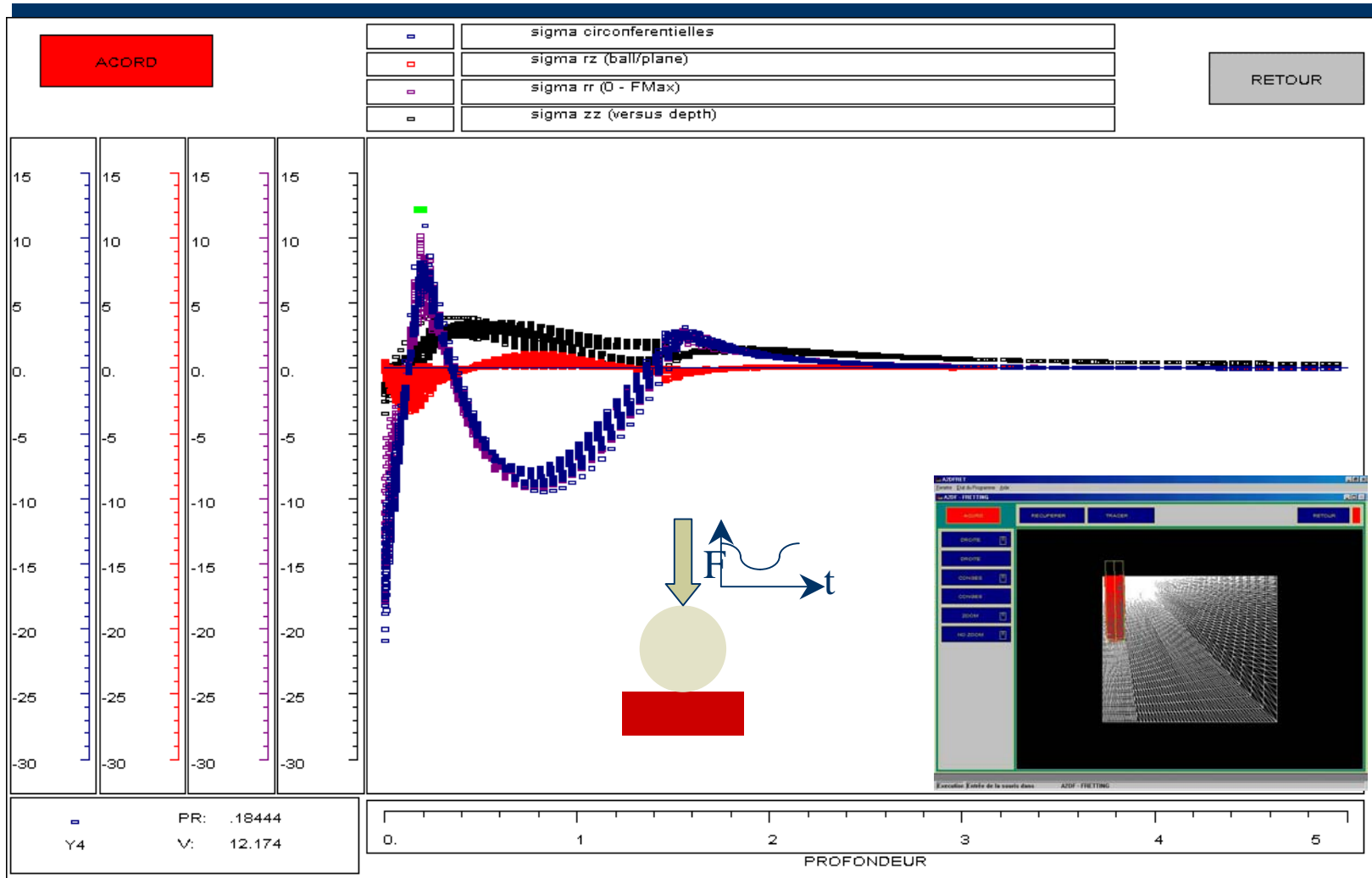
- localisation on rings : RMS4
- shakedown and life : A2DF6S

Disk / disk : numerical residual track



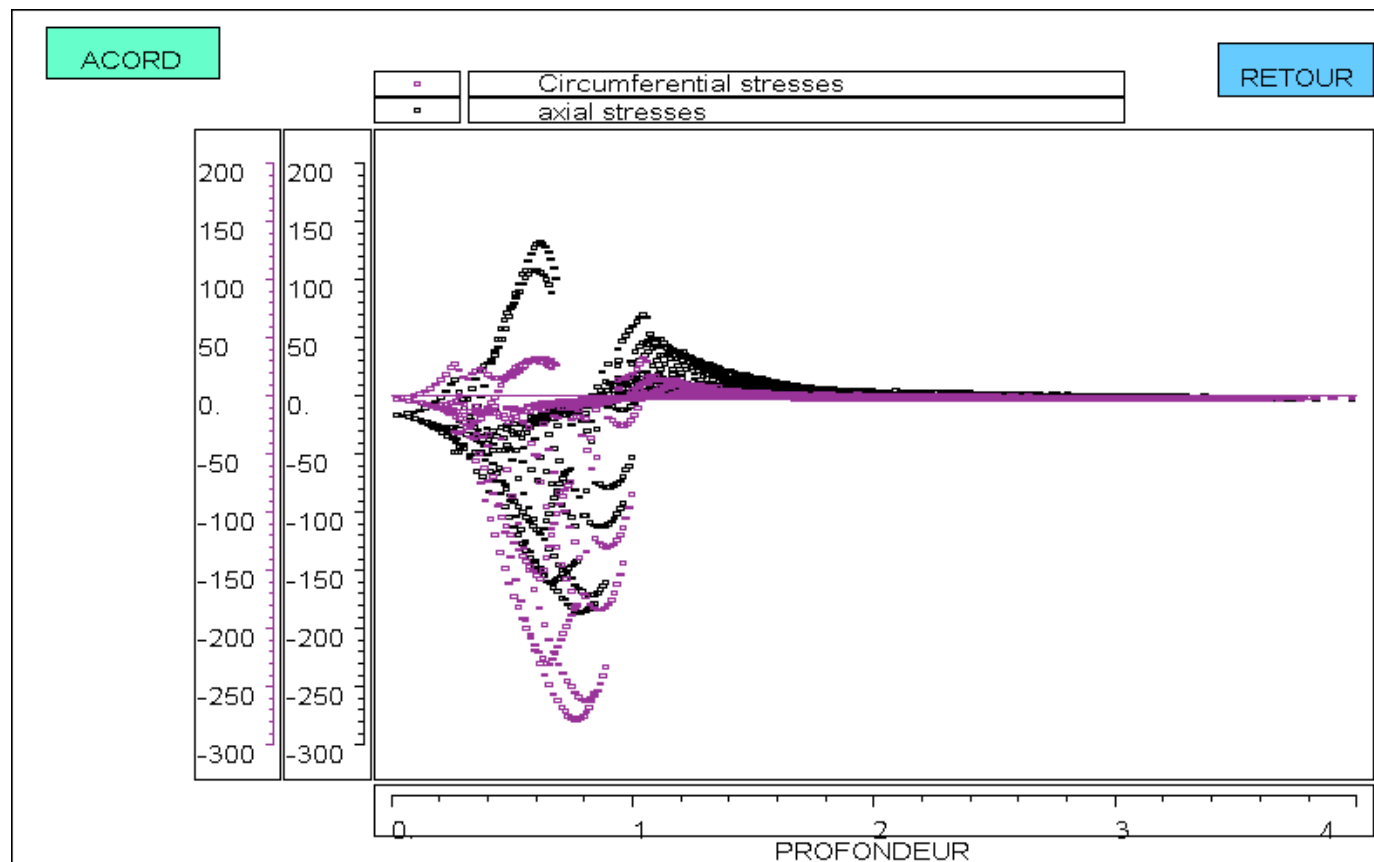
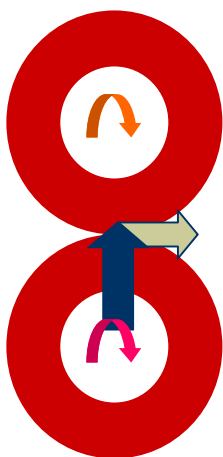
- ◆ 3 degrees of freedom for each node
 - radial, axial and circumferential displacements

Stresses vs. depth in a ball/plane test



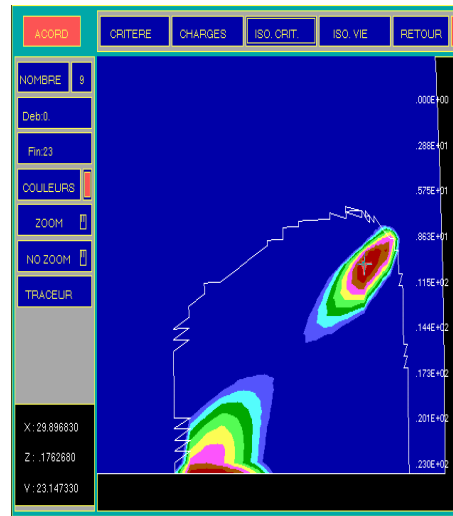
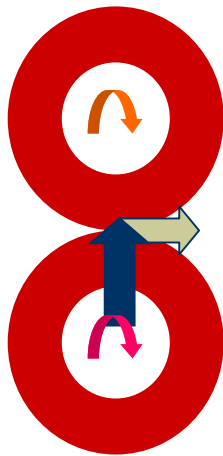
- ◆ Select of all numerical values along a straight line with given width

Example of stabilised residual stresses



under contact track (disk on disk)

Fatigue results on disk / disk test



Predicted crack initiation place



Observed crack

Observed fatigue crack has been found in the predicted place

RMS4 : Global to local loading on rings 1

- ◆ Bearing geometry and elastic behaviour (E, ν) mechanics for balls and inner and outer rings are defined

Parametres Roulement

OK Cancel

Reference TPO VUlcaïn1

DM (mm) 92.5

Delta (mm) 15.081

Nombre de billes 14

Courbure relative interieure f_i 0.525

Courbure relative exterieure f_e 0.52

Angle de contact geometrique (deg) 15

Angle de Cale interieur (deg) 0

Angle de Cale exterieur (deg) 0

B largeur bague (mm) 30

d3 (mm) 40

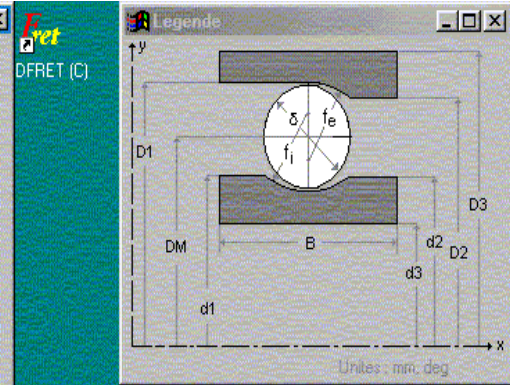
D3 (mm) 145

d1 (mm) 84.9595

d2 (mm) 84.9595

D1 (mm) 100.04

D2 (mm) 100.04



RMS4 : Global to local loading on rings 2

Parametres Fonctionnement

OK Cancel

Vitesse de rotation bague interieure (tr/min) 14500

Vitesse de rotation bague exterieure (tr/min) 0

Efforts appliques sur .

bague interieure

bague exterieure

Type de precharge .

souple

rigide

Effort axial impose suivant X (N) 22500

Deplacement radial impose suivant Y (micr.) 0

Deplacement radial impose suivant Z (micr.) 0

Basculement impose autour de Y (deg) 0

Basculement impose autour de Z (deg) 0

Parametres Contact/Lubrifiant

Ok Annuler Valider

Choix de la Lubrification : . Aucune

Choix du Modele : . Coulomb + Adaptation Elastique

Coef. de friction bille/bague interieure. 0.15

Coef. de friction bille/bague exterieure. 0.15

Cohesion bille/bague interieure. (MPa) . 0

Cohesion bille/bague exterieure. (MPa) . 0

Hysteresis elastique bille/bague interieure. (%) . 0.5

Hysteresis elastique bille/bague exterieure. (%) . 0.5

Nombre de tranches dans le contact 12

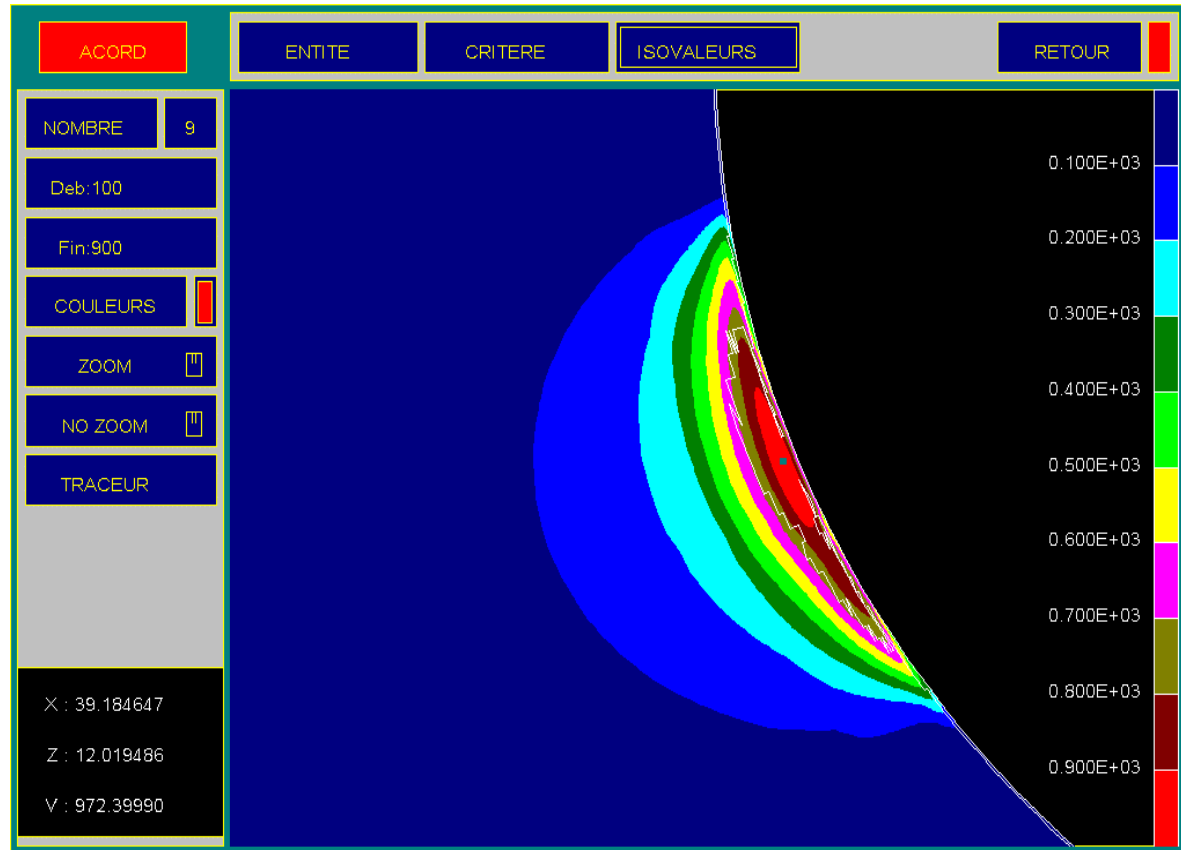
Nombre mini de points par tranche 5

Modele cinematique de la bille 4 ddl

Prise en compte des efforts transverses dans l'equilibre de bague

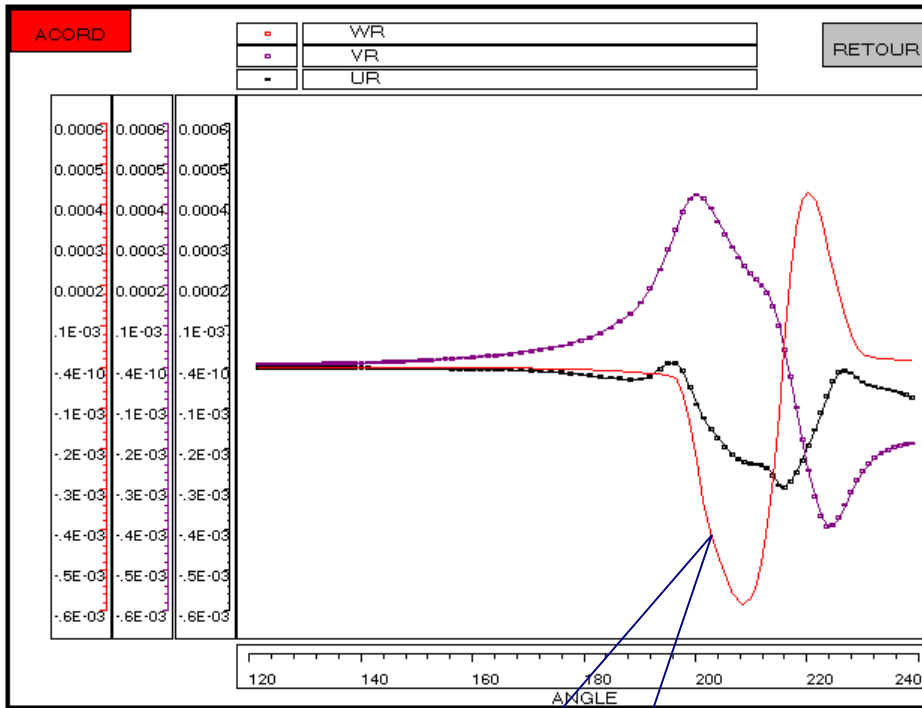
- ◆ External loading and lubrication conditions are defined
- ◆ Calculation gives the local loading on rings

Shakedown criterion



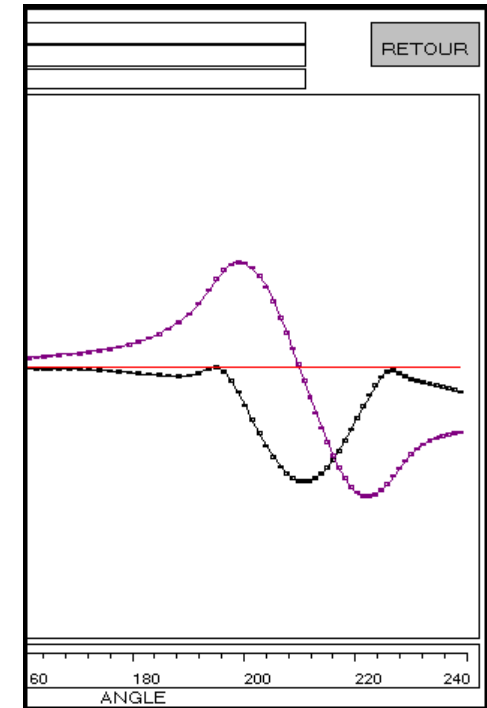
- ◆ Shakedown criterion :
 - maximal value should keep smaller than initial tensile yield stress (elasticity)

Residual displacements on an inner ring



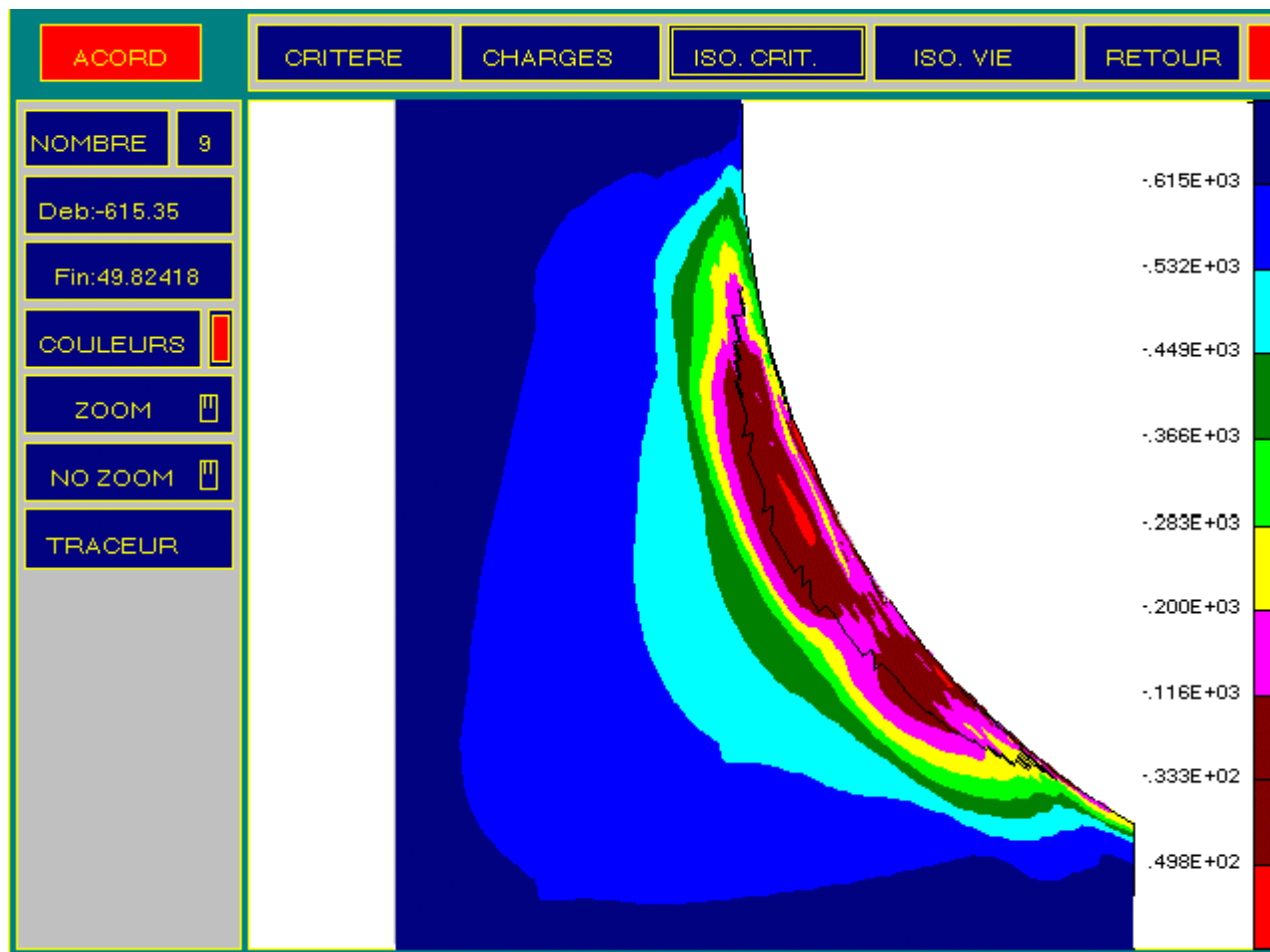
Spinning effect

Non radial loading



Radial loading

Life prediction for an inner ring



Conclusion (1st example)


- ◆ Present results on cryogenic ball bearings
 - Models
 - Crack initiation prediction
 - Life duration (validation going on)
 - Bearings life $\approx 12\ 000\ \text{s}$ ($20 \times$ present needs)
 - to be improved for reusable engines \Rightarrow lubrication, materials,...

- ◆ Other results :
 - Cryogenic
 - Fatigue & life of coated or uncoated titanium grooves
 - Lubricated (aerospace engines)
 - Fatigue and life of gears ; specific process for oil testing \Rightarrow friction factor

Combustion chambers or nozzles

- ◆ Extremely severe Thermal cycle
 - From 20K to 3500K
- ◆ Material properties
 - High thermal conductivity
 - Mechanical strength even at high temperature
 - Most likely involved damage
 - Thermal damage (local melting, ...)
 - Mechanical damage (inelastic strains, cracks, ...)
 - Chemical damage (loss of thermomechanical properties from corrosion or hydrogen embrittlement, ...)

Behavior description

- ◆ Classical practice
 - Isothermal elastoviscoplastic laws defined for a variety of temperatures
 - interpolations and extrapolations ?
- ◆ An attempt to define a unique law
 - Walker and Freed thermoelastoviscoplastic model
 -  Chemical damage is not in, neither fatigue
 - Possible discrepancy on yield stresses (or other parameters) for some temperatures

Walker and Freed model

Thermoelasticity

$$s_{ij} = dev(\sigma_{ij}) \quad \text{and} \quad e_{ij} = dev(\epsilon_{ij})$$

$$s_{ij} = 2\mu(e_{ij} - \epsilon_{ij}^p) \quad \text{and}$$

$$\sigma_{kk} = 3K(\epsilon_{kk} - \alpha(T - T_o)\delta_{kl})$$

Inelastic behavior

$$\epsilon_{ij} = \frac{1+\nu}{E} \sigma_{ij} - \frac{\nu}{E} \sigma_{kk} \delta_{ij} + \epsilon_{ij}^p$$

Yield stress and Thermal functions

$$Y = (1-f) \frac{(D - D_o)(C - D)}{C\delta} \quad \text{and} \quad L = \frac{f}{1-f} Y$$

$$\vartheta = \begin{cases} \exp(-Q/kT) & \text{when } T_t \leq T \leq T_m \\ \exp\left(\frac{-Q}{kT} \left(\ln\left(\frac{T_t}{T}\right) + 1\right)\right) & \text{when } 0 \leq T \leq T_t \end{cases}$$

$$Z = A \sinh^n \left[\left\langle \frac{\|S-B\| - Y}{D} \right\rangle \right] \quad \text{and} \quad r = A \sinh^n \left[\left\langle \frac{D - D_o}{C\delta} \right\rangle \right]$$

Inelastic flow rules

$$\dot{\epsilon}_{ij}^p = \frac{1}{2} \left\| \dot{\epsilon}^p \right\| \frac{S_{ij} - B_{ij}}{\|S - B\|} \quad \text{and}$$

$$\left\| \dot{\epsilon}^p \right\| = \vartheta(T) Z$$

$$\dot{B}_{ij} = 2H \left(\dot{\epsilon}_{ij}^p - \frac{B_{ij}}{L} \left\| \dot{\epsilon}^p \right\| \right)$$

$$\dot{D} = h \left(\left\| \dot{\epsilon}^p \right\| (1 - \Lambda) - r \vartheta(T) \right)$$

Norms and auxiliary functions

$$\left\| \dot{\epsilon}^p \right\| = \sqrt{2 \dot{\epsilon}_{ij}^p \dot{\epsilon}_{ij}^p} \quad \text{and}$$

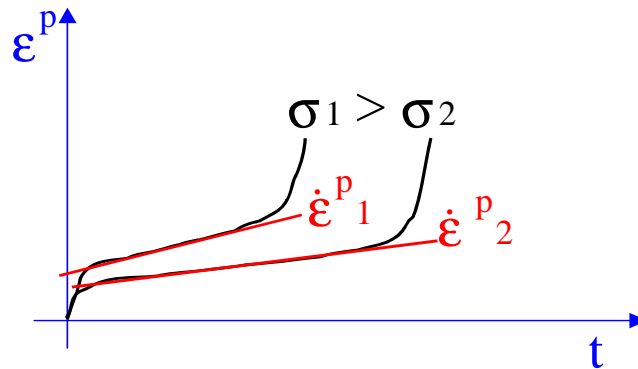
$$\|S - B\| = \sqrt{\frac{1}{2} (s_{ij} - B_{ij})(s_{ij} - B_{ij})}$$

$$H = \mu(0,1 + 0,9\xi) \quad \text{and} \quad \Lambda = l\xi$$

$$\xi = \sqrt{\frac{1}{8} \left(\frac{s_{ij} - B_{ij}}{\|S - B\|} - \frac{B_{ij}}{L} \right) \left(\frac{s_{ij} - B_{ij}}{\|S - B\|} - \frac{B_{ij}}{L} \right)}$$

Identification of material parameters for W & F viscoplastic law (I)

- ◆ Transition temperature T_t assumed usually as $T_t = 0,5 T_m$ (T_m melting temperature)
- ◆ Creep exponent n assumed : $4 \leq n \leq 5$
- ◆ Creep experiments at constant stress \Rightarrow identifying A , Q and C most easily :



at different temperatures

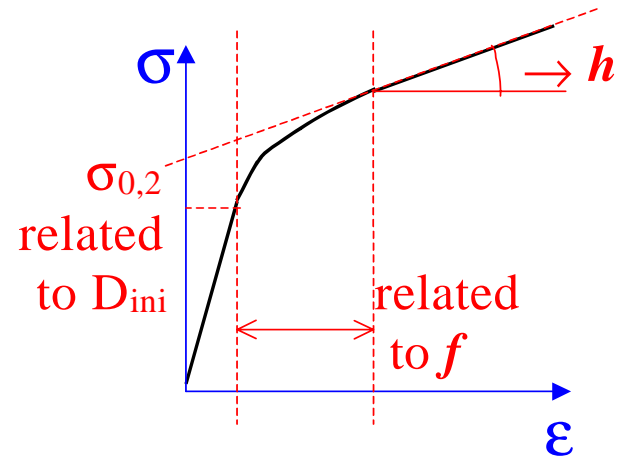
$$\dot{\epsilon}^P = \vartheta(T) A \sinh^n \left(\frac{\sigma}{C} \right)$$

$$\text{with } \vartheta(T) = \exp \left(\frac{Q}{kT} \right)$$

\Rightarrow Activation energy Q

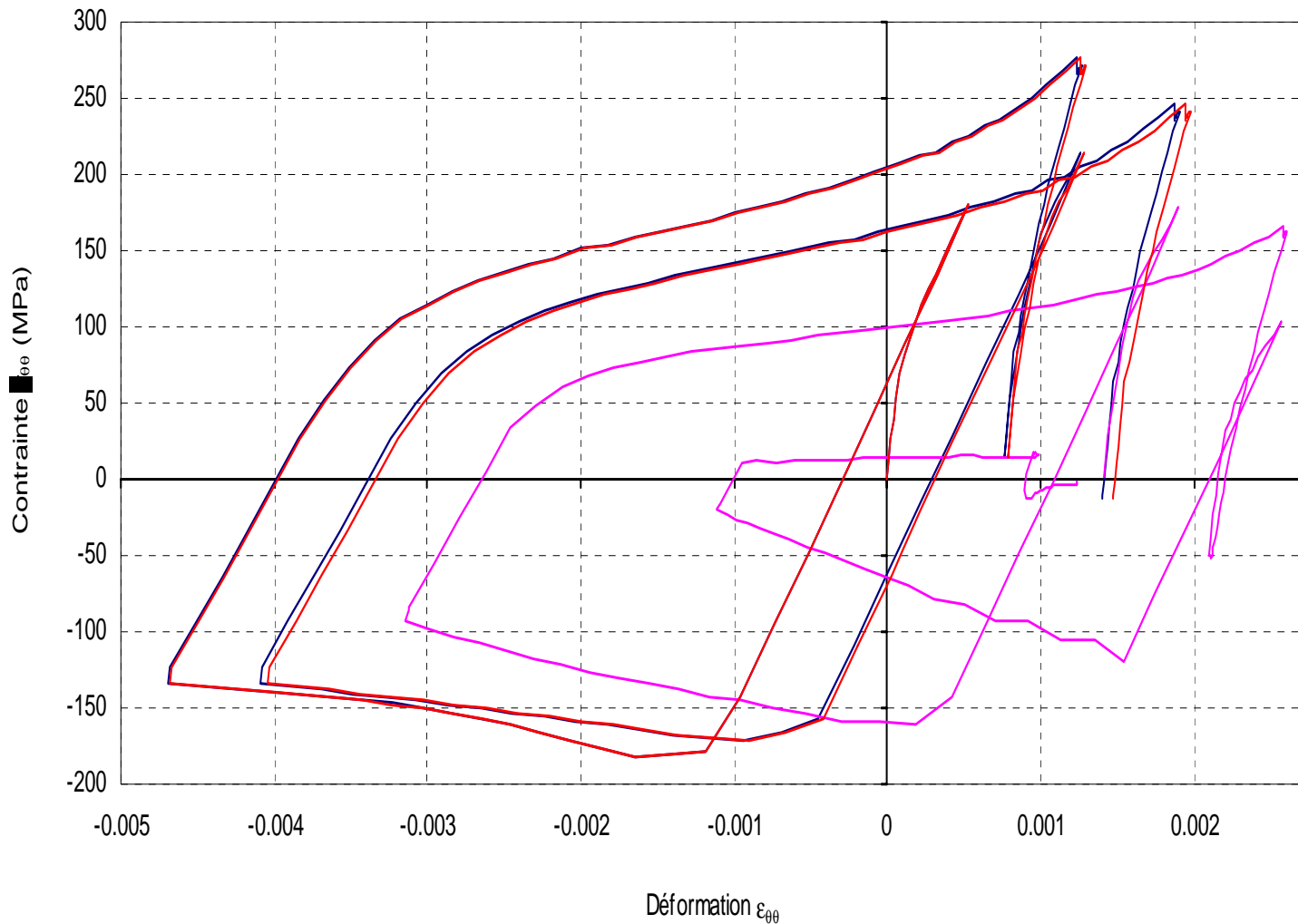
Identification of material parameters for W & F viscoplastic law (II)

- ◆ Minimal value of drag strength $D_0 \approx C / 100$
- ◆ Partition parameter f and hardening modulus h determined from tensile stress strain curves at known constant strain rate $\dot{\epsilon}$

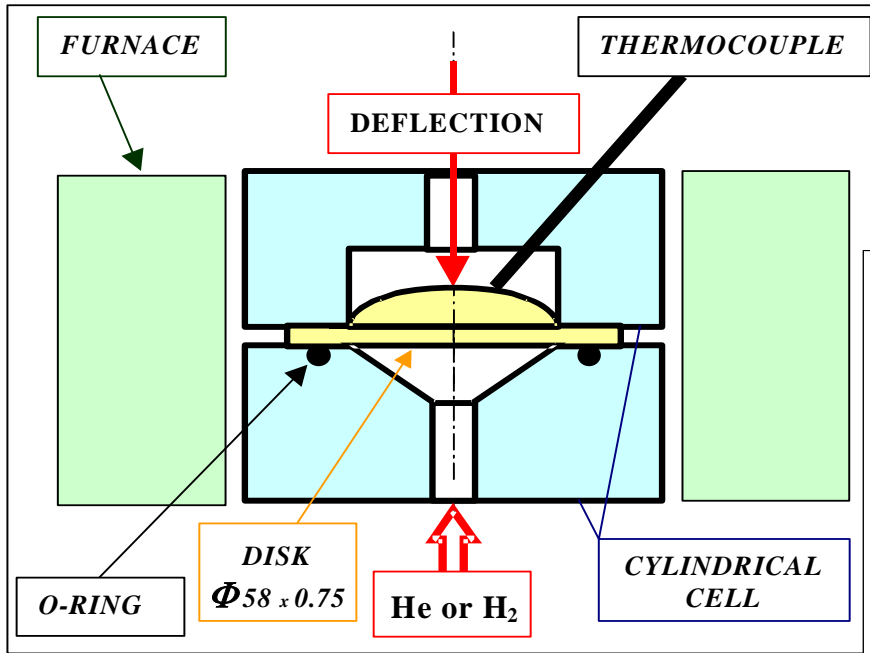


- ◆ Parameter δ determined from σ_{ultimate} at low temperature
- ◆ Cyclic / monotonic interaction parameter l from cyclic stress strain curves

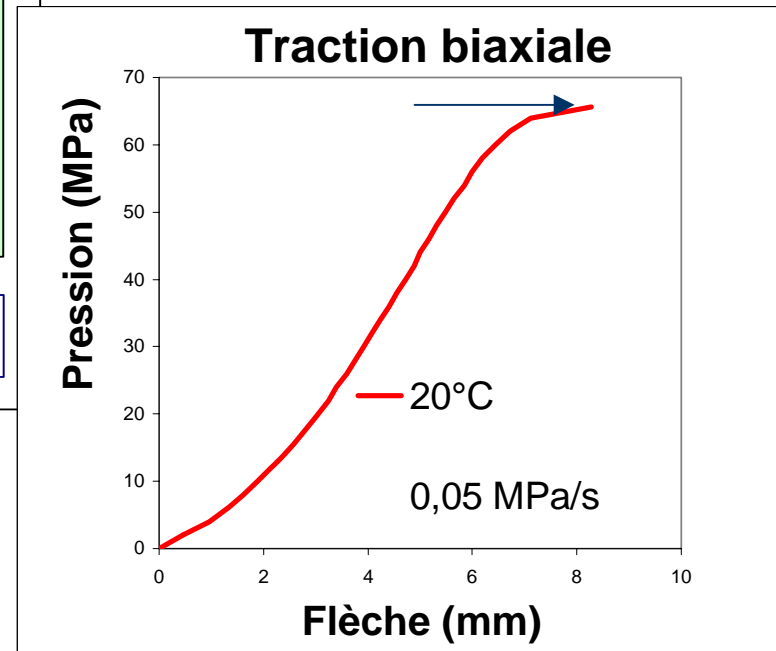
Thermomechanical stresses vs strains



Disk pressure test



- Loading speed
 10^{-1} à $2 \cdot 10^4$ MPa.mn⁻¹
- Temperature : 20 à 900°C

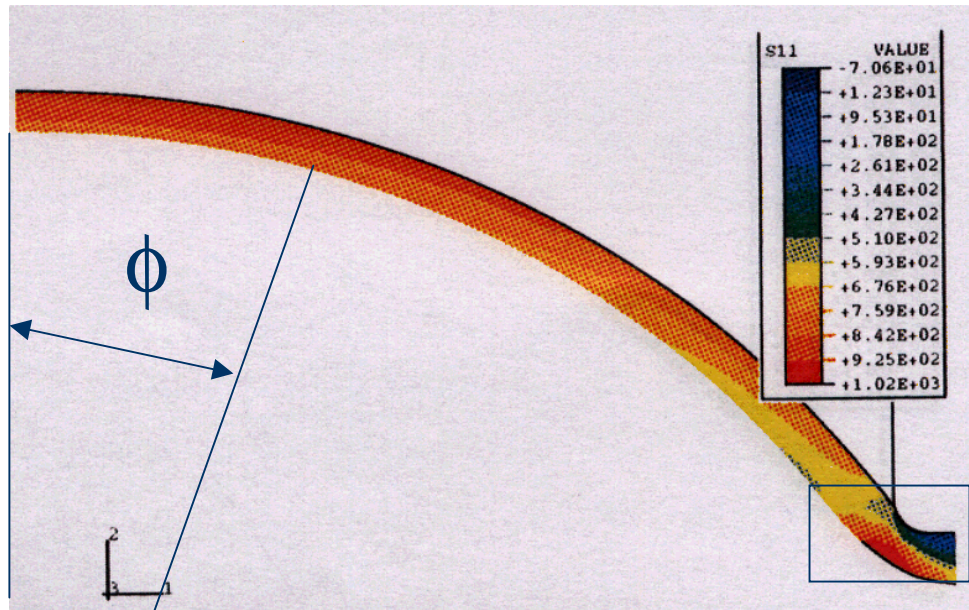


p_{He} or p_{H_2} : rupture pressure (He or H₂)

$p_{He}/p_{H_2} > 2 \Rightarrow$ No use under hydrogen

Embrittlement test

Cell for embrittlement tests => anchorage radius $r=0.5$



σ_ϕ : radial stress

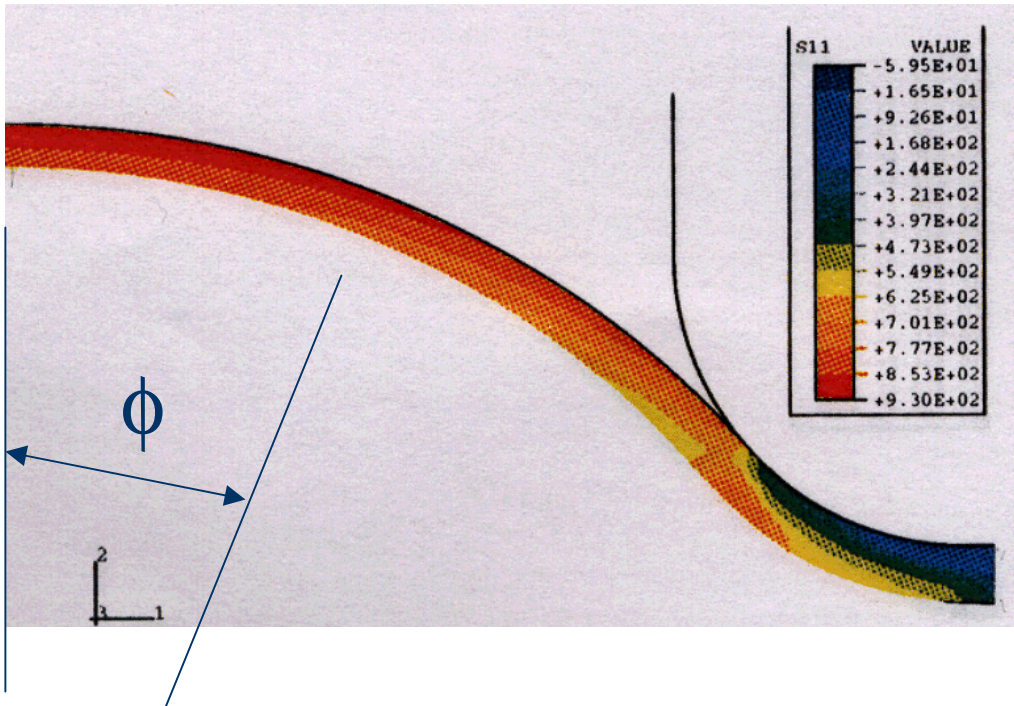
Local deformation

thickness ↘↘

σ_ϕ maximum near the anchorage

Biaxial tests

Cell for biaxial tests => anchorage radius $r=4$



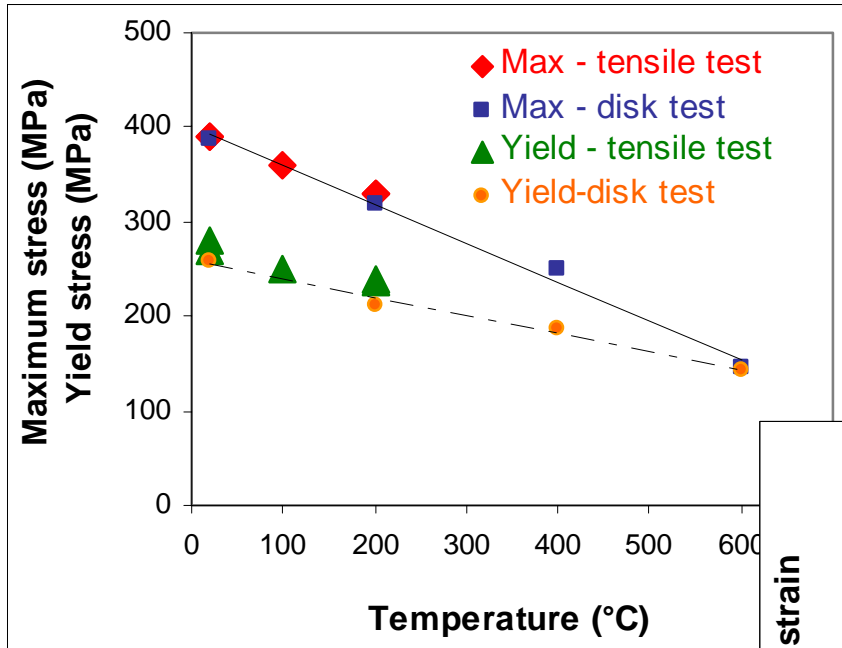
σ_{ϕ} : radial stress

**Homogeneous
deformation**

**Uniform
thickness**

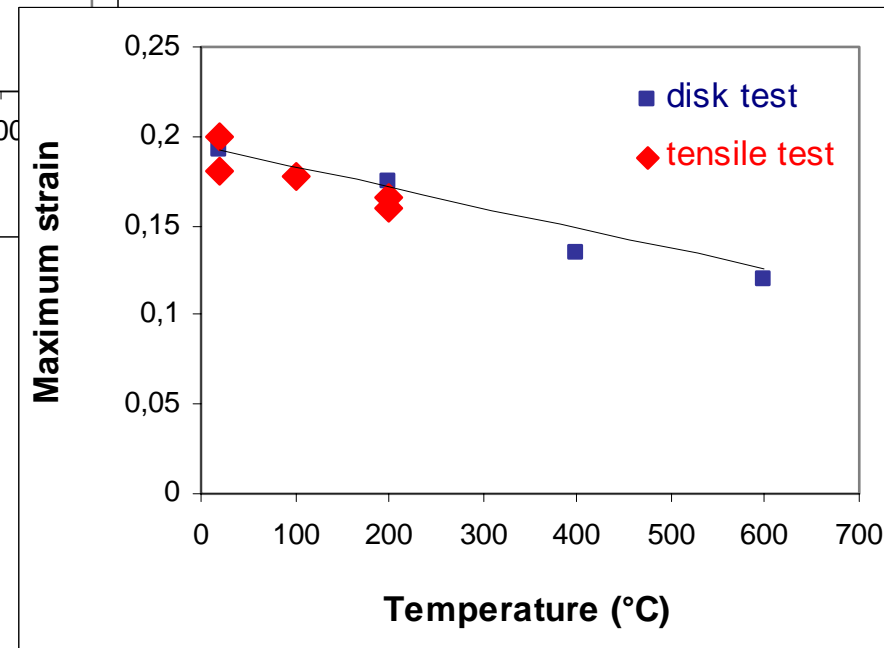
σ_{ϕ} maximum at the pole

Biaxial tests / Tensile tests



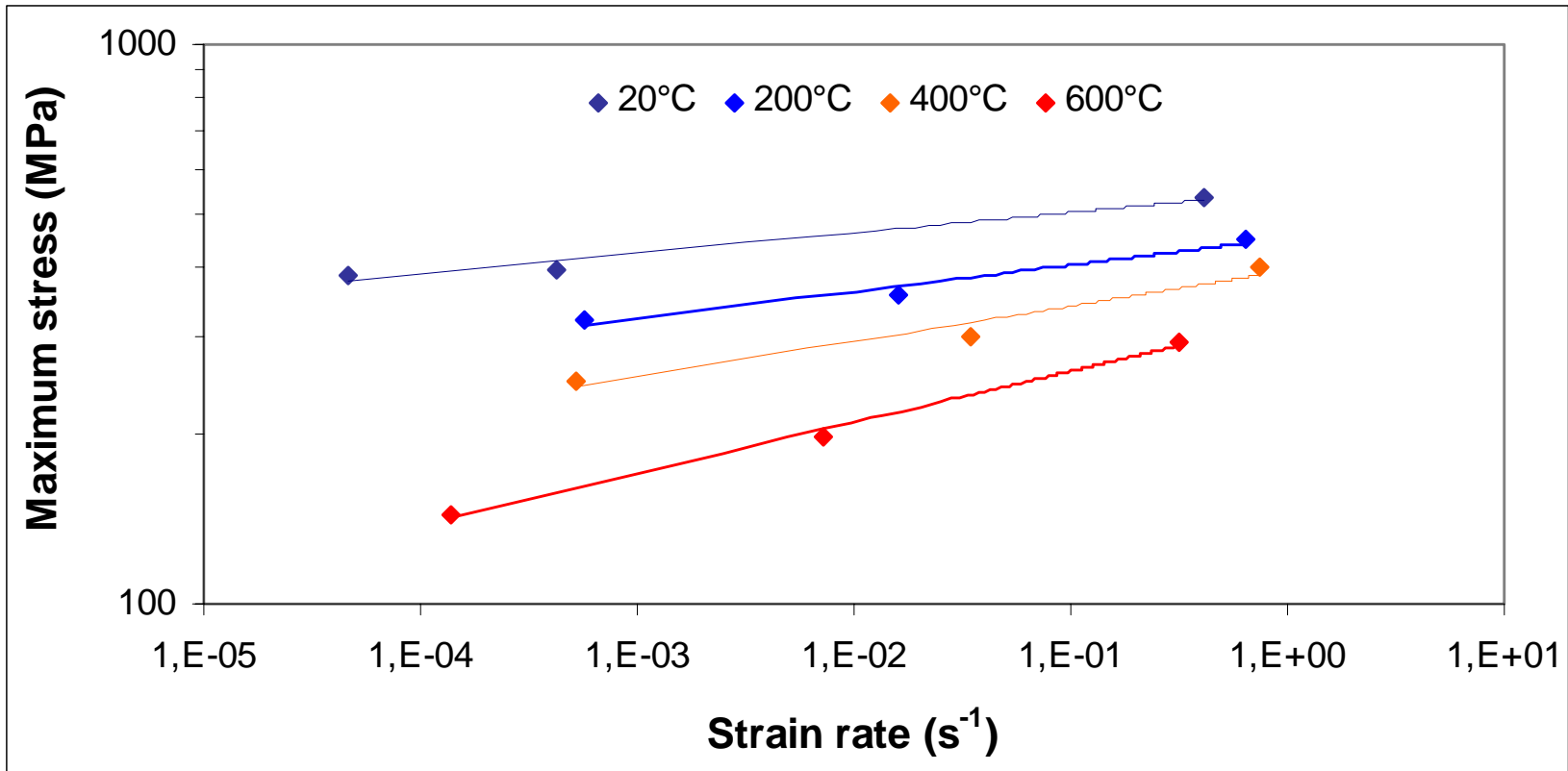
Yield and Peak Stresses
versus Temperature for
disk and tensile tests

Maximum Strains
versus Temperature for
disk and tensile tests

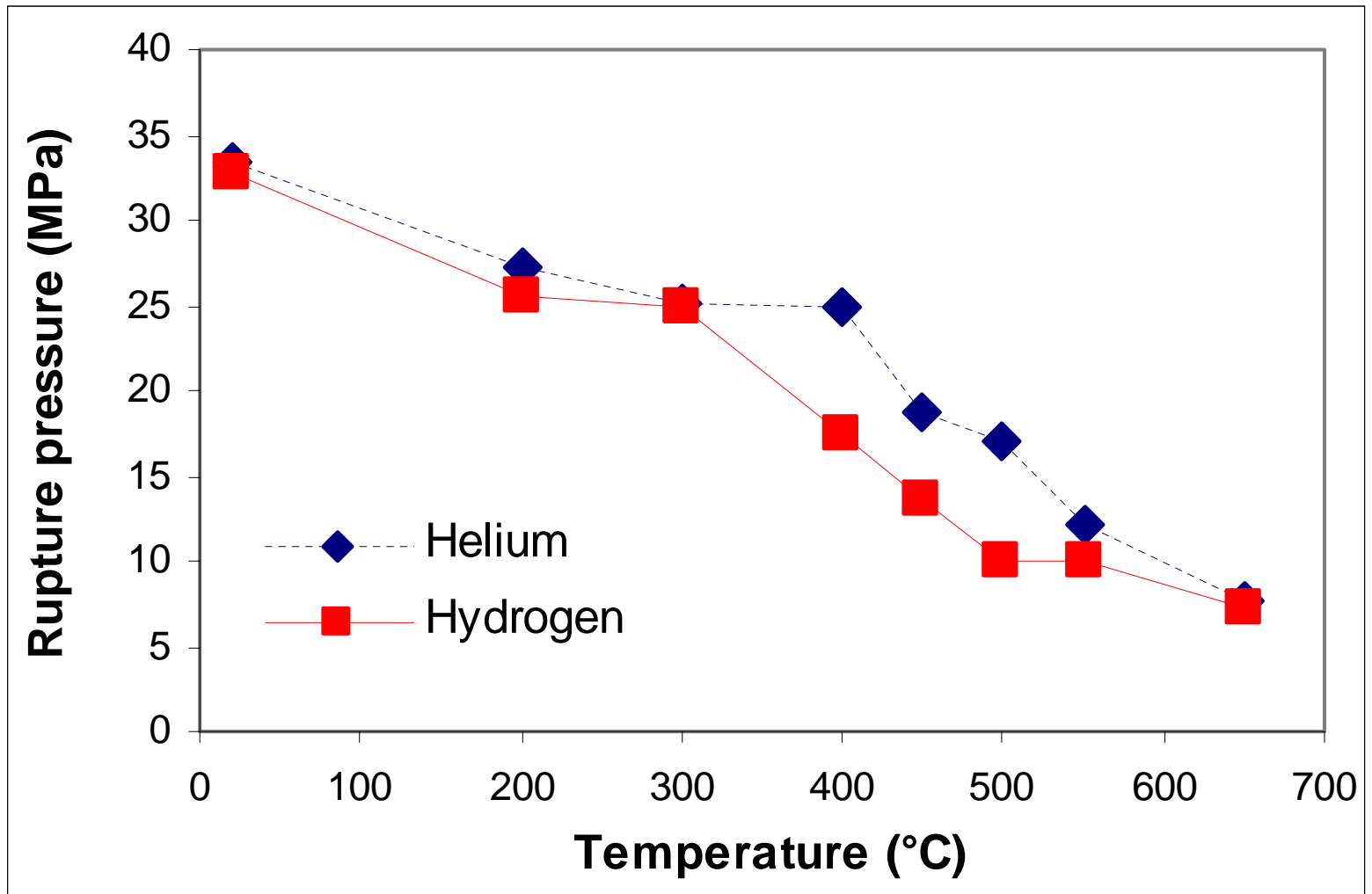


Biaxial tests

Influence of temperature and loading speed



EMBRITTLLEMENT TESTS



Conclusion

- ◆ Better choices of materials \Rightarrow Significant improvements
- ◆ Attention to be focused
 - Defining approximate thermal, mechanical and chemical loading conditions,
 - Selecting materials which can stand this loading
 - Checking significant damage mechanisms
 - Select significant behavior laws
 - Select associated tests programs for identification

Acknowledgements

- ◆ Thanks to CNES (French National Space Agency) and SNECMA Moteurs fusées for years of fruitful scientific cooperation in the field of contact mechanics
- ◆ Thanks to our partners of INTAS project on combustion chambers : CNES, DLR (Germany National Space Agency) and KeRC (Russian National Space Agency)

MATERIAL REQUIREMENTS AND LIMITATIONS FOR LIQUID ROCKET ENGINES

G. Inglebert, R. Gras

Laboratoire d'Ingénierie des Systèmes Mécaniques et des Matériaux, groupe Tribologie,
EA2336, ISMCM-CESTI, France

ABSTRACT

Liquid propulsion is currently used for spatial launchers. High power engine are required in the smallest size and the lightest weight. All parts of the engine are submitted to strong thermo-mechanical loadings. An optimum design of mechanical systems is strongly linked to some choice of appropriate materials. A fair knowledge of behavior laws of these materials and specific modeling of problems are necessary to reach sufficient reliability. Three examples of critical parts are presented with their specific modeling: ball bearing guiding of the rotor of the turbopumps, fretting fatigue in contacts of splined shaft, heat transfer in the nozzle.

INTRODUCTION

Spatial activities require design and manufacturing of complex systems such as launchers, space probes and planes, orbiting stations. All these have to work in severe environments: vacuum, hot gases (more than 3500K) cryogenic fluids and so on.

Mechanical links, guiding and power transmission systems, static and dynamic sealing are key parameters for successful operations. So today engines for launchers generally use combustion of hydrogen and oxygen to obtain high specific thrust. Propellants (LH₂ and LO_x) are carried out as liquids from tanks, compressed up to 100 bars or more, through turbopumps and burned in the combustion chamber where the gases are burnt at 3500K ; the turbopumps are moved by hot gases issued from hot gases generator (800 to 900K) or combustion nozzle through several actuators (hot gases valves) and allow to control fluxes.

All parts of these components undergo heavy thermo-mechanical loadings and have to be precisely defined at the design stage. A deep knowledge of materials and material behavior laws, in the really high and / or low temperature range, is required to ensure accurate enough reliability of the design.

Our presentation will try to enlighten some mandatory properties and behavior modeling of materials under thermo-mechanical loadings from a few examples.

- contact fatigue in ball-bearings,
- fretting contact in parts (splined shafts, blade fir trees)
- combustion chambers

MATERIAL REQUIREMENTS

VULCAIN engine as designed for ARIANE V is funded on a gas generator cycle. In such engines, an extremely wide range of thermal, mechanical (static and dynamic) and chemical conditions is encountered.

- Hot parts are surrounded with steam and hydrogen saturated reducing gases, which can induce hydrogen embrittlement; they undergo pressures up to 100 bars, and temperatures between 1000K (turbines, gases generators, nozzle, turbine feed lines and exhaust lines) and 3500K in the combustion chamber.

- Cold temperatures (20K or 90K) are supported by cold parts such as pumps, injection elements for gases generators and combustion chambers, feed lines and cooling channels, valves,...).
- Walls and separators between hot and cryogenic fluids are submitted to strong thermal gradients inducing very high mechanical stresses in self clamped components.

The whole set of constraints (thermal, mechanical, chemical) leads to choose specific materials such as Nickel based alloys, high quality Steels, Titanium alloys, and even Copper base alloys for the walls of combustion chambers... Their manufacturing processes have to be optimized, and, for design purposes, their behavior laws have to be identified in the whole range of thermal and mechanical loading.

These laws should take into account initial properties of materials, including stresses due to manufacturing processes, variations of these properties due to the thermo-mechanical loading or chemical effects, and damage mechanisms (creep during hot run, fatigue, hydrogen embrittlement) likely to lead to collapse of a component.

MATERIALS FOR CRYOGENIC TURBOPUMPS

In a rocket engine, turbopumps are the crucial components which feed the combustion chamber with high flow and high pressurized propellants. High power (about 12 MW for VULCAIN Hydrogen turbopump) is needed together with the lightest weight possible (240 Kg).

Manufacturing these turbopumps implements highly efficient solutions and high quality materials. In this presentation, we focus on two decisive points, belonging to the contact problems family:

- guiding components of the rotor
- blades and splined-shafts of turbine.

GUIDING COMPONENTS

The guiding of the rotor is provided by angular contact ball-bearings, submerged in cryogenic fluids. These bearings are run at high speed (35000 Rpm), NDm products between 2 and 2.5×10^6 mm \times rpm and Hertzian contact pressure (ball on rings) over 3 or 3.5 GPa.

Classical lubrication cannot be used due to liquid propellants LH2 and LOx. So bulk material for balls and rings is a martensitic stainless steel EZ100CD17 (440C) treated at 58 to 60 HRC. The monobloc cage is machined in a glass fiber PTFE composite insuring a solid lubrication by a transferred film of PTFE from cage to balls contacts.

An electrolytic Nickel, silver MoS2 coating is applied to the rings generating a significant improving of the bearing behavior.

Nowadays, many developments are performed about nature and composition of materials for balls, rings and cages (ceramics, nitrogen martensitic stainless steels, and new composite for cages),

New technologies are investigated to find reliable answers to ultra high rotating speeds and long life requirements (magnetic or fluid bearings).

PREDICTIVE TOOLS

For a better understanding and predictive design of ball bearings, a dedicated tool (A2DF6S GDR916 CNES, SNECMA Moteurs fusées, CNRS) has been developed for elastic shakedown and high cycle fatigue analysis. Associated experiments (to be run for behavior identification) such as disk on disk contact tests can be studied with this tool. It deals with the

fundamental question : predicting ball bearings life in the elastic shakedown range from high cycle fatigue multiaxial criteria and a complete 3 dimensional contact loading : complete 3D displacement fields and stress tensors are allowed, assuming they are the same in any meridian plane. Friction, rolling and spinning effect in the ball on race contact are taken into account and up to 8 steps of time can be associated to each selected ball on race contact.

General equilibrium of the bearing and localization of its global loading on the ball to races contact is achieved using a dedicated software RMS4 (CNES-GLCS) which creates the elastic loading data.

This approach has been extended to any cyclic loading in the elastic shakedown range with a particular attention to fretting conditions. A2DFretting deals with 2D structures submitted to any combination of classical FEM and Hertzian contact loading. Cyclic loading definition and more general elastoplastic behavior laws for materials were implemented. For each step of the time discretization, the cyclic loading in an element is a combination of classical FEM solution for given boundary conditions and analytically calculated contact stresses. These contact stresses are defined through their maximum Hertzian pressure and half length a and b of the elliptic contact area and calculated in the half plane of symmetry normal to the displacement of the contact (i.e; xy or rz plane). Up to now, the effect of tangential contact forces have only been introduced for circular contact area from Hamilton and Mindlin analytic calculations to compare our fretting-fatigue or fretting-wear experiments with numerical solutions.

A tentative damage accumulation law was implemented in both software to predict life under sequential levels of cyclic loading on the basis of a Miner rule (linear accumulation). The critical number of cycles for one level of loading is estimated through a multiaxial approach involving stabilized residual stresses for this level. So a non linear accumulation is generated through residual stresses evolution.

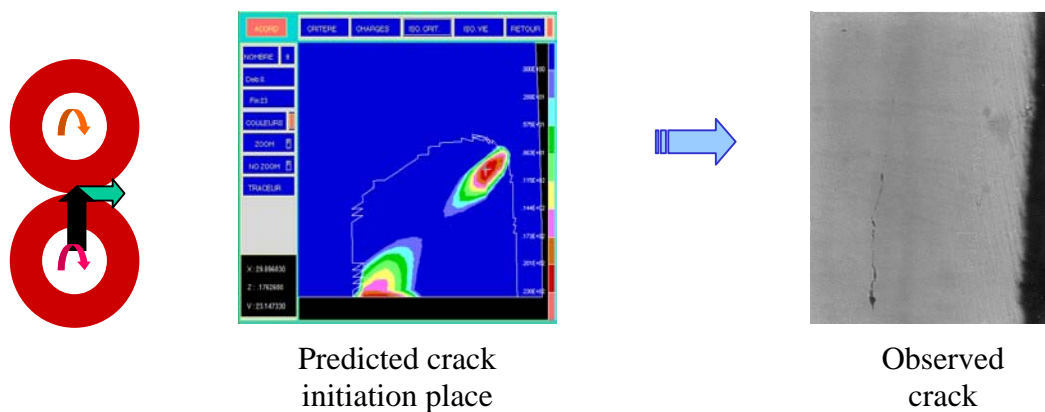


Figure 1: predicted and observed crack in a disk on disk experiment

ASSOCIATED EXPERIMENTAL DEVICES

Software prediction could only give valuable results if adequate material properties and physical phenomenon were entered in the model. Provided that High Cycle Fatigue is the main failure mechanism, elastoplastic and fatigue properties of the upper layers of the material have to be known.

Dedicated experimental devices may be used: disk on disk machine for rolling sliding contact or Vibrocryotribometer (VCTM) for fretting conditions.

Fretting occurs whenever quasi static loading is subjected to cyclic vibration. Its damage is manifested by either crack initiation (fretting fatigue) or wear (fretting wear). This phenomenon has been subject to a detailed study in the case of a Titanium alloy, Ti6Al4V,

with aerospace applications. This alloy is particularly appropriate to applications in which the ratio of mechanical resistance to density is the main criterion when seeking to lighten structures.

In service, the grooves in cryogenic turbopump shafts in Ti6Al4V can crack when undergoing fretting fatigue. In order to reduce damage caused by fretting fatigue, increasing use of coatings or treatments has been made. Experimental plastic evolution was determined by geometric measurement of inelastic print, and Resistance to fretting fatigue was determined using crack-initiation threshold.

Material parameters of the selected elastoplastic and High Cycle Fatigue behavior laws were adjusted to fit the experimental data. This hybrid method which combines experimental results (in term of crack initiation or no crack) and numerical analysis, has been applied on a titanium alloy, Ti6Al4V. A Silver P.V.D. coating (Physical Vapor Deposition) and an ionic nitriding in cryotechnical environment. This method has been validated on TiN P.V.D. and Cupper – Nickel P.V.D. coatings.

For the fretting tests, the apparatus, a Vibrocryotribometer (V.C.T.M.), has received a detailed description in Koenen's paper the V.C.T.M. applies a normal and a tangential force to the specimen thereby reproducing the fretting phenomenon on the specimen. Figure 2 shows its general principles. The contact is usually a ball-on-plane type (a spherical pin in the present case). The pin is linked to the normal load which is applied by means of a hanging weight. The track, bathed in a cryostat of liquid nitrogen, is set into motion with respect to the pin by a magnet. Oscillatory sliding motion between the track and the pin is measured by detached sensor that allows servo-positioning. Tangential loads are measured by a piezo-electric sensor.

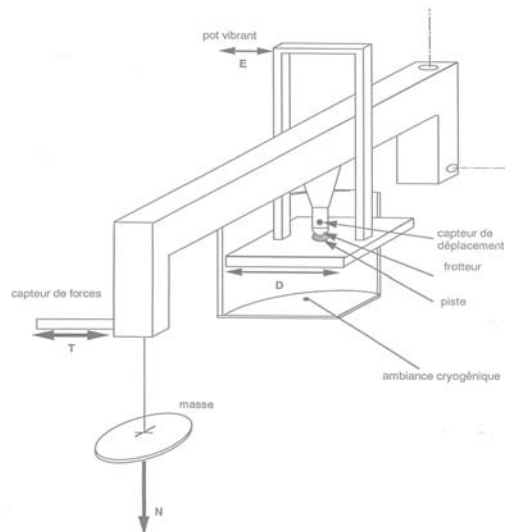


Figure 2 : V.C.T.M.

In precedent works, we find different domains in the space defined by the shear stress τ_{zx} (dependant of P and Q) versus constant normal stress P. Three zones appear , figure 3:

- 1 : sollicitation is partial slip and the damage is fatigue crack,
- 2 : sollicitation is partial slip and the damage is adhesion,
- 3: sollicitation is total slip and the damage is wear.

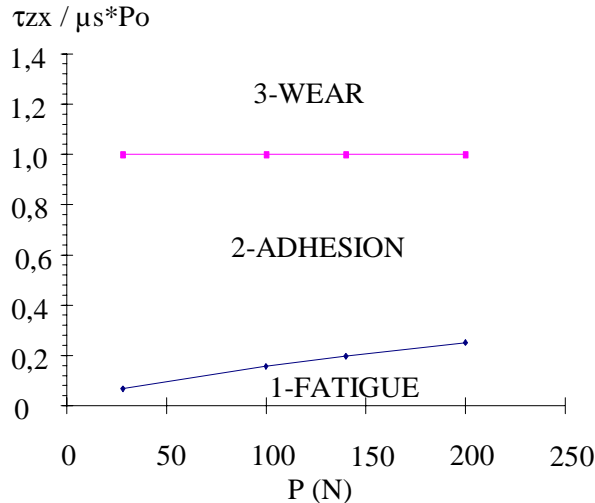


Figure 3 : damage of material versus solicitation

MATERIAL FOR COMBUSTION CHAMBERS AND NOZZLE

These parts undergo an extremely severe thermal loading. Material behavior has to be defined from LH2 temperature (20K) to ultra high temperature (1300K for nozzle and 3500K for combustion chamber). As soon as the engine is fired, strong thermal gradients occur across thin walls (less than 1mm), in a self clamped configuration. Combined complex mechanical loading due to hot gases flow inside, coolant pressure in the wall, and atmosphere or vacuum outside is superimposed. This loading give rise to viscoplastic strains, associated stresses, creep and fatigue damage.

First rate properties of heat conditions are essential. They have to be associated to high enough mechanical strength even in the high temperature range.

So, high strength copper based alloys are used for combustion chambers. Material works in hydrogen surroundings, and especially on the hot gases side, sensitivity to hydrogen embrittlement should be investigated.

A predictive calculation of the combustion chamber evolution during one run of the engine implies calculation of the fluid-structure thermomechanical coupling; successive map of temperatures are estimated from thermal properties; associated inelastic stresses and strains are then derived (giving new conditions for the thermal problem).

Material behavior law has to be defined in the whole range of temperature. Various solutions are used:

- complete integration of temperature in a global thermoelastoviscoplastic law such as defined by Walker and Freed (about 13 material constants).
- Interpolation (usually linear) between isothermal viscoplastic laws, settled for various temperatures; a proper selection of temperatures has to be done (about 10 material constants for each selected temperatures).

Damage evolution laws have to be added, such as creep damage during the hot run, law cycle fatigue, and hydrogen embrittlement if critical temperatures are detected somewhere; some more material constants have to be identified.

Thermal ratcheting of the wall submitted to temperature gradients is possibly obtained.

Quality of the prediction is strongly dependent on:

- how reliable is the calculation of the thermal exchanges, governing temperatures estimation,

- how reliable is the behavior law.

This last point depends on a good estimation of the main feature of the material behavior (inelastic behavior and damage); no key damage parameter should be neglected. Moreover, enough experimental evidence has to be used. In this case, some ten to twenty or even much more material constants have to be identified. These constants should describe thin walls behavior at various temperature. Isothermal tests on disks submitted to increasing or cyclic gas pressure (hydrogen or helium) at various temperature will give interesting data including sensitivity to hydrogen.

CONCLUSION

Significant improvements (in terms of performances, reliability and costs) may be achieved in design of rocket engines thanks to better choices of materials (chemical composition, manufacturing process, surface treatments and coatings) and progresses in components life prediction (thermo-mechanical fluid structure calculations).

Regarding materials, attention should be focused on an accurate enough description of material behavior:

- defining approximate thermal, chemical and mechanical loading conditions,
- selecting materials which can stand this loading,
- checking significant damage mechanisms: plastic or viscoplastic strains, fatigue, creep, chemical damage,... according to these loading conditions,
- select significant behavior laws and associated tests program for identification purpose.

Reliability will be achieved if adequate physical phenomena have been introduced in the model, and if enough and adequate experimental evidence has been taken into account.

ACKNOWLEDGEMENT

The authors express their thanks to CNES (French National Space Agency), and SNECMA Moteurs Fusées for years of fruitful scientific cooperation in the field of contact mechanics. They don't forget their partners of INTAS project on combustion chambers: CNES, DLR (Germany National Space Agency) and KeRC (Russian National Space Agency).

BIBLIOGRAPHY

1. G. Inglebert, T. Hassine, M. Pons, "Shakedown and damage analysis in the Ariane V program", Euromech 335 (*Inelastic analysis of Structures under variable loads*), Aachen, Allemagne, 8-11 September 1998
2. J. Riccius, V. Gantchenko, P. Jouinot, "Elastoplastic and fatigue tests of a typical combustion chamber material with different sample geometries", 4th international conference on launcher technology, Liège, Belgium, 3-6 December 2002
3. I. Caron, J.M. De Monicault, R. Gras "Influence of surface-coatings on titanium-alloy resistance to fretting fatigue in cryogenic environment", *Tribology international* 34 4 (2001) 217-223 Elsevier
4. M. Quillien, R. Gras, L. Collongeat, Th. Kachler "Rolling sliding device in harsh environment : twin disk cryotribometer", *Tribology international*, 34 4 (2001) 287-292 Elsevier
5. L. Manes, J.M. De Monicault, R. Gras "Monitoring damage by acoustic emission in bearing steels in cryogenic environment", *Tribology international*, 34 4 (2001) 247-253

6. L. Manes, J.M. De Monicault, R. Gras "Behavior of the nitrogen bearing martensitic stainless steel : XD15NW in cryotechnical environment", J. Phys. IV France 11(2001) Pr4-303-309 EDP Sciences
7. F. Robbe-Valloire - B. Paffoni - R. Progre "Prediction of the amount of load transmitted by elastic, elastoplastic or plastic deformed asperities at a rough interface", Mechanics of Materials - Vol. 33 (2001), p. 617 à 633
8. I. Caron, J.M. De Monicault, D. Ohier, G. Inglebert "Effect of silver PVD coatings on mechanical properties of a titanium alloy", Euromech Mecamat, 4th European Mechanics of Materials Conference, Metz – 26-29 juin 2000
9. L. Manes, J.M. De Monicault, R. Gras "Behaviour of the XDI5NV steel in cryogenic environment", Euromech Mecamat, 4th European Mechanics of Materials Conference, Metz – 26-29 juin 2000
10. G. Inglebert, G. Louradour, D. Le Nizerhy, M. Pons "A shakedown and life prediction software integrating initial and contact stresses", European Congress on Computational Methods in Applied Sciences and Engineering, Eccomas 2000, Barcelona, 11-14 Septembre 2000
11. I. Caron, J.M. De Monicault, R. Gras "Effect of coatings on mechanical properties and fretting fatigue strength of a titanium alloy in cryotechnical environment", 14th conf. On Surface Modification Technologies, Paris, Septembre 2000
12. Freed A. D. and Walker K. P. (1993) "Viscoplastic model development with an eye towards characterisation", in *Material Parameter Estimation for Modern Constitutive Equations*. L. A. Bertram & al editions, MD Vol : 43, and AMD Vol : 168, ASME, New York, pp. 57.
13. Koenen & al "A machine for fretting fatigue and fretting wear testing in cryotechnical and normal environment" Wear 197, 1996, pp 192-196

Materials Issues Arising from Transient and Unsteady Loads in Combustion Devices

T.N. Farris

*School of Aeronautics and Astronautics, Purdue University,
315 N. Grant St, West Lafayette, IN 47907-2023 U.S.A.*

<http://roger.ecn.purdue.edu/~farrist>

5th International Symposium on Liquid Space Propulsion



Rocket Engine Advancement Program 2 (REAP2)



Overview

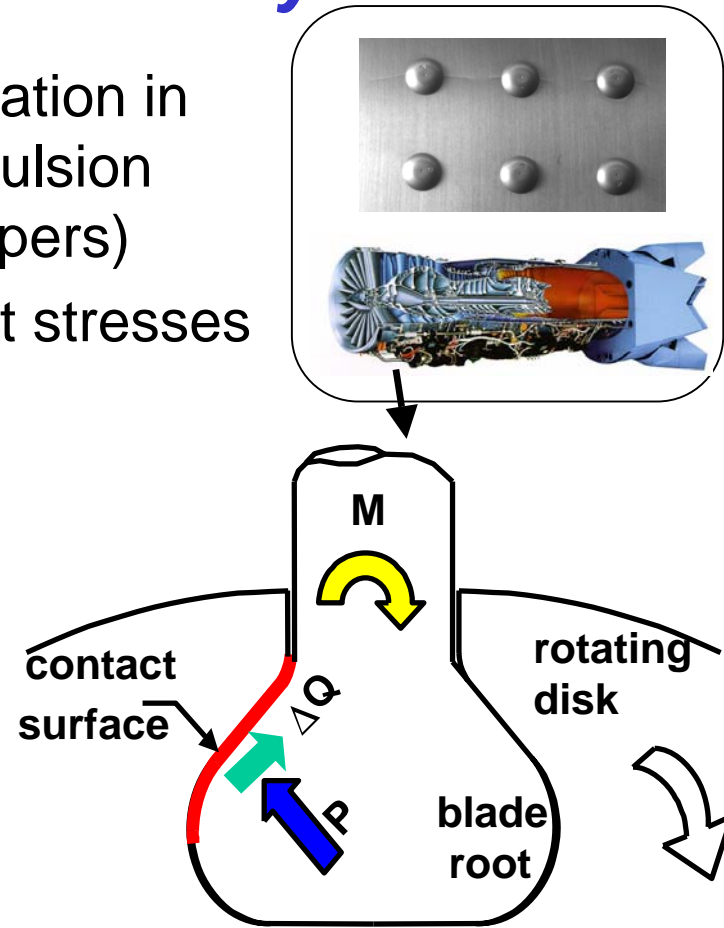
- Fretting fatigue is used as an example of failure arising from unsteady loads
- Topics
 - Successful prediction of fretting fatigue lives at room temperature
 - Elevated temperature experiments
 - Overview of experimental results
 - Fractography
 - Analysis of the experiments
 - Conclusions and future work

Fretting Fatigue

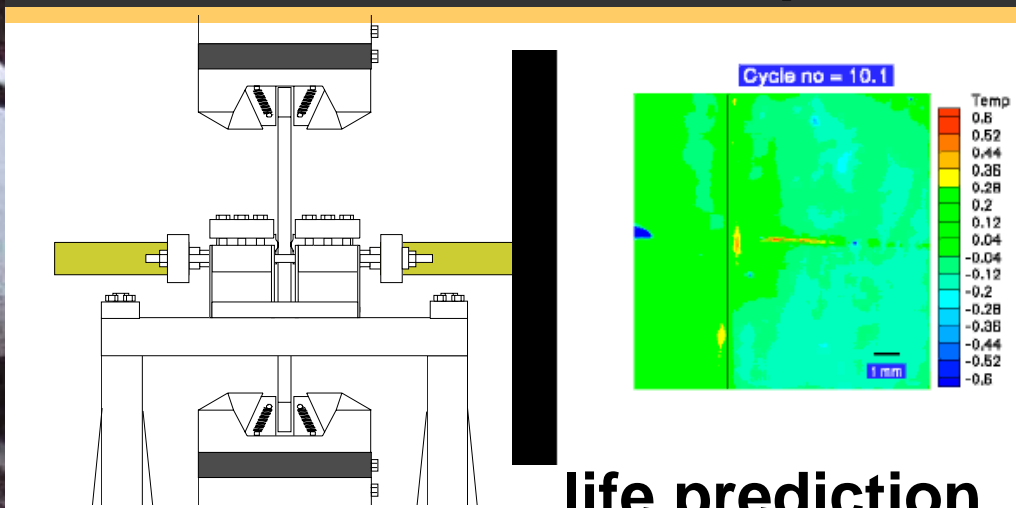
- ***Fretting is caused when two bodies nominally clamped together undergo oscillatory loads***
- Fretting is a prime cause of crack nucleation in riveted assemblies (lap joints) and propulsion components (dovetail joints, blade dampers)
- Fretting is characterized by high contact stresses and micro-slip at the contact interface

Tool for fretting fatigue prediction

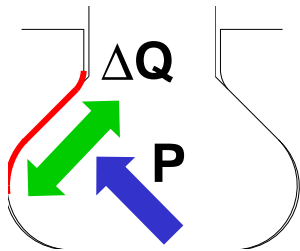
- Model contact conditions: Temperature, Tribology, Loads
- Fretting fatigue experiments
- Evaluate structural integrity using design-based metrics



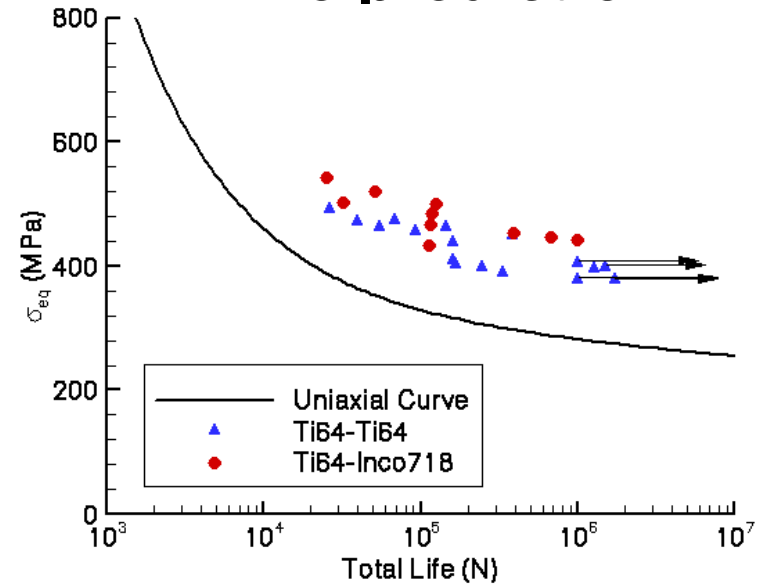
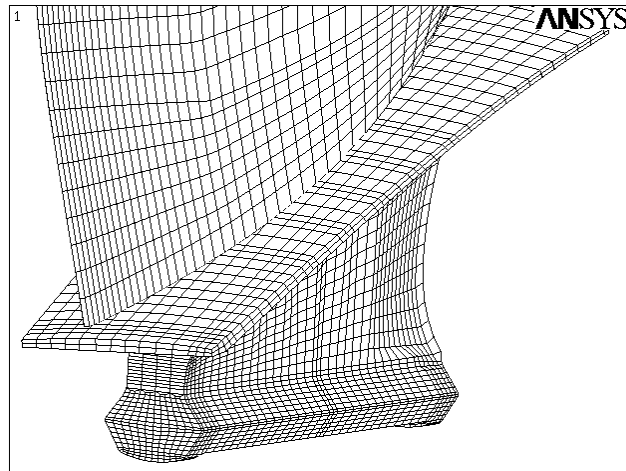
Overview of Approach well-characterized experiments



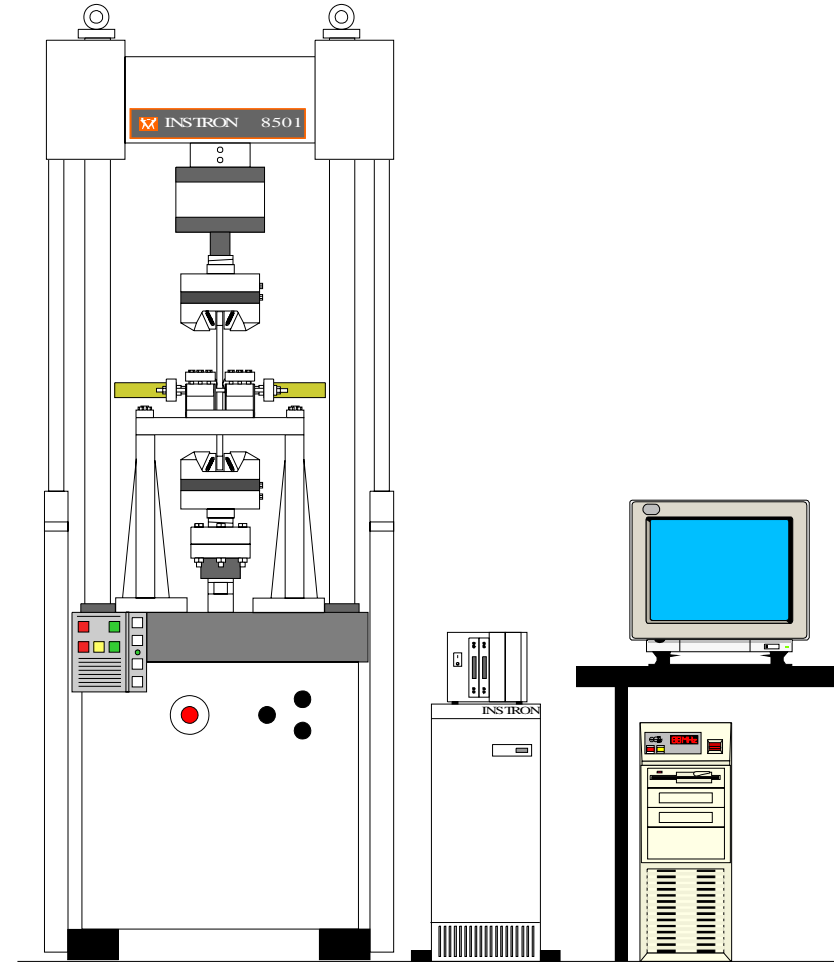
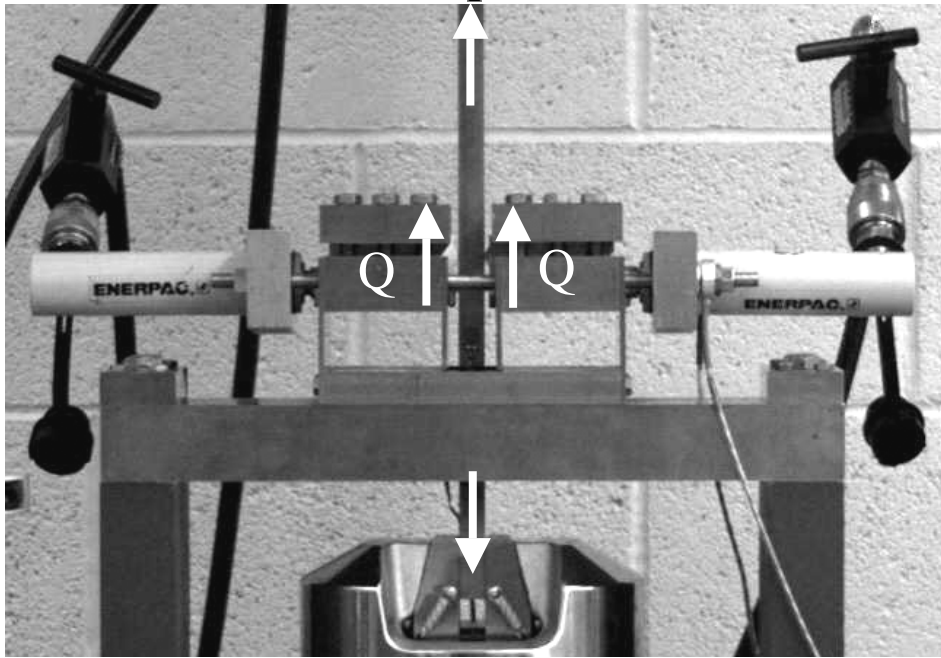
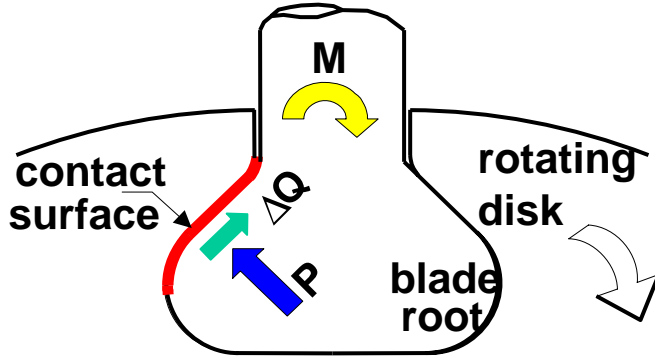
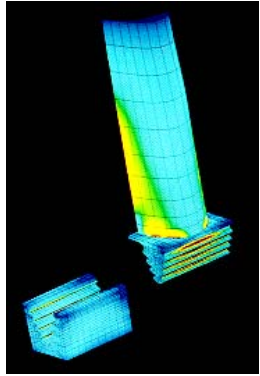
life prediction



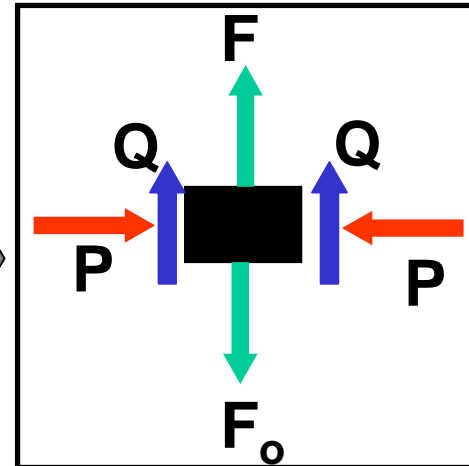
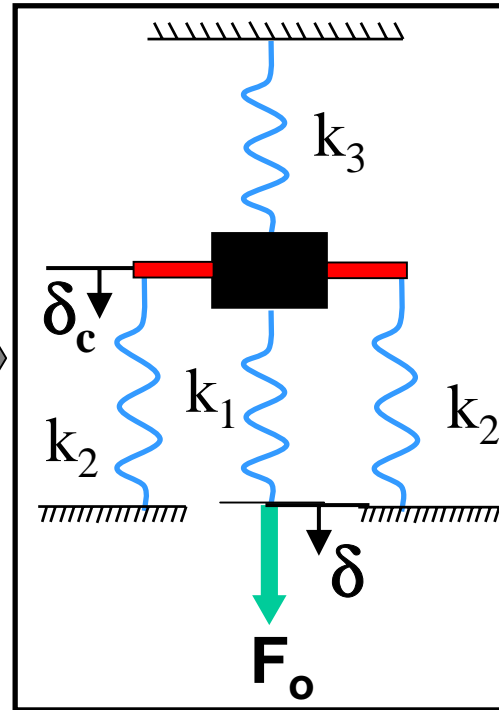
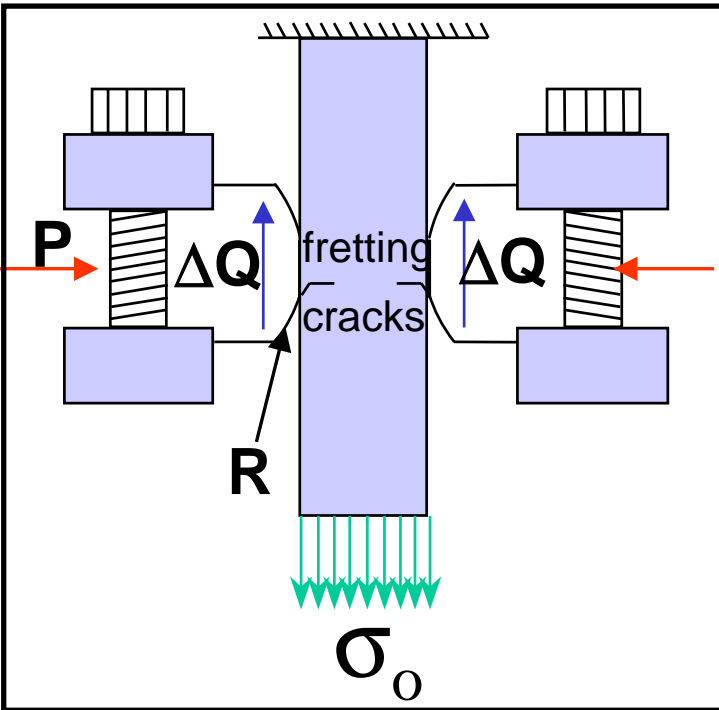
Global and
local model
of contact



LabView based DAQ



Mechanics of the Rig



A_s = cross-sectional area of specimen
 A_d = cross-sectional area of diaphragm
 E_s = Young's modulus of specimen
 E_d = Young's modulus of diaphragm
 l_1 = length of specimen below contact
 l_3 = length of specimen above contact

$$k_1 = A_s E_s / l_1$$

$$k_3 = A_s E_s / l_3$$

$$k_2 = A_d E_d / l_d$$

$$F_o = k_1 (\delta - \delta_c)$$

$$F = k_3 \delta_c$$

$$Q = k_2 \delta_c$$

$$Q = \frac{F_o}{2 + (k_3 / k_2)}$$

$$Q = \frac{F_o}{2 + (k_3 / k_2)}$$

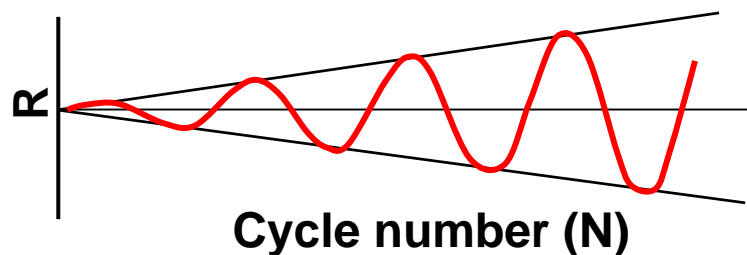
Q/P can be decreased by increasing $k_3 \Rightarrow$ decreasing l_3

Evolution of Coefficient of Friction for Titanium

Run fretting test for a predetermined number of cycles using cylindrical pads

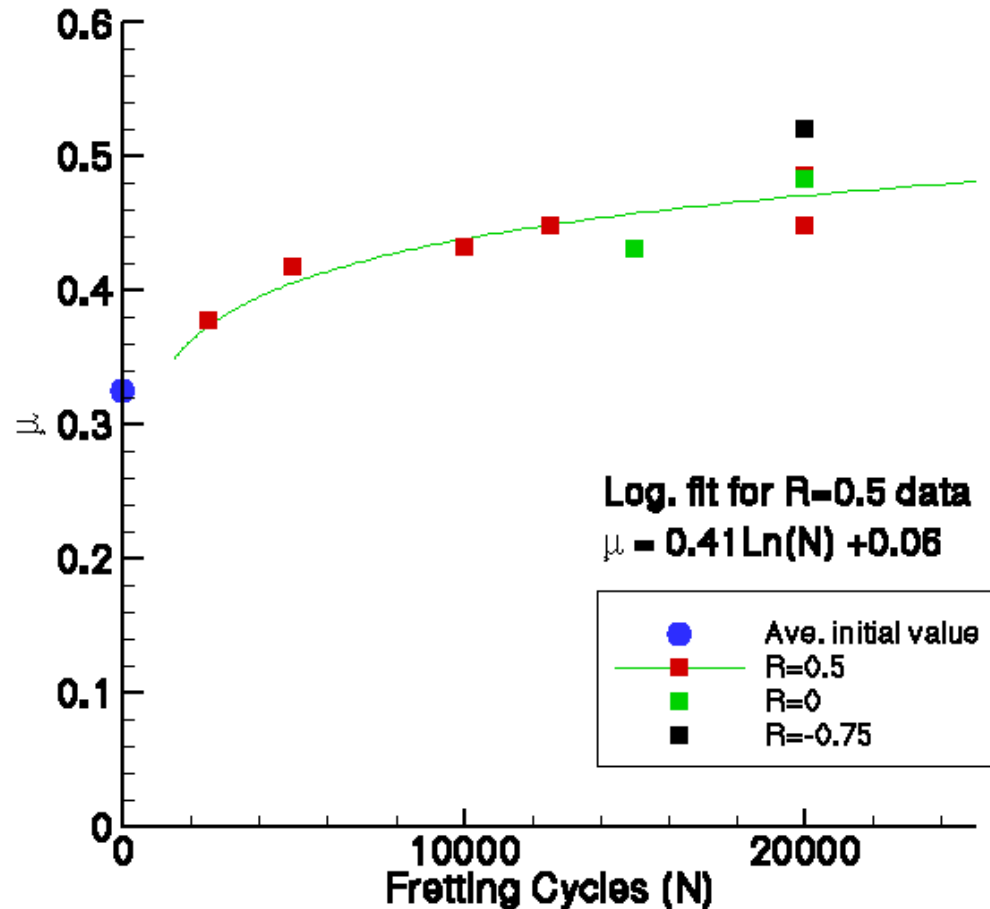


Leaving contact intact run increasing amplitude waveform R(N) to force sliding

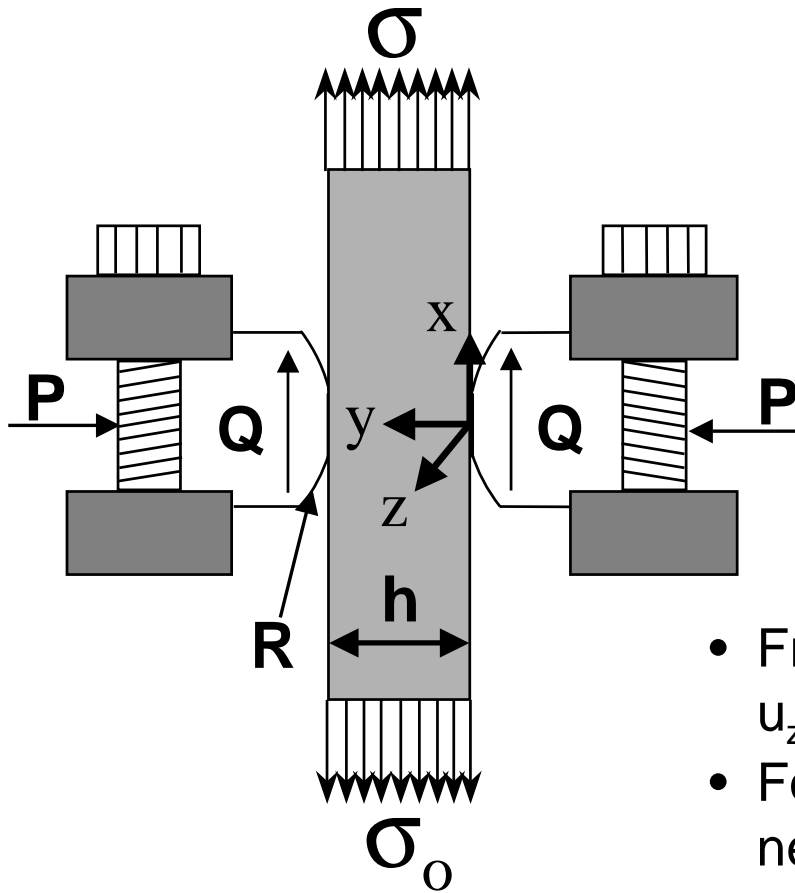


On onset of slip determine

$$\mu_{ave} = Q/P$$

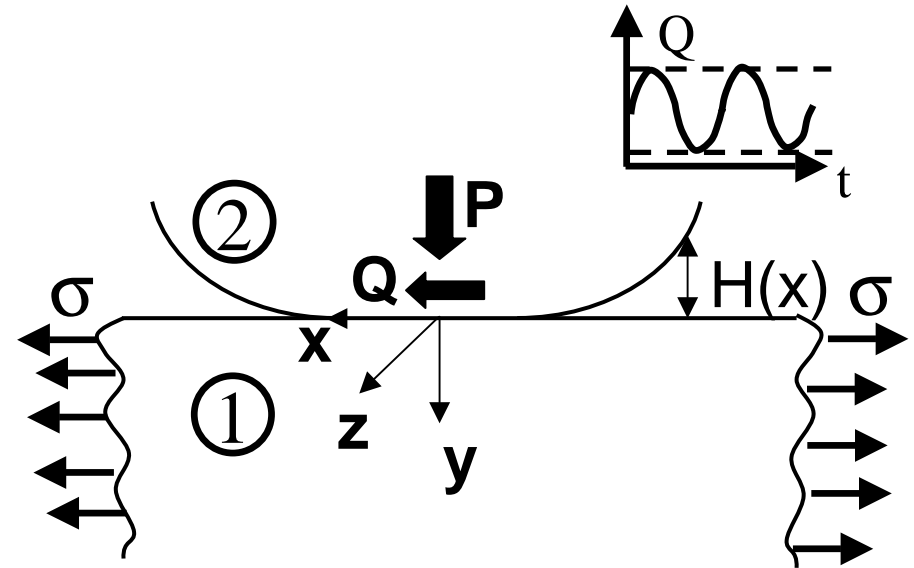


Analysis of Fretting Tests



$$2Q = h (\sigma_0 - \sigma)$$

$$h = 0.60 \text{ in}$$

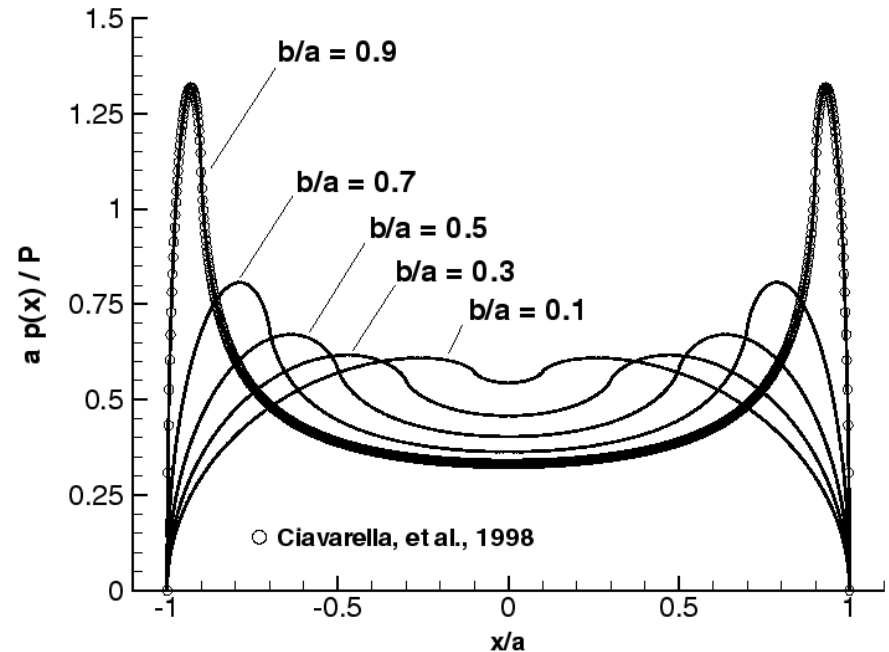
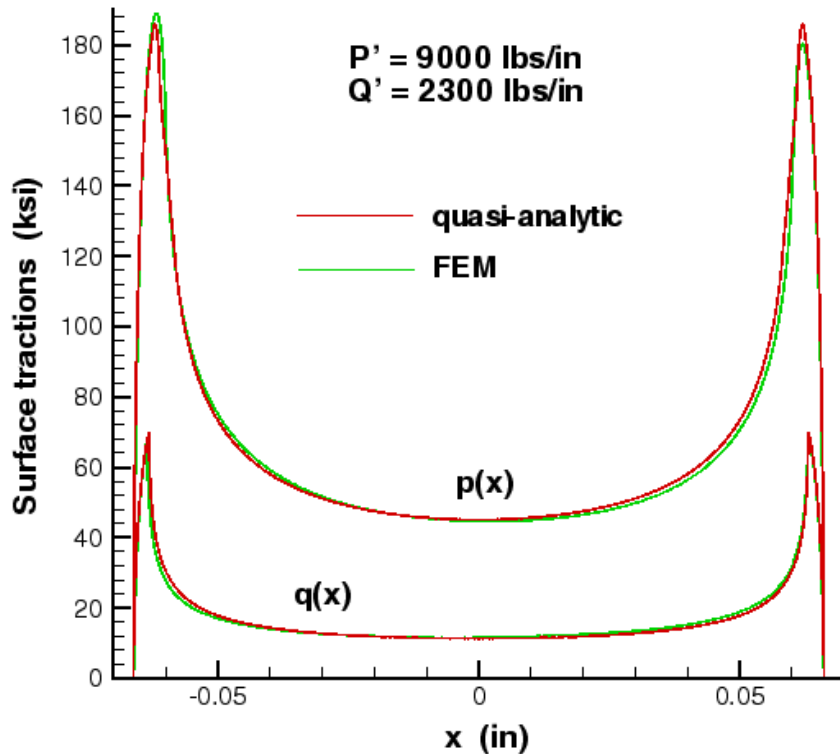


- Fretting contact is modeled as 2D, i.e., u_x , u_y , u_z only depend on x and y .
- For anisotropic materials $u_z(x,y)$ is not necessarily zero \Rightarrow out of plane relative slip \Rightarrow out of plane shear traction.
- The specimen is modeled as a half-space subject to remote stress.

Validation of Formulation

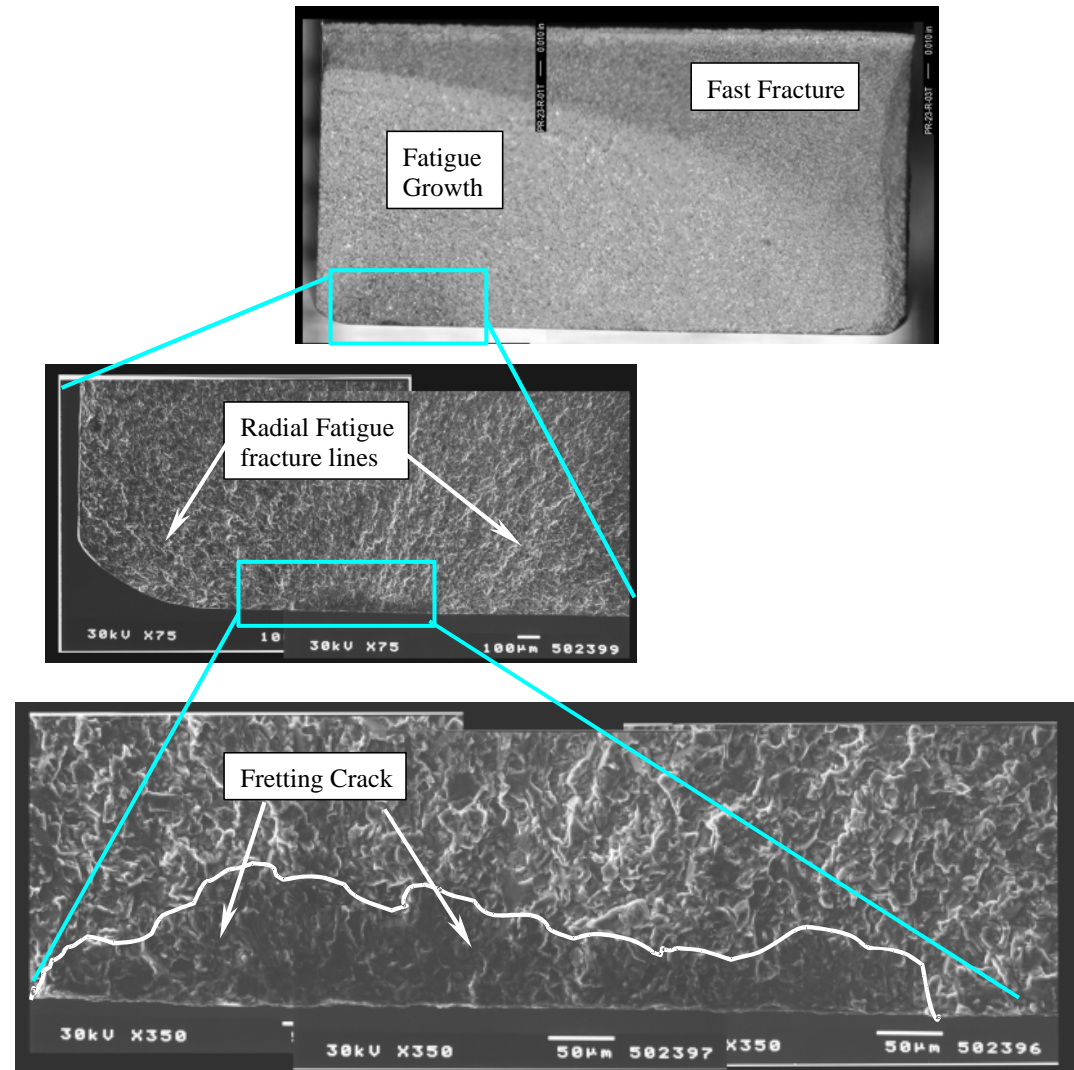
- Comparison of tractions obtained from integral equations with results from other methods for a flat with edge radius

b = flat length
 $a = b + r$ (r = radius)

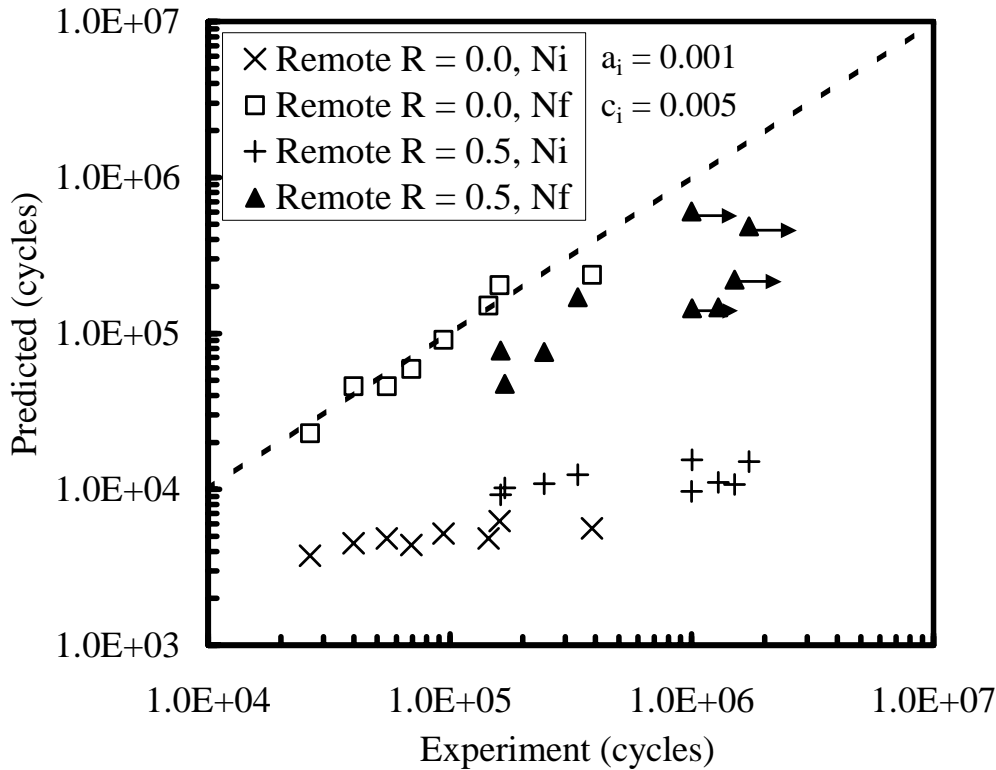


Fractography of Contact Pads for Titanium

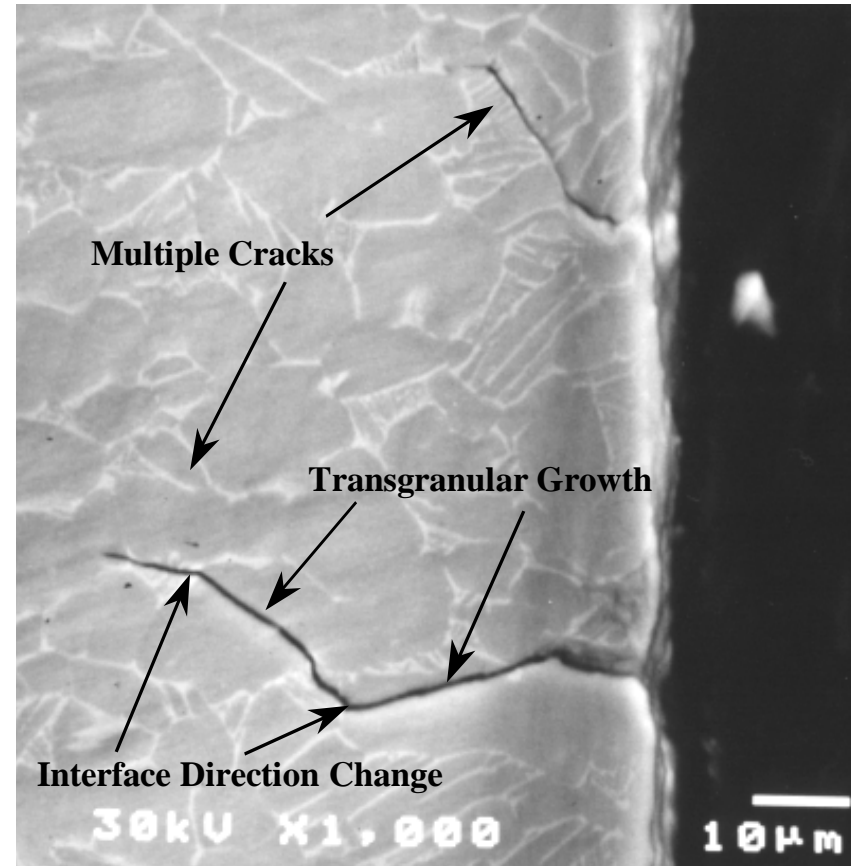
- Use fatigue fracture surface indicators to deduce fretting cracks
- Fracture lines emanate from fatigue initiation zone
- Photographs indicate location and method for finding fretting cracks in Ti-6Al-4V



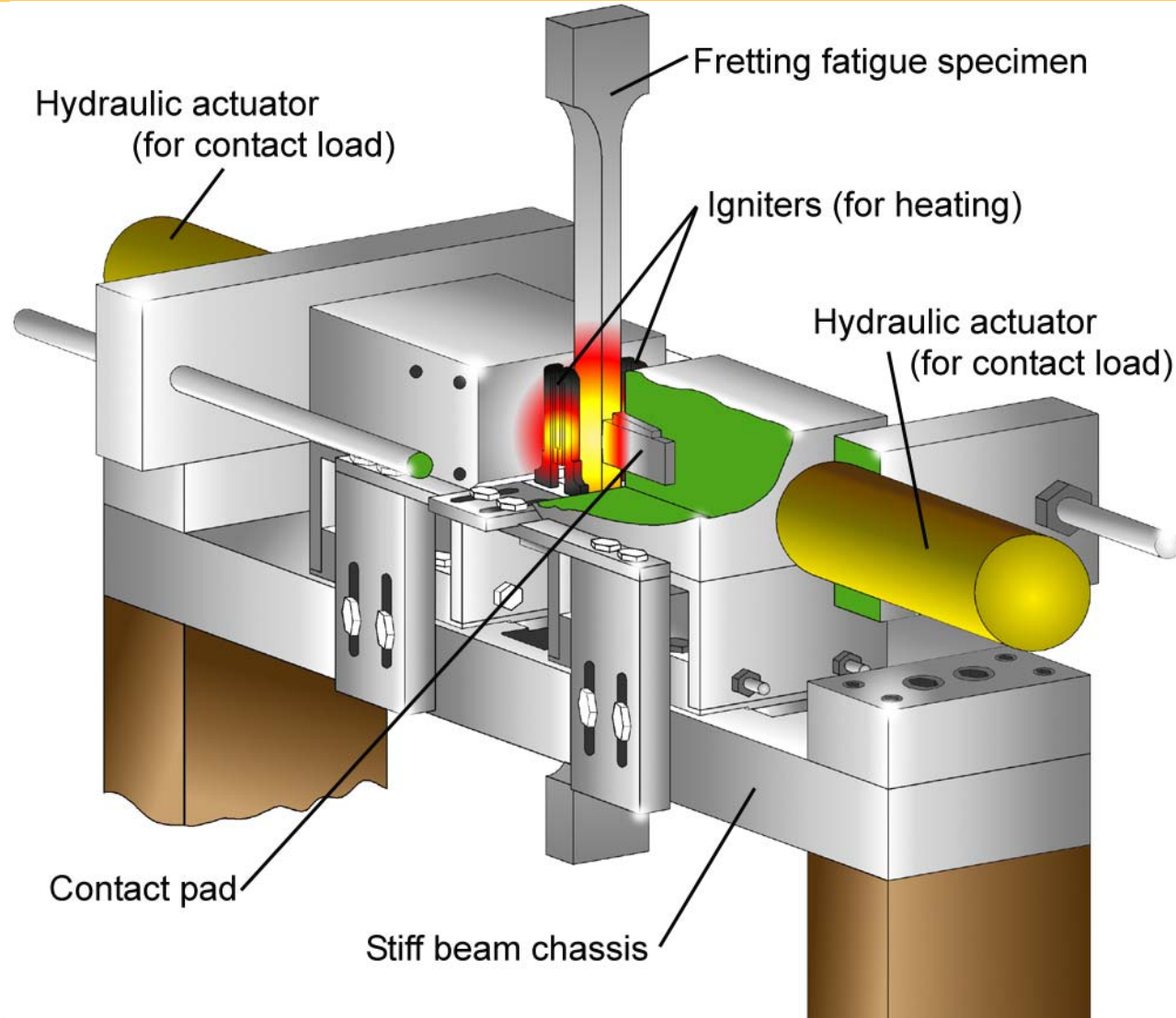
Successful Total Life Prediction



Golden and Grandt, 2002

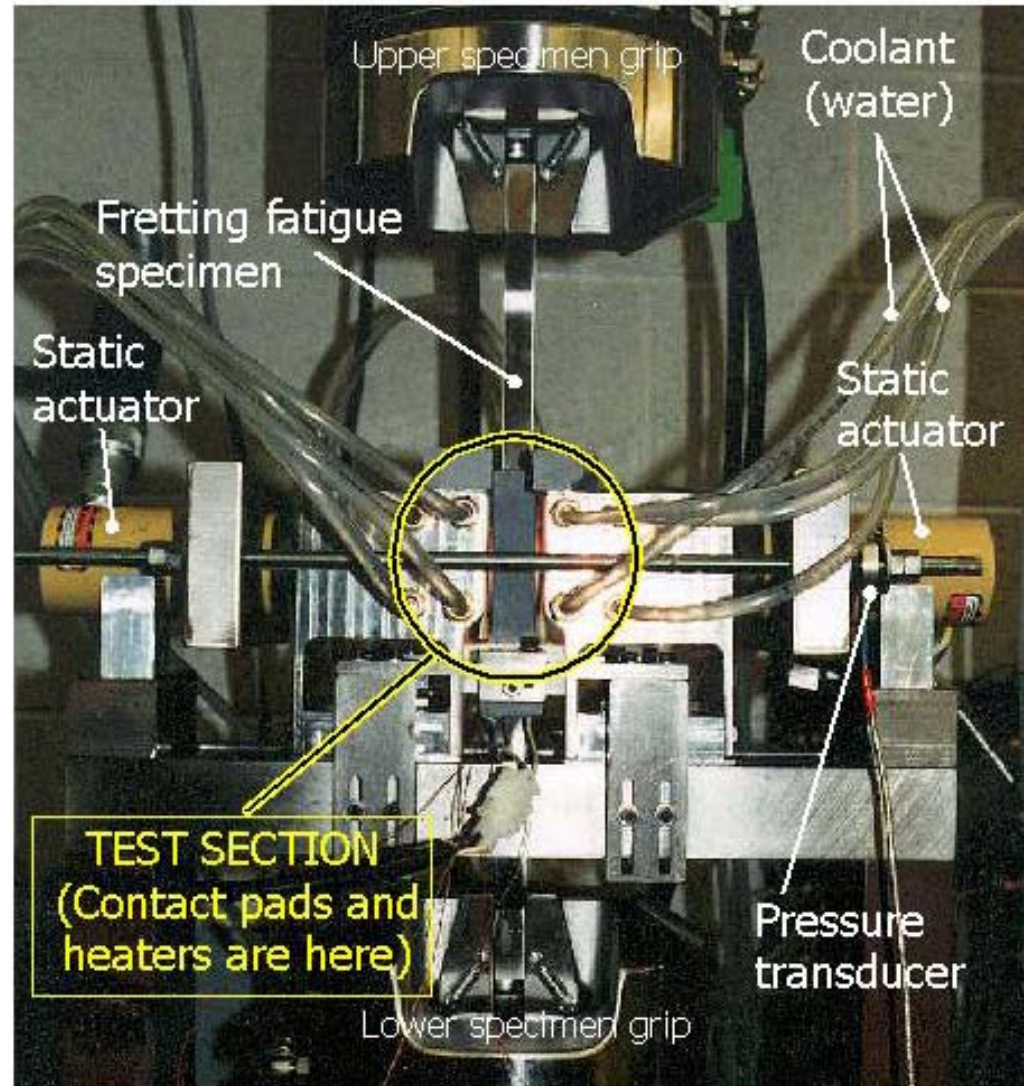


High Temperature Rig Schematic

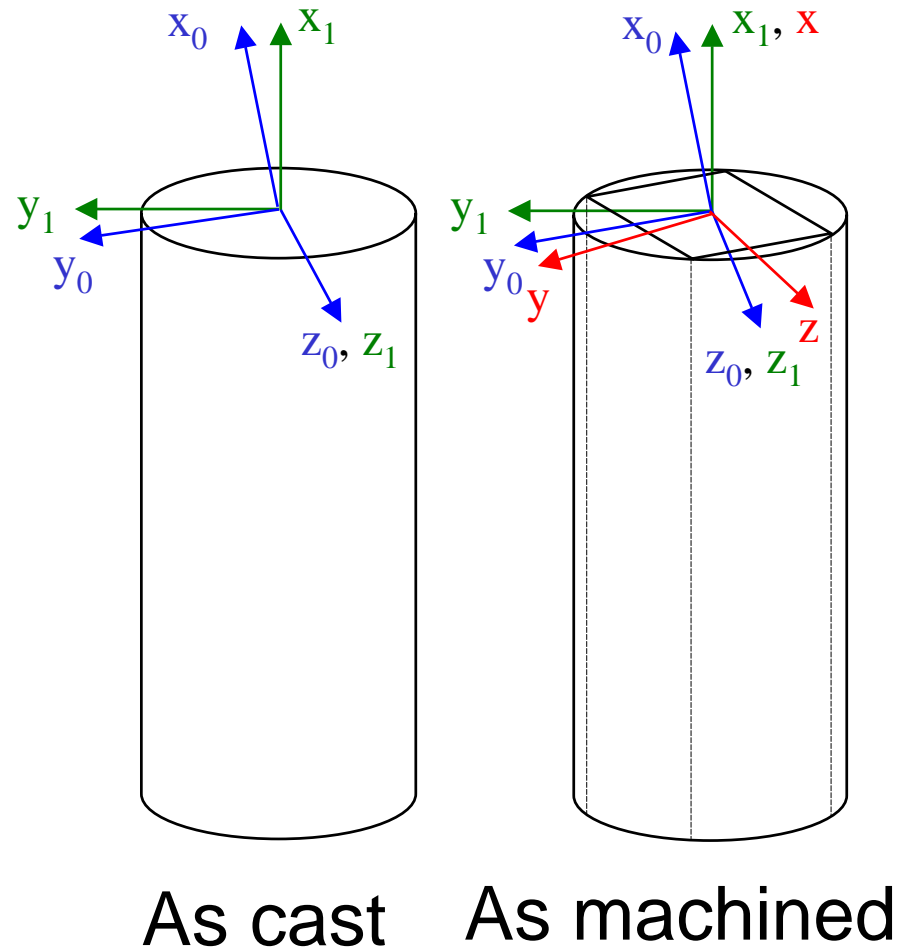


Rig for High Temperature Testing

- Load transfer based on a principle similar to that of standard fretting rig
- Igniters used for heating the specimen and the pads, locally, to high temperature
- Temperature controller unit designed using the output of thermocouple as input signal
- Ceramic shields to prevent loss of heat
- Water used to cool the chassis and the wedges that grip the specimen



SCN Specimens for FF Tests



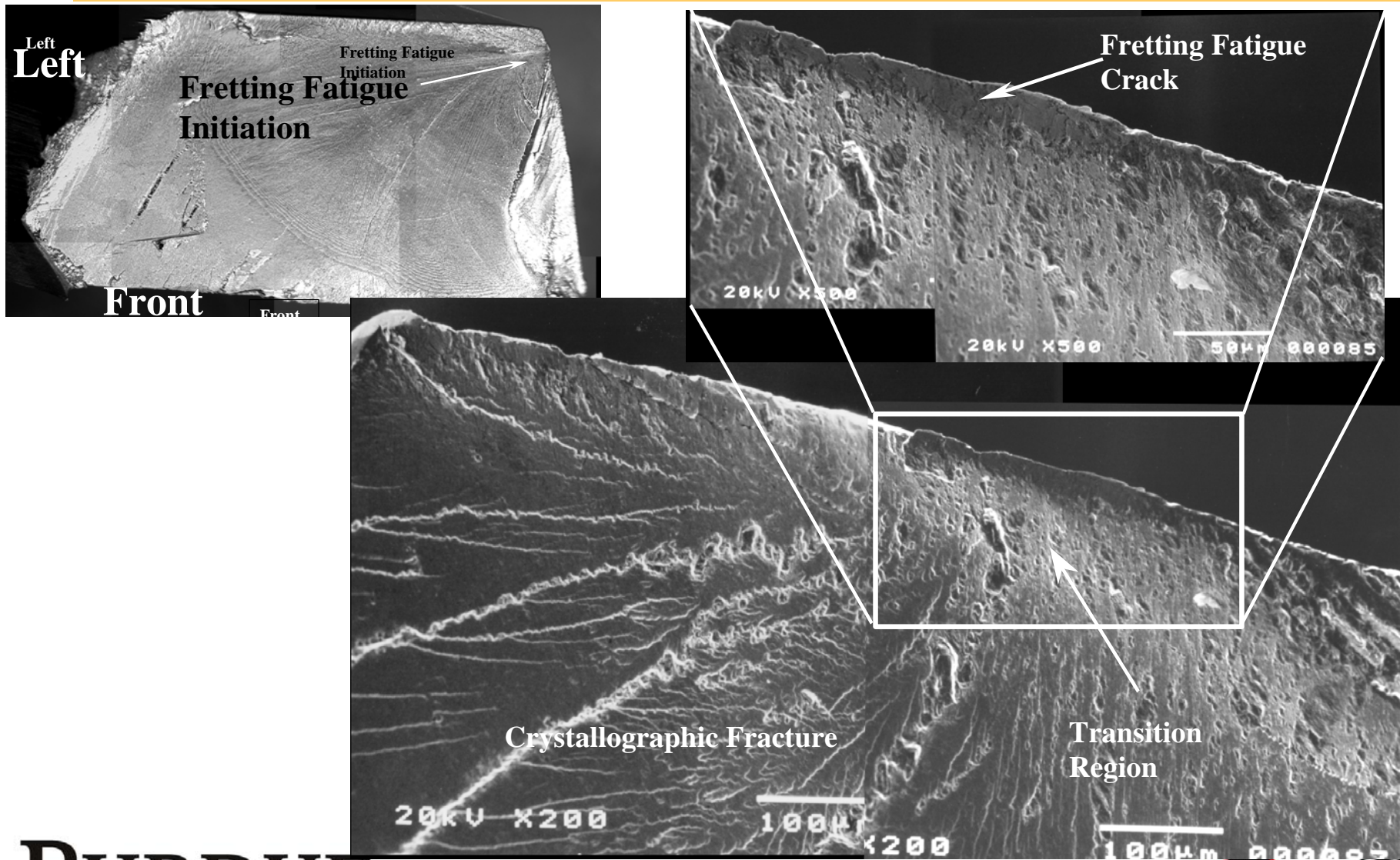
- The primary principal axis (x_0) is possibly tilted from the cylinder axis (x_1) by a small angle ($< 10^\circ$).
- A rectangular cross section (0.6in x 0.38in) oriented at an **arbitrary** angle about the x_1 -axis was machined.
- Tabs made from WASP alloy were inertia welded to the ends to produce a “dog-bone” FF specimen.
- The nominally flat fretting pads were made from IN100.

Experimental Results

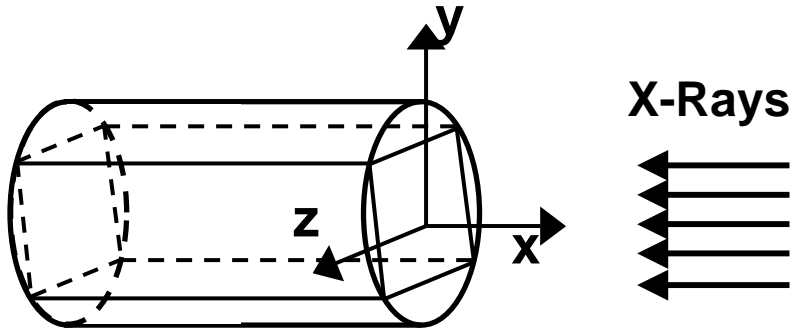
Expt. No.	Controllable Loads			Measured loads				Total Life (Cycles)
	P (lb/in)	σ^t_{max} (ksi)	σ^t_{min} (ksi)	σ^b_{max} (ksi)	σ^b_{min} (ksi)	Q _{max} (lb/in)	Q _{min} (lb/in)	
HTFF01	10695	30.7	7.5	46.9	0.6	4871	-2084	415,000 ^s
HTFF02	10575	58.0	7.7	64.1	2.0	1799	-1696	944,495
HTFF03	12522	42.1	11.3	51.9	3.3	2964	-2410	2,000,000 ^r
HTFF04	19100	58.2	12.9	77.3	2.1	5733	-3249	174,973
HTFF05	19380	59.0	12.2	72.8	0.1	4128	-3620	169,815
HTFF06	19592	48.9	10.3	64.5	-0.1	4688	-3101	61,900
HTFF07	19791	53.5	14.5	64.0	0.3	3141	-4260	491,292
HTFF08	20892	52.7	8.7	69.1	0.1	4929	-2577	18,810
HTFF09	19262	45.3	8.4	68.0	4.6	6804	-1155	16,044
HTFF10	19619	39.2	2.2	65.3	2.4	7837	87	21,800
HTFF11	19234	15.6	-9.0	43.8	0.1	8454	2704	45,496
HTFF12	19675	24.7	0.3	45.1	1.6	6116	391	49,306
HTFF13	15583	27.9	2.7	45.3	1.2	5209	-438	779,232
HTFF14	14171	41.6	2.9	69.6	1.5	8396	-421	37,528
HTFF15	15297	27.2	1.8	45.1	0.9	5369	-276	29,616
HTFF16	15079	41.9	3.7	67.0	1.1	7509	-801	4,438
HTFF17	15305	25.9	0.5	45.4	1.6	5859	334	148,384
HTFF18	18624	17.8	-1.6	35.5	1.7	5314	989	1,000,000 ^r

(^s Stopped due to problem with data acquisition, ^r Runout, ^t top load cell, ^b bottom load cell)

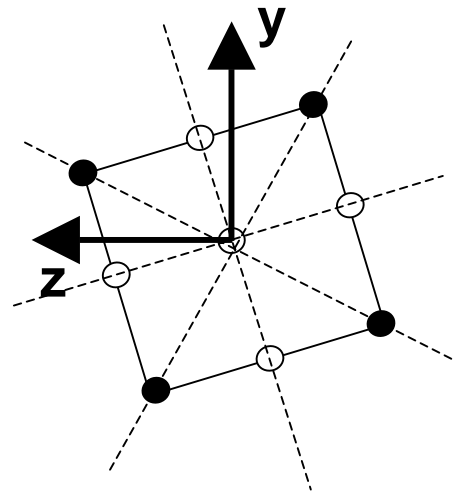
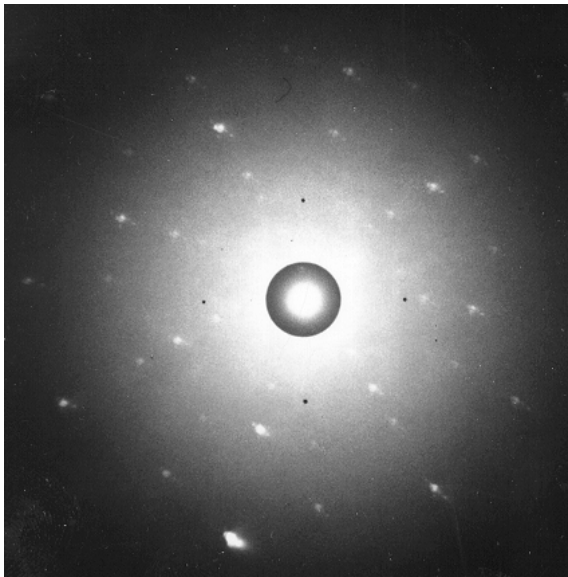
Fractography



Laue Diffraction Method

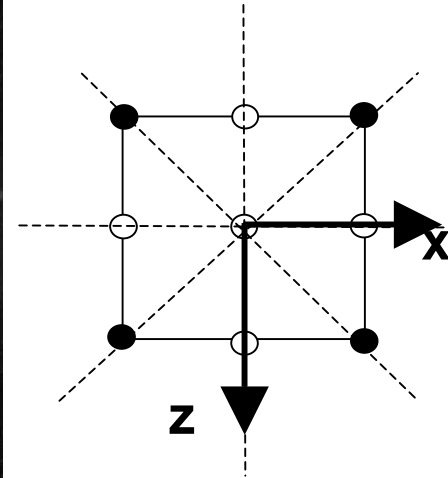
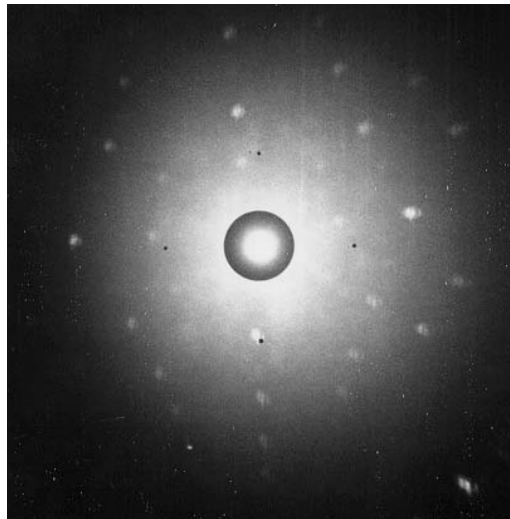
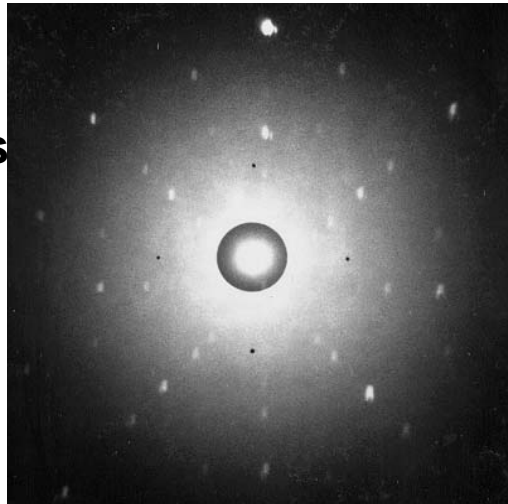
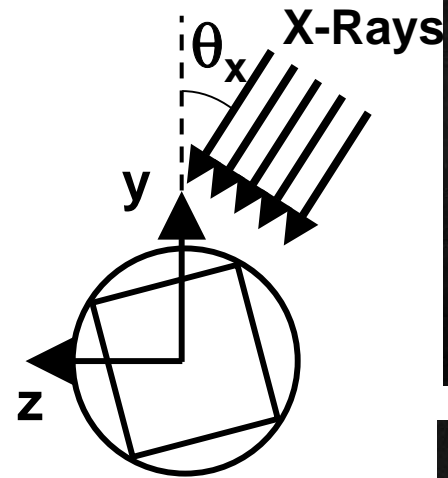


[1 0 0] is x-axis



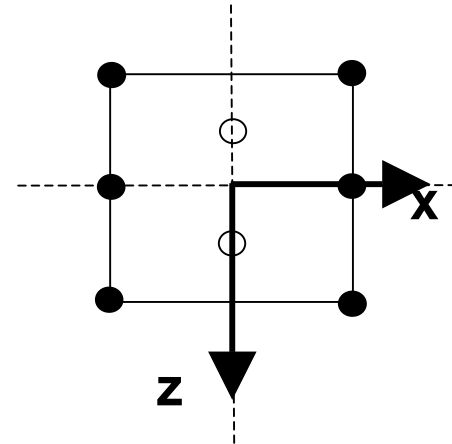
- Understanding material axis orientation is required for accurate stress calculation
- Manufacturer specified primary material axis $\langle 100 \rangle$ was oriented along the length of the specimen
- X-rays were oriented along the length of the specimen to identify potential secondary and tertiary axis orientations
- Laue diffraction results show four symmetric planes inherent to FCC crystal structure

Secondary Axis Determination



Case 1:
4 symmetry planes

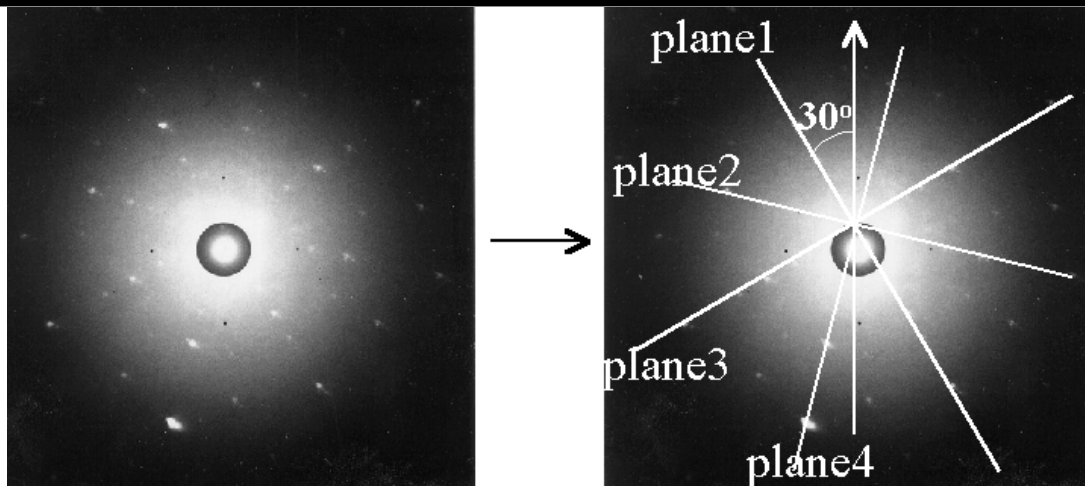
$$\theta_x = \theta_{x_0}$$



Case 2:
2 symmetry planes

$$\theta_x = \theta_{x_0} + 45^\circ$$

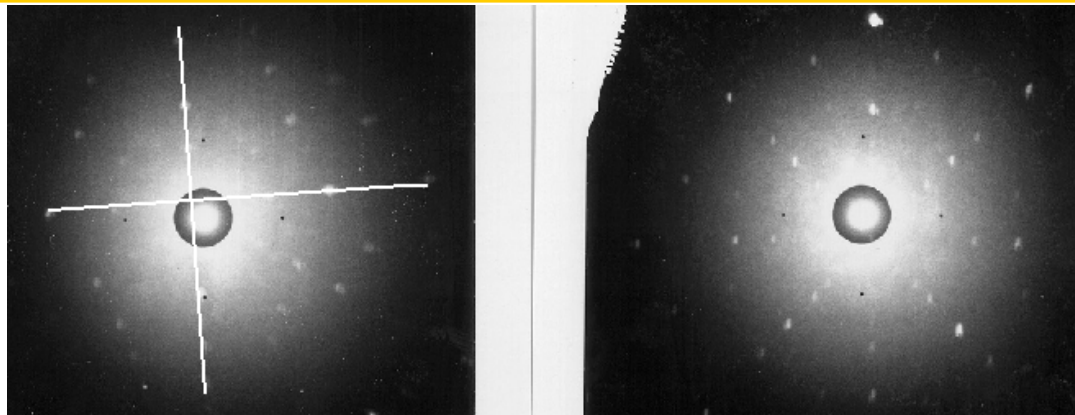
Determination of Secondary Axis



(a) Pattern along $\langle 1\ 0\ 0 \rangle$

Laue Pattern of ZOKKA

- Pattern along $\langle 1\ 0\ 0 \rangle$
- Two sets of mutually perpendicular symmetry planes can be observed
- One set corresponds to the secondary axis and the other set is at 45° to secondary axis



(b) $\theta = 30^\circ$

(c) $\theta = -15^\circ$

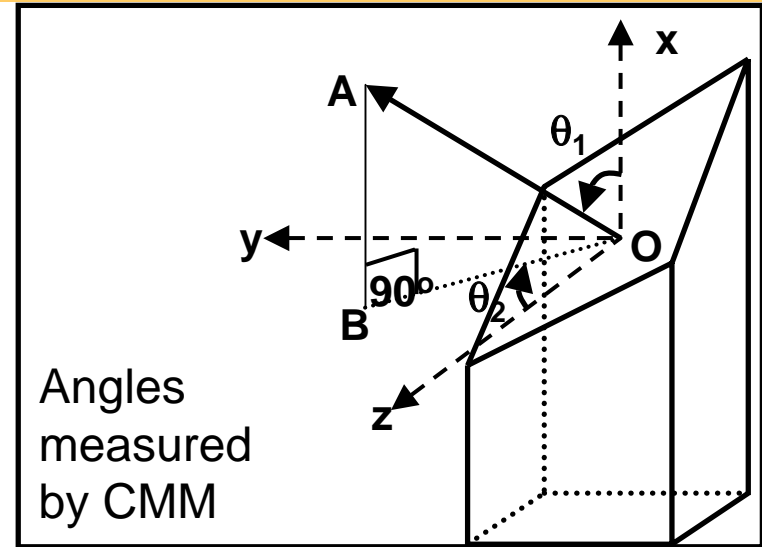
- (b) Laue pattern along $\langle 0\ 1\ 1 \rangle$. Only one set of mutually perpendicular symmetry planes

- (c) Laue pattern along $\langle 0\ 1\ 0 \rangle$. Two sets of mutually perpendicular symmetry planes

Fractography



Fracture was observed to occur along $\langle 1\ 1\ 1 \rangle$ plane in all cases

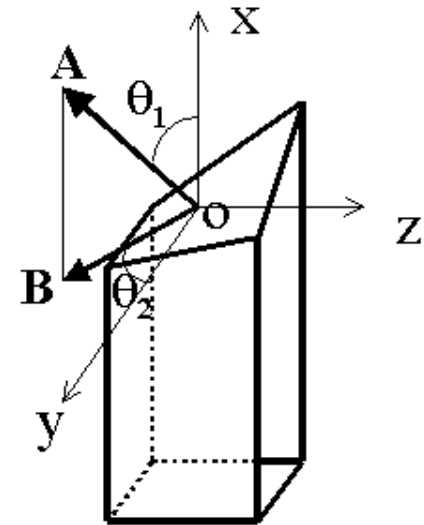


Expt. No.	Specimen	Laue Pattern		Angles from CMM			
		Primary axis	Secondary axis	Plane 1		Plane 2	
		θ_z	θ_x	θ_1	θ_2	θ_1	θ_2
2	ZOKLE	2.8	15	52	28		
4	ZOKJW	6.3	-14	50	58		
5	ZOKKE	2.4	45	54	90	51	2
6	ZOKKD	1.9	-40	56	85	56	-7
7	ZOKKA	3.2	-15	57	60.5		
8	ZOKFR	1.1	23	52	24		

Material and Fracture Orientations

Expt. No.	Specimen	Laue Pattern		Angles from CMM			
		Primary axis	Secondary axis	Plane1		Plane2	
		θ_z	θ_x	θ_1	θ_2	θ_1	θ_2
2	zokle	2.8	15	52	28		
4	zokjw	6.3	-14	50	58		
5	zokke	2.4	45	54	90	51	2
6	zokkd	1.9	-40	56	85	56	-7
7	zokka	3.2	-15	57	60.5		
8	zokfr	1.1	23	52	24		

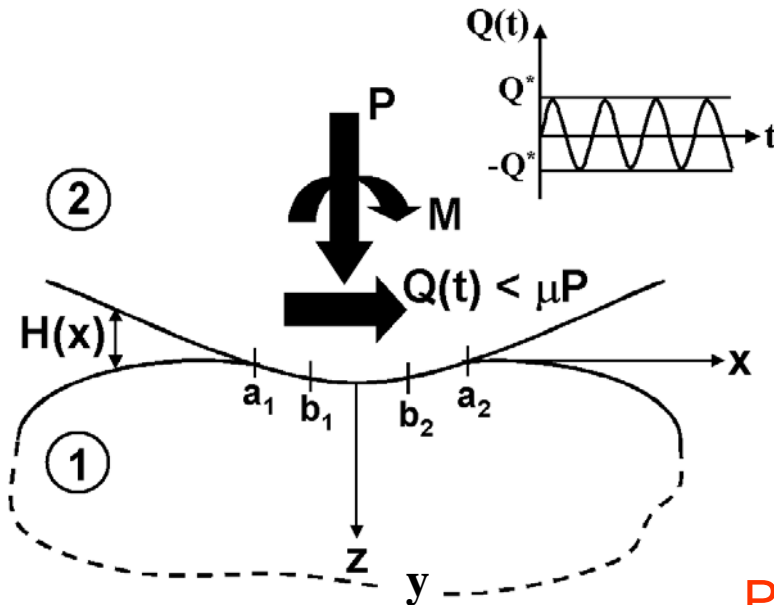
Fracture plane was along [1 1 1]
Transition from fretting crack to macroscopic crystallographic fracture is monoplanar transprecipitate noncrystallographic (TPNC)
2 mutually perpendicular fractures when secondary orientations $\sim 45^\circ$



Contact of Dissimilar Materials

Contact pressure and shear traction are related to the slip and gap functions by means of a pair of coupled singular integral equations (SIEs) as,

$$\frac{\partial}{\partial x} \begin{Bmatrix} s(x) \\ H(x) \end{Bmatrix} = \begin{bmatrix} \alpha_{11} & \alpha_{12} \\ \alpha_{21} & \alpha_{22} \end{bmatrix} \begin{Bmatrix} q(x) \\ p(x) \end{Bmatrix} + \begin{bmatrix} \beta_{11} & \beta_{12} \\ \beta_{21} & \beta_{22} \end{bmatrix} \int_{a_1}^{a_2} \begin{Bmatrix} q_x(t) \\ p(t) \end{Bmatrix} \frac{dt}{t-x}$$



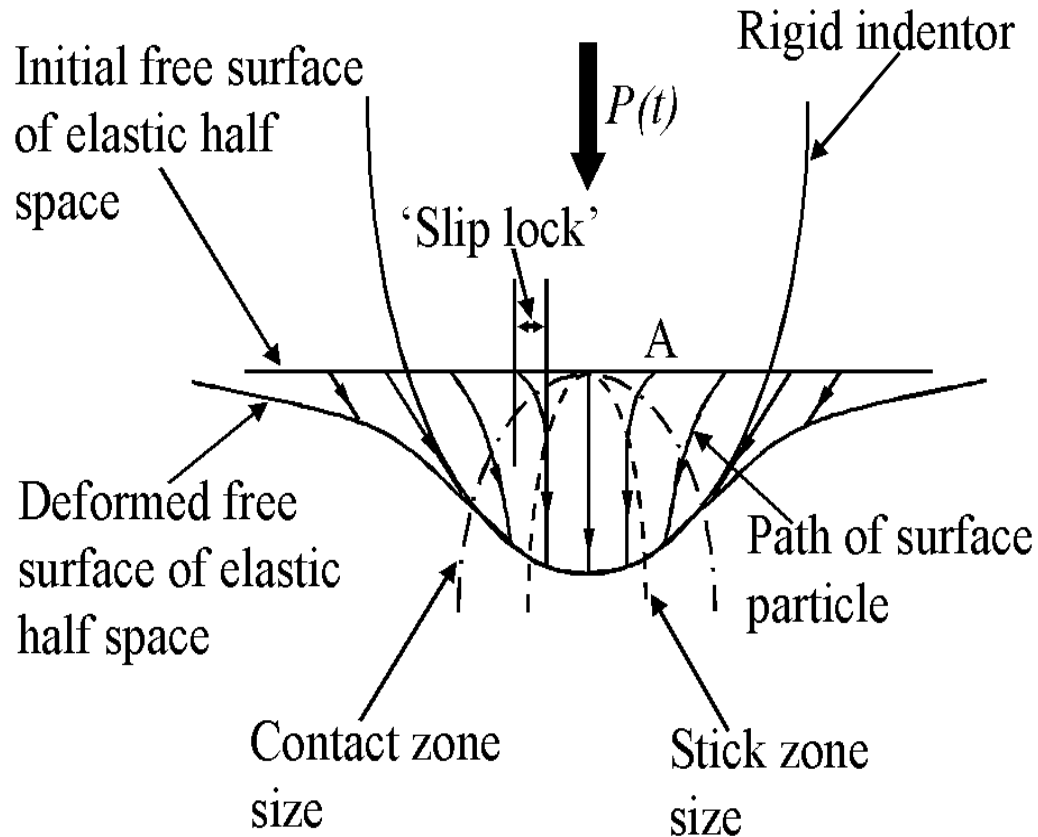
Dissimilar isotropic case:

$$\alpha_{12} = -\alpha_{21} = -\frac{(1-2\nu_2)(1+\nu_2)}{E_2} + \frac{(1-2\nu_1)(1+\nu_1)}{E_1}$$

$$\beta_{11} = \beta_{22} = -\frac{2(1-\nu_2^2)}{E_2} - \frac{2(1-\nu_1^2)}{E_1}$$

P.T. Rajeev and T.N. Farris, *JSA*, 2002

Slip Function



- Relative slip at a given loading stage cannot be known beforehand
- As the stick zone grows $s(x)$ in the surrounding slip zone gets 'locked in'
- Contact problem has to be solved incrementally
- $s(x)$ is known only over the stick zone

2D Fretting Contact Model for SCN

- Incorporating stick/slip behavior in the out-of-plane direction would mean solving **three coupled** SIEs to obtain $p(x)$, $q_x(x)$, $q_z(x)$.
- Problem can be simplified by assuming that the frictional traction acts only to resist motion in the x-direction, i.e., $\mu_x = \mu$ & $\mu_z = 0$.
- Since $q_z(x) \equiv 0$, the number of coupled SIEs is reduced to two.
- Effect of the remote stress on the relative slip function and hence the contact tractions can be included as,

$$s(x) = s_c(x) - \frac{(1 - \nu_{zx}\nu_{xz})}{E_x} \sigma_0 x$$

where $s_c(x)$ is the relative slip due to the contact tractions alone and σ_0 is the applied remote stress.

Single Crystal Nickel (SCN)

- SCN is a tri-axially symmetric orthotropic material used in high temperature applications. Its material properties along the principal material axes at 1150°F are

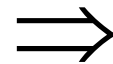
$$E_x = E_y = E_z = 15.4 \text{ Msi}$$

$$G_{xy} = G_{yz} = G_{zx} = 15.7 \text{ Msi}$$

$$\nu_{xy} = \nu_{yz} = \nu_{zx} = 0.4$$

- It can be shown that (Lekhnitskii, 1981), for an orthotropic material, if the z-axis is one of the material principal axes then the stress-strain relationship is of the following form,

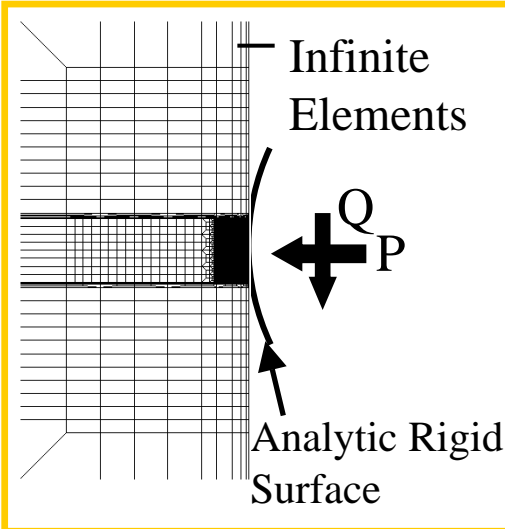
$$\begin{Bmatrix} \sigma_{xx} \\ \sigma_{yy} \\ \sigma_{zz} \\ \sigma_{yz} \\ \sigma_{zx} \\ \sigma_{xy} \end{Bmatrix} = [C] \{ \varepsilon \} = \begin{bmatrix} * & * & * & 0 & 0 & * \\ * & * & * & 0 & 0 & * \\ * & * & * & 0 & 0 & * \\ 0 & 0 & 0 & * & * & 0 \\ 0 & 0 & 0 & * & * & 0 \\ * & * & * & 0 & 0 & * \end{bmatrix} \begin{Bmatrix} \varepsilon_{xx} \\ \varepsilon_{yy} \\ \varepsilon_{zz} \\ \varepsilon_{yz} \\ \varepsilon_{zx} \\ \varepsilon_{xy} \end{Bmatrix}$$



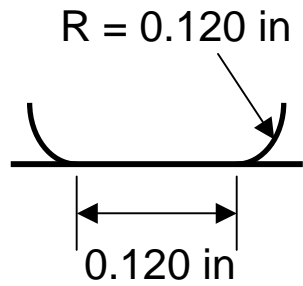
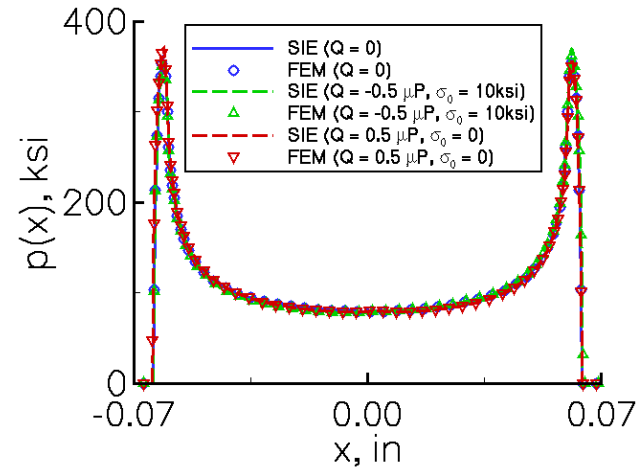
In-plane loads and out-of-plane displacements are decoupled

$$\therefore q_z(x) \equiv 0$$

Verification of SIE (Dissimilar Aniso.)

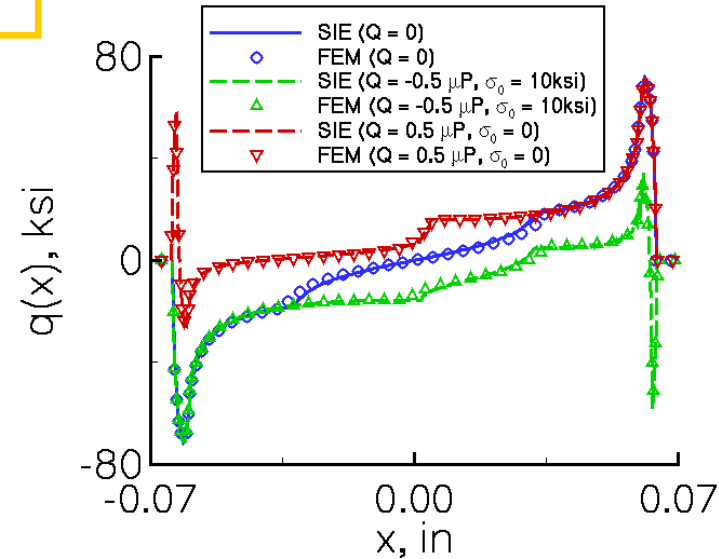
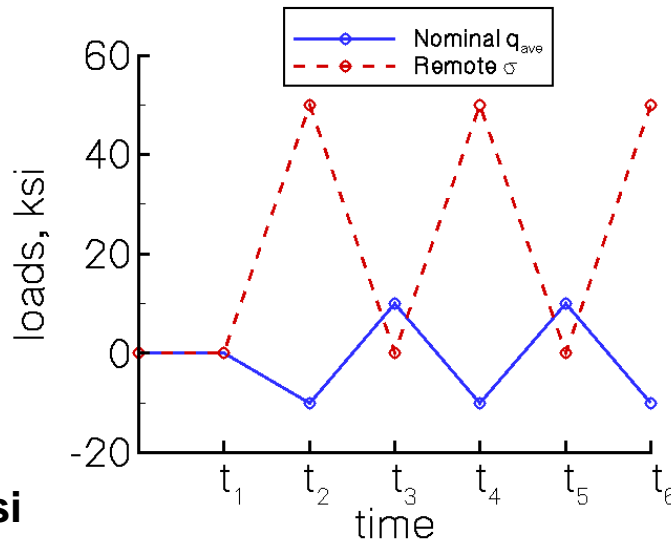


- 2D FEM analysis to validate the SIE model when one of the material principal axes is parallel to the z-axis.
- 16400 elements with 300 elements in contact
- Rigid indenter used to save analysis time
- Infinite elements to simulate elastic half space

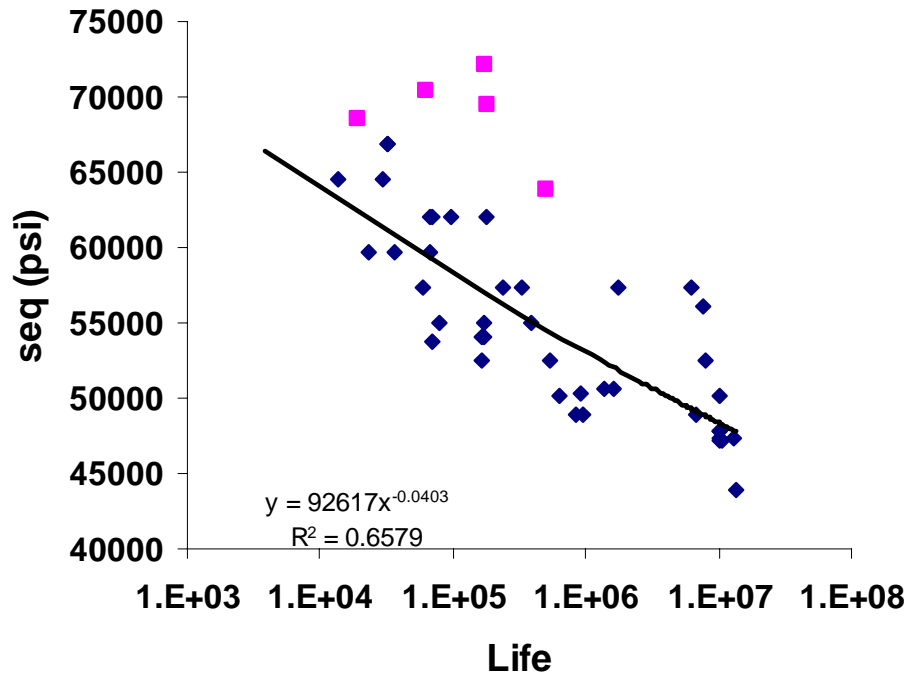


$\mu = 0.2$
 $\theta_z = 45^\circ, \theta_x = 0^\circ$

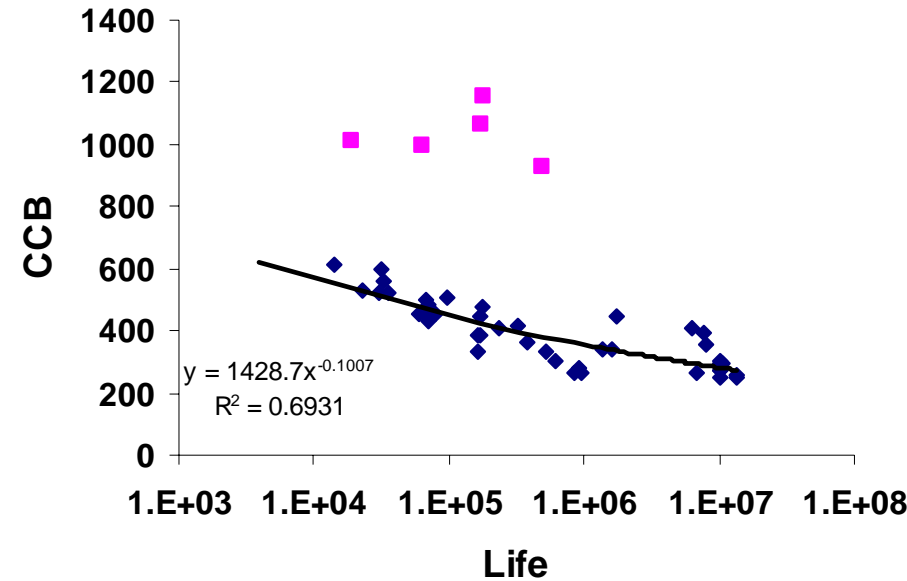
Nominal $p_{ave} = 100$ ksi



Life Estimation Using Stress Area



Chu-Conle-Bonnen



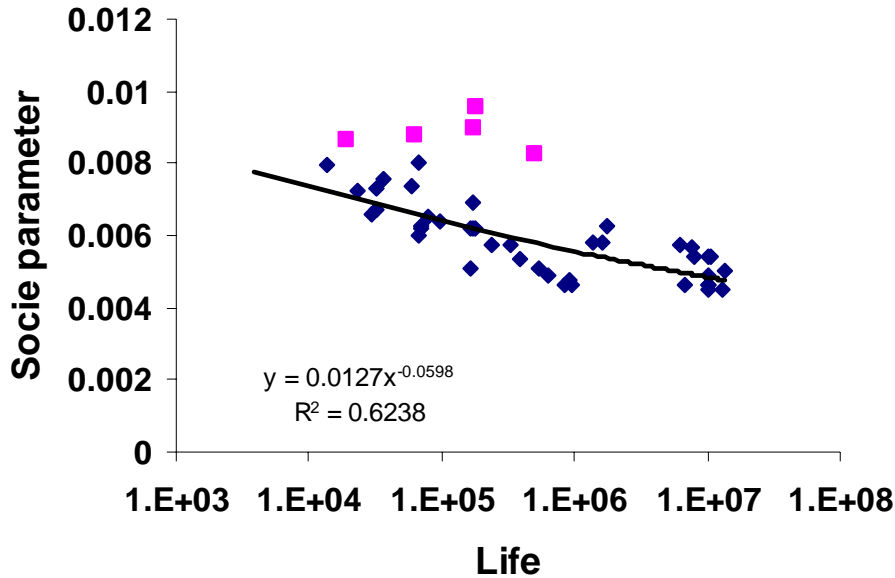
$$CCB = 2\gamma_a \tau_{\max} + \varepsilon_a \sigma_{\max}$$

Uniaxial data obtained from tests conducted by GEAE and PW

Reference for parameters: *G. R. Swanson, N. K. Arakere, NASA/TP-2000-210074, PWEH, HCF Quarterly report*

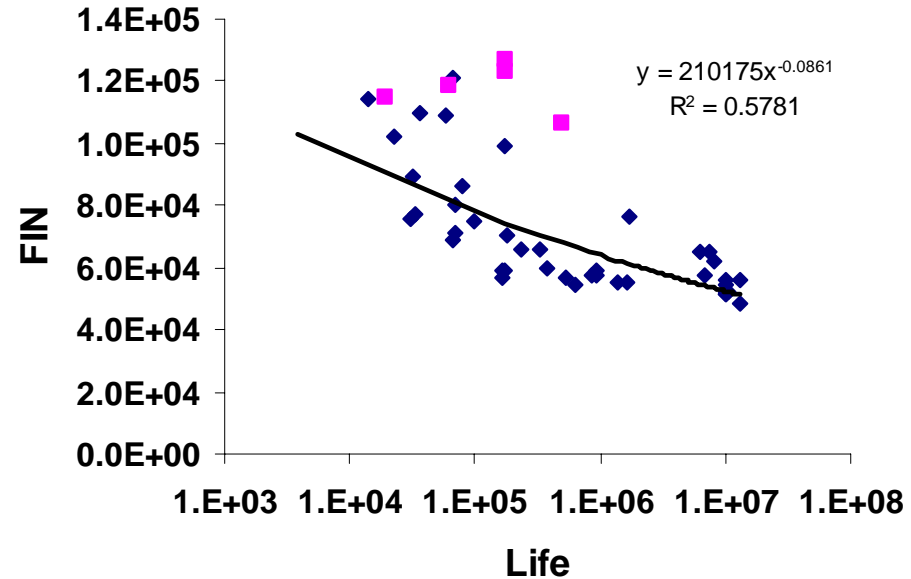
Life Estimation (Contd.)

Socie Parameter



$$SOC = \frac{\Delta\gamma}{2} + \frac{\Delta\varepsilon}{2n} + \frac{\Delta\sigma}{2E}$$

Findley Parameter



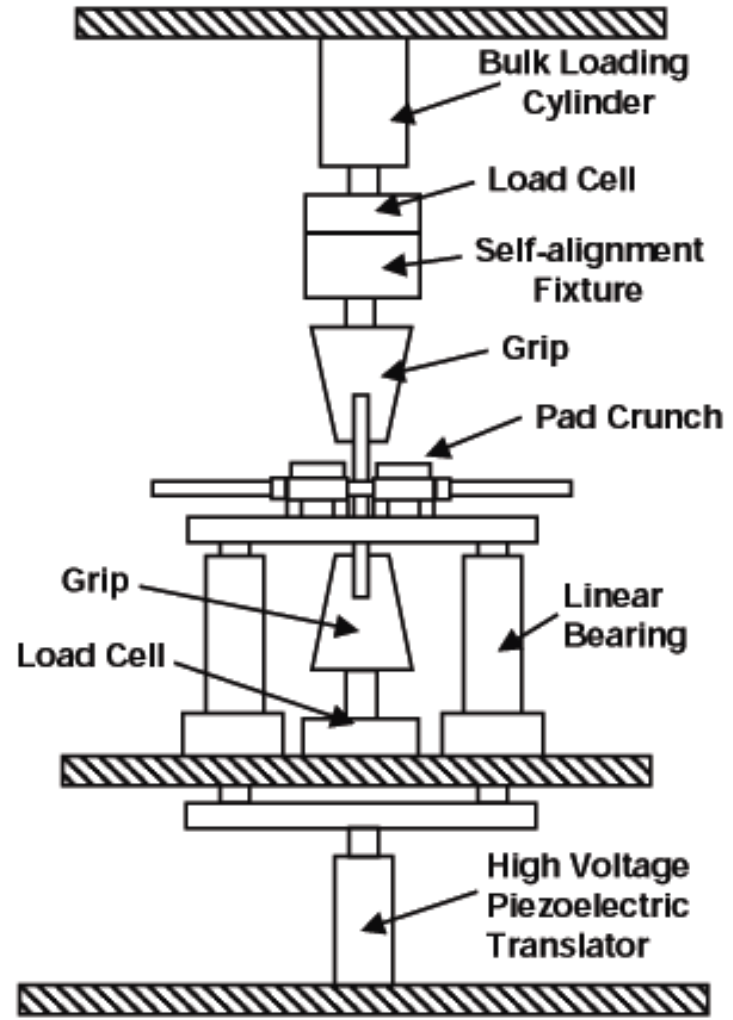
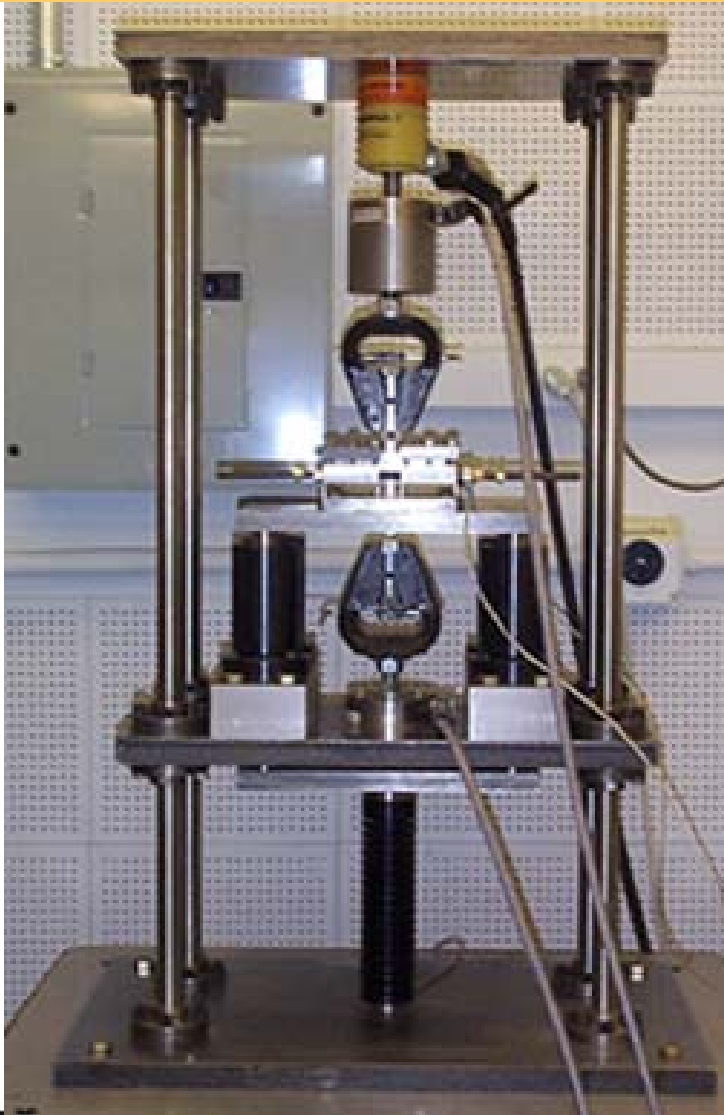
$$FIN = \tau_a + k\sigma_{\max}$$

Uniaxial data obtained from tests conducted by GEAE and PW
 Reference for parameters: *G. R. Swanson, N. K. Arakere, NASA/TP-2000-210074, PWEH, HCF Quarterly report*

Conclusions

- An experimental setup for elevated temperature tests (610°C) has been established based on the load transfer principle used with success for room temperature tests
- An experimental procedure has been designed to minimize the pad rotation and the moment at the contact location and obtain partial slip conditions representative of engine hardware
- Observations of fracture planes are consistent with uniaxial loading
- A numerical analysis technique developed by Rajeev, (*JSA 2002 PE Publishing Award*) is used to analyze the experiments, leading to nucleation life prediction
- Ongoing work is focused on crack propagation for inclusion in total life prediction
- **Fretting fatigue of advance materials can be analyzed with mechanics-based life prediction tools at high temperature**

High-Frequency Setup



-
-
-
- **5th International Symposium on Liquid Space Propulsion:**
- **Long Life Combustion Devices Technology**
- **October 27-30, 2003**
-
-

Damage Assessment of Combustion Devices

Peter J. Bonacuse
US Army Research Laboratory
Vehicle Propulsion Directorate
@ NASA Glenn Research Center
Cleveland, OH

•
•
•

Outline

- Driving Forces
- Damage Mechanisms
- Life Models
- Examples of Material Behavior
- Summary

-
-
-

Driving Forces

- Thermal gradients
 - Differential thermal expansion
- Elevated temperatures
 - Peak temperature
 - Time at temperature
- Loads/Stresses
- Environment
 - Oxidizing
 - Reducing
- Cycles (thermal/deformation)

-
-
-

Variables Affecting Damage Accumulation

- Gas Temperature
- Severity of Thermal Transients
- Cooling Flows
- Chamber Pressure
- Component Geometry
- Material Properties

-
-
-

Damage Mechanisms

- Creep
 - Void nucleation, GB sliding
- Metallurgical instabilities
 - Grain growth, precipitation/dissolution of phases
- Environmental attack
 - Oxidation
 - Effects of Hydrogen
- Fatigue crack initiation
 - Persistent slip, defects
- Fatigue crack growth

-
-
-

Damage Interactions

- Many of these damage mechanisms tend to interact synergistically
 - Creep-Fatigue
 - Fatigue-Oxidation
 - Hydrogen embrittlement-Fatigue
 - Dwell crack growth

Net effect is reduced available life

- Orders of magnitude in some cases

-
-
-

Damage Models

- Creep deformation
 - Diffusion based - power law
 - Unified visco-plastic models
- Creep rupture
 - Larson-Miller
 - Minimum Commitment Method
- Fatigue crack initiation
 - Strain-life
 - Stain Range Partitioning
 - Many others
- Fracture Mechanics

-
-
-

Strain Range Partitioning (SRP)

- Developed to calculate the extent of creep-fatigue interaction
- Creep damage due to time-dependent deformation and damage caused by high rate plastic deformation in the in tensile and compressive halves of fatigue cycles can contribute to damage in distinct ways
- Any arbitrary cycle can be 'partitioned'. Measured or calculated creep and/or plastic strain in the tensile and compressive halves of the cycle
- Requires creep-fatigue characterization

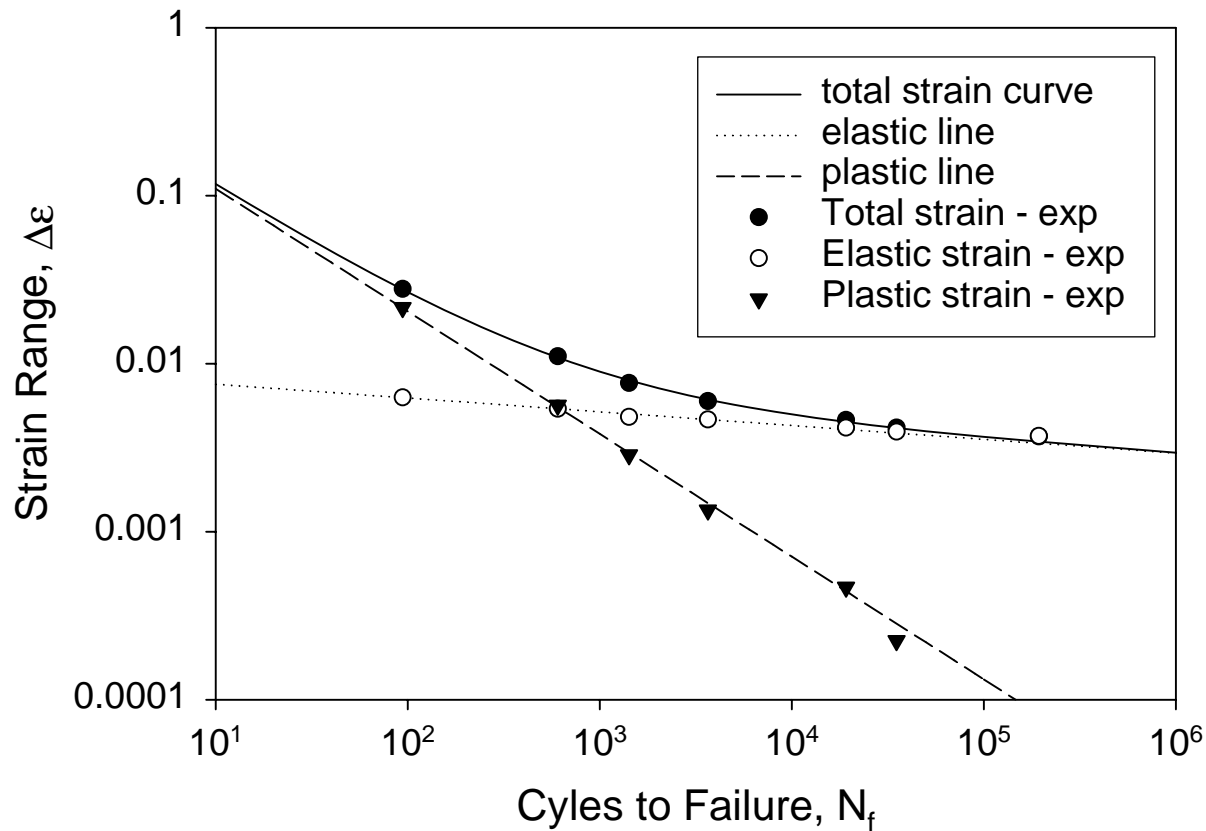
-
-
-

Model Material - Haynes 188

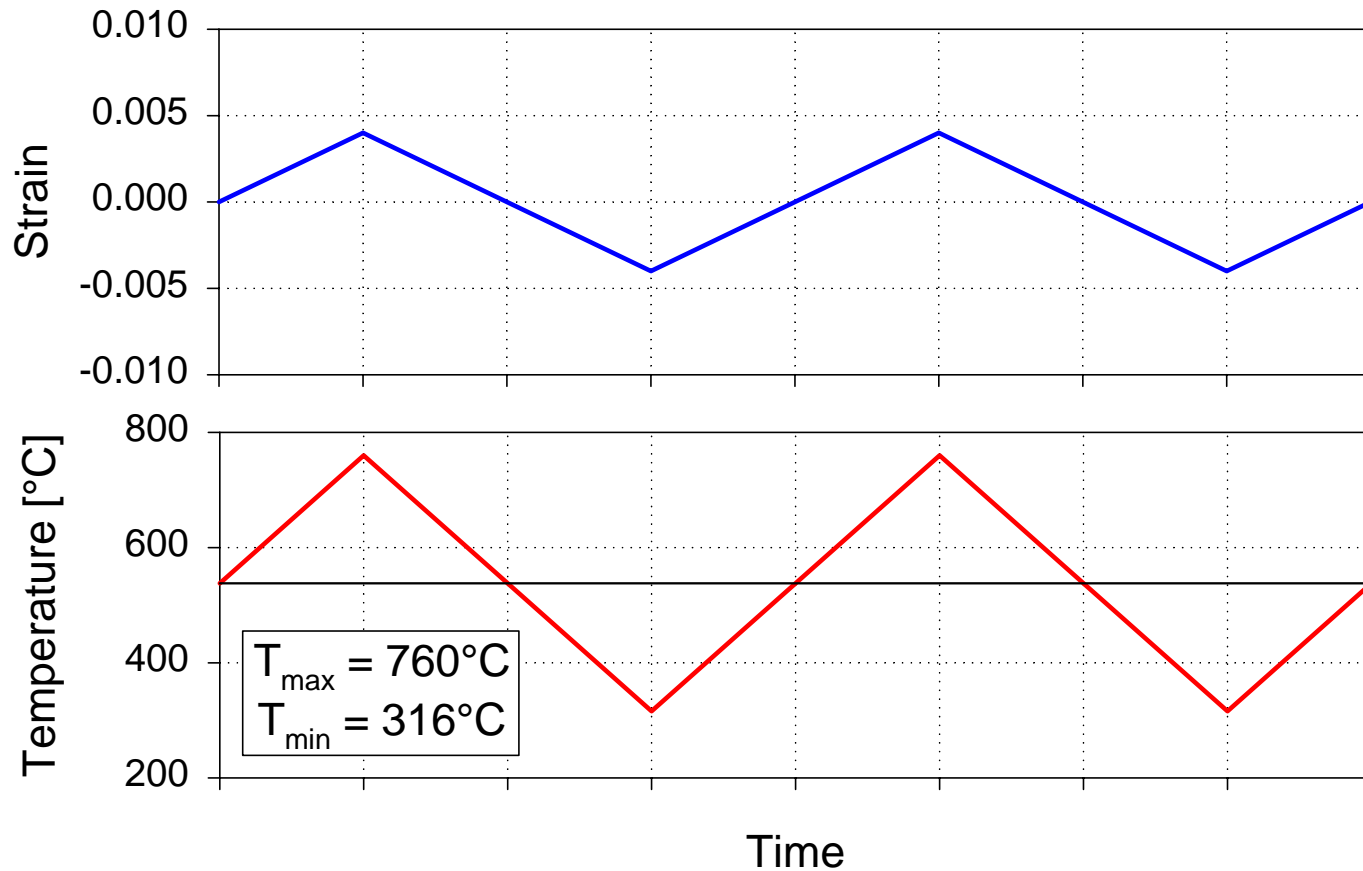
- Solid solution strengthened Cobalt-base superalloy
- Used in both gas turbine and rocket engine combustor applications
- Large and diverse database collected at NASA Glenn Research Center
 - Fatigue
 - Creep
 - Creep-fatigue
 - Thermomechanical
 - Multiaxial
 - Cumulative damage
 - Various combinations of the above

Strain Life Plot for Haynes 188 @760°C

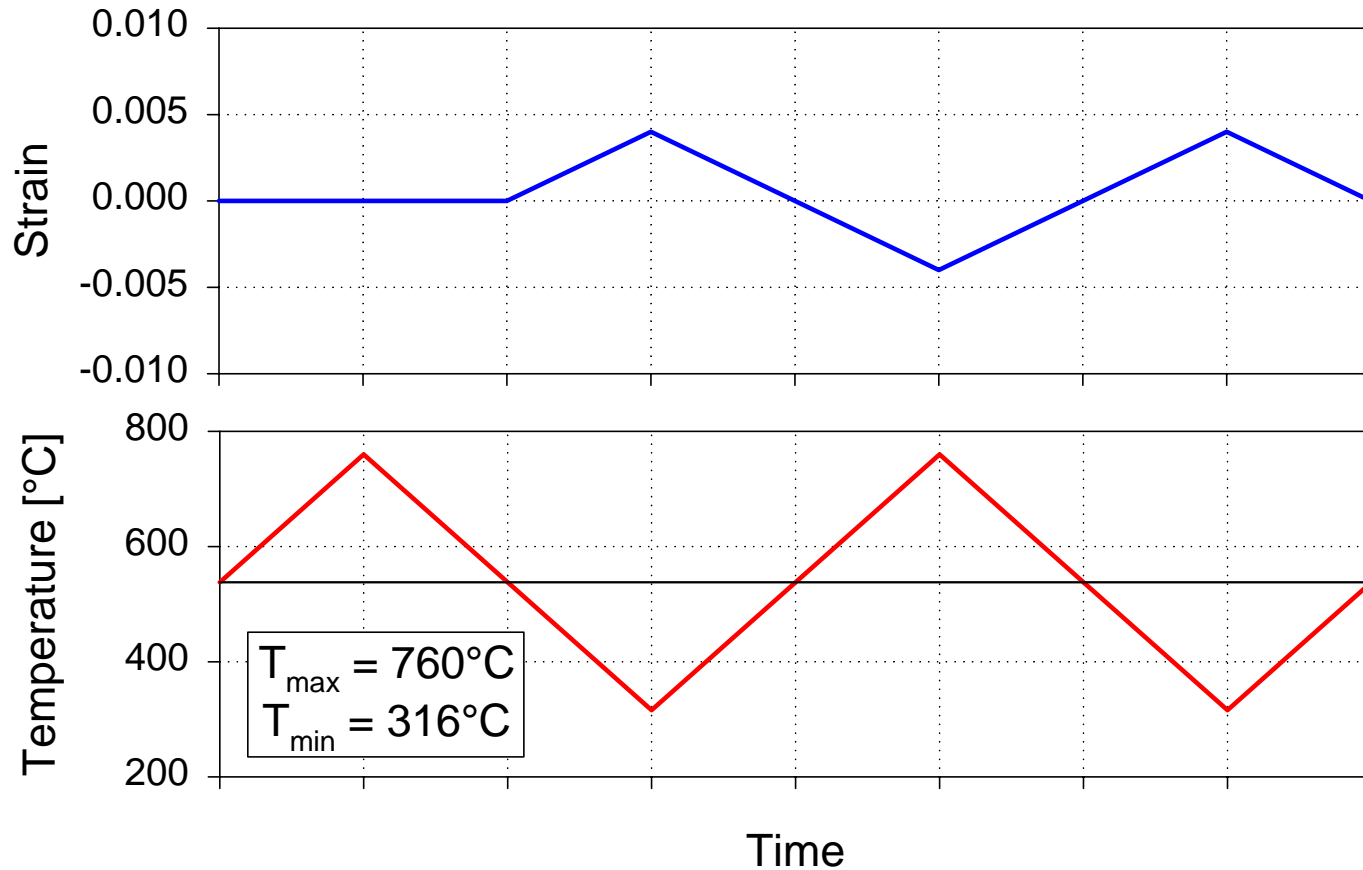
$$\Delta\varepsilon = 0.0091(N_f)^{-0.082} + 0.590(N_f)^{-0.730}$$



TMF Cycle Schematic - Thermally In-Phase



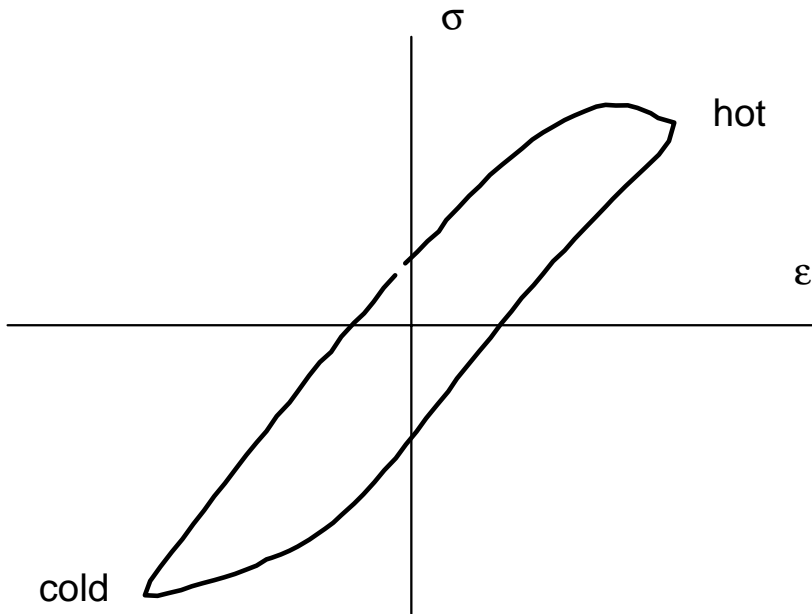
TMF Cycle Schematic - Thermally Out-of-Phase



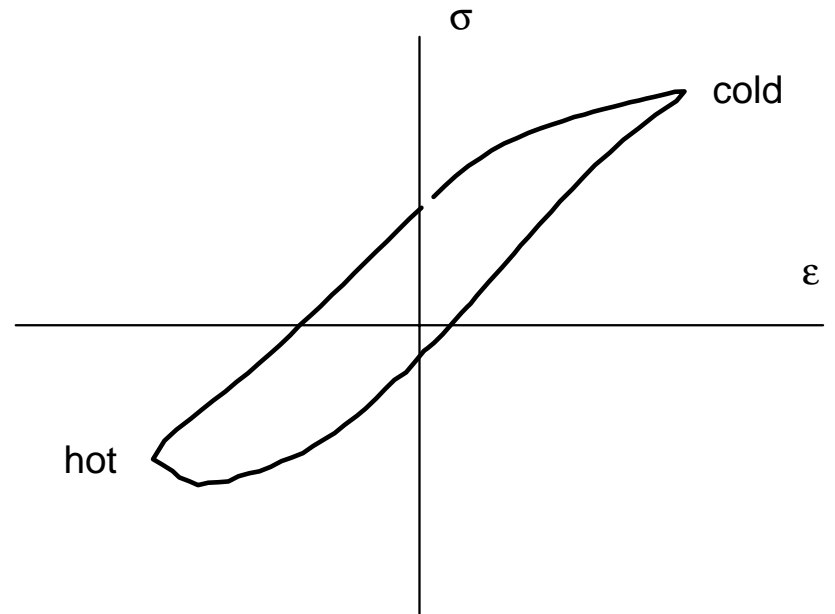
-
-
-

TMF Fatigue Cycles

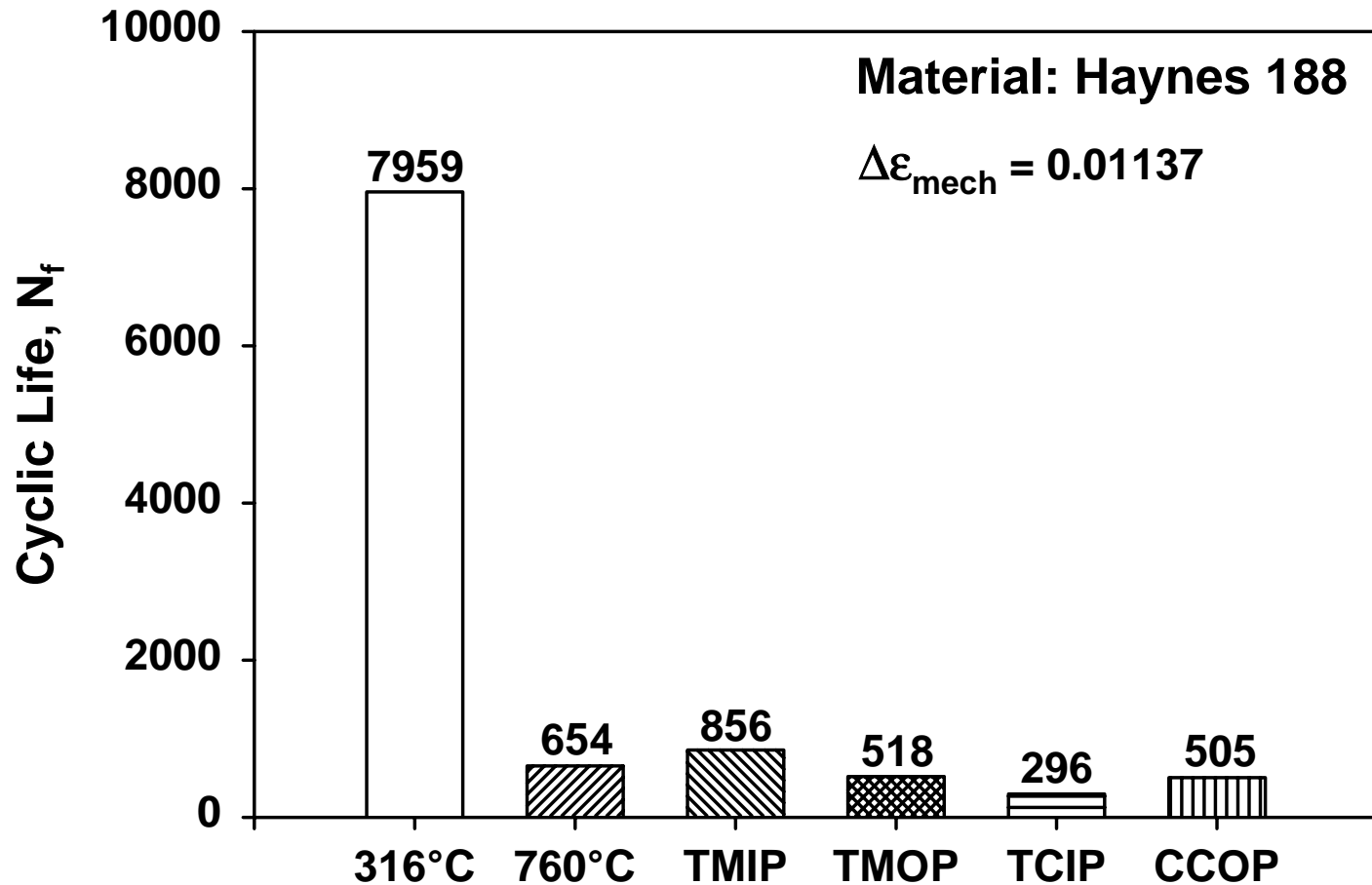
Thermally In-Phase (TMIP)



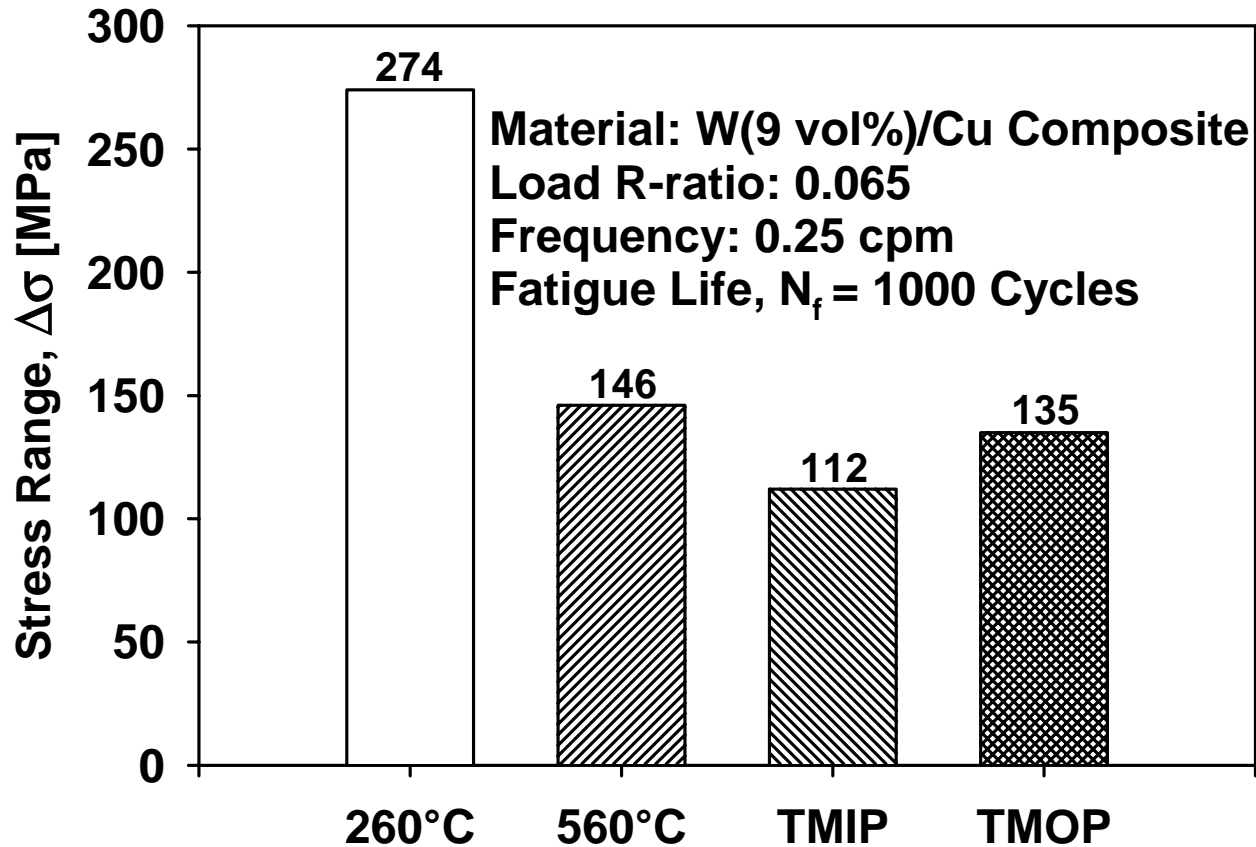
Thermally Out-of-Phase (TMOP)



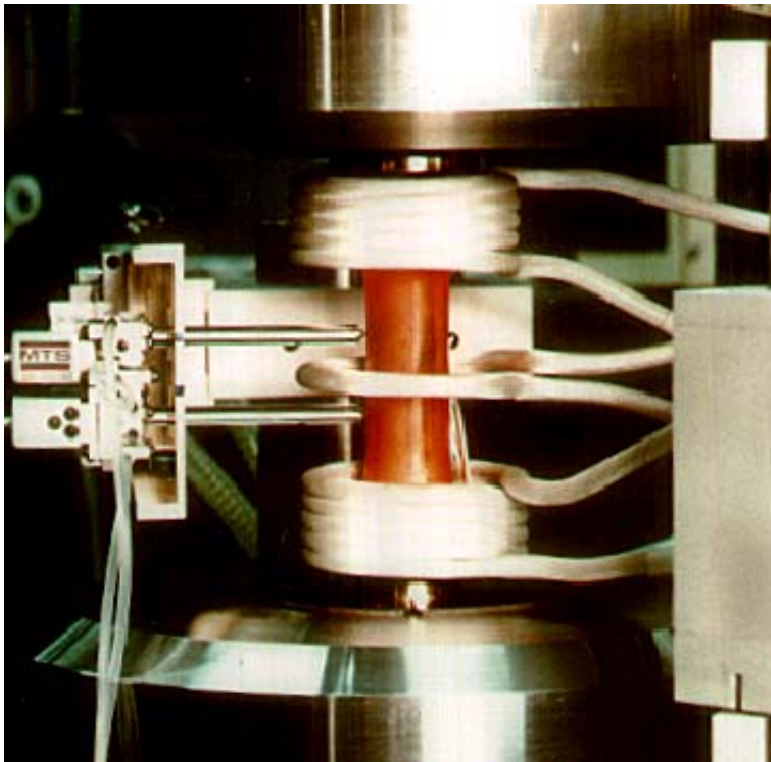
Comparison of Uniaxial Isothermal and TMF Fatigue Lives



Comparison of Uniaxial Isothermal and TMF Stress Ranges

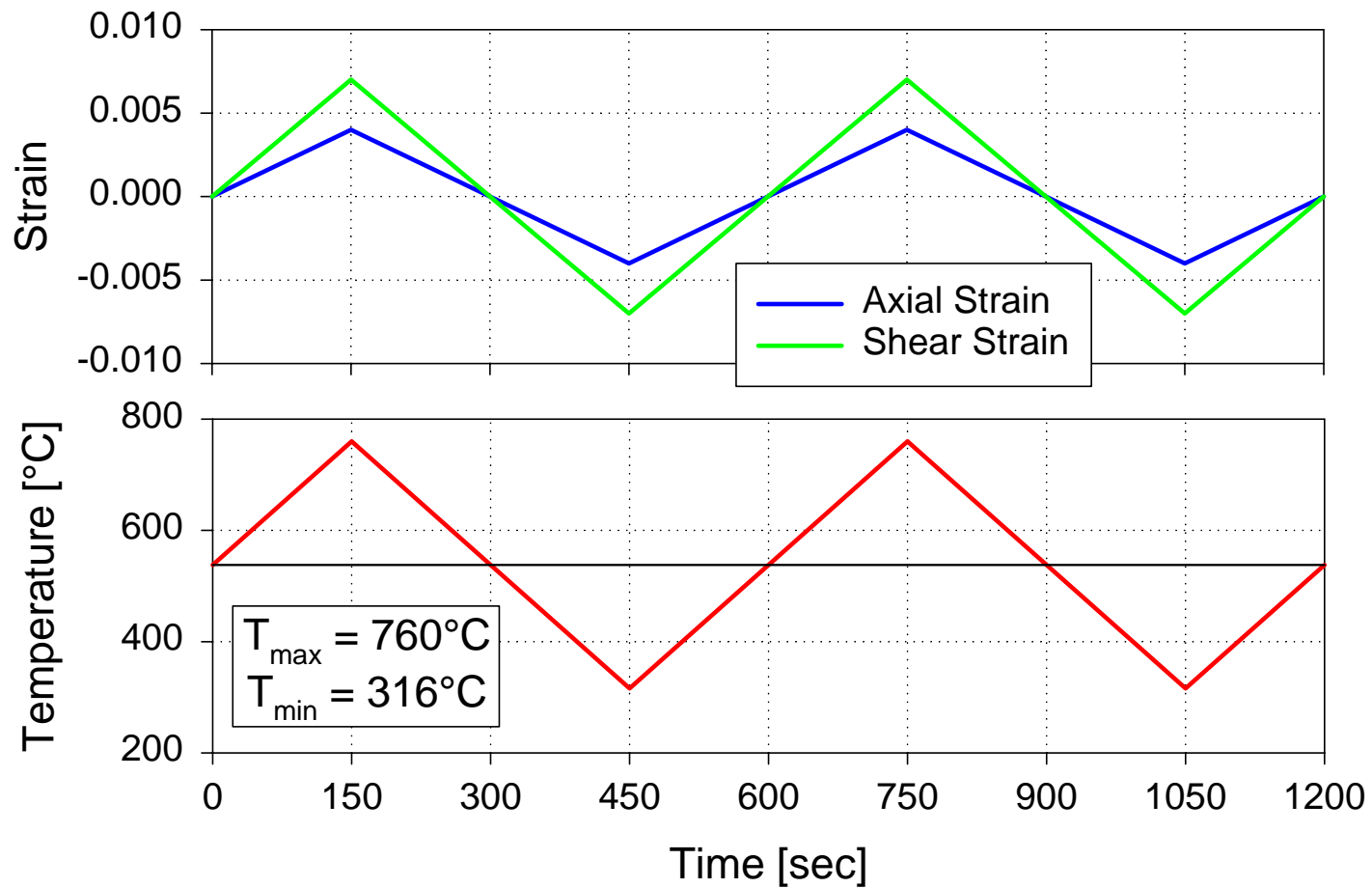


Combined Thermomechanical and Multiaxial Testing of High Temperature Materials

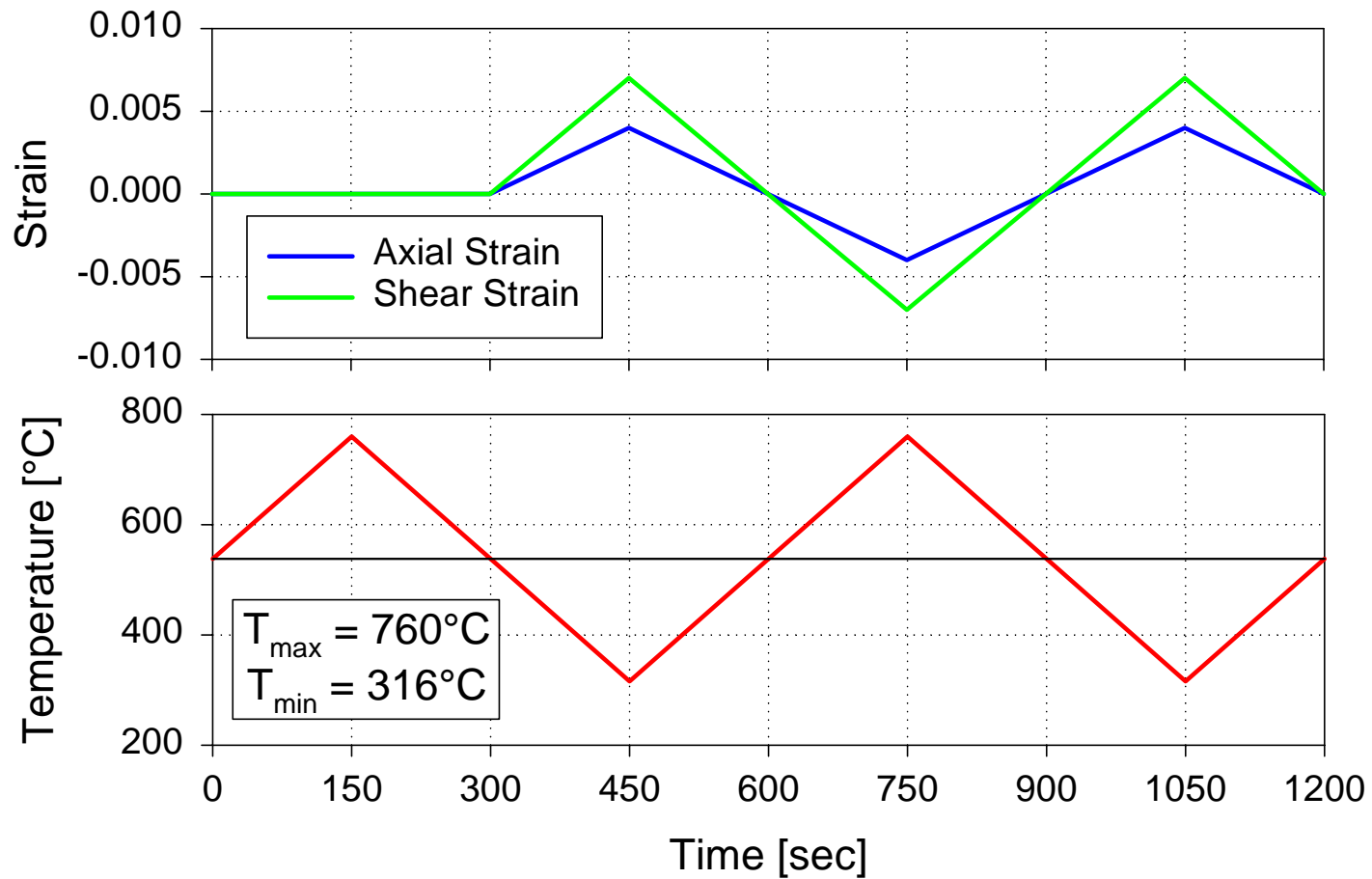


- Materials are typically characterized under isothermal, uniaxial loading
- Components in service generally experience multiaxial, thermomechanical loading
- Complex loading can trigger damage and deformation mechanisms not revealed in typical characterization
- To validate/calibrate material deformation and damage models for multiaxial, non-isothermal conditions, experiments must be performed under more complex loading

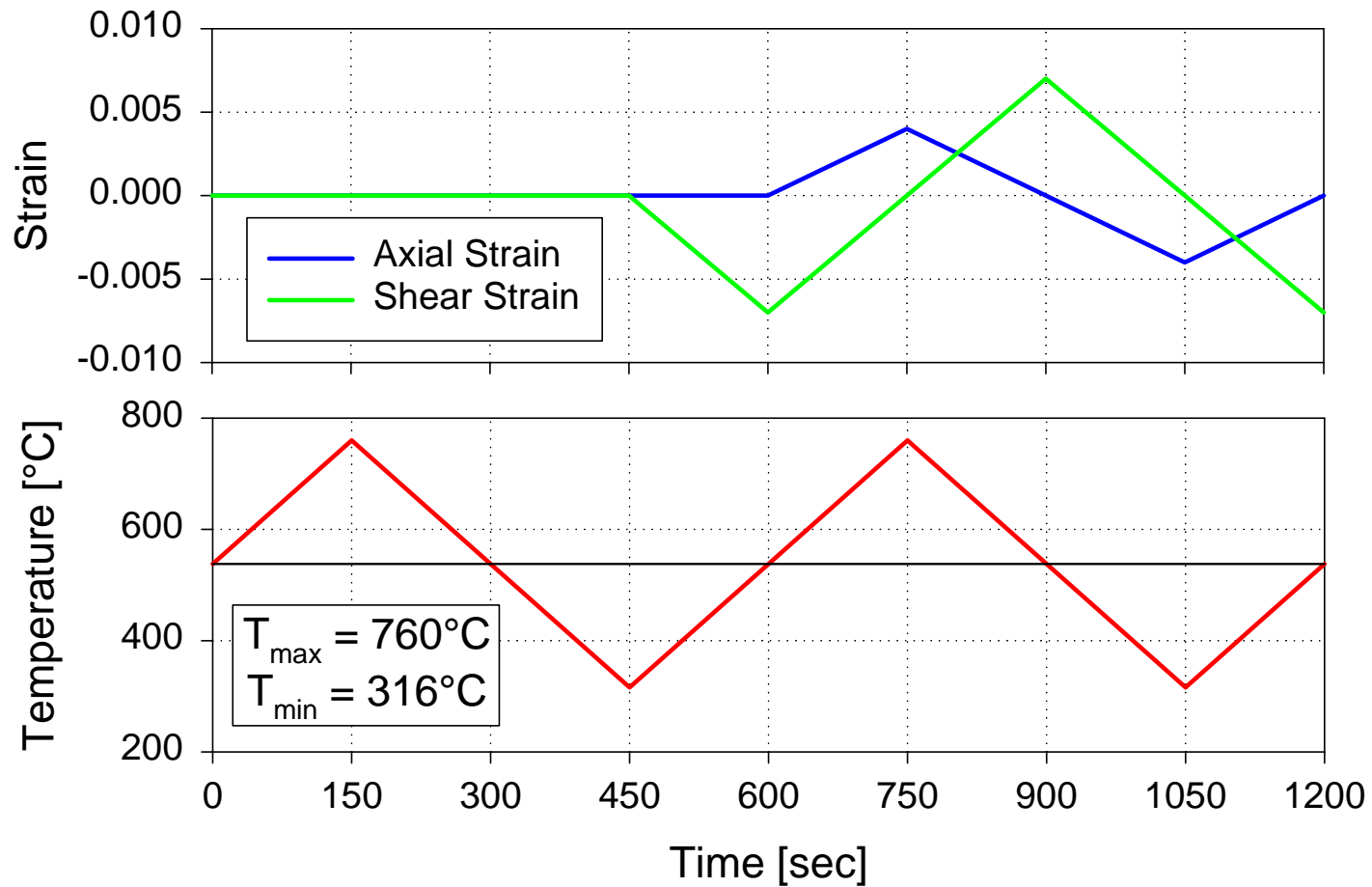
Mechanically In-Phase, Thermally In-Phase (MIPTIP)



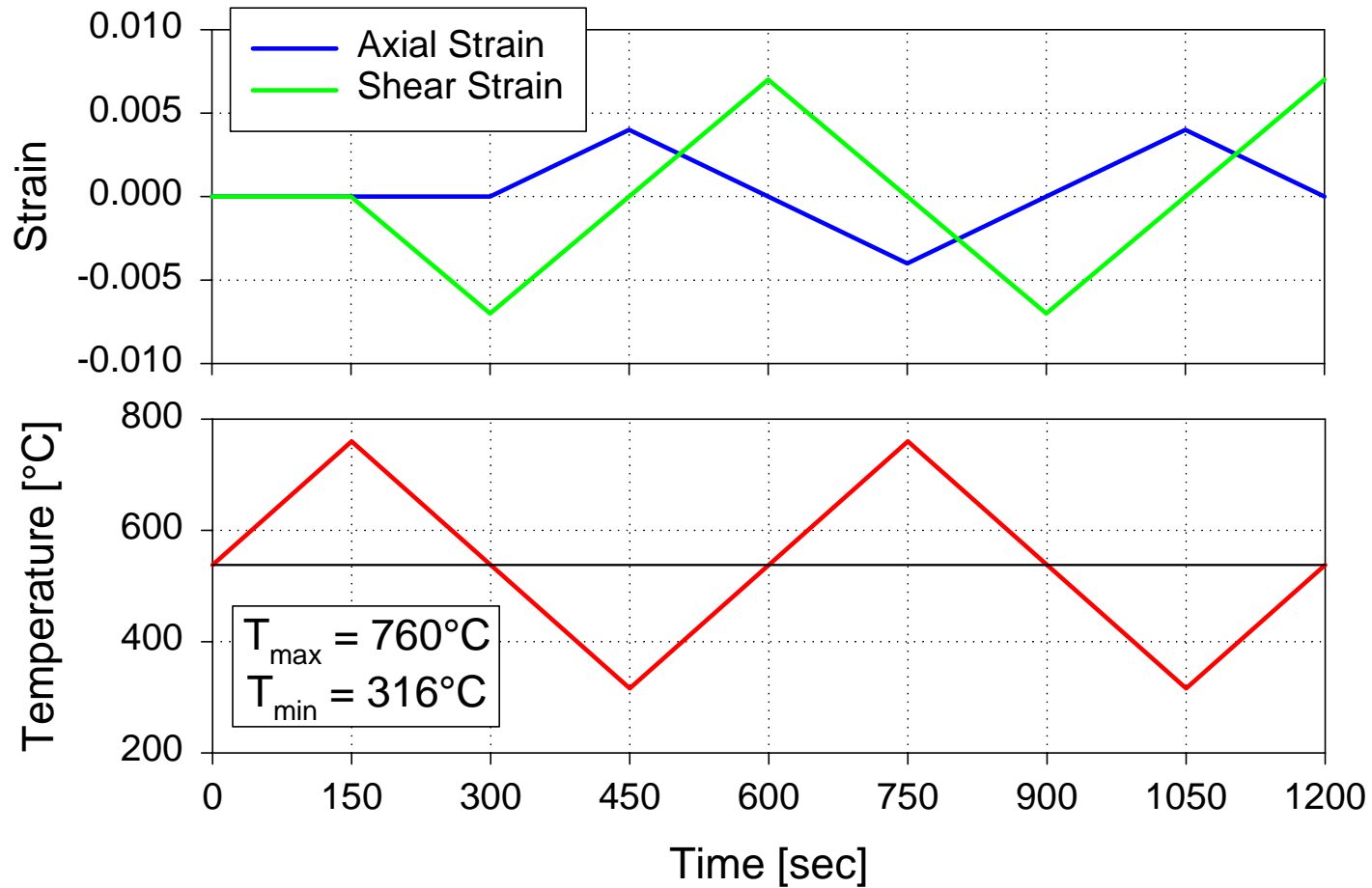
Mechanically In-Phase, Thermally Out-of-Phase (MIPTOP)



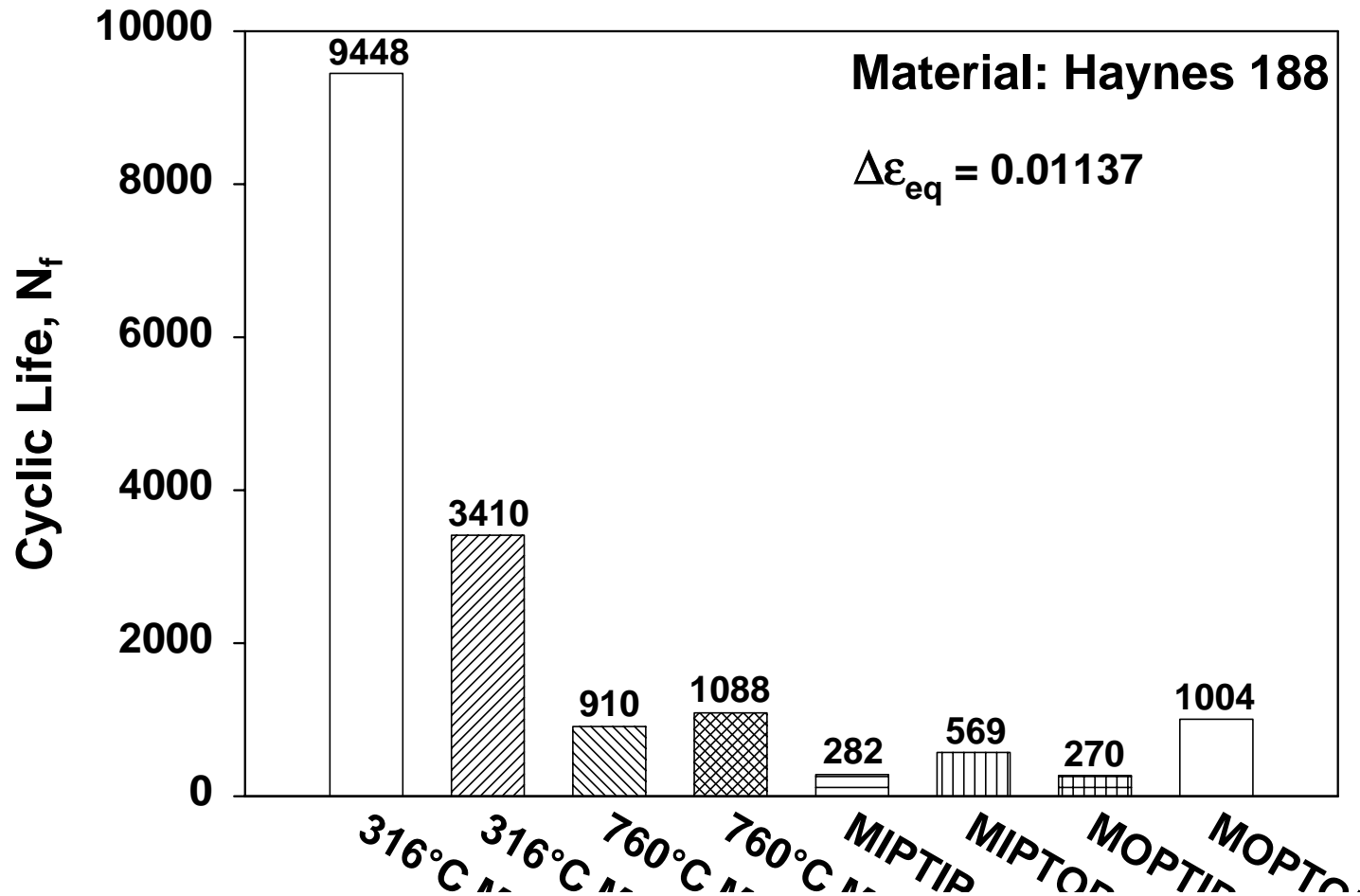
Mechanically Out-of-Phase, Thermally In-Phase (MOPTIP)



Mechanically Out-of-Phase, Thermally Out-of-Phase (MOPTOP)



Comparison of Thermomechanical, Axial-Torsional Fatigue Lives



-
-
-

Summary

- Damage in combustion devices is largely driven by thermal transients.
- The variety of competing and interacting damage mechanisms make life assessment challenging.
- Experimental characterization of material durability should explore conditions similar to the operating environment.
- Given the nonlinear relationship between stress/strain and life, accuracy of model inputs is critical

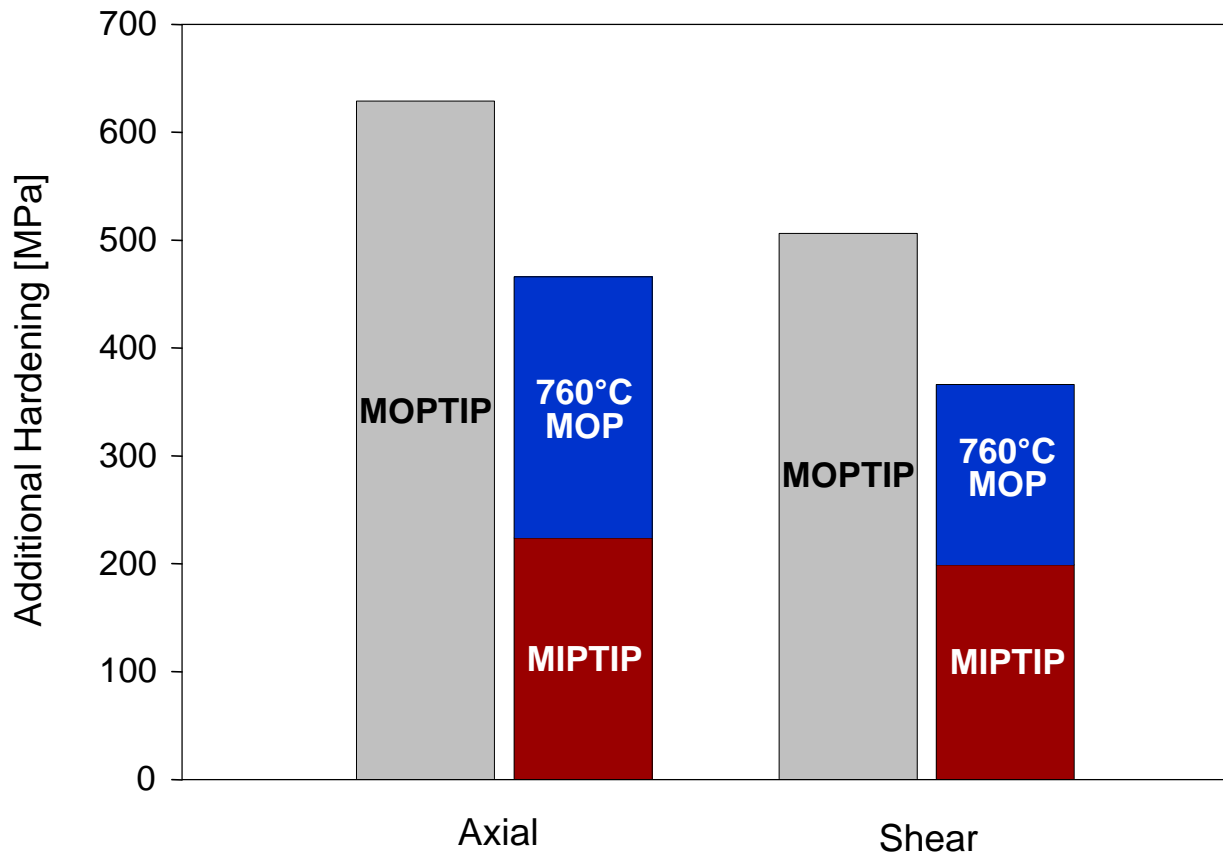
-
-
-

Increase Durability/Reliability

- Reduce the severity of thermal gradients
 - start up – shut down sequence/fuel flows
 - apply thermal barrier coatings (TBCs)
 - change the component geometry
- lower the peak temperatures
 - increased cooling flows
 - reduce severity of the thermal transients
- reduce the effect of environment
 - apply environmental barrier coatings (EBCs)
 - select more capable materials

Additional Hardening Comparison

760°C mechanically in-phase data used as baseline



DAMAGE ASSESSMENT OF COMBUSTION DEVICES

Peter J. Bonacuse

U.S. Army Research Laboratory
Vehicle Propulsion Directorate
NASA Glenn Research Center
Brook Park, OH

Sreeramesh Kalluri

Ohio Aerospace Institute
NASA Glenn Research Center
Brook Park, OH

ABSTRACT

The process of estimating the accumulated damage in a combustion devices can range from cursory with little or no data on either the boundary conditions or the material properties to elaborate and expensive with many repeated experiments to calibrate/validate the damage accumulation model. Confidence in the accuracy of the many possible analysis paths is typically proportional to level of testing required to properly calibrate the models. The various driving forces are discussed for thermally induced damage in combustion devices such as: thermal gradients, high temperatures, and environment. The damage mechanisms associated with these driving forces include: excessive deformation/creep ratcheting, creep rupture, fatigue, and oxidation/environmental attack. A small subset of the many proposed models for estimating the durability of combustion components is presented. Many potential damage mechanisms may be present in any given application. These mechanisms may compete or interact synergistically to increase the rate of damage accumulation.

INTRODUCTION

The accumulation of “damage” in combustion components is dependent on many variables, including: gas temperature, thermal transients, cooling flows, chamber pressure, combustor geometry, and the properties of the combustor materials. The materials chosen dictate the range of allowable temperatures, time of exposure, and mechanical loads and therefore place limits on the overall performance of the system. The components in the combustion system directly exposed to the hot gas stream tend to have relatively light mechanical loads. Often the life limiting driving force is the stress generated within the component due to the thermal gradients that are typically most severe during system transients. The magnitude of the thermal stress and strain is dependent on the severity of the thermal transient, the component geometry, and the material’s modulus of elasticity, thermal expansion, thermal conductivity, and heat capacity. The additional stress induced by mechanical loads and pressure differentials could also contribute to the damage process and should not be ignored.

Although the driving forces for damage accumulation apply to all classes of materials, the damage mechanisms outlined in the following sections occur mostly in metallic materials. Accurate assessment of the component temperature and stress/strain distributions is critical for reliable life estimation. Given the highly non-linear relationship between induced strain/stress and life, small differences between the input and the actual boundary conditions can lead to large errors in the predicted life.

DRIVING FORCES FOR DAMAGE ACCUMULATION

The driving forces for damage accumulation in combustion devices are independent of the materials chosen. All materials suffer varying degrees of degradation in the presence of highly transient heat fluxes, high peak temperatures, cyclic loading, and aggressive environments.

Since most materials tend to expand with increasing temperature, thermal gradients within a structure, particularly in the presence of geometric constraints that prevent free thermal expansion, can cause severe local distortions with associated high stresses and inelastic deformation. Thermal gradients tend to be largest during transients, i.e. start-up, shut-down, and throttle excursions. Forced cooling, which is utilized in nearly all current combustion devices to reduce peak material temperatures, causes thermal gradients. To minimize the damaging inelastic deformation in these cooled systems, high thermal conductivity materials (for example, Oxygen Free High Conductivity (OFHC) copper or alloys of copper) are often selected to minimize thermal gradients. Even un-cooled components will have thermal gradients during engine transients. Ironically, these transient induced thermal gradients tend to be exacerbated by the generally lower thermal conductivities of materials capable of withstanding the higher temperatures (e.g.: carbon/carbon composites, ceramics, and ceramic matrix composites). Stresses and inelastic strains generated within the material as a result of the imposed thermal gradients lead to thermal fatigue. Halford and Sehitoglu have provided excellent references describing the thermal fatigue problem in more detail [1, 2].

All materials have time at temperature limits imposed by their composition and microstructure. Approaching or exceeding these limits can cause significant changes in the material properties and an exponential increase in the rate of damage accumulation.

The requirement that the propulsion systems be reusable puts additional constraints on the design and material selection. Cyclic loading tends to stimulate damage mechanisms that do not typically occur in single use designs.

Environment also plays a crucial role in the accumulation of damage in combustion system materials. Oxidation (in oxygen rich combustion systems) and the effects of atomic hydrogen, (in fuel rich reducing environments), are often factors that require consideration in the durability assessment of combustion components.

DAMAGE MECHANISMS

A major challenge in predicting the expected life of components exposed to cyclic loading at elevated temperature is the variety of available, potentially competing or interacting, damage mechanisms. In elevated temperature environments all materials experience changes in their microstructure if the temperature is high enough for a long enough time. Alloys designed to operate in high temperature environments can undergo a variety of microstructural changes. Recrystallization may occur or grains may begin to grow and coarsen; age hardened alloys may lose strength as their secondary phases coarsen; and rogue phases may begin to precipitate often preferentially at grain boundaries. The environment also tends to become exponentially more active as temperature increases.

Creep is often defined as accumulation of time-dependent inelastic deformation. Creep deformation in metals is usually associated with void nucleation and grain boundary sliding. Plastic deformation is typically associated with crystallographic slip but some slip will also occur in creep deformation with additional dislocation mechanisms (climb and additional slip systems) activated at elevated temperatures. In addition other microstructural changes may take place including: subgrain formation, precipitation of additional intermetallic phases or dissolution of existing phases. The rate of creep deformation is dependent on temperature, applied stress, and the intrinsic properties of the material. Creep rupture in metallic materials occurs when voids, typically nucleating at grain boundaries and microstructural inhomogeneities such as inclusions or precipitates, grow and coalesce to form a crack that eventually causes the structure to fail. The structure might also be considered to have “failed” if its shape changes enough under creep deformation, to impact the overall system performance beyond a desired threshold. A crude rule of thumb for metallic materials is that the maximum use temperature must be kept below half the absolute melting temperature to preclude significant creep deformation and damage.

One of the most common causes of failure in high temperature components is fatigue crack initiation induced by cyclic loading. If inelastic strains are large enough, metallic materials will typically suffer fatigue crack initiation at multiple locations and some of those cracks may begin to propagate. The number of cycles a component subjected to fatigue loading can sustain before initiating a propagating fatigue crack is dependent upon a number of details that encompass both the material and the loading conditions. In general, when there is a prospect of measurable inelastic strains under cyclic loading, the material chosen must have sufficient ductility to absorb this deformation without initiating and propagating fatigue cracks within the expected life of the component. Once a crack has initiated, the structure may still be able to perform its function while the crack propagates. At some point, the crack may propagate to a size that will cause structural or functional failure of the component.

Oxidation, by itself, is not often a life limiting damage mechanism in combustion system components. General oxidation leads to loss of material cross section and reduction in strength of the component. Localized oxidation along fast diffusion paths such as grain

boundaries can make it easier for cracks to initiate in the more brittle oxide. Hydrogen, because of its small atomic cross-section, can diffuse into the lattice of metallic materials at high temperatures and slow or arrest the motion of dislocations, making the material more brittle. This mechanism has been shown to have the most significant detrimental effect in high strength materials with body centered cubic and hexagonal close packed crystal structures. Copper and its alloys also suffer deleterious effects from hydrogen in high temperature reducing environments in the form of surface blistering due to the formation of water vapor in the reaction of hydrogen with Cu_2O .

Many of these damage mechanisms cannot be modeled independently because they tend to interact in synergistic ways. For example, cyclic loading in the presence of an oxidizing environment will tend to accelerate the crack initiation process because the oxides produced tend to be more brittle than the base material and also tend to accumulate along grain boundaries (oxide spikes) [3, 4]. Another example of interacting damage mechanisms is the creep-fatigue interaction. This has been studied extensively [1, 5] and has been found to often cause a significant life debit. The extent of the creep-fatigue life debit is dependent on a number of parameters including: material properties, temperature regime, hold time at temperature, and strain rate (or cycle frequency), etc.

Observations have shown that different materials can have very different damage accumulation rates, different types of active damage mechanisms, and different levels of interaction among the active mechanisms, when subject to similar loading conditions. This makes the task of developing life models that apply uniformly to a variety of materials and operating conditions extremely challenging.

DAMAGE MODELS

A number of models for estimating the evolution of various damage mechanisms will be described. This is not intended to be a comprehensive list but merely a brief introduction to some of the more commonly used models. References are provided to allow the reader to obtain additional details on the implementation of the models described in this paper as well as to explore more accurate (and typically more complex) and data intensive life prediction models.

Many damage accumulation models currently in use require an estimate of the expected inelastic deformation in the material under the loads and constraints dictated by the structure. Recently developed unified visco-plastic models have come a long way toward accomplishing this goal [6]. The testing requirements to calibrate these models can vary from a few simple experiments to an elaborate test matrix, depending on the desired fidelity. Often estimates of model parameters can be made from prior experience with similar material systems with the recognition that this places additional uncertainty on the model's accuracy.

Creep Deformation – If one can neglect primary creep, a simple diffusion based steady state creep model may be all that's required to calculate the amount of creep deformation

that one can expect over the life of a component. In this type of model the steady state creep rate is a function of the local stress and the absolute temperature (in Rankine or Kelvin). The model parameters must be fit from steady state creep experiments performed at several temperatures and stress levels. One would hope that the stresses and temperatures chosen for the creep model calibration would approximate the expected conditions of the components whose creep life is to be estimated. In the general case where the temperature and stress level fluctuate with time, the function can be integrated over the loading cycle, or design life, to arrive at an estimate of the accumulated creep strain [7].

Creep Rupture – Time and temperature models for estimation of time to creep rupture of materials abound [8]. The one of the earliest, and still in common use, is the Larson-Miller (L-M) parameter [9]. This parameter collapses rupture data from various temperatures and stresses down to a single design curve. Given a calculated L-M parameter for a specific material the time-to-rupture at a specified temperature and applied stress can be calculated. Constant load creep rupture experiments should be performed under conditions that match the service conditions as closely as is practical. For extrapolation of short-time creep-rupture data to longer times, the Minimum Commitment Method [10] typically provides more accurate rupture time estimations.

Fatigue Crack Initiation – If it can be shown that the variation in temperature within the fatigue cycle of interest has little influence on the cyclic life of the material, a relatively straight forward strain-based approach to fatigue life estimation can be applied where the total strain range in the cycle is expressed in terms of the cyclic life. The constants are established from linear fits of the logarithms of elastic and inelastic strain ranges versus the fatigue life. Data for this calibration is typically obtained from strain controlled fatigue experiments [11, 12]. In the absence of fatigue data, these constants can be estimated from tensile properties [13] with an associated increase in uncertainty in the estimated fatigue life.

Cumulative Damage – In most applications, the loading cycle is not a simple repeated load up to maximum and down to a minimum stress/strain. When there are many other load excursions of smaller amplitudes, or the minor cycle amplitudes are a significant fraction of the major cycle, some account of the minor cycle damage will be required. The most common means of accomplishing this is a linear damage (Palmgren/ Miner) rule [14] which works remarkably well for a variety of variable amplitude loading conditions. This simple rule breaks down however when a material is subjected to both large strain low-cycle fatigue (LCF) cycles and low amplitude high-cycle fatigue. Detrimental nonlinear interaction can occur leading to significant deviation from the linear damage rule [15, 16, 17]. Nonlinear damage accumulation methods such as the Damage Curve Approach or the Double Linear Damage Rule are available to accurately estimate cumulative fatigue damage in materials when load ordering effects are present [15].

Creep-Fatigue Interactions – Many models have been developed to characterize the high temperature fatigue behavior of metallic materials [18, 5]. Strain Range Partitioning

(SRP), developed at the NASA Glenn Research Center, has shown promise as a tool for estimating the effect of arbitrary creep-fatigue cycles on the cyclic life [18]. SRP was developed to calculate the extent of creep-fatigue interaction for materials subjected to either isothermal or thermomechanical loading. The working hypothesis of this model is that creep damage due to time-dependent deformation and damage caused by high rate plastic deformation in the in tensile and compressive halves of fatigue cycles can contribute to the damage accumulation in distinct ways. If one has access to experimental data where the four possible permutations of creep or high rate inelastic deformation in either tension or compression have been explored, one can take any arbitrary cycle and by determining the proportions of creep or plastic strain in the tensile and compressive halves of the cycle, one can arrive at an accurate estimate of the cyclic life. A total strain range version of the Strain Range Partitioning method was also developed at NASA Glenn Research Center to estimate fatigue lives of cycles that exhibit small amounts of inelastic strain ranges. Additional explanation of the implementation of the SRP methodology can be found in reference [19].

Crack Propagation – If the material contains a flaw or a physical process initiates a crack of sufficient size to allow it to overcome microstructural barriers to its growth, linear elastic fracture mechanics (LEFM) may be applied to predict its subsequent growth. Information about the crack propagation properties of the material at the appropriate temperature and environment and the expected stress levels within a loading cycle are necessary to calculate the propagation life. LEFM relates crack growth rate and the computed range of the stress intensity. The stress intensity is a function of the stress field, the instantaneous crack length, and the component geometry. The parameters of the LEFM equation are typically fit from large crack growth data. The LEFM relationship tends to break down where inelastic strains are large, time dependent behavior of the material is an issue, and when there are large thermal gradients in the vicinity of the crack. Dwell time in tension at elevated temperature can lead to time dependent extension of the crack [20].

MATERIAL BEHAVIOR AND DISCUSSION

Uniaxial, isothermal, constant amplitude fatigue experiments remain the primary means of characterizing material durability despite the fact that studies have shown that this approach can be unconservative for thermal fatigue life prediction. More elaborate characterizations that include temperature variations, multiaxial loads, and variations in the loading cycle may not reveal damage mechanisms that occur in service if the testing conditions do not accurately reflect the service environment of the component.

A tungsten-copper composite tested in load-control under thermomechanical fatigue displayed a decreased cyclic load carrying capability than an experiment where the entire cycle was performed at the peak TMF cycle temperature (Figure 1) [21]. TMIP and TMOP in the figure refer to constant amplitude thermomechanical fatigue tests where TMIP was in-phase (the maximum temperature coincides with maximum stress in the

cycle) and TMOP was out-of-phase (the maximum temperature coincides with the minimum stress).

A comprehensive and diverse fatigue database has been collected at the NASA Glenn Research Center on the wrought, cobalt-base superalloy, Haynes 188; an alloy commonly used in both gas turbine and rocket engine combustor applications. The database contains data generated from experiments that include constant amplitude isothermal, fatigue, creep, creep-fatigue, thermomechanical, multiaxial, cumulative damage, and various combinations of the above [22, 23, 24, 25, 16, 17].

Fatigue life under thermomechanical loading (TMF), where both the temperature and mechanical load are changing simultaneously, has sometimes been predicted by taking the simple expedient of assuming that the entire loading cycle takes place at the peak temperature. For Haynes 188, loaded thermomechanically from 316°C to 760°C under thermally in-phase and out-of-phase conditions, this simplification worked well (Figure 2) [23]. This is not always the case with other materials, temperature regimes, or loading conditions [2]. Additional hardening of the material under thermomechanical loading can mean a loss of available ductility and reduced fatigue life.

Multiaxial loading can lead to additional complications in component life prediction. To predict the fatigue life under multiaxial loading conditions an equivalent stress/strain approach based on yield criteria, with von Mises being the most common, is often adopted. This has proven to work in many instances, particularly when the loading is proportional. However, out-of-phase, or non-proportional, mechanical loading (where peak mechanical stresses/strains in one loading axis do not correspond with peak stresses/strains in another axis on a temporal basis) can lead to additional hardening that can be detrimental to fatigue life. In combined thermomechanical and axial-torsional loading of thin-walled tubular specimens of Haynes 188, a large variation in fatigue life was observed at similar equivalent calculated strain ranges [25]. Figure 3 shows the phase shift between the axial strain, torsional strain, and temperature for the four types axial-torsional TMF experiments performed. Figure 4 shows effect of these loading schemes on cyclic life as compared to isothermal experiments.

The durability of components in service always shows variability. Even if all the component boundary conditions (temperatures, heat fluxes, and loads) are known to high precision (a rare happenstance) there will still be an intrinsic variability in life that is dictated by inhomogeneities in the material. In the laboratory, under conditions that can be much more tightly controlled than a service environment, repeated fatigue experiments show the range of observed cyclic lives that can exceed a factor of two on the mean fatigue life. In general, the longer the cyclic life the greater the variability in life and the more defect dominated the failure initiation.

To increase the durability/reliability of a combustion component the following measures can be implemented: 1) reduce the severity of thermal gradients by altering fuel flow schedules, apply thermal barrier coatings (TBCs), change the component geometry, etc.; 2) lower the peak temperatures of the materials through increased cooling flows,

reduction in the severity of the thermal transients, etc.; 3) reduce the effect of environment by applying environmental barrier coatings (EBCs) or selection of more capable materials. If either TBCs or EBCs are applied to the component, cyclic life of the material coated with the appropriate coating should be evaluated with additional fatigue experiments at the relevant temperature. Many of these recommendations may be mutually exclusive and, as is usual, compromises will be necessary.

SUMMARY

Complex interactions among damage mechanisms are possible depending on material, temperature range, loading conditions, and environment. Extrapolations from limited data can lead to unconservative and inaccurate life prediction of the combustor devices. Conditions representative of the service environment in the durability testing of materials and components are highly desirable.

The accuracy of all life prediction models is highly dependent on the accuracy of the model inputs (temperatures, stresses/strains, material properties). It is important to identify the mechanisms causing damage in the combustor device and utilize the appropriate models to estimate the durability of the component in a reliable manner.

There is always a distribution in the number of cycles or time to failure in materials subjected to repeated loading. Multiple experiments are necessary to quantify this variability, especially at longer expected lives (typically result in higher variability in life).

To minimize damage in combustion devices: reduce thermal gradients, lower peak temperatures, reduce the effect of environment, and reduce the severity and number of thermal excursions.

REFERENCES

- [1] Halford, G. R., "Low-Cycle Thermal Fatigue," in Thermal Stresses II, Elsevier Science, 1987.
- [2] Sehitoglu, H., "Thermal and Thermomechanical Fatigue of Structural Alloys," Heat Resistant Materials, an ASM Specialty Handbook, J. R. Davis, Ed., ASM International, Oct. 1997, pp. 454-485.
- [3] Reuchet, J. and Remy, L., "Fatigue Oxidation Interaction in a Superalloy – Application to Life Prediction in High Temperature Low Cycle Fatigue," Met. Trans. A, Vol. 14A, Jan. 1983, pp. 141-149.
- [4] Sehitoglu, H. and Boismier, D. A., "Thermo-mechanical Fatigue of Mar-M247, Part 1: Experiments," J. Eng. Mater. Technol. (Trans. ASME), Vol. 112, 1990, pp. 68-80.

- [5] Halford, G. R., "Creep-Fatigue Interaction," Creep Resistant Materials, an ASM Specialty Handbook, J. R. Davis, Ed., ASM International, Oct. 1997, pp. 499-517.
- [6] Allen, D. H. and Harris, C. E., "A Review of Nonlinear Constitutive Models for Metals," NASA TM 102727, December 1990.
- [7] Dieter, G. A., Mechanical Metallurgy, 3rd edition, McGraw-Hill, 1986.
- [8] Manson, S. S. and Ensign, C. R., "A Quarter-Century of Progress in the Development of Correlation and Extrapolation Methods of Creep Rupture Data," J. of Eng. Mat. and Tech., Vol. 101, 1979, pp. 317-324.
- [9] Larson, F. R. and Miller, J., "A Time-Temperature Relationship for Rupture and Creep Stresses," Transactions of ASME, Vol. 74, 1952, pp. 765-771.
- [10] Manson, S. S. and Kalluri, S., "Long Time Extrapolation of Creep Rupture and Creep-Fatigue Properties," Proceedings of the Conference on Life Prediction for High Temperature Gas Turbine Materials, EPRI AP-4477, April 1986, pp. 6-1 to 6-34.
- [11] E606-92, "Standard Practice for Strain-Controlled Fatigue Testing", 2003 Annual Book of ASTM Standards, Vol. 03.01, ASTM International, 2003.
- [12] E2207-02, "Standard Practice for Strain-Controlled Axial-Torsional Fatigue Testing with Thin-Walled Tubular Specimens," 2003 Annual Book of ASTM Standards, Vol. 03.01, ASTM International, 2003.
- [13] Manson, S. S., "Fatigue: A Complex Subject – Some Simple Approximations," Exp. Mech., Vol. 5, No. 7, 1965, pp. 193-226.
- [14] Miner, M. A., "Cumulative Damage in Fatigue," Journal of Applied Mechanics, Vol. 12, No. 3, September 1945, (Transactions of the American Society of Mechanical Engineers, Vol. 67, 1945), pp. A159-A164.
- [15] Halford, G. R., "Cumulative Fatigue Damage Modeling – Crack Nucleation and Early Growth," Int. J. Fatigue, Vol. 19, No. 1, 1997, pp. S253-S260.
- [16] Kalluri, S. and Bonacuse, P. J., "Cumulative Axial and Torsional Fatigue: An Investigation of Load-Type Sequencing Effects," Multiaxial Fatigue and Deformation: Testing and Prediction, ASTM STP 1387, S. Kalluri and P. J. Bonacuse, Eds., American Society for Testing and Materials, West Conshohocken, PA, 2000, pp. 281-301.
- [17] Bonacuse, P. J. and Kalluri, S., "Sequenced Axial and Torsional Cumulative Fatigue: Low Amplitude Followed by High Amplitude Loading," Biaxial/Multiaxial

Fatigue and Fracture, ESIS STP 31, A. Carpinteri, M. de Freitas, and A. Spagnoli, Eds., Elsevier, 2003, pp. 165-182.

- [18] Manson, S. S., "A Critical Review of Predictive Methods for Treatment of Time-Dependent Metal Fatigue at High Temperatures," Pressure Vessels and Piping: Design Technology -1982- A Decade of Progress, S. Y. Zamrik and D. Dietrich, (Eds.), ASME, 1982, pp. 203-225.
- [19] Saltsman, J. F. and Halford, G. R. "Procedures for Characterizing an Alloy and Predicting Cyclic Life with the Total Strain Version of Strainrange Partitioning," NASA TM 4102, June 1989.
- [20] Anderson, T. L., Fracture Mechanics: Fundamentals and Applications, 2nd edition, CRC Press, Boca Raton, FL, 1995
- [21] Verrilli, M.J., Kim, Y., and Gabb, T. P., High Temperature Fatigue Behavior of Tungsten Copper Composites, NASA TM-102404, 1989.
- [22] Halford, G. R., et al., "Thermomechanical and Bithermal Fatigue Behavior of Cast B1900 +Hf and Wrought Haynes 188," in Advances in Fatigue Lifetime Predictive Techniques, ASTM STP 1122, M. R. Mitchell and R. W. Landgraf, Eds., American Society for Testing and Materials, Philadelphia, 1992, pp. 120-142.
- [23] Kalluri, S. and Halford, G. R., "Damage Mechanisms in Bithermal and Thermomechanical Fatigue of Haynes 188," in Thermomechanical Fatigue Behavior of Materials, ASTM STP 1186, H. Sehitoglu, Ed., American Society for Testing and Materials, Philadelphia, 1993, pp. 126-143.
- [24] Dreshfield, R. L., "Long Time Creep Rupture of HaynesTM Alloy 188," Superalloys 1996, R. D. Kissinger, D. J. Deye, D. L. Anton, A. D. Cetel, M. V. Nathal, T. M. Pollock, and D. A. Woodford, Eds., The Minerals, Metals & Materials Society, 1996, pp. 383-389.
- [25] Kalluri, S. and Bonacuse, P. J., "An Axial-Torsional, Thermomechanical Fatigue Testing Technique," in Multiaxial Fatigue and Deformation Testing Techniques, ASTM STP 1280, S. Kalluri and P. J. Bonacuse, Eds., American Society for Testing and Materials, West Conshohocken, PA, 1997, pp. 184-207.

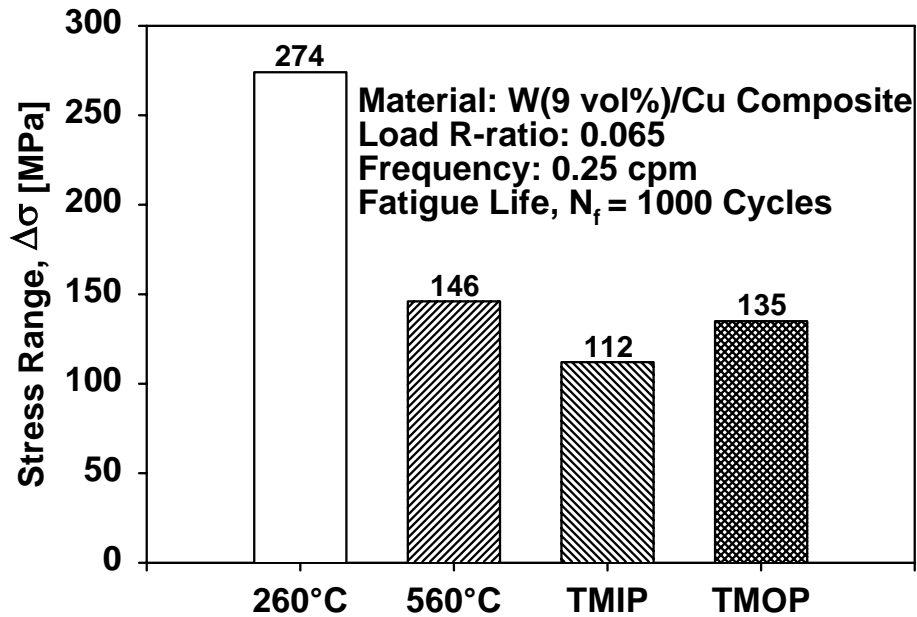


Figure 1: Stress ranges which yield 1000 cycle average life in LCF test specimens of a 9% tungsten-copper composite for isothermal and in-phase and out-of-phase thermal cycles.

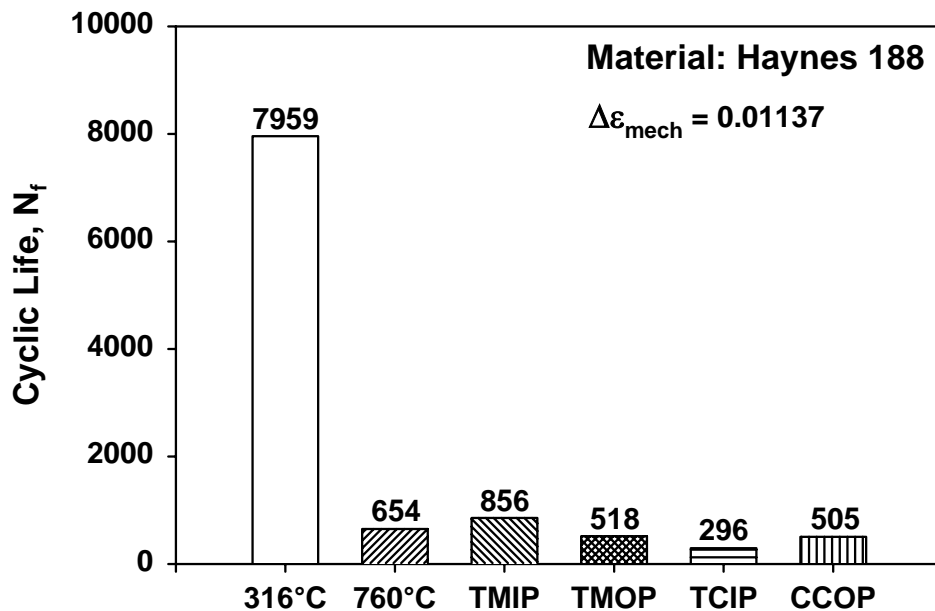


Figure 2: Comparison of isothermal fatigue, TMF (TMIP and TMOP), and creep-fatigue (TCIP and CCOP) lives with the same nominal axial mechanical strain range. All tests performed with uniaxial fatigue specimens under mechanical strain control with a fully reversed ($R_\epsilon = -1$) cycle.

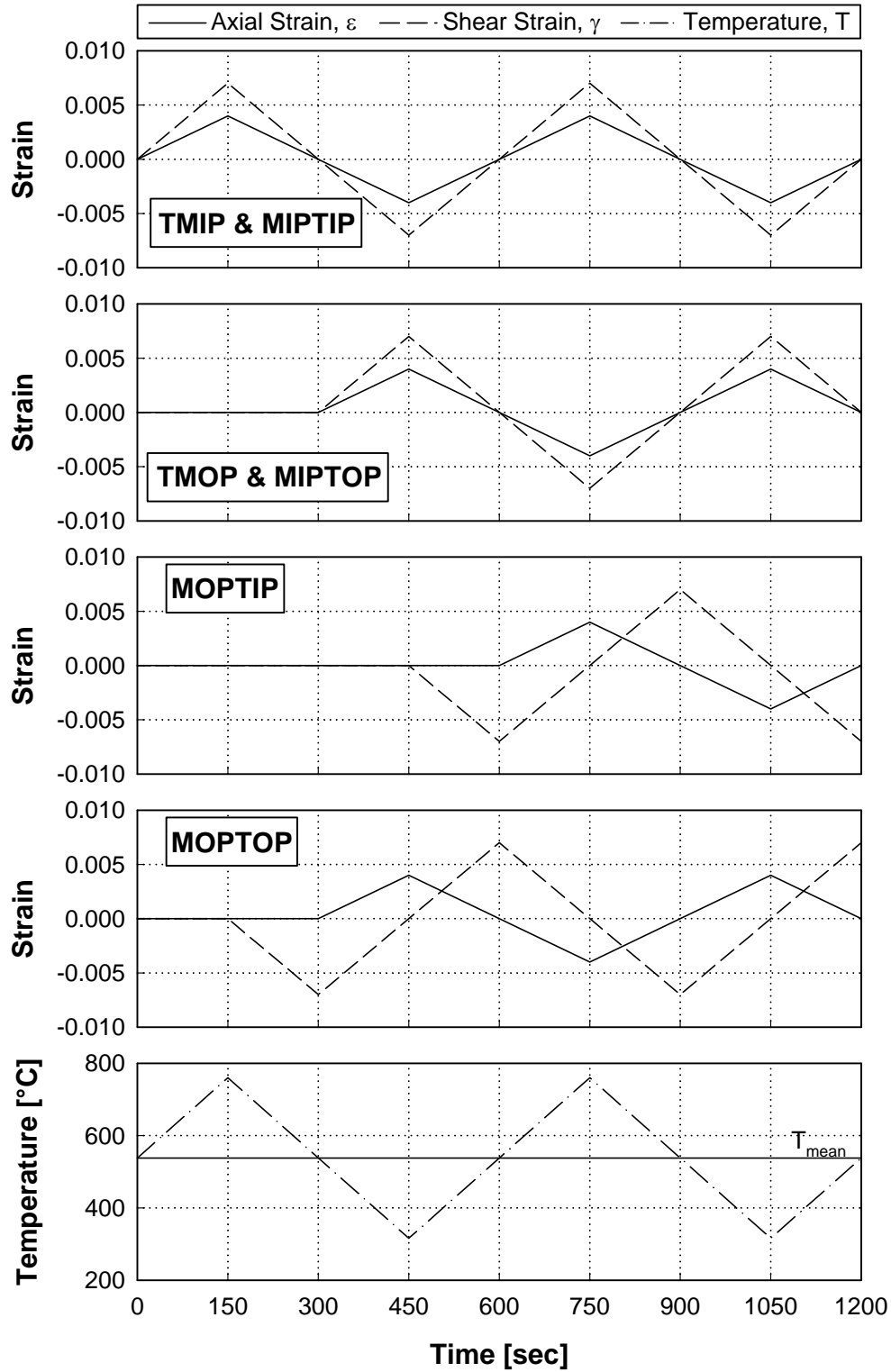


Figure 3: Schematic of axial and torsional strain and temperature command waveforms for each of the AT-TMF experiments. The uniaxial TMIP and TMOP experiments are described by simply ignoring the torsional waveform in the top two plots.

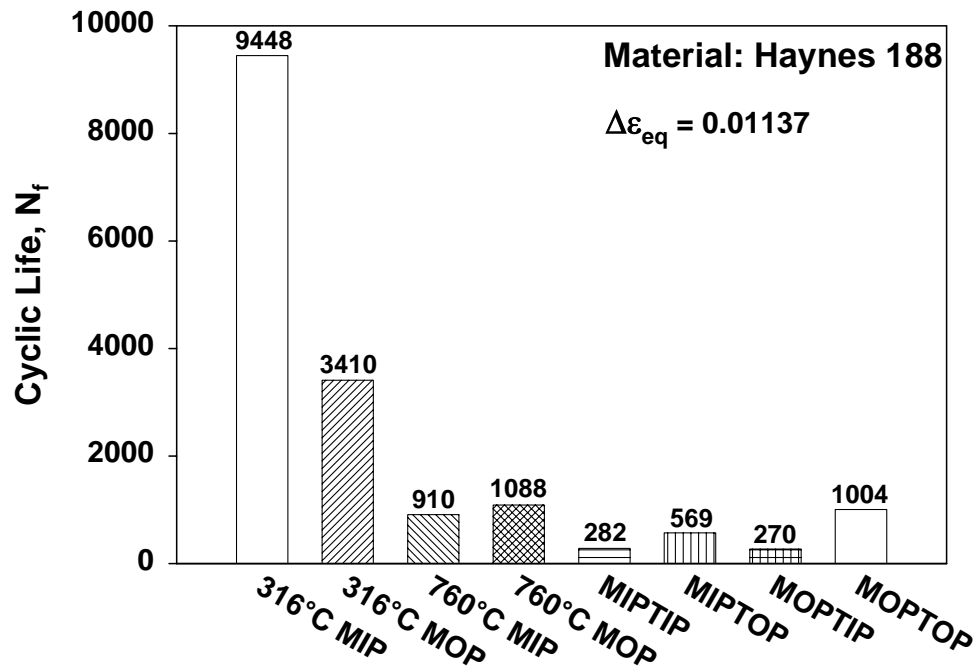


Figure 4: Comparison of isothermal, axial-torsional fatigue lives with combined axial-torsional TMF lives. All tests performed on thin-walled tubular specimens under fully reversed strain controlled fatigue cycling.

Advances In High Temperature (Viscoelastoplastic) Material Modeling for Thermal Structural Analysis



Dr. Steven M. Arnold
Senior Research Engineer
Life Prediction Branch
NASA Glenn Research Center



and

Prof. Atef F. Saleeb
The University of Akron
Civil Engineering Department

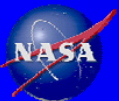


Presented

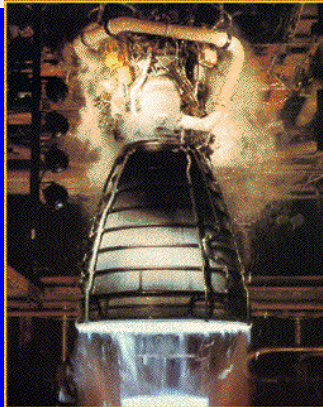
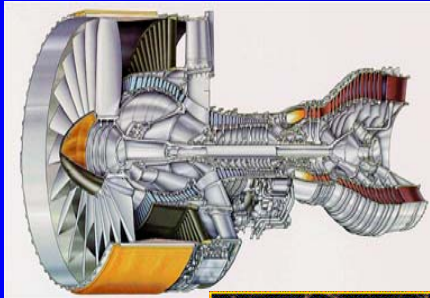
5th International Symposium on Liquid Space Propulsion,
Chattanooga , TN Oct 27-30th , 2003

OUTLINE

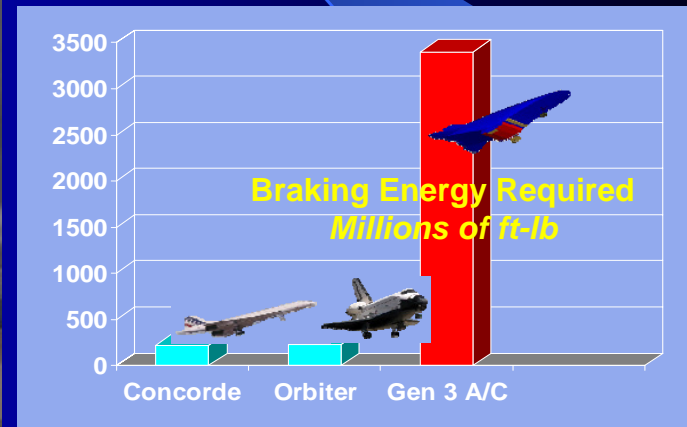
- **Background/Philosophy**
 - Elevated Material Behavior
 - Impact on Analysis
 - Multiscale Framework/Vision
- **Recent Advances**
 - Theoretical Modeling/Testing
 - Numerical Integration
 - Material Characterization



Typical High Temperature Applications Demand High Performance Materials



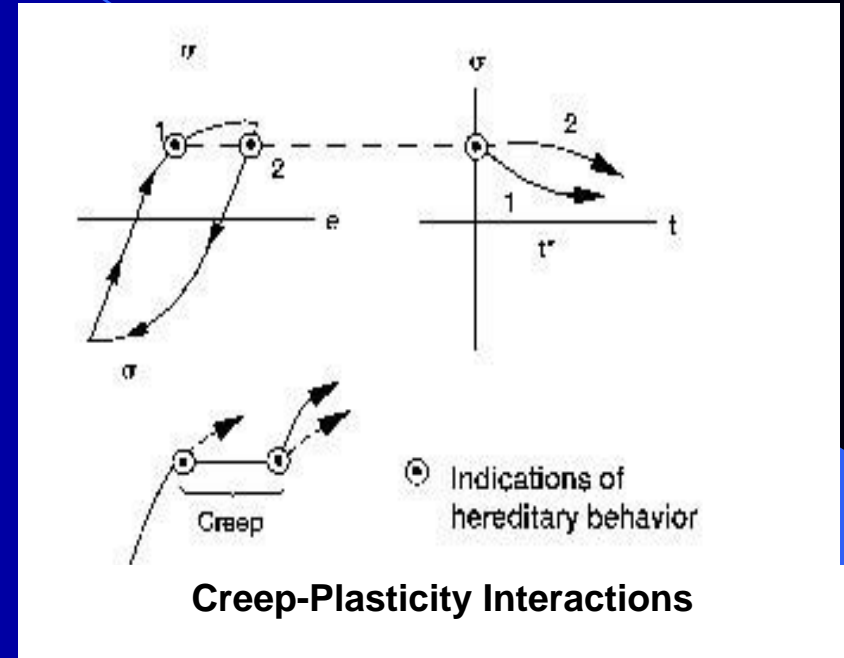
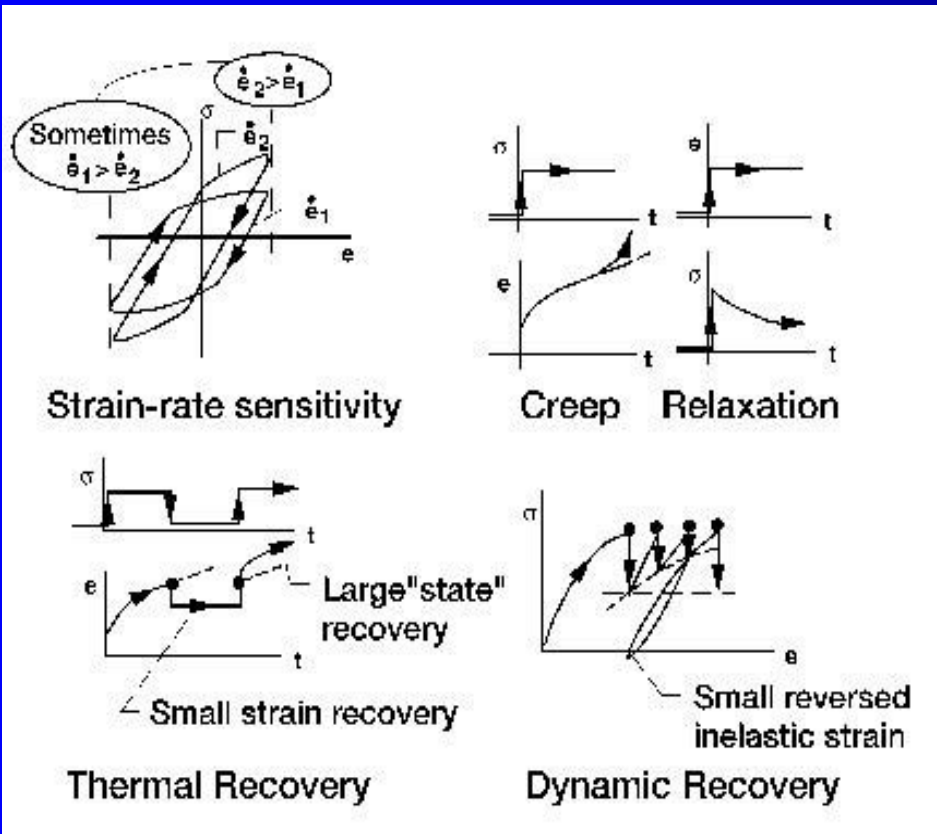
HTHL/SSTO



- Complex Thermomechanical Loading
- Complex Material response requires Time-Dependent/Hereditary Models: Viscoelastic/Viscoplastic
- Comprehensive Characterization (Tensile, Creep, Relaxation) for a variety of material systems



Important Phenomenological Observations of Behavior of Metals at High Homologous Temperatures ($T/T_m > 0.3$)

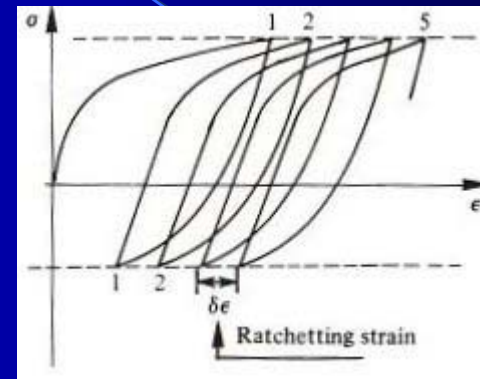
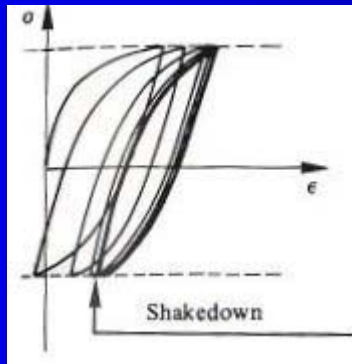


Classic Reason for Introducing Unified Viscoplastic Models (e.g., **GVIPS Class**)

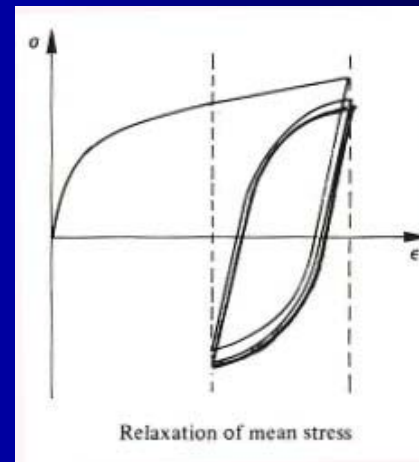
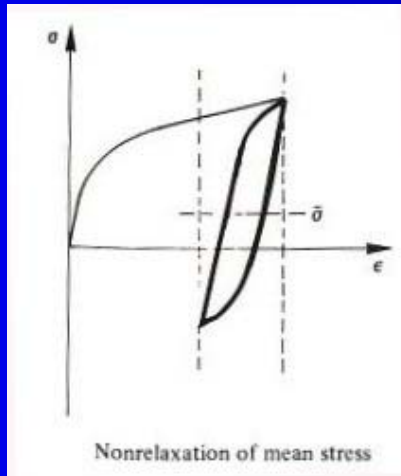
Important Phenomenological Observations of Behavior of Metals at High Homologous Temperatures ($T/T_m > 0.3$)

Cyclic Behavior

Stress-controlled



Strain-controlled



Shakedown Behavior

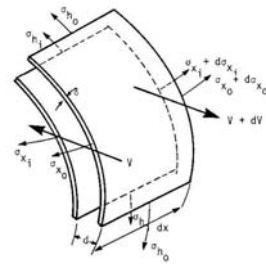
Ratchetting Behavior

Material Behavior Can Significantly Impact Structural Response (e.g. Recovery Mechanisms)

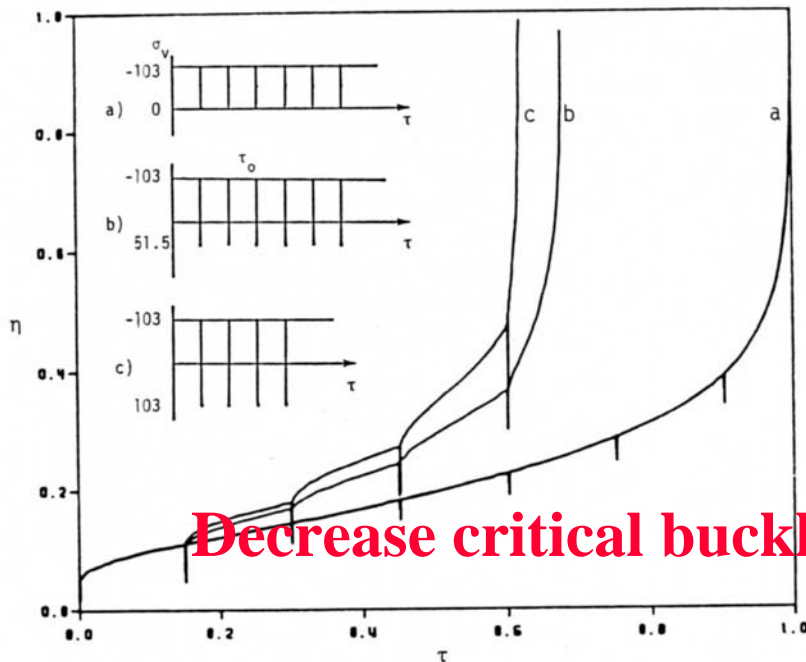
Applied Compressive Stress/Euler Stress = 0.095

Normalized Initial imperfection – 0.01

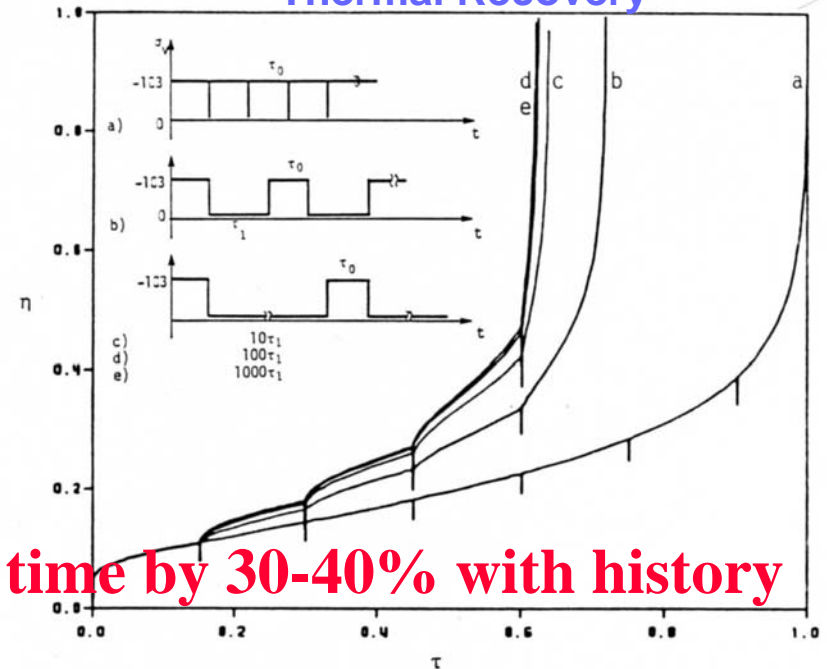
Arnold et al., "Creep Buckling of a Cylindrical Shell Under Variable Loading", Jnl of Eng Mech., ASCE, Vol. 115, No. 5, pp. 1054-1074, 1989.



Dynamic Recovery



Thermal Recovery



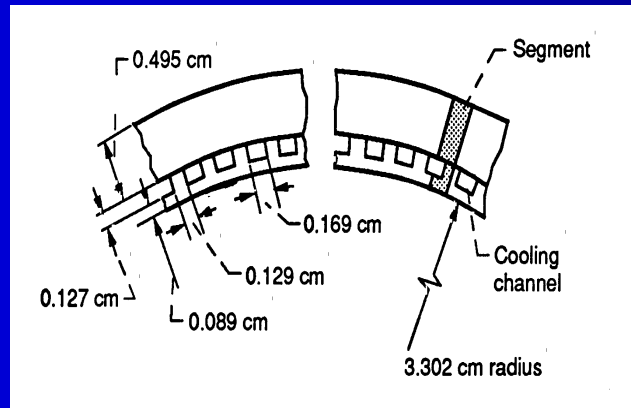
Normalized radial displacement versus normalized time for variable loading histories given in inserts

Unified Viscoplastic Models Capture Deformation Response in Rocket Engine Nozzle Liners

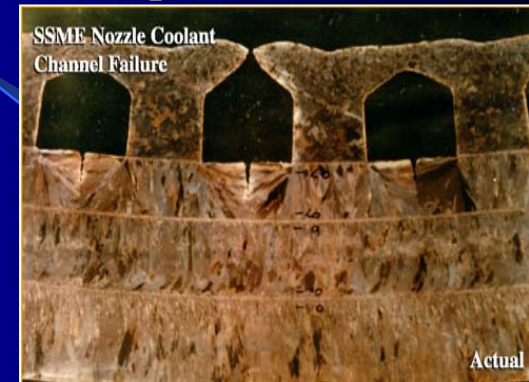
SSME



Nozzle Liner Geometry

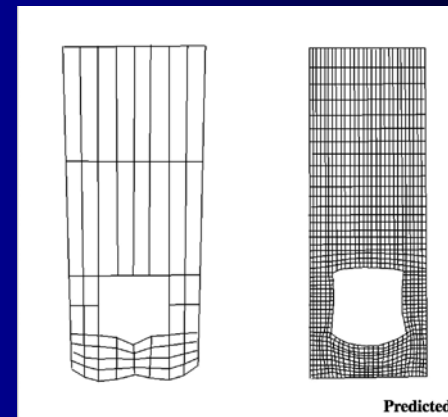


Experiment (GRC)



Prediction

Classical (Lockheed) Unified (GRC)



- Severe thermomechanical loading conditions result in irreversible strains
- Unified viscoplastic models successfully predict the experimentally observed deformation trends
 - Arya and Arnold, AIAA, Vol 30, No. 3, 1992

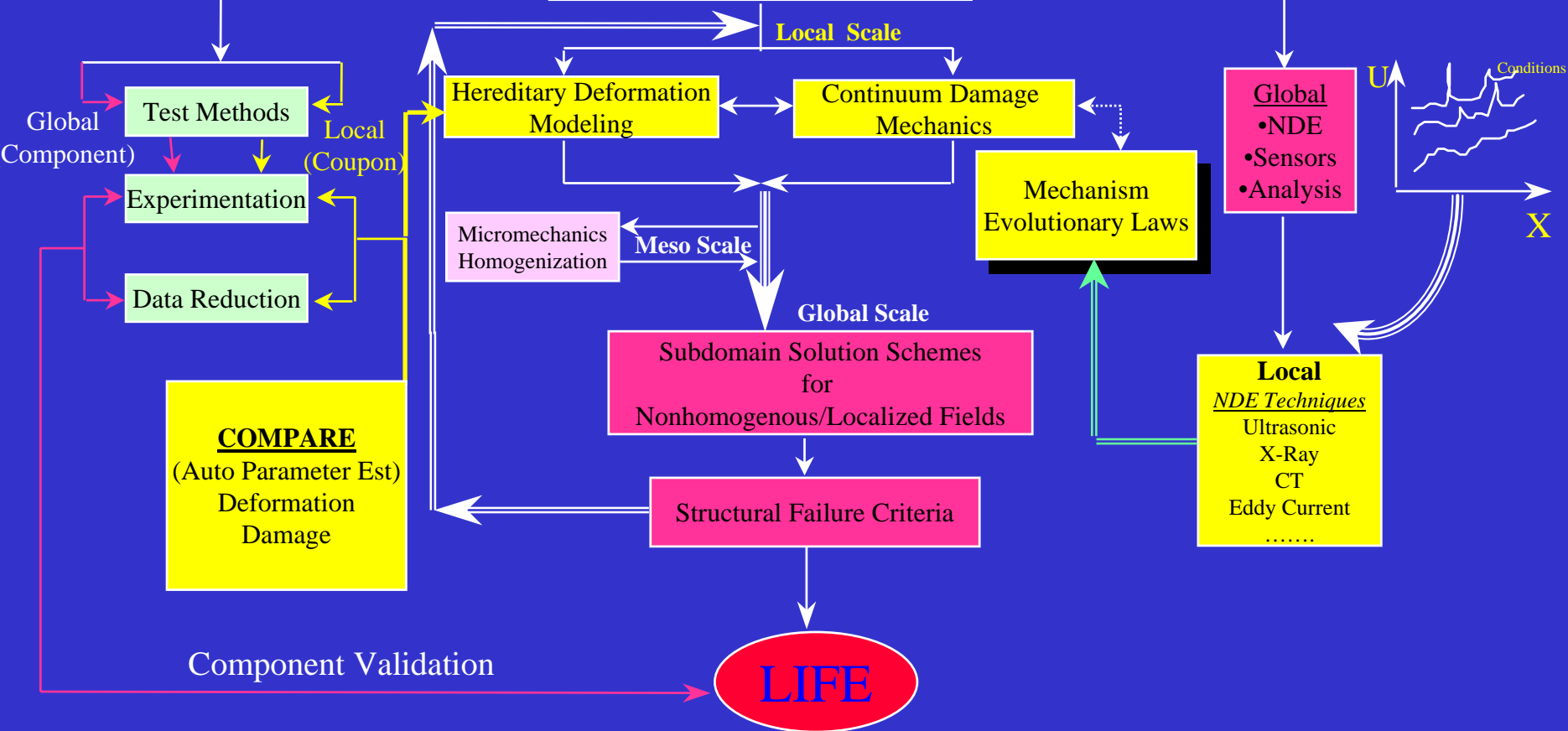


Multiscale Functional Framework for Deformation and Life Modeling

Characterization/Validation

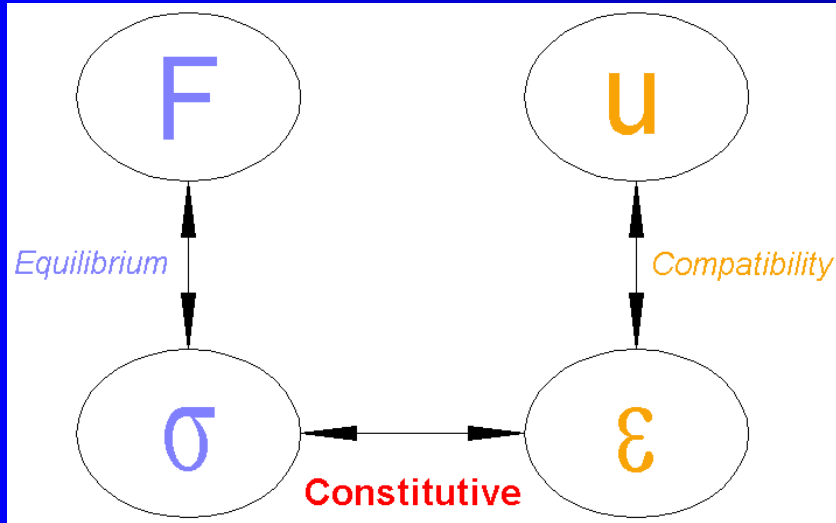
Structural Analysis

Detection Techniques



CONSTITUTIVE MODELING

Structural Mechanics Problem



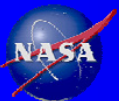
Knowledge of the material's life and constitutive behavior is a prerequisite for assessment of component performance/reliability

Need to concurrently address three important and related areas:

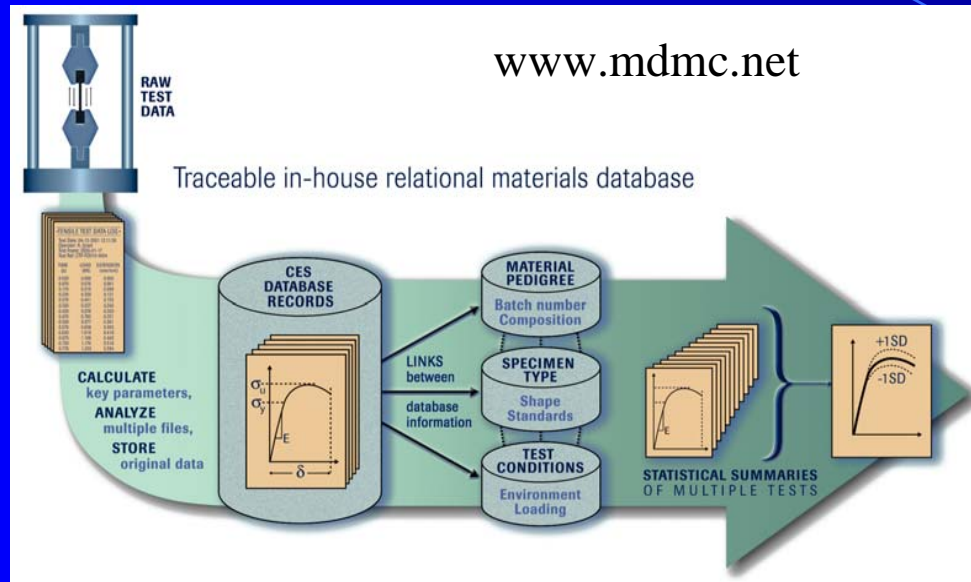
- i) mathematical formulation for the accurate multiaxial representation
GVIPS Classes
- ii) algorithmic developments for the updating (integrating) of external and internal state variables - FEA User Definable Subroutines
- iii) parameter estimation - COMPARE

This approach allows one to overcome the two major obstacles for practical utilization of sophisticated time-dependent (hereditary) models:

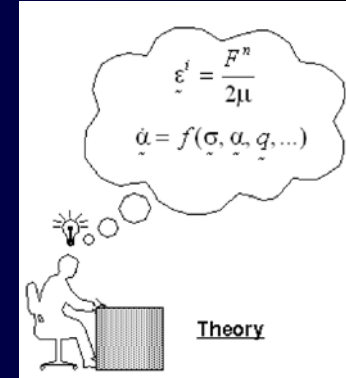
- 1) lack of efficient and robust integration algorithms - FEA Linkage issues
- 2) difficulties associated with characterization of large number of material parameters and appropriate experimental “data content” - COMPARE & sensitivities



The Desired Vision For Design and Analysis



Mathematical Characterization Of Material Behavior

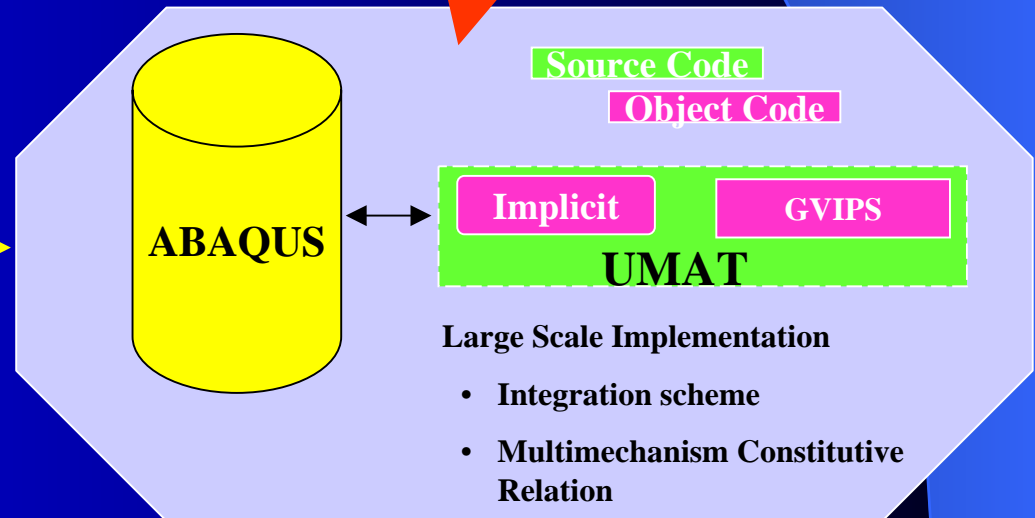


COMPARE

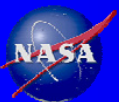
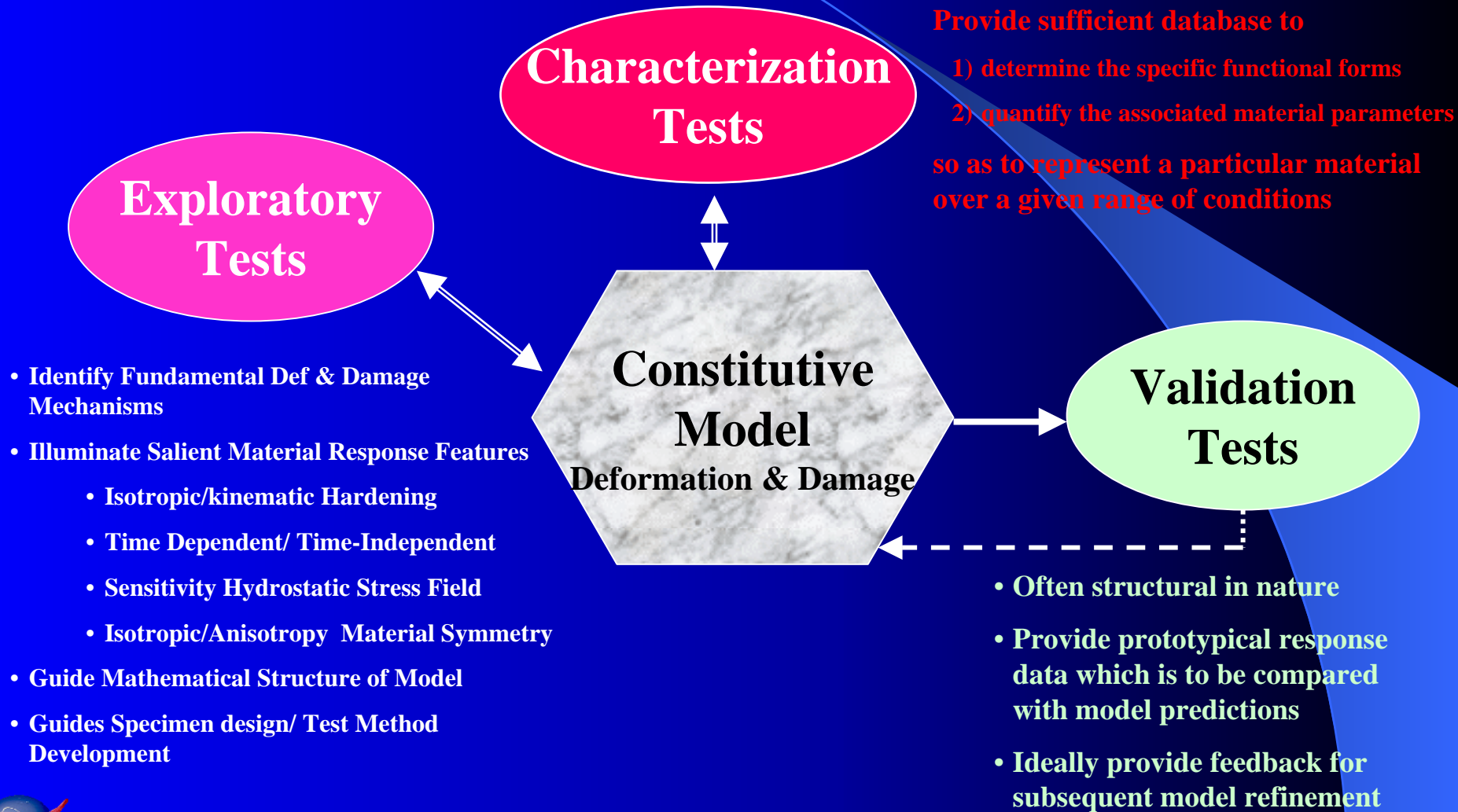
Automatically write required input information



FEA Analysis of component



Thermomechanical Testing in Support of Constitutive Model Development



Experimental Observations

• Reversibility

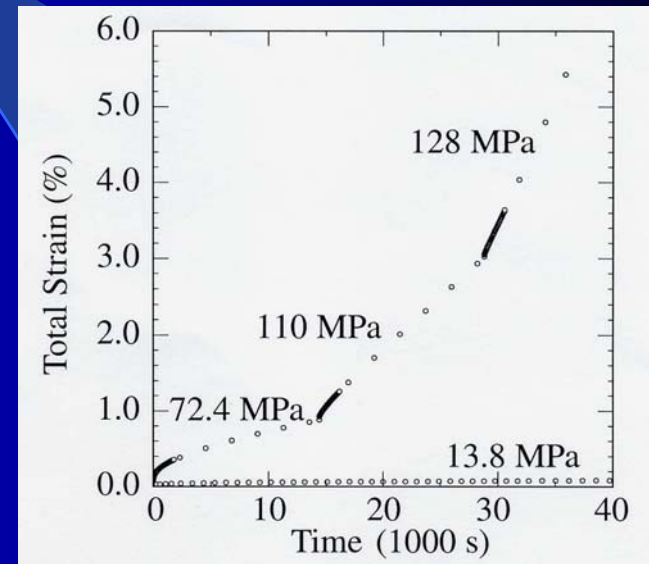
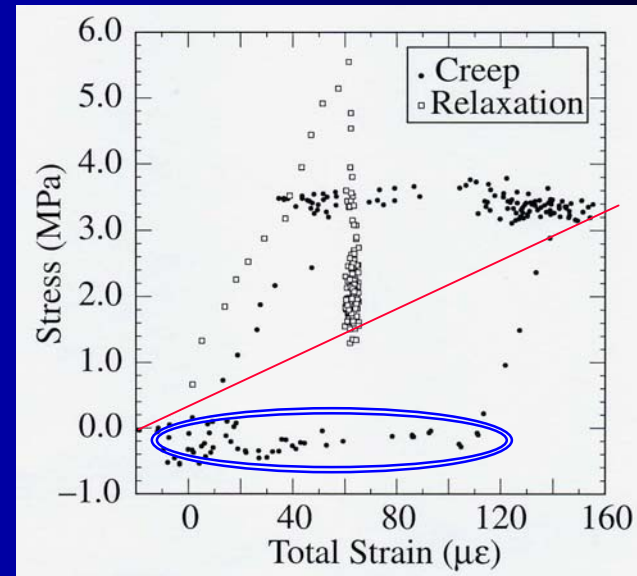
- rate-dependent instantaneous stiffness
- transient creep/relaxation
- **limit equilibrium state**

• Theoretical demarcation (Exp. Verified)

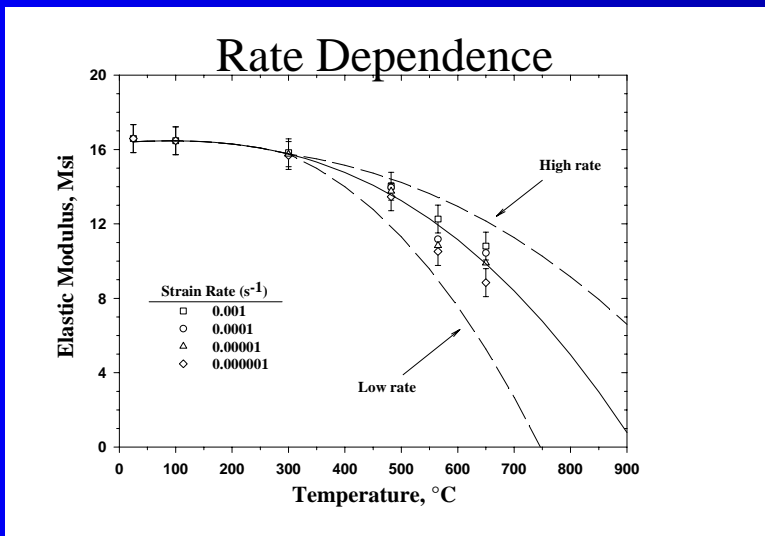
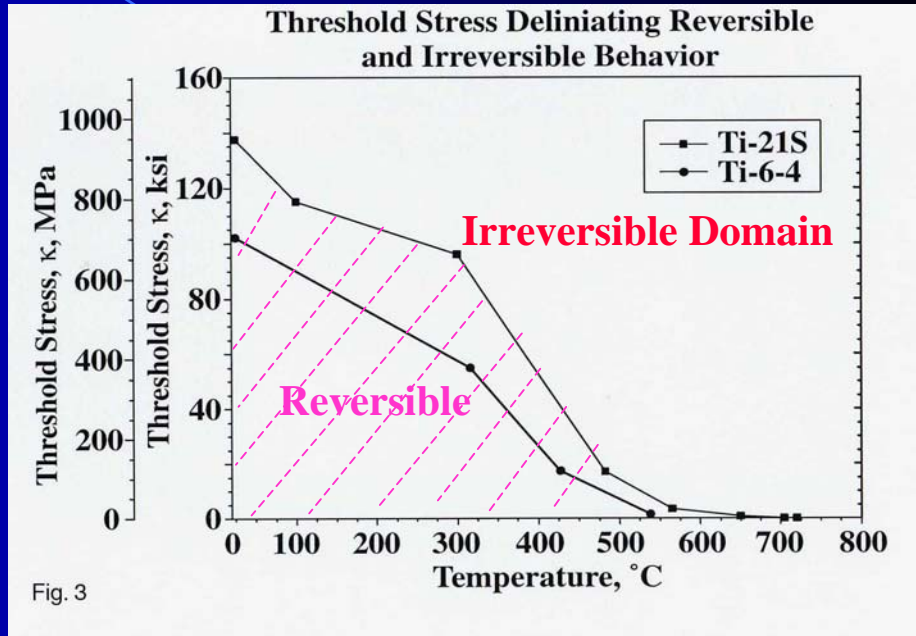
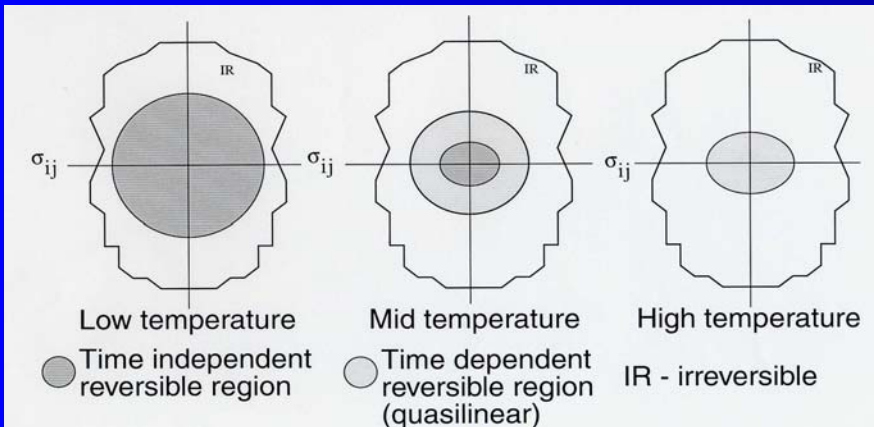
• Irreversibility

- strain-stress dependent
- nonlinearity
- strain rate dependence
- creep with steady-state
- relaxation with finite residual state
- creep/plasticity interaction
- thermal recovery
- nonlinear kinematic/isotropic hardening

- Anelastic recovery during reversal in both quasilinear and fully developed inelastic regions



Experiments Indicated Existence of Reversible and Irreversible Threshold Surface



*Experimentally verified for both
TIMETAL 21S and Ti-6-4*

*GRCop-84 doesn't appear to
exhibit strong viscoelastic response*



Theoretical/Computational Motivation

In view of four + decades of active research in the area of inelastic behavior modeling, the **need** still exists for an:

Accurate representation of material response details over an extensive domain of time, stress, temperature, loading conditions ...

Assessment

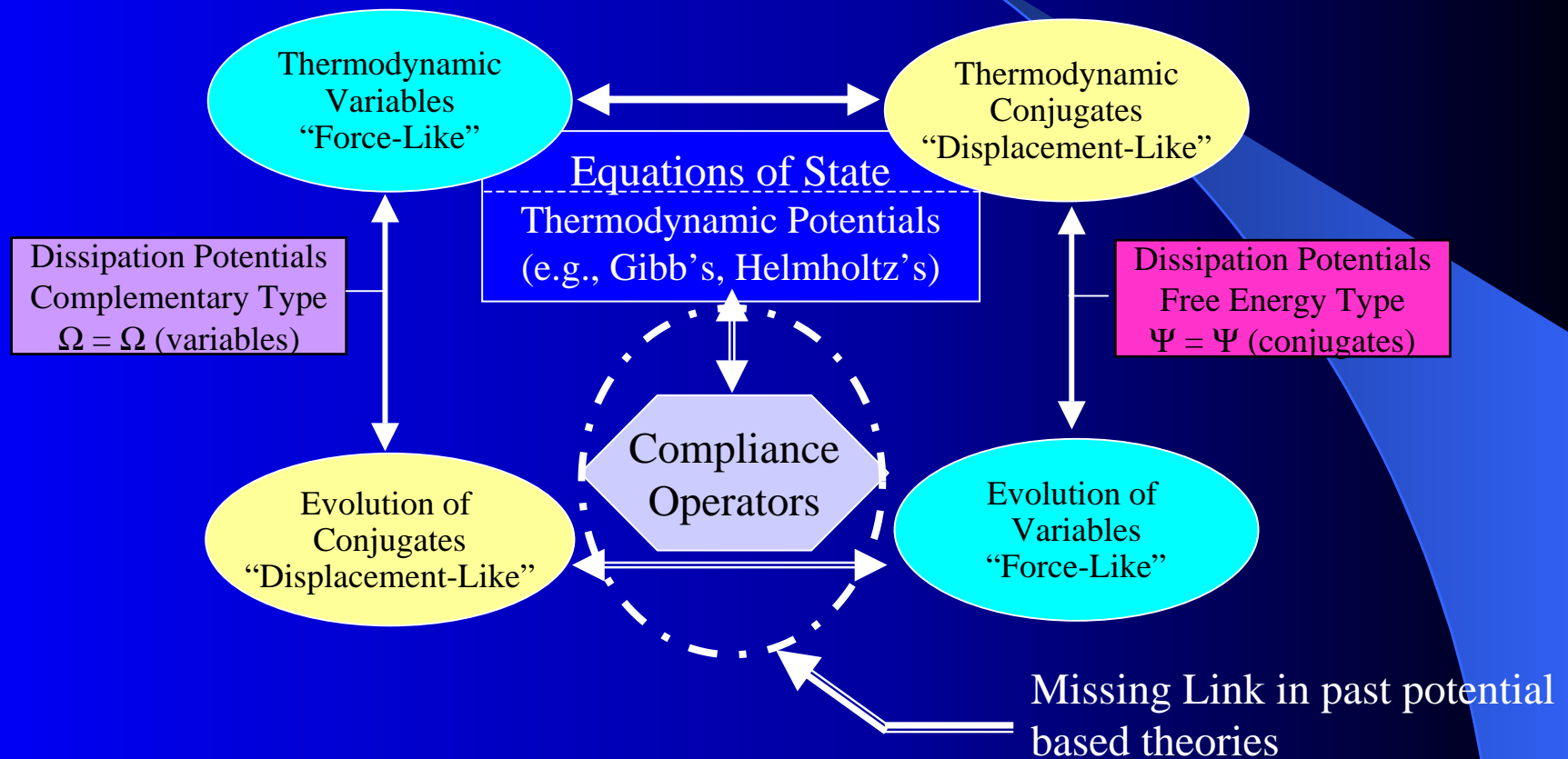
Technical

Practical Implication

Non-associative - Nonsymmetric Tangent Stiffness - Coupled system of Stiff Diff. Eq.	⇒ Non-uniqueness of solution ⇒ Implementation into large scale FEA codes problematic ⇒ Difficult to integrate
Numerous nonphysical material parameters	⇒ Requires expertise to characterize model
Single-mechanism models	⇒ Qualitatively capable, yet quantitatively limited in response spectrum

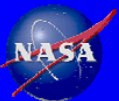


Utilize Concept of Thermodynamic Internal State Variables to Obtain Constitutive Equations

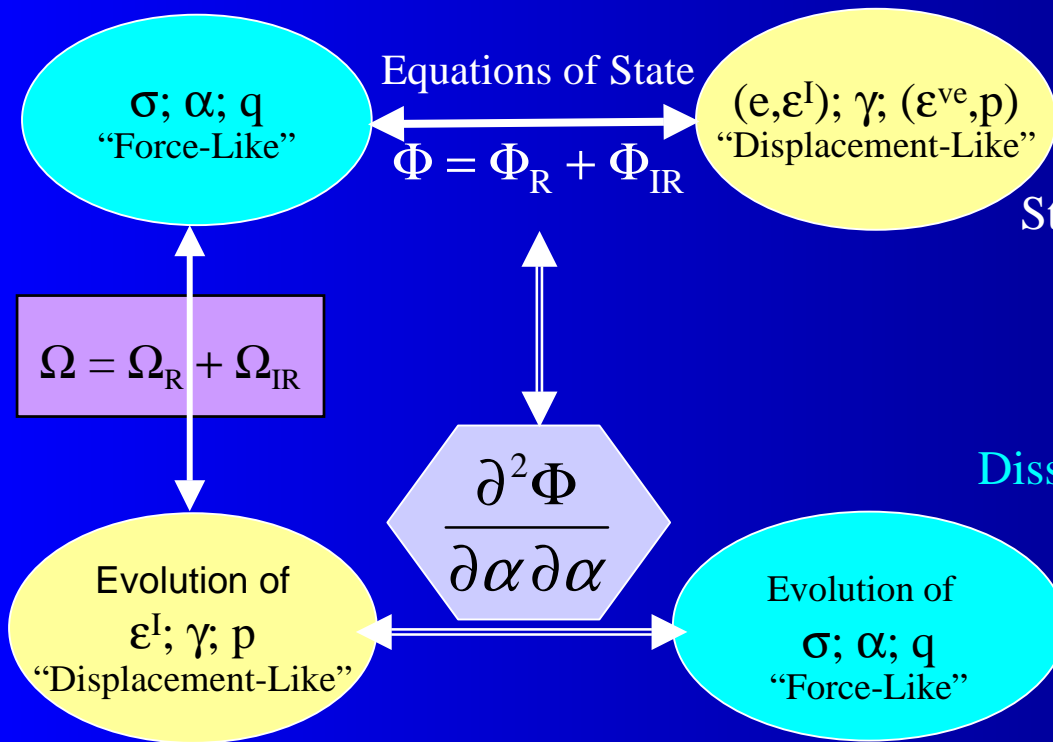


Advantages and Attributes of Potential Formulation

- Provides a consistent framework for deformation and damage modeling
 - Nonisothermal and/or anisotropic extension straight forward
 - Nonproportional loading histories automatic
 - Automatic satisfaction of the Dissipation Inequity of Thermodynamics
- Eliminates the “ad-hoc” nature of model development
- Provides sufficiently general variational structure.
- Constitutes cornerstone of regularity and bounding (or limit) theorems in plasticity and viscoplasticity.
- Lends itself to robust numerical implementation



Physical Mechanisms Underlying The Partitioning of Energy : Complementary Type



Total = Stored + Dissipated

$$\sigma e = \Phi + \Omega$$

Stored (Φ) = Reversible + Irreversible

Lattice Distortion Dislocation Pile-up

Reflects change in microstructure

Dissipation (Ω) = Reversible + Irreversible

Dislocation bowing Deformation & Thermally driven Mechanism

Reflects mobility/rate of evolution in microstructure

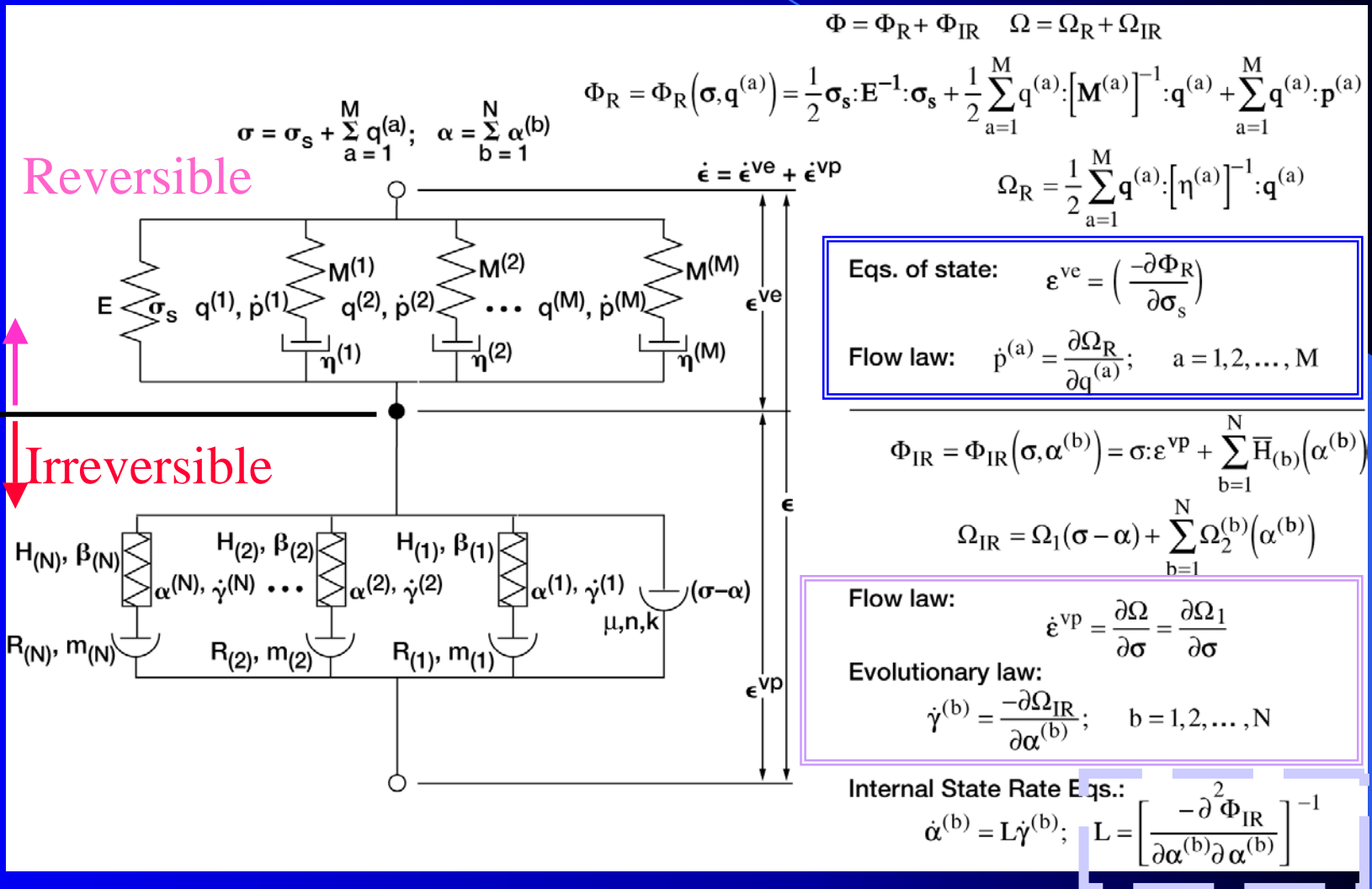
Irreversible = Ω_1 (deformation) + Ω_2 (diffusional; mass/vacancy)

Glide/plastic Slip

- Thermal recovery
- Dislocation/boundary interaction
- Formation of cell structure



General Multimechanism Hereditary Behavior Model of the GVIPS Class



Specific Choice of Energy Potentials and Material Functional Forms

$$\Phi_R = \Phi_R(\boldsymbol{\sigma}_{ij}, \mathbf{q}_{ij}^{(a)}) = \frac{1}{2}(\boldsymbol{\sigma}_s)_{ij} \mathbf{E}_{ijkl}^{-1}(\boldsymbol{\sigma}_s)_{kl} + \frac{1}{2} \sum_{a=1}^M \mathbf{q}_{ij}^{(a)} [\mathbf{M}_{ijkl}^{(a)}]^{-1} \mathbf{q}_{kl}^{(a)} + \sum_{a=1}^M \mathbf{q}_{ij}^{(a)} \mathbf{P}_{ij}^{(a)}$$

$$\Phi_{IR} = \Phi_{IR}(\boldsymbol{\sigma}_{ij}, \boldsymbol{\alpha}_{ij}^{(b)}) = \boldsymbol{\sigma}_{ij} \boldsymbol{\varepsilon}_{ij}^{up} + \sum_{b=1}^N \bar{H}_{(b)}(G^{(b)})$$

Stored Energy

and

$$\Omega_R = \frac{1}{2} \sum_{a=1}^M \mathbf{q}_{ij}^{(a)} [\boldsymbol{\eta}_{ijkl}^{(a)}]^{-1} \mathbf{q}_{kl}^{(a)}$$

$$\Omega_{IR} = \Omega_1(F) + \sum_{b=1}^N \Omega_2^{(b)}(G^{(b)})$$

Dissipation

where

$$F = \frac{1}{2\kappa^2} (\boldsymbol{\sigma}_{ij} - \boldsymbol{\alpha}_{ij}) \mathcal{M}_{ijkl} (\boldsymbol{\sigma}_{kl} - \boldsymbol{\alpha}_{kl}) - 1$$

$$G^{(b)} = \frac{1}{2\kappa_{(b)}^2} (\boldsymbol{\alpha}_{ij}^{(b)} \mathcal{M}_{ijkl} \boldsymbol{\alpha}_{kl}^{(b)})$$

and the specific functions :

$$\Omega_1(F) = \int \frac{\kappa^2 F^{\alpha}}{2\mu} dF$$

$$\Omega_2^{(b)}(G^{(b)}) = \kappa_{(b)}^2 \int \frac{r(G^{(b)})}{h(G^{(b)})} dG^{(b)}$$

$$\bar{H}_{(b)} = \kappa_{(b)}^2 \int \frac{1}{h(G^{(b)})} dG^{(b)}$$

$$h_{\text{const}}(G^{(b)}) = \frac{H_{(b)}}{[G^{(b)}]^{\beta_{(b)}}}$$

$$r(G^{(b)}) = R_{(b)} [G^{(b)}]^{m_{(b)}}$$

$$h_{\text{sat}}(G^{(b)}) = H_{(b)} \left\langle 1 - \sqrt{G^{(b)}} \right\rangle^{\beta_{(b)}}$$



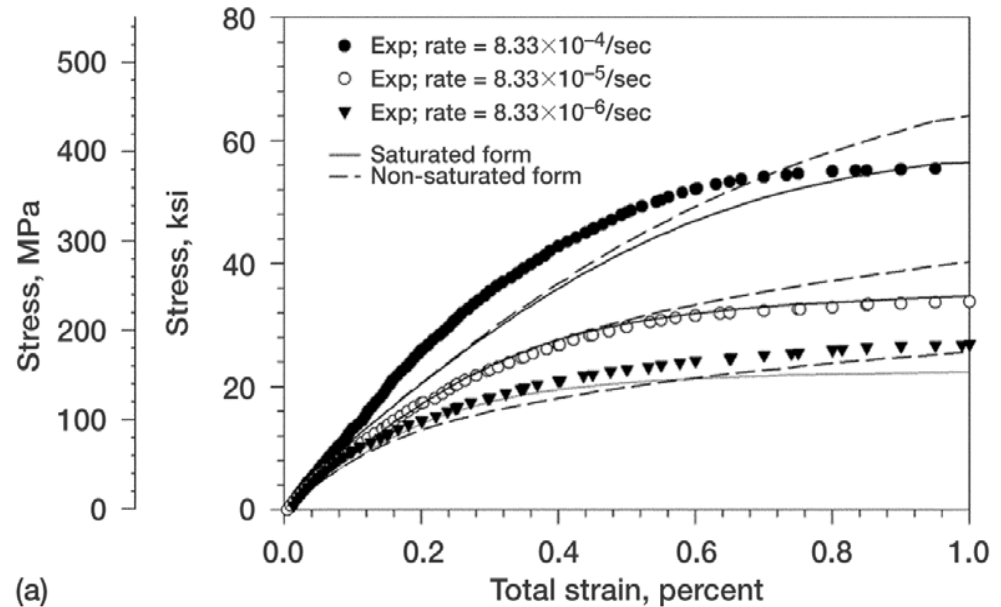
Results Illustrating Recent Improvements Made to the Hardening Functional Form in GVIPS Model

Previous Non-saturating
 $g(G) = H / G^\beta$

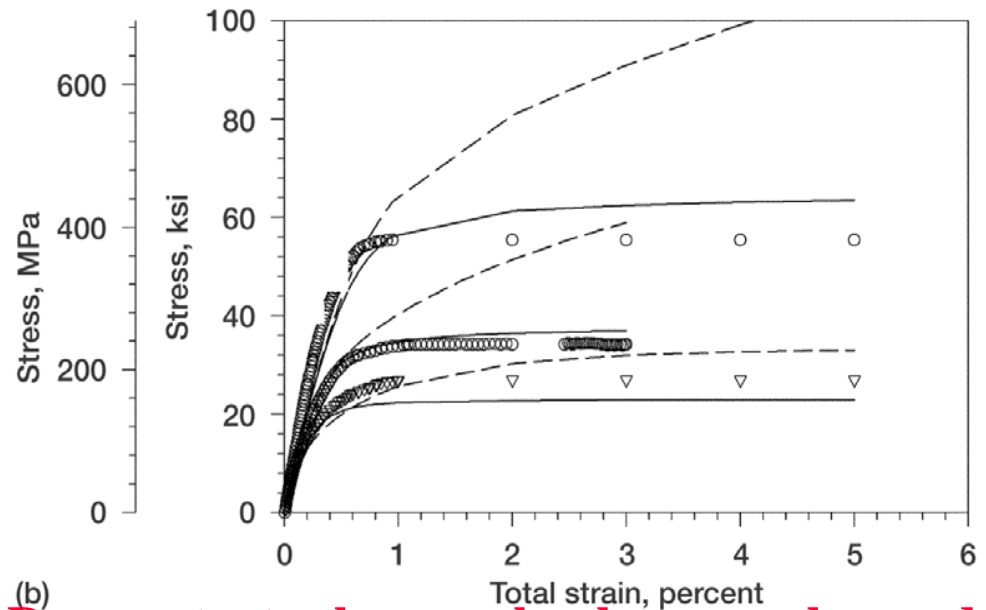
Current Saturating Form
 $g(G) = H(1-G)^\beta$

$$G = [1/2(\alpha_{ij} \alpha_{ij}) / K^2_{(b)}]^{0.5}$$

TIMETAL 21S: 650°C
 Strain Controlled Tensile
 Single Mechanism



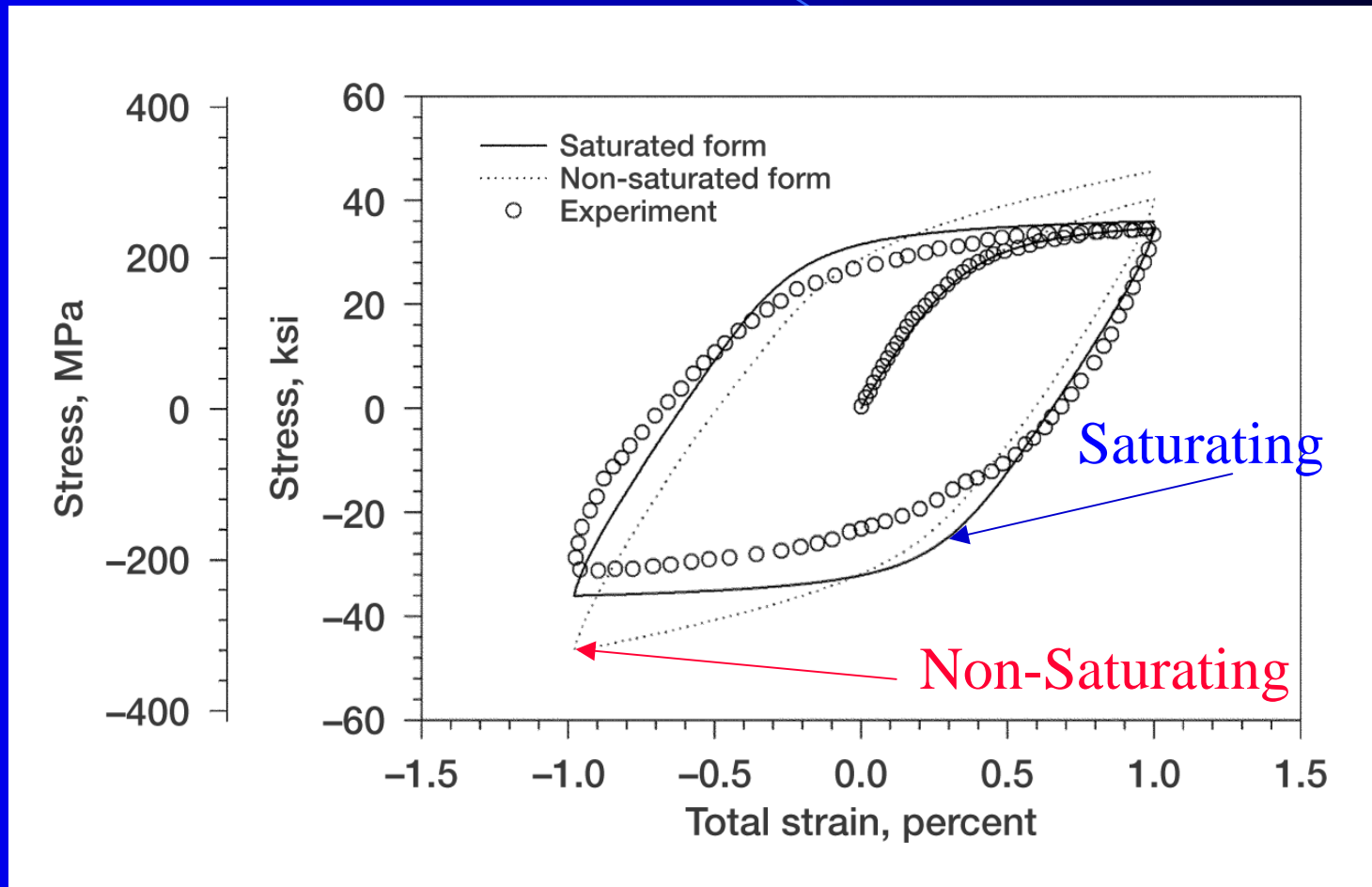
(a)



(b)

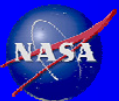
Demonstrates how scale-abuse can be used

Comparison of Specific Hardening Forms Under Cyclic Loading



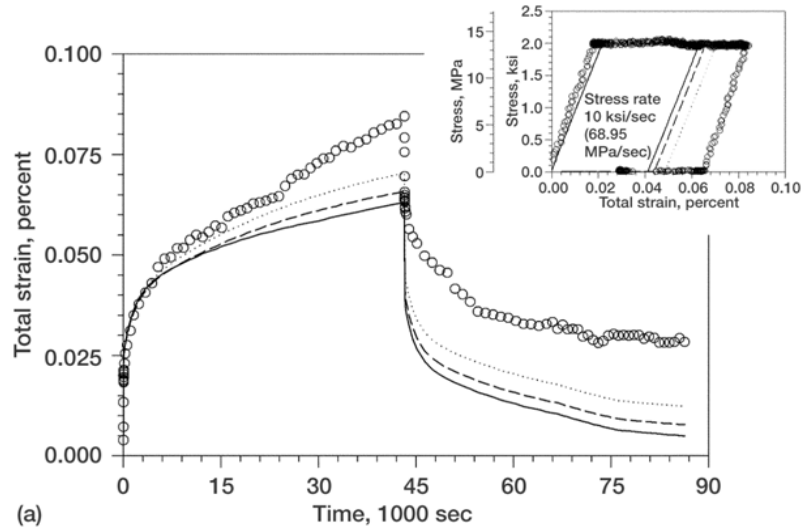
TIMETAL 21S: 650°C

Strain Controlled

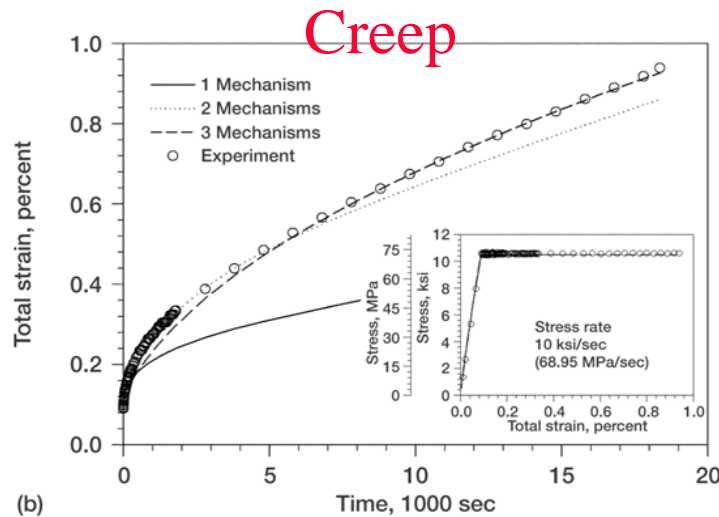


New Saturating Form Does Not Adversely Impact Ability to Represent Creep/Relaxation

- But need at least two mechanisms to capture both creep and relaxation well

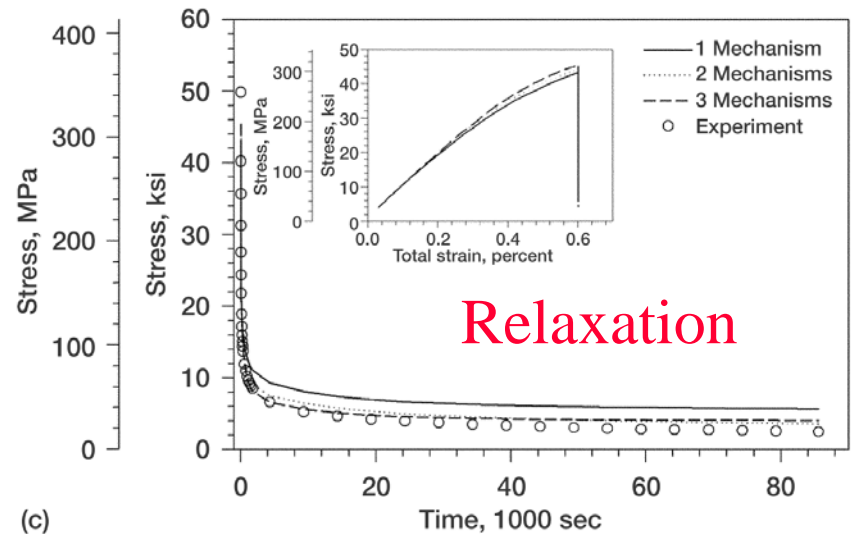


(a)



Creep

(b)



Relaxation

(c)



Robust Integration Scheme Key For Efficient Inelastic Finite Element Analysis

Common approaches for integration of rate equations:

1) Non-Iterative: explicit; semi-implicit

No local iterations less overhead
stability problems

2) Iterative: fully-implicit

Requires local iterations additional overhead

Unconditional stability

Consistent Tangent Stiffness

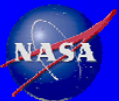
Quadratic Convergence of global
Newton-Raphson Iterations

Selected:

Backward Euler with Line Search

Advantages of Implementation

- Directly applicable for 3-D and sub-space loading(plane strain, axisymmetric, etc)
- Generalized Material Symmetry Operators (which influence flow, hardening, recovery, relaxation spectrum, etc.)
- Efficiency (through explicit algorithmic tangent stiffness)
- Robustness (through “slack” line search)

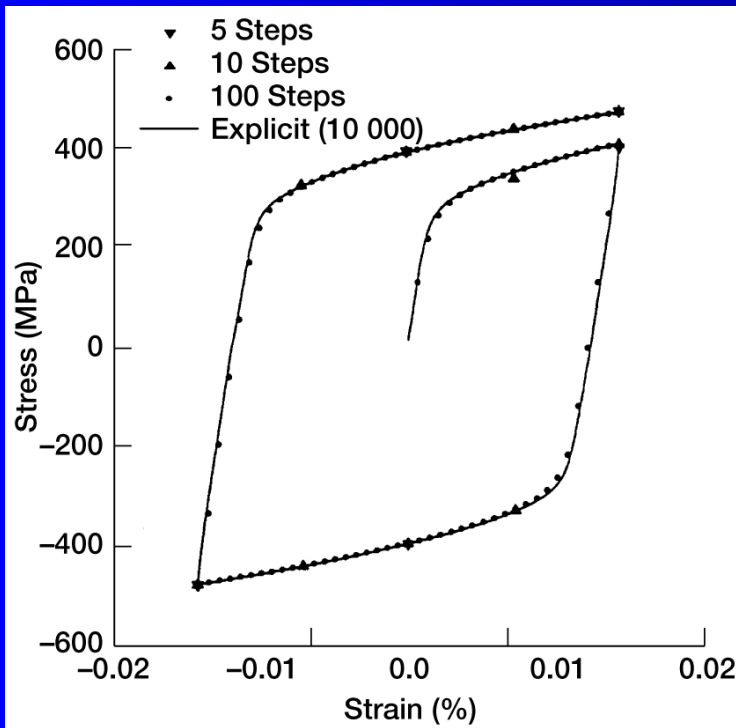


Results Illustrating the Efficiency of The Numerical Implementation of GVIPS

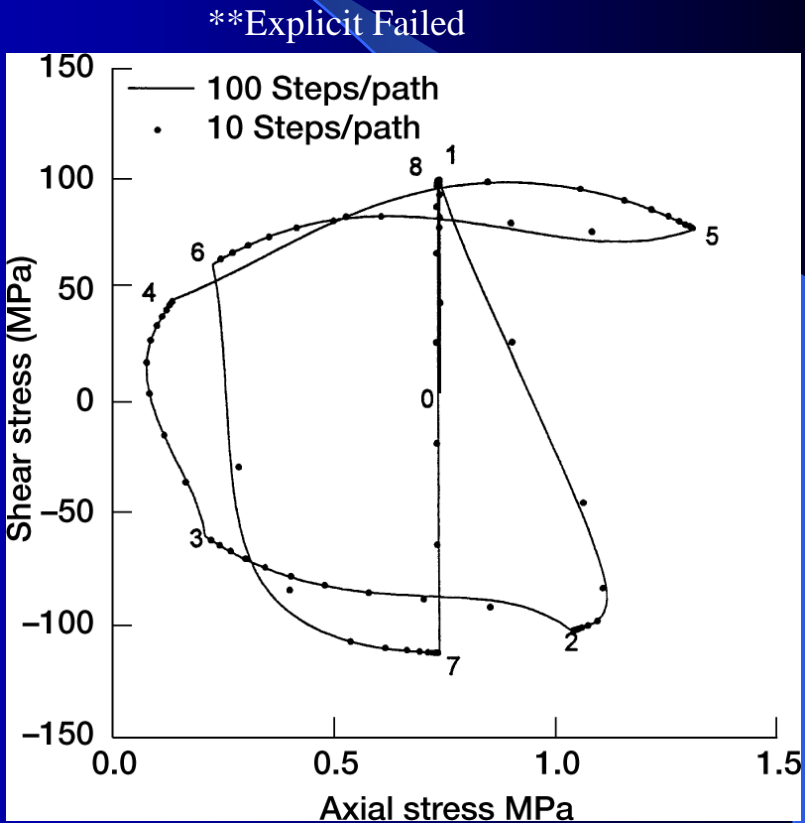
Backward Euler with Line Search

W/Kanthal , $\dot{\epsilon}=2 \times 10^{-3} / s$, $\epsilon_{max}=0.0144$

method	number of load steps	CPU time	GIT	LIT
explicit	10,000	180.0	3	0
implicit	100	5.0	2	4
implicit	10	1.05	4	10
implicit	5	1 (54 s)	10	20



Under cyclic conditions



Under nonproportional loading conditions



Key to Accurate Characterization of GVIPS Involves Sufficient “Data Content”

Viscoelastic Material Parameters

2+2M number, i.e., E_s , ν , $(M_{(a)}, \rho_{(a)})$

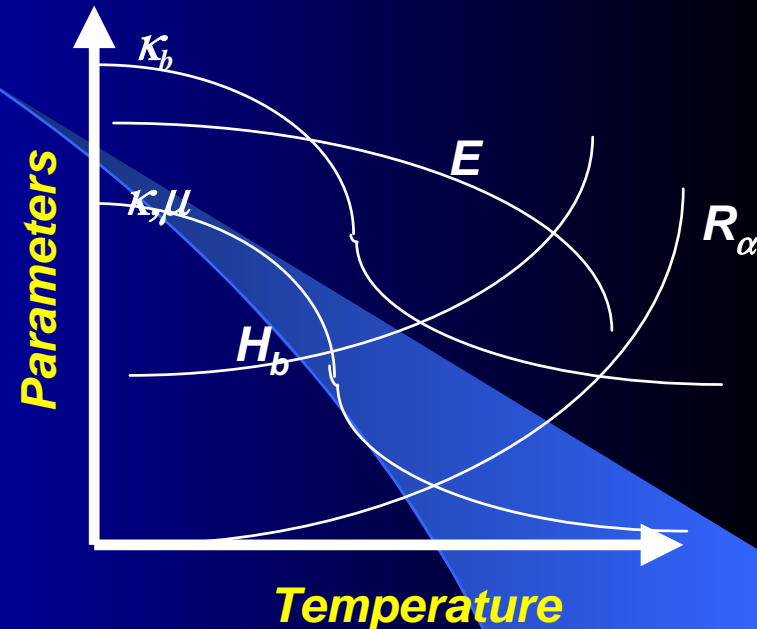
Viscoplastic Material Parameters

- Flow κ , μ , n
- Hardening H_b , K_b and β ,
- Recovery: R_b and m_b

3 + 5N irreversible material constants

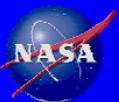
Types of Experimental Tests

- Strain controlled Tensile Tests (multiple rates)
- Creep Test (Monotonic and/or step)
- Relaxation (Monotonic and/or step)
- Cyclic Tests (Fully reversed, ratcheting)
- Biaxial Tests (tensile, creep, relaxation, cyclic)

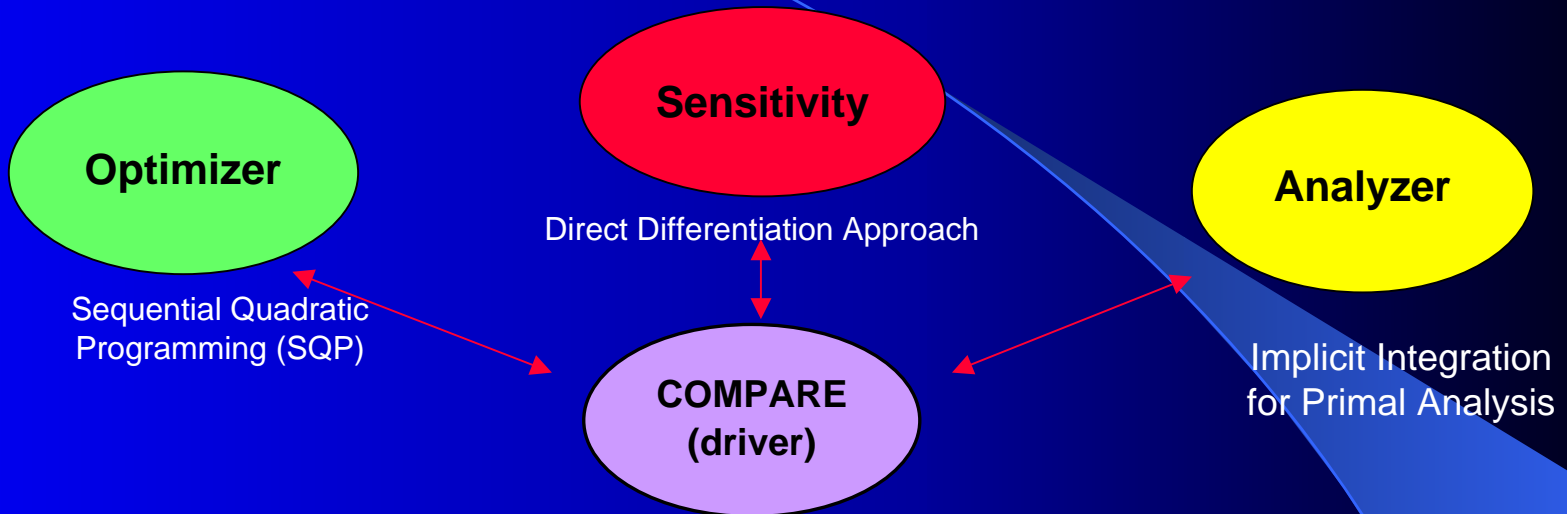


Desire a **mixture** (rather than numerous of one type) **of tests** at numerous temperatures

Quality vs. Quantity



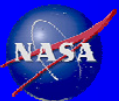
COMPARE CORE



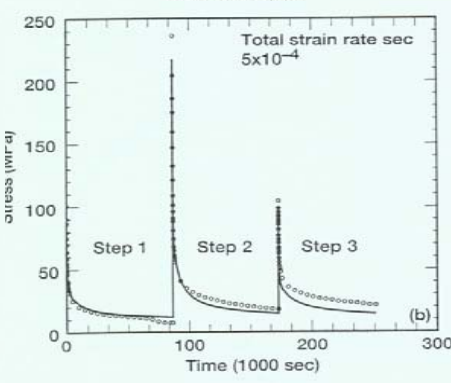
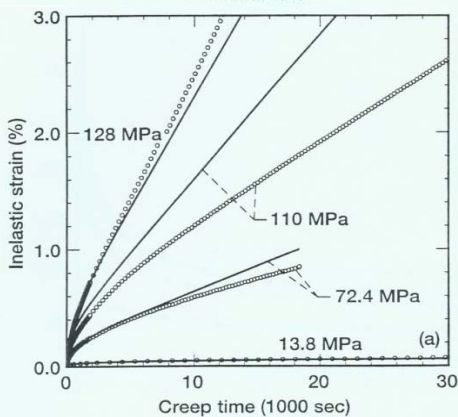
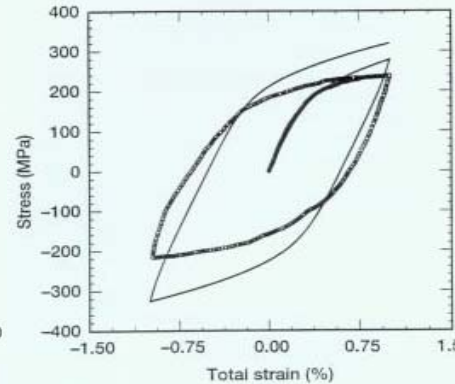
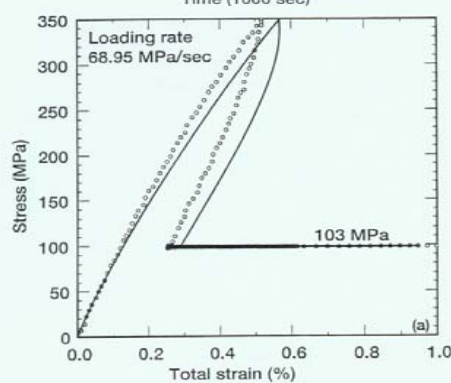
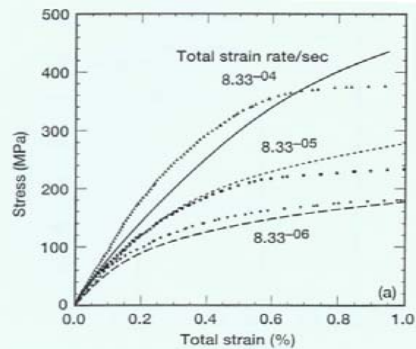
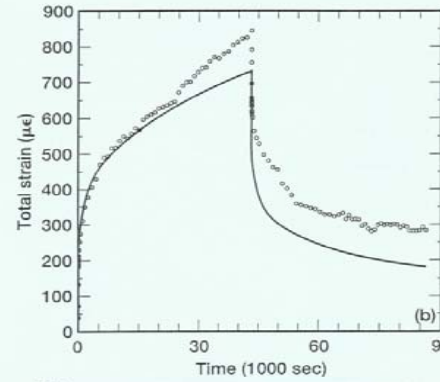
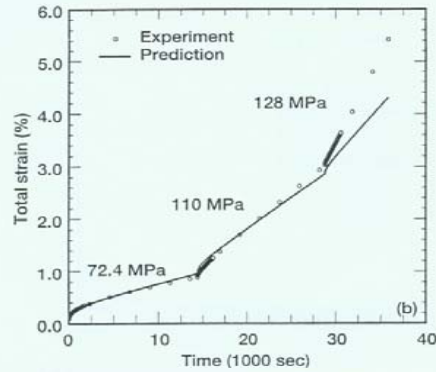
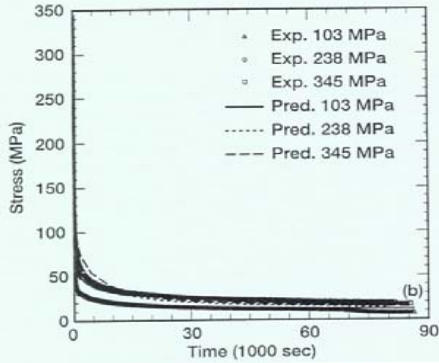
- Identify active/passive variables for a test
- Scaling design variables and objective function
- Formulating a single design optimization problem weighted objective function.
Constraints
sensitivities

Results

- Final Optimum Material Parameters
- Combined & Individual Error Functions



Comprehensive Characterization of The Deformation Response of TIMETAL21S

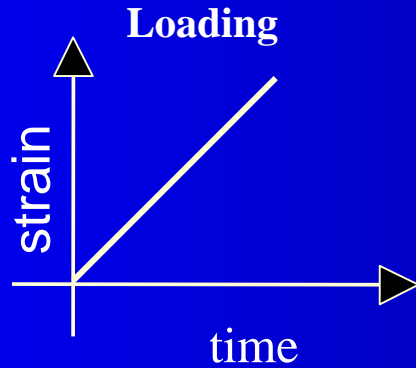


“DATA CONTENT” IS HUGE ISSUE

Wide Range of Application

- Stress: 1 → 60 Ksi
- Time: 2 → 90000 sec
- Temp: 650 C
- Loading Rates: $10^{-2} \rightarrow 10^{-10}$

Characterization of IN738LC @ 850 °C

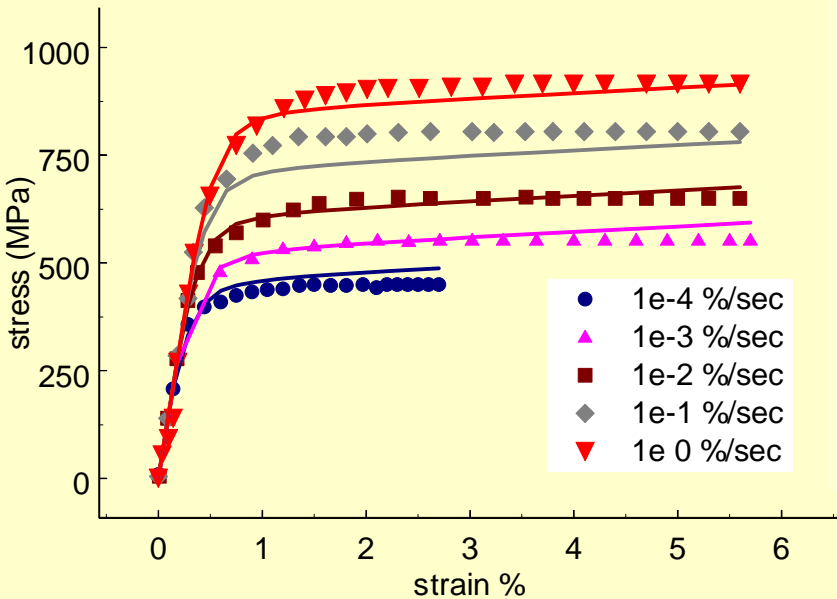


Elastic + 4 Viscoplastic Mechanisms

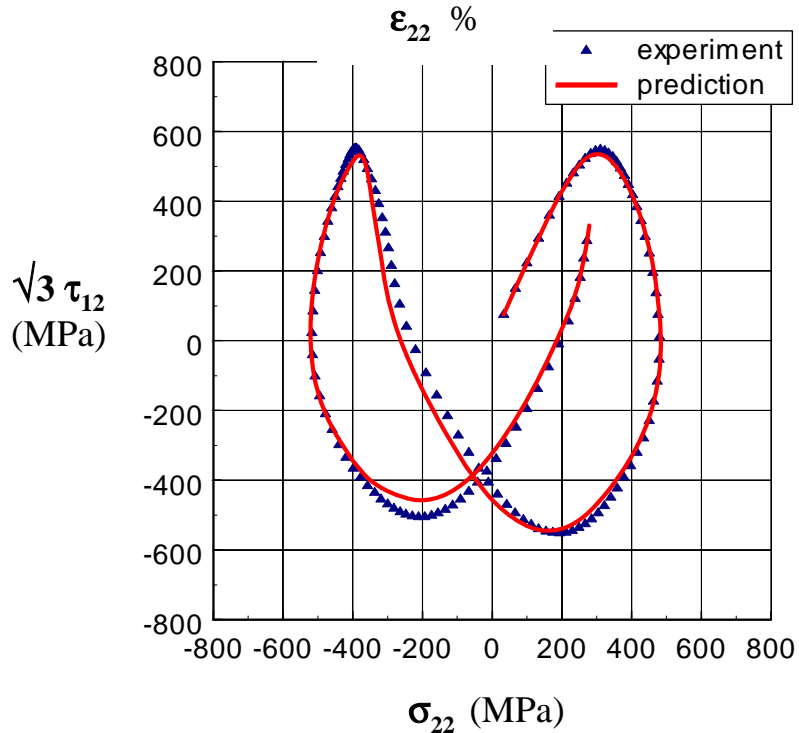
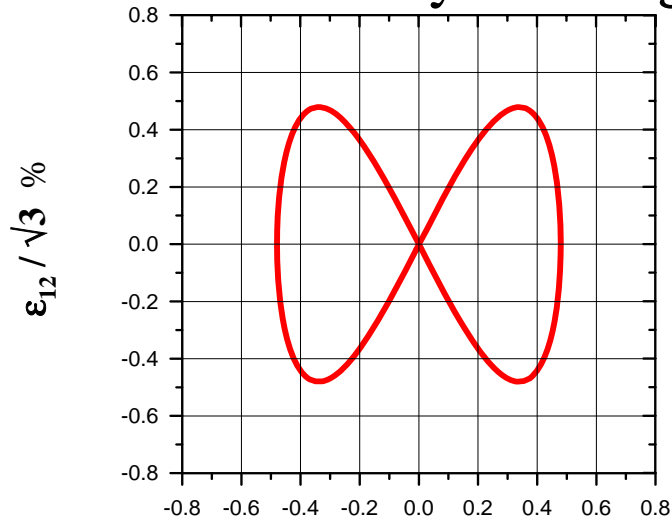
Final characterized parameters using four Viscoplastic mechanisms for IN738LC @850⁰ C

Material Parameter	Units	Value	Material Parameter	Units	Value
E	MPa	1.5×10^5	β_1	-	1 (6)*
ν	-	0.33	β_2	-	1 (6)*
κ	MPa	0.1	β_3	-	1 (6)*
κ_1	MPa	61.43	β_4	-	1 (6)*
κ_2	MPa	64.37	R_1	1/s	1.0×10^{-21}
κ_3	MPa	62.30	R_2	1/s	1.0×10^{-21}
κ_4	MPa	75.08	R_3	1/s	1.0×10^{-21}
n	-	1.486	R_4	1/s	1.0×10^{-21}
μ	MPa -s	3.79×10^{14}	H_1	MPa	4.6×10^4
m_1	-	0.001	H_2	MPa	5.13×10^4
m_2	-	0.001	H_3	MPa	8.33×10^7
m_3	-	0.001	H_4	MPa	9.458×10^7
m_4	-	0.001			

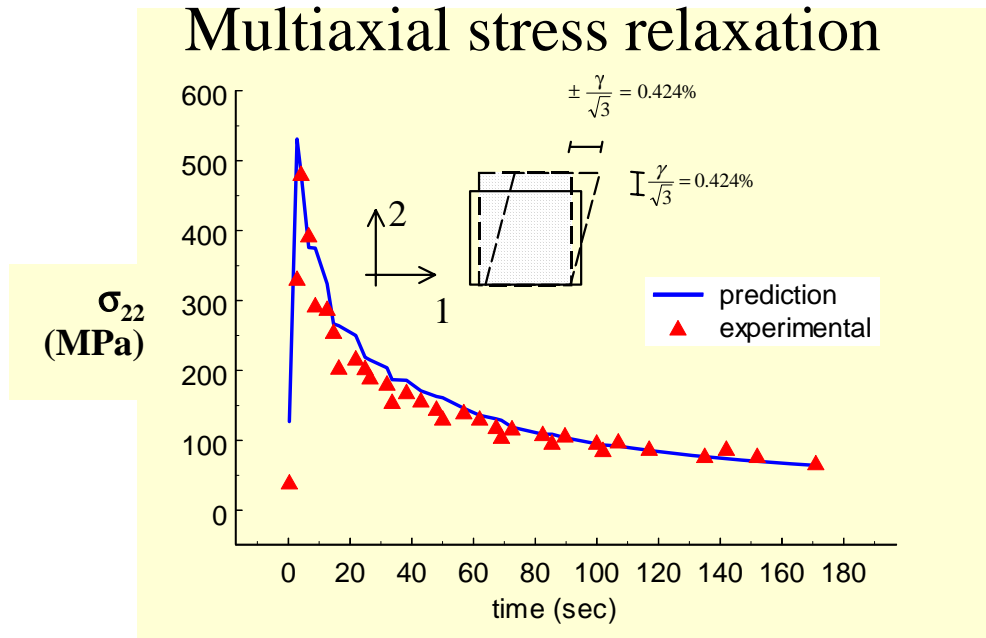
* the value between parentheses was determined in the FE simulation of the experiment



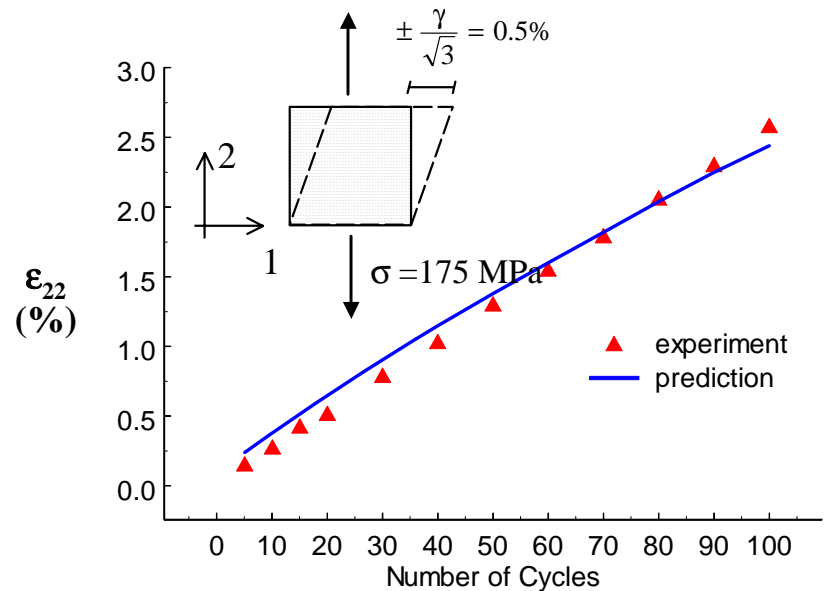
Butterfly Loading



Multiaxial stress relaxation

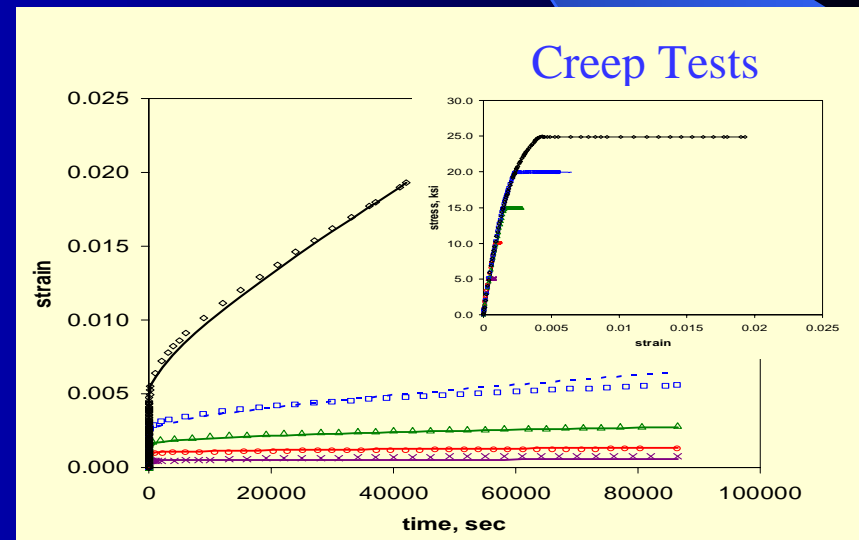
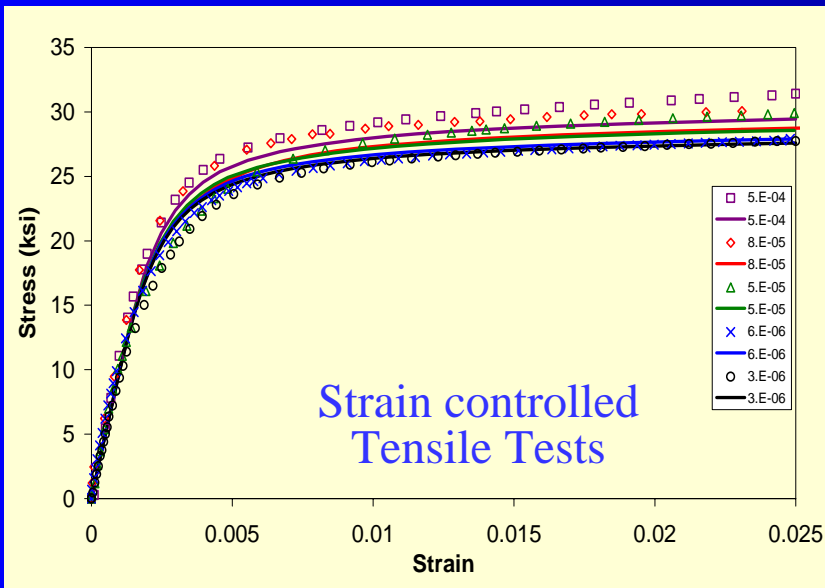
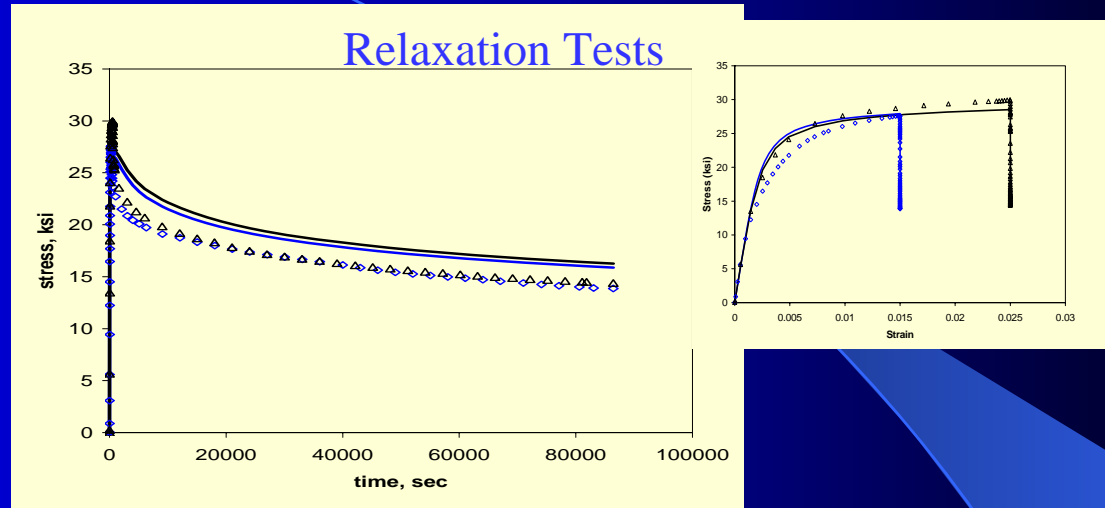


Multiaxial ratchetting



Correlation of GRCop-84 Utilizing Multimechanism GVIPS Model

1 VE mechanisms
4 VP mechanisms



Structural Verification Testing

- Ideally should provide feedback for subsequent model refinement
- Provide prototypical response data which is to be **compared** with model predictions



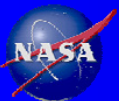
Consequently:

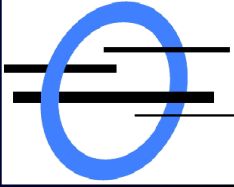
- Need accurate temperature, strain and load information at a variety of locations - **required for any true validation**
- Number of cycles to failure (alone) not enough
- Instrumentation incredibly challenging (sever environment)



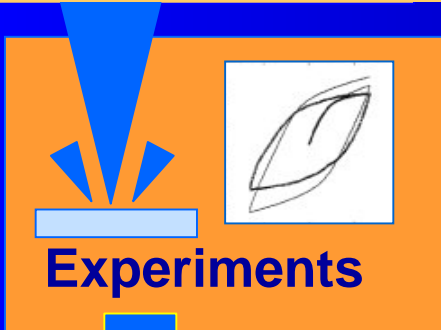
Summary of Advances in Material Modeling (Synergistic Technology)

- Generalized, Fully Associative, Multimechanism, Viscoelastoplastic Model Available
 - Reversible/Irreversible Regimes
 - Spanning wide time, stress, temperature spectrum
 - Nonlinear Hardening with Saturation
 - Ability to capture ratcheting
 - Stiffness and/or Strength Reduction
- Automated Material Model Characterization
 - via **COMPARE**
 - **Materials thus far:**
 - Ni based; Cu based; Ti
 - MMC and PMC
- Implicit Integration Algorithms
 - Directly applicable for 3D/sub-space loading
 - Generalized Material Symmetry Operators (which influence flow, hardening, recovery, relaxation spectrum, etc.)
 - Efficiency (through explicit algorithmic tangent stiffness)
 - Robustness (through “slack” line search)
- Now Commercially Available
 - COMPARE
 - GVIPS – via UMATs





www.openchannelfoundation.org



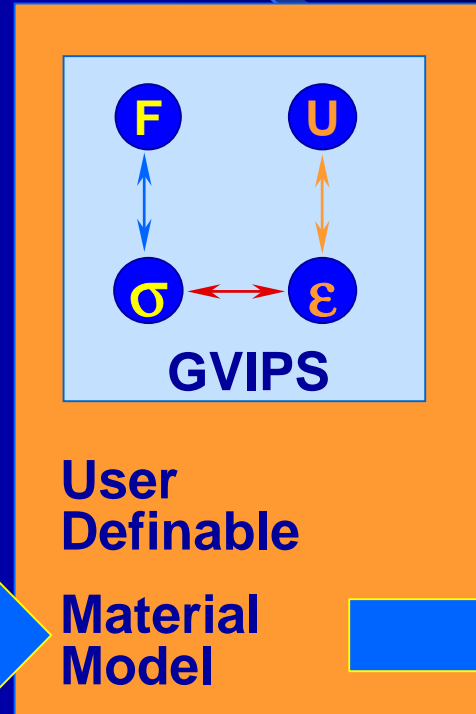
Multiple Experiments produce data

3	37446.27292	0.838069
3	37446.27292	0.838069
3	37446.27292	0.838069
3	37448.29514	1.320609
3	37450.27153	1.793447
3	37453.27222	1.005082
3	37455.28194	1.068973
3	37457.26597	1.040952
3	37460.45486	1.268637
3	37461.67014	1.357503
3	37462.34931	1.089025
3	37464.27778	1.13265
3	37467.28403	1.096359
3	37469.27153	1.064865

Data



COMPARE fits the GVIPS material parameters to experimental data within minutes.

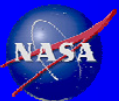


The resulting UMAT can be immediately accessed by the Finite Element Analysis



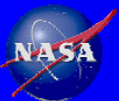
Future Work

- Extend formulation to account for
 - Coupled Nonisothermal Issues
 - Probabilistic Material Behavior
- Characterize additional material systems
- Verify under prototypical loading histories
- Implement softening (damage) mechanisms into COMPARE – theory complete
 - Characterize strength/stiffness reduction parameters to account for softening effects



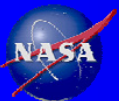
Thank You

Questions?



Selected References

- Arnold, S. M., and Saleeb, A.F., “On the Thermodynamic Framework of Generalized Coupled Thermoelastic-Viscoplastic -Damage Modeling”, *Jnl of Int. Plasticity*, Vol. 10, No. 3.,pp. 263-278, 1994
- Arnold, S. M., Saleeb, A.F. and Wilt, T.E., “An Investigation of the Modeling of Thermal/Dynamic Recovery and Nonlinear Hardening in Potential Based Viscoplasticity”, *Int. Jnl. of Engng. Mat. & Tech.*, Vol. 117, No. 2, pp. 157-167, 1995
- Arnold, S. M., Saleeb, A.F., Castelli, M.G., “A Fully Associative, Nonisothermal, Non-Linear Kinematic, Unified Viscoplastic Model For Titanium Based Matrices”, *Thermo-Mechanical Fatigue Behavior of Materials: Second Volume*, ASTM STP 1263, M. Verrilli and M.G. Castelli, Eds. , 1996, pp.146-173.
- Saleeb, A.F. and Arnold, S. M.; “A General Reversible Hereditary Constitutive Model: Part I Theoretical Developments”, *JEMT*, Vol. 123, 2001, pp.51-64.
- Arnold, S. M., Saleeb, A.F., Castelli, M.G.; “A General Reversible Hereditary Constitutive Model: Part II Application To Titanium Alloys”, *JEMT*, Vol. 123, 2001, pp. 65-73.
- Saleeb, A.F., Arnold, S.M., Castelli, M.G , Wilt, T.E., and Graf, W.E., “A General Hereditary Multimechanism-Based Deformation Model With Application to The Viscoelastoplastic Response of Titanium Alloys, *Int. Jnl. Of Plasticity*, Vol. 17, No. 10, pp. 1305-1350. Oct. 2001
- Saleeb, A.F. and Arnold, S.M. ; “Specific Hardening Function Definition and Characterization of A Multimechanism Generalized Potential-Based Viscoelastoplasticity Model”, accepted *Int. Jnl of Plasticity*, 2003



Using CFD as a Rocket Injector Design Tool: Recent Progress at Marshall Space Flight Center

Kevin Tucker, Jeff West, Robert Williams, Jeff Lin, Francisco
Canabal, Marvin Rucker, Bryan Robles, Robert Garcia
NASA

Marshall Space Flight Center
Huntsville, AL

James Chenoweth
CRAFT Tech
Huntsville, AL

**FIFTH INTERNATIONAL SYMPOSIUM
ON LIQUID SPACE PROPULSION**

Long Life Combustion Devices Technology

Chattanooga, Tennessee

October 27-30, 2003

- **Background on Issues Related to using CFD as an Injector Design Tool**
- **MSFC Vision for CFD as an Injector Design Tool**
- **How Do We Accomplish this Vision for Injector Design?**
 - **Parallel Efforts in Program Support & Technology Development**
 - **Key Roadmap Concepts**
- **Simulations for Program Support**
- **Validation Process**
 - **Issues**
 - **Current Data Acquisition Efforts**
- **Summary**



Why Use CFD as an Injector Design Tool?



**The NGLT Program is focused on improved hardware reliability
& reduced costs**

Requires better understanding of environments

- Historical tools focus on:
 - Performance first
 - Environments second (typically 1-d)
- Environments are almost always multi-dimensional
- **American designers are inexperienced with NGLT engine cycle**
 - Empirical tools based on historical databases
 - These tools/databases apply only marginally to NGLT injector concepts

Meeting NGLT goals requires new injector design tools



What Are the Major Obstacles to Using CFD as an Injector Design Tool?



1. Inability to model details of the physics and geometry

- Ideal gas, simple chemistry and turbulence assumptions are typical
- Most solutions are axisymmetric
- Very few 3-d, multi-element solutions

2. Slow solution turnaround time

- Many solutions must be accomplished early in the design phase
- For injectors, a few single element solutions are done in this time frame

3. Lack of demonstrated accuracy

- There is no agreed upon validation process
- Very little quantitative validation work has been done
- Relevant data at appropriate conditions is scarce



Injector design tools are in a transitional period between exclusive use of empirically-based tools and extensive reliance on CFD. Currently--

- Legacy tools are still overwhelmingly used
- CFD is not typically in the original design plan, budget or schedule
- CFD is mostly used for qualitative trend analysis focused on a specific issue
- CFD is sometimes used in the "there is no other option" mode
- Occasionally CFD is used to provide improved inputs to classical analysis tools (e.g., combustion stability)



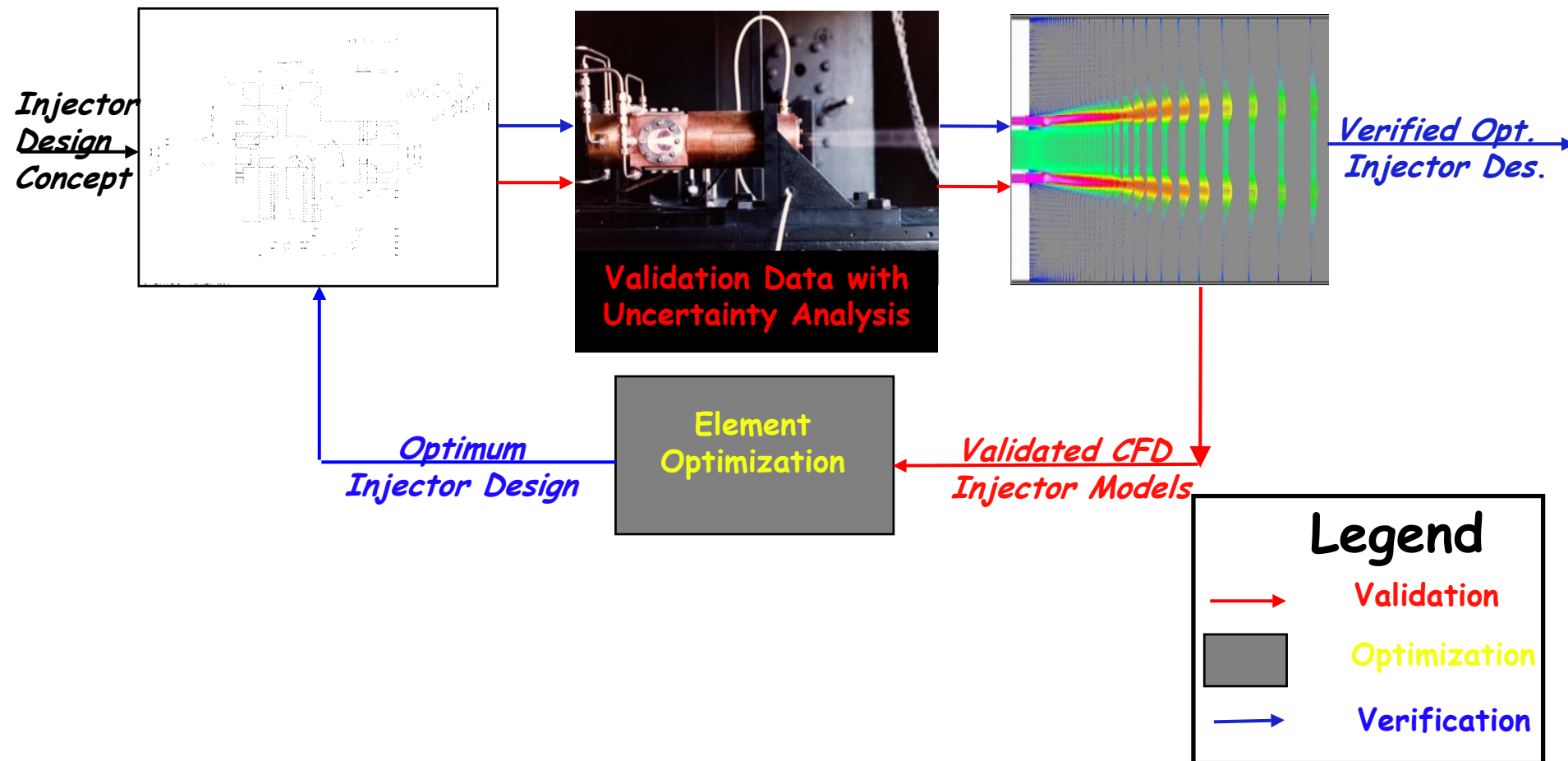
Overall MSFC/TD64 Vision for use of CFD in Combustion Devices Design:

To enable the use of CFD for Simulation of Preburners, Ducting, Thrust Chamber Assembly and Supporting Infrastructure in terms of Performance, Life, and Stability so as to affect the design process in a timely fashion.

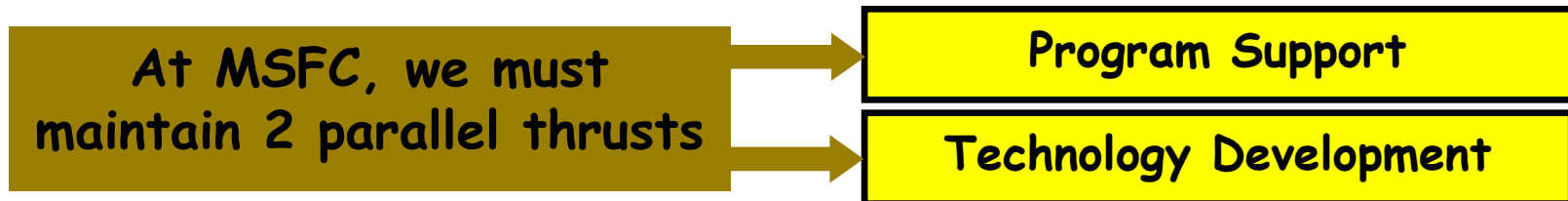
•Injector design is the heart of this overall goal

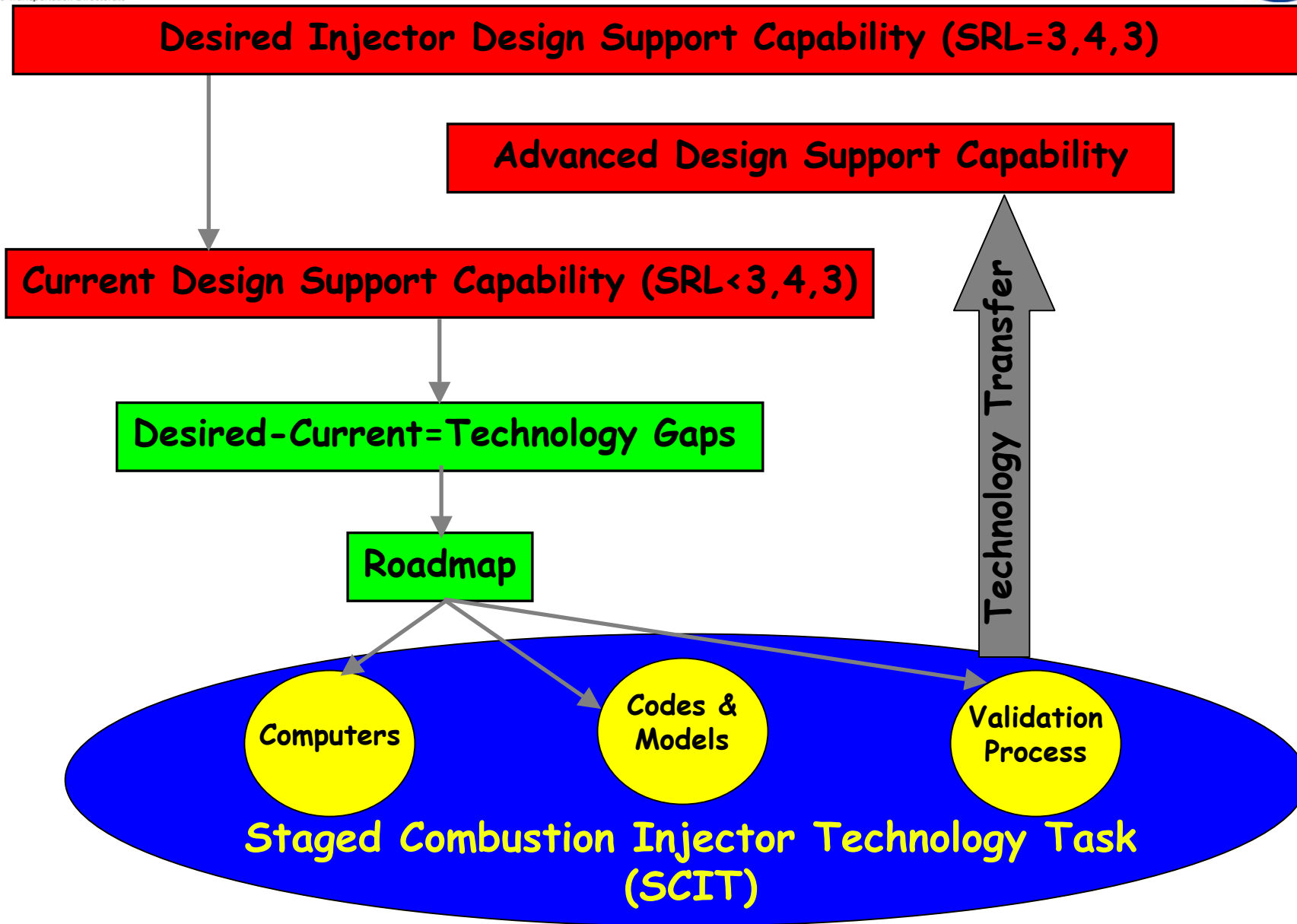
- Injector design details and physical processes occurring here govern:
 - Performance
 - Environments in the entire combustor or TCA
- Large parametric spaces for both single and multi-element injector issues must be explored to insure a reliable robust design

Generic CFD-Based Single Element Injector Design & Optimization Process



- Marshall is a Space Flight Center, so we must support Programs with the current, albeit limited capability for injector design
- Concurrently, CFD simulation capability improvements must be made in at least 3 areas:
 1. **Fidelity**-the ability to model the key details of the physics and geometry
 2. **Robustness**-solution turnaround must be sufficient to cover a large parametric space of independent design variables and operating conditions
 3. **Accuracy (demonstrated)**-we must be able to quantify accuracy; both current and threshold level for design



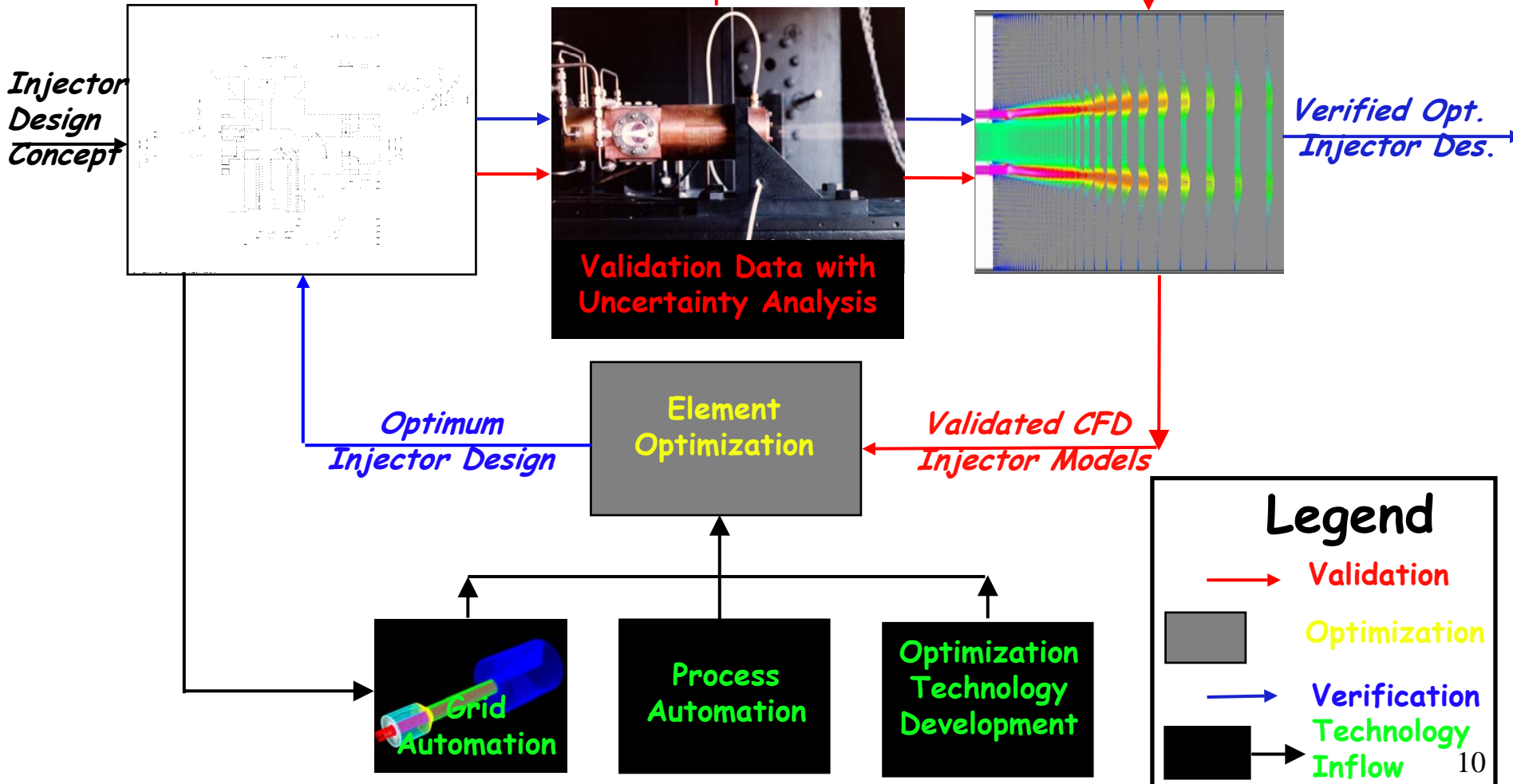




CFD-Based Single Element Injector Design & Optimization Process-Including Technology Inflow

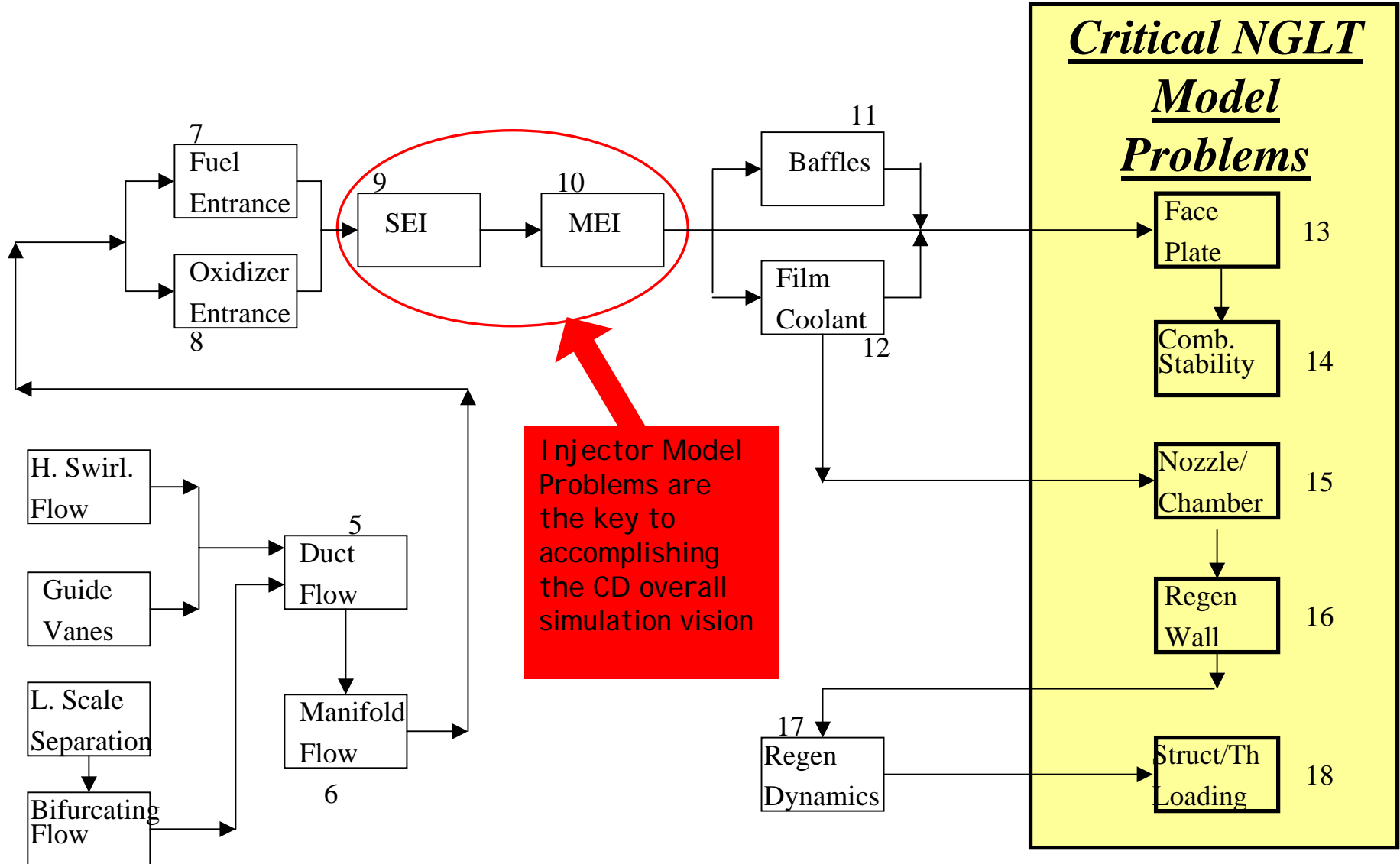


CFD-Based Single Element Injector Design & Optimization Process



Legend

- Validation
- Optimization
- Verification
- Technology Inflow



9.1 Steady

9.1.1 Supercritical reactants

9.1.1.1 H₂/O₂

9.1.1.1.1 Shear Coaxial*

9.1.1.1.2 Swirl Coaxial*

9.1.1.1.3 Impinger

9.1.1.2 RP-1/O₂

9.1.1.2.1 Shear Coaxial*

9.1.1.2.2 Swirl Coaxial*

9.1.1.2.3 Impinger

9.1.1.2.4 Hybrid *

9.1.1.3 RP-1(cracked)/O₂

9.1.1.3.1 Shear Coaxial

9.1.1.3.2 Swirl Coaxial

9.1.1.3.3 Impinger

9.1.1.4 JP-N/H₂O₂

9.1.1.4.1 Shear Coaxial

9.1.1.4.2 Swirl Coaxial

9.1.1.4.3 Impinger

9.1.2 Subcritical reactants

9.2 Unsteady

9.3 Transient

* Areas of Current Work

Simulation Readiness Level (SRL) SRL=(f,r,a)

Level	Fidelity	Robustness	Accuracy
0	Extremely simple physics, boundary conditions and geometry	Have not completed any simulations	Not evaluated other than historical quality of simulation tool
1	Reasonably precise geometry and boundary conditions, extremely simple physics	Have completed some simulations	Qualitative agreement with existing results of related problems
2	Reasonably precise physics with extremely simple boundary conditions and geometry	Simulations with proven convergence and conservation	Quantitative agreement with existing results of related problems
3	Reasonably precise physics, boundary conditions and geometry **	Simulations with proven convergence, conservation and grid independence	Qualitative agreement of relevant measures for one representative problem **
4	Reasonably precise physics, completely precise boundary conditions and as-built geometry	Fire and Forget (95%+) simulations with convergence, conservation and grid independence **	Qualitative agreement of relevant measures over parametric space of actual problems
5	Completely precise physics, completely precise boundary conditions and as-built geometry	Fire and Forget (95%+) simulations with convergence, conservation and grid independence plus the ability to complete 100 or more problems within 3 weeks	Quantitative agreement of relevant measures over parametric space of actual problem

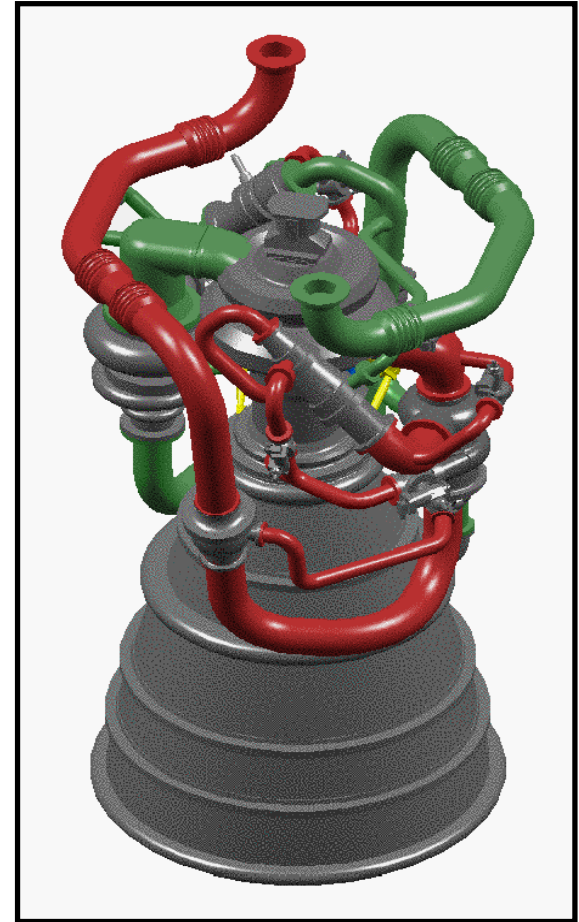
**** Minimum level for significant design impact**

Current Areas of Program Support

- **Integrated Powerhead Demonstrator**
 - Single Element
 - Multi-Element
- **NGLT ORSC Cycle**
 - TR-107 (single element)
 - RS-84 (single element)

Full Flow Staged Combustion Cycle (H_2/O_2)

- All propellants flow through preburner
- Propellants are gaseous as they enter Main Injector
- Faceplate environment concerns stem from:
 - Faceplate coolant is relatively hot gas
 - Combustion occurs closer to faceplate with gaseous propellants

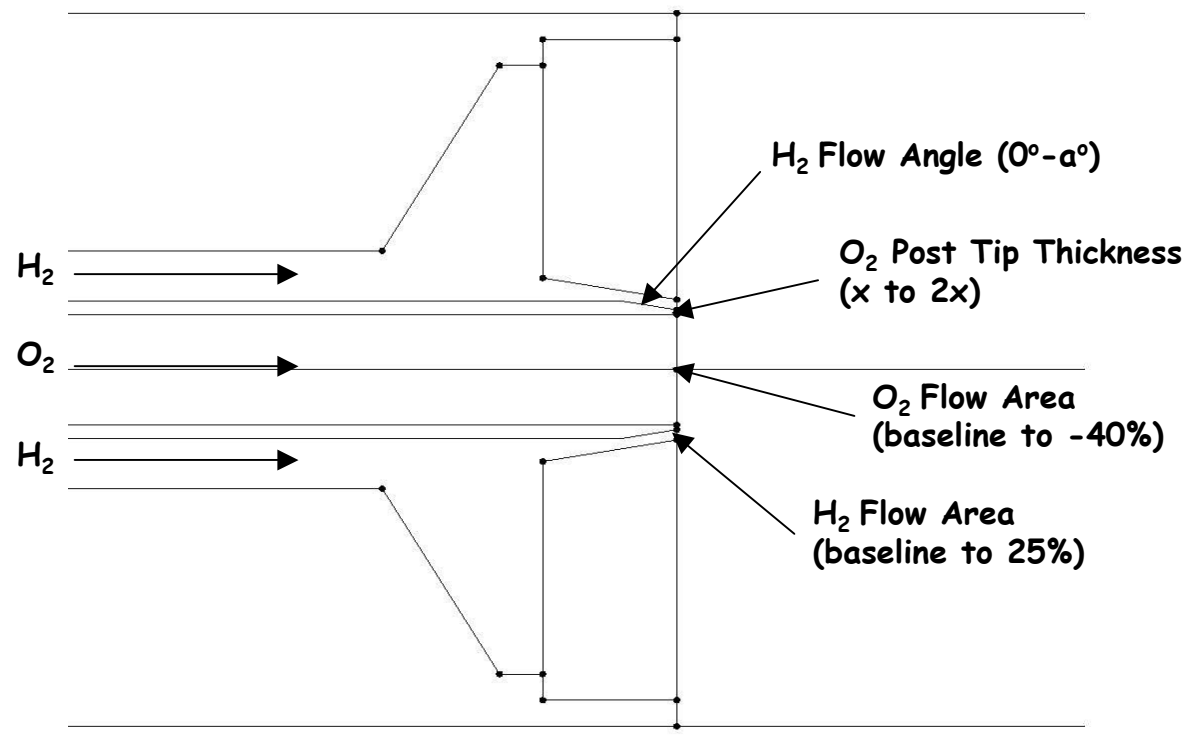


IPD Engine

OBJECTIVE

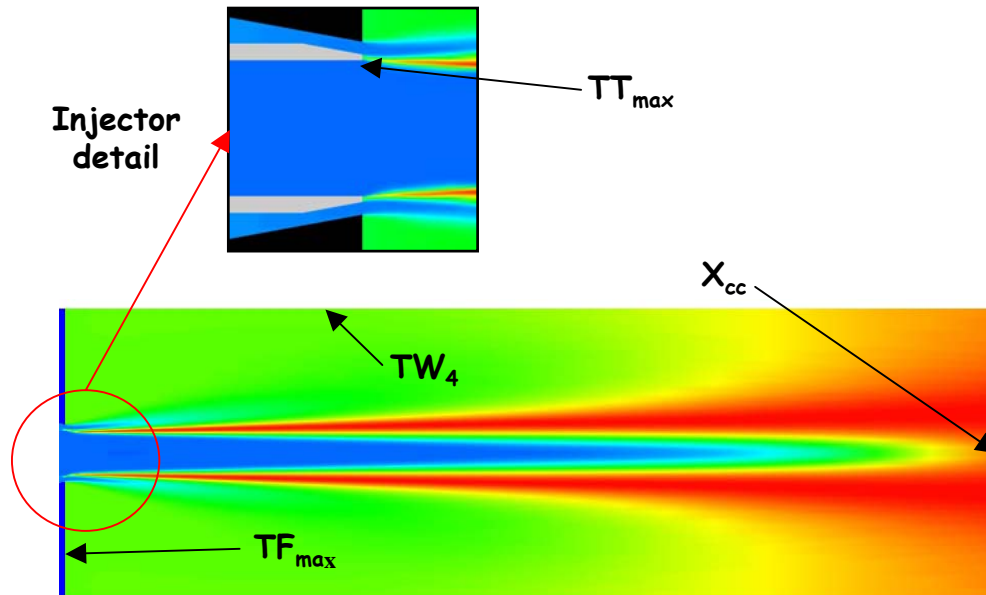
Starting with a baseline concept, optimize a GO_2/GH_2 element for performance and life (Model Problem 9.1.1.1)

APPROACH



- Generated DOE matrix
- Ran 54 cases
- Constructed Response Surfaces
- Conducted optimization trades with performance & life

RESULTS



The Boeing Company, US patent 6253539

Simulation Readiness Level

Fidelity-3

➤ Axisymmetric assumption is good

Robustness-5

➤ 54 cases run in one week

Accuracy-1

➤ Qualitative agreement on a similar problem

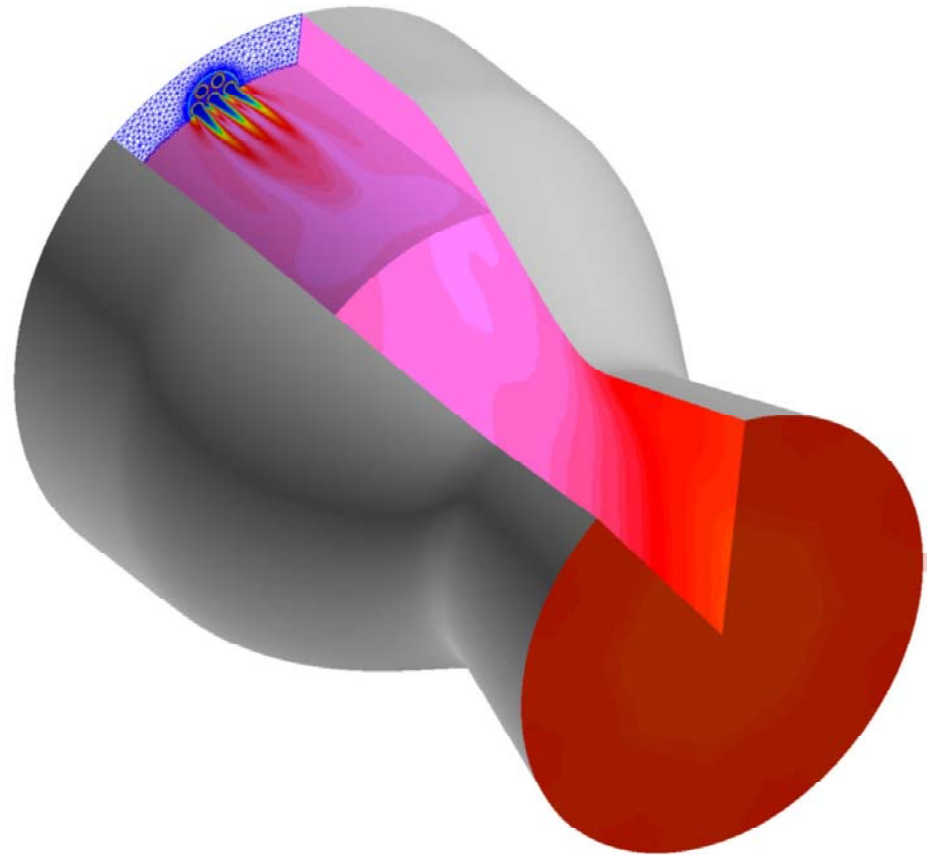
- All temperatures are life indicators
- The combustion length, X_{cc} , is a performance indicator
- The multi-variable optimization resulted in a different element design than any of the single element optimizations
- Robust design **requires** all relevant independent variables to be modeled early in the design process

OBJECTIVE

Construct a model to evaluate Main Injector and Chamber Wall Environments (Model Problem 10.1.1.1.1)

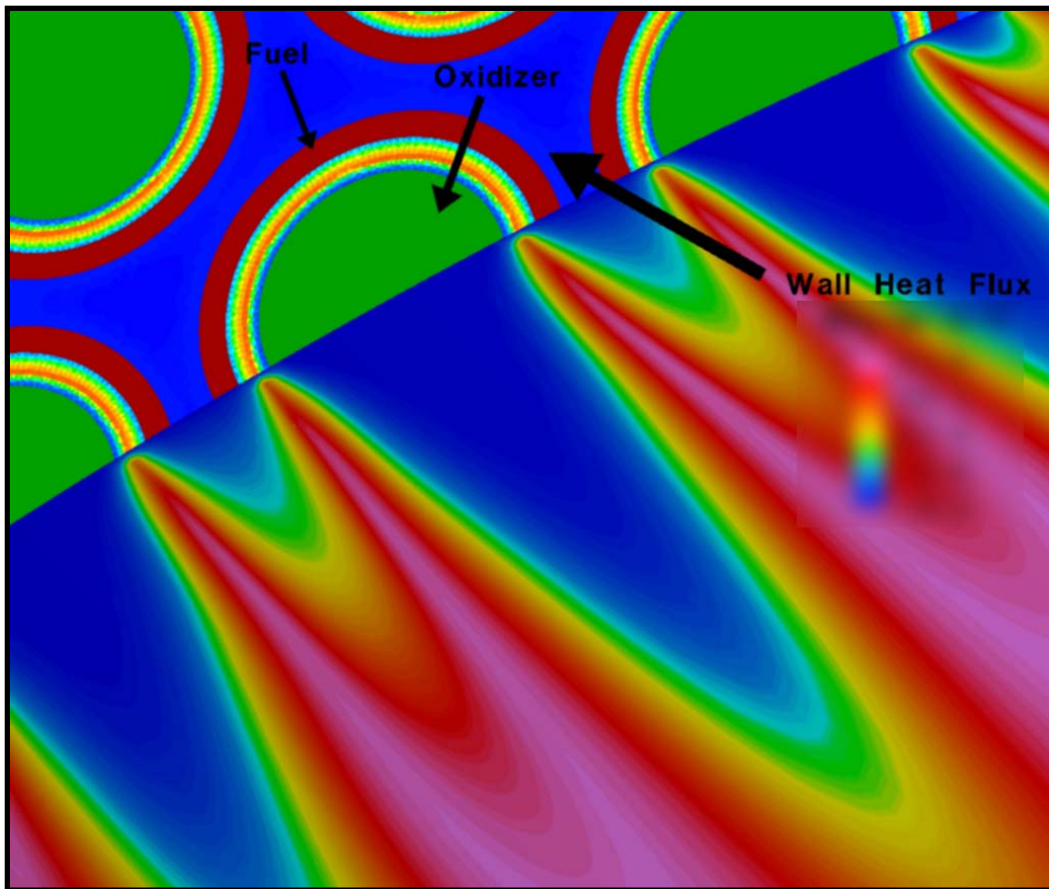
APPROACH

- Use full scale geometry
- Model must be:
 - Representative
 - Computationally tractable
 - 2 to 4 M grid points



IPD Multi-Element Simulation

RESULTS



IPD Injector Heat Fluxes and Hot Gas Temperature Field

Simulation Readiness Level

Fidelity-1

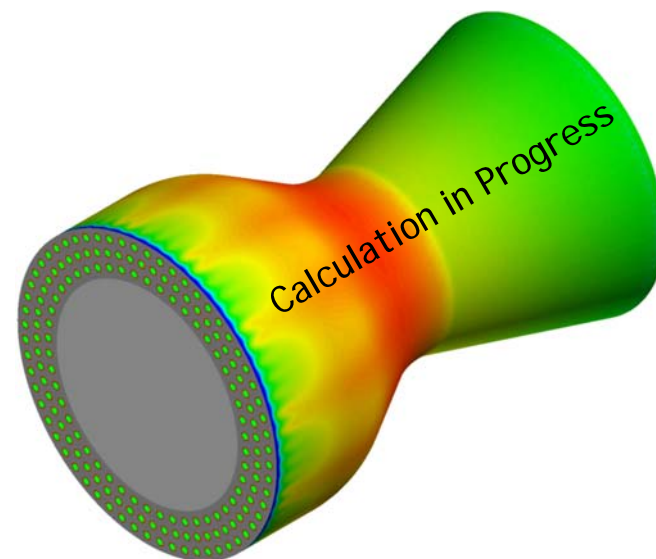
- Geometry & BC's extremely simple

Robustness-1

- Only a few cases have been run

Accuracy-0

- No evaluation of accuracy to date





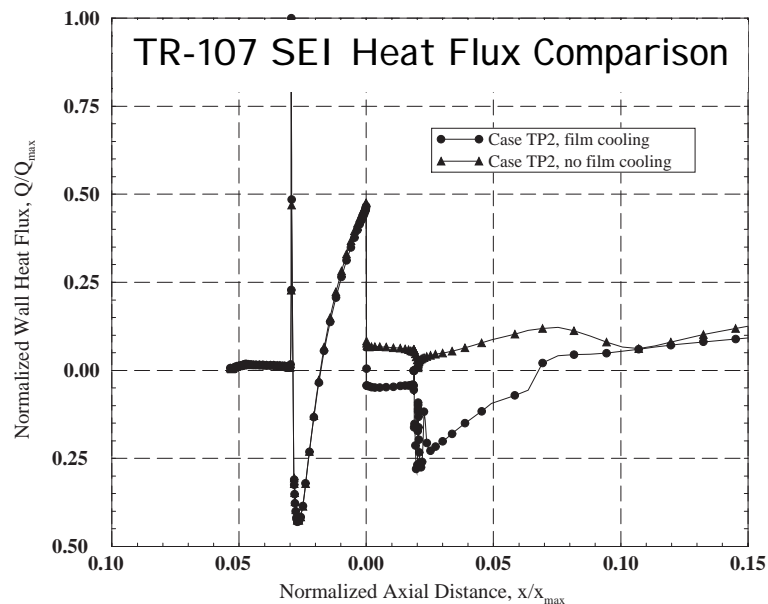
OBJECTIVE

- Construct subscale models to be validated for simulation of large scale combustors
- Use these models to evaluate thermal environments
- Model Problem 9.1.1.2.4

APPROACH

- Start with Single Element, axisymmetric geometry
- RP-1 modeled as ideal gas
- Finite rate multi-step chemistry

RESULTS



Simulation Readiness Level

Fidelity-0

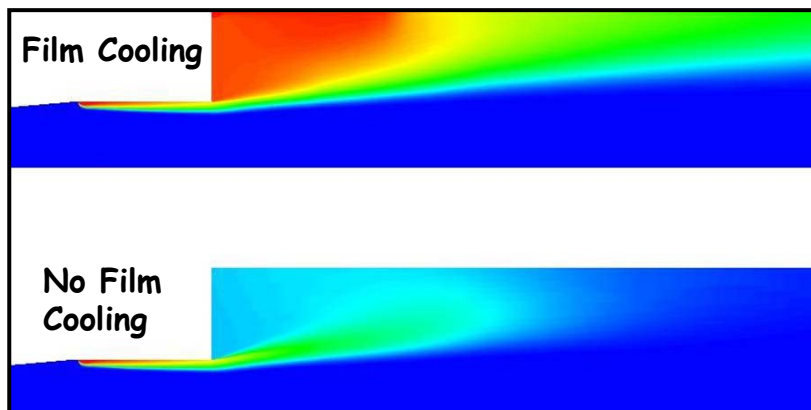
➤ Geometry & Physics extremely simple

Robustness-3

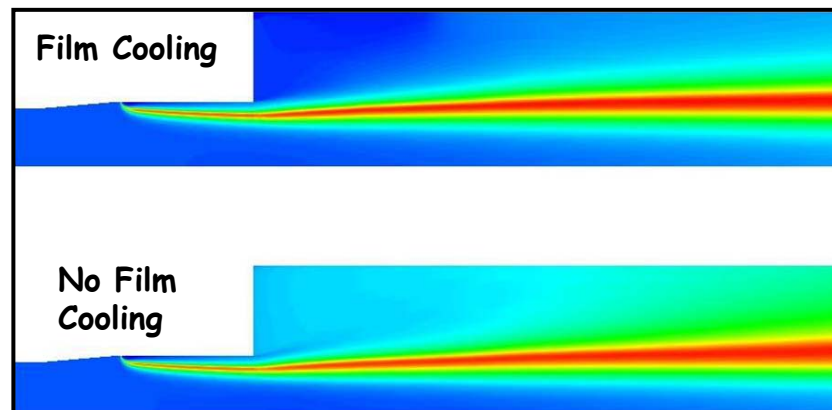
➤ Many good quality solutions completed

Accuracy-0

➤ No evaluation of accuracy to date



RP-1 Contours

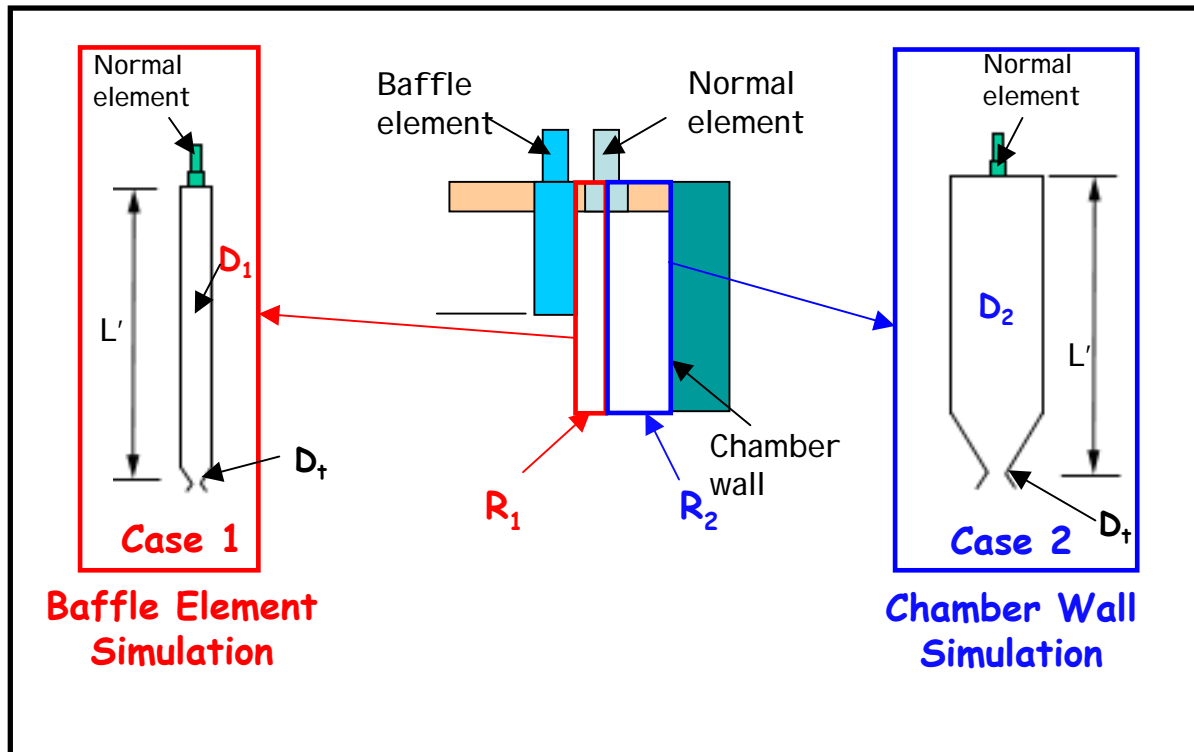


Temperature Contours

OBJECTIVE

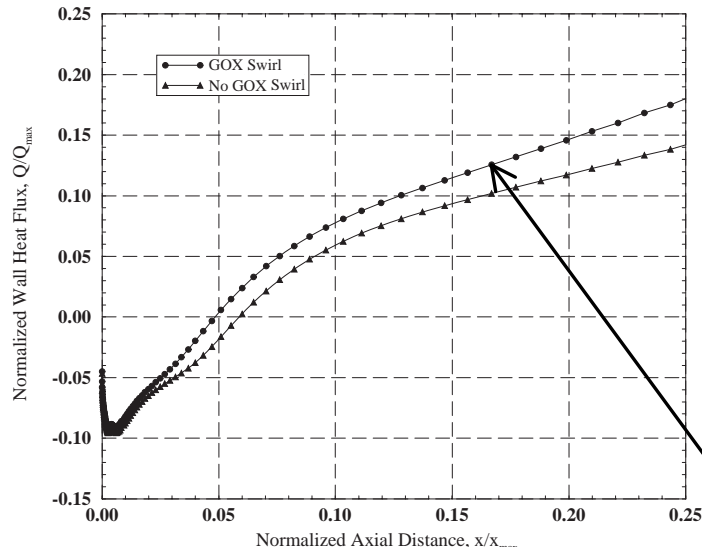
- Mitigate design risk by better characterization of thermal environments on baffle elements and on chamber wall
- Model Problem 9.1.1.2.4

APPROACH

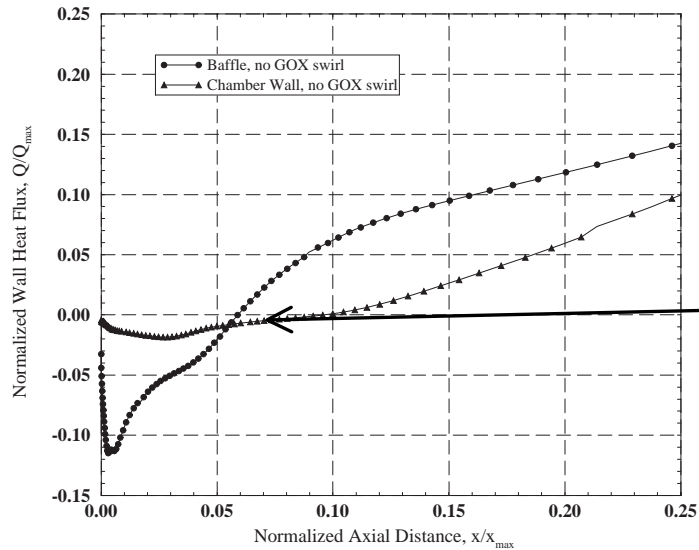


- Start with Single Element, axisymmetric geometry
- RP-1 modeled as ideal gas
- Finite rate multi-step chemistry
- Evaluated different GOX injection schemes
- Evaluated different turbulence models

RESULTS



RS-84 SEI Heat Flux Comparisons



Simulation Readiness Level

Fidelity-0

- Geometry & Physics extremely simple

Robustness-3

- Many good quality solutions completed

Accuracy-0

- No evaluation of accuracy to date

•GOX swirl promotes mixing , thus increasing the near-injector wall heat flux

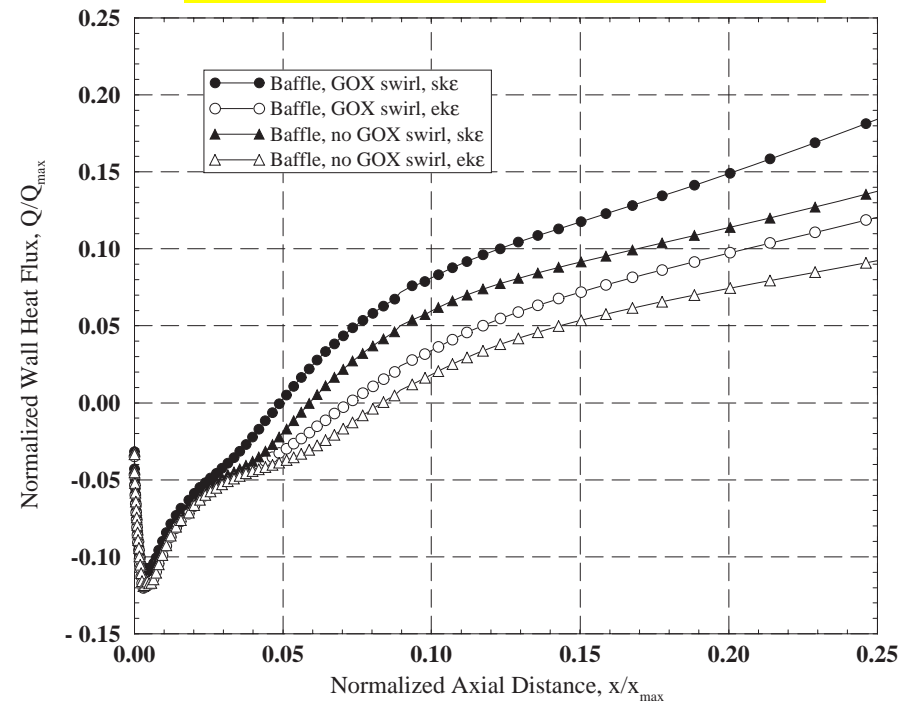
•Large recirculation zone in the larger chamber mixes gases causing a flat heat flux profile in the near injector region

- At MSFC we can produce injector solutions that:
 - Are grid independent
 - Satisfy the conservation equations

• What next??

- MSFC continues to work to improve codes and acquire computer resources. However--
- Validation of codes to **demonstrate** accuracy for injector flows is the most pressing issue identified to date

Impact of Turbulence Model on RS-84 Heat Flux Results



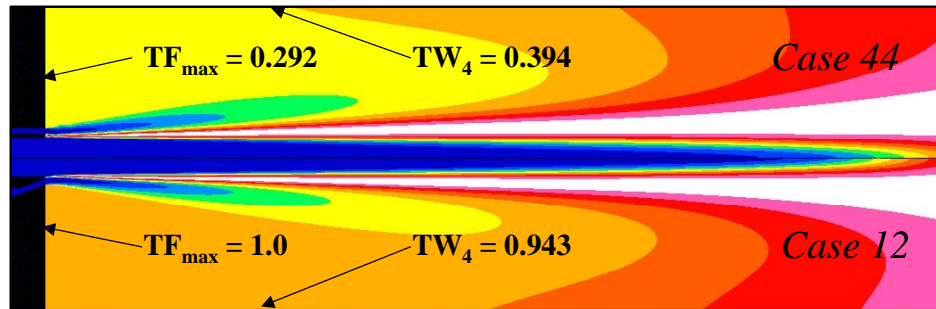
Spread between GOX swirl & no GOX swirl is the same order as between the standard $k\epsilon$ and extended $k\epsilon$ models

Code Validation is a Process

1. Use existing data from related problems (demonstrate accuracy up to level of 2)
2. Acquire additional data (demonstrate accuracy up to level of 5). This requires:
 - Careful experimental planning-including focused CFD analysis
 - Careful experimental execution
 - Use of the new data to demonstrate increased accuracy

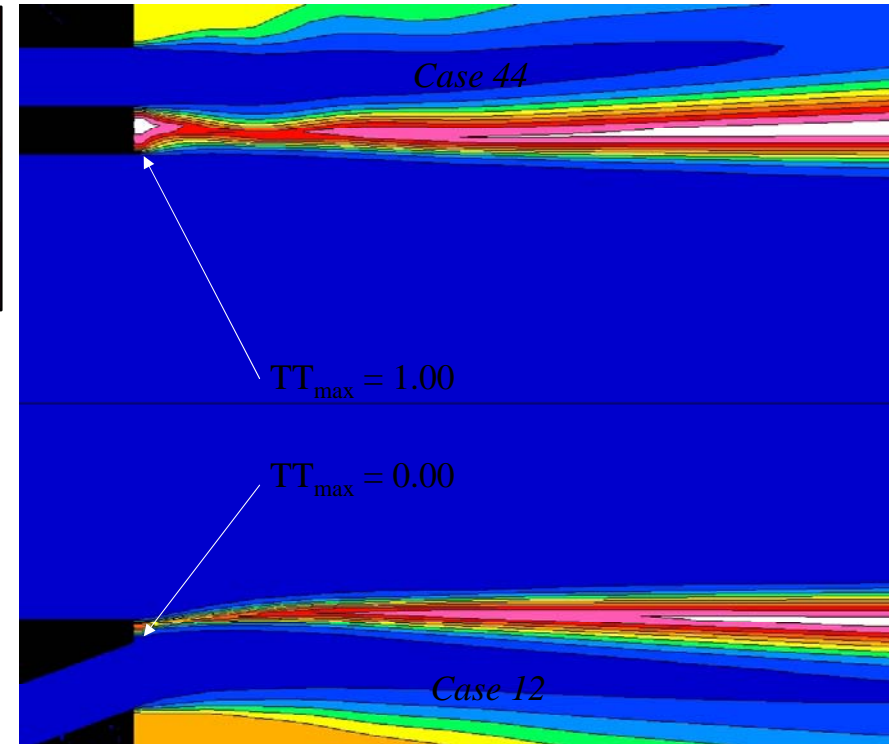
In the Experimental Planning Phase --

- CFD must be used to simulate test conditions
- If the code is to be used for design, the experiment must be conducted over a relevant range of independent geometry variables



Case 12 performed well, but had the highest wall and injector temperatures

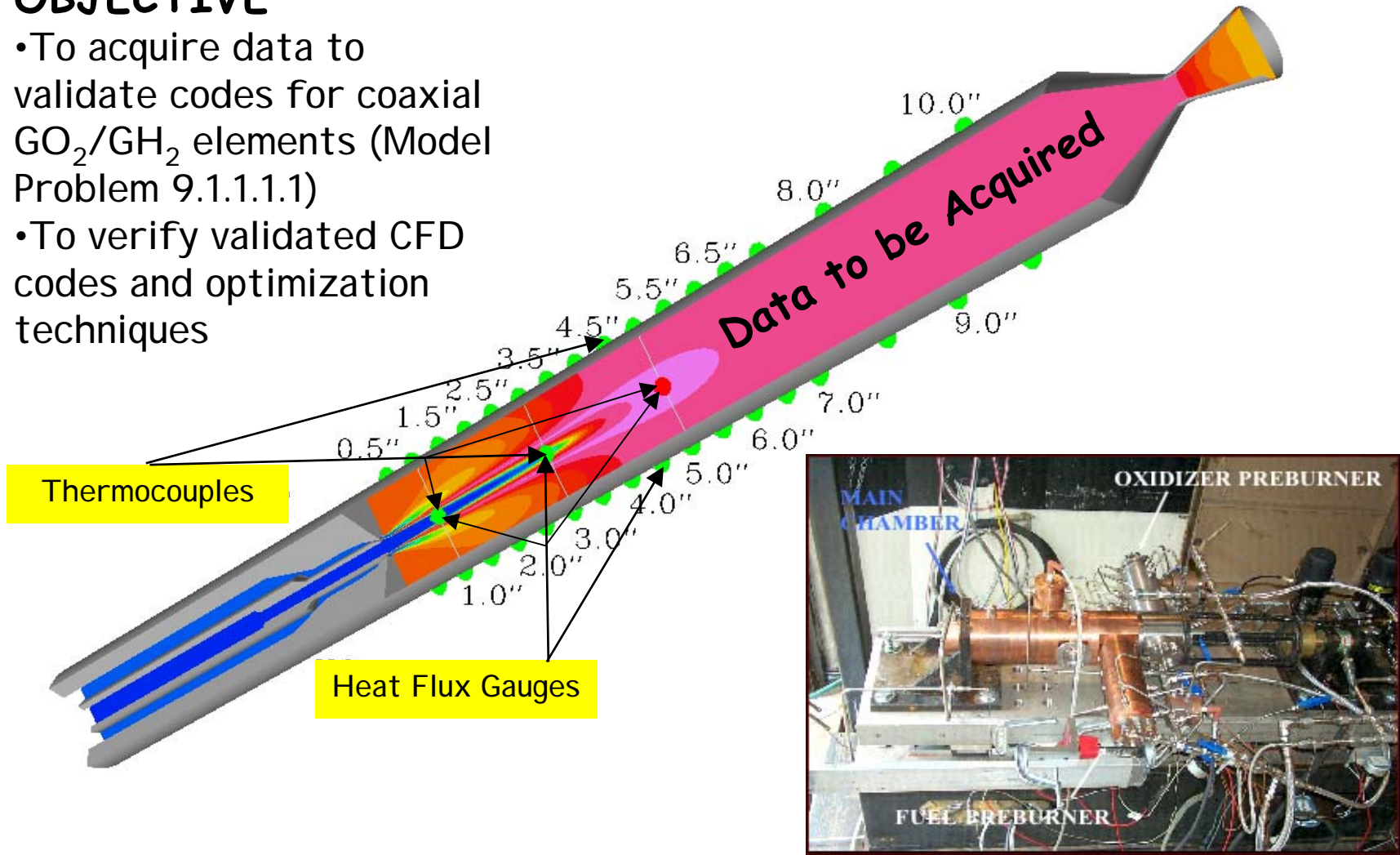
- CFD analysis during planning phase must be used to assess dependent variable ranges in order to select and place instrumentation
- Formal uncertainty analyses of both the facility and the rig must be done to understand, and where necessary, improve data accuracy



Case 12 also had the lowest injector tip temperature

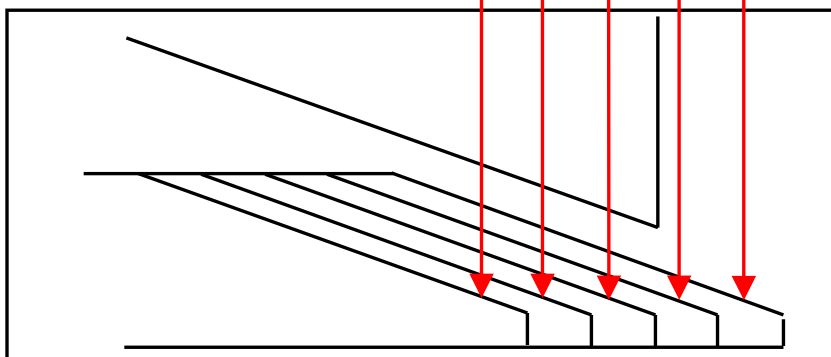
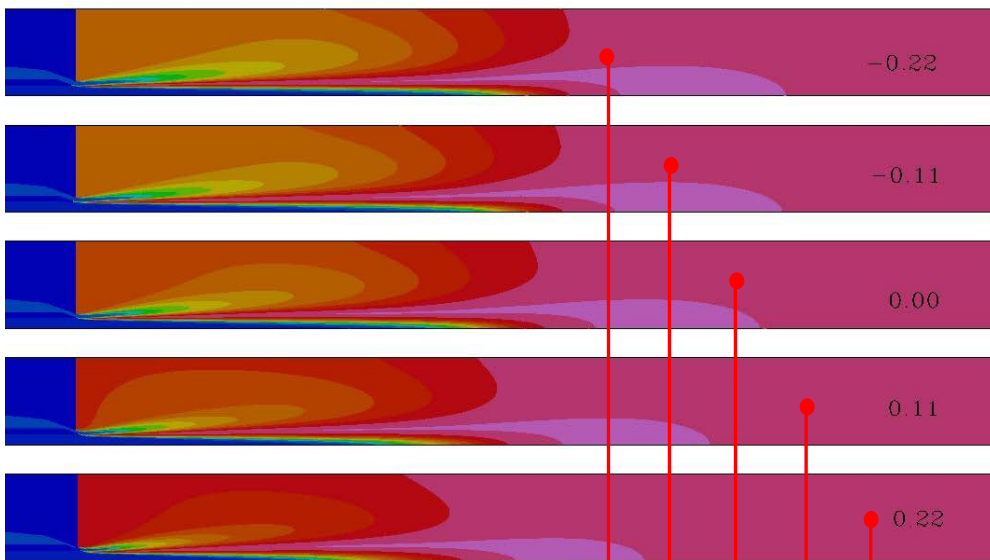
OBJECTIVE

- To acquire data to validate codes for coaxial GO_2/GH_2 elements (Model Problem 9.1.1.1.1)
- To verify validated CFD codes and optimization techniques



Test Rig at Penn State

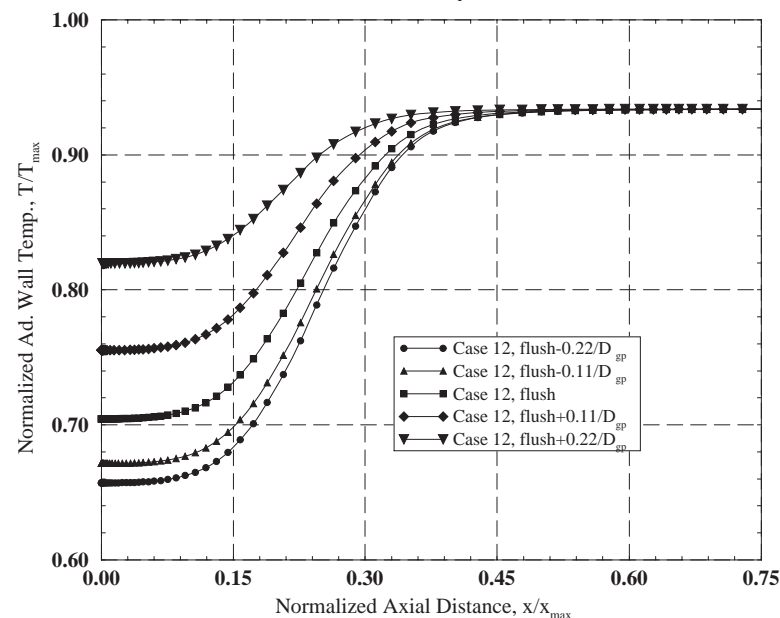
Pre-Test CFD Temperature Fields for 5 Different Tip Locations



as-built tip geometry



Wall Temperature Profiles for 5 Different Tip Locations

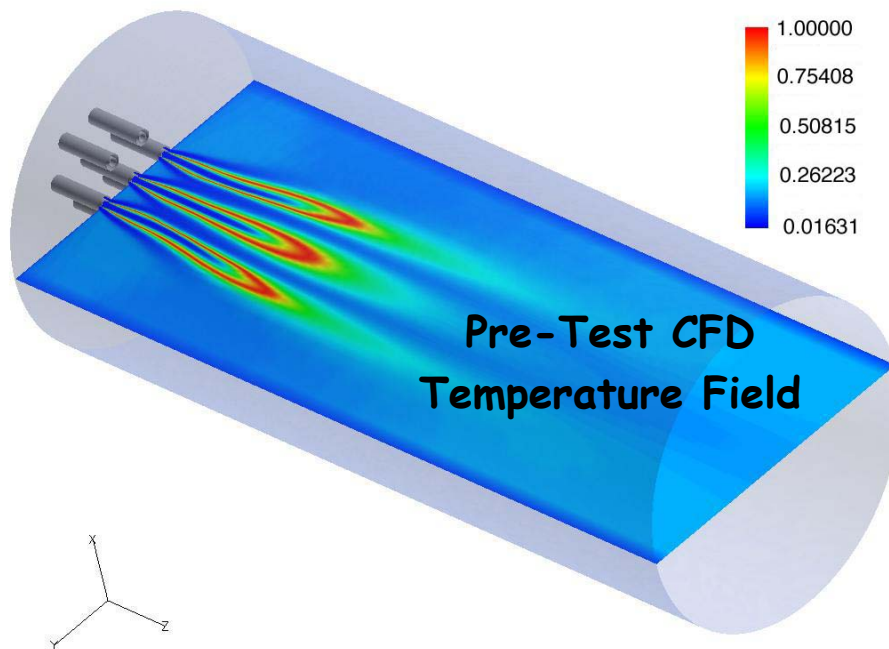
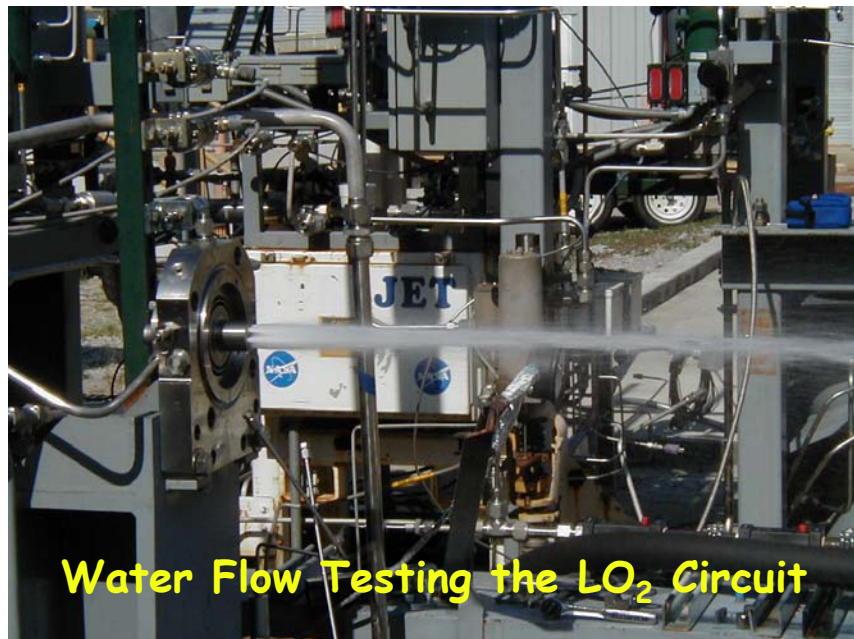
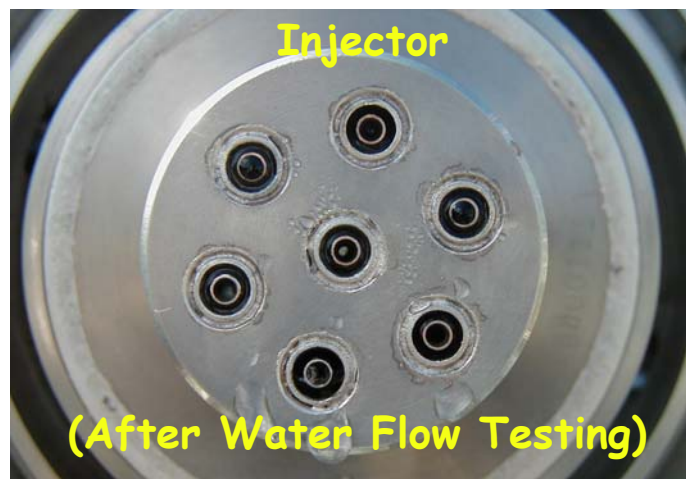


• Demonstrates importance of pre-test simulations

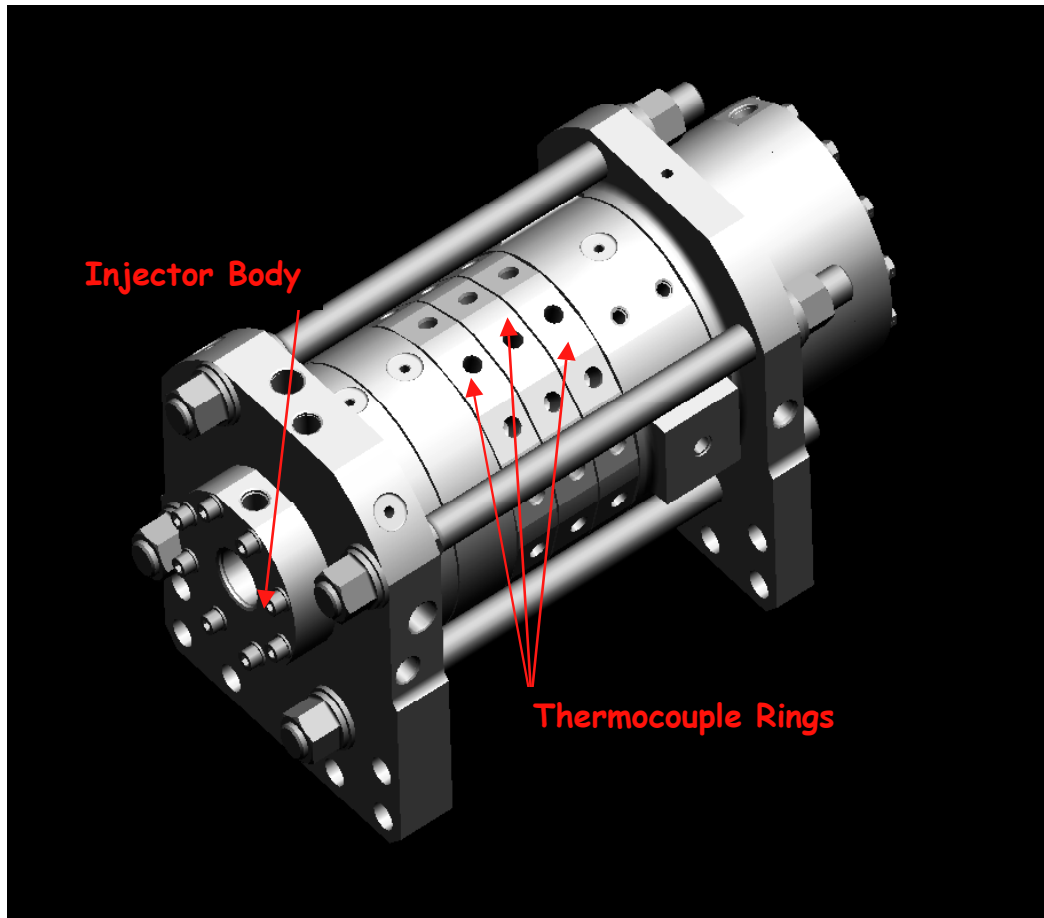
• Also shows knowledge of tip location to be critical

OBJECTIVE:

To acquire data to validate codes for multi-element coaxial LO₂/LH₂ injector (Model Problem 10.1.1.1.1)



CAD Model of MCTA-One TC Ring Configuration

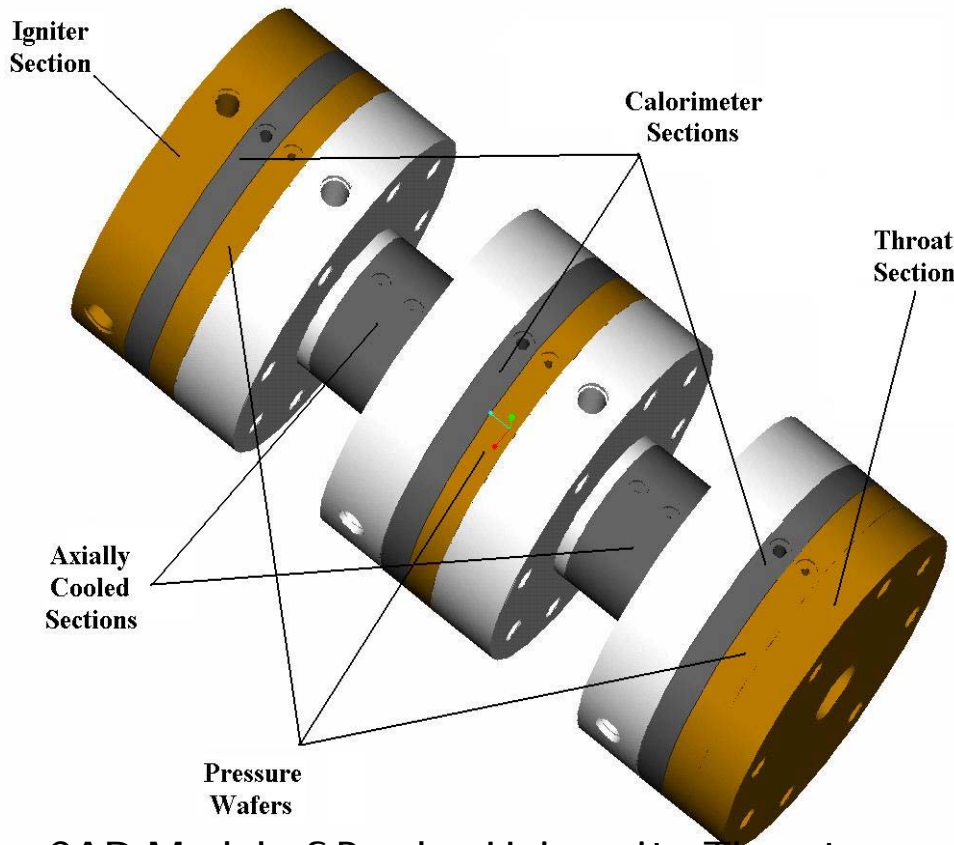


Data to be Acquired

- Spatially resolved temperature field via multiple TC ring configurations
- Shadowgraph near injector
- Wall Heat Fluxes (with calorimeter spool)
- Downstream species and temperatures in chamber and/or plume
 - Emission spectroscopy-Boeing
 - Raman Spectroscopy-Vanderbilt University
- High speed pressure transducers

OBJECTIVE:

To acquire data to validate codes for single -element $GO_2/RP-1$ injector (Model Problem 9.1.1.2.4)

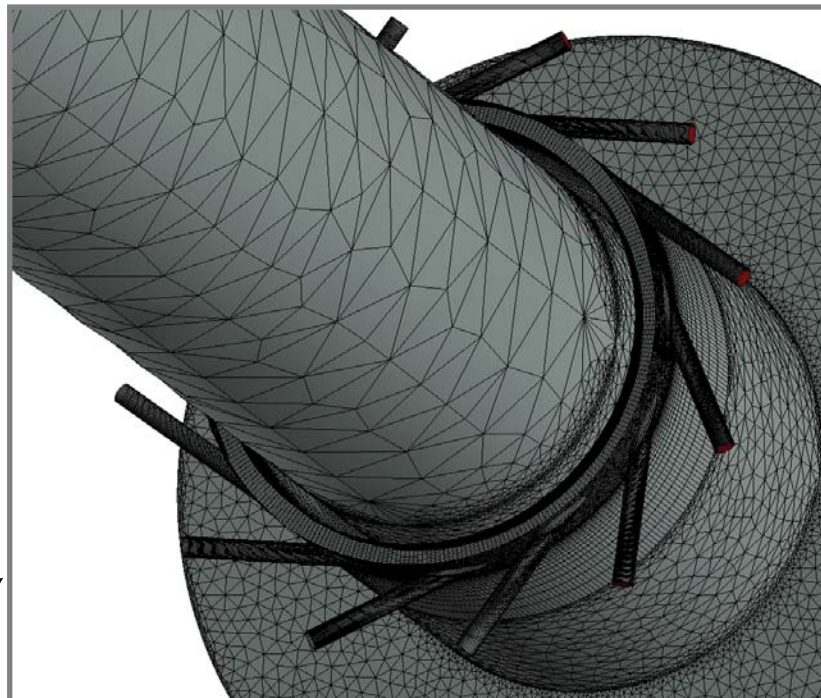


CAD Model of Purdue University Thruster

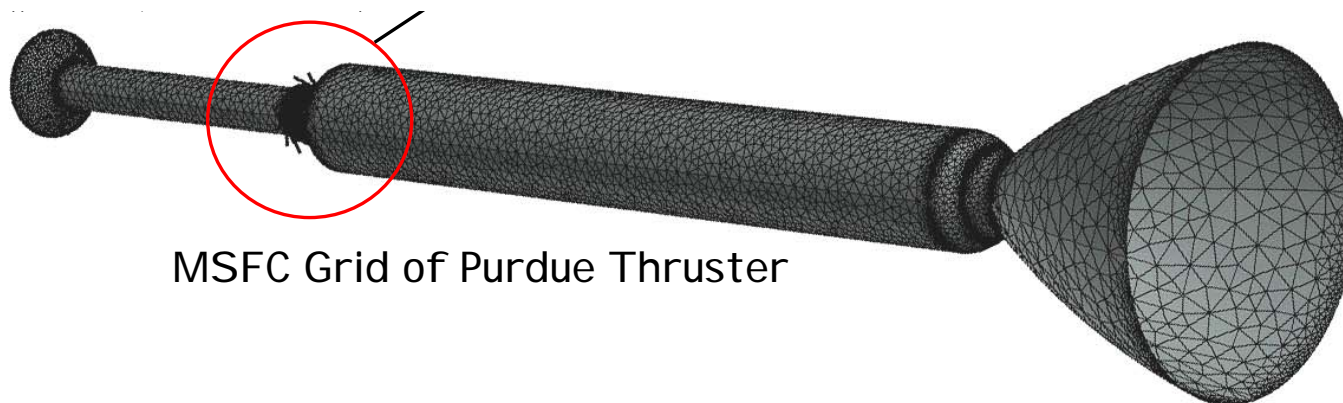
Data to be Acquired

- Propellant temperatures and pressures
- Near-injector heat flux
- Chamber barrel section heat flux
- Near-injector temperatures
- Chamber axial pressure profile

GO_2



Close-up of RP-1 inlet detail



MSFC Grid of Purdue Thruster

- **New programs have generated new design requirements for costs and reliability**
- **Meeting these new requirements demands higher environmental resolution early in the hardware design phase**
- **MSFC has established a vision to meet the need with improved CFD tools**
 - Results in concurrent efforts along two parallel paths
 - Program support
 - Technology development and integration via SCIT Task
 - These two paths are connected by the MSFC CD Simulation Capability Roadmap

- **MSFC is supporting IPD, TR-107 and RS-84 with current capability**
- **SRL's of these efforts indicate a critical need for code validation**
 - MSFC has begun to formulate a validation process
 - MSFC will initiate efforts to use existing data to demonstrate accuracy up to a level of 2
 - Three validation efforts involving new experiments are underway to extend accuracy levels to 3 and above
 - Lessons learned to date include--
 - Good experimental design requires significant CFD support in the planning phase for instrumentation selection, placement, etc.
 - Single design point experiments are not suitable to validate codes that will be used for injector design
 - Uncertainty analysis must be performed on the facility and the test article to quantify and improve the data quality

USING CFD AS A ROCKET INJECTOR DESIGN TOOL: RECENT PROGRESS AT MARSHALL SPACE FLIGHT CENTER

Kevin Tucker, Jeff West, Robert Williams, Jeff Lin, Marvin Rocker, Francisco Canabal, Bryan Robles and Robert Garcia

NASA
Marshall Space Flight Center,
Huntsville, Alabama 35812

James Chenoweth
CRAFT Tech
Huntsville, Alabama

ABSTRACT

The choice of tools used for injector design is in a transitional phase between exclusive reliance on the empirically based correlations and extensive use of computational fluid dynamics (CFD). Without commitment to a focused effort, completion of this transition is several years away at best. The Next Generation Launch Technology (NGLT) Program goals emphasizing lower costs and increased reliability have produced a need to enable CFD as an injector design tool in a shorter time frame. This is the primary objective of the Staged Combustor Injector Technology Task currently under way at Marshall Space Flight Center (MSFC).

The documentation of this effort begins with a very brief status of current injector design tools. MSFC's vision for use of CFD as a tool for combustion devices design is stated and discussed with emphasis on the injector. Long solution turnaround times and questionable accuracy are noted as the primary obstacles to widespread reliance on CFD for injector design. The concept of the Simulation Readiness Level (SRL), comprised of solution fidelity, robustness and accuracy, is introduced and discussed. This quantitative measurement is used to establish the gap between the current state of demonstrated capability and that necessary for regular use in the design process. Current examples of CFD calculations for injector design are presented and evaluated in terms of the SRL. The resultant technology gaps are examples of information used to develop the Combustion Devices CFD Simulation Capability Roadmap. Highlights of the injector portion of the Roadmap process are noted along with key concepts used in its development.

The Roadmap process, augmented by the SRL evaluations, highlights the critical need for code validation for injector flows. MSFC's view of the validation process is presented and issues associated with obtaining the necessary data are noted and discussed. Three current experimental efforts aimed at generating validation data are presented. The case for extensive CFD analysis during the design of the experiment is made and examples of MSFC-generated CFD solutions are presented for each effort. The importance of uncertainty analysis to understand the data quality is also demonstrated.

INTRODUCTION

The Next Generation Launch Technology (NGLT) goals focus design efforts on reducing costs and improving hardware reliability. The two efforts are related since increasing reliability typically reduces operational costs. Rocket engine component reliability can be increased in the design phase by a better understanding of the environments, both thermal and pressure, that will be imposed on critical parts during operation. It is known that the details of the injector design govern not only injector performance, but also environments in the entire thrust chamber assembly. Historically, design tools focus primarily on performance and evaluate environments secondarily, generally in a one-dimensional sense. Environments in the actual hardware are almost always multi-dimensional. Additionally, the NGLT goals have driven cycle selection to an oxygen-rich staged combustion (ORSC) cycle with which designers in the United States have very little experience. The historical design tools apply only marginally to the accompanying injector concepts. Therefore, meeting the NGLT goals will require a new tool that evaluates performance along with multi-dimensional environments with the design goal being to maintain a threshold performance level while generating environments conducive to reliability and long life. Also, robust injector designs require that significant numbers of design evaluations be accomplished over a parametric space during the time frame of the conceptual and preliminary portions of the design phase.

Computational fluid dynamics (CFD) is the tool on the near term horizon most capable of successfully addressing these issues. Theoretically, CFD can be used to determine injector performance and multi-dimensional environments as functions of injector design details. However, CFD has typically not been included in the injector design process. There are at least two fundamental reasons. First, solutions have been time consuming to generate. At best, a few single element solutions may be generated during the early phase of the design cycle. Multi-element solutions have been almost out of the question in this time frame. Secondly, lack of code and model validation has caused injector designers to rightly question whether CFD solutions are of sufficient accuracy to positively impact the injector design. Both of these issues must be addressed before CFD can contribute significantly to improved injector design.

The natural tendency of designers in private industry, enforced by tight budgets and aggressive schedules, is to continue using tools with which they are experienced. This reality dictates that government entities lead the effort to move CFD to the point of acceptance as a reliable injector design tool by the rocket propulsion community. The Marshall Space Flight Center (MSFC) Staged Combustor Injector technology (SCIT) Task has, over the last two years, served to focus technology at MSFC to enable CFD as a reliable and useful tool in an injector design methodology capable of addressing the goals of the NGLT and future propulsion programs. This paper attempts to document both the process developed to meet and the progress made toward achieving the vision for CFD as an injector design tool.

First, a brief status of current injector design tools is provided as context for the current effort. Next, the MSFC vision for using CFD as an injector design tool is stated. Implementation of this long-term goal produces a requirement to evaluate injector CFD capability in terms of both current and desired states. The measuring stick to facilitate this evaluation, Simulation Readiness Level, is presented and discussed in terms of solution fidelity, robustness and accuracy. A generic CFD-based injector design methodology is also outlined and briefly discussed.

Since Marshall is a Space Flight Center, engineering line organizations must provide support for existing and new programs. In the case of the line organization tasked with providing CFD analyses, there must also be technology development and implementation in terms of tools. This is especially true relative to injector CFD analyses. There must then be a parallel effort to prudently use CFD within its current limitations for program support in terms of injector design and analysis while concurrently working technology efforts to improve its capability and usefulness in those areas. Three areas where MSFC is using injector CFD analyses for program support will be discussed. These include the Integrated Powerhead Development (IPD) engine which uses hydrogen and oxygen propellants in a full flow staged combustion (FFSC) cycle and the TR-107 and the RS84 engine both of which use RP-1 and oxygen in an ORSC cycle. The solutions presented facilitate the discussion of current capability. The gaps between current and desired capability serve to motivate the following sections on technology development.

Next, addressing the technology gaps via roadmap development and implementation is discussed. The necessary partitioning and classification of the combustion devices problems into Model Problems is presented. Then, for the model problems, current and desired capability is quantified in terms of Simulation Readiness Level. The gaps thus identified are inputs to the roadmap where they are used to generate and prioritize specific technology tasks.

One of the key areas that emerges from the technology roadmap development process is the critical need for high quality validation data for every propellant combination. So, the status of current MSFC-sponsored validation efforts is presented. Lessons learned from recent experience and attempts to incorporate them into the current efforts are noted. The importance of using CFD to help design the experiment is discussed.

Finally, an attempt is made to objectively summarize what progress has been made at MSFC in enabling CFD as an injector design tool.

SUMMARY STATUS OF CURRENT INJECTOR DESIGN TOOLS

The tools used for injector design are in a transitional period between exclusive use of the empirical tools and extensive reliance on CFD. Although injector designers have begun to use CFD on a limited basis, empirical design tools continue to be used the great majority of the time. The empirical correlations that support the historical tools were developed by extensive use of previously gathered experimental data for similar designs,

propellant combinations and flow conditions. Some of these methodologies also require additional experimental data as input (e.g., drop size distribution, oxidizer core length, etc.) for a specific design. All are necessarily rooted in and bounded by their respective historical databases. Accordingly, these methodologies are not easily extended to address novel design concepts as required by programs like NGLT. These tools focus primarily on performance, with one-dimensional environments a secondary consideration. CFD, as noted earlier, has the potential to evaluate advanced injector concepts both in terms of performance and multi-dimensional environments. Unacceptably long solution turn-around times and questionable accuracy are the main issues that currently limit use of CFD for injector design.

The legacy tools are still overwhelmingly used. In most current injector design programs, CFD is usually not in the original design plan in terms of budget or schedule. The main use of CFD is to evaluate discrete design issues as they arise. Oftentimes this use is a last resort because no other analytical technique is applicable and/or there is no time or money for testing. Since the models are largely unvalidated, the results are typically used qualitatively for trend analyses. There are also occasional uses of CFD results as inputs to historical methods such as for combustion stability. It is primarily the need for new injector concepts driven by new programs that has begun to force the still very limited use of CFD for injector design.

MSFC VISION FOR CFD AS AN INJECTOR DESIGN TOOL

Advancing CFD from the current state of occasional use, often in the ‘there is no other option’ mode, to the primary tool in injector design requires a goal. At MSFC, a long-term goal for using CFD for combustion devices design has been established. That goal is to enable the use of CFD for simulation of preburners, thrust chamber assemblies, and supporting ducting and infrastructure in terms of performance, life and stability so as to affect hardware design in a timely manner. Extensive use of CFD for injector design is the heart of this vision since the physical processes that occur at the injector govern performance and environments in the entire combustor or thrust chamber assembly. Realizing even the injector portion of this vision will require that CFD demonstrate the capability to evaluate large parametric design spaces in both the single- and multi-element contexts in the early portion of the design. These notions have become part of the MSFC Combustion Devices CFD Simulation Capability Roadmap and will be discussed in more detail later.

Pushing CFD into the forefront of injector design requires solution improvement in at least three major areas. In addition to the previously noted issues of solution time and accuracy, the other area requiring attention is solution fidelity, both in terms of geometry and physics. Since this aspect has direct influence on the other two, it will be discussed first. The details of the injector design govern both performance and environments, so the design details must be modeled faithfully. Depending on the design, some single element simulations can be axisymmetric while others must be three-dimensional. All meaningful multi-element injector simulations must be three-dimensional. In terms of physical

processes, the major issues are chemistry treatments, propellant thermodynamic and phase modeling, and the ability to appropriately model heat transfer to and through solid surfaces.

Another solution aspect that must be addressed is robustness. In the design context, robustness refers to the ability to complete simulations of a given fidelity level in terms of convergence, mass conservation and grid independence. Since a large number of simulations must be completed, robustness also involves the ability to pre-process, execute and post-process this large number of solutions in a time frame that fits the design cycle.

The last major area of concern is solution accuracy. There must be quantitative solution capability if CFD is to be more extensively used for injector design. The degree of solution accuracy must be known in order to evaluate its usefulness. It will be shown later that the current degree of demonstrated accuracy is generally very low. This gives rise to the issue of code validation. What do we actually mean by code validation? How do we acquire the data that will be useful for code validation? These and other relevant questions regarding validation will be addressed later.

Quantified levels of simulation fidelity, robustness and accuracy are shown in Table 1. The use of these metrics will be demonstrated in the subsequent sections on program support and the Roadmap where current and desired capabilities are accessed.

Assuming that progress is made in improving CFD capability in the injector design area, some thought must be given to the process in which a useful CFD tool would be an integral part. Figure 1 depicts an embryonic notion of such a CFD-based design optimization process. This process produces an optimized design and then verifies that design by testing. Robust designs require that a range of design parametrics be evaluated. Some optimization capability is needed to help the designer efficiently manage the large amounts of data that will be generated. Since designs will be produced as the CFD capability evolves, Figure 1 also indicates some of the areas where development and integration of technology into the existing capability is required.

The single element design process is one in which issues such as orifice sizes, post tip thickness, cup details, etc. would be evaluated. The initial loop through the process accomplishes the validation and optimization. The green arrows in Figure 1 depict this part of the process. Here, the first step in the single element portion of the process is generation of one or more initial concepts. Next, if it does not already exist, suitable validation data is acquired to validate the CFD model to the required level. If the code to data comparison is not good enough, code improvements will be necessary to increase the accuracy. When the comparisons are good enough, the validated model can then be exercised to provide data for the single element optimization. Independent design parameters are selected over an applicable range to build a design of experiments (DOE) matrix. Based on the DOE matrix, the grids are generated, cases set up, run and post-processed. Process automation in terms of preprocessing is very important because of the time saved in setting up a large number of cases and the need to minimize human error in

Table 1. Quantification of Fidelity, Robustness and Accuracy for Simulation Readiness Level.

Level	Fidelity	Robustness	Accuracy
0	Extremely simple physics, boundary conditions and geometry	Have not completed any simulations	Not evaluated other than historical quality of simulation tool
1	One of reasonably precise geometry or boundary conditions or physics	Have completed some simulations	Qualitative agreement with existing results of related problems
2	Two of reasonably precise geometry or boundary conditions or physics	Simulations with proven convergence and conservation	Quantitative agreement with existing results of related problems
3	Reasonably precise physics, boundary conditions and geometry	Simulations with proven convergence, conservation and grid independence	Qualitative agreement of relevant measures over a parametric space of a representative model problem
4	Reasonably precise physics, completely precise boundary conditions and as-built geometry	Fire and Forget (95%+) simulations with convergence, conservation and grid independence	Quantitative agreement of relevant measures over parametric space of model problems
5	Completely precise physics, completely precise boundary conditions and as-built geometry	Fire and Forget (95%+) simulations with convergence, conservation and grid independence plus the ability to complete 100 or more problems within 3 weeks	Quantitative agreement of relevant measures over parametric space of actual problem

the case set up. The dependent variables extracted from the CFD solutions are some measure of performance, and environmental information relevant to the particular design, like injector face temperature, tip temperature, chamber wall temperature, etc. Here again, because of the large amounts of data involved, automation of the post processing is important. Each independent variable is then correlated in terms of the dependent variables and fed to an optimizer. The optimizer allows the designer to deal objectively with the inherent tradeoffs of injector design in the context of multiple independent and

dependent variables, large amounts of data and often-competing trends. Reliable optimization techniques that make efficient use of the available data are essential to the process. The optimum design will likely be a compromise having performance that is acceptable and environments that are conducive to long life. This optimum single element design is then verified with additional single element testing as shown by the blue arrows in Figure 1.

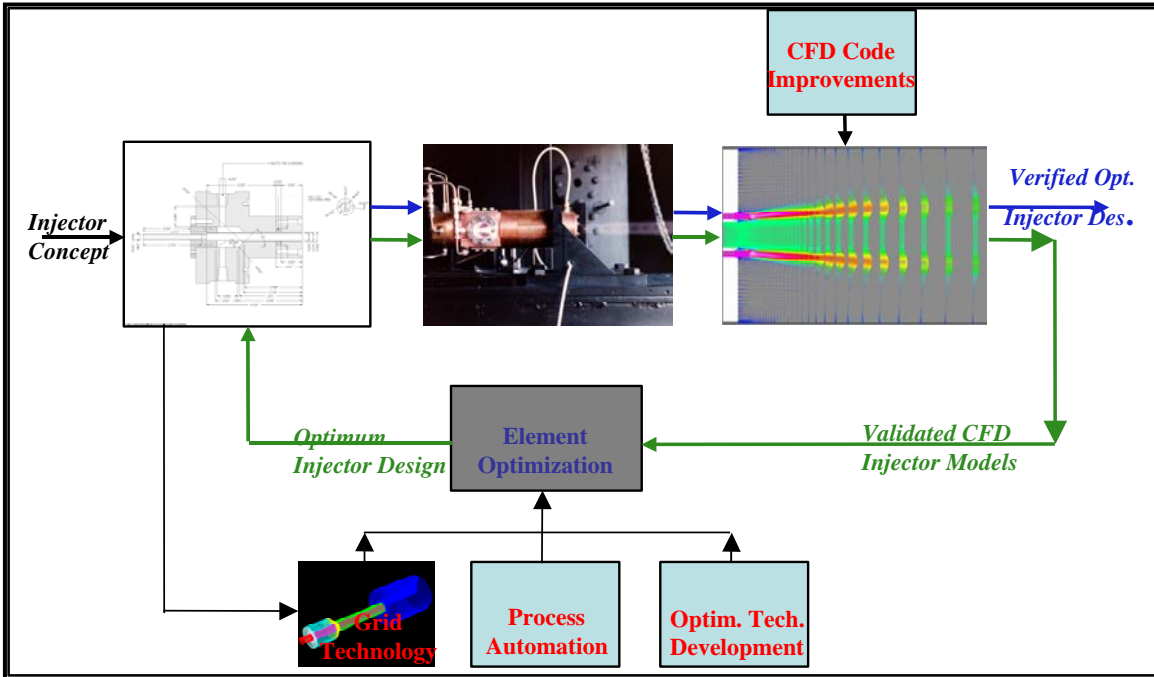


Figure 1. Generic CFD-Based Injector Design Optimization Process.

This optimum single element design would then be used to generate a subscale multi-element design concept that would be carried through a similar process. Here, independent variables such as element spacing, patterns, film cooling, etc. would be evaluated.

CURRENT EXAMPLES OF PROGRAM SUPPORT

MSFC is providing CFD support to main injector design and analysis for three programs. First, MSFC has single and multi-element simulation efforts under way in support of the main injector for the Integrated Powerhead Demonstrator (IPD) Program. The IPD burns O₂ and H₂ in a full flow staged combustion (FFSC) cycle. MSFC is also conducting single element simulations to support main injector designs for both the TR-107 and RS-84 engines in the NGLT Program. The TR-107 engine is a Northrop Grumman Corporation concept while the RS-84 is a Boeing Corporation (Rocketdyne Propulsion and Power Division) concept. Both engines consume O₂ and RP-1 in an oxygen-rich staged combustion (ORSC) cycle.

INTEGRATED POWERHEAD DEMONSTRATOR

In the IPD FFSC cycle, all of the propellants go through preburners before being fed to the main injector. Hence, both the oxygen and hydrogen propellants are gaseous as they enter the main injector. In addition to the general environment issues that accompany any new injector design, there is concern that the IPD main injector faceplate may be hotter than normal since the fuel used to cool it is warm gas and not a cold liquid. Also, the gaseous propellants do not have to atomize and vaporize thus allowing combustion to occur closer to the injector face and increasing the potential for even harsher environments. An initial single element optimization has been completed and a multi-element model of the full-scale main injector is underway at MSFC.

IPD-Single Element

A scaled IPD element is part of validation work that is ongoing at Penn State University. Since validation data is forthcoming, the decision was made to start with the baseline concept and attempt an optimization of that element. The idea was to model performance and environmental indicators as functions of an array of independent geometry variables. The independent geometry variables considered are shown with ranges of interest in Figure 2.

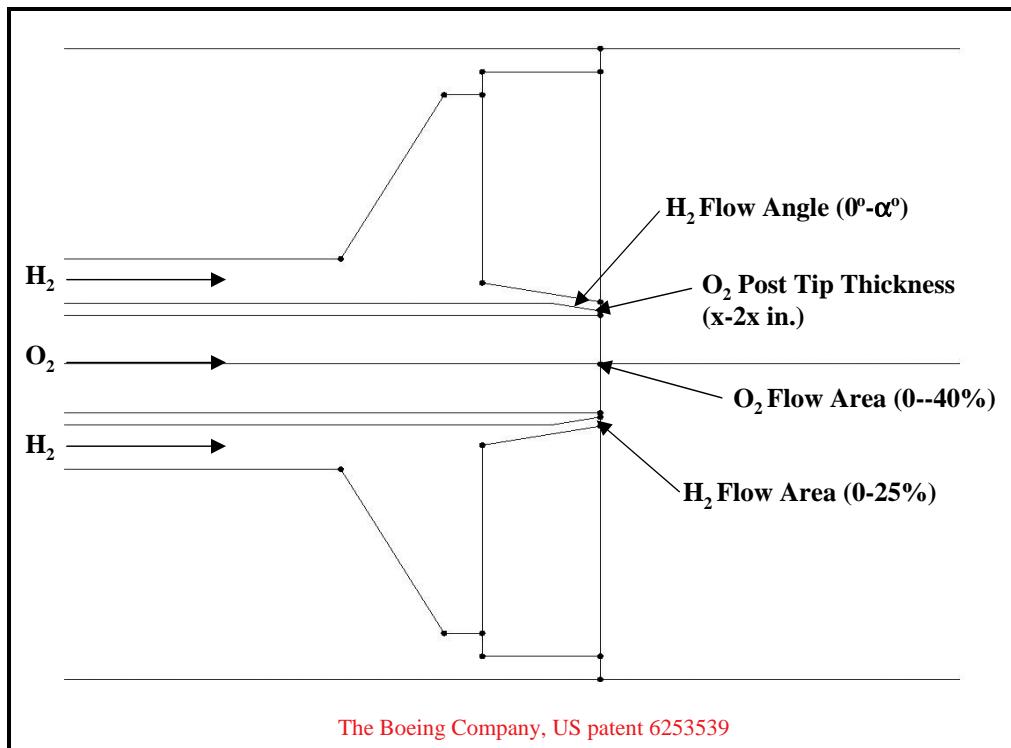


Figure 2. Independent Variables for Element Optimization.

From an initial concept baseline, both propellant flow areas were modified; the H_2 flow area being increased by up to 25% and the O_2 flow area decreased by up to 40%. The O_2 post tip thickness was increased by as much as 100% from the baseline. The H_2 flow angle was modified over a range of plus and minus 100% of the baseline flow angle. A design of experiments matrix was constructed yielding a total of 54 cases to be run.

The sample solution in Figure 3 highlights the dependent variables. Here the combustion length, X_{cc} , is taken to be a measure of combustion efficiency with shorter combustion lengths indicating more efficient designs. Three temperatures, all calculated as adiabatic wall temperatures for this effort, were taken as environmental indicators. The maximum temperature on the O_2 post tip, TT_{max} , the maximum temperature on the injector face, TF_{max} , and the wall temperature two inches from the injector face, TW_3 , all have direct bearing on life. For this relatively crude optimization, the objective was to trade performance (better performance occurring when the combustion length is shorter) versus life of the various parts (longer part life occurring when the part temperature is lower).

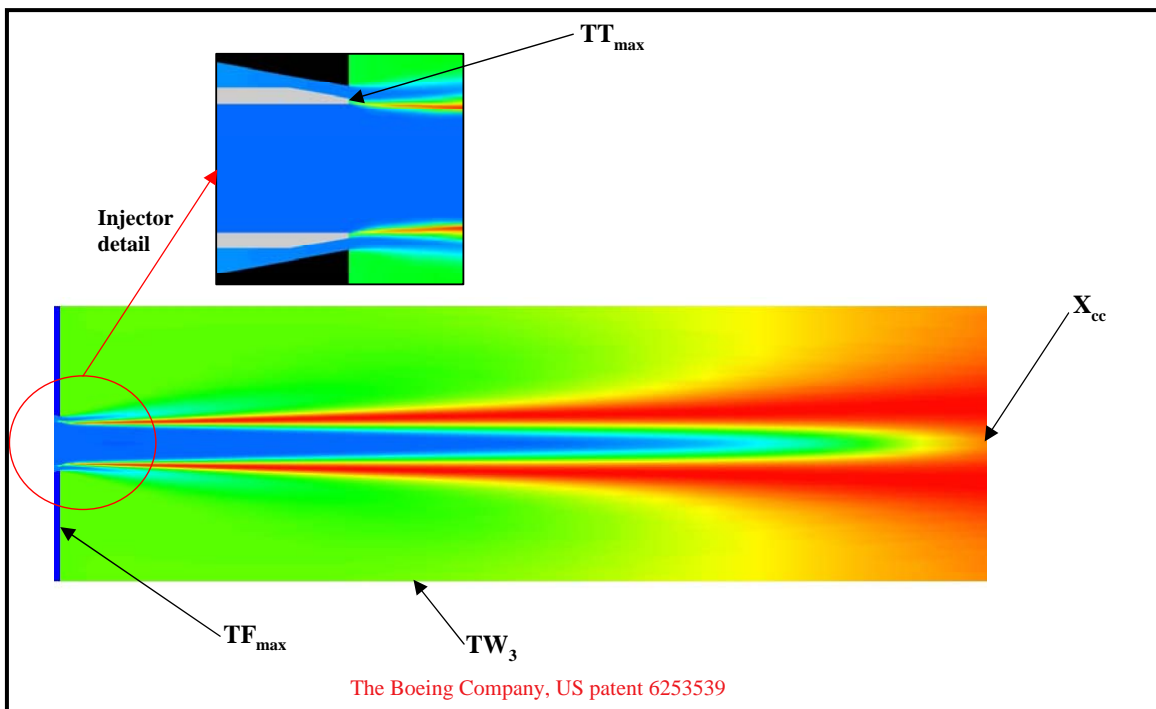


Figure 3. Sample Results and Dependent Variables.

Grids for the 54 cases were generated from a database in less than an hour. The cases were set up and run on a local PC cluster, with each case being run on a single CPU. All cases were completed in approximately five days. The results were post processed to extract the data of interest, which was then used to generate response surfaces (usually quadratic polynomials) for each dependent variable. During this process, problems were noticed with the quality of the polynomial fit for the combustion length. Investigation of the situation indicated insufficient grid resolution at the end of the flame region. New individual solutions were run until grid independence was achieved. The new grid density

was used to regenerate the grids for the 54 cases all of which were then rerun. The new combustion length correlation was much improved.

Before continuing, it should be noted that a significant amount of effort went into automating both the pre and post processing of these cases prior to the optimization. Reducing the amount of “hand labor” via process automation accomplishes two important things. First, when running large numbers of cases concurrently, there must be an efficient and verifiable process that is used to set up, run and post process the cases. It is infinitely easier and surer to verify a good process than it is to individually check to ensure that all the grids, input files and initial conditions are accurate and in the proper directories. Secondly, automation saves significant amounts of time in getting to the point where the results can be used for engineering.

After the individual response surfaces were generated, they were linked together into a composite surface so that multi-variable optimizations, which enable the performance versus life trades, could be accomplished. Both single and multi-variable optimizations were performed. Single variable optimizations were performed mainly to test the optimizer, since the individual dependent variable minimums were known. The optimizer worked well for these simple cases. One result of note was that each single variable optimization resulted in a different element geometry. The multi-variable optimization allows some or all of the dependent variables to be optimized simultaneously. This is the mode most useful to injector designers. Here, the dependent variables can be weighted either equally or unequally depending on the design priorities. Notably, when the multi-variable optimization was done with all dependent variables equally weighted, the design producing that result was different than that for any of the single variable optimizations. The clear message is that design of a robust injector that performs well and promotes long component life requires that as many of the relevant independent variables (i.e., the design details) be included and modeled as early in the design process as possible. Simply put, this requires an efficient, validated CFD code, sufficient computer resources to run the simulations and an optimizer to enable the designer to objectively manage the large amounts of data generated.

Completion of this initial design optimization was valuable in terms of experience gained in managing the process. However, evaluation of the CFD calculations in the context of the SRL concept reveals the additional work required before this process can have a significant design impact. The fidelity level of the single element simulations is approximately 3. The element is designed to be axisymmetric so the two-dimensional axisymmetric assumption is reasonable here. Both propellants are gases and the chamber pressure is such that the ideal gas assumption is also reasonable. The robustness level is 5. Convergence, mass conservation and grid independence have all been demonstrated. Fifty four cases were assembled and run in less than two weeks so 100 cases in three weeks could be done comfortably assuming processor availability. The accuracy level of the simulations is 1. Qualitative agreement has been obtained on a similar problem that used ambient propellants. Thus the key issue here is lack of proven accuracy at a level that could quantitatively affect design.

IPD-Multi-Element

Since the environments seen on the injector face and the near-injector chamber wall are functions of not only the element design, but also the number of elements, element spacing, injector pattern, etc., a three dimensional model is required to provide these environments. The initial focus of this model is environments with a lesser emphasis on performance.

A fifteen-degree slice of the main injector and main combustion chamber was modeled. The key assumption in the model is that the thermal environment at any point on the injector face or chamber wall is significantly affected only by the elements in the immediate area. Thus, the remaining elements are assumed to have only an indirect effect through the bulk flow in the chamber. This bulk flow is modeled by assuming that outside the area where the elements are modeled in detail, the flow is assumed to be completely mixed at equilibrium conditions. These assumptions permit the generation of a discrete mesh of a manageable size (i.e., approximately 2-4 million grid points). According, seven elements were simulated to model the propellant mixing and combustion in detail, while the remainder of the flow field is modeled as equilibrium bulk flow. The faceplate is modeled as a solid so the transpiration cooling is not part of this simulation. Figure 4 shows the domain modeled and the calculated temperature field. Typical results for the heat flux on the injector are shown in the close-up in Figure 5.

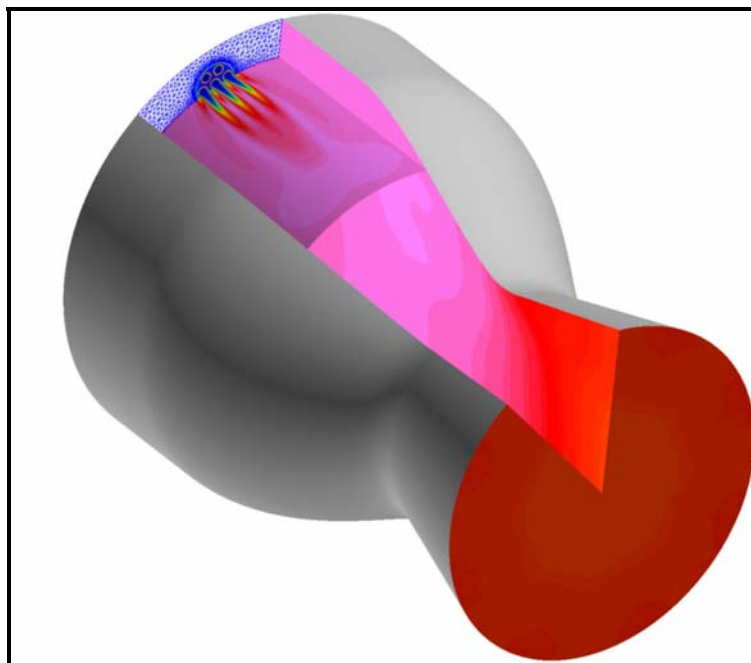


Figure 4. IPD Main Injector Temperature Contours.

Another simulation of the IPD main injector and main chamber is currently underway. The outer three element rings are simulated to give a better indication of the environments on the wall. Again, the remainder of the injector flow is assumed to be

completely mixed and is modeled as equilibrium bulk flow. Main chamber wall heat flux contours from this developing solution are shown in Figure 6.

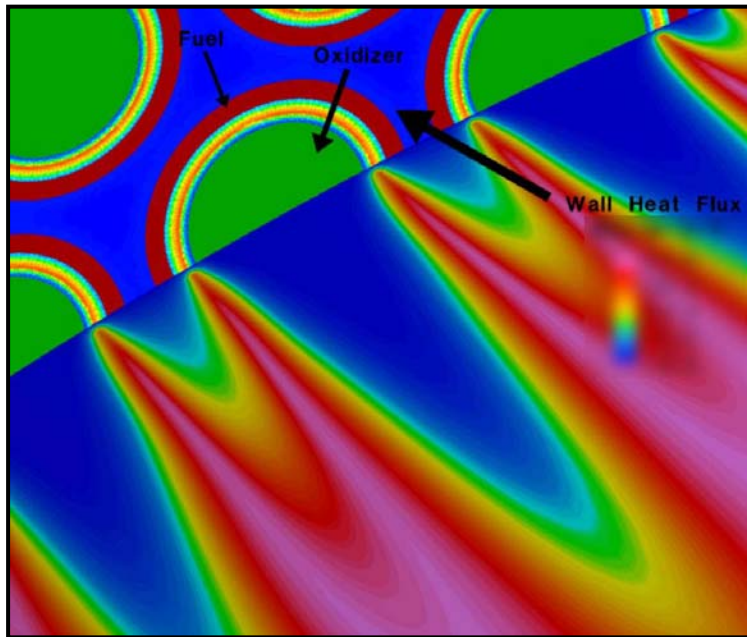


Figure 5. IPD Injector Face Heat Fluxes and Gas Field Temperatures.

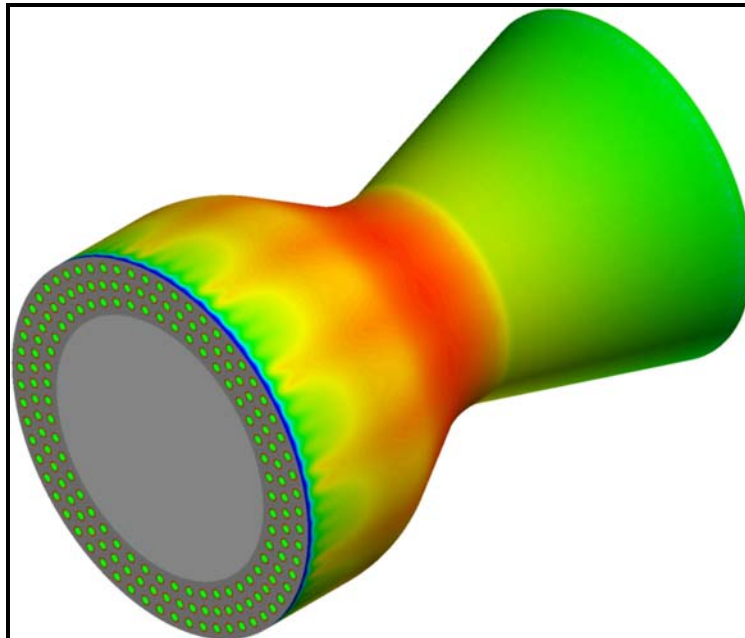


Figure 6. Developing Heat Flux Contours on the IPD Main Chamber Wall.

This ongoing effort represents the first attempt at MSFC to model the three-dimensional details of a multi-element injector. The level of immaturity of this type of calculation is revealed in the SRL evaluation. Since the geometry and boundary conditions are extremely simple, the fidelity is approximately one. Only a few calculations have been completed so the robustness level is also about one. The accuracy level has not been evaluated at all resulting in a demonstrated accuracy level of zero.

NEXT GENERATION LAUNCH TECHNOLOGY

Because of the increased emphasis the NGLT program places on engine life, the thermal environments generated by the TR-107 and RS-84 main injectors have taken on a higher priority than usual. The injector-generated thermal environments imposed on the injector and main chamber wall need to be at low levels relative to past programs to address the NGLT goals for long life. That means environmental dependencies on injector design details must be well understood and appropriately characterized. Since American designers are relatively inexperienced with the ORSC cycle, there is very little existing data that can be applied to the current designs. Ill characterized thermal environments in the near-injector area lead to designs that are likely to fail to meet at least one of the design requirements. If the thermal environments used for the design are too high, more fuel than actually necessary will be used to cool the wall and other solid surfaces in the near injector part of the chamber. This results in poor injector performance. If the thermal environments used for the design are too low, insufficient fuel coolant will be used likely causing some of the parts of the TCA to fail to meet life requirements. CFD is thus being used in an attempt to gain more insight into the problem.

Northrop Grumman TR-107

The TR-107 is an ORSC cycle engine concept using RP-1 and oxygen propellants in the NGLT program. Support of the TR-107 main injector is provided through a government task agreement (GTA) with the Northrop Grumman Corporation. The objective of the analyses is to validate a CFD tool to accurately predict performance and environments for main injectors ranging from subscale test articles to the full-scale injector. A single element test program will be conducted that will provide data for the code validation.

Numerous two-dimensional axisymmetric cases have been set up to model the uni-element test article. This represents a compromise since the propellant injection scheme is actually three-dimensional. All cases run thus far use an ideal gas assumption for both propellants. Wall temperatures have been fixed so that convective heat fluxes can be calculated. Cases have been run with and without film coolant, with different film coolant levels, at different propellant flow rates and mixture ratios and with varying cup depths. Cases with and without film cooling were run to judge the effectiveness of the film coolant. Figure 7 shows the static temperature distributions for Case TP-2 with and without the film cooling just downstream of the injector. Figure 8 shows the fuel mass fraction profiles for both cases. These cases were run to help judge the film coolant effectiveness. The wall heat flux profiles for both cases are shown in Figure 9. They are

identical up to the end of the cup where the film coolant is introduced for one case. The initial large spike at $x/x_{\max}=0.03$ is where the combustion is initiated at the injector fuel inlet. The fuel between the flame and the wall is warmed by the wall very briefly until heating by the flame causes the near wall gas temperature to rise, thus causing the heat flux to increase fairly sharply until the end of the cup is reached. As the corner is turned to the injector face, the heat flux falls off rapidly for both cases, though the film coolant injected at the face causes that heat flux for that case to be lower. The heat flux for the case with film coolant rises to meet that of the no film coolant case at $x/x_{\max} = 0.11$, thus indicating the end of its effectiveness.

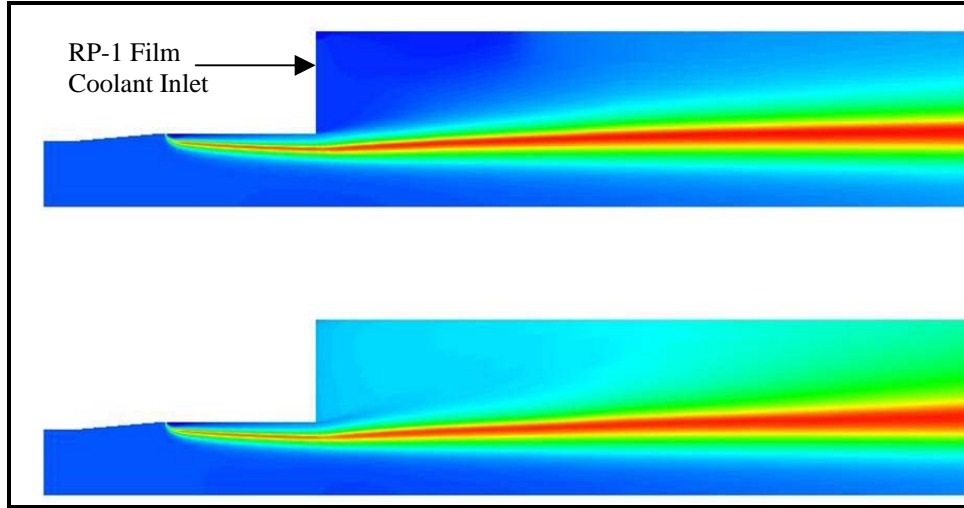


Figure 7. Static Temperature Contours for Case TP-2 with and without Film Coolant.

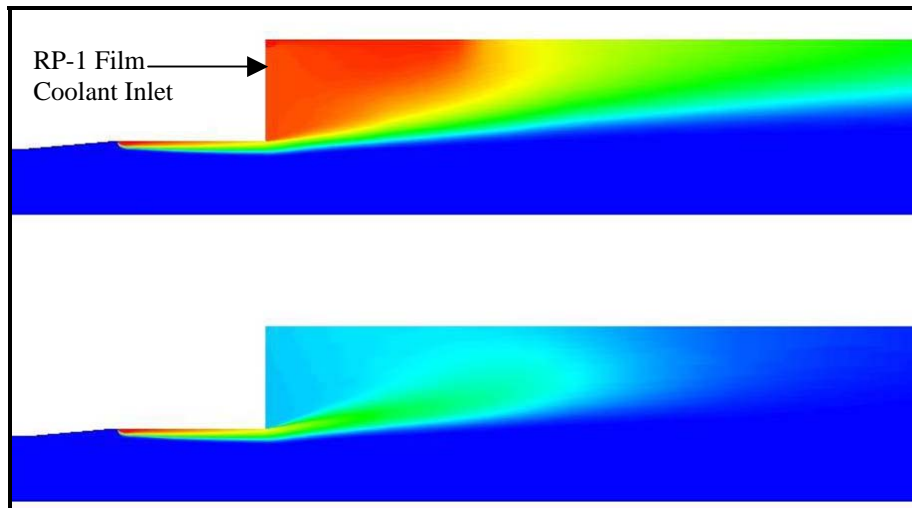


Figure 8. RP-1 Mass Fraction Contours for Case TP-2 with and without Film Coolant.

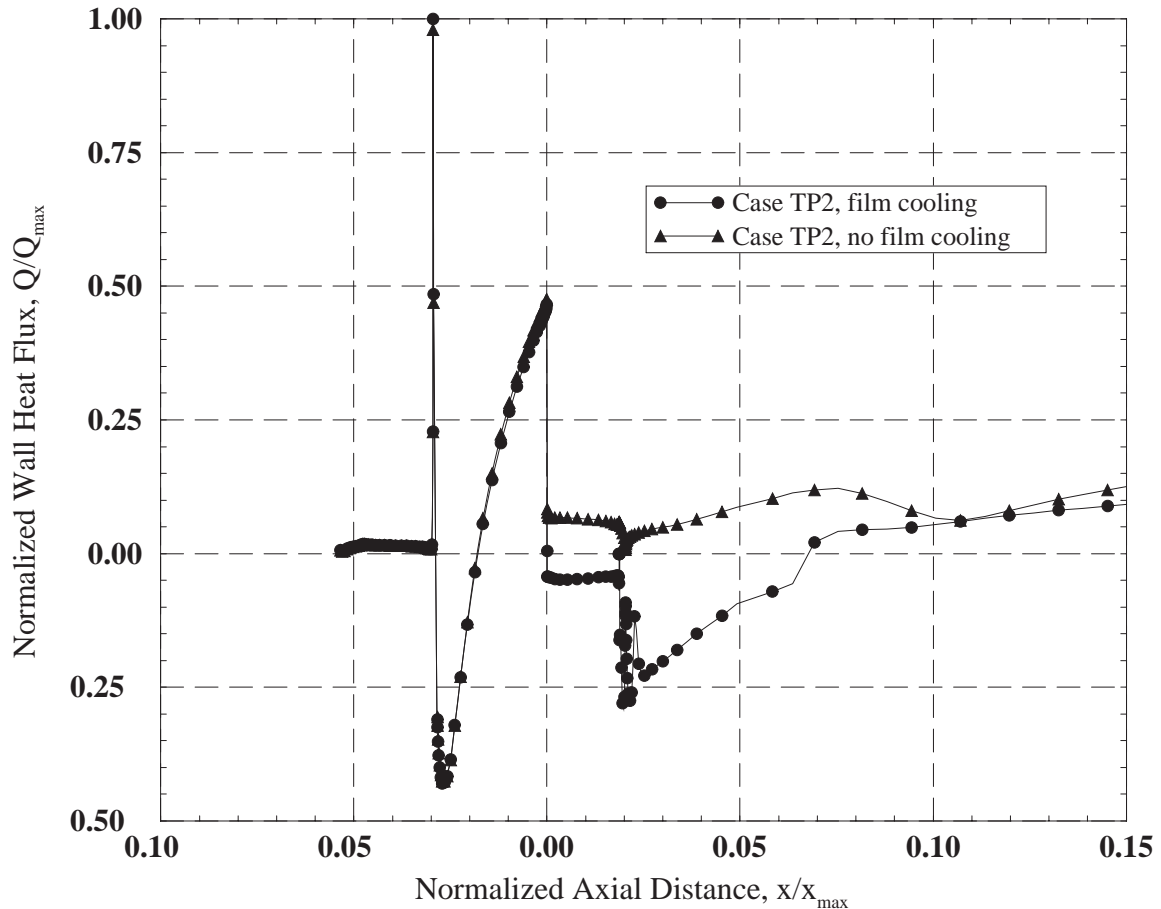


Figure 9. Wall Heat Flux Profiles for TR-107 Case TP-2 with & without Film Cooling

Again, there are several issues with the calculations that are identified in the context of the notion of SRL. In terms of the fidelity, the level is essentially zero since both the geometric and physical representations are extremely simple. However, it should be noted that an RP-1 decomposition model was employed (for some cases) to account for cracking as the film coolant heats up. A three dimensional grid slice of the problem has been generated and is currently running.

The robustness level of the two dimensional, axisymmetric simulations is approximately at level three. Numerous solutions have been completed with convergence both from a residual standpoint and with temperature probes inserted at key points in the flow field. Both overall mass conservation and plane-by-plane species balances have been achieved. Also, grid independence has been demonstrated.

There have been no validations of the code with similar problems. The accuracy level is therefore essentially zero.

Boeing (Rocketdyne Propulsion and Power) RS-84

The RS-84 engine is an NGLT concept that uses the oxygen-rich staged combustion (ORSC) cycle with oxygen and RP-1 as propellants. The objective of the RS-84 CFD injector design support is to mitigate risk by better characterizing the injector-generated thermal environments on the baffle elements and on the chamber wall. Two-dimensional axisymmetric single element representations of both situations were developed. For the baffle element simulation, the distance from a typical element centerline to the baffle element wall is taken to be the single element chamber radius. For the chamber wall simulation, the distance from an outer row element centerline to the chamber wall was taken to be the chamber radius. The single element chamber radius for the chamber wall simulation is the larger of the two chambers. These situations are represented notionally in Figure 10.

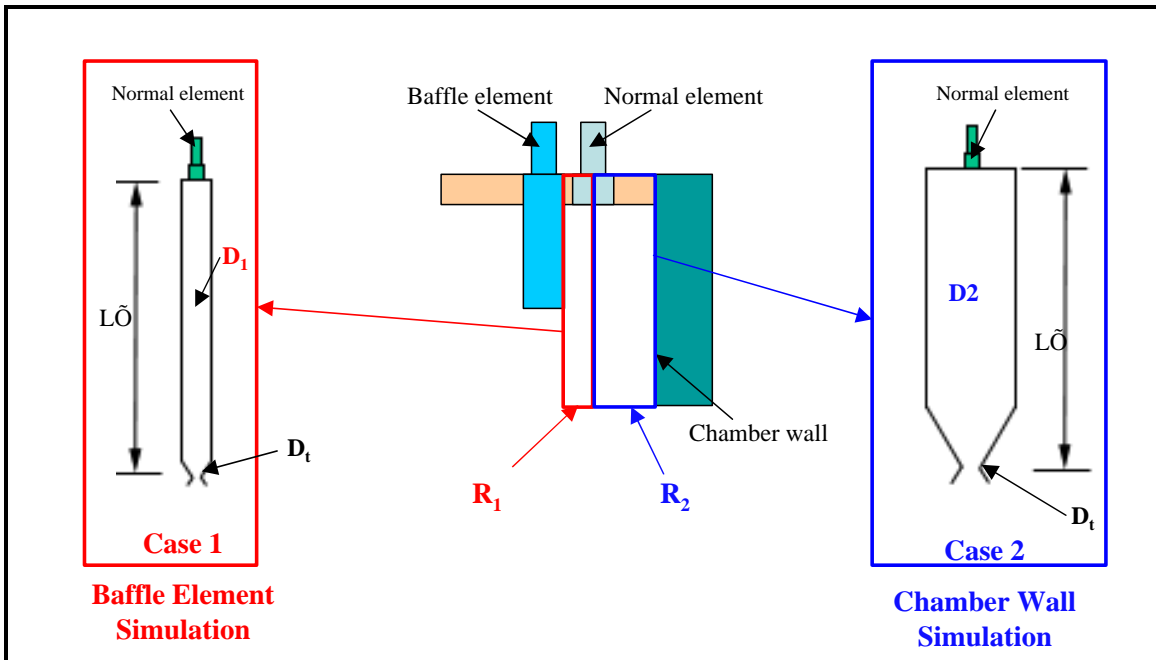


Figure 10. Single Element Baffle and Chamber Wall Representation.

For both chamber diameters, two variations of the same element were evaluated. In the first variation, some of the oxygen is introduced axially, while the remainder is introduced tangentially. The second element is similar except all the oxygen is introduced axially. All of the fuel is introduced tangentially in both variations. Full-scale propellant conditions were used while the flow rates were scaled from the full-scale power balance. Propellants in both cases were modeled as ideal gases. In all cases, the wall temperature was fixed to enable heat flux calculations. The chamber was modeled in such a way that the distance from the injector to the throat is the same as in the full-scale main chamber. Grid independent solutions were obtained for all cases.

In Figure 11, the effect of oxygen swirl is shown for the baffle simulation. The heat flux for the case where a portion of the oxygen is swirled is higher than for the case where all

of the oxygen is introduced axially. The effect of swirling a portion of the oxygen is to enhance mixing with the fuel, thus leaving less of the cool fuel to cool the wall.

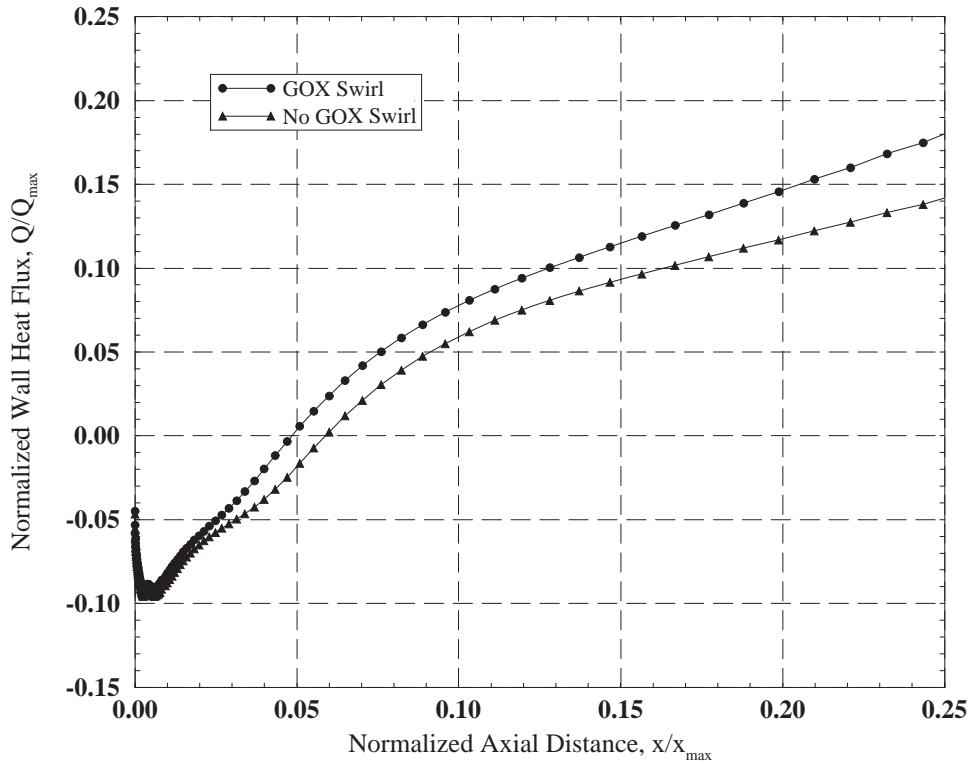


Figure 11. Effect of GOX Swirl on RS-84 Near-Injector Wall Heat Flux

Figure 12 shows the comparison between heat fluxes for the baffle (smaller chamber) case versus the chamber wall (larger chamber) case where all the oxygen is introduced axially. Here, the heat flux for the baffle case is negative at the injector face ($x/x_{max}=0.0$) due to the wall being warmer than the fuel. It rises steadily from just near the injector to the end of the domain of interest. The heat flux for the chamber wall case is essentially flat for the first third of the domain shown. This is primarily due to the recirculation zone near the injector in the larger chamber that is almost nonexistent in the smaller chamber. The gases in the recirculation zone are essentially constant temperature, thus accounting for the flat heat flux profile. After reattachment, the heat flux begins to rise at a rate similar to that in the small chamber. The heat flux for the baffle wall case is higher throughout most of the domain because of higher near wall velocities and temperatures.

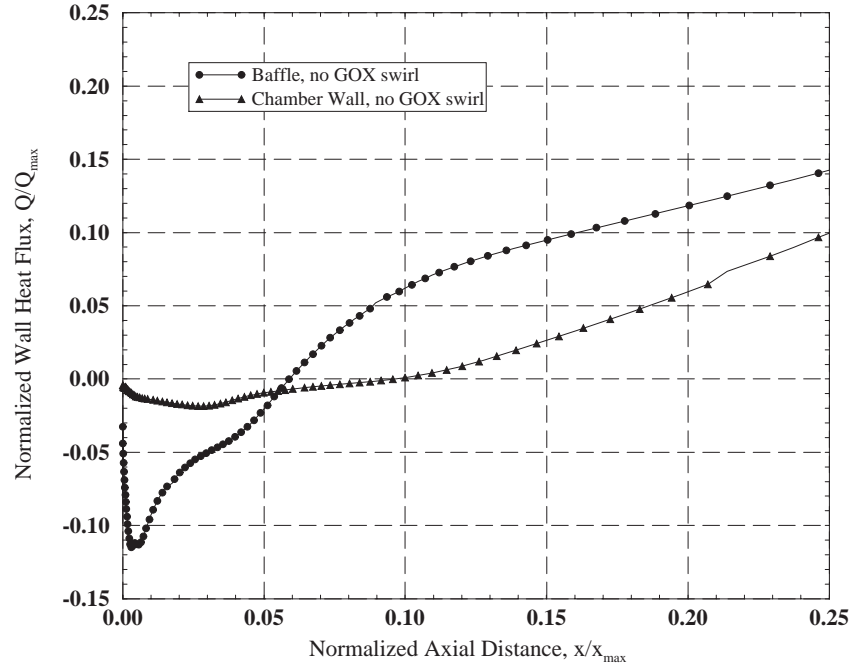


Figure 12. Baffle versus Chamber Wall Heat Flux Comparison for RS-84.

There are several issues with these calculations that will be highlighted in terms of the SRL notion discussed earlier. In terms of fidelity, these simulations are essentially at the 0 level since the geometric and physical representations are extremely simple. Geometrically, the tangential propellants cause the element to be three-dimensional instead of the two-dimensional representation used in these simulations. In terms of physics, the ideal gas representation of the RP-1 at the RS-84 operating conditions results in a fluid density that is 20-30% high relative to the real fluid. The robustness level of the simulations is approximately at level 3. Numerous solutions have been generated with proven convergence from a residual standpoint along with temperature probes inserted at key points in the flow field. Both overall mass and plane-by-plane species balance have been achieved. Also, grid independence has been demonstrated. There have been no validations of the code with similar problems. The accuracy level is therefore essentially at the zero level. Thus, significant improvements must be made for these calculations to be useful for design.

Figure 13 highlights the accuracy issue. The baffle case is used to show the difference in heat fluxes due to a physical aspect of the problem, the effect of swirling a portion of the oxygen, versus those differences resulting from choice of turbulence models. Figure 13 shows that the heat flux difference caused by swirling a portion of the oxygen versus introducing it all axially is on the same order as the difference resulting from using the standard $k\epsilon$ versus an extended $k\epsilon$ turbulence model. Without good quality validation data to give guidance on turbulence model selection, it is thus impossible to quantify the effect of oxygen swirl on the heat flux for this problem. At this point, the only meaningful conclusion is that swirling a portion of the oxygen produces a slightly higher heat flux than with no oxygen swirl.

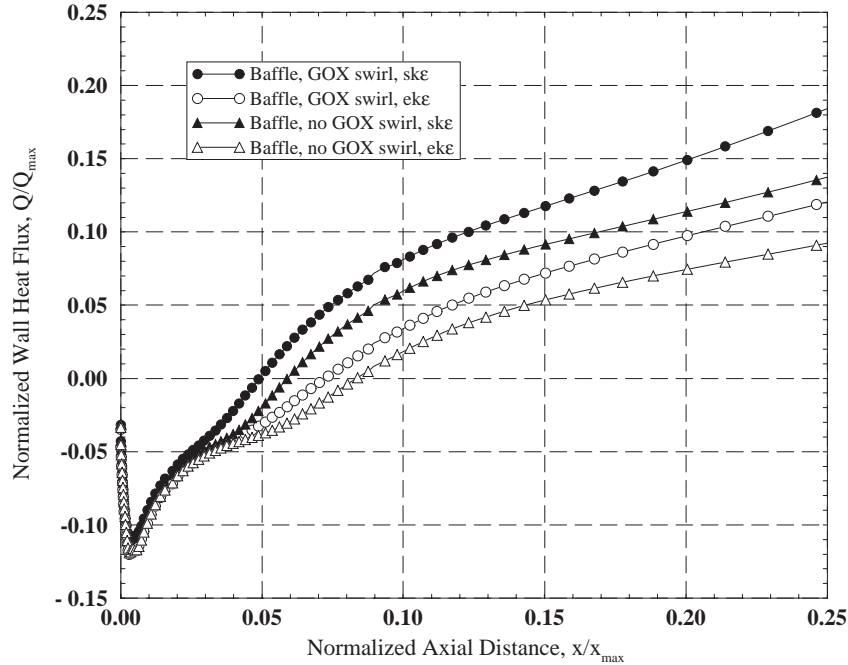


Figure 13. Effect of Turbulence Model Selection on Heat Flux Prediction.

COMBUSTION DEVICES CFD SIMULATION CAPABILITY ROADMAP

The examples of program support for injector design and analysis are evidence that significant progress has been made at MSFC in the last two years. It is also apparent that much work remains to be done before CFD can be relied on as the primary injector tool.

At MSFC the recent work on injector design fits into a larger effort embodied in a long-term goal for CFD in the context of combustion devices design. Although stated earlier, that goal bears restating here. It is to enable the use of CFD for simulation of preburners, thrust chamber assemblies, and supporting ducting and infrastructure in terms of performance, life and stability so as to affect hardware design in a timely manner. The scope of simulation capability required to meet this goal is extremely broad and deep. Flow regimes ranging from low subsonic to supersonic and from single phase to multi-phase must be modeled. Physical processes that must be modeled include turbulence, finite rate chemical reactions, heat transfer to solid surfaces, evaporation, etc. Some propellants flow through the injector axially, some swirl while others impinge into each other. There is a range of fuels and oxidizers in use, each combination of which has its own set of reactions and in some cases other issues, to be modeled. The high pressures and temperatures in the chamber sometimes negate the assumption of the ideal gas equation of state and require other more complex treatments.

This daunting array of issues has been one of the things that has stymied logical, consistent development of CFD in the general area of combustion devices design and especially for injectors. The first step to making progress is understanding what needs to

be done. Secondly, priorities must be established in terms of technical issues, budgets, manpower requirements and schedule. Finally, there must be an implementation plan in place that generates and manages technology tasks. This plan must also anticipate the newly developed technology so that the work continues with minimal disruption.

MSFC is in the process of developing a Combustion Devices CFD Simulation Capability Roadmap to facilitate an orderly technology development process that meets the above-noted goal. The function of the Roadmap is made clear by looking at its users. First the Roadmap is useful at a high level to programs and projects since it can be used at a high level to provide a vision of technology development strategy-both short and long term. It conveys to them a realistic view of current capability and the resources required to advance that capability to higher SRL's. Secondly, the Roadmap provides the line organization management with the necessary tools for capability evaluation and resource planning. Thirdly, it allows the engineer in the line organization to identify critical weaknesses in capability and to specify detailed technology tasks that will bridge the gaps. Finally, the Roadmap will provide the research community with detailed requirements in terms of new technology including required physical models and tool improvements and experimental designs required for simulation certification.

The aforementioned depth and breadth of the entire problem requires some linearization to break it up into something more tractable. MSFC has chosen the Model Problem approach. The notional cutaway of the Space Shuttle Main Engine (SSME) shown in Figure 14 is presented to facilitate the discussion. Eighteen model problems are identified

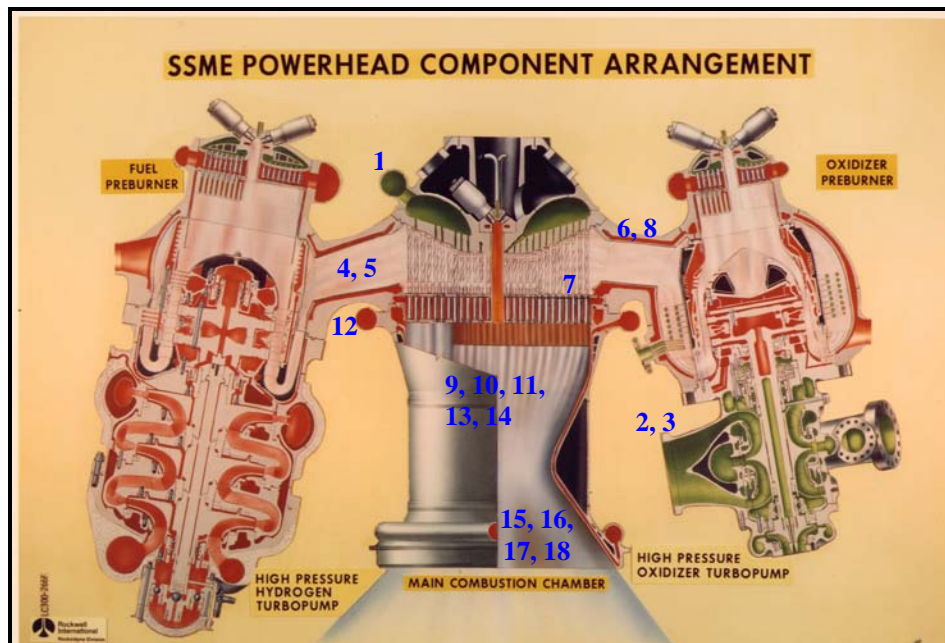


Figure 14. Model Problems Located Notionally on SSME Cutaway.

in the combustion devices area. The first six have to do with propellant flowing through hardware that feeds the injector. They are identified and organized logically in Figure 15. Next, model problems 7-12 cover the flow into and through the injector. They are also

shown in Figure 15. Finally, model problems 13, 14, 15, 16, and 18 are the environmental problems of interest to NGLT. They are also grouped in Figure 15. These Model Problems are associated with the thermal, and in some cases structural, loads on the hardware. It should be noted that Model Problem 14, combustion stability, is a very long-term goal.

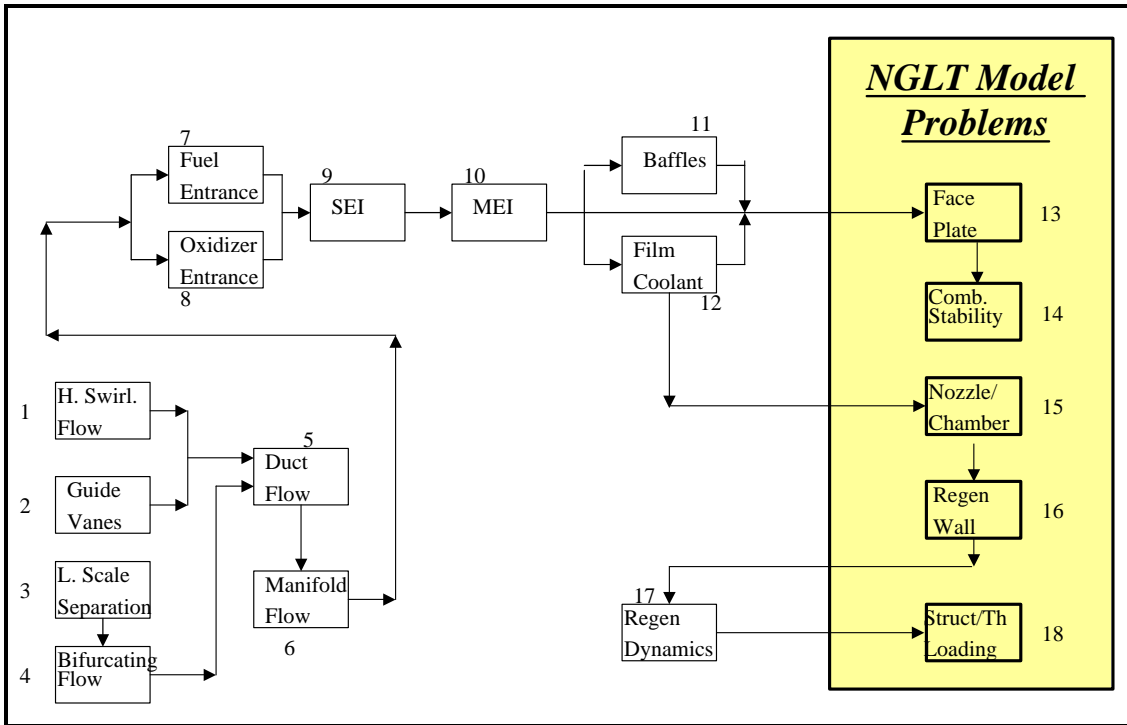


Figure 15. Model Problem Identification and Grouping.

Figure 15 supports the notion that the heart of the overall Roadmap should be the injector problem. Advances in grid generation techniques and increases in computing power have made the non-reacting duct flow problems embodied by Model Problems 1-6 considerably more tractable. The characteristics of the flow issuing from the injector are what govern Model Problems 13-18 (with the exception of problem 17). In addition to performance, these are the real problems of interest to NGLT in its effort to create designs that extend hardware life. The ability to evaluate the life of combustion devices components depends on the ability to accurately predict the environments imposed on them during operation. These environments are primarily a function of injector design. Thus, meeting the MSFC long-term goal requires the initial focus to be on the injector.

The initial focus on the injector portion of the model problem group also addresses the most difficult of the model problems. There are several viable fuels and oxidizers and even more combinations. Depending on the flow conditions, the propellants can be either thermodynamically subcritical or supercritical. The injector geometry may be shear coaxial, swirl coaxial or impinging or any hybrid combination. All of these issues have important ramifications on how, or even whether, the injector can be modeled. Somehow, the Roadmap must address this complexity. After setting the injector problem as the

initial Roadmap focus, it is divided into two Model Problems, the single element injector (SEI) and the multi-element injector (MEI) to make it more approachable. Further division of the injector problem is required to make the technology development problem tractable. The route chosen is based on the notion of degeneracies or subdivisions. Each model problem is further classified based on propellant selection, propellant state, injector geometry and whether the simulation is steady, unsteady, or transient. The requirement to quantitatively establish current and desired simulation levels also demands such subdivisions. Figure 16 shows the degeneracies for Model Problem 9 - the Single Element Injector. The red stars indicate areas of current work at MSFC.

<p>9.1 Steady</p> <p><u>9.1.1 Supercritical reactants</u></p> <p> 9.1.1.1 H2/O2</p> <p> 9.1.1.1.1 Shear Coaxial *</p> <p> 9.1.1.1.2 Swirl Coaxial *</p> <p> 9.1.1.1.3 Impinger</p> <p> 9.1.1.2 RP-1/O2</p> <p> 9.1.1.2.1 Shear Coaxial *</p> <p> 9.1.1.2.2 Swirl Coaxial *</p> <p> 9.1.1.2.3 Impinger</p> <p> 9.1.1.2.4 Hybrid *</p> <p> 9.1.1.3 RP-1(cracked)/O2</p> <p> 9.1.1.3.1 Shear Coaxial</p> <p> 9.1.1.3.2 Swirl Coaxial</p> <p> 9.1.1.3.3 Impinger</p> <p> 9.1.1.4 JP-N/H2O2</p> <p> 9.1.1.4.1 Shear Coaxial</p> <p> 9.1.1.4.2 Swirl Coaxial</p> <p> 9.1.1.4.3 Impinger</p> <p><u>9.1.2 Subcritical reactants</u></p> <p>9.2 Unsteady</p> <p>9.3 Transient</p>
--

Figure 16. Model Problem 9 (Single Element) Degeneracies.

For each Model Problem of interest, the current SRL is quantified in terms of fidelity, robustness and accuracy. The current SRL is then contrasted with the minimum SRL level required to impact injector design, in this case for NGLT. This minimum level has been established at SRL = (3, 4, 3). At this level, the simulation must be based on reasonably precise physics, boundary conditions and geometry. The capability must exist to run simulations in the “hands off mode” to convergence 95% of the time with mass conservation and grid independence. The simulations must be based on qualitative validation of relevant measure for at least one relevant problem. The difference in current and minimum required SRL levels forms the basis by which technology tasks are defined.

Since it is not possible to address all of the degeneracies of even a single Model Problem simultaneously, general priorities are set by the requirement to support current programs. Sometimes these general priorities are modified to an extent by technical issues. For

instance, even though the TR-107 and RS-84 projects currently have very high priority, considerable effort is being expended on the IPD support-both in single element and multi-element injectors. The justification is that the GO_2/GH_2 propellant combination, with its relatively simple physics and well understood chemistry, make it an efficient and effective arena in which to validate certain fundamental aspects of injector flow, investigate many aspects of simulation requirements and to develop processes and procedures that are very useful for all other injector simulations.

Technology tasks identified to support current programs are then organized in terms of technical priority, schedule, budget and available manpower. The result is a local map for each degeneracy of each model problem. The local maps are then prioritized and collated into Model Problem maps. The overall Roadmap is comprised of the Model Problem maps.

A summary of the SRL levels of the simulations done thus far to support MSFC programs is shown in Table 2. Some immediate conclusions can be drawn from this data. First, with the exception of the IPD single element simulation, the fidelity level is at zero. The IPD single element fidelity is at level three because the element is axisymmetric (i.e., there are no significant geometry simplifications) and the ideal gas assumption is good for the GO_2 and GH_2 propellants.

Table 2. SRL's of Program Support Simulations

Simulation	f	r	a
IPD Single Element	3	5	1
IPD Multi-Element	1	1	0
TR-107 Single Element	0	3	0
RS-84 Single Element	0	3	0

The other single element analyses actually use axisymmetric geometry assumptions for three-dimensional elements and the ideal gas assumption for RP-1 is generally not very good. The fidelity level of the IPD multi-element simulation is at a low level mainly because of all the simplifying geometry assumptions. Having the capability to generate three-dimensional grids for complex element geometries will increase fidelity levels. Additional computer resources to run the resulting large jobs are also necessary. A robust real fluids model also increases the fidelity level, especially for the hydrocarbon models.

In general, the robustness level of the calculations is higher, especially for the single element simulations. The single element IPD calculations were started and run to successful completion without operator intervention. Thus far, the hydrocarbon simulations have to be run in the non-reacting mode for a time, stopped, examined for a suitable ignition location and restarted in the reacting mode. Currently, the IPD multi-element simulation requires significant operator attention to achieve a solution.

The current demonstrated accuracy level of all the simulations is very low-either zero or one. This problem cannot be addressed by simply having a more precise model or more computer power, although both of these would be helpful. The initial and most important issue here is lack of relevant validation data. The ability to obtain and use high quality validation data is currently the most significant roadblock to using CFD for designing rocket engine injectors. The next section will examine some of the issues and concerns about data for validation and the validation process itself.

CFD CODE VALIDATION

The fact that the designers' lack of confidence in the solutions is one of the primary obstacles to CFD being used as an injector design tool was noted earlier. This notion of lack of proven accuracy was confirmed via the SRL discussion in the last section. MSFC, along with others in the community, has produced CFD solutions for injectors that are grid independent and satisfy the conservation equations for mass, momentum, energy and other auxiliary equations along with balance of species. Achievement of good quality solutions, while currently somewhat of an accomplishment for these complex flows, is really only the beginning. The accuracy of a code for a given simulation must be demonstrated on relevant problems to overcome the designers' reluctance. This requires a validation process.

MSFC engineers view the validation process as four basic phases. The first phase is to use existing data for related problems from the literature to increase the demonstrated accuracy level from the current level of zero or one to two. This concept is shown in Table 1. To further increase the accuracy level, new experimental data must be acquired. So the second phase is experimental planning. The third phase is experimental execution. Finally, the newly acquired data is used for validation to increase the demonstrated accuracy level of the code.

Lack of relevant, high quality validation data is the major initial obstacle in the validation process. Today, this obstacle looms so large it is difficult to see beyond it to others that surely must be conquered en route to real code/model validation. This data is needed now to provide guidance to many remaining questions that relate directly to solution accuracy. Are the simplifying geometry assumptions appropriate? Is the appropriate equation of state being used? Are the physical sub-models appropriate? And so on.

Since MSFC engineers do not yet have experience in a complete cycle of validation process, at this point the discussion will focus on current issues relative to the first two phases of the process. In this context, there are two major concerns. First, careful design of the experiment is critical in obtaining the data necessary to advancing the simulation accuracy to the required level. Second, the accuracy of the data must be well characterized in order for it to be truly useful.

Prior efforts at MSFC have shown that the users of the data must be intimately involved in the design of the test in order for the data to be useful as originally intended. MSFC

engineers are currently heavily engaged in this area for three experimental efforts. This phase involves much more than mechanical design of a test article and establishing a test matrix. CFD simulation of test conditions must be an integral part of this up front planning. For instance, the object is to increase the confidence of the code for injector design, so the code must be capable of discerning the effect of changes in geometry details and flow conditions on performance and environments. Just comparing the CFD solution to data from one design or one set of conditions is not sufficient validation for a design tool. An experiment must then be designed that spans a relevant range of geometries and conditions. The CFD code must be exercised over this parametric range of independent variables in order to assess the effect on the dependent variables. This must be done before the dependent variables to be measured can be established. Also, the range of the dependent variable response across the experimental space must be broad enough to be measured confidently. All of this is necessary to establish requirements for the type of instrumentation required and its location.

The issue of confidence in the experimental data leads to the notion of uncertainty analyses. A formal uncertainty analysis of both the experimental facility and the test rig must be conducted prior to finalizing the rig design, instrumentation selection and placement, and test matrix. The confidence level of the variables to be measured must be known before testing to ensure that the data will be useful for validation.

Both of these issues place requirements on the validating organization. It is clear the up front work requires a consistently high level of coordination between the organization that needs the data and the organization that provides the data. Engineers from both organizations must work together in an iterative process between data requirements and experimental capability to arrive at a test article design, instrumentation selection and placement, and data uncertainty levels. If these pre-test tasks are not taken seriously, it is unlikely that even successful execution of the experiment will yield the required data.

The validation process consumes significant amounts of valuable resources if it is done correctly. Manpower requirements to consistently achieve the above-noted coordination level are high. Many CFD simulations must be run before the experimental design is completed. Also, the high-pressure hot-fire experiments require large amounts of funding. Successful validation requires a long-term commitment from all of the involved organizations

The remainder of this section will provide brief overviews of three MSFC-sponsored validation experiments and MSFC involvement in each to date.

GO₂/GH₂ EXPERIMENT AT PENN STATE UNIVERSITY

The single element validation experiment to be performed at Penn State University will address Model Problem 9.1.1.1.1, which is the GO₂/GH₂ single element coaxial injector. This effort not only supports the IPD simulations noted earlier, but also a more general effort to validate CFD codes for injector design. The flow conditions are shown in Table 3. The test rig with the main chamber and both preburners is shown in Figure 17. Note that both propellants are fed to the scaled main injector as hot gases after having passed through preburners.

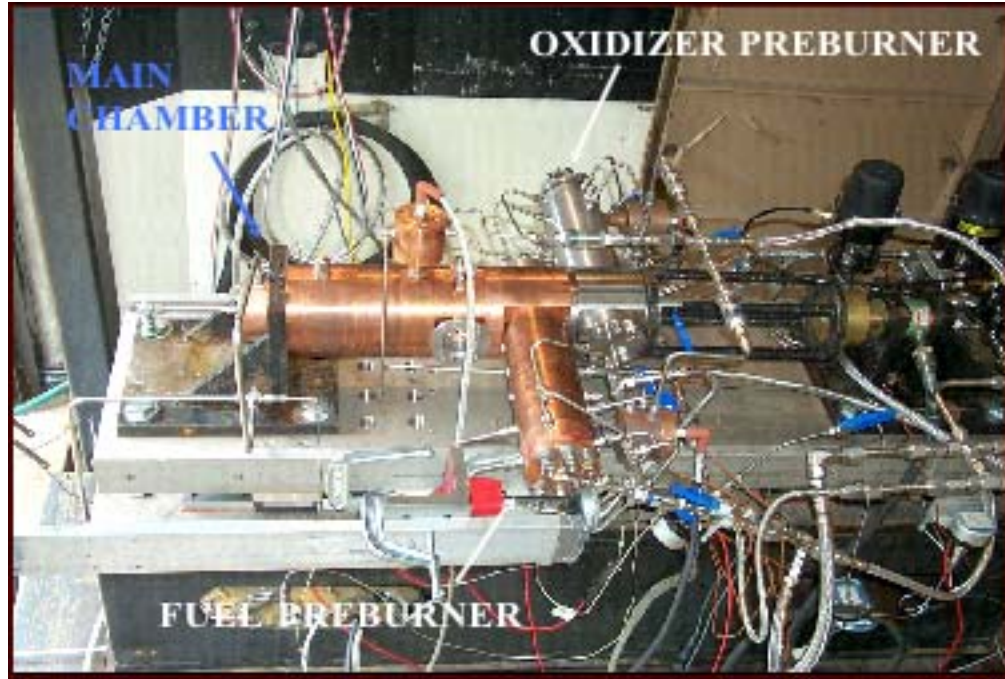


Figure 17. GO₂/GH₂ Test Rig at Penn State University.

The objective of the current task is three-fold. First, data will be taken for two injectors to validate the CFD codes. Second, the validated codes will then be used to design an optimum injector in terms of performance and environments. Finally, this optimized injector will be built and tested to verify the design optimization process. The pre-test CFD work to date has highlighted two issues. The first relates to the type and location of instrumentation required to validate the code for design in this effort. The second has to do with uncertainty in the test rig.

The initial work done to optimize a GO₂/GH₂ element (discussed earlier) required that a fairly large parametric design space be evaluated with CFD. Evaluation of the mixing data (radial species profiles at various axial stations) and environmental data (temperatures on the injector and chamber wall) led to a change in the data to be taken in the upcoming test. Originally, Raman spectroscopy was to be used to measure radial species profiles at two or three axial stations to validate mixing. The mixing of the propellant streams governs the performance and environments. Careful evaluation of the CFD data showed that the near-injector wall temperature profile, an indirect measure of

mixing, showed a much broader response range than the species profiles. Accordingly, a decision was made to measure the wall temperatures and heat fluxes down the length of the chamber. Calculated adiabatic wall temperatures for the two extreme cases are shown in Figure 18. An attempt was made to use this data to aid in placement of the instrumentation in the main chamber. However, uncertainty in the current model predictions and space constraints led to a decision to equally space the thermocouples and heat flux gauges along the chamber as shown in Figure 19.

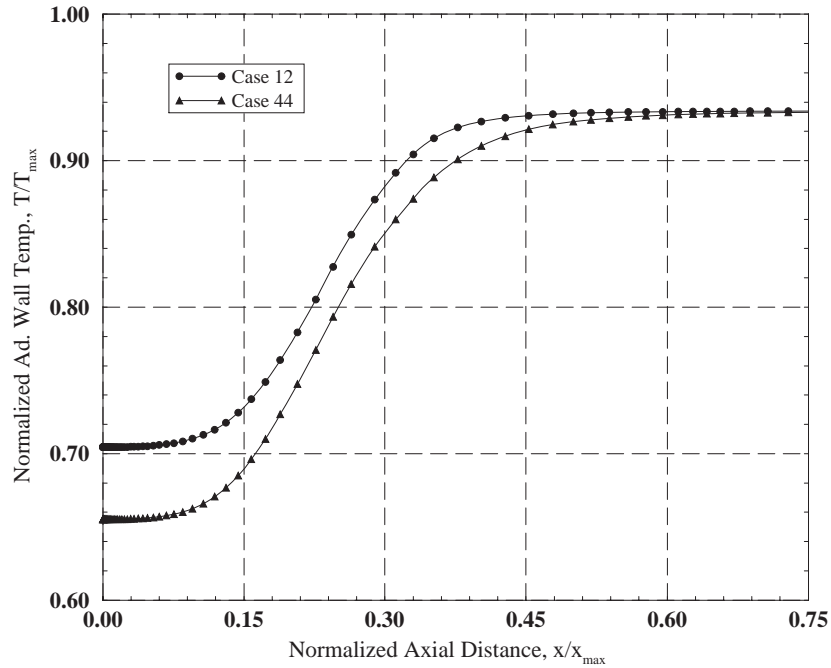


Figure 18. Adiabatic Wall Temperature Comparison for Two Extreme GO_2/GH_2 Cases.

The second issue where pre-test CFD has played a role concerns uncertainty relative to the injector design itself. A diagram of the injector end section of one of the elements to be tested is shown in Figure 20. This diagram depicts the “as built” condition. Since the hot gases from the preburner flow along both walls of the GO_2 tube, the tube heats up and grows in length. This growth is calculated to be $0.22 D_{gp}$, where D_{gp} is the inside diameter of the GO_2 post. Accordingly, the tube is built $0.22 D_{gp}$ short so when tested it should grow to be flush with the injector face. Figure 21 shows the temperature field for five cases of injector tip locations ranging from $0.22 D_{gp}$ upstream of the face to $0.22 D_{gp}$ downstream of the face. The adiabatic wall temperatures from these calculations are plotted in Figure 22. This parametric analysis of the injector indicates the tip location must be well known. It can be seen that the wall temperature spread from high to low is on the order of the extreme cases shown in Figure 18 that were due to intentional design changes.

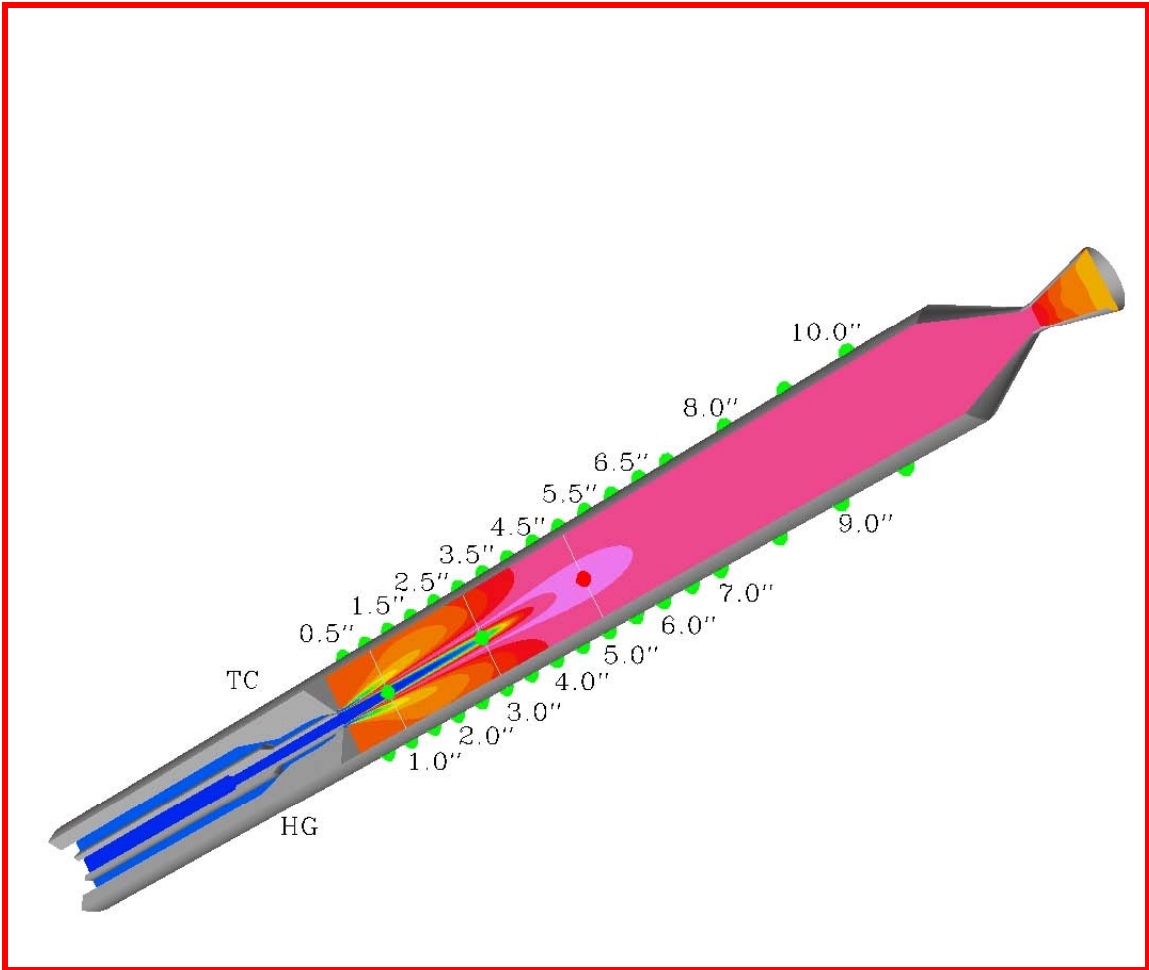


Figure 19. Instrumentation Layout for the GO_2/GH_2 Validation Test.

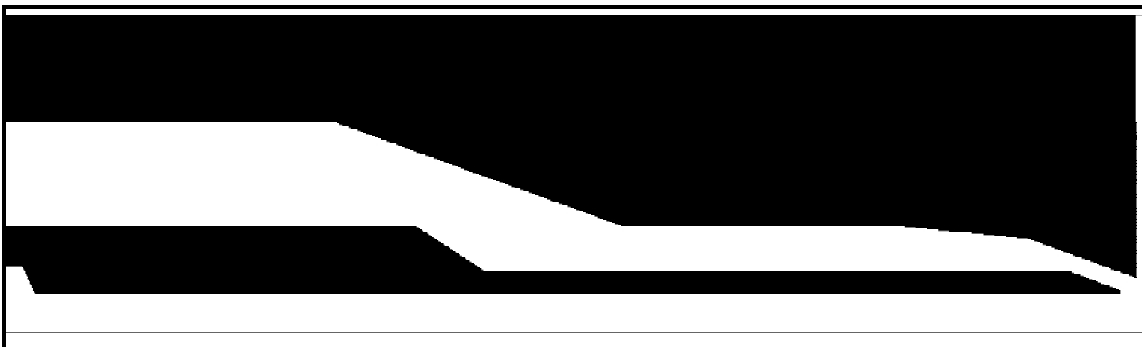


Figure 20. Injector Assembly with GO_2 Post in the As-Built Condition.

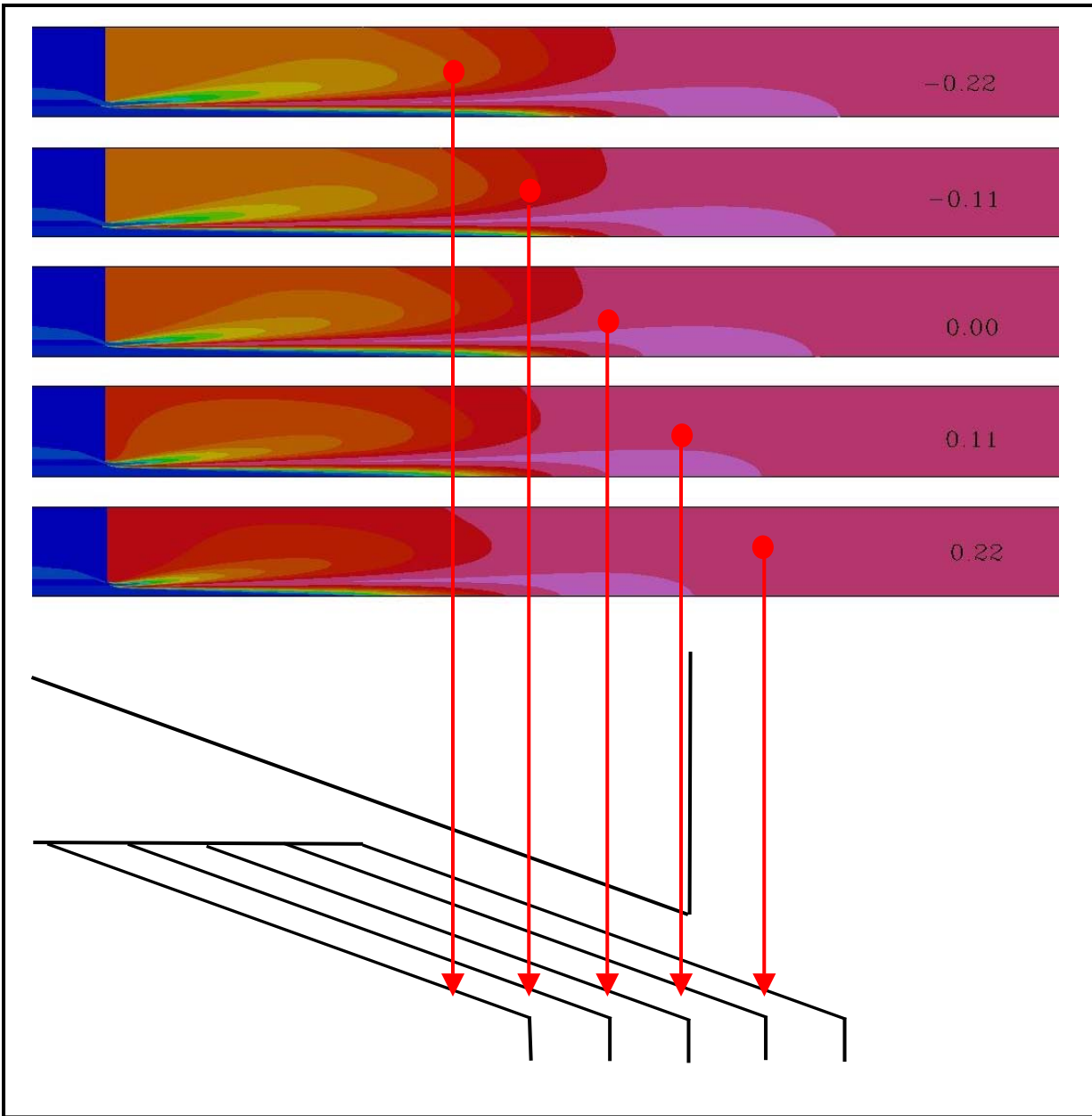


Figure 21. Temperature Fields Resulting from Various GO_2 Post Positions.

There are other potential issues with the experiment. The wall temperature rise shown in Figure 18 needs to be well characterized by the experiment. It is not certain equal spacing of the instrumentation will adequately capture the rise rate. The thermocouples and heat flux gauges have not been used in this rig before and so there is some concern about their ability to survive what are known to be relatively harsh start transients.

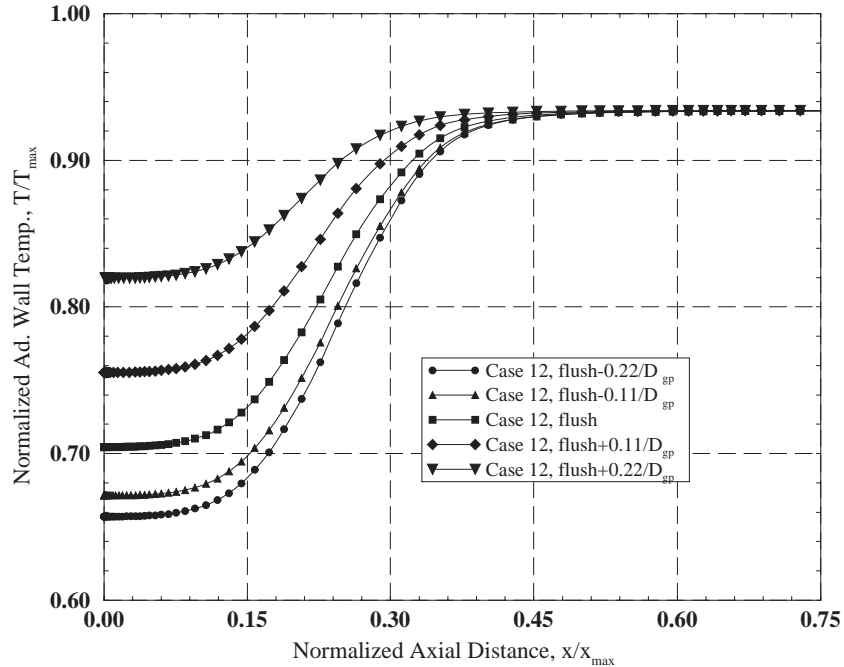


Figure 22. Wall Temperature Comparisons Resulting from Various GO_2 Post Tip Positions.

LO_2/LH_2 EXPERIMENT AT MSFC

The multi-element validation experiment to be performed at MSFC Test Stand 115 will address Model Problem 10.1.1.1.1, which is the LO_2/LH_2 multi-element shear coaxial injector. The objectives of the experiment are to evaluate the mixing accomplished by the injector and to collect data to validate chamber wall heat flux calculations at preburner-type conditions.

This effort is actually a carry over from the RS-83 program. The RS-83 engine design included a preburner that used liquid propellants. This task was already well under way when the RS-83 program was cancelled. Despite the fact that with the cancellation this task does not fit in the near-term roadmap, a decision was made to continue the work. The task was fairly far along (much of the hardware had been designed and fabricated) and it was felt the experience testing multi-element hardware would be beneficial in the long term. Also, just working through doing the CFD analysis to support the test at least peripherally supports the IPD CFD effort. If the test effort is successful, the data will likely be useful for other programs.

A picture of the injector that will be tested in the Modular Combustor Test Article (MCTA) is shown in Figure 23. The injector has seven elements; one at the center surrounded by six on the outside arranged in a circular pattern. Figure 24 shows the injector during water flow check out testing at TS 115. The test matrix, encompassing about 40 tests, is based on four sets of conditions—two chamber pressures, both



Figure 23. LO₂/LH₂ Multi-Element Injector.

supercritical, and two propellant mixture ratios - 0.66 and 0.78. Since the mixture ratios are low, the bulk temperature will also be fairly low. A series of thermocouple spool sections will be employed to evaluate the mixing by making spatially resolved gas temperature measurements. An example of one of the several thermocouple ring configurations to be tested is shown in Figure 25. The rings can be rearranged from test to test to give the desired axial resolution. Within each ring the thermocouples can be moved in or out to provide spatial resolution in the radial direction. The chamber will also be fitted with a window section to enable shadowgraph visualization of the near-injector combustion process. A calorimeter section will be installed for some tests to obtain wall heat flux measurements.

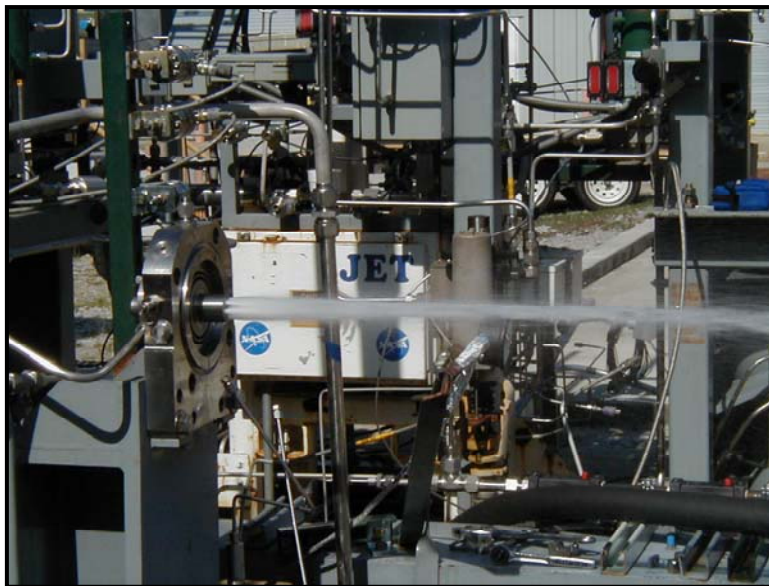


Figure 24. Water Flow Checkout Testing of the LO₂/LH₂ Multi-Element Injector Test 115.

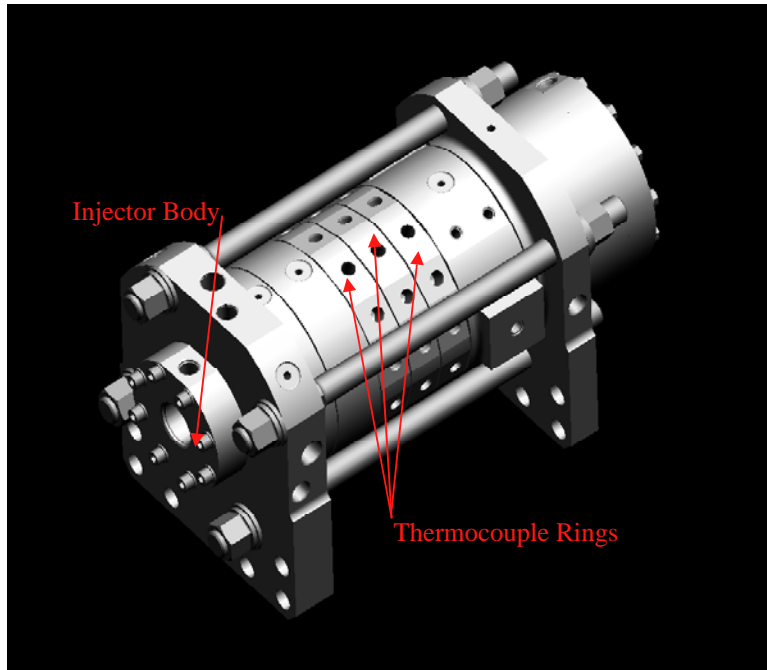


Figure 25. CAD Model of MCTA Showing One Thermocouple Ring Configuration

Pre-test calculations have been made to simulate the three-dimensional flow field in the chamber. A sample calculation of the temperature field is shown in Figure 26. The center element, because it is surrounded by the other elements is probably most representative of an actual preburner element.

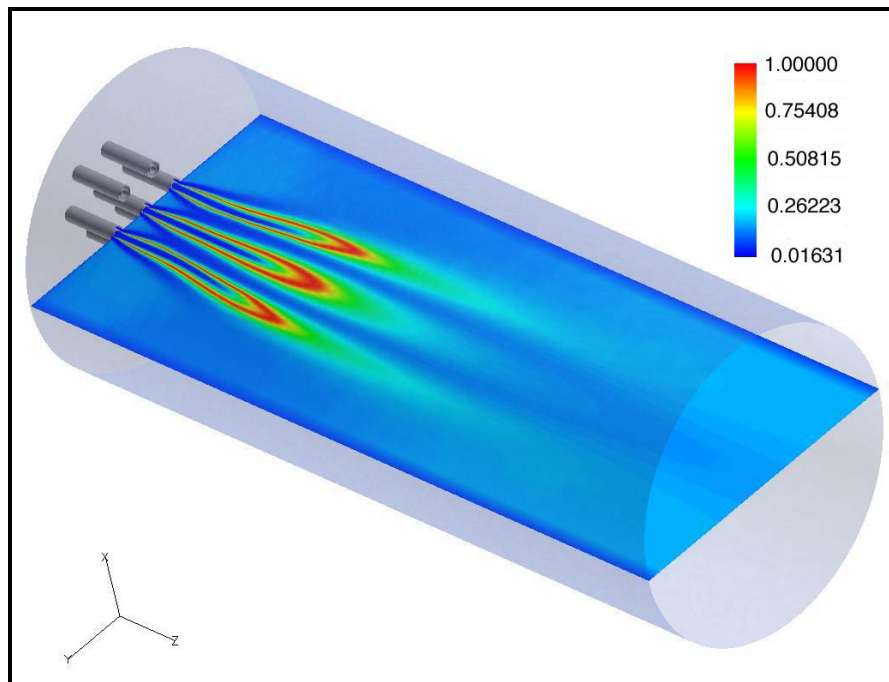


Figure 26. Normalized Temperature Field from Pre-Test MCTA Solution

The most significant potential shortcoming of this experiment is that MSFC has never attempted a test like this for code validation. Since the CFD codes are absolutely unproven for these flows, use of the pre-test analyses to place the instrumentation is risky at best. It is most prudent to start flow field temperature measurements in the far field and work upstream to minimize loss of instrumentation.

GO₂/RP-1 EXPERIMENT AT PURDUE UNIVERSITY

The single element validation experiment to be performed at Purdue University will address Model problem 9.1.1.2.2, which is the GO₂/RP-1 swirl coaxial single element. The objectives of the experiment are to provide a better understanding of several issues related to the ORSC cycle. A portion of the data taken will be used at MSFC for code validation. The validation effort following this data acquisition will support the work being done for both the TR-107 and RS-84 programs.

Two to three elements will be designed and tested at Purdue. A cross section of the baseline line element is shown in Figure 27. The oxidizer stream exits a preburner and enters the element axially. The RP-1 fuel enters tangentially behind a collar just above the cup. The two streams mix and begin to combust in the cup. The nominal chamber pressure is 2266 psia and the nominal mixture ratio is 2.87.

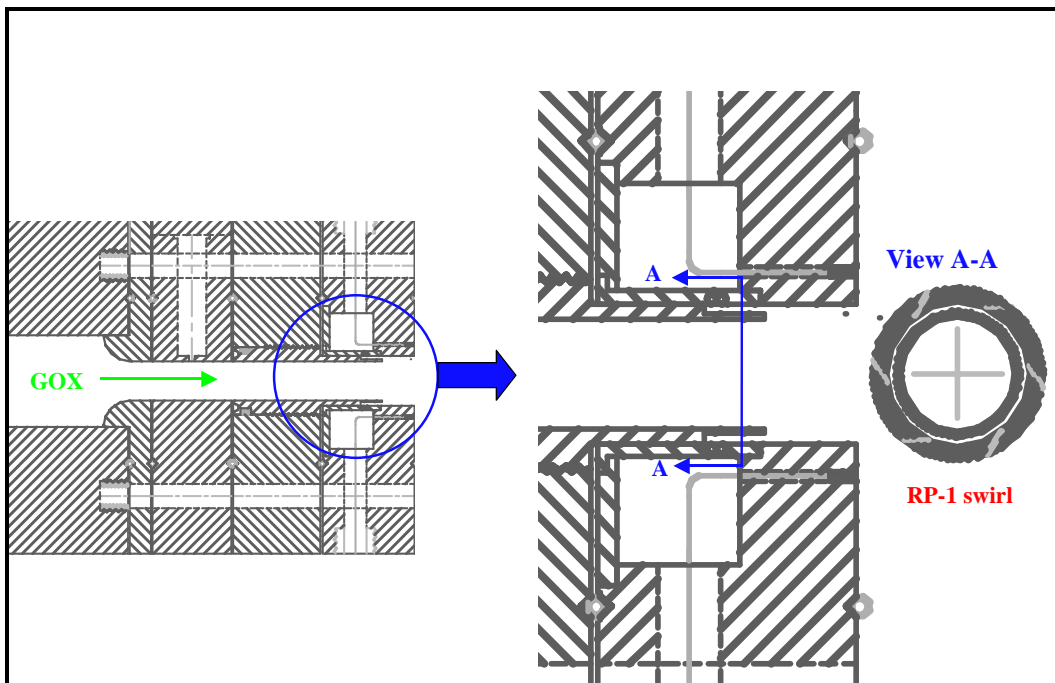


Figure 27. Cross Section of Purdue University ORSC Baseline Element.

A CAD model of the chamber is shown in Figure 28. Calorimeter sections allow wall heat flux measurements. Delta pressure gauges will be installed along the chamber axis to measure the energy release profile. Also, plans are in place to measure overall performance and film cooling efficiency.

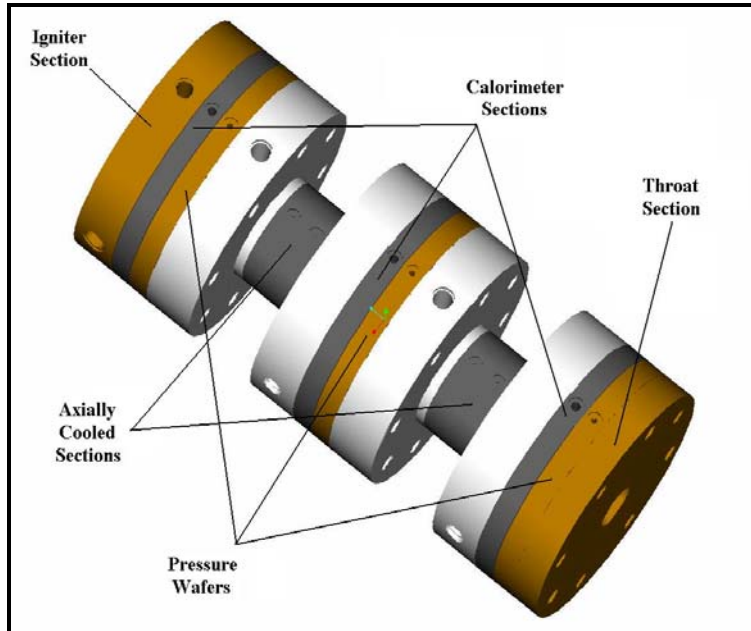


Figure 28. CAD Rendering of Purdue University Single Element Test Chamber

The pre-test CFD effort at MSFC has just begun. Figure 29 shows the three-dimensional grid that will be used for the baseline element and chamber calculations. Figure 30 shows a close-up of the grid focusing on the tangential fuel inlets. MSFC will participate with Purdue in designing the other elements to be tested when the baseline element testing is complete.

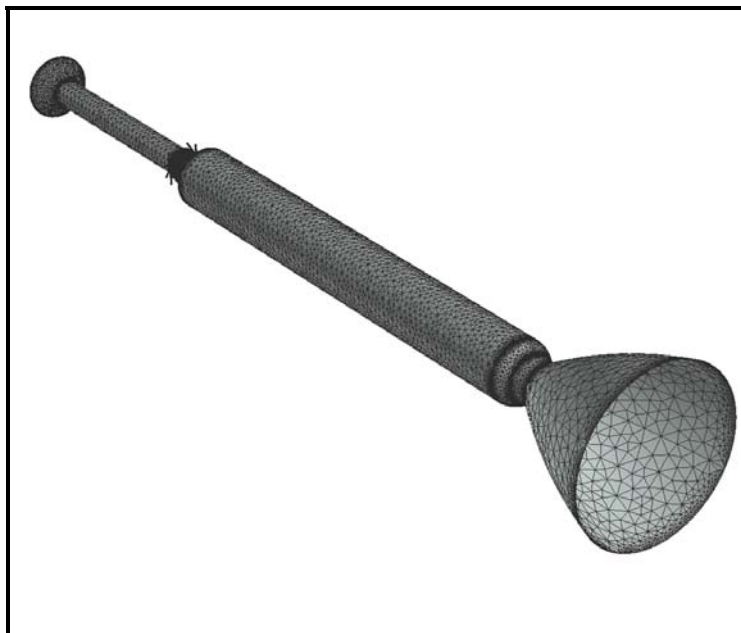


Figure 29. Grid for Purdue University ORSC Baseline Element and Chamber

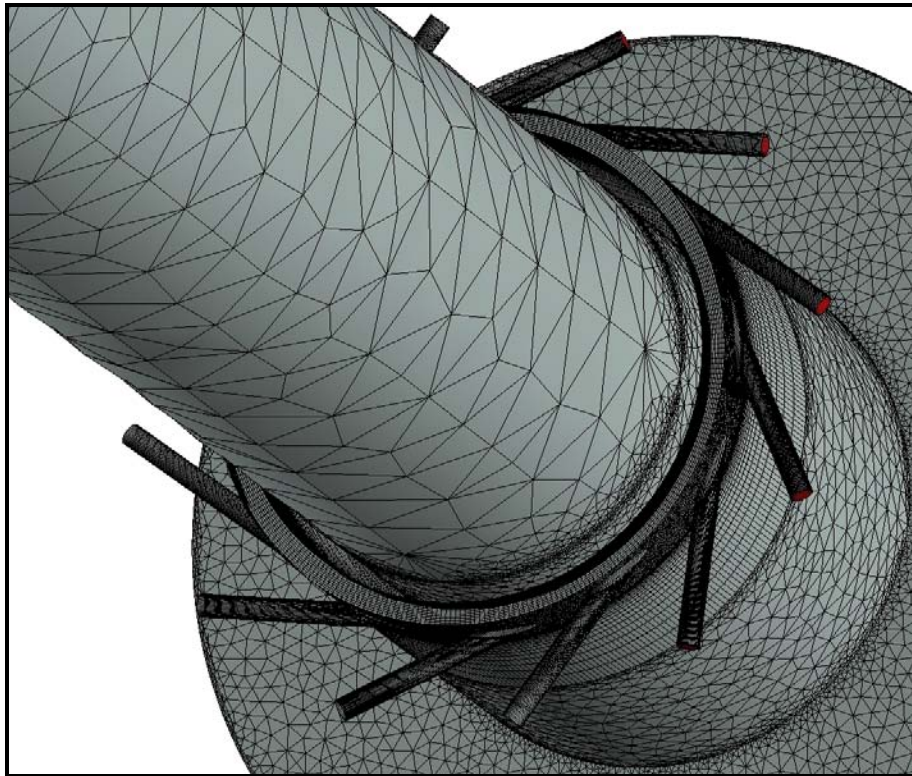


Figure 30. Close-up of the Grid Showing the Tangential Fuel Inlets.

SUMMARY

New programs are forcing American propulsion system designers into unfamiliar territory. For instance, industry's answer to the cost and reliability goals set out by the Next Generation Launch Technology Program are engine concepts based on the Oxygen-Rich Staged Combustion Cycle. Historical injector design tools are not well suited for this new task. The empirical correlations do not apply directly to the injector concepts associated with the ORSC cycle. These legacy tools focus primarily on performance with environment evaluation a secondary objective. Additionally, the environmental capability of these tools is usually one-dimensional while the actual environments are at least two- and often three-dimensional.

CFD has the potential to calculate performance and multi-dimensional environments but its use in the injector design process has been retarded by long solution turnaround times and insufficient demonstrated accuracy. This paper has documented the parallel paths of program support and technology development currently employed at Marshall Space Flight Center in an effort to move CFD to the forefront of injector design. MSFC has established a long-term goal for use of CFD for combustion devices design. The work on injector design is the heart of that vision and the Combustion Devices CFD Simulation Capability Roadmap that focuses the vision.

The SRL concept, combining solution fidelity, robustness and accuracy, has been established as a quantitative gauge of current and desired capability. Three examples of current injector analysis for program support have been presented and discussed. These examples are used to establish the current capability at MSFC for these problems. Shortcomings identified from this experience are being used as inputs to the Roadmap process.

The SRL evaluation identified lack of demonstrated solution accuracy as a major issue. Accordingly, the MSFC view of code validation and current MSFC-funded validation efforts were discussed in some detail. The objectives of each effort were noted. Issues relative to code validation for injector design were discussed in some detail. The requirement for CFD support during the design of the experiment was noted and discussed in terms of instrumentation placement and experimental rig uncertainty.

In conclusion, MSFC has made significant progress in the last two years in advancing CFD toward the goal of application to injector design. A parallel effort focused on program support and technology development via the SCIT Task have enabled the progress.

ONERA



CFD CODE VALIDATION FOR SPACE PROPULSION APPLICATIONS

F. Vuillot, ONERA/DSNA

D. Scherrer, M. Habiballah, ONERA/DEFA

ONERA, BP72, 92322 CHATILLON CEDEX, FRANCE

PRESENTATION

- **SPACE PROPULSION (launcher applications):**
 - Present : Liquid and solid rocket propulsion,
 - Future : Hypersonic airbreathing propulsion.
- **COMPETITIVE MARKET:**
 - Costs and delays,
 - Usefulness of numerical simulations:
 - Selecting appropriate designs,
 - Validating specific solutions,
 - Helping design test benches and instrumentation/measurement plans,
 - Analyzing static firings, hot testings and flight data.
- **IMPORTANCE OF CODE VALIDATION:**
 - Accuracy
 - Reliability

VALIDATION : importance to ONERA

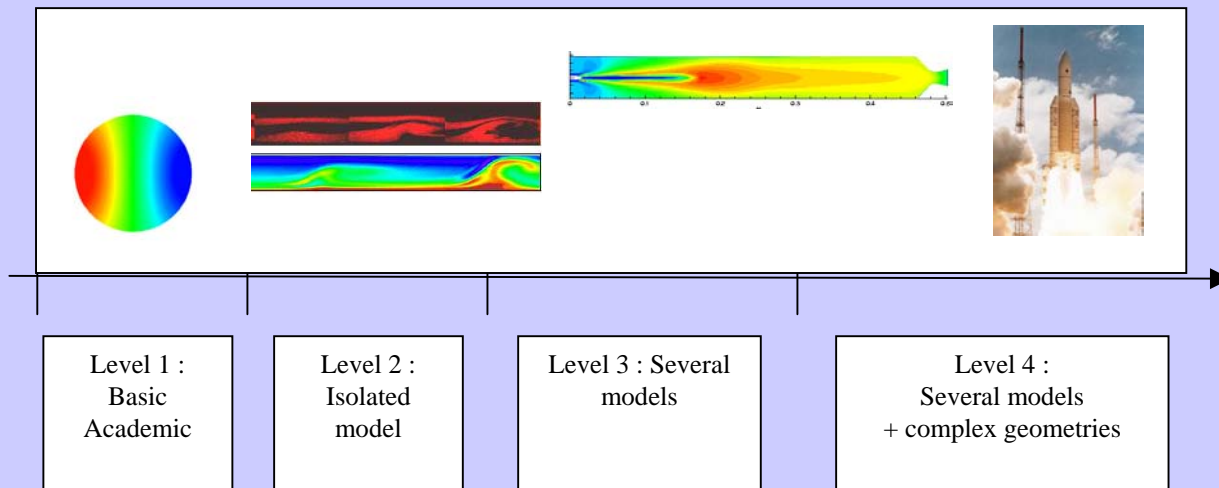
- Codes are a natural place to capitalize research activities.
- Trends towards multi-scale and multi-physics researches:
 - non-linear couplings of existing models,
 - codes are the vectors giving access to these complex physics.
- Bring together researchers from many different areas:
 - physical modeling,
 - numerical and computational methods,
 - data processing, experimental techniques.
- Codes are essential to design and understand complex systems that are used in space propulsion.
- Codes can be transmitted to industrial partners and are part of national and European research activities.
- Code releases include a "validation file".

ONERA codes for energetics and propulsion

- **MSD 3.1 (released, April 2003)**
 - more than 15 years in service,
 - multi-block, structured meshes, chimera and moving meshes,
 - explicit and implicit ADI time integrations up to $O(2)$,
 - several families of flux-splitting schemes up to $O(3)$,
 - elaborated models, multi-species, turbulent reactive flows, two-phase flow (eulerian + lagrangian), LES,
 - parallel and vectorized, external coupling capabilities (MpCCI).
- **CEDRE 1.2 (released, November 2003)**
 - new generation code (started in 1996, from scratch) builds on MSD,
 - multi-domain, generalized unstructured meshes,
 - explicit and implicit (GMRES) time integrations,
 - flux-splitting schemes,
 - multi-solver approach: multi-species, turbulent reactive flows (CHARME), two-phase flow (eulerian (SPIREE) + lagrangian (SPARTE)), thermal (ACACIA) and radiative (ASTRE), LES,
 - parallel and vectorized, external coupling capabilities (MpCCI),
 - integrated graphical user interface,
 - geometric preprocessors (fusion, splitting, refinements).

VALIDATION : Procedure

- **Follows code and model verifications.**
- **Progressive approach:**
 - Allow positive analysis of discrepancies,
 - Involve experimentalists and numericians.
- **Four levels:**
 - Level 1 : Basic Academic,
 - Level 2 : Isolated model,
 - Level 3 : Several models,
 - Level 4 : Several models + complex geometries.
- **Specific to each application.**



VALIDATION: experiments \Leftrightarrow computations

- **For each application:**
 - Define the path from level 1 to level 4,
 - Define and fund relevant experiments and model inputs.
- **For each level,**
 - Define the common scope of investigation:
 - extent of the physical domain to be simulated,
 - relevant models,
 - boundary conditions,
 - accuracy of data.
 - Harmonize data processings (spatial, temporal resolutions, ...).
- **In any case**
 - provide meeting points,
 - thoroughly analyze discrepancies,
 - revise experiments and computations when needed.

MAIN CONCERNS

LIQUID PROPULSION

Unsteady operations

- ignition transients,
- instabilities.

Steady operation

- heat loads, temperature stratification,
- combustion efficiency,
- performance.

SOLID PROPULSION

Unsteady operations

- ignition transients,
- flow stability,
- instabilities,
- two-phase flow effects.

Steady operation

- heat loads,
- performance,
- two-phase flow effects.

HYPERSONIC PROPULSION

Steady operation

- complex flow organization,
- chemistry interactions with aerodynamics and turbulence,
- combustion efficiency, performance.

EXAMPLES (see paper)

- **Liquid propulsion,**
 - unsteady operations,
 - elementary acoustics,
 - acoustic interaction of two cavities.
 - steady state operations: Mascotte set-up.
- **Solid propulsion,**
 - cold flow simulators: Vecla set-up,
 - flow stability,
 - acoustic resonance,
 - turbulent transition.
 - laboratory scale motors: C1xb,
 - two-phase flow effects.
- **Hypersonic propulsion,**
 - level 1: simple shock flow,
 - level 3: Laerte experiment,
 - level 4: Japhar scramjet.

LINEAR ACOUSTICS

LP: Level 1

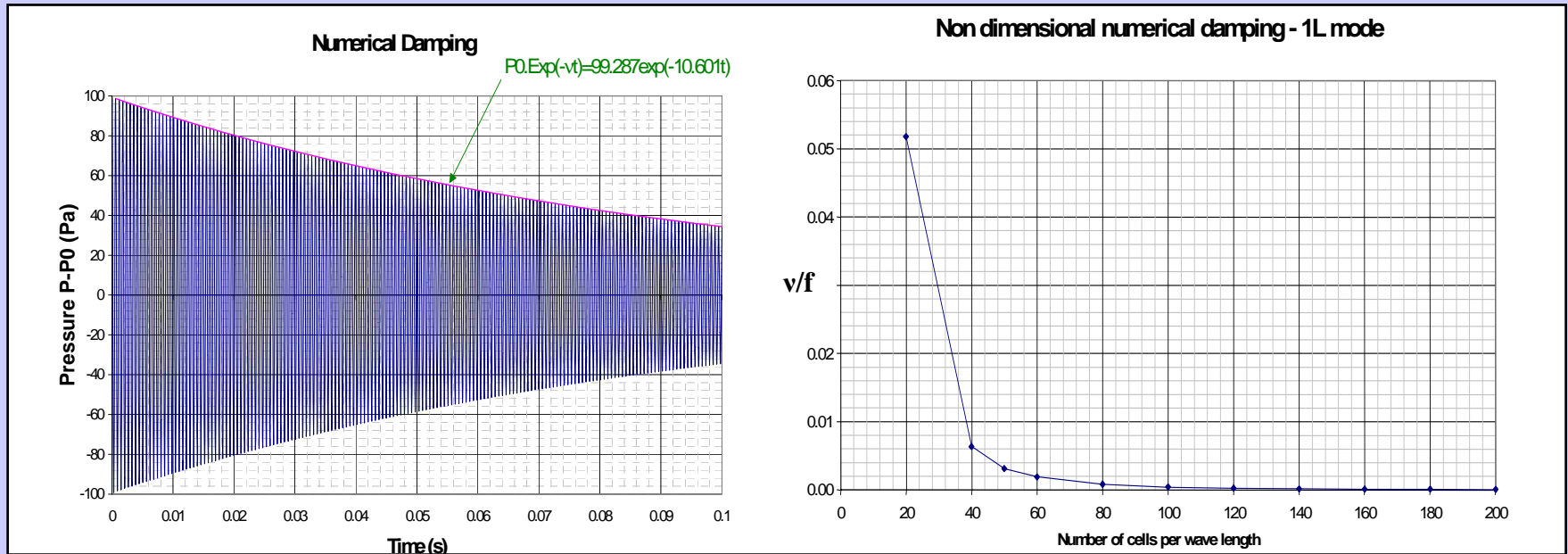
Mode 1L in a chamber (L=0.5 m, f=1675 Hz)

$$P_{ini} = P_0 \left(1 + \varepsilon \cos\left(\frac{\pi x}{L}\right) \right)$$

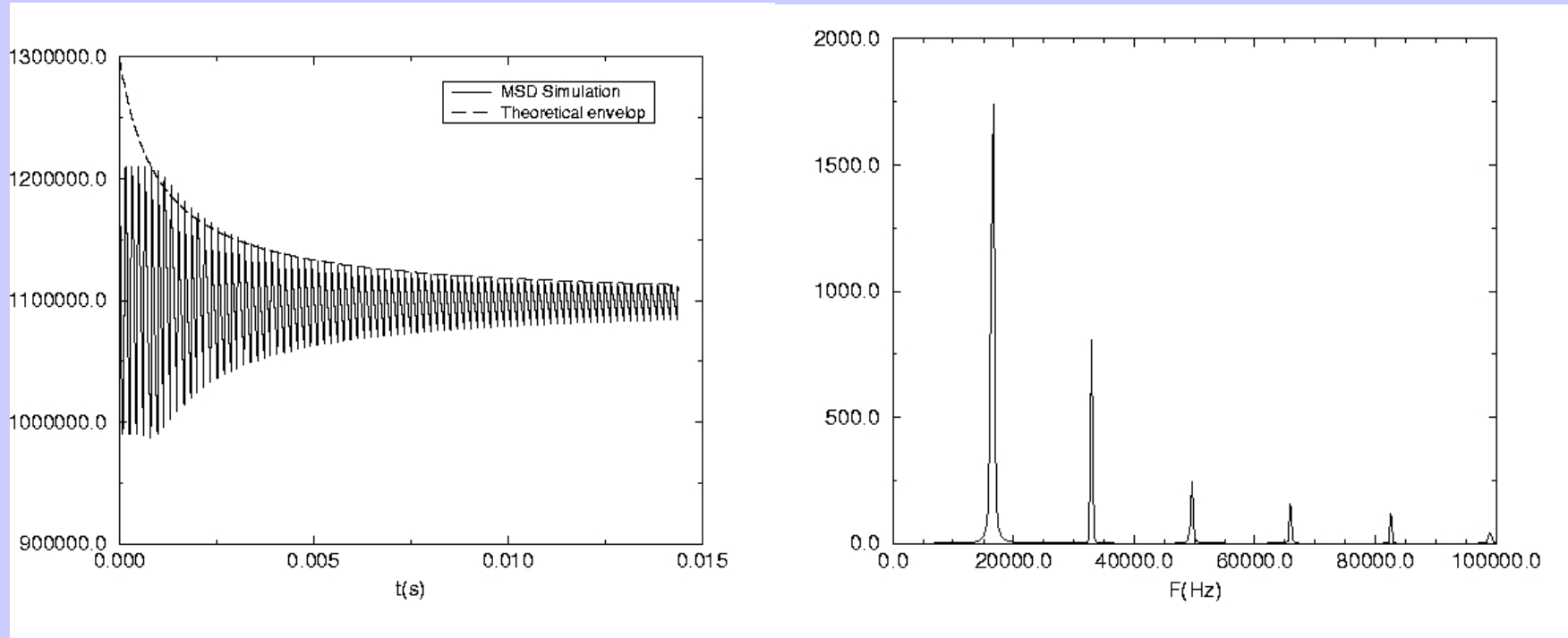
Numerical damping

$$P' = P_0 \varepsilon \cos(2\pi f t) \cos(kx) e^{-\nu t}$$

Schemes and meshes



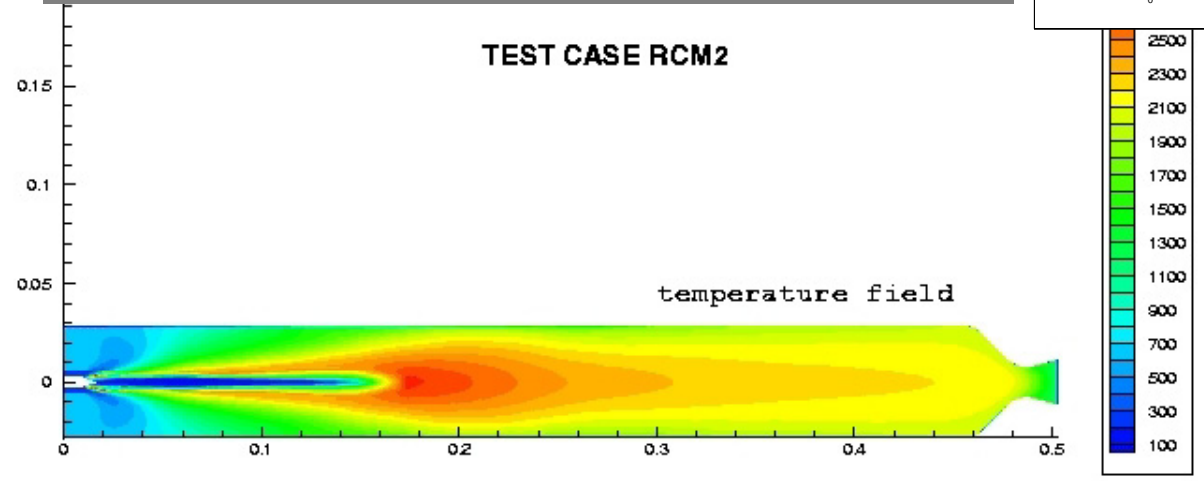
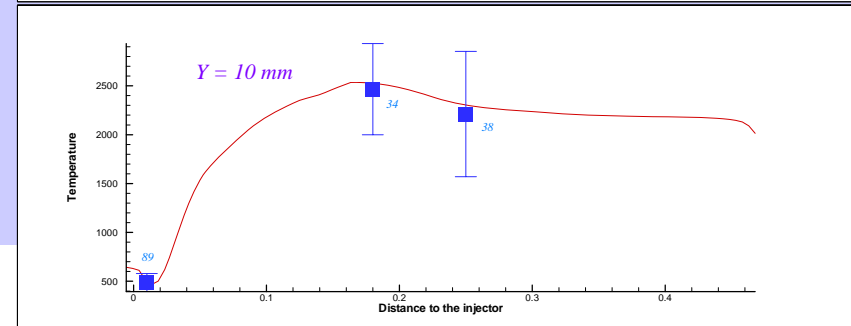
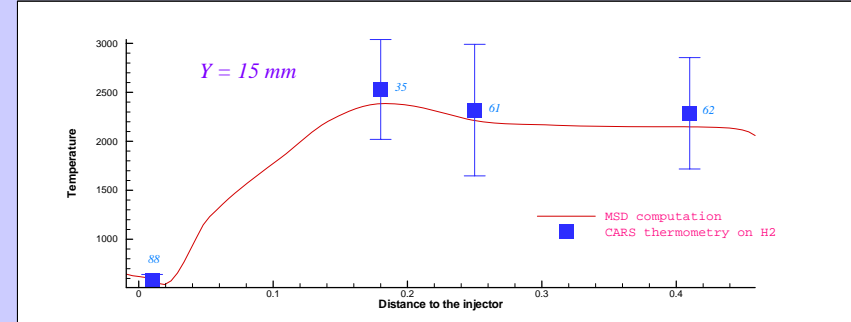
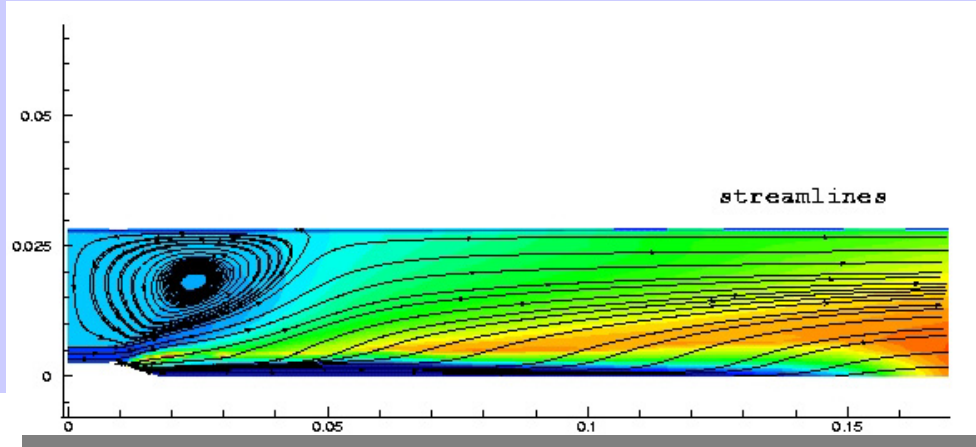
N-wave in a chamber Theoretical solution



MASCOTTE test case

LP: Level 3

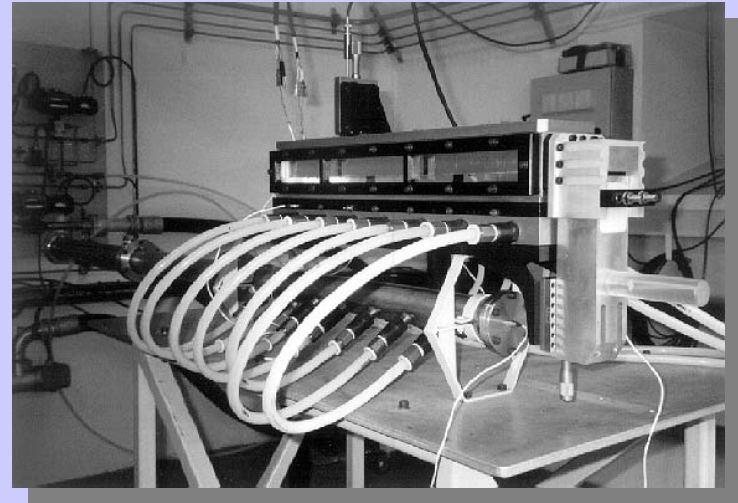
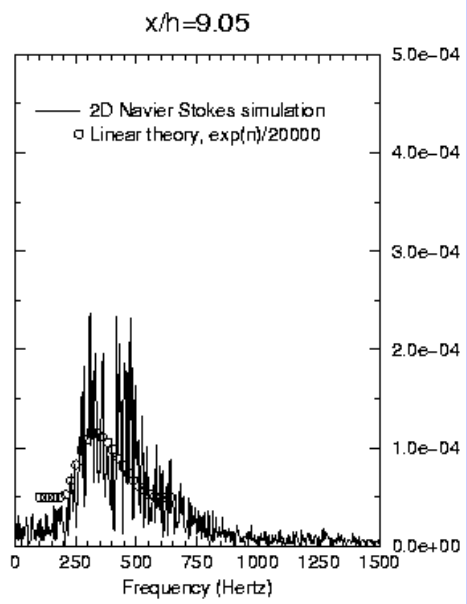
Reacting two-phase flow (LOX/GH2),
lagrangian approach



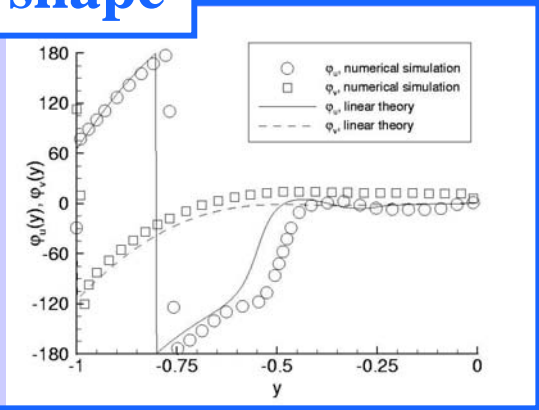
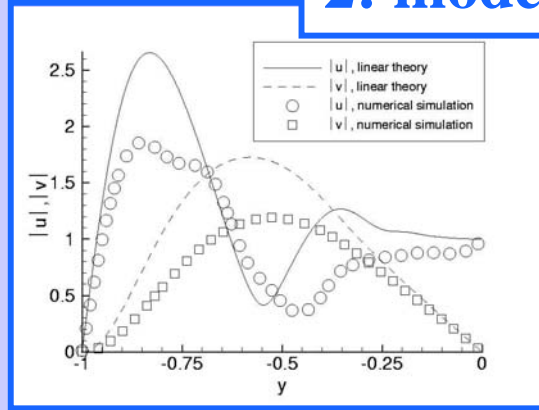
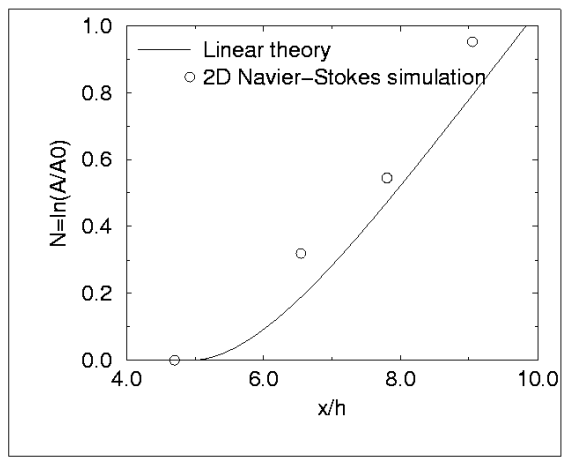
VECLA set-up (1/3)

SP: Level 1

1: natural instabilities

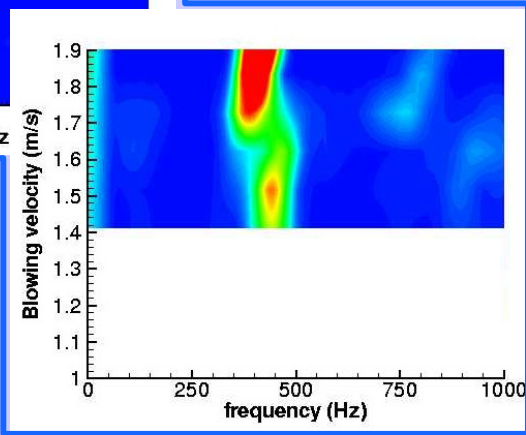
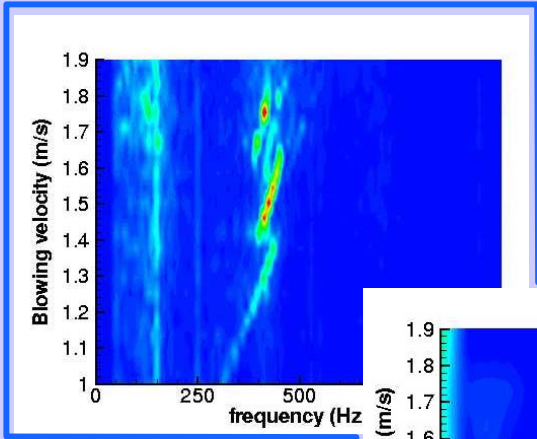


2: mode shape

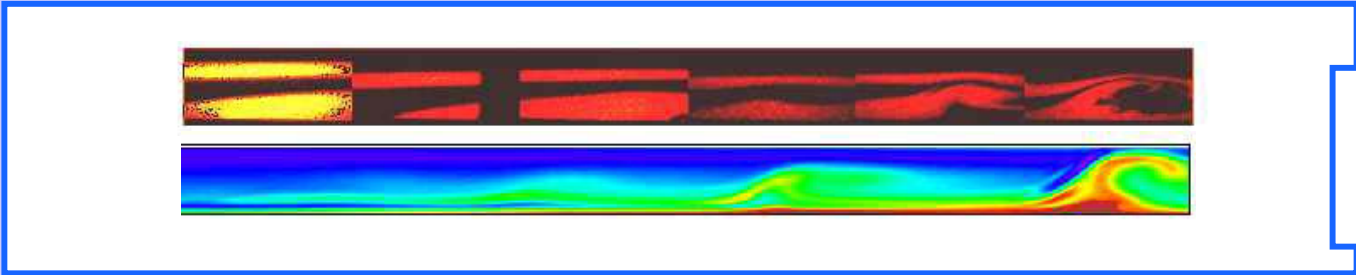
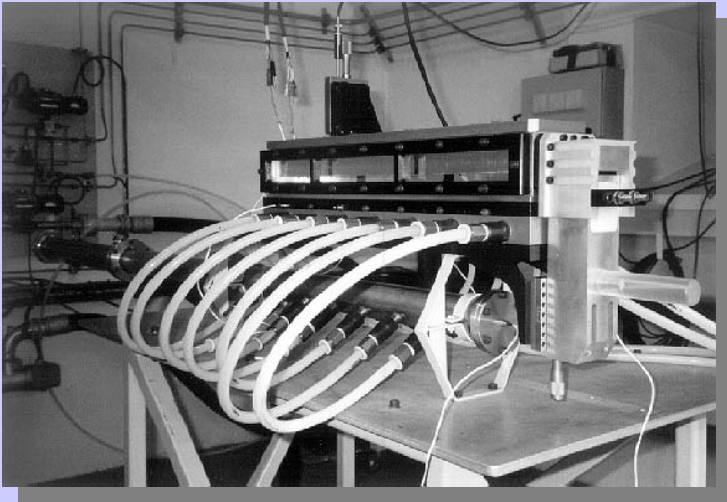


VECLA set-up (2/3)

SP: Level 2



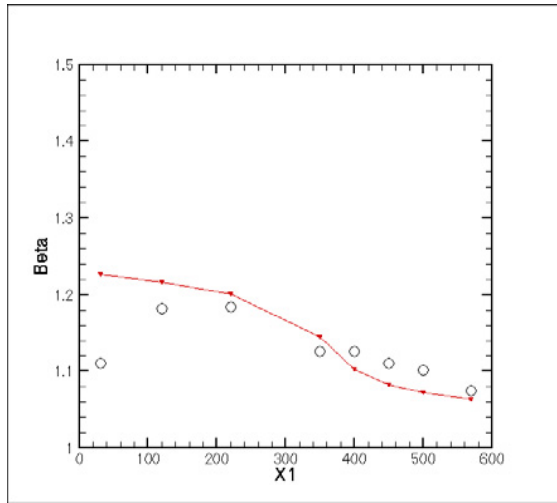
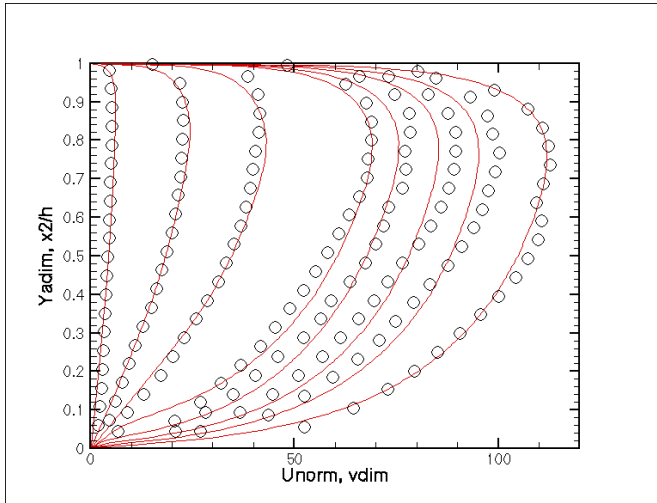
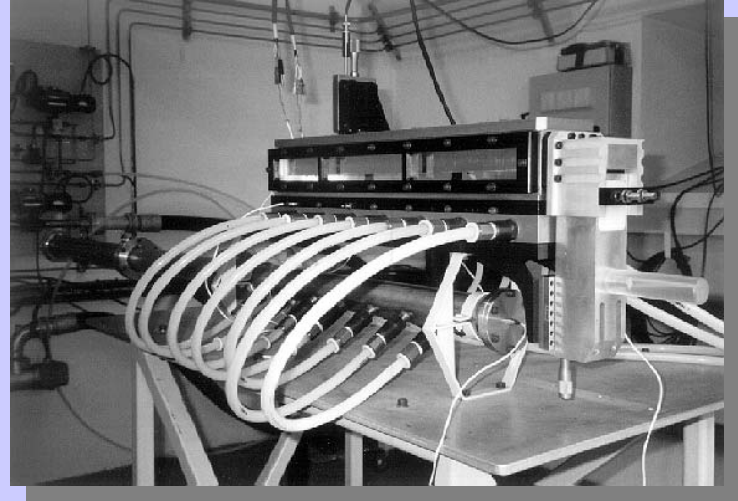
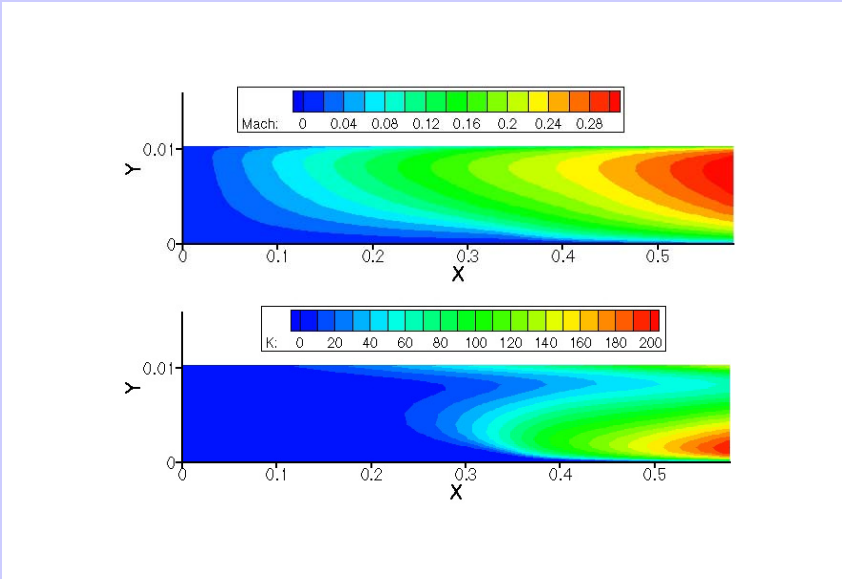
3: acoustic resonance



4: flow visualization

VECLA set-up, $h=10\text{mm}$ (3/3)

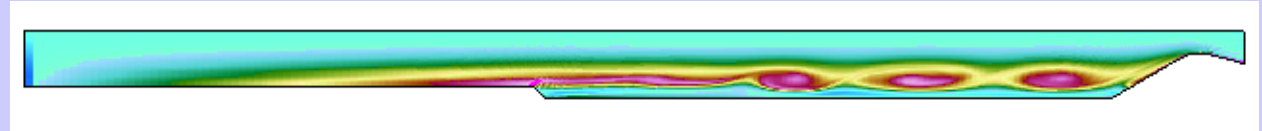
SP: Level 2



5: turbulent transition

Laboratory motor: C1xb

SP: Level 3



Propellant response function

$$R_{MP}(\omega) = \frac{\dot{m}'(\omega) / \bar{\dot{m}}}{p'(\omega) / \bar{p}}$$

$$\dot{m}(t) = \bar{\dot{m}} + \frac{\bar{\dot{m}}}{\bar{p}} \int_0^{t-t_0} R(\tau)(p(t-\tau) - \bar{p}) d\tau$$

$$R(t) = \text{TF}^{-1}[R_{MP}(\omega)]$$

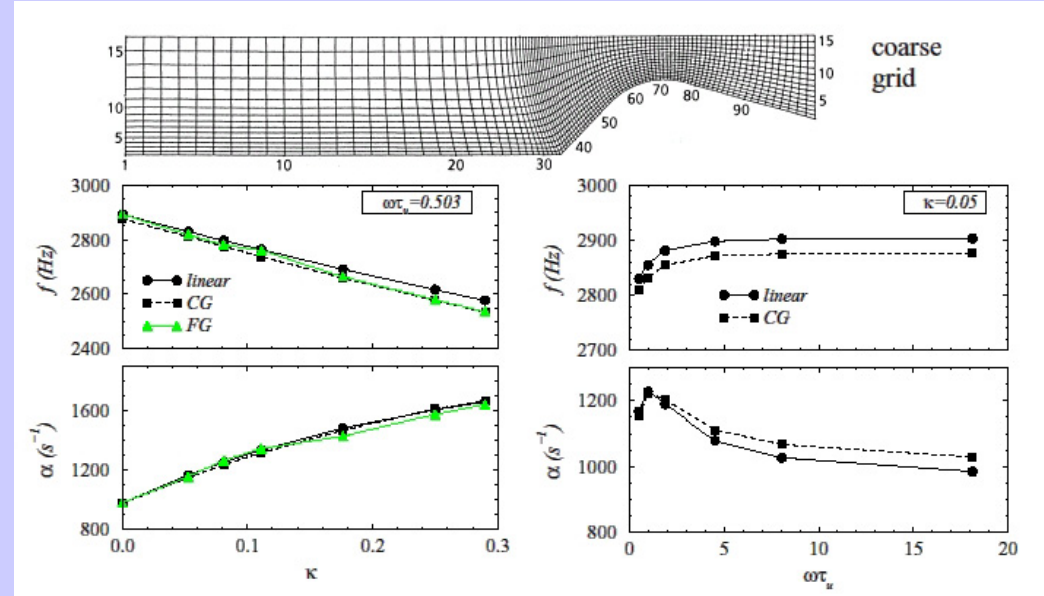
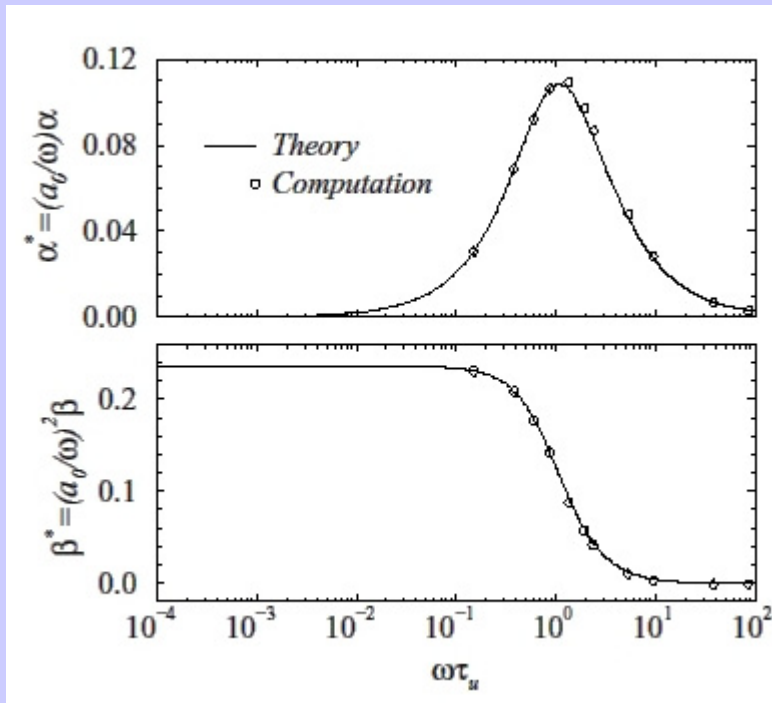
	No response	Response #1 (mne)	Response #2 (glk)	Experiment
Head-end amplitude (hPa) (relative error)	12.7 (71%)	28.5 (35%)	43.1 (2%)	43.9
Aft-end amplitude(P_{C6}) (hPa) (relative error)	15.5 (39%)	20.6 (20%)	26.6 (4%)	25.6
Frequency (Hz) (relative error)	740 (3.8%)	720 (1.0%)	715 (0.3%)	713
Frequency resolution (Hz)	23	23	23	10

Unsteady two-phase flow effects

SP: Level 2

Particle acoustic damping

- Theoretical solution
- 1D, linear acoustic balance solution

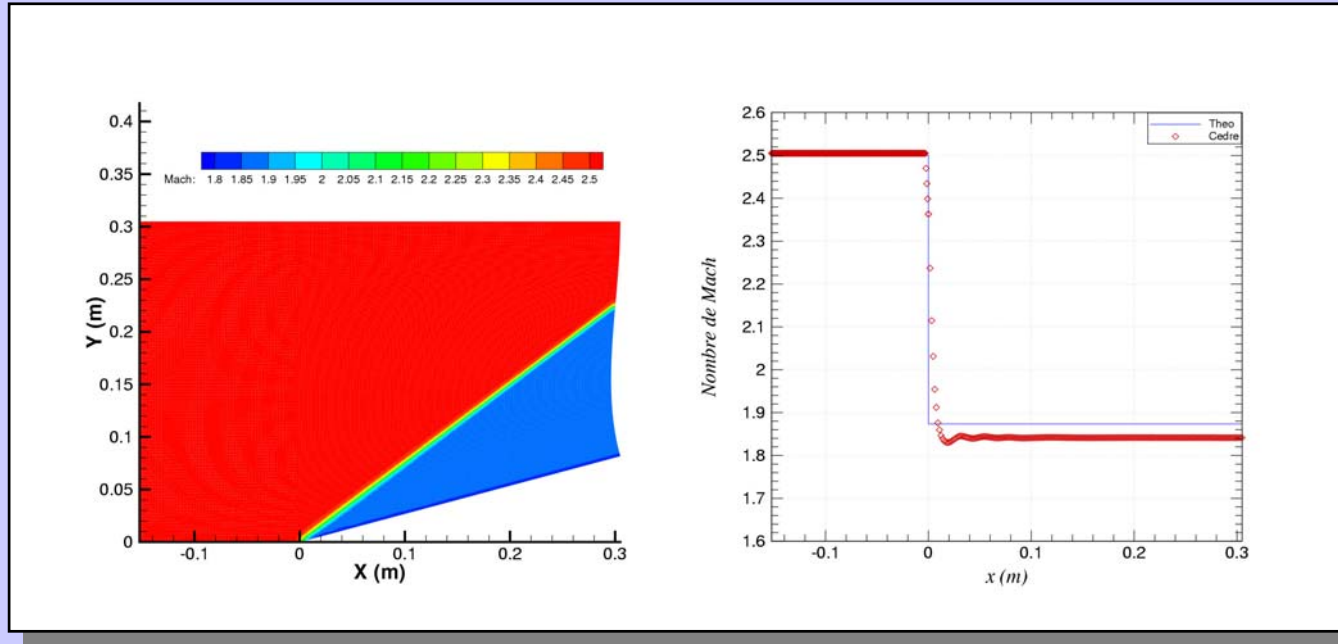


ONERA

Shocked flows

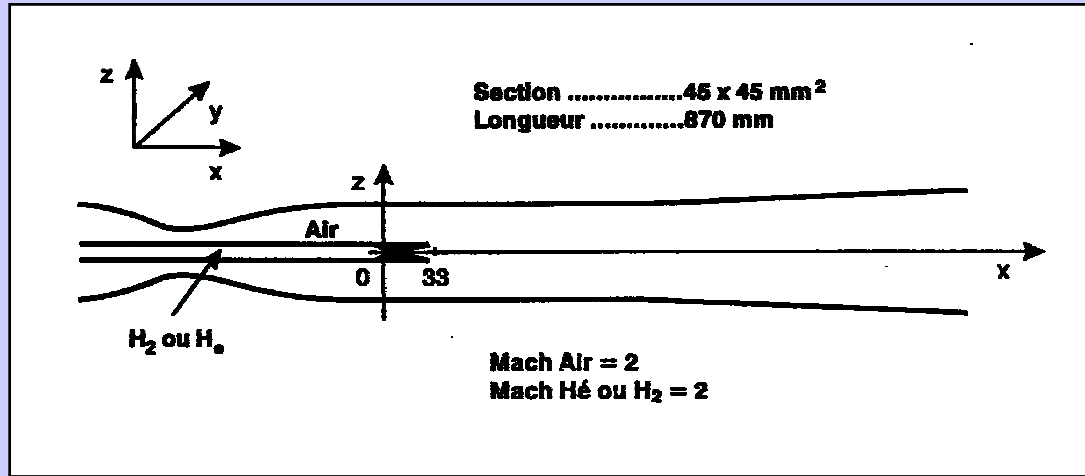
HP: Level 1

Mach 2.5 wedge flow

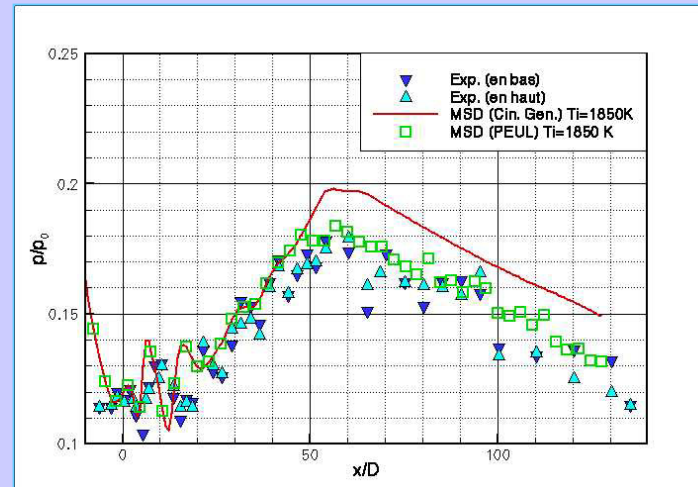


LAERTE experiment (M=2)

HP: Level 3

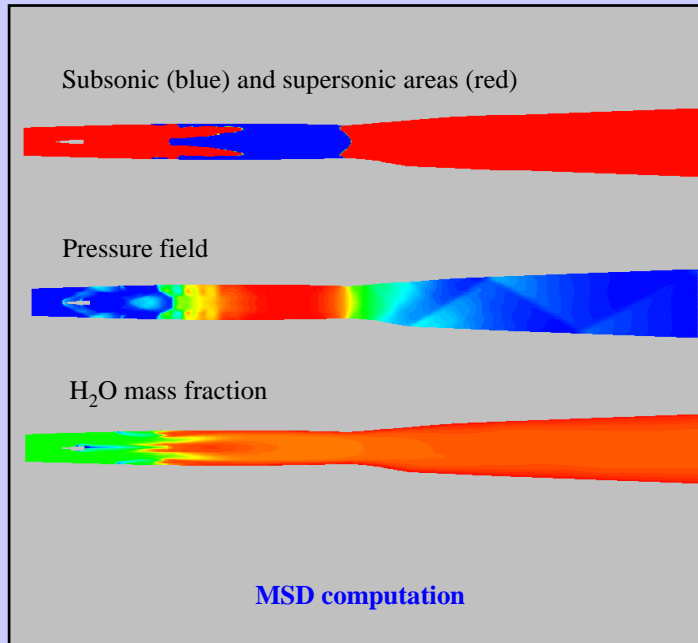
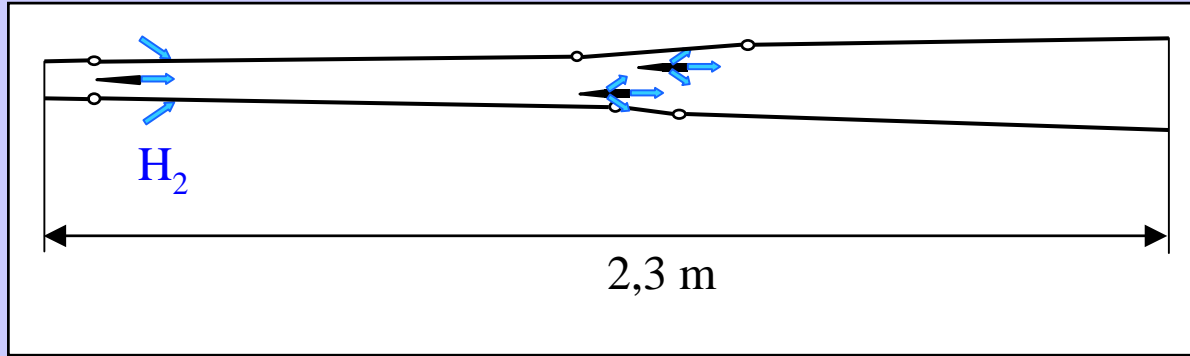


Wall pressure
profile

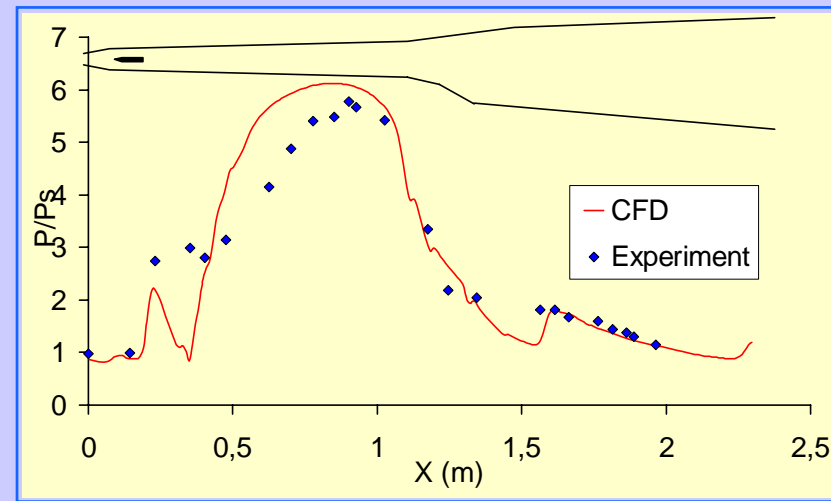


JAPHAR scramjet (M=7.6)

HP: Level 4



Wall pressure profile



CONCLUSIONS

- **Space propulsion applications have been considered**
 - competitive market: costs and delays,
 - liquid, solid and hypersonic propulsion.
- **Codes are valuable assets:**
 - complex physics implies several models, code/solver couplings,
 - need for thorough validation:
 - progressive approach (one difficulty at a time),
 - 4 levels to be addressed by each application.
 - need for experiments and model inputs (separate experiments),
 - need for close cooperation between all actors (experiments, numerical simulation, physical modeling),
 - benefit from agencies and industrial partners through their needs and expertise.
- **Validation implies a full spectrum of research activities and requires continuous supports to deliver its benefits.**
- **ONERA is quite concerned and fully involved.**

ACKNOWLEDGEMENTS

The essential roles of agencies, CNES, DGA and industry, SNECMA Moteurs, SPS, SME and MBDA are kindly acknowledged.

Thanks also to colleagues who contributed to the presented works: A. Nicole, I. Dubois, E. Laroche, M. Pourouchottamane, F. Dupoirieux, V. Burnley, J. Troyes, G. Avalon, B. Ugurtas, G. Casalis, N. Lupoglazoff, J. Dupays and D. Gaffié.

Special thanks to P. Kuentzmann who never failed in working out ONERA supports through internal fundings and encouragements.

CFD CODE VALIDATION FOR SPACE PROPULSION APPLICATIONS

F. Vuillot, D. Scherrer, M. Habiballah
ONERA
BP72
92322 Châtillon Cedex, France

1- INTRODUCTION

Looking at space propulsion from the launcher point of view implies considering engines which are capable of delivering the several hundreds tons of thrust which are needed for lift off from the launch pad and reaching appropriate transfer orbits. Present technology relies on rocket engines using liquid or solid propellants. Some hybrid designs exist and have been tested, up to full scale, but they lack the log charts of either solid or liquid motors to be considered as a practical solution for the present day systems and missions. In the future, airbreathing space propulsion may become a reality and many efforts are carried out in this direction. One of the key technology for such space planes is supersonic combustion.

During the development and operation of space engines, several phases can be mentioned, starting from the design phase, to the development phase and later the operation/upgrade phases. In any of these phases, that take place in a competitive market, where delays and cost reduction become a priority, numerical simulations can bring advantages in selecting appropriate designs, validating specific solutions, helping design test benches and instrumentation/measurement plans and analyzing static firings and flight data. Since testing of such complex systems is quite expensive and intricate, there is a definite need to use simulations in a reliable way. The parallel development of multi-purpose codes including state of the art modelisations has rendered possible the use of the numerical simulations to address complex experimental situations. This implies that the codes that are to be used need to be validated, that is to say that one knows the validity of the simulations and their reliability.

This importance of code validation has been recognized at ONERA for several years. From its missions and expertise, ONERA is in the core of the business of developing simulation codes. Several reasons exist for such an implication :

- codes are a natural place to capitalize research activities for further use
- trends are clearly towards multi-scale and multi-physics researches that implies non-linear coupling of existing models, so that codes are the vector giving access to these complex physics
- codes also provide a very powerful way to bring together researchers from many different areas : ranging from physical modeling, numerical and computational methods, but also data processing, experimental techniques,
- codes are essential to design and understand complex systems that are used in space propulsion,
- codes can be transmitted to industrial partners and are part of national and European research activities.

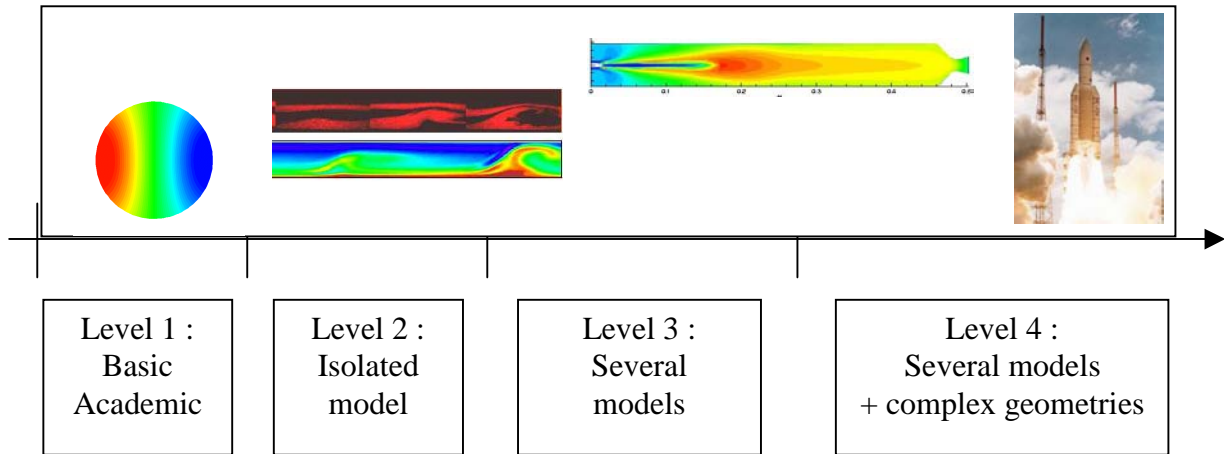
As a consequence, code validation is viewed as a key issue that makes use of the entire ONERA research spectrum, from numerical methods, physical modelings, experimental know how, including measurement techniques, and test benches.

Concerning space propulsion, ONERA has been developing and releasing several versions of its MSD software package for more than 15 years. This code works on block-structured grids, including overlapping and moving grids, and comprise a multi-species reactive Navier-Stokes solver completed by two dispersed phase solvers (Eulerian and Lagrangian) and some specific modules for solid propulsion. It is a fully parallel code, with external code coupling capabilities (e.g. coupling with a thermo-mechanic codes such as Abaqus). Since 1995 ONERA has been developing a next generation code, called CEDRE, which will extend MSD capabilities to generalized unstructured grids. This code is a complete rewriting, starting from scratch, of the MSD code. The generalized unstructured capability is an original development that allows to use cells with any number of faces, each face having any number of nodes. Of course this naturally includes usual structured and unstructured grids, but also allows for additional capabilities in term of grid generation and refinements. The first release of the CEDRE code occurred in December 2001 and since then it has been extensively used at ONERA. Next release will occur before the end of 2003. Both codes are produced by ONERA, following quality management procedures and are used for in house research activities, as well as for industrial partners needs. Both codes are released with a validation file that demonstrates the capability and accuracy of the codes for selected test cases.

The definition of the validation file is detailed in reference ¹ and follows guidelines presented in reference ². Code verification is treated in a separate file and although of major importance, it will not be described here. This entails verifying that the coding of a particular model is actually conform to the intent of the model. In other words, that the coded version of the model produces expected results and that no programming errors remain in the code.

Once the code is verified it can be "validated". The validation of the code is the subject of this paper and some definition of "validation" must be given before going further. In some sense validation means that the results produced by the code are indeed the actual results observed in an experiment or a test firing. Insuring validation would insure that the results can be used as actual results from the reality of the real world. Since the real world is quite complex, one has to define what is the real world he will refer to and what is the measure of reality.

In order to validate the code results one has to compare them to results that bear some of the reality the code is intended to simulate. Then it is useful to introduce some sort of ordering of the reality. The simplest way is to follow the complexity of the situation that is to be simulated. The first level should include only one complexity and it seems wise to consider one level of modeling in a geometrically simple configuration. Very often this permits to develop analytical solutions against which the numerical results may be checked. This level will be referred to as "basic and academic level". This will implies only the flow model or another model for a uniform flow : examples are boundary layer flows, acoustics or two-phase flows in a uniform flow. The next level should introduce an additional model, other than the flow model, in a still simplified geometry : examples are simple burners or two-way coupling of two-phase flow models with the gas flow model in a simple geometrical configurations. Level three will address complex situations that occurs in simplified systems, such those considered in research lab for proof of concept activities. It should include several models in actual situations, representing simplified or subscale models of actual systems. Finally a fourth level will consider actual industrial applications, up to full scale. This hierarchy of validation test cases is summarized by the schematic below :



This hierarchy of validation levels should be followed progressively in order to gain confidence in code performances before considering more complex situations. Indeed this will be of major importance when analyzing difficulties encountered at one level. For instance the causes for a given code to produce improper results at level 3, using model 1 and model 2 will be much easier to analyze if one knows that model 1 and model 2, when used separately, produced satisfactory results at level 2. We shall also emphasize that if analytical solutions must be used as often as possible at level 1, they cease to produce valuable results at level 2 and above. So the validation effort should imply the definition of ad hoc experiments to pave the way of code validation up to level 4, which is the ultimate goal. It must be stressed that those are essential steps in code validation and that these steps are proper to each application. Indeed, we want to make the point that in order to reach level 4, each community should work out the relevant steps to appear at levels 1 to 3 and to ensure that the proper experiments are available to fulfill them. This will imply to :

- identify the physical models that are needed and ensure their verification,
- insure that the necessary steps are taken to provide the needed inputs for the models,
- define the proper experiments where these models are involved in a gradual way to fulfill level 3 requirements.

Finally, the core of the validation procedure, excepting level 1 (where the conditions are clearly known) and level 4 (where the conditions cannot be controlled) is to compare results produced by a numerical code with results obtained experimentally in a controlled environment. The quality of the work is logically very dependent on the quality of the possible matching between the simulations and the experiments. The ideal situation is when both the computations and the experiments are designed together in order to insure that :

- the proper measures are taken to define the boundary conditions for the simulations,
- the extent of the simulated experiment is clearly defined and corresponds to some portion of the experiment that can be "isolated",
- the data processing is clearly defined and should be as close as possible between the two approaches,
- the simulations are viewed as a numerical experiment and should follow similar procedures.

From this it appears that a good code validation implies good communications between the experimentalists and the numericians. They must realize that they share similar requirements and objectives and that they need each other, to define both the experiment/simulation plans and the data processing methodologies. Difficulties such as the spatial and temporal

resolutions, reduced quantities and global coefficients, should be discussed together at the earliest stages of the validation activities.

Another notion that will be developed when considering the level 4, stems from the difficulty to exactly describe the complexity of the reality. This will introduce the notion of relative validation. The explanation comes from the fact that it may be very difficult to produce positive comparisons on quantitative data in a real life situation (for instance the exact level of pressure oscillations in a solid rocket motor). Then the search for an absolute comparison (produce identical data) will be usefully shifted towards the search of a qualitative validation. In other word, the emphasis will be put on the tendencies rather than on the absolute values, that cannot be matched. The usual reason for the impossibility to match absolute values comes from the difficulty to properly define the boundary conditions of an actual system (vibrations, mass flow rate fluctuations, heterogeneities, ...), its geometrical limits or the proper model inputs (e.g. : droplet size and distribution, ...). Then code validation will ensure that the code will produce the right tendencies (for instance : a decrease in the burning rate will produce reduced oscillations) for a change in one of the identified parameters. This relative validation represent a valuable goal for a complex situation and requires that the confidence in the code results has been acquired in the lower levels of the validation procedure.

The complexity of the proper definition of the actual system to be reproduced by the simulation is one limiting factor from the experimental point of view. It is equally matched by a more than real difficulty from the numerical point of view, which entails to grid issues. Grid convergence is a classical pre-requisite for any numerical simulation. However this is a real limit that offers in many practical cases no solutions. Indeed the simulation of complex systems implies grid tailoring, which means that the grid is defined following an a priori knowledge of the physical mechanisms to reproduce (one knows that a shear layer requires from 10 to 20 grid points across it or that an acoustic wave needs roughly the same amount of grid points per wave length to be correctly propagated, etc ...). The geometrical complexity of the system quite often consumes most of grid point resources so that very little margin is left for grid independence issues. At this level 4 position, one should realize that a given computation that produces usable results may do so by a delicate balance between resolved scales (assumed to be controlling the observed behavior) and unresolved scales (that are properly taken care of by the grid construction choices, that ensure that they are dissipated). Changing the grid resolution may break this delicate balance by shifting part of the unresolved scales into a badly resolved scale range where their damping is no longer ensured by the numerical scheme. This may pollute the computation and produce erroneous results until the grid resolution is further increased for that range of scale; but in doing so other unresolved scales will appear and so on. So the grid issue may appear much like a Pandora box This difficulty presently limits the full scale *a priori* use of numerical simulation for complex system and explains the relative validation notion that represents the best of what can be obtained from a purely numerical procedure. Of course the efforts currently made in the simulation community aim to reduce this limitation and to permit to extend the range of absolute simulations from first principles.

In the remaining of the paper, specific code validation works will be detailed for the three aspects of space propulsion, namely, liquid, solid and hypersonic propulsion. In each case examples will be given of the progressive approach from level 1 to level 4.

2- LIQUID PROPULSION

In liquid propulsion, the design of a combustion device needs characterization of the system in the whole operating range, from startup to shutdown. Analysis tools need then to be validated in order to handle the operation of the combustion device in the operating range. In particular, numerical simulations are needed to prove the device has sufficient margin with regards to operational risks like :

- excessive heat loads
- hard transients
- combustion instability
- low performance

Thus suitable models are needed to be implemented in the CFD code, depending on the operation : transient, main stage or unsteady operation. Those models may need specific research programs³ involving different teams and expertise.

As an illustration for liquid propulsion applications, we present two examples of code validation for unsteady operation (for combustion instability investigation purpose) and one example for steady-state combustion (for performance, heat transfer or temperature stratification analysis).

2-1 Unsteady operation

The first step in calibrating a CFD code, intended to be used in assessing combustion stability of a liquid rocket engine, is to investigate its capabilities to propagate correctly linear and nonlinear acoustics in simple configurations of geometry and fluid flow.

The code that has been assessed for unsteady and steady-state flows simulation is the MSD code. The discretization is based on finite volume techniques on curvilinear structured grids, with upwind schemes derived from the Roe scheme. The time integration can be either explicit, then a predictor-corrector scheme is used, or implicit with first or second-order accuracy. The implicit algorithm uses a classical ADI factorisation. Eulerian and Lagrangian solvers are also implemented in the code for spray combustion applications. Several turbulence models are also available.

2-1.1 Elementary acoustic test cases

a) Methodology

Numerical simulations are conducted in simple configurations of geometry and flow field for which analytical solutions exist. Computational data are then compared to those solutions. For classical acoustics, two cases were considered : 1D closed cavity and a 2D (disc) cavity. The 2D configuration is representative of what happens in a slice of combustion chamber. For 2D configurations, two kinds of meshes were compared (O mesh and H mesh).

The initial condition is a uniform solution plus a pressure perturbation, corresponding to a first longitudinal (for 1D computations) or transverse (for 2D configurations) acoustic mode. For instance, for the first longitudinal mode, the initial solution is given by:

$$P_{ini} = P_0 \left(1 + \varepsilon \cos\left(\frac{\pi x}{L}\right) \right) \quad (1)$$

Depending on the initial perturbation amplitude (ϵ) the solution belongs to the linear or nonlinear regime. Typically, the linear regime corresponds to ϵ of the order of 10^{-4} and the nonlinear regime to ϵ of the order of 0.1. The linear solution corresponds to the mode initially prescribed, whereas in the nonlinear solution, the acoustic energy initially present in this mode gradually cascades to its harmonics. More details about the processes involved can be found below.

No initial velocity perturbation is prescribed. The process is assumed to be adiabatic, which gives :

$$\rho_{ini} = \rho_0 + \frac{\epsilon P_0}{a^2} \quad (2)$$

Figure 1 gives an overview of the solution obtained for a 1T steady mode, at two successive instants. The pressure signal is then analyzed either through a peak to peak evaluation or a Fourier transform.

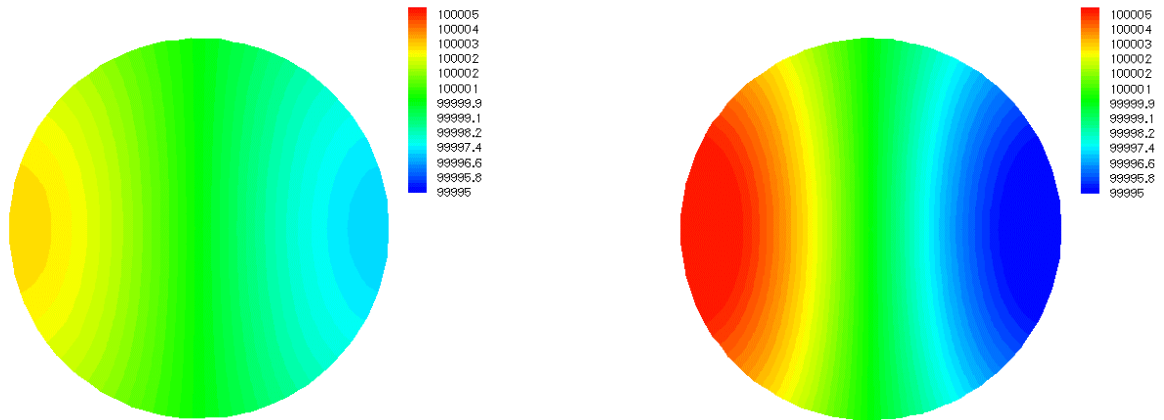


Figure 1 : Pressure field at two successive times

b) Linear acoustics

A good description of an acoustic signal requires to minimize the dissipation and dispersion induced by the numerical scheme. Here, we focus on the numerical damping inherent to the scheme, and its relation to the mesh density expressed in terms of number of cells per wavelength (NCPWL). The damping obtained in the process described above has its origin in numerical viscosity. No other source of dissipation is present here. In order to determine this numerical damping for the MSD solver, several acoustics test cases were carried out⁴⁻⁵. Both longitudinal and transverse waves were simulated.

Figure 2 gives an example of the pressure signal in the 1D case. The cavity has a length of a 0.5 m and is filled with water steam at 3200 K and a pressure of 10 bar. The numerical damping is given by ν ($P' = P_0 \epsilon \cos(\omega t) \cos(kx) e^{-\nu t}$). Figure 3 shows the non dimensional numerical damping (ν/f) versus the number of cells per wave length :

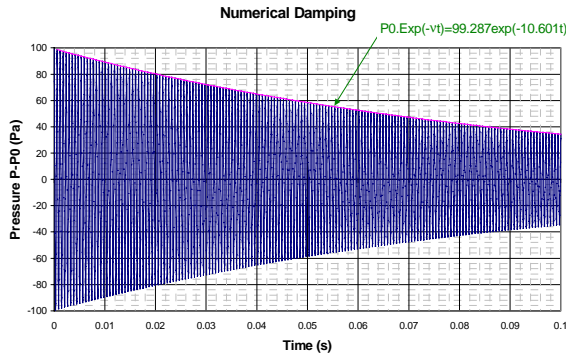


Figure 2 : Numerical damping

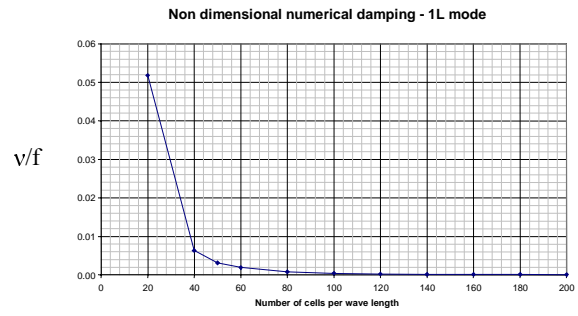


Figure 3 : Non dimensional numerical damping

We can also consider the concept of numerical damping per cycle (NDPC) which can be defined as $\%NDPC = 100(1 - e^{-v/f})$. Table 1 gives, for the 1L mode, non dimensional damping v/f and $\%NDPC$ versus the number of cells. As it can be seen, a grid including 80 cells per wave length (40 cells for the cavity) gives a reasonable damping without increasing too much the computational time.

Number of cells	NCPWL	v	-v/f	%NDPC
10	20	-87.40	0.05180	5.05
20	40	-10.67	0.00635	0.63
25	50	-5.22	0.00311	0.31
30	60	-3.18	0.00190	0.19
40	80	-1.37	0.00082	0.08
50	100	-0.73	0.00044	0.04
60	120	-0.44	0.00026	0.03
70	140	-0.28	0.00016	0.02
80	160	-0.19	0.00011	0.01
90	180	-0.14	0.00008	0.01
100	200	-0.10	0.00006	0.01

Table 1: Numerical damping – 1L mode

Similar calculations were carried out for transverse acoustics modes.

c) Nonlinear acoustics

When the amplitude of the initial perturbation is strong, in a few cycles the initial sinusoidal wave turns into a N shape wave, whose amplitude gradually decreases with time. This N shape wave corresponds to the superposition of the harmonics of the initial signal. Because of nonlinear phenomena, the energy initially introduced on the fundamental gradually cascades to the harmonics. An analysis of the N-wave formation as well as of the decay of the perturbation energy can be found in⁶. Figure 4 shows a comparison between the values predicted by Morse and Ingard and those obtained with the MSD solver, with 80 points in the cavity and an explicit integration (CFL = 0.5). The spectral analysis (Figure 5) reveals a DSP

similar to the predictions by Morse and Ingard, i.e a decrease with $1/N^2$, where N indicates the Nth harmonics of the signal.

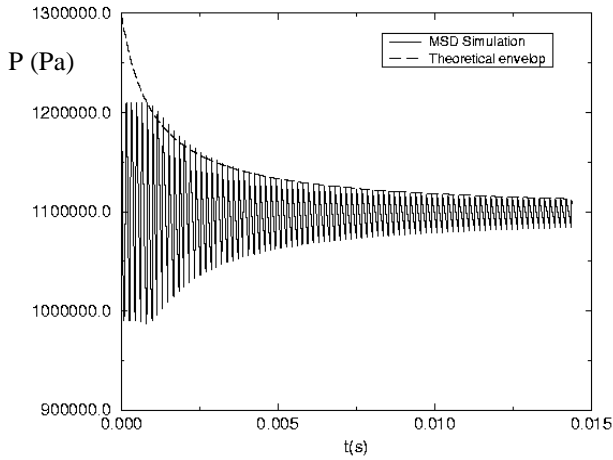


Figure 4 : End of cavity pressure signal

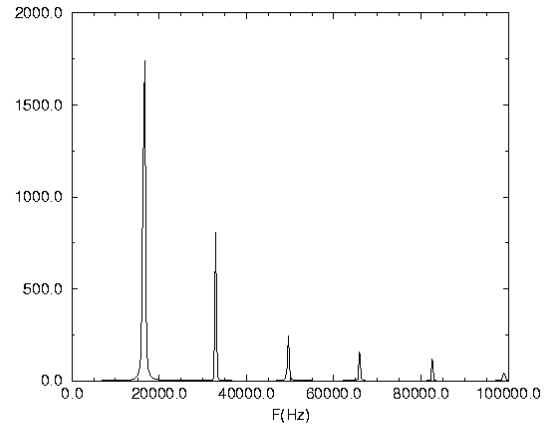


Figure 5 : Spectral analysis of the pressure signal

d) Time integration issues

The O or H mesh topologies used for transverse modes involve large variations of the cell sizes, and of the CFL numbers. There is therefore a strong need for an implicit integration, corresponding to relatively high CFL for a few cells (around 3 for instance), and moderate for the majority of them (around 1). For a H-topology, the ‘corner’ cells can mostly be treated with high time steps without a deterioration of the signal in the chamber. Figure 6 shows the results obtained for 3 different time integration schemes : explicit, implicit with first order accuracy, implicit with second order accuracy and an upwind parameter of 1, implicit of second order accuracy with an upwind parameter of 0.5.

The only satisfactory solution is obtained with an explicit integration or an implicit integration with second order accuracy and an upwind parameter of 0.5. The implicit integration of order 1 induces a strong damping whereas the upwind parameter of one carries out a very pronounced dispersion of the signal.

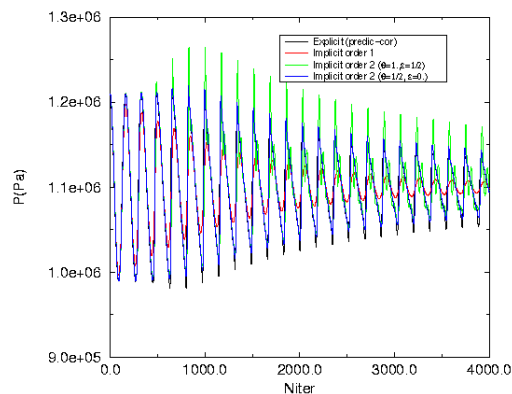


Figure 6 : Influence of the time integration scheme

2-1.2 Acoustic interaction of two cavities

One the most effective method to prevent combustion instabilities is the use of damping devices such as baffles or acoustics cavities. The objective of this second acoustic test case is to assess the code to handle correctly the acoustic interaction of two cavities, one representing a slice of the combustion chamber and the other one representing a quarter-wave resonator, particularly when the temperature is not uniform inside the resonator ⁴. Indeed one of the most important problem in designing acoustic cavities is to know their resonance frequency which depends itself on the temperature distribution inside the cavity. Temperature distribution is not always well known and may change during the engine operation.

2-1.2.1 Influence of a temperature gradient on resonant frequency of a quarter-wave resonator

a) Theoretical analysis

The linear constant temperature theory of a quarter-wave resonator was extended by P. Kuentzmann ⁷ to the case of non uniform temperature assuming a linear distribution in a the cavity.

$$\frac{T(x)}{T(0)} = \frac{a^2}{a_0^2} = 1 + \alpha x, \alpha = \frac{1}{L} \left(\frac{T_L}{T_0} - 1 \right) \quad (3)$$

Where T_0 and T_L are temperatures at the closed and open ends of the cavity, respectively. The analysis shows that the acoustic modes of the cavity are given by

$$J_0(kz)Y_1(z) - J_1(z)Y_0(kz) = 0 \quad (4)$$

where, $k = \sqrt{(1 + \alpha L)} = \sqrt{\frac{T_L}{T_0}}$, $z = \frac{2\omega}{a_0\alpha}$, J and Y are Bessel's functions of first and second kinds.

The fundamental mode corresponds to the first root z_1 of this equation and is given by:

$$f_1 = \frac{a_0}{4L} \frac{(k^2 - 1)z_1(k)}{\pi} \quad (5)$$

If the temperature gradient in the chamber is small, i.e if $z_1 \gg 1$, the Bessel functions in Eq.(4) become sinusoidal functions. Eq. (4) can then be solved easily, and

$$z_1 = \frac{\pi}{2(k-1)}, \frac{f_1^A}{f_0} = \frac{\sqrt{\frac{T_L}{T_0}} + 1}{2} \quad (6)$$

where f_0 is the frequency that would correspond to a uniform temperature distribution in the cavity (equal to T_0) and f_1^A is the resonance frequency within the approximation ($z_1 \gg 1$) as given by Eq. (6). Eq. (4) was solved numerically to get the root $z_1(k)$ and thus the resonance frequency, for k ranging from 1 to 5. For instance, the case $T_L = 4T_0$ (a realistic value for liquid-propulsion applications), i.e. $k = 2$, we find $f_1/f_0 = 1.71$. In other words, the acoustic mode in the cavity is 1.71 times higher than the mode based on T_0 . The quarter-wave resonator being a narrow band device, this is of crucial importance.

b) Numerical simulation

To check the ability of the code to handle this case and to compare CFD results (resonance frequency) with the theory, numerical simulations were performed in a closed-open cavity. A no-slip condition is prescribed for $x = 0$ (closed end) and a constant pressure for $x = L$ (open end). The mean temperature profile is prescribed via a density profile, the pressure being assumed constant in the resonator. The disturbances on pressure and density are identical to those detailed above. Several temperature ratios are tested, for T_L/T_0 between 1 and 4. The results are summarized in Table 2 and Figure 7. The temperature gradient increases the acoustic mode value, and carries out the appearance of harmonics. For $k = 2$, the ratio between the two frequencies present in the signal is 2.68, which is the exact ratio between the first and second roots of Eq.(4), for this value of k .

T_L/T_0	f_1^A / f_0 Eq.(6)	f_1 / f_0 (solution Eq.(4))	f_1 / f_0 numerics (MSD)
1	1	1	1
2	1.207	1.295	1.3
4	1.5	1.71	1.72

Table 2 : Effect of temperature gradient on acoustic modes

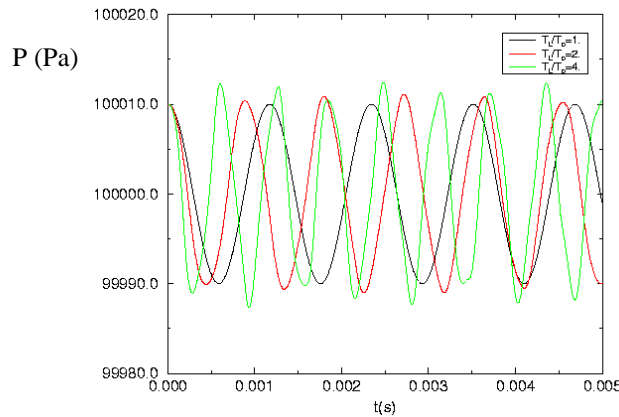


Figure 7 : Effect of temperature gradient on the pressure signal

2-1.2.2 Numerical simulation of a quarter-wave resonator/combustion chamber coupling

These elementary test cases being judged satisfactory, the damping effect generated by a quarter-wave resonator on an acoustic transverse perturbation in a slice of combustion chamber can then be investigated numerically for linear as well as nonlinear regimes. Here only the first tangential mode (1T) with uniform temperature in the resonator is studied for illustration. The method is identical to that explained above. There is no initial disturbance in the quarter-wave. An overview of the geometry can be found in Figure 8. The flow pattern strongly depends on the resonator geometry (through l/d), and the perturbation amplitude. If the amplitude is sufficiently high, the flow is going out from the resonator, and the jet induces two counter-rotating vortices (Figure 9).

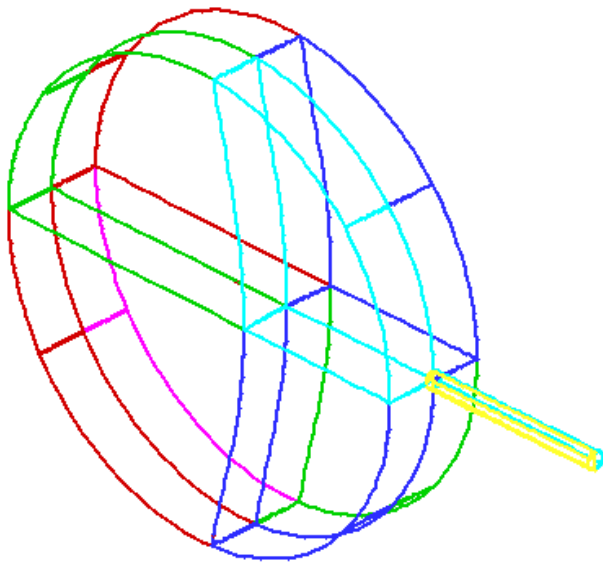


Figure 8 : Overview of the geometry

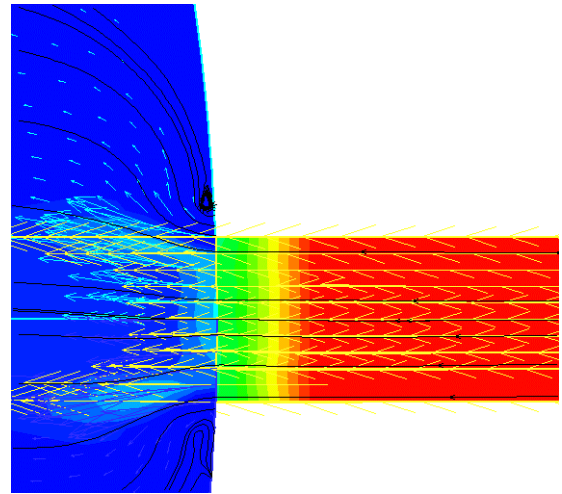


Figure 9 : Streamlines and pressure field

2-2 Steady-state operation – The Mascotte test case

To be used for steady-state analysis of spray combustion (for performance, heat transfer or stratification evaluation, for instance), the CFD tool needs to be calibrated in more realistic conditions. Thus, a more complex case is considered, the Mascotte test case. Mascotte is a cryogenic test facility using LOX/GH₂ and LOX/CH₄ propellants^{3, 8-10}. The test case consists in computing the spray reacting flow in a single shear-coaxial windowed combustor. A lot of data, both qualitative (OH imaging) and quantitative (CARS technique) have been obtained with this facility at low (10 bar) and high (60 bar) pressure. This test case deals with the 10 bar situation, it has been proposed at two workshops on Rocket Combustion Modeling¹¹⁻¹².

At this stage it should be noticed that numerical results will depend on physical modeling of main processes involved (secondary atomization, vaporization, turbulent combustion...) as well as on the boundary conditions (inlet conditions) which are not always well known. In the present test case, one issue is droplet and velocity distribution at the inlet. Indeed in the Mascotte combustor, flow visualization showed that the atomization process is very complex and far from being complete (presence of ligaments) in the near exit region. Nevertheless, using some PDPA (Phase Doppler Particle Analyzer) measurements, an estimation of these data have been obtained. For details on specifications of this test case see references^{11, 12}.

2-2.1 Operating point and injection conditions

The operation point is named A-10 which characteristics are

PRESSURE	O/F	\dot{m} (LOX)	\dot{m} (H ₂)
10 bar	2.11	50 g/s	23.7 g/s

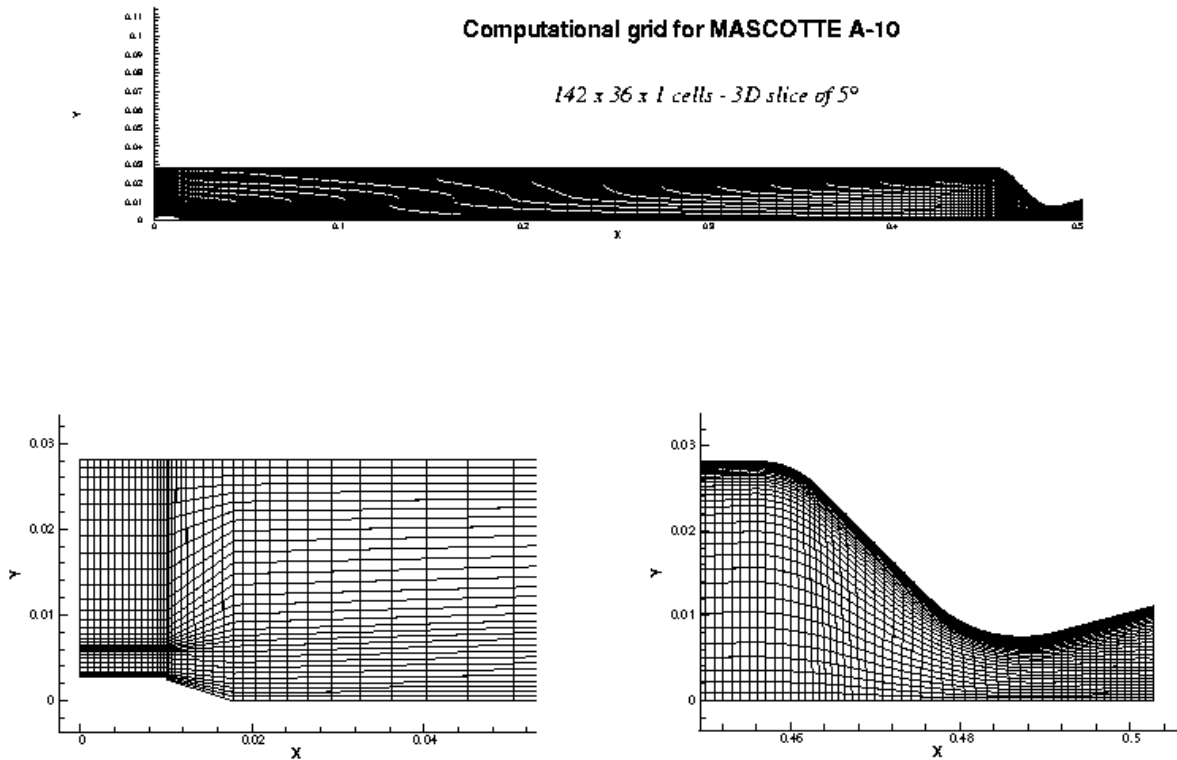


Figure 10 : Computational geometry and grid

Computations were performed using the MSD code. Droplets are tracked using the Lagrangian solver DLS. A two-way coupling is performed between the liquid phase and the gas phase. Gas phase turbulence is computed with the $k-\varepsilon$ turbulence model. The turbulent dispersion is treated by the Gossman and Ionnides Eddy Life Time dispersion model with an additional spatial decorrelation criterion to better account for crossing trajectory effect. Vaporization is computed with the standard "D²" model with Ranz-Marshall correction to account for convection around the droplet. Four combustion models were used for these computations : two kinetic models (the Rogers and Chinitz model and the Eklund⁵² model) and two turbulent models (the Magnussen's Eddy break-up model and the CLE model). Although experimental data including OH imaging and Coherent Anti-Stokes Raman Scattering (CARS) indicated a highly turbulent flame, kinetic combustion models were used for comparison. The CLE turbulent combustion model assumes an infinitely fast single scalar chemistry with a β -function pdf and a thermodynamical equilibrium limitation.

2-2.2 Results

Both kinetic models predict a longer flame than expected and a still stratified temperature field at a distance of 200 mm from the injector exit which contradicts experimental observation.

Computations were then performed using the turbulent combustion models: the Magnussen model and the CLE model. After some preliminary computations, the CLE model was chosen

to continue the analysis using a single droplet size of $82\ \mu\text{m}$. Figure 11 shows the temperature field and streamlines where the recirculation zone can be observed.

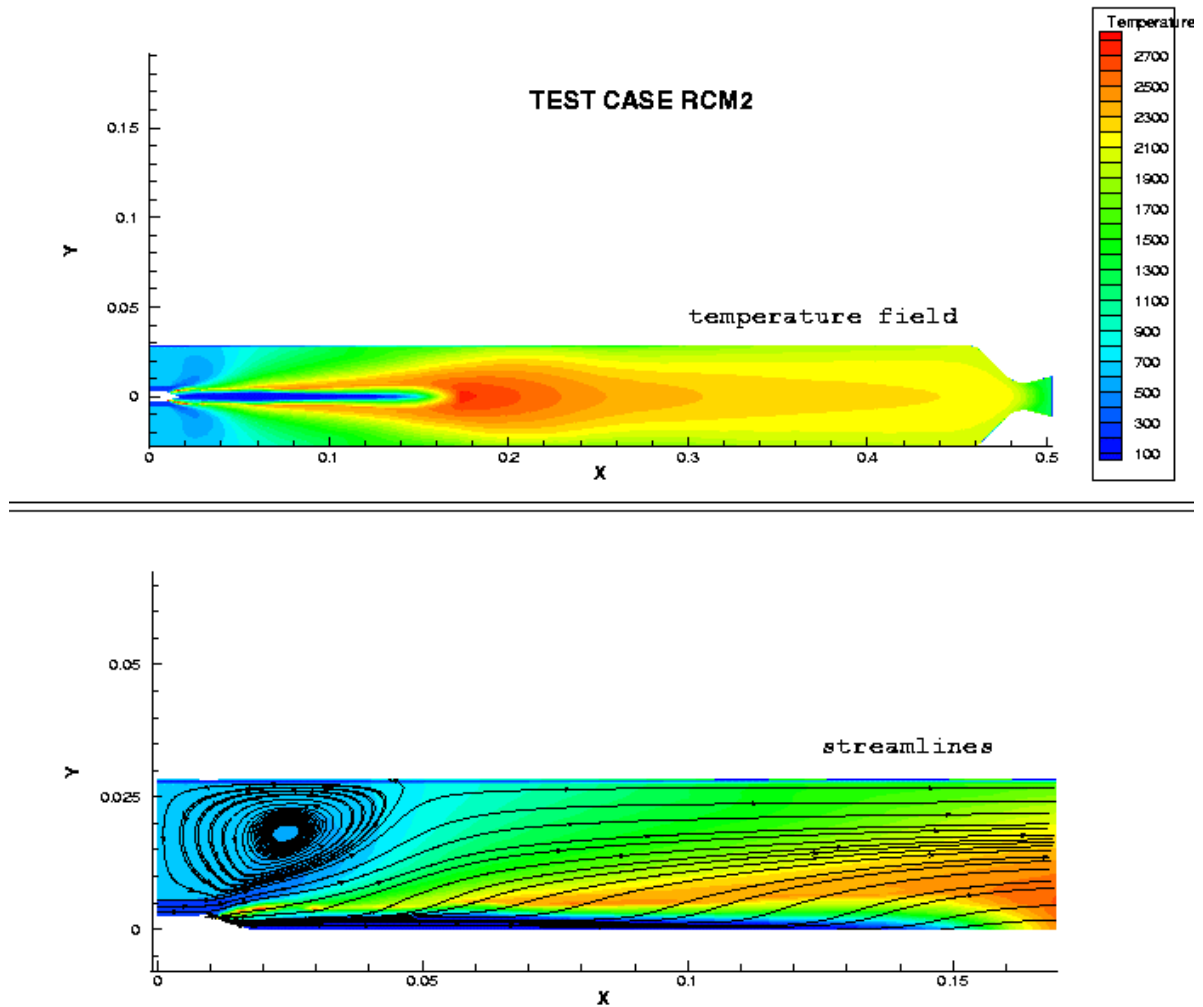


Figure 11 : Temperature field and streamlines - CLE model, $D = 82\ \mu\text{m}$.

Figure 12 and Figure 13 show a comparison of computed temperature profiles with experimental data obtained by means of the CARS technique. The CARS technique, using in this case hydrogen as a probe molecule, allows to measure instantaneous gas temperature at a given spatial location. The number on the experimental data (Figure 12 and Figure 13) represents the validation rate which is the ratio of the number of CARS signals successfully processed to the total number of laser shots acquired during a Mascotte run. Nearly 100 laser shots are acquired during a run. At a fixed location, each CARS signal gives an instantaneous temperature. From the instantaneous values one can obtain a mean value and a standard deviation. Of course precision of the measurements depends on the validation rate, higher is this number, better are the statistics. The interval that bounds the experimental data (Figure 12 and Figure 13) represents the standard deviation. The high values of the standard deviation indicate the turbulent character of the flow field.

Figure 12 compares temperature radial profiles at four axial locations: 10, 180, 250, and 410 mm from the injector exit. At 10 mm, one can observe a good agreement between computed results and experimental data. This region corresponds to the recirculation zone with high concentration of hydrogen which also explains the observed high validation rate. As we move downstream, we have a relatively good agreement with the experimental data. It can be also noticed that the validation rate is low on the axis ($x = 180$ mm and $x = 250$ mm) and increases as we move to the chamber wall where more hydrogen is present. No hydrogen is detected on the axis at $x = 10$ mm

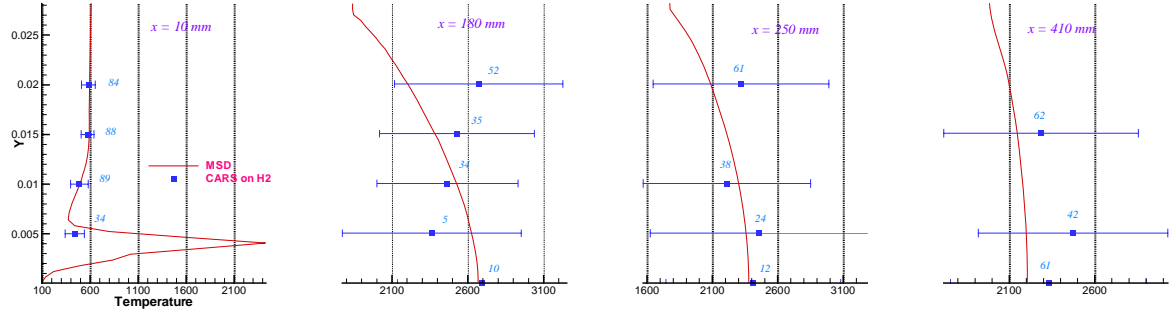


Figure 12 : Temperature radial profiles – Comparison of computations and experimental data

Figure 13 shows temperature axial profiles at two radial locations ($y = 10$, and 15 mm). Computed profiles are compared with the experimental data. The agreement is fairly good.

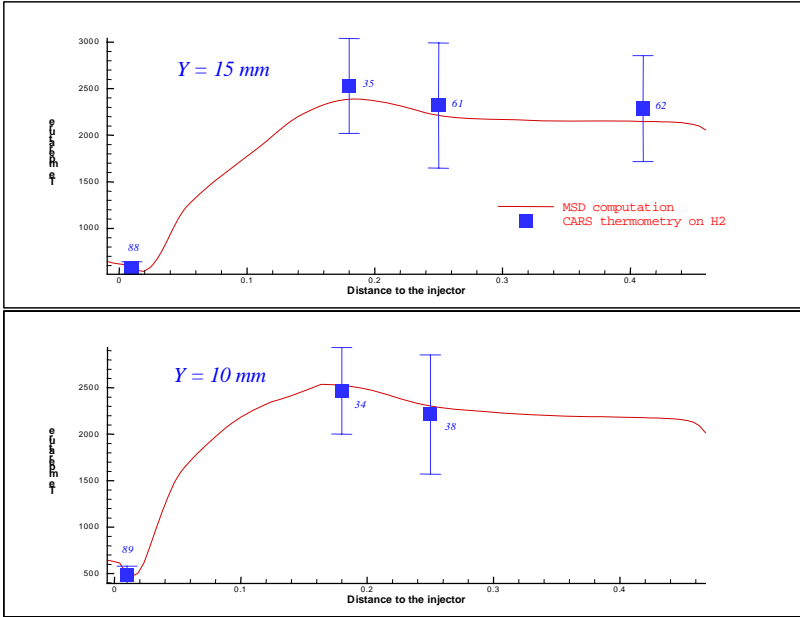


Figure 13 : Temperature axial profiles - Comparison of computations and experimental data ($y = 10$ mm and $y = 15$ mm)

2-3 Conclusion - Liquid propulsion

For liquid propulsion application use of CFD codes is more and more required to optimize combustor device design, and predict the system operation. At ONERA, the propulsion MSD-CEDRE family solvers are being developed for this purpose. Validation of these codes is an

important issue that needs careful attention. Through the examples presented in this paper, it has been shown that this new generation of codes have a promising potential to be used for practical devices in space propulsion. The validation approach that has been used for MSD is being extended to the new code CEDRE. Nevertheless, it should be noticed that use of such codes for complex systems need powerful computing capabilities and physical modeling. In general, building such models needs suitable experiments with sophisticated diagnostics. For instance, for combustion instability in liquid rocket engine, an European program is being conducted¹³ to get insight in physical mechanisms of combustion instability and to build up models, to represent this phenomenon, and that could be implemented in CFD codes. For steady-state combustion, European teams have been working on cryogenic combustion¹ to investigate combustion processes and a good amount of data are now available for code calibration. Only with all these efforts in computing capabilities, numerical and experimental investigations it will be possible to use CFD codes in the design loop of liquid propellant combustion devices.

3- SOLID PROPULSION

One of the key aspects of solid propulsion comes from the fact that the flow field originates from the burning propellant surface, which is distributed all along the combustion chamber. If one excludes end burning grains (cigarette like burning) the propellant grain has the shape of a hollow cylinder radially burning from inside. Mass injection is thus distributed along the chamber ensuring a continuous flow acceleration, while turning towards the nozzle. An other aspect of flow in solid propellant rocket motors is that combustion mechanisms take place in the very vicinity of the propellant surface (typical flame height of tens to hundreds of microns) and only aluminum (or other metallic additive) particles, when present, may burn away from the surface, depending on their effective sizes. As a consequence, most flow studies concerning unmetalized composite propellant can safely consider the flow of a non reactive mixture of reaction products (pure aerodynamic analysis). The presence of condensed matters, for instance in the form of alumina droplets, can be treated as a diluted two-phase flow problem, in which the motion of the particulate phase is computed from a separate, although coupled, set of equations. The case of burning aluminum droplets has been considered only recently (e.g. ref ¹⁴) and will not be addressed in this paper, due to inherent difficulties in characterizing the droplet properties and reaction mechanisms, which presently render very premature any validation works. The following cases will consider only non reactive flows.

Other aspects of solid propellant motors are more trivial but must nevertheless be addressed before any detailed simulations can be considered. First, as the propellant burns, the chamber geometry continuously changes. However, due to the relative densities of solid propellant and combustion products (typical ratio solid/gas is 1000) the propellant regression rate is three order of magnitude smaller than gas velocities. This permits to uncouple the two mechanisms and the entire burn can be represented by a succession of fixed geometries in which the flow solution is computed. This implies that an ad hoc procedure is available to provide the successive geometries as the motor firing proceeds. Second, due to extraordinary conditions that prevail inside the chamber (> 1 MPa and > 2600 K) and the relative short durations of the motor burn (full scale Ariane 5 boosters burn for a maximum of 120s, while a typical lab scale motor burn lasts for less than 10 s), measurements are very difficult in such unfriendly conditions. Most of the time, only limited pressure measurements are carried out (the number of allowed "holes" in a pressurized vessel is always a matter of discussion), limiting available data to validate computational data.

Under such conditions, cold flow simulators which use cold air injection through porous surfaces (representing the burning propellant surfaces at a given time) present many advantages over actual rocket firings : test duration can be extended to allow for the necessary measurements, detailed pressure and velocity measurements can be performed, using available and well proven techniques and optical access to the flow field can be easily provided, for detailed visualizations and analyses. However, and especially for unsteady flow studies the cold flow apparatus presents serious drawbacks that come from the injection device. The porous plates that are used (most often sintered bronze) produce turbulent flows that may differ from what would result from propellant combustion and their acoustic response tends to attenuate acoustic waves present in the chamber while propellant combustion is known to amplify certain frequencies. This means that cold flow set-up will not be sufficient for code validation and that there is a need for a laboratory scale motor set-up that provides actual firing data in conditions simple enough to be reproduced by the code. In

the course of the ASSM program (see refs. ¹⁵⁻¹⁷) this motivated the development of small scale motors to complement the cold flow apparatus.

The basic properties of the flow solver that need to be validated are the following:

- laminar flow
- turbulent flow transition
- acoustic motions
- two-phase flow
- motor instabilities driven by flow instabilities that couple with acoustic modes of the chamber

To achieve this validation cold flow set-ups as well as laboratory scale motors were designed and operated in the course of the ASSM program to provide the necessary data for code validation^{18, 19}. A progressive approach was followed in order to permit the analysis of discrepancies in a positive way. Some characterizations were also performed to secure key data for the models operated inside the codes, such as propellant response measurements and particle properties and size distributions.

Some of the results will now be succinctly presented.

3.1 Cold flow set-up : VECLA

The cold flow VECLA set-up is a 2D rectangular chamber (Fig. 14). Air is injected through a porous plate placed at the bottom of the chamber and the flow is exited to the atmosphere from the right. The porous plate has a length of 581 mm and is 60 mm wide²⁰.

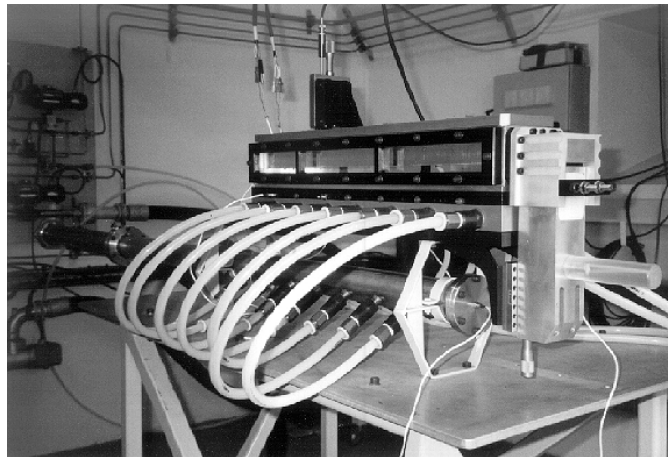


Figure 14 : The VECLA set-up

The VECLA cold flow set-up of ONERA was extensively used to understand the VSP (so-called parietal vortex-shedding, see ²¹) mechanism and to validate the full numerical approach for unsteady regimes²²⁻²⁷. The length to height ratio can be varied through variation of chamber height (the height can be varied from 30 to 10 mm). It can be tested with or without a choked nozzle. In the configuration without nozzle, the injection velocity can be easily varied by changing the air mass flow rate. This provided a very convenient mean to control the flow field inside the VECLA set-up.

At least three different behaviors were documented :

- a) For small length to height ratio ($h=30\text{mm}$) no acoustic resonance nor turbulent transition are observed. However, the flow exhibits local instabilities that can be compared to the stability analysis.
- b) For moderate length to height ratio ($h=20\text{mm}$) acoustic resonance could be produced for a definite range of injection velocities.
- c) For large length to height ratio ($h=10\text{mm}$) transition to turbulence was observed inside the chamber.

All three regimes were used to validate the numerical results, as described below.

3.1.1 Flow stability

The VECLA set-up, in configuration a) served as a first level academic validation, where the computed mean flow could be compared to known theoretical solution of the Taylor’s or Culick’s flow^{28, 29}. Then the comparison was carried out one step further by looking at the stability properties of the flow. These properties can be derived from the knowledge of the mean flow and were compared to detailed, time resolved, velocity measurements^{22, 23}. Next, the code results were compared against linear stability theory results²⁴⁻²⁷. Simulations were performed and the unsteady field was extracted from the full Navier-Stokes solutions by discrete Fourier transforms at chosen frequencies. Unstable wave frequency range and spatial growth rate were found to match the stability results as illustrated by figure 15 below.

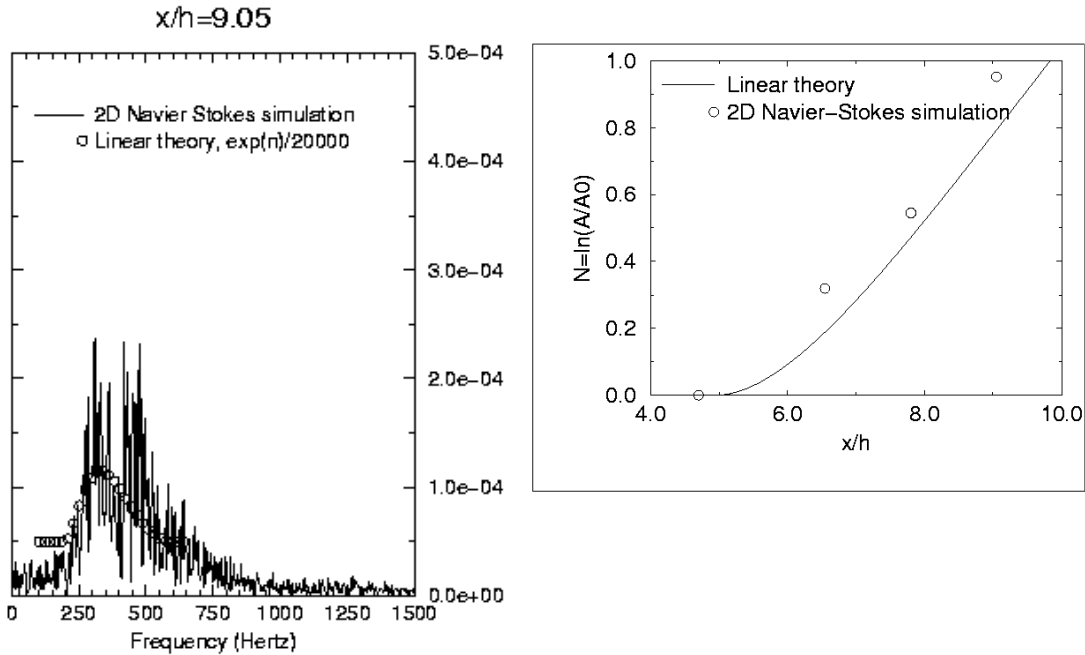


Figure 15 : Comparison of the Navier-Stokes results with the linear stability analysis : velocity spectrum and exponential growth rate.

At the chosen frequency, the unstable mode shape, in both amplitude and phase, was also extracted from the numerical solution and showed good agreement with the linear stability results, as depicted in figure 16.

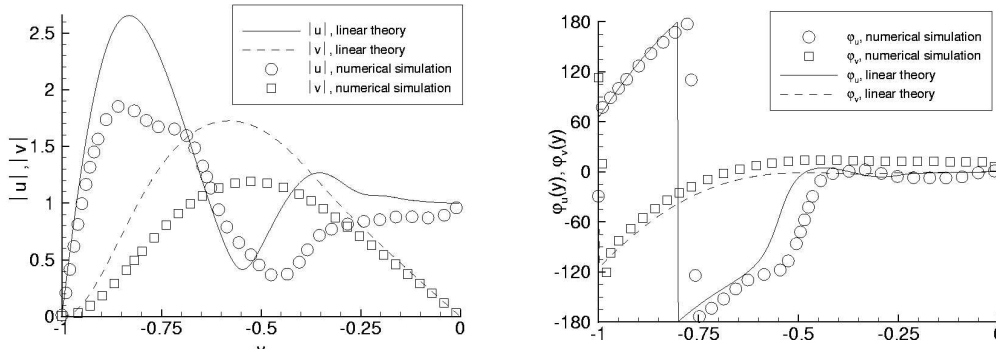


Figure 16 : Comparison of the Navier-Stokes results with the linear stability analysis : velocity amplitudes and phases at a selected frequency.

This established the ability of the Navier-Stokes solver to properly describe the early destabilization processes of the Taylor’s flow and provided a key validation step at the first level.

3.1.2 Acoustic resonance

Case b) was also used to check the ability of the full Navier-Stokes approach to reproduce acoustic resonance regimes in the simple geometry of VECLA, progressing to the second level of the validation procedure. For this case, the ratio V_{inj}/h could be adjusted so as the unstable stability wave frequencies match the chamber longitudinal mode frequencies. Clear cases of acoustic resonance could be observed in a definite injection velocity range. By imposing a time variation of the injection velocity in the Navier-Stokes simulations, resonances could be simulated in good agreement with the experimental results. This is illustrated by figure 17 below.

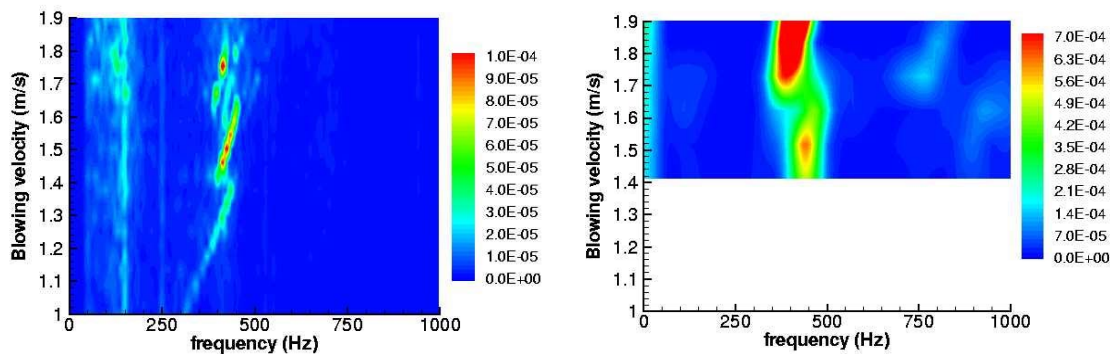


Figure 17 : Comparison of the Navier-Stokes results (right) with the experimental results (left). Velocity psd as a function of the injection velocity.

Satisfactory qualitative agreement is observed, establishing the ability of the full approach to reproduce resonant regimes in VSP situations. However, the oscillatory amplitudes were found to be over-estimated. Reference ³⁰ presents an effort to bridge the amplitude gap. In that work, the negative response function of the porous wall was included in the simulation (as mentioned earlier and on the contrary to burning propellant, the porous wall has a negative response to pressure waves, resulting in significant damping of the excited acoustic waves). In an attempt to better stick to the experiment, the flow destabilization in the numerical solution relied on a white noise, introduced at the porous surface vicinity, whose characteristic was matched with the measured injection noise. This produced a marked decrease of the simulated

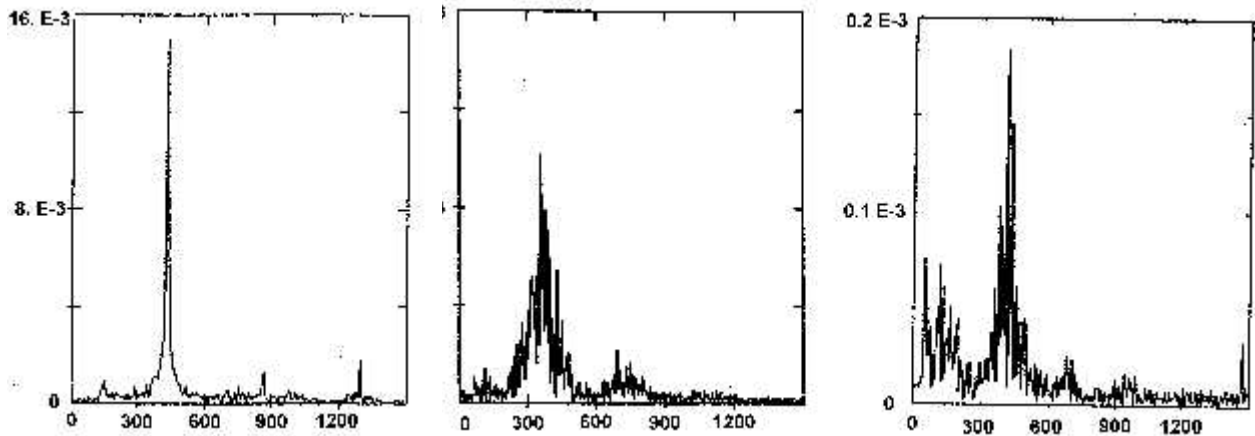


Figure 18 : Head-end pressure spectra. From left to right : a) Initial Navier-Stokes solution; b) Navier-Stokes with porous wall response and white noise model; c) Experiment.

oscillatory amplitude being now comparable to actually measured amplitudes, as displayed in figure 18.

The exemplary simplicity of the VECLA set-up permitted to go one step further in establishing the validity of the full numerical approach and to actually see the so-called parietal vortices. Following Prof. Culick's suggestion, the injected flow was seeded with acetone and laser induced fluorescence permitted to actually see the vortices in the VECLA

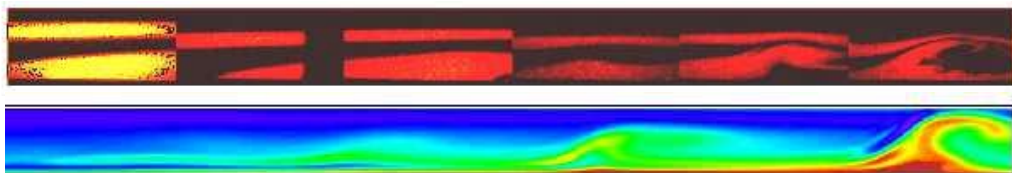


Figure 19 : PLIF images of vortices in VECLA set-up(top) compared to the computed vorticity field (bottom).

set-up ³¹. It must be stressed that this constituted a world premiere that confirmed that the computed vortices were indeed present in the experimental set-up. Figure 19 above illustrates this result.

3.1.3 Turbulent transition

At the same level "2" of the validation procedure, the VECLA set-up in configuration c) was used to check the ability of the codes to reproduce the flow turbulent transition. Several traversing positions are available along the chamber length (0.031, 0.120, 0.220, 0.350, 0.400,

0.450, 0.500 and 0.570 mm) and are used for two component hot wire measurements. Observations show a laminar region in the range $0^+ < x/h < 20$ (here 0^+ means that the region very close to the head end has not been investigated thoroughly and shows complex flow organization that is outside the scope of this paper) followed by a transitional region $20 < x/h < 30$ where fluctuations occur without affecting the mean velocity profiles and finally by a fully turbulent region $30 < x/h < L/h$ where the mean flow profiles undergo transition³². This flow field organization recovers similar descriptions by other researchers e.g. 33, 34. Computations have been carried out in the course of the validation file of the CEDRE code. A standard (k, L) model is used, except for the low Reynolds number damping functions that have been turned off (it has been shown that they should not be used in such injection driven flows³⁵). Boundary conditions are the following :

- inert walls are considered as adiabatic,
- porous wall : air is injected with $T_i = 303$ K, $\rho v = 2.62$ kg/m²/s, $k=0.011$ m²/s², $L=1.$ mm
- exit boundary : $P_s=137$ 400 Pa

The grid comprises 151x61 nodes, with a uniform x distribution and stretching in the y direction (minimum spacing being 1.10^{-3} mm on both upper inert and lower injecting walls). Figures 20 below show the Mach number and the turbulent kinetic energy maps after convergence (2000 time steps, using local time stepping).

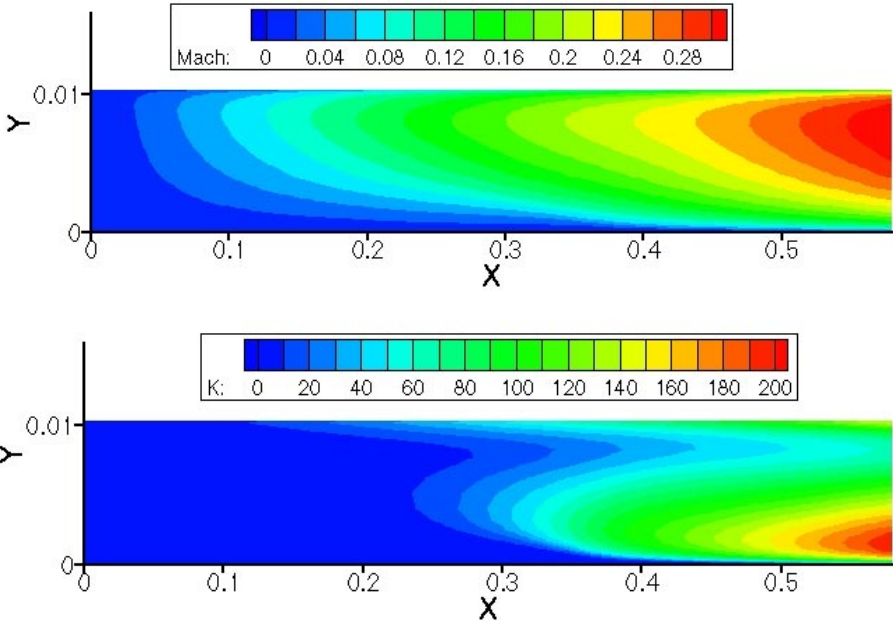
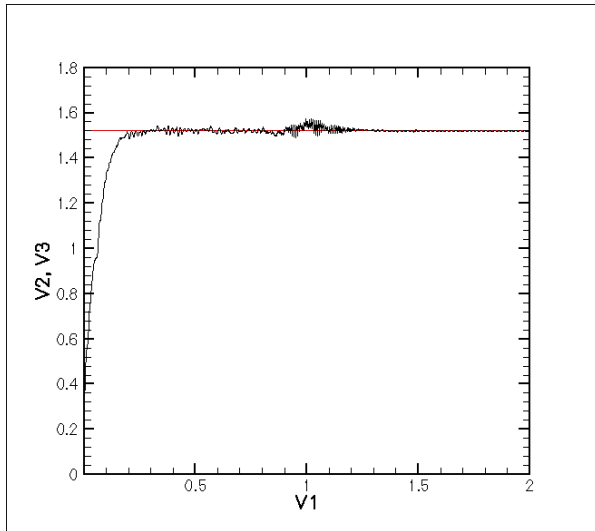
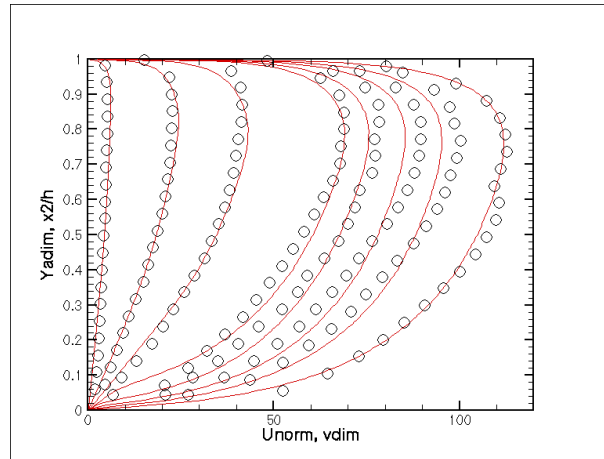


Figure 20 : Mach number and turbulent kinetic energy fields (Vecla 10 mm)

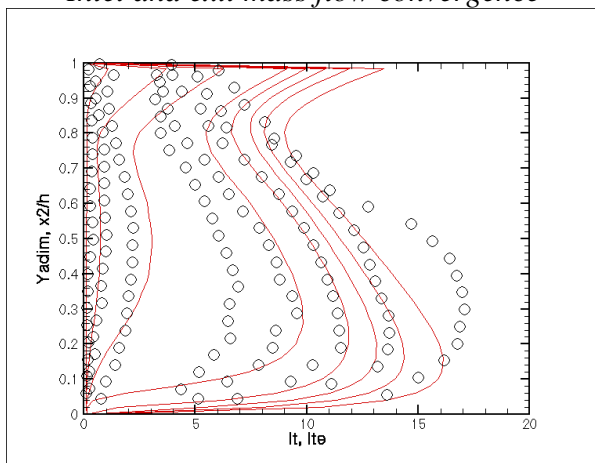
Comparisons with experimental data are based on the velocity and turbulent intensity profiles at several axial positions : They are illustrated by the figures 21 below (open circles show measurements).



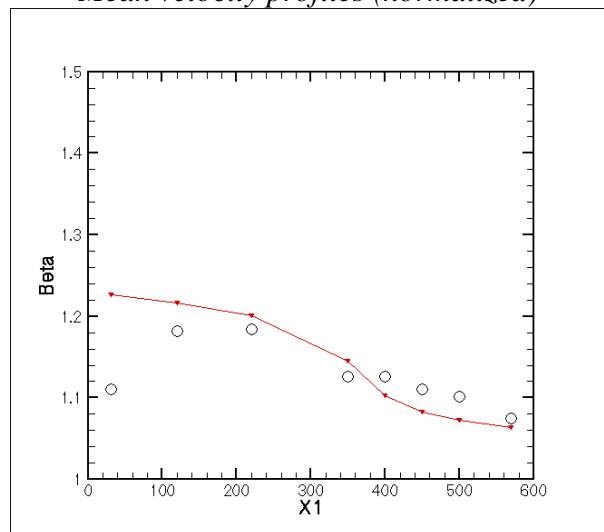
Inlet and exit mass flow convergence



Mean velocity profiles (normalized)



Turbulent intensity profiles
 $\text{sqrt}(u^2 + v^2) = \text{sqrt}(2k^*)$ with $k^* = 2k/3$



Axial variations of the β parameter
 $(= \langle U^2 \rangle / \langle U \rangle^2)$

Figure 21 : Convergence and comparisons with experimental data (Vecla 10 mm)

Due to slight variations in the injected mass flow rate in the VECLA set-up, mean velocity are normalized with respect to the experimental mass flow rates. The β parameter is a measure of the velocity profile shape ($\beta = \langle U^2 \rangle / \langle U \rangle^2$, for an incompressible flow). The results indicate that the mean flow transition is well recovered, while the transitional region is found to begin at an earlier position (turbulent intensities are over estimated upstream of the fully turbulent region). Over estimation of the computed turbulent intensities can be observed on the upper inert wall and is a consequence of turning off the low Reynolds damping functions. This will be corrected by a code development permitting to turn on and off these functions on selected walls. It is also interesting to note that in the laminar region, the code properly recovers the well known sine and cosine profiles (Taylor's or Culick flows, for which the theoretical value for β is $\beta = 1.23$). These results also compare well to recent computations of the same test case by Chaouat, using a RSM model³⁵.

3.1.4 Conclusions on Vecla set-up

This case illustrated that a well documented test case in three different configuration has proven its usefulness in validating codes in simple situations where only one type of modelization is at stake (second level). The presence of a laminar flow regime also fulfills the first level of validation against academic solutions.

However, it must be stressed that the inlet conditions are not fully modeled neither fully measured. First order variations, such as the nonuniformity of the injected mass flow rate have been well documented in the experiment and permitted a proper normalization of computed results (that use a uniform mass flow rate) for comparison. However, the injected turbulence and the complex flow organization at the head end (likely 3D effects) were not experimentally documented and introduce some uncertainties that exclude more detailed comparisons. In particular, parametric computations showed that to certain extents, the flow field was sensitive to the properties of the turbulence at the injection surface. In this case, the researcher is left to best guess. Nevertheless the comparisons were judged sufficient and the objectives were considered as attained.

3.2 Laboratory scale motor : C1xb

Another very important aspect of solid propellant rocket motor operation is stability provisions. Reference ³⁶ presents a recent review of available results and methods. In particular, large motors for space launchers (such as the US Space Shuttle, TITAN or European Ariane 5) are known for developing low level pressure oscillations on their first acoustic modes ³⁷⁻⁴¹. Flandro and Jacobs ⁴² were the first to mention the "vortex-shedding" as a possible additional driving to the motor stability balance. It was viewed as a coupling between a shear layer instability (in the hydrodynamic sense) and the chamber acoustic. In order to provide a proper validation case for the code developments undertaken in the ASSM program relative to the numerical simulations of such unsteady flow regimes, it was decided to design a specific lab scale motor named C1xb ⁴³⁻⁴⁶. Indeed, cold flow set-up, such as the VECLA set-up, were used intensively to analyze flow stability, but it was thought that they could not provide sufficient data for code validation in such coupled regimes. The reason is that the porous wall acts like an acoustic damper while burning propellant is known to have a positive response, leading to amplification.

From the beginning, the C1xb motor was designed as to be a first stage of validation at the laboratory scale (level 3). As described in references ^{44, 45}, the emphasis was put on the two-phase flow effects, combined with vortex-shedding driven oscillations. Following first demonstration of effective motor destabilization, the motor was fired with propellants having different inert particle loadings. Although this work produced unprecedented results, in particular on the influence of the inert particles on oscillatory levels (to the contrary of the ideas inherited from the acoustic balance approach, amplitudes were not always decreased by the presence of condensed phase) it was limited by the difficulties in characterizing the propellant combustion response. A quantitative comparison in term of frequency and amplitude was nevertheless conducted few years later, once propellant characterization became available, only for the reference propellant without inert particle loading. This is described in ⁴⁷ and the main results are presented below. The propellant response function is treated as an unsteady boundary condition that is derived from the linear relationship defining

the pressure coupled response function $R_{MP}(\omega) = \frac{\dot{m}'(\omega)/\bar{\dot{m}}}{p'(\omega)/\bar{p}}$. Here \dot{m} is the injected mass flow rate, prime denotes unsteady components and overbar mean values. Then the resulting unsteady injected mass flow rate is expressed as a convolution integral:

$$\dot{m}(t) = \bar{\dot{m}} + \frac{\bar{\dot{m}}}{\bar{p}} \int_0^{t-t_0} R(\tau)(p(t-\tau) - \bar{p})d\tau$$

with $R(\tau)$ being the impulse response associated to the frequency response $R_{MP}(\omega)$ that has to be measured :

$$R(t) = \text{TF}^{-1}[R_{MP}(\omega)]$$

This simple boundary condition proved to be quite effective and produced quasi-perfect agreement between the experimental measurements and the computations. Due to uncertainties in the propellant characterization, two response curves were considered. Although these curves largely differed, the results were found to be significantly improved with both response functions. The figure 22 below presents the unsteady flow field in the C1xb motor at the 10.7 mm web distance burned, which was chosen for the comparison, and the following table summarizes the quantitative results, in terms of pressure amplitudes and frequency.

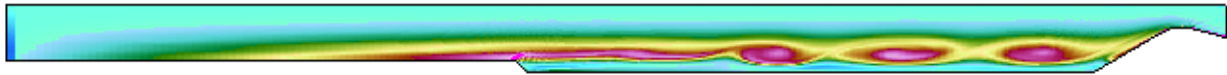


Figure 22 : C1xb flow field at 10.7 mm of web distance burned

	No response	Response #1 (mne)	Response #2 (glk)	Experiment
Head-end amplitude (hPa) (relative error)	12.7 (71%)	28.5 (35%)	43.1 (2%)	43.9
Aft-end amplitude(P_{C6}) (hPa) (relative error)	15.5 (39%)	20.6 (20%)	26.6 (4%)	25.6
Frequency (Hz) (relative error)	740 (3.8%)	720 (1.0%)	715 (0.3%)	713
Frequency resolution (Hz)	23	23	23	10

The "no response" results were found to be improved for both response functions. In particular, the ratio of head-end to aft-end pressure amplitudes together with the oscillation frequency were found to better match the experimental measurements. Best results were obtained with the second response curve with an almost perfect agreement. It must be stressed that it was the first time that numerical results could be compared to actual firing test measurements. The rather satisfactory agreement was seen as an evidence that the numerical approach was sound and could provide quantitative stability data, such as frequency and amplitude of limit cycle oscillations in actual motors. This level of validation belongs to the third level and is a pre-requisite to level 4 applications.

3.3 Two-phase flow effects

Although the C1x motor was fired with propellants loaded with inert particles (see ^{44, 45}) these could not be used to validate the two-phase flow computations, due to a lack of fundings that precluded measurement of propellant response functions for all the fired propellants. Here

again it must be stressed that validation may require specific experiments to secure key input data for model operation. This has to be acknowledged early enough in the program funding to avoid such embarrassing situations. Nevertheless, code validation was obtained from analytical results and linear acoustic balance results, as described in ⁴⁸⁻⁵⁰. The main objective was to check the ability of the two-phase flow solver to describe acoustic wave damping in particle laden flows. The figure 23 below compares the computational results for a planar acoustic wave travelling in a duct filled with and gas-inert particle mixture. The real and imaginary parts of the wave number k ($\exp(i(kx - \omega t))$) were plotted as $\alpha = k^{(i)}/2$ and $\beta = (k^{(r)})^2 - (\omega/a_0)^2$, versus the Stokes number $\omega\tau_u = \omega\rho D^2/18\mu$, where ρ is the particle density, D the particle diameter and μ the gas viscosity. The very good agreement provided a validation of the two-phase flow solver at the first level.

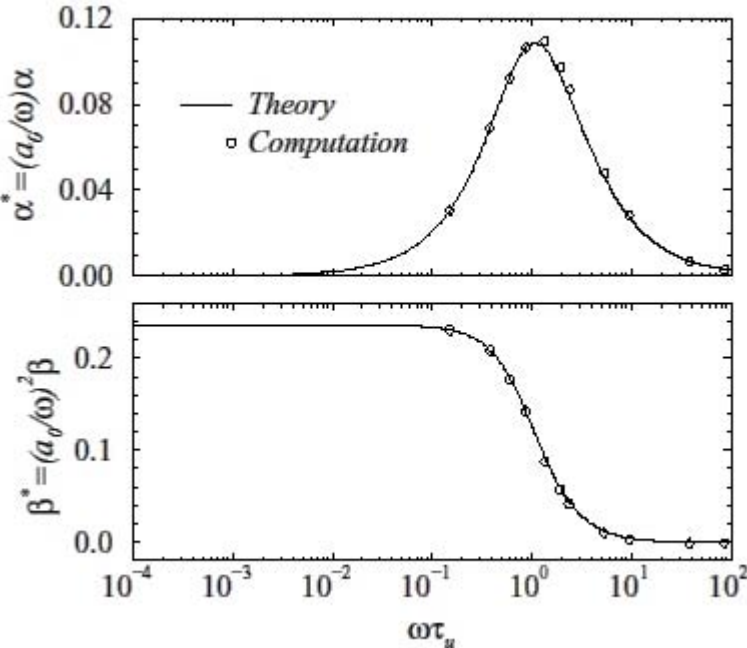


Figure 23 : Real and imaginary part of the wave number as a function of the Stokes number

Finally, two-phase flow computations were performed in the configuration of a small rocket motor mock-up and were compared to the available acoustic balance results, as described in references ^{49, 51}. This provided level 2 validation, with good agreement (discrepancies were related to the non-linear aspects of the full Navier-Stokes results, as opposed to the linear treatment inherent to the acoustic balance results) as depicted in figure 24.

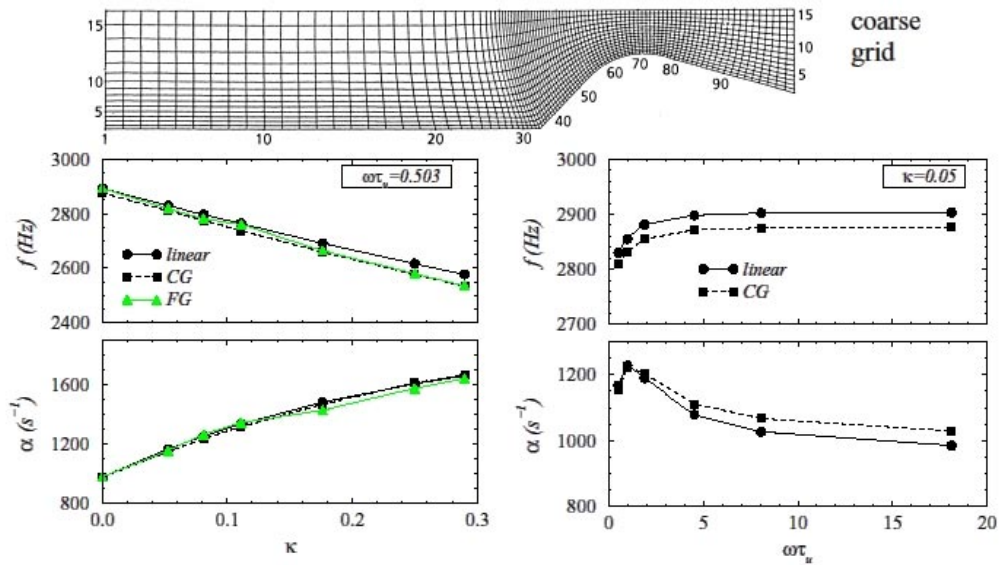


Figure 24 : Computational results for two-phase flow effects in a small scale rocket motor mock-up, as compared to the linear acoustic balance results. Variations of the frequency and damping with the particle loading parameter κ (left) and with Stokes number (right)

3.4 Conclusion - Solid propulsion

The progressive approach followed in the solid propulsion research activities, permitted to validate numerical codes up to level 3. This opened the way to full scale applications of the numerical codes, that are now used to analyze full scale firing results. Although some difficulties remain, they are limited to the level 4 problems. They mainly concern the proper way to couple several models in the practical situations encountered at that level 4. The results of several years of research works have permitted to increase the confidence in the numerical results and to delimit the areas where the research efforts should be concentrated. In the course of this research activity, several discoveries have been made, thanks to the validation effort at the earlier levels of the validation procedure, that produced clear cases of comparisons where discrepancies could be discussed and analyzed in fruitful details.

4- HYPERSONIC PROPULSION

Hypersonic propulsion generally involves scramjets. The structure of the flow is very complex in these engines and represents a difficult challenge for CFD, due to strong interactions between chemistry, aerodynamics and turbulence. For these engines, CFD is a precious help to understand the structure of the flow and is also the only way to predict the performance of the engine at very high flight Mach number, when ground testing becomes impossible. For these reasons, the need for validation is particularly important in the field of propulsion. Basic test cases (level 1) are used to test the ability of numerical schemes to capture shocks and contact discontinuities. Level 2 and 3 test cases are used to validate the modeling in simplified configurations, with no or restricted interactions. Level 4 test cases are used to validate the codes in a real configuration.

4-1. Level 1 test case : oblique shock wave

A basic oblique shock test case is included, at level 1, in the MSD and CEDRE validation files. It is a Mach 2.5 flow incoming onto a 15 degrees wedge, for which theoretical solution is available. Figure 25 displays the Mach number field where the shock is clearly captured by the code. Figure 26 compares the Mach number along the bottom boundary with theoretical results. This basic test case permits to check the good behavior of the numerical scheme.

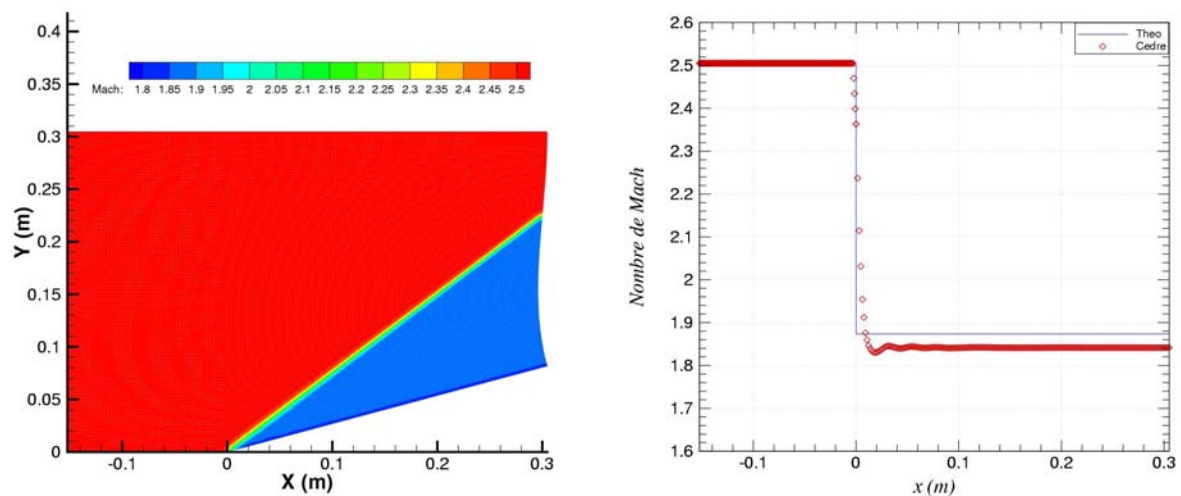


Figure 25 : Basic wedge flow at Mach = 2.5 and 15 degrees

4.2. Level 3 : LAERTE experiment

The LAERTE experiment located at ONERA Palaiseau is used to validate turbulent mixing and combustion of hydrogen in a supersonic air flow. It consists of an axial cylindrical jet of 6 mm diameter in a square channel of 45 x 45 mm² (figure 26). The typical conditions for air flow are a stagnation temperature of 1800 K and a stagnation pressure of 7 bar, with a Mach number of 2. This provides a static temperature of 1100K which ensures self ignition of the hydrogen jet. The entrance Mach number of the jet is 2, which leads to a convective Mach number of 0.38 to 0.62, if the hydrogen is heated up to 500 K.

Quite a complete database has now been acquired on this configuration. It includes:

- wall pressure measurement,
- OH radical visualisation by OH spontaneous emission and PLIF, that also provides OH concentration (the calibration of the PLIF signal allows to determine the mass fractions with an uncertainty of about 20%),
- H₂ jet visualisation by PLIF with acetone seeding,
- temperature measurement by CARS on N₂ and H₂ molecules,
- velocity measurement by laser interferometric velocimetry,
- stagnation temperature at the exit of the test channel.
- Particle Imaging Velocimetry (in cooperation with DLR Lampoldshausen that operated the PIV system)

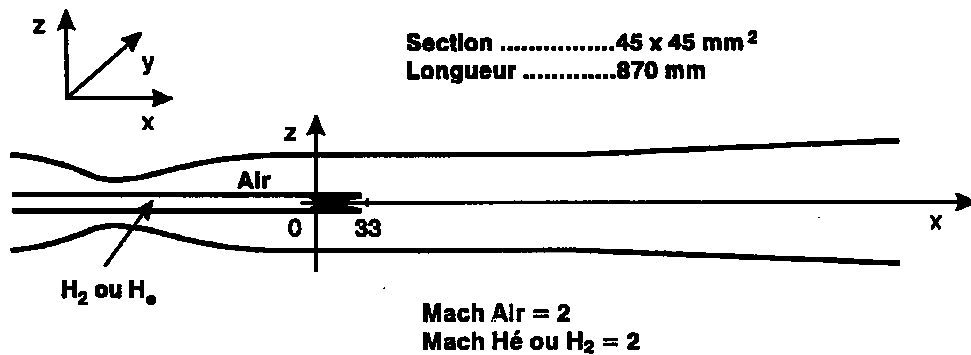


Figure 26 : sketch of the LAERTE experiment

Figure 27 shows images produced by PLIF on OH and acetone. PLIF on OH allows to visualize the combustion region, at the boundary of the jet, and PLIF on acetone (which seeds the jet) allows to visualize the jet. Test results were used to validate compressibility effects in

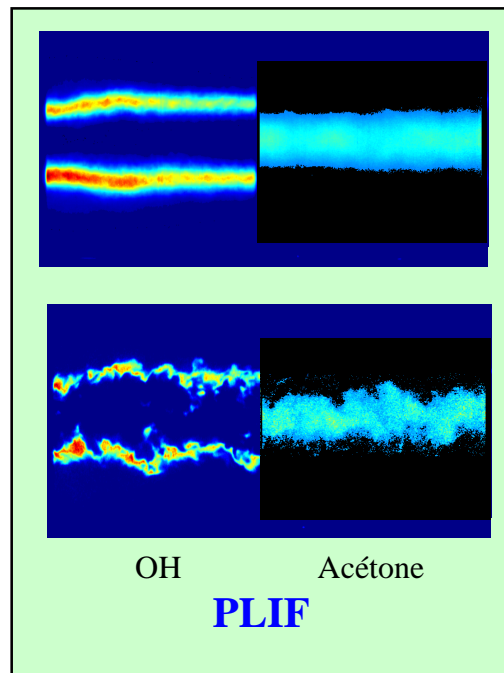


Figure 27 : Visualisation of hydrogen supersonic combustion by PLIF

the turbulence model and to compare several combustion models.

Figure 28 presents some validation results obtained on this configuration for two combustion models : the first one is the pure kinetics Eklund⁵² model, the second one is the PEUL+ model developed at ONERA, which allows to take into account the influence of turbulence on kinetics through an Eulerian-Lagrangien coupled approach. One can see that the kinetics model overestimates the heat release, whereas the PEUL+ model gives a better agreement with test results.

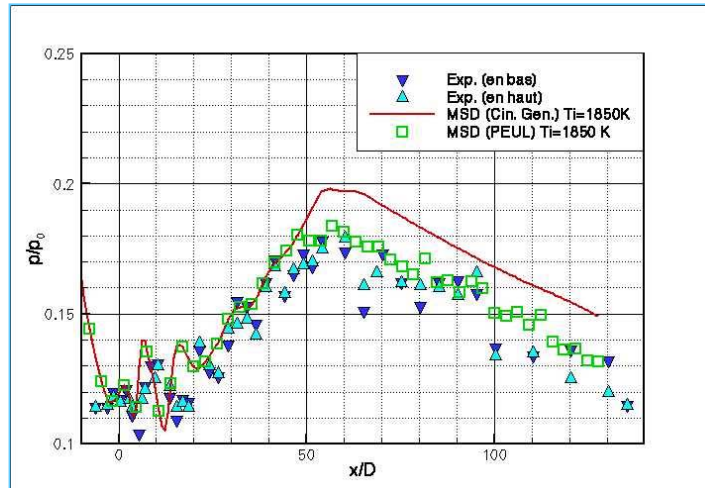


Figure 28 : Wall pressure in the LAERTE experiment

4-3 Level 4 : JAPHAR scramjet

The JAPHAR scramjet is an experimental engine designed to operate with a fixed geometry from Mach 4 to Mach 8. For this purpose, a double combustion chamber concept is retained in order to match the combustion constraints at the various Mach numbers and combustion regimes. It is illustrated on Figure 29 below.

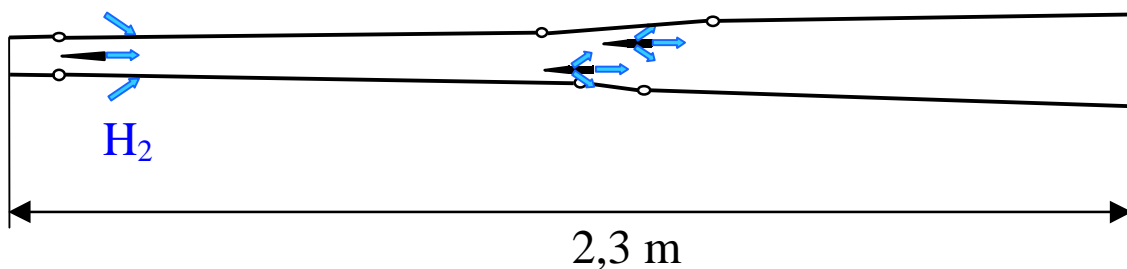


Figure 29 Sketch of JAPHAR scramjet

In supersonic combustion, at high Mach number, the best combustion process is obtained in a constant area duct. Then, the first part of the combustor, the cross section of which is nearly constant, is used, the fuel being injected from the first level of injection located at the beginning of the duct.

When the Mach number decreases, combustion can no longer take place at high equivalence ratio in a constant area duct. Then, only a part of hydrogen is injected from the first level of injection and burns in the first chamber at the end of which the Mach number is reduced to a bit more than 1. The rest of the fuel is injected through the second level of injection located at

the beginning of the second combustion chamber, the cross section of which is diverging. The ratio of injection between the first level and the second one is decreased when the Mach number increases.

Comparison between test and computation is illustrated on figure 30 in the case of operation at Mach 7.6 for an equivalence ration equal to 1. Computations were performed with MSD code, with k-l turbulence model and the Eklund kinetics model (6 species, 7 reversible reactions). One can see, on the left, the structure of the flow from the MSD computation, and on the right the wall pressure contour for both test and computation. Combustion begins in a supersonic flow, after a rather large ignition delay, and then continues in a subsonic flow after a quasi-normal shock due to the thermal choking. The computed pressure contour is in good agreement with the test measurements, excepted in the vicinity of the normal shock, where probably boundary layer separations are not correctly captured by the computation.

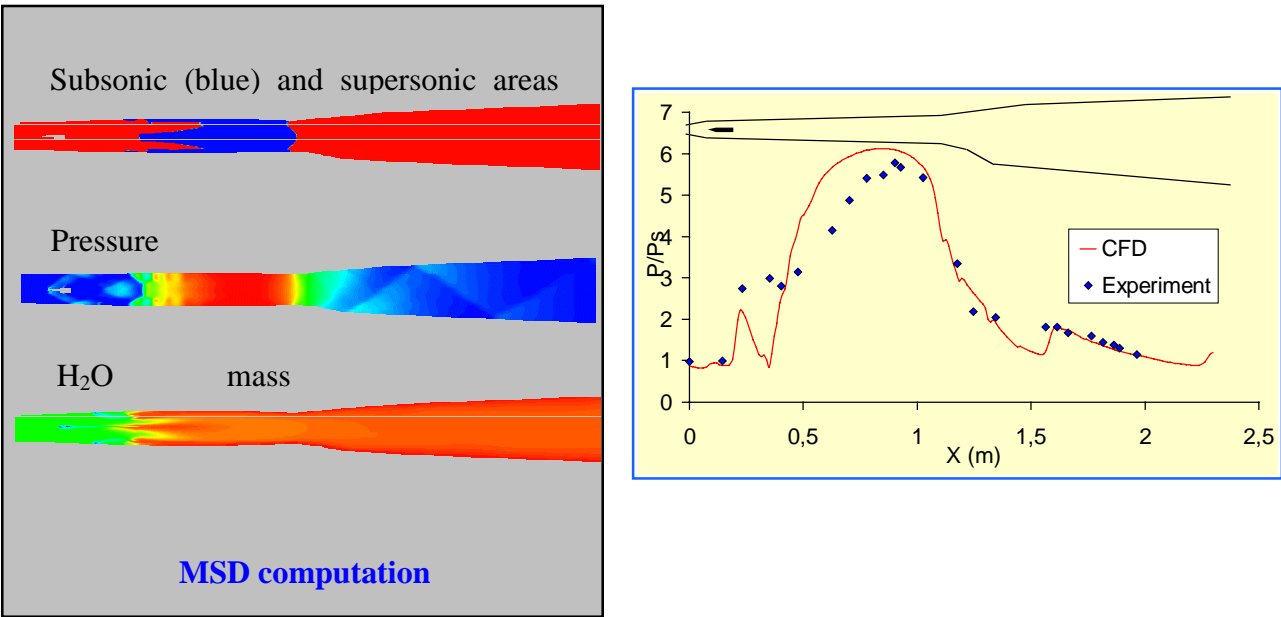


Figure30 : JAPHAR scramjet operation at Mach 7.6

5- CONCLUSIONS

Space propulsion evolves in a competitive market where delays and cost reductions are important aspects in developing and testing complex propulsion devices. In such a context, complex multi-physics codes are essential assets that need full validation before they can deliver their benefits. ONERA from its large research spectrum is in the core of the business of developing and validating such codes, for its own research needs and also for the needs of research and industrial partners. This implies numerous ties with basic research labs, in the frameworks of coordinated research programs, who bring in their expertise, as well as with industrial partners or agencies, who contribute through their identified needs.

This paper addressed this issue from three major fields of space propulsion: liquid, solid and hypersonic propulsion. In each of these fields a progressive approach was illustrated, covering four levels of the complexity of the physical reality : basic academic (level 1), isolated model (level 2), multiple models in simplified geometry (level 3) and finally actual systems in complex geometry (level 4). In each case, proper validation implies that a proper path is established to move from one level to the next one. This is essential to allow for positive analysis of observed discrepancies. Another important aspect of validation work is the necessary coordination between experiments and computations. Indeed in order to provide valuable confrontation points, the boundaries of the system under scrutiny must be properly defined and agreed on and key inputs to the numerical computations must be secured. Similarly the data processings must be, as much as possible, rendered comparable between experiments and computations. Issues such as spatial and temporal resolution, as well as durations (which entails frequency resolution), must be addressed in common.

With such requirements in mind, examples were provided for the three areas of liquid, solid and hypersonic propulsion, showing key results that permitted to validate the code results. Most of the presented results come from the validation files of ONERA MSD and CEDRE codes. These codes are produced by ONERA and released to partners in the aerospace research and industrial communities under quality management rules. They represent valuable assets in capitalizing research works and rendering possible the study of present days complex systems.

Future works are clearly directed towards multi-physics and multi-scale applications entailing code coupling, parallel computing, LES or DES simulations and associations of several models and solvers. The new generation CEDRE code is already designed for such an evolution, that will render possible the analysis of systems of ever increasing complexity, provided that the necessary validation steps are recognized and supported. ONERA with the support of concerned agencies is engaged in such a challenging endeavor.

ACKNOWLEDGEMENTS

The authors wish to acknowledge A. Nicole, I. Dubois, E. Laroche, M. Pourouchottamane, F. Dupoirieux, and V. Burnley for their contribution to CFD activities for the liquid propulsion part, J. Troyes, G. Avalon, N. Lupoglazoff and J. Dupays for their contributions to the solid propulsion part and D. Gaffié for contributing to the supersonic combustion part. J. Troyes also provided the first hypersonic propulsion test case.

REFERENCES

- [1] DESCAMPS L., "Spécifications de vérification et de validation du code MSD", MSDH/SPE-001, oct.2000.
- [2] FRENCH J., "Guide for the Verification and Validation of CFD Simulations", Technical Report AIAA G-077-1998.
- [3] HAIDN O., HABIBALLAH M., "Research on high pressure cryogenic combustion". Aerospace Science and Technology, Volume 7, Issue 6, pp. 473-491, (September 2003).
- [4] LAROCHE E., HABIBALLAH M., KUENTZMANN P., "Numerical analysis of liquid rocket combustion instability : preliminary 3D acoustic calculations", AIAA paper 2000-3497, Huntsville, Alabama, July 2000.
- [5] NICOLE A., HABIBALLAH M., "Numerical Analysis of Acoustic Instability", 4th International Conference on Launcher Technology "Space Launcher Liquid Propulsion", 3-6 December, 2003, Liege (Belgium).
- [6] MORSE AND INGARD, "Theoretical Acoustics", International Series in Pure and Applied Physics, Mc Graw-Hill Book Co, 1968
- [7] KUENTZMANN P., Private communication, 1999
- [8] HABIBALLAH M., VINGERT L., TRAINÉAU J.-C., VUILLERMOZ P., "MASCOTTE : a test bench for cryogenic combustion research", IAF-96-S.2.03, 47th International Astronautical Congress, (Beijing, China), October 7-10, 1996.
- [9] VINGERT L., HABIBALLAH M., TRAINÉAU J.-C., "MASCOTTE : a research facility for high pressure combustion of cryogenic propellants", 12th European Aerospace Conference, 3rd European Conference on Space Transportation Systems; November 29 – December 01, 1999, Paris.
- [10] VINGERT L., HABIBALLAH M., VUILLERMOZ P., ZURBACH S., "MASCOTTE, a test facility for cryogenic combustion research at high pressure", IAF-00-S.3.06, 51th International Astronautical Congress, (Rio de Janeiro, Brazil), October 2 - 6, 2000.
- [11] Proceedings of "Workshop on Rocket Combustion Modeling : Atomization, Combustion and Heat Transfer", ONERA, March 11-13, 1998, Toulouse, France.
- [12] Proceedings of the Second Workshop on Rocket Combustion Modeling : Atomization, Combustion and Heat Transfer, DLR Lampoldshausen, March 25-27, 2001, Edited by Oskar, J. Haidn.
- [13] G.SEARBY, "The French-German high frequency combustion instability program" in 4th International conference space launcher liquid propulsion, Liège, 3-6 Dec. 2002.
- [14] LUPOGLAZOFF N., VUILLOT F., DUPAYS J., FABIGNON Y., "Numerical simulations of the unsteady flow inside segmented solid-propellant motors with burning aluminum particles", AIAA paper 2002-0784, AIAA 40th Aerospace Sciences Meeting, Reno, Nevada, USA, Jan. 2002.
- [15] VUILLOT F., KUENTZMANN P., "Programme de R&T ASSM (Aerodynamics of Segmented Solid Motors)", Colloque CNES/ONERA/CNRS sur les Ecoulements propulsifs dans les systèmes de transport spatial, Bordeaux, France, 11-15 sept., 1995.
- [16] FABIGNON Y., KUENTZMANN P., VUILLOT F., PRÉVOST M., BEC R., ROBERT E., MARION-DUVAL P., "A survey of French research and technology program on the internal aerodynamics of segmented solid motors", 2nd European Conference on Launcher Technology, Space Solid Propulsion, Rome, Italy, 21-24 November 2000.
- [17] VUILLOT F., CASALIS G., "Recent Advances on the Stability of Large Segmented Space Boosters", Second European Conference on Launcher Technology, Space Solid Propulsion, November 21-24, 2000, Rome, Italy
- [18] GUERY J.-F., VUILLOT F., AVALON G., PLOURDE F., ANTHOINE J., PLATET B., "Use of cold flow experiments in the ASSM program - Lessons and results", 2nd

- European Conference on Launcher Technology, Space Solid Propulsion, Rome, Italy, 21-24 November 2000.
- [19] PRÉVOST M., DOMMÉE, Y., MAUNOURY J., TRAINÉAU J.C., VUILLOT F., "On the representativity of small scale motor test", 2nd European Conference on Launcher Technology, Space Solid Propulsion, Rome, Italy, 21-24 November 2000.
- [20] AVALON G., COMAS P., "Simulative study of the unsteady flow inside a solid rocket motor", AIAA paper 91-1866, AIAA 27th Joint Propulsion Conference Sacramento, California, June 1991.
- [21] LUPOGLAZOFF N., VUILLOT F. "Parietal vortex-shedding as a cause of instability for long solid propellant motors. Numerical simulations and comparisons with firing tests ", AIAA paper 96-0761, AIAA 34th Aerospace Sciences Meeting, Reno, Nevada, USA, Jan. 1996.
- [22] AVALON G., CASALIS G., GRIFFOND J., "Flow instabilities and acoustic resonance of channels with wall injection" AIAA paper 98-3218, AIAA 34th JPC, Cleveland, July 13-15, 1998.
- [23] CASALIS G., AVALON G., PINEAU J.-Ph., "Spatial instability of planar channel flow with fluid injection through porous walls", Phys. Fluids, 10 (10), october 1998.
- [24] UGURTAS B., AVALON G., LUPOGLAZOFF N., VUILLOT F., "Numerical computations of hydrodynamic instabilities inside channels with wall injection", AIAA 99-2505, 35th AIAA-/ASME/SAE/ASEE Joint Propulsion Conference - 20-24 June, 1999, Los Angeles, CA, USA.
- [25] UGURTAS B., AVALON G., LUPOGLAZOFF N., VUILLOT F., CASALIS G., "Stability and acoustic resonance of internal flows generated by side injection", in AIAA Progress in Astronautics and Aeronautics, Volume 185, Solid Propellant Chemistry, Combustion, and Motor Interior Ballistics, Vigor Yang, Thomas B. Brill, Wu-Zhen Ren editors, pp. 823-836.
- [26] UGURTAS B., "Etudes numérique et expérimentale des instabilités hydrodynamiques et du couplage aéro-acoustique dans un écoulement de Taylor", Thesis dissertation, Paris 6, décembre 2000.
- [27] GRIFFOND J., "Instabilité pariétale et accrochage aéroacoustique dans les conduits à parois débitantes simulant les moteurs à propergol solide d'Ariane 5", Thesis dissertation, ENSAE, septembre 2001.
- [28] TAYLOR G., "Fluid flow in regions bounded by porous surfaces", Proceedings of the Royal Society Series A, Vol. 234, No. 1199, 456-475, London, 1956.
- [29] CULICK F.E.C., "Rotational Axisymmetric Mean Flow and Damping of Acoustic Waves in a Solid Propellant Rocket", AIAA J., Vol.4, No.8, Aug. 1966, pp. 1462-1464.
- [30] LUPOGLAZOFF N., VUILLOT F., "Numerical simulations of parietal vortex-shedding phenomenon in a cold flow set-up", AIAA 98-3220, 34rd AIAA/ASME/SAE/ASEE Joint Propulsion Conference - July 13-15 1998, Cleveland, USA.
- [31] AVALON G., UGURTAS B., GRISCH F., BRESSON A., "Numerical computations and visualization tests of the flow inside a cold gas simulation with characterization of a parietal vortex shedding", AIAA 2000-3387, 36th AIAA/ASME/SAE/ASEE Joint Propulsion Conference and Exhibit, Huntsville, AL., 16-19 July 2000.
- [32] G. AVALON, L. LEBON, "Étude de la Turbulence sur le Montage VECLA pour un Écoulement en Transition", RTS ONERA n°6/2486 EY, Septembre 1993.
- [33] BEDDINI R.A., "Injection induced flows in porous walled ducts", AIAA Journal, Vol.24, No.11, pp.1766-1773, November 1986
- [34] APTE S., YANG V., "Effect of acoustic oscillation on flow developement in a simulated nozzleless rocket motor", in AIAA Progress in Astronautics and Aeronautics,

- Volume 185, Solid Propellant Chemistry, Combustion, and Motor Interior Ballistics, Vigor Yang, Thomas B. Brill, Wu-Zhen Ren editors, pp.791-822.
- [35] CHAOUAT B., "Numerical Simulations of Channel Flows with Fluid Injection Using Reynolds Stress Model.", J. of Propulsion and Power, Vol. 18, No.2, March-April 2002.
- [36] KUENTZMANN P., "Combustion instabilities," AGARD LS 180, Sept. 91.
- [37] MASON D.R., FOLKMAN S.L., BEHRING M.A., "Thrust oscillations of the space shuttle solid rocket booster motor during static tests", AIAA Paper 79-1138, AIAA 15th Joint Propulsion Conference, Las Vegas June 18-20, 1979
- [38] MATHES H.B. "Assessment of chamber pressure oscillations in the shuttle solid rocket booster motors" AIAA paper 80 1091, AIAA 16th Joint Propulsion Conference, Hartford CT, June 1980.
- [39] BROWN R.S., DUNLAP R., YOUNG S.W. AND WAUGH R.C. "Vortex Shedding as a Source of Acoustic Energy in Segmented Solid Rockets", J. of Spacecraft and Rocket, Vol.18, No.4 pp.312-319. July-August 1981.
- [40] BLOMFIELD F., MATHES H.B., "Pressure oscillations in post-Challenger Space Shuttle redesigned solid rocket motors", Journal of Propulsion and Power, Vol.9, No.2, March-April 1993, pp.217-221
- [41] VUILLOT F., TISSIER P.Y., DE AMICIS R., "Prédiction de stabilité des gros moteurs segmentés à propergol solide", AAAF, 5ème symposium international sur La Propulsion dans les Transports Spatiaux - 2.13-2.27, 22-24 Mai 1996, Carré des Sciences, Paris.
- [42] FLANDRO G.A., JACOBS H.R., "Vortex generated sound in cavities" , AIAA paper 73 1014, Seattle, Wa., USA, October 1973.
- [43] VUILLOT F., "Vortex-Shedding phenomena in solid rocket motors", Journal of Propulsion and Power, Vol. 11, NO. 4, pp 626-639, July - August 1995.
- [44] DUPAYS J., "Contribution à l'étude du rôle de la phase condensée dans la stabilité d'un MPS pour lanceur spatial", Thesis dissertation, INPT, novembre 96.
- [45] DUPAYS J., PREVOST M., TARRIN P., VUILLOT F., "Effects of particulate phase on vortex shedding driven oscillations in solid rocket motors", AIAA 96-3248, AIAA 32nd Joint Propulsion Conference- July 1-3 1996, Orlando, USA.
- [46] VUILLOT F., CASALIS G., "Motor Flow Instabilities", VKI-RTO-AVT Lecture Series, Internal Aerodynamics in Solid Rocket Propulsion, May 27-31, 2002
- [47] LUPOGLAZOFF N., VUILLOT F., "Simulations of solid propellant rocket motors instability including propellant combustion response", 6th International Congress on Sound and Vibration, 5-8 July 1999, Lingby, Denmark.
- [48] DUPAYS J., "Two-phase unsteady flow in solid rocket motors", Aerospace Science and Technology, 6(2002), pp. 413-422.
- [49] VUILLOT F., BASSET T., DUPAYS J., DANIEL E., LUPOGLAZOFF N. "2D Navier-Stokes stability computation for solid rocket motors : rotational, combustion and two-phase flow effects", AIAA 97-3326, 33rd AIAA/ASME/SAE/ASEE Joint Propulsion Conference- July 6-9 1997, Seattle, USA.
- [50] DUPAYS J., VUILLOT F., "Propagation of acoustic waves in a two-phase vaporizing mixture", J. of Propulsion and Power (TN), Vol. 18, No. 1, January-February 2002, pp.222-224.
- [51] DUPAYS J., WEY S., FABIGNON Y., "Steady and unsteady reactive two-phase computations in solid rocket motors with eulerian and lagrangian approaches", AIAA 2001-3871, AIAA 38th Joint Propulsion Conference, July 2001, Salt Lake City, USA.
- [52] EKLUND D. R., DRUMMOND, HASSAN, "Calculation of supersonic turbulent co-axial jets", AIAA J., 28, Sept. 90, pp. 1633-1641.



Liquid-Propellant Injection, Mixing, and Combustion at Supercritical Conditions

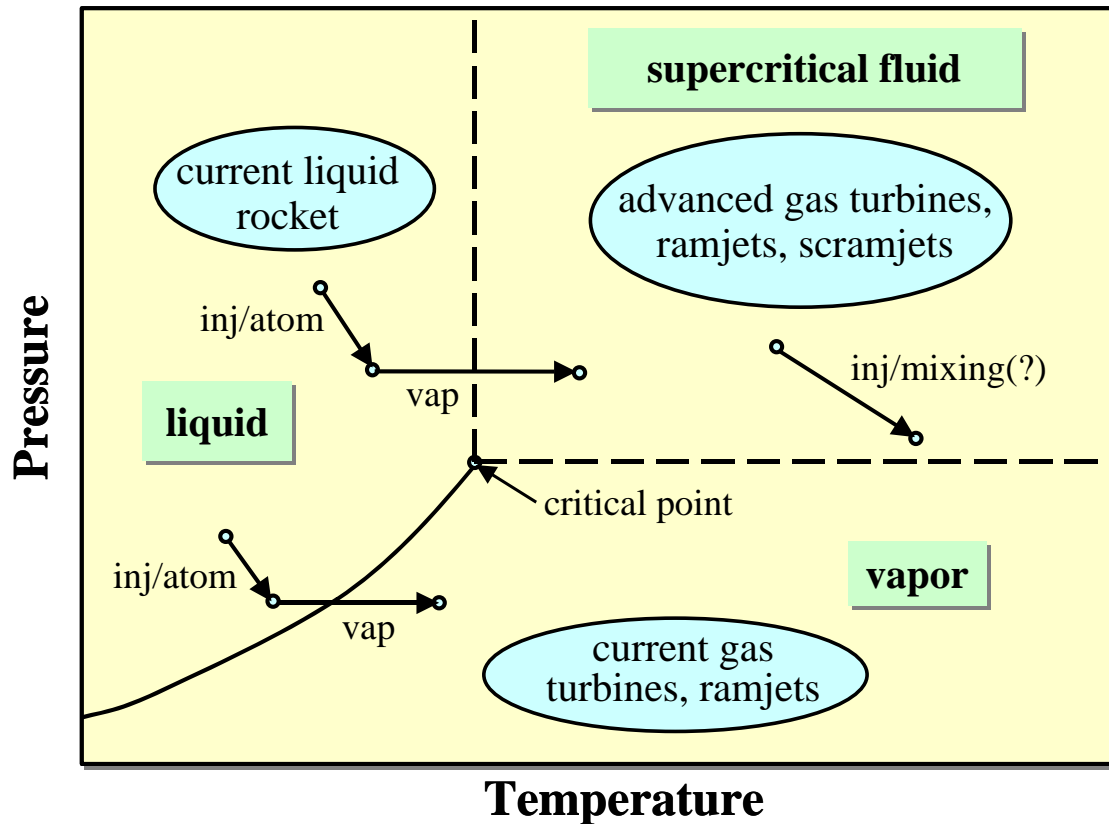
Vigor Yang
The Pennsylvania State University
University Park, Pennsylvania 16802, U.S.A.
**Email: vigor@psu.edu*

Presented at
Fifth International Symposium on Liquid Space Propulsion
October 27-29, 2003



Why Supercritical Combustion Research?

- most booster engines operate at supercritical conditions
- current understanding not sufficient to support design optimization





Liquid Rocket Chamber Conditions

Critical Properties of Propellants

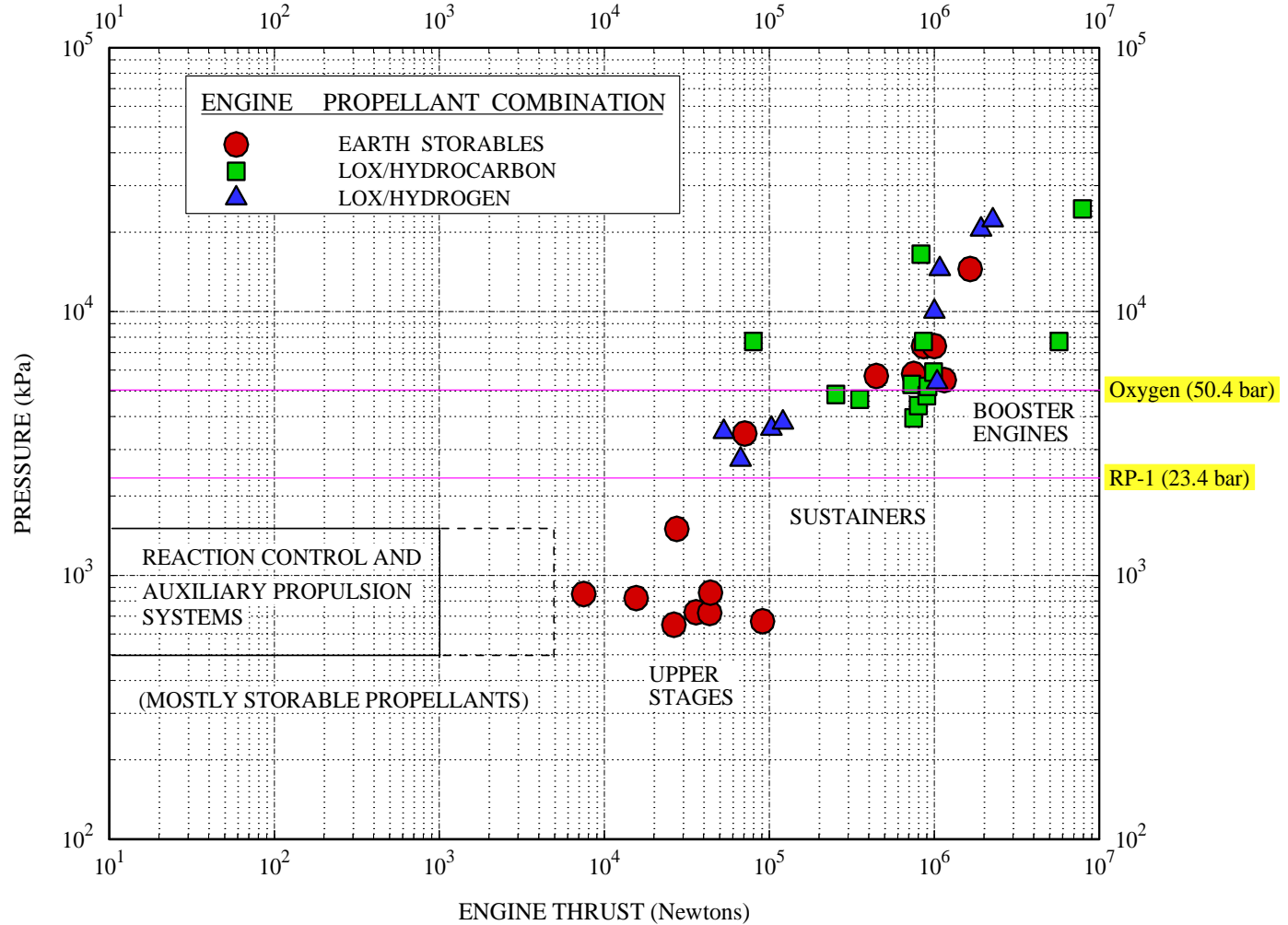
	Pcr (MPa)	Tcr (K)
H ₂	1.3	33.3
Oxygen	5.04	154.4
RP-1	2.344	685.95

F-1 Engine (Saturn V)

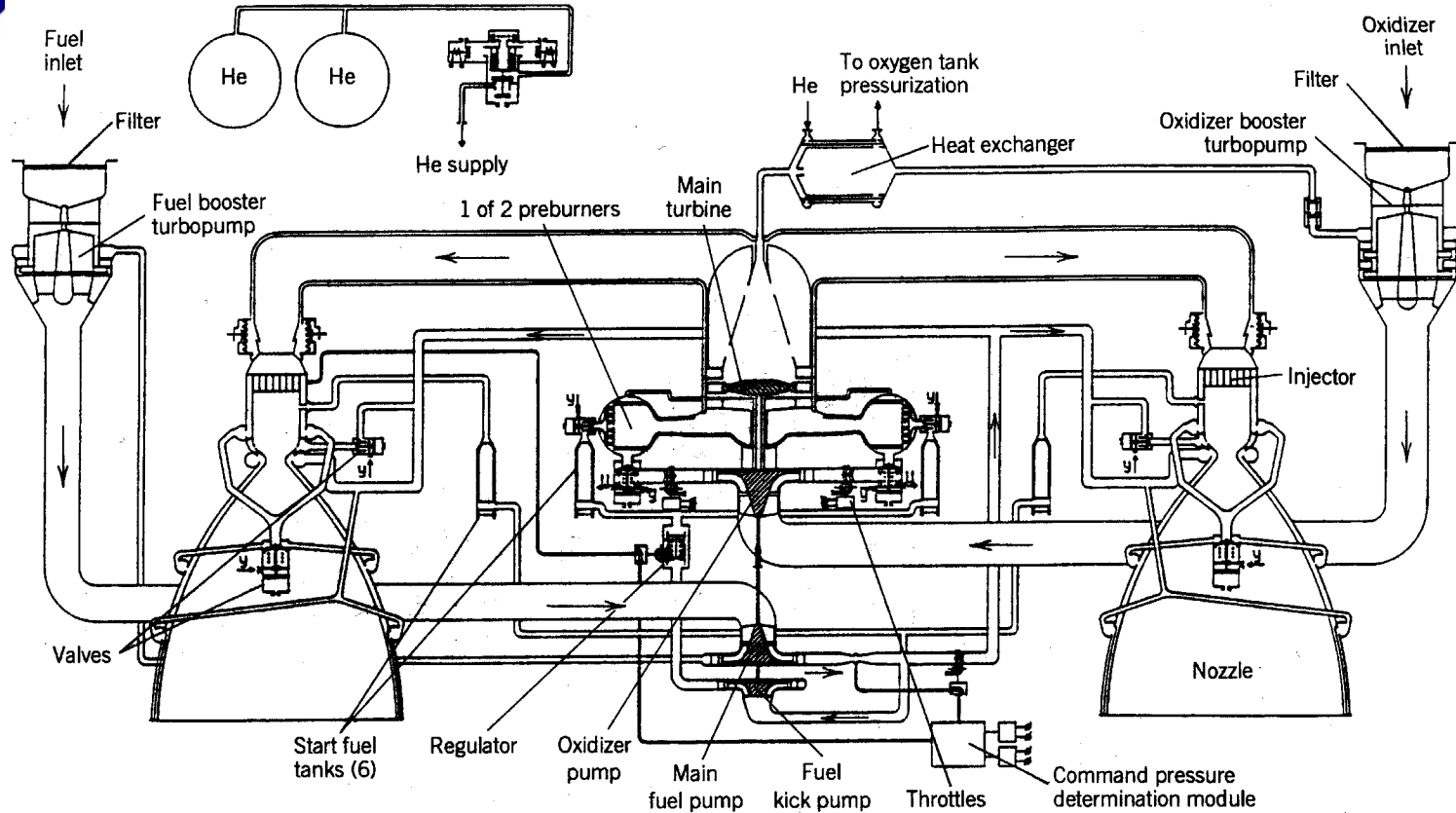
	Fuel Inj.	Oxy Inj.	Cham.
T (K)	294.3	89.5	3546
P (MPa)	7.9	8.8	7.8

Space Shuttle Main Engine

	Fuel Inj.	Oxy Inj.	Cham.
T (K)	879.0	126.0	3700
P (MPa)	24.8	33.0	22.58



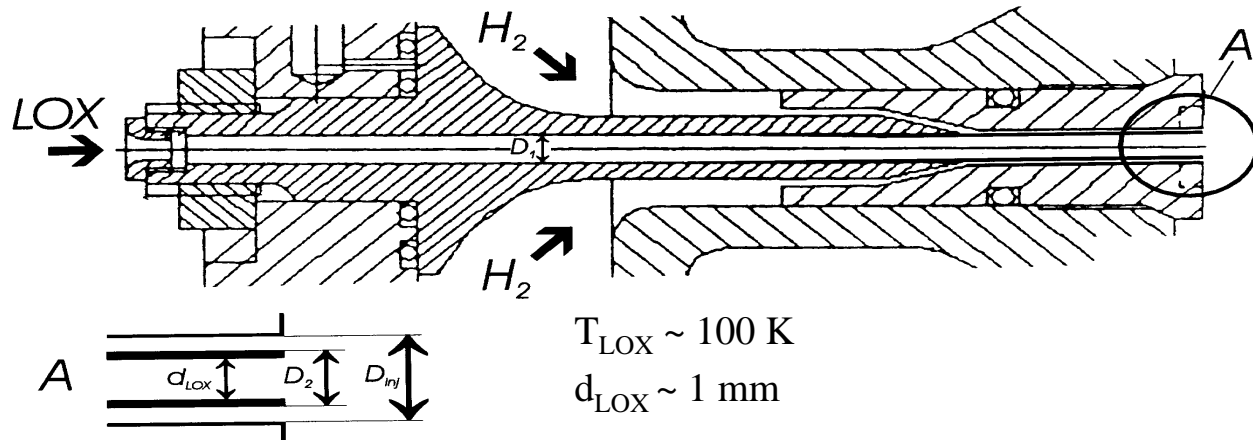
Flow Diagram of RD-170 Engine

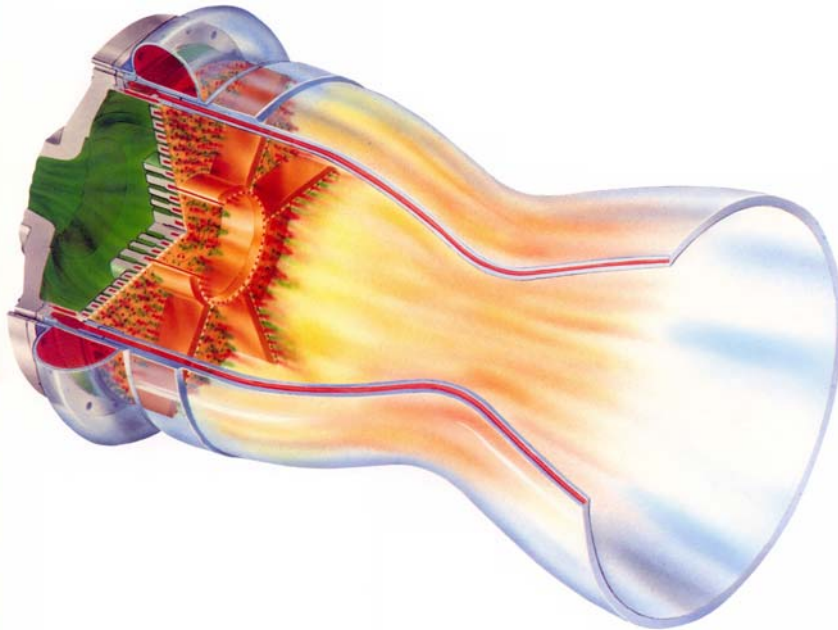
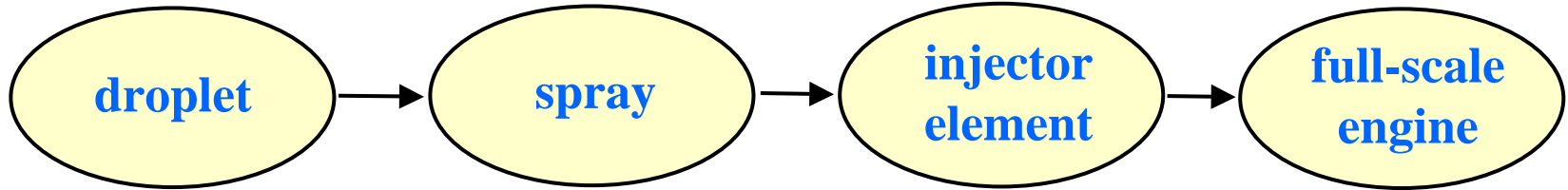


- Energia booster and Zenit first stage, up to 10 flights.
- LOX/kerosene, one main two boost turbopumps
- 806 ton thrust (vacuum), 337 seconds of I_{sp} , O/F ratio of 2.63
- Chamber pressure 250 bar, turbine inlet pressure 519 bar and temperature 772 K



- Tamura et al. / NAL (Japan)
- Mayer, Oswald, Haidn, etc. / DLR (Germany)
- Habiballah, Vingert, Grisch, etc. / ONERA (France)
Candel et al. / Ecole Central Paris (France)
- Woodward, Pal, Santoro, etc. / Penn State (USA)
Talley, Chehroudi, etc. / AFRL (USA)
Blevins, Morris, etc. / NASA Marshall (USA)

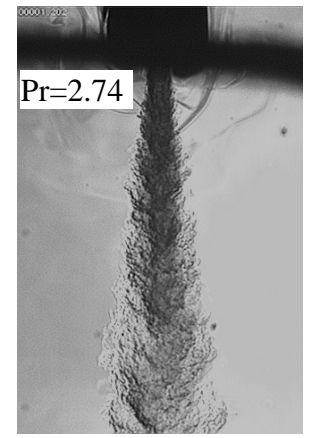
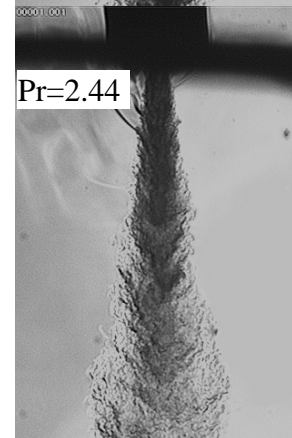
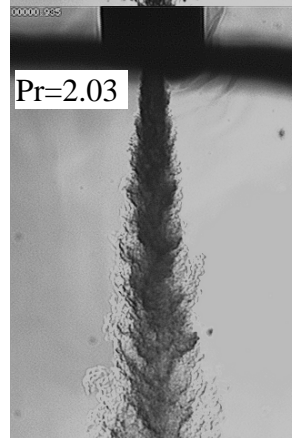
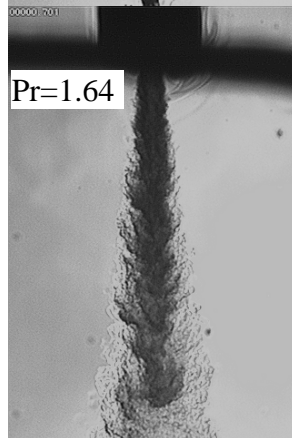
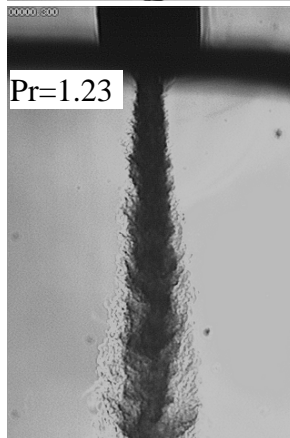
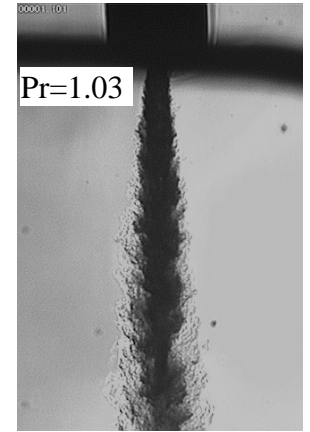
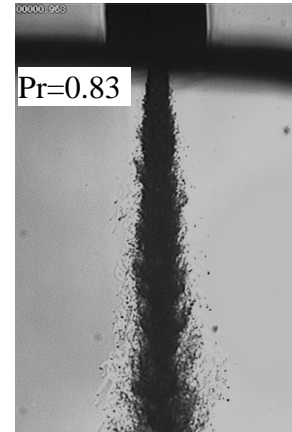
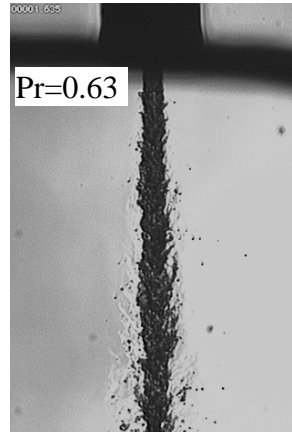
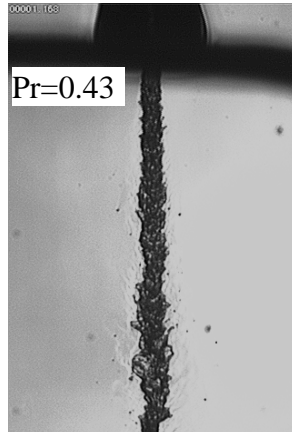
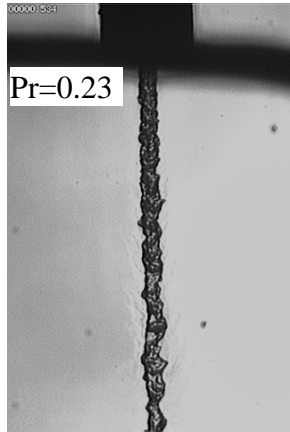




- Oefelein / DoE Sandia Lab. (USA)
- Bellan / NASA JPL (USA)
- Farmer / U. of Nevada (USA)
- Habiballah, et al. / ONERA (France)
- Yang / Penn State (USA)

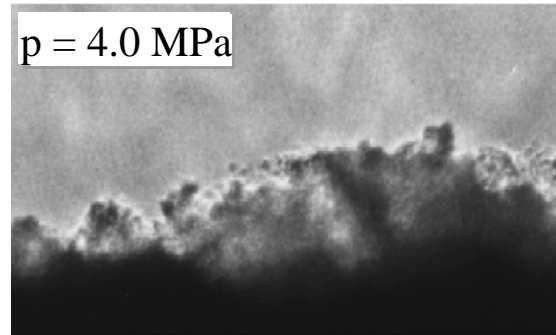
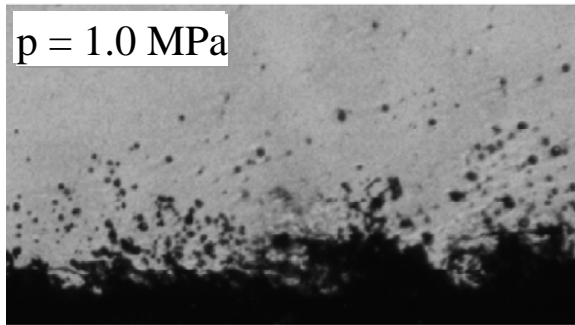
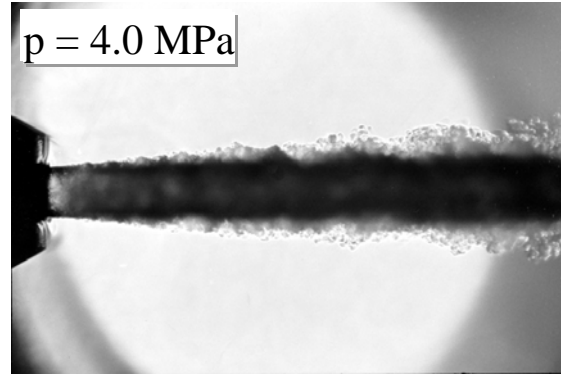
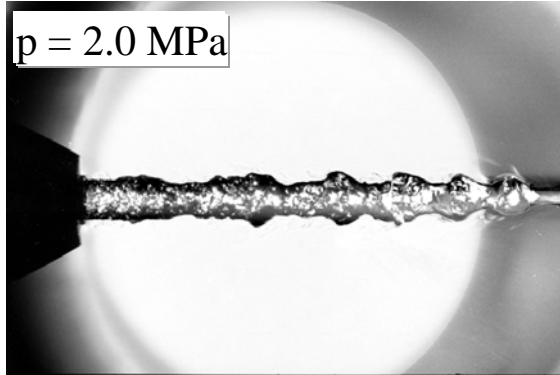


$p_{cr} = 3.39 \text{ MPa}$, $T_{cr} = 126 \text{ K}$, $T_{\infty} = 300 \text{ K}$, $T_{in} = 99 \sim 120 \text{ K}$
 $u_{in} = 10 \sim 15 \text{ m/s}$, $D_{in} = 0.254 \text{ mm}$, $Re = 25,000 \sim 75,000$





Characteristics of Supercritical Fluid Jet

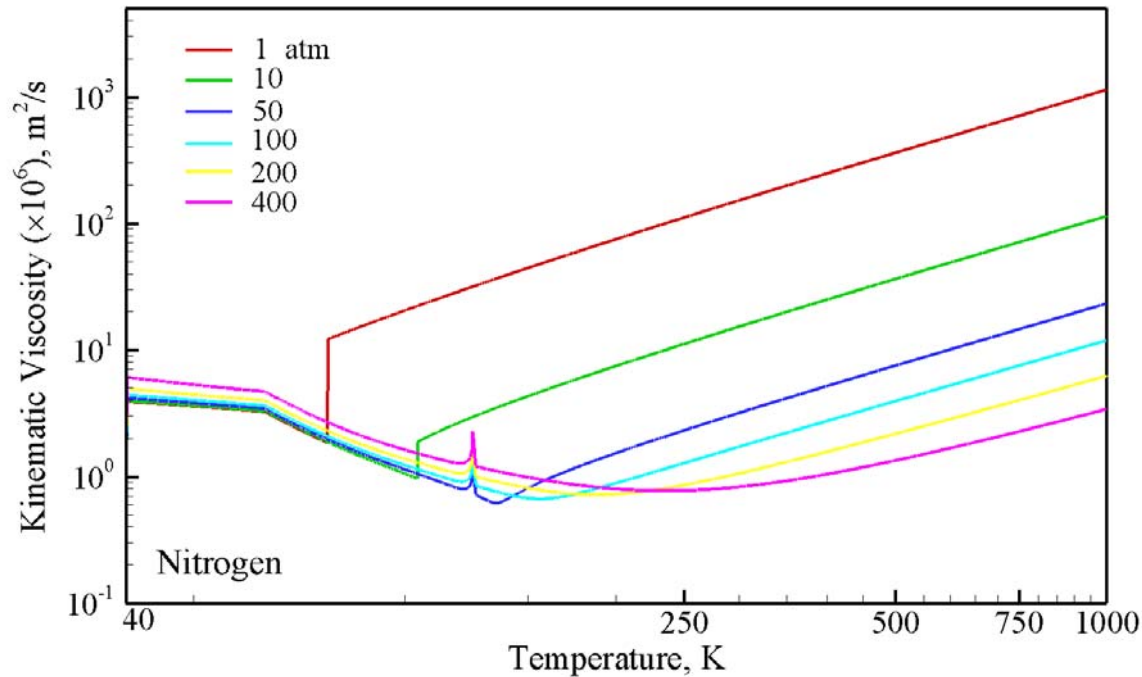


Mayer et al.
AIAA 1996-2620
 $T_{LN2} = 105 \text{ K}$
 $T_{GN2} = 300 \text{ K}$
 $u_{LN2} = 10 \text{ m/s}$
 $D_{in} = 1.9 \text{ mm}$

- **Thermodynamic non-idealities and transport anomalies in transcritical regime**
 - rapid property variations
 - large density gradient
- **Diminishment of surface tension and enthalpy of vaporization**
- **Pressure-dependent solubility**
- **High Reynolds number**



Effect of Pressure on Turbulence Scales



- Pressure increases from 1 to 10^2 atm, Re_t increases by 10^2
- Kolmogorov microscale $\eta_t/l_t \sim Re_t^{-3/4}$ (decrease by 1.5 order)
- Taylor microscale $\lambda_t/l_t \sim Re_t^{-1/2}$ (decrease by 1.0 order)



• Favre-filtered conservation equations

• Closure requirements

$$\frac{\partial \bar{\rho}}{\partial t} + \frac{\partial (\bar{\rho} \tilde{u}_j)}{\partial x_j} = 0$$

$$\frac{\partial (\bar{\rho} \tilde{u}_j)}{\partial t} + \frac{\partial (\bar{\rho} \tilde{u}_i \tilde{u}_j + \bar{p} \delta_{ij} - \bar{\tau}_{ij})}{\partial x_j} = - \frac{\partial (R_{ij} + L_{ij} + C_{ij})}{\partial x_j}$$

$$\frac{\partial (\bar{\rho} \tilde{E} + q)}{\partial t} + \frac{\partial [(\bar{\rho} \tilde{E} + \bar{P}) \tilde{u}_j - \overline{u_i \tau_{ij}}]}{\partial x_j} = - \frac{\partial (K_j + Q_j + q_j)}{\partial x_j}$$

- Thermodynamic and transport properties $Z, C_p, \mu, \lambda, D_{im}$
- Subgrid-scale turbulence interaction R, L, C
- Chemical kinetics $\bar{\dot{\omega}}_i$



Equations of State

- Soave-Redlich-Kwong (SRK)

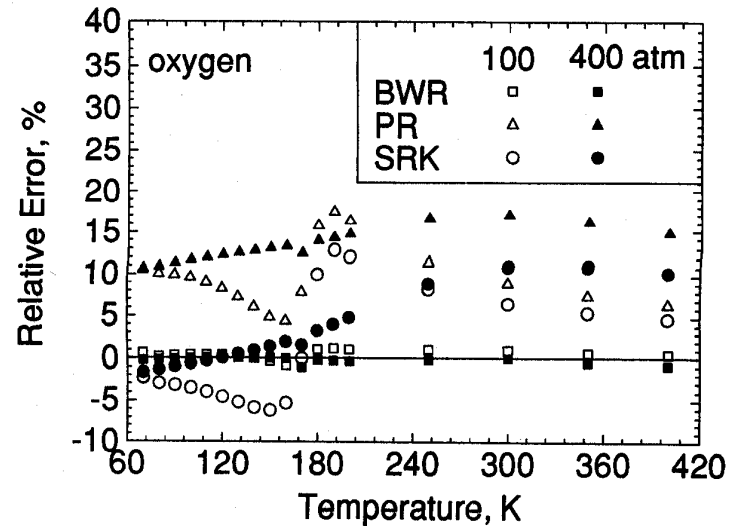
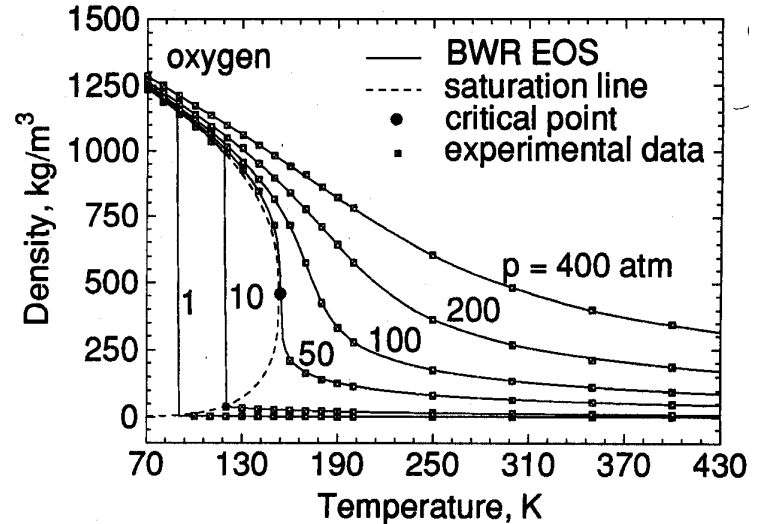
$$p = \frac{RT}{v-b} - \frac{a}{v(v+b)}$$

- Peng-Rubinson (PR)

$$p = \frac{RT}{v-b} - \frac{a}{v(v+b)+b(v-b)}$$

- Benedict-Webb-Rubin (BWR)

$$p = \sum_{n=1}^9 a_n \rho^n + \sum_{n=10}^{15} a_n \rho^{2n-17} e^{-\gamma \rho^2}$$





- Sensible enthalpy: $h(\rho, T) = h^0(T) + \Delta h_{exc}(\rho, T)$
 - Internal energy: $u(\rho, T) = u^0(T) + \Delta u_{exc}(\rho, T)$
 - Specific heat $C_p(\rho, T) = C_p^0(T) + \Delta C_{p,exc}(\rho, T)$
- $\Delta h_{exc}, \Delta u_{exc}, \Delta C_{p,exc}$ = dense fluid corrections
 $h^0(T), u^0(T), C_p^0(T)$, = values in dilute-gas limit

Pressure-explicit type of EOS:

$$\Delta h_{exc} = \int_0^\rho \left[\frac{p}{\rho^2} - \frac{T}{\rho^2} \left(\frac{\partial p}{\partial T} \right)_\rho \right] d\rho + RT(Z - 1)$$

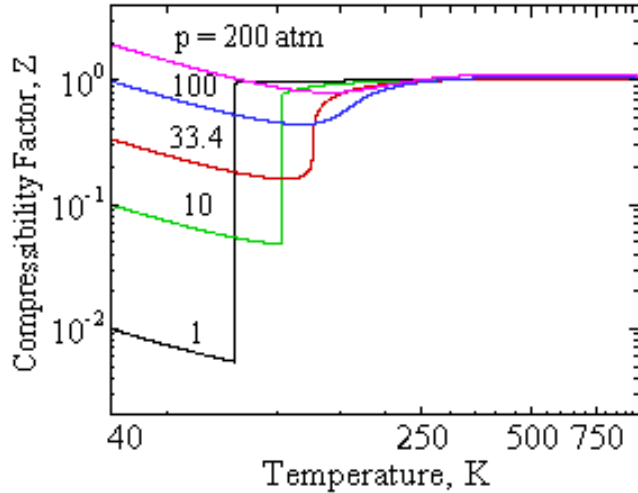
$$\Delta u_{exc} = \int_0^\rho \left[\frac{p}{\rho^2} - \frac{T}{\rho^2} \left(\frac{\partial p}{\partial T} \right)_\rho \right] d\rho$$

$$\Delta C_{p,exc} = -T \int_0^\rho \left[\frac{1}{\rho^2} \left(\frac{\partial^2 p}{\partial T^2} \right) d\rho + \frac{T(\partial p / \partial T)_\rho^2}{\rho^2 (\partial p / \partial \rho)_T} \right] - R$$

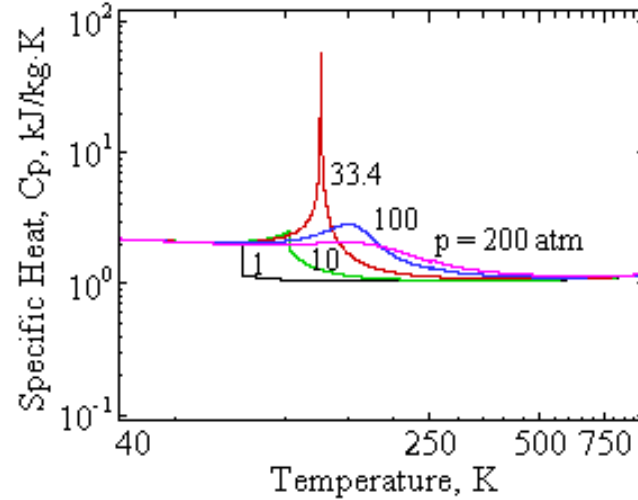


Thermophysical Properties of Nitrogen

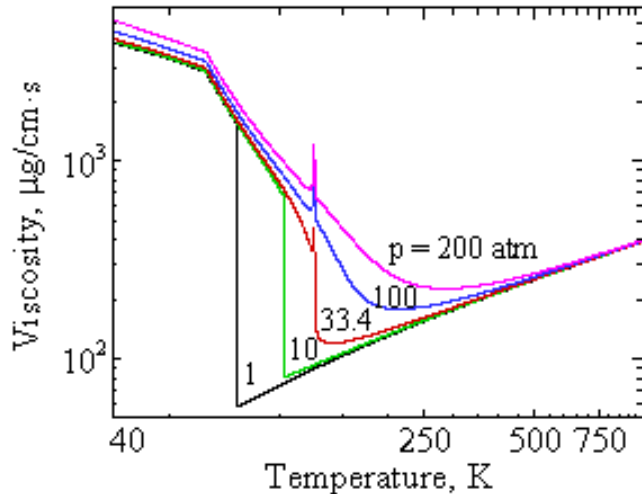
• compressibility factor



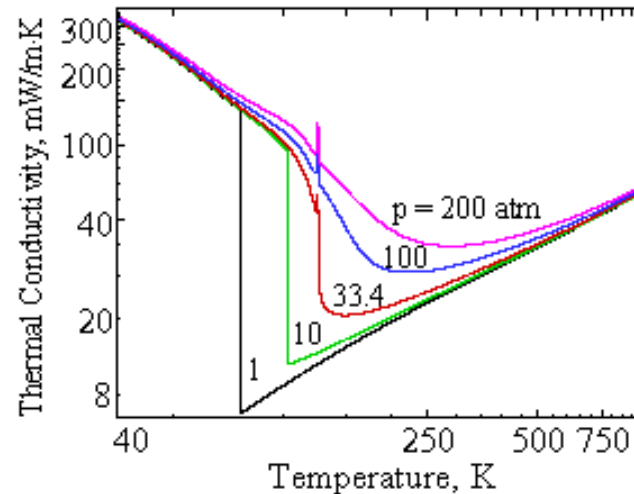
• specific heat



• dynamic viscosity



• thermal conductivity



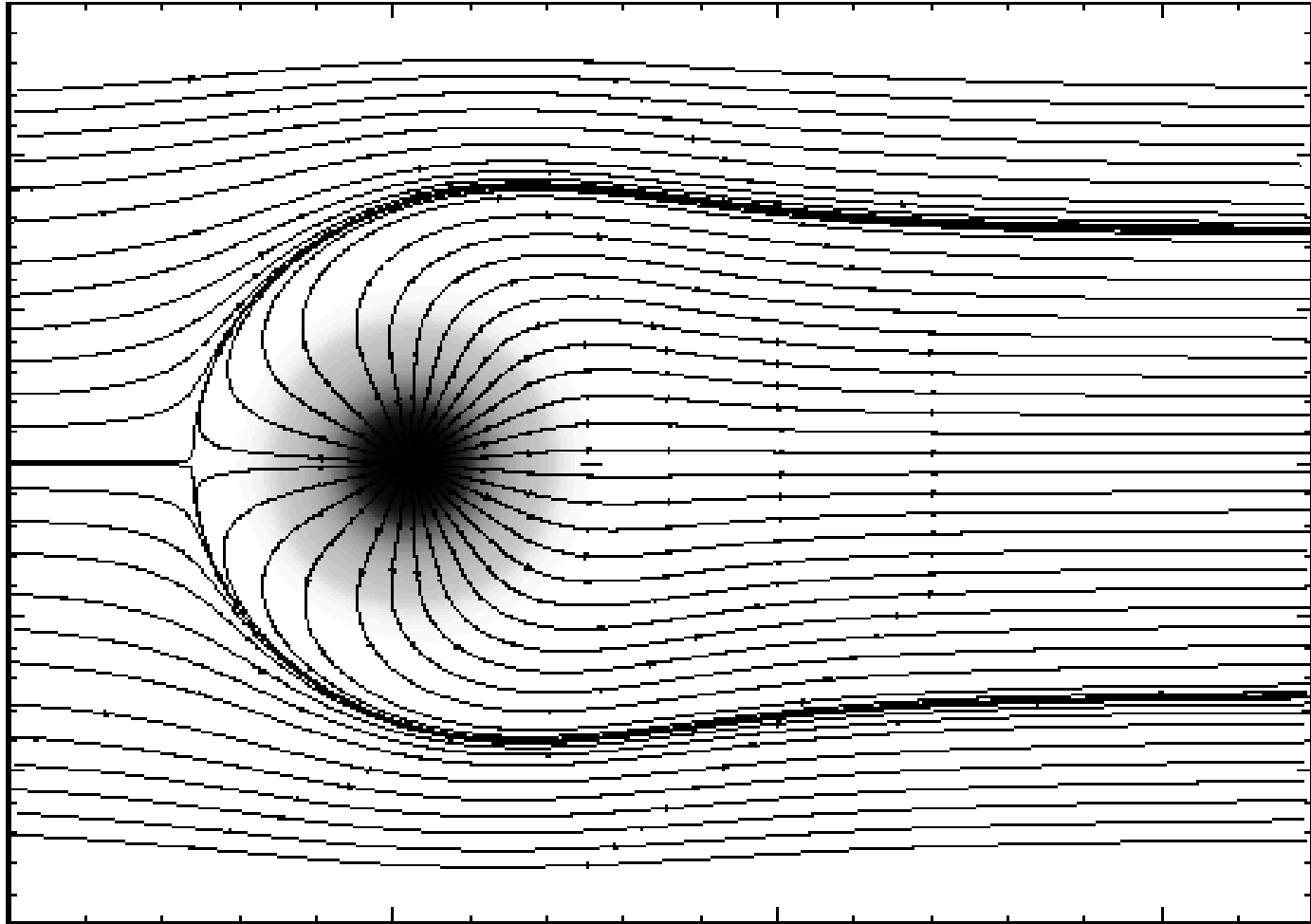


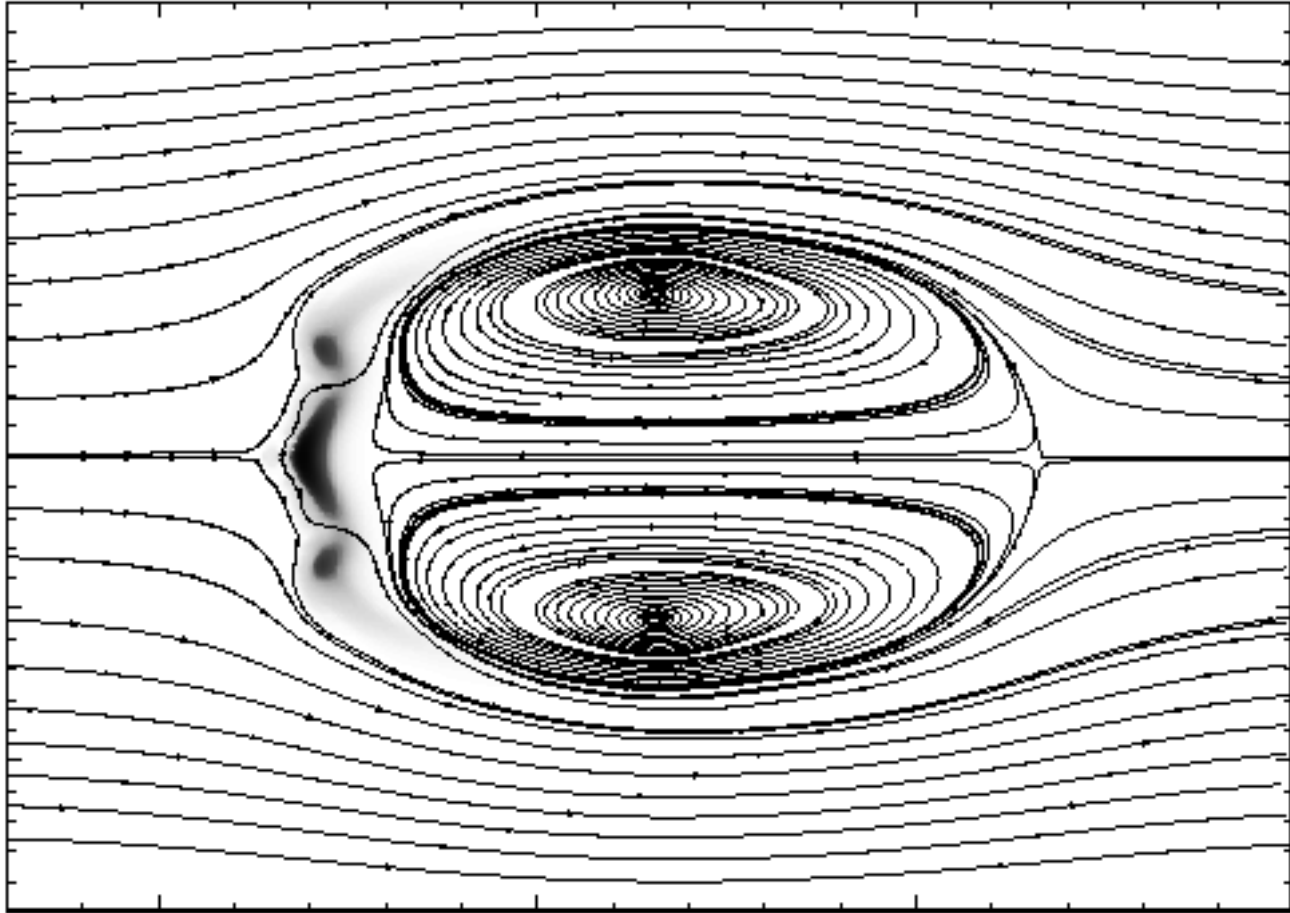
Droplet Vaporization and Combustion in Quiescent and Convective Environments

- **Liquid oxygen (LOX) droplet vaporization & combustion in hydrogen and water**
 $5 < p_{\infty} < 300 \text{ atm}$
 $500 < T_{\infty} < 2500 \text{ K}$
 $50 < D_0 < 300 \mu\text{m}$
- **Hydrocarbon droplet vaporization & combustion in air and oxygen**
 $5 < p_{\infty} < 200 \text{ atm}$
 $300 < T_{\infty} < 2500 \text{ K}$
 $100 < D_0 < 1000 \mu\text{m}$
- **Unsymmetrical dimethylhydrazine (UDMH) droplet vaporization and decomposition combustion**
 $1 < p_{\infty} < 180 \text{ atm}$



Spherical Mode (100 atm, 0.2 m/s; $t=610 \mu\text{s}$)





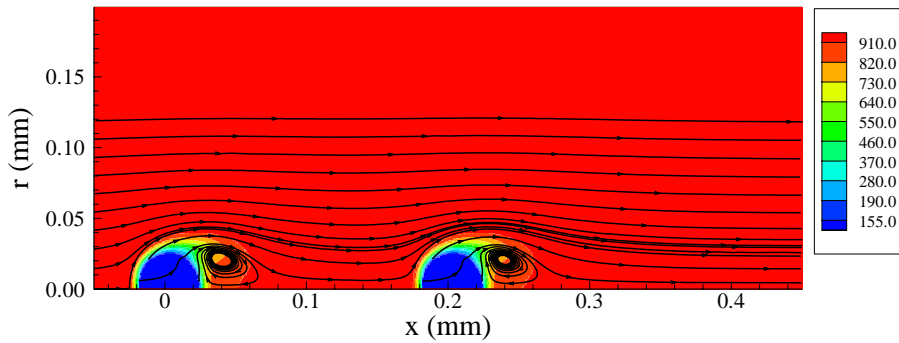


Flow and Temperature Fields

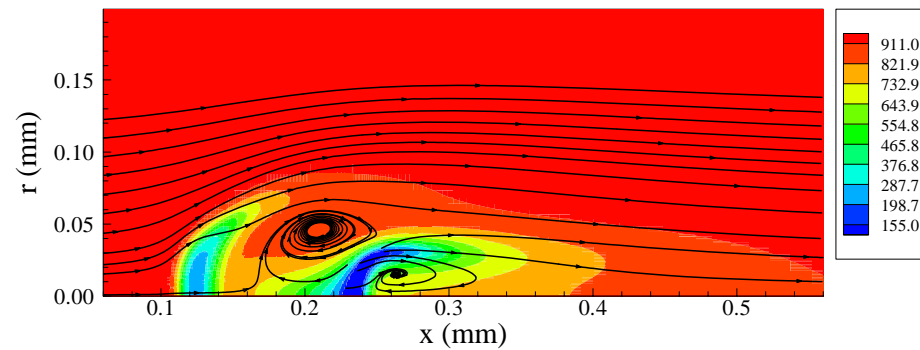
Department of Mechanical & Nuclear Engineering

$P_\infty=100$ atm, $T_\infty=1000$ K, $u_\infty=20$ m/s, $T_0=100$ K, $d_0=50$ μm , $H/R=8$

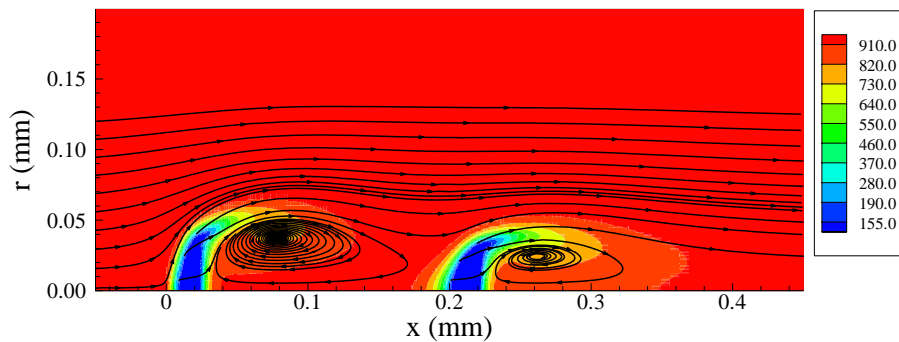
$t=8$ μs



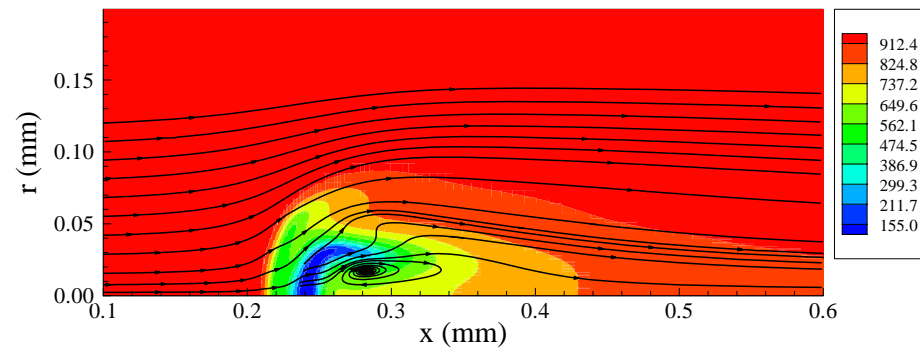
$t=90$ μs

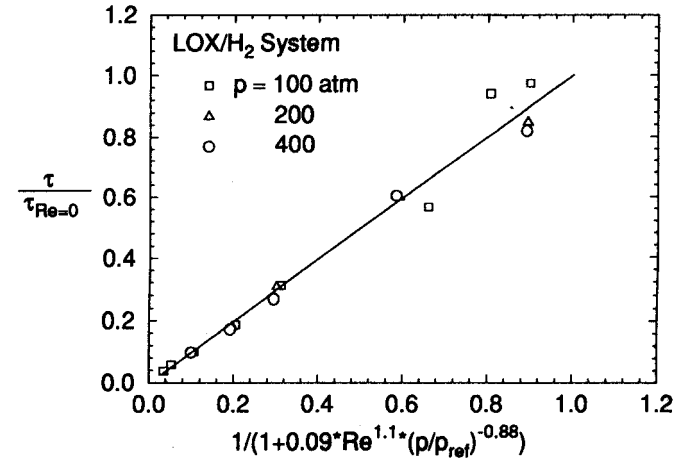
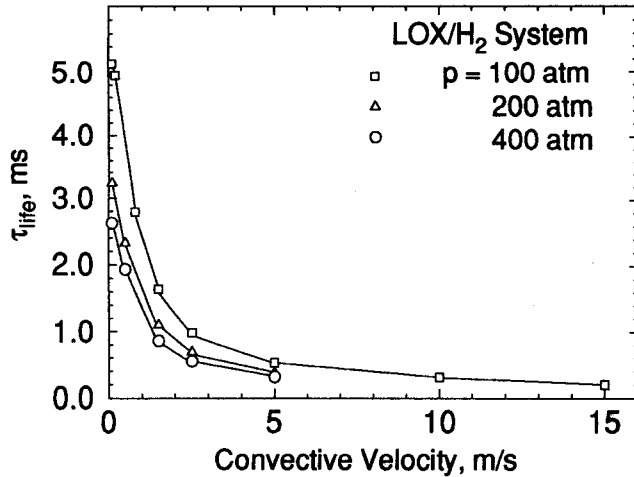


$t=40$ μs



$t=110$ μs





- **effect of ambient pressure on**
 - thermophysical properties
 - critical mixing state
 - convective heat transfer
- **effect of ambient velocity on**
 - convective heat transfer

- **atmospherical condition**

- Ranz and Marshall's correlation

$$\frac{\tau_f}{\tau_{f,Re=0}} \propto \frac{h_{Re=0}}{h} = \frac{1}{1 + 0.3 Re^{1/2} Pr^{1/3}}$$

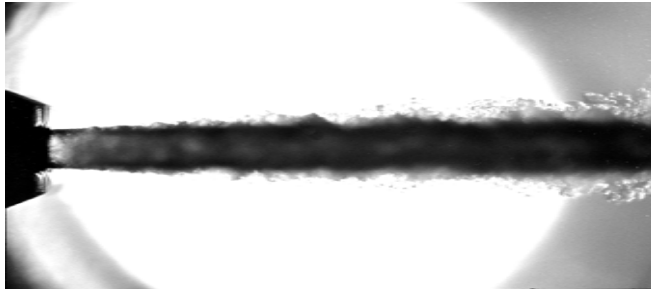
- **supercritical condition**

- LOX/hydrogen system

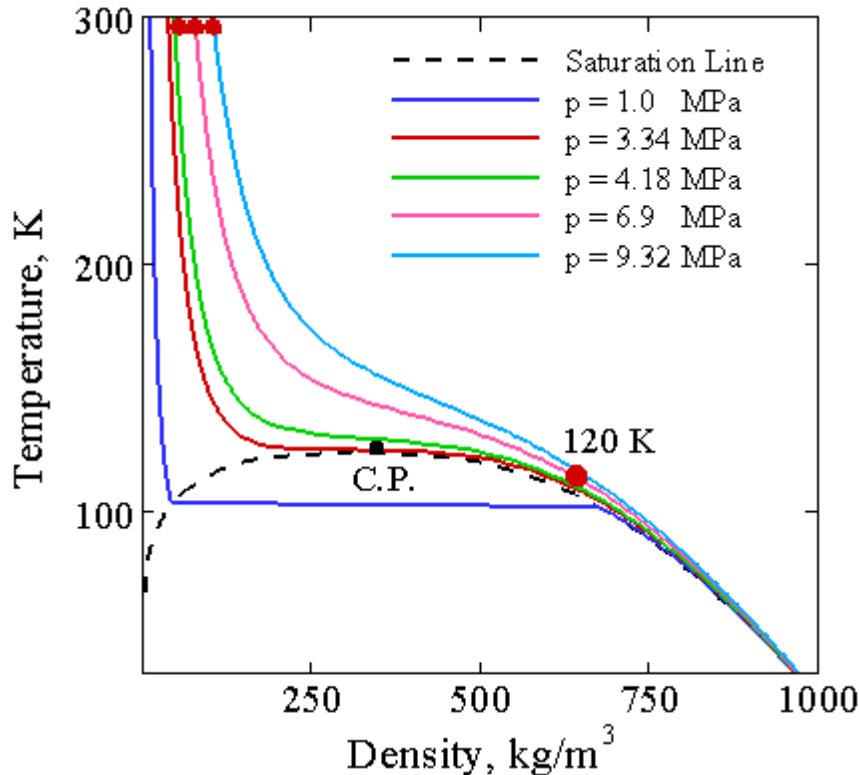
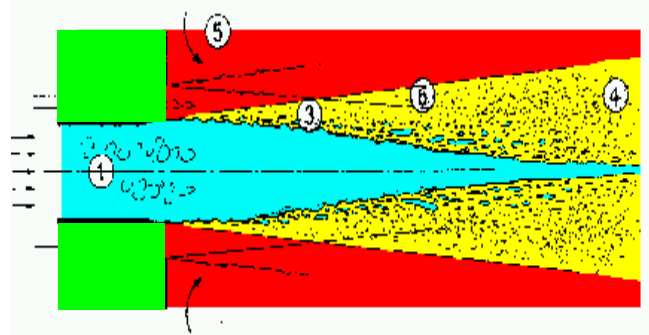
$$\frac{\tau_f}{\tau_{f,Re=0}} \propto \frac{h_{Re=0}}{h} = \frac{1}{1 + 0.15634 Re^{1.1} Pr_{O_2}^{-0.88}}$$



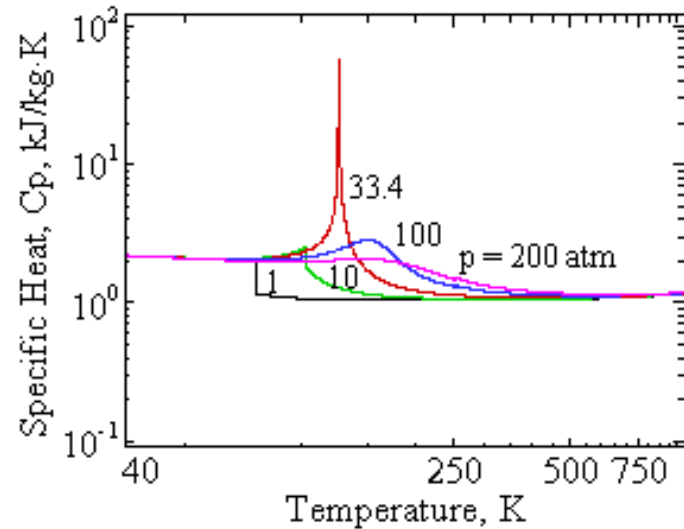
Supercritical Fluid Injection



$p_{ch} = 4.0 \text{ MPa}$
 $T_{LN2} = 105 \text{ K}$
 $T_{GN2} = 300 \text{ K}$
 $u_{LN2} = 10 \text{ m/s}$
 $D_{in} = 1.9 \text{ mm}$



$p_{\infty} = 3.4 - 10.0 \text{ MPa}$, $T_{\infty} = 300 \text{ K}$,
 $T_{in} = 120 \text{ K}$, $D_{in} = 0.254 \text{ mm}$,
 $u_{in} = 15 \text{ m/s}$, $Re = 20000 - 40000$



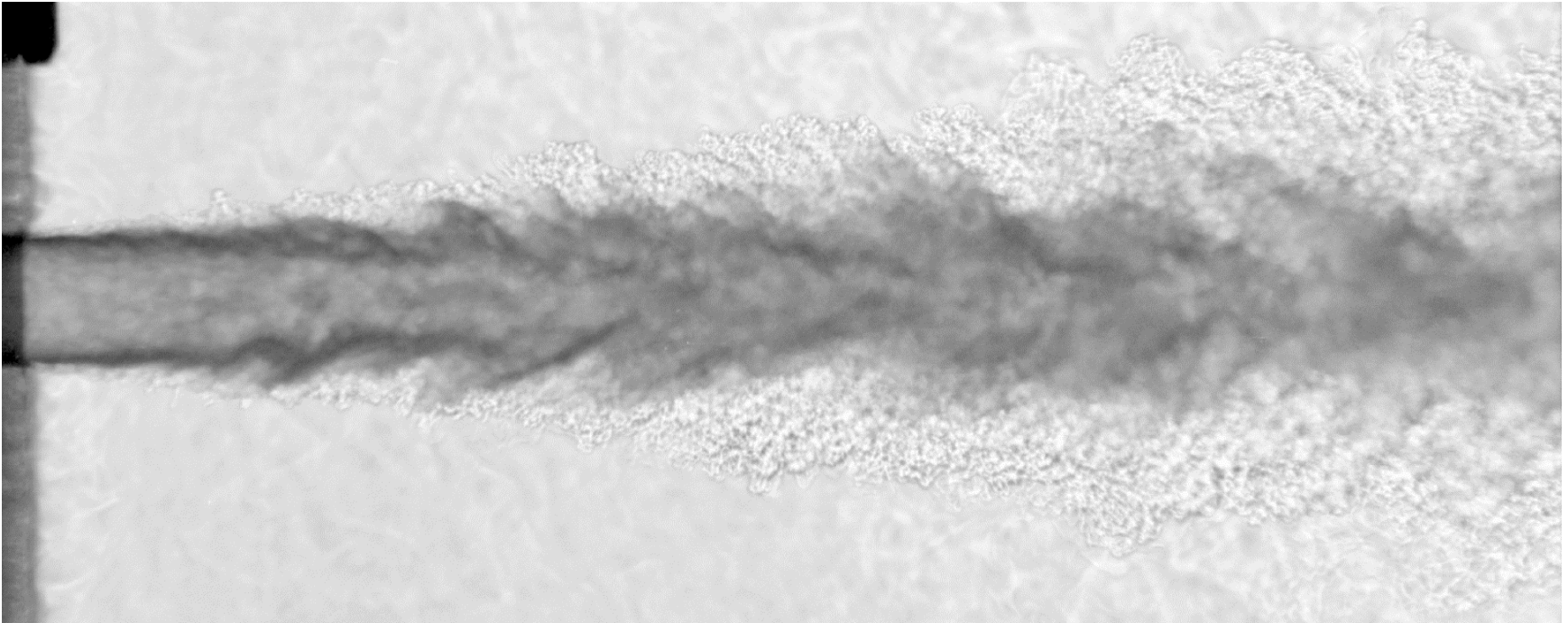


Shadowgraph Images of Cryogenic Nitrogen Injection

Mayer et al. AIAA 2001-3275

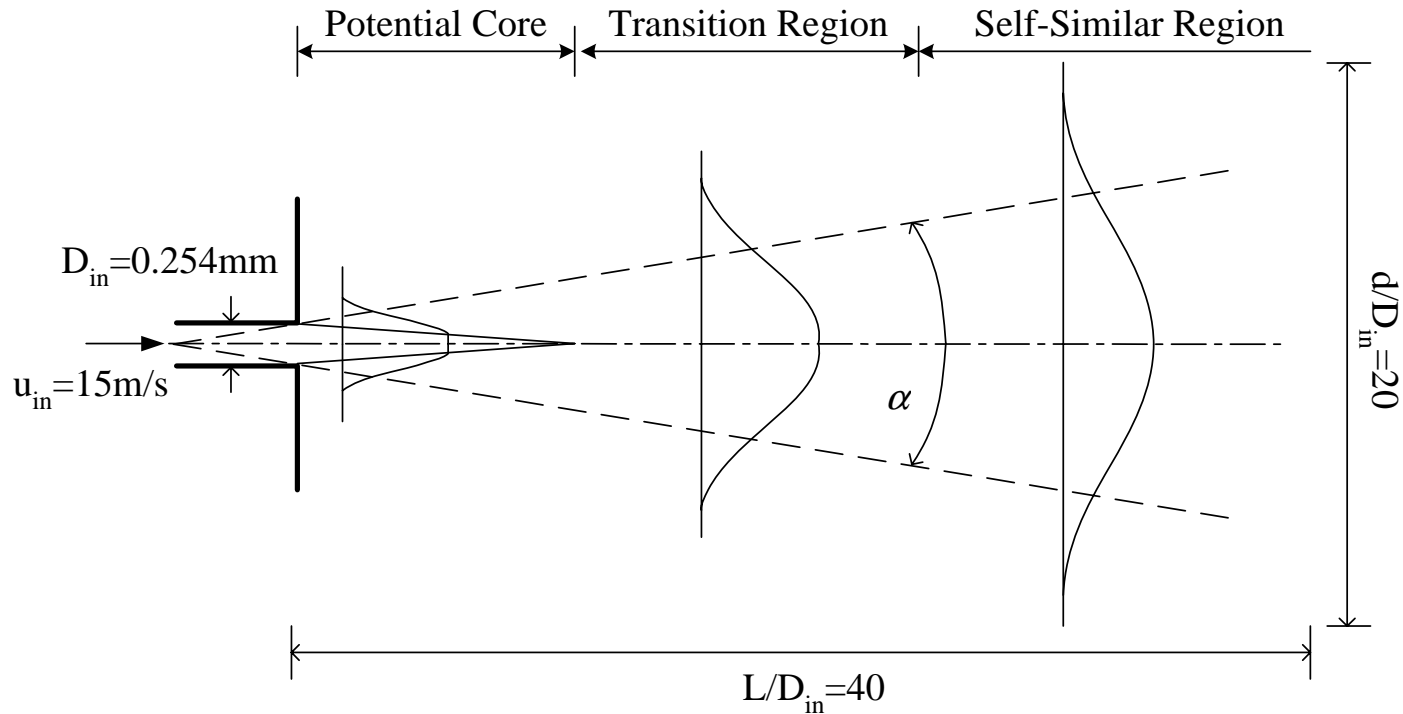
1 8 5 5 Department of Mechanical & Nuclear Engineering

($p_\infty = 6.0$ MPa, $T_\infty = 300$ K, $u_{in} = 4.9$ m/s, $T_{in} = 132$ K, $D_{in} = 2.2$ mm)





Computational Domain and Grids



- Kolmogorov microscale $\eta_t/l_t \sim Re_t^{-3/4}$
- Taylor microscale $\lambda_t/l_t \sim Re_t^{-1/2}$
- $3.4 \leq p_{ch} \leq 10.0 \text{ MPa}$ and $D_{in} = 0.254 \text{ mm}$
- $3 < \lambda_t < 5 \text{ }\mu\text{m}$



total grids

$$225 \times 75 \times 72 = 1,215,000$$

mean grid spacing in
near injector region

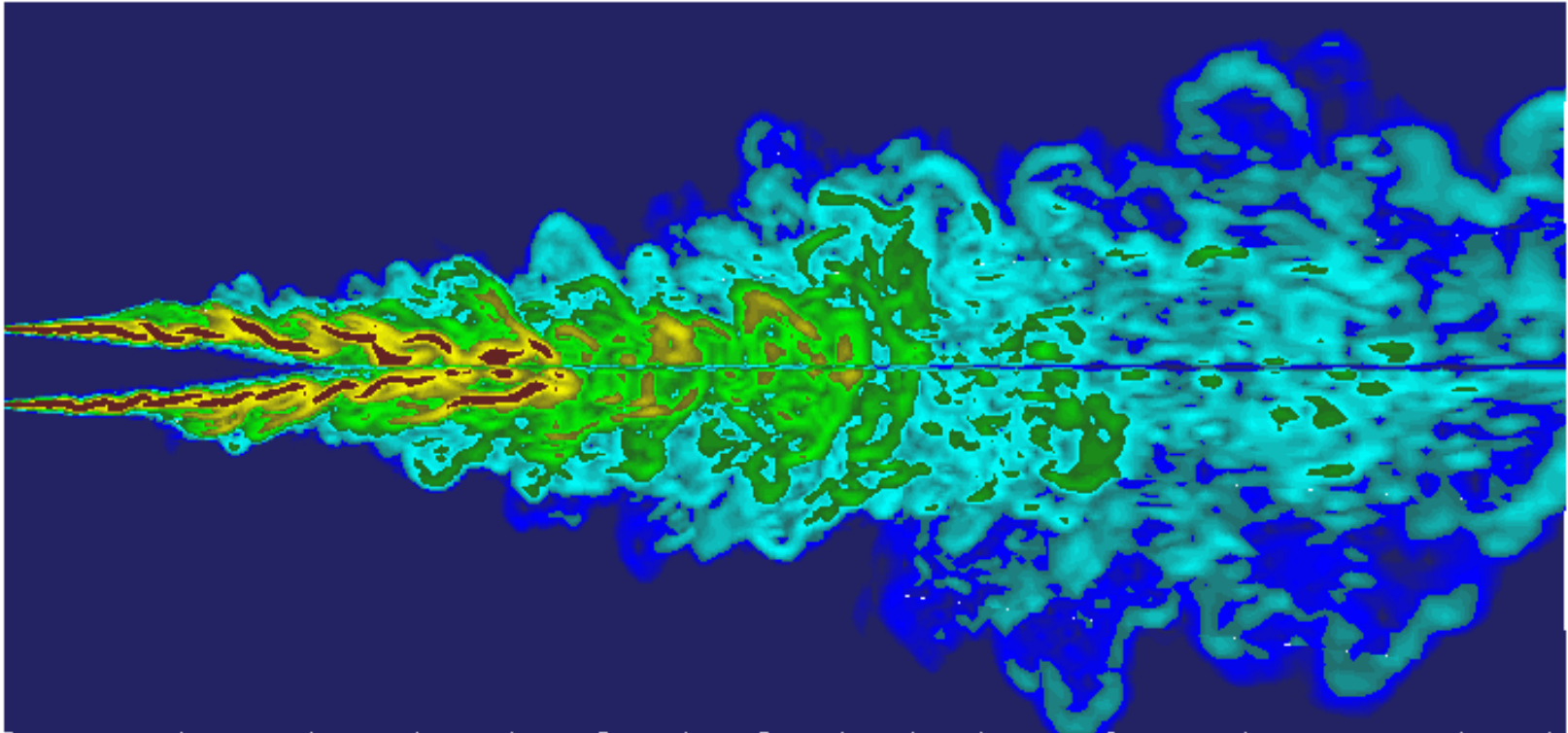
$$\Delta = 5 \text{ }\mu\text{m}$$



Density Gradient Field

Department of Mechanical & Nuclear Engineering

$(p_\infty = 9.3 \text{ MPa}, T_\infty = 300 \text{ K}, u_{in} = 15 \text{ m/s}, T_{in} = 120 \text{ K}, D_{in} = 254 \text{ }\mu\text{m})$



$|\nabla\rho| \text{ (kg/m}^4\text{)}$



1.0000E+04 3.9401E+04 1.5524E+05 6.1167E+05 2.4100E+06

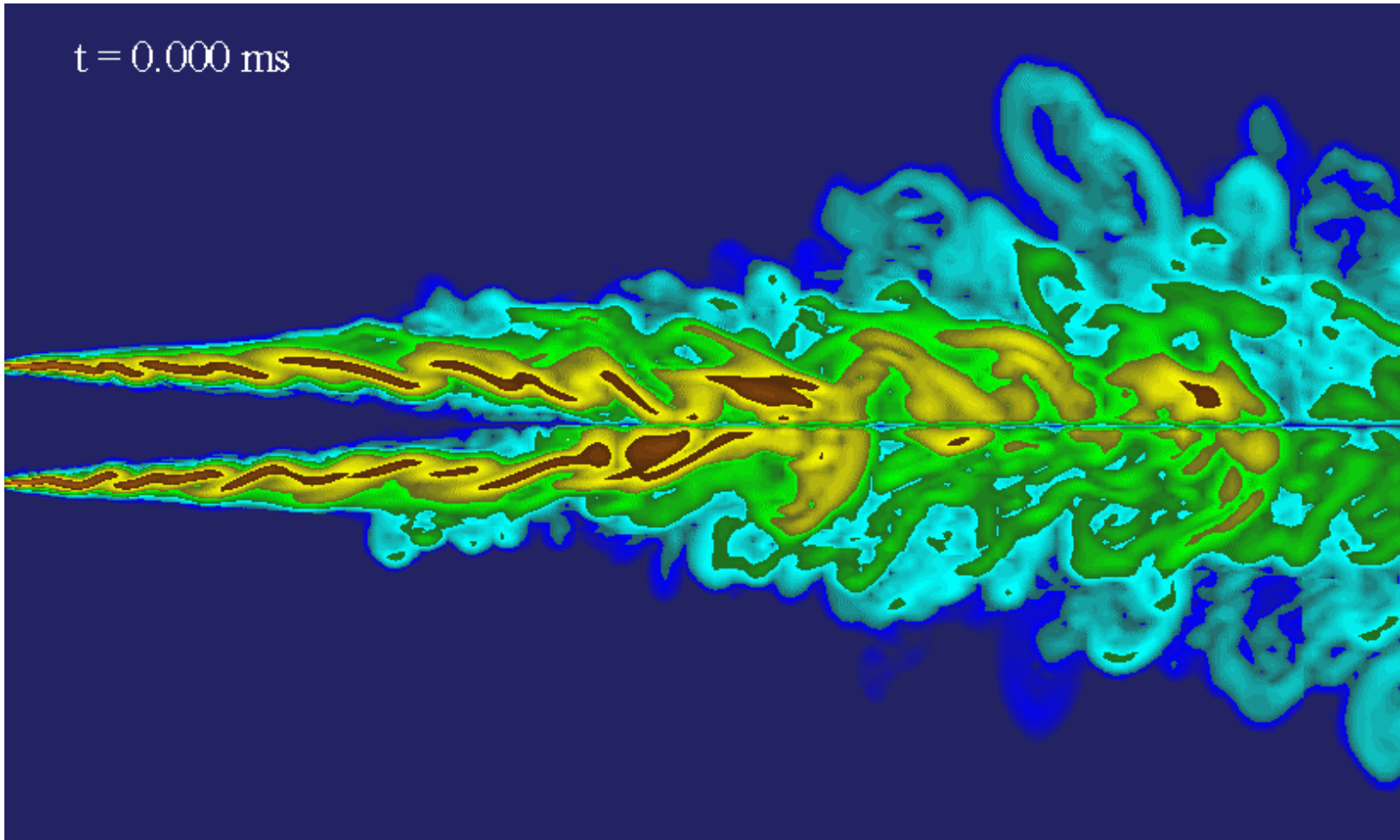
Time Evolution of Density Gradient Field



Department of Mechanical & Nuclear Engineering

$(p_\infty = 6.9 \text{ MPa}, T_\infty = 300 \text{ K}, u_{\text{in}} = 15 \text{ m/s}, T_{\text{in}} = 120 \text{ K}, D_{\text{in}} = 254 \mu\text{m})$

$t = 0.000 \text{ ms}$

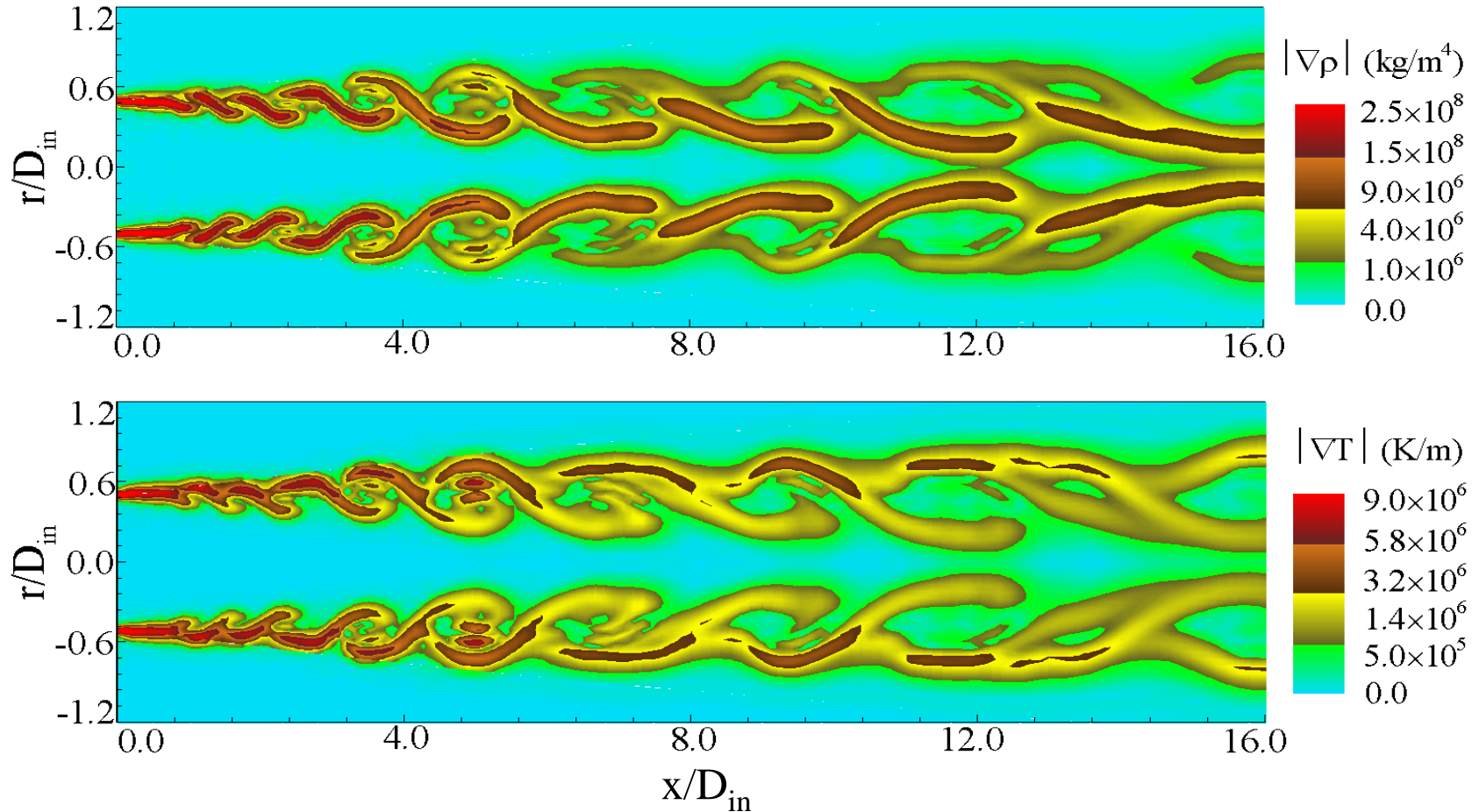




Snapshots of Density and Temperature Gradient Fields

Department of Mechanical & Nuclear Engineering

($p_\infty = 9.3\text{MPa}$, $T_\infty = 300\text{K}$, $u_{in} = 15\text{m/s}$, $T_{in} = 120\text{K}$, $t = 1.550\text{ms}$, $D_{in} = 254\mu\text{m}$)





Most Energy Containing POD Modes of Axial Velocity

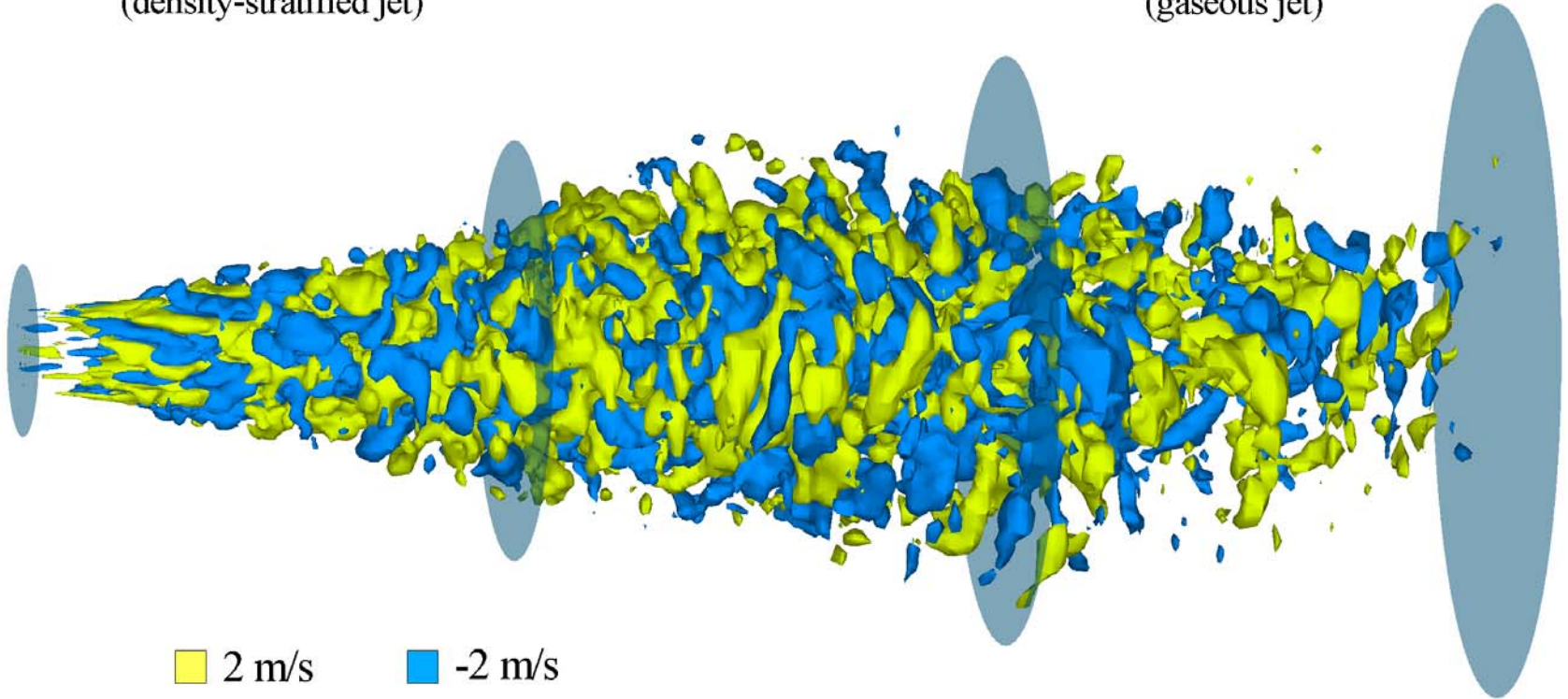
1 8 5 5 Department of Mechanical & Nuclear Engineering

$(p_\infty = 9.3 \text{ MPa}, T_\infty = 300 \text{ K}, u_{in} = 15 \text{ m/s}, T_{in} = 120 \text{ K}, D_{in} = 254 \mu\text{m})$

pre-burst region
(density-stratified jet)

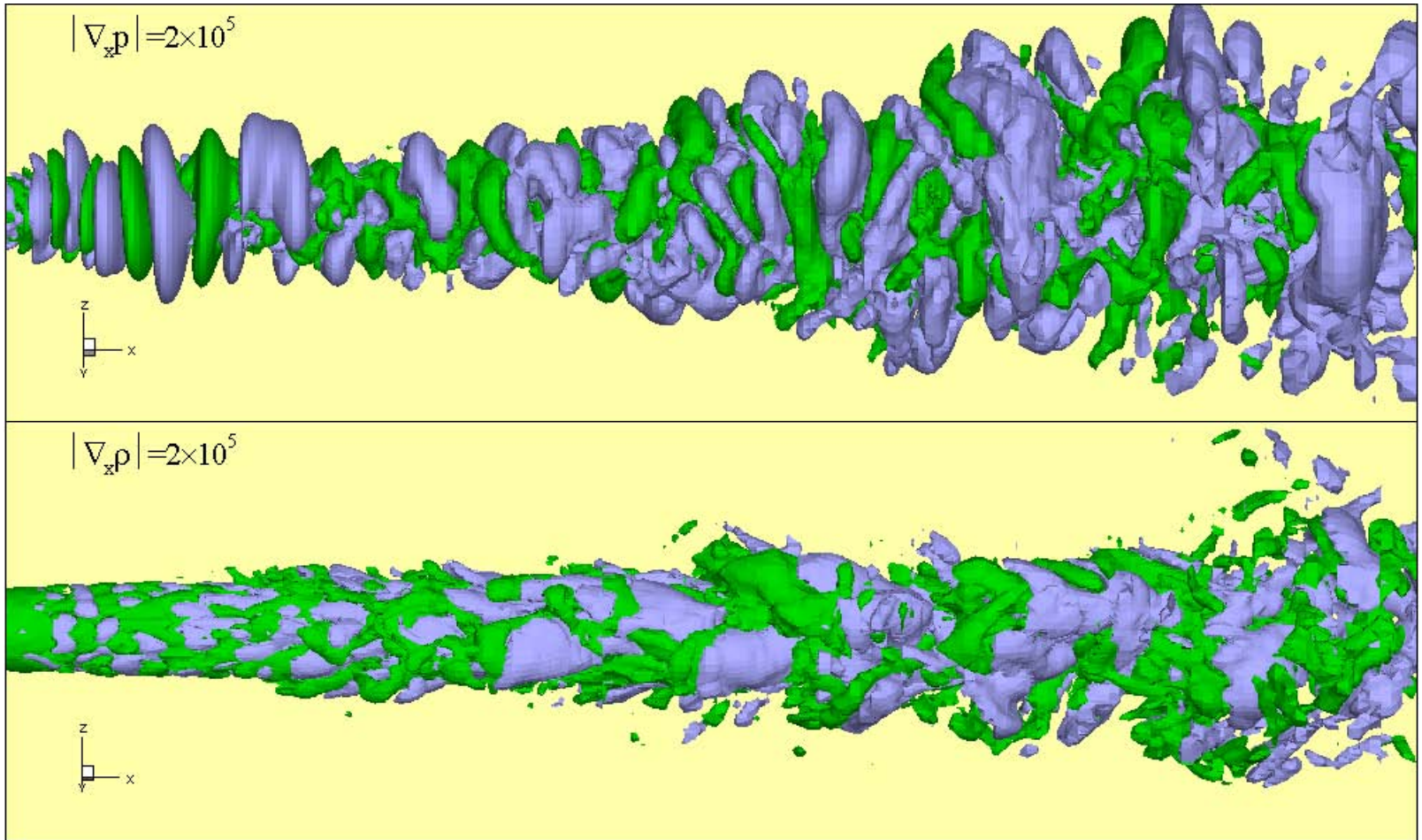
burst region

post-burst region
(gaseous jet)





$(p_\infty = 9.3 \text{ MPa}, T_\infty = 300 \text{ K}, u_{in} = 15 \text{ m/s}, T_{in} = 120 \text{ K}, D_{in} = 254 \mu\text{m})$

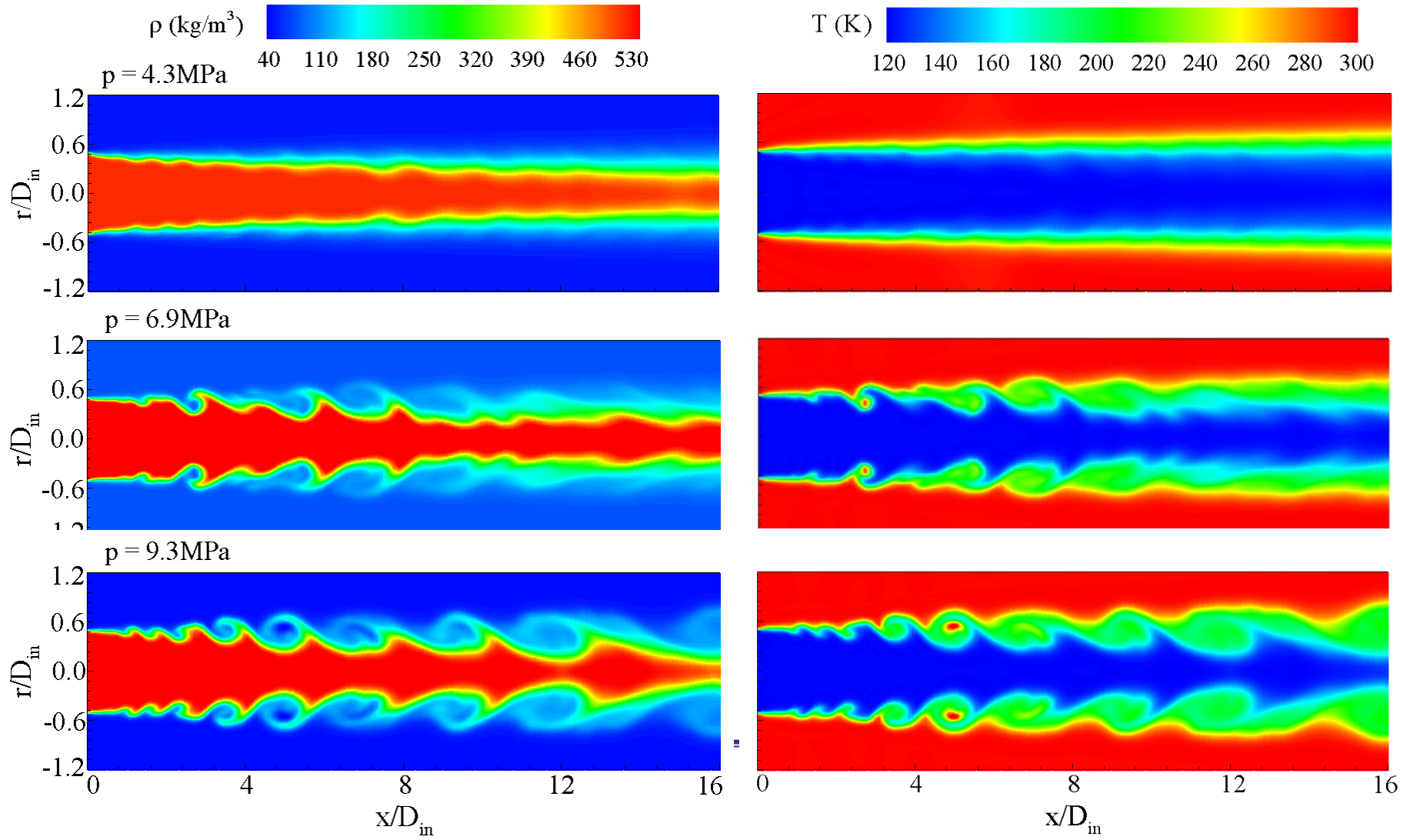




Effect of Pressure on Density and Temperature Fields

Department of Mechanical & Nuclear Engineering

$$T_\infty = 300\text{K}, u_{\text{in}} = 15\text{m/s}, T_{\text{in}} = 120\text{K}, D_{\text{in}} = 254\mu\text{m}$$

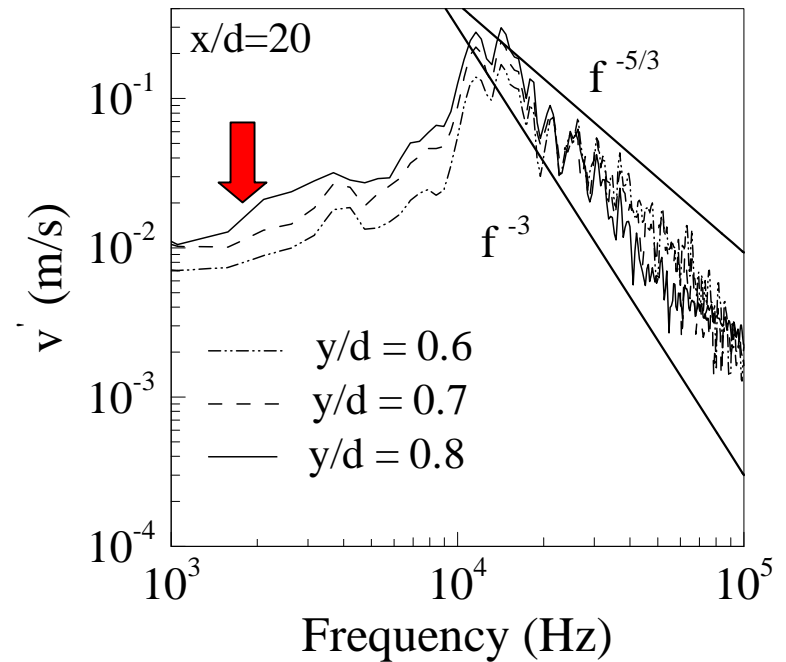
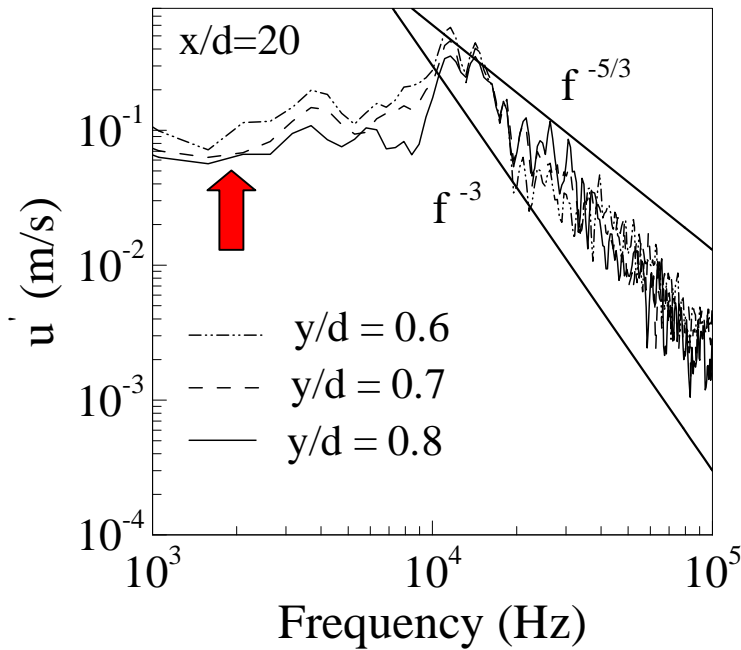




Power Spectral Densities of Velocity Fluctuations

Department of Mechanical & Nuclear Engineering

$(p_\infty = 9.3\text{MPa}, T_\infty = 300\text{K}, u_{in} = 15\text{m/s}, T_{in} = 120\text{K}, D_{in} = 254\mu\text{m})$

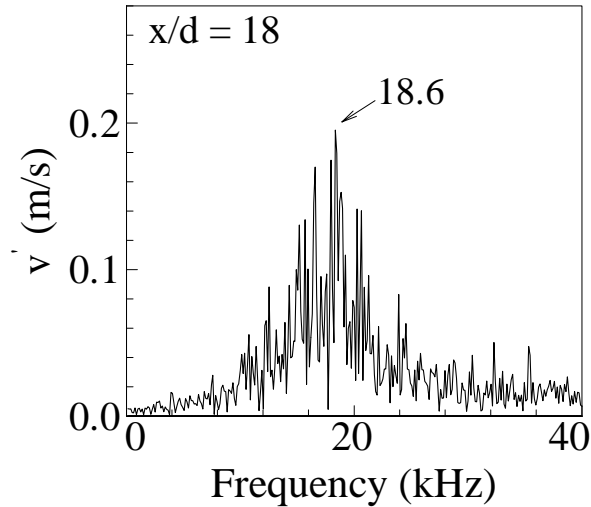
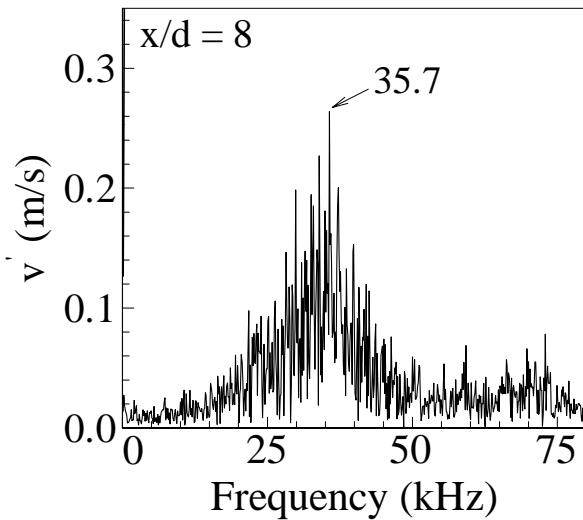
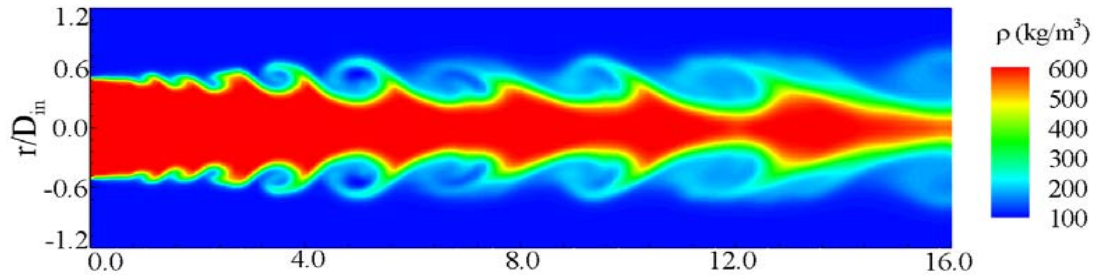


Large density-gradient regions act like a solid wall that amplifies the axial turbulent fluctuation but damps the radial one.



Vortex Shedding Frequency

$(p_\infty = 9.3\text{MPa}, T_\infty = 300\text{K}, u_{in} = 15\text{m/s}, T_{in} = 120\text{K}, D_{in} = 254\mu\text{m})$



Jet flow instability analysis

$$St_j = f_j \theta_0 / \bar{U}$$

where $0.044 \leq St_j \leq 0.048$

$$\bar{U} = 15 \text{ m/s}$$

Momentum thickness

$$\theta_0 = 0.02 \text{ mm}$$

$$\theta_0 = \int_0^\infty \frac{u}{U_{\max}} \left(1 - \frac{u}{U_{\max}}\right) dy$$

choose

$$St_j = 0.046$$

then

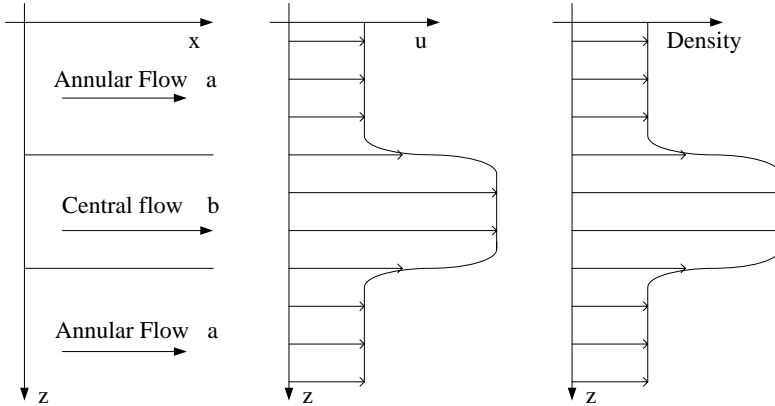
$$f_1 = 34500$$

$$f_2 = 17250$$



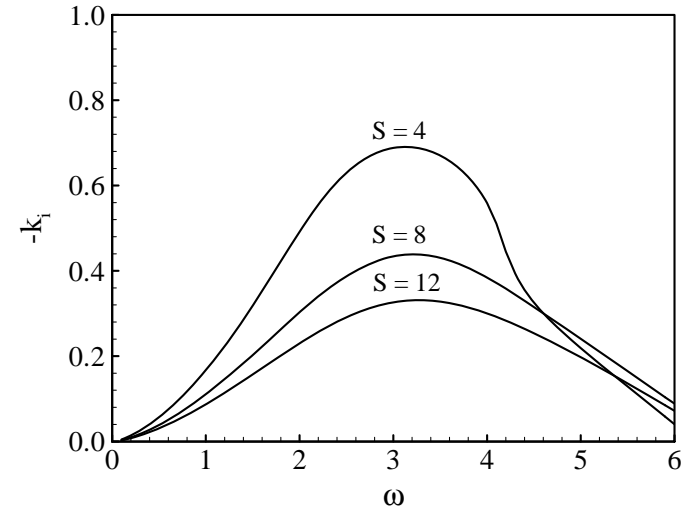
Approach

- Two-dimensional fluid jet instability at supercritical conditions.
- Unified treatment of real-fluid thermodynamics and transport phenomena.
- Disperse equation solved by Newton-Ralpson method.



Conclusions

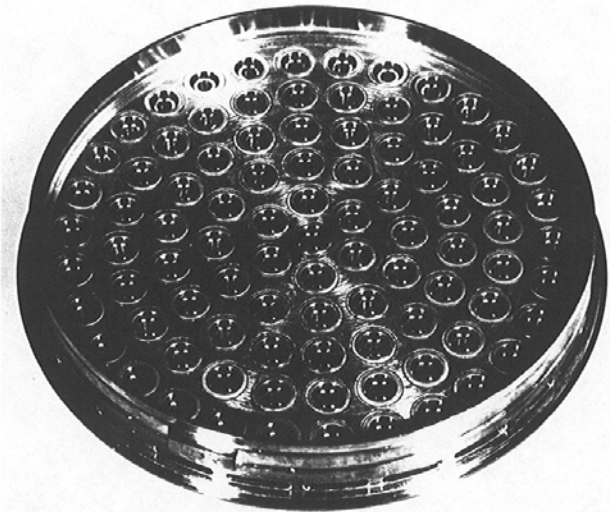
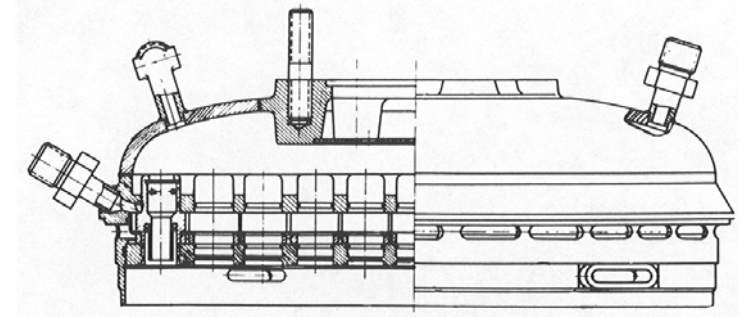
- As the density ratio increases, the spatial growth rate of the interfacial instability wave decreases. ➡ Density stratification tends to stabilize the mixing layer.
- Density stratification has little effect on the frequency of the most unstable mode.





Bi-Propellant Swirl Co-Axial Injector

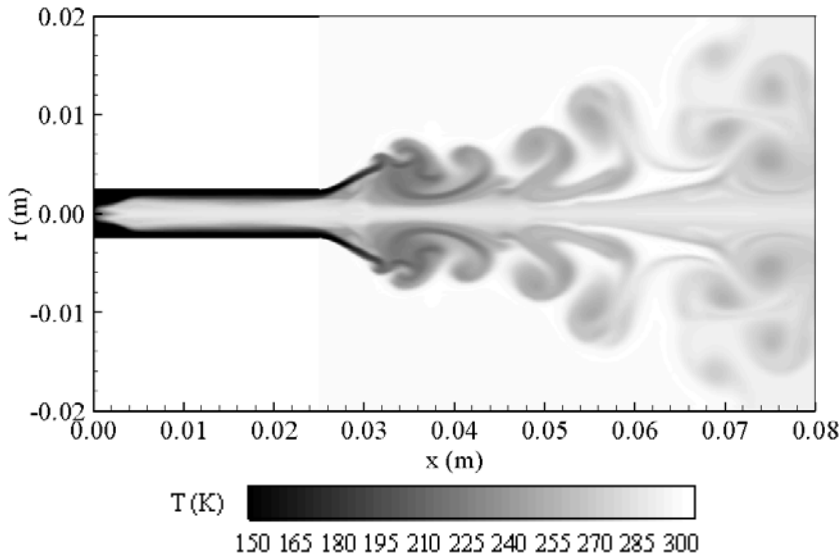
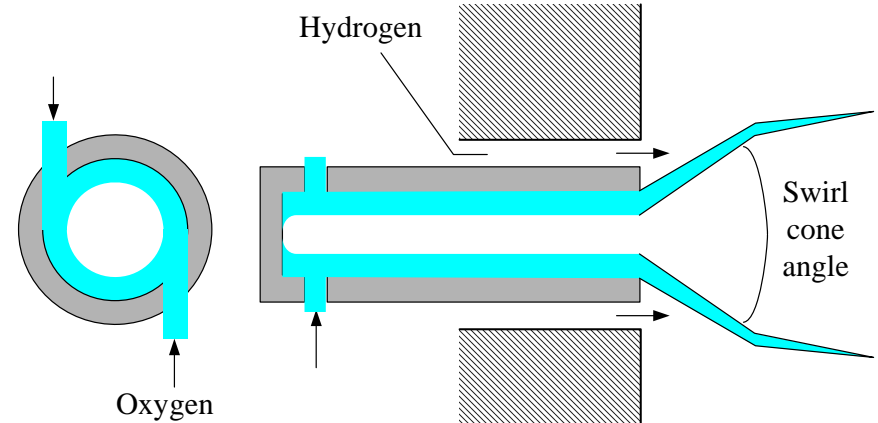
Component	Geometrical characteristic	Spray-cone angle	Pressure drop	flow rate
oxidizer	2	80	0,426	172,9
fuel	24,5	135	0,696	64,8
oxidizer	-	-	0,426	172,3
fuel	-	-	0,696	64,8





Issues

- Swirling jet dynamics at supercritical conditions.
- Flame stabilization mechanisms of swirl co-axial injector.
- Liquid rocket thrust chamber dynamics.

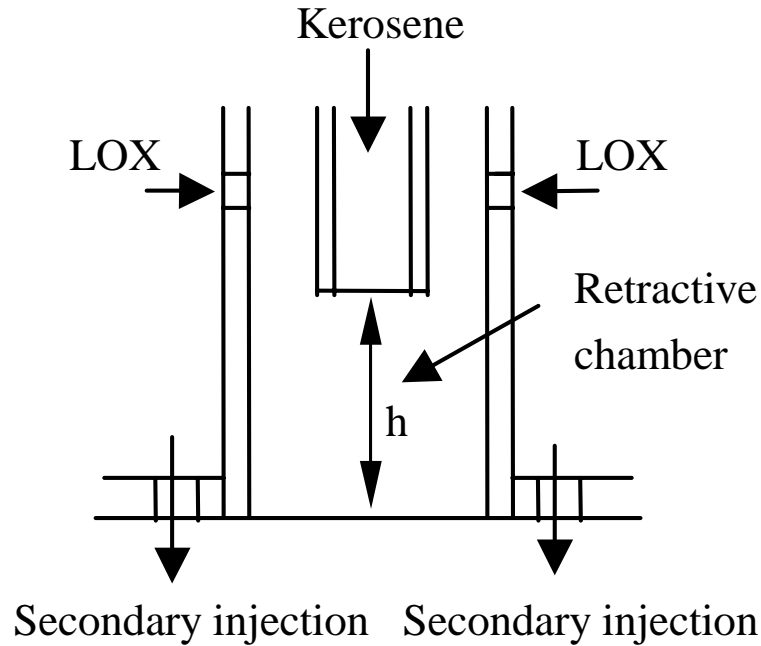


Major Results

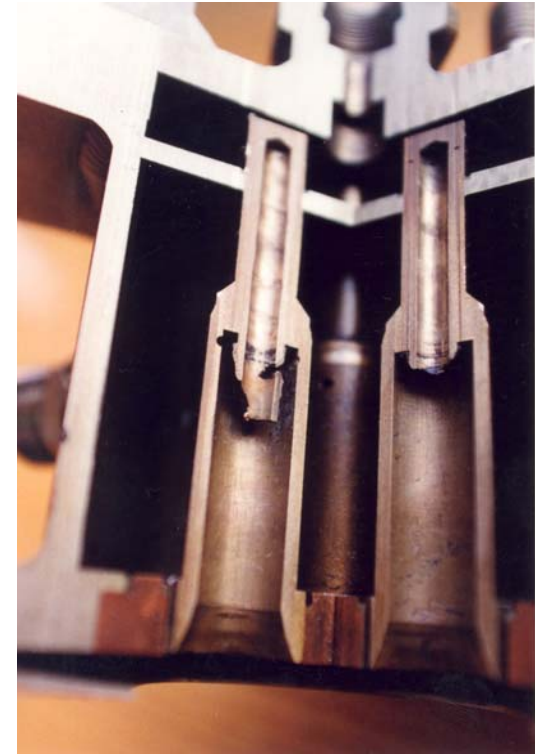
- Liquid film thickness and swirl cone angle.
- Detailed flow structures, including central recirculation zone, surface instability, etc.
- Response of injector dynamics to external forcing.

LOX/Kerosene Preburner Swirl Injector

(Wu, et al., unpublished data, 2003)



oxidizer-rich preburner injector



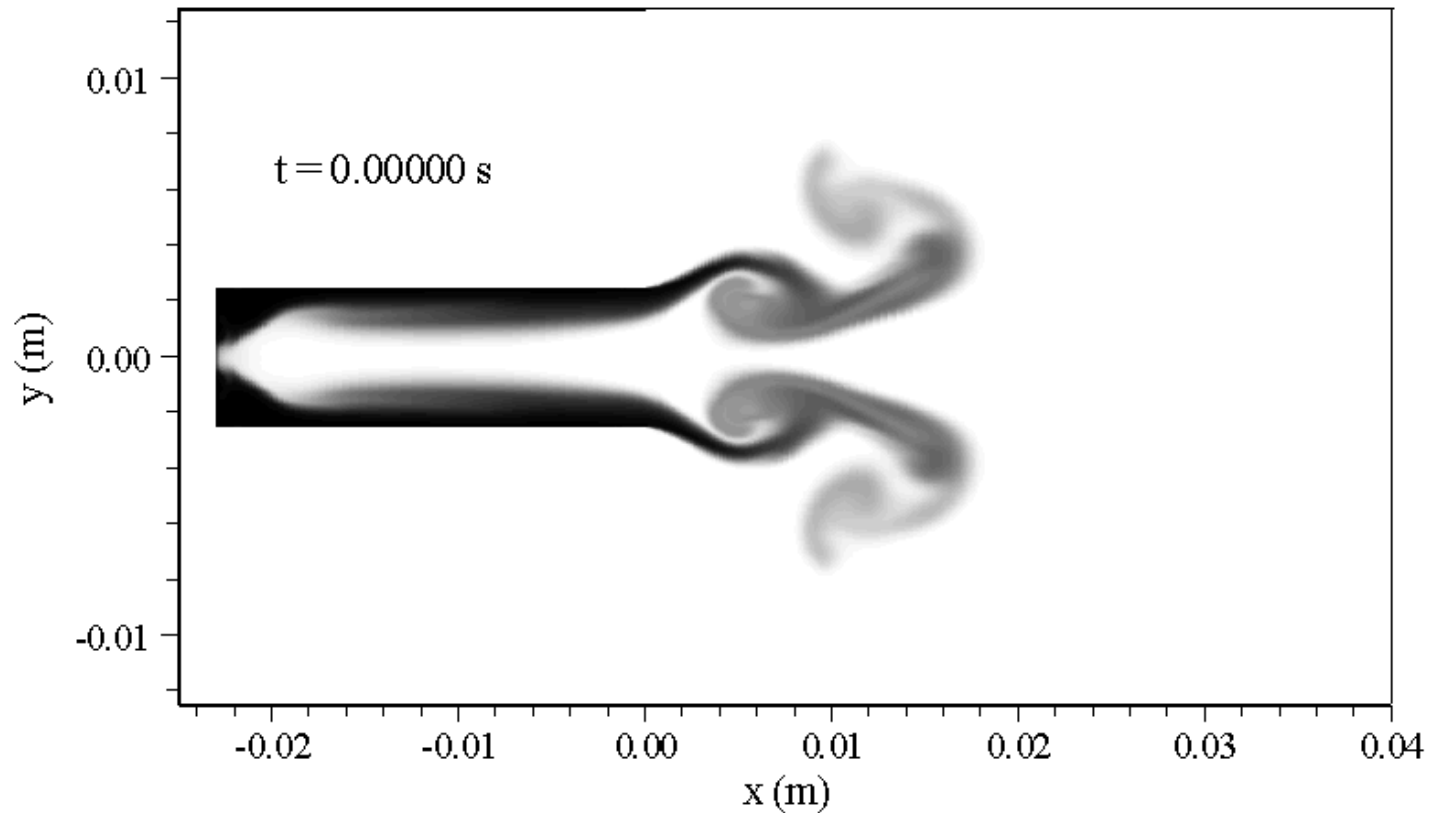
damaged inner centrifugal injector



Time Evolution of Swirling Jet

Department of Mechanical & Nuclear Engineering

($p_\infty=10.0$ MPa, $T_\infty=300$ K, $u_{inj}=30$ m/s, $T_{inj}=120$ K, $\theta=30^\circ$, nitrogen)

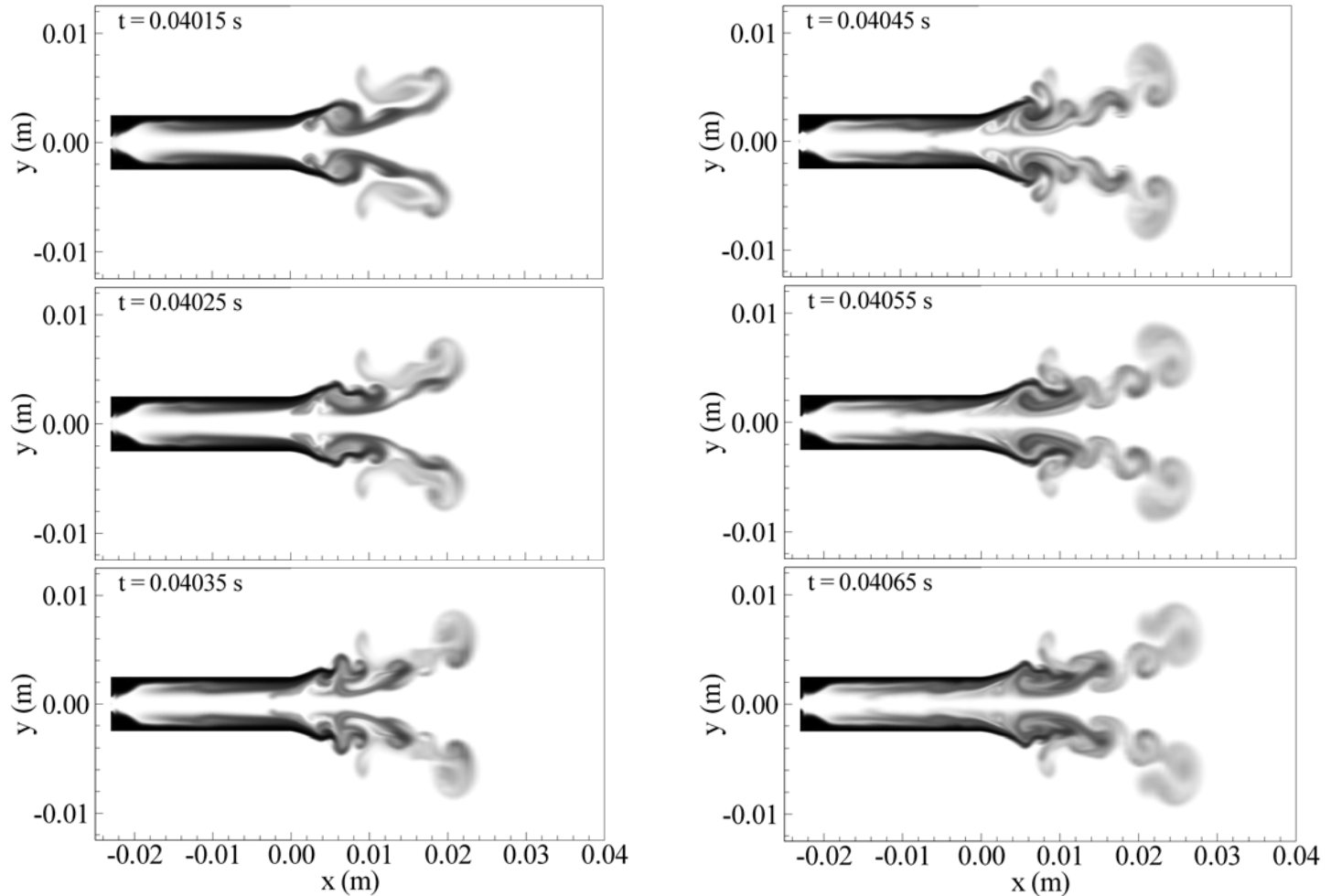




Time Evolution of Swirling Jet

Department of Mechanical & Nuclear Engineering

($p_\infty = 10.0$ MPa, $T_\infty = 300$ K, $u_{inj} = 30$ m/s, $T_{inj} = 120$ K, $\theta = 30^\circ$, nitrogen)



Temperature (K)

120 140 160 180 200 220 240 260 280 300

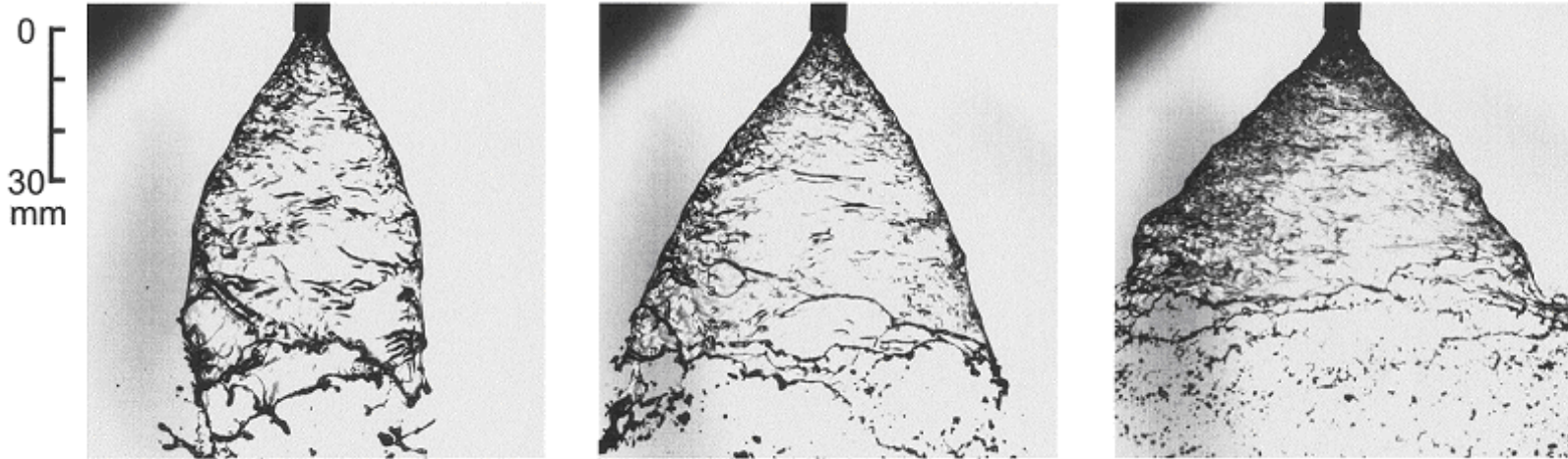


Disintegration of Swirling Water Jet

(Inamura, Tamura and Sakamoto, JPP, 2003)

1855 Department of Mechanical & Nuclear Engineering

Water Injection, $L/D=11.67$, $K=1.0$



(1) $M_l = 26.1$ g/s

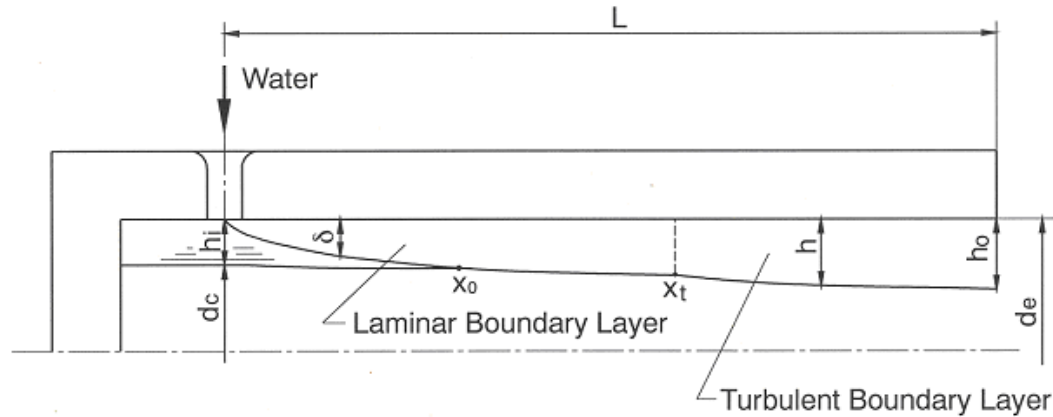
(2) $M_l = 32.5$ g/s

(3) $M_l = 48.6$ g/s

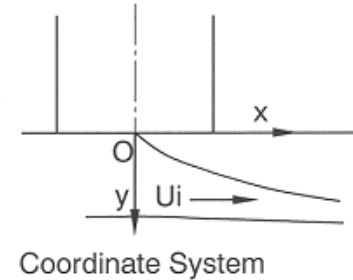
- A hollow cone sheet forms around the injector exit.
- The conical sheet fluctuates vigorously and disintegrates into ligaments and droplets at the sheet tip.
- The sheet breakup point approaches the injector as the liquid flow rate increases.



Theoretical Analysis of Swirl Injector (1/2)



(Inamura et al. *JPP*, 2003)



$$x < x_0$$

$$\frac{d}{dx} \int_0^\delta (U_i u - u^2) dy = \frac{\tau_w}{\rho_l} \quad \text{where} \quad \tau_w = \rho_l \nu_l \left(\frac{\partial u}{\partial y} \right)_{y=0} \quad \text{and} \quad \delta^* = 5.84 \sqrt{x^* / \text{Re}}$$

$$Q = U_i h_i = \int_0^\delta u dy + U_i (h - \delta) \quad \rightarrow \quad h^* = 1 + (3/10) \delta^*$$



Theoretical Analysis of Swirl Injector (2/2)

$$x_0 < x < x_t$$

$$h^* = 1.429 / \{1 + A(x^* - x_0^*)\} \quad A = 1.682(v_l / Q)$$

$$x_t < x$$

$$h^* = 0.02798(x^* / \text{Re}^{1/4}) + C_1 \quad x_0^* = 0.0598 \text{Re}$$

$$C_1 = 1.429\{1 + A(x_t^* - x_0^*)\} - 0.0279(x_t^* / \text{Re}^{1/4})$$

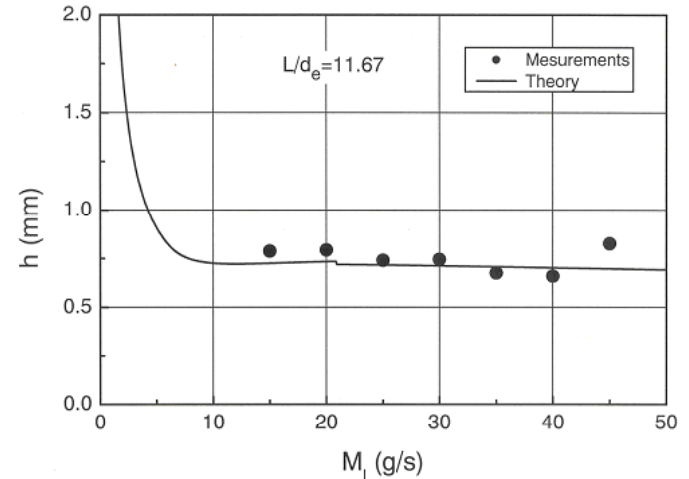
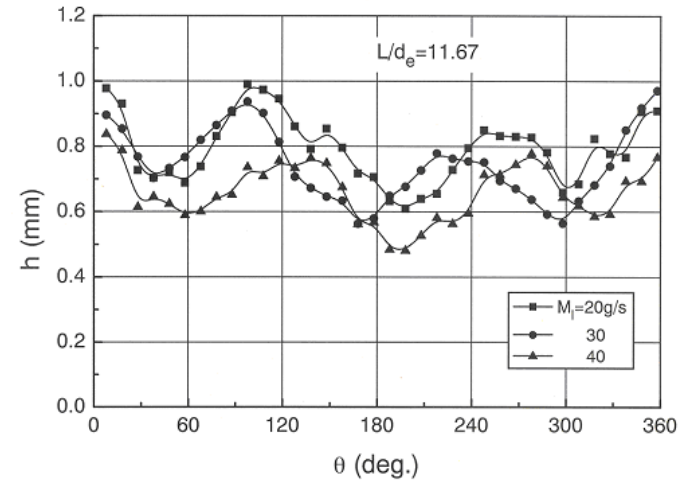
$$x_t < x < x_0$$

$$h^* = 0.02798(x^* / \text{Re}^{1/4}) + C_3$$

$$C_3 = 1.143 - 0.02798(x_0^* / \text{Re}^{1/4})$$

$$x_0^* = \{(1.182 - C_2) / 0.2893\} \text{Re}^{1/4}$$

Film Thickness at Post Exit

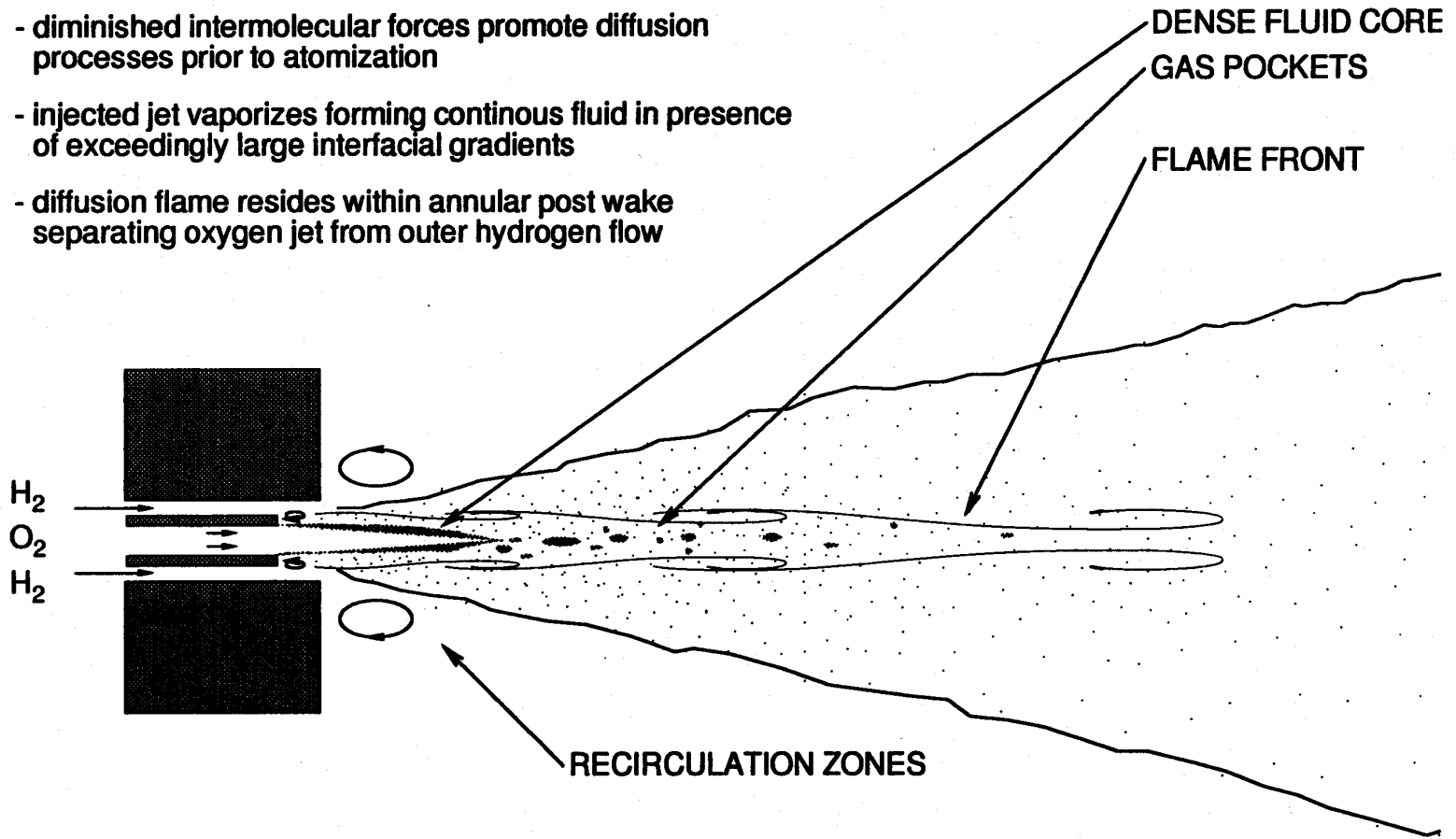




Limiting Extremes: 2) Diffusion Processes Dominate

- "High" Heating Rates

- diminished intermolecular forces promote diffusion processes prior to atomization
- injected jet vaporizes forming continuous fluid in presence of exceedingly large interfacial gradients
- diffusion flame resides within annular post wake separating oxygen jet from outer hydrogen flow



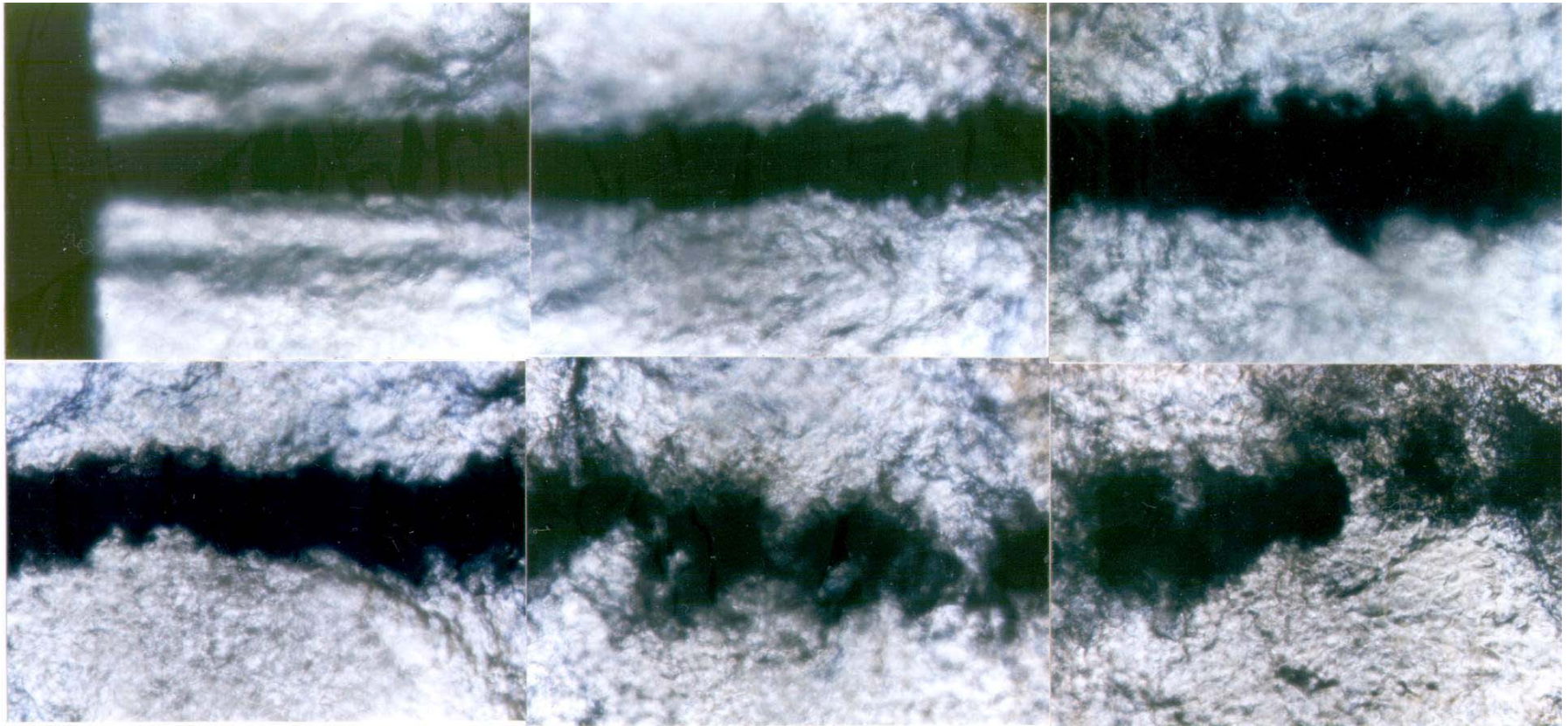


Burning LOX Jet at Supercritical Pressure

(Mayer, DLR, Germany; Tamura, NAL, Japan)

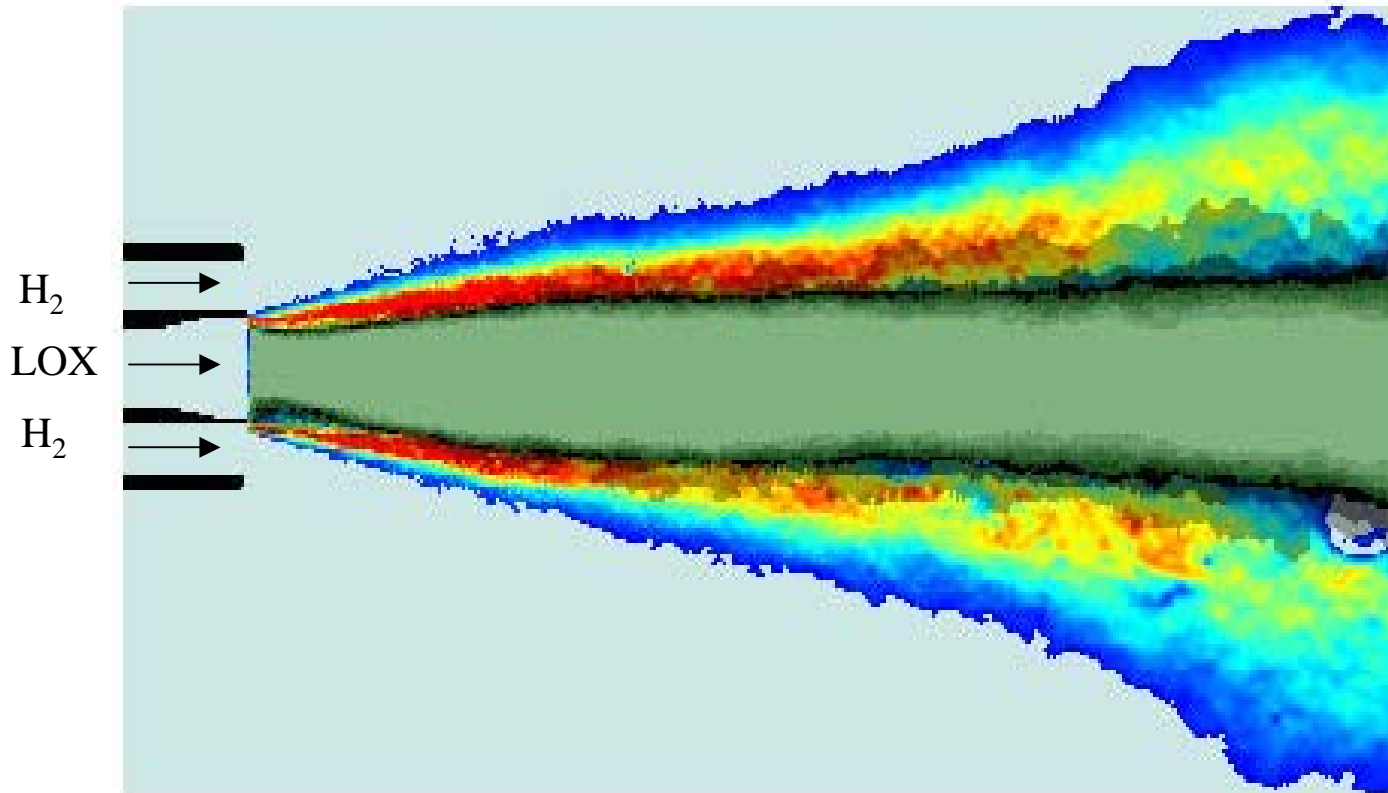
1 8 5 5 Department of Mechanical & Nuclear Engineering

$(u_{\text{LOX}} = 30 \text{ m/s}, u_{\text{H}_2} = 300 \text{ m/s}, T_{\text{LOX}} = 100 \text{ K}, T_{\text{H}_2} = 300 \text{ K}, p = 6 \text{ MPa})$



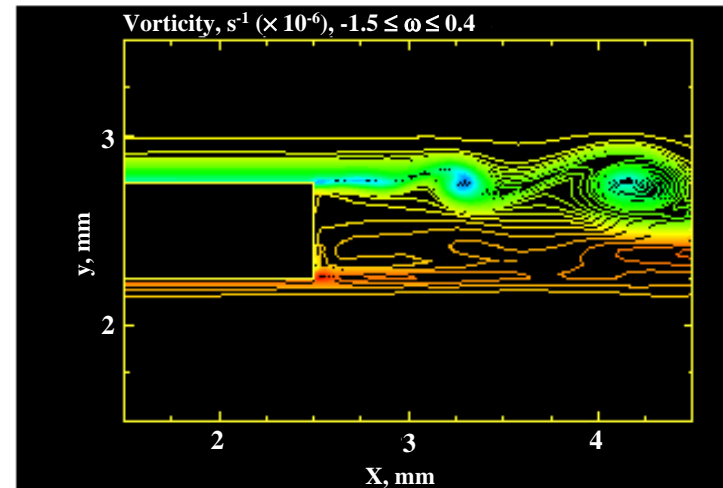
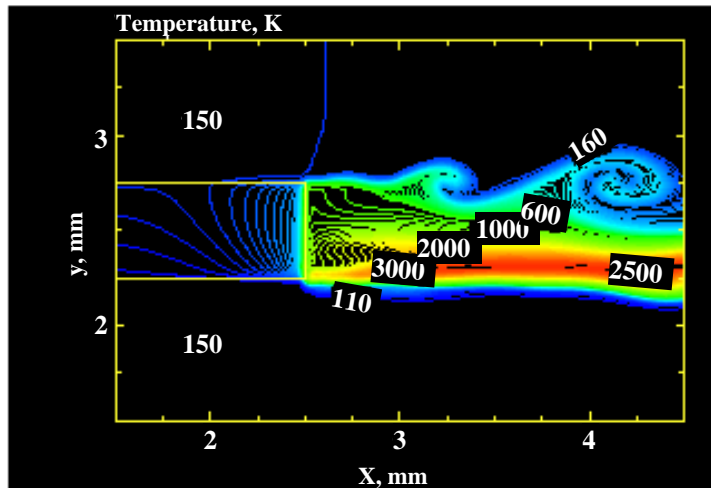
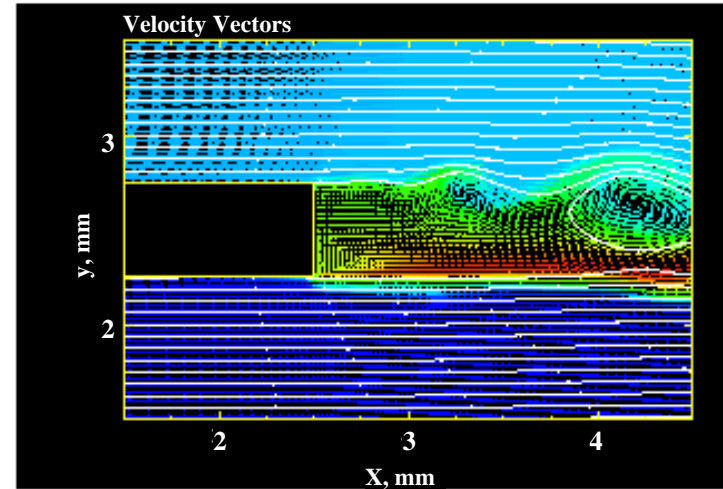
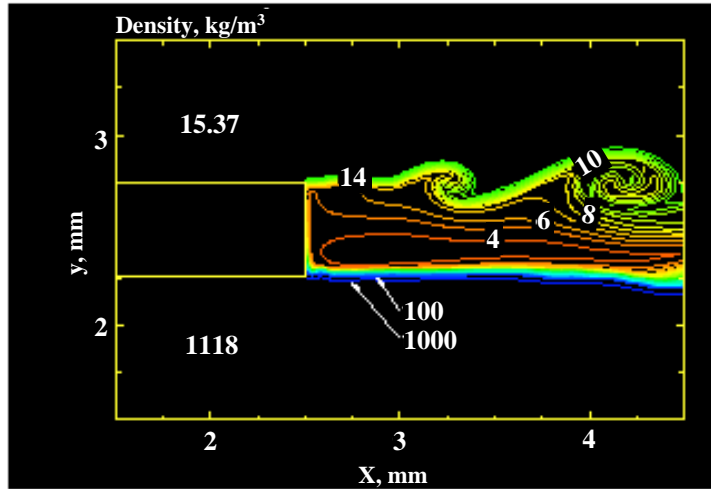


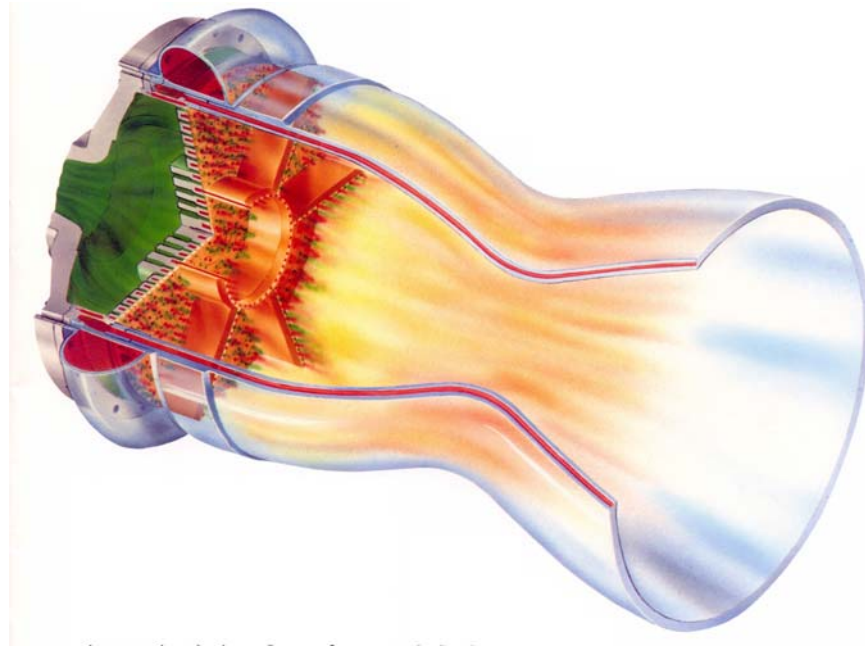
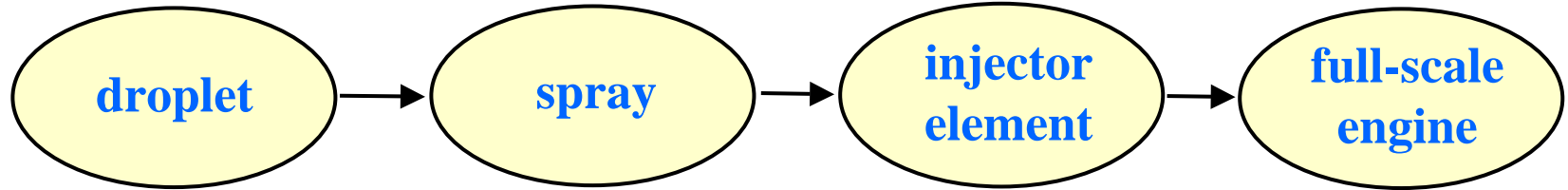
Supercritical Injector Flow and Flame Dynamics



Combined OH emission and backlighting images (Ph.D thesis of Matthew Juniper)

LOX/Hydrogen Shear-Coaxial Injector Dynamics



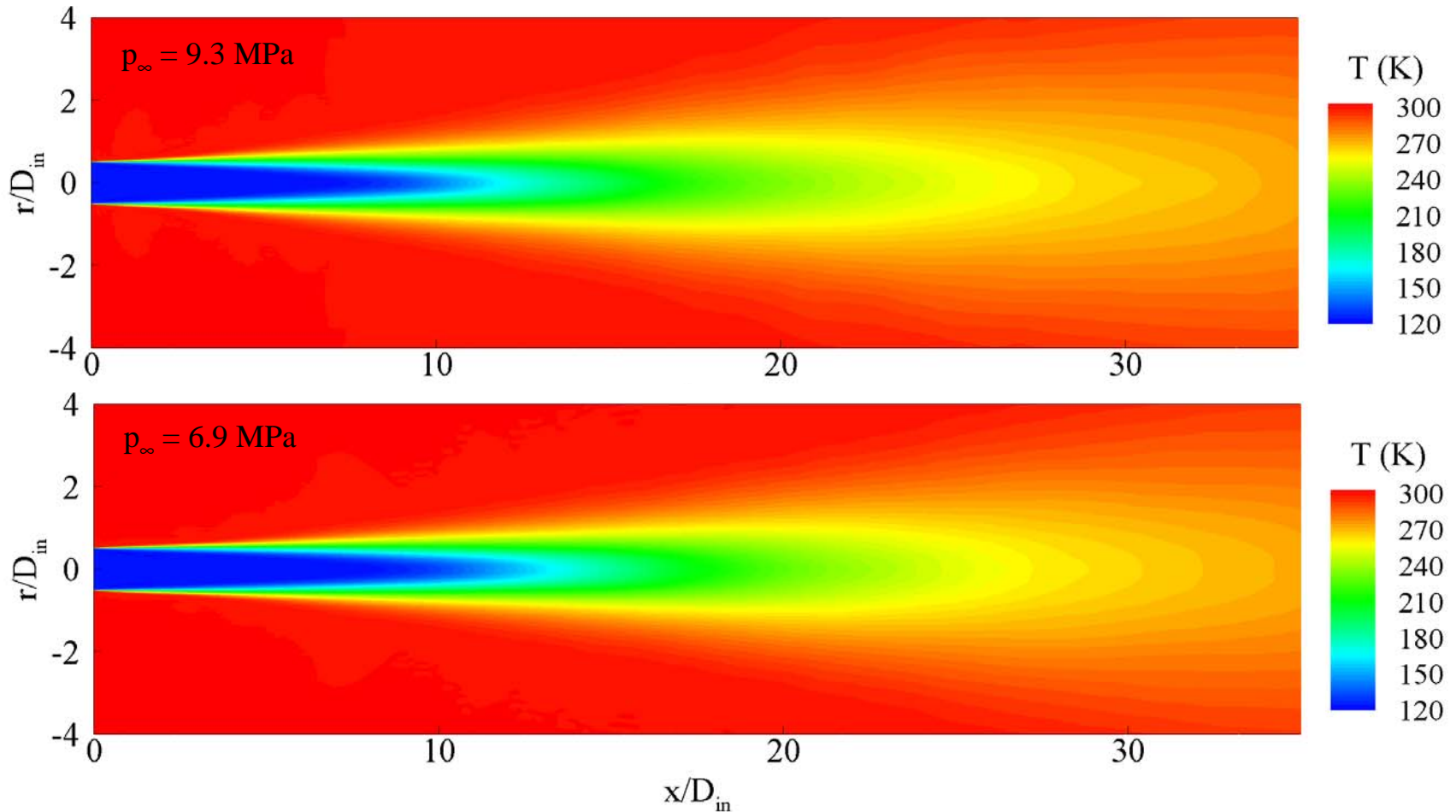




Effect of Pressure on Mean Temperature Distributions

Department of Mechanical & Nuclear Engineering

$(T_\infty = 300 \text{ K}, u_{in} = 15 \text{ m/s}, T_{in} = 120 \text{ K}, D_{in} = 254 \mu\text{m})$

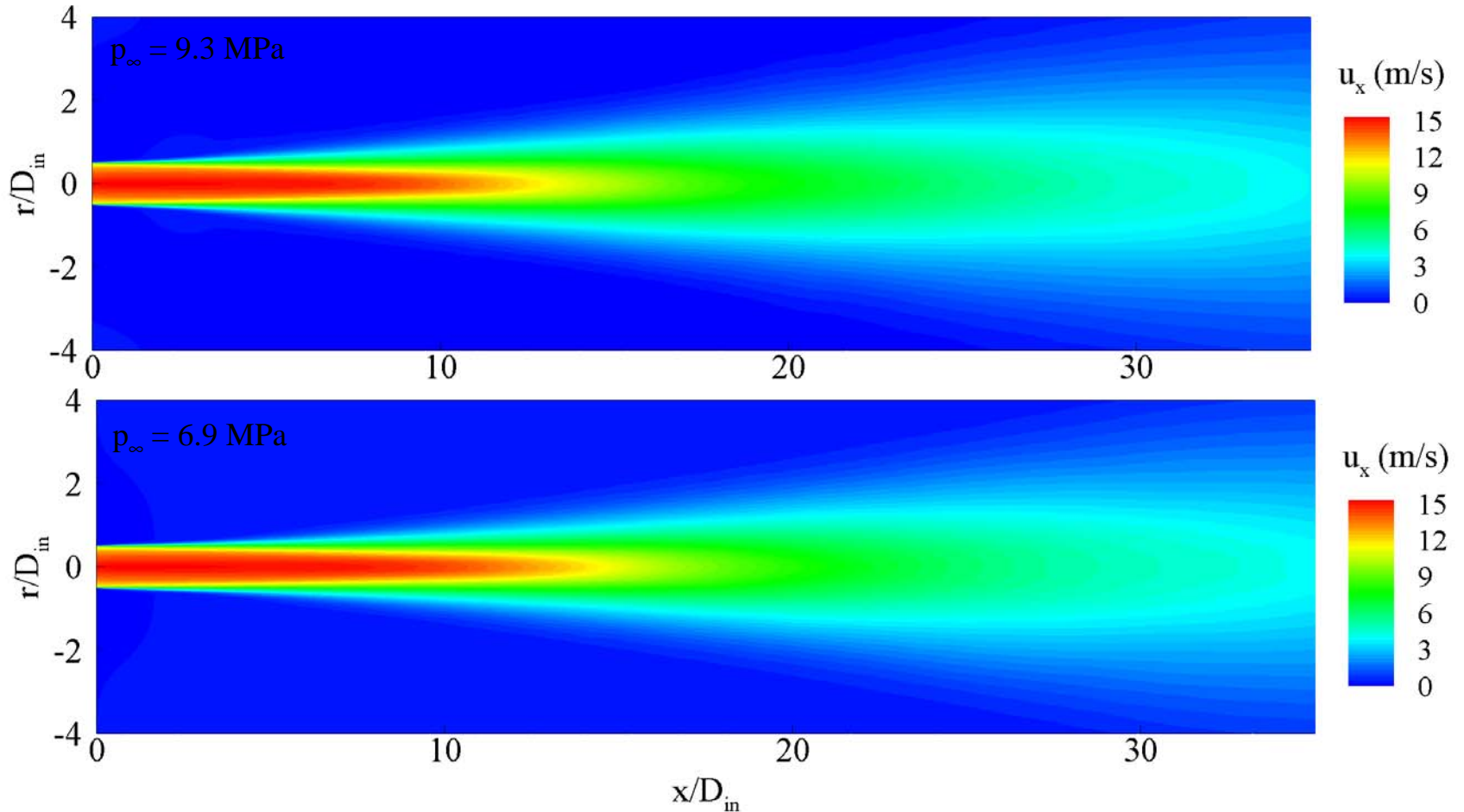




Effect of Pressure on Mean Velocity Distributions

Department of Mechanical & Nuclear Engineering

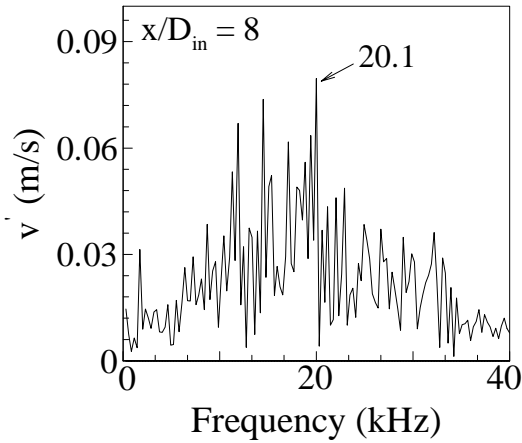
$(T_\infty = 300 \text{ K}, u_{in} = 15 \text{ m/s}, T_{in} = 120 \text{ K}, D_{in} = 254 \text{ }\mu\text{m})$



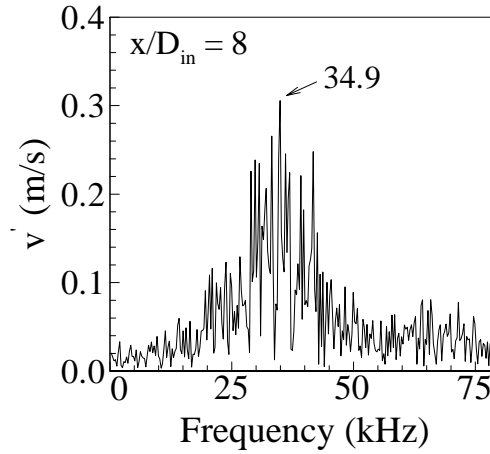


Frequency Spectral of Radial Velocity Oscillations

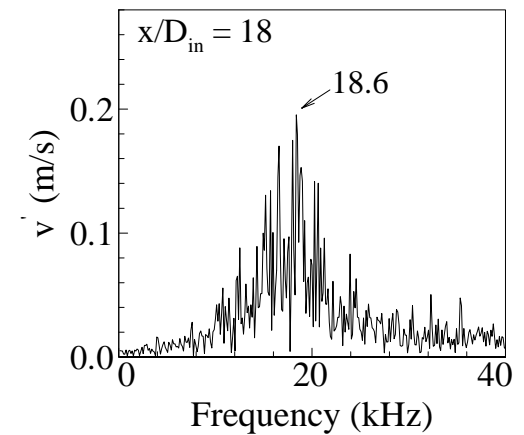
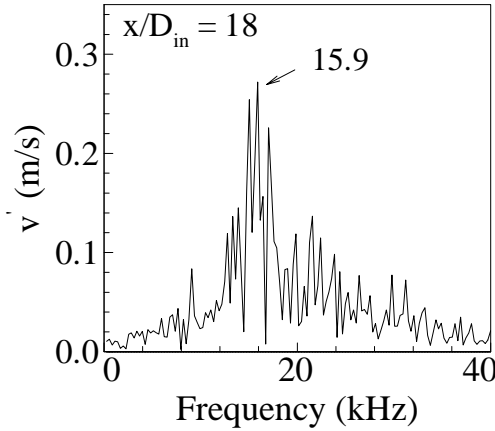
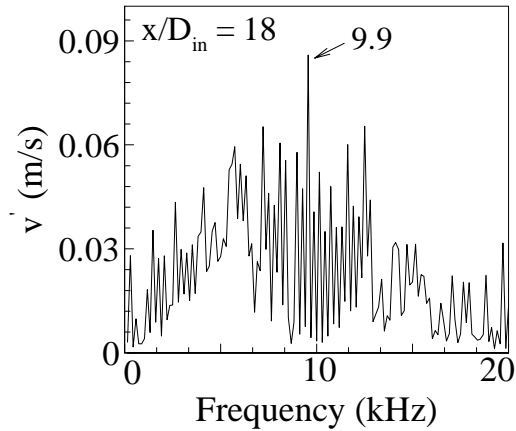
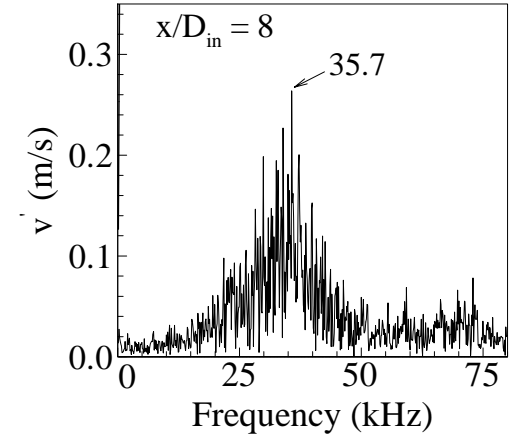
$p = 4.2 \text{ MPa}$



$p = 6.9 \text{ MPa}$



$p = 9.3 \text{ MPa}$

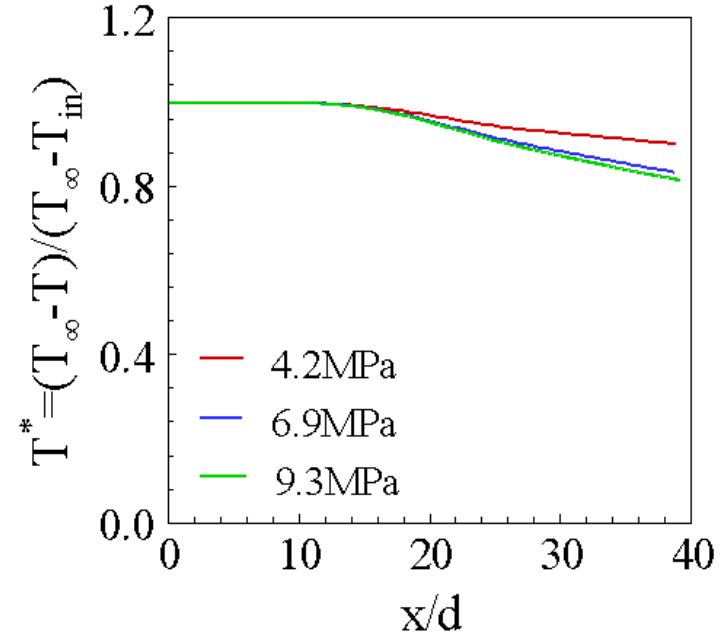
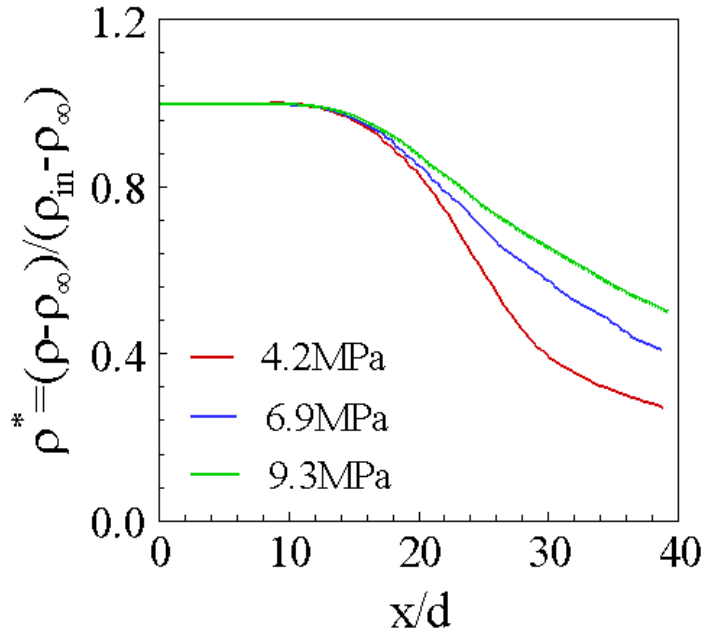




Normalized Density and Temperature Distributions along Radial Direction

Department of Mechanical & Nuclear Engineering

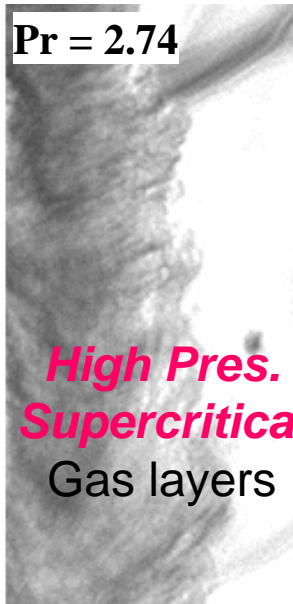
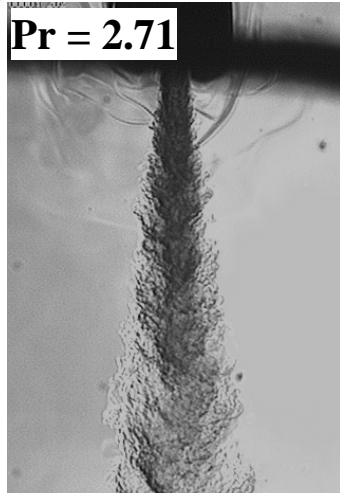
$T_\infty = 300\text{K}$, $u_{in} = 15\text{m/s}$, $T_{in} = 120\text{K}$, $D_{in} = 254\mu\text{m}$



- Thermal diffusivity of nitrogen is relatively lower in the region where the temperature is near the critical temperature.
- Most thermal energy transferred from the hot ambient gaseous nitrogen to the cold jet is used to facilitate volume expansion.



Numerical Challenges



Challenges

- machine round-off errors at low speeds
- eigenvalue disparity
- time accuracy
- real-fluid behavior
- robust and efficient numerical treatment

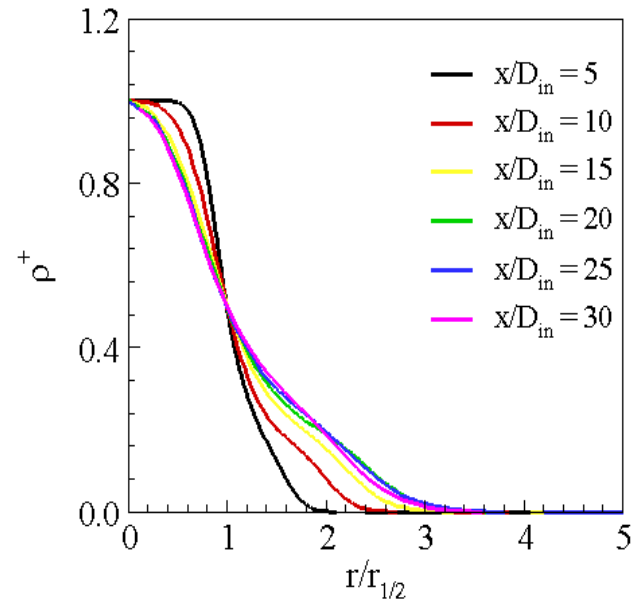
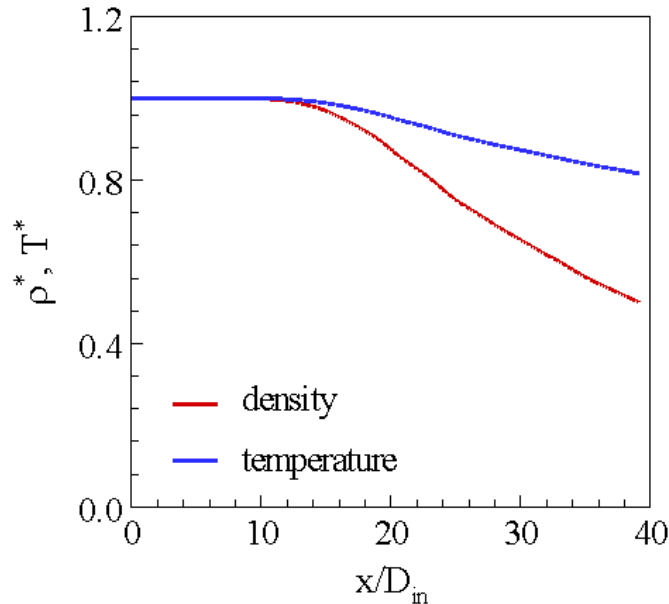
Solutions

- pressure decomposition
- preconditioning method
- dual time-stepping integration technique
- partial mass/molar properties
- derivation of numerical Jacobians and thermodynamic properties based on fundamental thermodynamic theories



Normalized Density and Temperature Distributions

$(p_\infty = 9.3\text{MPa}, T_\infty = 300\text{K}, u_{in} = 15\text{m/s}, T_{in} = 120\text{K}, D_{in} = 254\mu\text{m})$



- Due to the “near critical slow down”, the temperature of nitrogen fluid increases slowly along the jet centerline.
- A self-similar density profile exist when $x/d > 15$.

PENNSTATE



1 8 5 5 *Department of Mechanical & Nuclear Engineering*

Thank You!

Injector Issues with Different Propellant Combinations

D. Haeseler, C. Mäding,
EADS SPACE Transportation, Munich, Germany

V. Rubinski, V. Kosmatcheva, V. Berezhnoy, N. Bratukhin,
KBKhA, Voronezh, Russia

5th International Symposium on Liquid Space Propulsion
“Long Life Combustion Devices Technology”
27 - 30 October 2003 / Chattanooga, TN, USA

Overview:

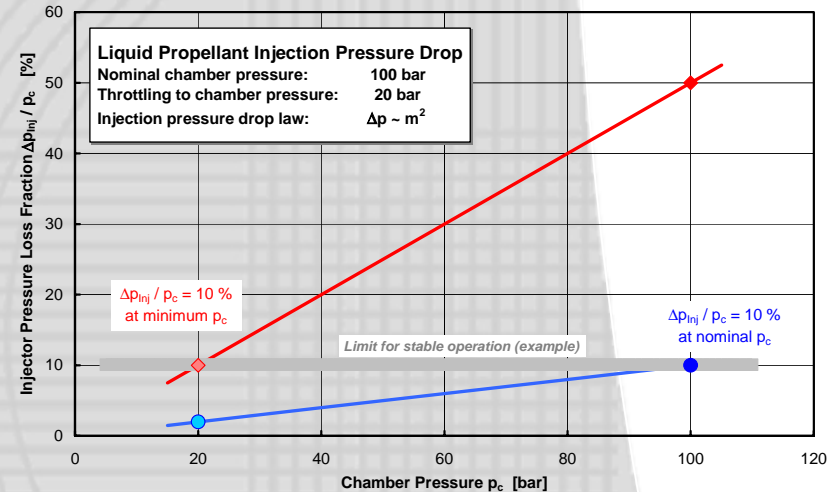
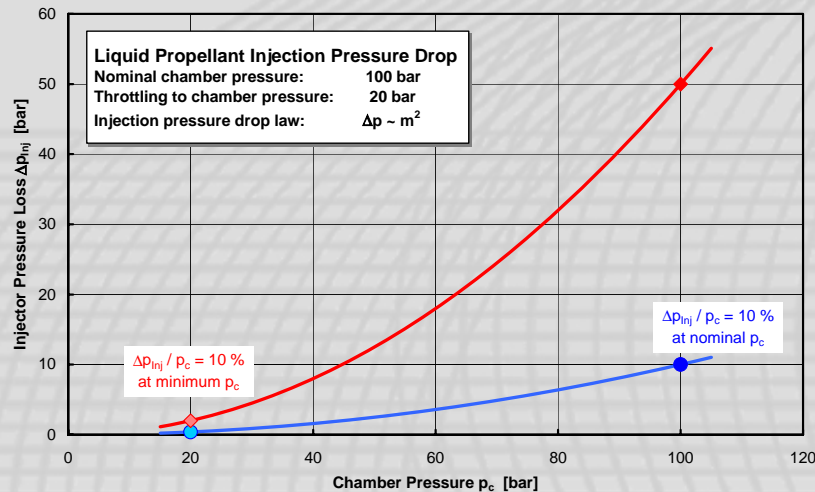
Experimental characterization of operation, efficiency, heat flux of:

- Injection element concepts for wide throttling range.
- Injection element concepts for large flowrate.
- Injection element concepts for hydrocarbon fuels (LOX-Methane and LOX-Kerosene).

Activities in cooperation with KBKhA/Russia since 1993

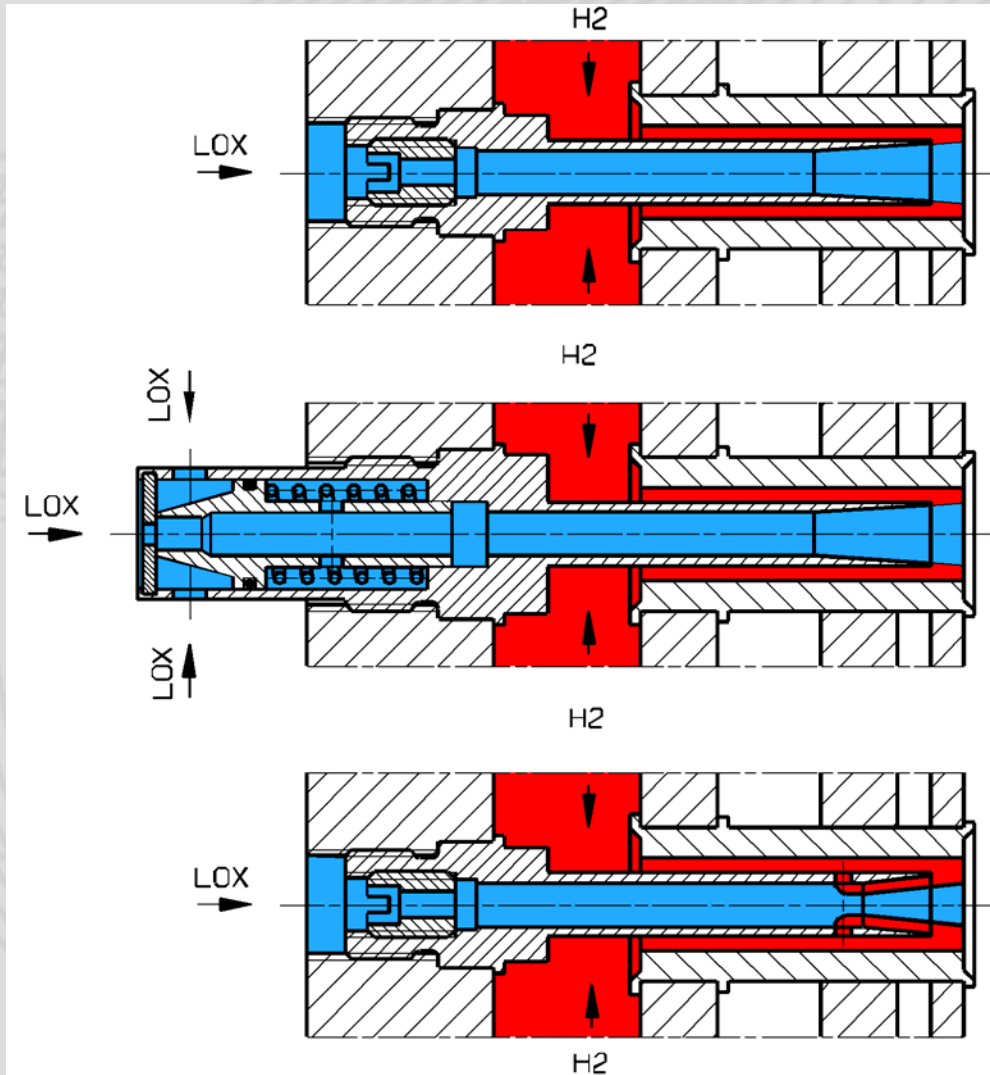
Injection element concepts for wide throttling range.

Throttlable Injection Element Goals



- Usual coaxial elements produce liquid propellant pressure drops according to the square law $\Delta p_{inj} \sim m^2$.
 - The pressure drop fraction $\Delta p_{inj} / p_c$ is one indicator (of several) for the stable operation without feedline-coupled combustion instabilities. A minimum of e.g. 10% needs to be present for stable operation.
 - Keeping the pressure drop fraction required for stable operation $\Delta p_{inj} / p_c$ (typical 10%) at deeply throttled conditions results in excessive pressure drop at nominal operations.
- ➔ Develop an element concept with a (ideally) constant pressure drop fraction $\Delta p_{inj} / p_c$.

Tested Throttlable Injection Elements



1. Regular Coax-Element

2. Mechanically Throttled

3. Gasdynamically Throttled

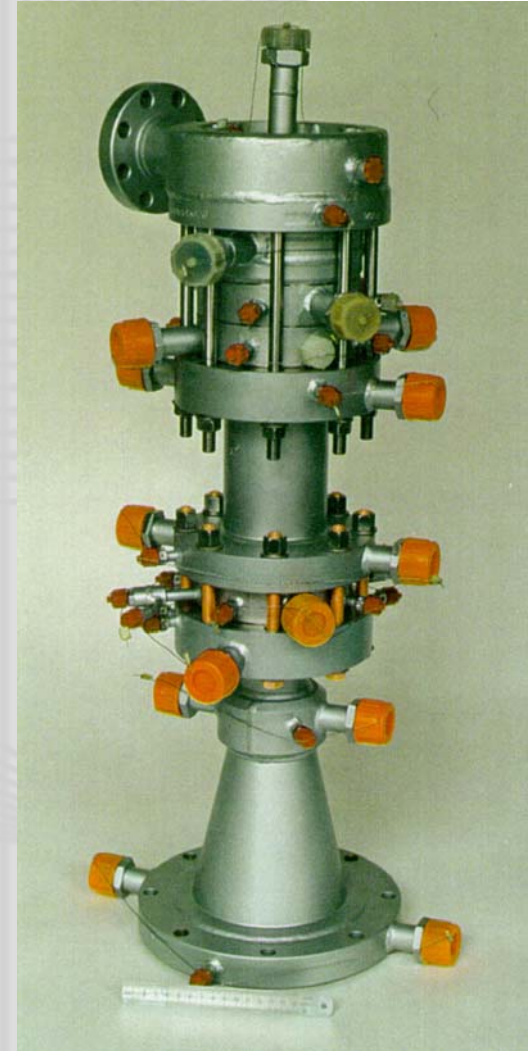
Throttlable Injection Element Test Hardware

Operating Conditions:

Propellants: LOX at 105 K
GH2 at room temp.

Test duration: 30 s

Water cooling of faceplate and chamber sections.



Throtttable Injection Element Tests

Unregulated Coax Element:

Mechanically regulated element

Gasdynamically regulated element (different versions)

Chamber pressure range:

Mixture ratio range:

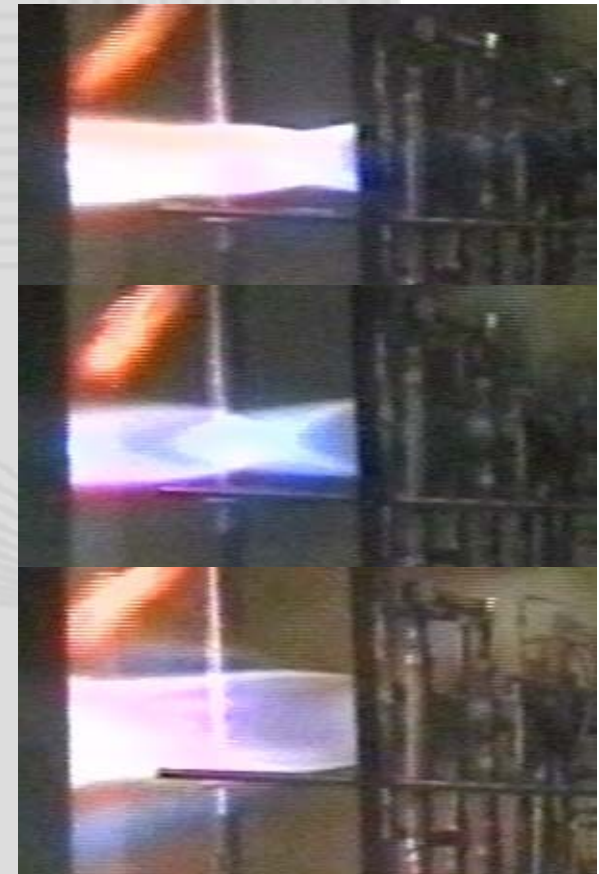
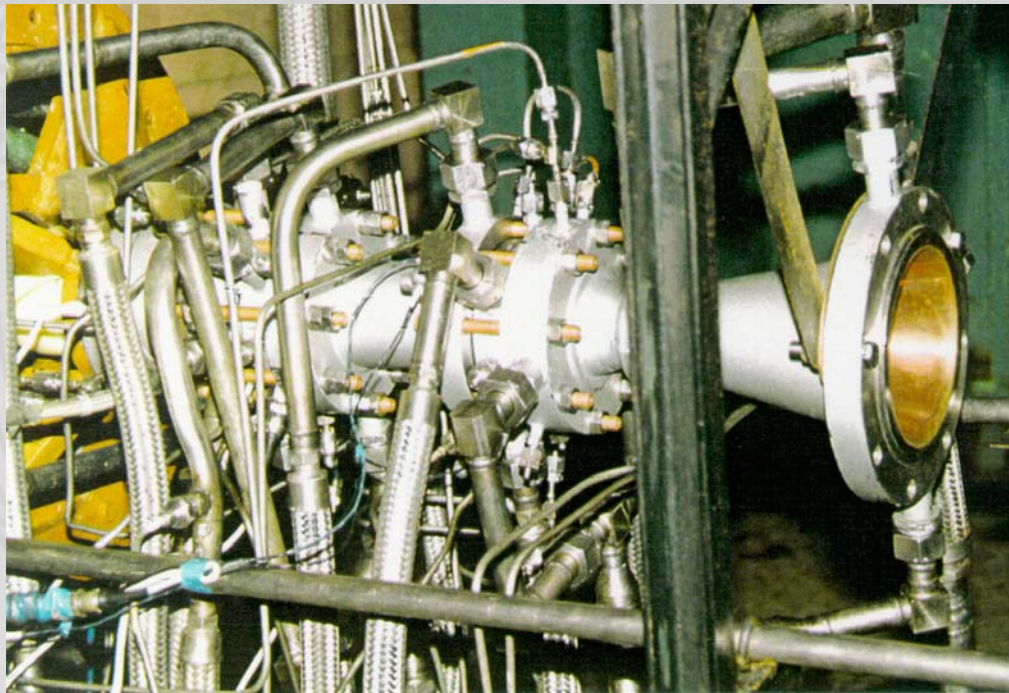
4 tests

4 test

15 tests

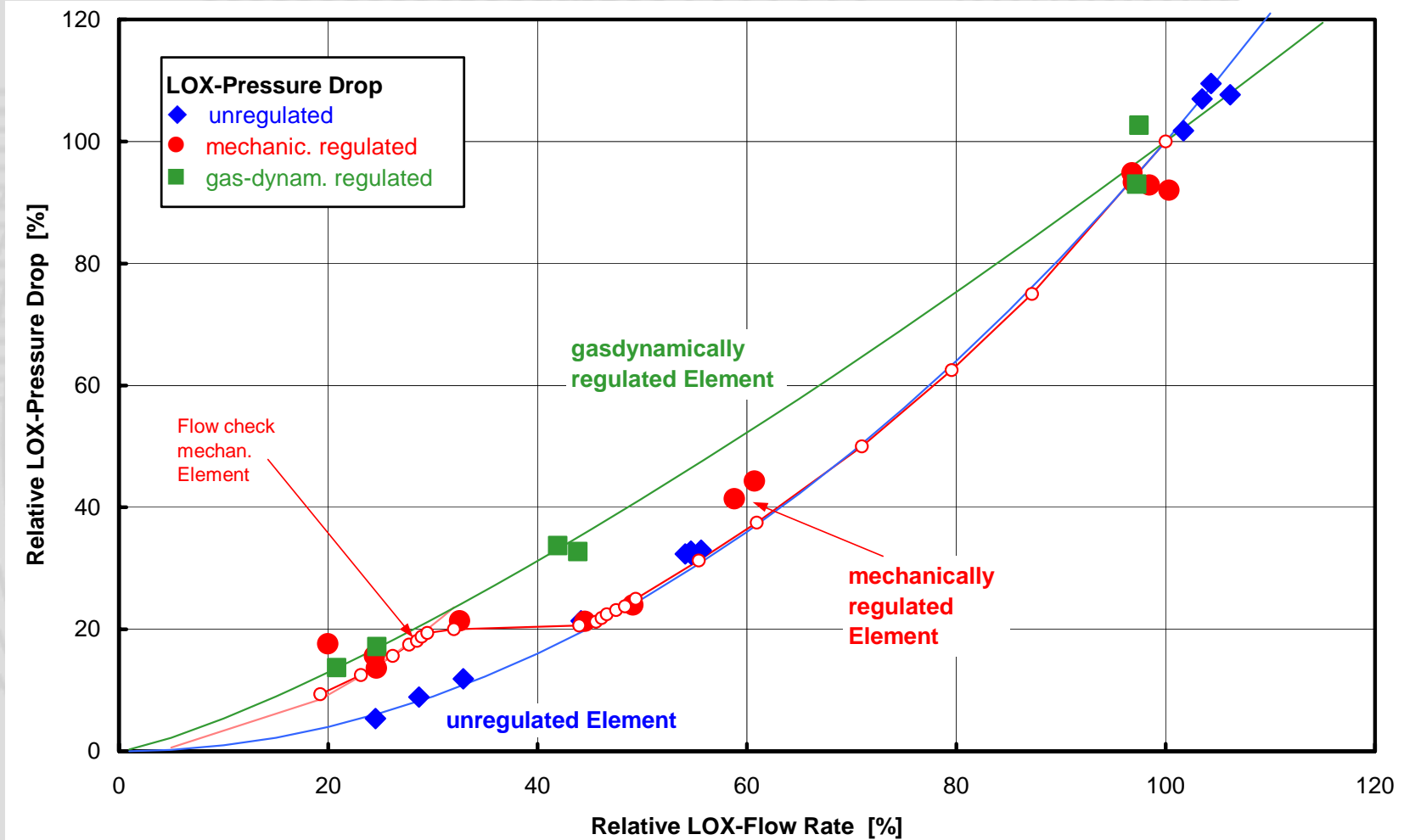
19.4 – 108 bar

5.0 – 8.2



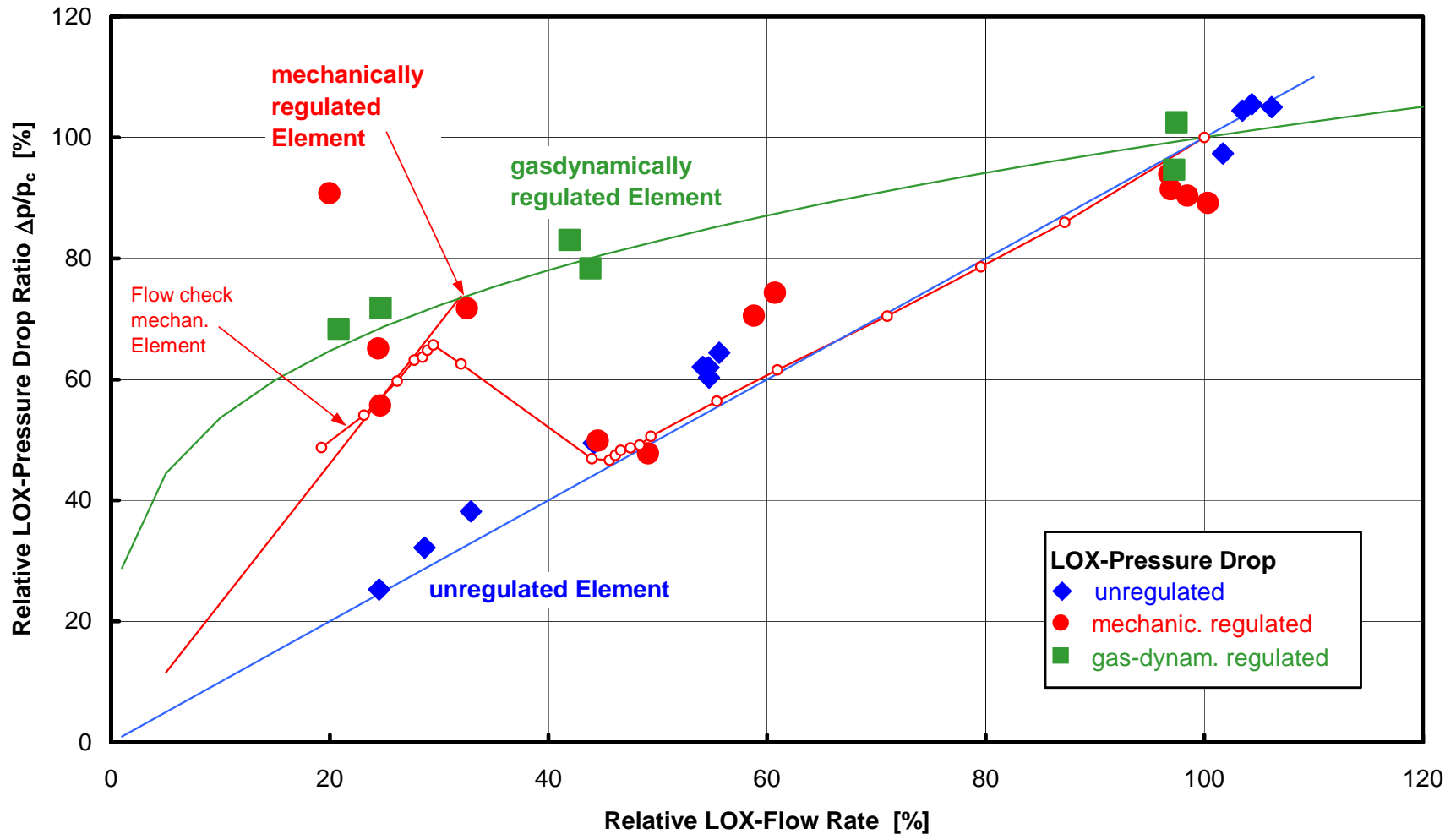
Throttlable Injection Element Test Results

LOX-Pressure Drop Characteristics of the 3 Tested Element-Concepts



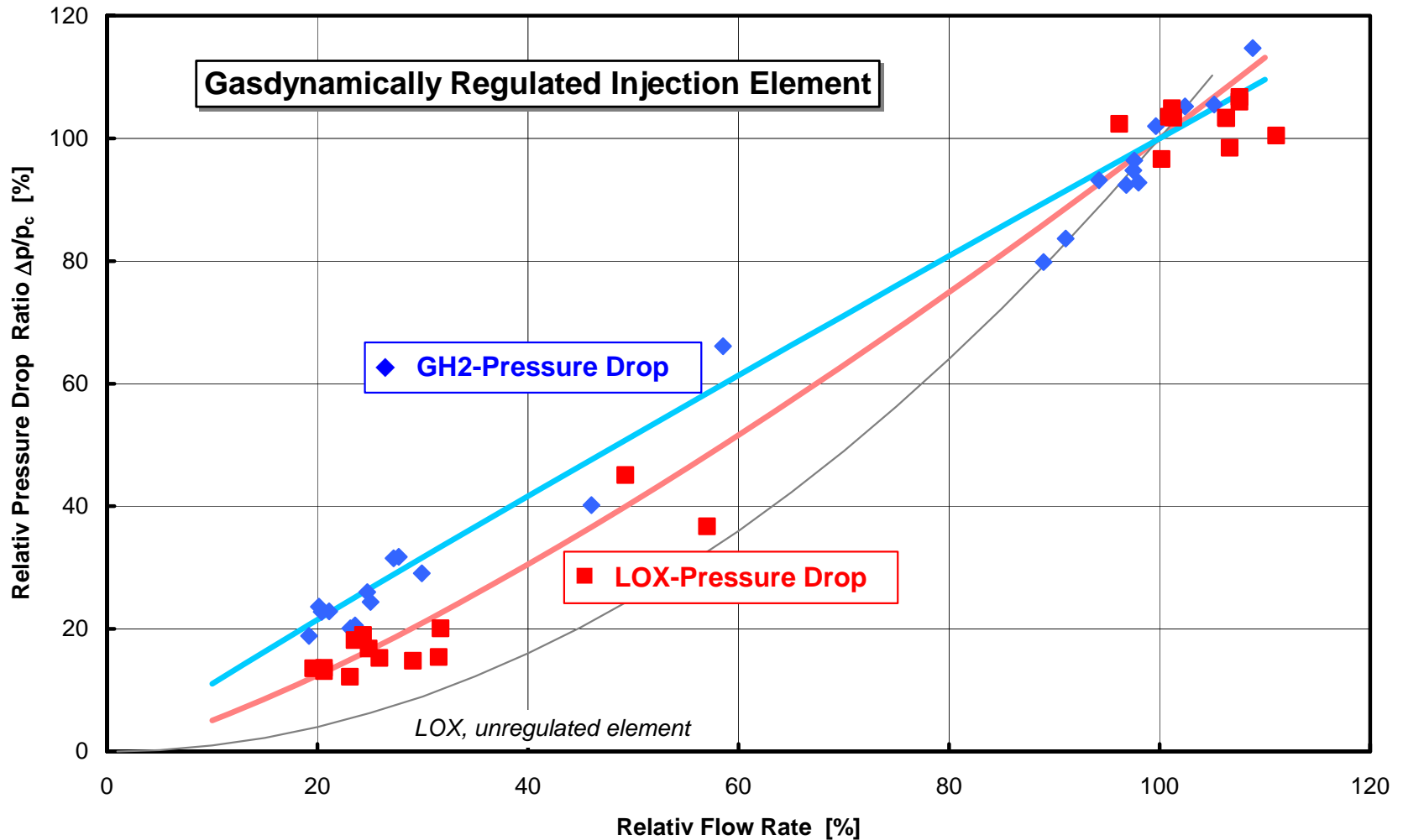
Throttlable Injection Element Test Results

LOX-Pressure Drop Characteristics of the 3 Tested Element-Concepts



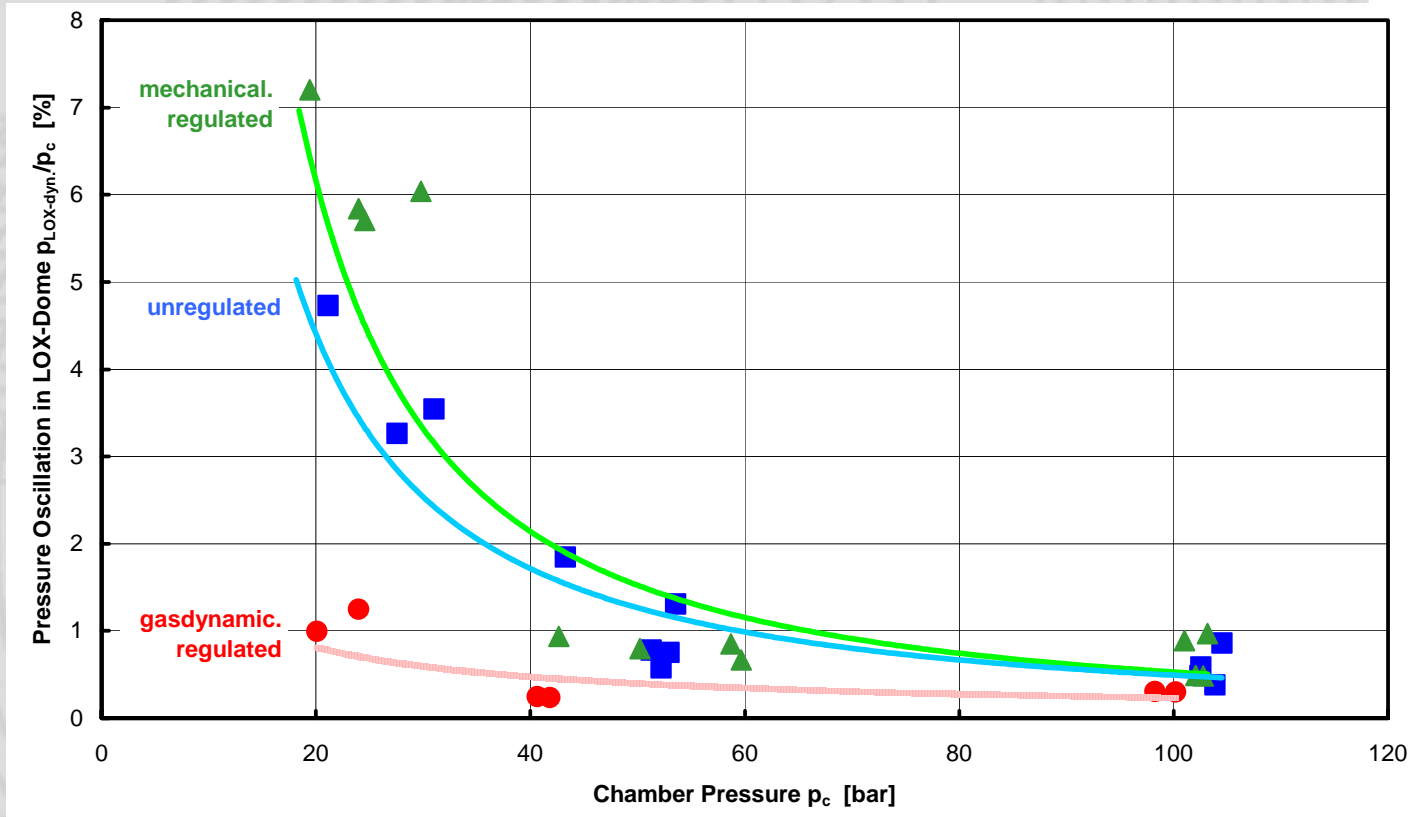
Throttlable Injection Element Test Results

Pressure Drop Characteristics of the Gasdyn. Regulated Element-Concept



Throttlable Injection Element Test Results

Experimental Pressure Oscillations in LOX-Dome



- The mechanically regulated element creates significant higher pressure oscillations due to springs.
- The gasdyn. element creates significant lower pressure oscillations due to pre-mixing of GH2 and LOX.

Conclusions on Throttlable Injection Elements

- Three different injection element concepts with higher pressure drop at throttled operation were designed and tested successful. 23 tests were performed with LOX/GH2 at 19 – 108 bar chamber pressure and at mixture ratios O/F = 5.0 – 8.2,
- The functionality of all three element concepts was demonstrated.
- The characteristic of the **unregulated element** was identical to the known characteristic of usual coaxial elements in the hot tests.
- The characteristic of the **mechanically regulated element** in the hot tests was in agreement to the characteristic derived from flow checks with water. The pressure drop was increased by a factor of 2.3 for throttling below 30%. The transition at throttling range 30 – 50% is not recommended for steady-state operation.
- The relative LOX-pressure drop of the **gas-dynamically regulated element** was increased threefold at 20% throttling.
- The interaction of the propellants cannot be modeled in the flow checks with simulating fluids.
- The pressure oscillations in the LOX-dome and in the combustion chamber was slightly lower in comparison to the unregulated element.
- No significant difference in the combustion efficiency of all element concepts could be observed. Some scatter in the data was present.

Injection element concepts for large flowrate.

Large Injection Element Size Considerations

Current engine injection systems contain a large number of injection elements: *Vulcain* - 516; *SSME* - 600; *RD-0120* - 444; *RS-68* – 628

Cost reduction due to reduced number of elements:

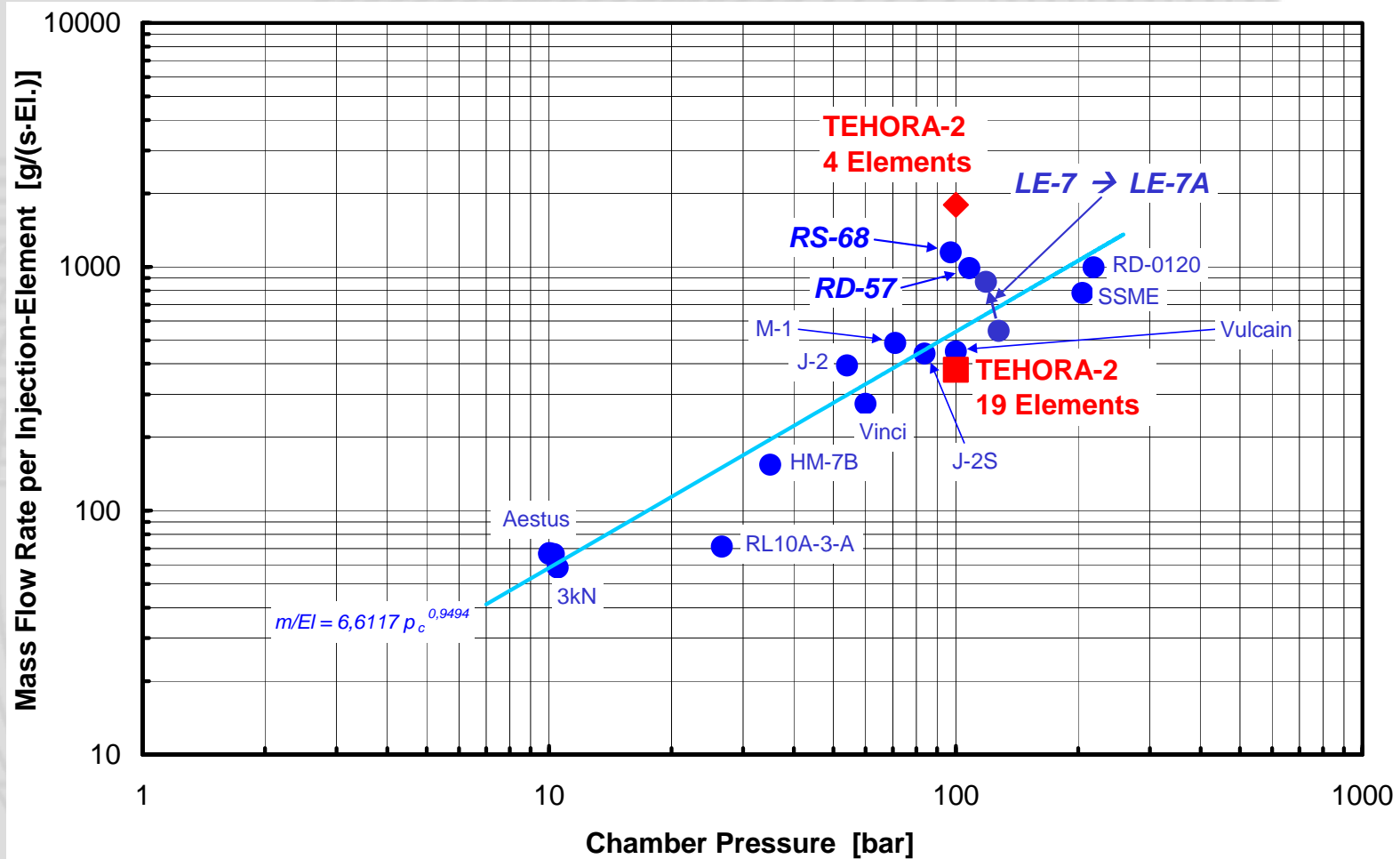
- Reduced number of parts to be manufactured.
- Reduced number of subassemblies to be integrated into the injector body.
- Relaxed tolerances may be allowed for manufacturing of enlarged element parts.

Expected Disadvantages:

- Reduced combustion efficiency due to less complete mixing.
- Enhanced variation of heat load to chamber wall due to the less uniform flow profile.
- Large injection elements may be more susceptible to combustion instabilities.

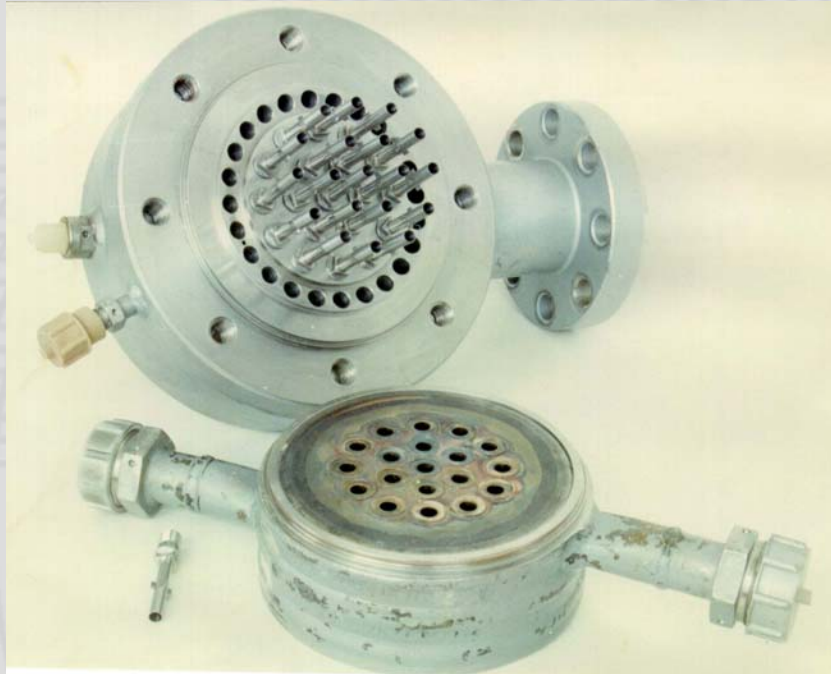
➔ **Experimental investigation to study combustion behaviour**

Injection Element Size Trend

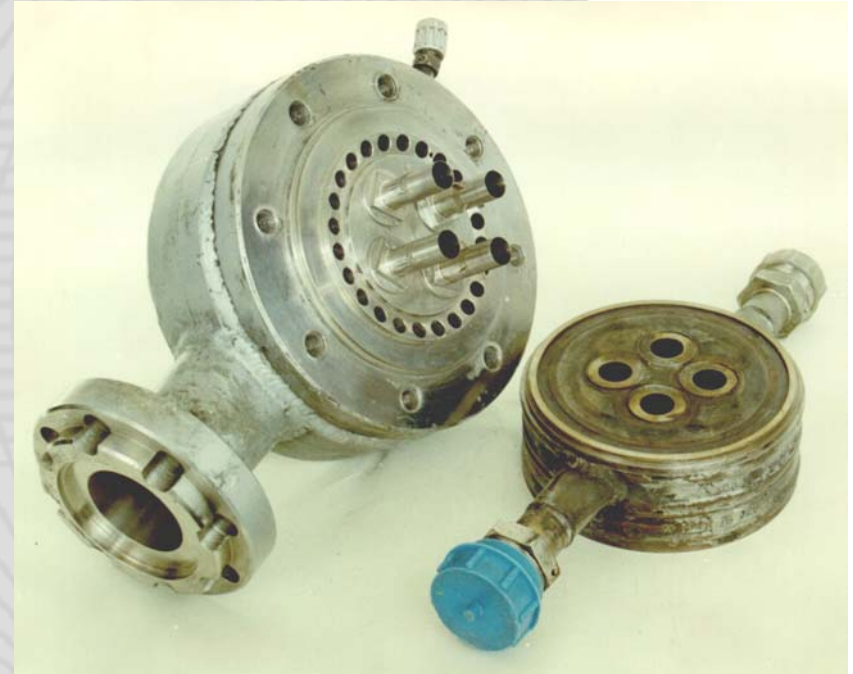


Propellant flow rate per element is related to chamber pressure

Tested Subscale Injection Heads



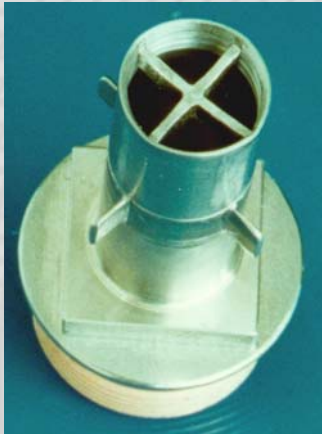
19 Reference Injection Elements
Flowrate per element: 0.38 kg/s



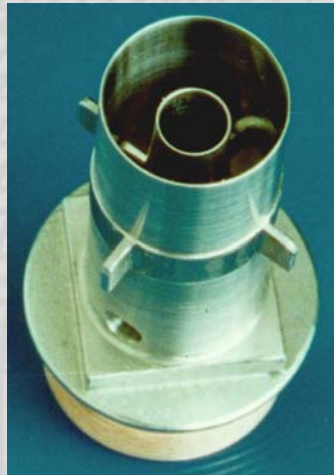
4 High-Flowrate Injection Elements
Flowrate per element: 1.8 kg/s

Flowrate per element increased by a factor of 4.75

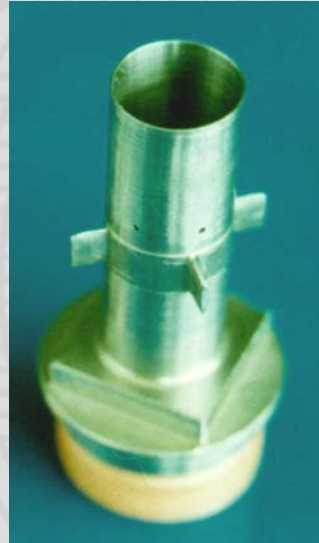
Tested Injection Elements



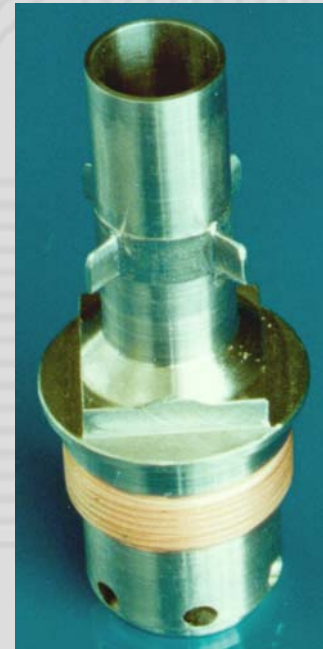
cross coaxial



tri-coaxial



gasdynamic
coaxial

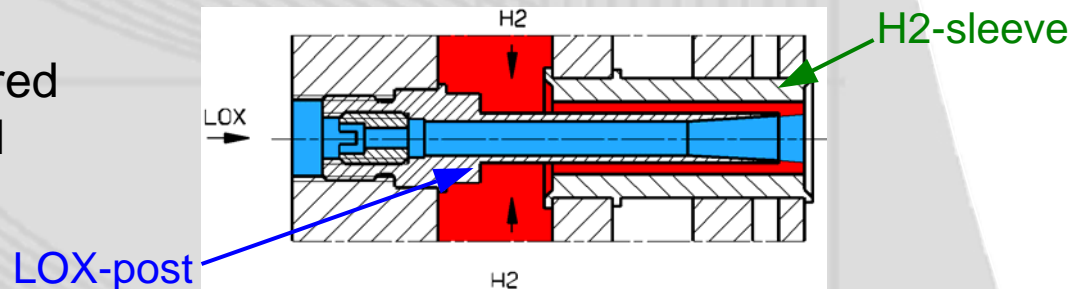


swirl coaxial



shear coaxial

Shown LOX-posts are centered in H2-sleeves to form coaxial LOX-H2 injection elements



Flowcheck of Injection Elements



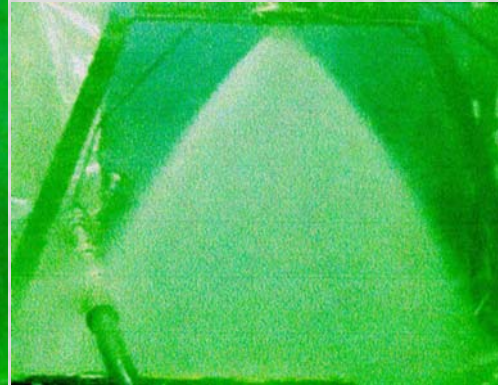
cross coaxial



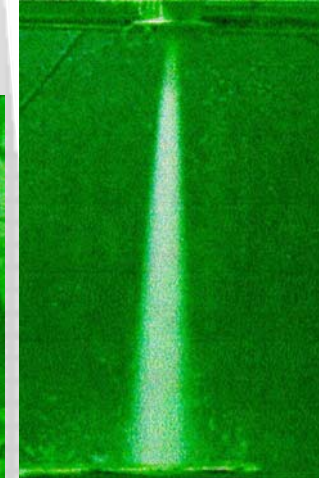
tri-coaxial



gasdynamic
coaxial



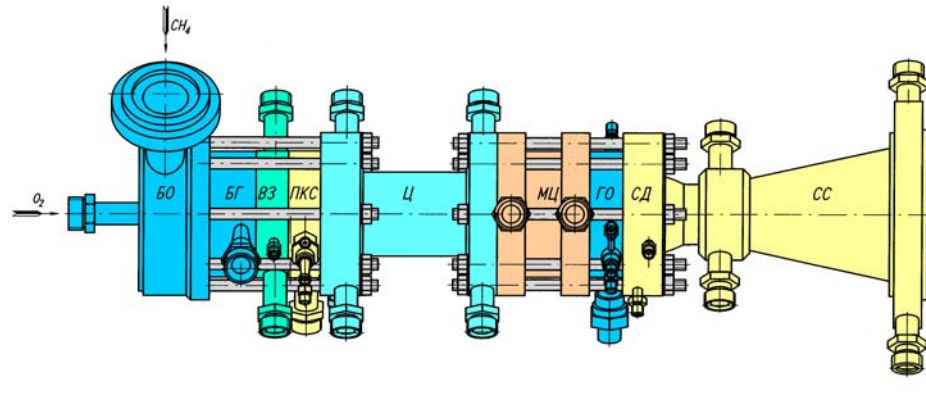
swirl coaxial



shear coaxial

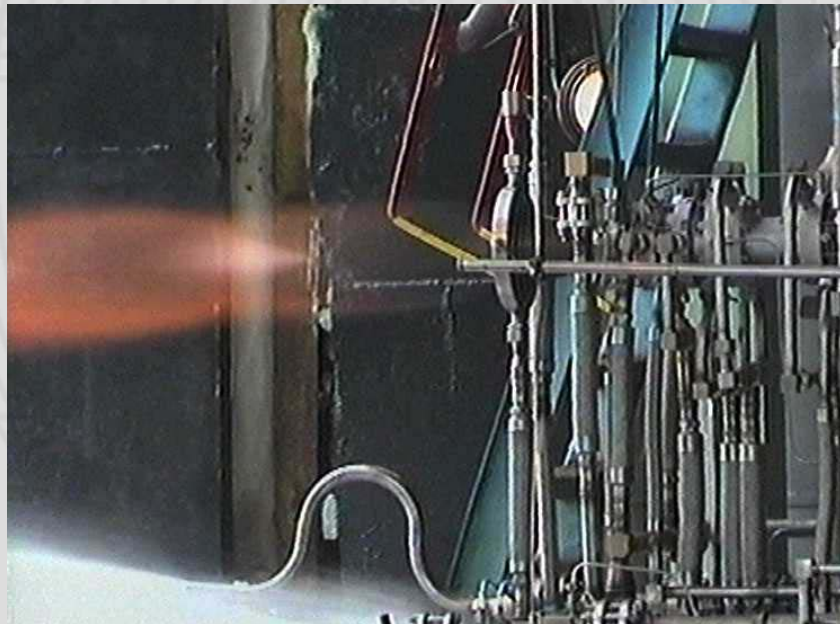
Flow checks with water and air were performed to assess the LOX-flow pattern of the various injection elements:

- LOX-posts with swirl produces widest LOX-injection cone.
- Cross flow-divider has some positive effect
- Flow from inner annulus of tri-coaxial element is almost axial.
- Gasdynamical element produces dense liquid-gaseous mixture.



KBKhA/EADS Subscale chamber:

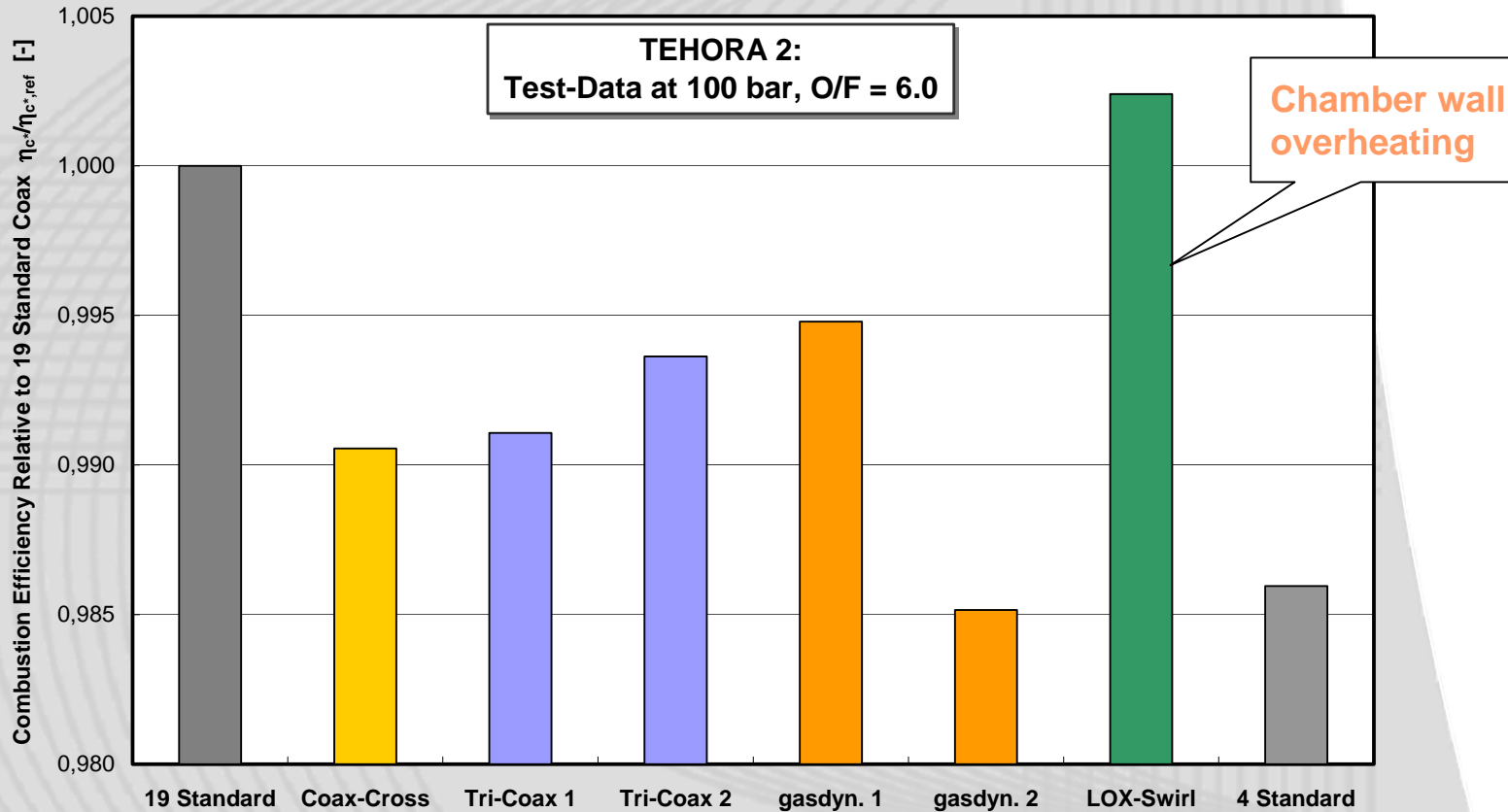
- Tested in past cooperation with LOX-GH2
- 8 water-cooled sections
- LOX-GH2
- Propellant flow rate ~7 kg/s
- Chamber pressure 52 - 104 bar
- Mixture ratio 3.9 - 7.3
- 5 different injector types



Test Objectives:

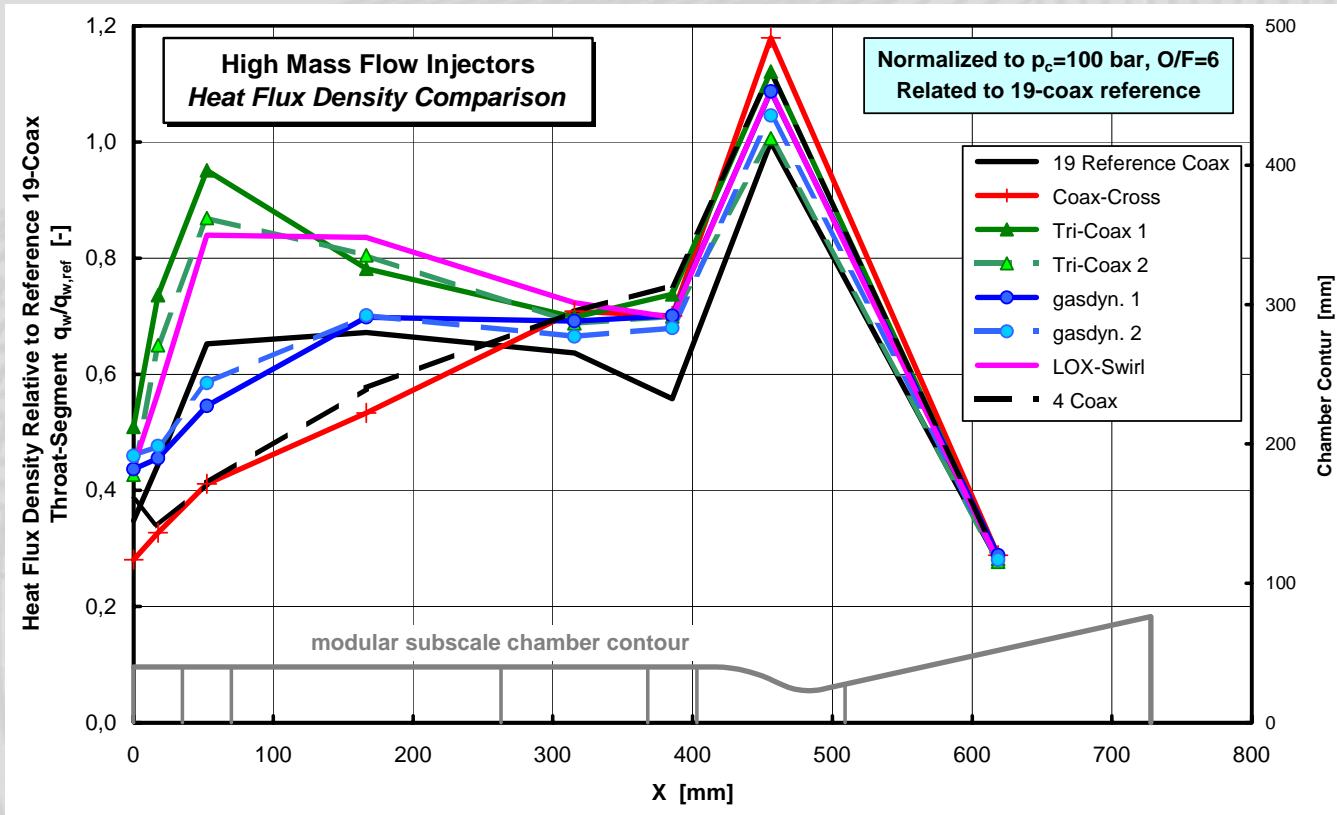
- ➔ Assess different injector elements
- ➔ Demonstrate injector performance
- ➔ Assess chamber heat flux
- ➔ Demonstrate stable operation and reliable ignition

Combustion Efficiency of Large Injection Elements



- ➔ Combustion efficiency related to reference 19-element injection head
- ➔ About 1.5% efficiency loss by element simply scaled up.
- ➔ Partly recovery of the efficiency loss possible with tri-coax and gasdynamic elements.

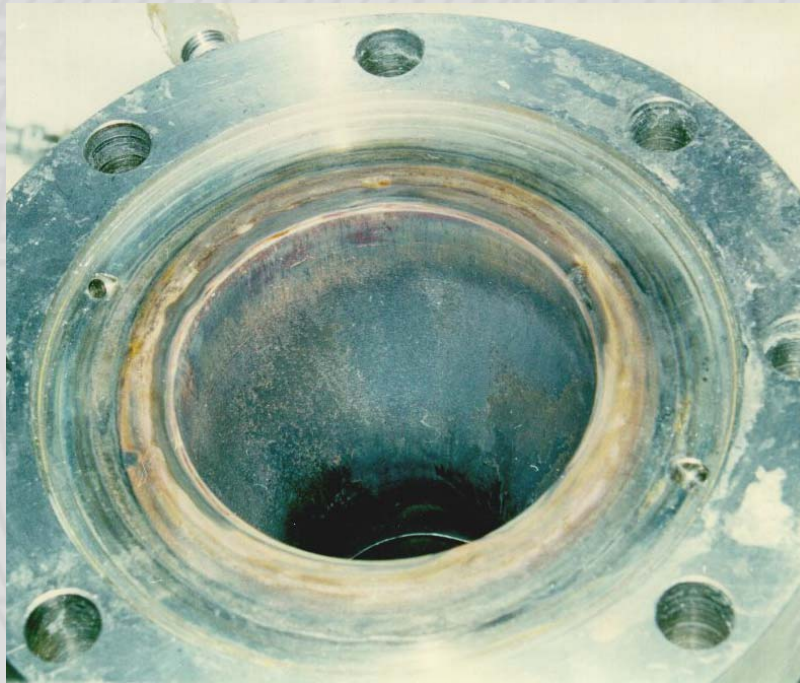
Heat Flux of Large Injection Elements



- ➔ Heat flux averaged over chamber section length and normalized to nominal operation and related to measured maximum of reference 19-element injection head.
- ➔ Extended atomization and mixing length for less performing elements.
- ➔ Heat flux peak near injector from tri-coax and from LOX-swirl elements.
(Chamber wall damage experienced by overheating from LOX-swirl element)

Hardware Status After Testing

→ No damage to chamber and injector observed except some discoloration in line with injection elements



Chamber throat after 31 tests and 1000 s run-time



Faceplate with large gasdynamical elements after 3 tests and 100 s run-time

Conclusions for Large Elements

- ➔ 22 Subscale tests with large elements in cooperation with KBKhA/Russia:
 - Combustion efficiency loss of about 1.5% by element simply scaled up.
 - Partial recovery of efficiency loss achieved with tri-coax and gasdyn. elements.
 - Best performance achieved with LOX-swirl element, but wall compatibility in large chambers to be demonstrated.

- ➔ Transfer of results to flight-type engines:
 - 4 large elements in square pattern may not be representative for large injector head, therefore, prediction of thrust chamber performance based on available test experience is difficult and questionable.
 - Tests with HM-7 or Vinci thrust chamber with 19 elements (instead of 90) in same pattern as reference subscale would probably be far more representative.
 - Significant cost reduction expected for reduction of element number by factor 4+.

Injection element concepts for hydrocarbon fuels (LOX-Methane and LOX-Kerosene).

Typical Main Chamber Injection Conditions

Full Scale Main Combustion Chamber Injection Conditions							
	Gas Generator Cycle			Staged Combustion Cycle			
	<i>fuel-rich gas generator</i>			<i>fuel-rich preburner</i>		<i>ox.-rich preburner</i>	
	Hydrogen	Methane	Kerosene	Hydrogen	Methane	Methane	Kerosene
LOX	95 K	95 K	95 K	95 K	95 K	—	—
Fuel	100 K	250 K	390 K	—	—	250 K	390 K
TEG	—	—	—	~650 K fuel-rich		~600 K oxygen-rich	

Full-Scale Main Chamber Injection Conditions for LOX-HC Engines:

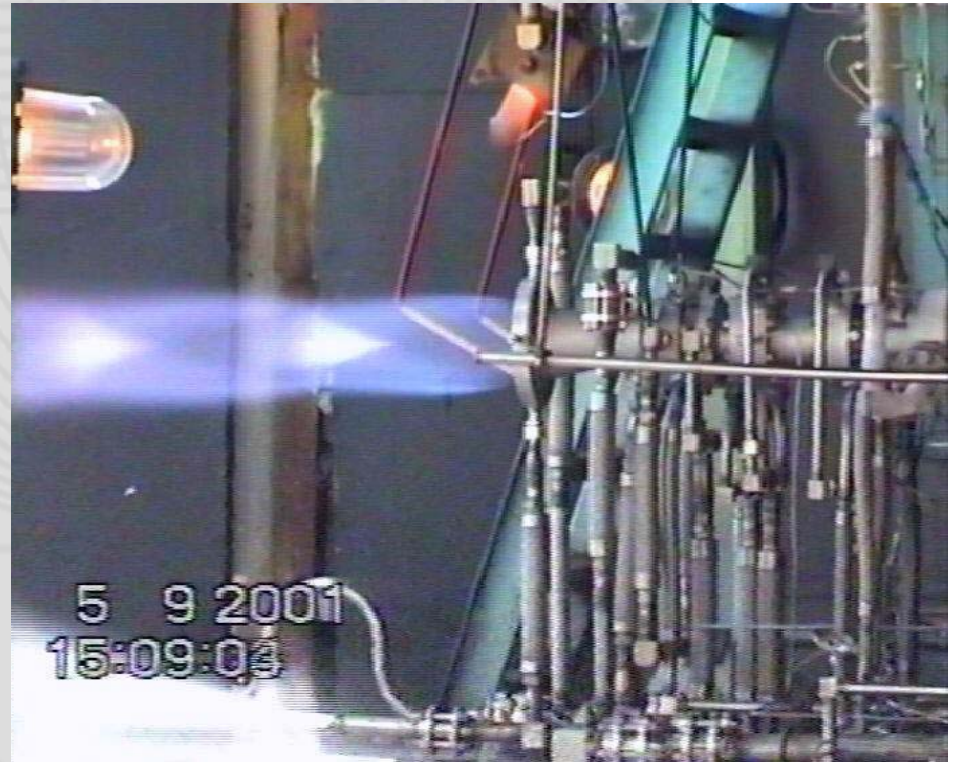
- LOX in Gas Generator cycle comparable to H₂-O₂ engines (e.g. SSME, Vulcain).
- Fuel heated to room temperature or even higher by chamber cooling.
- Injection of hot ox.-rich turbine exhaust in stage comb. cycle different to H₂-O₂ engines.

Simulation of Injection Conditions on Subscale Level:

- Hot ox.-rich turbine gas in staged combustion cycle simulated by ambient GOX.
- Natural gas at room temperature to simulate methane heated in chamber cooling.

LOX-Methane Subscale Testing

- ➔ 12 hot-tests with 8 injection element variants
- ➔ Chamber pressure 40 - 70 bar, mixture ratio 3.1 – 3.8
- ➔ Reliable and safe ignition by GOX-GCH4 torch-igniter

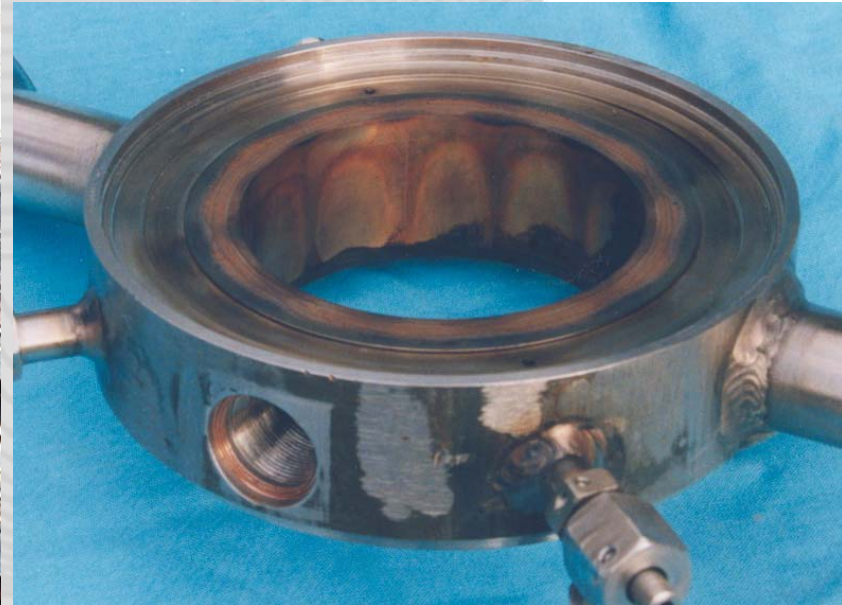


LOX-Methane Subscale Testing

→ Only very slight soot layer on chamber wall, easily removable

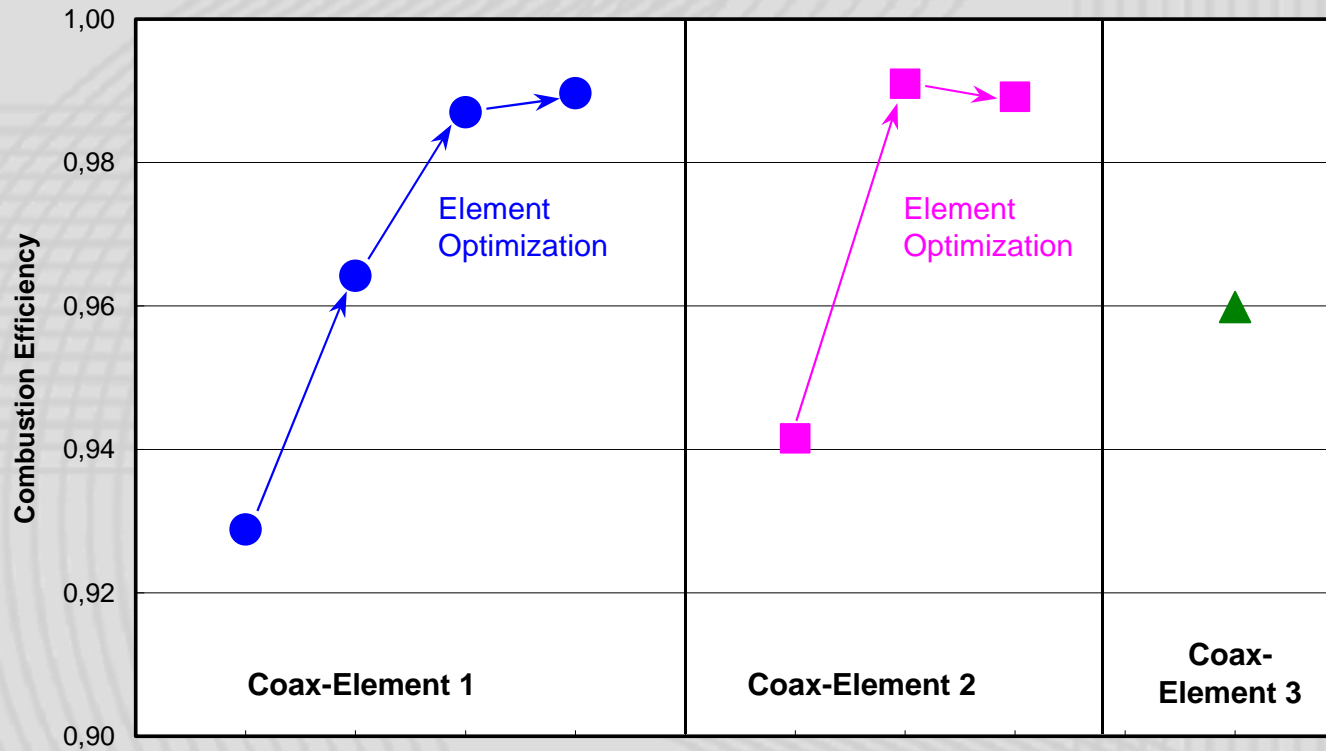


Faceplate after 3 tests and 115 s run-time



Chamber wall after 12 tests and 450 s run-time

LOX-Methane Subscale Testing

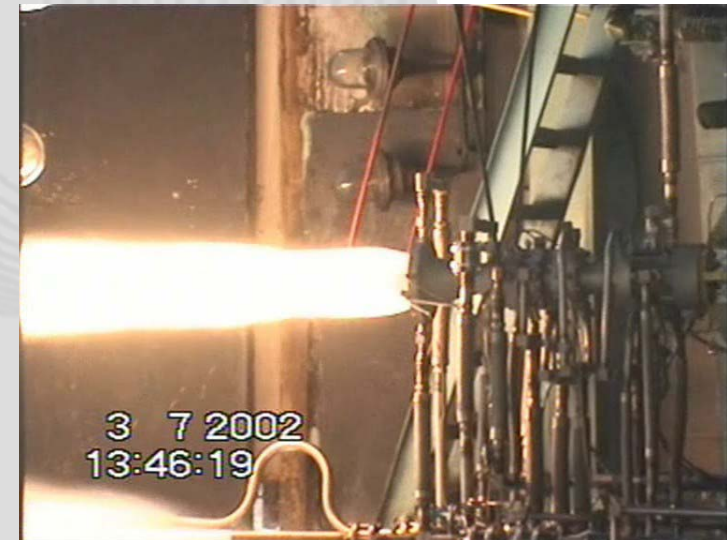


- ➔ Stable operation of three injection element types
- ➔ Optimization of combustion efficiency by variation of element geometry
- ➔ Combustion efficiency similar to LOX-H2 experience obtained

LOX-Kerosene Subscale Testing

Goal: Experimental study of various injection concepts

- Design and manufacturing of 3 injection heads and an igniter at KBKhA and EADS.
- Design and manufacturing an GOX-kerosene spark igniter at KBKhA.
- EADS injection head adapted to KBKhA chamber design
 - ➔ Experience with brazing of mechanically loaded structures.
- 7 Hot tests in June/July 2002 with LOX-Kerosene and 3 generic element-types
 - ➔ Characteristics of combustion stability and performance obtained for three heads.
 - ➔ Stable operation of the EADS head but slight leaks at brazing.
 - ➔ Reliable ignition.



LOX-Kerosene Subscale Testing

- Good performance of the injection elements, but two test-stops due to combustion instabilities.
- Slight soot deposition on faceplate and chamber wall, supposedly created during shut-off transients. Soot could be easily cleaned away.
- Although faceplate darkened during tests, no erosion or structural damage could be observed.



→ 12 Subscale tests with **LOX-methane** in cooperation with KBKhA/Russia:

- Combustion efficiencies comparable to LOX-H₂ experience obtained by variation of injection element parameters.
- Clean combustion of LOX-methane-rich natural gas (>98% CH₄), only slight soot layer on chamber wall, which could be easily removed.

→ 7 **LOX-kerosene** subscale test in cooperation with KBKhA/Russia:

- Good performance of the injection elements, but two test-stops due to combustion instabilities.
- Slight soot deposition on faceplate and chamber wall, no erosion or structural damage was observed.
- Good operation of the EADS injection head, but slight leaks at brazing.

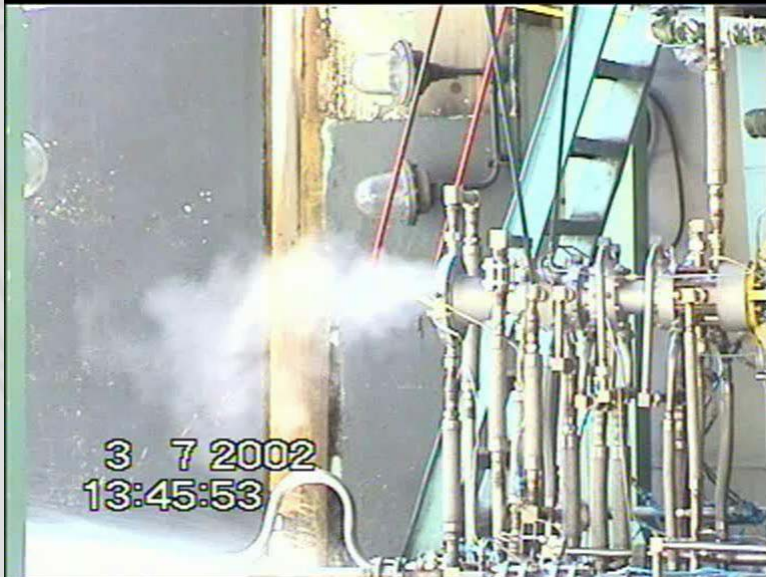
LOX-Hydrocarbon Subscale Testing



LOX-methane subscale test

Chamber pressure: 40 / 67 bar

Mixture ratio O/F: 3.37 / 3.48



LOX-kerosene subscale test

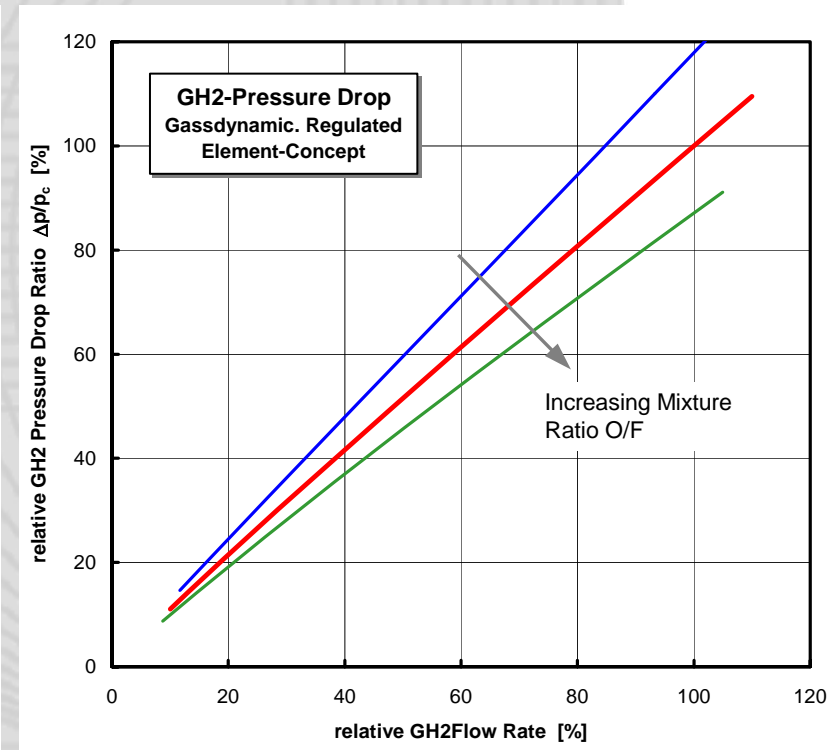
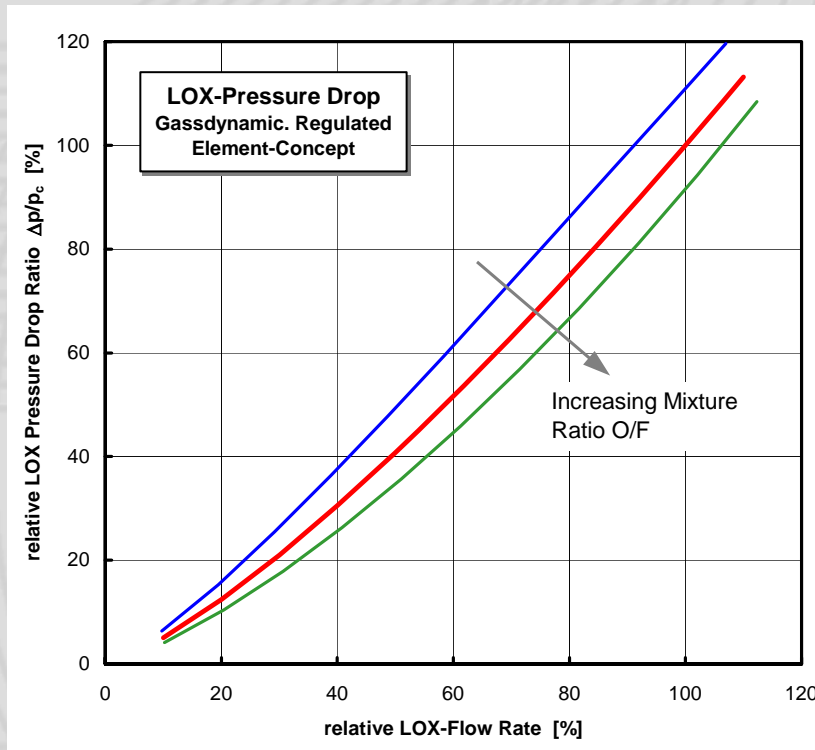
Chamber pressure: 43 / 68 bar

Mixture ratio O/F: 3.18 / 3.22

Back-up Charts

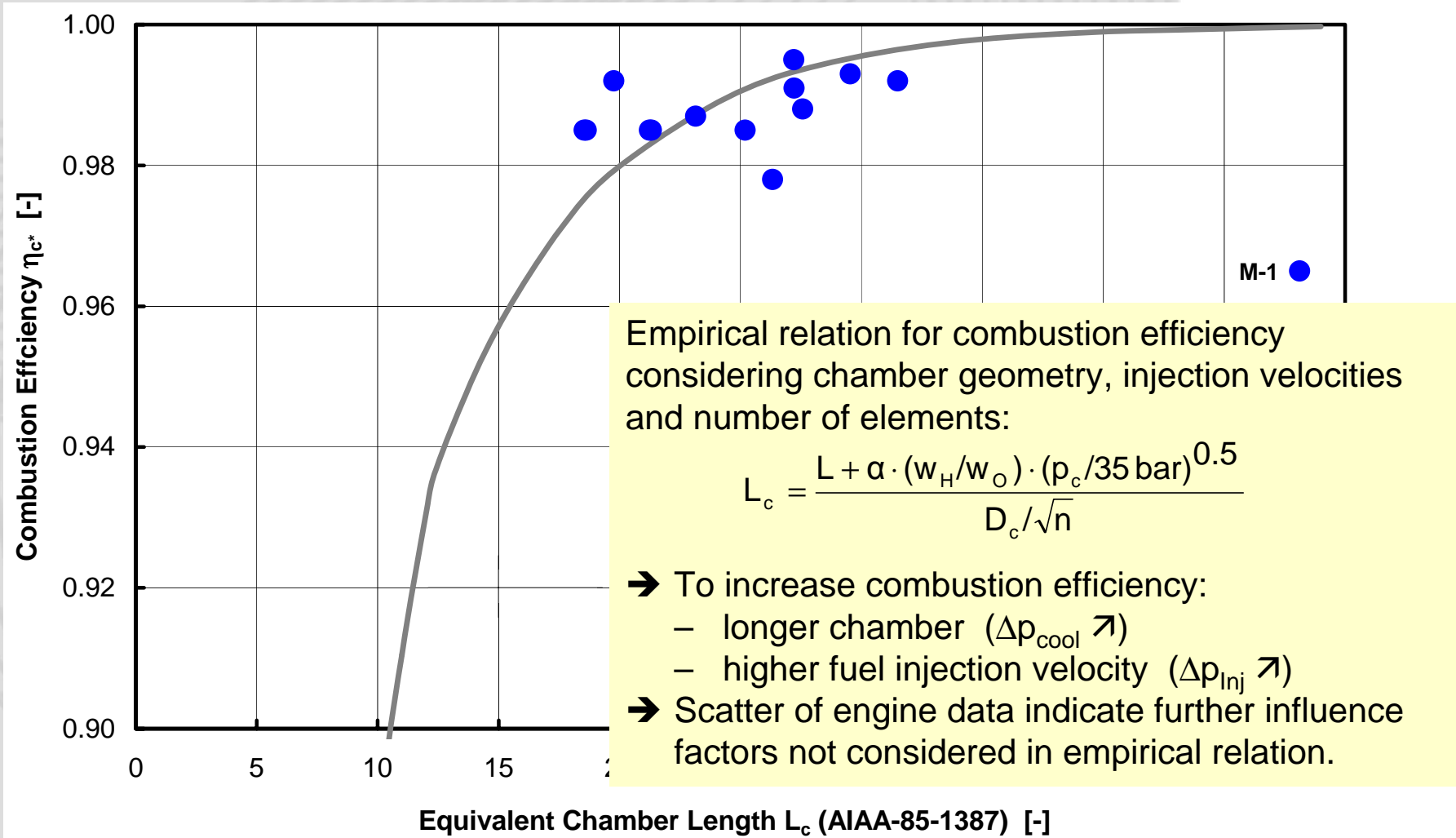
Throttlable Injection Element Test Results

Pressure Drop Characteristics of the Gasdyn. Regulated Element-Concept



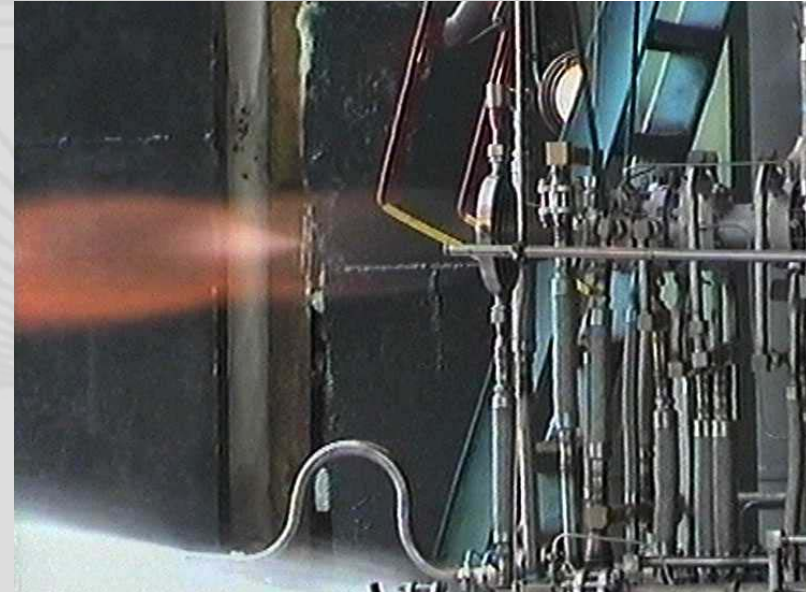
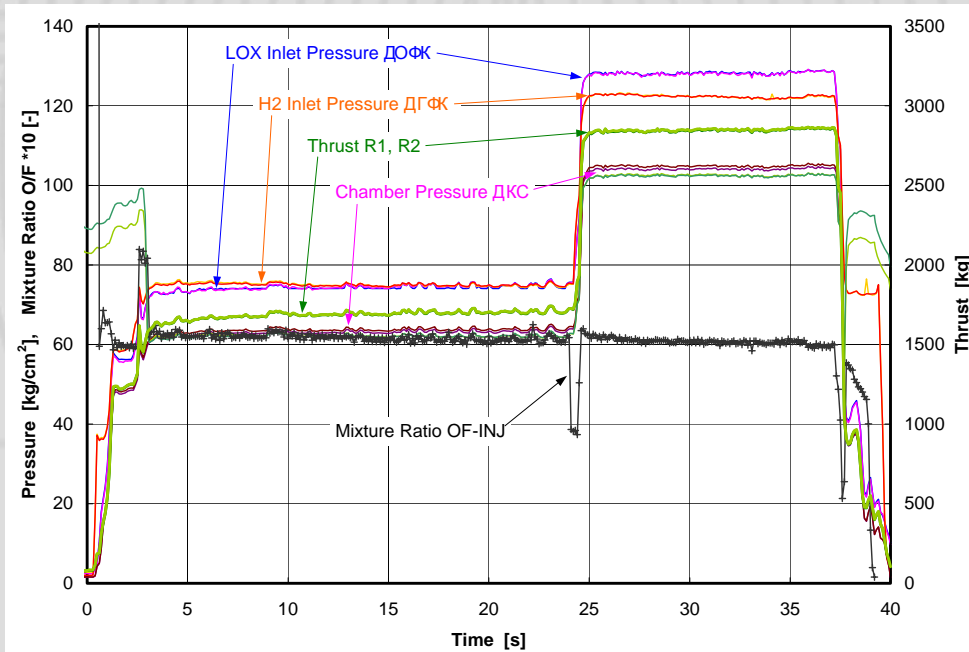
Mixture ratio variations have an influence on both LOX and GH2 pressure drop due to the coupling of the propellant flows within the injection element.

Injection Element Size Trend



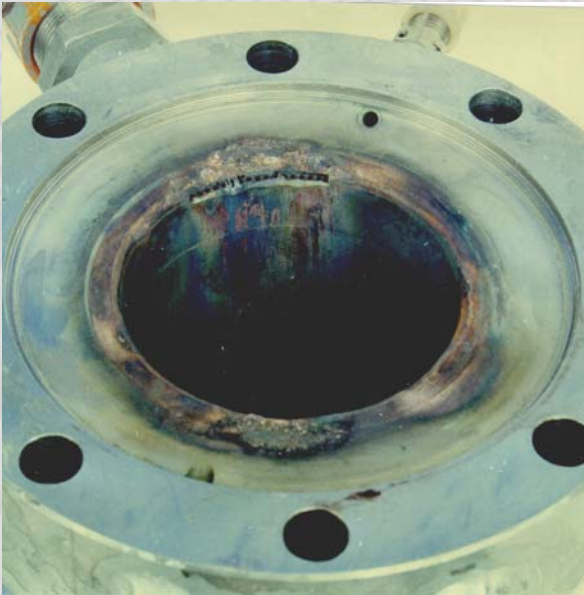
Large Flowrate Injection Element Subscale Testing

- 22 hot-tests with 8 injection element variants (incl. 19-element reference).
- Two chamber pressures (~55 bar and ~100 bar) realized in each test at various mixture ratios.
- Stable operation in all tests.
- Chamber wall overheating caused by LOX-swirl in two tests.

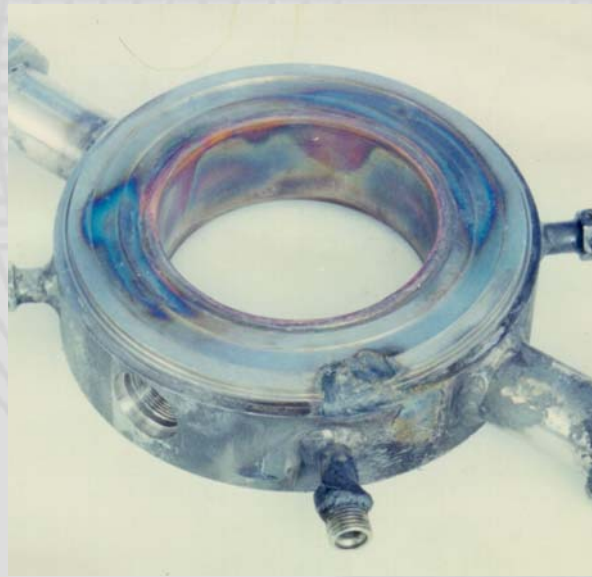


Hardware Status After Testing with LOX-Swirl

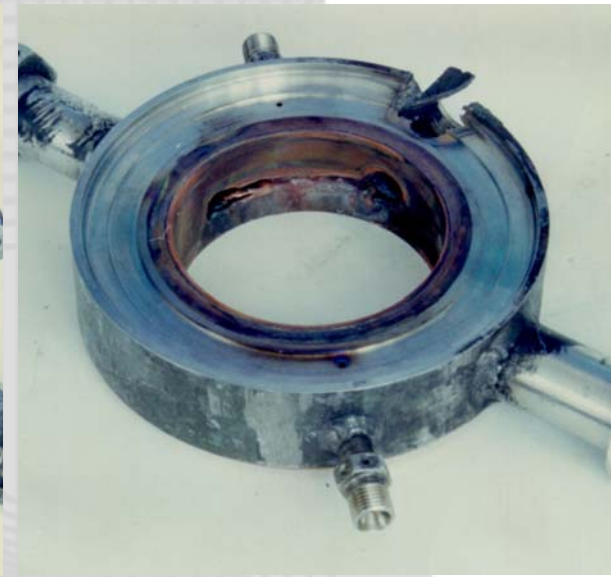
→ Damage to chamber and injector observed after tests of LOX-swirl elements



Chamber cylinder after test



Chamber sections near injector after test

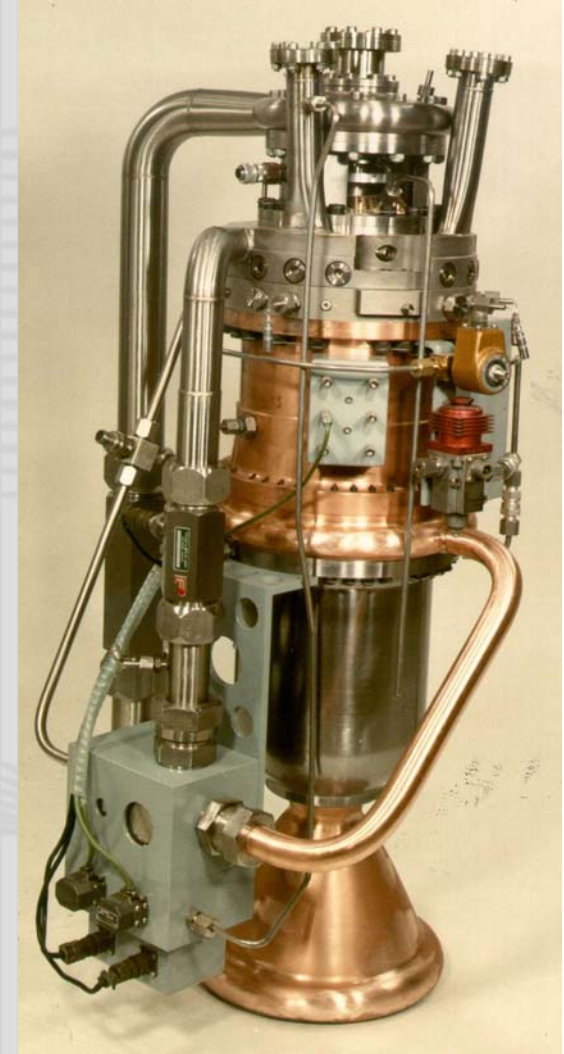


LOX-Kerosene Engine P111:

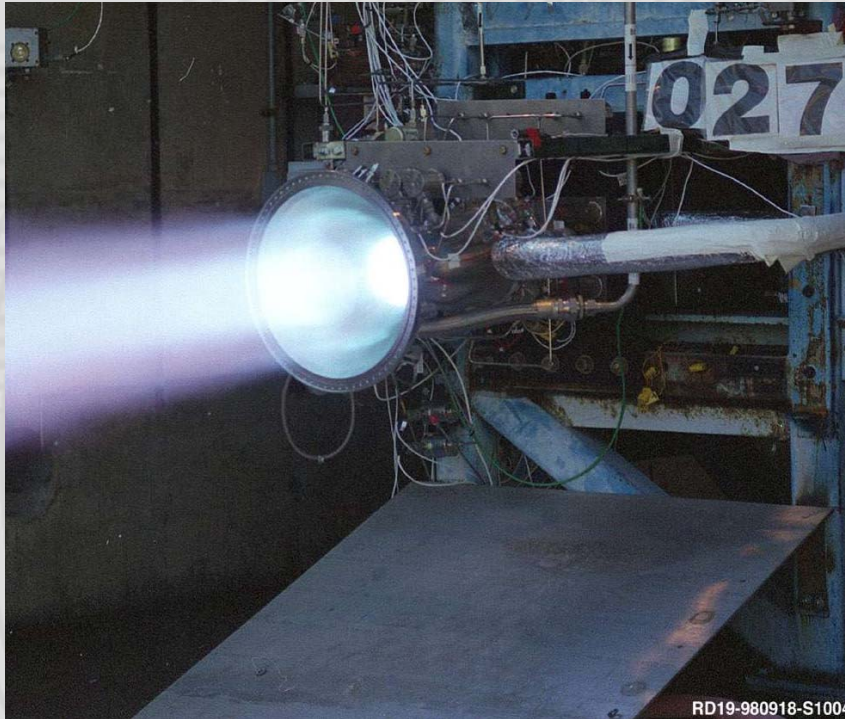
- Development 1956 – 1967 by Bölkow.
- LOX–Kerosene, staged combustion cycle, ox.-rich preburner.
- Single shaft turbopumps, axially integrated with preburner and main chamber.
- LOX-regeneratively cooled main chamber.
- Copper liner with milled cooling channels, electro-deposited copper and nickel close-out.

Performance Data:

Propellants:	LOX – Kerosene
Sea-level thrust:	49 kN (4.9 – 49 kN) (11 klb (1.1 – 11 klb))
Chamber pressure:	85 bar (1233 psia)
Mixture ratio:	2.7 (2.1 – 4)
Nozzle area ratio:	10.6
Spec. impulse:	306 s
Preburner pressure:	116 bar (1680 psia)
Preburner temperature:	920 K (1660 R)



Aestus Engine LOX-Ethanol Testing



Aestus engine used in Ariane 5 upper stage:

- NTO - MMH
- Chamber pressure 10 bar (145 psi)

Aestus tested with LOX-Ethanol with unchanged injector, but two necessary modifications:

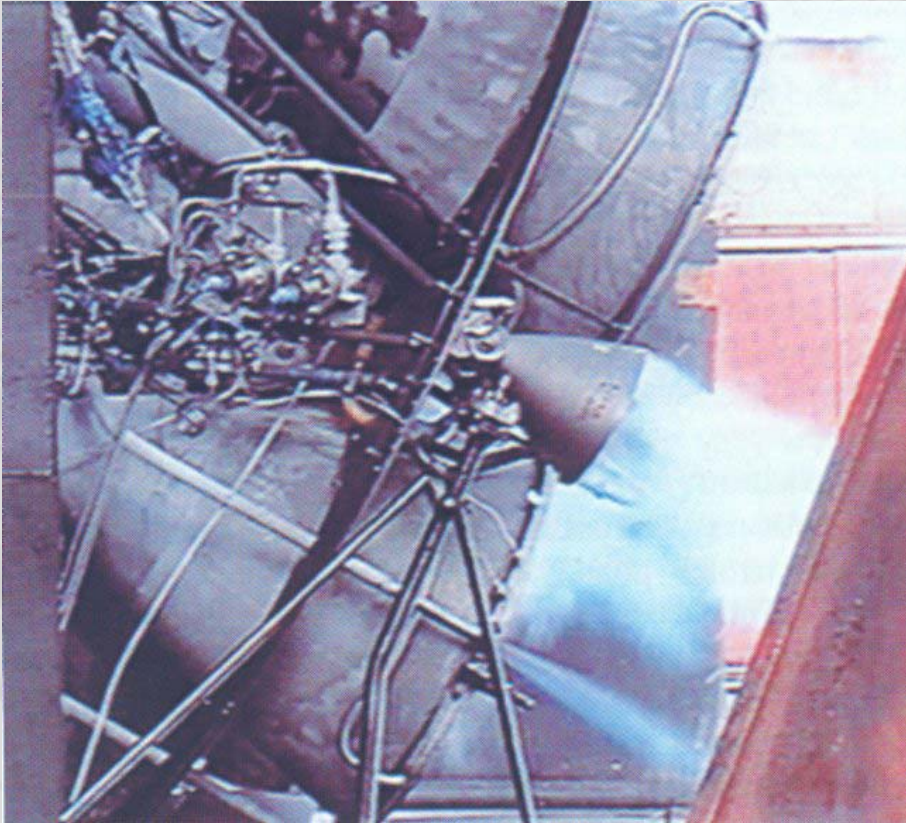
- Igniter added
- Seal material changed

16 tests with LOX-Ethanol +
8 Test with LOX-Methanol:

- ➔ Performance prediction confirmed
- ➔ Cooling prediction confirmed
- ➔ Ignition and stable operation demonstrated

Tests performed in cooperation with Boeing Propulsion & Power under NASA contract, 1999

RD-0110MD Engine LOX-Methanol Testing



RD-0110 engine used in Soyuz 3rd stage:

- LOX - Kerosene
- Chamber pressure 68 bar (986 psi)

RD-0110MD tested with LOX-LNG (liquefied natural gas). Some modifications of the test bench for LNG supply.

Two tests with LOX-LNG:

- ➔ Study of start-up transient
- ➔ Chamber pressure 54 bar (782 psi)
- ➔ Operational data of preburner, combustion chambers and turbopumps

Tests performed by KBKhA in Voronezh, 1998

Injector Issues with Different Propellant Combinations

D. Haeseler, C. Mäding,

EADS SPACE Transportation GmbH, Propulsion and Equipment, Munich, Germany

V. Rubinski, V. Kosmatcheva, V. Berezhnoy, N. Bratukhin,
 Chemical Automatics Design Bureau, Voronezh, Russia

Introduction

The reliable and effective propellant injection is a vital requirement for any rocket engine. EADS-ST (formerly MBB, Dasa, and Astrium, in succession) is responsible for the thrust chambers including the injection heads of the European liquid rocket engines like HM7, Vulcain, Aestus. A cooperation was set up since 10 years now with the Russian rocket engine developer KBKhA (Chemical Automatics Design Bureau), see e.g. [1] to prepare technologies for various future applications, studying injection elements for different propellants. This cooperation was supported by the respective space agencies DLR, and Rosaviakosmos. In the frame of this long cooperation named TEHORA the following injection technologies were explored theoretically and experimentally in subscale chambers:

- Characterization of different LOX-H₂ injection concepts for wide throttling range.
- Characterization of different LOX-H₂ injection concepts for large flowrate.
- Characterization of different injection concepts for LOX-methane and LOX-kerosene.

LOX-H₂ Injection Concepts for Wide Throttling Range

Introduction

Throttling of rocket engines in a wide range is required for certain reusable launch vehicle concepts studied currently, which are to perform a soft vertical landing with deeply throttled engines. A first vehicle concept DC-X was demonstrated successfully in 1998. Other TSTO vehicle concepts need throttling in the upper stage engines during stage separation for balance of forces. These concepts envisage high-performance reusable rocket engines. Furthermore, payload increase of current launchers like Ariane 5 may be achieved by throttling back the main engine after ignition at liftoff until throttling-up after booster separation. (the main launch thrust is provided by the two boosters for the Ariane 5 launcher).

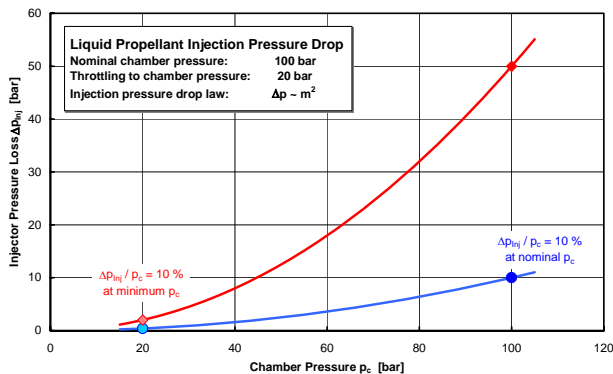


Figure 1: Injector pressure drop characteristics

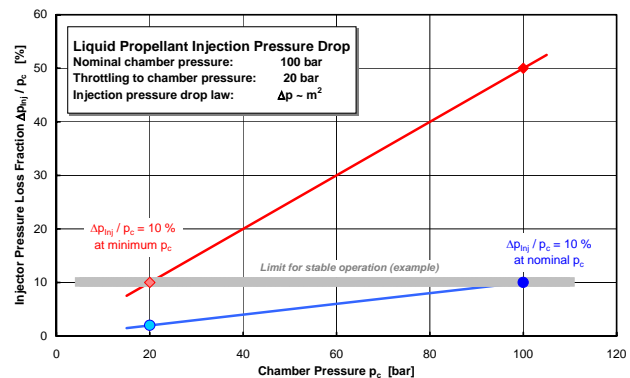


Figure 2: Relative injector pressure drop characteristics

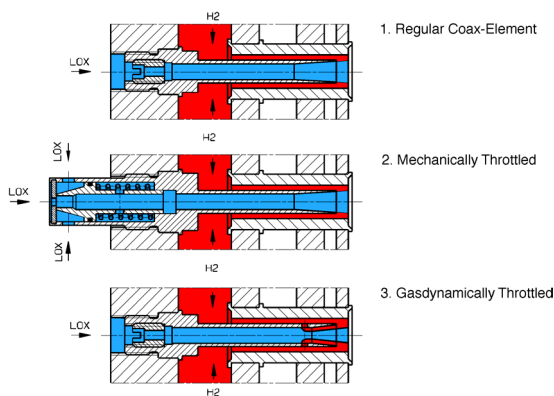
Usual coaxial elements produce liquid propellant pressure drops according to the square law $\Delta p_{inj} \sim m^2$. The pressure drop fraction $\Delta p_{inj}/p_c$ is one indicator (of several) for stable operation without feedline-coupled combustion instabilities. A minimum of typically 10% needs to be present for stable operation. Keeping the pressure drop fraction required for stable operation $\Delta p_{inj}/p_c$ (e.g. 10 %) at deeply throttled conditions results

in excessive pressure drop at nominal operations as illustrated in Figure 1 and Figure 2. Therefore, the goal is to develop an element concept with a (ideally) constant pressure drop fraction $\Delta p_{inj}/p_c$.

Application of regulated injection elements can provide a reduction of the pressure drop at nominal (100%) operation of throttling engines, which should lead to a significant reduction of the required turbopump load. This is important in particular for future long-life, reusable high-performance, high-chamber-pressure engines.

Injection Element Concepts

Injection elements were designed for liquid oxygen LOX and gaseous hydrogen GH₂ as they were present on the test bench for subscale testing. The usual coaxial injection element and two variations were tested, see Figure 3.



The mechanical regulated element incorporates a movable cylinder, which opens an axial and several lateral orifices for the liquid oxygen at high flow rate, while at low flow rate the cylinder moves such that the flow comes only through the axial orifice into the post.

The gasdynamically regulated element allows a small fraction of gaseous hydrogen GH₂ to flow into the LOX through some lateral orifices, such that the pressure drop in the LOX-post increases depending on the GH₂-flow into the LOX. That flow establishes itself autonomous with the occurring pressure cascade.

Figure 3: Tested element concepts

Subscale Test of Throttling Injection Element Concepts

Cold tests with water were performed to check the pressure drop characteristics of single elements of all three concepts. Several modifications of the gasdynamic element were tested with water and air.

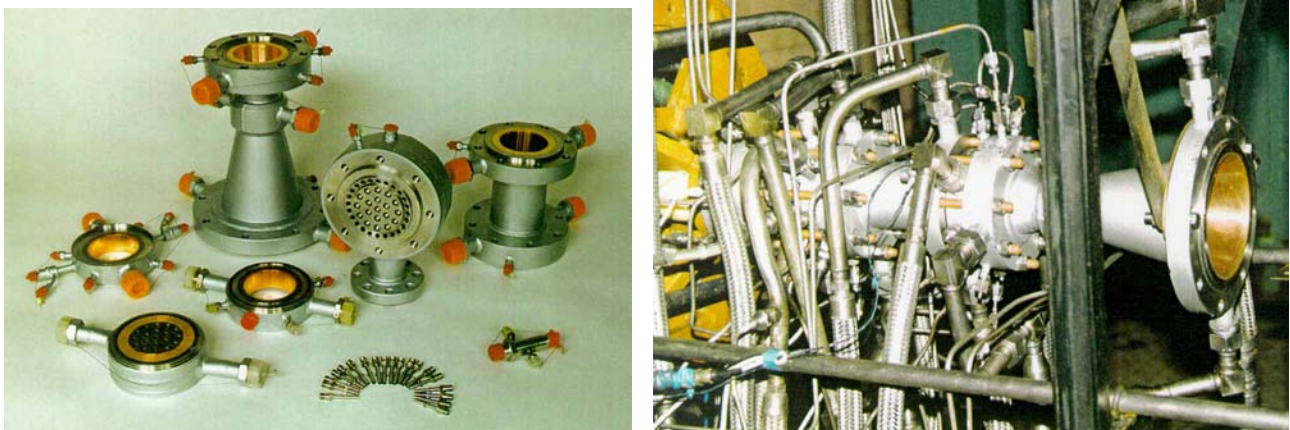


Figure 4: Subscale chamber and injection head parts (left) and assembly on test bench (right)

23 hot tests with a 19 element injection head in a subscale chamber were performed on a test bench of KBKhA in Voronezh, see Figure 4, including 6 variations of the gasdynamic element. The chamber pressure was varied in the range 19–108 bar and the mixture ratio in the range 5.0–8.2. The functionality of all three element concepts was demonstrated in the tests. Figure 5 shows operation at full throttle.

Figure 6 shows the LOX-pressure drop characteristics achieved in the tests reduced to the pressure drop and flow rate at nominal operation. The unregulated coaxial element showed the expected pressure drop characteristics $\Delta p \sim m^2$.

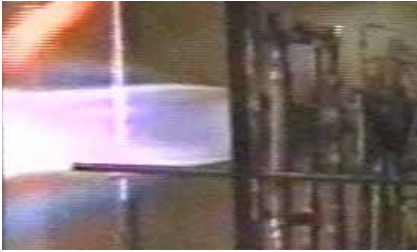


Figure 5: Throttled hot-tests: $p_c=98$ bar, O/F=6.4

The position change of the cylinder in the mechanically regulated element causes a change between two such characteristics. This characteristic of the mechanical element in the hot tests was in agreement with the characteristic derived from flow checks with water. The pressure drop was increased by a factor of 2.3 for throttling below 30%. Below 30% flow the cylinder is located at one stop, while for

flows above 50% it resides at the other stop. The transition range between 30 and 50% should not be used in steady-state operation to avoid oscillations of the free-moving cylinder.

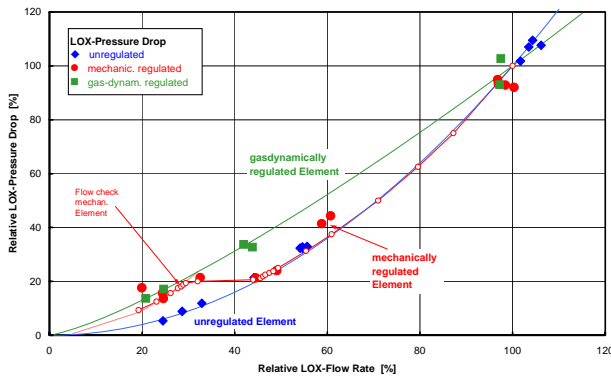


Figure 6: LOX-Pressure drop characteristics of the 3 tested element-concepts

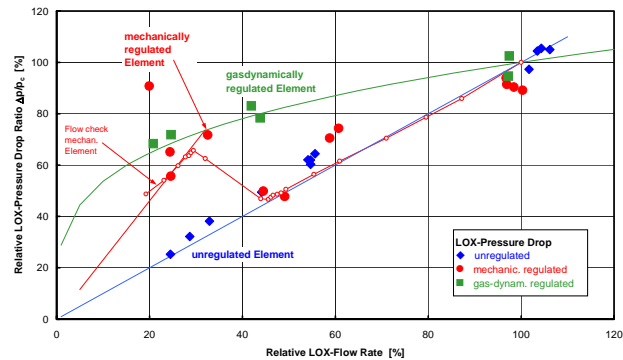


Figure 7: LOX-Pressure drop ratio characteristics of the 3 tested element-concepts

The relative LOX-pressure drop of the gas-dynamically regulated element was increased threefold at 20% throttling, while the pressure drop characteristic was followed a law of $\Delta p \sim m^{1.3}$. A comparison with flow test data demonstrated that the interaction of the two propellants in the LOX-post cannot be modeled reliably in the flow checks with inert simulating fluids. A significant influence of the mixture ratio variations on both LOX and GH₂ pressure drop due to the coupling of the propellant flows within the injection element has been observed.

The mechanically regulated element creates significant higher pressure oscillations compared to the coaxial element at deep throttling due to the springs used for the mechanical actuation while the gasdynamic element creates significant lower pressure oscillations due to pre-mixing of GH₂ and LOX.

A significant increase of the pressure drop at deep throttling relative to the pressure drop at nominal flow rate can be achieved with both the gasdynamic and the mechanical element types. No significant difference in the combustion efficiency of all three element concepts could be observed.

LOX-H₂ Injection Concepts for Large Flowrates

Injector Enlargement Objective

Current thrust chambers for rocket engines employ a high number of injection elements, for example the Vulcain engine employs 516 elements, the Space Shuttle Main Engine SSME has 600 elements, and the recent RS-68 thrust chamber has 628 elements. A high effort is spent for precise manufacturing of several parts, integration, and calibration in order to archive a homogenous flow field and a high combustion efficiency. A significant reduction of the number of elements is expected to lead to a considerable cost reduction due to the reduced number of parts to be manufactured and integrated into the injector body. Relaxed tolerances may be allowed for the manufacturing of the enlarged element parts. However, some disadvantages may be expected like reduced combustion efficiency due to less complete mixing, enhanced variation of heat load to chamber wall due to the less uniform flow profile in the chamber, and higher tendency to combustion instabilities.

The application of large injection elements requires a compromise between cost reduction and performance loss. Modifications of the injectors to counteract the performance loss may be applied, but probably will increase the cost.

Injector Size Consideration

The definition of the injection element size and the number of elements depends on many factors like elements type (e.g. shear coaxial, swirl coaxial), engine cycle (open gas generator cycle vs. closed staged combustion cycle), propellant temperature, pressure and density, chamber thrust and flow rate, etc. The propellant atomization and mixing for a complete as possible energy release is initiated by the injection element and continues downstream the length of the combustion chamber.

An empirical parameter for combustion efficiency deduced from LOX-H₂ combustor experiments is given in reference [2]. Two possibilities to counteract the performance loss follow for given chamber pressure:

1. Increase of the velocity ratio w_H/w_O . A certain minimum flow velocity for the oxidizer is necessary to obtain realistic dimensions for the LOX-post, thus the fuel velocity should be increased. The injection pressure drop will increase drastically while the acceptable injector inlet pressure is limited.
2. Increase of the total chamber length. A longer chamber will increase coolant pressure drop.

In consequence, the best mean to limit the efficiency loss of large injection elements seems to be additional design features to increase the propellant atomization and mixing, thus the combustion efficiency. Several large injection element variants with specific atomization and mixing design features were tested to check the associated performance loss and the heat load to the chamber wall. It was decided to test large elements in a pattern of only 4 elements in the injection head, compared to the reference of 19 elements, thus enlarging the elements by a factor of 4.75. The large injector elements were designed by KBKhA and EADS-ST.

Figure 8 shows the hardware for both the reference injection head with 19 coaxial elements and the injection head with 4 large standard coaxial elements. The modular design offers the possibility to exchange the LOX-posts for several design variants, use different fuel sleeve dimensions, and change the recess.

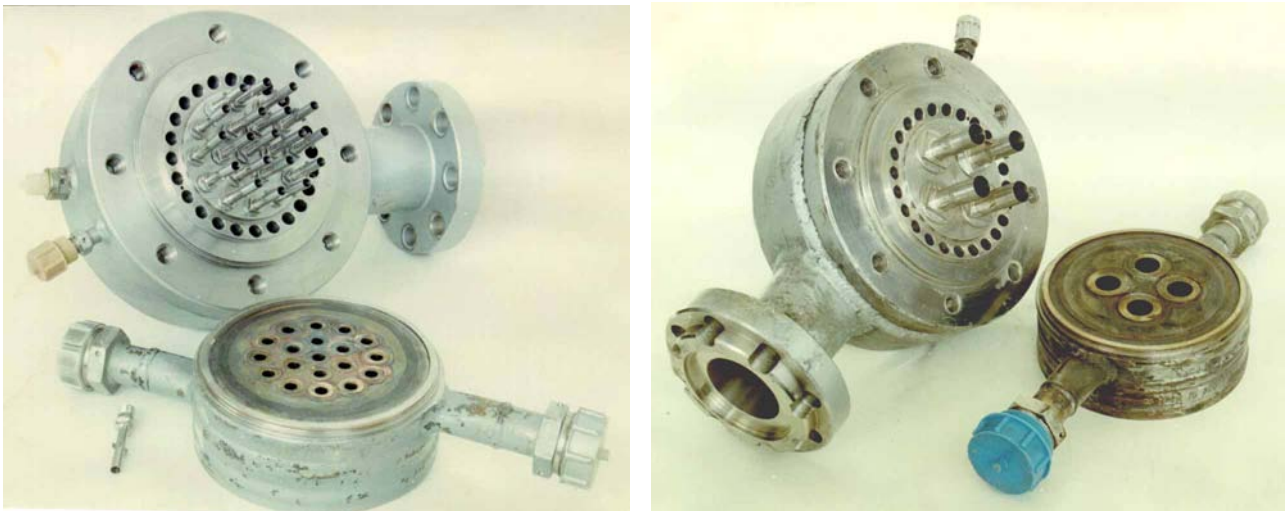


Figure 8: Reference 19-element injection head (left) and 4-standard large element injection head (right)

Injector Element Types

Following coaxial injection element types, composed of a LOX-posts and a hydrogen sleeves were studied:

Cross coaxial element: This element is like a shear-coaxial element with a cross mounted at the LOX-post exit intended to split the liquid oxygen stream and thus to enhance the LOX-atomization.

Tri-coaxial element: In the tri-coaxial element a part of the hydrogen flows through the central post while the remaining hydrogen flows through the outer annulus. Both hydrogen flows enclose the oxygen stream in the inner annulus, thus acting from both sides in order to atomize the liquid flow into droplets by shear forces. The contact area per flow rate is greatly increased in comparison to the usual coaxial element. Two different hydrogen flow distributions between center and outer annulus were tested. Tri-coaxial elements have already been tested for a future LOX-LH₂ gas generator [3]. In that investigation the obtained radial temperature distribution was more important than the achieved combustion efficiency.

Gasdynamic coaxial element: This element type was originally developed for high throttling ratios, see above. Two different hydrogen flow fractions for premixing in the LOX-post were tested.

Swirl coaxial element: The LOX-flow is swirled in the post by tangential injection through several orifices at the post inlet to enhance the interaction between oxygen and hydrogen. However, the oxygen flow cone may hit the wall and cause local overheating due to strong combustion adjacent to the chamber wall.

Shear coaxial element: The standard shear coaxial element was scaled up by a factor of 4.75 to compare directly a 19-element injection pattern to a 4-element pattern.

Injector Cold-Tests

All injector elements were cold-tested with water and air to define the pressure drop characteristics. A backpressure of 30 bar was provided in order to avoid local cavitation. Figure 9 compares the simulated LOX-flow of the different posts. Shown at far right is the almost axial flow from the large standard post for reference. The cross divides the flow and increases the flow cone. The flow from the inner annulus in the tri-coaxial element is almost as axial as the standard coaxial element. The gasdynamic post was tested with water and some air flow to simulate the gasdynamic effect inside the post. This creates a narrow and less dense flow cone. The broadest cone is created by the swirl LOX-post as intended.

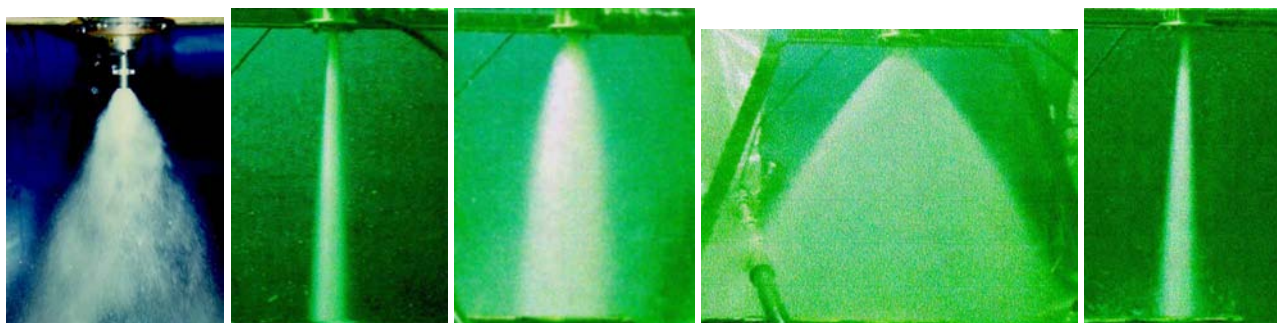


Figure 9: Water flow tests of the LOX-posts: Cross coaxial, tri-coaxial, gasdynamic coaxial, swirl coaxial, shear coaxial (left to right)

Subscale Injector Tests

The test specimen consists of a subscale chamber with several interchangeable injection heads. The chamber consists of several water-cooled sections to allow the evaluation of the heat fluxes. Liquid oxygen was injected at about 105 K while gaseous hydrogen was supplied at room temperature, i.e. about 280 K. At 100 bar chamber pressure, the propellant mass flow rate is about 7.2 kg/s. Ignition was performed by an electric igniter using GOX and H₂ provided by the Russian partner KBKhA.

Figure 10 shows the installation of the subscale chamber on the test bench in Voronezh. The chamber is mounted with the injection head end to a yellow thrust structure which includes a thrust measuring device. The nozzle end is supported laterally by two steel bands. The feedline for cryogenic oxygen is covered by a dark green insulation. The cooling water is supplied to the various chamber sections by numerous flexible connections. This installation allows some axial movement of the chamber with the thrust measurement.

Test results

A total of 22 tests were performed in the chamber pressure range 52 – 104 bar at mixture ratio in the range 3.9 – 7.3. Eight different injection element types were tested including the 19-element reference injection head. Figure 11 shows a typical test with an almost invisible flame, which becomes more opaque downstream of the typical Mach-disk. Most tests were conducted without problems. However, the two tests with the 4 coax elements with LOX-swirl experienced overheating of the chamber wall near the location where the swirl cone intersects the wall.

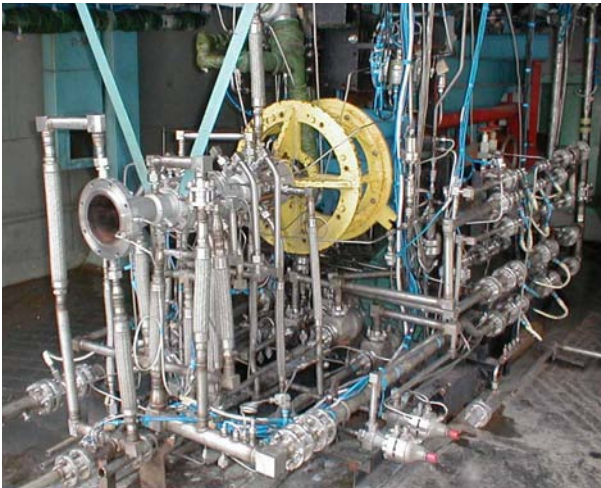


Figure 10: Subscale chamber on KBKha's test bench

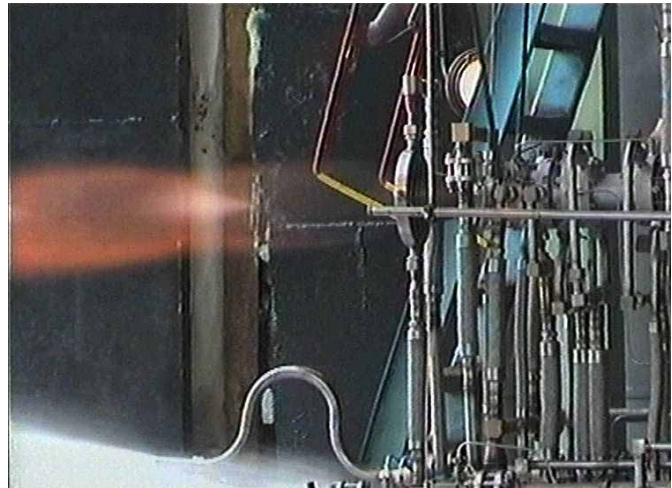


Figure 11: LOX-H2 large gasdynamical coaxial injection element test

Combustion Efficiency

Performance comparison was based on the combustion efficiency resulting from the experimental characteristic velocity and the theoretical value calculated according to the realized chamber pressure, mixture ratio, propellant inlet enthalpies, and water cooling heat flux, reduced to nominal chamber pressure of 100 bar and mixture ratio 6.0. Figure 12 compares the achieved combustion efficiency relative to the reference of 19 shear coax elements.

The scaled-up coaxial element showed a c^* -loss of 1.4% compared to the reference. The LOX-swirl element performed best, but overheated the chamber wall, thus this good performance may be reduced by necessary additional wall protection means (e.g. film-cooling or mixture ratio bias). The splitting of the LOX-flow by the cross could increase the performance, thus reducing the performance loss by ca. 0.5%.

The two variants each of the tri-coax element and of the gasdynamic element demonstrated the influence of the varied parameters on the performance. With optimized parameters the performance loss can probably be reduced to ca. 0.6% or even less. However, the available data for two variations each do not allow an estimation of the optimized parameters and their performance.

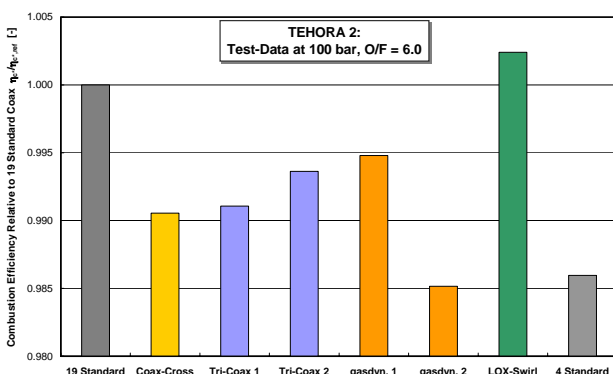


Figure 12: Achieved combustion efficiencies for the various injection elements relative to the reference efficiency of 19 standard shear coax elements

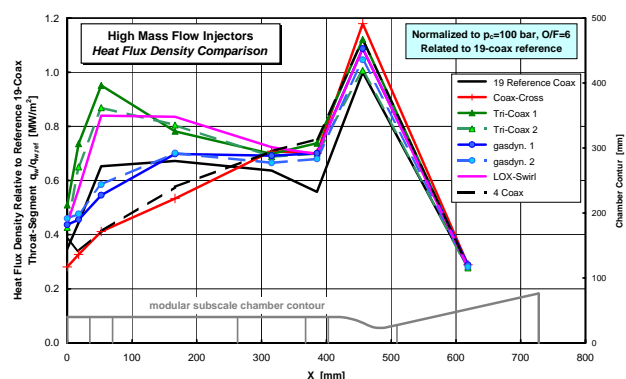


Figure 13: Heat flux along chamber wall for tested injection elements, normalized to reference conditions and relative to heat flux of throat-section with 19 elements

Heat Flux

Figure 13 compares the heat flux evolution along the chamber contour for the various elements tested. The heat flux data were normalized to the nominal operation conditions for better comparison. The peak heat flux near the throat does not show the real maximum but the average for the chamber throat section.

Both the scaled-up coax elements as well as the coax-cross element show heat flux profile indicating a longer extension of the atomization and mixing length. The heat flux plateau in the chamber barrel section is obtained more than 300 mm from the injection. The gasdynamic coax elements enhance the combustion process, thus the heat flux plateau is obtained already at about 150 mm from the injection.

The coax-swirl element and the two tri-coax variants show a quick mixing and combustion process resulting in a heat flux peak near the faceplate. In case of the swirl element overheating and damage to the chamber wall was observed, while the chamber wall remained undamaged in tests with the tri-coaxial elements.

Pressure Oscillation

Dynamic pressure oscillations were measured in the chamber, in the LOX-dome and in the hydrogen cavity. All tests showed a stable combustion. The coax-cross and the gasdynamic coax elements showed slightly higher pressure oscillations, the pressure oscillations with the coax-swirl and the large coax elements were even a bit higher. The tri-coax elements showed pressure oscillations depending on the hydrogen distribution to center and outer annulus. Higher performance was experienced with lesser pressure oscillations.

Hardware status after the tests

The chamber wall was in good condition after 22 and about 800 s tests. Some discoloration could be observed in the chamber cylinder in line with the large injection elements, see Figure 14 and Figure 15.

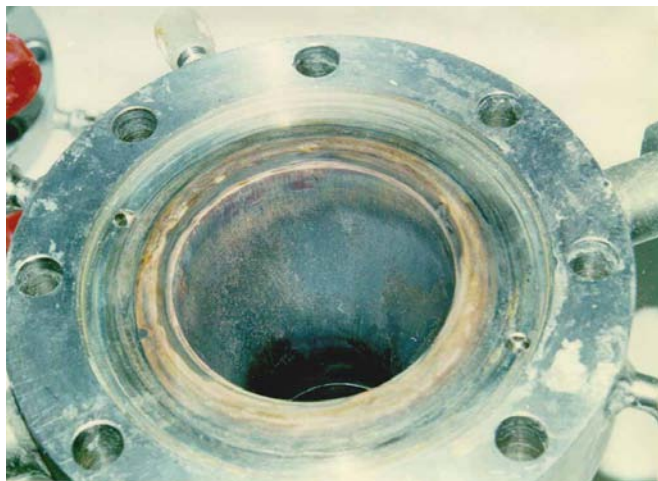


Figure 14: Subsonic chamber throat after 31 tests and 1000 s run time



Figure 15: Injection head with large gasdynamic coax elements after 3 tests

Prediction for utilization in large rocket engine chambers

A small chamber with 4 large injectors represents a large operational combustion chamber with many large elements to a far lesser degree than the small experimental chamber with 19 elements of standard size represents a full-scale chamber with many standard elements. In injector patterns of large chambers the majority of elements is situated in the flow core while only a limited number of elements is adjacent to the chamber wall. Global performance is influenced both by the interaction between the elements as well as by the interaction of elements and the chamber wall. In small chambers with few elements the ratio between both interactions is shifted significantly towards the wall-element interaction. Therefore, it is assumed that the performance loss experienced in the small chamber is much pronounced in comparison to a large chamber with large elements of the same type. For example, reducing the number of injection elements from more than 560 by a factor of 5 to 120 elements may result in an insignificant performance loss.

LOX-Hydrocarbon Injection Concepts

Previous Experience with Hydrocarbon Fuels

Recent investigations into the use of non-toxic propellants, also called hydrocarbon (HC) propellants, for propulsion of reusable first stages for medium launchers or booster stages for TSTO launch vehicles show

the potential to satisfy the market's performance and cost requirements. The expected advantages are high propellant density, reduced handling effort, and reduced safety precautions, see ref. [4, 5, 6, 7, 8]. Problem areas like sooting of combustion products on the hot gas side, coking of the fuel in the cooling channel, and material compatibility with combustion products and hot oxidizer-rich gases are reported. [9, 10, 11, 12, 13].

Several LOX-methane engine concepts have been developed, see ref. [14, 15, 16]. In 1998 KBKhA carried out two hot tests of the experimental demonstrator engine RD-0110MD with LOX-LNG (liquefied natural gas) while the engine was designed originally for LOX-kerosene, see ref. [17].

Tests of the Ariane 5 upper stage engine "Aestus developed by EADS-ST for the storable propellants NTO-MMH were carried out with LOX-methanol and LOX-ethanol in a cooperation of EADS-ST and Boeing Propulsion & Power towards a non-toxic orbital maneuvering engine OME for the Space Shuttle [18]. The successful ignition and stable operation was demonstrated.

First activities focused on the injection concepts, compatibility of current liner materials copper and copper-alloys with the hydrocarbon fuel and its combustion products, and electrical igniters.

Injection

LOX is injected almost at tank temperature in the gas generator cycles from the pump discharge into the main chamber and into the gas generator, while the fuel is heated in the chamber cooling, thereby lowering its density to the gaseous range at supercritical state in case of hydrogen and methane.

In the fuel-rich staged combustion cycles the hot fuel-rich turbine exhaust gas is injected into the main chamber at low mixture ratio. In the ox.-rich staged combustion cycles the turbine exhaust is injected into the main chamber at high mixture ratio like hot oxygen gas. The heating of the fuel in the chamber cooling is comparable to the gas generator cycles.

Coaxial injectors are used today in the European engines HM-7B, Vulcain, Aestus, and Vinci. The liquid-liquid injection for LOX-kerosene gas generator engines is similar to the liquid-liquid injection of storable propellants, while the gaseous methane from the chamber cooling is similar to gaseous hydrogen injection.

Ignition

The current European engines all use pyrotechnic ignition, while an electric spark igniter is foreseen for the Vinci engine. Electrical spark igniters for GOX-methane and GOX-kerosene were developed by KBKhA for the subscale testing. The operation was verified in ignition tests at various spark power levels.

Further preparatory research work is currently conducted by Stork Product Engineering and TNO PML, both in the Netherlands, aiming at an electrical GOX-HC igniter. EADS-ST is supporting this work in view of implementation of such an igniter in an European LOX-HC thrust chamber.

Subscale Injector and Chamber

The tests were performed with the subscale chamber described above. A temperature probe for measurement of the igniter hot gas is mounted at the nozzle exit, which is blown out of the nozzle immediately after ignition. Some 90 measurements of pressures, temperatures, vibrations, and flow rates are recorded.

Both LOX-methane and LOX-kerosene were chosen for experimental investigation from the system studies. Subscale tests were performed at gas-generator-cycle-like conditions. Liquid oxygen is injected around 105 K. Commercial natural gas from an urban gas station with about 98% methane content and liquid kerosene are injected at room temperature. The injection heads consist of body, LOX-posts, and fuel section with the faceplate. Several variants could be created by exchanging parts of the injection head, thus allowing variations of functional parameters of the injection elements.

LOX-Methane Testing

A total of 12 tests with LOX-methane were performed in 2001 on KBKhA's test bench in Voronezh in the chamber pressure range 35-70 bar at mixture ratio in the range 3.1-3.8. Three different basic injection element types designed by KBKhA and EADS-ST were tested. The tests demonstrated successful and reliable ignition and operation of all three injector types. Figure 16 shows a typical test with its characteristic blue flame colour, which is a pronounced contrast to tests with hydrogen. Reliable ignition was achieved in all tests in the subscale chamber.

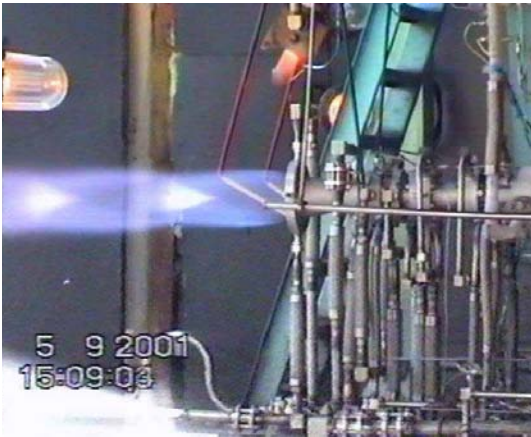


Figure 16: LOX-methane subscale chamber test by EADS-ST and KBKhA

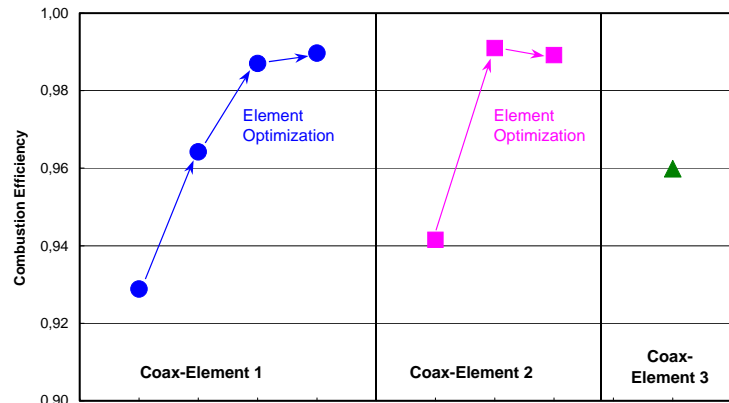


Figure 17: Results of injection element testing with LOX-methane

All three tested injection elements were of the coaxial type building upon the similarity to the experience acquired in past LOX-H₂ development programs. Impinging elements were not considered. During the test program some parameters like element geometry and injection velocity could be varied thanks to the modular design of the test hardware. Figure 17 shows the progress in optimization of the combustion efficiency achieved by this variation. It could be shown that with LOX-methane combustion efficiencies comparable to the experience from LOX-H₂ thrust chambers can be obtained.

The pressure drop oscillations measured in the combustion chamber and upstream of the injection elements did not show significantly higher values than those experienced in similar tests with LOX-H₂. The measured coolant water heating agreed well with the prediction based on theoretical heat transfer relations.

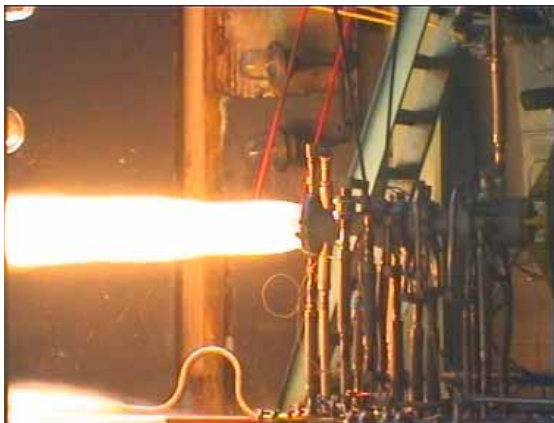


The chamber wall was in good condition after 12 tests. Some discoloration could be observed from the injector to downstream of the throat, see Figure 18. A slight soot layer was observed, which did not grow with increasing test duration and which could be cleaned easily. The injector faceplate was in good condition after 3 three tests.

Figure 18: Chamber wall section after 12 tests and 450 s run time

LOX-Kerosene Testing

Similar tests with LOX-kerosene were performed in 2002. Three basic injection element types designed for the injection of liquid oxygen and liquid kerosene were tested. Two of them are based on designs for KBKhA gas generator cycle engines like RD-0110. The coaxial EADS-ST injection element was based upon the experience gained during the joint Boeing-Rocketdyne/EADS-ST RS-72 Pathfinder program [18] with NTO/MMH propellants. The injection element was adapted to the different propellant densities and flow rates imposed by LOX-kerosene while keeping the same liquid/liquid injection principle.



7 tests were conducted at a mixture ratio of around 2.6-3.2 and chamber pressures of 40-70 bar. The burn times achieved per test are around 37 sec. The ignition was always smooth and reliable. The flame showed a yellow colour typical for kerosene combustion, see Figure 19.

Figure 19: Subscale chamber test with LOX-kerosene

The most tests were performed fully successfully. However, combustion instabilities occurred during the transition phase into the main stage leading to an automatic test stop in two cases. Both the KBKhA and the EADS-ST injection elements showed smooth transients and stable operation, except those two cases noted above. The combustion efficiency was evaluated up to 98%, which compares well with our experience of RS-72 tests using the NTO-MMH propellants combination.

The chamber wall turned out to be in good condition. Some slight soot layer was wiped away between tests. This soot layer was caused primarily not during the steady-state operation of the chamber but during the shut-down transients when the combustion is poor due to transient mixture ratio variations. Figure 20 shows this effect of soot deposition on the injector.

The continuation of the successful cooperation with KBKhA in the frame of the TEHORA project is initiated with further design and experimental work. Tests of subscale chambers and injectors are planned simulating the injection conditions of a staged-combustion cycle main chamber with LOX-Kerosene. In addition the cooling characteristics of the fuel shall be explored.



Figure 20: LOX-kerosene injector head before and after 3 tests and 110 s run-time showing soot deposition

Summary and Conclusion

Injection elements for an increased propellant flow rate may offer the possibility to reduce manufacturing costs by a reduction of parts and integration effort and by possibly less demanding tolerance requirements. Design features may be incorporated into large elements like flow dividers, LOX-swirl, gasdynamic pre-mixing, or tri-coaxial elements to limit the expected performance losses.

Subscale chamber tests with different large injection elements with LOX-H₂ demonstrated successful operation of those elements except for the coax-swirl elements, which caused overheating and damage of the chamber wall. The added design features could reduce the performance loss compared to scaled-up shear coaxial elements by a factor of 2. The most promising performance increase could be obtained with gasdynamic coax elements and with tri-coaxial elements. The design parameters need to be optimized.

It is very difficult to predict the performance losses to be expected in large combustion chambers with many large elements from the 4 element pattern tested in the small experimental chamber. The performance loss in large chambers may be less pronounced, making large injection elements more interesting. Further testing with a seven-element pattern is in progress to get additional experimental performance and heat flux data.

Non-toxic hydrocarbon propellants have gained interest recently promising better environmental conditions for easier handling and thus reduced space transportation costs. Liquid methane provides the best performance and chamber cooling capability but requires cryo-cooling and no operational engine has been developed so far. Kerosene is denser and easily storable but the chamber requires thermal protection coating or film-cooling due to the low coking temperature limit. A huge experience is available for LOX-kerosene in particular from Russian engines. The danger of corrosion due to small impurities in methane was observed independently by various authors and needs to be checked for the envisioned liner material.

Tests with LOX-methane demonstrated successful ignition and operation of three injector types. The combustion efficiency could be increased by variation of injector parameters to values as high as the past experience with LOX-H₂. A GOX-methane torch igniter was used successfully.

Tests for LOX-kerosene with three injection element designs for liquid-liquid injection were performed. Most of the tests were conducted successfully and indicate good injector element behavior including reliable ignition using a GOX-kerosene spark igniter. In two cases the tests had to be stopped due to excessive combustion instabilities. A slight soot layer that had formed could be cleaned away easily.

Acknowledgements

The studies were performed in the frame of a project co-funded by the German Aerospace Center (DLR) under project number 50JR9911. This support is gratefully acknowledged here. The LOX-HC injector element tests were contracted by KBKha with coordination by Rosaviakosmos. The fruitful cooperation with these two institutions is acknowledged here as well.

References

1. D. Haeseler, C. Mäding, V. Rubinskiy, V. Gorokhov, S. Khrisanfov: *Experimental Investigation of Transpiration-cooled Hydrogen-Oxygen Subscale Chambers*, AIAA 98-3364, 34th AIAA Joint Propulsion Conference, July 1994, Cleveland, OH.
2. N. Yatsuyanagi, H. Gomi, H. Sakamoto: *An Empirical Expression of the C* Efficiency of LO₂/Hydrogen Rocket Combustor with Coaxial Injector*, AIAA-85-1387, 21st AIAA Joint Propulsion Conference, July 1985, Monterey, CA.
3. J. Berque, M. Sion, J-L. Thomas: *Tricoaxial Injector Technology Development*, AIAA 99-2492, 35th AIAA Joint Propulsion Conference, June 1999, Los Angeles, CA.
4. H. Burkhardt, M. Sippel, J. Klevanski, A. Herbertz: *Comparative Study of Kerosene and Methane Propellants for Reusable Liquid Booster Stages*, AIAA-2002-5235, 11th AIAA/AAAF International Space Planes and Hypersonic Systems and Technologies Conference, October 2002, Orleans, France.
5. J. Hopkins: *Selection of Lockheed Martin's Preferred TSTO Configurations for the Space Launch Initiative*, IAC-02-V.4.03, 53rd International Astronautical Congress, October 2002, Houston, USA.
6. D. Haeseler, C. Mäding, V. Roubinski, S. Khrissanfov: *LOX-Hydrocarbon Rocket Engines and Thrusts Chamber Technologies for Future Launch Vehicle Applications*, IAC-02-S.2.01, 53rd International Astronautical Congress, October 2002, Houston, USA.
7. D. Haeseler, A. Götz, A. Fröhlich: *Non-Toxic Propellants for Future Advanced Launcher Propulsion Systems*, AIAA-2000-3687, 36th AIAA Joint Propulsion Conference, July 2000, Huntsville, AL.
8. A. Götz, C. Mäding, L. Brummer, D. Haeseler: *Application of Non-Toxic Propellants for Future Advanced Launch Vehicles*, AIAA-2001-3546, July 2001, Salt Lake City, USA.
9. L. Schoenmann: *LOX/Propane and LOX/Ethanol Combustion Chamber Heat Transfer*, J. Propulsion Vol. 7 No. 4 pp. 538-548 (AIAA-87-1857)
10. R. Hernandez, S. Mercer: *Carbon Deposit Characteristics of LO₂/HC Propellants*, AIAA 87-1855, 23rd AIAA Joint Propulsion Conference, June 1987, San Diego, USA.
11. S. Rosenberg, M. Gage: *Corrosion Prevention in Copper Combustion Chamber Liners of Liquid Oxygen/Methane Booster Engines*, AIAA 90-2119, 26th AIAA Joint Propulsion Conference, June 1990, Orlando, USA.
12. K. Liang, B. Yang, Z. Zhang: *Investigation of Heat Transfer and Coking Characteristics of Hydrocarbon Fuels*, J. Prop. and Power, Vol. 14 No. 5 (Sept.-Oct. 1998), pp. 789-796.
13. B. Stiegemeier, M. Meyer, R. Taghavi: *A Thermal Stability and Heat Transfer Investigation of Five Hydrocarbon Fuels: JP-7, JP-8, JP-8+100, JP-10, and RP-1*, AIAA 2002-3873, 38th AIAA Joint Propulsion Conference, July 2002, Indianapolis, USA.
14. P. Pempie, H. Gorecki: *High Thrust LOX-CH₄ Engine*, ISTS 2000-A-01V, 22nd International Symposium on Space Technology and Science, Morioka, Japan, 2000.
15. I.A. Klepikov, B.I. Katorgin, V.K. Chvanov: *The New Generation of Rocket Engines, Operating by Ecologically Safe Propellant "Liquid Oxygen and Liquefied Natural Gas (Methane)"*, IAF-97-S.1.03, 48th International Astronautical Congress, October 1997, Turin, Italy.
16. W.A. Visek: *LOX/Hydrocarbon Booster Engine Concepts*, AIAA-86-1687, Huntsville, 1986.
17. V.D. Gorokhov, V.S. Rachuk: *CADB's Development of the LRE Operating with Liquefied Natural Gas and Liquid Oxygen*, Green Propellant Conference, ESTEC, Noordwijk, The Netherlands, June 2001.
18. A. Darby, A. Little, C. Tang, G. Langel, G. Taubenberger, G. Obermaier, *Development of the Storable Upper Stage Engine for Global Market*, AIAA-2000-3783, 36th AIAA Joint Propulsion Conference, Huntsville, AL, July 2000



INJECTORS FOR LONG LIFE COMBUSTION DEVICES

Prof. Vladimir Bazarov

Purdue University

FIFTH INTERNATIONAL SYMPOSIUM ON
LIQUID SPACE PROPULSION

Long Life Combustion Devices Technology

Chattanooga, TN 27-30 October 2003

School of Aeronautics and Astronautics





Life-limiting factors in LRE combustion devices

- High local heat fluxes, caused by high pressure, gas density and high velocity of combustion products
- Concentration non-uniformity and local zones of oxidizer-rich gases
- High level and wide spectrum of mechanical vibrations
- Combustion instability
- Combustion unsteadiness, accompanied by high amplitude and wide frequency range of gas pressure, velocity and vorticity pulsation
- Most of them depend on injector design and operation.





Propellant injection parameters that influence LRE life

Stationary parameters

- Composition and temperature fields of combustion products
- Flow velocity and intensity of reverse flows near the wall
- Spectrum and quality of atomization

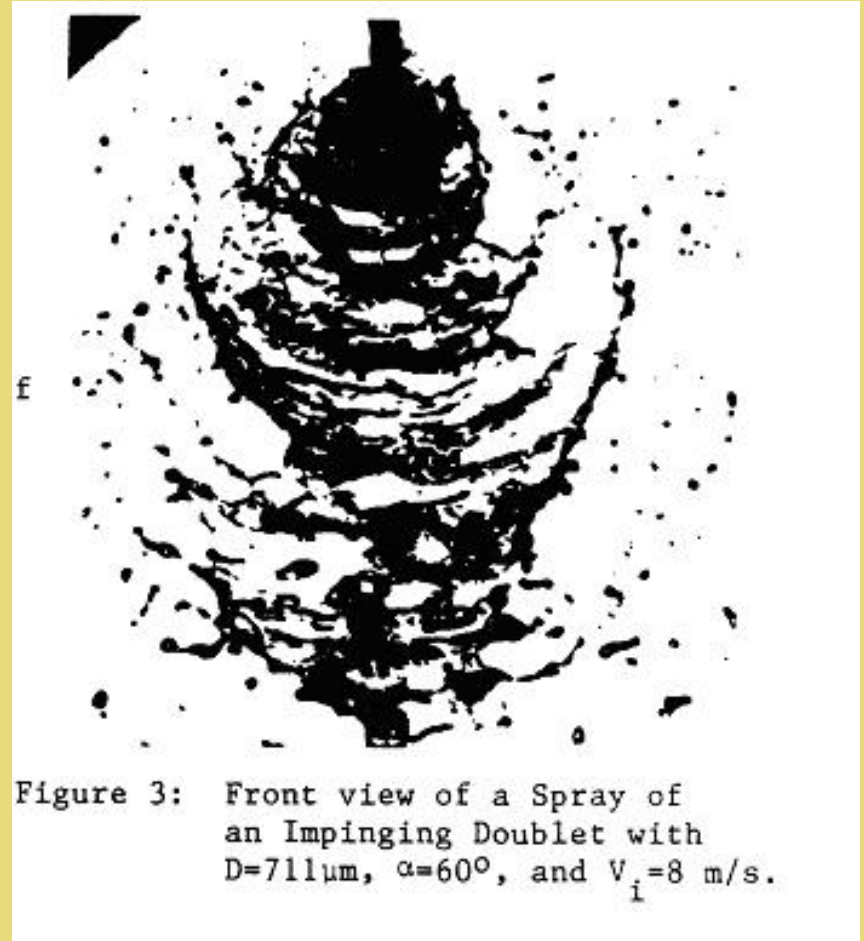
Dynamic parameters

- Chaotic fluctuations of droplet diameter, specific mass flow rate and distribution of concentration due to pulsation of liquid flow disintegration
- Bifurcations of atomizing and mixing processes
- Regular self-oscillations
- Sensitivity of injectors to pressure pulsation in the combustion chamber and propellant supply systems
- Sensitivity of atomization and mixing processes to velocity pulsation in the combustion chamber



Dynamic characteristics of injectors

- Chaotic fluctuations of droplet diameter, specific mass flow rate and distribution of concentration due to turbulent fluctuations and liquid flow disintegration [1].
- Process of two-phase flow formation is entirely non-stationary: continuous flows of gas and liquid transform into disperse media flow.
- Disintegration of liquid jets or sheets into droplets is accompanied by instability of liquid flow, which leads to non-uniformities of the two-phase flow.



Bifurcations of atomizing and mixing processes

- Some types of injectors are characterized by existence of at least two different stable operational regimes of the flow for the same input parameters. Occasional change in pressure or pressure drop, appearance of oscillations can lead to bifurcations of injection process. It was observed in swirl-jet injectors [2], where central liquid jet with growth of pressure touched the interior surface of rotating liquid film, swirled by it and finally disappeared, outflowing together with the rotating liquid. Shear coaxial injectors also have possibility for bifurcation. In recessed shear/coax injector elements, two regimes can be observed: or liquid jet do not touch exterior gas nozzle and atomization occurs by coaxial gas spray, or liquid flow can attach the exterior wall. In the latest case, the angle of the spray strongly increases, as well as efficiency of atomization and mixing.

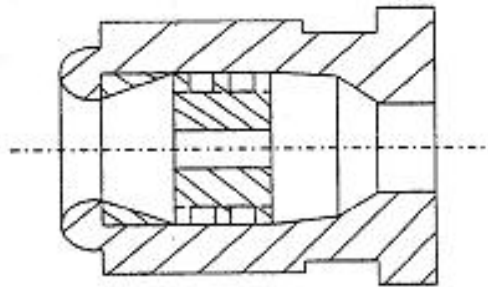
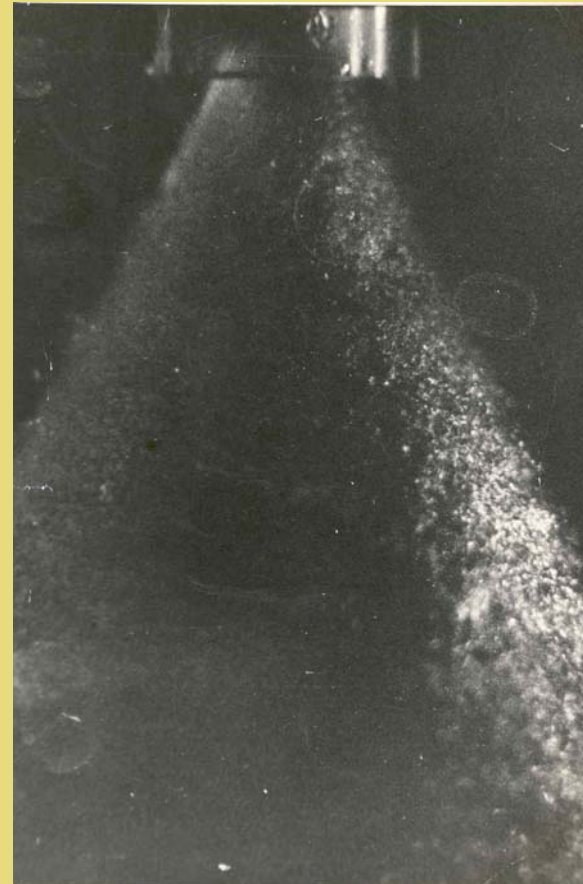


Fig. 18 Schematic diagram of a mixed jet-swirl liquid injector.

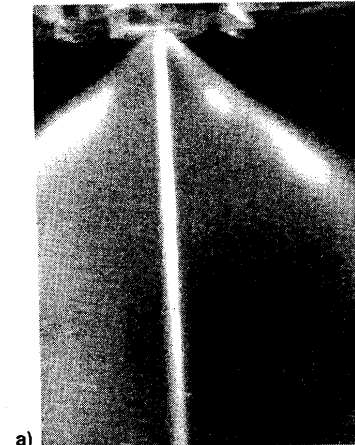
Regular self-oscillations

- usually appear in injectors with centrally positioned liquid swirl stage, coaxial to the exterior swirled or non-swirled gas flow [3]

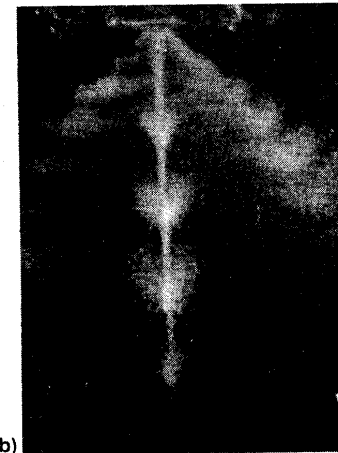


Injector sensitivity to pressure pulsations

As it was shown in several works [5,6], injectors are usually sensitive to pressure drop pulsation and respond to them by pulsation of outlet parameters such as mass flow rate, angle of spray, size of droplets, outlet velocity, that cause secondary pulsation of heat release and pressure. Even in the absence of coupling and stable combustion, injector sensitivity leads to elevated noise in the combustion chamber.



a)



b)

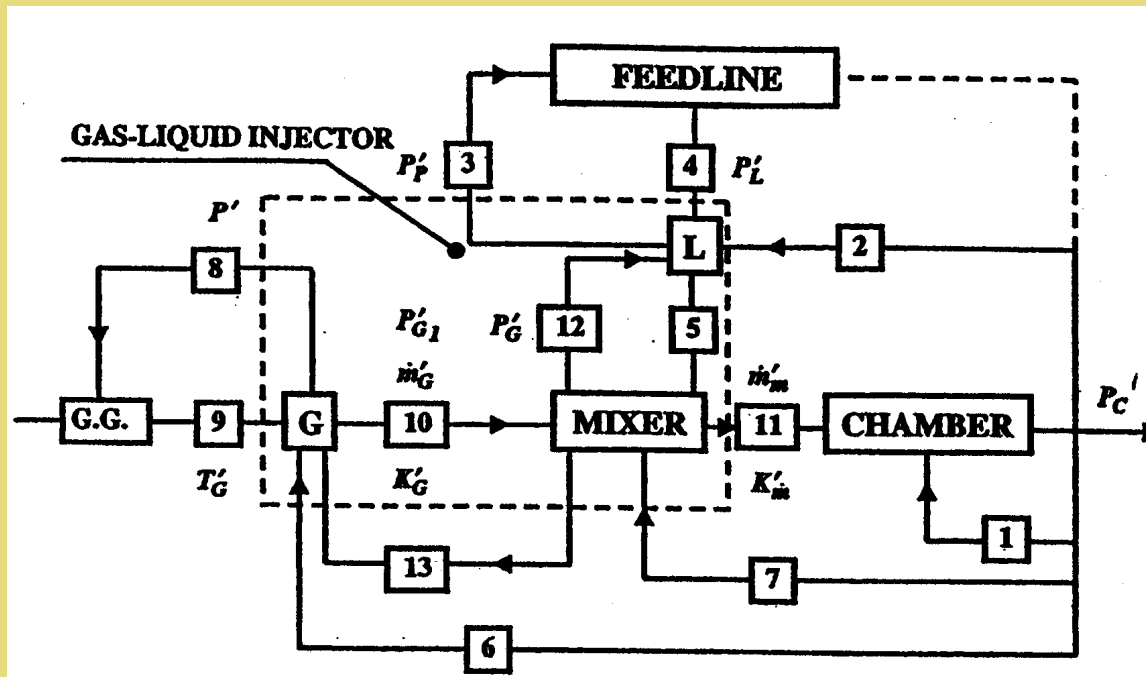
Fig. 19 Spray fields of a mixed jet-swirl liquid injector under a) stationary and b) externally forcing conditions.

Sensitivity to velocity oscillations

- Sensitivity of atomization and mixing process to transverse velocity pulsation in the combustion chamber is typical for impinged jets and crossed films of fuel and oxidizer of mono-propellant swirl injectors. This sensitivity provides pulsation of concentration and atomization efficiency and finally leads to the strong increase in heat fluxes in the injector fire face and combustion chamber walls

Injector as a link in LRE dynamic system

Scheme of LRE dynamic processes interaction



Injector in LRE dynamic system serves as:

1. Sensitive element;
2. Amplifier;
3. Phase shifter;
4. Actuator;
5. Generator of pulsation;
6. Modulator.

Dynamic characteristics of injectors – jet injectors

Within assumption that its length is strongly less than the pressure wave length comprise plain inertial elements [2]. They have rather high sensitivity to combustion chamber pressure pulsation, but shift angle does not exceed 90° . Sensitivity can be decreased by increasing the length of the liquid channel.

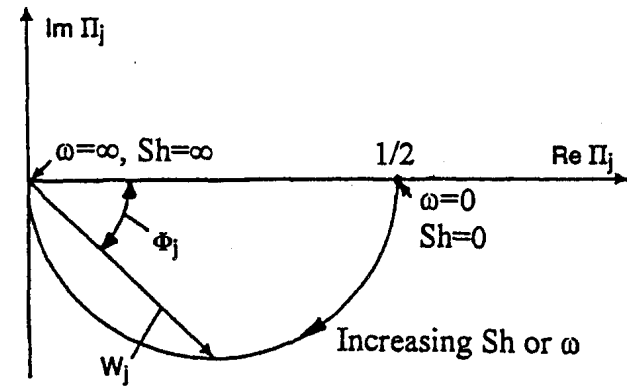


Fig. 3 Amplitude-phase diagram of the response function of a short jet injector.

Dynamic characteristics of injectors – swirl injectors

Swirl injectors are more complicated, as injector from the dynamic point of view comprise a combination of inertial elements (tangential channels), capacitance (vortex chamber) and transport element (nozzle). Cooperation of these elements give the chance to design injectors with the desired dynamic e.g., with no response to pressure drop pulsation in the required frequency range

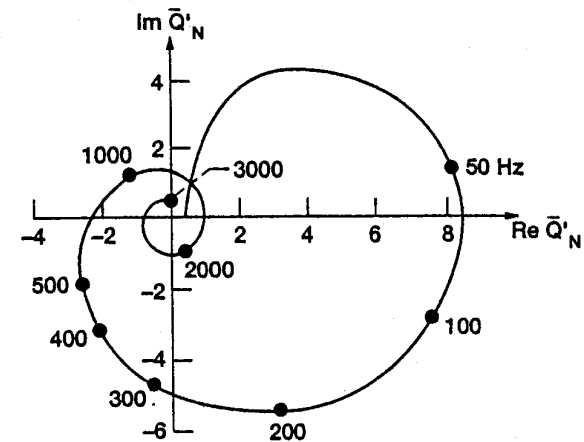


Fig. 9 Amplitude-phase diagram of the response function of a typical liquid swirl injector.

Comparison of injection methods

Liquid – liquid injectors - impinged jets.

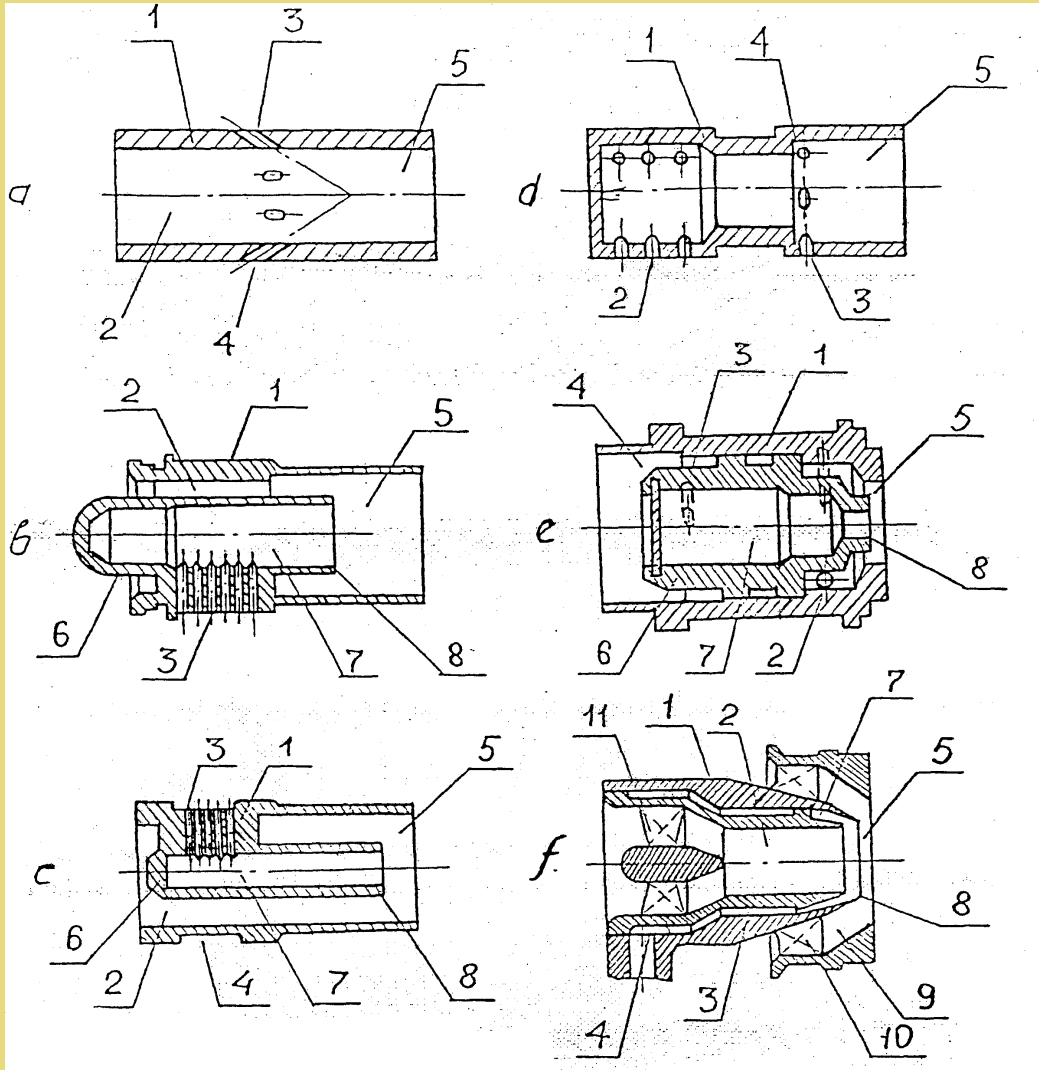
- Positive features: simple design and calculation, good atomization, low inertia.
- Negative features: high sensitivity to rectangular velocity pulsation of combustion products, non-uniformity of local O/F ratio, absence of fire face heat protection.
- Preferable area of usage: low thrust impulse working combustion chambers for reaction control engines.

Comparison of injection methods

Liquid – liquid injectors – swirl injectors.

- Positive features: durable, fool-proof, low sensibility to manufacture mistakes, low noise, good atomization, good preservation of injector fire face from overheating, no self-oscillations.
- Negative features: mono-propellant swirl injectors produce non-uniform combustible mixture, sensitivity to transverse velocity pulsation.
- Preferable area of usage: mono-propellant – for cooling of fire face and combustion chamber walls; bipropellant with internal mixing – in high pressure combustion chambers and gas generators.

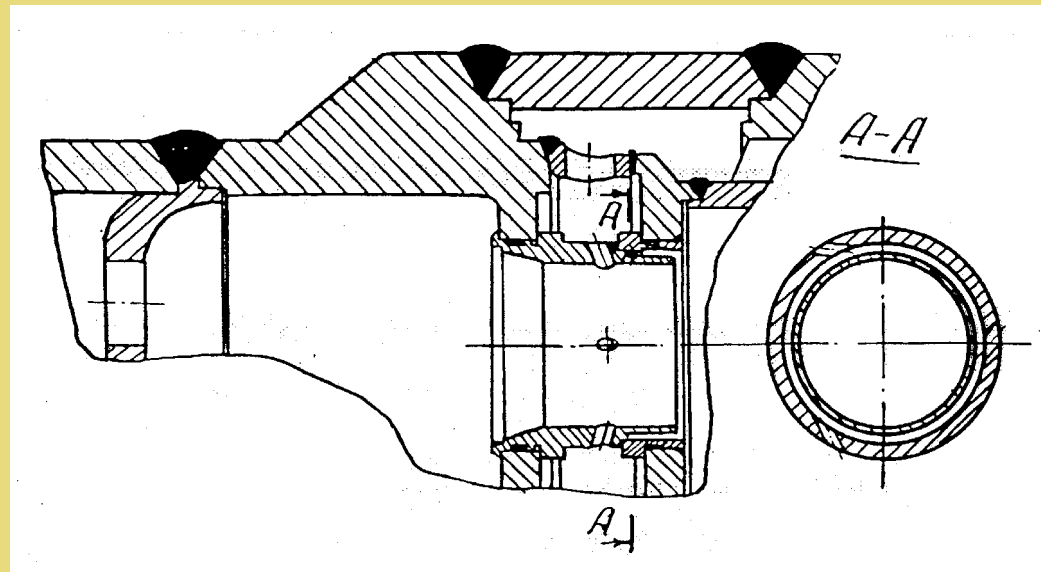
Main combustion chamber injectors



a) spray to spray, up to 200 g/sec; b, c) swirl to spray (b) with constant damper; up to 2.0 kg/sec.); d) swirl to swirl, up to 10 kg/sec.), e) bipropellant liquid/liquid injector, = 220 g/sec.; f) gas-liquid injector, up to 2 kg/sec. (1 – body, 2 – channels for gasified or less density propellant, 3 – channels for liquid propellant, 4 – gas cavity, 5 – mixer, 6 – resonant damper, 7 – swirl chamber, 8 – nozzle for liquid propellant, 9 – nozzle for gaseous propellant, 10 – gas swirler).

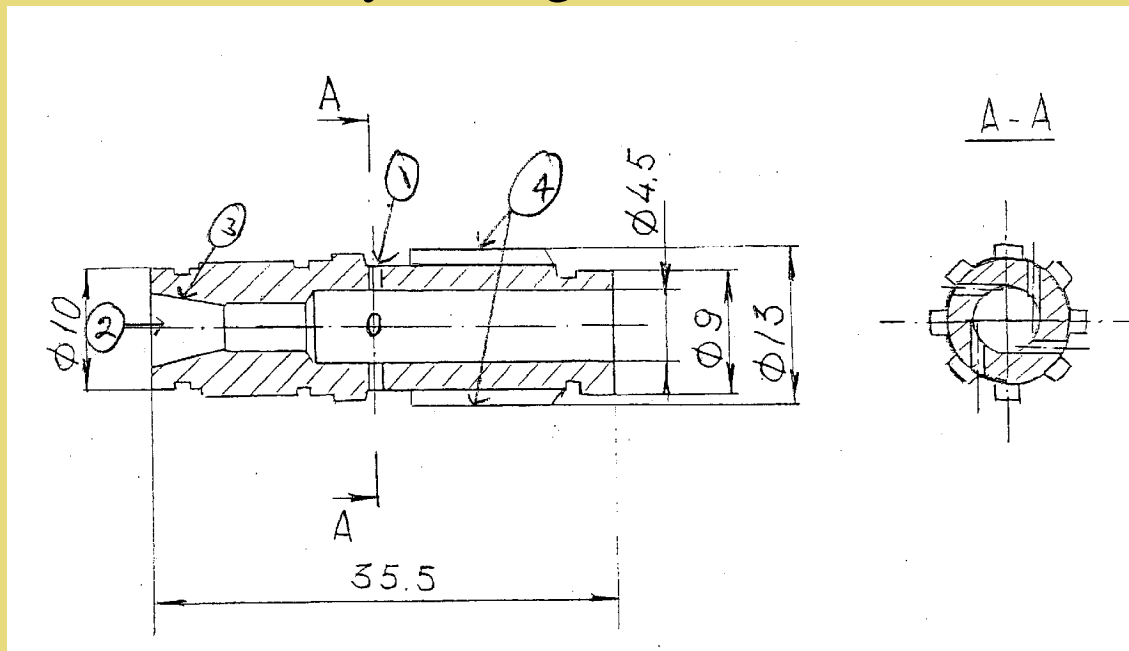
Transverse jet injector

- Most wide-spread type of injector in Russian LRE.
- Positive features: very simple in the design and production, good atomization and mixing, no regular self-oscillations.
- Negative features: high sensitivity to pressure pulsation, bad protection of fire face, strong reverse flows.
- Preferable area of usage: medium size LRE using storable propellants.



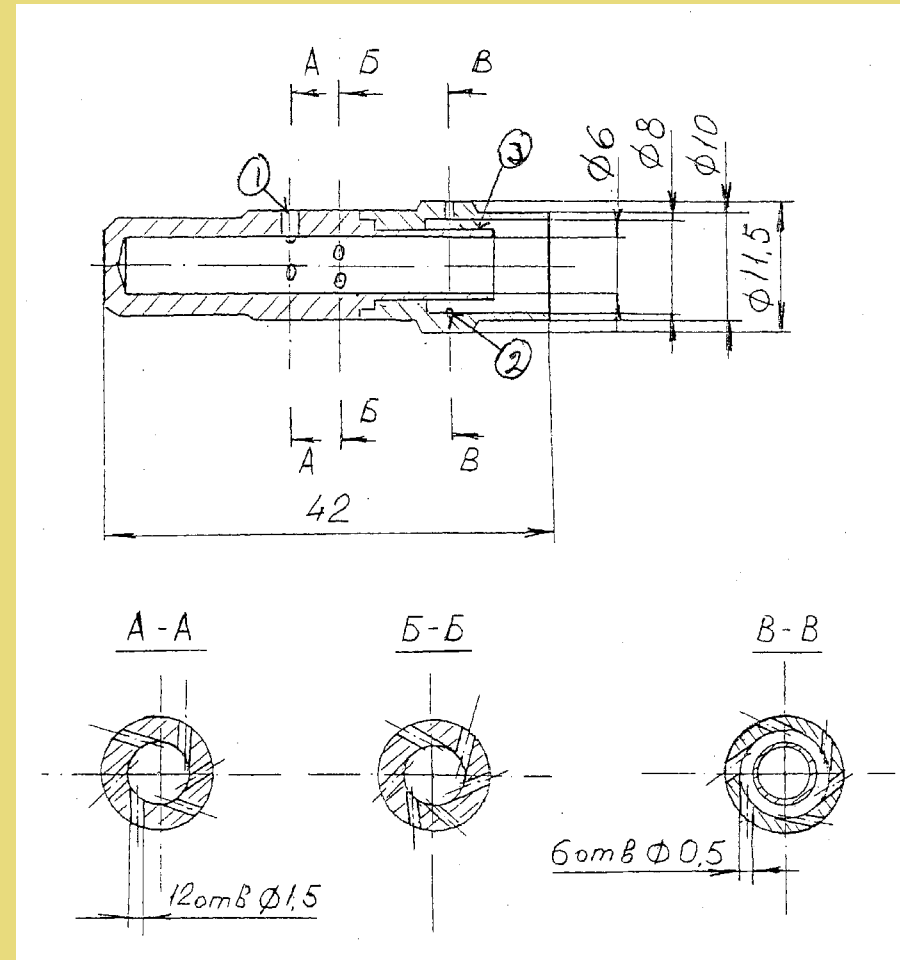
Axial gas core with swirled liquid annulus

- Positive features: liquid flow stabilized along walls, good heat protection, no self-oscillation recorded, low noise, more uniform atomization, possibility of gas injector acoustic tuning.
- Negative features: non-even mixing via radius of the flow, worse atomization at low pressures.
- Preferable area of usage: high-pressure Ox-rich staged combustion cycle engines



Swirled gas core with liquid annulus

- Positive features: better atomization and mixing, elevated mass flow rate per unit, formation of the reverse flow zone of stability, usage of gas vortex chamber as a Helmholtz resonator decrease acoustic energy in the combustion chamber.
- Negative features: more complicated design and production.
- Preferable area of usage: LOX/methane, propane, hypergols with high thrust.



Shear coaxial injector

- Positive features: compact design, high combustion efficiency.
- Negative features: high inclination to formation of self-oscillations, bad heat protection of fire face, highly sensitive to pressure and velocity pulsation, very noisy.
- Preferable area of usage: LOX/H₂ engines of different sizes.

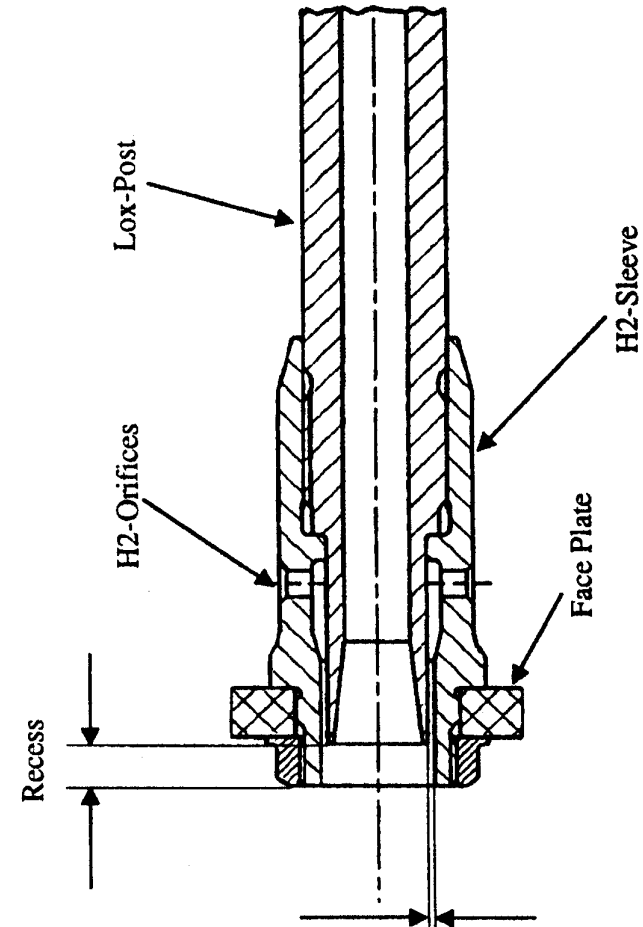
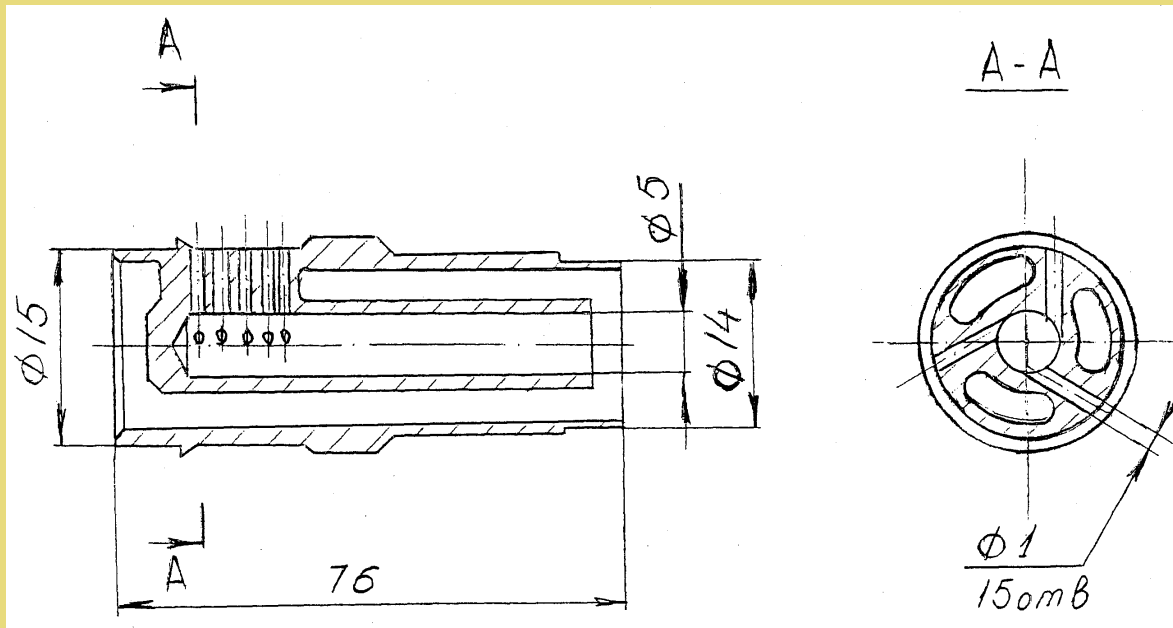


Figure 6: Coaxial Injection Element

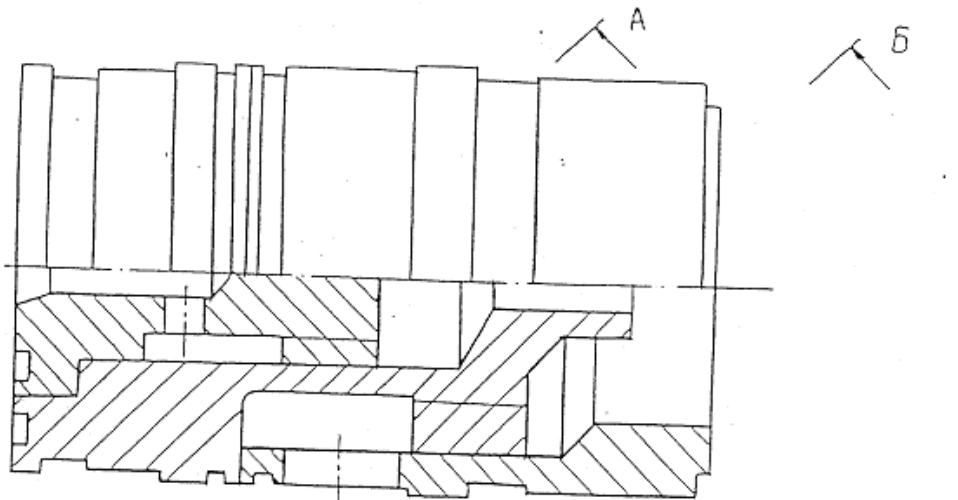
Swirl coaxial injector

- Positive features: elevated atomization and mixing efficiency, stability of combustion.
- Negative features: inclined to strong self-oscillation, more complicated design and production.
- Preferable area of usage: LOX/H₂ engines of high thrust.



Bicentrifugal swirl injector

- Positive features: most high atomization efficiency, absence of bifurcations
- Negative features: inclination to self-oscillations, high sensitivity to pressure pulsation.
- Preferable area of usage: medium and low thrust LOX/kerosene and LOX/H₂ engines.

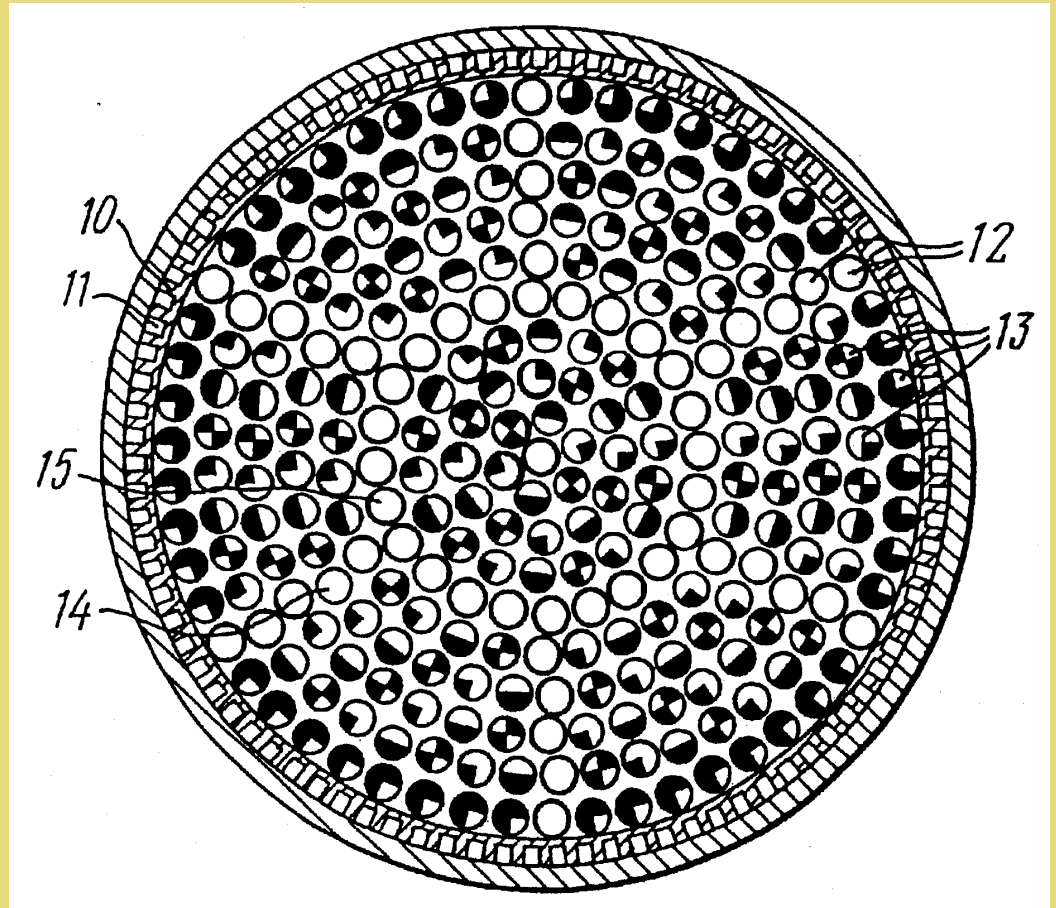
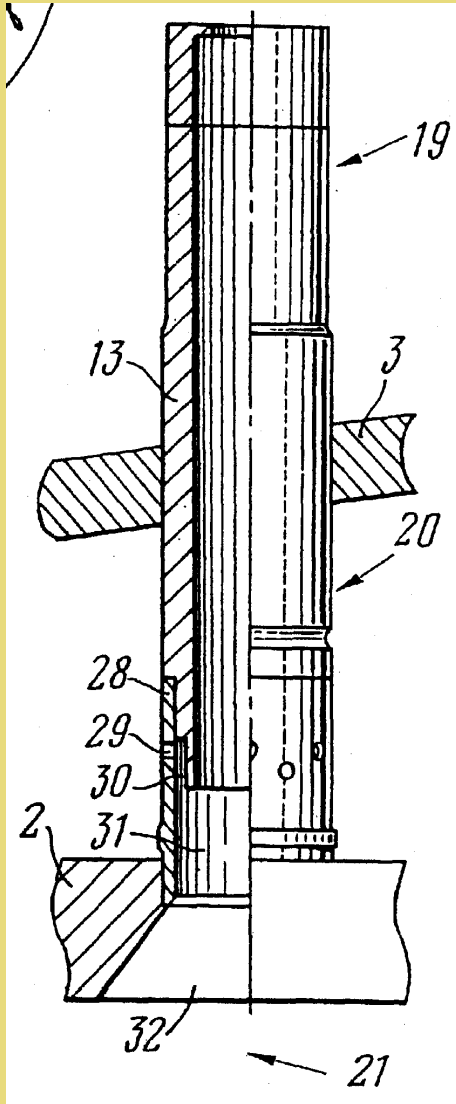


Alternative injector type

Gas from both sides of liquid flow

- Positive features: highest mixing and combustion efficiency, high acoustic admittance.
- Negative features: very complicated design and production, sensitivity to pressure and velocity pulsation.
- Preferable area of usage: medium and low thrust LOX-kerosene engines (OMS Buran, Block DM).

ORSC MC injector





Injector requirements for long life applications

- Stable steady-state parameters: absence of bifurcations, unexpected change of the regime.
- Absence of the destructive self-oscillations.
- Minimum of noise and arbitrary pulsation.
- Minimum sensitivity on liquid side of the injector to pressure pulsation.
- Desirable – self-sustaining stability of operational process.





Recommendations for future research

- Experimental research of injector dynamic characteristics in full scale and modeling conditions
- Develop means of measurement stationary parameters of atomization: local concentration, dispersity, specific mass flow rate in real conditions of high density, pressure, vibration etc.
- Develop means for measurement of dynamic parameters: thickness of liquid film pulsation, pulsation of mass flow rate, size of droplets, velocity, concentration.



Conclusions

- Each type of injectors developed and used in LRE has its preferable area of usage.
- For LOX/H₂ staged combustion cycle engines, best results with the respect of life duration showed bipropellant injectors with central swirl LOX flow and external fuel rich gas flow. Shear/coax injectors are also usable if special means will eliminate sources of self-oscillations, bifurcations and noise.
- For LOX/hydrocarbon high pressure staged combustion cycle LRE, best results showed bipropellant injector with central Ox-rich gas supply and external swirled fuel flow supply in open vortex chamber that serves as an atomizer and mixer. If properly designed, such injectors have very low sensitivity to pressure pulsation and provide servo-stabilization of operational process.



References

- Ashgriz N., Brocklenhurst W., Talley D.G. On the Mixing Mechanisms in a Pair of Impinging Jets. Paper AIAA-95-2421, 31st AIAA/ASME/SAE/ASEE Joint Propulsion Conference and Exhibit, July 10-12, 1995, San Diego, CA.
- Bazarov V., Yang V. Liquid Propellant Rocket Engine Injector Dynamics. Journal of Propulsion and Power, v. 14, #5, September-October 1998.
- Bazarov V. Self-Pulsations in Coaxial Injectors with Central Swirl Liquid Flow. Paper AIAA-95-2421, 31st AIAA/ASME/SAE/ASEE Joint Propulsion Conference and Exhibit, July 10-12, 1995, San Diego, CA.
- Woodward R.D., Miller K.L., Guerin G.F., Pal S., Bazarov V. and Santoro R.S. Injector Research for Shuttle OMS Upgrade Using LOX/Ethanol Propellants. Paper AIAA-98-3816, 34th AIAA/ASME/SAE/ASEE Joint Propulsion Conference and Exhibit, July 13-15, 1998, Cleveland, OH.
- Bazarov V. Dynamics of Liquid Injectors. Moscow, Mashinostroenie Publishing House, 1967.
- Andreev A., Bazarov V., Dushkin A., Lul'ka L. and Grigoriev S. Dynamics of Gas – Liquid Injectors. Moscow, Mashinostroenie Publishing House, 1991.
- Vasin A. et al. US Patent # 6244041, B1, June 12, 2001.
- Andreev A., Chepkin V. and Fanciullo T. The Development of the D-57 Advanced Staged Combustion Engine for Upper Stages. AIAA Paper # 94-3378, June 1994.
- Dexter C., Fisher M., Hulka J and Denisov K. Scaling Technologies in Liquid Rocket Engine Combustion Devices Testing. Proceedings of the Second International Symposium on Liquid Rocket Propulsion, ONERA – Chatillon, France, June 19-20, 1995.



INJECTORS FOR LONG LIFE COMBUSTION DEVICES

Prof. Vladimir Bazarov
Purdue University

Abstract

Factors that decrease the life time of combustion devices were considered with the respect of liquid-propellant rocket engines (LRE), including some new ones as vibroactivity of combustion, and comparative analysis of injectors for gas generators and for main combustion chambers was fulfilled respectively to the decreasing of these factors and expanding the life time of combustion devices. Experimental data and qualitative analysis showed that the best way to eliminate unevenness of the heat flux, pulsation of heat release via time and space and to stabilize combustion process in ox-rich gas generator is to hide the most sensitive part of the flame inside the vortex chamber of bi-propellant swirl-swirl injector that comprise in this case a small cyclone pre-burner. It works with much higher O/F ratio than the gas generator as a whole, swirled liquid oxygen cools vortex chamber walls from inside and then mix and cool the products of combustion. For combustion chambers the most keen conditions for fire face and combustion chamber walls produce bi-propellant gas-liquid injectors with central gas flow and liquid film, rotating along the surface of the gas channel. Unlike shear coaxial gas-liquid injectors, widely used in combustion chambers of fuel-rich staged cycle LRE, they are characterized by absence of any self-oscillations and other sources of noise and unsteady pulsation, forms conical films that protect fire face from overheating. Peculiarities of the mechanism of disturbances propagation via length of the opened vortex chamber allow to reach zero response of the liquid stage of such an injector to pressure drop pulsation. Acoustic tuning of the gas stage by means of the length of the gas pipe and variations of its inlet area allow to withdraw significant part of acoustic energy from the combustion chamber to the gas manifold. Finally, such an injector, if properly designed, can provide servo-stabilization of the combustion chamber with the respect of pressure, mass flow rate and temperature pulsation and thus to improve its reliability and increase life time.

1. Factors that influence life time of combustion devices in liquid rocket engines:

- High local heat fluxes, caused by high pressure, gas density and high velocity of combustion products;
- Concentration non-uniformity and local zones of oxidizer-rich gases
- High level and wide spectrum of mechanical vibrations
- Combustion instability
- Combustion unsteadiness, accompanied by high amplitude and wide frequency range of gas pressure, velocity and vorticity pulsation

Most of them depend on injector design and operation.

2. Parameters of propellant's injection that influence LRE life duration

2.1. Stationary parameters

- Composition and temperature fields of combustion products
- Flow velocity and intensity of reverse flows near the wall of the combustion chamber
- Spectrum and quality of atomization

2.2. Dynamic parameters

- Chaotic fluctuations of droplet diameter, specific mass flow rate and distribution of concentration due to turbulent fluctuations and liquid flow disintegration [1].

Process of two-phase flow formation is entirely non-stationary: continuous flows of gas and liquid transform into disperse media flow. Disintegration of liquid jets or sheets into droplets is accompanied by instability of liquid flow, which leads to non-uniformities of the two-phase flow.

- Bifurcations of atomizing and mixing processes.

Some types of injectors are characterized by existence of at least two different stable operational regimes of the flow for the same input parameters. Occasional change in pressure or pressure drop, appearance of oscillations can lead to bifurcations of injection process. It was observed in swirl-jet injectors [2], where central liquid jet with growth of pressure touched the interior surface of rotating liquid film, swirled by it and finally disappeared, outflowing together with the rotating liquid. Shear coaxial injectors also have possibility for bifurcation. In recessed shear/coax injector elements, two regimes can be observed: or liquid jet do not touch exterior gas nozzle and atomization occurs by coaxial gas spray, or liquid flow can attach the exterior wall. In the latest case, the angle of the spray strongly increases, as well as efficiency of atomization and mixing.

- Regular self-oscillations – usually appear in injectors with centrally positioned liquid swirl stage, coaxial to the exterior swirled or non-swirled gas flow [3]. The consequences of such self-oscillations usually are rather severe. In the case of the development of RD-57 40-ton thrust LOX/H₂ engine, strong pressure pulsation (0.9 MPa of amplitude with frequency about 5.5 KHZ) in the LOX manifold led to cracks in nipple connections. Self-oscillations also appeared in bi-propellant swirl injectors of LOX/ethanol model combustion chamber [4] when LOX with elevated temperature, vapor pressure of which exceeded the combustion chamber pressure, was used. In this case, strong decrease in combustion efficiency was observed due to formation of strong non-uniformities of combustible mixture composition. Not only swirl-jet or swirl-swirl injectors can behave in such a manner. Shear/coax injectors with recessed central nozzle, though do not generate regular pulsation as swirl ones, but also realize several mechanisms of self-oscillations, both in liquid stage and in the mixer. Oscillations of liquid spray can appear due to separation of liquid flow in the tapered part of the liquid nozzle. Due to this separation, the spray flows along the side wall of the nozzle in inclined direction. This leads to the formation of vortices in the gas flow across the inclined spray and consequently, non-uniformities of O/F ratio in the combustible mixture. It is dangerous mainly in gas generators, where local Ox-rich zones may be formed.

- Sensitivity of injectors to pressure pulsation in the combustion chamber and propellant supply system.

As it was shown in several works [5,6], injectors are usually sensitive to pressure drop pulsation and respond to them by pulsation of outlet parameters such as mass flow rate, angle of spray, size of droplets, outlet velocity, that cause secondary pulsation of heat release and pressure. Even in the absence of coupling and stable combustion, injector sensitivity leads to elevated noise in the combustion chamber.

- Sensitivity of atomization and mixing process to transverse velocity pulsation in the combustion chamber is typical for impinged jets and crossed films of fuel and oxidizer of mono-propellant swirl injectors. This sensitivity provides pulsation of concentration, atomization efficiency and finally leads to the strong increase in heat fluxes in the injector fire face and combustion chamber walls.

3. Injector as a link in LRE as a dynamic system

3.1. The scheme of LRE dynamic processes interaction is presented in Fig. 1.

It can be seen from this picture that additionally to the main function of the injector – to prepare combustible mixture, injector also serves in an engine as a sensitive element, amplifier and phase shifter. In some cases it has internal feedback connections 12 and 13, which allow injector to generate its own self-oscillations and serve as a generator. Recent studies showed also that for finite amplitudes injector can modulate oscillations and change accordingly its mean characteristics of atomization and mixing.

3.2. Dynamic characteristics of injectors

- Jet injectors.

Within assumption that its length is strongly less than the pressure wave length comprise plain inertial elements [2]. They have rather high sensitivity to combustion chamber pressure pulsation, but shift angle do not exceed 90° . Sensitivity can be decreased by increasing the length of the liquid channel. It is dangerous to have sudden increase in the liquid passage as cavitation or occasional bubbles can strongly change dynamic characteristics and lead to the increase in the injector sensitivity.

- Swirl injectors.

Dynamic characteristics of swirl injectors are more complicated, as injector from the dynamic point of view comprise a combination of inertial elements (tangential channels), capacitance (vortex chamber) and transport element (nozzle) [5]. Cooperation of these elements give the chance to design injectors with the desired dynamic qualities, for instance with no response to pressure drop pulsation in the required frequency range.

4. Comparative analysis of injection methods used in contemporary LRE with the respect of combustion devices long life

4.1. Liquid – liquid injectors for combustion chambers and gas generators.

- Impinged jets.

Positive features: simple design and calculation, good atomization, low inertia.

Negative features: high sensitivity to rectangular velocity pulsation of combustion products, non-uniformity of local O/F ratio, absence of fire face heat protection.

Preferable area of usage: low thrust impulse working combustion chambers for reaction control engines.

- Pintle injectors.

Pintle injector actually is a kind of impinged jet injector assembly.

Positive features: more uniform mixing, ability of thrust variations, high combustion stability.

Negative features: bad fire face heat protection, low combustion efficiency when high mass flow rate per element.

Preferable area of usage: medium – thrust OMS combustion chambers with thrust variations.

- Swirl injectors.

Positive features: durable, fool-proof, low sensibility to manufacture mistakes, low noise, good atomization, good preservation of injector fire face from overheating, no self-oscillations.

Negative features: mono-propellant swirl injectors produce non-uniform combustible mixture, sensitivity to transverse velocity pulsation.

Preferable area of usage: mono-propellant – for cooling of fire face and combustion chamber walls; bipropellant with internal mixing – in high pressure combustion chambers and gas generators.

4.2. Main combustion chamber injectors

Fig. 2 presents schemes of gas-liquid injectors, used in main combustion chambers of staged combustion cycle LRE.

4.2.1. Crossed jet sprays, liquid from outside, injected through inclined drills into the gas flow.

It is the most widely spread type of injector in Russian LRE.

Positive features: very simple in the design and production, good atomization and mixing, no regular self-oscillations.

Negative features: high sensitivity to pressure pulsation, bad protection of fire face, strong reverse flows.

Preferable area of usage: medium size LRE using storable propellants.

4.2.2. Gas spray from inside, swirled liquid from outside (see, for instance [7]).

Positive features: liquid flow stabilized along walls, good heat protection, no self-oscillation recorded, low noise, more uniform atomization, possibility of gas injector acoustic tuning.

Negative features: non-even mixing via radius of the flow, worse atomization at low pressures.

Preferable area of usage: high-pressure Ox-rich staged combustion cycle engines

4.2.3. Swirled gas – inside, swirled liquid – outside

Positive features: better atomization and mixing, elevated mass flow rate per unit, formation of the reverse flow zone of stability, usage of gas vortex chamber as a Helmholtz resonator decrease acoustic energy in the combustion chamber.

Negative features: more complicated design and production.

Preferable area of usage: LOX/methane, propane, hypergoles with high thrust.

4.2.4. Gas spray – outside, liquid spray – inside (shear coax).

Positive features: compact design, high combustion efficiency.

Negative features: high inclination to formation of self-oscillations, bad heat protection of fire face, highly sensitive to pressure and velocity pulsation, very noisy.

Preferable area of usage: LOX/H₂ engines of different sizes.

4.2.5. Gas spray – outside, swirled liquid – inside (from [8]).

Positive features: elevated atomization and mixing efficiency, stability of combustion.

Negative features: inclined to strong self-oscillation, more complicated design and production.

Preferable area of usage: LOX/H₂ engines of high thrust.

4.2.6. Swirl bi-propellant, liquid from inside

Positive features: most high atomization efficiency, absence of bifurcations

Negative features: inclination to self-oscillations, high sensitivity to pressure pulsation.

Preferable area of usage: medium and low thrust LOX/kerosene and LOX/H₂ engines.

4.2.7. Alternative gas and liquid flows – gas from both sides of liquid flow.

Positive features: highest mixing and combustion efficiency, high acoustic admittance.

Negative features: very complicated design and production, sensitivity to pressure and velocity pulsation.

Preferable area of usage: medium and low thrust LOX-kerosene engines (OMS Buran, Block DM).

5. Requirements, applied to long life LRE injectors.

- Stable steady-state parameters: absence of bifurcations, unexpected change of the regime.
- Absence of the destructive self-oscillations.
- Minimum of noise and arbitrary pulsation.
- Minimum sensitivity on liquid side of the injector to pressure pulsation.
- Desirable – self-sustaining stability of operational process.

6. Necessary works to develop injectors with the respect of LRE long life and stability of combustion.

- Experimental research of injector dynamic characteristics in full scale and modeling conditions
- Develop means of measurement stationary parameters of atomization: local concentration, dispersity, specific mass flow rate in real conditions of high density, pressure, vibration etc.
- Develop means for measurement of dynamic parameters: thickness of liquid film pulsation, pulsation of mass flow rate, size of droplets, velocity, concentration.

References:

1. Ashgriz N., Brocklenhurst W., Talley D.G. On the Mixing Mechanisms in a Pair of Impinging Jets. Paper AIAA-95-2421, 31st AIAA/ASME/SAE/ASEE Joint Propulsion Conference and Exhibit, July 10-12, 1995, San Diego, CA.
2. Bazarov V., Yang V. Liquid Propellant Rocket Engine Injector Dynamics. Journal of Propulsion and Power, v. 14, #5, September-October 1998.
3. Bazarov V. Self-Pulsations in Coaxial Injectors with Central Swirl Liquid Flow. Paper AIAA-95-2421, 31st AIAA/ASME/SAE/ASEE Joint Propulsion Conference and Exhibit, July 10-12, 1995, San Diego, CA.
4. Woodward R.D., Miller K.L., Guerin G.F., Pal S., Bazarov V. and Santoro R.S. Injector Research for Shuttle OMS Upgrade Using LOX/Ethanol Propellants. Paper AIAA-98-3816, 34th AIAA/ASME/SAE/ASEE Joint Propulsion Conference and Exhibit, July 13-15, 1998, Cleveland, OH.
5. Bazarov V. Dynamics of Liquid Injectors. Moscow, Mashinostroenie Publishing House, 1967.
6. Andreev A., Bazarov V., Dushkin A., Lul'ka L. and Grigoriev S. Dynamics of Gas – Liquid Injectors. Moscow, Mashinostroenie Publishing House, 1991.
7. Vasin A. et al. US Patent # 6244041, B1, June 12, 2001.
8. Andreev A., Chepkin V. and Fanciullo T. The Development of the D-57 Advanced Staged Combustion Engine for Upper Stages. AIAA Paper # 94-3378, June 1994.
9. Dexter C., Fisher M., Hulka J and Denisov K. Scaling Technologies in Liquid Rocket Engine Combustion Devices Testing. Proceedings of the Second International Symposium on Liquid Rocket Propulsion, ONERA – Chatillon, France, June 19-21, 1995.

Figures:

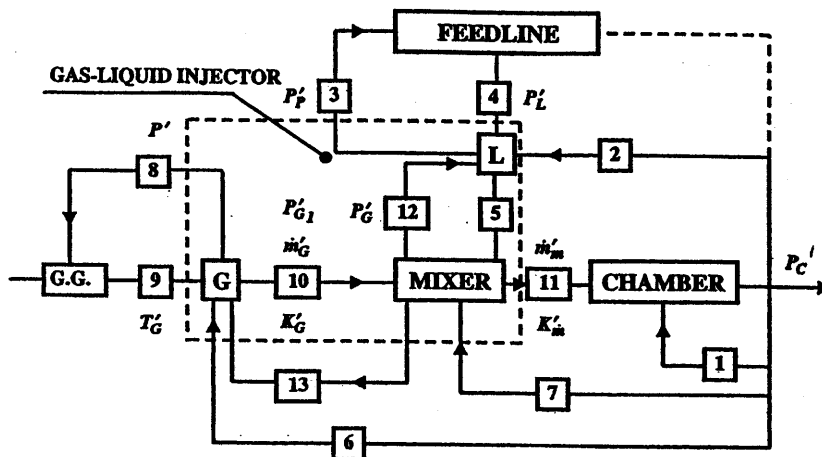


Fig. 1. Scheme of LRE dynamic processes interaction

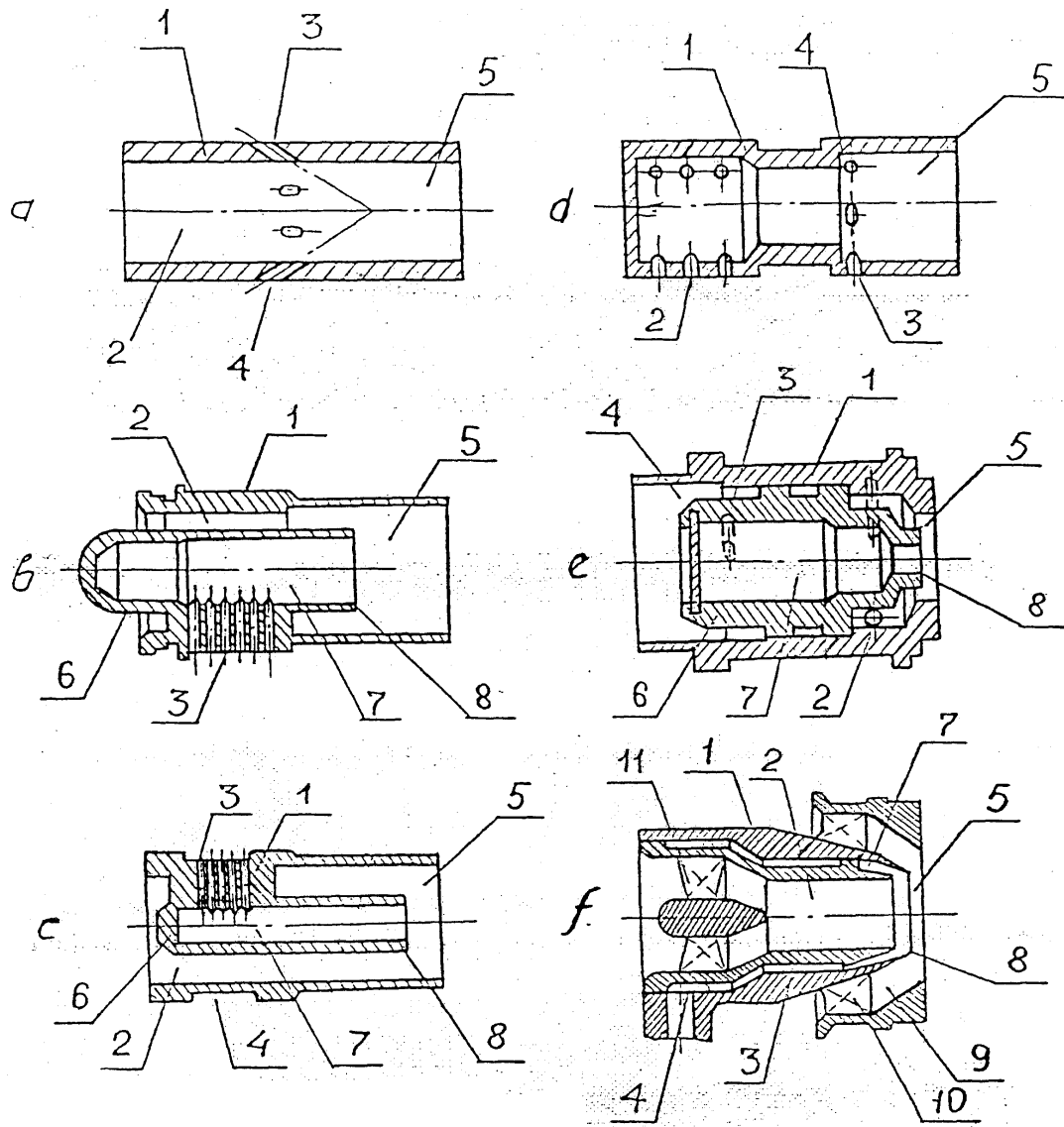


Fig 2. Design schemes of injectors used in main combustion chambers.

a) spray to spray, \dot{m}_E up to 200 g/sec; b, c) swirl to spray (b) with constant damper; \dot{m}_E up to 2.0 kg/sec.); d) swirl to swirl, \dot{m}_E up to 10 kg/sec.); e) bipropellant liquid/liquid injector, $\dot{m}_E = 220$ g/sec.; f) gas-liquid injector, \dot{m}_E up to 2 kg/sec. (1 – body, 2 – channels for gasified or less density propellant, 3 – channels for liquid propellant, 4 – gas cavity, 5 – mixer, 6 – resonant damper, 7 – swirl chamber, 8 – nozzle for liquid propellant, 9 – nozzle for gaseous propellant, 10 – gas swirler).

Gas-Centered Swirl Coaxial Liquid Injector Evaluations

5th International Symposium on Liquid Space
Propulsion

October 27-30, 2003



P.A. Strakey
R.K. Cohn
D.G. Talley

Propulsion Directorate
Air Force Research Laboratory



Introduction



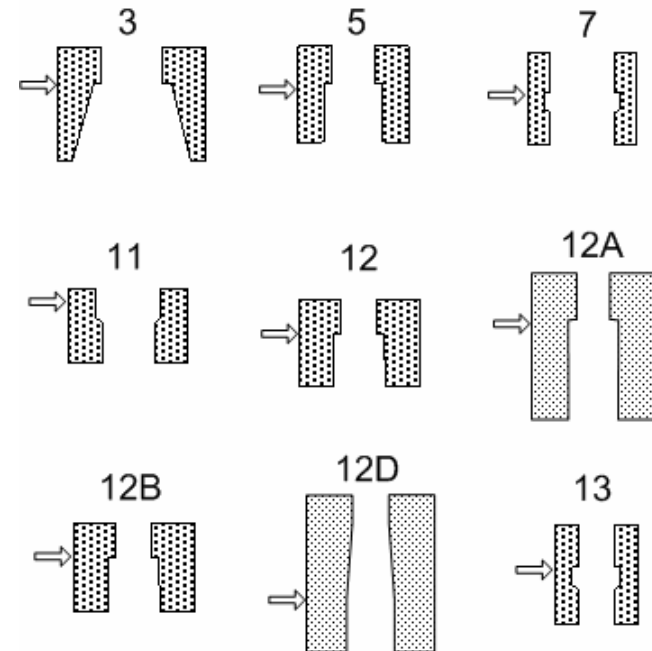
- **Development of Liquid Rocket Engines is expensive**
 - Extensive testing at large scales usually required
- **In order to verify engine lifetime, large number of tests required**
- **Limited Resources available for development**
- **Sub-scale cold-flow and hot-fire testing is extremely cost effective**
 - Could be a necessary (but not sufficient) condition for long engine lifetime
 - Reduces overall costs and risk of large scale testing
- **Goal: Determine knowledge that can be gained from sub-scale cold-flow and hot-fire evaluations of LRE injectors**
 - Determine relationships between cold-flow and hot-fire data



Approach



- Selected GOX-centered, swirl element
- Performed cold flow and hot-fire evaluations of single element
- 3 general injector types:
 - Converger, ex #11
 - Diverger
 - Sudden expansion, ex #5
 - Gradual expansion, ex #3
 - Prefilmer, ex #13
- Several variations of each general type were examined

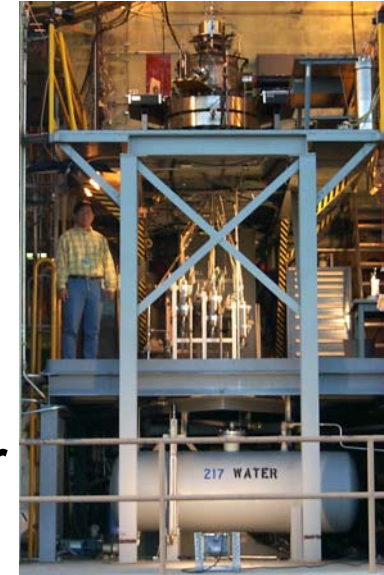




Cold Flow Evaluations



- **Water/GN2 used as simulants for fuel/oxidizer**
- **Diagnostics**
 - Back-lit strobe imaging
 - Mechanical patternation
 - Phase Doppler Interferometry
- **Data collected 2.54-15.24 cm downstream of injector**
 - Majority collected at 5.08 cm downstream of injector
- **Conditions designed to simulate hot-fire conditions**
 - Butane Fuel, Oxygen Oxidizer
 - $P_{\text{chamber}} = 1.72, 3.44 \text{ MPa (250, 500 psia)}$
 - Two scaling methodologies
 - Match momentum ratio between fuel/oxidizer
 - Results not indicative of performance
 - Match absolute momentum difference between fuel/oxidizer



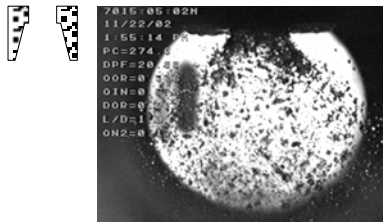


Cold Flow Measurements Back-Lit Imaging

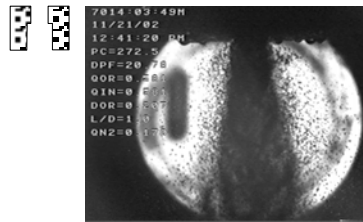


- Without gas flow, rapidly expanding liquid cone
 - Half-angle $> 75^\circ$
 - Wetted injector face plate
- With gas flow, liquid pulled towards gas core
 - #3 has widest entrainment, large liquid drops thrown outward
 - Others produced relatively fine spray with fewer droplets

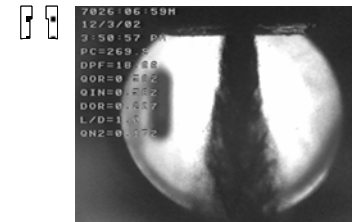
Sierra #3



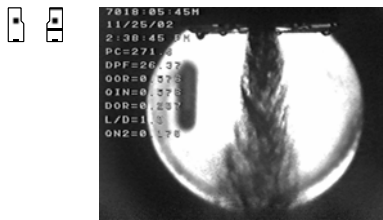
Sierra #5



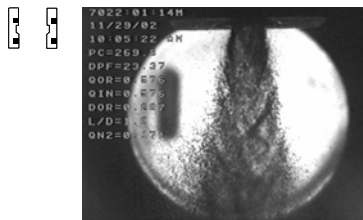
Sierra #12



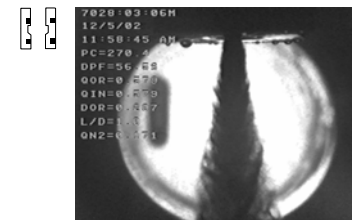
Sierra #11



Sierra #7



Sierra #13





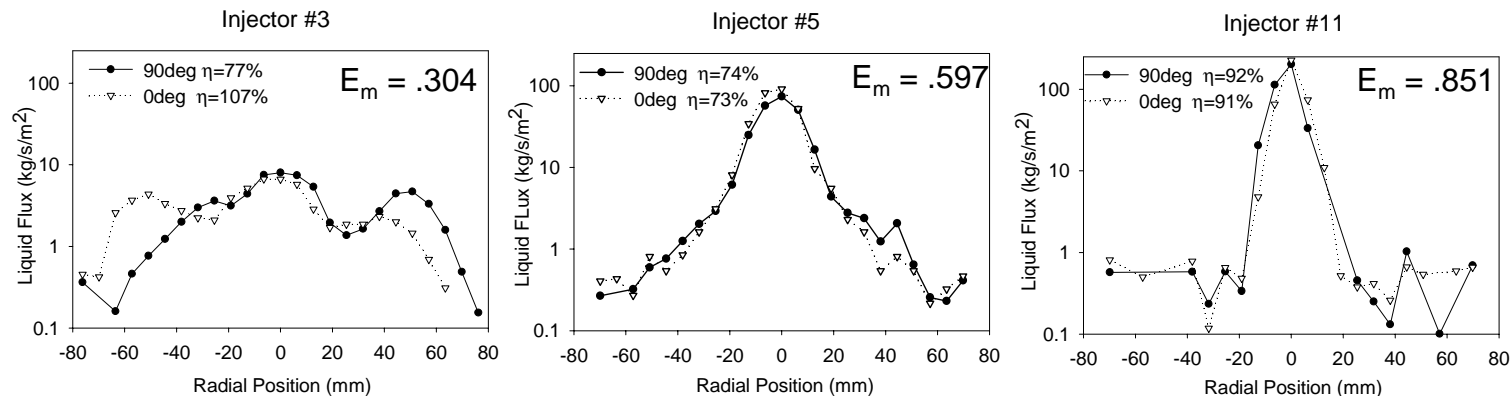
Cold-Flow Measurements

Quantitative Diagnostics



- **Mechanical Patternation**

- Corrected for collection efficiency
- Most solid-cone structure, #3 semi-hollow cone
- Wide variation of mixing efficiency



- **Sauter Mean Diameter**

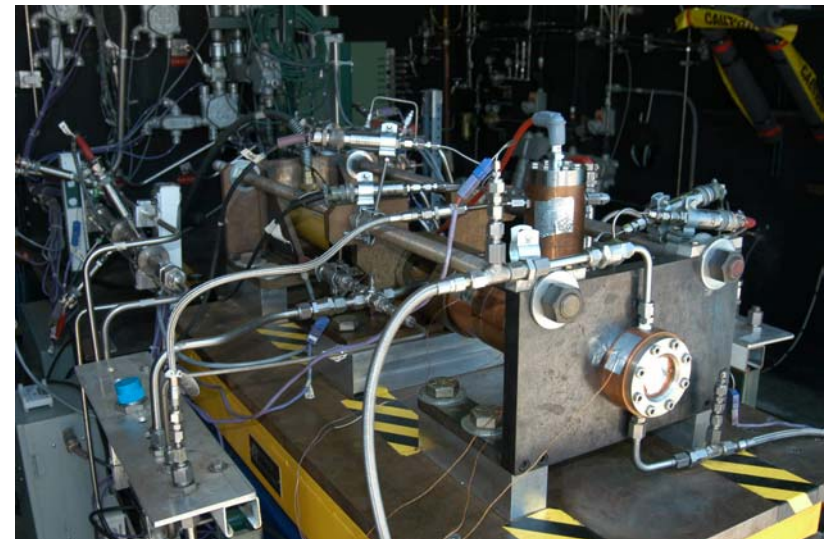
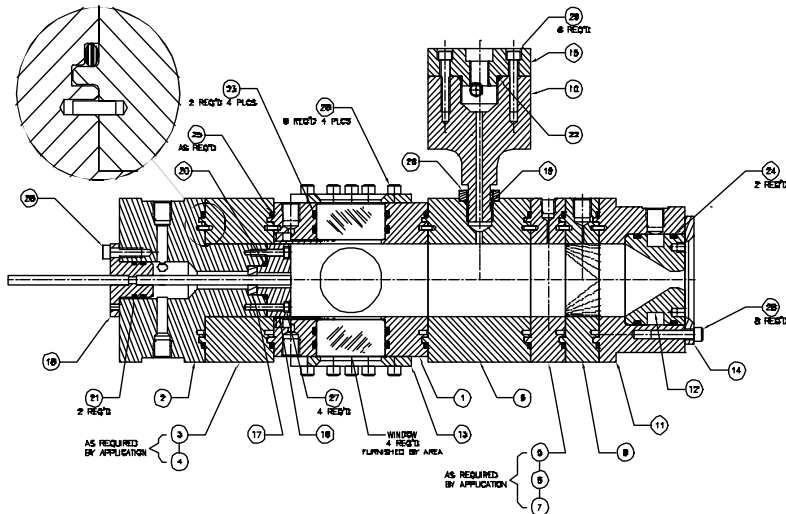
- Except for #3, all less than 75 um which indicates good atomization
- Smaller Sauter Mean Diameter correlates with larger gas bulk velocity



Hot-Fire Measurements



- Conducted in uni-element combustor test facility (EC-1)
- Copper heat-sink chamber
- Allows for optical access (not used during these tests)
- Nearly 1000 tests conducted using these injectors (all results not shown in presentation)





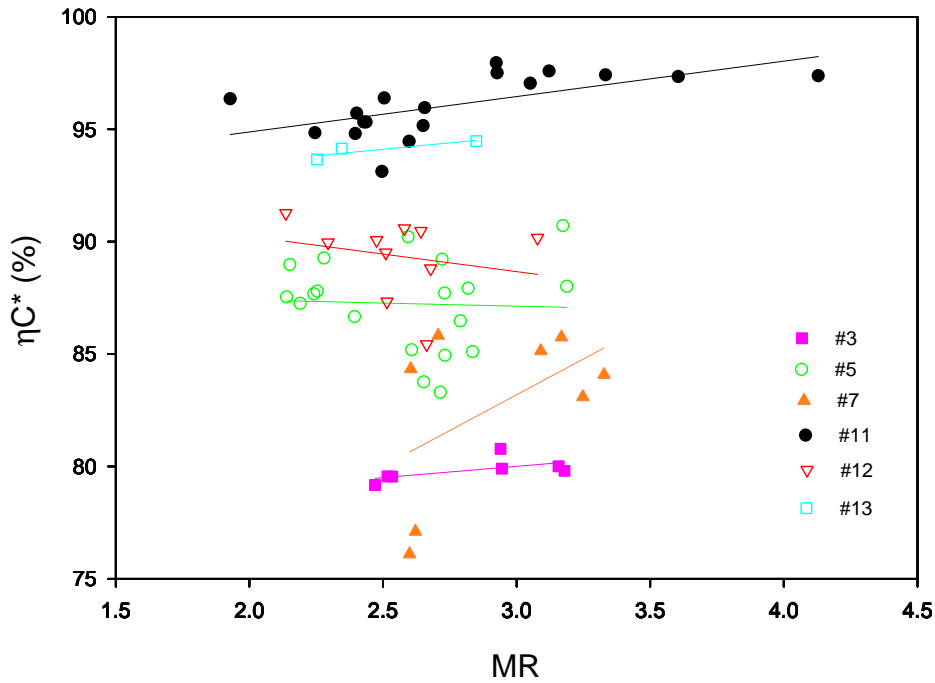
Hot-Fire Measurements Uncertainties



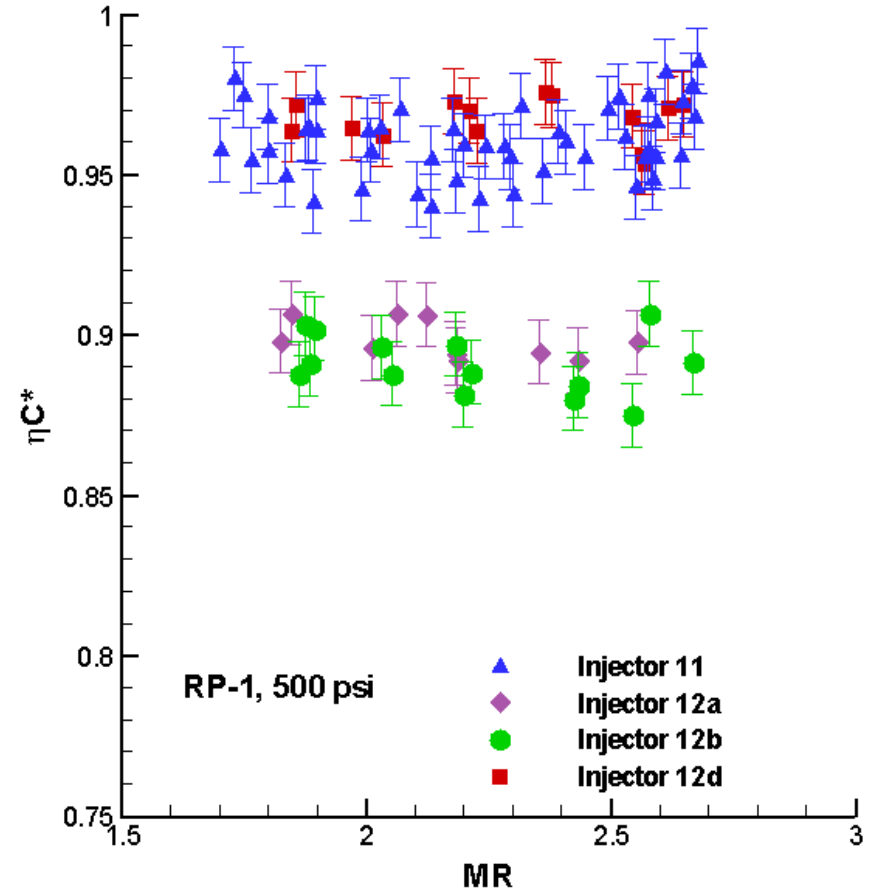
- **Uncertainty in $C^* = \pm 1\%$ (1σ)**
 - Largest source of error: Nozzle diameter = $\pm .44\%$,
 - Liquid flow rate: uncertainty of $\pm 1\%$, but contribution to overall uncertainty only $\pm .33\%$.
 - Mainly due to calibration uncertainty
- **Results averaged over 0.4 s (400 data points)**
 - Typical steady state is 2 s.
- **Initial Butane testing had uncertainty of $\pm 2\%$**



Hot-Fire Measurements Injector Comparison



Butane

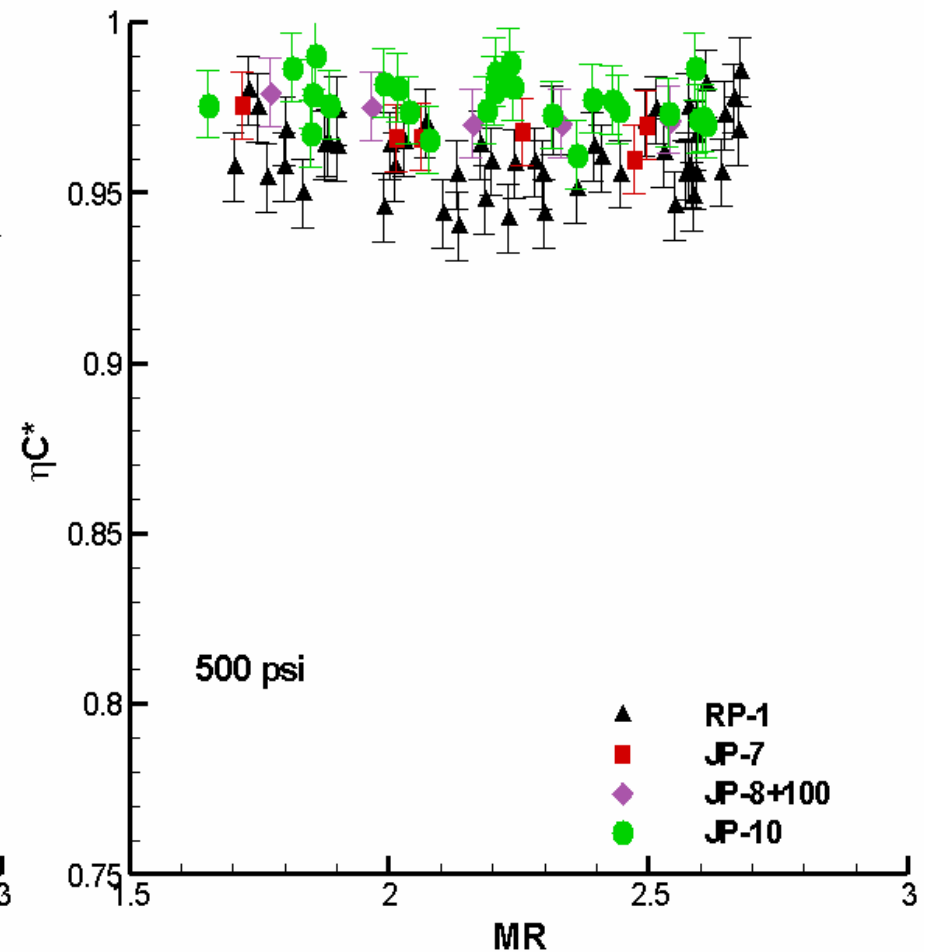
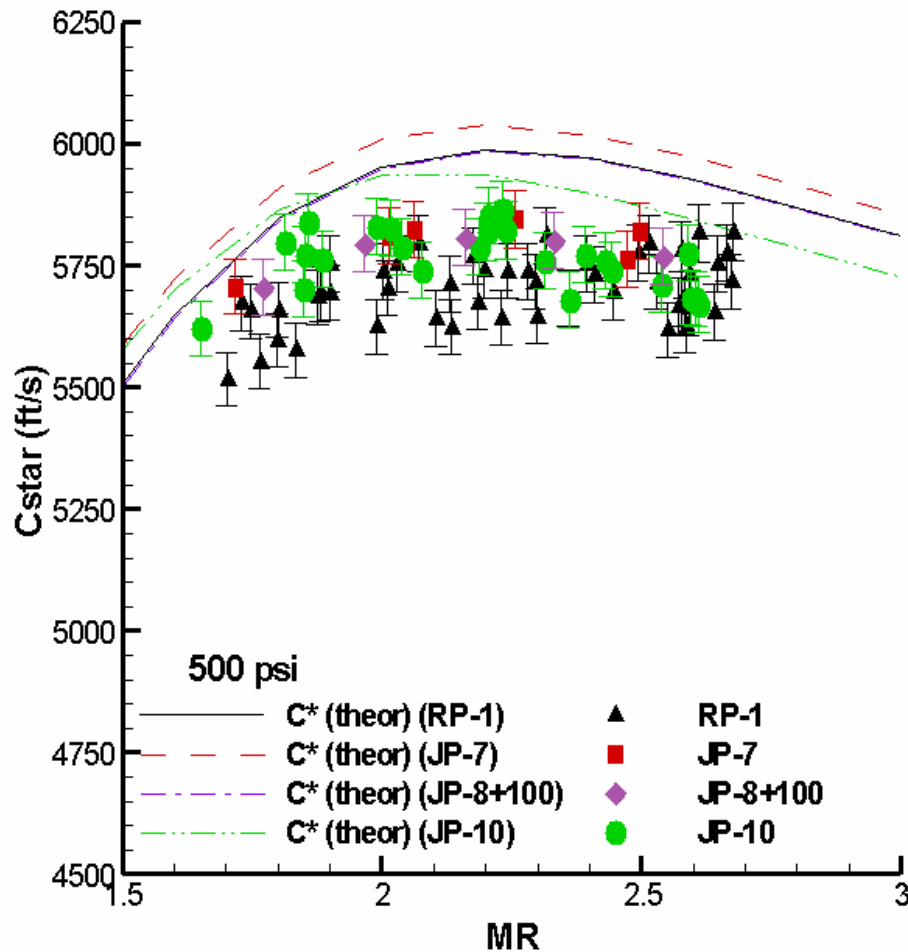


RP-1

• Injectors 3, 5, 7, and 12 exhibited 200 Hz chamber pressure oscillation



Hot-Fire Measurements Fuels Comparison



750 psi results show identical trend



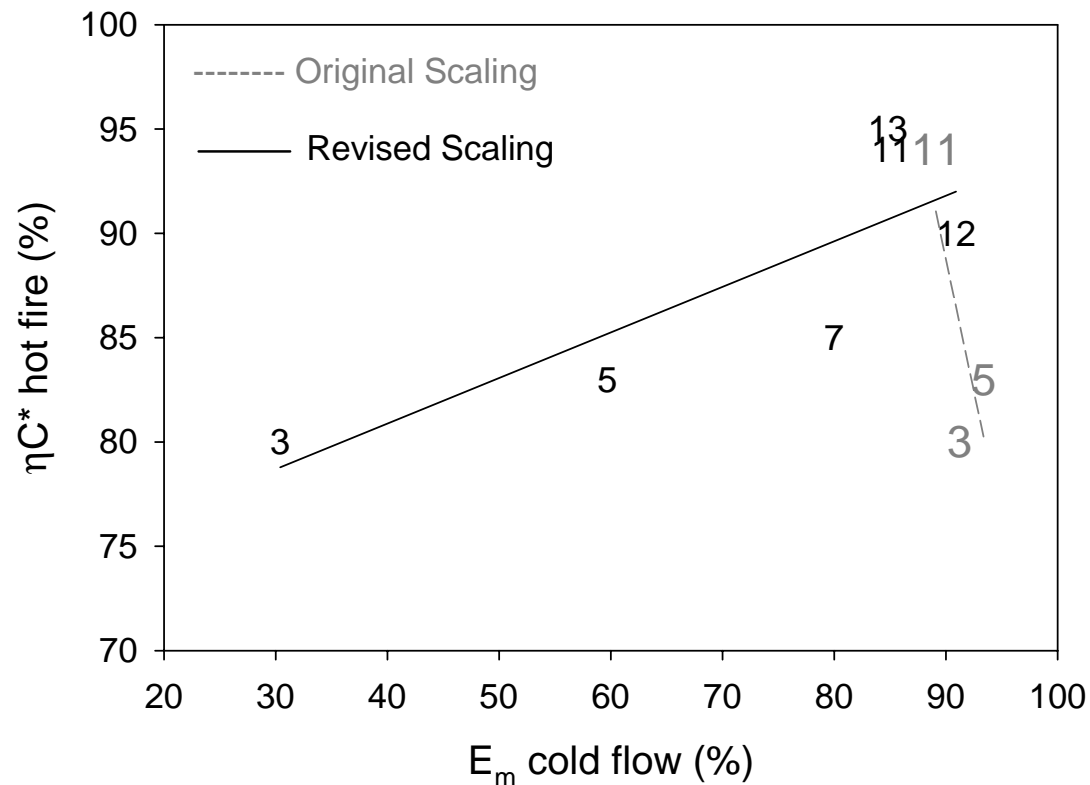
Cold-Flow/Hot-Fire Comparison

Mixing Efficiency



- **Rupe Mixing Efficiency**

- Original Scaling is based on momentum ratio
- Revised Scaling is based upon absolute momentum difference





Cold-Flow/Hot-Fire Comparison

Break-Up Time Analysis



- **Combustion performance is dependent upon the ratio of the film residence time to the break-up time of the fuel film**
- **Break-up time found from correlation proposed by Mayer (1961). Reformulated to:**

$$\frac{t_r}{t_b} = \frac{C_1 L}{\tau_f} \left[\frac{\mu_l \left(\frac{\rho_g}{\rho_l} \right)^2 (V_g - V_l)^4}{V_l^3} \right]^{1/3}$$

- **C_1 arbitrary constant set so that $t_r/t_b = 1$ when $\eta c^* = 100\%$**
- **Dominated by relative velocity between gas and liquid (or just gas velocity)**



Cold-Flow/Hot-Fire Comparison

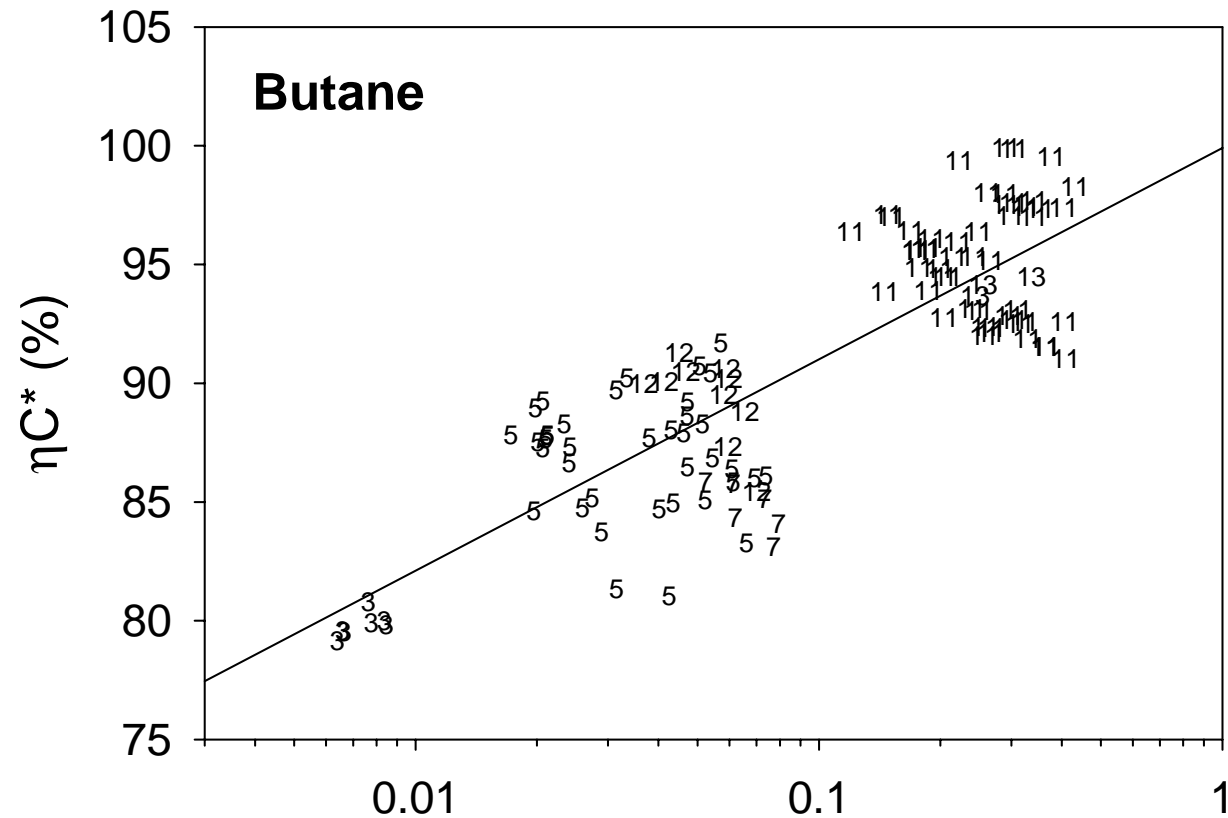
Break-Up Time Analysis



- **Initial attempts to use correlation using bulk (average) gas velocity**
 - Did not correlate with combustion performance
- **Velocity profile measurements found that flow was not a plug flow**
- **Appropriate gas velocity is the interface velocity**
 - Estimated as gas phase velocity, at the exit plane, one film thickness from wall
 - Measurements made with Phase Doppler Interferometry without injector liquid circuit flowing
 - Film thickness calculated from inviscid flow theory



Cold-Flow/Hot-Fire Comparison Break-Up Time Analysis



- Injector effects dominate

- Determination Coefficient (R^2) = 0.71

- Plot contains data for cases: 1.3 MPa < Pc < 6.5 MPa, 1.8 < MR < 4.1



Cold-Flow/Hot-Fire Comparison Break-Up Time Analysis



- Small, but measurable effect of the fuel selection
- Simplifying the break-up time correlation (for high performing injector):

$$\frac{t_r}{t_b} = \frac{C_1 L}{\tau_f} \left[\frac{\mu_l \left(\frac{\rho_g}{\rho_l} \right)^2 (V_g - V_l)^4}{\sigma_l V_l^3} \right]^{1/3}$$

$\dot{m}_g / \rho_g A_l \leftarrow V_g$ since $V_g > V_l$ for inj 11
 $\dot{m}_l / \rho_l A_l \leftarrow V_l$

$$\frac{t_r}{t_b} = \frac{C_1 L}{\tau_f} \left[\frac{A_l^3 \mu_l \rho_l}{A_g^4 \sigma_l} \frac{1}{\rho_g^2} \frac{\dot{m}_g^4}{\dot{m}_l^3} \right]^{1/3}$$

- Effect of fuel found in parameter $\mu_l \rho_l / \sigma_l$
- Mass flow of fuel and oxidizer nearly constant for constant MR and P_c



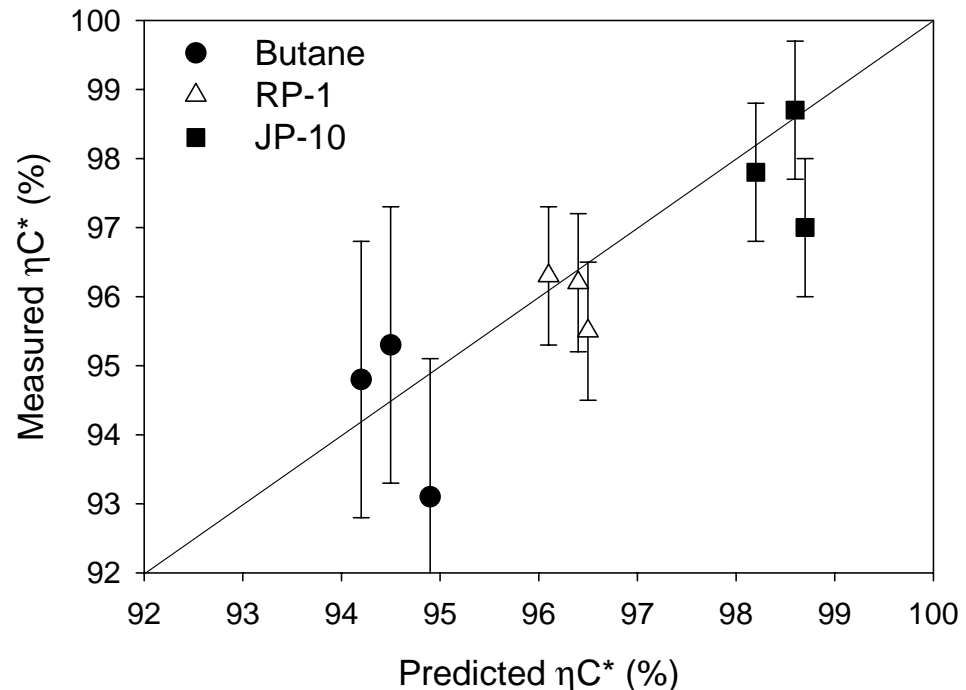
Cold-Flow/Hot-Fire Comparison Break-Up Time Analysis



- Fuel effect contained within the $\mu_l \rho_l / \sigma_l$ parameter
 - Testing performed with Injector 11 (converging design)
 - All cases are MR = 2.5, $P_c = 3.3$ MPa
 - Nearly order of magnitude change in this parameter
 - Small effect on η_c^*

Fuel	Density (kg/m ³)	Viscosity (N s/m ²)	Surface Tension (N/m)	$\frac{\mu \rho}{\sigma}$
Butane	579	1.68e-4	1.2e-2	8.11
RP-1	806	7.70e-4	2.8e-2	22.2
JP-10	929	3.50e-3	3.0e-2	108.4

Properties of Selected HC Fuels





Conclusions



- **Three basic styles of gas-centered swirl injectors studied**
 - **Converger**
 - **Diverger**
 - **Prefilmer**
- **Demonstrated that injector performance (ηc^*) is dependent upon ratio of residence time to break-up time**
- **Relative velocity between fuel and oxidizer is primary indicator of performance**
- **Effect of fuel properties is small but measurable**
- **Smaller Sauter Mean Diameter (less than $75 \mu\text{m}$) did not correlate with combustion performance**
- **Cold-flow data, when scaled properly, can be a strong indicator of hot-fire performance**



Supplemental Material



- You never know when you might need it....



Cold Flow Evaluations

Scaling Methodologies

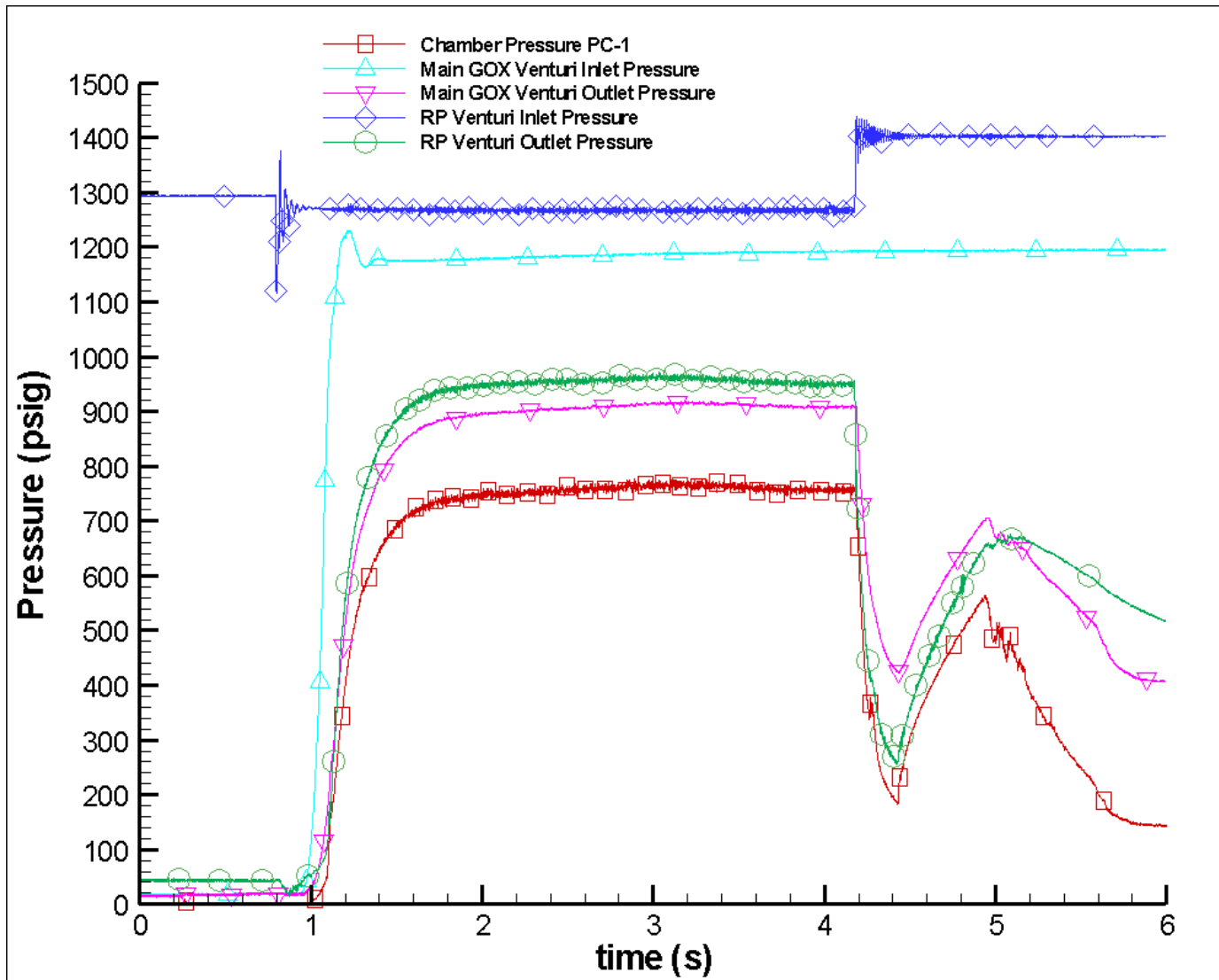


- **Two cold-flow scaling methods used**
 - **Goal is to gain data indicative of hot-fire performance**
 - **Match momentum ratio between fuel/oxidizer**
 - **Match liquid injection velocity and gas density to hot-fire conditions**
 - **Adjust gas flow rate to match momentum ratio**
 - **Results not indicative of performance**
 - **Match absolute momentum difference between fuel/oxidizer**
 - **Match gas density and injection velocity to hot-fire conditions**
 - **Adjust water flow rate to match absolute momentum difference**



Hot-Fire Measurements

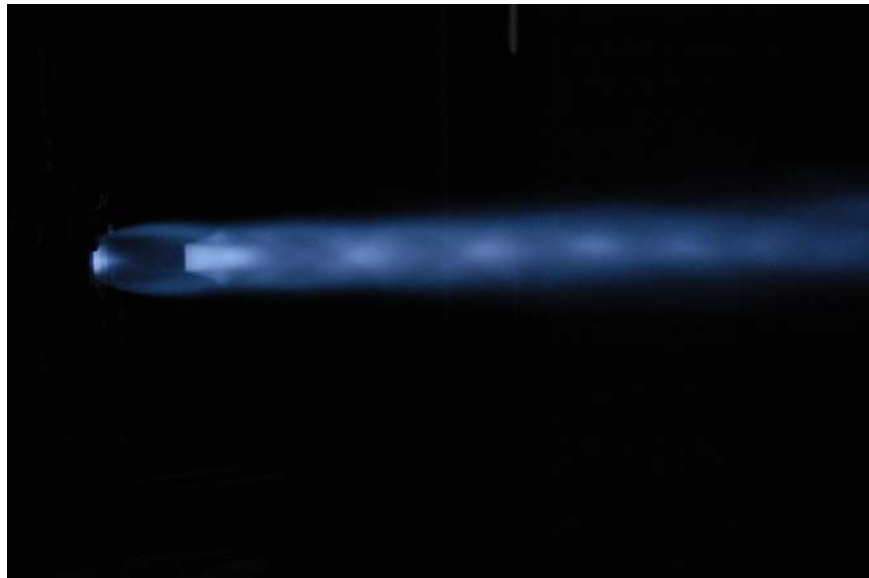
Sample Pressure Traces





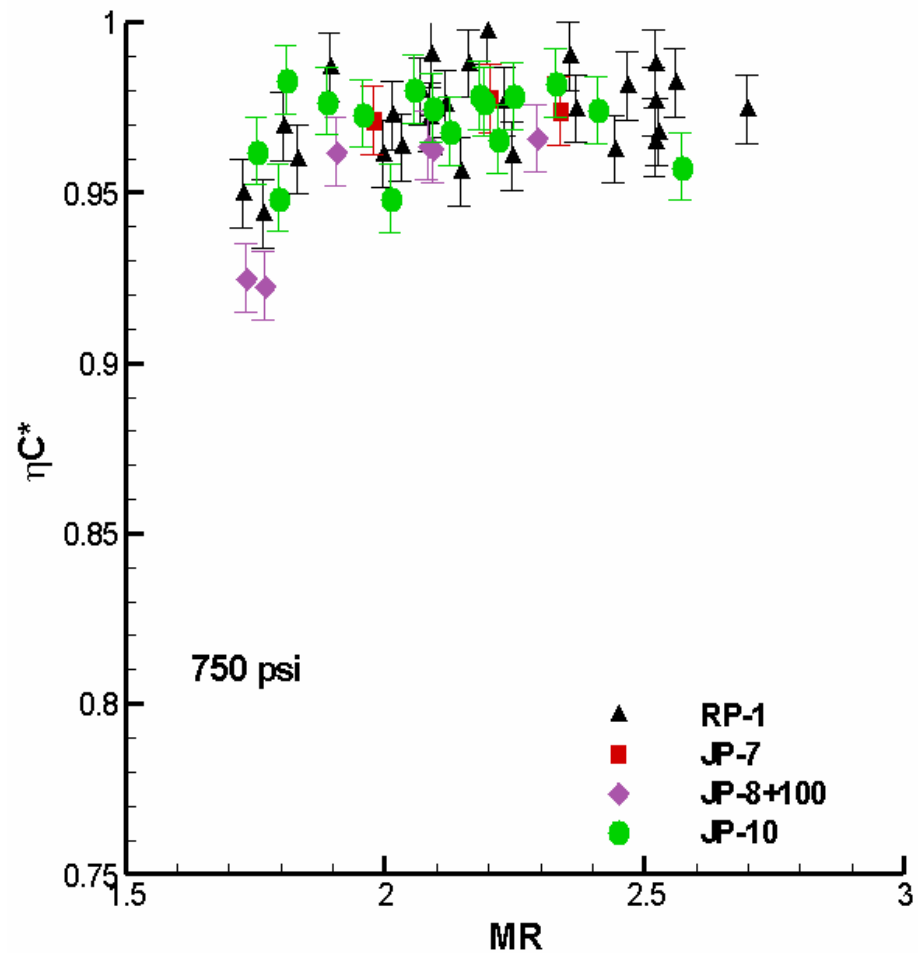
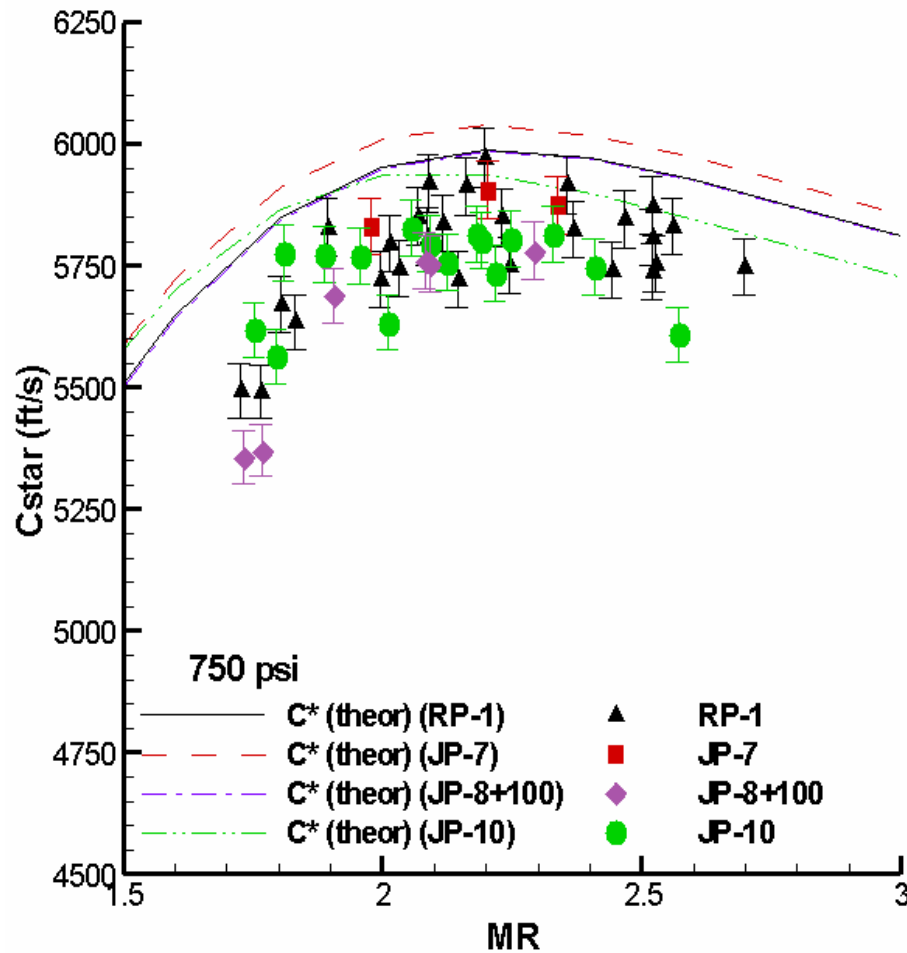
Hot-Fire Measurements

Sample Firings





Hot-Fire Measurements Fuels Comparison



500 psi results show identical trend

GAS-CENTERED SWIRL COAXIAL LIQUID INJECTOR EVALUATIONS

P.A. Strakey, R.K. Cohn, and D.G. Talley
Air Force Research Laboratory, Edwards AFB, CA

ABSTRACT

Uni-element cold flow and hot fire evaluations were performed on variants of gas-centered swirl coaxial injectors. Gaseous oxygen and various liquid hydrocarbons were used in the combustion evaluations, while water and gaseous nitrogen were the simulants in the cold flow experiments. The connections between the two sets of data were examined.

The cold flow experiments demonstrated that the mixing efficiency of the various injector designs was highly sensitive to the internal geometry of the injector as well as the scaling methodology used to simulate the hot-fire conditions. When proper scaling methodology was employed, a correlation between the measured cold-flow mixing efficiency and hot-fire c^* performance was observed. A semi-empirical correlation was developed based on a film stripping mechanism that relates the measured c^* efficiency of these injectors to the injector geometry and fuel properties. The correlation was able to capture the general trends of injector geometry and c^* performance.

The correlation also implies a relative insensitivity of injector performance to fuel properties. Hot-fire testing of several common hydrocarbon fuels including RP-1, Butane, JP-10, JP-7 and JP-8 confirmed the insensitivity to fuel properties and demonstrated that c^* efficiency in excess of 95% is achievable with all of these fuels.

INTRODUCTION

The development of a liquid rocket engine is an arduous task typically involving extensive testing at both large and small scales. Since testing at large scales is extremely expensive, it is of interest to understand how modeling and simulation and inexpensive cold flow and hot fire evaluations on a uni-element scale can best be combined to advance the injector design before committing to larger scales. In addition to being inexpensive, evaluations on a uni-element scale are often capable of producing a large amount of information within a short period of time. Accordingly, it was decided to develop such an understanding of scaling for the coaxial class of injectors. An oxygen-rich staged combustion liquid

hydrocarbon engine was selected as the baseline cycle.

A reasonable design principle for coaxial injectors is to attempt to shroud the oxidizer in the central flow with the fuel as the annular flow. The goal is for the oxidizer to be completely encapsulated and consumed by the fuel, thus preventing it from reaching the combustion chamber walls. In some applications, the oxidizer injected into the main combustion chamber is a liquid, for example liquid oxygen, while the fuel is injected as a gas, for example gaseous hydrogen. In an oxygen-rich staged combustion liquid hydrocarbon engine, however, it would be the oxygen which is the gas and the fuel which is a liquid. The difference leads to fundamentally different injector designs. In the present study, a gas-centered swirl coaxial injector concept was selected, where swirl is imparted to the annular liquid fuel flow, while the central gaseous oxygen (GOX) flow is not swirled. Atomization of the fuel is accomplished through the development of surface instabilities on the liquid sheet by shear from the high-speed gas, which initiates ligation and ultimately atomization.

Design guidance in the US for liquid swirl-type injectors commonly comes from industrial applications that include industrial boilers, gas turbines, and spray drying. The guidance has been compiled in various monographs, such as refs. 1 and 2. However, these applications concern sprays which are introduced into a quiescent or co-flowing gas, with the gas typically being the oxidizer. These applications are more consistent with liquid-centered injectors. As such, this guidance is not directly applicable to gas-centered swirl coaxial injectors.

The following sections describe the injector designs, the cold flow uni-element test results, hot fire uni-element test results, and the connections found between these results. CFD calculations were also performed [3,4], but are not discussed here.

INJECTOR DESIGN

The basic gas-centered swirl coaxial element design can be conceptualized as a straight-run post for the gas. The post includes a discrete set of liquid injection orifices near the downstream exit of the gas post. The orifices are tangentially oriented to

generate a swirling liquid film around the periphery of the element. The liquid film is thus subjected to a combination of cross-flow shear and centrifugal forces. The liquid is stripped from the film inside the element by the central gas jet, which entrains the droplets, transporting the resultant spray downstream. The parameters that can be varied in this design include the number of liquid injection orifices, the axial location of the orifices relative to the final injection location, and most importantly the post geometry near the liquid injection orifices. Three basic injector concepts were identified for comparative evaluation: diverging elements, converging elements, and pre-filming elements. These elements are shown schematically in Figure 1.

The diverging element design injects the fuel downstream of a sudden expansion, with the expansion having a characteristic expansion angle. A set of six parametric diverging elements was designed, as shown in Figure 1.

For the converging element, the liquid is injected tangentially into the outer annulus. Then, the outer annulus necks down to accelerate both the liquid and gaseous flows. Out of an initial set of four parametric converging element designs, one design was selected (#11) for evaluation.

The pre-filming element is an adaptation of designs commonly used in gas turbines and industrial boilers (1). The liquid is injected tangentially into a recessed groove (Fig. 1, #7 & #13). The axial dimension of the groove should be large enough to permit the liquid film to homogenize before being exposed to the high-speed gaseous core flow. The film is then circumferentially accelerated as the groove diameter narrows to the main gas port diameter. Two parametric pre-filming element designs were developed as shown in Figure 1.

COLD FLOW EVALUATIONS

Cold flow evaluations used water to simulate the liquid fuel and gaseous nitrogen to simulate GOX. The cold flow evaluations were performed in a vessel pressurized with gaseous nitrogen. The vessel design allows the back pressure to be adjusted and includes windows for optical access. The diagnostics utilized for this study included back-lit strobe imaging of the spray, mechanical patterning for measurement of liquid flux distribution and phase Doppler interferometry for droplet size and velocity measurement. The axial station for all diagnostics can be varied between 2.54 and 15.24 cm downstream of the injector exit, although most of the subject test data was collected at 5.08 cm.

The cold flow conditions were designed to simulate hot fire conditions with respect to propellant conditions at the point of injection. At the time of the cold flow evaluations, hot fire test pressures were projected to be 1.72 MPa (250 psia) and 3.44 MPa (500 psia) using butane as the fuel. Later the hot fire conditions were extended both in pressure range and in number of fuel types.

The cold flow injector operating conditions were designed to match to the hot fire operating condition in the following manner. First, the gas injection velocity was set to the corresponding hot fire operating velocity. Second, the injected gas density was matched to the hot fire density by setting the chamber back pressure. Since the density of nitrogen and oxygen at a given temperature and pressure are very similar, the second condition is achieved with only a slight variation in chamber back pressure relative to the hot fire chamber pressure. With oxidizer injection velocity and density equivalent to the hot fire case, the final adjustment was to match the hot fire gas-to-liquid momentum difference by adjusting the mass flow rate of liquid water. Using the above matching conditions, the injectors were tested at chamber pressures of 1.97 MPa (271 psig) and 3.93 MPa (556 psig), compared to 1.72 MPa (250 psia) and 3.44 MPa (500 psia) for the hot-fire conditions. Most of the cold-flow data presented here are for the 1.97 MPa (271 psig) condition. Higher pressure cold flow data is not presented due to dense spray effects which limited the ability to obtain optical diagnostic measurements. Selected elements were also tested over a range of injected mixture ratios. A comparison of the 1.72 MPa (250 psia) hot fire operating condition and the analogous cold flow simulation operating condition is included in Table 1.

Several different measurements were made of each element's performance characteristics, some qualitative and others quantitative. Back-lit strobe images were used to qualitatively compare the near-field spray patterns of the different injection elements. Tests were run with only the liquid circuit operating and then with both fluid circuits operating. The "liquid only" tests produced a rapidly expanding liquid cone. The cone typically expanded with half-angles exceeding 75° and often wet the injector face plate. However, when the gas and liquid circuits were run simultaneously, the free liquid film was pulled inwards towards the gas core and rapidly entrained. The images for the 1481 N (333 lb_f) equivalent operating condition are presented in Figure 2. The largest angle diverging element (#3), appears to have the widest spray pattern with relatively large liquid droplets being thrown toward the periphery of the

spray, while the other diverging elements (#5 and #12) show better entrainment of the liquid film into the gas flow. This is due to the higher gas velocity and improved liquid stripping of these designs.

The converging element (#11) produced a narrower spray cone with what appears to be finer droplet sizes. The large bore pre-filming element (#7) produced a well entrained spray but with a somewhat larger droplet size near the periphery of the spray, similar to element #5. The small bore pre-filming element (#13) produced a very narrow solid cone spray with excellent atomization.

More quantitative measurements were performed using a combination of mechanical patterning and phase Doppler velocimetry. The liquid (and gas) entering the mechanical patterner tubes drain into collection bottles where the liquid level was measured using a capacitance probe accurate to $\pm 2\%$. Although the gas vents off to a common manifold that connects back to the chamber, the pressure drop through the patterning system only allows about 25% of the gas to pass through the tubes. This generated a partial stagnation region at the entrance of the patterner tubes and prevented some of the smaller droplets from entering the tubes. The larger droplets have enough momentum to penetrate the stagnation zone and enter the tubes. The collection efficiency of the patterner was defined as the ratio of the integrated liquid mass flux to the injected liquid flow rate. The high gas flow rates and injection velocities generated by these swirl coaxial elements combined with the small droplet sizes resulted in measured collection efficiencies were sometimes much less than 100%. The measured collection efficiencies were in the range of 60% - 100%.

Droplet size and velocity were measured using a phase Doppler interferometer. The instrument simultaneously measures the size and velocity of individual droplets as they pass through a $60\ \mu\text{m}$ by $75\ \mu\text{m}$ probe volume. The optical configuration in this experiment was set to measure droplet sizes ranging from $3.8\ \mu\text{m}$ to $440\ \mu\text{m}$ and velocities ranging from $-50\ \text{m/s}$ to $250\ \text{m/s}$. The average velocity of droplets less than $20\ \mu\text{m}$ in diameter was taken as a good estimate of the average gas phase velocity (5). The extreme density of the spray prevented phase Doppler measurements at element flows above equivalent thrusts of $1481\ \text{N}$ ($333\ \text{lb}_f$). At this flow condition, data validation rates for droplet sizing were as low as 15% in the center of the spray, where the liquid mass flux was the highest. In comparison, data validation rates as high as 90% were achieved at the edges of the spray. The

validation rates for the velocity measurements were much larger than those for the droplet sizing, typically greater than 97% throughout the spray.

In order to account for the low collection efficiency of the mechanical patterner, the raw liquid mass flux data were corrected by the measured collection efficiency for each radial profile. For example, if the collection efficiency was 80%, the liquid flux data were multiplied by a factor of 1.25. Radial profiles of liquid mass flux measured at 5.08 cm downstream of the injection point are displayed in Figure 3 for three of the injectors. The patterner collection efficiency is annotated on each plot. For each element, two radial slices oriented at right angles to one another apart were measured with the patterner to check for spray symmetry, they are denoted by the 90° and 0° markings. Most of the sprays appear to have a solid-cone structure when both the gas and liquid circuits are flowing. The diverging element (#3) generated a significantly wider spray pattern with only some of the liquid entrained into the central gas flow. Most of the liquid exited the injector in the form of a hollow cone as evidenced by the peaks in the liquid mass flux profiles at a radial location of 60 mm on each side of center (Fig. 3). This was also seen in the images in Fig. 2. The six other elements tested produced solid cone sprays with varying degrees of radial spreading.

Most of the mass flux patterns appeared to be well behaved, reaching a maximum value at the centerline and falling off with an approximately Gaussian distribution and good spray symmetry. One exception was the largest angle diverging element (#3) that showed a significant asymmetry in the liquid flux distribution. The extent of the asymmetry in the liquid flux profile of element #3 can be seen in Figure 3 for the two radial slices which are oriented 90° apart. The outboard peak in the liquid flux profile at 60 mm shifts from one side of the spray to the other. This type of behavior typically results in poor combustion performance.

The gas velocity profiles were all Gaussian-like in shape and were typical of simple turbulent jets. The mixture ratio distribution for each injector was calculated from the gas velocity and liquid flux profiles. The mixture ratio profiles provided an indication of the degree of mixing between the gas and liquid. An element with large deviations in mixture ratio from the average in regions where there is significant mass flow (such as #3) will result in poor combustion performance.

A more quantitative measure of mixture ratio uniformity that has commonly been used in the past is the Rupe mixing efficiency (6). The mixing

efficiency is calculated by dividing the spray into a series of concentric rings or stream-tubes. Each ring has a measured liquid and gas mass flux. A modified version of the Rupe mixing efficiency was used here and is given by Equation 1.

$$E_m = 1 - \underbrace{\sum_{r_i < R} \frac{m_{f_i}(R - r_i)}{R}}_{r_i < R} - \underbrace{\sum_{r_i > R} \frac{m_{f_i}(R - r_i)}{(R - 1)}}_{r_i > R}$$

$$r_i \equiv \frac{MR}{(1 + MR)} \quad R \equiv \frac{\overline{MR}}{(1 + \overline{MR})} \quad (1)$$

In eq. 1, m_{f_i} is the mass fraction in each ring, and MR is the measured mixture ratio. The modification here is that the integrated liquid and gas flowrates are used instead of the injected flowrates. This is necessary because the integrated gas mass flowrate differs from the injected amount due to entrainment. The converging element design (#11) as well as the small bore diverging element (#12) and the pre-filming element (#13) all generated well mixed sprays with E_m on the order of 85% or better. Element #3 produced the poorest mixing with an E_m of only 30.4%, while element #5, with an E_m of 59.7%, and #7, with an E_m of 80.0%, were deemed to be of intermediate mixing. The element mixing is believed to play a direct role in combustion performance and will be discussed further in relation to the hot-fire results.

A comparison of the Sauter mean diameter for the six elements evaluated is provided in Figure 4. The Sauter mean diameter (SMD) was found to be inversely proportional to the gas velocity in the cup region, as would be expected. As the relative velocity between the liquid film and gas flow, and thus the Weber number, is increased, the shearing force on the liquid droplets also increases resulting in a smaller final drop size. Except for element #3 all of the elements provided good atomization with a SMD less than 75 μm .

The conclusions of the uni-element cold flow testing, which guided the selection of elements for the uni-element hot fire testing, were that the element designs which maintain high relative velocity between the gas and liquid film and allow sufficient residence time for liquid stripping and entrainment should perform the best. All of the element designs produced sprays that were hollow-cone with only the liquid flowing, but became solid-cone sprays with both the gas and liquid circuits flowing. Except for injector #3, the injection element concepts all produced sprays with adequate symmetry.

HOT FIRE TEST RESULTS

Hot fire evaluations were conducted using a copper heat-sink combustor with chamber lengths of 17.78 cm and 20.32 cm and a nominal contraction ratio of 25.2. Each test was several seconds in duration with at least a half-second of steady state operation. Details of the facility and the test hardware can be found in previous publications (7,8).

Nearly 1000 separate firings were conducted of the various elements. Chamber pressures have ranged from 1.37 MPa (200 psia) to in excess of 6.87 MPa (1000 psia). Two series of evaluations were conducted. First, butane and RP-1 fuels were evaluated for a variety of injector geometries. Then, a variety of fuels were evaluated using one of the injector designs (#11). This was motivated by a need to validate the capability of the facility to make measurements of the required accuracy, and by the expectation that was developed during the progress of this study that the performance of injector #11 should be relatively insensitive to the identity of the fuel. Injector #11 also demonstrated low combustion noise characteristics.

The metrics used to characterize the hot fire data include characteristic velocity (c^*), heat load, and chug stability. The c^* efficiency measurements assume the ideal c^* can be calculated using the CEA chemical equilibrium code assuming a finite area combustor. Heat loss to the walls and other losses are neglected. Despite this, it is reasonable to assume that these losses will be similar between the different injector types, thus allowing for comparisons between the elements.

Propellant flow rates were measured with cavitating venturis and sonic nozzles. The liquid venturis were calibrated with water, RP-1, and JP-10. The calibrations were then compared with each other, after correcting for vapor pressure and density. Typically, these three calibrations agreed to within 1%. The sonic nozzles were also calibrated using GN2 to develop the appropriate discharge coefficient for the nozzle. Spot-check calibrations with GOX provided suitable confidence in these results. Uncertainty estimates for the liquid venturi flow rates are less than 1%. Primarily, this uncertainty is the result of the process of converting results between the different fluid media. Estimate for the gas-side flow rate uncertainty is 0.5%. Both of these values can be reduced by performing all calibrations with the requisite propellant.

The chamber pressure transducers used for these experiments were accurate to 0.05% of their

full-scale value. Since measurements were typically made at $\frac{1}{4}$ of their full-scale output, the typical pressure measurement uncertainty is 0.20%. Another significant player in the uncertainty is the nozzle diameter. Combined in this uncertainty are the accuracy of the measurement of the nozzle as well as the change in the nozzle diameter as it heats during the test. It is estimated that this error is less than 0.05 mm. Using the nominal nozzle diameter of 1.14 cm, this yields an uncertainty of 0.44%.

Using these values the estimated uncertainty in the c^* measurements is $\pm 1.0\%$. This uncertainty is dominated by the uncertainties of the throat diameter and the propellant flow rates. The butane data that is presented here is from an older set of experiments and the uncertainty in the c^* measurements of this data set is approximately 2.0%.

Figure 5 shows a comparison of several of the element types at a nominal pressure of 3.44 MPa (500 psi) except for elements #3 and #7 which were only evaluated at a pressure of about 1.72 MPa (250 psi). The converging element (#11) produced the highest c^* efficiency. Qualitatively, one would expect that this element would have a high heat load due to the mixing and burning that likely occurs within the cup. This was confirmed by the heat markings seen on the element. However, the heat loads were not high enough to damage the element. The c^* efficiency increases slightly with increasing MR, i.e., with the resulting increased oxidizer injection velocity. This injector has shown no signs of chug instability. In fact, very little combustion noise is seen in the data with the standard deviation of chamber pressure less than 0.7% of the mean chamber pressure. This can be seen in Figure 6 which is a plot of a typical pressure trace from the experiments.

The pre-filming element (#13) which has a relatively small inside diameter also showed excellent combustion performance, but resulted in a much higher pressure drop than the converging element design (#11). Figure 7 shows the measured gas and liquid side injector pressure drops, normalized by the chamber pressure for six of the elements in cold-flow and hot-fire conditions. The pressure drop for injector #13 was much higher than the cold-flow pressure drop. It is believed that combustion was occurring within the element which caused significant propellant acceleration and pressure drop.

The pre-filming element (#7) demonstrated lower performance than the converging design. However, this element showed the most heat marking. In fact, the marking was so severe, that

testing was not conducted at chamber pressures exceeding 3.44 MPa (500 psi). Both of these pre-filming injectors experienced a 200 Hz chamber pressure oscillation.

Figure 8 is a comparison of the measured cold flow mixing efficiencies and the hot-fire c^* performance using two different scaling methodologies with butane as the fuel. The original scaling between hot-fire (butane/GOX) and cold-flow (water/gN₂) conditions was based upon typical momentum ratio scaling used for shear coaxial injectors. The procedure was to match the liquid injection velocity and the gas density to the hot fire conditions, then to adjust the gas flowrate to match the gas-to-liquid momentum ratio. As can be seen by the dashed line in Figure 8, this methodology resulted in a very poor correlation between the cold flow and the hot fire results. Further investigation indicated that the gas-to-liquid momentum ratio might not be the appropriate scaling parameter for gas-centered swirl injectors. A revised scaling approach was then adopted which involved matching the gas density and injection velocity to the hot-fire conditions and adjusting the water flowrate to match the absolute momentum difference between the gas and liquid flows, as shown by the solid line in Figure 8. This approach resulted in a much better correlation between the cold flow and hot fire results, and demonstrates the importance of understanding the proper physical mechanisms when scaling between cold flow and hot fire evaluations.

Although mixing efficiency is only partially related to c^* performance, there is a distinct correlation between the hot fire and the cold flow data. Note that the cold-flow mixing efficiency was measured 5.08 cm downstream from the injector exit, while the hot fire experiments were conducted with an 20.32 cm long chamber. The longer chamber provides more time for mixing to occur, which improves performance. In the limit of an infinitely long chamber with no losses all of the injectors would perform at 100% efficiency. Thus the correlation between cold flow and hot fire evaluations should depend on the hot fire combustion chamber length.

After this initial screening, three more diverging element designs were examined. These designs were labeled 12A, 12B, and 12D. Due to facility changes, these three new diverging designs were evaluated with RP-1 instead of Butane. The results of these evaluations are shown in Figure 9. Note that design 12D had a c^* efficiency in excess of 95%. This is approximately 5% higher than that of 12A and 12B. Figure 10 shows c^* efficiency results from RP-1 testing for injector 11. As can be seen from comparing these results with those in Figure 5, the c^*

efficiency was approximately the same for RP-1 as it was for butane.

In order to demonstrate the capability of the facility to perform accurate combustion performance measurements, additional evaluations were performed with injector 11 using JP-7, JP-8, and JP-10 as fuels. The densities of these fuels varies by nearly a factor of two, and their viscosities vary by an order of magnitude, as indicated in table 3. The results of the combustion performance evaluations are shown in Figure 11. The results confirm the fuels performed nearly the same as predicted. The results also show that, despite the difference in densities and viscosities, injector #11 is not only highly performing but relatively insensitive to fuel type, as well as being relatively insensitive to chamber pressure for the two pressures examined.

ANALYSIS OF THE RESULTS

In an effort to better understand the effect of injector design and operating conditions on combustion performance, an analysis of the film breakup process was conducted. The cold-flow results indicate that the best performing injectors are the ones in which the swirling liquid film is completely stripped and entrained into the gas flow. Incomplete stripping of the liquid film inside the cup region results in the remaining film being thrown radially outward away from the central gas core, resulting in poor mixing. This is supported by the correlation between cold-flow mixing efficiency and hot-fire c^* performance, to be shown below. A search of the literature revealed a liquid stripping correlation used for shear coaxial injectors originally proposed by Mayer (9). The breakup rate, or rate of mass removal from the liquid core (per unit area) is given by;

$$\dot{m}_b = C_1 \left[\frac{\mu_l (\rho_g V_r)^2}{\sigma_l / \rho_l} \right]^{1/3} \quad (2)$$

where V_r is the relative velocity between the gas and liquid streams, and C_1 is an empirically determined constant. In a first order analysis, one could calculate the breakup time as;

$$t_b = \frac{\dot{m}_l}{\dot{m}_b P V_l} \quad (3)$$

where "P" is the perimeter of the contact area between the liquid and gas phase ($P=\pi D$) and V_l is the axial component of the liquid film velocity inside the

cup region. This would be the time to fully strip the liquid film assuming that the flow conditions inside the cup region are constant in the axial direction. The residence time of the film can be calculated by:

$t_r = \frac{L}{V_l}$ where "L" is the length of the cup, or the con-

tact length between the gas and liquid phases. Since the mass flowrate of the thin liquid film is approximately equal to: $\dot{m}_l = \rho_l V_l \pi D \tau_f$, where τ_f is the thickness of the swirling liquid film, the ratio of the film residence time to the breakup time (t_r/t_b) can be expressed as;

$$\frac{t_r}{t_b} = \frac{C_1 L}{\tau_f} \left[\frac{\mu_l \left(\frac{\rho_g}{\rho_l} \right)^2 (V_g - V_l)^4}{V_l^3} \right]^{1/3} \quad (4)$$

It is hypothesized that when the ratio of t_r/t_b is increased, the mixing efficiency or c^* performance should also increase. The key parameter in the breakup rate is the relative velocity, V_r , which is equal to $(V_g - V_l)$. In calculating V_r we have used the liquid film axial velocity, V_l , calculated from inviscid flow theory, which yields an average film velocity (10). Since the bulk gas velocity in the cup region is roughly an order of magnitude larger than the film velocity, one might speculate that V_l has only a small effect on relative velocity. Using the "bulk flow" or average gas velocity inside the cup region produced only a very weak correlation between the measured hot fire performance and the film-stripping analysis described above. Further cold flow investigation revealed that the axial velocity profiles at the exit-plane of the injectors were not plug-flow for many of the diverging element designs. It is believed that a more appropriate gas velocity to use in the film-stripping correlation would be the gas velocity at the gas-liquid interface.

In an effort to estimate the interface velocity, cold flow axial velocity profiles were measured for each of the injector types without the liquid circuit flowing. This was accomplished by seeding the gas flow upstream of the injector with a fine mist of water droplets in the size range of 1 to 10 μm . Droplet size and velocities were measured with the phase Doppler interferometer and gas velocity was estimated by extrapolating the size-velocity relationship to the limit of zero size. The interface velocity was then taken to be the gas-phase velocity at one film thickness from the wall. The film thickness was calculated using inviscid flow theory (10). Table 2 provides bulk-flow velocity, measured interface velocity and calculated film thickness for each of the injec-

tors. The gas velocity at the film interface for the diverging element designs (nos. 3, 5, and 12) was found to be significantly lower than the bulk flow velocity due to flow separation in the expansion region of the cup.

Using the gas velocity at the film interface, the correlating parameter (t_f/t_b) was calculated for the GOX/butane hot-fire conditions, and is presented in Figure 12 as a function of the measured c^* efficiency. Although there is a significant degree of scatter in the plot, a fairly strong correlation can still be seen. The constant, C_1 , in Eq. 4 was determined to be 0.01177 by setting the correlating parameter to be equal to 1.0 at a c^* efficiency of 100%. This is somewhat arbitrary, but is based upon the hypothesis that combustion efficiency should be maximized when the ratio of residence time to breakup time is greater than or equal to 1.0.

The coefficient of determination, R^2 , of the first order fit in Figure 12 was 0.71. Figure 13 is a plot of the correlating parameter versus c^* efficiency for injectors 5, 11 and the 12 using RP-1 and JP-10 as fuels. The curve fit line in the plot in Figure 13 is the same as that from the Butane data (Fig. 12). With the possible exception of injector 5, Figure 13 demonstrates the ability of the correlating parameter to capture both the geometrical effects of the 12-series injectors and also the effect of fuel type. The results for injector 5 may be questionable because of the 200 Hz instability for this injector that was evident during the tests.

The effect of fuel type is better isolated from other effects such as gas velocity and density in Figure 14. Whereas Figure 13 contains all mixture ratios and chamber pressures, Figure 14 extracts data for a fixed injector type #11, a fixed nominal chamber pressure of 3.3MPa, and a fixed mixture ratio of 2.5. For each of the runs, the measured chamber pressure and propellant flowrates were used along with the corresponding ambient condition fuel properties from Table 3 to calculate the value of the correlating parameter. The actual fuel temperature at the gas-liquid interface is unknown due to the possibility of combustion occurring inside the injector, therefore the fuel properties at the nominal inlet temperature of 298K are used as a basis for comparison. The relationship between c^* and the correlating parameter from the first order curve fit in Figure 12 was used to predict c^* for each of the test cases. Figure 14 shows a plot of the predicted c^* versus the measured c^* efficiency for each test case. Figure 14 shows that the fuel density and viscosity play a small but measurable role in combustion performance. The higher viscosity of JP-10 results in an increase in the strip-

ping rate as given by Eq. 2. Also, the higher density of JP-10 results in a lower liquid film velocity and hence an increase in residence time and relative velocity in the cup region of the injector. Both factors result in an increase in the correlating parameter as well as combustion performance. It is important to point out that the relatively wide variation in fuel properties studied here results in only a small variation in combustion performance compared to the strong effect of injector geometry on performance as shown in Fig. 12.

Finally, it may be observed that many of the chamber pressures achieved in the hot fire evaluations in fact exceeded the critical pressure of the respective fuels, yet the correlation parameter still captures the effects of fuel and injector type. Supercritical pressures potentially cause effects such as reducing the surface tension to zero which could invalidate the physical basis of Eq. 4. However, absorption and diffusion of gaseous oxygen into the fuels is known to significantly increase the critical pressure of the mixture. Phase equilibrium calculations of butane/oxygen mixtures reveal that the critical mixing pressure could be as high as 20 MPa, whereas most of the hot fire chamber pressures did not exceed 5 MPa. Therefore it may be expected with reasonable confidence that the mixtures were subcritical, surface tension existed, and the physical basis of Eq. 4 remains sound.

SUMMARY

Design guidelines are being developed for gas-centered hydrocarbon swirl injectors. Three basic element concepts have been identified. A set of parametric injection elements has been designed in an effort to identify key design features and acceptable parameter values. Detailed cold-flow testing was performed on each of the elements with the goal of identifying unique injector characteristics. The cold flow data showed that the internal injector geometry played a key role in the measured mass distributions, mixture ratio distributions and atomization characteristics.

Extensive hot-fire data was also collected with the same injectors used in the cold-flow phase of the program. The injectors were tested over a range of chamber pressures and mixture ratios and with a variety of hydrocarbon fuels. Within the range of fuels studied, it has been found that the converging element injector #11 is both high performing and relatively independent of fuel selection. The effect of injector geometry on the spray patterns and mixing uniformity observed in the cold-flow experiments was also observed in the hot-fire-results in the form of combustion performance. An increase in the cold-

flow mixing uniformity resulted in an increase in combustion performance.

A film-stripping correlation developed for shear-coaxial injectors has been used to estimate the stripping rate of the liquid film inside the injector cup. The correlation takes into account both fluid property effects as well as injector geometry effects. The hot-fire performance data correlates reasonably well with the film-stripping correlation over a broad range of injector designs and a significant variation in fuel properties. The correlation also reveals an important parameter for injector scaling between cold-flow and hot-fire, which is the relative velocity between the liquid film and gas stream in the injector post.

ACKNOWLEDGEMENTS

The authors would like to thank Jeff Muss and Curtis Johnson of Sierra Engineering for their work in designing the injectors and for their valuable suggestions regarding the material in this paper. A portion of this work was supported by NASA-Glenn Research Center under the direction of Mike Meyer.

REFERENCES

1. Lefebvre, A.; Atomization and Sprays. Hemisphere Publishing Corp, 1989.
2. Doumas, M. and Laster, R.; "Liquid-Film Properties for Centrifugal Spray Nozzles", *Chemical Engineering Progress*, Vol. 49, No. 10, Oct. 1953.
3. Muss, J.A., Johnson, C.W., Cheng, G.C., and Cohn, R.K. "Numerical Cold Flow and Combustion Characterization of Swirl Coaxial Injectors." AIAA 2003-0125, 41st AIAA Aerospace Sciences Meetings and Exhibit, Reno, NV, 6-9 Jan 2003.
4. Cheng, G.C., Davis, R.R., Johnson, C.W., Muss, J.A., Greisen, D.A., Cohn, R.K., "Development of GOX-Kerosene Swirl Coaxial Injector Technology". AIAA 2003-4751 39th AIAA Joint Propulsion Conference and Exhibit, Huntsville, AL, 20-23, July, 2003.
5. P. A. Strakey, D. G. Talley, L. K. Tseng and K. I. Miner, "The Effects Of LOX Post Biasing On SSME Injector Wall Compatibility", *Journal of Propulsion and Power*, Vol. 18, No. 2, March-April 2002.
6. Nurick, W. H., "Analysis of Sprays from Rocket Engine Injectors", *Journal of Spacecraft*, Vol. 8, No. 7, July, 1971, pp. 796-798.
7. Cohn, R.K., Strakey, P.A., Bates, R.W., Talley, D.G., Muss, J.A. and Johnson, C.W., "Swirl Coaxial Injector Development", AIAA 2003-0124, 41st AIAA Aerospace Sciences Meeting and Exhibit, Reno, NV, 6-9 Jan., 2003.
8. Cohn, R.K., Danczyk, S.A. and Bates, R.W., "A Comparison of the Performance of Hydrocarbon Fuel in an Uni-element Combustor", AIAA 2003-4752, 39th AIAA Joint Propulsion Conference and Exhibit, Huntsville, AL, 20-23, July, 2003.
9. Mayer, E., "Theory of Liquid Atomization in High Velocity Gas Streams", *ARS J.*, Vol. 31, pp. 1783-1785, 1961.
10. Yule, A.J. and Chinn, J.J., "Swirl Atomizer Flow: Classical Inviscid Theory Revisited", *Presented at: The 6th International Conference on Liquid Atomization and Spray Systems, ICLASS-94, Rouen, France, July, pp. 334-341, 1994.*

Test (Hot-Fire or Cold-Flow)	Pc (MPa)	Fvac (kN)	m ^{Gas} (kg/s)	m ^{Liq} (kg/s)	V ^{Gas} (m/s)	V ^{Liq} (m/s)	mV ^{Gas} - mV ^{Liq}	V ^{Gas} /V ^{Liq}	MR
Butane/GOX	1.72	1.48	0.078	0.028	43.3	14.1	2.99	3.1	2.8
H ₂ O/N ₂	1.97	NA	0.078	0.036	43.3	10.8	2.99	4.0	2.1

Table 1: Comparison of element operating conditions, hot fire to cold flow (hot fire MR=2.8)

Injector	Gas Bulk Velocity (m/s)	Gas Inter- face Veloc- ity (m/s)	Film Axial Velocity (m/s)	Relative Velocity (m/s)	Film Thickness (μ m)
3	12	1.5	3.2	1.7	193
5	51	15	5.4	9.6	247
7	43	22	3.5	18.5	332
11	65	59	4.9	51.1	295
12	83	25	6.4	18.6	256
12A	83	25	6.4	18.6	256
12B	83	25	6.4	18.6	256
12D	127	64	7.3	56.7	280
13	157	79	7.2	71.8	322

Table 2: Gas and liquid properties in cup region. Pc=1.97 MPa, N₂=0.078 kg/s, H₂O=0.036 kg/s

Fuel	Density (kg/m ³)	Viscosity (N s/m ²)	Surface Tension (N/m)
Butane	579	1.68e-4	1.2e-2
RP-1	806	7.70e-4	2.8e-2
JP-10	929	3.50e-3	3.0e-2

Table 3: Properties of selected hydrocarbon fuels @ 298K and 0.1 MPa

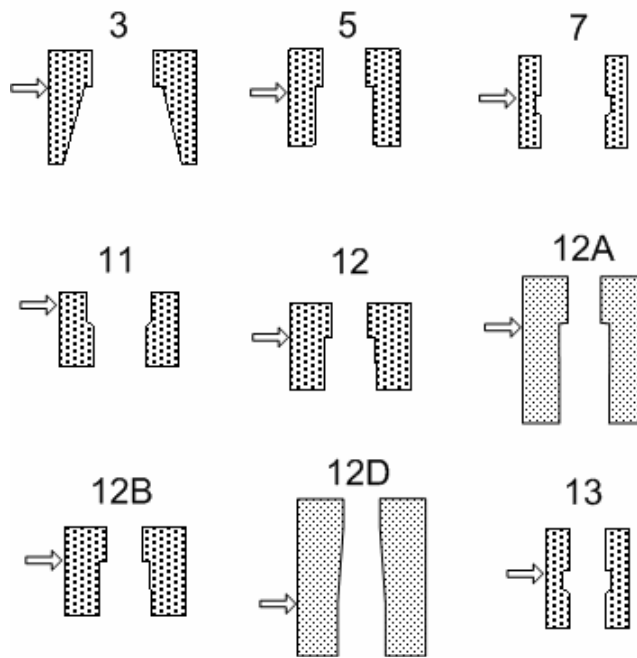


Figure 1 : Schematic drawings of the nine elements tested. Gas enters from the top and the location of the tangential liquid inlets are shown by arrows.

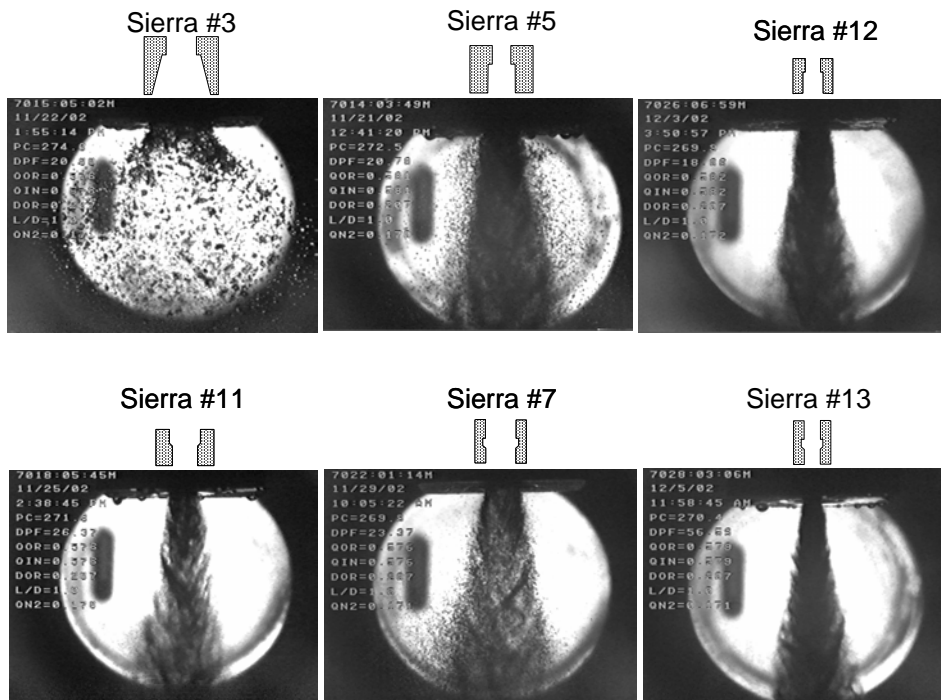


Figure 2: Strobe Back-Lit Images of Six Element Types, Pc=1.97 MPa (271 psig)

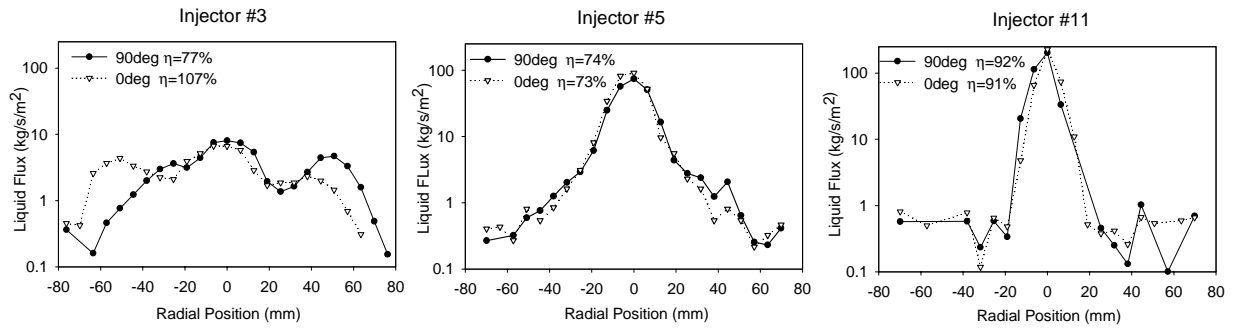


Figure 3: Corrected liquid mass flux profiles for injectors 3,5 and 11 at an axial location of 5.08 cm and a chamber pressure of 1.97 MPa (271 psig) (see Table 1).

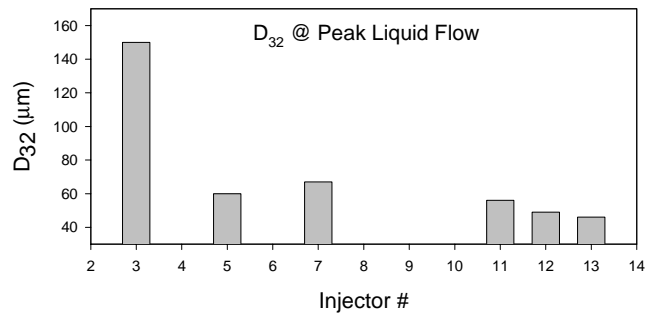


Figure 4: Sauter mean diameter at location of peak liquid flow.

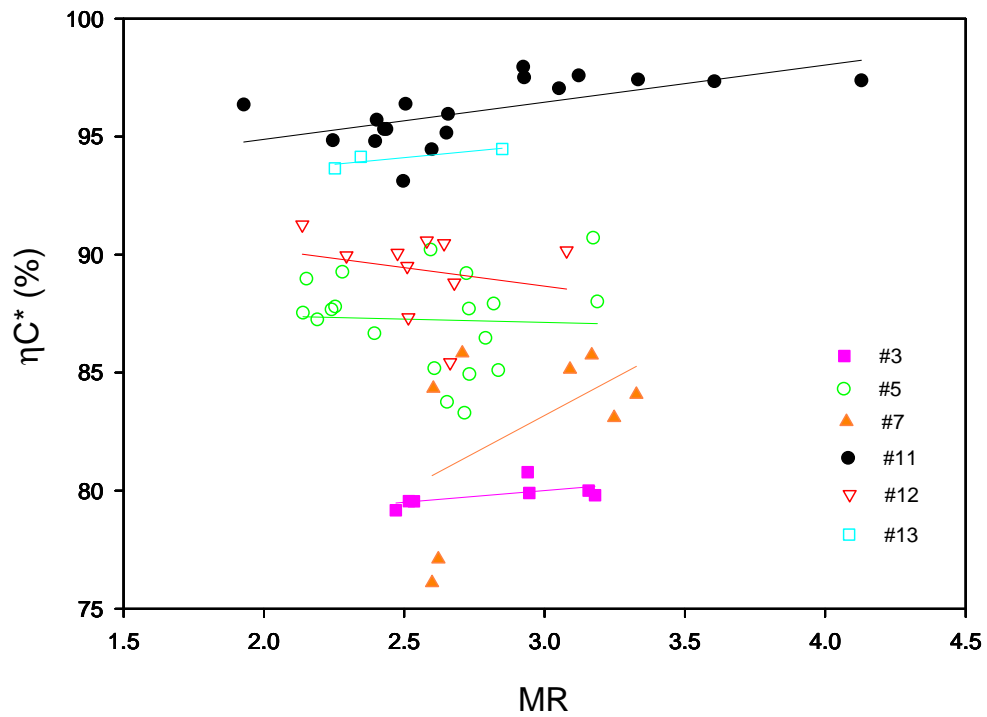


Figure 5: C* efficiency versus MR for Diverging (#3, #5 and #12), Pre-filming (#7 and #13) and Converging (#11) Elements. $P_c \sim 1.72$ to 3.42 MPa (250 to 500 psi), butane as fuel.

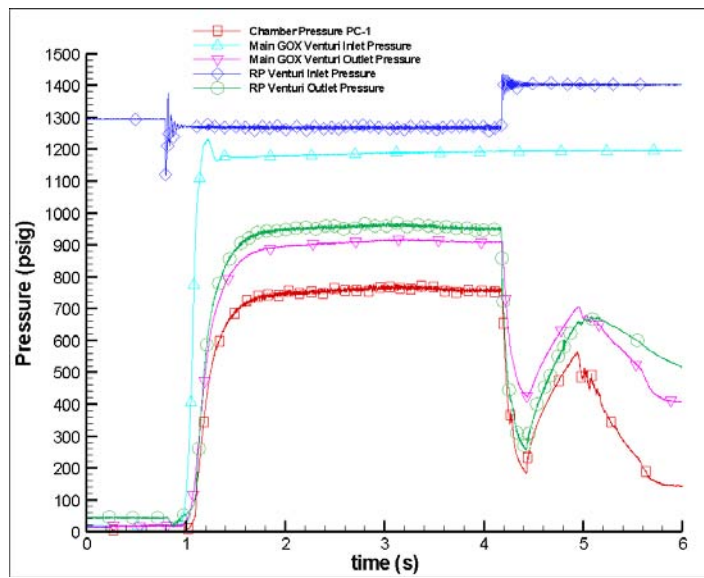


Figure 6: Sample pressure plot for Hydrocarbon fuel testing.

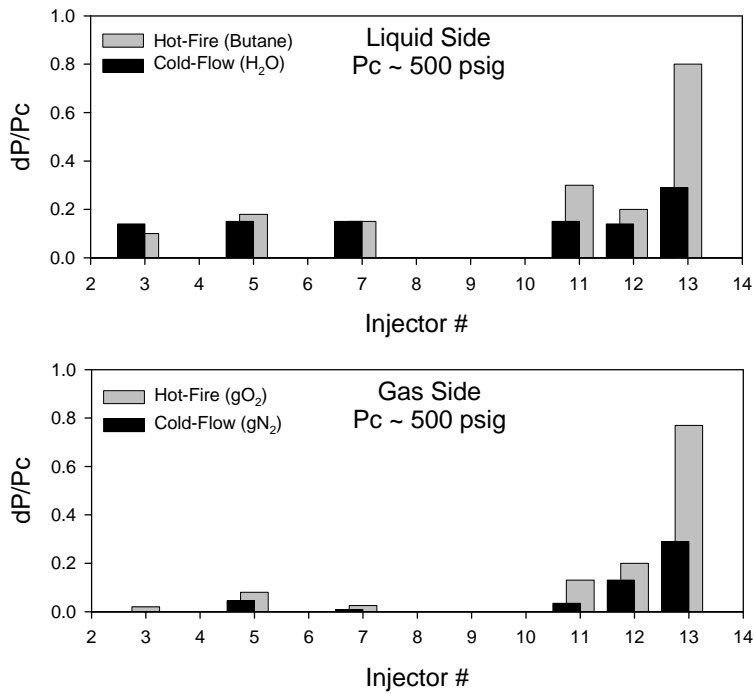


Figure 7: Hot-fire and cold-flow pressure Drop Data (dP/Pc) for Liquid and Gas Sides

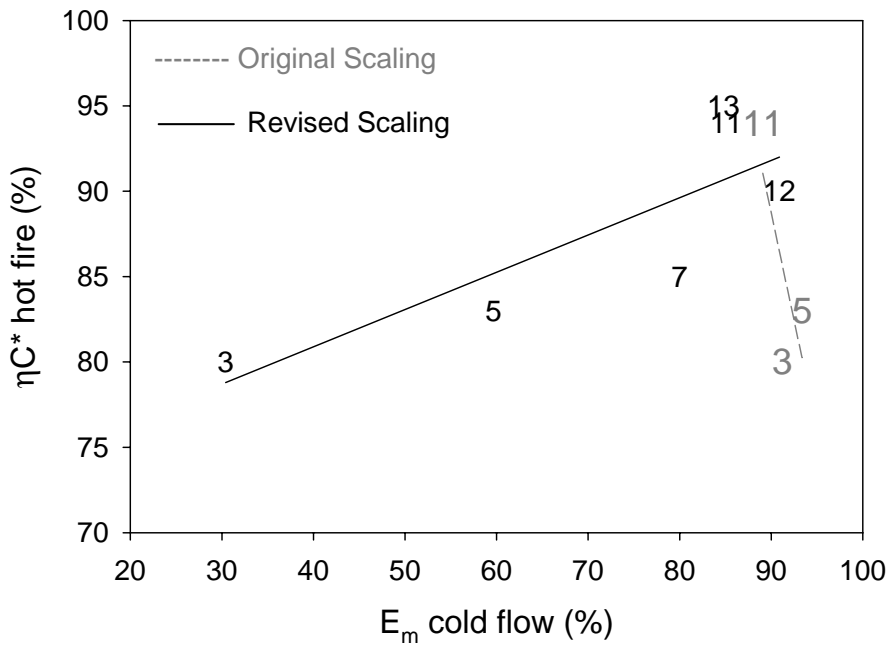


Figure 8: Correlation between hot-fire c^* efficiency (MR=2.8, $P_c=1.37$ to 3.42 MPa (200 to 500 psia)) and cold-flow mixing efficiency ($P_c=1.97$ MPa (271 psig)) for six of the injector designs.

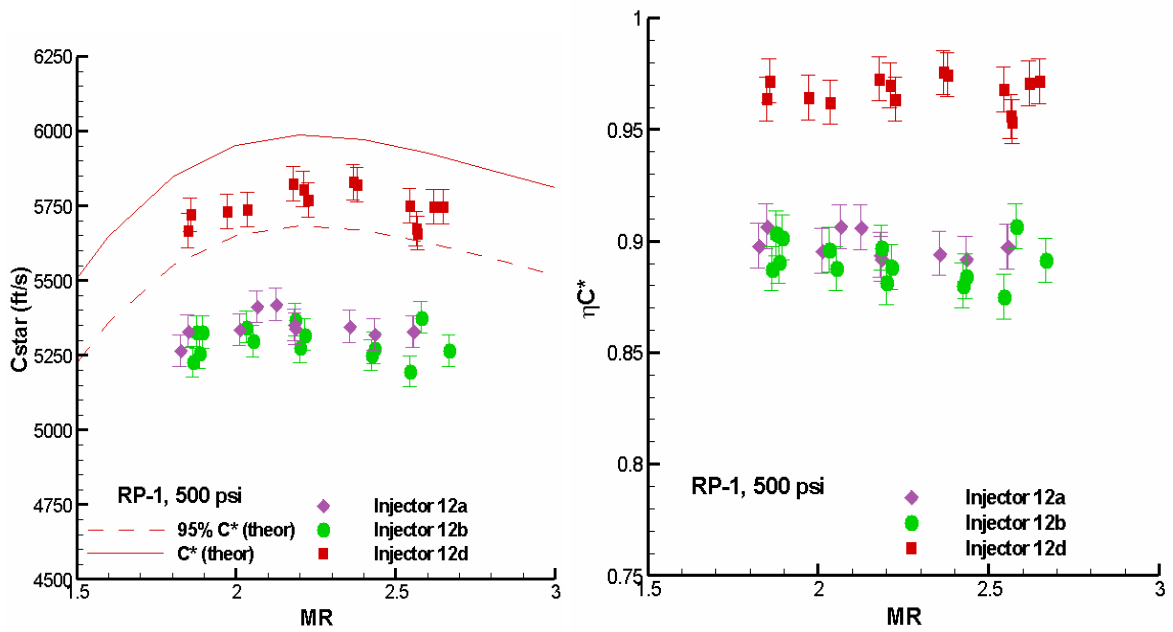


Figure 9: c^* (a) and c^* efficiency (b) for 3 different diverging injectors.

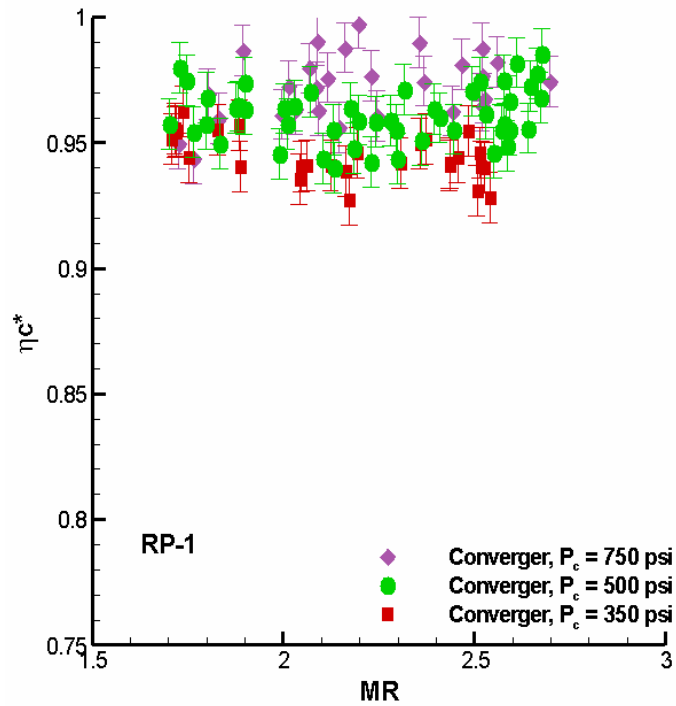


Figure 10: c^* efficiency for RP-1 with Injector 11.

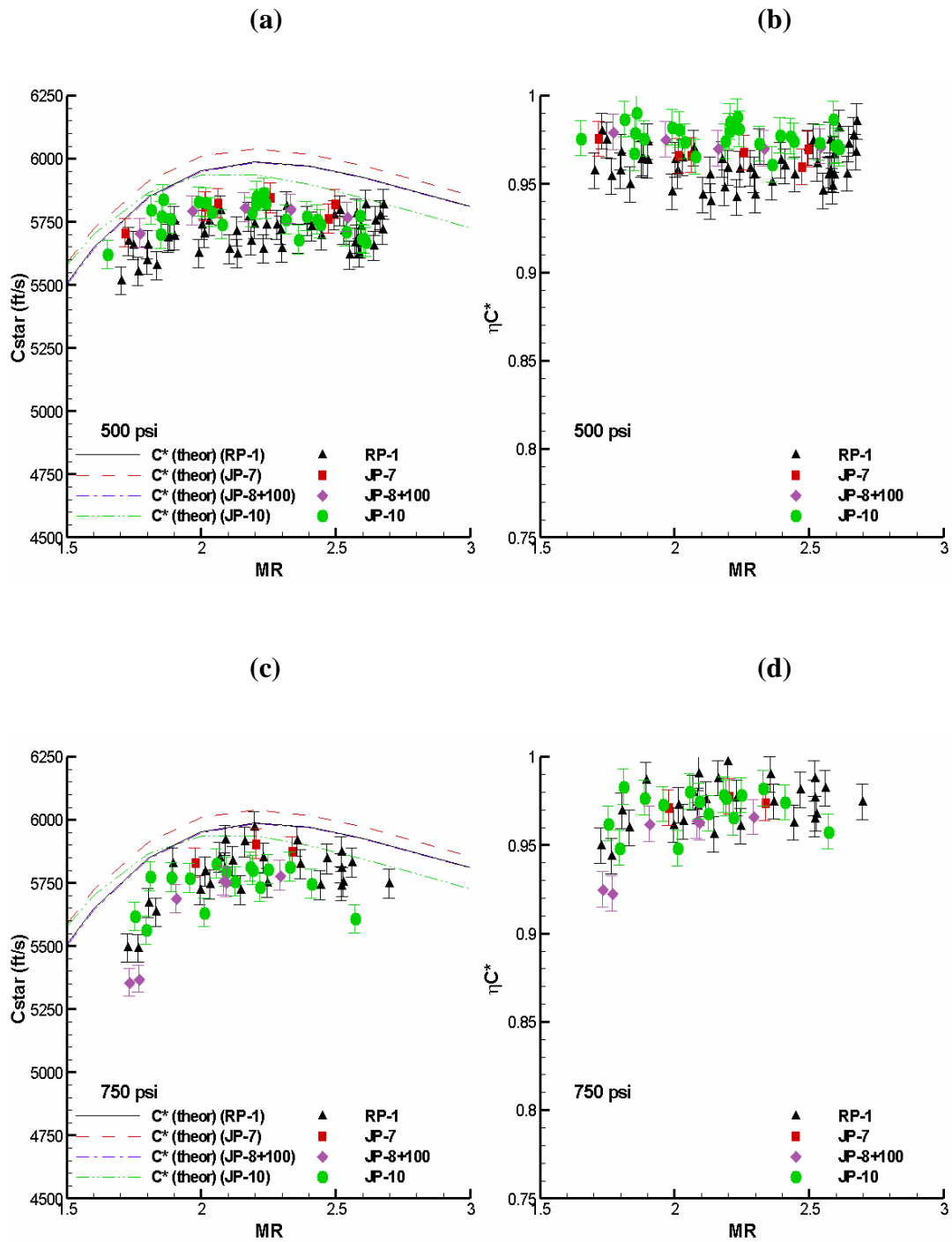


Figure 11: Performance of Injector 11 (converging injector) with a variety of hydrocarbon fuels. (a) c^* for 3.42 MPa (500 psi). (b) c^* efficiency for 3.42 MPa. (c) c^* for 5.15 MPa (750 psi). (d) c^* efficiency for 5.15 MPa.

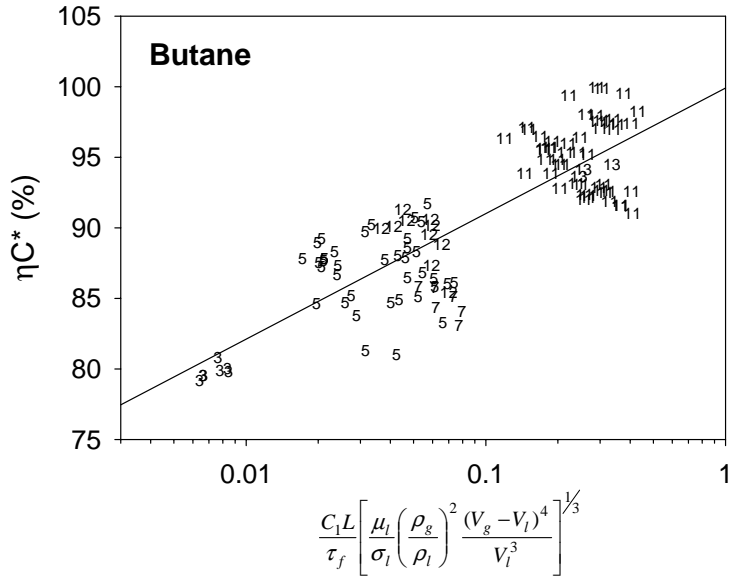


Figure 12: C* versus correlating parameter for all injectors (Butane data) using the interface velocity for gas side. Pc=1.3 to 6.53 MPa (190 to 950 psia), MR=1.8 to 4.1 and chamber length of 17.8 to 20.3 cm.

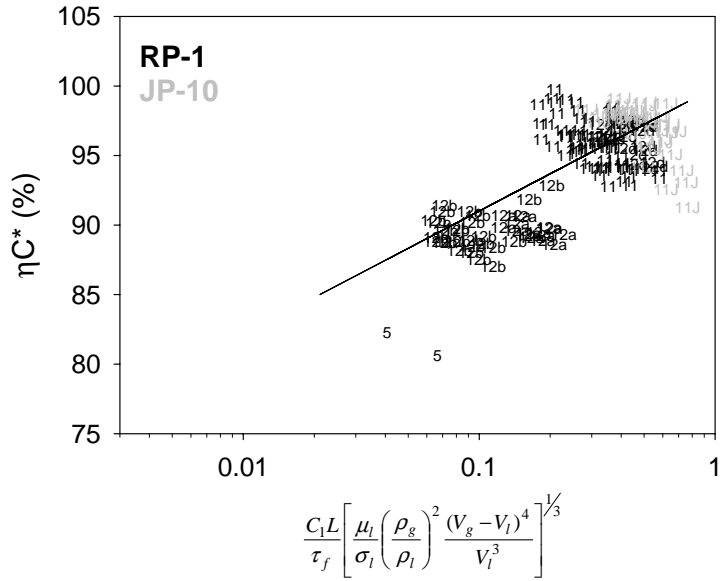


Figure 13: C* versus correlating parameter for injectors 5,11,12*(RP-1 and JP-10) using the interface velocity for gas side. Pc=1.49 to 5.36 MPa (217 to 780 psia), MR=1.5 to 5.0 and chamber length of 20.3 cm.

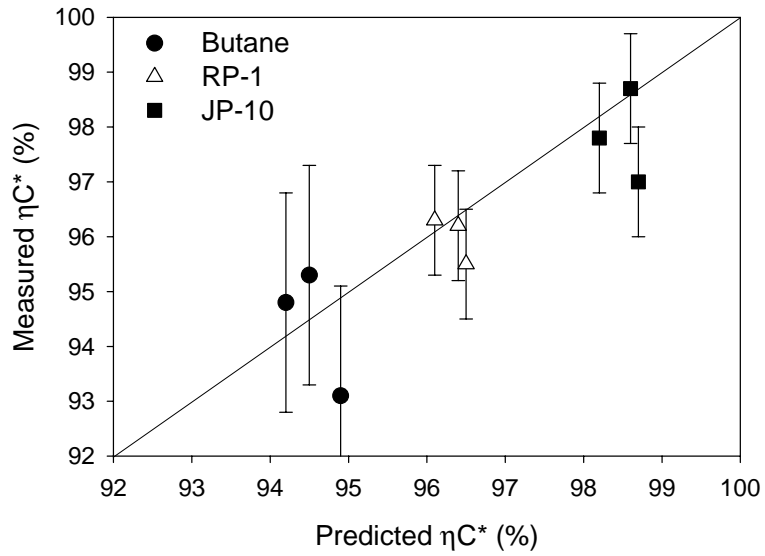


Figure 14: Predicted versus measured C* efficiency for Butane, RP-1 and JP-10 with injector #11. $P_c=3.07$ to 3.70 MPa (447 to 539 psig), $MR=2.4$ to 2.6 .



Required Data for Code Validation

Richard Farmer
University of Nevada, Reno

Fifth International Symposium on Liquid
Space Propulsion, Chattanooga, TN
October 27-30, 2003



THE ISSUES

Computational Fluid Dynamics (CFD) is a mature and powerful methodology

Neither CFD nor experimentation can quantify all aspects of a design

CFD is not used without a preliminary validation exercise

The validation experiment is usually not sufficiently definitive or appropriate



ANALYSIS & EXPERIMENT

Purpose of investigation

Identify critical flowfield characteristics

Does the validation experiment address the issues critical to the design?

Does the CFD analysis substantiate the critical measurements?

SCOPE OF CFD VALIDATION CONSIDERATIONS

Purpose	Critical Phenomena	Additional Phenomena	Measurements Desired	Examples	Typical References
Operational LRE performance	Thrust & propellant flowrates	O/F distributions	Thrust, flowrates & local compositions and temperatures	SSME	Wang & Chen ⁵
LRE thermal environment	Wall heat-fluxes, coolant conditions, hot-gas conditions	Gas-side compositions	Stream temperatures & flowrates	H-1 & F-1; Hot gas test nozzle*	Hale ⁶ Back ⁷
Base heating	Exit-plane conditions; geometry	Flight trajectory	Structural temperatures; flowfield velocities	Saturns; Space Shuttle; Cold flow model*	Payne & Jones ⁸ Greenwood, et al ⁹ Wang ¹⁰
Characterize injector elements	O/F uniformity, atomization efficiency	Wall heating, combustion mechanics	Local temperatures & mixture and phase ratios	PSU; IWRCM experiments	Santoro ¹¹ ; Vingert & Habiballah ¹² ; Thomas, et al ¹³
Characterize regenerative cooling system	Local flow & thermal state of coolant; configuration	External & internal wall conditions	Temperatures, local flowrates & flowfields	Cooling system for the ST SSME	Wang ¹⁴
Investigate combustion stability Start-up & shut-down	Transient internal pressure- & flow-fields	Accurate configuration specification	Local temperature & compositions Thermal environments		Muss ¹⁵ Grenda, et al ¹⁶ Habiballah ¹⁷ Wang ¹⁸
Revolutionize combustor configuration	Mixing efficiency & thermal environments	Ignition sequence	Thrust, flowrates, & local compositions in the exit-plane	Pulsed detonation engine concepts	Strehlow ^{19*}
Catalyze propellant combustion	Catalysis kinetics	Catalyst life	Thrust, flowrates, & local compositions in the exit-plane	Peroxide LRE	Harlow ²⁰
Material/hot-gas compatibility	Materials & propellants	Local temperatures & compositions	Material response to operating conditions	Carbon deposition	Lausten ²¹



Potential of CFD Methodology

Only way to analyze 3-D steady and unsteady flowfields.

Can utilize any averaged turbulence model.

Can use real thermodynamic & transport fluid properties.

Can compute finite-rate combustion.

Accurately accounts for coupling between heat, mass & momentum transfer.

Only practical means of treating multiphase flows.



The Dilemma

Lack of basic experimental research---

Instead many project oriented studies.

Multitude of successful CFD analyses give CFD analyst confidence, but not the design community.



Instrumentation Choices

Optical measurements

Classical measurements

Validation

CFD/experimental integration

DEMONSTRATED INSTRUMENTATION SYSTEMS

PARAMETER	INSTRUMENT TYPE	EXAMPLE	COMMENTS	INVESTIGATOR/ REFERENCE
pressure	inlet, wall & exit plane transducers		<ul style="list-style-type: none"> • distribution along wall • high frequency transducers at selected locations & thermally protected 	T. Nesman, MSFC J. Wiley, MSFC
temperature	thermocouple	Medtherm instruments	wall distribution	L. Jones, Medtherm, Inc. Huntsville, AL
wall heat flux	total & radiation calorimeters	Medtherm instruments	selected wall stations	L. Jones
temperature	emission/absorption radiation	Rocketdyne experiments	exit plane values	Herget
stable species concentration	optical E/A IR radiation	Rocketdyne experiments Spectraline	<ul style="list-style-type: none"> • exit plane values • major species only 	Herget
stable species concentrations	probes & gas chromatography		<ul style="list-style-type: none"> • cooled probes to freeze reactions • all species to determine mixture ratios 	Drummond*
radical species	laser-induced fluorescence	MASCOTTE data	distinction between thermal & chemiluminescence req'd	A.C. Eckberth ²⁹ J.L. Thomas
plume photographs	visible & IR photographs	shock structure and plume boundaries	criticality depends on exit-plane pressure field	A. Ratliff ³⁰

Mixing efficiency is the key to combustor efficiency and thermal loads

CFD can be used now to predict mixing effects

Reynolds or Favre averaged turbulent transport equation solutions will answer essentially all of the important design issues

Experiments can be designed & accomplished to evaluate these predictions





Transient Phenomena

Transient CFD simulations can be made for combustion stability, start-up & shut-down thermal environments

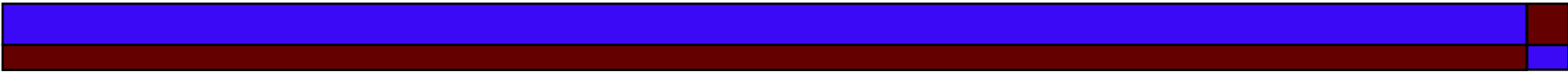
Suitable experiments to validate the transient analyses can be designed and performed

A determined effort backed by adequate funding is necessary for this methodology to be developed



Recommendations:

- ❑ A baseline set of CFD validation experiments should be selected and/or performed
- ❑ Parametric variation of operational variables must be included in the baseline studies
- ❑ Refrain from selecting a standard CFD code, instead utilize validated codes
- ❑ Develop and calibrate critical instrumentation systems



REQUIRED DATA FOR CODE VALIDATION

Richard Farmer, University of Nevada, Reno

ABSTRACT

Current computational fluid dynamics provides a powerful design tool for liquid rocket engines; however, its use is limited because combustion device designers feel it is not sufficiently validated. This paper reviews available experimental methodology and suggests the synergism necessary for CFD analysts, hardware designers, and experimentalists to establish sufficient code validation to utilize CFD simulations more efficiently. The ultimate goal is to establish an experimental data base that can qualify CFD codes to be stand-alone design tools.

INTRODUCTION

Despite modern computers having revolutionized our ability to analyze liquid rocket propulsion systems, any major computational design must still include a validation step before it is considered useful. Unfortunately, the validation step is frequently the weak link in the entire process, a result of the experimental and analytical research being independently supported. Several factors have caused this dichotomy and have created the need for this paper.

Both computational fluid dynamics analysts and experimentalists value their work by the totality of successes they have accumulated in using their methodology. Seldom, if ever, is an experiment designed for validating analyses of liquid rocket engine combustion devices. Rather, experiments are performed to investigate problems and concepts in operational engines. A classic example was the experiment which led to the solution of the combustion stability problem in the F-1 engine¹. Table 1 shows the range of experiments that are likely to be available for any validation. Review of these experiments indicates that the first criteria for successful CFD code validation is the establishment of the **purpose for which the analysis is to be used**.

The second criteria is to determine the **important flowfield characteristics** which control the phenomena of interest. If thrust and wall heating are the improvements a novel design is supposed to offer, then thrust and wall heating must be both predicted and measured. Since full scale experiments are cost prohibitive, subscale experiments can usually be devised for capturing the unique feature(s) of the design. The CFD analysis can be validated by reproducing the experimental results and used to scale the results to the full size device.

The third criteria is the experimental determination of the **phenomena critical to the design**. Historically, liquid rocket engine (LRE) performance predictions are made with the JANNAF standard codes. These codes were validated by experiments at Rocketdyne² and Aerojet³. Before the accuracy of performance predictions could be ascertained, one must determine how accurately the performance can be measured. Some years ago Remtech⁴ undertook an investigation to determine the accuracy of thrust stand measurements. The validation of the performance predictions must be interpreted in light of such evaluations. Today the measurements and predictions are still considered to be accurate to about 1/4 of a percent.

Since no universal CFD code for analyzing liquid rocket engine phenomena has been envisioned, much less developed, data requirements for specific combustion device test programs will be addressed in the remainder of this presentation. CFD uniquely offers the means to simulate three-dimensional, unsteady flowfields. Application to LRE technology must also include combustor, multiphase flows effects. The impressive capabilities of CFD methodology are shown in Table 2. To be useful to the designer the CFD analysis must relate the injector and combustor geometry to the performance and thermal environment of the device. Current CFD methodology can accomplish this requirement without resorting to: probability density function (PDF), large eddy simulation (LES), and direct Navier-Stokes (DNS) turbulence models. In fact, even if these elaborate turbulence models were now available, combustor flowfield simulations typical of LREs would not be practical. However, some important physical phenomena cannot be simulated and/or measured; therefore, engineering judgment is still necessary to complete the design process. The following considerations are offered to insure rigorous validation of practical CFD design tools.

Basic research sufficient to validate CFD codes for application to LRE analyses has never been accomplished. Such research would involve measuring the relevant parameters, systematically varying these parameters (including propellants used), and evaluating the accuracy with which the CFD simulations predicted the result of the parametric changes. Rather, experiments to determine the behavior of a particular combustion device, usually an injector element, and propellant system are conducted. Although the experiment was predicated on providing CFD validation data, this objective was seldom satisfied. All too often the reported test data reflect only the capability of the performing laboratory. Many experiments are conceived as being axisymmetric to facilitate simulations. In reality, flow symmetry is usually compromised to facilitate instrumentation systems, for example using flat, excessively cooled optical windows. However, if a CFD code has been used to simulate a significant number of the applications listed in Table 1 and validated with the admittedly incomplete test data available for each application, a good case can be made for trusting the results of further simulations with that code.

A disproportional amount of research resources has gone into the investigation of spray phenomena. First, spray vaporization is a thermodynamic process. If the combustor provides a long enough residence time for evaporation, the only effect of the delayed vaporization is to modify the mixture distribution. For essentially all liquid space propulsion engines, the residence time far exceeds the vaporization time. This is a most valid statement for supercritical combustor pressures. Even if some drops can be observed under supercritical chamber conditions, they are extremely unstable. Furthermore, attempts to measure drop-size distributions in dense sprays have proven to be unsuccessful, and are likely to remain so. Since high pressure, dense sprays cannot be adequately simulated with a practical CFD analysis or measured in experiments, consider an alternative. The spray can be approximated with a real fluid CFD model which accounts for density variation from liquids to gases. The local quality can be converted to number density of drops with an assumed mean drop size (or drop size distribution). The conversion of drops to vapors does not have to be assumed to be in equilibrium. A finite-rate conversion process could be implemented in the CFD code. The pseudo rate conversion process should be based on a model which does not include an unrealistic surface tension. Such a vaporization model is described by Muss and Ngyen²². The presence of

evaporated drops (or for supercritical conditions globules of dense fluid) would modify the mixing, but this effect cannot be adequately predicted, i.e. turbulent mixing of drops and gases cannot be accurately modeled. This effect can also be lumped into the finite-rate conversion model. This rate expression could be improved if and when suitable test data could be obtained. The suggested methodology would provide practical computation times to simulate spray combustion. If the mixture ratio distribution is determined in a cross-plane, even in the engine exit, exceedingly valuable validation data would be generated. Attempts to obtain such data within the chamber have invariably distorted the symmetry of the flow.

MEASUREMENT OPTIONS

Consider a combustion device which is a small scale LRE that has a "simple" injector. Simple will be defined subsequently. The chamber diameter should be sized to match the mass flux expected in a full-scale engine. It should not look like a dump combustor. We wish to characterize the specific impulse produced by this device and its internal thermal environment and combustion stability in sufficient detail to use the results to validate a CFD analysis of the system. The measurement options and a recommended measurement system will be established for such an experiment.

Elementary combustor characterization involves measuring propellant flowrates and pressure (somewhere). Thrust should be considered a basic measurement, but it frequently is not. Thrust should be measured even if a horizontally mounted combustor makes the measurement difficult. Flowrates obviously need to be accurately measured. If any other streams are used, they must also be measured. The next most important measurement is the temperature distribution down the chamber wall. Simulation of the RCM-2 test case²³ indicates that the temperature changes 300%, whereas the pressure changes only 6%. Obviously, the temperature measurement is the more important indicator of the accuracy of the numerical simulation. However, pressure at least in the head-end and preferably also down the wall should be measured. Appropriate attention to the wall heating boundary condition must be given to interpret such data. At least some of the pressure transducers should have a high enough frequency response to determine in any instability occurs. The high-frequency pressure transducers should be located both up- and down-stream of the injector faceplate. The high frequency data would indicate the roughness of the combustion. Although valid simulation methodology to quantify this roughness is not available, a data base for future validation would be established. To more accurately validate the simulation, a Foelsch nozzle should be used. This nozzle is designed to produce one-dimensional nozzle flow which eliminates the need to account for nozzle shocks and which simplifies exit-plane optical and/or probe measurements. This is not essential, but if the experiment is truly designed to validate the CFD analysis such a nozzle should be used.

Mixing efficiency is generally believed to be the driving force in LRE design. One philosophy is to use many injector elements to insure uniform mixing while destroying such uniformity as necessary to provide wall cooling for combustor longevity. The many elements in themselves are a life reducing design feature. Other designs utilize a few large injector elements which are believed to be more robust. Undoubtedly incomplete mixing causes a loss of efficiency, the question is how much? CFD simulations can accurately determine this efficiency, NOW (Ratliff²⁴). There is substantial evidence that convective mixing at the injector element is

responsible for mixing the propellants, and that turbulent mixing (although faster than laminar mixing) through out the chamber and nozzle contributes negligible additional mixing. Such behavior is illustrated in Figure 1 for a radiation cooled nozzle. The hot and cold streaks, which extend all the way to the nozzle exit plane, correspond one-to-one with the injector elements. Most of the recommended measurements involve a direct determination of mixing inefficiencies, just as most new design concepts attempt to improve mixing. A simple injector may consist of a single element or a small number of clustered elements. Note, even a simple unlike pair of injector elements create an asymmetrical flowfield. Thus the simple injector configuration might require a three-dimensional flowfield simulation. This is a most acceptable situation and should not be avoided simply to make calculations faster. Simulation simplification at this point begs the issue and creates no acceptable validation.

Mixing can generally be determined in the exit-plane by optical and/or probe measurements. This is questionable for an injector with many elements, but data from such a combustor is probably unnecessary. If the flow is not symmetric, sufficient measurements must be made to establish its actual character. Infrared emission/absorption (E/A) spectroscopy has been proven adequate for this purpose if the flowfield is axisymmetric²⁵. However, no systematic study to determine the accuracy of the E/A methodology has been performed. Optical tomography may be used for asymmetric flows²⁶. Optical point measurements could be used (Raman, etc.), if they can be developed to withstand the environment and the extraneous gases and vapor which obscure the view. There is nothing wrong with using probe measurements for both temperature and composition, if proper techniques are employed. The ramjet dump combustor experiment reported by Drummond²⁷ is excellent for validating purposes. It is the only one this investigator has found sufficiently definitive for justifying making a temperature correction to the k- ϵ turbulence model. However, the upstream boundary conditions (the inlet velocity profiles) on the primary and secondary streams were not measured - they had to be estimated. The shape of these profiles had a strong effect on the solution. The simulation had to be started far upstream of the combustor to successfully simulate the flow. When considering hydrocarbon propellants, the measurement and prediction of soot formation is critical.

The combustion chamber should be axisymmetric, even if the injector and/or injector elements are inherently three-dimensional. This would preclude the use of large flat windows and their accompanying coolant flow. Trying to make optical measurements within the chamber has resulted in studying chambers of larger diameter than the streamtube which they would feed in an actual engine. This mismatch of mass fluxes makes the validation questionable. If optical measurements were made in the chamber, they would have to be made at several axial stations, including the exit plane (otherwise the thrust and flowfield data could not be reconciled). Since optical measurements in the chamber are not sufficient for validation, such measurements should not be made forsaking wall temperature and/or pressure measurements.

The optical measurement system should also include the measurement of temperature. Inside wall temperatures and boundary layer gas temperatures should also be made. Radiation and total heat flux calorimeters should also be used to measure fluxes to the chamber wall to duplicate the flux deducted from the thermocouple measurements.

WHERE ARE WE NOW?

Is such an ambitious measurement program necessary? This author believes it is. The situation now is that hundreds of experiments have been reported, none of which are definitive enough to convince designers that CFD methodology is a valuable design tool.

Major efforts for producing CFD validations data for LRE systems have been and are being accomplished by Pennsylvania State University, ONERA, and DLR. This work was reported by the workshops for Fluid Dynamic Applications in Rocket Propulsion and Launch Vehicle Technology conducted by NASA/MSFC, and the previous International Workshops on Rocket Combustion Modeling hosted by ONERA and DLR. No concerted effort has been given to simulating all of these experiments or to determining if existing CFD simulations are even partially validated by benchmark test cases.

The measurement systems suggested and examples of their prior use are shown in Table 3. Load cells, pressure and heat flux transducers, and thermocouples are readily available. Composition measurements require more consideration. The entries in Tables 1 and 3 marked with * should be used as part of the data base for validating CFD codes for LRE analysis.

Extracting samples is the only method to measure all of the stable species at a point in the flowfield. E/A measurements conceptually can be used to determine temperature species distributions - H_2O in a H_2/O_2 system and CO_2 , CO , H_2O , and soot in a hydrocarbon/ O_2 system. Even if only one species is accurately measured temperature profiles and estimates of mixing will be produced for validation data. Although new spectrometers²⁸ are available that expedite this measuring system, the accuracy of such measurements is yet to be demonstrated. A calibration for such a measurement system is necessary. Even though all of the potential of this system might not be achievable, significant validation data could be obtained with a system which could be operated on an engine test stand.

Other optical systems might also be developed for interrogating rocket combustion processes. However, none of these systems appear to have been used successfully on high Reynolds' number, high pressure combustion systems typical of LREs. Extensive work has been reported on low pressure, low Reynolds number turbulent flames and on modest-pressure gas-turbine engine experiments. The International Workshops on Measurement and Composition of Turbulent Nonpremixed Flames (www.ca.sandia.gov/tdf/Workshop) have emphasized the study and development of time-resolved optical point measurements. For the high Reynolds number LRE applications, time-averaged and high Reynolds number turbulence CFD models are very adequate for describing the flowfields of interest. In fact, if no time averaging is considered, real design issues cannot be addressed for LREs in the foreseeable future. Some of the measurement systems developed for these studies might be appropriate for liquid rocket engine validation, but this has not proven to be the case up to this point.

Other research areas that might offer new instrumentation methodology for the study of LREs are those of gas-turbine engines and industrial furnaces. This research is typified by the excellent studies conducted at the University of California at Irvine's Combustion Laboratory. The thrust of their research is "to use and apply conventional diagnostics, laser diagnostics, and

state-of-the-art numerical modeling to develop an understanding of the processes of fuel injection, fuel/air mixing, reactant and product transport, and the formation of soot and gaseous pollutants." (www.uci.edu/about/index.htm) This could be the goal of LRE research studies EXCEPT - these combustion devices have lower flowrates, operate at lower pressures, and more importantly use air as the oxidizer thereby producing lower flame temperatures and much slower combustion reactions.

RECOMMENDATIONS

1. A baseline set of experiments should be designed and executed for establishing a data base for validating CFD codes which are suitable for analyzing liquid rocket engines. CFD analysts, instrumentation specialists, and experimentalists must work in concert to accomplish this task.

2. Prepare and run a test matrix with the baseline combustors to measure the cause and effect of various operational variables.

3. Refrain from selecting a single CFD code for the entire community to use. Rather, accept good simulations of the set of baseline benchmark-cases as evidence that a given code is acceptable for design studies. Otherwise, interest in improving CFD methodology would be stifled and no improvements in computational technology would be forthcoming.

4. Identify critical, promising instrumentation systems which require further development/calibration and collectively undertake their research.

REFERENCES

1. Levine, R.S., "Experimental Status of High Frequency Liquid Rocket Combustion Instability," Tenth Symposium (International) on Combustion, The Combustion Institute, pp. 1083-1099, 1965.
2. Sutton, R.D., et al, "Development and Application of a Comprehensive Analysis of Liquid-Rocket Combustion," AIAA J, 10, pp. 194-203, 1972.
3. Valentine, R.S., et al, "An Improved Method for Rocket Performance Prediction," J. Spacecraft, pp.1409-1414, 1966.
4. Praharaj, S.C., and R.L. Palko, "Measurements for Liquid Rocket Engine Performance Code Verification," RTR 157-01, Remtech, Inc., Huntsville, AL, 1986.
5. Wang, T.S., and Y.S. Chen, "Unified Navier-Stokes Flowfield and Performance Analysis of Liquid Rocket Engines," J. of Propulsion and Power, 9, pp. 678-685, 1993.
6. Hale, D.V., "A Turbulent Distributed Injection Boundary Layer Computer Program," LMSC/HREC A783452, Lockheed Missiles & Space Co., Huntsville, AL, 1966.
7. Back, L.H., and R.F. Cuffel, "Turbulent Boundary Layer and Heat Transfer Measurements Along a Convergent-Divergent Nozzle," J. of Heat Transfer, pp. 397-407, 1971.
8. Payne, R.G., and I.P. Jones, "Summary of Saturn I Base Thermal Environment," J. Spacecraft, 3, pp.489-497, 1966.
9. Greenwood, T.F., et al, "Space Shuttle Base Heating," AIAA Paper 83-1544, 1983.
10. Wang, T.S., "Grid-Resolved Analysis of Base Flowfield for Four-Engine Clustered Nozzle Configuration," J. of Spacecraft and Rockets, 33, pp. 22-29, 1996.
11. Santoro, R.J., "An Experimental Study of Characteristic Combustion-Driven Flow for CFD Validation," Final Rpt. on NAS8-38862, PSU, University Park, PA, 1997.

12. Vingert, L., and Habiballah, "Test Case RCM 2: Cryogenic Spray Combustion at 10 bar at MASCOTTE," Presented 2nd International Workshop of Rocket Combustion Modeling, Lampoldshausen, Germany, March 25-27, 2001.
13. Thomas, J.L., et al, "Test Case RCM 3: Supercritical Spray Combustion at 60 bar at MASCOTTE," Presented 2nd International Workshop of Rocket Combustion Modeling, Lampoldshausen, Germany, March 25-27, 2001.
14. Wang, T.S., and V. Luong, "Hot-Gas-Side and Coolant-Side Heat Transfer in Liquid Rocket Engine Combustors," J. of Thermophysics and Heat Transfer, 8, pp. 525-530, 1994.
15. Muss, J.A., "Instability Phenomena in Liquid Oxygen/Hydrocarbon Rocket Engines," in Liquid Rocket Engine Combustion Instability, V. Yang and W.E. Anderson, Eds., AIAA Publ., pp. 73-88, 1994.
16. Habiballah, M., and I. Dubois, "Numerical Analysis of Engine Instability," *ibid.*, pp. 475-502, 1994.
17. Grenda, J.M., et al, "Application of Computational Fluid Dynamics Techniques to Engine Instability Studies," *ibid.*, pp. 503-524, 1994.
18. Wang, T.S., "Numerical Study of the Transient Nozzle Flow Separation of Liquid Rocket Engines," Comp. Fluid Dynamics J., 1, pp.319-328, 1992.
19. Strehlow, R.A., Fundamentals of Combustion, International Textbook Co., pf. 339, 1968.
20. Harlow, J., "Hydrogen Peroxide Engines: Early Work on Thermal Ignition at Wstcott," presented at 2nd International Hydrogen Peroxide Propulsion Conference, Purdue Univ., Nov. 7-10, 1999.
21. Lausten, M.F., "Carbon Deposition Model For Oxygen-Hydrocarbon Combustion," Bimonthly Prog. Rpt. 2427-M-2, on NAS8-34715, Aerojet Liquid Rocket Co., Sacramento, CA, 1982.
22. Muss, J.A., et al, "User's Manual for Rocket Combustor Interactive Design (ROCCID) and Analysis Computer Program," NASA CR 187110, 1991.
23. Cheng, G.C., and R.C. Farmer, "CFD Spray Combustion Model for Liquid Rocket Engine Injector Analysis," submitted to J. of Propulsion and Power, 2003.
24. Ratliff, A.W., "The Effect of Nozzle Flow Striations on Engine Performance," LMSC/HREC A784646, Lockheed Missiles & Space Co., Huntsville, AL, 1967.
25. Limbaugh, C.C., "The Infrared Emission-Absorption Method for Temperature and Species Partial Pressure Determination in Flames and Plumes," in Infrared Methods for Gaseous Measurements, Ed. J. Wormhoudt, publ. Marcel Dekker, Inc., pp. 197-246, 1985.
26. Goulard, R., and R.J. Santoro, "Optical Tomography for Flow Field Diagnostics," Int. J. of Heat and Mass Transfer, 24, pp.1139-1150, 1981.
27. Wang, T., et al, "Numerical Study of Reactive Ramjet Dump Combustor Flowfields with a Pressure Base CFD method," AIAA Paper 89-2798, 1989.
28. Sivathanu, Y., www.spectraline.com
29. Eckbreth, A.C., Laser Diagnostics for Combustion Temperature and Species, 2nd ed., publ. Gordon & Breach, 1996.
30. Ratliff, A.W., "Comparison of Experimental Supersonic Flow Fields with Results Obtained by Using a Method of Characteristics Solution," LMSC/HREC A782592, Lockheed Missiles & Space Co., Huntsville, AL, 1966.

TABLE 1. SCOPE OF CFD VALIDATION CONSIDERATIONS

Purpose	Critical Phenomena	Additional Phenomena	Measurements Desired	Examples	Typical References
Operational LRE performance	Thrust & propellant flowrates	O/F distributions	Thrust, flowrates & local compositions and temperatures	SSME	Wang & Chen ⁵
LRE thermal environment	Wall heat-fluxes, coolant conditions, hot-gas conditions	Gas-side compositions	Stream temperatures & flowrates	H-1 & F-1; Hot gas test nozzle*	Hale ⁶ Back ⁷
Base heating	Exit-plane conditions; geometry	Flight trajectory	Structural temperatures; flowfield velocities	Saturns; Space Shuttle; Cold flow model*	Payne & Jones ⁸ Greenwood, et al ⁹ Wang ¹⁰
Characterize injector elements	O/F uniformity, atomization efficiency	Wall heating, combustion mechanics	Local temperatures & mixture and phase ratios	PSU; IWRCM experiments	Santoro ¹¹ ; Vingert & Habiballah ¹² ; Thomas, et al ¹³
Characterize regenerative cooling system	Local flow & thermal state of coolant; configuration	External & internal wall conditions	Temperatures, local flowrates & flowfields	Cooling system for the ST SSME	Wang ¹⁴
Investigate combustion stability	Transient internal pressure- & flow-fields	Accurate configuration specification	Local temperature & compositions		Muss ¹⁵ Grenda, et al ¹⁶ Habiballah ¹⁷ Wang ¹⁸
Start-up & shut-down			Thermal environments		
Revolutionize combustor configuration	Mixing efficiency & thermal environments	Ignition sequence	Thrust, flowrates, & local compositions in the exit-plane	Pulsed detonation engine concepts	Strehlow ^{19*}
Catalyze propellant combustion	Catalysis kinetics	Catalyst life	Thrust, flowrates, & local compositions in the exit-plane	Peroxide LRE	Harlow ²⁰
Material/hot-gas compatibility	Materials & propellants	Local temperatures & compositions	Material response to operating conditions	Carbon deposition	Lausten ²¹

TABLE 2. POTENTIAL OF CFD METHODOLOGY

1. Only way to analyze 3-dimensional, steady and unsteady flowfields.
2. Can utilize any averaged turbulence model.
3. Can use real thermodynamic & transport fluid properties.
4. Can compute finite-rate combustion.
5. Accurately accounts for coupling between heat, mass, & momentum transfer.
6. Only practical means of treating multiphase flows.

FIGURE 1. RADIATION-COOLED NOZZLE



TABLE 3. DEMONSTRATED INSTRUMENTATION SYSTEMS

PARAMETER	INSTRUMENT TYPE	EXAMPLE	COMMENTS	INVESTIGATOR/ REFERENCE
pressure	inlet, wall & exit plane transducers		<ul style="list-style-type: none"> • distribution along wall • high frequency transducers at selected locations & thermally protected 	T. Nesman, MSFC J. Wiley, MSFC
temperature	thermocouple	Medtherm instruments	wall distribution	L. Jones, Medtherm, Inc. Huntsville, AL
wall heat flux	total & radiation calorimeters	Medtherm instruments	selected wall stations	L. Jones
temperature	emission/absorption radiation	Rocketdyne experiments	exit plane values	Herget
stable species concentration	optical E/A IR radiation	Rocketdyne experiments Spectraline	<ul style="list-style-type: none"> • exit plane values • major species only 	Herget
stable species concentrations	probes & gas chromatography		<ul style="list-style-type: none"> • cooled probes to freeze reactions • all species to determine mixture ratios 	Drummond*
radical species	laser-induced fluorescence	MASCOTTE data	distinction between thermal & chemiluminescence req'd	A.C. Eckberth ²⁹ J.L. Thomas
plume photographs	visible & IR photographs	shock structure and plume boundaries	criticality depends on exit-plane pressure field	A. Ratliff ³⁰



Subscale Test Methods for Combustion Devices

Fifth International Symposium on

Liquid Space Propulsion

28-30 October 2003

Chattanooga TN

W.E. Anderson, J.C. Sisco, M.R. Long, and I.-K. Sung

School of Aeronautics and Astronautics

Purdue University



Outline

- Motivation for Scaled Experiments
- Brief Scaling History
 - Steady-State Combustion
 - Combustion Stability
 - Life Prediction
- Scaling Approaches Presently Used at Purdue

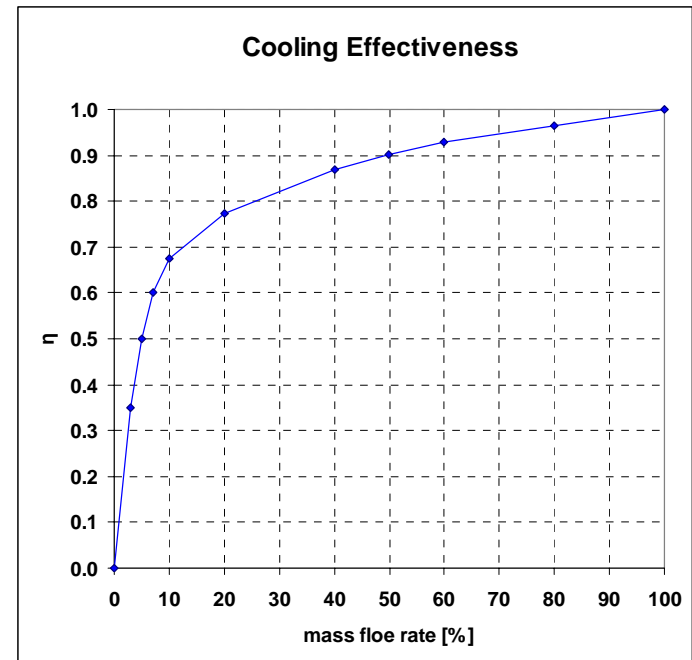
Background

- Stated goals for long-life LRE's have been between 100 and 500 cycles
 - Inherent technical difficulty of accurately defining the transient and steady state thermochemical environments and structural response (strain)
 - Limited statistical basis on failure mechanisms and effects of design and operational variability
 - Very high test costs and budget-driven need to protect test hardware (aversion to test-to-failure)
- Ambitious goals will require development of new databases
 - Advanced materials, e.g., tailored composites with virtually unlimited property variations
 - Innovative functional designs to exploit full capabilities of advanced materials
 - Different cycles/operations
- Subscale testing is one way to address technical and budget challenges
 - Prototype subscale combustors exposed to controlled simulated conditions
 - Complementary to conventional laboratory specimen database development
 - Instrumented with sensors to measure thermostructural response
 - Coupled with analysis

SSME Film Cooling Analysis

- Configuration
 - Propellant = LOX + LH2 with O/F = 6.02
 - $M_{\dot{LOX}} = 64,000$ liter/min
 - $M_{\dot{LH2}} = 178,000$ liter/min
 - $M_{\dot{coolant}}$ for regen cooling = 29.06 lb/sec
- Chamber condition
 - $P_c = 3300$ psi
 - $T_c = 3500$ K (5840 F)
 - $D_{throat} = 10.88''$
 - $E = 77$
- Cooling channel
 - Wall thickness = 0.03''
 - Width = 0.04 ''
 - Height = 0.12 ''
 - $Pressure_{throat} = 3851$ psi
- Thermal condition at throat
 - Heat flux = 80 Btu/in²-s
 - $hg = 58000$ W/m²-K
 - $T_{wg} = 1100$ F
- Wall adiabatic temperature
 - $T_{aw} = T_r - \eta(T_r - T_{co})$
 - Where T_r = recovery temperature
 - η = film cooling efficiency
 - T_{co} = initial coolant temperature

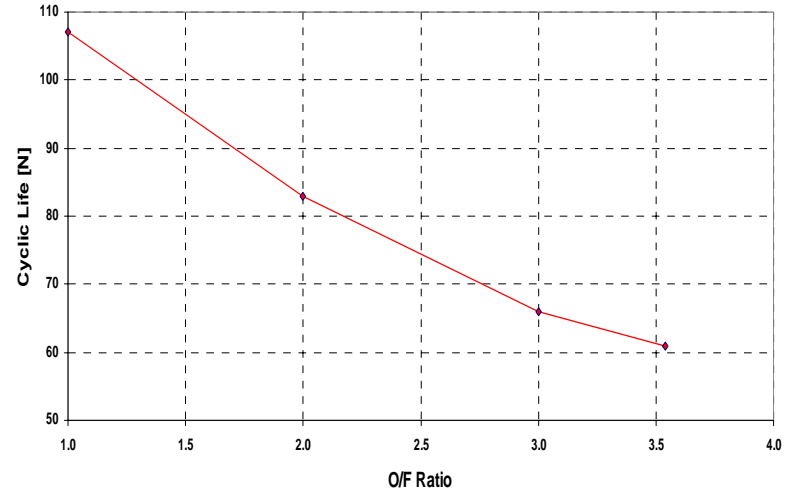
- Current near wall O/F ratio
 - $\dot{q} = hg(T_{aw} - T_{wg})$
 - Where $\dot{q} = 80$ Btu/in²-s
 - $hg = 58000$ W/m²-K
 - $T_{wg} = 1100$ F
 - $T_{aw} = 3125$ K
 - $\eta = 0.5$
 - $T_{co} = 2750$ K
 - O/F_{nw} = 3.54 from Flame temperature vs O/F ratio chart



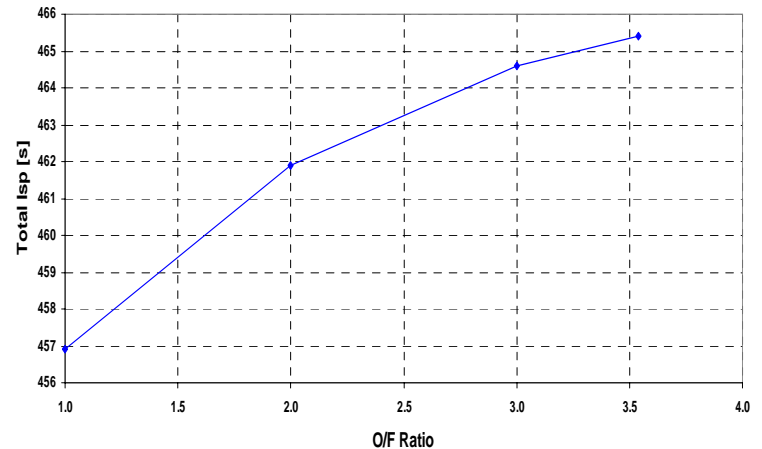
SSME Film Cooling Analysis

- Current film cooling condition
 - $O/F_{nw} = 3.54$
- Parametric study with fixed film flow rate (5 %)
 - *Porowski et al. method (AIAA Journal Vol. 2 No. 2, 1985)
 - O/F_{nw} change = $3.54 \rightarrow 1.0$
 - Life change = $61 \rightarrow 107$ (75.4% increase)
 - Isp change = $465 \rightarrow 457$ (1.83 % decrease)

SSME O/F vs Life



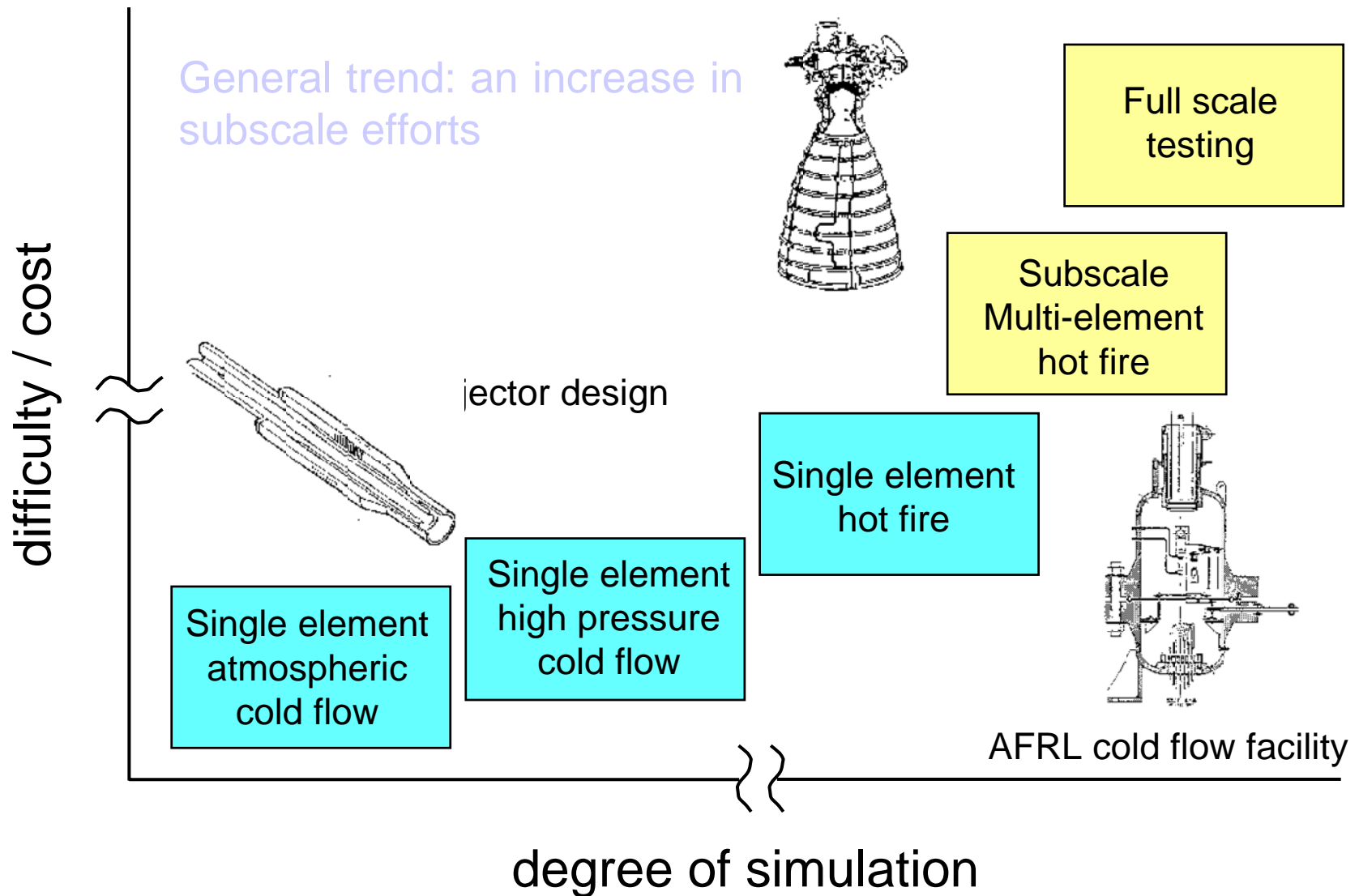
Isp vs O/F Variation
(coolant $\dot{m} = 5.0\%$)



Scaling Objectives and Approaches

- Combustor characterization is goal
 - Validation data for design analysis models
 - Assess innovative functional design, materials, operation
 - Investigations into specific physics
- Single element, multi-element, 40K, 250K
- Cold flow and hot fire
- Performance, heat transfer, life, stability
- Experimental objective needs to define scaling approach and measurement
 - Well-instrumented combustors linked to analysis
 - Thrust level and number of elements
 - Element scaling and configuration

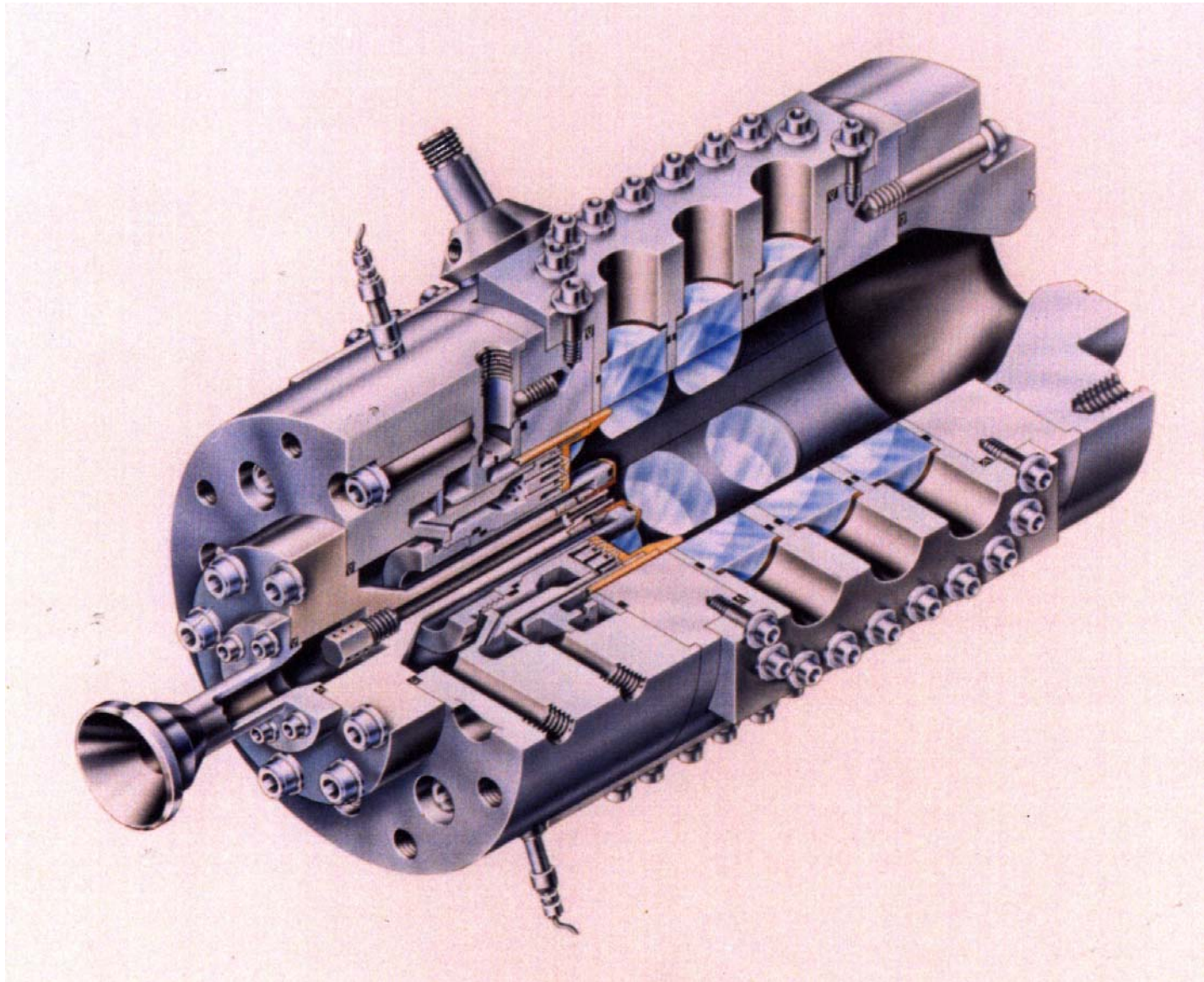
Hierarchy of injector experiments



Brief History of Scaling in the US – Steady State Combustion

- JPL studies of mixing efficiencies of impinging jets
- Bell Aerospace/AFRL holographic and shadowgraphic studies of combusting flows
- Rocketdyne development of LISP methodology for SDER
- Aerometrics development of PDPA
- Rocketdyne studies of flameholding behind LOX post
- PSU measurements of chemical species in HO combustors
- AFRL studies of supercritical jets

Single Element Test Chamber



Stability Scaling

- Simulation of chamber dynamics in subscale configuration is very difficult
 - Acoustic frequencies scale as $\sim 1/d$
 - Pressure ν velocity sensitivity
- Scaling approaches
 - Wedges, T-burners, 2-d chambers
 - $1T = 3T$ scaling
- Single element rarely used in US, but is more typical in Russia

Experimental Approach of Bazarov

This facility screened Injector elements for Liq/liq and gas/liq Injectors for over 20 Years (1965-85)

Typical $P_c = 750$ psi,
Total flowrate of 5 lb/s

‘self-oscillation’ and response to pulsations measured

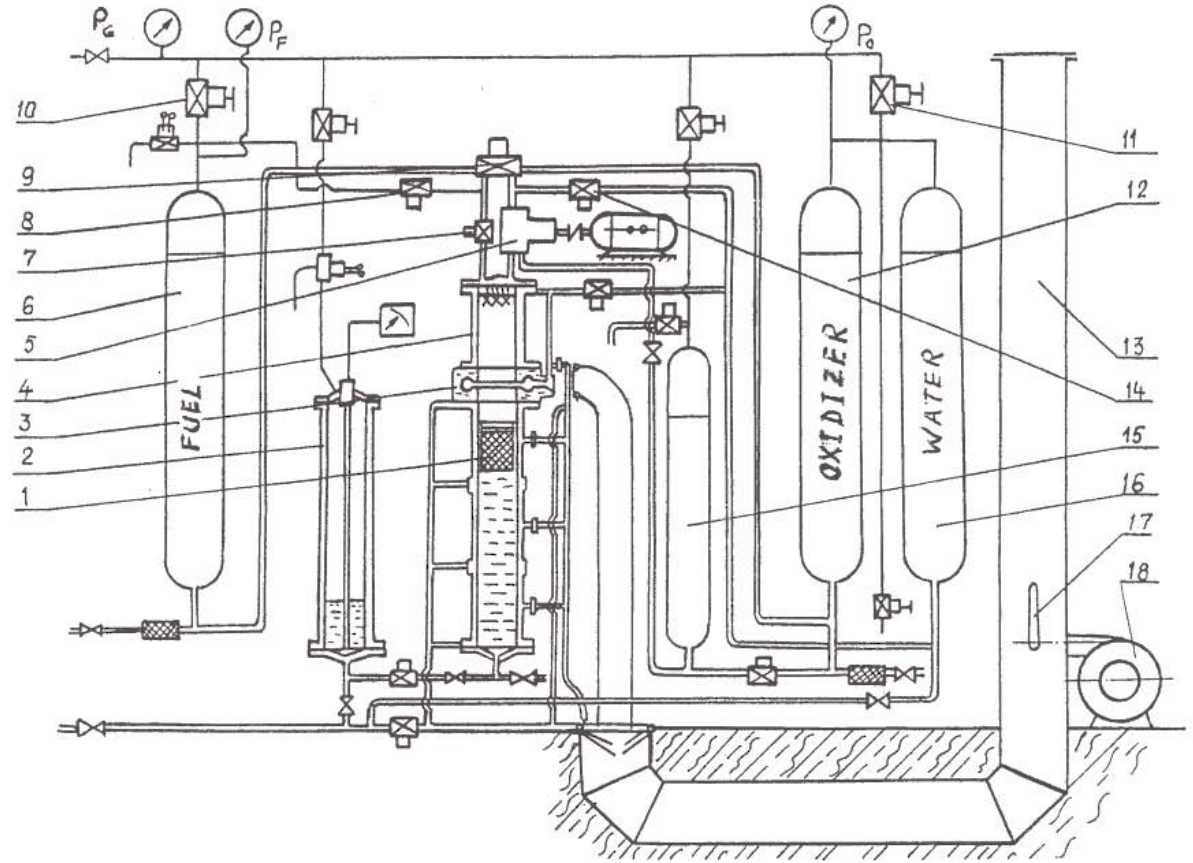


Fig.8 Pneumatic and hydraulic scheme of fire stand

1-piston, 2-measuring vessel, 3-nozzle collector, 4-combustion chamber, 5-pulsator, 6-fuel tank, 7-time delay valve, 8-blow through valve, 9-main bi-propellant valve. 10,11-pressurising gas reducers, 12-oxidizer tank, 13-exhaust tubes, 14-water valve, 15-oxidizer return tank, 16-pressurised water tank, 17-ejector, 18-air compressor

Experimental Approach of NIICHIMMASH

- Use full-scale injector elements
- Experiment designed to simulate controlling process - mixing
- Match equivalence ratio and volumetric flowrates using diluted gaseous propellants
- Combustor acoustics matched by using appropriately sized low-pressure chamber
- Stability boundaries determined by varying flowrates
- Relative boundaries indicate stability ranking

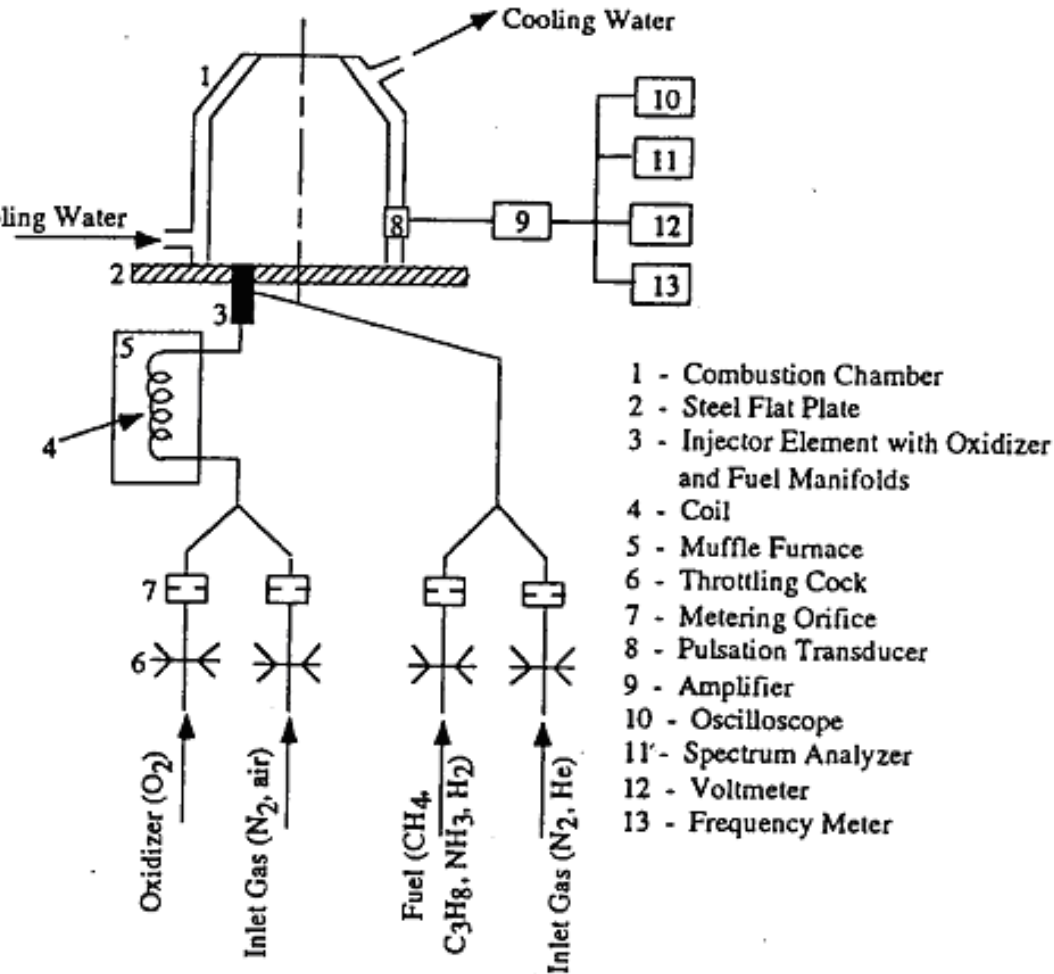


Figure 6. Schematic of Single Element Model Set-up and Instrumentation

Propellant Distribution Effects

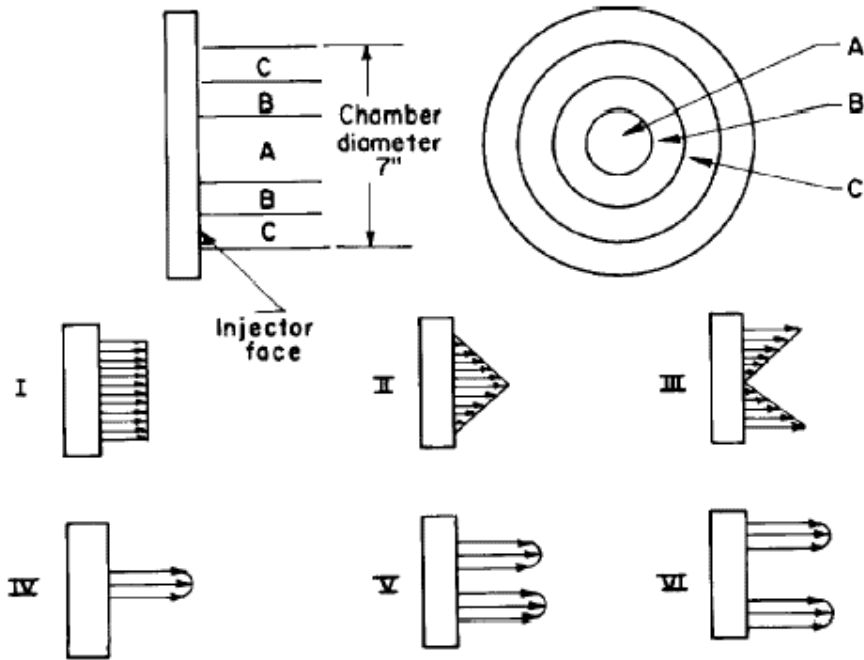


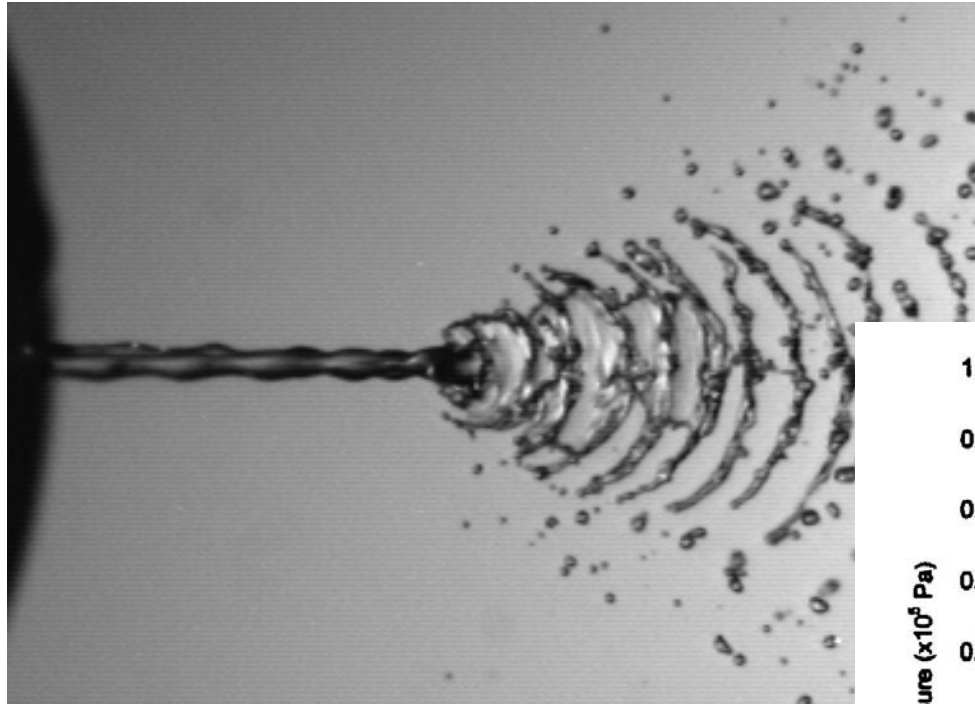
FIGURE 7.2.5a.—Injection radial profile comparison.

TABLE 7.2.5a.—GAS ROCKET TEST HISTORY WITH VARIOUS INJECTION PROFILES

[Instabilities initiated spontaneously and linearly; mean chamber pressure, 150 psia; combustion chamber diameter, 7 in.; combustion chamber length, 6 in.]

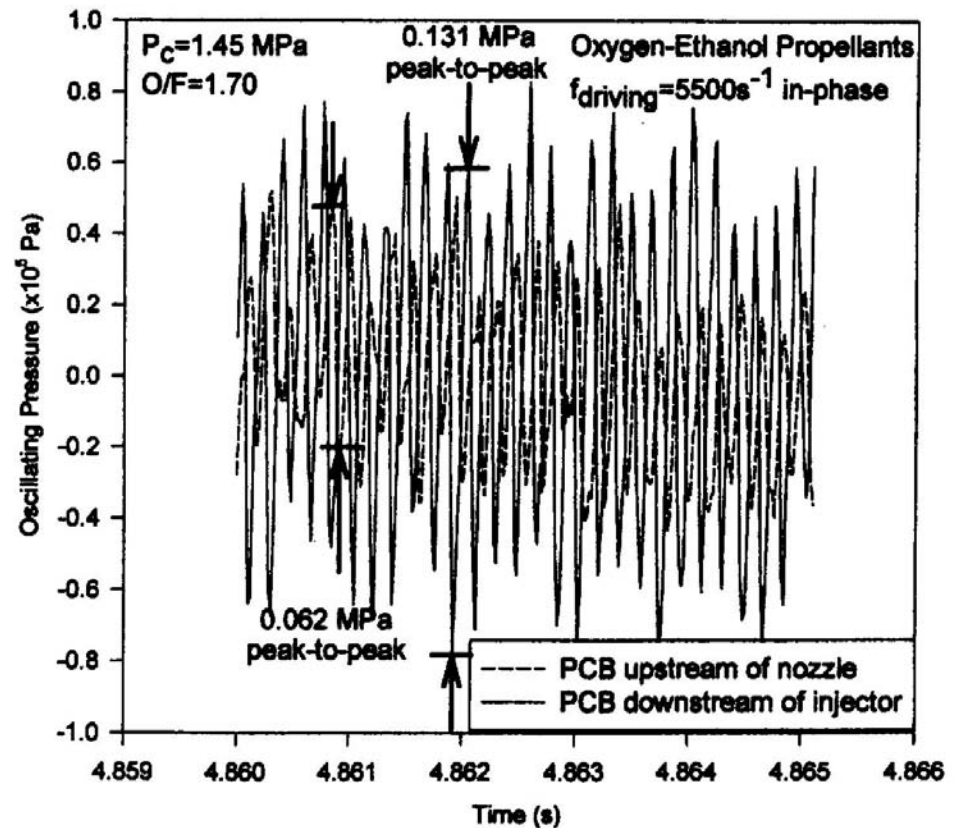
Profile	Amplitude, psi	Mode
I	7	1st tangential
II	0	Stable
III	11	1st tangential
IV	13	1st radial
V	0	Stable
VI	40	1st tangential

Single Element 'Instability'

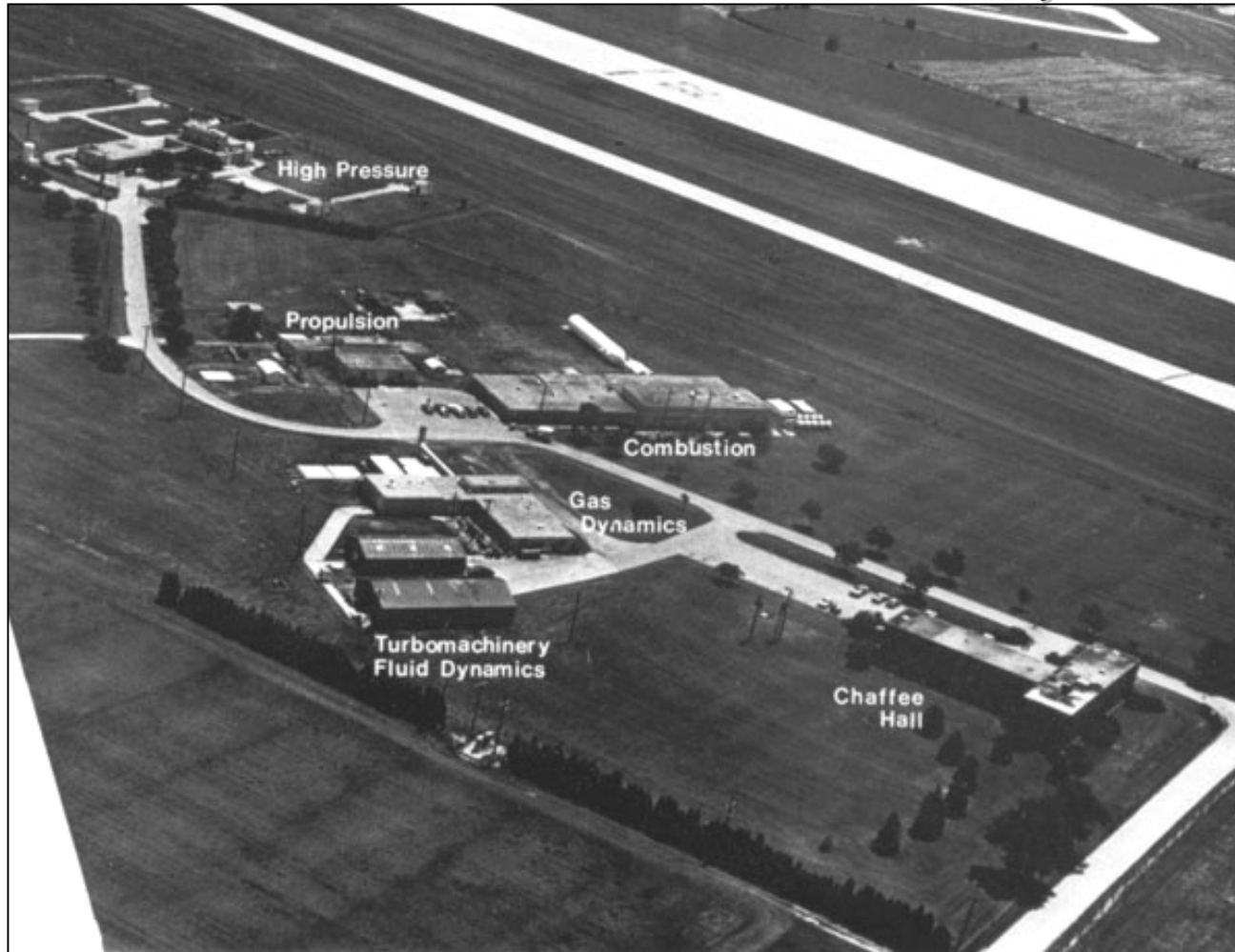


Combustor oscillations at driven atomization frequency

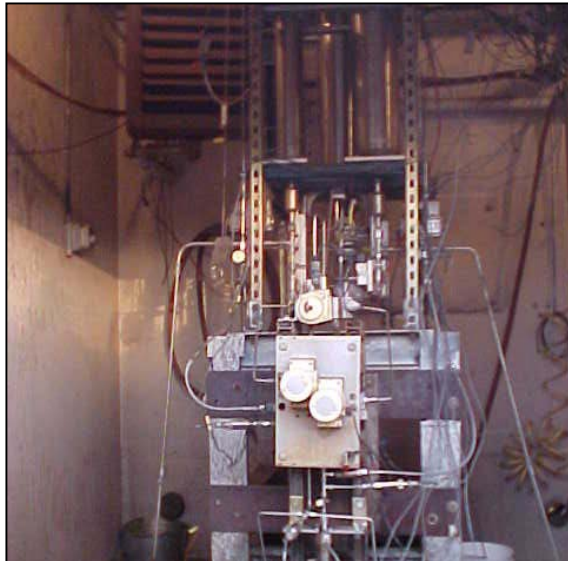
Impinging jets driven by piezoelectric actuator



Subscale Test Activities at Purdue - Maurice Zucrow Laboratory



Advanced Propellants and Combustion Lab



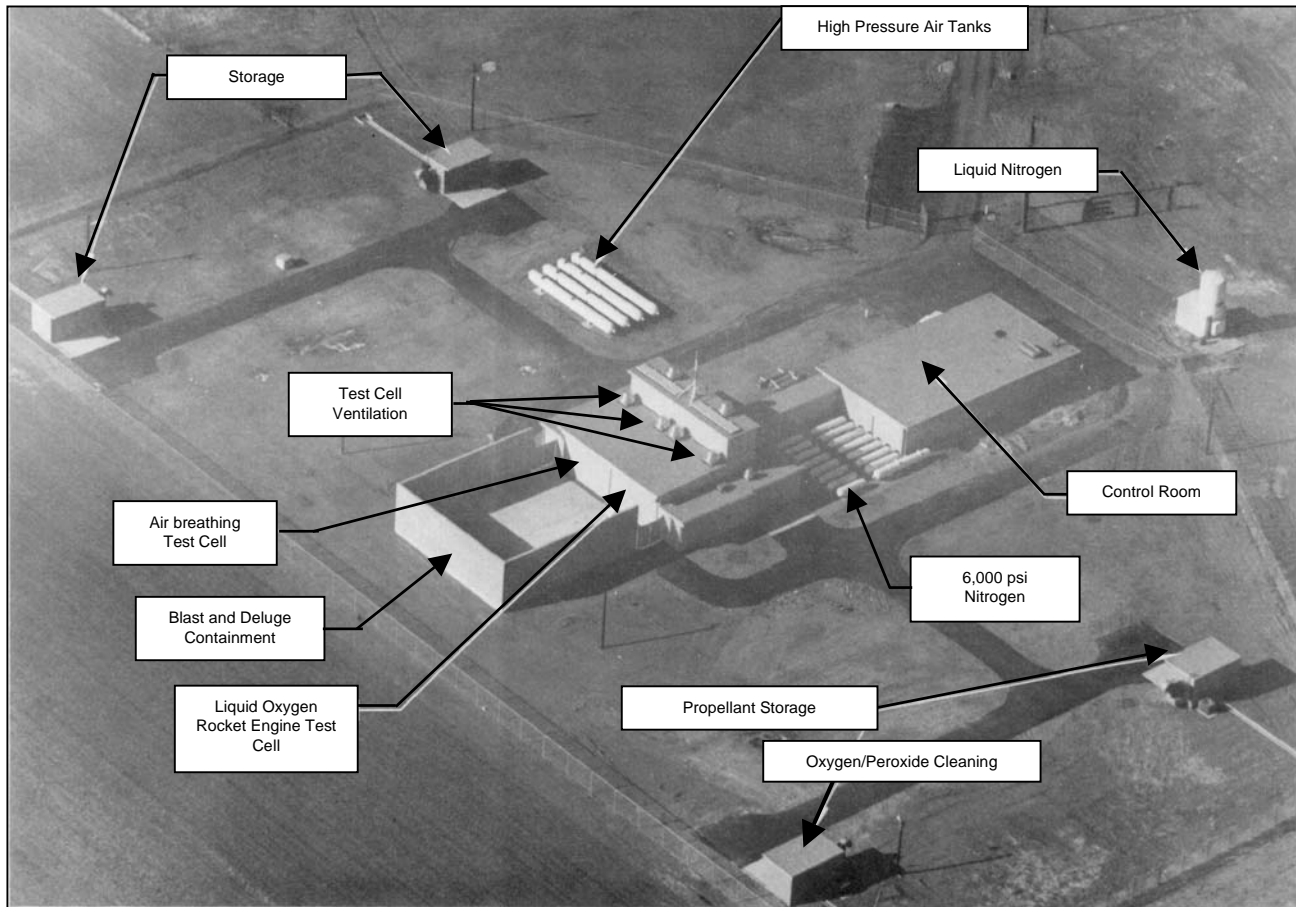
- Two cells w/ 1 Klbf thrust stands
- Propellant supply of 1800 psia
- 2 - 4 gallon oxidizer tanks
- 1 & 4 gallon fuel tanks
- National Instruments hardware & LabView software
 - 32 channels pressure
 - 32 channels temperature



- All valves computer controlled
- Rapid test article installation
- Design/Build/Test course

High Pressure Lab

Renovation funded thru Indiana 21st Century R & T Fund –
Propulsion and Power Center of Excellence
Facility activated in May '03



6,000 psi Nitrogen System



- Pressurization, Actuation and Purge Gas
- 2,400 gallon Liquid Nitrogen Tank w/ 6,000 psi Pump
- 253 ft³ 6,000 psi Nitrogen Tube Trailer
- Computer Controlled Pressurization Systems

Propellant/Coolant Tanks



- 22 gal 5,000 psi LOx
- 16 gal 5,000 psi Fuel
- 220 gal 5,000 psi H₂O
- 400 gal 800 psi H₂O₂
- Hydraulic Control Valves



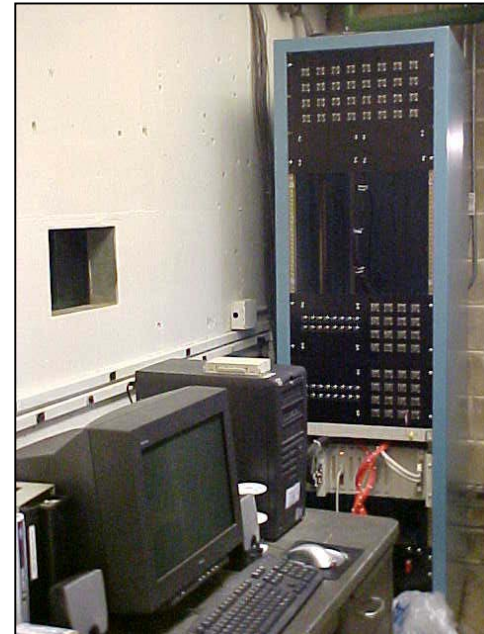
10,000 lbf Thrust Test Cell



- LabView 6.1-based DACS
- 10,000 lbf thrust measurement
- 64 channels pressure
- 96 channels thermocouples
- 18 channels analog control
- 32 channels on/off control

Control System Operation

- Data System Located Adjacent to Test Cell
- Operation Remoted to Control Room (KVM Extender) for Testing
- Video Recorded Directly to DVD



Test Cells



- 18” Thick Reinforced Concrete Test Cell Walls
- High Flow Capacity Test Cell Exhaust Fans
- Heated High Pressure Air Plumbed to Both Cells
- Walled Containment Area

Injector Characterization Scaling Approach

- Study Objectives

- Steady state and dynamic characterization of ORSC MC injector elements

- Approach

- Investigate full-scale elements at realistic operating conditions

- No film cooling (if possible)

- Evaluate different injector design configurations

- Couple with analysis

- Measurements

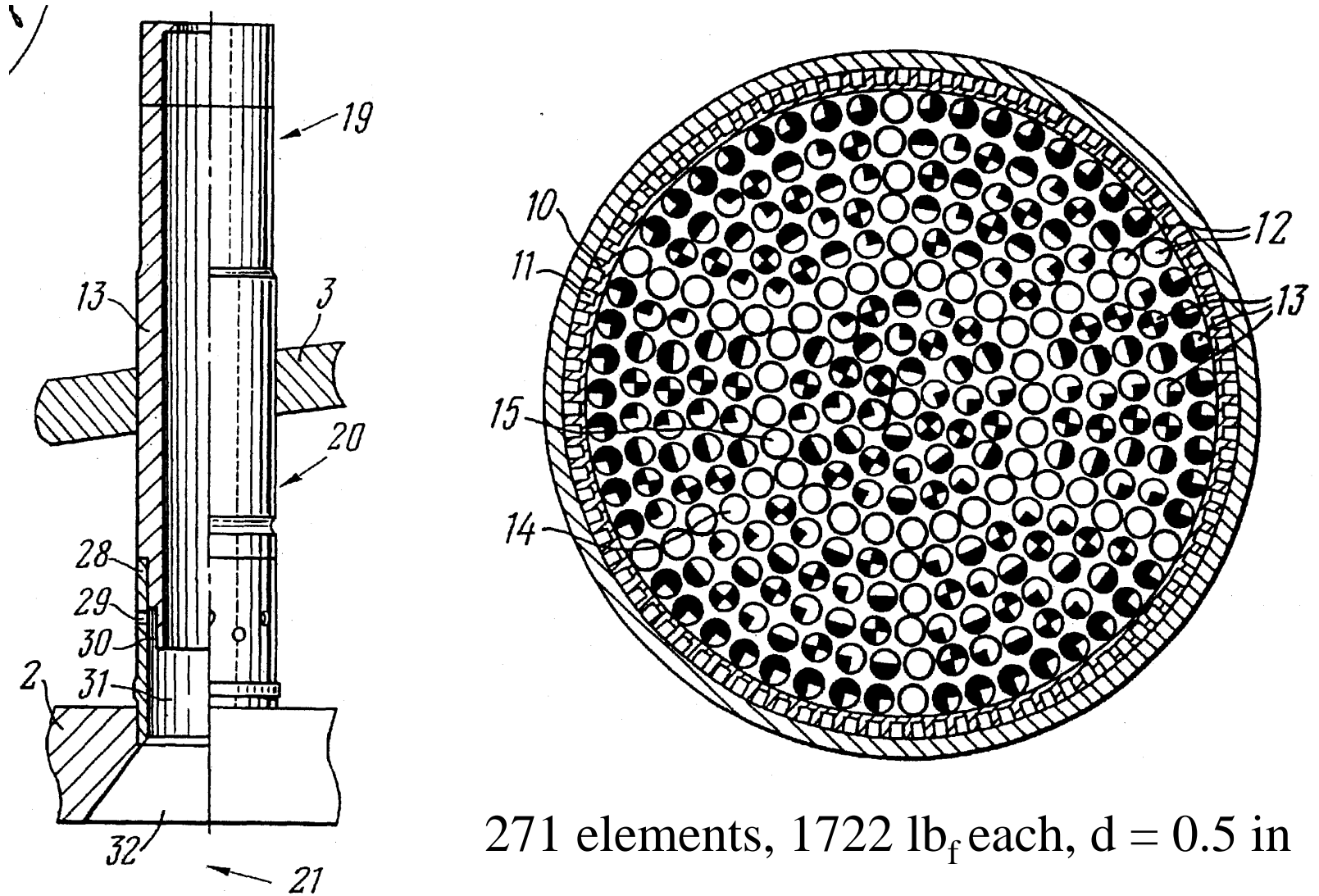
- Energy release profile from axial pressure gradient

- Injector face and chamber wall thermal environments

- Plume signature with IR tomography

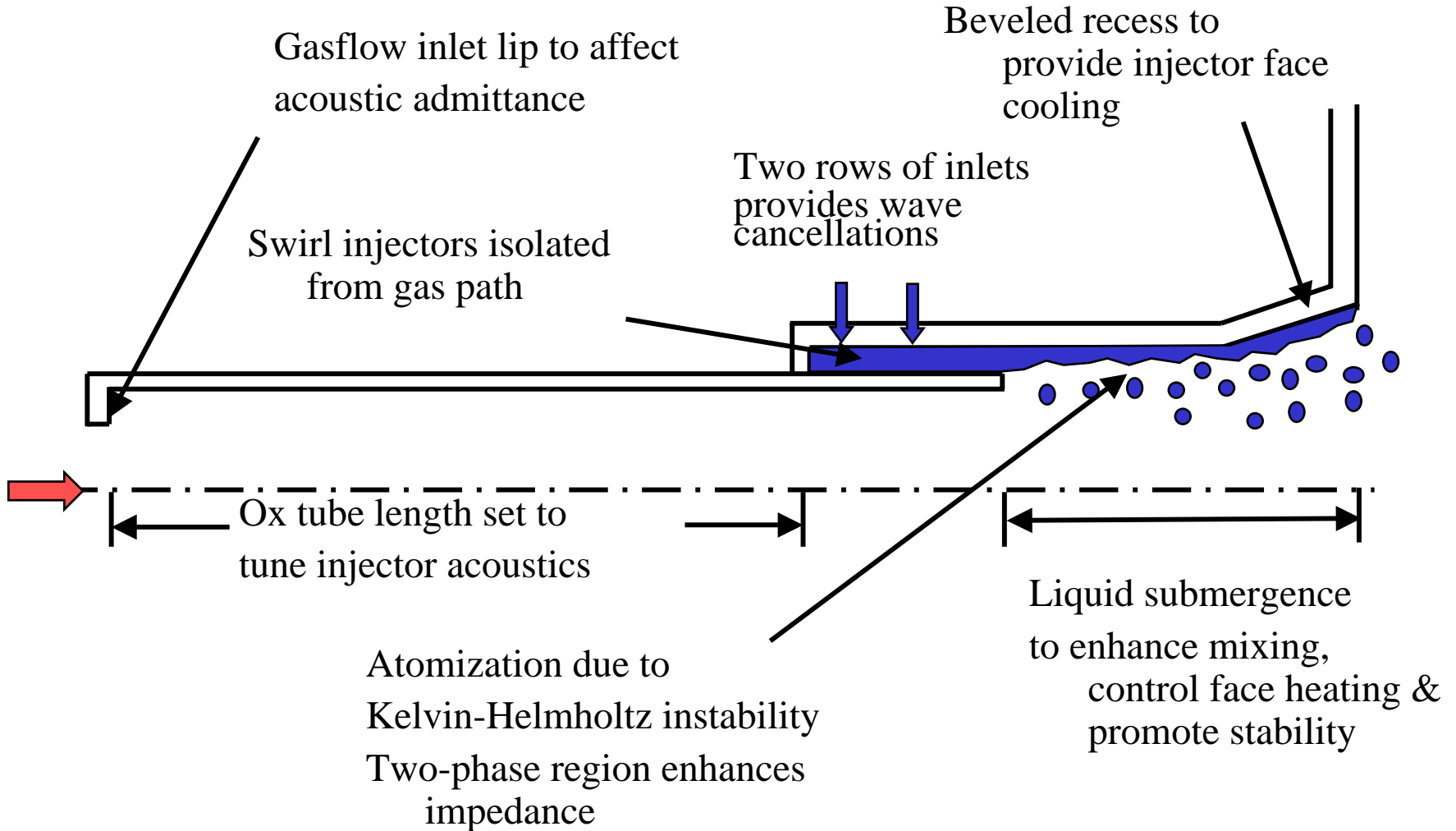
- Manifold, injector and chamber p'

ORSC Main Combustor Components

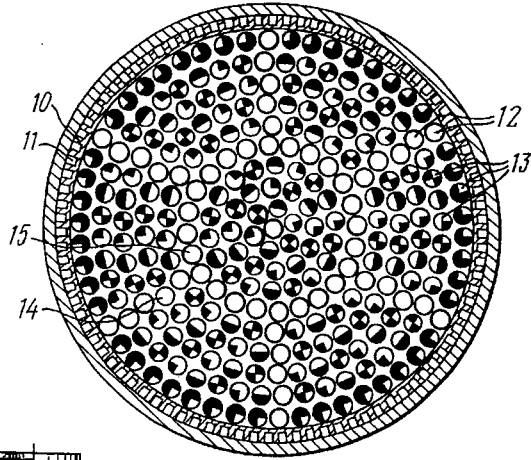


271 elements, 1722 lb_f each, d = 0.5 in

Principle Design Features



Single Element Sizing Exercise



Approach

- use full scale F/element ($1722 \text{ lb}_{\text{fvac}}$)
 - ➔ $\text{mox} = 3.6 \text{ lb/s}$, $\text{mf} = 1.2 \text{ lb/s}$
- test at 'full' P_c (2250 psia)
 - ➔ $A_t = 0.39 \text{ in}^2$, $d_t = 0.70 \text{ in}$
- match injection pressure drops (10%)
 - ➔ $d_{\text{inj, ox}} = 0.43 \text{ in}$, $d_{\text{inj}} = 0.57 \text{ in}$

Possible scaling methods:

Contraction ratio (1.61) ➔ $d_c = 0.89 \text{ in}$

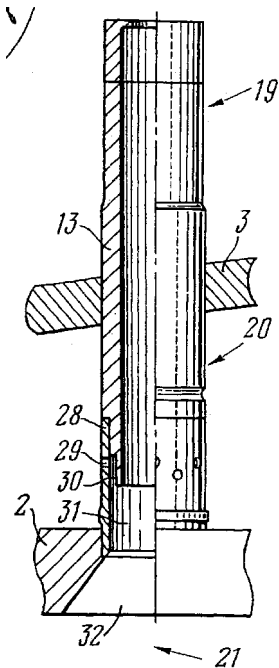
Element to chamber area ratio (0.30) ➔ $d_c = 1.04 \text{ in}$

Element-element spacing ($0.60d$) ➔ $d_c = 0.91 \text{ in}$

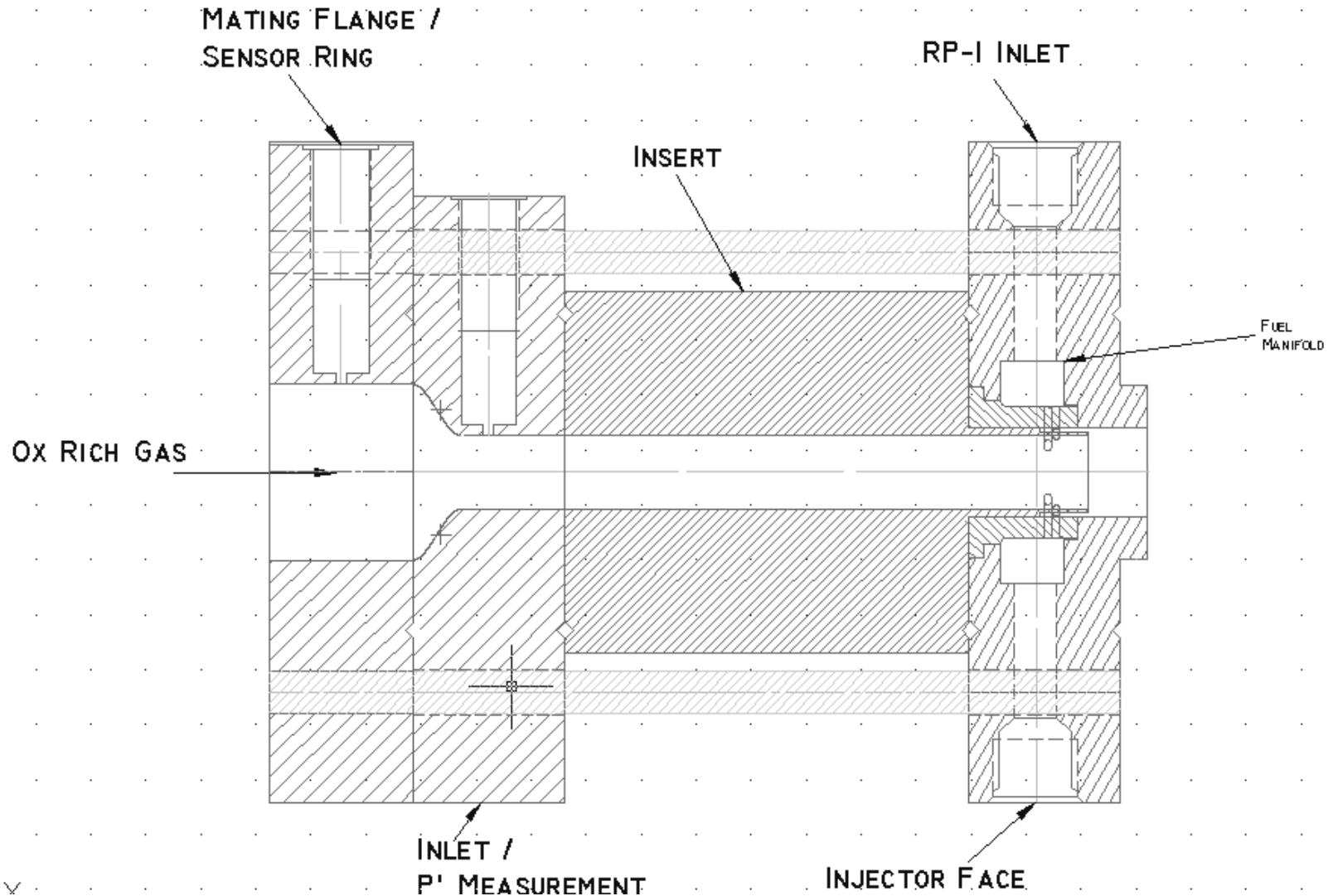
Element-wall spacing ($0.60d$?) ➔ $d_c = 0.91 \text{ in}$

Element area (0.65 in^2) ➔ $d_c = 0.91 \text{ in}$

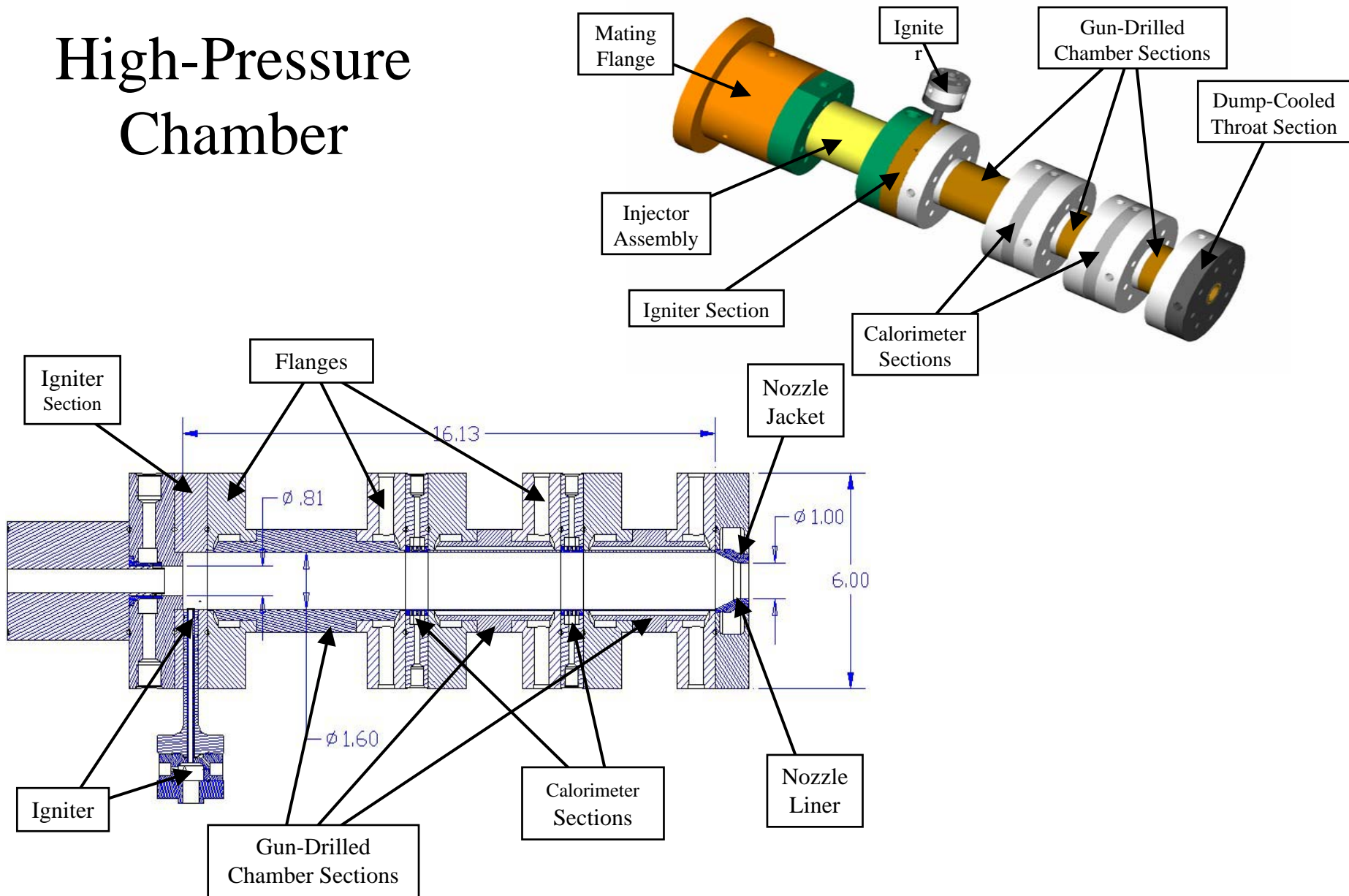
Chamber length based on $L^* \sim 30 \text{ in}$ (??)



Baseline Injector Design

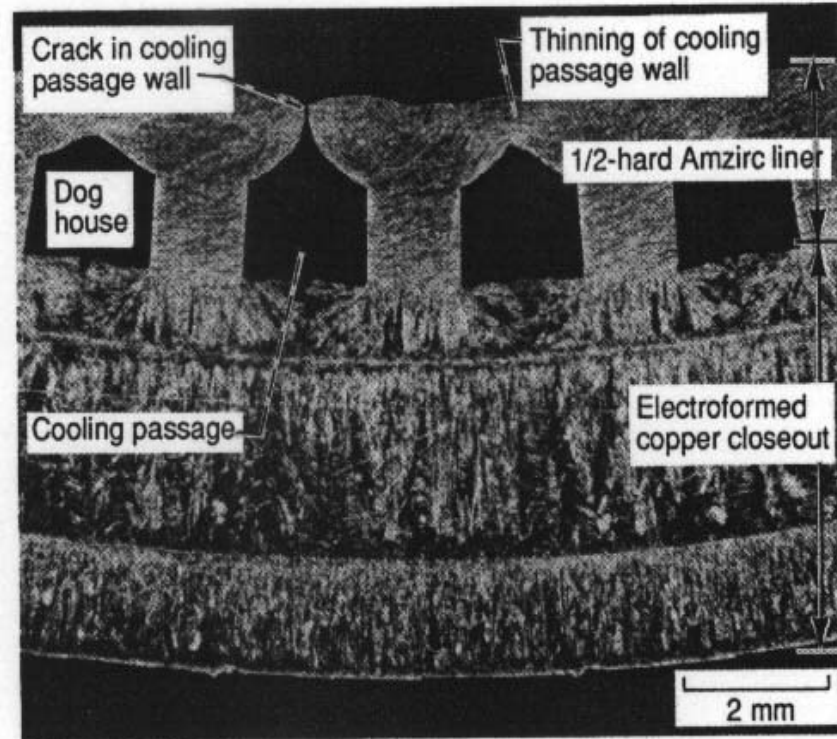


High-Pressure Chamber



Life Prediction - Background

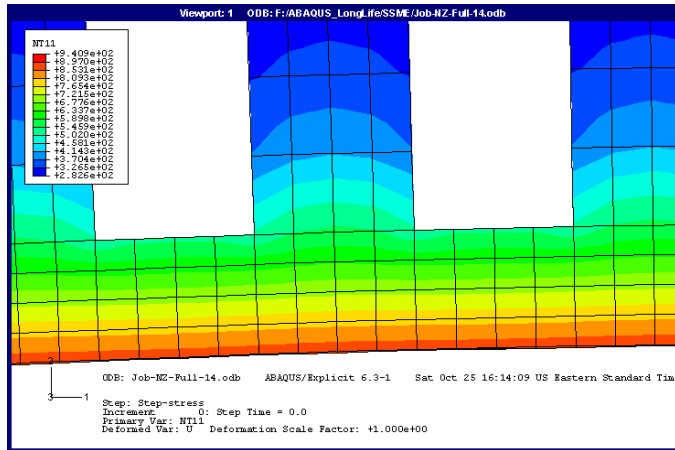
- Rocket combustor liner such as SSME operated at high temperature (6000F) and pressure (3000 psi) ranges as well as extreme heat flux (80 Btu/in²-s) requires active cooling devices to prevent material failure.
- Combustor liner experiences high thermal structural stress (~100 MPa) during mission profile (SSME 8 min)
- Experiments by Quentmeyer and Jankovsky showed bulging and thinning of liner due to cyclic loading
- Kasper and Porowski developed analytical life prediction methods using simple fatigue and creep model
- Robinson, Arnold and Freed developed visco-plastic model for fatigue-creep interaction phenomena which is believed to be a main failure mechanism



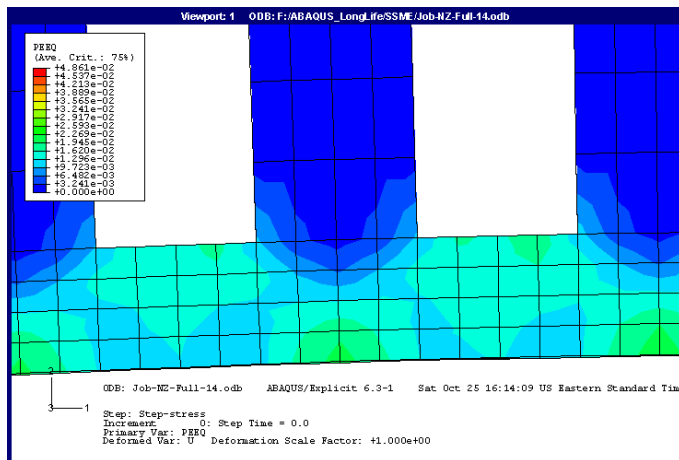
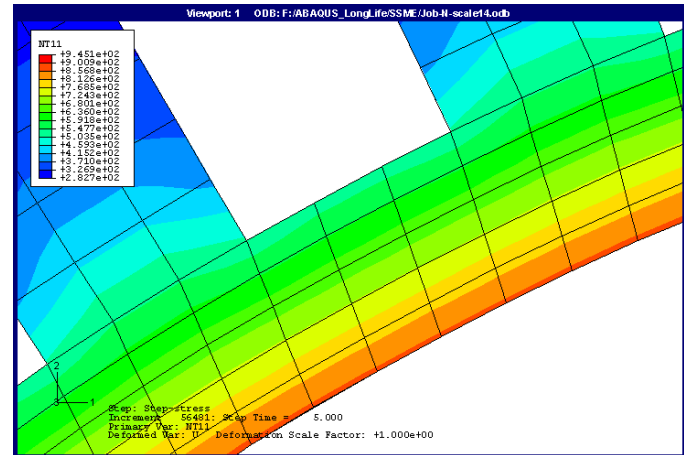
Typical failure mode of combustor liner at throat so called “dog house effect” per Quentmeyer

Full Scale – Subscale Life Comparison

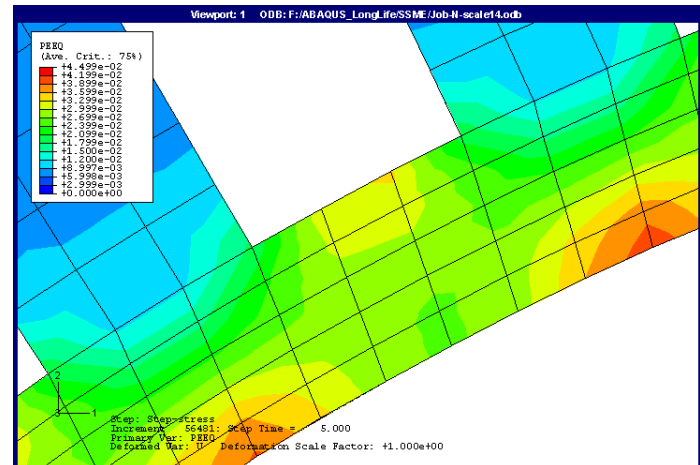
– $P_c = 3300$ psi, $T_c = 3500$ K



T



ε



Full scale engine

Strain_max = 2.4

Life = 120

1/10 scale model

Strain_max = 3.94

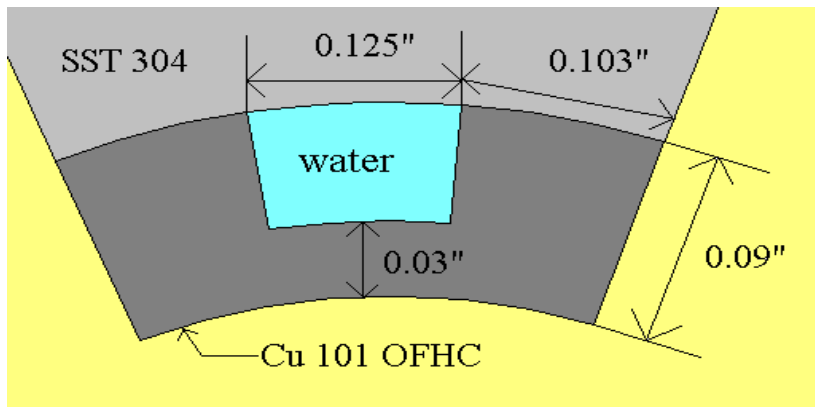
Life = 48

Approach

- Develop DBT course with life prediction as part of AAE curriculum
- Develop design requirements
 - Controlled hot-gas environments – use ‘pre-combustor’
 - Creep-fatigue interaction failure of cooled liner
 - Failure within reasonable number of cycles
- Life prediction analysis using conventional methods
 - Chemical equilibrium in pre-combustor
 - One-dimensional heat transfer analysis for initial design
 - critical heat flux and cooling requirements, duty cycle
 - FEM for stress and plastic strain
 - Strain-life curves for cycle life
 - More advanced life modeling by graduate student following project
- Cyclic testing of test article
 - Ten cycles per test
 - Validation of cooling analysis
 - Regular inspection
- Test-to-failure

Combustor Design Parameters

- Top level requirements
 - Less than 200 life cycle
 - Test should produce verifiable results
 - Liner has no melting prior to the LCF failure
 - All parts had to be manufactured in ASL at Purdue
- Under these requirements, the coolant pressure, flow rate and cooling channel aspect ratio (0.5) were determined.



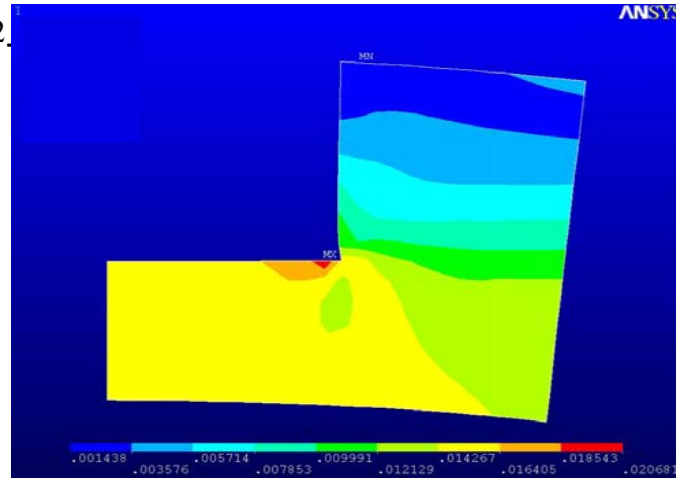
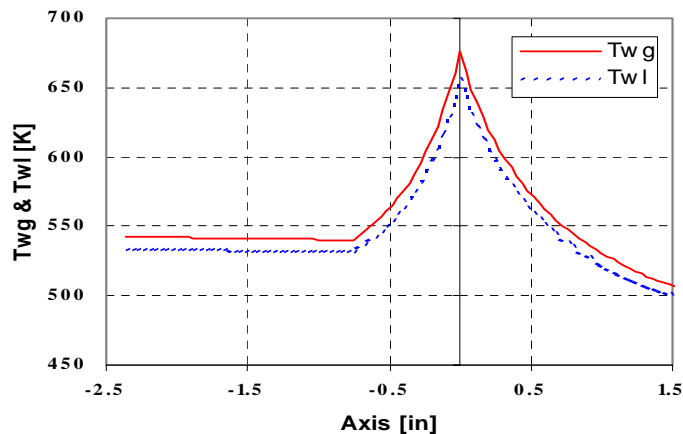
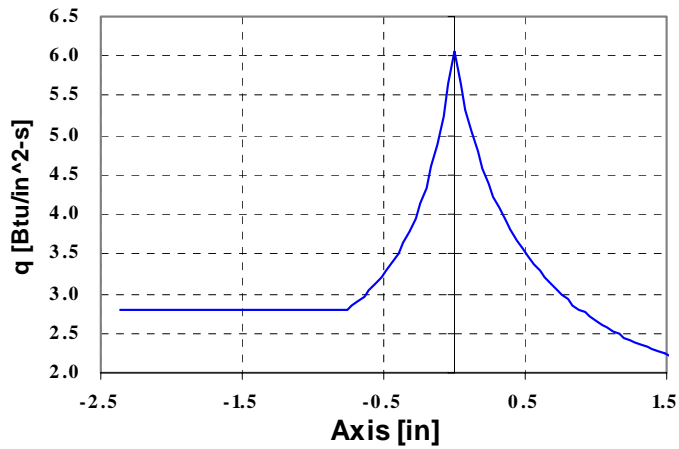
Parameter	Value
Propellant	90% H ₂ O ₂ + JP-8
Propellant mixture ratio (O/F)	4.0
Propellant flow rate	1.25 lb/s
Chamber pressure (P _c)	200 psia
Chamber temperature (T _c)	3440 °F
Characteristic velocity (C*)	4961 ft/s
Throat area (A _t)	0.915 in ²
Characteristic length (L*)	70
Test liner diameter	2.0 in
Test liner length	5.0 in
No. of cooling channel	30
P _{coolant}	110 psi
M _{dot} _{coolant}	0.8 lb/s

Table 1 : Combustor design parameters

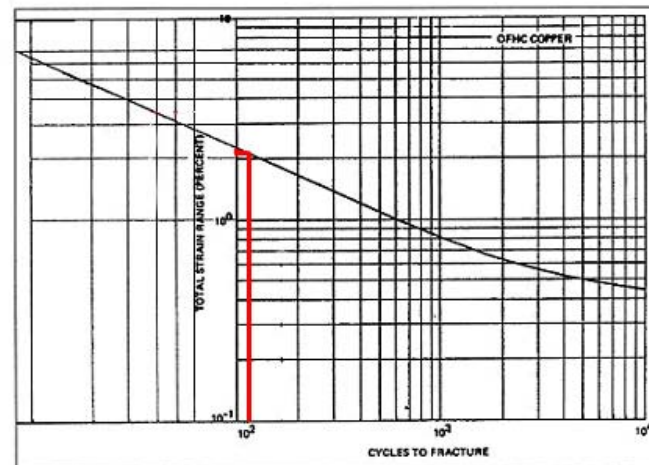
Thermal Structural Prediction

Thermal analysis

- Burn out heat flux --- 6.54 Btu/in²
- Max wall temp --- 670 K



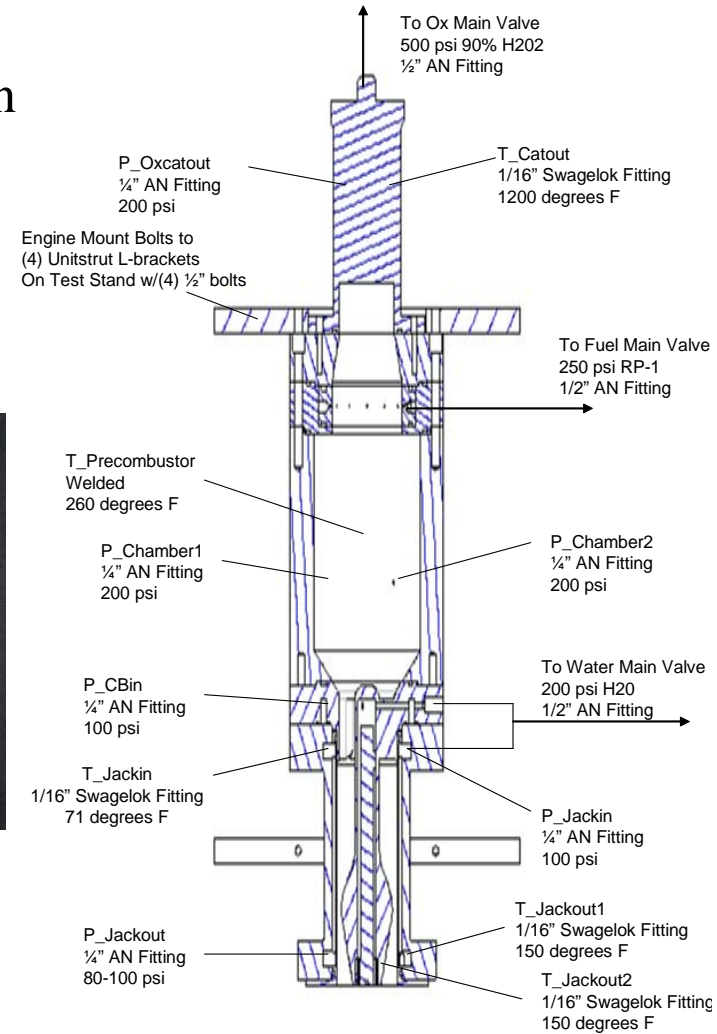
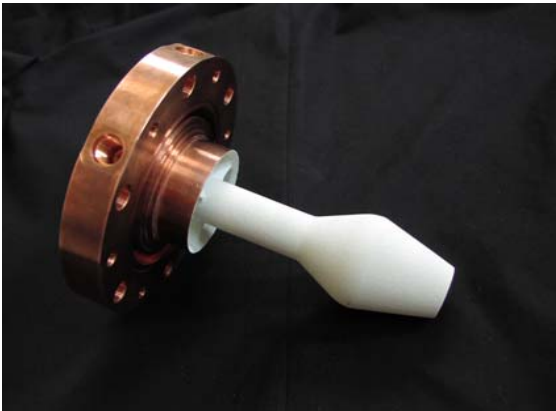
Total strain predicted by ANSYS around rectangular cooling channel.
-Total strain --- 2.0 %
-Life expected --- 115 cycles



Strain-life curve for OFHC at 810 K from NASA CR-134806, 1975

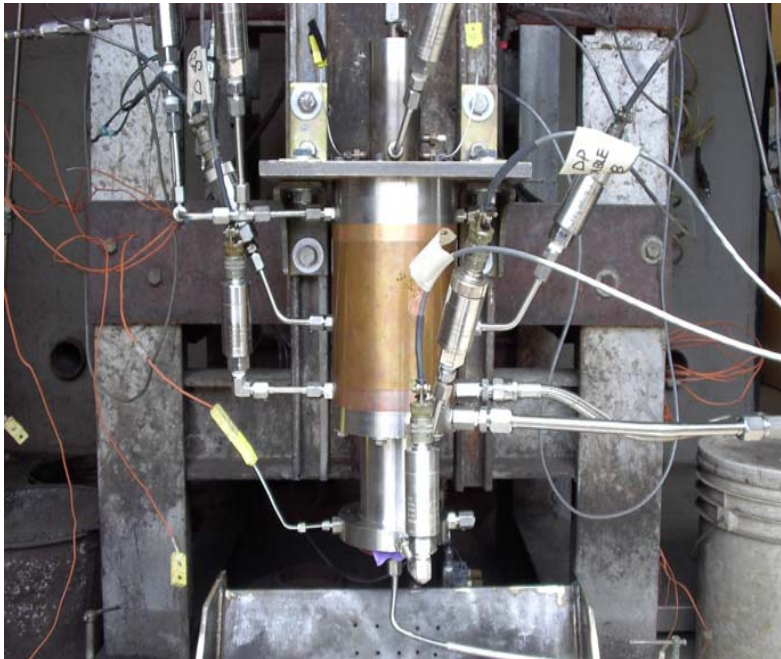
Test Article

- Catalyst bed for decomposing H_2O_2
- Heat sink dump combustor for hot gas generation
- Chamber liner --- water cooling
- Center body --- water cooling with TBC (0.01" thick)



Testing

- Tests were conducted in the APCL at Purdue University
- Propellant flow timing sequence was automatically controlled by pneumatically actuated valve with LABVIEW system



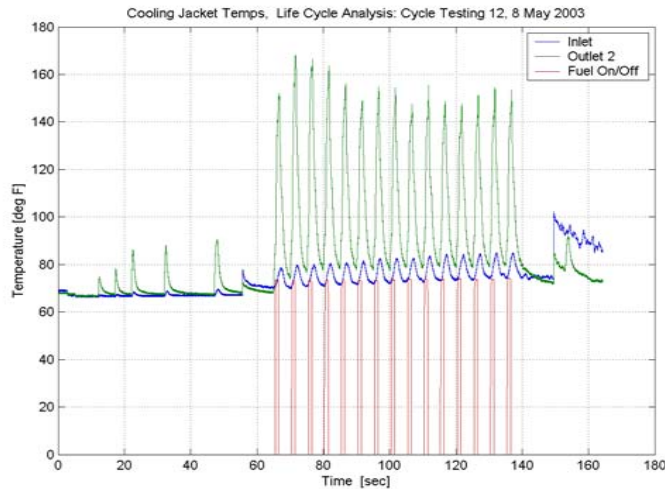
Test article assembly on test stand



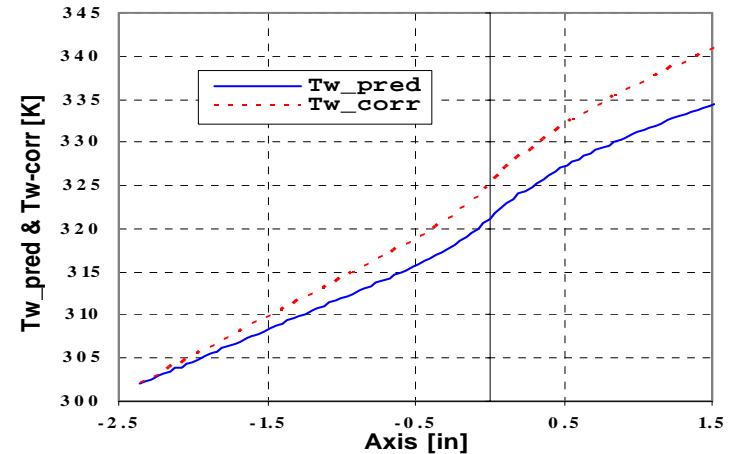
Cyclic test

Test Results

- Chamber pressure, C^* efficiency, propellant mass flow rate, coolant temperature and pressure were measured and calculated
- Data reduction was performed using in-house code written by students using MATLAB
- Validation procedure
 - Measure coolant ΔT , wall thinning rate
 - $2.15E-5$ in/cycle ($0.032'' \rightarrow 0.029''$)
 - Verify 1D thermal model
 - Compute updated thermo-structural environment
 - Make life prediction



Coolant temperature



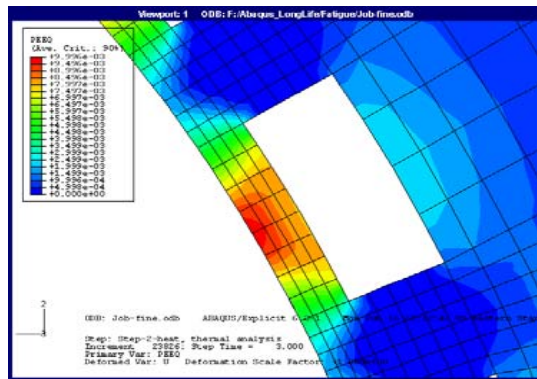
Predicted and measured coolant temperature
 $\Delta T = 4.0K$ at throat



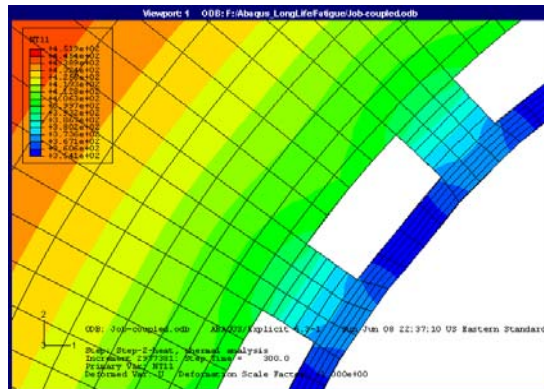
Discoloration and deformation at
90 cycles ($1.5'' \times 0.6''$)

Updated Structural Analysis

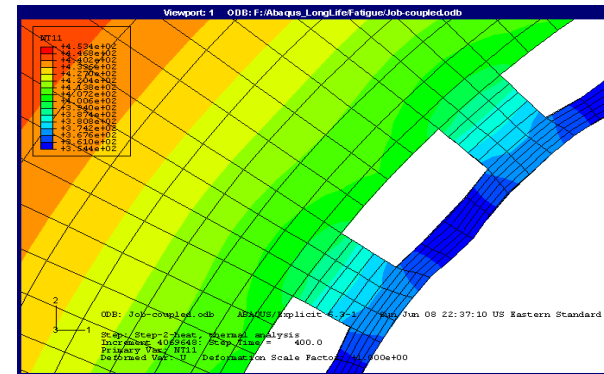
- Simulation of temperature, strain and deformation (bulging, thinning) using ABAQUS explicit module
- Maximum strain : 1.2 % at middle of ligament
- Only bulging of ligament was simulated



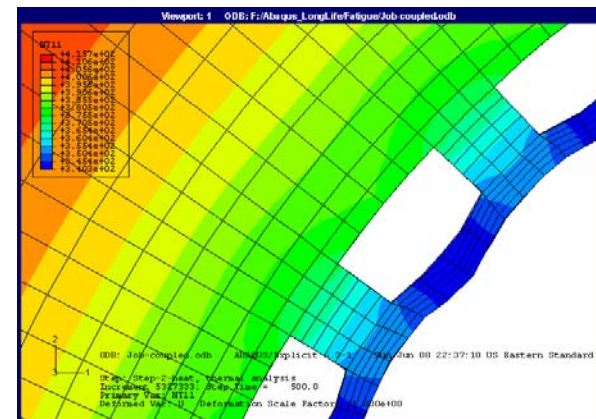
Plastic strain distribution



Deformation after 60 cycle



Deformation after 80 cycle



Deformation after 100 cycle

Summary and Conclusions

- Small-scale rocket combustor was designed and tested to verify life prediction models for low cycle fatigue and fatigue-creep interaction.
- Several life prediction methods were applied to predict combustor life and were compared with test results.
- Correlation data used to improve predictions.
- Improvements would include fixing the liner lands to the structural jacket, and testing at more severe conditions.

Prediction method	Estimated life cycle	Determined life cycle by experiment
Effective stress-strain	115	
ANSYS	115	
Porowski	51	270
Dai and Ray with Freed model	260	
ABAQUS	320	

Comparison of life prediction with test

Summary and Conclusions

- 100's of cycle goal is very challenging and verification would be very expensive
 - Question of economic feasibility
- Improved life prediction methodology for expanding range of design and operational scenarios is needed
 - Probabilistic life prediction design analysis
 - Testing methodologies with *in situ* thermostructural response measurements
 - Environments definition
 - Improved material database and understanding of damage mechanisms

Acknowledgements

- Work sponsored under NAG8-1856, -1876, -1894
 - Huu Trinh, Robert Williams, and Terri Tramel COTR's
- Professor Steve Heister and senior engineer Scott Meyer
- Machinists Madeline Chadwell and Jerry Hahn
- Students of AAE 590
- School of Aeronautics and Astronautics

Investigations of subcritical and transcritical cryogenic combustion using imaging and laser techniques

S. Candel, M. Juniper, P. Scoufflaire, C. Rolon
EM2C Laboratory, CNRS, Ecole Centrale Paris,
92295 Chatenay-Malabry, France

W. Clauss, D. Klimenko, M. Oswald
DLR Lampoldshausen, Institute of Space Propulsion
D-74239 Hardthausen, Germany

F. Grisch, P. Bouchardy and L. Vingert
ONERA Palaiseau, France

October 15, 2003

Abstract

The detailed understanding of liquid propellant combustion is necessary to the development of improved and more reliable propulsion systems. This article describes experimental investigations aimed at providing a fundamental basis for design and engineering of combustion components. It reports recent applications of imaging techniques and laser diagnostics to cryogenic combustion at high pressure. The flame structure is investigated in the transcritical range where the pressure exceeds the critical pressure of oxygen but the temperature of the injected liquid oxygen is below its critical value. Data are obtained from imaging of OH* radicals emission, backlighting and Coherent Anti-Stokes Raman Scattering of H₂ and H₂O molecules. Results from these different diagnostics provide a detailed view of the flame structure and some quantitative temperature profile measurements at various pressure. The data may be used to guide numerical modeling of transcritical flames and the theoretical and numerical analysis of the stabilization process. Results obtained may also be employed to devise engineering methodologies for component development aimed at service life extension.

1 Introduction

Progress in liquid rocket propulsion technology during the second half of the 20th century has allowed extensive commercial utilization of space and a continuous growth of the launching market of telecommunications and earth observation satellites. Developments in space transportation systems have initially relied on full scale testing accumulated experience, engineering analysis and application of basic combustion principles. In this context, research carried out during the last fifteen years has brought new insights on the processes controlling combustion in high performance rocket motors. Detailed experiments have provided a stream of data allowing design improvement and optimization. The data have been used to assist modeling efforts and validate numerical simulation tools. These in turn will allow a renewal of design methodologies for improving engine components and augmenting their service life.

Cryogenic combustion investigations described in this article are concerned with physical processes occurring in the chamber. The research effort focuses on combustion of liquid propellants, which are stored at low temperatures and require ignition to initiate the chemical reaction. Such cryogenic reactants, like liquid oxygen and hydrogen, are used in high performance propulsion systems like the Vulcain motor of the Ariane 5 first stage and the Space Shuttle main engines.

While early research into liquid rocket motors relied heavily on full scale testing with some model scale experiments but with limited diagnostic and data acquisition capabilities, the recent effort has exploited new model scale facilities and a set of optical and laser diagnostics. The state of the art some forty years ago is well

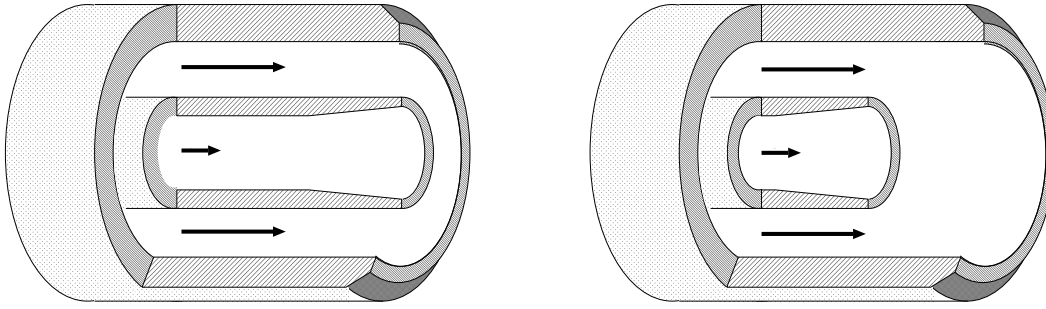


Figure 1: Coaxial injectors of the type used in rocket motors. Liquid oxygen flows through the central tube and gaseous hydrogen through the annular passage. Left, the oxygen tube is set flush with the hydrogen channel. Right, the oxygen tube is recessed

synthesized in the textbook of Barrère et al.¹. Tests on a wide variety of injection systems led to rapid adoption of certain configurations²⁻⁵. These include coaxial injectors like those represented schematically in figure 1. The coaxial geometry is considered in this research project because it is generic and also equips most high performance engines. While the engineering know-how in practical design has become substantial fundamental scientific questions relating to the physical processes at work in the chamber have remained unanswered. These mainly relate to ignition transients, initial flame spreading, flame stabilization, flame spread and conversion efficiency, heat transfer to the chamber walls and injection backplane, sensitivity to impulsive perturbations, triggering of combustion instabilities, combustion dynamics and coupled phenomena.

An understanding of the flame structure is prerequisite to the solution of many technical problems. This question has been difficult to tackle because of the harsh conditions prevailing in the chamber. Rocket engines release powers of several GW - the equivalent of a few large nuclear powerplants - and such powers are expanded in volumes of only a fraction of a cubic meter and at temperatures in excess of 3000 K. The power density may reach 50 to 100 GW m⁻³. Even model scale testing is highly energetic. Most experiments carried out in the early days were restricted by sensor performance, data acquisition equipment and processing devices. Much of the technological developments were carried out without a detailed understanding of the parameters controlling the structure of the reactive flow and the dynamics of ignition and flame spreading during the engine start. Models or numerical simulation tools could not reproduce the complexity of the physical situation. One critical aspect has been to ensure a smooth ignition transient leading to a stable nominal operation. Another permanent problem has been that of instabilities associated with the resonant coupling of combustion and acoustic eigenmodes. These phenomena increase heat transfer to the walls and often lead to chamber burn-out. The scientific analysis of cryogenic combustion has essentially begun during the later period of the twentieth century and these investigations have benefitted from advances in laser diagnostics, digital imaging cameras, experimental instrumentation and high speed data acquisition. Research facilities like Mascotte and P8 developed by Onera and DLR were made available during the same period and could be exploited for hot fire investigations under realistic injection conditions. In this general context research has focused on the following items :

- Processes controlling liquid jet break-up, atomization and mixing
- Spray vaporization and combustion
- Stabilization and flame spread near the injection backplane
- Experimental diagnostics applicable to cryogenic flames under high pressure conditions
- Effect of pressure and transcritical phenomena

Theoretical and numerical modeling efforts have been carried out in parallel to integrate knowledge from experiments and advance engineering design methods.

The present article reports results of recent experimental investigations of high pressure cryogenic combustion. Other results are available in the previous literature (see Ref. 6 to 16). Experimental investigations are also

reported in Refs. 17 to 20. A series of papers by Juniper and Candel^{21–23} covers important issues in flame stabilization. This subject has been approached by analyzing a series of generic problems which reveal the controlling parameters in carefully defined steps. Theoretical and numerical modeling helps resolve some of the difficult questions raised in the experimental studies.

The present paper focuses on experiments and reports data on the following aspects : (a) High pressure supercritical flame structure, (b) Stabilization and flame spread in the nearfield, (c) Temperature distribution measurements based on Coherent Anti-Stokes Raman Scattering (CARS) of H₂ and H₂O species. While the emphasis is on transcritical flames some of the CARS data corresponds to subcritical flames.

The next section describes essential features of the Mascotte and P8 cryogenic combustion test facilities. The flame structure is then discussed on the basis of emission imaging and backlighting. The injector nearfield is characterized with the same diagnostics. Principles of CARS are then briefly reviewed and quantitative measurements of temperature based on CARS are reported. Interpretation of these measurements raises questions which are considered in the same section.

2 Cryogenic combustion facilities

2.1 Mascotte test rig

The Mascotte test facility was developed by ONERA to allow studies of elementary processes of atomization, vaporization and turbulent combustion involved in cryogenic jet flames. The combustion chamber is equipped with a single-element injector fed by liquid oxygen (LOX) and gaseous hydrogen (GH₂). The injection head, holding the coaxial injector element, is cooled by liquid nitrogen (LN₂) to prevent heating of the LOX during injection. The injector element consists of a central tube fed with LOX surrounded by a parallel annular duct delivering gaseous hydrogen (see figure 1). Liquid oxygen is injected at a temperature of 85 K, while gaseous hydrogen is injected either at room temperature or may be cooled down to a temperature of 100 K. The test combustor can be operated up to pressures of 7 MPa exceeding the critical pressure of oxygen. The maximum LOX mass flow rate is of 200 g s⁻¹ but most studies are carried out with mass flow rates of 50 or 100 g s⁻¹. The combustion chamber is a square duct of 50 mm inner dimension made of stainless steel fitted with four fused silica windows for optical access.

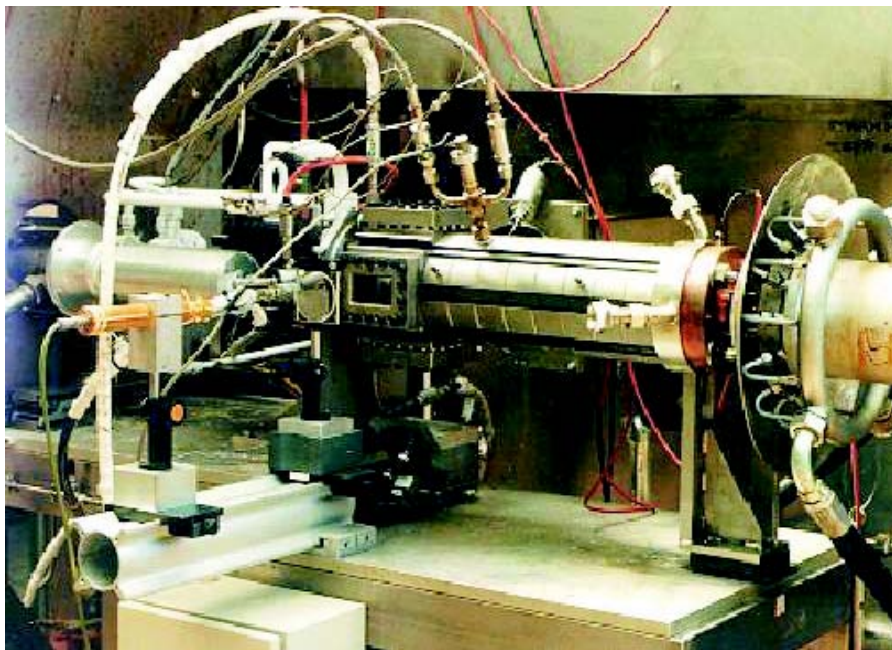


Figure 2: The Mascotte combustor.

The two lateral windows are 100 mm long and 50 mm high. Their internal face is cooled by a gaseous helium film. The upper and lower windows are 100 mm long and 10 mm wide. They may be used to transmit a longitudinal

Run Condition	Pressure (MPa)	LOX mass flow (g s ⁻¹)	Gas mass flow (g s ⁻¹)	E	J
A	0.1	50	15.0	3.3	13.4
C	0.1	50	10.0	5.0	6.3
A-10	1.05	50	23.7	2.1	14.5
C-10	0.95	50	15.8	3.2	6.5
A-30	3	50	25.2	2.0	15.5
C-30	2.8	54	17.0	3.2	6.6
A-60	6.6	100	70.0	1.4	14.4
C-60	5.8	100	45.0	2.2	6.8

Table 1: Operating conditions of the Mascotte facility.

light sheet for laser imaging. The test section comprises interchangeable modules, allowing explorations of chamber sections located at various distances from the injection plane. (the total chamber length is 425 mm). This is achieved by moving the visualization module to different longitudinal positions. Interchangeable nozzles terminate the chamber and their throat diameter is selected to obtain the desired pressure level. There is no water cooling and the chamber design based on simplified thermomechanical models allows 30 s of operation at atmospheric pressure, with a maximum mass flow rate of 120 g s⁻¹ at a mixture ratio of 6. This test duration is reduced to 20 s at higher pressures. The combustor may be fired six to ten times a day, with 5 to 10 minutes between successive runs. Besides the mixture ratio $E = \dot{m}_{LOX}/\dot{m}_{GH2}$, one important similarity parameter, for the liquid jet break-up process, is the ratio of momentum fluxes at the injection plane, defined as:

$$J = \frac{(\rho v^2)_{H_2}}{(\rho v^2)_{LOX}} = \frac{\text{gas momentum flux}}{\text{liquid momentum flux}}$$

The operating conditions (see Table 1) are chosen to preserve the LOX mass flow rate or equivalently the power and the J ratio roughly constant at the different pressure levels. To fulfill this condition, the injector had to be changed by reducing the hydrogen annulus outer diameter (D_g). However, at pressures exceeding 5 MPa, i.e., above the critical pressure of oxygen, new operating points have been defined by keeping the values of the J ratio, further reducing the outer diameter, but doubling the LOX mass flow rate. Trying to reach a pressure of 6.5 MPa in the combustor with a mass flow rate of 50 g s⁻¹ of LOX, would have led to technological problems. The nozzle throat would have been too small and difficult to cool properly.

2.2 The P8 facility

The European research and technology test bench P8, located at the DLR-Institute in Lampoldshausen, designed for high pressure LOX/GH2 combustion investigations, is jointly used by French and German researchers. Operation of subscale combustors is possible using liquid oxygen and gaseous or liquid hydrogen as propellants. Thus, the installed equipment consists of tanks for liquid oxygen (LOX), gaseous and liquid hydrogen (GH2, LH2), cooling water (H₂O). A heat exchanger operated with liquid nitrogen (LN2) is used to cool down gaseous hydrogen to approximately 100 K. The facility is equipped with two test cells allowing test campaigns with different combustors operating in parallel. Due to safety requirements the entire experiments are remotely controlled from a room which located about 100 m from the P8 test stand. Optical diagnostics and data acquisition systems are placed in two rooms located on both sides of each test cell.

For research purposes, the combustion chamber ‘‘C’’ (BKC), equipped with a single coaxial injector with a square layout of 50mm × 50mm, may be operated at pressures of up to 10 MPa. The chamber consists of modules made of a special copper alloy (see figure 3. Water cooling of all modules allows long run times. The visualization module features lateral windows of 50 mm × 100 mm size for imaging, spectroscopy, CARS and LIF detection. A laser sheet can be transmitted into the chamber through smaller windows of 20 mm × 100 mm for LIF and PLIF diagnostics. Windows are cooled and protected on their inner side by a gas flow of hydrogen or helium. For CARS measurements, the BKC was run at 6 MPa with a LOX mass flow of 240 g s⁻¹ at 120 K and a GH2 mass flow of 80 g s⁻¹ at 110 K. Window cooling mass flow was GHe of 160 g s⁻¹. These mass flow rates, although still higher than in Mascotte, represent the lowest operating regime of P8.

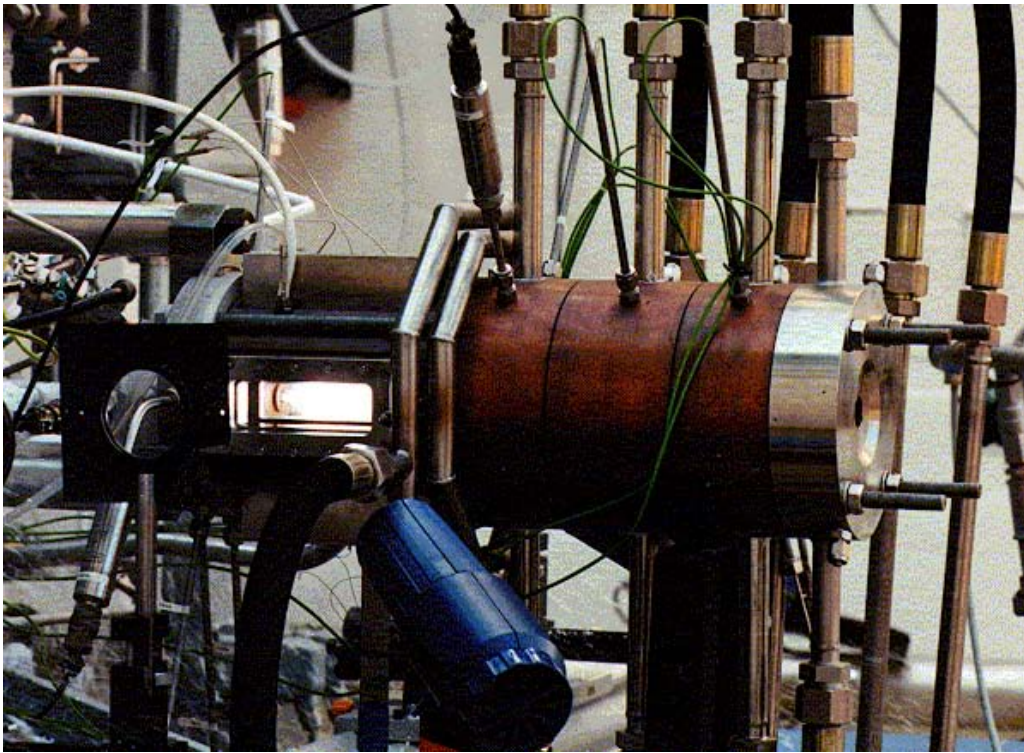


Figure 3: Combustion chamber ‘C’ at P8

Coherent Anti-Stokes Raman spectroscopy (CARS) is used to measure temperature under supercritical pressure conditions.

Operating conditions are gathered in table 2.

The laser system was set at an acquisition frequency of 10 Hz. With a test duration of 20 seconds, 200 CARS spectra could be recorded during a test.

Due to severe vibrations experienced at the test site, the laser system was placed in the diagnostics room adjacent to the engine test cell. The beam guiding optics and focussing lenses mounted around the combustion chamber could be traversed along three axes to allow mapping of the flame. This translation module is made of heavy duty linear stages, welded steel brackets and X95 optical profiles.

3 Structure of high pressure cryogenic flames

Observations of cryogenic combustion at low operating pressures (less than 1. MPa) have provided a wealth of information on the flame structure in the injector vicinity and in the farfield. It has been possible to envisage effects of injection parameters and propose reasons for the effects observed. This has guided further experiments and numerical modeling efforts. On this basis, it has been possible to identify controlling parameters and propose physical descriptions of the flame structure. This section discusses selected high pressure data and proposes a physical description of the flame structure in the transcritical regime.

Among the many parameters affecting the flame it has become standard to consider the Reynolds numbers of each stream, the Weber number of the liquid flow (when the pressure is below critical), the velocity ratio $V = v_{H_2}/v_{LOx}$, the injector diameter ratio d_{H_2}/d_{LOx} , the momentum flux ratio $J = \rho_{H_2}v_{H_2}^2/\rho_{O_2}v_{O_2}^2$, the mixture ratio $E = \dot{m}_{O_2}/\dot{m}_{H_2}$ and the operating pressure p or the ratio of the pressure to the critical pressure $\pi_c = p/p_{crit}$. A limited number of variables can be altered on a model scale test facility, such as injector geometry, exhaust nozzle throat diameter and mass flowrates. Consequently it is not possible to vary each parameter separately. Instead, it is necessary to study only parameters which are judged to be the most influential.

From cold flow experiments and theoretical considerations^{24–26}, it was suggested that the momentum flux ratio

H ₂ Temperature (K)	117
O ₂ Temperature (K)	115.5
H ₂ Density (kg m ⁻³)	11.95
O ₂ Density (kg m ⁻³)	1133.8
H ₂ Mass flow rate (kg s ⁻¹)	0.06
O ₂ Mass flow rate (kg s ⁻¹)	0.29
H ₂ Injection Reynolds no.	3.0×10^6
O ₂ Injection Reynolds no.	7.9×10^5
Injection Velocity Ratio	11.5-12
Injection Mixture Ratio (O/F)	5
Chamber Pressure (MPa)	5.94

Table 2: Operating conditions of the P8 cryogenic test facility.

	Previous work (VO1/VO2)	New results (VO3)
p (bar)	1, 5, 10	10, 70
J	Point C: $J = 6.3 \rightarrow 6.5$ Point D': $J = 9.8 \rightarrow 10.2$ Point A: $J = 13.4 \rightarrow 14.5$	Point C: $J = 3.0 \rightarrow 8.0$ Point A: $J = 9.0 \rightarrow 13.0$
Recess (d_{LOx})	0, 1	0, 1, 1.5
T_{H_2} (K)	298 K	298 K \rightarrow 100 K

Table 3: Operating points of the cryogenic test facility

was the most influential parameter in determining the rupture of the central fluid in a coaxial jet at least under subcritical conditions where break-up and atomization determine the liquid droplet sizes. This dimensionless group has served as the main scaling parameter in the experimental investigations carried out in the Mascotte test facility. Low pressure range experiments, have confirmed that J controls the flame spread⁶⁻⁹. Initial hot fire tests were carried out in the low pressure range up to 1 MPa ($\pi_c = 0.2$). In that range, the oxygen stream behaves like a liquid jet which is broken down into ligaments. These are subsequently atomized by aerodynamic shear stresses induced by the high speed hydrogen flow. When the chamber pressure is increased beyond 5.05 MPa (when $\pi_c > 1$), the oxygen jet passes from a subcritical to a supercritical state and its general structure is modified¹⁵. Break-up and atomization prevailing at low pressure are replaced by a turbulent mixing process which determines the rate of transfer between dense oxygen at a temperature lower than the critical temperature and light oxygen at a temperature exceeding the critical value.

It has also been observed that recessing the LOx tube inside the hydrogen annulus has a significant effect on flame spread when the chamber pressure is below critical¹¹⁻¹³. Cold flow experiments at low pressures²⁷ indicate that post biasing may be used to shift the liquid flux distribution away from the chamber wall.

Other experiments have focused on the effect of inlet hydrogen temperature. This temperature affects the stabilization of the flame and the near field flow configuration. It was found that under cold flow conditions some of the water vapor produced by the chemical reaction could be condensed and form an annular cloud surrounding the oxygen stream. At low injection temperatures the cloud was sufficiently dense to block most of the light emitted by the flame¹⁵.

The operating conditions of hot fire tests are summarized in Table 3. Values of the momentum flux ratio J have been selected to change the quality of atomization (imperfect at low values of J , suitable at high values of this parameter). The value of J is the hardest to keep constant because it depends on the ratio of the square of the velocities. The desired pressure is also difficult to achieve every time and there is some dispersion in the values of these parameters.

A large set of optical diagnostics has been used during the various test series including OH* emission detection, backlighting, spectroscopy, planar laser light scattering and planar laser induced fluorescence of OH radicals (see Table 4, Ref. 28 for a review of optical diagnostics for cryogenic flames and Ref. 10 for a synthesis of

	Laser induced Fluorescence OH, O ₂	Emission imaging, Emission tomography	Backlighting, Light scattering	Combined imaging
Flame structure	[8],[10], [20]	[6], [9], [17]	[6], [17]	
Injection parameters	[8]		[8], [18]	[8]
Effect of pressure		[14], [15]	[14], [15], [19]	[15]
Stabilization	[7]			
Effect of recess		[11], [12] [13]	[16]	[16]

Table 4: Experimental investigations of cryogenic combustion.

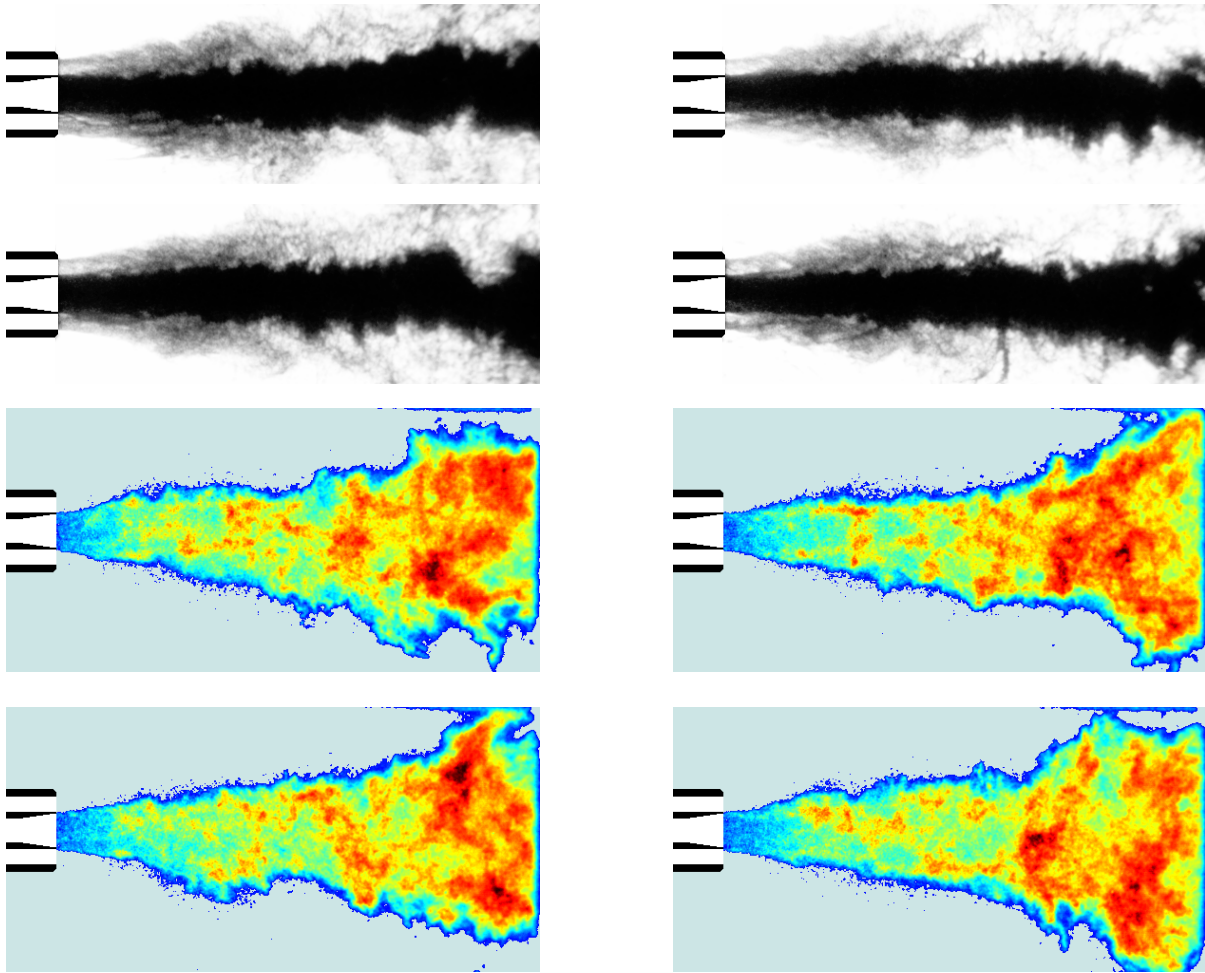


Figure 4: A sample of instantaneous backlighting images (top) and instantaneous OH* images (bottom) for the broad field. The operating points and camera position are identical in both sets of images: Point C, $p = 70$ bar.

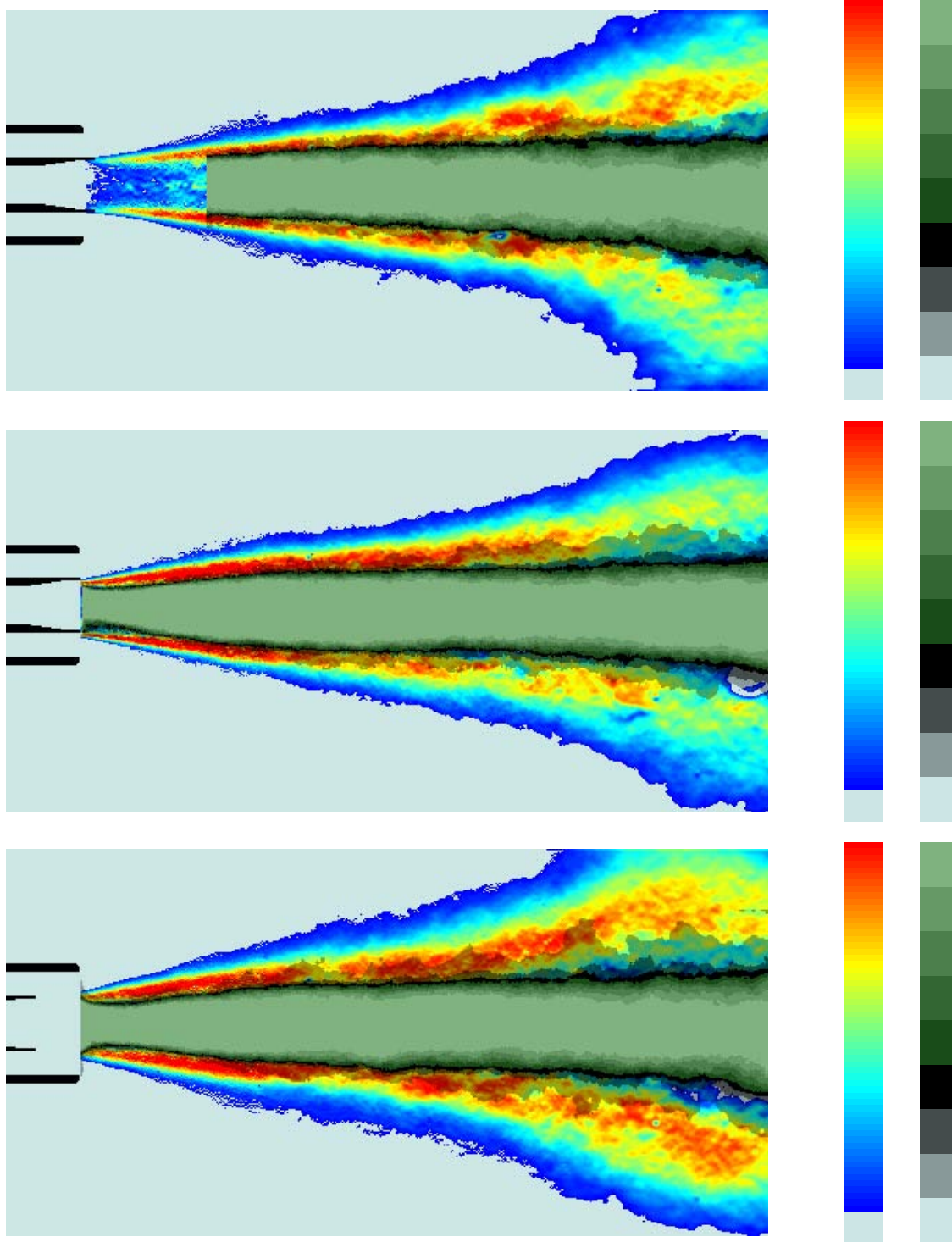


Figure 5: Combined emission and backlighting images. The colour scale corresponds to a slice of OH* emission and the grayscale to the average jet position. Top: Point A, zero recess. Middle: Point C, zero recess. Bottom: Point C, recess of $1 \times d_{LOx}$.

experiments in the low pressure range). The first three techniques were exploited in the high pressure range since fluorescence is not applicable due to excessive quenching. A selection of backlighting images is presented in figure 4. These show the dense oxygen jet and the regions containing steep refractive index gradients in the gas. The intensity of light defines the edge of the oxygen jet which is taken to be the position where the intensity gradient changes most rapidly. Using this method, the oxygen jet position was found for all images in a sequence. These were then averaged to give a residence time along the line of sight. One obtains in this way a qualitative indication of the rate of expansion of the dense jet of oxygen.

A selection of instantaneous OH* emission images is shown in figure 4. These images, taken just after the backlighting images, correspond to exactly the same operating point and camera position. These images can also be averaged and processed with the Abel inversion. This process yields the position of the average flame. These data may then be merged with the average oxygen jet position deduced from backlighting to form composite images as in figure 5. (Note that in the top picture the average jet position near the injector was not available due to a partial icing of the visualization window).

As in the low pressure range, the flame begins at the injector, it spreads in the vicinity of the oxygen jet and does not penetrate in the central core occupied by a dense stream of oxygen. In the high pressure range, the flame expansion angle is much smaller than that found in the low pressure experiments. It is also found that the momentum flux ratio has less influence in this pressure range. A detailed examination of the data gathered is carried out in Ref. 15 . It is found that the low pressure flames are controlled by droplets produced by the liquid jet break-up and subsequent atomization. The momentum flux ratio J determines the break-up process. In the high pressure range, beyond the critical pressure of oxygen ($p > 5.05$ MPa), the flame spreading rate is controlled by turbulent mixing of the dense stream of oxygen with the lighter surroundings. The controlling mechanism is now mass transfer from the dense jet to the lighter surrounding gas. Under these circumstances, the momentum flux ratio is less influential. The change in flame structure as pressure exceeds the critical pressure of oxygen is illustrated schematically in figure 6.

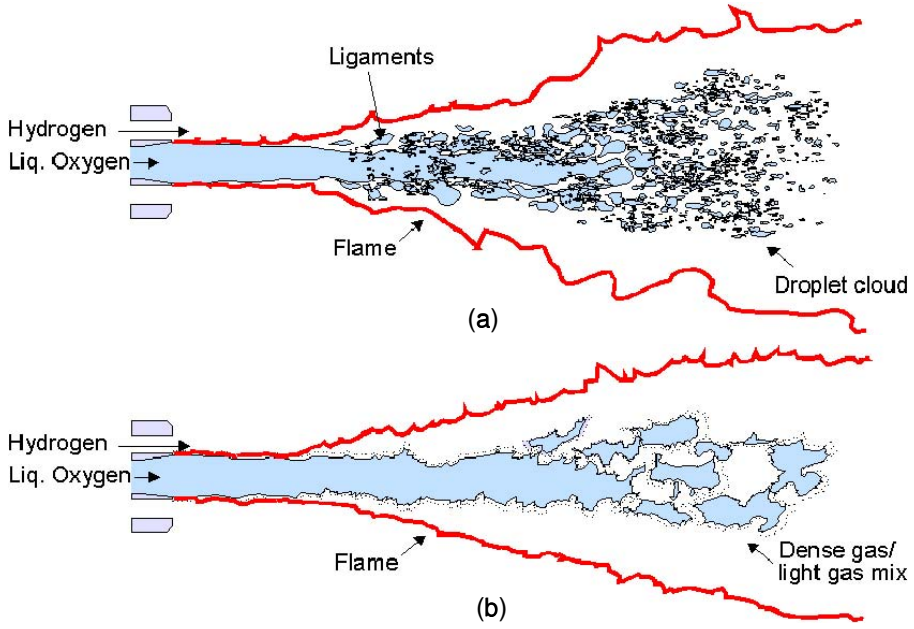


Figure 6: Schematic representation of subcritical (a) and supercritical (b) cryogenic jet flames.

4 Flame stabilization in the nearfield

Flame spread in the nearfield is fundamental to flame holding. It is therefore important to focus on this region. This is accomplished by using the same optical techniques combining emission and backlighting imaging¹⁶. The backlighting setup is influenced by Schlieren effects because ray deviations are strong enough to deflect light out of the light cone which is captured by the camera. When these images are averaged, the darkness of a

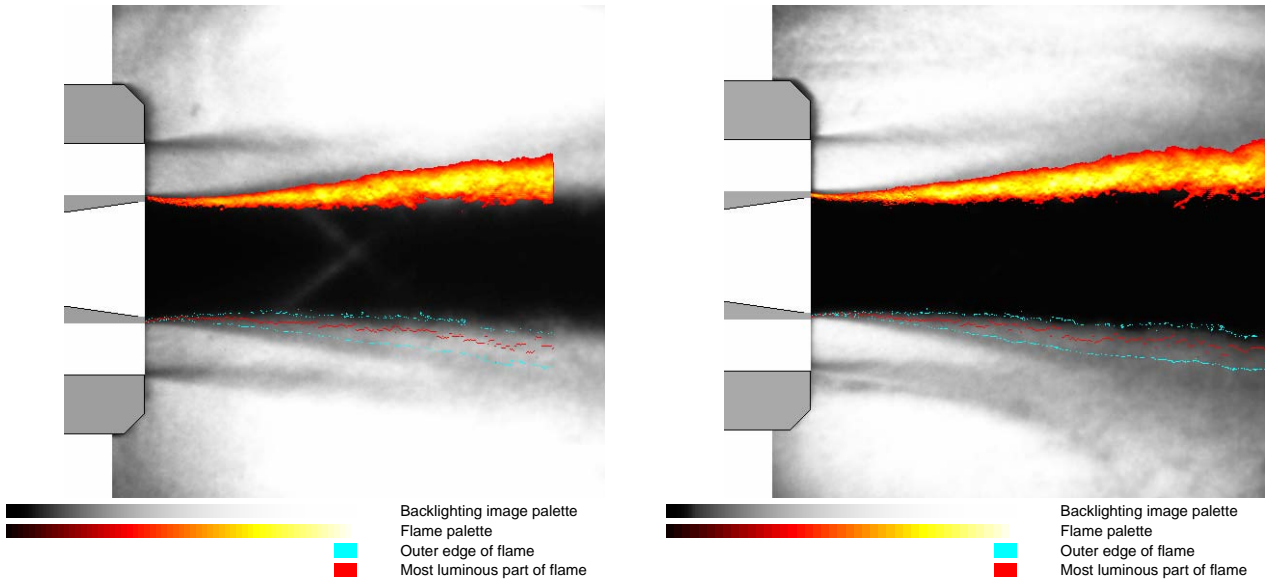


Figure 7: Combined emission and backlighting images. The colour scale corresponds to a slice of OH^* emission and the grayscale to the average backlighting image. Left, point A, 70 bar, zero recess. Right point C, 70 bar, zero recess.

pixel corresponds to the average time that a strong gradient has existed at that pixel's position. The strongest deviation occurs where gradients are perpendicular to the ray direction, which is in a slice through the jet's axis. Thus, to a first approximation, the images can be considered to be a slice of this plane and can be compared with the Abel-inverted emission images.

Instantaneous emission images obtained in the nearfield can be averaged and processed with the Abel inversion. They can then be superimposed on the average backlighting images, as shown in figures 7. The flame edge is located in the near vicinity of the LOx injector and the flame then closely follows the dense oxygen boundary. Heat released by chemical conversion taking place near the dense oxygen stream induces a gradient of temperature and a steep change in oxygen density. The experimental data indicate that the flame is attached to the oxygen injector lip over the complete range of pressures, inlet velocities and hydrogen temperatures studied. This is illustrated in figure 8 which shows the flame structure near the injection plane and a closeup of the vicinity of the LOX post lip. The flame edge is located just behind the lip at a small distance from this boundary. It is shown in a recent article by Juniper and Candel²² that the backwall serves to stabilize the flame. Theoretical considerations and simulations of this region indicate that the most influential parameter is a nondimensional step height ψ which measures the size of the lip with respect to the flame thickness $\psi = h_s/\delta$. When this is large, the flame tucks behind the lip and is affected little by the Damköhler number. When this is small, the flame is thicker than the lip and it is exposed to the high speed hydrogen stream and becomes very sensitive to the Damköhler number. Figure 8 corresponds to a case where $\psi > 1$ and one expects that the flame will be well stabilized.

5 CARS and applications to cryogenic combustion

Quantitative measurements of temperature and species may be carried out using Raman or Coherent AntiStokes Raman Scattering CARS and probing H_2 and H_2O molecules. The application of Raman scattering is explored in Ref. 29 which illustrates the possibilities and limitations of this technique. This section is concerned with CARS applications. It begins with a short summary of principles and contains a description of specific properties of probe molecules and of practical details. Measurement results are discussed in the next section.

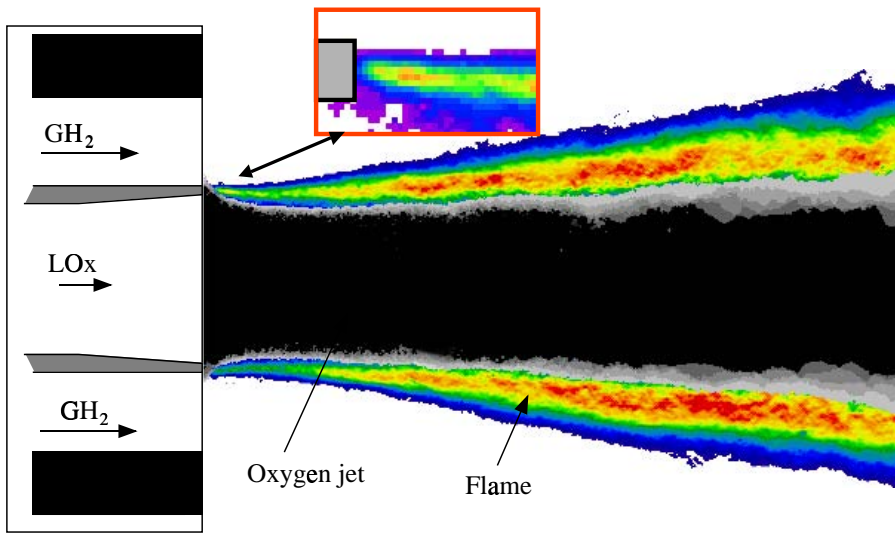


Figure 8: Combined emission and backlighting images. The colour scale corresponds to a slice of OH* emission and the grayscale to the average backlighting image.

5.1 CARS principles

The achievements in nonlinear optics and quantum electronics have significantly broadened concepts of the interaction of light with matter, thereby opening the way on a number of fundamentally new spectroscopic diagnostic techniques that employ tunable lasers as the excitation sources.

Presently most widely employed is the Coherent Anti-Stokes Raman Scattering (CARS). CARS is a Raman-resonant direct four photon parametric interaction process in a medium with the third order nonlinear susceptibility $\chi^{(3)}(\omega)$, based on the nonlinear response of molecules to the incident electric fields of the exciting laser beams. Three photons of frequencies ω_P , ω_P and ω_S (to simplify experimental setup, two photons can be taken from one laser, suffix P denotes the so called pump laser, suffix S the so called Stokes laser) are sent into a probe volume (created by the three laser beams to focus in the same volume) in this medium where a fourth photon $\omega_{CARS} = 2\omega_P - \omega_S$ is generated.

This new wave results from the inelastic scattering of one photon ω_P by the molecular vibrations of the third order nonlinear susceptibility which are excited by the interaction of the two photons ω_P and ω_S .

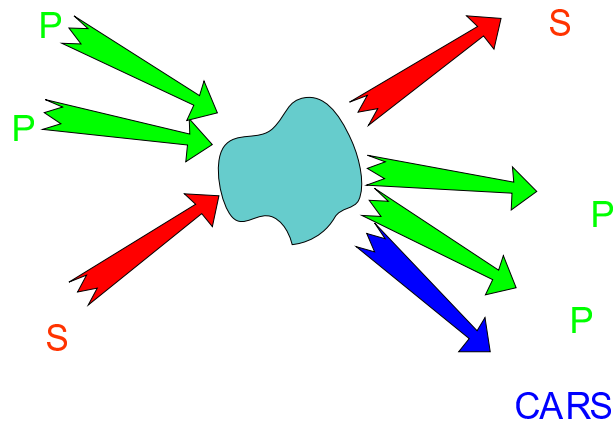


Figure 9: The CARS principle

In principle, ω_{CARS} is generated from all kinds of molecules within the probe volume. If the frequency difference

$\Delta\omega = \omega_P - \omega_S$ is equal to a Raman-active molecular transition of a specific molecule, the vibrations of this molecule are coherently and resonantly driven by the waves ω_P and ω_S and ω_{CARS} from this molecule is resonantly enhanced in intensity.

Experimentally, a CARS signal is produced by focussing three pulsed laser beams into the same probe volume. A CARS spectrum is obtained by scanning the Stokes laser frequency ω_S or by using a broadband Stokes laser, thus generating the whole spectra over the frequency difference $\omega_P - \omega_S$ in one laser shot of 5ns duration which makes CARS well suited for combustion diagnostics.

The CARS signal is detected and recorded by a photodiode-array or a CCD detector attached to the output of a conventional optical spectrometer. The detector can be intensified by a microchannel plate. Gating of the detector is desirable to reject background emission.

Deducing the temperature from experimental CARS spectra is done by analyzing the spectral profile formed by the different intensities of the excited rotational-vibrational transitions of the probe molecules. The effects of temperature and concentration on the CARS spectrum are contained in the squared modulus of $\chi^{(3)}(\omega)$. Changes in temperature and concentration markedly modify the shape of CARS spectra and form the basis for measurements.

The third-order non-linear susceptibility is calculated for the specific molecule as a function of temperature. Here, specific molecular data like rotational and vibrational levels, polarizability, transition probability and linewidth broadening effects must be included. Knowledge of the linewidths of individual transitions is not sufficient if high pressure combustion is studied. Because of interference effects arising from line overlap, the CARS process is sensitive to the linewidths of the molecular transitions. Here, it is necessary to also specify the rates of inelastic energy transfer between vibrational-rotational states in the active molecule. This is the cause for the phenomenon of spectral collapse which is commonly known as collisional narrowing. This illustrates, that the successful application of CARS on technical combustion requires a thorough understanding of the basic physics, which is necessary for a reliable modeling of the CARS spectra of probe molecules. For more on CARS see Ref. 30 .

5.2 Probe molecules in LOX/GH₂ combustion

CARS thermometry is usually performed with major species. For LOX/GH₂ rocket engine applications, the possible Raman-active probe species are H₂, H₂O and O₂. Since rocket combustors are operated in fuel rich conditions, hydrogen is present downstream of the flame front and is the prominent probe molecule into the flowfield. O₂ is only present in vapor in the thin shear reactive mixing layer located around the LOX jet while the major product of combustion, H₂O, is available in abundance everywhere. We concentrated our efforts on simultaneous and synchronous CARS of H₂ and H₂O because this gives valuable information on the mixing processes in the turbulent reacting flow.

5.3 Hydrogen-CARS at high pressure

Obtaining data on hydrogen line broadening by collisions with foreign molecules at elevated temperatures (> 1000 K) still stays an actual problem. At this point in time, hydrogen line broadening coefficients at temperatures not exceeding 1800 K have been measured in Ref. 31 for collisions with N₂, H₂, and H₂O. In order to perform such an investigation, one has to apply high-resolution scanning CARS techniques with CW single-frequency tunable pump sources to a stationary medium in a heatable high-pressure vessel³¹. Possible alternatives to static vessel measurements are the hydrogen Raman linewidth measurements directly in a hydrogen-oxygen burner where continuous refreshment of the medium takes place. A high-pressure repetitively pulsed (up to 10 Hz) hydrogen-oxygen burner was designed. Running such a burner that has a small - about 2 cm³ volume of the combustion chamber in a repetitively pulsed mode allows obtaining high (100 bar) values of the pressure of combustion products at about 2800 K, while keeping both fuel and oxidizer consumption and mean overall heat production at reasonably low levels. This design concept diminishes the amount of problems connected with chemical activity of combustion products, device overheating, limited amounts of available fuel, etc and allows to conduct the measurements within several hours without interruption.

Specific operation mode of such a pulsed non-stationary object requires that all the necessary spectral information should be obtained within a single short laser pulse synchronized with a burner pulse. In our case the analysis of the line shapes of individual hydrogen Q-branch lines with a necessary spectral resolution was performed by CARS spectroscopy with the help of a Fabry-Perot interferometer and an Optical Multichannel Analyzer (OMA). Simultaneously with Fabry-Perot pattern a broadband CARS spectrum of the complete H₂

Q-branch structure together with the ν_1 band of water has been recorded in order to measure the probe volume temperature. A piezoelectric pressure sensor has monitored combustion chamber pressure and its temporal dependence. Thus, during every shot of the burner, a pressure pulse together with CARS spectra both of H_2 and H_2O delivering the information on individual line shapes and medium temperature have been recorded. Figure 10 presents the results of our measurements of hydrogen Q-branch linewidth for $J=1,3,5,7$ versus water vapor density. The line-broadening coefficients derived in this way are displayed in figure 11. It should be noted that the values are in good agreement with the linewidth data experimentally obtained in Refs. 31-33 in the range of 600 K - 1800 K extrapolated to 3000 K in Ref. 31 .

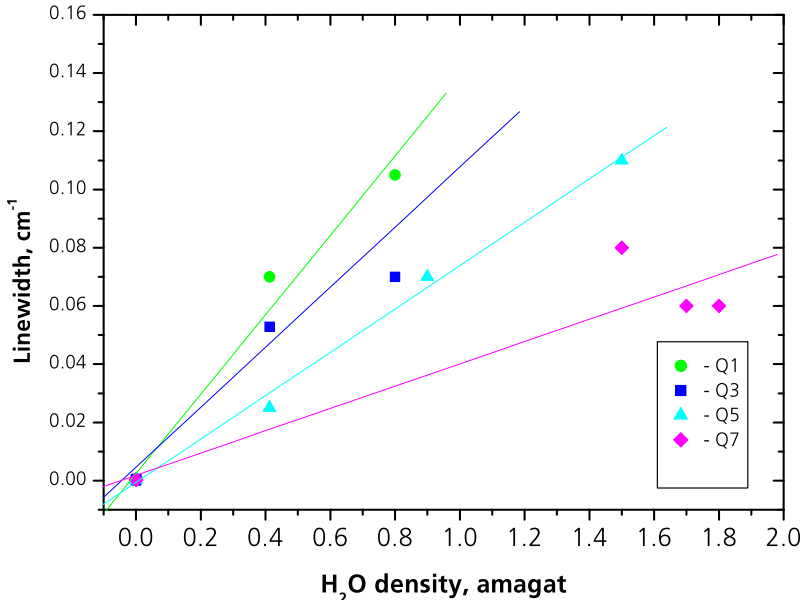


Figure 10: The dependence of H_2 Q-branch linewidths on water vapor concentration at 2700 K.

Determination of temperature from hydrogen CARS spectra is obtained by two analytical procedures depending on the pressure prevailing in the combustion chamber. At low density (i.e., pressure below 0.1 MPa), the Raman linewidths are equally broad when the J -dependent Raman linewidths are much smaller than Doppler broadening. In this case, the temperature can be deduced by plotting the amplitudes of the Q-lines in a Boltzmann diagram. When the density is higher (i.e., when the pressure exceeds 0.1 MPa), pressure broadening and Dicke narrowing become important and temperature must be deduced by modeling the spectral shape of the Q-lines.

The important parameter in this situation is the collisional broadening. This coefficient depends on density, J quantum number, temperature and composition of the mixture. In the Mascotte investigation, collisional linewidths are calculated using a methodology developed by Michaut³².

5.4 Water-CARS

The CARS spectra have been processed both for temperature and for H_2O concentration. Temperature and H_2O concentration measurement were deduced by fitting the experimental CARS spectra to the theoretical ones using a non-linear least-squares fitting procedure. Calculation of H_2O CARS spectra follows the treatment given by Grisch et al.³⁴. The code has been expanded to simulate the interference between resonant and nonresonant CARS signals.

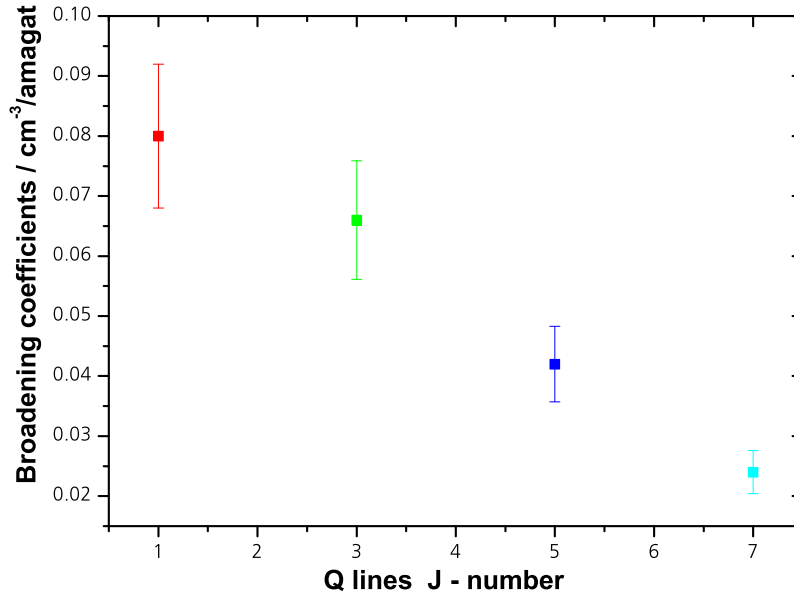


Figure 11: The dependence of H₂ Q-branch linewidths on water vapor concentration at 2700 K.

5.5 CARS Spectrometry at Mascotte

The laser system is composed of two separate optical benches which produce the pump and Stokes beams (ω_P and frequencies ω_S) required for H₂ and H₂O CARS spectroscopy.

For H₂, the pump beam is the doubled-frequency output of a Nd:YAG laser chain composed of a single-mode Q-switched oscillator followed by an amplifier. The laser delivers 140 mJ in 13 ns pulses with a frequency rate of 10 Hz, thus providing single-shot measurements which can be used to study the dependence/variability of the process. Half of the green energy is used to pump the Stokes dye laser which emits the broadband ω_2 beam. At the output of the laser bench, the pump beam is split in two parallel beams and one of them is overlapped with the ω_2 beam (planar BOXCAR arrangement). The energy per pulse of the beams are 30 mJ for each of the pump beams and 4 mJ for the Stokes one. All beams are horizontally polarized.

The H₂O pump laser is a Quanta-Ray DCR 3D Nd:YAG unstable oscillator-amplifier system whose multimode output is also frequency-doubled to produce a 532 nm laser pulse with a duration of 8 ns. The green output is split by a dichroic mirror in order to pump a broadband dye laser and to act as the pump beam in the CARS process. The USED-CARS (Unstable-resonator Spatially Enhanced Detection) beam geometry was chosen because it is easier to align and not so sensitive to loss of beam overlap caused by refractive index variations than BOXCAR.

The H₂ beams are focused first in an atmospheric pressure flow of argon where a nonresonant CARS signal is created to monitor the shot to shot fluctuations of direction and of pulse energy of the lasers beams and of the spectral shape of the Stokes laser. This reference signal is then split off and the H₂ laser beams are combined spatially with the H₂O laser beams onto the same path using a single mirror (i.e., the H₂ beams passed over the mirror while the H₂O beams are reflected on the mirror). All laser beams are then transmitted to the testing facility through optical windows. They are focused in the chamber by means of a single 200 mm-focal-length achromat yielding a 1 mm-long and 50 μ m in diameter probe volume for H₂ and 2 mm-long and 100 μ m diameter for H₂O.

Both lasers systems are synchronized, the H₂ CARS laser serving as the master. A TTL signal issued from the electronics of this laser and delayed by a delay generator was used to fire the flashlamps of the H₂O CARS laser. A synchronous operation of both lasers is achieved at 10 Hz with a jitter of less than 200 ns.

The H₂ CARS signal is sent to the spectrograph by a series of mirrors. Reference and sample H₂ CARS spectra are dispersed using two separate spectrometers. The hydrogen spectrum and the broadband reference

are formed in the output plane of the spectrographs and detected by means of intensified 512-photodiode arrays. After leaving the combustion chamber, the H₂O CARS signal which was geometrically separate from the H₂ CARS signal, was guided off from the optical path by using a prism. The H₂O laser beams were blocked by a dichroic filter and the CARS signal was focussed into a single 550 μm diameter quartz fiber and guided to the spectrograph.

The water vapor spectra have been sequentially recorded using an intensified gated diode array. The 10 Hz sequence of H₂O CARS spectra was stored to a PC harddrive and simultaneously displayed in near realtime on the PC monitor.

Both data acquisition systems were started using the same single external trigger which was performed manually after combustion was stabilized in the chamber.

5.6 CARS spectrometry at P8

A frequency doubled single mode Nd:YAG laser was used to pump two amplified modeless dye lasers in a Dual-Broadband-CARS configuration. This allows for a good spectral averaging in each laser shot and referencing of the H₂-CARS is not necessary. A drawback is the low energy in the water region.

The 3700-4000 cm^{-1} difference between the central frequencies of the two dye lasers and their bandwidth enables the Q-branch of hot Hydrogen and Q-branch of Water to be probed.

The laser beams were combined in a planar BOXCARS and angled configuration. Longitudinal spatial resolution for planar and angled CARS was approximately 2mm and 2.5 mm respectively. The detection system received the CARS signal via a 6m long 600-mm-diameter fused silica fiber. This was necessary due to excessive vibrations experienced within the test facility. A 46-cm spectrograph was employed for spectral acquisition. This was used in conjunction with a detection system consisting of a back illuminated 256×1024 CCD detector.

6 Temperature measurements based on CARS and interpretation

Temperature measurements using CARS on H₂ are already discussed in Ref. 10. The data correspond to subcritical flames at pressures not exceeding 1 MPa. A more recent effort has been made to obtain temperature from CARS on H₂O and H₂ simultaneously and operate at pressures up to 6.5 MPa. Experiments were carried out on the Mascotte and P8 facilities. While the emphasis is on transcritical flames, this section discusses selected data corresponding to atmospheric (0.1 MPa), moderate pressure (1 MPa), high pressure subcritical (3. MPa) and high pressure transcritical (6.5 MPa) flames.

6.1 Subcritical tests on the Mascotte facility

At atmospheric pressure, an ensemble of 150 instantaneous measurements is recorded during each run for both species. Under stationary conditions, the test run can be characterized by histograms, mean values and standard deviations of temperature.

Figure 12 shows typical data on H₂ corresponding to different positions. The data are displayed with a temperature interval of 100 K matching the apparatus uncertainty. The scatter in the results, larger than the measurement uncertainty, gives insight into the degree of turbulence in the flow. This depends primarily on the mixing of H₂ and O₂. Figs. 12(a-b) show the temperature probability density functions (PDF) within the flame region. Both PDF's feature a skewed-bimodal type of distribution with one dominant peak. The cold gas peak corresponds to temperatures which are preheated by the recirculation zone and the hot gas peak is close to the flame temperature. A finite probability of intermediate temperatures also exists in both temperature PDF's suggesting the presence of gas in the partially burned-unburned state moving randomly in space and time. Further downstream, the environment becomes more uniform indicating that mixing progresses. The PDF's are centered around the hot gas peak with a symmetric and narrower distribution (see Fig. 12 d).

Radial mean temperature and H₂O concentrations deduced from the data reduction of H₂ and H₂O CARS spectra are displayed in Fig. 13 for different axial sections. The bars represent rms fluctuations in measured temperatures. The validation percentage of the measurements is also indicated.

Near the centerline, the data show an absence of detection of H₂ CARS signals up to an axial location $x=200$ mm. This indicates that combustion occurs in a layer bounding the two propellants and that the flame constitutes a surface ("a shell") separating the two fluids, preventing any diffusion of H₂ into the oxygen core flow. This is in agreement with the fluorescence imaging data of Refs. 8 and 10 and with the average flame structure deduced from emission imaging⁹⁻¹².

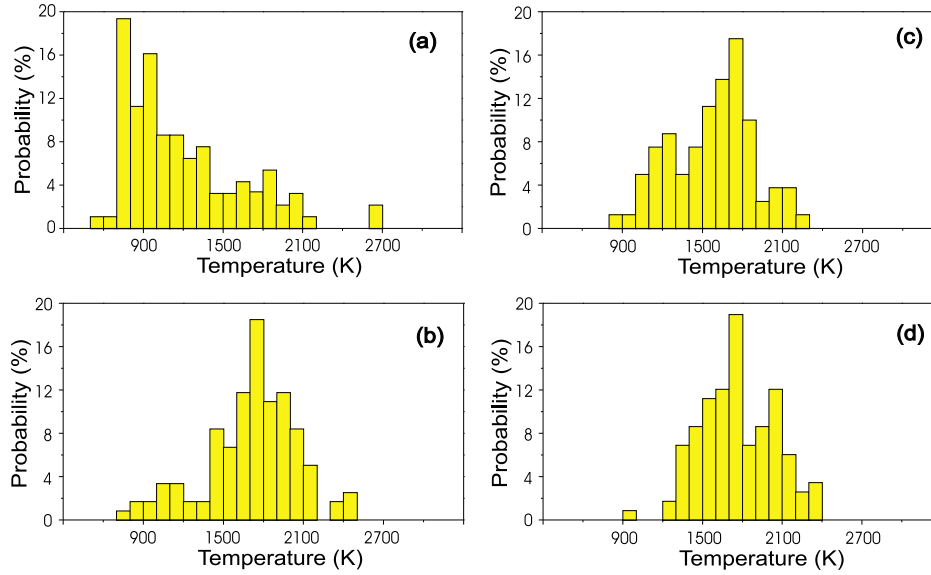


Figure 12: Probability density function for H_2 -temperatures. Operating conditions A, $p = 0.1$ Mpa. Radial location $y = 20$ mm (a) $x = 80$ mm, (b) $x = 180$ mm, (c) $x = 215$ mm, (d) $x = 250$ mm.

Further downstream, progressive H_2 diffusion occurs into the core of the flow due to intense mixing and the validation percentage increases. The mean temperature increases with distance from the injector and reaches 2800 K at $x=200$ mm and remains constant thereafter. Similar trends are also observed in the outer periphery of the flame where the temperature profiles measured at several radial locations behave in a similar fashion. Finally, whatever the location downstream of the injector, the H_2 radial temperature increases monotonically from the walls to the centerline indicating that some flow stratification persists to downstream sections.

For H_2O , the temperature and concentration profiles present some analogy with those usually observed in gaseous diffusion flames. In the initial sections the H_2O temperature on the combustor centerline is low and temperature increases in the radial direction and reaches a maximum in the flame region where fuel and oxygen diffuse and react. Profiles of H_2O mole fraction also feature similar shapes with a peak coinciding approximately with the peak of the temperature.

It is interesting to note that the mean radial temperature profiles deduced from H_2O CARS spectra differ from those determined from H_2 CARS. A maximum difference between temperatures of about 2000 K is obtained at $x=100$ mm. Beyond this axial location, the difference decreases progressively. One also finds that the difference in measured temperatures is extreme along the axis and vanishes close to the chamber walls.

The different distributions are due in part to a possible bias of temperature measurements and to the nature of the flow mixing processes occurring in this combustion. Concerning the H_2 measurements, the rejection of some distorted spectra in the data reduction may bias the mean temperature of H_2 towards higher values because of systematic detection of H_2 at elevated temperatures. Existence of these high temperatures probably derive from conditionally sampled data on H_2 mainly present in the outer region surrounding the flame. For H_2O , the cooler temperature in the central flow region could be attributable to thermal effects induced by the presence of the spray of liquid oxygen droplets. The H_2O molecules, initially produced at high temperature in the reactive zone, are transported as a relatively stable product into the core of the flow formed by a two-phase mixture of LOX ligaments, droplets and gaseous oxygen and water. During these processes, thermal transfer occurs between the two fluids leading to a decrease of the energy of the water vapor penetrating into the core flow. As a consequence, the H_2O temperature level will be cooler on the centerline than in the flame front. These

thermal processes control the combustion process in this region where they determine the rate of vaporization and the distribution of liquid and gaseous oxygen and the rate of combustion. The fact that detection of high H_2 temperatures and cooler H_2O temperatures occur is probably the result of the presence of large-scale turbulent mixing taking place around the LOX spray with the appearance of smaller packets of burning fuel separated by nonreacting regions of mixture of products of combustion and LOX. Outside the inner region, the large validation percentage of the measurements and the well-correlated temperatures for both species indicate a presence of a gaseous mixture of H_2 and H_2O in thermodynamic equilibrium. All these results confirm visual features of the processes responsible for the instantaneous flame shapes deduced from OH-LIF, O_2 -LIF (see Refs. 8 and 10) and for the time average flame structures derived from emission measurements in the same configuration^{9–11}. Measurements indicate that the mean flame can be considered initially as a thin, cylindrical surface which expands downstream into a thick “shell” surrounding the LOX spray formed after jet break-up. Further downstream, the mean flame becomes annular. The inner and outer diameters of the flame volume slowly decrease with axial distance as the oxygen convected in the central region is being consumed.

Further downstream ($x=400$ mm), the inner jet is fully atomized due to the dominance of the outer hydrogen jet. On the centerline, the measurement validation rate rises considerably, indicating that hydrogen starts to be entrained and mixed with reactant products within the inner jet flow. Complementary measurements devoted to probing O_2 with CARS at the exit of the combustor also show that combustion is still not complete at this location. A validation rate as high as 40% was obtained while detecting O_2 by CARS on the centerline of the combustor. All these results confirm that the observed decrease in validation rate of H_2 measurements near the axis is linked to a stratification of the flowfield near the injector, which progressively vanishes further downstream when mixing is achieved.

At higher pressure (i.e., $p > 0.1$ MPa), temperature and H_2O mole fraction were measured in sections located between 10 and 300 mm downstream from the injector. The combustor runs during 15 s, reducing the CARS data to 75 samples per measurement point. Figures 14 and 15 display the radial temperature profiles recorded respectively for the conditions $A-p = 1$ MPa and $A-p = 3$ MPa at several axial locations.

Similar trends are observed at a pressure of 1 MPa. The difference between H_2 and H_2O temperatures is still present. However, the length of the zone where there is a difference is reduced to 200 mm, compared to the one observed at 0.1 MPa. The mean temperature reaches 2500 K, with a standard deviation of 600 K related to intense turbulent fluctuations in the flow. Between $x= 100$ mm and $x=200$ mm and on centerline, the low validation percentage of measurements of H_2 indicates that the H_2 mole fraction is quite low in the core flow, confirming that LOX and gaseous oxygen and water dominate in that region. The difference between temperatures, smaller than the one measured at 0.1 MPa, indicates that atomization and vaporization of LOX is enhanced with pressure leading as expected to faster burning. This explanation is also in agreement with results observed at positions farther downstream: larger validation percentage of measurements and similar temperature distributions suggesting that droplets have disappeared and that the flow is more homogenous. Increasing the pressure to 3 MPa enhances these trends. Distributions of the mean temperature of H_2 and H_2O become similar from the location $x=50$ mm, indicating the presence of a homogeneous mixture at this position. The mean H_2O concentration profiles present flat shapes with peak concentration of about 25% indicating that the flame produces more H_2O which is in accordance with the lower mixture ratio level used at these pressure regimes. All these results lead to the conclusion that an increase in pressure enhances the atomization and vaporization of LOX, which in turn leads to a faster mixing of gaseous O_2 with the fuel and a reduction in flame length.

6.2 Transcritical tests on the Mascotte facility

Another question of importance is the applicability of CARS at pressures above the critical value representative of the conditions encountered in real liquid-fueled engines.

When LOX is injected at an initially subcritical temperature into an environment which exceeds the critical temperature and pressure of oxygen ($T_{crit}=154$ K and $p_{crit}=5.05$ MPa), LOX undergoes a transition to a supercritical state as it is heated and burned, leading to different behaviors than the ones occurring under low pressure subcritical conditions. This is well illustrated in previous studies by Juniper et al.¹⁴ or by Mayer et al.¹⁷ and in the first sections of the present article.

The data reveal differences in behavior, leading to different types of fluid disintegration and flame structures under subcritical and supercritical conditions as sketched in figure 6

Measurements with H_2 CARS have been carried out at a chamber pressure of 6.5 MPa which is well above the O_2 critical pressure. Regarding the quality of the spectra and assuming that the collisional linewidth model is

still valid in this pressure range, the accuracy of the temperature measurements can be assumed to be similar to that obtained under subcritical conditions.

Figure 16 presents typical examples of PDF's deduced from a series of 300 instantaneous measurements acquired during two successive runs and taken at a radial location of 8 mm from the combustor centerline and at axial locations of 15 mm, 50 mm and 150 mm downstream of the injection plane. These results provide PDF's from the recirculation zone to the reacting shear layer. The validation rate of the CARS measurements exceeds 60 % for all the probed locations. These large validation rates support the illustration of the present capabilities of CARS in such conditions. This finding is also confirmed by the fact that the PDF's are relatively smooth whatever the positions explored. At $x=15$ mm, a narrow and symmetric temperature distribution with a mean temperature of 700 K is observed indicating that hot gases formed downstream recirculate in this region (fig. 16a). The bimodal nature of the PDF confirms the presence of large-scale coherent structures within the reacting shear layer (fig. 16b). These structures form as folds around the flame edge, and then grow in size downstream, entraining reactants and products and thickening the reacting shear layer as shown in figure 16c.

6.3 Transcritical tests on the P8 facility

Measurements at four and five radial locations were carried out in two axial sections located at 50 mm and 80 mm from the injection plane. Strong beam steering effects were observed at both cross-sections. Due to the low energy of the dye laser in the spectral region of water, only a few CARS water spectra were recorded. Data evaluation from water was not possible in this case.

Large density gradients exist between the liquid oxygen core and gaseous hydrogen annulus. The gradients cause beam defocusing with subsequent loss of efficiency of signal generation. Unsteady flame and turbulent flow behavior contribute to the beam steering problem which results in large disparities in shot-to-shot measurements. A very weak signal or a complete loss of signal was frequent, particularly in the high temperature regions.

Attempts were made to probe with cold H_2 injection conditions as low as 65K. However repeated attempts at various radial locations led to a total loss of signal. This signal depletion can be attributed to the excessive density gradients experienced under such hostile conditions. The density of H_2 increases by 2.5 times at such low temperatures, adding to the difficulties with signal loss. With H_2 injection temperatures descending below 80K, no signal could be measured due to refraction effects. These effects are also present near the combustor walls far away from the injected propellant jet.

To ensure accurate temperature estimation from the CARS spectra, it was necessary to use a fitting approach. After background subtraction, the CARS spectra were normalized to the appropriate spectral correction curve and then processed. A special software is used to determine the best fit to theoretically calculated spectra and thus obtain gas temperatures. H_2 line broadening coefficients of Q-branch for H_2 - H_2O mixtures were calculated using various data sets³³⁻³⁵ and applied to model the theoretical spectra. Densities of 15-30 amagat were typical for the experimental conditions investigated. The collisions can still be considered as binary and hence the total linewidth can be calculated as a sum of hydrogen-broadband and water-broadband contributions when appropriate hydrogen and water contents are taken into account.

Temperature histograms obtained at 50mm and 80mm from the injection plane at a radial position of 4mm are displayed in figure 17. The data was evaluated from separate 200-shot series obtained at the different axial and radial positions within the chamber. Bi-modal structures can be observed in the histograms at measurement points belonging to the 80mm downstream section (see figure 17). This bimodal distribution is due to combined effects of turbulent mixing of the stream of H_2 , and flame flapping around the core flow³⁶.

Figure 18 represents the temperature profiles for both sections within the chamber. For several measurement points two temperatures exist in accordance with the previously mentioned bimodal structures observed in the temperature histograms. A majority of the measured temperatures were below 1500K at the two axial sections investigated.

At the 80 mm downstream location, the effects of a flapping LOX core has a significant impact on the CARS results. Strong bi-modal temperature distributions are observed at 2, 4, 6, and 8 mm radial positions. This can be attributed to fluctuations of the LOX jet, shear layer and surrounding reaction zone. The low values in the histograms represent temperatures of slightly heated hydrogen stream. The higher temperatures measured are representative of heat release from the combustion zone ($T > 1000K$).

The 2mm radial point is close to the reactive shear layer. The temperature histogram at this point exhibits a broad temperature distribution between 200K-2000K. This suggests that the LOX core and shear layer are continuously occupying and escaping the probe volume. The outermost point (10 mm) is the only position at 80 mm downstream to exhibit a uni-modal temperature distribution heavily biased toward the lower temperatures.

A Gaussian fit of the data indicates a temperature of 620K. The 10 mm location escapes the shear layer and the surrounding high temperature environment and is mainly influenced by the H₂ stream.

The 50 mm axial position shows a different result. At all points probed, the tendency is toward lower temperatures. At the 50mm location, the temperature histograms exhibit a unimodal temperature distribution. The weighted average temperatures range between 400 and 500K. This indicates a strong influence of the hydrogen stream and a reduced combustion zone closer to the injector.

Data gathered do not indicate temperatures in the theoretical range of stoichiometric conditions. The reactive shear layer formed between the propellants is very thin and is at each moment surrounded by gases at much lower temperatures. The maximum temperature observed in this study was approximately 2000K. It is also possible that laser beam deflections reduce the validation rate considerably and bias the measurements towards lower values.

7 Conclusions and perspectives

This research effort has focused on the problem of cryogenic combustion in the high pressure range. Data described in this article originates from joint efforts carried out by teams from three laboratories using the Mascotte and P8 facilities. Experiments were carried out over a wide pressure range and at hydrogen temperatures between 100 K and 300 K. In these tests, the pressure ranges from 0.1 to 7 MPa and the gas to liquid momentum flux ratio from 4 to 15. Fundamental analyses based on optical diagnostics and the use of two synchronized ICCD cameras has produced high quality images which show the LOx jet and the flame simultaneously and reveal the main features of the flame structure.

In the low pressure range, below the critical pressure of oxygen (5.05 MPa) the flame burns in an external group combustion mode and has the shape of a shell surrounding the LOx jet and LOx droplet cloud. This is now well documented in previous studies. Detailed examination of the experimental results combined with simplified modeling indicates a change in behaviour when the pressure exceeds the critical pressure of oxygen. The experimental and theoretical results indicate that the rate of combustion is vaporization limited when the pressure is below the critical pressure and is mixing limited when the pressure is above the critical pressure. This suggests that, rather than improving atomization, one should attempt to increase mixing inside combustion chambers designed to operate above the critical pressure of the liquid reactant.

Experimental results also show that the flame remains attached to the lip of the oxygen injector over the complete range of pressure, inlet velocity and hydrogen temperatures studied. The stabilization mechanism has been elucidated by combining experimental information and detailed calculations.

Temperature measurements have been carried out using CARS on hydrogen and water. A complete set of profiles has been gathered in the Mascotte facility and some data also originates from the P8 test rig. In the low pressure range, (ie below the critical pressure of oxygen) the data indicate that the temperatures measured by CARS spectroscopy on H₂ and H₂O differ to a great extent. The main differences are found in the initial region and they can be interpreted by considering the flame structure determined from laser induced fluorescence and emission imaging. It is known from these studies that the flame separates a core region formed by a two-phase stream of liquid oxygen inclusions, ligaments and droplets mixed with gaseous oxygen and water vapor formed in the flame and an outer region mainly composed of gaseous hydrogen and water vapor. There is little hydrogen in the core and when some is detected this species has come from rare hot pockets of gases which penetrate the two-phase stream. The temperature detected under such circumstances will be relatively high because the gases come from the hot stream surrounding the two-phase core. Water vapor trapped in the core region is in contact with cool gases and its temperature will be low. In the core region the laser shots which yield a temperature measurement from H₂ differ from those which yield a measurement from H₂O. The measurements are conditioned by the presence of hydrogen and water molecules in the probe volume. The difference in measured temperatures vanishes in the downstream sections as mixing proceeds. This difference in temperatures also diminishes as the chamber pressure is increased because the rate of vaporization and burning is augmented and the length of the central core region is reduced. Measurements also indicate that a certain stratification in temperature persists in the downstream sections with a temperature maximum on the chamber axis. Histograms measured in the transcritical range of pressures feature a bimodal distribution in the injector near field indicating the presence of regions of low temperature dense gases and regions of high temperature lighter pockets. Further downstream the temperature histogram become monomodal and the mean temperature reaches higher values.

Research which has mainly concerned on stable cryogenic flames formed by liquid oxygen and gaseous hydrogen

now focuses on LOx/methane flames and on combustion dynamics and high frequency instabilities, a central problem in rocket propulsion. A program has been established by a French-German consortium formed by CNES, DLR, Snecma, Astrium, Onera and CNRS laboratories and a combination of experimental and computational investigations is underway.

Acknowledgments

We wish to thank CNES, Snecma, CNRS and DLR for their continuous and generous support of our work in rocket propulsion. The assistance of the “Mascotte” and P8 teams are gratefully acknowledged.

References

- ¹**Barrère, M., Jaumotte, A., Fraeijs de Veubeke, B. and Vandenkerckhove, J.,** *Rocket propulsion* Elsevier, Amsterdam, 1960.
- ²**Burick, R. J.,** “Atomization and mixing characteristics of gas/liquid coaxial injector elements,” *Journal of Spacecraft*, Vol. 9 , 1972, pp. 326-331.
- ³**Burick, R. J.,** “Optimum design of space storable gas/liquid coaxial injectors,” *Journal of Spacecraft*, Vol. 10 , 1973, pp. 663-670.
- ⁴**Gill, G. S.,** “A qualitative technique for concentric tube element optimization, utilizing the factor (dynamic head ratio-1),” AIAA Paper 78-76, 1978.
- ⁵**Haarje, D. T. and Reardon, F. M.,** “Liquid propellant rocket combustion instability,” NASA Report SP 194, 1972.
- ⁶**Herding, G., Snyder, R., Souffaire, P., Rolon, C. and Candel, S.,** “Emission and laser induced fluorescence imaging of cryogenic propellant combustion,” *Proceedings of the Conference on Propulsive Flows in Space Transportation Systems* (Bordeaux, France), CNES, 1995. pp. 1-14.
- ⁷**Herding, G., Snyder, R., Scouffaire, P., Rolon, C. and Candel, S.,** “Flame stabilization in cryogenic propellant combustion,” *Proceedings of the Combustion Institute*, Vol. 26, 1996, pp. 2041-2047.
- ⁸**Snyder, R., Herding, G., Rolon, C. and Candel, S.,** “Analysis of flame patterns in cryogenic propellant combustion,” *Combustion Science and Technology*, Vol. 124, Nos. 1-6 , 1997, pp. 331-373.
- ⁹**Herding, G., Snyder, R., Rolon, C. and Candel, S.,** “Investigation of cryogenic propellant flames using computerized tomography of OH emission images,” *Journal of Propulsion and Power*, Vol. 13, No. 2 , 1998, pp. 146-151.
- ¹⁰**Candel, S., Herding, G., Snyder, R., Scouffaire, P., Rolon, C., Vingert, L., Habiballah, M., Grisch, F., Pealat, M., Bouchardy, P., Stepowsky, D., Cessou, A. and Colin, P.,** “Experimental investigation of shear coaxial cryogenic jet flames,” *Journal of Propulsion and Power*, Vol. 14, No. 5 , 1998, pp. 826-834.
- ¹¹**Kendrick, D., Herding, G., Scouffaire, P., Rolon, C. and Candel, S.,** “Effet du retrait sur la stabilisation des flammes cryotechniques,” *Comptes Rendus de l’Académie des Sciences, Serie II b*, Vol. 326 , 1998, pp. 111-116.
- ¹²**Kendrick, D., Herding, G., Scouffaire, P., Rolon, C. and Candel, S.,** “Effects of a recess on cryogenic flame stabilization,” *Combustion and Flame*, Vol. 118 , 1999, pp. 327-339.
- ¹³**Tripathi, A., Juniper, M., Scouffaire, P., Rolon, C., Durox, D. and Candel, S.,** “ LOx tube recess in cryogenic flames investigated using OH and H2O emission,” AIAA Paper 99-2490, 1999.

- ¹⁴**Juniper, M., Tripathi, A., Scouffaire, P., Rolon, C. and Candel, S.**, "Structure of cryogenic flames at elevated pressures," *Proceedings of the Combustion Institute*, Vol. 28 , 2000, pp. 1103-1109.
- ¹⁵**Juniper, M., Tripathi, A., Scouffaire, P., Rolon, C. and Candel, S.**, "The structure of cryogenic flames at subcritical and supercritical pressures," *Proceedings of the Symposium "Combustion dans les moteurs fusées"*, (Toulouse), Cepadues, 2001. pp. 348-357.
- ¹⁶**Juniper, M., Tripathi, A., Leroux, B., Lacas, F. and Candel, S.**, "Stabilization of cryogenic flames and effect of recess," *Proceedings of the Symposium "Combustion dans les moteurs fusées"* (Toulouse), Cepadues, 2001. pp. 222-231.
- ¹⁷**Mayer, W. and Tamura, H.**, "Propellant injection in a liquid rocket oxygen/gaseous hydrogen rocket engine," *Journal of Propulsion and Power*, Vol. 12, No. 6 , 1996, pp. 1137-1147.
- ¹⁸**Mayer, W., Schik, A., Schweitzer, C. and Schaffler, M.**, "Injection and mixing processes in high pressure LOX/GH₂ rocket combustors," AIAA Paper 96-2620, 1996.
- ¹⁹**Mayer, W., Shick, A., Vielle, B., Chauveau, C., Gokalp, I., Talley, D. and Woodward, R.**, "Atomization and breakup of cryogenic propellants under high-pressure subcritical and supercritical conditions," *Journal of Propulsion and Power*, Vol. 14, No. 5, 1998, pp. 835-842.
- ²⁰**Cessou, A., Colin, P. and Stepowski, D.**, " Statistical investigation of the turbulent flame geometrical structures in a liquid oxygen / gaseous hydrogen shear coaxial jet," *Proceedings of the Combustion Institute*, Vol. 27, 1998, pp. 1039-1046.
- ²¹**Juniper, M. and Candel, S.**, "The stability of ducted compound flows and consequences for the geometry of coaxial injectors," *Journal of Fluid Mechanics*, Vol. 482 , 2003, pp. 257-269.
- ²²**Juniper, M. and Candel, S.**, "Edge diffusion flame stabilization behind a step over a liquid reactant," *Journal of Propulsion and Power*, Vol. 19 (3) , 2003, pp. 332-341.
- ²³**Juniper, M., Darabiha, N. and Candel, S.**, "The extinction limits of a hydrogen counterflow diffusion flame above liquid oxygen," *Combustion and Flame*, Vol. 135 (2), 2003. pp. 87-96.
- ²⁴**Hopfinger, E. and Lasheras, J. C.**, " Breakup of a water jet in high velocity co-flowing air", in *Proceedings of the 6th International Conference on Liquid Atomization* edited by A. J. Yule and C. Dumouchel, Begell House, New York, 1994, pp. 110-117.
- ²⁵**Villiermaux, E.**, "Mixing and spray formation in coaxial jets," *Journal of Propulsion and Power*, Vol. 14, No. 5 , 1998, pp. 807-817.
- ²⁶**Lasheras, J. and Hopfinger, E.**, "Liquid jet instability and atomisation in a coaxial gas stream," *Annual Reviews of Fluid Mechanics*, Vol. 32 , 2000, pp. 275.
- ²⁷**Strakey, P. A., Talley, D. G., Tseng, L. K. and Miner, K. I.** , "Effects of liquid-oxygen post biasing on SSME injector wall compatibility," *Journal of Propulsion and Power*, Vol. 18, No. 2, 2002, pp. 240-246.
- ²⁸**Brummund, U., Cessou, A., Oswald, M., Vogel, A., Grisch, F., Bouchardy, P., Pealat, M., Vingert, L., Habiballah, M., Snyder, R., Herding, G., Scouffaire, P., Rolon, C. and Candel, S.**, "Laser diagnostics for cryogenic propellant combustion studies," *Proceedings of the 2nd International Symposium on Liquid Rocket Propulsion* (Chatillon, France), 1995. pp. (19)1-(19)22.
- ²⁹**Yeralan, S., Pal, S. and Santoro, R. J.** "Experimental study of major species and temperature profiles of liquid oxygen/gaseous hydrogen rocket combustion," *Journal of Propulsion and Power*, Vol. 17, No. 4, 2001, pp. 788-793.

- ³⁰**Druet, S. A. J. and Taran, J. P.**, "CARS spectroscopy," *Progress in Quantum Electronics*, Vol. 7 , pp. 1-72.
- ³¹**Berger, J. P.**, "Etudes des mécanismes de relaxation rovibrationnelle pour les mélanges H₂-gaz rares H₂-N₂ et H₂-H₂O par spectroscopie Raman stimulé en vue du diagnostic de température dans un moteur fusée" Doctoral thesis, Université de Bourgogne, Dijon, France, 1994.
- ³²**Michaut, X., Berger, J. P., Saint-Loup, R., Chaussard, F. and Berger, H.**, "Détermination des paramètres physiques indispensables pour le diagnostic optique de la température," In *Proceedings of the Symposium "Combustion dans les moteurs fusées,"* Cepadues, Toulouse, 2001.
- ³³**Chaussard, F., Michaut, X., Saint-Loup, R., Berger, H., Joubert, P., Lance, B., Bonamy, J. and Robert, D.**, "Collisional effects on spectral line shape from Doppler to collisional regime : A rigorous test of a unified model," *J. Chem. Phys.*, Vol. 112 , 2000, pp. 158-166
- ³⁴**Grisch, F. and Péalat, M.**, "CARS studies of H₂O Motional narrowing in high-pressure and high-temperature H₂O-N₂ mixtures," *J. Raman Spectroscopy*, Vol. 25 , 1994, pp. 145-151.
- ³⁵**Clauss, W., Klimenko, D. N., Oswald, M., Vereschagin, K. A., Smirnov, V. V., Stelmakh, O. M. and Fabelinsky, V. I.**, "CARS investigation of hydrogen Q-branch linewidths at high temperatures in a high-pressure H₂-O₂ pulsed burner," *J. Raman Spectroscopy*, Vol. 33 , 2002, pp. 906-911.
- ³⁶**Smith, J., Klimenko, D. N., Clauss, W. and Mayer, W.**, "Supercritical LOX/Hydrogen Rocket Combustion Investigations using Optical Diagnostics," AIAA Paper 2002-4033, 2002.

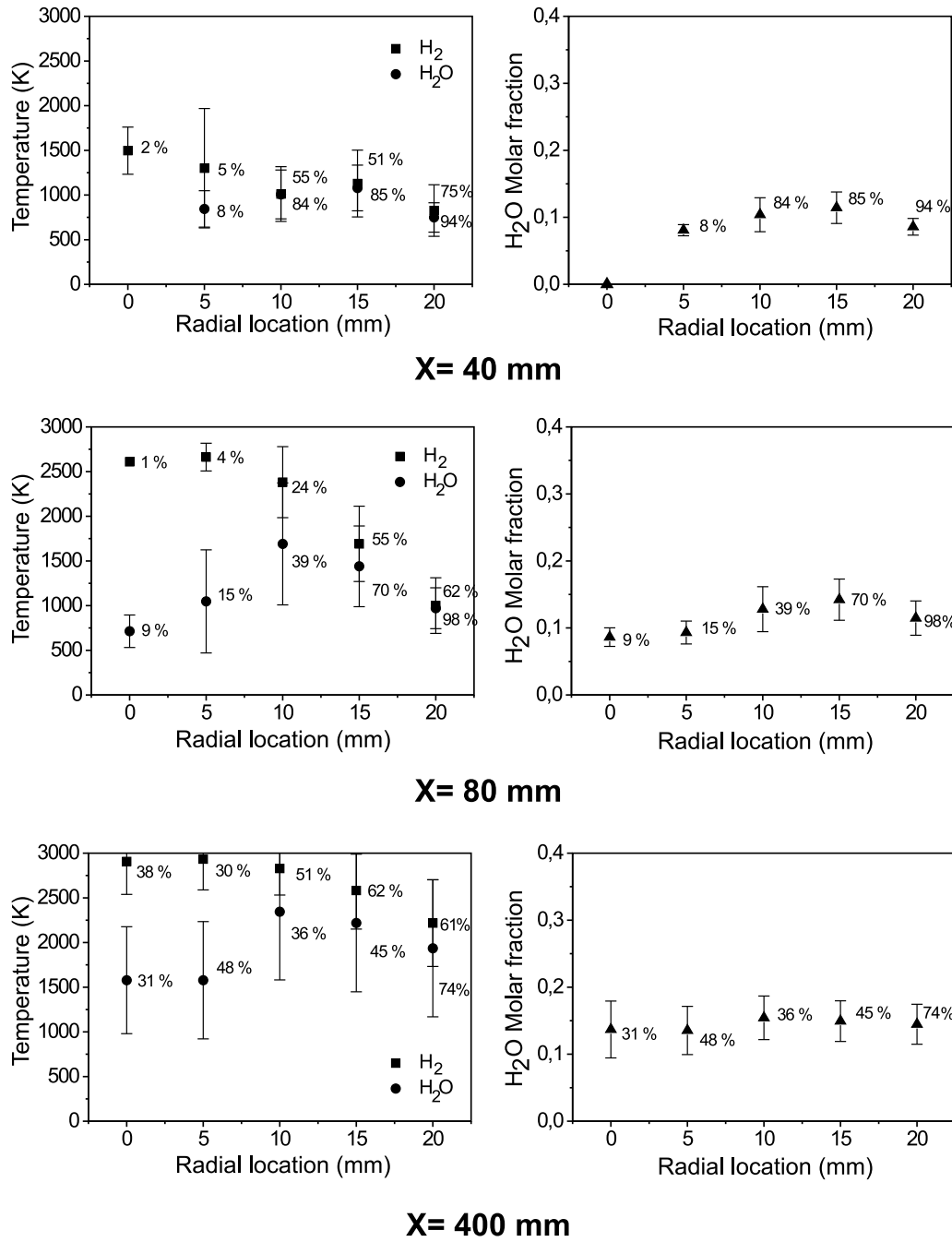


Figure 13: Mean Temperatures of Hydrogen and Water at different radial and axial positions. Conditions A, $p = 0.1$ MPa.

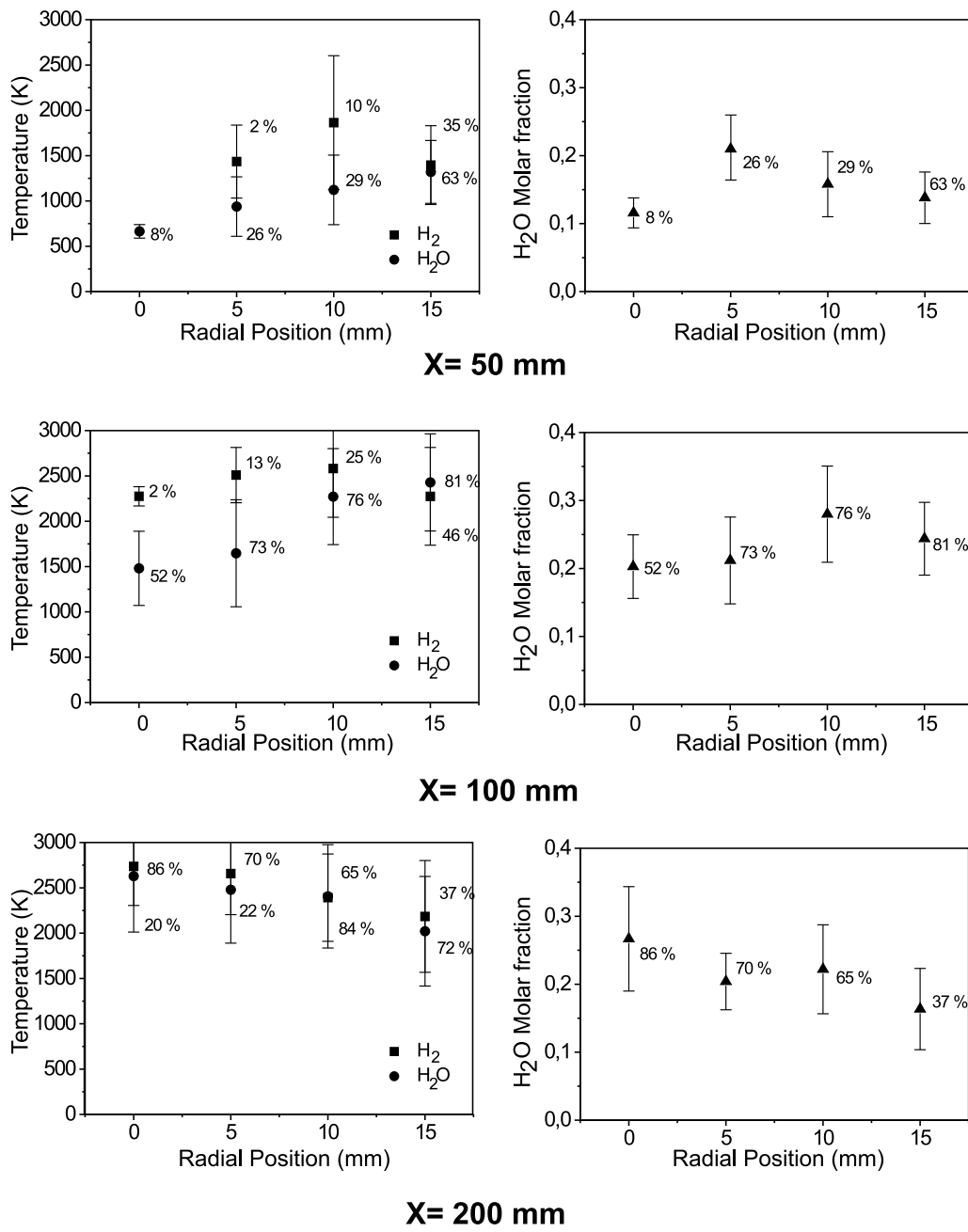


Figure 14: Mean Temperatures of Hydrogen and Water at different radial and axial positions. Operating conditions A. $p = 1$ MPa.

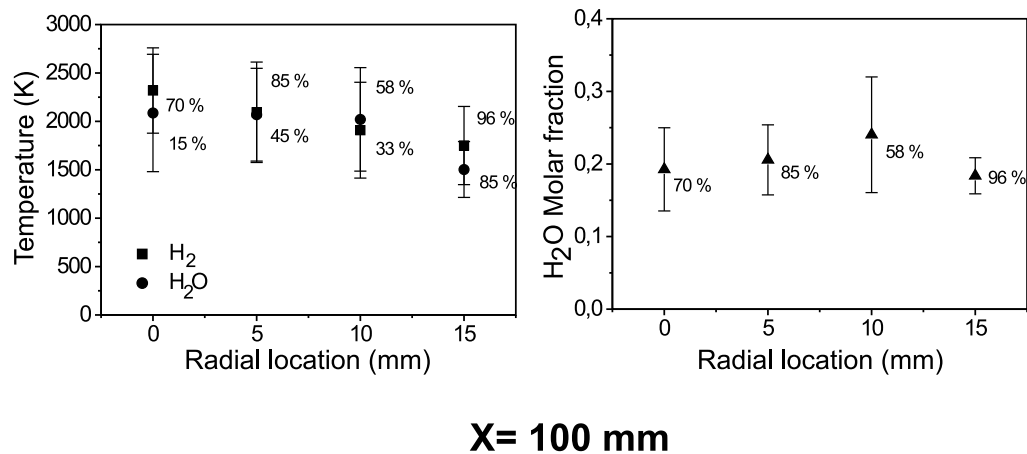
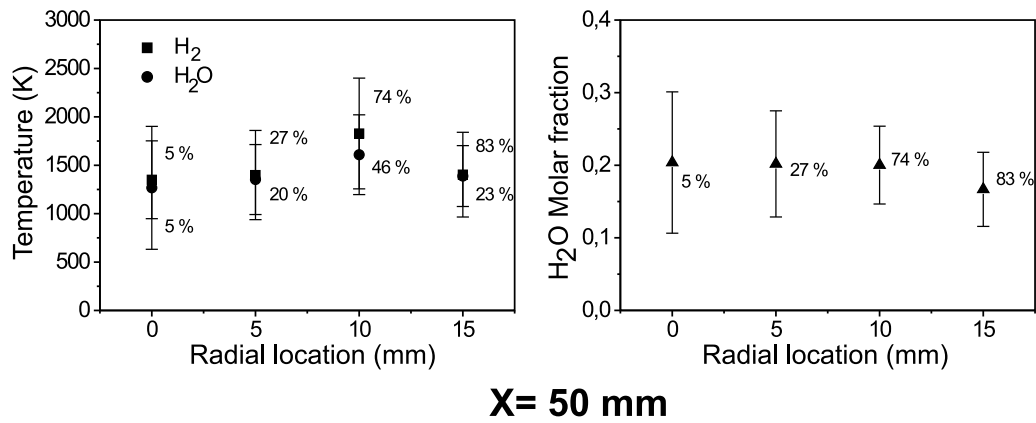


Figure 15: Mean Temperatures of Hydrogen and Water at different radial and axial positions. Operating conditions A. $p = 3$ MPa.

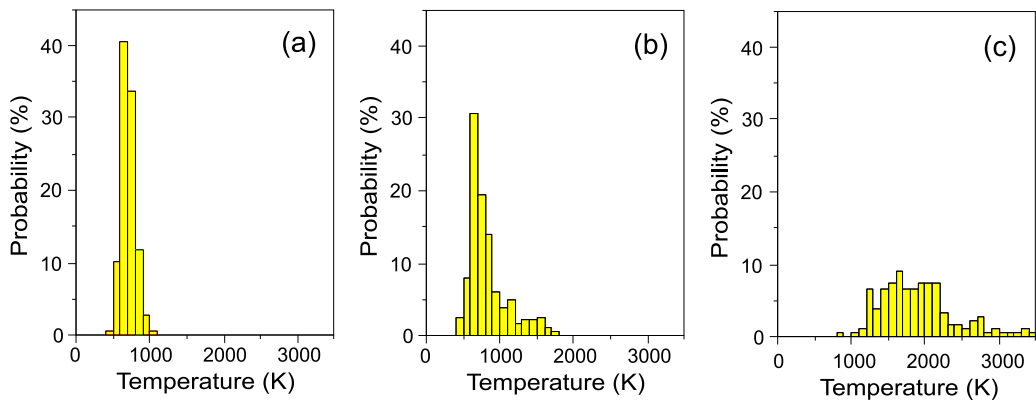


Figure 16: Probability density function for H₂-temperatures at 6.5 MPa. (a) $x = 15$ mm, (b) $x = 50$ mm, (c) $x = 150$ mm. Radial distance $y = 8$ mm.

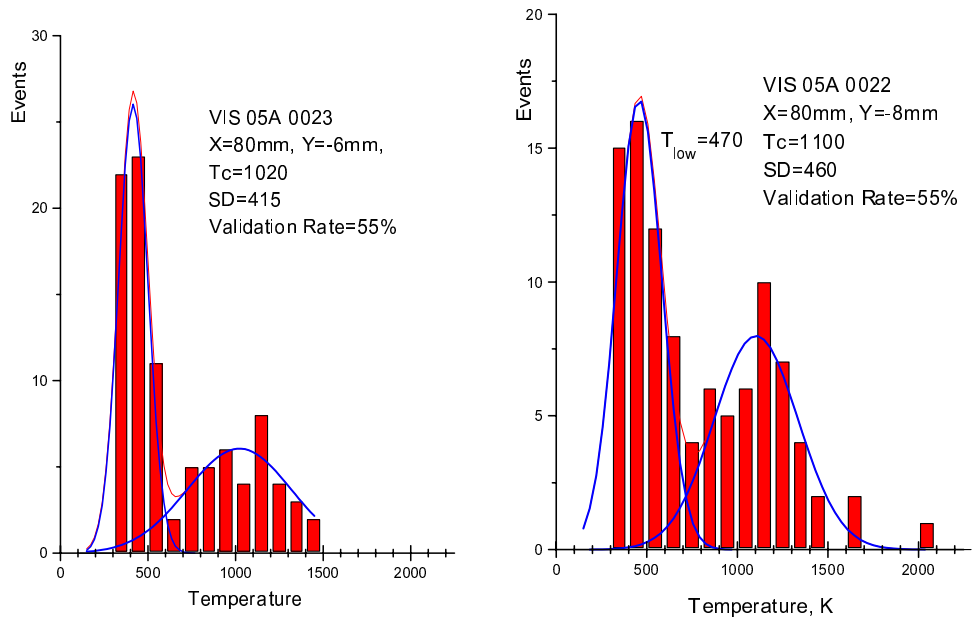


Figure 17: Probability density function for H₂-temperatures at 6 MPa

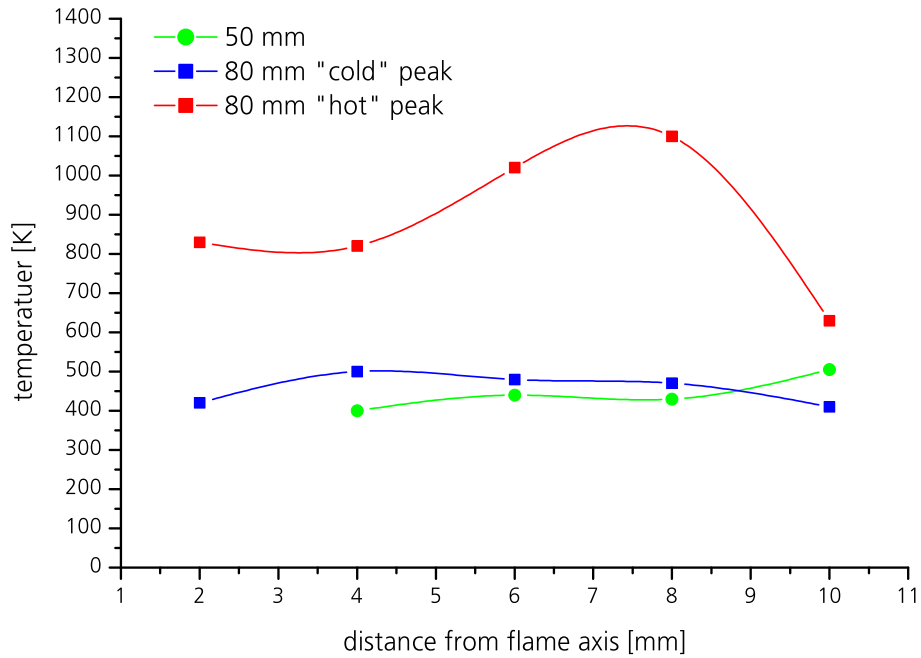


Figure 18: Mean temperature profiles at 6 MPa.



Understanding Injection Into High Pressure Supercritical Environments

***B. Chehroudi and D. Talley**

**Air Force Research Laboratory (AFRL), Propulsion Directorate,
United States**

***Engineering Research Consultants**

and

**W. Mayer, R. Branam, J.J. Smith, A. Schik, and M. Oswald
DLR Lampoldshausen, Institute of Space Propulsion, Germany**



Understanding Injection Into High Pressure Supercritical Environments



Motivation

- Typical liquid rocket engine pressures exceed the critical pressure of the injected propellants.
- Vanishing surface tension, vanishing enthalpy of vaporization, and other effects differ from conventional spray combustion assumptions.
- What are the governing mechanisms?

Objectives of this paper

- Consolidate and compare the findings of two independent laboratories related to the injection of cryogenic liquids into high pressure supercritical environments.

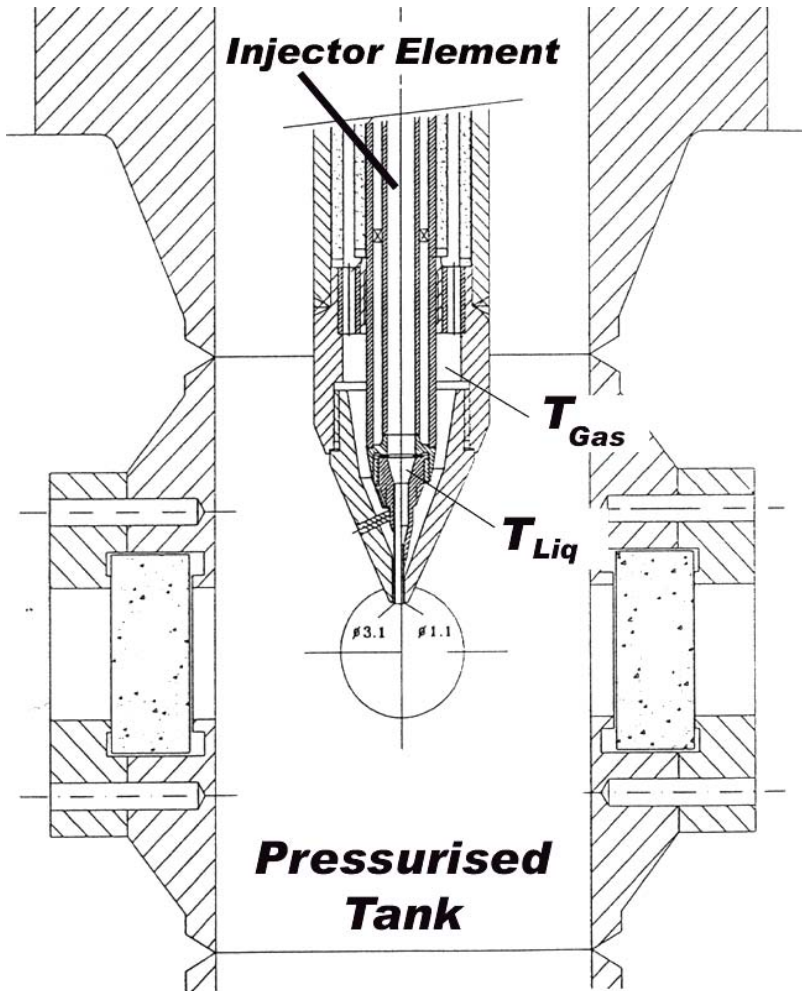


Paper outline



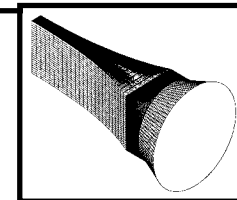
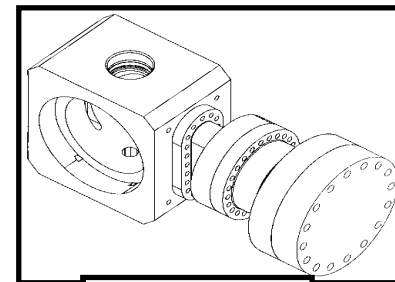
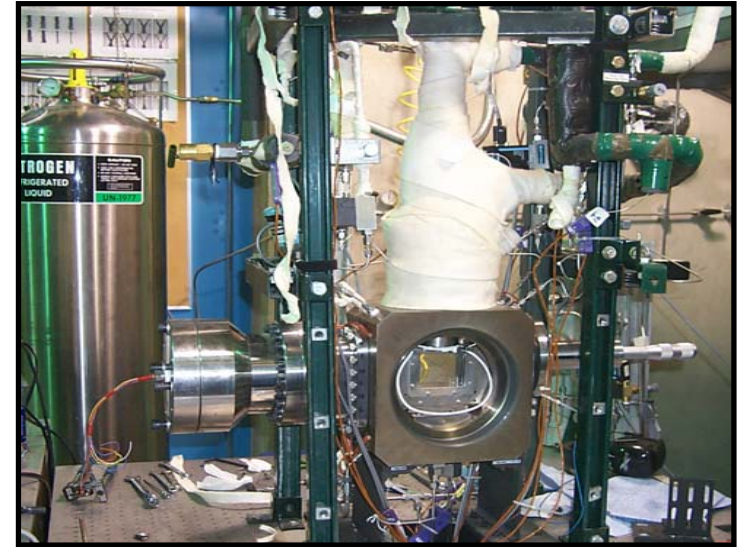
- Introduction
- Cold flow studies
 - Single jets
 - Shadowgraphy, the jet core region, jet growth rate, fractal analysis, Raman measurements, length scale results, interaction with external acoustic field, phenomenological model of the jet growth rate
 - Coaxial jets
 - Shadowgraphy, the core region, length scale analysis, Raman measurements, interaction with external acoustic field
- Combustion studies
 - Shadowgraphy, quantitative studies, OH fluorescence, CARS thermometry
- Summary and conclusions

DLR cryogenic cold flow facility

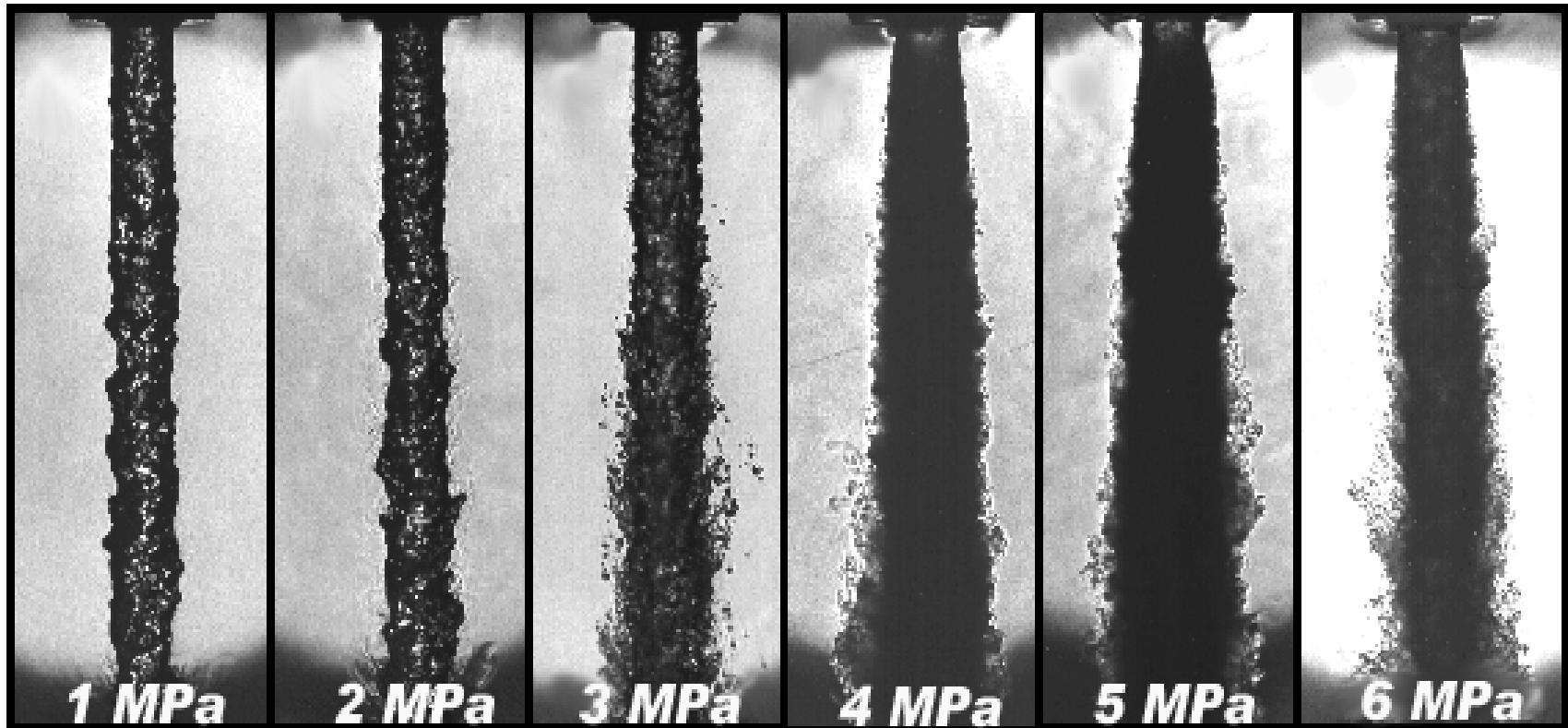


- Provide fundamental non-reacting information
- Optical access
- Single & binary systems
- Various injectants:
 - LN₂, GN₂
 - Helium
 - Ethanol
 - Hydrogen
- Adjustable injector dimensions
- Sub-, trans- & supercritical conditions (6 MPa)
- Accurate pressure, mass flow and temperature data
- Injector (cold flow): 1.9 mm dia. (L/D of 11.6) and 2.2 mm dia. (L/D of 40).

- Windowed pressure vessel operating at supercritical pressures (13 MPa).
- Cryogenic fluid capability (LOX, LN2)
- Capability to produce supercritical droplets and jets.
- Shadowgraph, Schlieren, and Raman visualization of concentration fields.
- Capability to drive flows with an acoustic driver
- $D = 0.2 - 0.5 \text{ mm}$, $L/D = 100 - 200$.



DLR results, N₂ into N₂



Pr = 0.3

Pr = 0.59

Pr = 0.85

Pr = 1.18

Pr = 1.47

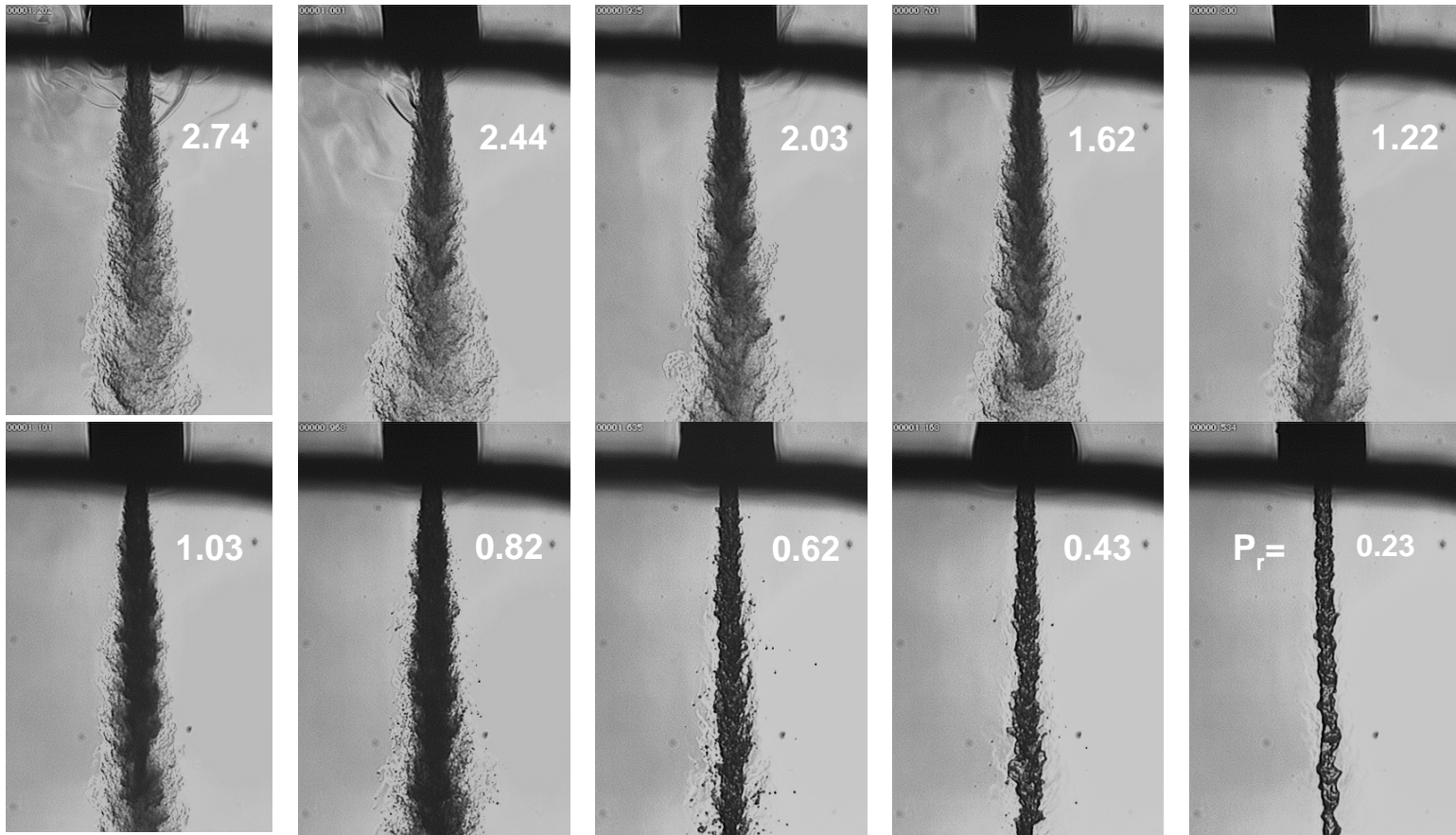
Pr = 1.77

LN₂ jets into ambient GN₂ at subcritical & supercritical conditions

LN₂ temperature: 100K, GN₂ temperature: 300K

AFRL results, N₂ into N₂

Back-illuminated images. Chamber is at a fixed supercritical temperature of 300 K but varying sub- to supercritical pressures ($P_{\text{critical}} = 3.39$ MPa). $Re = 25,000$ to $75,000$. Injection velocity: 10-15 m/s. Froud number = 40,000 to 110,000. Injectant temperature = 99 to 120 K.

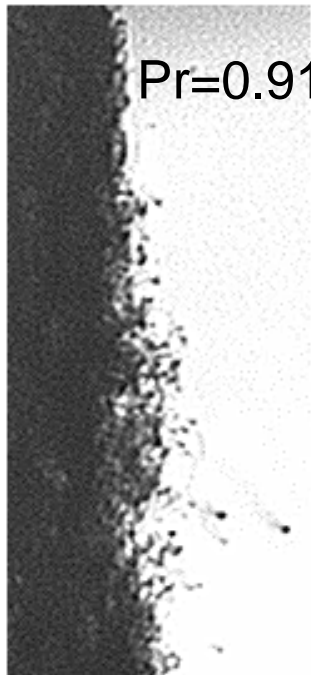




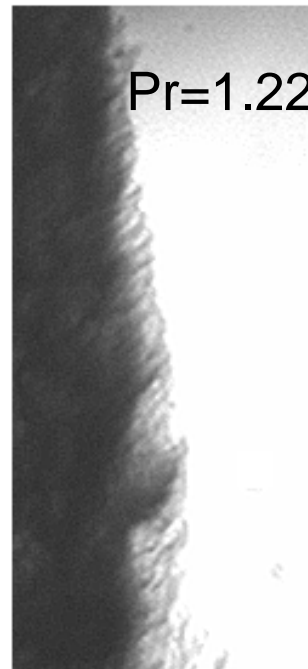
Mixing Layer Structure - N₂ into N₂ (AFRL)



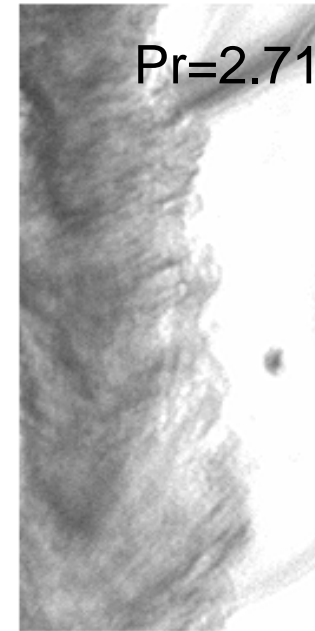
$$P_{cr} = 3.39 \text{ MPa}, T_{cr} = 126 \text{ K}, T_{inj} = 128 \text{ K}, T_{amb} = 300 \text{ K}$$



**Low Pres.
Subcritical**
Droplets



**Mod. Pres.
Supercritical**
Transition

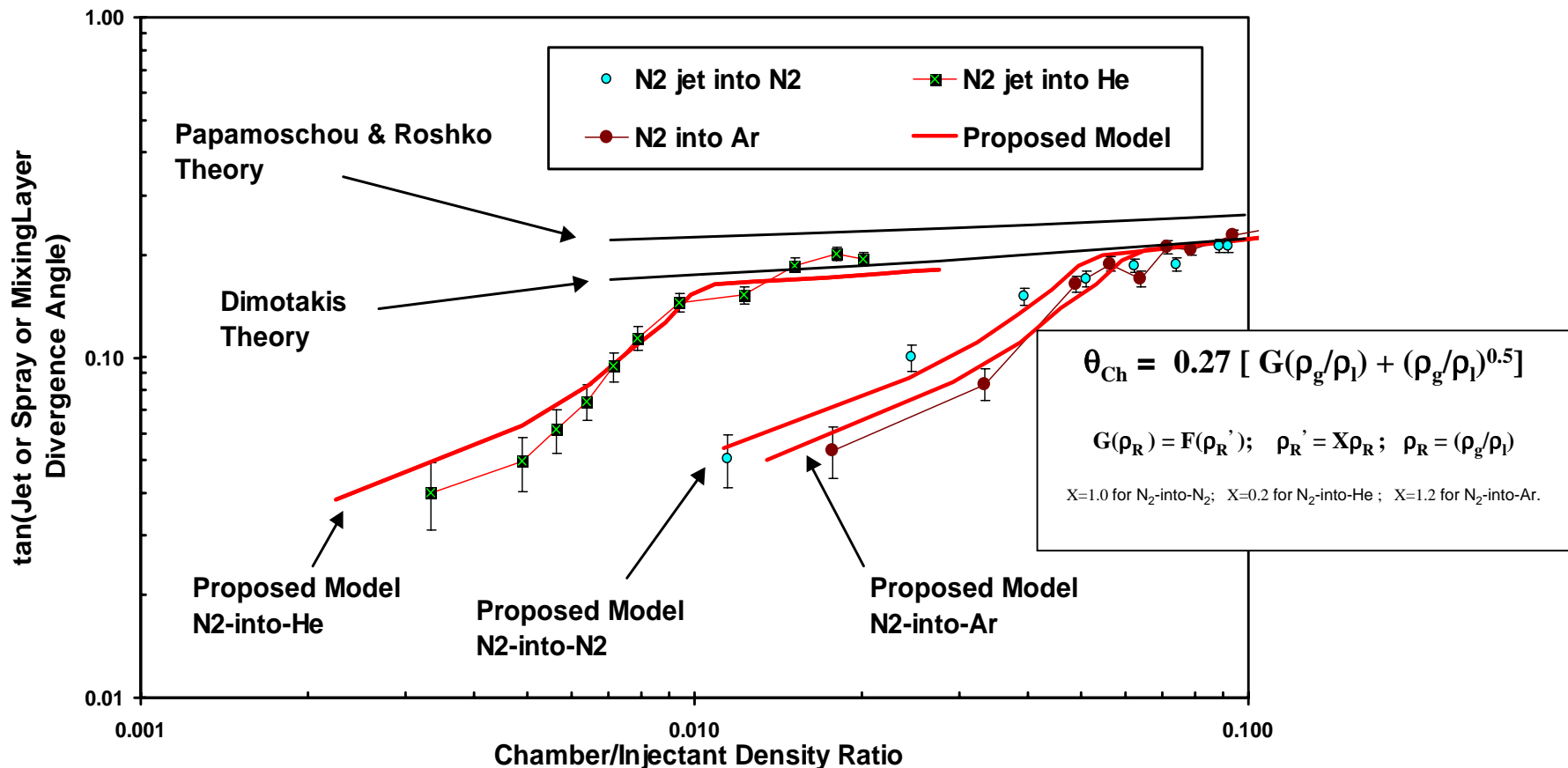


**High Pres.
Supercritical**
Gas layers

Comparing bulge separation times with vaporization times leads to a simple empirical model

Jet spreading angles

- Measurements from shadowgraphs indicate transition between spray-like and gas-like behavior.
 - Much more data exists than is shown here; sample is representative of both laboratories.

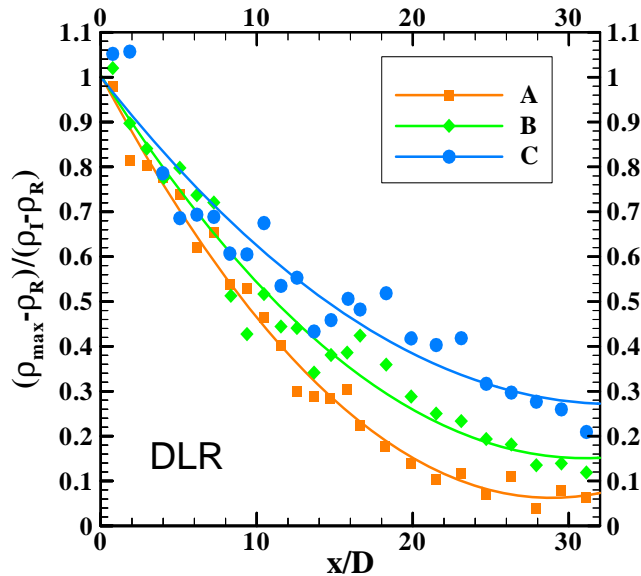


- AFRL analyzed the fractal dimensions of the jets.
 - The fractal dimension of supercritical jets is similar to that of gas jets.
 - The fractal dimension of subcritical jets is similar to that of sprays.
- DLR performed two-point pixel correlations to measure turbulent axial and radial length scales.
 - Measurements corresponded with numerically determined Taylor length scales.

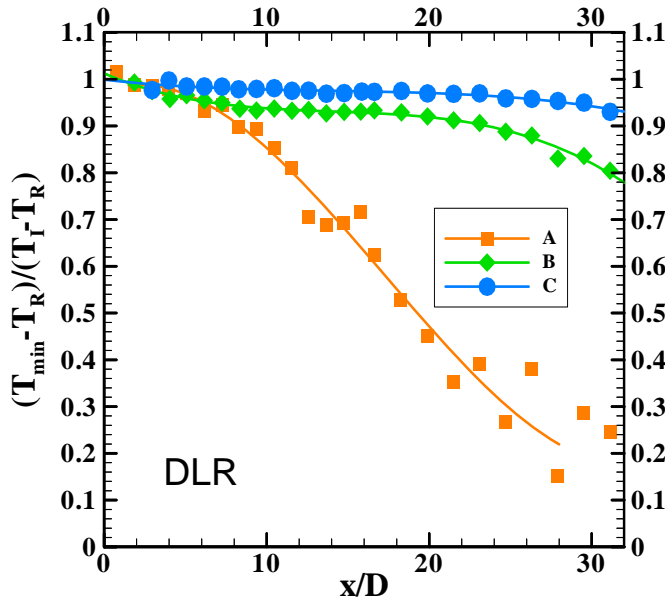




Raman measurements

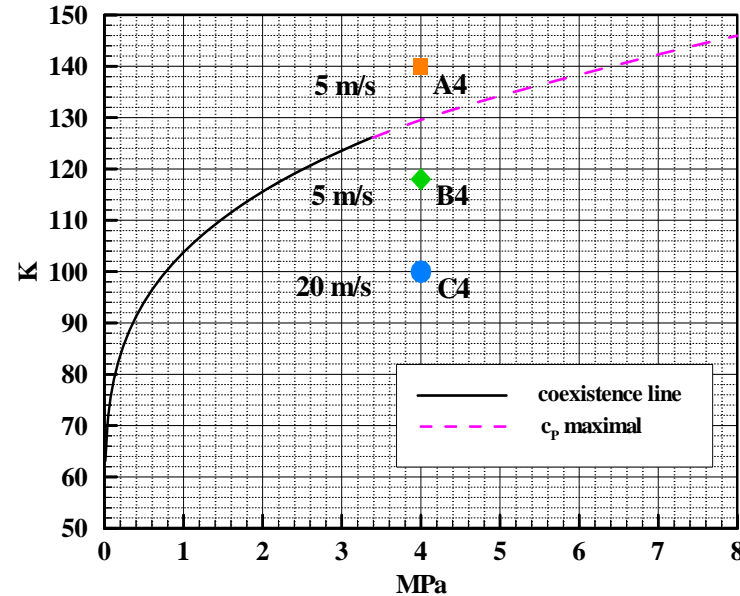


Variation of centerline density

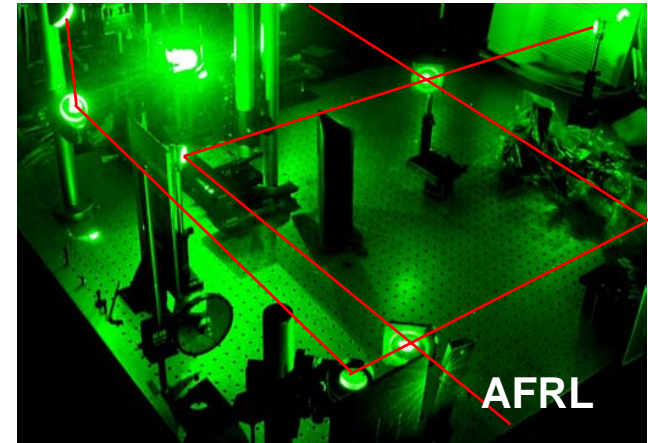
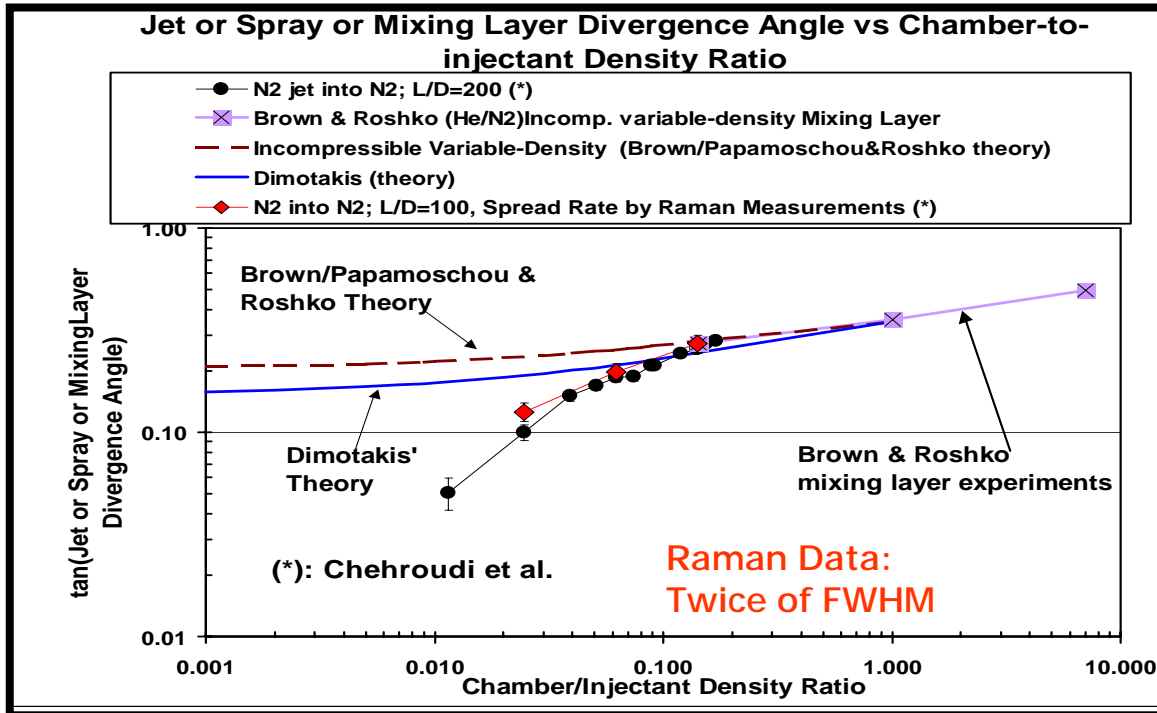


Variation of centerline temperature

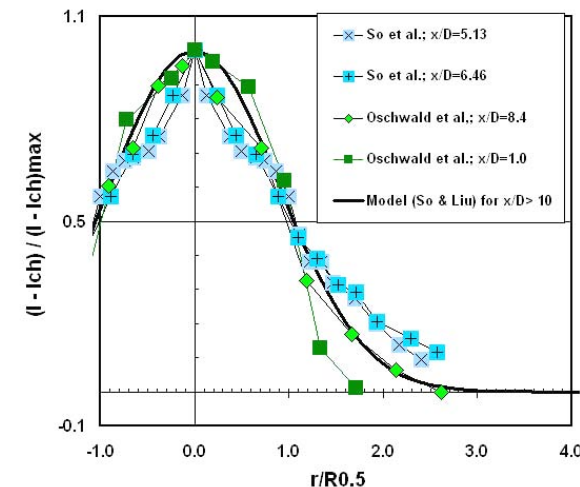
- Injection temperatures: A4: 140K, B4: 118K, C4: 100K
- Test cases B and C: quasi-boiling behavior for cold, trans-critical fluid



- An appropriate equation of state is used to calculate temperature
- The colder the initial temperature, the slower the growth and development of the jet
- For when $T_{\text{initial}} < T^*$ (cases B4 & C4) the heat exchange does not affect the centerline temperature due to maximal behavior of the specific heat (C_p)



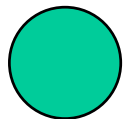
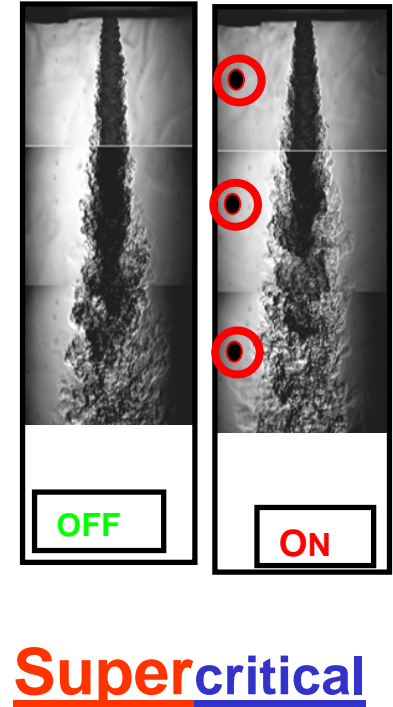
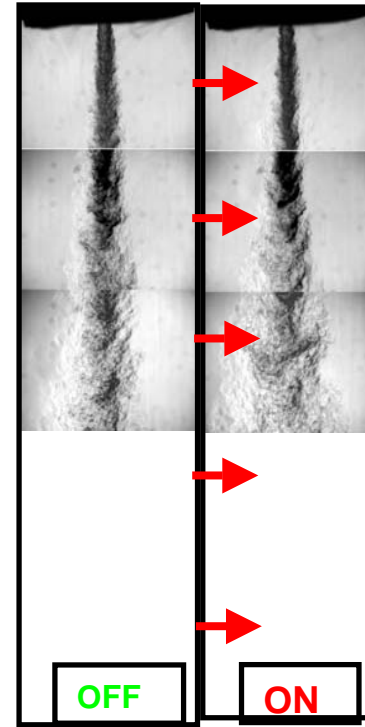
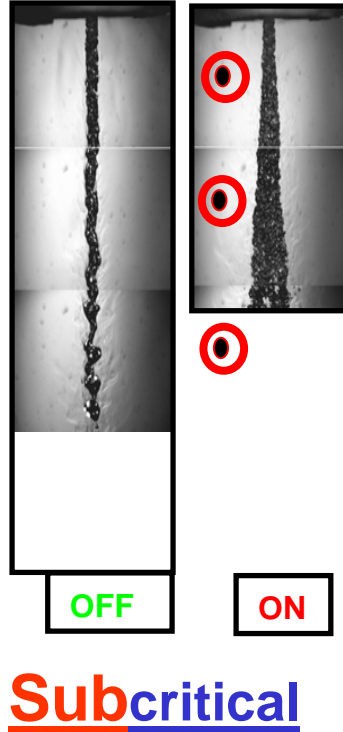
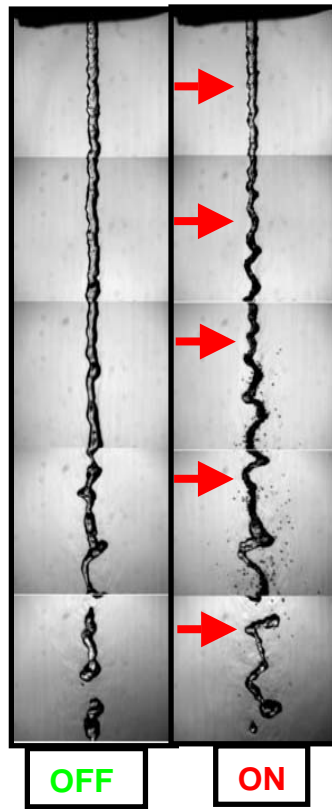
- AFRL and DLR found that 2 x FWHM of the Raman density profiles was consistent with shadowgraph spreading angles for $15 < x/D < 32$
- DLR found that 2 x FWHM under-predicted shadowgraph spreading angles when $0.5 < x/D < 14$.



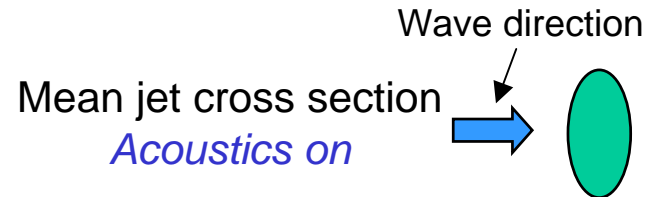
AFRL acoustic results

LN2 into GN2

SPL = 140 – 189 dB



Mean jet cross section
Acoustics off



- Subcritical jets were sensitive to acoustics while supercritical jets were not.
- Near-critical jets were the most sensitive.
- Coaxial jets exhibited a different trend (shown later).

Coaxial Injection Shadowgraphy

Binary liquid N₂/gaseous He system

$d_{\text{LN}_2} = 1.9 \text{ mm}$, $v_{\text{LN}_2} = 5 \text{ m/s}$, $v_{\text{He}} = 100 \text{ m/s}$, $T_{\text{LN}_2} = 97 \text{ K}$, $T_{\text{He}} = 280 \text{ K}$.

A: subcritical LN₂/GHe

$P_C = 1.0 \text{ MPa}$

B: transcritical LN₂/GHe

$P_C = 6.0 \text{ MPa}$

- reduced surface tension approaching the critical point
- spray formation at subcritical pressure
- turbulent mixing of dense and light fluid components at supercritical pressure
- visible boundary of LN₂-jet at high pressure assumed to correspond to the critical mixing temperature

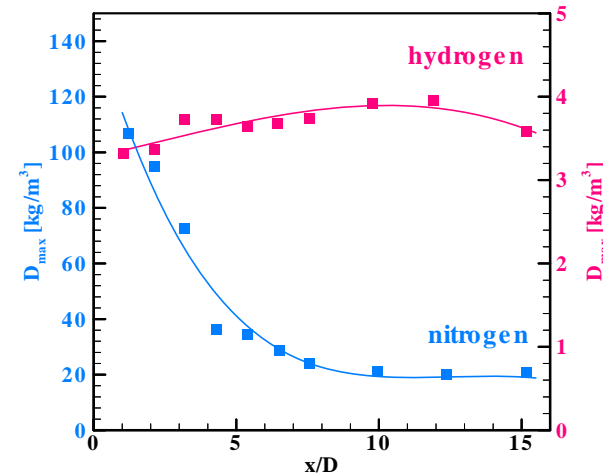


LN₂/GH₂-injection at 4 MPa

- radial N₂- and H₂-density profiles determined at various downstream axial positions

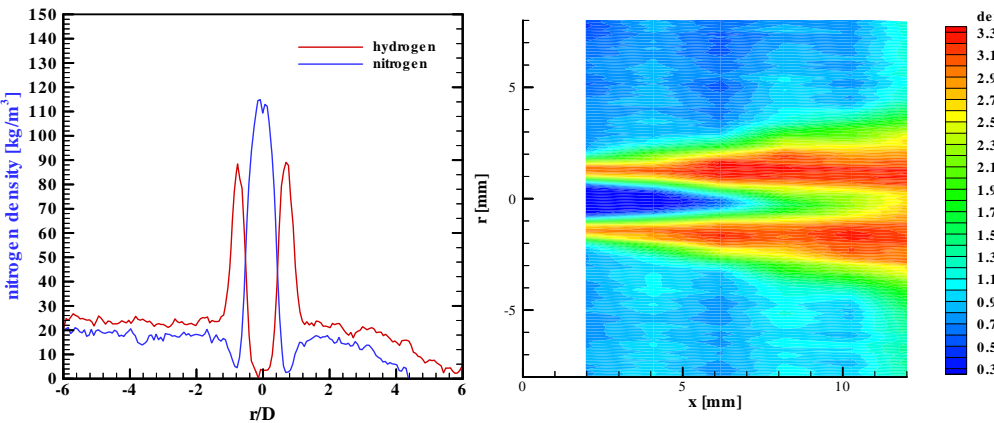
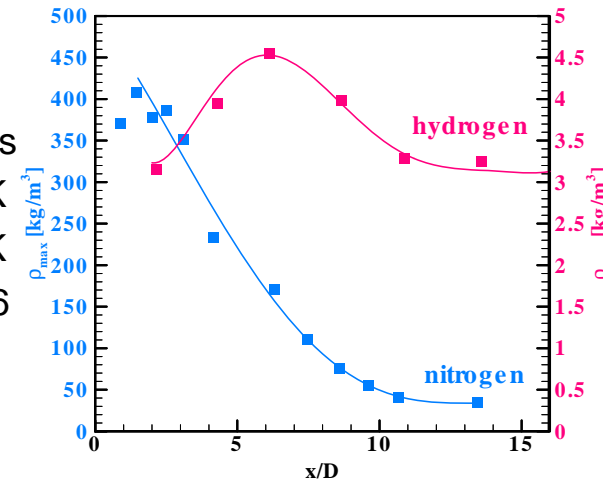
case D4

$v_{N_2} = 5 \text{ m/s}$
 $v_{H_2} = 60 \text{ m/s}$
 $T_{N_2} = 140 \text{ K}$
 $T_{H_2} = 270 \text{ K}$
 $\rho_{N_2}/\rho_{H_2} = 43$



case E4

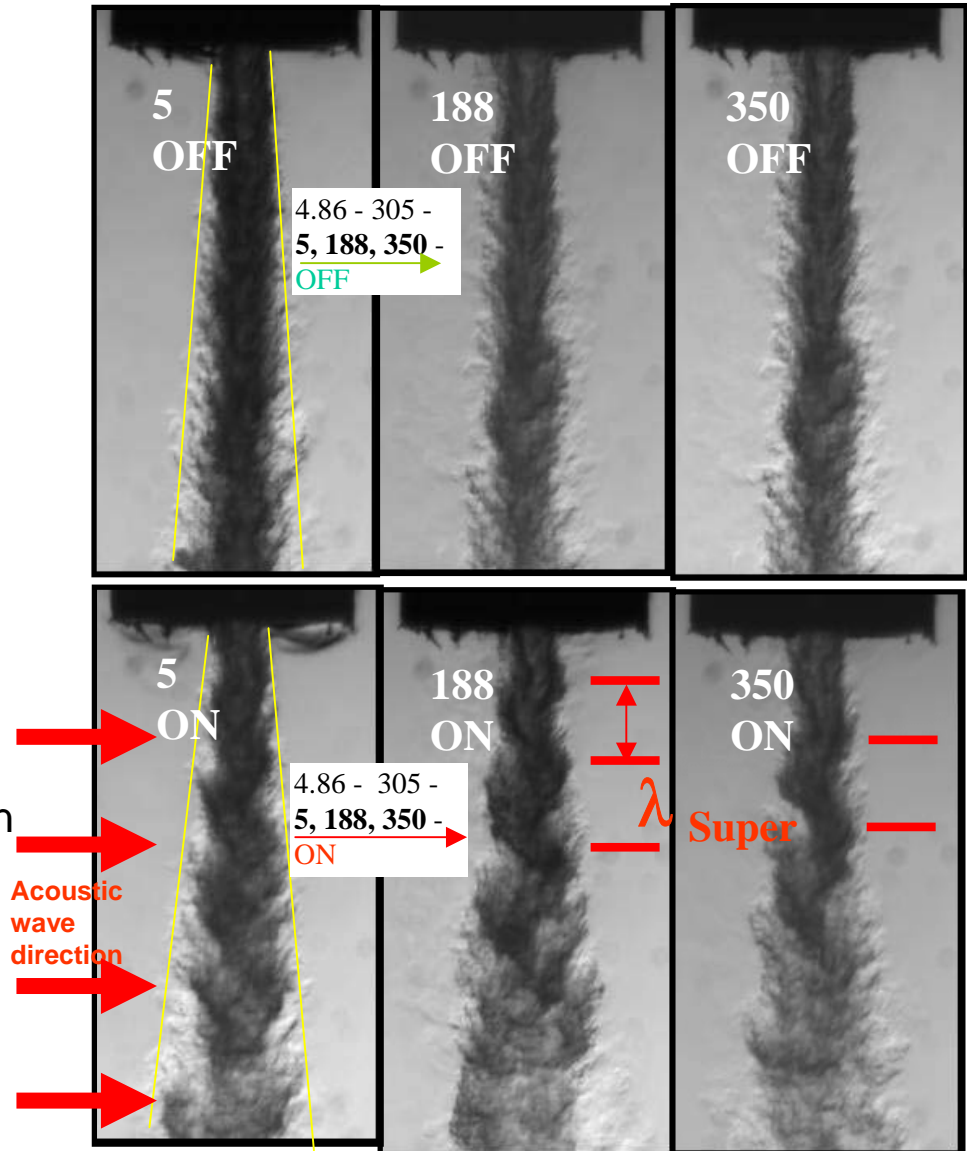
$v_{N_2} = 5 \text{ m/s}$
 $v_{H_2} = 60 \text{ m/s}$
 $T_{N_2} = 118 \text{ K}$
 $T_{H_2} = 270 \text{ K}$
 $\rho_{N_2}/\rho_{H_2} = 166$



- cooling of H₂ by LN₂, more efficient for high density N₂ (case E4)
- increasing LN₂-density results in less efficient atomization
- atomization efficiency more sensitive to N₂-density than to H₂-velocity ($v_{H_2}=60\text{m/s}$, 120m/s)

Supercritical ($P_r=1.43$)

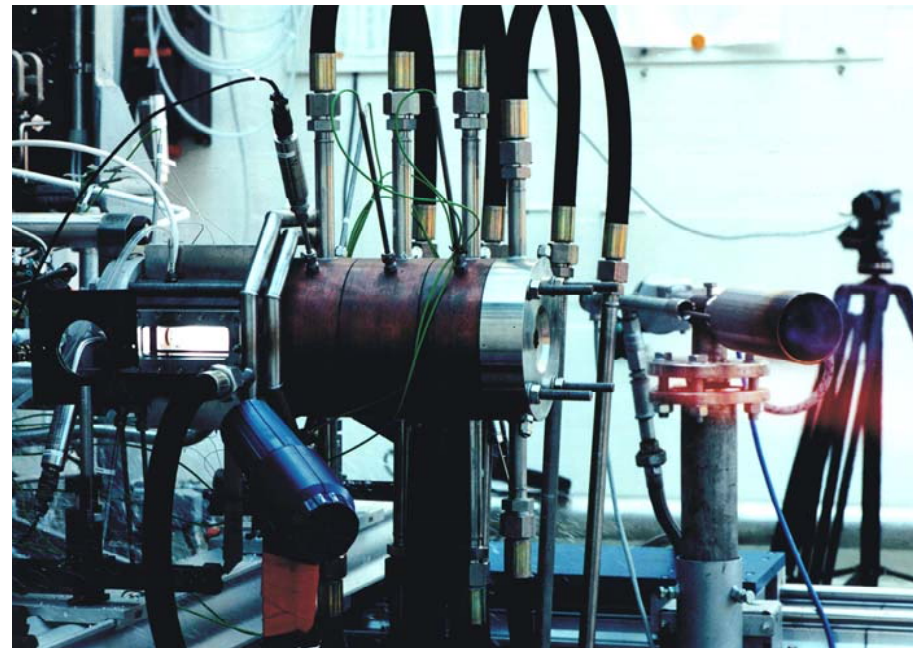
- GN2 in the annular region of the injector affected the thermodynamic condition of the LN2 jet near the inner wall surface, reducing the jet initial visual diameter, particularly at higher gaseous coflow rates
- Effects of the acoustic waves are, not only to increase the initial jet angle, but to impose a sinusoidal shape to the jet
- λ_{Super} is measured to be smaller than the corresponding values for the subcritical case (λ_{Sub}) due to the reduced penetration rate of the newly injected fluid under higher chamber pressures (supercritical)



results presented on coaxial injection at supercritical pressure are from tests at NAL (Mayer/Tamura) and DLR Lampoldshausen

DLR combustion chamber “C”

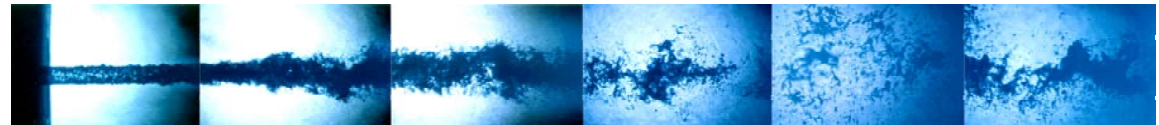
- single injector head
- LOX/GH₂-injection
- P_C up to 10 MPa, combustion at supercritical O₂-pressures
- optical access
 - shadowgraphy
 - OH-imaging
 - CARS



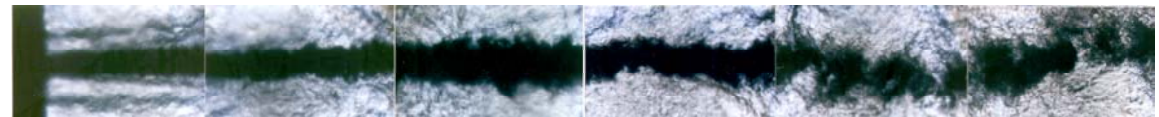
DLR combustion chamber “C”

LOX-jet disintegration:

- subcritical:
disintegration into
LOX-droplets
- supercritical:
disintegration into O₂-
clumps of larger size
than typical liquid
entities in subcritical
case

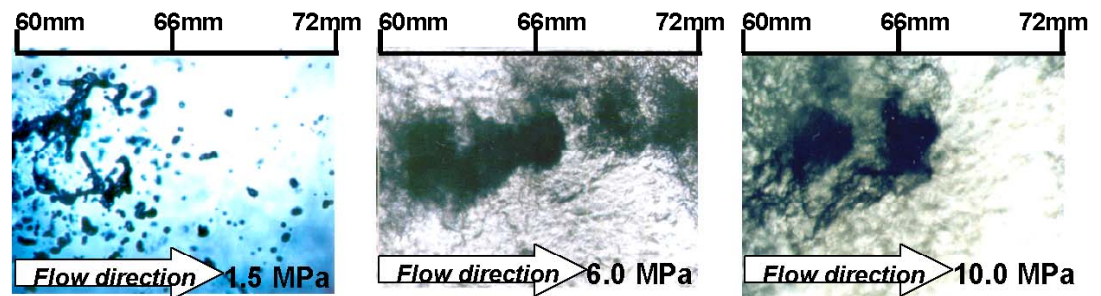


(a) Subcritical Pressure, 1.5 MPa Combustion



(b) Supercritical Pressure, 10 MPa Combustion

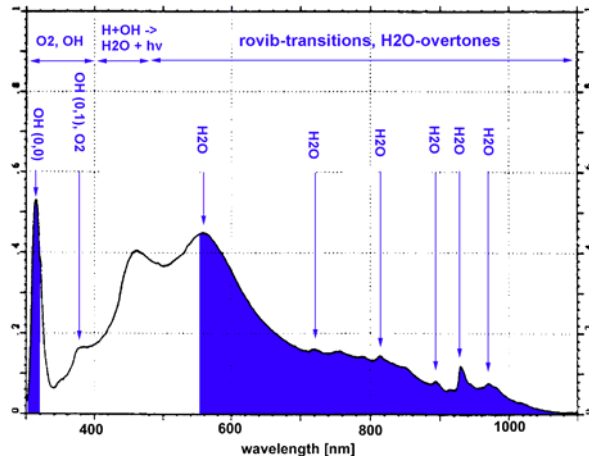
LOX-jet at subcritical (a) and supercritical (b) pressure conditions (from Mayer and Tamura)



Visualization of O₂-jet disintegration with varying chamber pressure (Mayer and Smith)

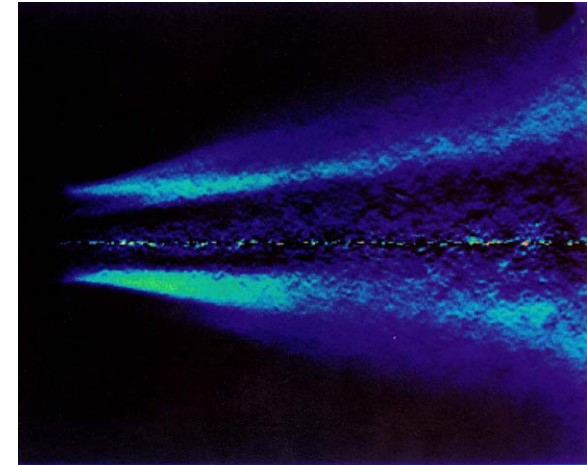
flame emission

- OH-radical: near 300nm
- H₂O: 500nm and above; non-linear increase with increasing pressure

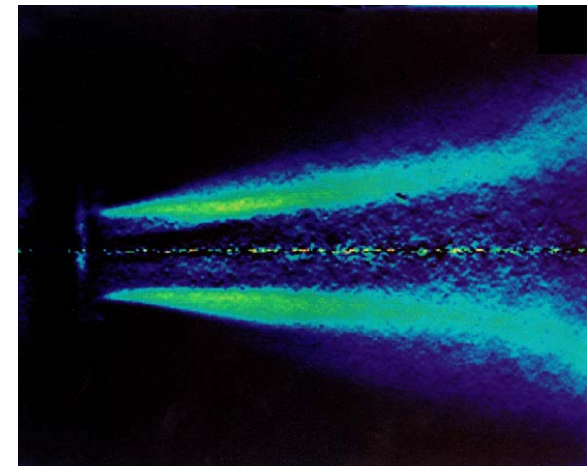


O₂/ H₂-flame spectra at 6 MPa

- flame anchors at the LOX-post
- H₂O-emission shows somehow larger extension in radial direction
- length scales extracted from OH-intensities between integral and Kolmogorov scales



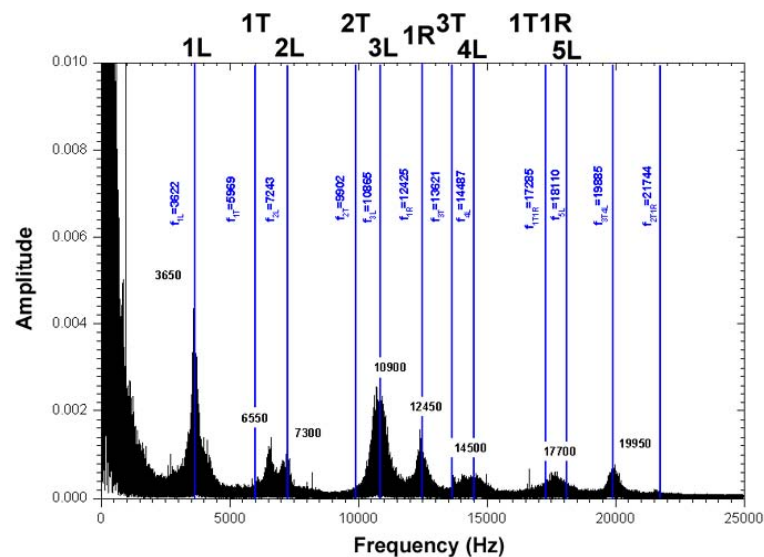
Deconvolution of the flame-emission of the OH-radical.



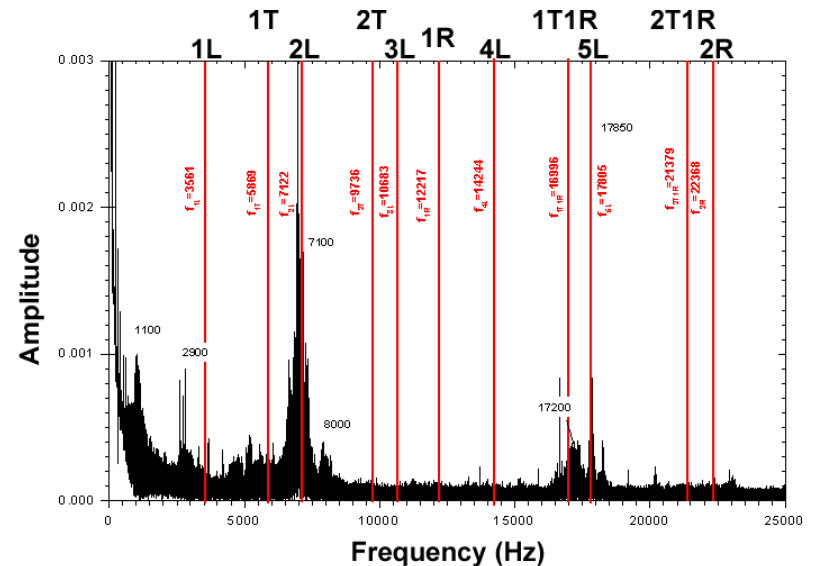
Deconvolution of the flame-emission of the H₂O-radical.

LOX/H₂-injection (L42-combustor) at 4 MPa and 6 MPa

- FFT of combustion chamber noise
- frequency distribution very well reproducible
- significant difference in chamber acoustics at sub- and supercritical pressure



4MPa



6MPa

Fourier spectra of combustion chamber pressure at 4MPa and 6MPa in a multi-injector combustion chamber



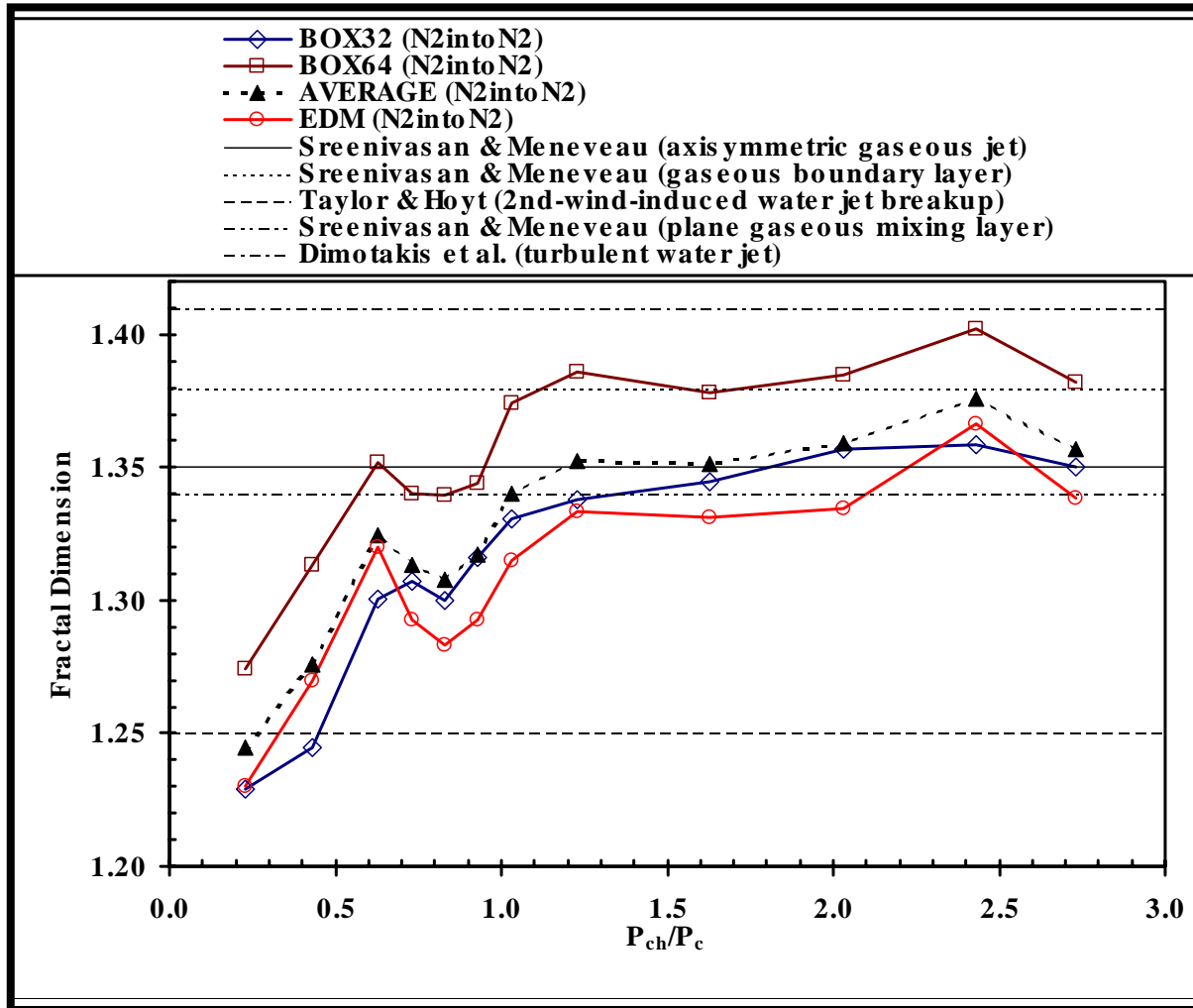
Major conclusions



- As pressure increases past the critical pressure, jet behavior changes from spray-like to gas-like.
 - No evidence of surface tension or droplets
 - At high enough pressures, the spreading rate of a single non-reacting jet is well predicted by variable density incompressible flow models.
- The evolution of the jet temperature and density is strongly dependent on the initial temperature and, for coaxial jets, on heat transfer between the flows.
 - The temperature at which the specific heat reaches a maximum is an important parameter.
- Reacting coaxial jet flames anchor to the LOX post.
- The acoustic behavior of subcritical jets is likely to be significantly different than the acoustic behavior of supercritical jets.
- Many of the above results have been independently confirmed by the research groups at AFRL and DLR.

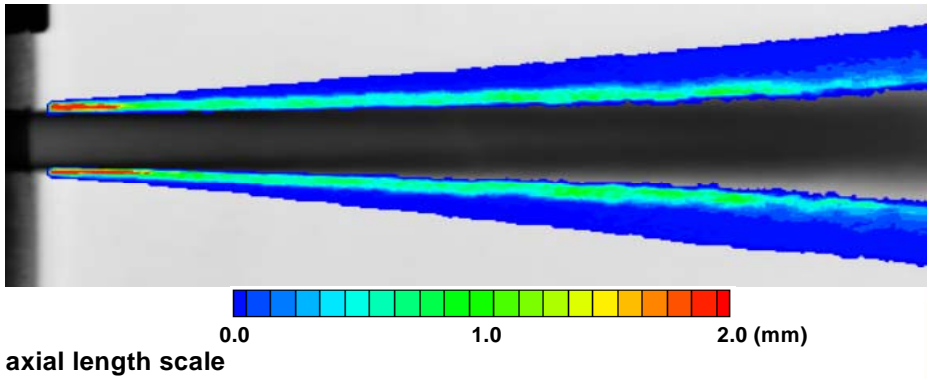
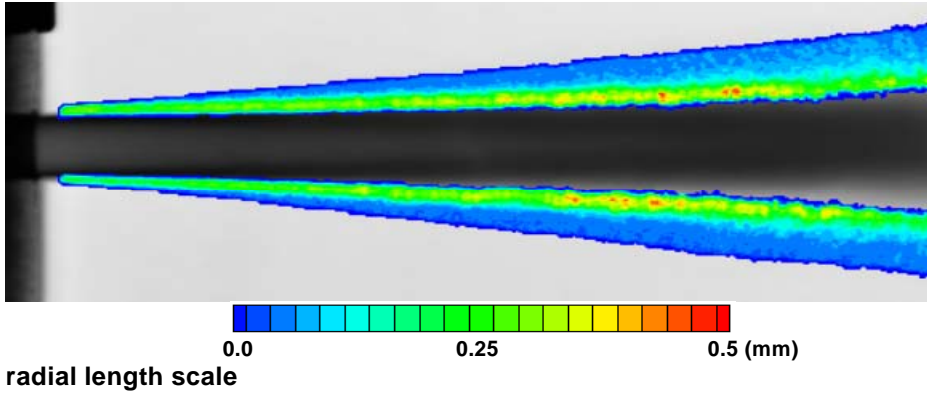


Supplemental slides



- Box-counting and Minkowski (EDM algorithm) fractal dimensions of the visual boundary of the jet as a function of the relative chamber pressure for N₂-into-N₂ injection.
- At supercritical condition fractal dimension of the jet boundary is similar to those of gaseous jets and mixing layers

Comparison with Numerical Length Scales

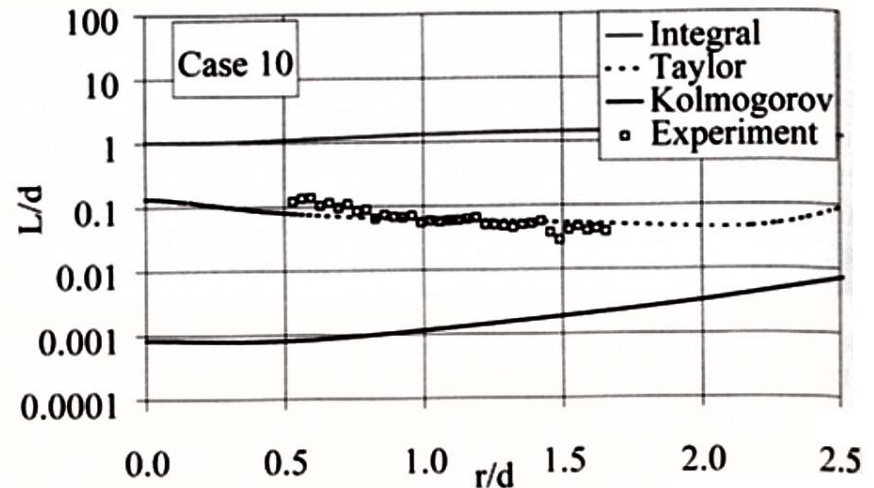


Experimental length scales from shadowgraphs

$$L = \sqrt{L_{ax} \cdot L_{rad}}$$

show good agreement with numerically determined Taylor length scale

$$L_{Tay} = \left(\frac{15 \nu \bar{u}^2}{\epsilon} \right)^{\frac{1}{2}}$$





Injection Into High Pressure Supercritical Environments

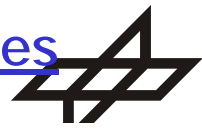


Properties

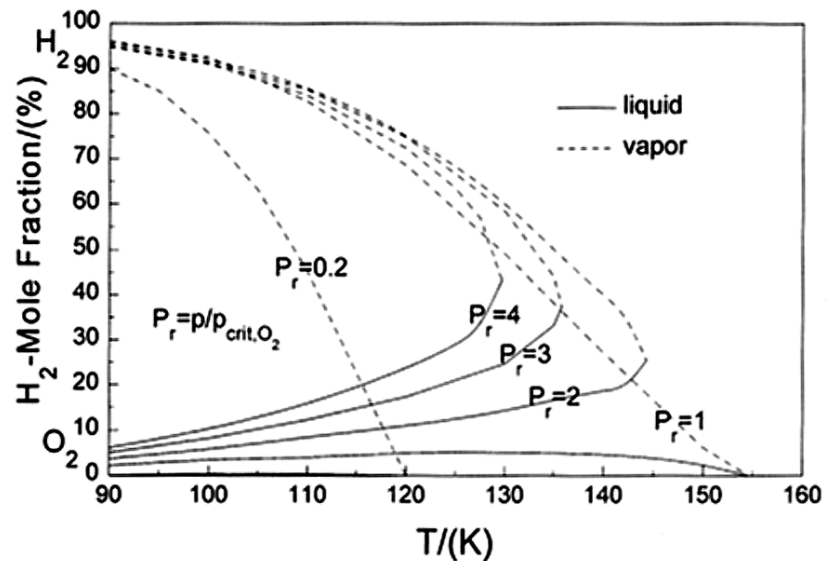
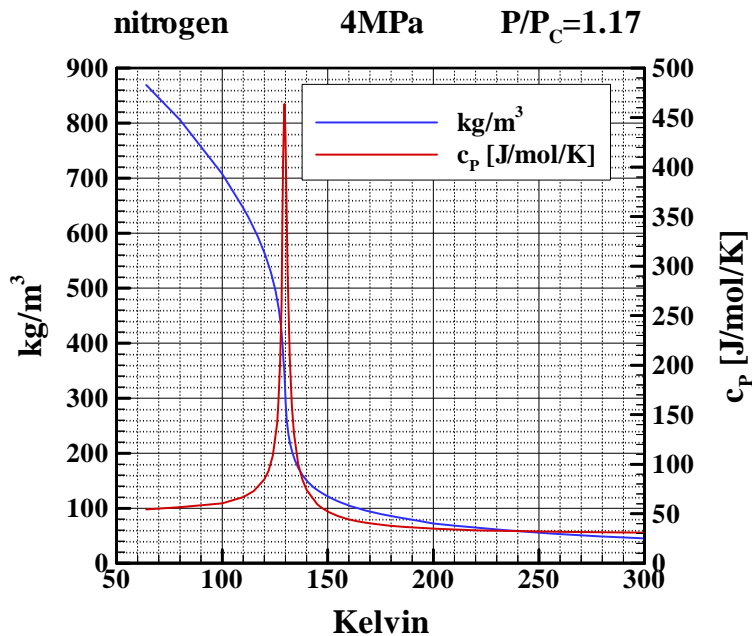
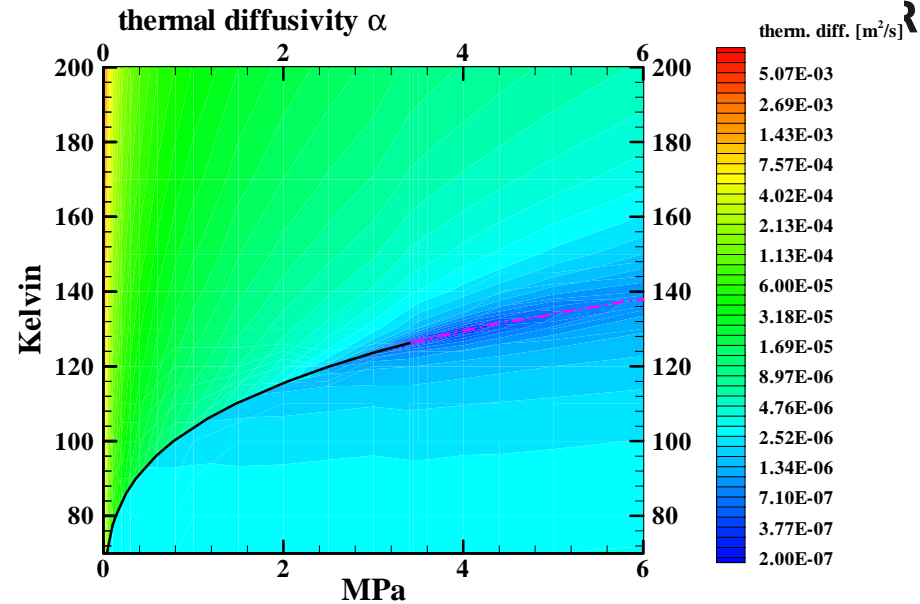
- Vanishing surface tension and enthalpy of vaporization.
- Equivalent “gas” and “liquid” phase densities.
 - Increased “gas” phase aerodynamic effects.
- Strongly enhanced solubility of one species (“gas”) into another (“liquid”).
- Reduced “gas” phase diffusivity (more liquid-like).
- Large property excursions near the critical point
 - Conductivity, viscosity, speed of sound, specific heats.
- Mixing induced critical point variations.
- Enhanced gas phase unsteadiness.

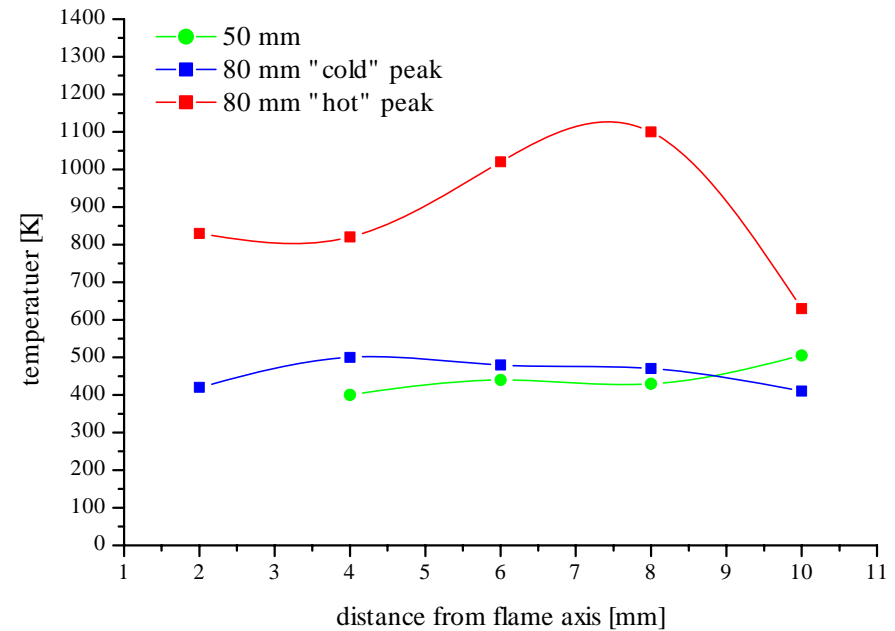
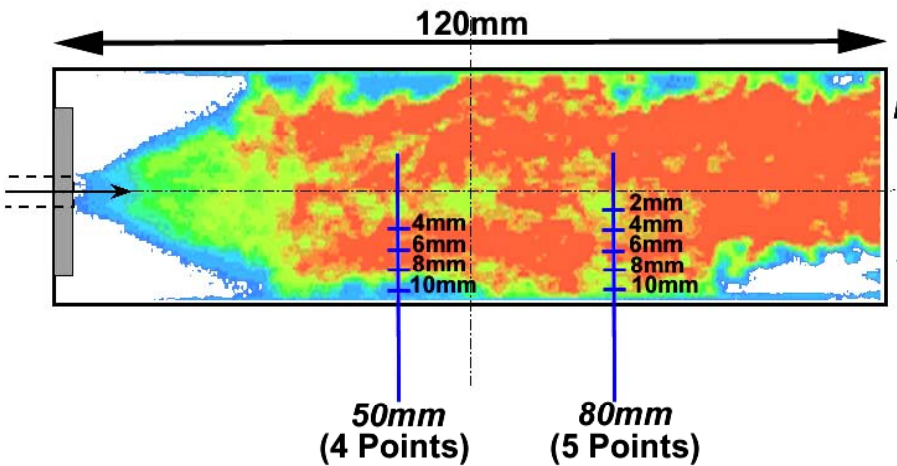


Anomalous Behavior in Thermophysical Properties



- Rapid changes in density near critical point (CP)
- Very large values of specific heat near CP and beyond
- Surface tension vanishes at and beyond CP
- Heat of vaporization vanishes at and beyond CP
- Enhanced solubility at supercritical state





Measurement locations for CARS thermometry in windowed combustion chamber "C"

Radial profiles of the mean temperature values for axial positions 50mm and 80mm.

SUBSCALE TESTING AND DESIGN ISSUES OF INJECTORS

Youngbin Yoon and In-Seuck Jeung

School of Mechanical and Aerospace Engineering
Seoul National Univ., KOREA 151-742

ABSTRACT

The breakup characteristics of liquid sheets formed by like-doublet injector were investigated in the cold-flow and atmospheric ambient pressure condition. The sheet breakup wavelength, which induces the sheet to be broken into ligaments, as well as the sheet breakup length, which is important for the flame location, was measured using a stroboscopic light. Since these spray characteristics are affected by the flow characteristics of two liquid jets before they impinge on each other, we focused on the effects of orifice internal flow such as the cavitation phenomenon that occurs inside the sharp-edged orifice. From the experimental results, we found that the liquid jet turbulence delays the sheet breakup and makes shorter wavelengths of sheet. Since the turbulent strength of sharp-edged orifice is stronger than that of round-edged orifice, the shape of orifice entrance results in large differences in the spray characteristics. Using these results, we proposed empirical models on the spray characteristics of the like-doublet injector, and these models are believed to provide some useful and actual data for designing liquid rocket combustors.

INTRODUCTION

Like-doublet injectors that atomize liquid mass into fine drops using the impinging momentum of two liquid jets are commonly used in liquid rocket engines due to their advantages: low manufacturing cost, potentially high flow rate, compatibility of chamber wall and so forth¹. Therefore, extensive experimental and analytical researches have been carried out on the spray formed by the injector^{2,3,4,5}. However, the experimental results have not agreed well with other experimental results as well as analytical models, and thus there have not been reliable models for the breakup characteristics of liquid sheets. One of the most important reason of this is thought that different orifices in material, inner surface roughness, treatment quality of orifice hole and so forth have been used because these may produce the differences in the flow characteristics in liquid jets. Since the laminar or turbulent characteristics of liquid jet dominate the breakup mechanism of liquid sheet³ and the turbulence strength of liquid jet is strongly affected by the internal flow of orifice, it is believed that the inner condition of orifice is very important for the spray characteristics of the injector.

It is known that the occurrence of cavitation phenomenon is significant for steady internal flow of orifice^{6,7,8}. An abrupt change in the flow direction at the entrance of the orifice reduces the local static pressure up to the saturation pressure, and then cavitation bubbles appear at the location. These bubbles make the internal flow very turbulent, and

thus jet characteristics become dependent on the flow time, which implies unsteady flow. The development of cavitation bubble can induce liquid flow to be separated from the orifice wall. This hydraulic flip phenomenon reduces the mass flow rate of propellant and causes the mis-impingement problem of impinging type injectors. Although it was found that the flip seldom occurs in high ambient pressure of liquid rocket combustors, the cavitation still remains inside the orifice and produces the turbulent jet flow⁷. Tamaki et al.⁸ conducted studies on the turbulence characteristics of sharp or round-edged orifice jets for diesel engine and measured the jet breakup lengths. As for liquid rocket injectors, Nurick⁶ reported that the cavitation reduces the mixing efficiency of unlike-doublet injector from the cold flow test. However, the cavitation effects on the spray characteristics of liquid sheets formed by like-doublet injectors have not been reported.

In this paper, we visualized internal flows of sharp or round-edged orifices and investigated their effects on the breakup characteristics of liquid sheets. The final objective of this study was to obtain empirical models on the breakup lengths and the breakup wavelengths or frequencies of sheet or ligament for the practical like-doublet injectors. Therefore, we proposed the models for the sharp-edged orifice that is more commonly used in practical system as functions of Weber number, impingement angle, and liquid properties.

EXPERIMENTAL METHOD

We designed both sharp and round-edged orifices for like-doublet injectors as shown in Figure 1. According to Vennard's experimental results⁹, the orifice of which entrance is rounded with 0.14 times of orifice diameter or much has no a vena contracta. In order to obtain the non-cavitation flow, therefore, the round-edged orifice was designed with a curvature radius of one diameter of orifice. In this case, it has been known that the internal flow of round-edged orifice is so smooth that there is no perturbation of the flow as shown in the schematic of Figure 1(a)⁸. Contrary to the round-edged orifice, the flow of sharp-edged orifice has to change its direction rapidly at the orifice entrance so that a cavity flow is formed (Figure 1(b)). In case that the static pressure of the cavity is lower than the saturation pressure, the cavitation occurs within the cavity. In addition, the change in the flow direction during the passing of the orifice makes the flow turbulent, especially for short orifices. According to Dombrowski and Hooper³, the ratio of orifice length to diameter has to be higher than 400 for the velocity profile to be fully developed. Since the lengths of present orifices are too short to stabilize the turbulence of internal flow, the sharp-edged orifice of Figure 1(b) is believed to form the turbulent jet.

As shown in Figure 2, the breakup length of liquid sheet ($x_{b,s}$) was defined as the distance from the impingement point to the edge of liquid sheet along the x-axis. The wavelength of the liquid sheet at the moment of the breakup of liquid sheet ($\lambda_{b,s}$) is important in validating the linear instability theory that there is a specific wavelength which induces the breakup of liquid sheet¹¹

FLOW CHARACTERISTICS OF LIQUID JETS

Figure 3 shows discharge coefficients C_d for round and sharp-edged orifices. The discharge coefficient of round-edged orifice was higher than that of sharp-edged orifice. In cases of sharp-edged orifice, the discharge coefficients decrease as the injection pressure increases after about 2.5 bars. Nurick ⁶ found that the discharge coefficient of sharp-edged orifice for the cavitation flow is determined by following equation:

$$C_d = 0.62 [(P_I - P_v)/(P_I - P_B)]^{0.5} \quad (1)$$

where P_I is total pressure in orifice chamber, P_v is liquid vapor pressure and P_B is ambient back pressure. Since the discharge coefficient of sharp-edged orifice followed above equation after 2.5 bars, the occurrence of cavitation flow inside the orifice could be expected.

The orifice internal flow can be separated from the wall after the cavitation bubbles are fully developed inside the orifice. This hydraulic flip phenomenon is very important for the impinging type injectors because it can result in the mis-impingement of liquid jets ⁷. According to Nurick ⁶, the flip can be expected from the discharge coefficient curve; it departs from Equation (1) and has a constant value that is lower than the coefficient of cavitation flow. However, the sharp-edged orifice did not show the flip in present experimental conditions because the orifice length is long enough for separated flows to be reattached.

Figure 4 shows the shapes of orifice internal flows and jet flows for water and kerosene simulants as a function of injection velocity that has been known as the most important parameter for the characteristics of liquid jet ¹². The injection velocities were calculated from the following equation ⁶:

$$U_j = C_d (2\Delta P/\rho_l)^{0.5} \quad (2)$$

Since the discharge coefficients of round and sharp-edged orifices as well as the liquid densities ρ_l of water and kerosene simulants were not same, the injection pressures ΔP were determined by using Equation (2) for the same jet velocities in each case.

From Figure 4(a), it was found that there were no significant differences in the water internal or external flow irrespective of the shape of orifice entrance when the jet velocity is 980 cm/s. In case of higher velocity ($U_j=1690$ cm/s), however, cavitation phenomenon occurred inside only the sharp-edged orifice; the cavitation bubbles are shown to be white images in the internal flow photos. From the images of jet flow, it is observed that the cavitation bubbles causes the liquid jet to become turbulent. When the velocity was 2180 cm/s, the cavitation bubbles were fully developed inside the sharp-edged orifice, and thus the turbulence strength of liquid jet became higher. In case of the round-edged orifice, however, the turbulence strength of jet flow did not increase greatly as compared with that of sharp-edged orifice.

Figure 4(b) shows that the turbulence strengths of kerosene jets are higher than those of water jets for the sharp-edged orifices under the same injection velocity. The reason may be explained by the fact that surface tension force of kerosene is lower than that of water so that the jet spreads rapidly at the exit of orifice. In case of round-edged orifice, the laminar jet is formed under the low injection velocity, 980 cm/s. For the higher injection velocity ($U_j=1690$ cm/s), the jet becomes semi-turbulent; it has both the turbulent core and laminar envelope as Lefebvre ¹² mentioned. According to

Dombrowski and Hooper³, the orifice can have the laminar liquid jet until the Reynolds number is 12000 only if its entrance is very smooth. Therefore, it is thought that all the liquid jets of round-edged orifices of Figure 4(a) are turbulent because their Reynolds number are higher than 12000.

In order to compare the turbulence strengths of liquid jets, we measured the diameters of liquid jets at the impingement location using 100 instantaneous images, and Figure 5 shows the results. Although the jet diameter may not exactly indicate the jet turbulence strength because it is based on not the internal jet structure but the outer jet shape, it is believed that it can give qualitative information on the turbulence strength. As shown in Figure 5, while the water jet diameter of round-edged orifice increases just slightly as the Weber number increases, that of sharp-edged orifice shows a S-curve; the water jet diameter increases rapidly when the cavitation occurs inside the sharp-edged orifice and increases slowly after the cavitation is fully developed. The kerosene jet diameter of sharp-edged orifice also shows the similar trends with the water jet diameter of sharp-edged orifice except the higher increasing rate. As for the kerosene jet of round-edged orifice, the rate of increase of jet diameter is much higher than the water jet diameter of round-edged orifice because the jet characteristics change rapidly from laminar into semi-turbulent or fully turbulent.

BREAKUP LENGTHS OF SHEET

We measured the breakup lengths of liquid sheet using instantaneous spray images obtained by a stroboscopic light. For the reliability of data, we analyzed 100 images for one experimental case, and the deviations of data were less than 10 percents of their mean values. Figure 6(a) shows the breakup length of liquid sheet as a function of Weber number of jet ($We_j, \rho_l U_j^2 d_o / \sigma$ where σ is surface tension). First of all, the breakup lengths decreases irrespectively of the orifice entrance shape or the kind of simulant as the Weber number increases. It could be expected that the sheet breakup length increase because the sheet velocity also increases as the Weber number increases. However, Figure 6(a) shows the opposite results to this expectation, and thus it is thought that the effect of the impact force of two liquid jets predominates the sheet breakup rather than that of the sheet velocity.

In cases of water sheets as shown in Figure 6(a), it is interesting that the breakup length of round-edged orifice (symbol ●) is much larger than that of sharp-edged orifices (symbol ■) when both Weber numbers are about 1500, although both jet diameters are similar as shown in Figures 4 and 5. According to Dombrowski and Hooper³, the impact waves formed by the impingement of two liquid jets are diminished by the boundary flow of jets. Since the boundary flow becomes thin as the turbulence strength of jet increases, the liquid sheet breaks easily by the impact waves. Therefore, it is believed that the jet inner turbulence of sharp-edged orifice is higher than that of round-edged orifice, although both jet outer shapes are similar. Consequently, it can be deduced that the shape of orifice entrance is the very important for the sheet breakup.

However, the difference in the water sheet breakup lengths of round and sharp-edged orifices decreases as the Weber number increases because the decrease rate of water sheet breakup length of sharp-edged orifice (proportional to $We_j^{-0.27}$) is lower than

that of round-edged orifice ($We_j^{-0.40}$) as shown in Figure 6(a). It is thought that this results from the increase of jet turbulence by the cavitation; in cases of sharp-edged orifices, the jet turbulence strength as well as the impact force of two jets increases as the Weber number increases, and the jet turbulence may relax the effect of impact force on the sheet breakup. Therefore, the Weber number effect on the sheet breakup length of sharp-edged orifice is lower than that of round-edged orifice of which jet turbulence effect is not significant. In addition, since the turbulence strengths of kerosene jets of both round and sharp-edged orifices also increase sensitively with the increase of Weber number as shown in Figure 5, the sheet breakup lengths of them show the similar trends ($We_j^{-0.21}$ and $We_j^{-0.27}$ for round and sharp-edged orifices, respectively) with the water sheet breakup length of sharp-edged orifice.

As for the breakup length of liquid sheet, Huang¹³ obtained a semi-empirical relation by using a vibrating membrane model as follows:

$$x_{b,s}/d_o = 7.1(\rho_g/\rho_l)^{-2/3} We_j^{-1/3} \quad (3)$$

when the Weber number is higher than 2000. Since he used perpendicularly impinging jets, he did not consider the effect of impingement angle. Ryan et al.¹¹ also suggested a breakup length model of a like-doublet injector based on the aerodynamic instability theories of Dombrowski and Hooper¹⁴ and Hasson and Peck¹⁵ as follows:

$$x_{b,s}/d_o = 5.451(\rho_g/\rho_l)^{-2/3} [We_j f(\theta)]^{-1/3}, \quad f(\theta) = (1 - \cos\theta)^2 / \sin^3\theta \quad (4)$$

Since both breakup length models are basically based on the aerodynamic instability theory, it can be known that the powers of the Weber number or the density ratio of gas to liquid are same in Equations (3) and (4).

The model of Ryan et al.¹¹ shows a similar trend with the present experimental data as shown in Figure 6(a), although it overestimate the breakup length quantitatively. However, the model predicts that the breakup length of kerosene (dashed line) is smaller than that of water sheet (solid line), which is contrary to the present results. According to the linear instability theory based on the balance between surface tension force and aerodynamic force, since the amplitude of sheet wave increases as the liquid density decreases, the liquid sheet of kerosene of which density is smaller than that of water is early broken. In case of the breakup of the present turbulent sheet, however, the impact force of two liquid jets is more important than the aerodynamic force³. Since the impact forces of both kerosene and water jets are same at the same Weber number, the sheet breakup lengths of them are determined by the turbulence strength of jets as we mentioned previously. Therefore, the breakup length of kerosene sheet becomes larger than that of water sheet at the same Weber number because the turbulence strength of kerosene jet is stronger than that of water jet as shown in Figures 4 and 5.

In order to identify the effects of impingement angle on the breakup of sheet, we measured the breakup lengths of sheet as varying the impingement angle at the fixed Weber number of 5900. Although the impact force of two liquid jets is proportional to the square of sine of half impingement angle θ^3 , the turbulence strength of jet may not be changed significantly because the Weber number was fixed. Therefore, it is believed that Figure 6(b) shows the effect of the impact force on the breakup characteristics to the exclusion of the effect of jet turbulence strength.

From Figure 6(b), it was found that the water sheet breakup lengths of both round and sharp-edged orifices are proportional to $(\sin^2\theta)^{-0.60}$, although they are proportional

to $We_j^{-0.40}$ and $We_j^{-0.27}$, respectively, in Figure 6(a). If considering that the impingement angle affects only the impact force while the Weber number affects the jet turbulence strength as well as the impact force, the differences in powers between We_j and $\sin^2\theta$ (i.e., $-0.40 - (-0.60) = +0.20$ for round-edged orifice and $-0.27 - (-0.60) = +0.33$ for sharp-edged orifice) are thought to indicate the degree of the effect of jet turbulence strength on the breakup length; since the jet turbulence increase the sheet breakup length by relaxing the impact force and the increase in turbulence strength of round-edged orifice is lower than that of sharp-edged orifice, the sheet breakup length of round-edged orifice becomes more sensitive to the Weber number than that of sharp-edged orifice.

From the results of Figure 6, it was found that the jet turbulence strength as well as the impact force of two liquid jets is important for both sheet and ligament breakup lengths. By using these experimental data, we could obtain empirical relations on the breakup lengths of sheet for the sharp-edged orifice as follows:

$$x_{b,s}/d_o = 97.3 We_j^{-0.27} (\sin\theta)^{-1.20} \quad (5)$$

BREAKUP WAVELENGTHS OF SHEET

Squire¹⁸ proposed the breakup wavelength that generates the highest amplitude of the liquid sheet using the linear instability theory as follows:

$$\lambda_{b,s}/d_o = 4\pi (\rho_g/\rho_l)^{-1} We_j^{-1} \quad (6)$$

However, present experimental data in Figure 7(a) show that this theory excessively overestimates the effects of Weber number so that underestimates the wavelength quantitatively. In addition, the Squire's model predicts that the breakup wavelength of kerosene sheet (dotted line) is shorter than that of water sheet (solid line) at the same Weber number, which is in contrary to the present results. This may be explained by the fact that Squire did not consider the impact force of liquid jets because his model is based on a flat expanding sheet injected from a rectangular slit hole. Consequently, Figure 7(a) shows that the linear instability theory based on only the aerodynamic force without the impact force or jet turbulence cannot be used to expect the breakup characteristics of liquid sheets formed by like-doublet injectors.

Figure 7(a) also shows the similar trends with the sheet breakup lengths; the water sheet wavelength of round-edged orifice (proportional to $We_j^{-0.34}$) is sensitive as compared with water sheet wavelength of sharp-edged orifice ($We_j^{-0.24}$) and kerosene sheet wavelength of round ($We_j^{-0.21}$) and sharp-edged orifices ($We_j^{-0.21}$). The reason also can be explained by the effects of the impact force and the jet turbulence strength. From Figure 7(b) that shows the effect of the impingement angle on the sheet wavelengths, it is found that the sheet wavelengths of round and sharp-edged orifices are proportional to $(\sin^2\theta)^{-0.37}$ and $(\sin^2\theta)^{-0.12}$, respectively. Since the water jet turbulence strength of round-edged orifice does not change significantly, the variation in the power of its sheet wavelength is not significant (i.e., from -0.37 to -0.34). On the other hand, since the turbulent jet may prevent the wave within the sheet from fully developing, the sheet wavelength of sharp-edged orifice decreases as the Weber number increases so that the variation in the power is relatively large (i.e., from -0.12 to -0.24); in other words, it is

believed that the decrement of -0.12 results from the effect of the increase of jet turbulence strength.

We obtained empirical relations on the breakup wavelengths of sheet from the results of sharp-edged orifices of Figure 7 as follows:

$$\lambda_{b,s}/d_o = 45.2 Oh^{0.096} We_j^{-0.24} (\sin\theta)^{-0.24} \quad (7)$$

where Ohnesorge number $(\mu/(\rho_l \sigma d_o))^{0.5}$, μ is liquid viscosity) was used in order to compensate the quantitative difference between water and kerosene simulants with their properties such as density, viscosity, and surface tension¹². Comparing Equation (7) with Squire's theory of Equation (6), the effect of Weber number is mitigated; the power of Weber number is changed from -1 into -0.24.

CONCLUSIONS

1. The turbulence strength of each jet as well as the impact force of two jets is an important factor for the breakup characteristics of liquid sheet. The turbulence strength of jet is affected by the orifice entrance shape, injection velocity, liquid properties, and so on. Especially, the cavitation bubbles that occur inside the sharp-edged orifice at high Weber numbers make the liquid jet very turbulent.
2. Although the impact force decreases the breakup length of liquid sheet, the liquid jet turbulence relaxes the effect of impact force on the liquid sheet. Therefore, the water sheet breakup length of round-edged orifice is more sensitive to the Weber number than that of sharp-edged orifice because its turbulence strength is not changed significantly as the Weber number increases.
3. The jet turbulence strength as well as the impact force reduces the sheet breakup wavelength because the jet turbulence may prevent the wave within the sheet from fully developing. Therefore, although the sheet wavelength of sharp-edged orifice becomes more sensitive to the Weber number by the jet turbulence, that of round-edged orifice is determined by only the impact force because the jet turbulence strength of round-edged orifice does not change significantly.
4. The surface tension force of kerosene is lower than that of water so that the jet diameter spreads rapidly at the exit of orifice. Therefore, the turbulence strength of kerosene jet irrespective of orifice entrance shape shows the similar tendency with that of water jet of sharp-edged orifice. Consequently, the spray characteristics of the kerosene sheet show similar trends with those of the water sheet formed by the sharp-edged orifice.

ACKNOWLEDGMENTS

The authors of this research would like to acknowledge the financial supports of the KSR-III project and the National Research Laboratory program (M1-0104-00-0058).

REFERENCES

1. Gill, G. S., and Nurick, W. H., "Liquid Rocket Engine Injectors," NASA, SP-8089, 1976.
2. Taylor, G. I., "Formation of Thin Flat Sheets of Water," *Proceedings of the Royal Society of London A*, Vol. 259, 1960, pp. 1-17.
3. Dombrowski, N., and Hooper, P. C., "A Study of the Sprays Formed by Impinging Jets in Laminar and Turbulent Flow," *Journal of Fluid Mechanics*, Vol. 18, Pt. 3, 1964, pp. 392-400.
4. Heidmann, M. F., Priem, R. J., and Humphrey, J. C., "A Study of Sprays Formed by Two Impinging Jets," NACA, TN-3835, 1957.
5. Anderson, W. E., Ryan, H. M., and Santoro, R. J., "Impinging Jet Injector Atomization," *Liquid Propellant Rocket Combustion Instability*, edited by V. Yang and W. E. Anderson, Vol. 169, Progress in Astronautics and Aeronautics, AIAA, Washington, DC, 1995.
6. Nurick, W. H., "Orifice Cavitation and Its Effect on Spray Mixing," *Journal of Fluids Engineering*, Dec. 1976, pp. 681-687.
7. Chew, T. J. C., "Hydraulic Flip Behavior in Typical Liquid Rocket Operating Regimes," NASA, 73N32630, 1973.
8. Tamaki, N., Shimizu, M., Nishida, K., and Hiroyasu, H., "Effects of Cavitation and Internal Flow on Atomization of a Liquid Jet," *Atomization and Spray*, Vol. 8, 1998, pp. 179-197.
9. Vennard, J. K., "Elementary Fluid Mechanics," Wiley, New York, 1961.
10. Kline, M. C., Woodward, R. D., Burch, R. L., Cheung, F.B., and Kuo, K. K., "Experimental Observation of Impinging Jet Breakup Utilizing Laser-Sheet Illuminated Photography", AIAA Paper 91-3596, 1991.
11. Ryan, H. M., Anderson, W. E., Pal, S., and Santoro, R. J., "Atomization Characteristics of Impinging Liquid Jets," *Journal of Propulsion and Power*, Vol. 11, No. 1, 1995, pp. 135-145.
12. Lefebvre, A. H., "Atomization and Spray," Hemisphere, Philadelphia, PA, 1989, pp. 45-48.
13. Huang, J. C. P., "The Break-Up of Axisymmetric Liquid Sheets," *Journal of Fluid Mechanics*, Vol. 43, Pt. 2, 1970, pp. 305-319.
14. Dombrowski, N., and Hooper, P. C., "The Effect of Ambient Density on Drop Formation in Sprays," *Chemical Engineering Science*, Vol. 17, 1962, pp. 291-305.
15. Hasson, D., and Peck, R. E., "Thickness Distribution in a Sheet Formed by Impinging Jets," *A.I.Ch.E. Journal*, 1964, pp. 752-724.
16. Hoyt, J. W., and Taylor, J. J., "Turbulence Structure in a Water Jet Discharging in Air," *Physics of Fluids*, Vol. 20, pt. 2, 1977, pp. 253-257.
17. Wu, P. -K., Miranda, R. F., and Faeth, G. M., "Effects of Initial Flow Conditions on Primary Breakup of Nonturbulent and Turbulent Round Liquid Jets," *Atomization and Spray*, Vol. 5, 1995, pp. 175-196.
18. Squire, H. B., "Investigation of the Instability of a Moving Liquid Film," *British Journal of Applied Physics*, Vol. 4, 1953, pp. 167-169.

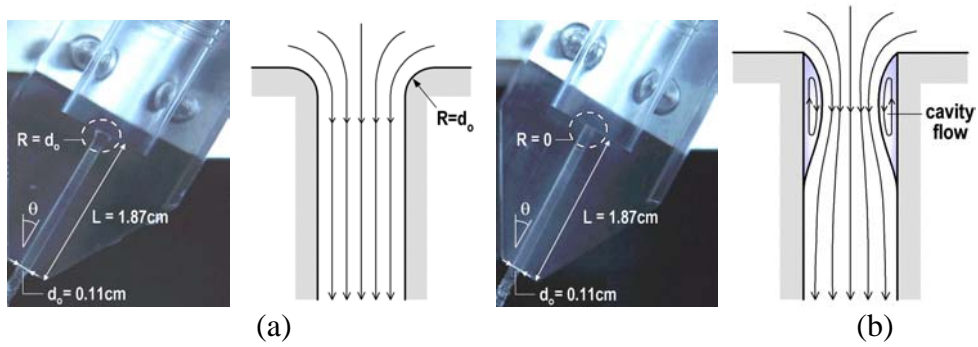


Figure 1: The orifice design and schematics of internal flow: (a) round-edged orifice and (b) sharp-edged orifice.

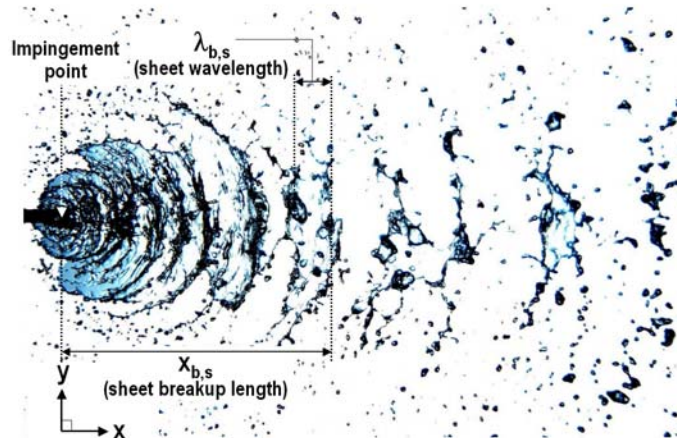


Figure 2: The breakup pattern of liquid sheet formed by like-doublet injector and definitions of breakup characteristic parameters.

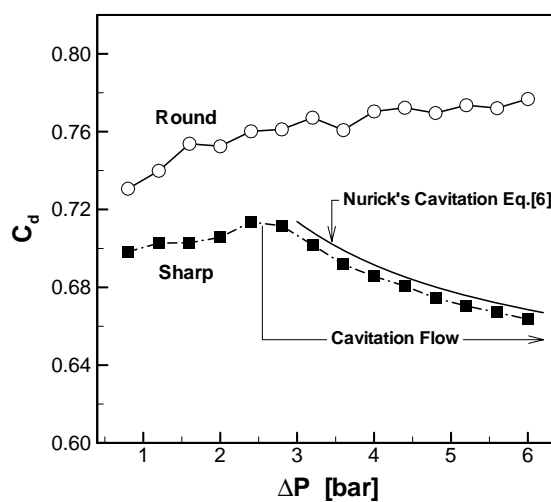


Figure 3: The discharge coefficients of round and sharp-edged orifices as a function of injection pressure.

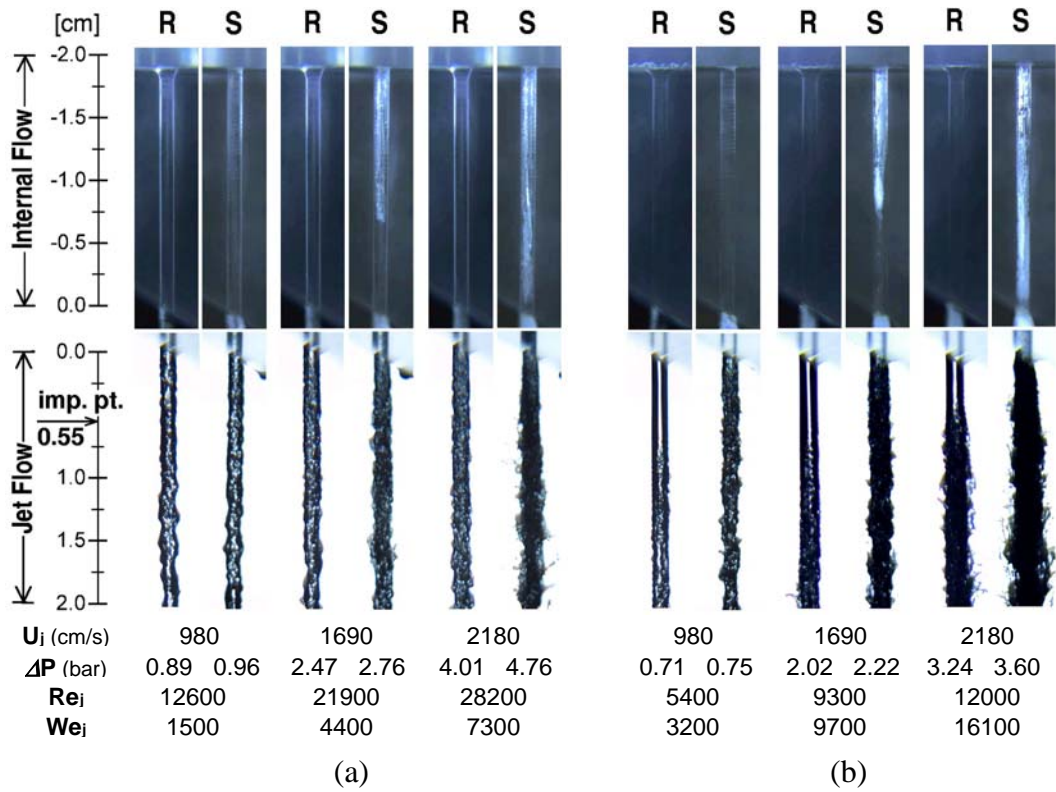


Figure 4: Visualization of internal flow and liquid jets for round and sharp-edged orifices as a function of injection velocity: (a) water simulant and (b) kerosene simulant.

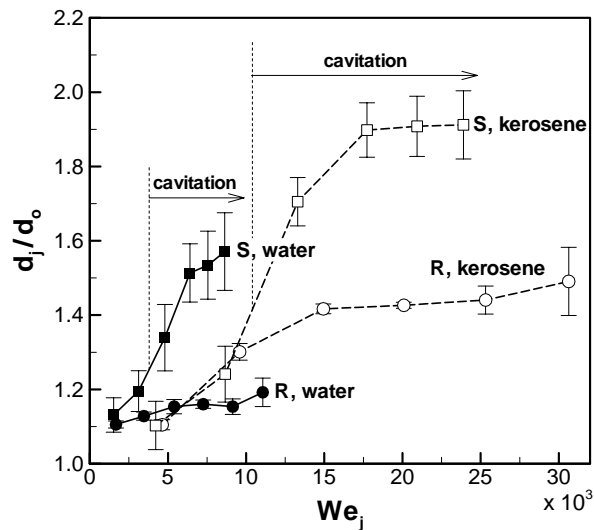


Figure 5: Single jet diameter at the impingement point as a function of Weber number of jet.

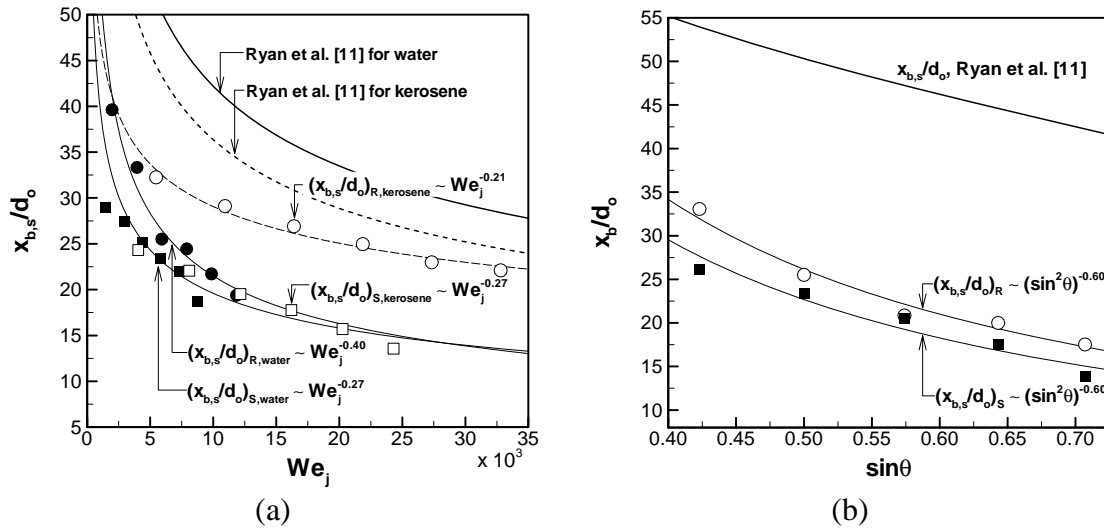


Figure 6: The breakup lengths of liquid sheet ($x_{b,s}$): (a) as a function of Weber number of jet ($\theta=30^\circ$) and (b) as a function of the sine of half impingement angle (water simulant, $We_j=5900$) (R and S indicate round and sharp-edged orifices, respectively).

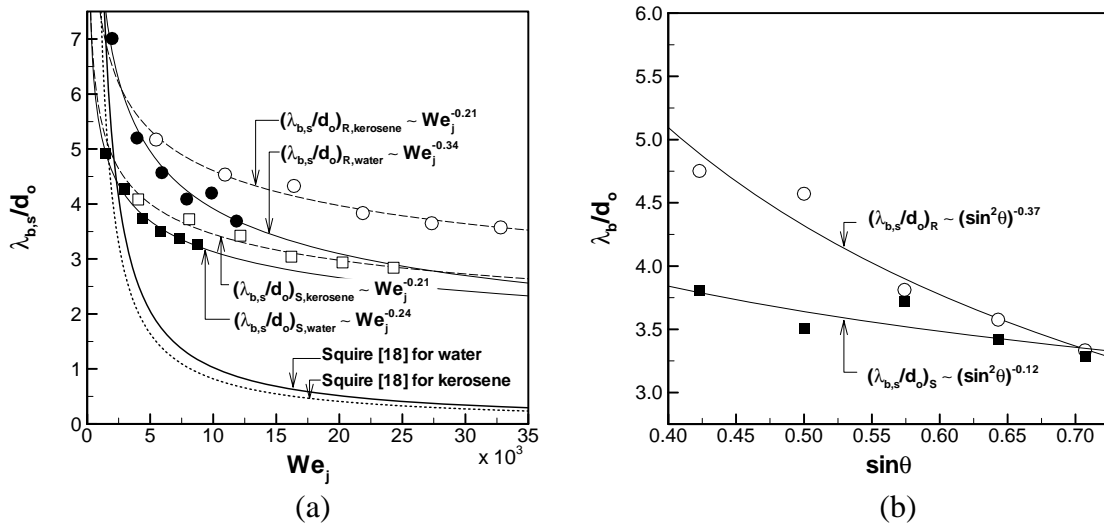


Figure 7: The breakup wavelengths of liquid sheet ($\lambda_{b,s}$): (a) as a function of Weber number of jet ($\theta=30^\circ$) and (b) as a function of the sine of half impingement angle (water simulant, $We_j=5900$) (R and S indicate round and sharp-edged orifices, respectively).

Name**Organization**

Anderson, Bill
765–496–2658
wanderso@ecn.purdue.edu

Purdue University

Arnold, Steven
216–433–3334
Steven.M.Arnold@nasa.gov

NASA Glenn Research Center

Ballard, Rick
256–544–7015
richard.o.ballard@nasa.gov

NASA MSFC

Bancroft, Steve
931–454–6418
steve.bancroft@arnold.af.mil

Arnold Air Force Base

Bazarov, Vladimir
7–095–214–8695
vgb2@nika.sokol.ru

Purdue University

Blevins, John
256–544–2590
john.a.blevins@nasa.gov

NASA MSFC

Bonacuse, Pete
216–433–3309
peter.j.bonacuse@grc.nasa.gov

Army Research Laboratory

Bordelon, Wayne
256–544–1579
wayne.bordelon@nasa.gov

NASA MSFC

Brown, Kendall
256–544–5938
kendall.k.brown@nasa.gov

NASA MSFC

Bullard, Brad
256–544–3787
brad.bullard@nasa.gov

NASA MSFC

Candel, Sebastien
33 1 41 1310 83
candel@em2c.ecp.fr

Ecole Centrale Paris

Caraccioli, Paul
256–544–0064
paul.c.caraccioli@nasa.gov

NASA MSFC

Chae, Yeon-Seok
82 42–860–2001
yschae@kari.re.kr

KARI

Chelkis, Feliks
7095 572 1173
energo@online.ru

NPO Energomash

Cheng, Gary
205–934–2038
gcheng@uab.edu

ME/UAB

Chenoweth, James
256–544–1713
james.d.chenoweth@msfc.nasa.gov

CRAFT Tech

Chow, Alan
256–544–7107
alan.s.chow@nasa.gov

NASA MSFC

Cikanek, Harry
216–433–6196
harry.a.cikanek@nasa.gov

NASA Glenn Research Center

Coates, R.H.
256–544–0549
r.h.coates@nasa.gov

NASA MSFC

Cohn, Richard
661–275–6177
richard.cohn@edwards.af.mil

Air Force Research Laboratory

Coote, David
228–688–1056
david.j.coote@nasa.gov

NASA Stennis Space Center

Dehaye, Michael
256–544–6807
michael.k.dehaye@nasa.gov

NASA MSFC

Deng, Z.T.
256–372–4142
AAMZXD01@AAMU.EDU

Alabama A&M

Dressler, Gordon
310–813–9286
gordon.dressler@ngc.com

Northrop Grumman

Duarte, Alberto
256–544–2944
alberto.duarte@nasa.gov

NASA MSFC

Fang, Jim
818–586–0351
james.j.fang@boeing.com

Boeing/Rocketdyne

Farmer, Richard
775–883–2417
farmers36@sbcglobal.net

SECA, Inc.

Farris, Thomas
765–494–5118
farrist@purdue.edu

Purdue University

Fears, Shawn
256–544–5562
shawn.d.fears@nasa.gov

NASA MSFC

Fisher, Steve
818–586–0356
steven.c.fisher@boeing.com

Rocketdyne

Ford, Mark
0031 71 5653497
mark.ford@esa.int

European Space Agency

Forde, Scott
916–355–2357
scott.ford@aerojet.com

Aerojet

Garcia, Robert
256–544–4974
roberto.garcia-2@nasa.gov

NASA MSFC

Goetz, Otto
256–828–3411
ottogoetz@aol.com

NASA MSFC

Greene, William
256–544–1038
william.d.greene@nasa.gov

NASA MSFC

Habiballah, Mohammed
33 (0)1 46 73 43 37
Mohammed.Habiballah@onera.fr

ONERA

Haeseler, Dietrich
49 89 607 23464
dietrich.haeseler@astrium-space.com

EADS Space Transportation

Haidn, Oskar
49 6298 28 214
oskar.haidn@dlr.de

DLR Lampoldshausen

Hammond, Matt
256–544–1255
john.m.hammond@nasa.gov

NASA MSFC

Hasegawa, Keiichi
81 224 683947
khasegawa@kakuda-splab.go.jp

National Aerospace Lab

Hedayat, Ali
256–544–6206
ali.hedayat-1@nasa.gov

NASA MSFC

Heister, Steve
765–494–5126
heister@ecn.purdue.edu

Purdue University

Hosangadi, Ashvin
215–766–1520
hosandagi@craft-tech.com

Combustion Research and Flow Tech

Hulka, Jim
256–544–0875
james.r.hulka@msfc.nasa.gov

Sverdrup/MSFC Group

Inglebert, Genevieve
33 1 49 452951
genevieve.inglebert@ismcm-cesti.fr

ISMCM SUPMECA

Jeung, In-Seuck
82 2 880 7387
enjis@snu.ac.kr

Seoul National University

Johnson, Curtis
775–885–0139
cwj@sierraengineering.com

Sierra Engineering

Jones, Preston
256–544–5716
carl.p.jones@nasa.gov

NASA MSFC

Kim, Yoo
82 42 821-5643
yookim@hanbat.chungnam.ac.kr

Chung Nam University

Kopicz, Charles
256–544–9317
chip.kopicz@msfc.nasa.gov

ERC/SvT-MSFC Group

Kuentzmann, Paul
33 1 46 734300
paul.kuentzmann@onera.fr

ONERA

Kumakawa, A.
81 224 68 4749
kuma@kakuda-splab.go.jp

JAXA

Lee, Soo-Yong
82 42 860-2431
sylee@kari.re.kr

Korea Aerospace Research Institute

Lide, George
256–971–7305
george.m.lide@saic.com

SAIC

Lu, Frank
425–885–5000
frank.lu@rocket.com

Aerojet

McDonald, Henry
Henry-McDonald@utc.edu

University of Tennessee

Martin, Mike
256–544–4478
michael.a.martin@nasa.gov

NASA MSFC

Merkle, Charles
merkle@purdue.edu

Purdue University

Mitchell, Michael
256–544–2491
michael.mitchell@nasa.gov

NASA MSFC

Monk, Jan
256–881–7790
jan.monk@comcast.net

Lee and Associates, LLC

Morris, Chris
256–544–6728
christopher.i.morris@nasa.gov

NASA MSFC

Oefelien, Joe
925–294–2648
oeifelei@sandia.gov

Sandia National Laboratories

Ordonneau, Gerard
33 1 4673 4333
gerard.ordonneau@onera.fr

ONERA

Oschwald, Michael
49 6298 28327
michael.oschwald@dlr.de

DLR Lampoldshausen

Popp, Mike
561–796–6085
michael.popp@pw.utc.com

Pratt & Whitney

Rhys, Noah
256–544–2386
noah.o.rhys@nasa.gov

NASA MSFC

Rodgers, Stephen
256–544–0818
stephen.l.rodgers@nasa.gov

NASA MSFC

Ruf, Joseph
256–544–4942
joseph.h.ruf@nasa.gov

NASA MSFC

Sackheim, Bob
256–544–1938
bob.sackheim@nasa.gov

NASA MSFC

Schafer, Charles
256–544–1642
charles.f.schafer@nasa.gov

NASA MSFC

Sciorelli, Frank
916–355–3115
frank.sciorelli@aerojet.com

Aerojet

Seal, Mike
757–827–2632
sealiim@saic.com

SAIC

Seo, Seong H.
82 42 860–2718
sxs223@kari.re.kr

Korea Aerospace Research Institute

Shimp, Nancy
916–355–4360
barbara.depew@aerojet.com

Aerojet

Simmons, Martha
931–454–4658
martha.simmons@arnold.af.mil

ATA; Arnold Air Force Base

Sims, Joe
256–544–4650
joseph.d.sims@nasa.gov

NASA MSFC

Sindir, Munir
818–586–1627
munir.m.sindir@boeing.com

Boeing/Rocketdyne

Singer, Chris
256–544–7058
christopher.e.singer@nasa.gov

NASA MSFC

Snyder, Lynn
317–230–8188
lynn.e.snyder@aadc.com

AADC

Souchier, Alain
alain.souchier@sneema.fr

SNECMA MOTEURS

Spotswood, Sherri
561–796–3377
sherri.spotswood@pw.utc.com

Pratt & Whitney

Starke, Bob
916–355–3915
robert.starke@aerojet.com

Aerojet

Stephenson, David
256–544–0211
David.D.Stephenson@nasa.gov

NASA MSFC

Talley, Doug
661–275–6174
douglas.talley@edwards.af.mil

Air Force Research Lab

Tanner, Larry
561–796–2725
lawrence.tanner@pw.utc.com

Pratt & Whitney

Tiller, Bruce
256–544–4695
bruce.tiller@nasa.gov

NASA MSFC

Tucker, Kevin
256–544–4185
paul.k.tucker@nasa.gov

NASA MSFC

Vuillot, Francois
33 1 46 73 6335
vuillotf@onera.fr

ONERA

Watkins, William
561–796–5840
william.watkins@pw.utc.com

Pratt & Whitney

West, Jeff
256–544–6309
jeffrey.s.west@nasa.gov

NASA MSFC

Williams, Robert
256–544–3998
robert.w.williams@nasa.gov

NASA MSFC

Wilson, Adrian
256–544–3578
adrian.wilson@msfc.nasa.gov

NASA MSFC

Woodward, Roger
814–863–6289
rdw100@psu.edu

Penn State University

Yang, Vigor
814–863–1502
vigor@psu.edu

Penn State University

Zeender, Peter
410–992–9950
pzeender@cpi.jhu.edu

John Hopkins University



Fifth International Symposium on Liquid Space Propulsion

Monday October 27, 2003

Welcome and Symposium Overview – Tennessee Aquarium

6:30 p.m.	Bob Sackheim	NASA MSFC, U.S.A	Welcome and Overview
6:45 p.m.	Dr. John Rogacki	NASA Headquarters, U.S.A.	Delivering the Future: NASA'S Integrated Space Transportation Plan
7:30 p.m.	All		Self-guided tour of the aquarium



Fifth International Symposium on Liquid Space Propulsion

Tuesday October 28, 2003

Technical Session I: Welcome and International Perspectives

8:30 a.m.	Wayne Bordelon	NASA MSFC, U.S.A	Symposium Logistics
8:45 a.m.	Bob Sackheim	NASA MSFC, U.S.A.	Overview of NASA's Space Transportation Plans
9:20 a.m.	Alain Souchier	Snecma, France	European Space Propulsion Perspective
9:55 a.m.	Break		
10:10 a.m.	Keiichi Hasegawa	National Aerospace	Overview of Japanese Research and Laboratory, Japan Development Program on Liquid Rocket Engine Combustor
10:45 a.m.	Yeon-Seok Chae	Director, Korea Aerospace	Korean Perspective: Development of a Research Institute, Korea Liquid Propellant Rocket, Korea Sounding Rocket (KSR)-3
11:20 a.m.	End of Session		
11:30 a.m.	Lunch - Broad Street Grill		



Fifth International Symposium on Liquid Space Propulsion

Tuesday October 28, 2003

Technical Session II: System Level Effects

12:35 p.m.	Jan Monk Otto Goetz	NASA MSFC, U.S.A. (retired) NASA MSFC, U.S.A. (retired)	Combustion Device Failures During Space Shuttle Main Engine Development
1:20 p.m.	Rick Ballard	NASA MSFC, U.S.A.	Operational Issues in the Development of a Cost-Effective Reusable LOX/LH2 Engine
1:55 p.m.	Gordon Dressler	Northrop Grumman, U.S.A.	Lifetime Issues for In-Space Propulsion Systems
2:30 p.m.	Break		
2:45 p.m.	Akinaga Kumakawa	National Aerospace	Research Achievements on Long-Life Thrust Laboratory, Japan Chambers at NAL/KPL
3:20 p.m.	Feliks Y. Chelkis	NPO Energomash, Russia	LOX/Kerosene Oxygen Rich Staged Combustion Rocket Engine Design and Life Issues
3:55 p.m.	James Fang	Boeing – Rocketdyne	Design of Next Generation Reusable Rocket Propulsion & Power, U.S.A. Engine
4:30 p.m.	End of session		
5:00 p.m.	Board Motor Coach for trip to Southern Belle Riverboat		
5:30 p.m.	Recognition Banquet - Southern Belle Riverboat		



Fifth International Symposium on Liquid Space Propulsion

Wednesday October 29, 2003

Technical Session III: Component Level Processes

8:00 a.m.	Bill Green David C. Seymour Michael A. Martin Huy H. Nguyen	NASA MSFC, U.S.A. NASA MSFC, U.S.A. (retired) NASA MSFC, U.S.A. NASA MSFC, U.S.A.	Startup and Shutdown Transients Engine System Issues
8:30 a.m.	Michael Oswald Mohammed Habiballah	DLR, Germany ONERA, France	Experimental Investigation and Modeling of the Ignition Transient of a Coaxial H ₂ /O ₂ -Injector
9:00 a.m.	Mike Popp	Pratt and Whitney, U.S.A	Combustion Chamber Cooling and Life Issues
9:30 a.m.	Joe Ruf David McDaniels	NASA MSFC, U.S.A. NASA MSFC, U.S.A.	Recent Aerospike Nozzle Test Results
10:00 a.m.	Break		

Technical Session IV: Material Considerations

10:15 a.m.	Genevieve Inglebert	ISMCM-CESTI (LISMMA Groupe Tribologie), France	Materials Requirement and Limitations for Liquid Rocket Engines
10:45 a.m.	Thomas Farris	Purdue University, U.S.A	Materials Issues Arising from Transient and Unsteady Loads in Combustion Devices
11:15 a.m.	Peter J. Bonacuse	NASA/Glenn Research Center, U.S.A.	Damage Assessment of Combustion Devices
11:45 a.m.	Steve Arnold	NASA/Glenn Research Center, U.S.A	Advances in High Temperature (Viscoelastoplastic) Material Modeling for Thermal Structural Analysis
12:15 p.m.	Buffet Lunch - Broad Street Grill		



Fifth International Symposium on Liquid Space Propulsion

Wednesday October 29, 2003

Technical Session V: Design Environments – Predictions

1:30 p.m.	Kevin Tucker	NASA/MSFC, U.S.A.	Using CFD as a Rocket Injector Design Tool: Recent Progress at Marshall Space Flight Center
2:10 p.m.	Francois Vuillot Mohammed Habiballah Dominique Scherrer	ONERA, France ONERA, France ONERA, France	CFD Code Validation for Space Propulsion Applications
2:45 p.m.	Vigor Yang	Pennsylvania State University, U.S.A	High Pressure and Supercritical Environments-Modeling
3:20 p.m.	Break		

Technical Session VI: Injector Design Technology

3:35 p.m.	Dietrich Haesler	EADS, Germany	Injector Issues with Different Propellant Combinations
4:10 p.m.	Vladimir Bazarov	Moscow International University of Engineering, Russia	Injectors for Long-Life Combustion Devices
4:45 p.m.	Doug Talley	AFRL, U.S.A	Gox-Centered Swirl Hydrocarbon Injector Design and Testing
5:20 p.m.	End of Session, Open Evening		



Fifth International Symposium on Liquid Space Propulsion

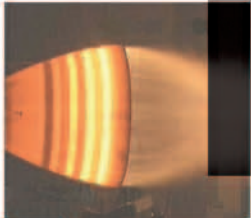
Thursday October 30, 2003

Technical Session VII: Design Environments – Measurements

8:00 a.m.	Richard Farmer Robert Santoro	University of Nevada, U.S.A Pennsylvania State University, U.S.A.	Required Data for Code Validation
8:35 a.m.	Bill Anderson	Purdue University, U.S.A.	Subscale Test Methods for Combustion Devices
9:10 a.m.	Sebastien Candel	Ecole Centrale de Paris, France	Investigations of Transcritical Cryogenic Combustion Using Imaging and Laser Techniques
9:45 a.m.	Doug Tally Wolfgang Mayer	AFRL,U.S.A DLR, Germany	High Pressure & Supercritical Environments- Experiments
10:20 a.m.	Youngbin Yoon In-Seuck Jeung	Seoul National University Seoul, Korea	Subscale Testing and Design Issues of Injectors
10:40 a.m.	Break		
11:00 a.m.	Panel Discussion/Closing		
12:00 p.m.	Buffet Lunch - Broad Street Grill		
1:00 p.m.	Technical Committee Meeting		



Long Life Combustion Devices Technology



October 27-30

Sponsored by National Aeronautics and Space Administration
Marshall Space Flight Center, Huntsville, Alabama



Chattanooga



- International Experts
- World Class Exhibits
- Technical Sessions
- Panel Discussion
- Recognition Banquet



2003

Program

www.nasa.gov

www.spacetransportation.com

Chattanooga



Executive Committee

Bob Sackheim – Chair

Keiichi Hasegawa
In-Seuck Jeung
Wolfgang Koschel
Alexander Kuznetsov
Paul Kuentzmann
Jue Wang

Technical Committee

Robert Garcia – Chair

Bill Anderson
Mohammed Habiballah
Oskar Haidn
Chuck Merkle
Mike Popp
Joe Ruf
Doug Talley
Vigor Yang

Organizing Committee

Vanessa Suggs – Chair

Wayne Bordelon
Robert Garcia
Bennie Jacks

October 27-30



FIFTH INTERNATIONAL SYMPOSIUM ON LIQUID SPACE PROPULSION

The International Liquid Space Propulsion Symposia provides the principal forum for all aspects of liquid rocket propulsion. The aim of the symposium series is to gather international experts in the field of liquid rocket engines on a regular basis for presentations and discussions of the current status of research and development. Besides an exchange of information about future trends it also fosters existing cooperations and acts as a nucleus to establish networks to enhance international scientific collaboration in the liquid rocket propulsion area.

THEME

The Fifth International Symposium on Liquid Rocket Space Propulsion is focused on Long Life Combustion Devices Technologies for Liquid Space Propulsion, including all aspects of analysis, modeling, and design. In addition to an introductory session on current national programs given by representatives from agencies and industries from across the world, recent technical work of particular relevance will be presented by invited speakers in the following main categories.

- * Component-level processes
Ignition, chamber life, injector life, nozzle loads
- * Engine cycle and material considerations
Transient load issues, oxygen rich environments, hydrocarbon environments, material limitations, hydrogen environment issues, injector considerations
- * Design Environments - Predictions
Damage assessment, CFD, validation of codes
- * Design Environments - Measurements
Data requirements, advance diagnostics, scaling considerations
- * System-level effects
Component interactions, in-space propulsion, tri-propellant engines

This symposium is of interest to researchers, scientists, engineers, and students from agencies, industry, research laboratories and universities working in the field of liquid rocket propulsion.

2003

5 Overview:

● MONDAY	October 27, 2003	3:00 p.m. – 9:30 p.m.
● TUESDAY	October 28, 2003	7:00 a.m. – 8:30 p.m.
● WEDNESDAY	October 29, 2003	7:00 a.m. – 5:30 p.m.
● THURSDAY	October 30, 2003	7:00 a.m. – 3:15 p.m.

AUTHORS

Bill Anderson
Steven Arnold
Rick Ballard
Vladimir Bazarov
Peter J. Bonacuse
GuoBiao Cai
Sebastien Candel
Yeon-Seok Chae
Feliks Chelkis
Gordon Dressler
Richard Farmer
Thomas Farris
Steven Fisher
Otto Goetz
William Greene
Mohammed Habiballah
Dietrich Haeseler
Keiichi Hasegawa
Geneviève Inglebert
Akinaga Kumakawa
Michael Martin
Wolfgang Mayer
David McDaniels
Charles Merkle
Jan Monk
Huy Nguyen
Michael Oschwald
Mike Popp
Joseph Ruf
Bob Sackheim
Robert Santoro
Dominique Scherrer
David C. Seymour
Alain Souchier
Doug Talley
Kevin Tucker
Francois Vuillot
Jue Wang
ZhenGuo Wang
Vigor Yang
EnZhao Zhang

SPONSORS

Aerojet
ATK
Atlantic Research Corporation
Boeing
Computer Sciences Corporation
Lockheed Martin
NASA
Northrup Grumman
Orbital
Pratt & Whitney
SAIC
Sverdrup

SPECIAL EVENTS

Monday, October 27

Opening Reception: An Evening at The Tennessee Aquarium
Board the motor coach at 6:00 p.m.
Return at 9:30 p.m.

Tuesday, October 28

Recognition Banquet Onboard The Southern Belle Riverboat
Board the motor coach at 5:00 p.m.
Return at 8:30 p.m.

GENERAL

SIGN-IN

Tables will be located in the main lobby of the hotel on Monday from 3:00 – 6:00 p.m. and Tuesday morning from 7:00 – 9:00 a.m.

AUTHORS

Please make sure that you have provided your session chair with presentation material and appropriate information for your presentation.

PHONE MESSAGES AND FAXES

- * The hotel fax number is 423-756-3404
- * Anyone needing to leave messages for symposium attendees during the session may call 423-756-3400.

DINING

All planned meals will be in the Broad Street Grille. Since meals are included in your symposium package, gratuities have been included.

HOTEL SAFETY

- * Safeguard your card key
- * Do not leave your valuables in the ballroom
- * Familiarize yourself with the nearest fire exit
- * In the event of fire, do not use the elevators
- * In the event of severe weather, the hotel staff will direct you to safety

SPECIAL ASSISTANCE

Please let a member of the symposium staff know if you require special assistance.

Agenda

● MONDAY	Oct 27
● TUESDAY	Oct 28
● WEDNESDAY	Oct 29
● THURSDAY	Oct 30

● MONDAY/27

3:00 p.m. – 6:00 p.m.

Symposium Sign-in

Main lobby of the Chattanooga

6:00 p.m.

Trip to the Tennessee Aquarium

Motor Coaches are located outside the main entrance of the Chattanooga

6:30 p.m. – 7:30 p.m.

Mayor's Welcome

Tennessee Aquarium Auditorium
Bob Corker, Mayor of Chattanooga

Welcome and Symposium Overview

Bob Sackheim, Executive Chair
Associate Director and Chief Engineer for Propulsion, Marshall Space Flight Center

Keynote Address

Dr. John Rogacki
Director, Space Transportation Technology,
Office of Aerospace Technology, NASA

Light hors d'oeuvres will be served.

7:30 p.m.

Self-guided tour of the Tennessee Aquarium

Heavy hors d'oeuvres served in Main Lobby
Cash bar available

9:30 p.m.

Return trip to the Chattanooga

Motor Coaches are located outside the main entrance to the Aquarium

● TUESDAY/28

7:00 a.m. – 8:30 a.m.

Buffet Breakfast

Broad Street Grill

Symposium Sign-in (continued)

Main lobby of the Chattanooga

Technical Session I: International Perspective

8:30 a.m. – 8:45 a.m.

Symposium Logistics

Ballroom I/II

Wayne Bordelon, NASA-MSFC, U.S.A.

8:45 a.m. – 9:15 a.m.

Overview of NASA's Space Transportation Plans

Bob Sackheim, NASA-MSFC, U.S.A.

9:15 a.m. – 9:45 a.m.

European Space Propulsion Perspective

Alain Souchier, Snecma, France

9:45 a.m. – 10:00 a.m.

Break

10:00 a.m. – 10:30 a.m.

The Status and Development of LRE in China

Jue Wang, Beijing Aerospace Propulsion
Institute, China

10:30 a.m. – 11:00 a.m.

Overview of Japanese Research and Development Program on Liquid Rocket Engine Combustor

Keiichi Hasegawa, National Aerospace
Laboratory, Japan

11:00 a.m. – 11:30 a.m.

Korean Perspective: Development of a Liquid Propellant Rocket, Korea Sounding Rocket (KSR)-3

Yeon-Seok Chae, Director, Korea Aerospace
Research Institute

11:30 a.m. – 12:45 p.m.

Buffet Lunch

Broad Street Grill

Technical Session II: System Level Effects

12:45 p.m. – 1:30 p.m.

Rocket Combustor Failure Modes

Jan Monk, retired, NASA-MSFC, U.S.A.
Otto Goetz, retired, NASA-MSFC, U.S.A.

1:30 p.m. – 2:00 p.m.

System Level Component Interactions

Steve Fisher, Boeing, U.S.A

2:00 p.m. – 2:30 p.m.

Lifetime Issues for In-Space Propulsion Systems

Gordon Dressler, Northrop Grumman, U.S.A.

2:30 p.m. – 2:45 p.m.

Break

2:45 p.m. – 3:15 p.m.

**Theoretical and Experimental Studies of
LO₂/Kerosene/GH₂ Tripropellant Engine**

ZhenGuo Wang, National University of Defense
Technology, China

3:15 p.m. – 3:45 p.m.

**Research Achievements on Long-Life Thrust
Chambers at NAL/KPL**

Akinaga Kumakawa, National Aerospace
Laboratory, Japan

3:45 p.m. – 4:15 p.m.

**Oxygen Rich Staged Combustion Operational
and Design Issues**

Feliks Y. Chelkis, NPO Energomash, Russia

4:15 p.m. – 5:00 p.m.

Break

5:00 p.m.

Trip to the Southern Belle Riverboat

Motor Coaches are located outside the
main entrance of the Chattanooga

5:30 p.m. – 8:30 p.m.

Recognition Banquet

Southern Belle Riverboat
Buffet provided; cash bar available

● WEDNESDAY/29

7:00 a.m. – 8:00 a.m.

Buffet Breakfast

Broad Street Grill

**Technical Session III:
Component Level Processes**

8:00 a.m. – 8:30 a.m.

Large Flow Rate Oxidizer-Rich Preburner

EnZhao Zhang, The 11th Research Institute in
Xian, China

8:30 a.m. – 9:00 a.m.

**Experimental Investigation and Modeling of the
Ignition Transient of a Coaxial H₂/O₂-Injector**

Michael Oswald, DLR, Germany
Mohammed Habiballah, ONERA, France

9:00 a.m. – 9:30 a.m.

**Transient Mathematical Modeling for Liquid
Rocket Engine Systems: Methods, Capabilities,
and Experience**

Bill Greene, NASA-MSFC, U.S.A.
David C. Seymour, NASA, Retired, U.S.A.
Michael A. Martin, NASA-MSFC, U.S.A.
Huy H. Nguyen, NASA-MSFC, U.S.A.

9:30 a.m. – 9:45 a.m.

Break

9:45 a.m. – 10:15 a.m.

Recent Aerospoke Nozzle Test Results

Joe Ruf, NASA-MSFC, U.S.A.
David McDaniels, NASA-MSFC, U.S.A.

10:15 a.m. – 10:45 a.m.

Combustion Chamber Cooling and Life Issues

Mike Popp, Pratt and Whitney, U.S.A.

10:45 a.m. – 11:15 a.m.

Liquid Rocket Thrust Chamber Flow Analysis

GuoBiao Cai, Beijing University of Aeronautics
and Astronautics, China

11:15 a.m. – 11:45 a.m.

Injectors for Long-Life Combustion Devices

Vladimir Bazarov, Moscow International University
of Engineering, Russia

12:00 p.m. – 1:00 p.m.

Buffet Lunch

Broad Street Grill

**Technical Session IV:
Material Considerations**

1:00 p.m. – 1:30 p.m.

Materials Requirements and Limitations

Geneviève Inglebert, ISMCM-CESTI
(LISMMA Groupe Tribologie), France

1:30 p.m. – 2:00 p.m.

**Material Issues Arising from Transient and
Unsteady Loads in Combustion Devices**

Thomas Farris, Purdue University, U.S.A.

● WED/29 CONTINUED

2:00 p.m. – 2:30 p.m.

Thermal Structural Modeling Advances

Steve Arnold, NASA-Glenn Research Center, U.S.A.

2:30 p.m. – 2:45 p.m.

Break

2:45 p.m. – 3:15 p.m.

Injector Issues with Different Propellant Combinations

Dietrich Haeseler, EADS, Germany

3:15 p.m. – 3:45 p.m.

Hydrogen-Fueled Reusable Engines Design and Operational Issues

Rick Ballard, NASA-MSFC, U.S.A.

3:45 p.m. – 4:15 p.m.

Gox-Centered Swirl Hydrocarbon Injector Design and Testing

Doug Talley, AFRL, U.S.A.

4:15 p.m. – 4:30 p.m.

Break

Technical Session V: Design Environments- Predictions

4:30 p.m. – 5:00 p.m.

Damage Assessment of Combustion Devices

Peter J. Bonacuse, NASA-Glenn Research Center, U.S.A.

5:00 p.m. – 5:30 p.m.

CFD as a Design Tool

Charles Merkle, Purdue University, U.S.A.
Kevin Tucker, NASA-MSFC, U.S.A.

Free Evening

● THURSDAY/30

7:00 a.m. – 8:00 a.m.

Buffet Breakfast

Broad Street Grill

Technical Session V: Design Environments- Predictions (continued)

8:00 a.m. – 8:30 a.m.

CFD Code Validation for Space Propulsion Applications

Francois Vuillot, ONERA, France
Mohammed Habiballah, ONERA, France
Dominique Scherrer, ONERA, France

8:30 a.m. – 9:00 a.m.

High Pressure and Supercrit Environments – Modeling

Vigor Yang, Pennsylvania State University, U.S.A.

Technical Session VI: Design Environments- Measurements

9:00 a.m. – 9:30 a.m.

Required Data for Code Validation

Richard Farmer, University of Nevada, U.S.A.
Robert Santoro, Pennsylvania State University, U.S.A.

9:30 a.m. – 10:00 a.m.

Subscale Test Methods for Combustion Devices

Bill Anderson, Purdue University, U.S.A.

10:00 a.m. – 10:30 a.m.

Investigations of Transcritical Cryogenic Combustion Using Imaging and Laser Techniques

Sebastien Candel, Ecole Centrale de Paris, France

10:30 a.m. – 11:00 a.m.

High Pressure & Supercritical Environments – Experiments

Doug Talley, AFRL, U.S.A.
Wolfgang Mayer, DLR, Germany

11:00 a.m. – 11:15 a.m.

Break

11:15 a.m. – 12:15 p.m.

Panel Discussion/Closing

12:15 – 1:15 p.m.

Buffet Lunch

Broad Street Grill

1:15 p.m. – 3:15 p.m.

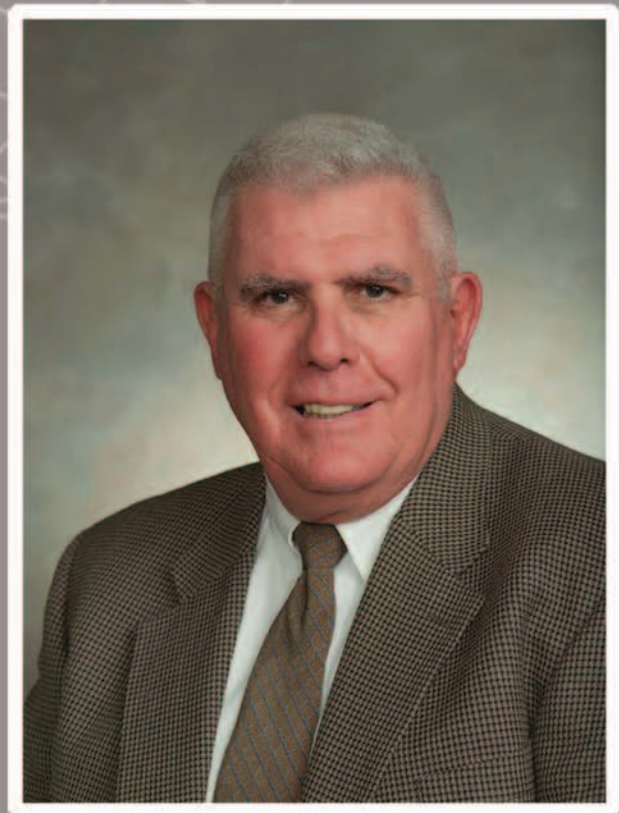
Technical Committee Meeting



Executive **CHAIR**

Robert L. Sackheim

Robert L. Sackheim, the Assistant Director and Chief Engineer for Propulsion at NASA's George C. Marshall Space Flight Center (MSFC), holds a B.S. degree from the University of Virginia and a M.S. degree from Columbia University. He has completed all doctoral coursework in chemical engineering at the University of California in Los Angeles. He joined MSFC after 35 years in various technical and management positions with TRW Space and Electronics Group. At MSFC he provides technical leadership and expertise for all propulsion and space transportation activities.



As a leader in the AIAA, Mr. Sackheim was formerly the chairman of the Liquid Propulsion Technical Committee, the chairman of the Los Angeles section, and the chairman of the Mississippi/Alabama section. He is a fellow of the AIAA and was elected in 2000 to the National Academy of Engineering. He has served on a number of NASA boards, including the Shuttle Independent Assessment Team, the Mars Climate Orbiter Mishap Investigation Board, and the Mars Polar Lander Mishap Board. He has authored more than 150 technical papers and holds eight patents for spacecraft and launch vehicle propulsion and control systems technology.

His awards and honors include the AIAA James Wyld Award for outstanding technical contributions to the field of rocket propulsion, the AIAA Sustained Service Award, 12 NASA Group Achievement Awards, 2 MSFC Director's Commendations, and the NASA Medal for outstanding technical leadership. While at TRW he received 3 Chairmen's Awards and a TRW patent of the year award. The AIAA Alabama/Mississippi section awarded him the Martin Schilling Award for outstanding service, the Herman Oberth Award "For Outstanding Individual Scientific Achievement in the Fields of Astronautics and Space Sciences," and the Holger Toftoy Award for outstanding technical management. He recently received an award from the Association of Aeronautics and Astronautics of France for "High Quality Contributions to the Propulsion Field".

Keynote **SPEAKER**

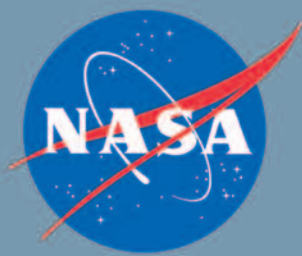
Dr. John R. Rogacki

Dr. "Row" Rogacki received a B.S. degree in Engineering Mechanics from the U.S. Air Force Academy in 1973; a M.S. degree in Mechanical Engineering from the University of Washington in 1983; and a Ph.D. in Mechanical Engineering from the University of Washington in 1992. He is currently assigned to NASA Headquarters in Washington, D.C., as Director of Space Transportation Technology, Office of Aerospace Technology. In that capacity, he is responsible for the Space Launch Initiative Theme and serves as Program Director for the Orbital Space Plane and Next Generation Launch Technology Programs.



Dr. Rogacki was the first Director of NASA's new Space Transportation Directorate at MSFC. His organization was responsible for executing the NASA Lead Center role assigned to MSFC for space transportation systems development activities, consolidating and integrating space transportation programs and projects together with space transportation and propulsion systems research and engineering departments. The Space Transportation Directorate built NASA's inaugural Integrated Space Transportation Plan, integrating Space Shuttle safety and supportability upgrades with the Space Launch Initiative (including the 2nd Generation Reusable Launch Vehicle Program) and the Advanced Space Transportation Program (including 3rd Generation RLV and In-Space propulsion efforts).

He is a former Deputy Director and Director of the Propulsion Directorate for the Air Force Research Laboratory at Wright-Patterson AFB, Ohio. He was Director of Phillips Laboratory's Propulsion Directorate at Edwards Air Force Base, California. He served at Wright-Patterson Air Force Base, Ohio, first as Chief of the Structures Division, then as Deputy Director of the Flight Dynamics Directorate. He has served as Associate Professor of Engineering Mechanics and Chief of the Materials Division at the U.S. Air Force Academy, Colorado, and as chief of the B-52 Branch, Standardization and Evaluation Division, 42nd Bomb Wing at Loring Air Force Base, Maine. Dr. Rogacki is a 26-year U. S. Air Force veteran with more than 3000 flying hours as a command pilot in aircraft ranging from motorized gliders to heavy bombers.



Guest

SPEAKER



Lee M.E. Morin, M.D., PH.D.

NASA Astronaut

U.S. Navy Captain Lee M.E. Morin graduated from the Western Reserve Academy, Hudson, Ohio in 1970; received a bachelor of science degree in mathematical/electrical science from the University of New Hampshire in 1974; a master of science degree in biochemistry from New York University in 1978, a doctorate of medicine and microbiology degrees from New York University in 1981 and 1982, respectively, and a Master of Public Health degree from the University of Alabama at Birmingham in 1988.

Selected as an astronaut candidate by NASA in April 1996, Morin reported to the Johnson Space Center in August 1996. Having completed two years of training and evaluation, he is qualified for flight assignment as a mission specialist. Initially assigned technical duties in the Astronaut Office Computer Support Branch, followed by the Astronaut Office Advanced Vehicles Branch. He is currently assigned to ISS training tasks in the Shuttle Operations Branch of the Astronaut Office. Morin served on the EVA crew of STS-110 (2002) and has logged over 259 hours in space, including over 14 EVA hours.

STS-110 Atlantis (April 8-19, 2002) was the 13th Shuttle mission to visit the International Space Station. Mission milestones included: the delivery and installation of the SO (S-Zero) Truss; the first time the station's robotic arm was used to maneuver spacewalkers around the station; and the first time that all of a shuttle crew's spacewalks were based from the station's Quest Airlock. Morin performed 2 EVAs totaling 14 hours and 9 minutes. The crew prepared the station for future spacewalks and spent a week in joint operations with the station's Expedition-4 crew. Mission duration was 10 days, 19 hours and 42 minutes.

Special honors include the 1994 Chairman of the Joint Chiefs of Staff Award for Excellence in Military Medicine (also known as the Fisher Award), a finalist of the 1995 Innovations in American Government Award from the John F. Kennedy School of Government at Harvard University and Ford Foundation, and the 1996 Sustaining Membership Lecture Award for the Association of Military Surgeons of the United States.

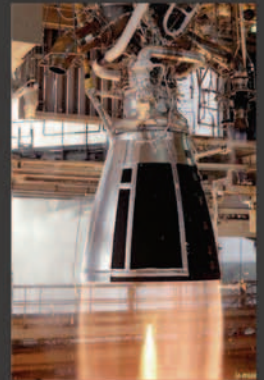
Special ACKNOWLEDGEMENTS

There are many teams and individuals who have worked tirelessly to support the website, program, logistics, audio-visual, special events, exhibits, and overall planning of the Fifth International Symposium on Liquid Space Propulsion.

Without their combined efforts and without significant contributions from the following, we would not have been able to host this event.

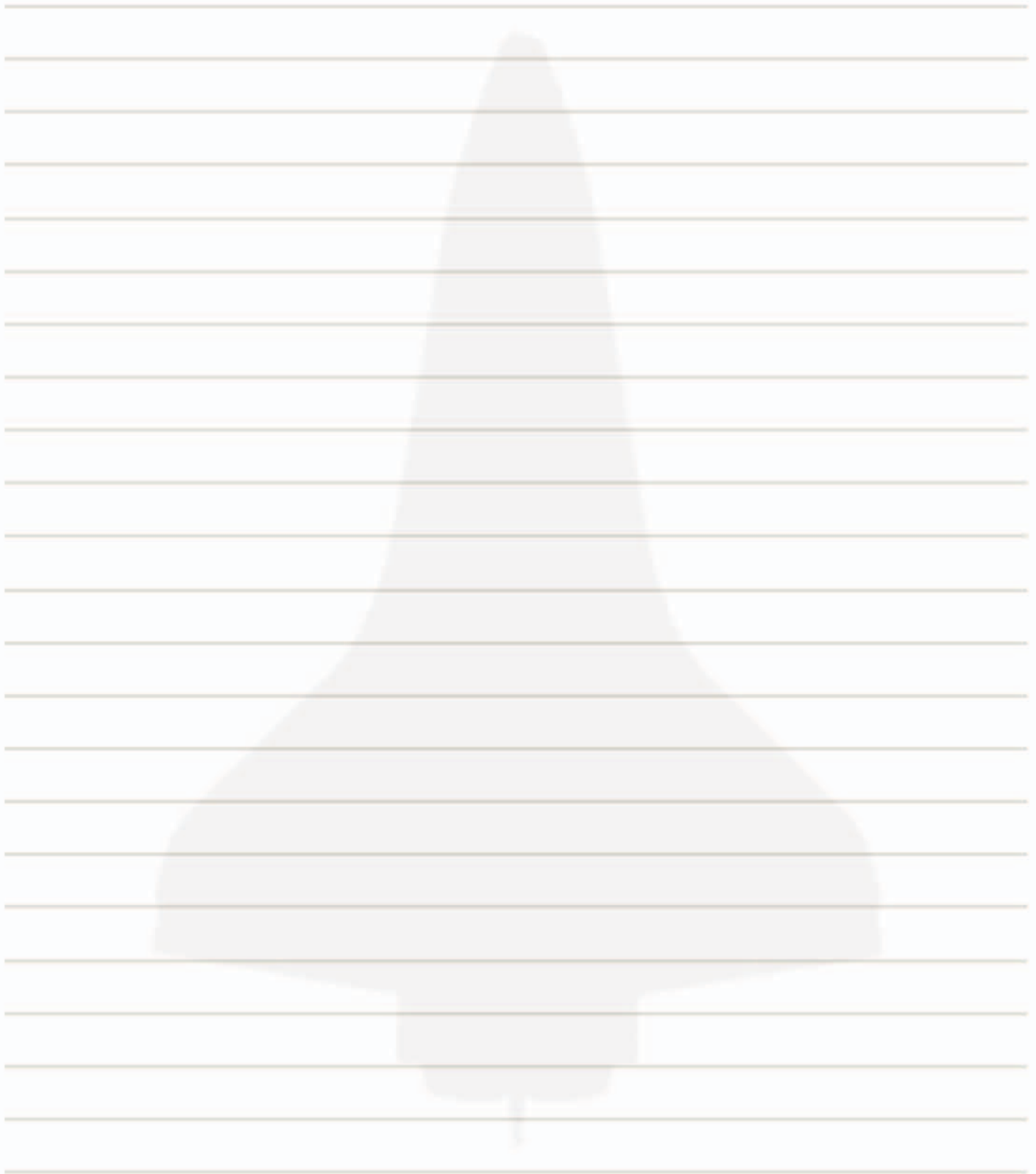
Center Operations Directorate-MSFC
Customer and Employee Relations Directorate-MSFC
Space Transportation Directorate-MSFC
AI Signal Research, Inc. (ASRI)
ARCATA
Mainthia
Computer Sciences Corporation
Office of the Director Staff

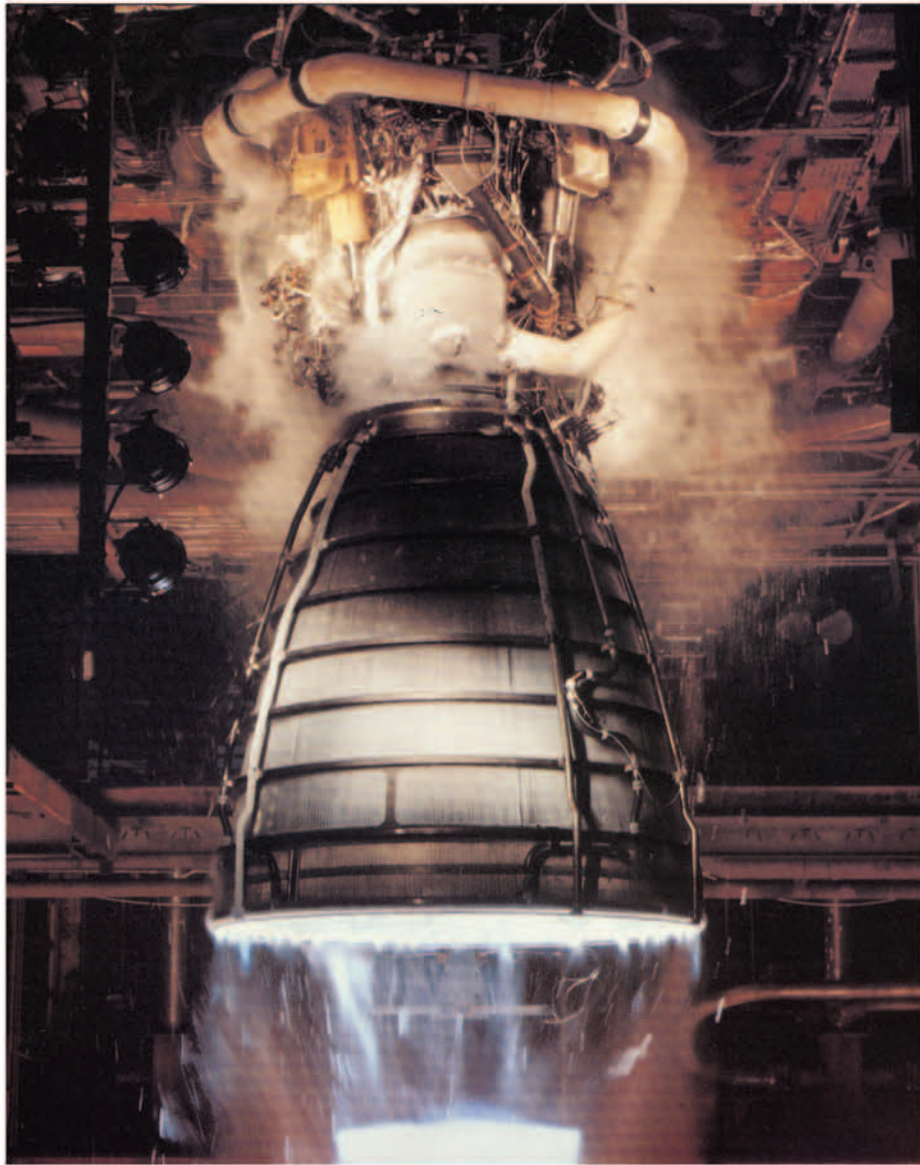
We would also like to thank Bob Corker, Mayor of Chattanooga; and our special guest, Dr. John Rogacki, Director of Space Transportation Technology Division for NASA, for generously giving their time to make this symposium a success.



5 Notes

Fifth International Symposium on Liquid Space Propulsion





National Aeronautics and
Space Administration

George C. Marshall Space Flight Center
Marshall Space Flight Center, Alabama 35812

REPORT DOCUMENTATION PAGE			Form Approved OMB No. 0704-0188	
Public reporting burden for this collection of information is estimated to average 1 hour per response, including the time for reviewing instructions, searching existing data sources, gathering and maintaining the data needed, and completing and reviewing the collection of information. Send comments regarding this burden estimate or any other aspect of this collection of information, including suggestions for reducing this burden, to Washington Headquarters Services, Directorate for Information Operation and Reports, 1215 Jefferson Davis Highway, Suite 1204, Arlington, VA 22202-4302, and to the Office of Management and Budget, Paperwork Reduction Project (0704-0188), Washington, DC 20503				
1. AGENCY USE ONLY (Leave Blank)	2. REPORT DATE January 2005	3. REPORT TYPE AND DATES COVERED Conference Publication		
4. TITLE AND SUBTITLE Fifth International Symposium on Liquid Space Propulsion			5. FUNDING NUMBERS	
6. AUTHORS R. Garcia, Compiler				
7. PERFORMING ORGANIZATION NAMES(S) AND ADDRESS(ES) George C. Marshall Space Flight Center Marshall Space Flight Center, AL 35812			8. PERFORMING ORGANIZATION REPORT NUMBER M-1129	
9. SPONSORING/MONITORING AGENCY NAME(S) AND ADDRESS(ES) George C. Marshall Space Flight Center Marshall Space Flight Center, AL 35812			10. SPONSORING/MONITORING AGENCY REPO NUMBER NASA/CP-2005-213607	
11. SUPPLEMENTARY NOTES Prepared by the Propulsion Systems Department, Engineering Directorate Technical Monitor: R. Garcia, NASA Marshall Space Flight Center				
12a. DISTRIBUTION/AVAILABILITY STATEMENT Unclassified-Unlimited Subject Category 20 Availability: NASA CASI 301-621-0390			12b. DISTRIBUTION CODE	
13. ABSTRACT (Maximum 200 words) This document contains the proceedings of the Fifth International Symposium on Liquid Space Propulsion, held October 27-30, 2003, in Chattanooga, TN. The International Liquid Space Propulsion Symposia provide the principal forum for all aspects of liquid rocket propulsion. The aim of the symposium series is to gather international experts in the field of liquid rocket engines on a regular basis for presentations and discussions of the current status of research and development. Besides an exchange of information about future trends, it also fortifies existing cooperation and acts as a nucleus to establish networks to enhance international scientific collaboration in the liquid rocket propulsion area.				
14. SUBJECT TERMS liquid propellant rocket engines, propulsion, combustion, combustion chambers, combustion physics			15. NUMBER OF PAGES 1171	
			16. PRICE CODE	
17. SECURITY CLASSIFICATION OF REPORT Unclassified	18. SECURITY CLASSIFICATION OF THIS PAGE Unclassified	19. SECURITY CLASSIFICATION OF ABSTRACT Unclassified	20. LIMITATION OF ABSTRACT Unlimited	